Power Systems

Farhad Shahnia
Sumedha Rajakaruna
Arindam Ghosh *Editors*

Static Compensators (STATCOMs) in Power Systems

Springer

Power Systems

More information about this series at http://www.springer.com/series/4622

Farhad Shahnia · Sumedha Rajakaruna
Arindam Ghosh
Editors

Static Compensators (STATCOMs) in Power Systems

Springer

Editors
Farhad Shahnia
Department of Electrical and Computer Engineering
Curtin University
Perth
Australia

Arindam Ghosh
Department of Electrical and Computer Engineering
Curtin University
Perth
Australia

Sumedha Rajakaruna
Department of Electrical and Computer Engineering
Curtin University
Perth
Australia

ISSN 1612-1287 ISSN 1860-4676 (electronic)
Power Systems
ISBN 978-981-287-280-7 ISBN 978-981-287-281-4 (eBook)
DOI 10.1007/978-981-287-281-4

Library of Congress Control Number: 2014957148

Springer Singapore Heidelberg New York Dordrecht London

Printed on acid-free paper

Springer Science+Business Media Singapore Pte Ltd. is part of Springer Science+Business Media (www.springer.com)

Preface

A static compensator (STATCOM), also known as static synchronous compensator, is a member of the flexible alternating current transmission system (FACTS) devices. It is a power-electronics-based regulating device which is composed of a voltage source converter (VSC) and is shunt connected to alternating current electricity transmission and distribution networks. The voltage source is created from a DC capacitor and the STATCOM can exchange reactive power with the network. It can also supply some active power to the network if a DC source of power is connected across the capacitor. A STATCOM is usually installed in the electric networks with poor power factor or poor voltage regulation to improve these problems. In addition, it is used to improve the voltage stability of a network.

Over the last 20 years, several researches have been carried out around the world on STATCOMs and their results are published as journal and conference papers or technical reports. So far, STATCOMs have only appeared as a chapter or part of a chapter in some of the books on FACTS, power electronics, power systems, and reactive power compensation. However, to the best of the editors' knowledge, no single book has covered the different aspects of STATCOMs until now. The interested readers had to search among several hundreds of papers on STATCOM through different databases in order to build up their knowledge on the subject. This book is the first one entirely on STATCOM and it is an effort to provide a research-oriented, well-developed, and coherent book on the subject for postgraduate students and researchers. As the editors of the book, we hope it will prove to be a valuable addition to the literature on STATCOMs and be helpful to those interested in the subject.

This book is benefited from the inputs and comments of a large number of researchers and experts from the academia and industry. It contains 21 chapters. The breakdown of the chapters is as follows:

- Chapter 1 reviews the different topologies for the converters and filters used in the STATCOMs.
- Chapter 2 describes several multilevel converter topologies for STATCOMs.

- Chapter 3 discusses the analysis and implementation of an 84-pulse STATCOM.
- Chapter 4 presents the mathematical modeling of STATCOMs and control algorithms for STATCOMs.
- Chapter 5 discusses some control strategies for the STATCOMs.
- Chapter 6 presents the robust nonlinear control method for the STATCOMs.
- Chapter 7 describes the utilization of multiple reference frames for versatile control of STATCOMs.
- Chapter 8 presents the different control algorithms for multilevel STATCOMs.
- Chapter 9 discusses the adaptive observer for capacitor voltages in multilevel STATCOMs.
- Chapter 10 presents different methods of modeling and control of STATCOMs.
- Chapter 11 studies the STATCOM operation in steady state and dynamic modes in abc framework.
- Chapter 12 presents a load flow method considering the presence of STATCOM in power systems.
- Chapter 13 reviews different methods for optimal placement and sizing of STATCOMs in power systems based on heuristic optimization techniques.
- Chapter 14 discusses a multi-objective optimization technique to define the optimal placement of STATCOMs in power systems against short-term voltage instability.
- Chapter 15 demonstrates the application of STATCOM for increasing the available power transfer capability in transmission networks
- Chapter 16 presents the application of STATCOM for decentralized secondary voltage control in transmission networks.
- Chapter 17 provides an analysis for damping of subsynchronous oscillations with the help of STATCOMs.
- Chapter 18 demonstrates the STATCOM application for mitigation of subsynchronous resonance in wind farms that are connected to series-compensated transmission lines.
- Chapter 19 introduces two case studies for the application of STATCOM on Mexican power systems.
- Chapter 20 presents the stability analysis of STATCOM in distribution networks.
- Chapter 21 discusses the network protection systems in the presence of STATCOMs.

As the editors of the book, we would like to thank all the contributors for their support and hard work. We also would like to thank the reviewers who provided valuable comments to improve the quality of the book. Also, we thank the publisher Springer for agreeing to publish this book. Last but not least, we would like to thank

our respective families—Farhad thanks his parents (Ali and Nahideh) and his spouse (Negar), Sumedha thanks his spouse (Gayani) and Arindam thanks his spouse (Supriya) for their encouragement and support.

September 2014

Farhad Shahnia
Sumedha Rajakaruna
Arindam Ghosh

Contents

About the Editors

Farhad Shahnia received his Ph.D. in Electrical Engineering from Queensland University of Technology, Brisbane, Australia in 2011. Currently, he is a Lecturer of Power Engineering in Curtin University, Perth, Australia. His professional experience includes 3 years at Research Office-Eastern Azarbayjan Electric Power Distribution Company, Tabriz, Iran. Prior to joining Curtin University, he was a research fellow in Queensland University of Technology, Brisbane, Australia. He has published five book chapters and over 80 research articles.

Sumedha Rajakaruna received his Ph.D. in Electrical Engineering from University of Toronto, Ontario, Canada in 1993. Currently, he is a senior lecturer of Power Engineering at Curtin University, Perth, Australia. Prior to joining Curtin University in 2007, he was with University of Moratuwa, Sri Lanka from 1994 to 2000 and with Nanyang Technological University, Singapore, from 2000 to 2007. He is the supervisor of more than ten Ph.D. graduates and has published two book chapters and over 40 research articles.

Arindam Ghosh received his Ph.D. in Electrical Engineering from University of Calgary, Canada in 1983. Currently, he is a Professor of Power Engineering at Curtin University, Perth, Australia. Prior to joining Curtin University in 2013, he was with Indian Institute of Technology (IIT), Kanpur, India, from 1985 to 2006 and with Queensland University of Technology, Brisbane, Australia from 2006 to 2013. He is a fellow of INAE and IEEE. He is also an IEEE PES distinguished lecturer. He is the supervisor of more than 30 Ph.D. graduates and has published two books, seven book chapters, and more than 350 research articles.

Reviewers

Akshaya Kumar Moharana, Powertech Labs Inc, Canada
Amit Kumar Jain, Intel Corporation, USA
Antonio Valderrabano-Gonzalez, Universidad Panamericana, Mexico
Anup Kumar Panda, National Institute of Technology-Rourkela, India
Aurelio Garcia-Cerrada, Comillas Pontifical University, Spain
Behrooz Vahidi, Amirkabir University of Technology, Iran
Cesar Angeles-Camacho, Universidad Nacional Autónoma de México, Mexico
Chung Choo Chung, Hanyang University, Republic of Korea
Dionisio Ramirez, Universidad Politécnica de Madrid, Spain
Ersan Kabalci, Nevşehir Hacı Bektaş Veli University, Turkey
Federico Serra, Universidad Nacional de San Luis, Argentina
Fernando Martinez, Universidad de Valladolid, Spain
Francisco Jurado, University of Jaén, Spain
Hasan Mehrjerdi, Research Institute of Hydro-Quebec, Canada
Juan M. Ramirez, Centro de Investigación y de Estudios Avanzados del Instituto Politécnico Nacional
Juan Segundo Ramirez, Universidad Autónoma de San Luis Potosí, Mexico
Leopold Herman, University of Ljubljana, Slovenia
Luis Carlos Herrero, Universidad de Valladolid, Spain
Miguel F. Escalante, Universidad Autónoma de Nuevo León, Mexico
Miguel Ochoa-Gimenez, Comillas Pontifical University, Spain
Nagesh Prabhu, N.M.A.M. Institute of Technology, India
Reza Sirjani, Cyprus International University, Northern Cyprus
Salah Kamel, Aswan University, Aswan, Egypt
Santhi Karthikeyan, Ryerson University, Canada
Santiago de Pablo, Universidad de Valladolid, Spain
Trapti Jain, Indian Institute of Technology Indore, India
Yan Xu, University of Newcastle, Australia

Abbreviations

AC	Alternating current
ACCC	Aluminum conductor composite core
ACO	Ant colony optimization
AIS	Artificial immune system
APF	Active power filter
ASD	Adjustable speed drive
ATC	Available transfer capability
AVR	Automatic voltage regulator
BCO	Bee colony optimization
BCOP	Base case of operation
BESS	Battery energy storage system
CBM	Capacity benefit margin
CCT	Critical clearing time
CHB	Cascade H-bridge
CLOD	Composite load model
COI	Center of inertia
CPF	Continuation power flow
CSB	Connected system bus
CSC	Current source converter
CT	Coupling transformer
DC	Direct current
DCT	Discrete cosine transform
DFIG	Doubly fed induction generator
DFT	Discrete Fourier transform
DQ	Direct-quadrature
DSC	Delayed signal cancellation
DSP	Digital signal processor
DSTATCOM	Distribution static compensator
DVR	Dynamic voltage restorer
EAF	Electric arc furnace
EMF	Electromotive force

EMI	Electromagnetic interference
EMRF	Efficient multiple-reference-frame
ES	Evolution strategy
ESS	Excitation system stabilizer
ETC	Existing transfer commitment
FACTS	Flexible alternating current transmission system
FC	Flying capacitor
FPGA	Field programmable gate array
GA	Genetic algorithm
GHS	Global harmony search
GTO	Gate turn-off thyristor
HB-PWM	Hysteresis band pulse width modulation
HIS	Improved harmony search
HM	Harmony memory
HMCR	Harmony memory considering rate
HMS	Harmony memory size
HS	Harmony search
HSRF	Harmonic synchronous reference frame
HV	High voltage
IDMT	Inverse definite minimum time
IEEE	Institute of electrical electronic engineering
IEEE.Std	Institute of electrical electronic engineering standard
IG	Induction generator
IGBT	Insulated gate bipolar transistor
IGCT	Integrated gate commutated thyristor
IOL	Input–output feedback linearization
IOLD	Input–output linearization with damping
IOLMD	Input–output linearization with a modified damping
IPC	Inter-phase power controller
KCL	Kirchhoff current law
KSP	Key system parameter
KVL	Kirchhoff voltage law
L	Inductor
LC	Inductor–capacitor
LCL	Inductor–capacitor–inductor
LPF	Low-pass filter
LSE	Least square estimation
LS-SPWM	Level shifted sinusoidal pulse width modulation
LV	Low voltage
LVRT	Low-voltage ride-through
MCSC	Multilevel current source converter
MCT	MOS-controlled thyristor
MCU	Microcontroller unit
MES	Mexican electrical system

MIDO	Mixed-integer dynamic optimization
MIMO	Multiple-input multiple-output
MINLP	Mixed-integer nonlinear programming
MIP	Mixed-integer programming
MLI	Multilevel inverter
MOEA	Multi-objective evolutionary algorithm
MOEA/D	Multi-objective evolutionary algorithm using decomposition
MOGLS	Multi-objective genetic local search
MOP	Multi-objective optimization problem
MPC	Model predictive control
MSA	Modified simulated annealing
MSR	Machine synchronous reactance
MSV	Minimum singular value
MV	Medium voltage
M2LC	Modular multilevel converter
NERC	North American electric reliability council
NPC	Neutral-point clamped
NR	Newton-Raphson
NR-CIM	Newton-Raphson current mismatch
NR-PCIM	Newton-Raphson power and current mismatches
NRPG	Northern regional power grid
NR-PM	Newton-Raphson power mismatch
NR-RCIM	Newton-Raphson revised current mismatch
NSGA-II	Non-dominated sorting genetic algorithm II
OASIS	Open access same time information systems
OHC	Overall harmonic compensation
OLP	Optimal load flow
OPF	Optimal power flow
PBC	Passivity-based control
PBCND	Passivity-based control with nonlinear damping
PC	Predictive control
PCC	Point of common coupling
PCH	Port-controlled hamiltonian
PEBS	Potential energy boundary surface
PF	Pareto front
PFC	Power factor correction
PI	Proportional-integral
PID	Proportional-integrative-derivative
PLL	Phase-locked loop
PNP	Power network partitioning
PR	Proportional-resonant
PS	Pareto set
PSM	Plug setting multiplier
PSO	Particle swarm optimization

PS-SPWM	Phase shifted sinusoidal pulse width modulation
PU	Per unit
PWM	Pulse width modulation
RC	Repetitive controller
RI	Risk index
RMS	Root mean square
SA	Simulated annealing
SCR	Short-circuit ratio
SHC	Selective harmonic compensation
SHE-PWM	Selective harmonic elimination pulse width modulation
SI	Sensitivity index
SISO	Single-input–single-output
SMES	Superconducting magnetic energy storage
SMIB	Synchronous machine infinite bus
SO	System operator
SPWM	Sinusoidal pulse width modulation
SRF	Synchronous-reference frame
SSCI	Subsynchronous current injector
SSDC	Subsynchronous damping controller
SSR	Subsynchronous resonance
SSSC	Static synchronous series compensator
STATCOM	Static synchronous compensator or static compensator
SVC	Static VAr compensator
SVG	Synchronous voltage generator
SVM	Space vector modulator
TCBR	Thyristor-controlled braking resistor
TCPST	Thyristor-controlled phase-shifting transformer
TCR	Thyristor-controlled reactor
TCSC	Thyristor-controlled series capacitor
TCVL	Thyristor-controlled voltage limiter
TF	Transfer function
TGR	Transient gain reduction
THD	Total harmonic distortion
TLR	Transformer leakage inductance
TOCC	Time-optimal current-control
TRM	Transmission reliability margin
TSC	Thyristor-switched capacitor
TSSC	Thyristor-switched series capacitor
TTC	Total transfer capability
TVAC	Time varying acceleration coefficient
TVSI	Transient voltage severity index
UEP	Unstable equilibrium point

UPFC	Unified power-flow controller
VSC	Voltage source converter
VSSC	Voltage-sourced switching converter
VUF	Voltage unbalance factor
WECC	Western electricity coordinating council

Chapter 1
Converter and Output Filter Topologies for STATCOMs

Ersan Kabalci

Abstract This chapter reviews different converter topologies and output filter configurations used in STATCOM applications. The output voltage and harmonic control of a STATCOM is obtained by individual control of each switch in the STATCOM. Several converter topologies can be considered for STATCOMs. The multi-pulse converters are developed using the most widely known 6-pulse configurations. The variations of multi-pulse converters such as 12-pulse, 24-pulse and 48-pulse that are built by combining 6-pulse converters via phase-shifting isolation transformers are introduced in terms of control methods and structures in this chapter. On the other hand, the multilevel converters are considered to be used in recent STATCOM topologies as an alternative to the multi-pulse configurations, owing to their multi MVA switching capability that is inherited from series or parallel connection of converter cells. The diode clamped, flying capacitor, and cascaded H-bridge configurations of multilevel converters, that are the most widely known topologies, are comprehensively introduced in this chapter. The multilevel converter topologies provide several advantages such as harmonic elimination, lower electromagnetic interference, better output waveforms, and increased power factor correction (PFC) capabilities together. Furthermore, each switch can be controlled individually to robustly tackle the unbalanced load operations even in higher switching frequencies relatively to the multi-pulse configuration. The related subsections propose control and operation properties of converters besides introducing the main topological issues. The filtering requirements of STATCOM are particularly considered in this chapter where the passive and active filters are introduced in detail. The passive filters designed with reactive components such as individual L and C or their combinations as LC or LCL are surveyed according to design and analytical criteria. Besides, active power filters (APFs) that provide several feedback control methods increasing the efficiency and controllability are discussed in the following part. The control methods of STATCOM converters are introduced in a separate section where the recent control approaches and analytical

E. Kabalci (✉)
Department of Electrical and Electronics Engineering, Faculty of Engineering and Architecture, Nevsehir Haci Bektas Veli University, 50300 Nevşehir, Turkey
e-mail: kabalci@nevsehir.edu.tr

F. Shahnia et al. (eds.), *Static Compensators (STATCOMs) in Power Systems*, Power Systems, DOI 10.1007/978-981-287-281-4_1

calculations required are presented in detail. The block diagrams of the industrial STATCOM applications are also discussed.

Keywords STATCOM · Converter · Inverter · Filter · Active power filter (APF)

1.1 Introduction

STATCOM is a reactive power (Q) compensation device that is shunt connected to the AC transmission and distributions systems. The basic topology is based on Voltage Source Converters (VSCs) where the emerging topologies consist of self-commutated switching devices while recent STATCOMs include line commutated switches such as thyristors. A STATCOM that is capable of generating or absorbing reactive power to compensate the transmission line is located between generators and load [1–3]. This operation principle of STATCOM makes it to act either as a source or a load for the transmission line. STATCOMs are considered as a member of the Flexible AC Transmission System (FACTS) devices. Furthermore, STATCOMs can replace Static VAr Compensators (SVC) in distribution systems [1, 2]. STATCOM can increase the power quality by performing several compensations such as dynamic voltage control, oscillation damping of power line, pursuing the stability during transients, voltage flicker and sag-swell controls, and active and reactive power (PQ) control in transmission and distribution systems. These are achieved since the STATCOM utilizes a VSC with power switches, a closed-loop control system which controls the on-off states of switches, and output filters [3, 4].

Figure 1.1 shows a double generator system and a transmission line where an ideal shunt compensator is connected to the middle of the line. The generators have an equivalent reactance of X_{G1} and X_{G2} while the transmission line has an equivalent reactance of X_{dL}. The voltages at Point of Common Coupling (PCC) of the generators are given as$V_1\angle\delta_1$ and $V_2\angle\delta_2$. The shunt compensator connected in the middle of the line is a voltage source that is continuously controlled to $V_{SC}\angle\delta_{SC}$.

Figure 1.2 depicts the phasor diagrams of the transmission system with the shunt compensator where δ_1 is assumed to be equal to $+\delta/2$ while δ_1 is assumed to be

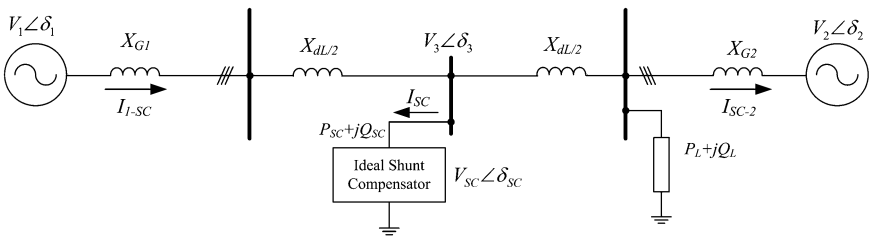

Fig. 1.1 Connection of an ideal shunt compensator to transmission line

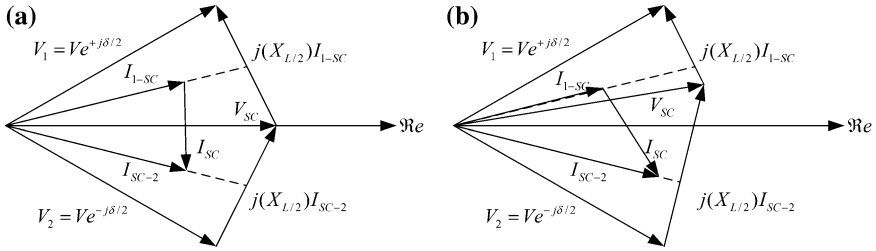

Fig. 1.2 Phasor diagram of shunt compensation, **a** reactive power compensation, and **b** reactive and active power compensation

equal to $-\delta/2$. The phase differences show that I_{1-SC} current flows from first generator to the line while I_{SC-2} flows from line to the second generator. The I_{SC} phasor is the derived current flowing through the shunt capacitor where it is orthogonal to the V_{sc} as seen in Fig. 1.2a. This means the compensator does not exchange active power (P) with the line. In this case, the compensator has only reactive power on its connections. Hence, the power transferred from V_1 to V_2 can be calculated as

$$P_1 = \frac{2V^2}{X_L}\sin(\delta/2) \tag{1.1}$$

where the P_1 is the active power supplied by V_1 while V is the vector sum of V_1 and V_2 sources. In case of any compensator was not included in the system, the transferred power would be expressed as given in the following,

$$P_1 = \frac{V^2}{X_L}\sin(\delta) \tag{1.2}$$

where the compensator increases the power control ability of the transmission line since $2\sin(\delta/2)$ yields higher value than $\sin(\delta)$ in the range of $[0, 2\pi]$. In case of the phase angles of V_1 and V_2 are different from $\delta/2$, this situation causes the power flowing through sources has active and reactive power components as shown in Fig. 1.2b. In this situation, the shunt compensator owing to its power electronics based structure can be operated to adjust one of active or reactive power. Besides, the device structure also varies according to requirement of active or reactive power compensation since they are different in terms of energy storage elements [1]. The connection type and switching device of compensators involve several different operating characteristics. The thyristor based topologies are classified into two main groups of self-commutated and force-commutated. The self-commutated devices consist of thyristors. On the other hand, the force-commutated devices are comprised of Gate Turn-Off thyristors (GTO), Integrated Gate-Commutated Thyristors (IGCT), MOS-Controlled Thyristors (MCT) and Insulated Gate Bipolar Transistors (IGBT) that use gate-controlled commutation [1, 2].

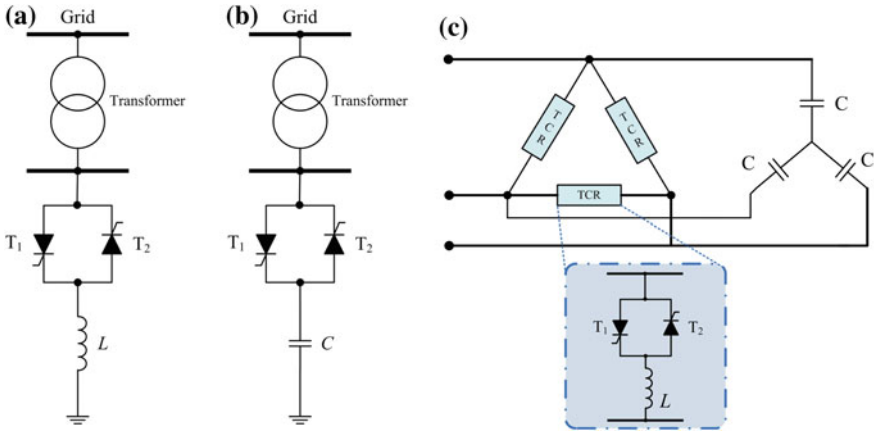

Fig. 1.3 Thyristor based FACTS devices, **a** thyristor-controlled reactor, **b** thyristor-switched capacitor, and **c** 6-pulse static VAR compensator

The self-commutated FACTS devices are Thyristor-Controlled Reactor (TCR), Thyristor-Switched Capacitor (TSC), SVC, Thyristor-Switched Series Capacitor (TSSC), Thyristor-Controlled Series Capacitor (TCSC) that all are based on aforementioned ideal shunt compensator methodology. The TCR seen in Fig. 1.3a is a specific shunt compensator that adjusts the equivalent inductive reactance of the transmission line by controlling the phase-angle. It is composed of a reactor in series with a bidirectional thyristor valve. The TSC is another device that is constituted by replacing the inductor of TCR with a power capacitor, as shown in Fig. 1.3b.

The limitation of these two compensators is that they are only capable of continuous inductive compensation or discontinuous capacitive compensation. Nevertheless, most industrial applications require continuous capacitive or inductive compensation. The SVC is designed to operate in both inductive and capacitive continuous compensation. The schematic diagram of a simple three-phase SVC is depicted in Fig. 1.3c. SVC consists of delta-connected three TCRs and a three-phase capacitor bank. The TCR stands for the basic controller of SVC while the capacitor bank serves as a TSC. The capacitance should generate the maximum reactive power that it is expected to be controlled by SVC. For this, the thyristors are switched off at $\alpha = 180°$. Another important point of the SVC configuration is related to inductor of TCR that should provide the maximum reactive power greater than that of the capacitor banks. For the SVC to generate the maximum inductive reactive power, the thyristors are switched on at the minimum angle of $\alpha = 90°$ [1, 2].

The emerging power systems and FACTS require more effective controllers such as STATCOMs, the Thyristor-Controlled Phase-Shifting Transformer (TCPST), the Static Synchronous Series Compensator (SSSC), the Unified Power-Flow Controller (UPFC), the Inter-phase Power Controller (IPC), the Thyristor-Controlled Braking Resistor (TCBR), the Thyristor-Controlled Voltage Limiter (TCVL), the

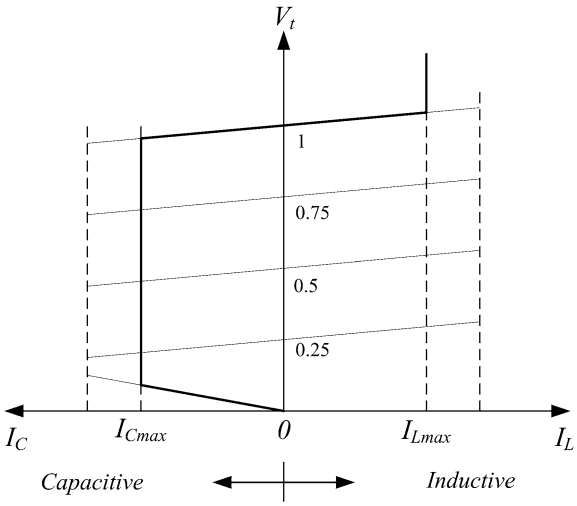

Fig. 1.4 The typical V-I characteristic of STATCOM

Battery Energy Storage System (BESS), and the Superconducting Magnetic Energy Storage (SMES) systems [3]. STATCOM is operated as a shunt SVC to adjust the AC system voltage managing the capacitive or inductive output current. A typical V-I characteristic of STATCOM, as shown in Fig. 1.4, illustrates this situation where the STATCOM can perform inductive or capacitive compensation regarding to its line current. Besides, the V-I characteristic shows that STATCOM can provide capacitive or inductive power even at very low voltages (e.g. 0.15 pu).

The converters used in STATCOM topologies are classified according to their multi-pulse or multilevel structures. The multi-pulse converters are switched in line frequency where it consists of line-commutated devices. On the other hand, multilevel converters including widely known VSC topologies are commutated by pulse width modulation (PWM) or its improved methods.

1.2 Multi-pulse Converters

1.2.1 Six-Pulse Converter

The preliminary STATCOM applications are based on multi-pulse converters owing to its lower losses and lower harmonic contents. The multi-pulse converter topologies consist of several 6-pulse VSC circuits that are also known as three-level VSC. A basic VSC STATCOM in the configuration of 6-pulse two-level is illustrated in Fig. 1.5 that is constituted with six GTOs and anti-parallel diodes where several other self-commutated devices such as IGBT, MCT or IGCT could also be used. The GTOs are the switching devices of the system where the converter can generate balanced three-phase AC output voltages from a DC capacitor. The frequency of the output

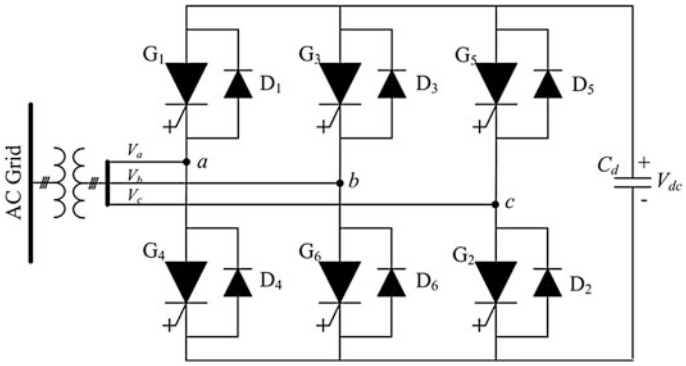

Fig. 1.5 Basic 6-pulse two-level VSC STATCOM

voltage is adjusted by the modulating frequency of GTO switches and the phase voltages are coupled to the AC grid through an interconnection reactor [3, 5, 6].

The power quality concept covers topics such as flicker, dip, rise, sag, and swells on voltage besides harmonic distortion rates. The operating principle of the STATCOM is based on generating a staircase waveform by synthesizing the DC input voltage levels. The VSC can be operated with 120° or 180° switching sequences where it allows conducting two or three switches at any time, respectively. Figure 1.6 illustrates the switching sequences; signals generated and applied to G_1 and G_4 switches, and output line voltage of v_{ab} in each axis.

The line voltage v_{ab} can be expressed in Fourier-series as

$$v_{ab} = a_0 + \sum_{h=1}^{\infty} a_h \cos(h\omega t) + \sum_{h=1}^{\infty} b_h \sin(h\omega t) \tag{1.3}$$

where coefficients a_0, a_h, and b_h can be determined by considering one fundamental period of v_{ab}. The average voltage is calculated as $a_h = 0$ since the v_{ab} waveform is symmetrical. On the other hand, the coefficient b_h is determined as seen in (1.4) since it also has odd-wave symmetry [3].

Therefore,

$$b_h = \frac{2}{\pi} \int_0^{\pi} V_{dc} \sin(h\omega t) d(\omega t) \tag{1.4}$$

$$b_h = \frac{2}{\pi} \int_{\alpha}^{\pi-\alpha} V_{dc} \sin(h\omega t) d(\omega t) = \frac{4V_{dc}}{\pi h} \cos(h\alpha) \tag{1.5}$$

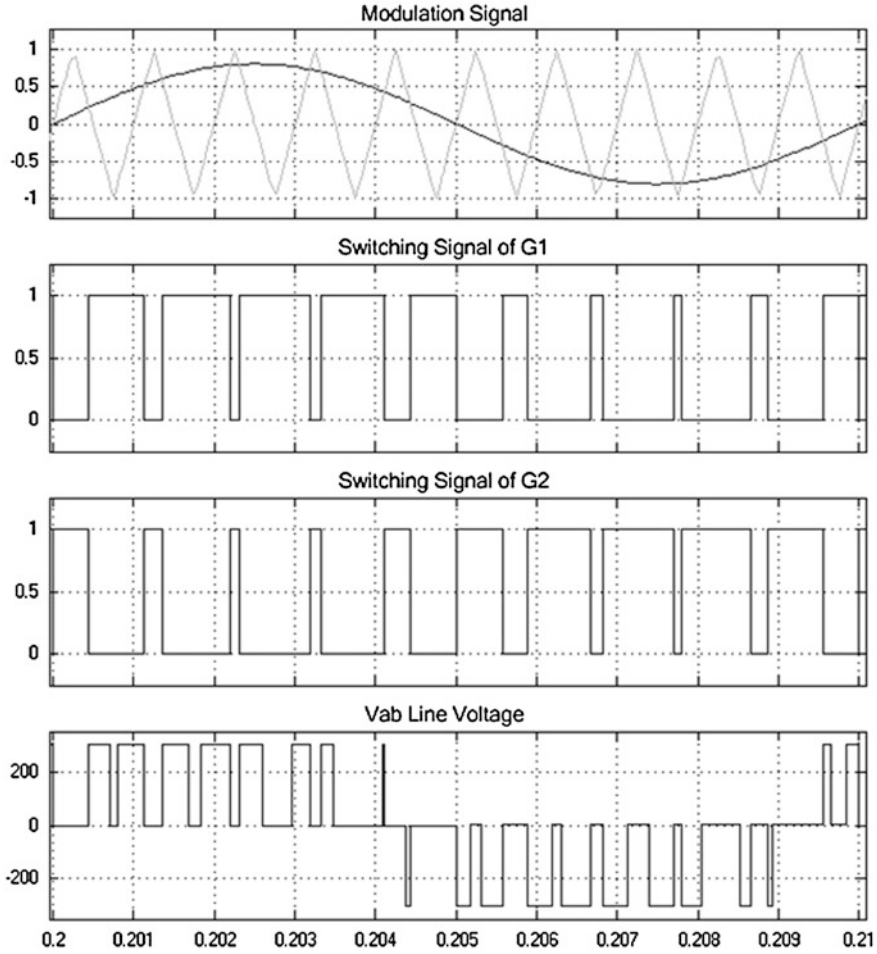

Fig. 1.6 Output line voltage of a VSC operated at 120° conduction sequence

$$\therefore V_{ab} = \sum_{h=1,3,5}^{\infty} \frac{4V_{dc}}{\pi h} \cos(h\alpha) \sin(h\omega t) \tag{1.6}$$

The triplen harmonics in the line voltage will be zero when the switching angle is set to $\alpha = 30°$ as seen from (1.5). It is also seen that the harmonic contents of the converter are occurred in the $(6n \pm 1)$. f_o orders where f_o is the fundamental frequency of line voltage and $n = 1, 2, 3, \ldots,$. It is obviously seen that the harmonic orders of 6-pulse VSC are 5th, 7th, 11th, 13th, …, and so on that makes the VSC impractical for power systems. In order to cope with this problem, increased pulse levels such as 12-pulse, 24-pulse, and 48-pulse are achieved by combining basic 6-pulse VSCs together.

1.2.2 12-Pulse Converter

The 12-pulse converters requires 6-pulse converters connected in parallel over the single DC bus where they are serially connected to transformers on the output side as seen in Fig. 1.7 [7, 9]. Two different topologies can be used to generate a 12-pulse static compensation. The first one consists of two level VSCs as shown in Fig. 1.5 while the second one is based on three level VSCs that is depicted in Fig. 1.8 [8]. The first approach requires a different transformer connection for each six pulse VSC, i.e. one is Δ-Y connected while the other is Y-Y connected to the AC grid. The Δ connected secondary of the transformer has three times higher winding turns and provides 30° phase shift comparing to the Y connected one. Therefore, the lower order harmonics are eliminated easily.

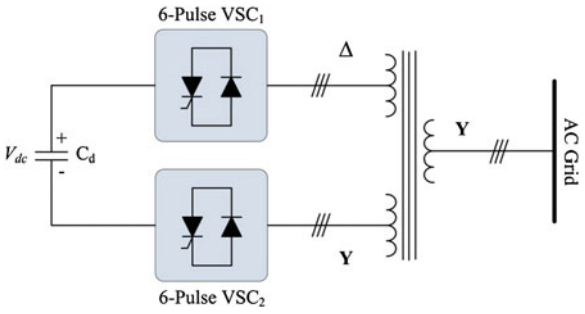

Fig. 1.7 Output line voltage of a VSC operated at 120° conduction sequence

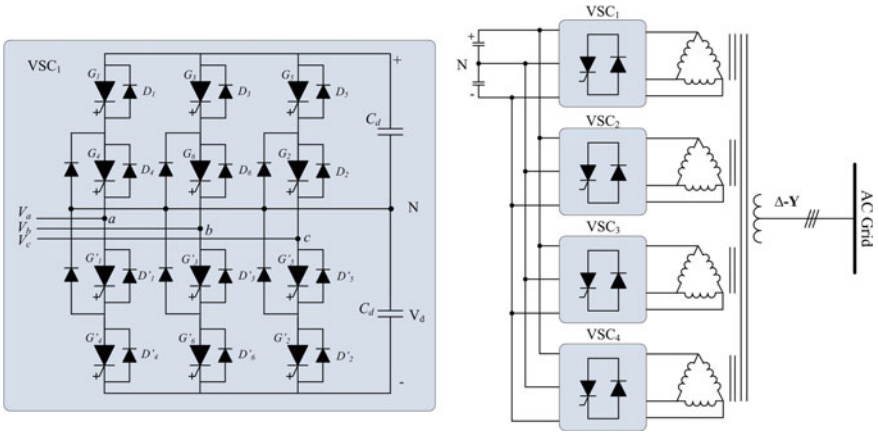

Fig. 1.8 Three-level 12-pulse STATCOM [8]

The phase-a output voltage of STATCOM in any instant can be calculated by using (1.7) where n_1 and n_2 are the voltage ratios of the corresponding VSC transformers while v_{a-Y} and $v_{a-\Delta}$ are the output voltages of the Y-Y and Δ-Y connected converters, respectively [7].

$$v_a = n_1 v_{a,Y} + n_2 \frac{v_{a,\Delta}}{\sqrt{3}} \tag{1.7}$$

The amplitude of VSC output voltage depends on the modulation index (m_i) of the controlling signal that allows obtaining the output voltage at $m_i V_{dc}$ where V_{dc} is the voltage across the capacitor. The control signal that is based on some variation of PWM generates the switching angle α which subsequently generates the STATCOM bus voltage. The Eq. (1.8) expresses the admittance of the transformer

$$Y = \frac{1}{R + jX} = G + jB \tag{1.8}$$

that manages the active or reactive power injection to the utility grid. The reactive power generation or absorption capability of STATCOM depends to the voltage that is generated by modulation of controller. The injected reactive power by the STATCOM can be presented as

$$Q = V^2 B - m_i V_{dc} V B \cos(\delta - \alpha) + m_i V_{dc} V G \sin(\delta - \alpha) \tag{1.9}$$

In case of $V > m_i V_{dc}$, Q will be positive that causes STATCOM to absorb reactive power and vice versa [7]. The active power generated by utility grid to charge the capacitor is expressed by

$$P = \frac{|V| m_i V_{dc}}{X} \sin(\delta - \alpha) \tag{1.10}$$

The three-level 12-pulse STATCOM requires 2α phase angle to vary the amplitude of VSC output voltage that controls the reactive power of utility grid. The phase angle δ between the AC bus voltage V_{ac} and STATCOM output voltage V sustains the DC line voltage V_{dc} at a constant value. The active and reactive powers are calculate as

$$P = \frac{V_{ac} V \sin \delta}{X} \tag{1.11}$$

$$Q = V_{ac} \left(\frac{V_{ac} - V \sin \delta}{X} \right) \tag{1.12}$$

where X is considered as the reactance along with STATCOM and utility grid [8–12].

The fundamental VSC voltage V regarding to operation modes is given as

$$V = 2V_1 \cos \alpha \tag{1.13}$$

where V_1 is the fundamental voltage of each VSC block seen in Fig. 1.8. The reactive power flows from utility grid to STATCOM while the capacitive operation mode supplies reactive power to utility grid from STATCOM. The operation of STATCOM given in Fig. 1.8 is carried out by applying 30° phase shift between VSC_1 and VSC_3 owing to their Y and Δ connection respectively on the primary windings of transformer. On the other hand, same connection and phase shift angles are supplied for VSC_2 and VSC_4 that are other sets of three-level 12-pulse VSC [8, 11, 12].

1.2.3 24-Pulse Converter

The self-commutated devices such as GTOs are widely preferred in VSC topologies since they can be used in square-wave or quasi-square wave modes. However, the GTO-based VSC technology is not preferred as much as before since the novel topologies are based on gate-commutated devices. The 24-pulse converter topology of STATCOM consists of 6-pulse converters where it eliminates the $6n \pm 1$ ordered harmonics. Since $n = 4$ for a 24-pulse converter, the 23rd, 25th, 47th, and 49th harmonics in the AC output waveform are naturally eliminated. The 24-pulse STATCOM constituting of two-level VSCs is illustrated in Fig. 1.9 where this topology is also known as quasi 24-pulse [13]. Each VSC and transformer

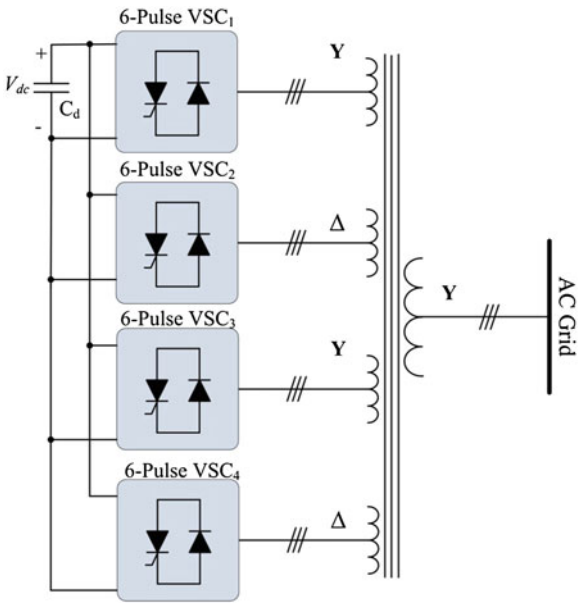

Fig. 1.9 Quasi two-level 24-pulse STATCOM

connection builds a stage that each stage is connected to the utility grid over Y-Y and Δ-Y connections of transformers. The transformers are connected in zigzag that generates 15° phase shift according to each other with −7.5°, 7.5°, 22.5°, and 37.5° angles [13, 14].

Another topology of quasi 24-pulse STATCOM is presented in [15] where the VSCs are constituted according to neutral point clamping (NPC) topology that is previously shown in Fig. 1.8. The conduction angle α defines the negative and positive cycles of intervals where $\alpha = 180 - 2\beta$, that 2β stands for the dead-band angle. The on–off spectral transitions are ensured by the dead-band angle where the output voltages of a 6-pulse three-level VSC is given by

$$V_1 = \frac{2\sqrt{6}}{\pi}\frac{v_{dc}}{2}\sin\left(\frac{180 - 2\beta}{2}\right) \tag{1.14}$$

On the other hand, output voltages of a 24-pulse three-level VSC is given as in (1.15) while the active and reactive powers are calculated by using (1.11) and (1.12) [15–17],

$$V_{c1} = np\frac{2\sqrt{6}}{6\pi}\frac{v_{dc}}{2}\sin\left(\frac{180 - 2\beta}{2}\right)\cos\frac{\pi}{24} \tag{1.15}$$

1.2.4 48-Pulse Converter

The most important benefit of the multi-pulse converters is the harmonic eliminating owing to the $6n \pm 1$ ratio. The 48-pulse converter based STATCOM is the most important VSC type to reduce lower ordered harmonics since harmonic orders appears at 47th, 49th, 95th, and 97th orders that are managed by $48n \pm 1$ ratio of eight 6-pulse VSCs. Furthermore, this facility of 48-puse converter allows using in high power FACTS without requiring any ac filter. The topology includes 6-pulse VSCs as introduced in previous devices where the phase shifts and transformer connections are depicted similarly in Fig. 1.10 [17].

The transformer connections are realized with zigzag type on primary side and Y/Δ types on secondary sides where the outputs of phase shifting sides are connected in series in order to eliminate lower order harmonics [18, 19]. The operation of 48-pulse STATCOM is depended on appropriate phase shift angles applied to VSCs and arranged between transformer connections. The proper shifting angles are shown in Table 1.1 where switching signals of each VSC are generated by considering these orders. The transformer connection types and phase shift angles are also done according to this order and therefore high quality sinusoidal output voltage is generated to compensate the utility grid [17, 19].

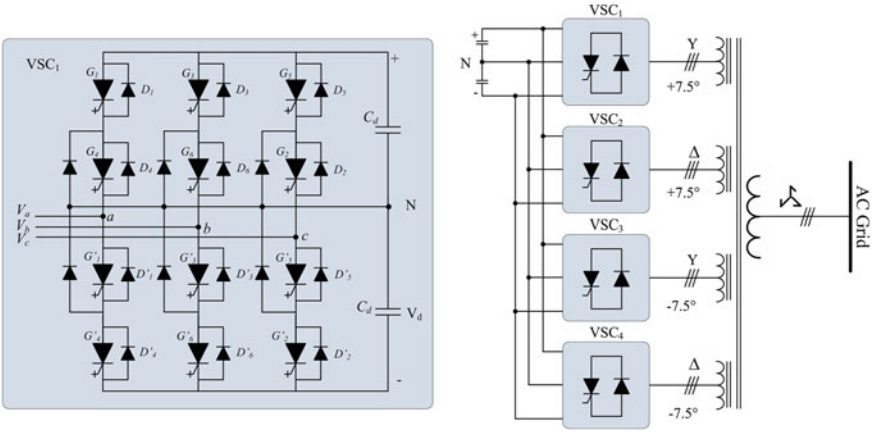

Fig. 1.10 Three-level 24-pulse STATCOM

Table 1.1 Phase shift angles for a 48-pulse VSC

Transformer connection	VSC switching angle (°)	Transformer phase shift angle (°)
Y–Z	+11.25	−11.25
Δ–Z	−18.75	−11.25
Y–Z	−3.75	+3.75
Δ–Z	−33.75	+3.75
Y–Z	+3.75	−3.75
Δ–Z	−26.25	−3.75
Y–Z	−11.25	+11.25
Δ–Z	−41.25	+11.25

Table 1.2 Phase shift angles for 48-pulse STATCOM including 12-pulse VSCs

Transformer connection	VSC switching angle (°)	Transformer phase shift angle (°)
Y–Z	+7.5	−7.5
Δ–Z	−22.5	−7.5
Y–Z	−7.5	+7.5
Δ–Z	−37.5	+7.5

Another 48-pulse topology is constituted with 12-pulse VSCs that is similar to the connection diagram and phase-shift angles as shown in Fig. 1.10. The 48-pulse converter requires 12-pulse transformers with phase shifting windings to match with 12-pulse VSCs [19]. In this situation, the phase shift angles of transformers are at −7.5° and 7.5° for Y and Δ connections respectively as shown in Table 1.2.

The switching angles α is calculated as shown below where the k is harmonic component to be eliminated

$$\alpha = 180\left(1 - \frac{1}{k}\right) \tag{1.16}$$

The switching angle of VSC is intended to eliminate desired harmonic contents depending to its frequency spectrum and the instantaneous phase voltage of the STATCOM is expressed by Fourier series expansion as

$$V_{an}(t) = \sum_{k=1}^{\infty} \sin\, k\omega t \tag{1.17}$$

$$V_{an_k} = \frac{2V_{dc}}{k\pi} \cos\, k\left(\frac{\pi - \alpha}{2}\right) \tag{1.18}$$

Once the $V_{an}(t)$ is calculated from (1.17) and (1.18), $V_{bn}(t)$ and $V_{cn}(t)$ can be easily calculated in a similar way where they are phase shifted by 120° and 240° respectively [18, 19, 21]. The four VSCs of the 48-pulse STATCOM generate phase shifted AC output voltages to compensate the utility grid voltage where the output line voltage is given by [20],

$$V_{ab48}(t) = V_{ab}(t)_1 + V_{ab}(t)_2 + V_{ab}(t)_3 + V_{ab}(t)_4 \tag{1.19}$$

$$V_{ab48}(t) = 8\left[\begin{array}{l} V_{ab1}\sin(\omega t + 30^\circ) + V_{ab47}\ \sin(47\omega t + 150^\circ) + V_{ab49}\sin(49\omega t + 210^\circ) \\ + V_{ab95}\sin(95\omega t + 330^\circ) + V_{ab97}\sin(97\omega t + 30^\circ) + \cdots \end{array}\right] \tag{1.20}$$

Voltages $V_{bn48}(t)$ and $V_{cn48}(t)$ can also be easily calculated in a similar way to phase voltages since they are phase shifted by 120° and 240° respectively [20].

1.3 Multilevel Converters

The MultiLevel Converters (MLC) are one of the extensively studied research area of power converters. Nabae introduces the initial studies on MLCs where a two-level converter is improved by utilizing neutral point of the DC line voltage to constitute the third level. This early device is presented as neutral point clamped (NPC) inverter [21, 22]. In the following years, several topologies and arrangements are proposed by numerous researches to increase the efficiency of MLCs while decreasing the switching losses. However, three topologies that are diode-clamped, flying capacitor (FC), and cascaded H-bridge (CHB) hold superior rate of utilization [21, 23]. The most important contribution of MLCs are related to their benefits such as lower voltage stress on switching devices, lower *dv/dt* in voltage source, higher power outputs, decreased electromagnetic interference (EMI), and staircase output voltages depending to multilevel generation [21].

The MLCs are widely used in active filters, FACTS, STATCOMs, and distributed generation interfacing beyond their conventional applications such as adjustable speed drive (ASD) or energy conditioning. Even though they are operated in medium voltage (MV), the MLCs used in transmission system STATCOMs are capable to control power rates from a few kVArs to multi MVArs. Almost all the STATCOM topologies introduced in multi-pulse section are implemented with three-level diode clamped-MLC where the switching devices were GTOs. Although the FC-MLI requires pre-charge arrangement in opposite to diode clamped-MLI, it eliminates the output filter requirement that decreases the entire system cost particularly in high power applications. On the other hand, the CHB topology requires the least number of switches compared to the other two topologies and can generate higher output levels in a simpler way. In addition to this, CHB involves several isolated DC sources for each H-bridge to generate a staircase output waveform [21, 24, 25]. The following sections are intended to introduce MLCs applications in STATCOM at a glance.

1.3.1 Diode Clamped MLC

The widely used diode clamped-MLC is based on the early NPC model of Nabae. The essential three-level topology is constituted by using the VSC_1 shown in Fig. 1.11. Besides, there are several experimental verifications are performed for four, five, and six-level diode clamped-MLI for STATCOM, FACTS, and ASD

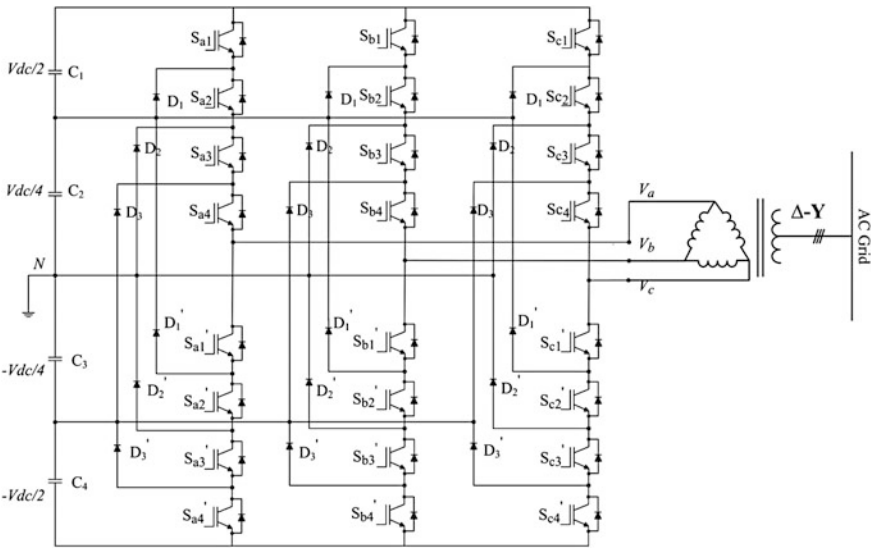

Fig. 1.11 Five-level diode clamped MLC based STATCOM

Table 1.3 Output voltages and switching sequence of a five-level diode clamped-MLC

Voltage V_{an}	Switching sequence							
	S_{a1}	S_{a2}	S_{a3}	S_{a4}	S'_{a1}	S'_{a2}	S'_{a3}	S'_{a4}
$V_4 = V_{dc}/2$	1	1	1	1	0	0	0	0
$V_3 = V_{dc}/4$	0	1	1	1	1	0	0	0
$V_2 = 0$	0	0	1	1	1	1	0	0
$V_1 = -V_{dc}/4$	0	0	0	1	1	1	1	0
$V_0 = -V_{dc}/2$	0	0	0	0	1	1	1	1

applications. However, multi MVA applications in high voltage operation require a robust and proven topology that is depicted in Fig. 1.11. A three-phase,five-level diode clamped-MLC STATCOM is based on sharing a common DC bus voltage over four capacitors. The DC bus voltage is equally shared by each capacitor and the diodes titled as D_1, D_2, D_3 and D'_1, D'_2, D'_3 limits the voltage stress on each IGBT.

The staircase output voltage is generated by switching each phase legs in eight various intervals where a switching table for a phase voltage V_{an} is given in Table 1.3. A group of four switches is at *on* state for any given interval as seen from table. In the first interval, the switches from S_{a1} to S_{a4} are switched and the resultant voltage level is increased to $V_{an} = V_{dc}/2$ where the left intervals generate the other voltage levels where they synthesizes a staircase output voltage.

V_{bn} and V_{cn} are also generated in a similar way where the modulating signals are phase shifted by 120° and 240° respectively [21, 22].

1.3.2 Flying Capacitor MLC

Meynard and Foch implement the FC-MLC in early 1990s as an alternative to diode clamped-MLC in order to be used on high voltage power conversion. The proposed MLC topology is capable of serial connection of several three-level modules while providing more simple control algorithms and more precise output voltage waveforms. A three-phase five-level FC-MLC based STATCOM is shown in Fig. 1.12. The voltage sharing capacitors are assisted by contiguous capacitors that are replaced with diodes in diode clamped-MLC topology [21, 26].

The contiguous capacitors are named as auxiliary capacitor and an m-level FC topology requires $(m - 1) \cdot (m - 2)/2$ auxiliary capacitor with $(m - 1)$ DC bus capacitors. This requirement of FC seems increasing the device number for a given level design. However, it enables voltage synthesis in more flexible and versatile way comparing to diode clamped MLC. The auxiliary capacitors (C_{a1}, C_{a2}, and C_{a3}) are pre-charged to the voltage levels of $V_{dc}/4$, $V_{dc}/2$, $3V_{dc}/4$ respectively [21, 26]. The FC-MLC also involves the completing switches as $(S_{a1} - S'_{a1})$, $(S_{a2} - S'_{a2})$, $(S_{a3} - S'_{a3})$, and $(S_{a4} - S'_{a4})$ as seen in Fig. 1.12.

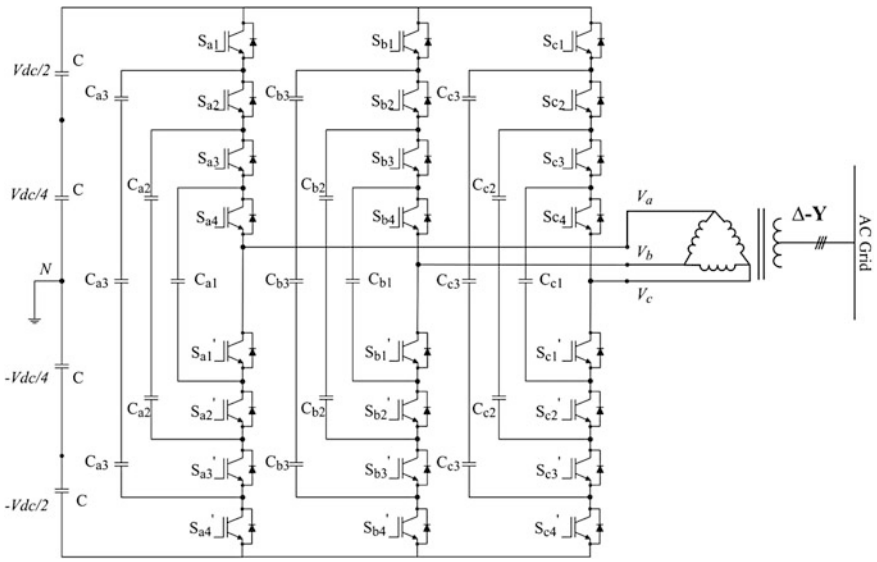

Fig. 1.12 Five-level FC-MLC based STATCOM

The switch pairs can differ owing to control method applied to MLC. However, improper selection of switching pairs may cause redundancy in terms of switching states. The optional switching states for voltage levels of $V_{dc}/4$, 0, $-V_{dc}/4$ shows the phase redundancies of FC-MLC as an advantage to decrease the phase duplications of diode clamped MLC. Table 1.4 shows the switching combinations for phase

Table 1.4 Output voltages and switching sequence of a five-level FC-MLI

Voltage V_{an}	Switching sequence							
	S_{a1}	S_{a2}	S_{a3}	S_{a4}	S'_{a1}	S'_{a2}	S'_{a3}	S'_{a4}
$V_4 = V_{dc}/2$	1	1	1	1	0	0	0	0
$V_3 = V_{dc}/4$	1	1	1	0	1	0	0	0
	0	1	1	1	0	0	0	1
	1	0	1	1	0	0	1	0
$V_2 = 0$	1	1	0	0	1	1	0	0
	0	0	1	1	0	0	1	1
	1	0	1	0	1	0	1	0
	1	0	0	1	0	1	1	0
	0	1	0	1	0	1	0	1
	0	1	1	0	1	0	0	1
$V_1 = -V_{dc}/4$	1	0	0	0	1	1	1	0
	0	0	0	1	0	1	1	1
	0	0	1	0	1	0	1	1
$V_0 = -V_{dc}/2$	0	0	0	0	1	1	1	1

voltage output (V_{an}) that is relative to neutral point of n. This advantage allows selecting charging control sequence of capacitors by defining the appropriate switching [21].

The FC-MLC topology prevents output filter requirement, and controls the PQ flow in an efficient way decreasing the phase repeating. In contrast, the increment of m level restricts the accurate charge control of capacitors. In case the required capacitors are increased, the installation cost increases and VSC gets more bulky [21].

1.3.3 Cascaded H-Bridge MLC

The most extended utilization of MLCs in STATCOMs belongs to CHB. The CHB topology consists of several H-bridge modules connected in series to generate a multilevel output voltage. Most important features of this topology compared to the other two topologies are higher switching frequency and increased power rate that is handled by the total device and equally shared to the each module. In addition to these, the CHB based STATCOM is capable to eliminate harmonics and compensate reactive power in superior in comparison with the other topologies. The outputs of CHB are series connected, thus the DC sources should be isolated. Therefore, CHB-MLCs can be easily integrated to separate energy sources

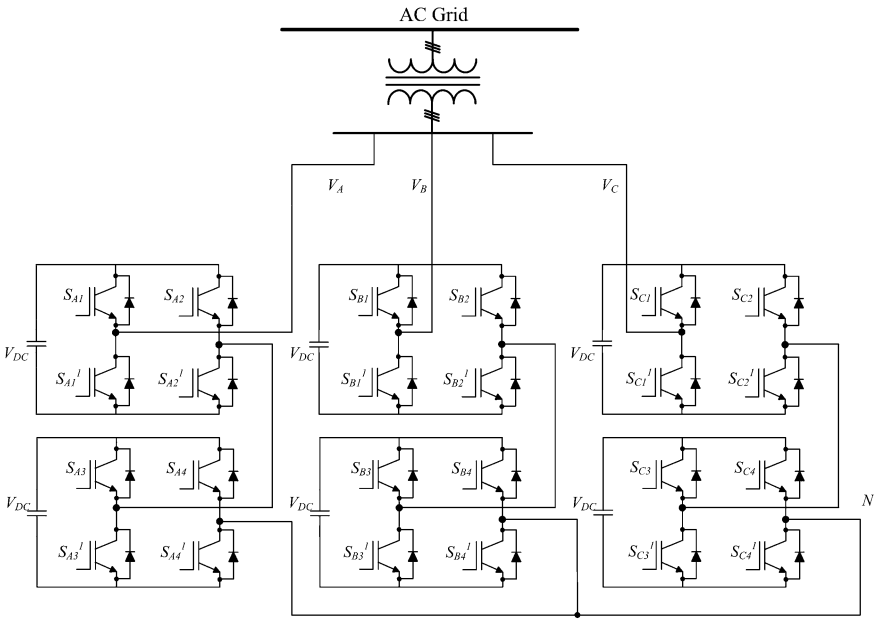

Fig. 1.13 Five-level CHB STATCOM

alternatively to capacitors to obtain higher output levels [21, 27, 28]. A five-level three-phase CHB STATCOM connection is seen in Fig. 1.13 where each phase leg includes two series connected H-bridge cells. Any H-bridge cell generates three voltage levels as $+V_{dc}$, 0, $-V_{dc}$ from the DC bus voltage and supplies the AC output by different combinations of four switches, S_{A1}, $S_{A1}^{'}$, S_{A2}, and $S_{A2}^{'}$. The CHB utilizes two sources for each phase to generate a five-level output voltage. To obtain $+V_{dc}$, S_{A1} and $S_{A2}^{'}$ switches are turned on, whereas $-V_{dc}$ level can be obtained by turning on S_{A2} and $S_{A1}^{'}$.

V_{a1} and V_{a2} voltages of series connected H-bridge cells synthesize the phase voltage V_{an} in a stepped waveform. The positive output voltage levels are indicated with P_1 and P_2 while the negatives are $P_1^{'}$ and $P_2^{'}$. Equation (1.21) expresses the Fourier series expansion of the general multilevel stepped output voltage while the transform applied to the STATCOM shown in (1.22), where n represents harmonic order of the output voltage. The switching angles θ_1, θ_3, …, θ_5 in (1.21) are selected to meet the minimum voltage harmonics [21, 27].

$$V_{an}(t) = \frac{4V_{dc}}{\pi} \sum_{n=1,3,5,\ldots}^{\infty} [\cos(n\theta_1) + \cos(n\theta_2) + \cdots + \cos(n\theta_5)] \frac{\sin(n\omega t)}{n} \quad (1.21)$$

$$V_{an5}(t) = \frac{4V_{dc}}{\pi} \sum_{n=1,3,5,\ldots}^{\infty} [\cos(n\theta_1) + \cos(n\theta_2)] \frac{\sin(n\omega t)}{n} \quad (1.22)$$

1.4 Filter Topologies

The multi-pulse STATCOM topologies have several drawbacks such as higher costs, bulky device structures, higher active power losses, and nonlinearities caused by multi-winding transformers when compared to the multilevel converter based topologies. The multilevel VSC STATCOMs are widely used owing to its advantages against aforementioned drawbacks and owing to its modular structure, independent phase control ability, and decreased costs [29–32].

On the other hand, the structure of VSC includes higher ordered harmonics at the output since the recent power switches are limited to operate at lower switching frequencies to reduce the switching losses. Thus, this situation causes line current harmonics at lower frequencies [30, 33]. However, low and high order harmonics can be eliminated by using a filter at the STATCOM output [34].

Although the conventional method to filter harmonics is connecting an inductor in series or shunt to the output of VSC, the output filter design requires more attention to operate the STATCOM in an efficient way [29, 33]. The filtering methods introduced in this section cover passive filters including L, LC, LCL filters; active filters and recently implemented filtering devices.

1.4.1 Passive Filters

The passive filters include three main types that are L filters, LC filters, and LCL filters where all the reactive components are connected to a small resistor to increase the stability in comparison to the pure reactive filters. The simplest passive filter is an inductor which is low cost and is expected to meet the ripple current requirements while the voltage drop across the inductor should be in an acceptable limit. The design criteria of L filter requires that the reactance of the inductor should be around 20 % of STATCOM while the ripple current should be lower than 25 %, and the voltage drop lower than 10 % [29, 31, 33]. The main drawback of the L filters is that they require higher inductance to decrease the total harmonic distortion (THD). On the other hand, in high power applications, the switching frequency is restricted to decrease the power losses. Other passive filter topologies are widely researched to cope with the drawbacks of simple L filter by increasing the reactive components. The LC filter is implemented to reduce the inductance of filter while obtaining the same filtering properties [33, 35, 36].

The most important properties of LCL filter are originated from its gain at low frequencies and harmonic elimination at high frequencies. The resonance peak of LCL filter requires special attention in design to obtain proper control of VSC and handling the utility grid disturbances. Hence, active and passive resonance damping methods are involved in controller designs that are depended to control strategy of current loops. Although several strategies such as direct current control and indirect current control are improved, the most widely used method is conventional Proportional-Integral (PI) current control that is managed by measuring VSC currents and utility grid voltages. The repetitive control and proportional resonant control methods are assumed as alternatives to conventional PI control method. However, the complex structures and phase delays occurred during the operation cannot restrain the resonance variations at the exact times [31, 34]. The passive filters of L filter, LC filter, and LCL filter are shown in Fig. 1.14a–c, respectively. The rest of this section presents two important aspects of passive filters that are designing criteria and control methods for each filter type.

1.4.1.1 L Filters

Let us consider Fig. 1.14a with an L filter at the output of the SATCTOM. i_s is the source current, i_L is the load current, i_c is the output current of the SATCTOM while i_{ref} is its reference value. R_S and L_S are the equivalent resistance and inductance of the source and line.

The switching signal block consists of a PWM modulator that generates the switching intervals regarding to the reference current. The transfer function (TF) of the L filter is presented as seen in Fig. 1.15 where T_S is the constant PWM delay time, k_{PWM} is the proportional gain of the switching signal, k_d is the feedback signal, and k_p is the proportional gain parameter. Since the integrative value of PI

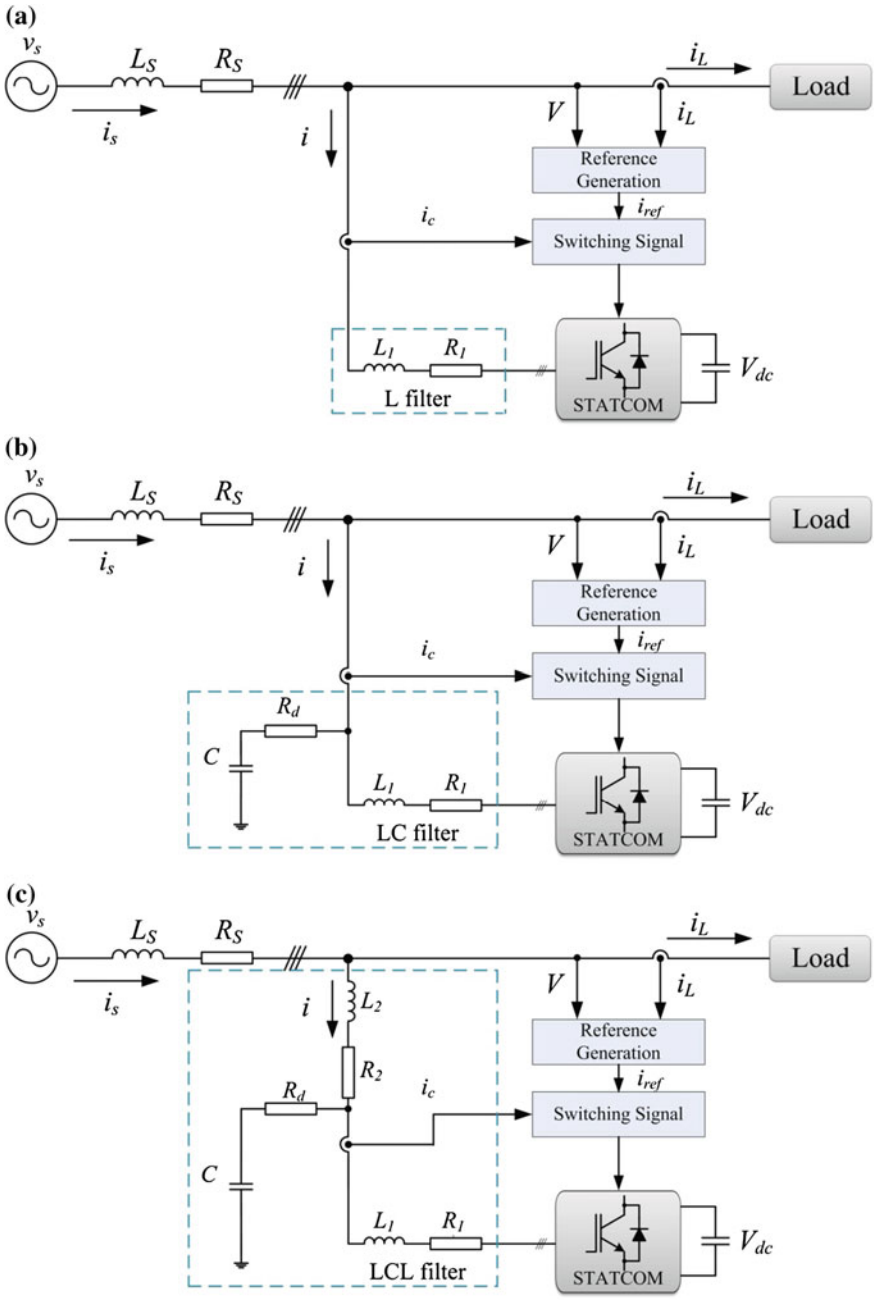

Fig. 1.14 STATCOM with passive output filter, **a** L filter, **b** LC filter, and **c** LCL filter

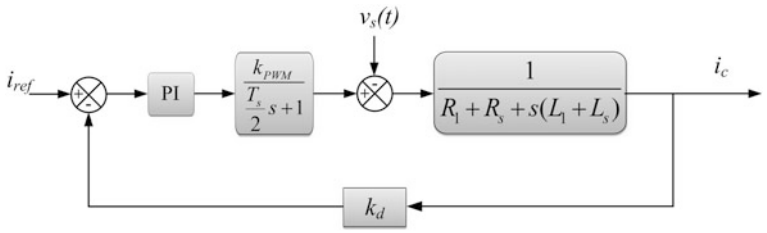

Fig. 1.15 Transfer function of L filter

controller is quite small, the TF is constituted by considering the proportional value. The open loop TF of the Fig. 1.15 can be calculated as [29, 30]

$$G(s) = \frac{k_D k_P k_{PWM}}{(s\frac{T_S}{2}+1)[R_1 + R_S + s(L_1 + L_S)]} \tag{1.23}$$

The cutoff frequency of the L filter affects its filtering efficiency. Increased value of R_1 increases the cutoff frequency and hence more low frequencies are eliminated. The cutoff frequency is inverse rated with L_1 i.e. increased L_1 decreases the cutoff frequency. On the other hand, L_1 is effective on the magnitude of medium and high frequencies while it is ineffective on the magnitude of low frequencies.

1.4.1.2 LC Filters

The LC filter provides more appropriate filtering compared to the L filter and most of the passive filters are constituted with LC filters. The STATCOM application with LC output filter is illustrated in Fig. 1.14b where v_s is the system source voltage, i_s is the source current, i_L is the load current, i_c is the output current of STATCOM and i_{ref} is its reference. The output filter of STATCOM includes L_1, R_1, C and R_d that can easily eliminate the higher ordered harmonics of the VSC.

The TF of the LC filter is shown in Fig. 1.16. The LC filter performance can be analyzed in two different ways depending on the location of the current sensors at the output of the STATCOM. In the first method, it is assumed that the feedback loop does not involve the capacitor as expressed below [29, 33, 36],

$$G(s) = \frac{k_d k_p k_{PWM}}{(s\frac{T_s}{2}+1)} \cdot \frac{s^2 L_s C + s(R_d + R_s)C + 1}{(sL_1 + R_1)[s^2 L_s C + s(R_d + R_s)C + 1] + s(R_d C + 1)(sL_s + R_s)} \tag{1.24}$$

where the resonance frequency is calculated by

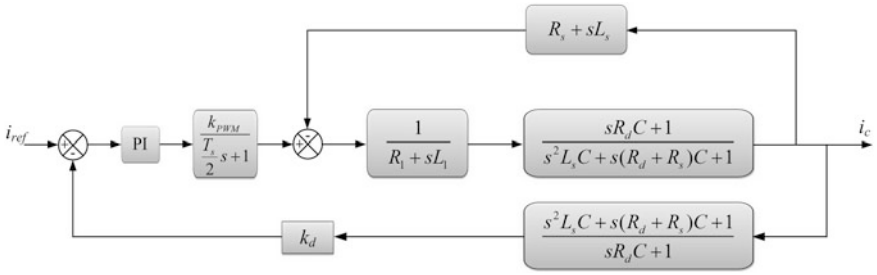

Fig. 1.16 Transfer function of LC filter

$$f'_{res} = \frac{1}{\omega'_{res}} = \frac{1}{2\pi}\sqrt{\frac{L_s + L_1}{L_s L_1 C}} \tag{1.25}$$

In the second method, it is assumed that the feedback loop considers the capacitor. Hence the open loop transfer function can be given as [29],

$$G(s) = \frac{k_d k_p k_{PWM}}{(s\frac{T_s}{2}+1)} \cdot \frac{sR_dC + 1}{(sL_1 + R_1)[s^2L_sC + s(R_d + R_s)C + 1] + s(R_dC + 1)(sL_s + R_s)} \tag{1.26}$$

The equations given in (1.24), (1.25) and (1.26) show that the value of inductor L_1 has inverse effect on the cut-off frequency ω_1 and the magnitude of medium and high frequency where the increment on inductor value decreases the others. On the other hand, the increment on the value of capacitor C deteriorates the noise attenuation by increasing the cut-off frequency [29]. The increased L_1 eliminates the high order harmonics in the output line currents of STATCOM while attenuating the EMI noises. However, for higher inductor values, higher voltage capacitors are required in the LC filter structure that increases the system costs. Similarly, smaller inductor leads to smaller size, lower costs and higher dynamic response [33]. The TF of LC filter presented in (1.24) and (1.26) can be reduced to (1.27) by assuming the no-load operation as

$$G(s) = \frac{v_o(s)}{v_{VSC}(s)} = \frac{sR_dC + 1}{s^2L_1C + sR_dC + 1} \tag{1.27}$$

where the $v_o(s)$ and $v_{vsc}(s)$ are respectively the output voltage of the filter and the VSC [33, 36].

1.4.1.3 LCL Filters

There are several STATCOM applications that use LCL output filters [34, 37–39] since the harmonic elimination ability of an LCL filter is better than inductive filter. Furthermore, filtering the high frequency harmonics is limited in L filter applications while LCL filter easily tackles it. The most important features of the LCL filter is related to its low frequency gain and high frequency attenuation that are demanded from an ideal filter [31].

The TF of the LCL filter is shown in Fig. 1.17. The LCL filter performance can be analyzed in two different ways by considering different current sensing points at the output of STATCOM. The first method is applied by assuming that the feedback loop does not consider the capacitor as [29, 33, 36],

$$G_{LCL}(s) = \frac{k_d k_p k_{PWM}}{(s\frac{T_s}{2}+1)} \cdot \frac{s^2(L_s+L_2)C + s(R_d+R_s+R_2)C + 1}{(sL_1+R_1)[s^2(L_s+L_2)C + s(R_d+R_s+R_2)C+1] + s(R_dC+1)[(s(L_s+L_2)+R_s+R_2)]} \tag{1.28}$$

It can be seen from (1.28) that the effects of L_1, R_d, and C are same with the LC filter. The additional inductor L_2 affects the gain in the low and medium frequencies while it has no effect on high frequency attenuation.

In the second method where the capacitor is considered in the feedback loop, the TF is rearranged as

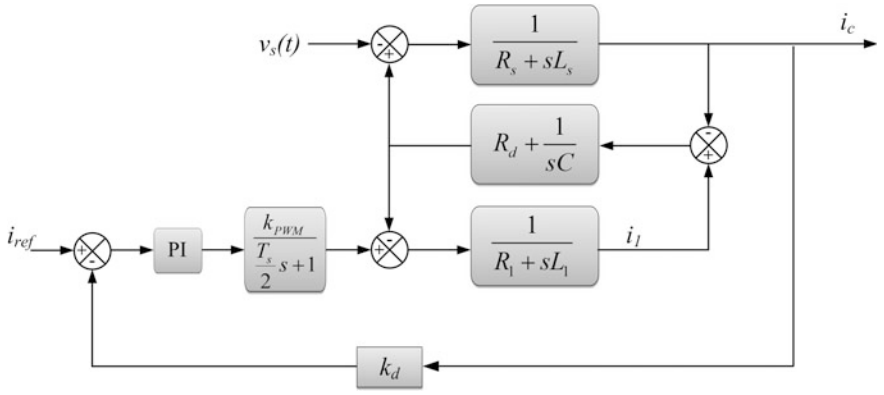

Fig. 1.17 Transfer function of LCL filter

$$G_{LCL}(s) = \frac{k_d k_p k_{PWM}}{(s\frac{T_s}{2}+1)} \cdot \frac{sR_dC+1}{(sL_1+R_1)[s^2(L_s+L_2)C+s(R_d+R_s+R_2)C+1]+s(R_dC+1)[(s(L_s+L_2)+R_s+R_2)]} \quad (1.29)$$

where the higher inductor L_1 value generates bigger phase margins. On the other hand, inductor L_2 presents inverse effect on phase margin with respect to L_1. Thus, the system shifts from unstable states to stable states. The TF of the LCL filter presented in (1.28) and (1.29) can be reduced to (1.30) by disregarding resistors R_1 and R_2 as [29, 31],

$$G(s) = \frac{v_o(s)}{v_{VSC}(s)} = \frac{sR_dC+1}{s^3L_1L_2C+s^2(L_1+L_2)R_dC+s(L_1+L_2)} \quad (1.30)$$

1.4.2 Active Power Filters

Passive filters found a wide application area in STATCOM mainly due to their low cost and simple structure. However, they require serious tuning methods to operate in wide range of frequencies. The active power filters (APF) that are based on PWM controlled VSCs provide versatile applications even for low and medium voltage distribution systems. The APFs can be connected in shunt or series to the network alone or along with passive filters. APFs are intended to compensate current harmonic and power factor [40–42].

On the other hand, the notable improvements seen in semiconductors promoted the speed and capacity of APFs that easily overcome the disadvantages of passive filters. A parallel-connected APF to the load is known as shunt APF operating as a controllable current source that eliminates the current harmonics by injecting a compensating current to the line. The shunt APF is more convenient type used in nonlinear loads [43, 44]. The series APFs can be assumed as controllable voltage sources that are used to compensate load voltage harmonics [40]. Both of these APFs are implemented from a VSC and a DC bus capacitor, as shown in Fig. 1.18a, b. The series-shunt APF connection that is shown in Fig. 1.18c is constituted with dual VSCs to operate as separate series and shunt APFs. The controller is capable to generate reference voltage values for series APF and reference current values for shunt APF as seen in the block diagram.

A STATCOM controller block diagram is shown in Fig. 1.19 that compensates harmonic components of load current. The controller includes a current reference generator, a voltage controller and VSC switching signals generator. The instantaneous active and reactive powers are calculated from the load currents [40].

The DC component elimination block removes the DC values in active and reactive power and provides feedback signals to reference current generator block.

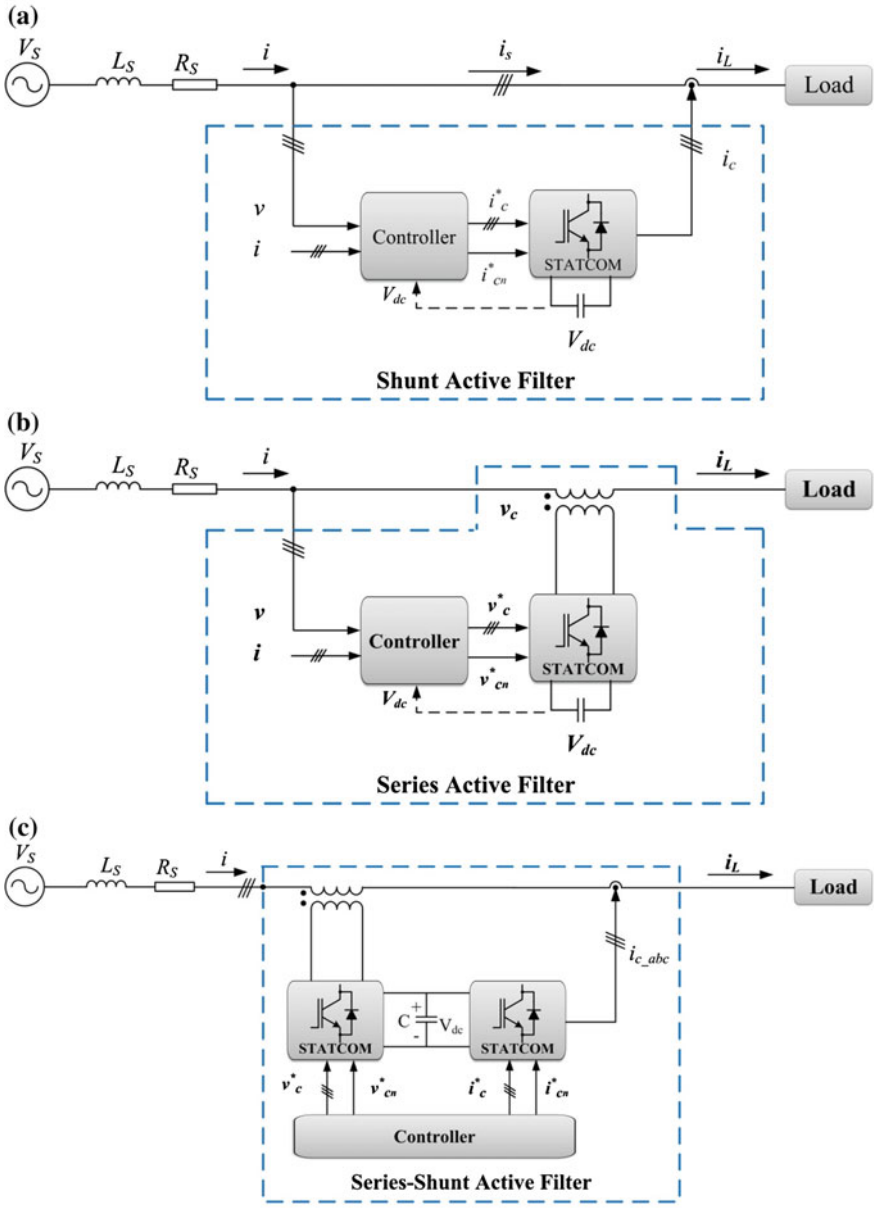

Fig. 1.18 Active STATCOM filters, **a** shunt active filter, **b** series active filter, **c** series-shunt active filter

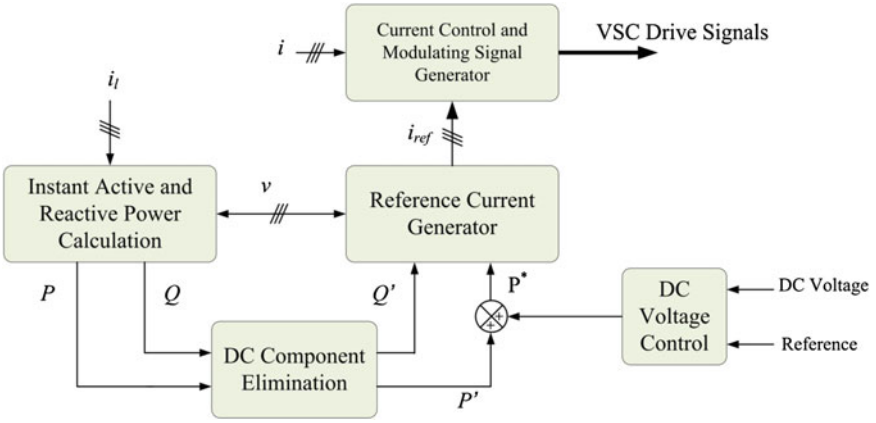

Fig. 1.19 The block diagram of an APF for current harmonic compensation

The DC voltage controller tracks the voltage level of DC capacitor and provides the required tracking signal to reference current generator. The modulating signal generator produces the switching signals to drive the semiconductors of VSC [40].

1.5 Control Methods of STATCOM Converters

The STATCOM control methods are studied in terms of PWM controls of VSC since the recent advanced STATCOMs are based on multi-pulse or multilevel VSCs. The efficiency of a VSC depends on the proper control method that is the most important parameter to decrease the switching losses and harmonic elimination properties. The outstanding and robust control methods applied in VSCs are sinusoidal PWM (SPWM), space vector PWM (SVM), selective harmonic elimination PWM (SHE-PWM), optimal PWM (OPWM), and hysteresis control PWM that all are derivatives of regular PWM method [21, 22, 45–49]. Besides these modulation methods; sigma-delta, linear, fuzzy, proportional-resonant (PR) and optimized current control methods are also used to manage the switching signal generating algorithm of regular PWM [21, 45]. The control methods of VSCs are introduced at a glance in this section.

1.5.1 Sinusoidal PWM (SPWM)

SPWM is one of the most widely used control method in VSCs owing to its simplified mathematical requirements and easy implementation even with basic microcontrollers. The SPWM method is based on comparing a sinusoidal

modulating signal with a triangular carrier waveform that is arranged according to required switching outputs. The fundamental frequency SPWM is proposed to minimize the switching losses in low and higher frequency applications. On the other hand, the performance feature of the modulator is increased by multi-carrier operations that are achieved by arranging the carrier waveforms either in horizontal or in vertical positions by the modulator. The ratio of the modulating waveform amplitude to carrier amplitude is known as modulation index (m_i) that is one of the most important parameter of an SPWM modulator with switching frequency (f_s). The output voltage of STATCOM is obtained in linear operating mode ($0 < m_i \leq 1$) and over-modulation mode ($m_i > 1$) where the phase voltage limits are expressed as [21, 22],

$$V_{An} = V_{Bn} = V_{Cn} = m_i \frac{\sqrt{3}V_d}{2} \quad 0 < m_i \leq 1 \tag{1.31}$$

$$\frac{\sqrt{3}V_d}{2} < V_{An} = V_{Bn} = V_{Cn} < \frac{4}{\pi}\frac{\sqrt{3}V_d}{2} \quad m_i > 1 \tag{1.32}$$

Another important point of SPWM modulator design is the amplitude distortion which is caused by the variations of the DC voltage capacitor of the STATCOM. This situation presents the most significant impact on the "on–off" spectral errors. The amplitude distortion of the PWM waveforms declines the amplitude of the fundamental component and introduces unexpected low order harmonic contents as [21, 50–53].

$$V_O(t) = \frac{m_i V_{dc}}{2}\cos(\omega_r t) + \frac{2V_{dc}}{\pi}\sum_{k=1}^{\infty} J_0\left(k.m_i\frac{\pi}{2}\right)\sin\left(k\cdot\frac{\pi}{2}\right)\cos(k\cdot\omega_c t) + \frac{2V_{dc}}{\pi}\sum_{k=1}^{\infty}\sum_{l=\pm 1}^{\pm\infty}\frac{J_n\left(k\cdot m_i\frac{\pi}{2}\right)}{k}\sin\left[\left((k+l)\cdot\frac{\pi}{2}\right)\right]\cos(k\cdot\omega_c t + l\cdot\omega_r t) \tag{1.33}$$

where

m_i	amplitude of modulation ratio,
V_{dc}	DC supply voltage,
ω_r	sinusoidal reference frequency,
ω_c	triangular reference frequency,
J_0, J_n	Bessel function

The first part of (1.33) presents the amplitude of fundamental component of a regular SPWM while Colak et al. [53] have implemented the second and third parts. The second part indicates the elimination of side band harmonics of the carrier signal while the last part considers elimination of the harmonics in multiples of the carrier signal [53].

1.5.2 Space Vector PWM (SVM)

SVM is probably the most widely used modulation method in MLCs since it can generate 15 % higher output voltage compared to other control methods. The switching signals of an SVM modulator is generated by using the switching vector as a point in complex space of (α, β) shown in Fig. 1.20. The sector definition and look-up table requirements make SVM method quite complicated comparing to others.

However, some of the repeating switching states except zero voltage vectors, small and medium vectors are ignored by defining exact switching orders as seen in Table 1.5 where the switching orders are prepared for a three-level VSC.

The vectors given in Fig. 1.20 are classified into three groups that are named as small vectors (V_1 to V_6), middle vectors (V_8, V_{10}, V_{12}, V_{14}, V_{16} and V_{18}), and the large vectors (V_7, V_9, V_{11}, V_{13}, V_{15} and V_{17}).

The SVM modulator of a STATCOM shown in Fig. 1.21 contains a three-phase generator, low-pass bus filter, α-β transformation, α-β vector sector, ramp generator, and switching time calculator. Three-phase generator produces 120° phase shifted modulating signals and the α-β transformer performs the three-phase to two-phase conversion for sector preparation. The low-pass bus filter is used to remove fast

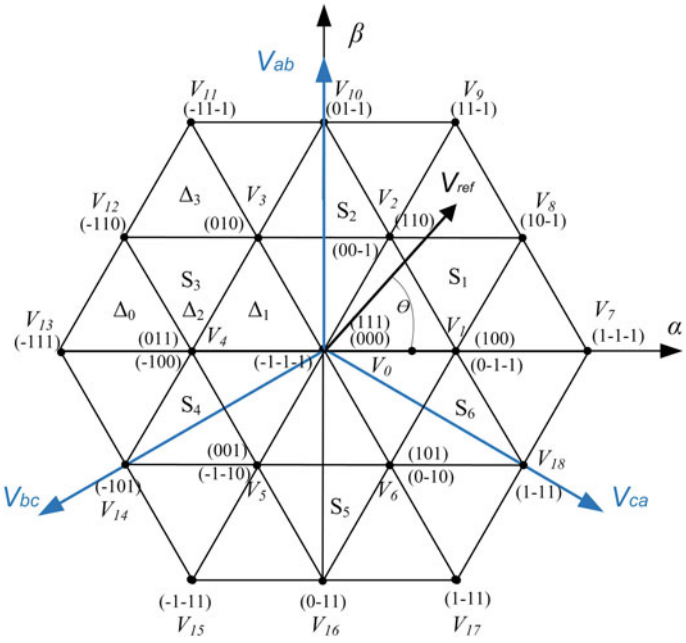

Fig. 1.20 Space vector diagram designed for a three-level VSC to be used in SVM control of STATCOM

Table 1.5 SVM switching states of a three-level VSC

Switching symbol	Switching states						Phase voltage
	S_1	S_2	$S_1^{'}$	$S_2^{'}$	D_1	D_2	
1	ON	ON	OFF	OFF	OFF	OFF	$V_{dc}/2$
0	OFF	ON	ON	OFF	Depend on polarity of load voltage		0
−1	OFF	OFF	ON	ON	OFF	OFF	$-V_{dc}/2$

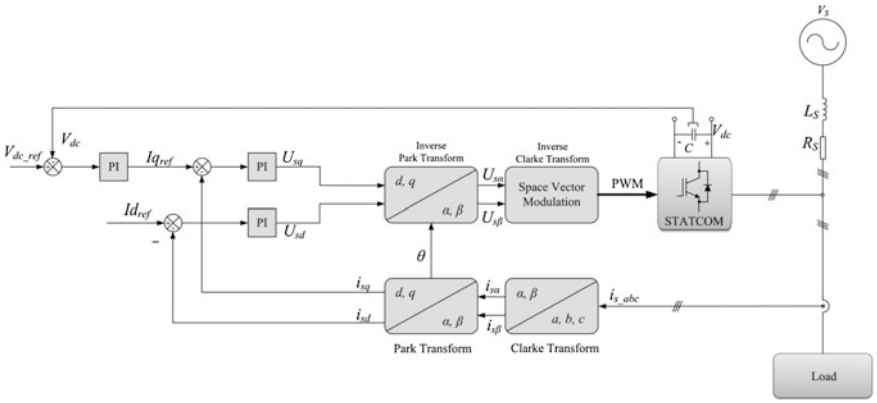

Fig. 1.21 Space vector controlled STATCOM

transients from the dc bus voltage measurement. The feed-forward method is used to compute the voltage vector applied to the loads [54].

This control method is also known as field oriented control of any load in SVM modulated VSCs that is easily applied to STATCOM applications. The controller scheme is based on two separate controllers that are responsible for direct axis (d-axis) current controller which generates i_{dref} reference and for quadrature axis (q-axis) current controller which generates i_{qref} reference. PI controllers generate the required values and converts to voltage signals to generate the switching signals of STATCOM [54, 55].

The Clarke transformation resolves the load currents to d-axis and q-axis components where the d-axis component is in phase with the DC voltage while the q-axis component that provides the reactive power is 90° out of phase [54, 55].

1.5.3 Selective Harmonic Elimination PWM (SHE-PWM)

Patel and Hoft proposed the SHE-PWM method that is implemented using fundamental frequency theory [56]. The basic idea is to eliminate predefined harmonic

orders as its name implies. This is carried out by defining the exact switching angles to eliminate the predefined harmonics. The Fourier series expansion for output voltage of STATCOM is operated with Newton-Raphson iteration as given below for a 7-level VSC,

$$V(\omega t) = \sum_{n=1,3,5,..}^{\infty} \frac{4Vdc}{n \cdot \pi} \cdot [\cos(n \cdot \theta_1) + \cos(n \cdot \theta_2) + \cos(n \cdot \theta_3)] \frac{\sin(n \cdot \omega t)}{n} \quad (1.34)$$

where the m_i to eliminate for 5th, 7th, 11th, and 13th harmonic orders is calculated by solving,

$$\left.\begin{aligned} &\cos(\theta_1) + \cos(\theta_2) + \cos(\theta_3) = 3m_i \\ &\cos(5\theta_1) + \cos(5\theta_2) + \cos(5\theta_3) = 0 \\ &\cos(7\theta_1) + \cos(7\theta_2) + \cos(7\theta_3) = 0 \\ &\cos(11\theta_1) + \cos(11\theta_2) + \cos(11\theta_3) = 0 \\ &\cos(13\theta_1) + \cos(13\theta_2) + \cos(13\theta_3) = 0 \end{aligned}\right\} \quad (1.35)$$

The switching angles are obtained at the values of $\theta_1 = 6.57°$, $\theta_2 = 18.94°$, and $\theta_3 = 27.18°$ by assuming $m_i = 0.8$ and solving with Newton-Raphson Iteration [21, 49, 56]. The calculated switching angles of the harmonic series are saved to a look-up table and are operated by the modulator for each measurement cycle of STATCOM. The complex analytical calculation of the harmonic orders to be eliminated is assumed as the drawback of SHE-PWM method.

1.5.4 Hysteresis Band PWM (HB-PWM)

The current controlled PWM methods are classified as linear methods including PI, feedback, and predictive controllers while the non-linear controllers are known as hysteresis band, ramp, and delta modulator based controllers. The hysteresis band PWM (HB-PWM) is widely used among other current control methods since it is easy to be implemented. The current controller in a HB-PWM is claimed to continuously track the load current to force it to remain in a reference band.

This operation is performed by switching the VSC properly to keep the output current in the desired hysteresis band where it is allowed oscillating between upper and lower band. In order to achieve this situation, the load currents are measured and are compared to reference values by hysteresis comparators. The d-axis and q-axis vectors generate the switching signals as done in SVM modulator and hysteresis controller forces dead band in the α-β plane as shown in Fig. 1.22 [21, 57, 58].

The voltage and current vectors defined as follows are applied to hysteresis current controller by considering the phase shift θ between voltage vector and real axes [57].

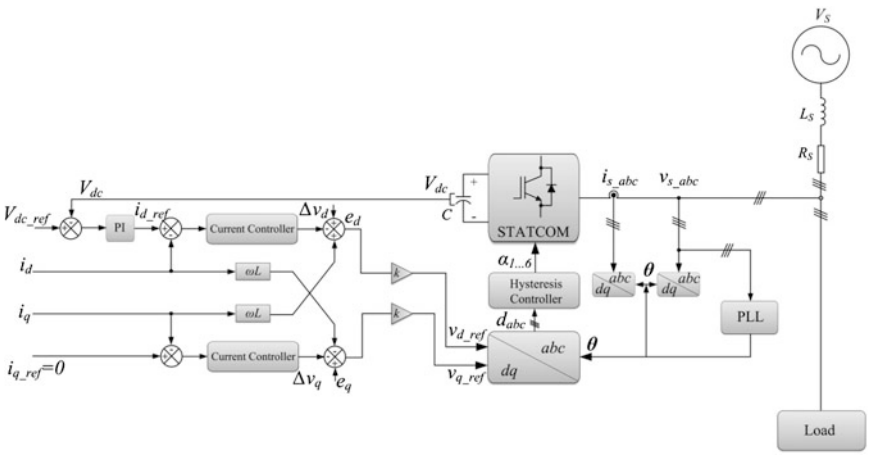

Fig. 1.22 HB-PWM controlled STATCOM

$$v(t) = \frac{2}{3}\left[v_a + e^{\frac{j2\pi}{3}}v_b + (e^{\frac{j2\pi}{3}})^2 v_c\right] \tag{1.36}$$

$$i(t) = \frac{2}{3}\left[i_a + e^{\frac{j2\pi}{3}}i_b + (e^{\frac{j2\pi}{3}})^2 i_c\right] \tag{1.37}$$

References

1. Watanabe EH, Aredes M, Barbosa PG, de Araújo Lima FK, da Silva Dias RF, Santos G Jr (2011) 32—Flexible AC transmission systems. In: Rashid MH (ed) Power electronics handbook, 3rd edn. Butterworth-Heinemann, Boston, pp 851–877
2. Acha E, Agelidis V, Anaya O, Miller TJE (2002) Power electronic control in electrical systems. Newnes Power Engineering Series. ISBN-13: 978-0750651264
3. Mathur RM, Varma RK (2002) Thyristor-based facts controllers for electrical transmission systems. Wiley-IEEE Press, Hoboken, ISBN: 978-0-471-20643-9
4. Kasikci I (2004) Analysis and design of low-voltage power systems: an engineer's field guide. Wiley, ISBN: 978-3-527-30483-7
5. Luo FL, Ye H, Rashid M (2005) Digital power electronics and applications. Elsevier, USA, ISBN: 0-1208-8757-6
6. Barik SR, Nayak B, Dash S (2014) A comparative analysis of three level VSC based multi-pulse STATCOM. Int J Eng Technol (IJET) 6(3):1550–1563
7. Kouadri Benatman, Tahir Yamina (2008) Power flow and transient stability modelling of a 12-pulse STATCOM. J Cybern Inf 7:9–25
8. Singh B, Srinivas KV (2009) Three-level 12-pulse STATCOM with constant DC link voltage. In: Annual IEEE India conference (INDICON), 18–20 Dec 2009, pp 1–4
9. Anadol MA, Aydin M, Yalcinoz T (2013) A real-time extraction of active and reactive current using microcontrollers for a multipulse STATCOM. Turk J Electr Eng Comput Sci 21 (4):1044–1060

10. Chandrasekhar S, Brahmmam J, Srinu M (2013) Mitigation of voltage flicker and reduction in THD by using STATCOM. Int J Electr Comput Eng (IJECE) 3(1):102–108
11. Agiwara MH, Akagi H (2005) An approach to regulating the DC-link voltage of a voltage-source BTB system during power line faults. IEEE Trans Ind Appl 41(5):1263–1271
12. Hagiwara M, Fujita H, Akagi H (2003) Performance of a self-commutated BTB HVDC link system under a single-line-to-ground fault condition. IEEE Trans Power Electron 18 (1):278–285
13. Voraphonpiput, N, Chatratana, S (2004) Analysis of quasi 24-pulse STATCOM operation and control using ATP-EMTP. In: IEEE region 10 conference TENCON 2004, 21–24 Nov 2004, vol C, pp 359–362
14. Singh B, Saha R (2006) A new 24-pulse STATCOM for voltage regulation. In: International conference on power electronics, drives and energy systems, 12–15 Dec 2006, pp 1–5
15. Srinivas KV, Singh B (2010) Three-level 24-pulse STATCOM with pulse width control at fundamental frequency switching. In: IEEE industry applications society annual meeting (IAS), 3–7 Oct 2010, pp 1–6
16. Khorrami Navid (2012) Simulation and modeling of 24-pulse STATCOM in EMTDC/PSCAD program in order to regulate voltage and dynamic stability improvement. Res J Appl Sci Eng Technol 4(3):152–158
17. Geethalakshmi B, Dananjayan P (2009) A combined multipulse-multilevel inverter based STATCOM for improving the voltage profile and transient stability of power system. Int J Power Electron 1(3):267–285
18. Padmaja SM, Tulasiram Das G (2011) A novel controller based 48-pulse STATCOM for reactive power compensation and voltage stabilization in high voltage applications. ACEEE Int J Electr Power Eng 2(1):43–49
19. Molina Marcelo G, Mercado Pedro E (2013) Primary frequency control of multi-machine power systems with STATCOM-SMES: a case study. Electr Power Energy Syst 44:388–402
20. El-Moursi MS, Sharaf AM (2006) Novel reactive power controllers for the STATCOM and SSSC. Electr Power Syst Res 76:228–241
21. Colak Ilhami, Kabalci Ersan, Bayindir Ramazan (2011) Review of multilevel voltage source inverter topologies and control schemes. Energy Convers Manage 52(2):1114–1128
22. Colak Ilhami, Kabalci Ersan (2011) Practical implementation of a digital signal processor controlled multilevel inverter with low total harmonic distortion for motor drive applications. J Power Sources 196(18):7585–7593
23. Gultekin B, Gerçek CO, Atalik T, Deniz M, Biçer N, Ermis M, Kose KN, Ermis C, Koç E, Çadirci I, Açik A, Akkaya Y, Toygar H, Bideci S (2012) Design and implementation of a 154-kV ± 50-Mvar transmission STATCOM based on 21-level cascaded multilevel converter. IEEE Trans Ind Appl 48(3):1030–1045
24. Shaha NM, Soodb VK, Ramachandran V (2009) Modeling, control and simulation of a chain link STATCOM in EMTP-RV. Electr Power Sys Res 79:474–483
25. Muñoz Javier A, Espinoza José R, Baier Carlos R, Morán Luis A, Guzmán Johan I, Cárdenas Víctor M (2014) Decoupled and modular harmonic compensation for multilevel STATCOMs. IEEE Trans Ind Electron 61(6):2743–2753
26. Meynard TA, Foch H (1992) Multi-level conversion: high voltage choppers and voltage-source inverters. In: 23rd Annual IEEE power electronics specialists conference, vol 1, pp 397–403
27. Soto Diego, Green Tim C (2012) A comparison of high-power converter topologies for the implementation of FACTS controllers. IEEE Trans Ind Electron 49(5):1072–1080
28. Gultekin Burhan, Ermis Muammer (2013) Cascaded multilevel converter-based transmission STATCOM: system design methodology and development of a 12 kV ± 12 MVAr power stage. IEEE Trans Power Electron 28(11):4930–4950
29. Zhao G, Liu J, Han M (2011) Design of input filters considering the stability of STATCOM systems. J Power Electr 11(6):904–913
30. Wang Bingsen, Cathey Jimmie J (2003) DSP-controlled, space-vector PWM, current source converter for STATCOM application. Electr Power Syst Res 67:123–131

31. Xia Zhenglong, Shi Liping, Yang Xiaodong (2014) Parameters design and control strategy of cascade STATCOM based on LCL filter. Int J Control Autom 7(1):307–320
32. Okou FA, Dupuis D, Akhrif O, Tarbouchi M (2009) A robust nonlinear controller for a StatCom based on a 3-phase neutral point clamped converter. In: 35th Annual conference of IEEE industrial electronics, pp 3623–3630
33. Wang C, Yin X, Wen M, Jian L, Xiong Q, Zhang B (2010) Structure and parameters design of output LC filter in D-STATCOM. In: International conference on power system technology (POWERCON), pp 1–6
34. Lauttamus P, Tuusa H (2011) Model-based cascade control of three-level STATCOM with a tuned LCL-filter. In: Twenty-sixth annual IEEE applied power electronics conference and exposition (APEC), 6–11 Mar 2011, pp 1569–1575
35. Escobar G, Stankovic AM, Mattavelli P(2000) Reactive power, imbalance and harmonics compensation using D-STATCOM with a dissipativity-based controller. In: Proceedings of the 39th IEEE conference on decision and control, vol 4, pp 3051–3055
36. Ping T, Xianggen Y, Zhe Z (2011) Topology analysis of the output filter in D-STATCOM and its parameters multi-objective optimal design. In: International conference on advanced power system automation and protection, 16–20 Oct 2011, vol 2, pp 998–1002
37. He Chao, Xie Xin, Yan Hui, Xie Chuan, Chen Guozhu (2011) A novel grid-connected converter with active power filtering function. Energy Procedia 12:348–354
38. Tavakoli Bina M, Eskandari MD, Panahlou M (2005) Design and installation of a ± 250 kVAr D-STATCOM for a distribution substation. Electr Power Syst Res 73(3):383–391
39. Nakamura S, Kojima H, Matsui K, Mori H, Ueda F (2005) STATCOM circuit having active filter function for lower order harmonics. In: The international conference on electrical engineering, vol 1, pp 1–6
40. Morán L, Dixon J, Espinoza J, Wallace R (1999) Using active power filters to improve power quality. In: 5th Brasilian power electronics conference, 19–23 Sept 1999, pp 501–511
41. Afonso JL, Aredes M, Watanabe E, Martins JS (2000) Shunt active filter for power quality improvement. In: International conference UIE 2000—electricity for a sustainable urban development, Lisboa, Portugal, 1–4 Nov 2000, pp 683–691
42. Basu TS, Bhattacharya A, Chakraborty C (2010) Shunt active power filter/STATCOM topology for medium/high power applications: parallel inverters operating at different switching frequencies. In: 36th annual conference on IEEE industrial electronics society, 7–10 Nov 2010, pp 2669–2674
43. Kanaan HY, Hayek A, Al-Haddad K (2007) Averaged-model-based nonlinear control of a PWM three-phase four-leg shunt active power filter. In: Canadian conference on electrical and computer engineering, 22–26 Apr 2007, pp 1002–1005
44. Kalyankumar D, Kirubakaran V (2010) D-STATCOM based voltage regulation and harmonic damping. Int J Comput Appl 7(4):39–43
45. Sanz-Bobi MA (ed) (2014) Use, operation and maintenance of renewable energy systems, green energy and technology. Springer International Publishing, Switzerland. doi:10.1007/978-3-319-03224-5_7
46. Routray SK, Nayak N, Rout PK (2010) A robust fuzzy sliding mode control design for current source inverter based STATCOM application. Procedia Technol 4:342–349
47. Fukuda S, Imamura R (2005) Application of a sinusoidal internal model to current control of three-phase utility-interface converters. IEEE Trans Ind Electron 52(2):420–426
48. Filizadeh S, Gole AM (2005) Harmonic performance analysis of an OPWM-controlled STATCOM in network applications. IEEE Trans Power Delivery 20(2):1001–1008
49. Cetin A, Ermis M (2009) VSC-based D-STATCOM with selective harmonic elimination. IEEE Trans Ind Appl 45(3):1000–1015
50. Lin W (2006) A new approach to the harmonic analysis of SPWM waves. In: Proceedings of the 2006 IEEE international conference on mechatronics and automation, 25–28 June 2006, pp 390–394

51. Ghuo Pan Z, Peng FZ (2007) A novel SPWM method with voltage balancing capability for multilevel rectifier/inverter systems. In: Twenty second annual IEEE applied power electronics conference, 25 Feb–1 Mar 2007, pp 1109–1115
52. Hua CC, Wu CW, Chuang CW (2007) Fully digital control of 27-level cascade inverter with variable DC voltage sources. In: 2nd IEEE conference on industrial electronics and applications, 23–25 May 2007, pp 2441–2448
53. Colak Ilhami, Kabalci Ersan (2013) Developing a novel sinusoidal pulse width modulation (SPWM) technique to eliminate side band harmonics. Int J Electr Power Energy Syst 44 (1):861–871
54. Kabalci E (2014) Power electronics and drives used in automotive applications. In: Bizon N, Dascalescu L, Tabatabaei NM (eds) Autonomous vehicles: intelligent transport systems and smart technologies. ISBN: 978-1-63321-324-1, 3rd Quarter
55. Sao CK, Lehn PW, Iravani MR, Martinez JA (2002) A benchmark system for digital time-domain simulation of a pulse-width-modulated D-STATCOM. IEEE Trans Power Delivery 17 (4):1113–1120
56. Patel HS, Hoft RG (1973) Generalized harmonic elimination and voltage control in thyristor converters: part I—harmonic elimination. IEEE Trans Ind Appl 9:310–317
57. Mohapatra M, Babu BC (2010) Fixed and sinusoidal-band hysteresis current controller for PWM voltage source inverter with LC filter. In: Students' technology symposium (TechSym). 3–4 Apr 2010, IEEE, pp 88–93
58. Venkata Ranganadh B, Mallikarjuna Prasad A, Sreedhar M (2013) Modelling and simulation of a hysteresis band pulse width modulated current controller applied to a three phase voltage source inverter by using matlab. Int J Adv Res Electr Electron Instrum Eng 2(9):4378–4387

Chapter 2
Multilevel Converter Topologies for STATCOMs

Anshuman Shukla and Alireza Nami

Abstract To implement the STATCOMs for transmission and distribution applications, high power converters are needed. A multilevel converter is a logical choice for such applications as it can meet the imposed line side current and voltage harmonic distortion standards without extending its device ratings. Several types of monolithic multilevel converters have been proposed based on different structures of a DC link voltage (or current) to generate staircase output voltage (or current) levels. The multilevel current source converters (CSC) are also a potential configuration for STATCOM. Multilevel CSCs using fully controllable switches have the advantages of low output harmonics and controllable active and reactive power. During the last decade, modular multilevel converters have shown a breakthrough and have made their way to commercial high power applications. Modularity, in general, refers to a technique to develop comparably large systems by combining smaller subsystems. For power converter topologies, this means, a cascaded connection of converter cells seems to be an interesting solution to reach high voltage and high quality waveforms with a minimum complexity. This chapter provides an overview on monolithic and modular multilevel converter topologies, targeting high-power applications and in particular STATCOM. Modular multilevel converters can be built either straightforward by applying the modular building block cells or by a combination of cells with monolithic multilevel topologies. The monolithic and modular CSCs can also be realized by employing the duality concept on each corresponding Voltage Source Converter (VSC). This chapter summarizes the most recent developments made for multilevel converter

A. Shukla (✉)
Department of Electrical Engineering, Indian Institute of Technology Bombay, Mumbai, India
e-mail: ashukla@ee.iitb.ac.in

A. Nami
RDPTEPS, ABB AB, Corporate Research, Västerås, Sweden
e-mail: alireza.nami@se.abb.com

F. Shahnia et al. (eds.), *Static Compensators (STATCOMs) in Power Systems*, Power Systems, DOI 10.1007/978-981-287-281-4_2

topologies, by covering new promising topologies and operational issues. In addition, emerging trends, challenges, and possible future directions of the multilevel converter technologies are outlined.

Keywords VSC · CSC · STATCOM · Multilevel · Submodule · Modular

2.1 Introduction

The most important component in a STATCOM is a power electronic based static converter. The main objective of this converter is to produce an AC output waveform from a DC power supply. According to the type of DC source used, i.e., voltage or current, there are two types of converter topologies prevailing: VSC and CSC, as illustrated in Fig. 2.1. These converters are constructed using power switches, like IGBTs. In a VSC, each basic switching element is composed of a fully controllable, unidirectional semiconductor switch with a diode connected in antiparallel to it. In a CSC, each switching element is required to block bipolar voltage when open and to conduct at least unidirectional current when closed. A bidirectional current conducting switch may also be used for enhanced flexibility and functional improvements. A reverse blocking device can be composed by a fully controllable switch in series with a diode. The fully controllable semiconductor switch considered in this chapter is the IGBT as it suits the high frequency switching operation for both low and medium voltage distribution system compensation as well as can meet the high voltage and power requirements for transmission system compensation [1–11].

There are various converter configurations available for both single and three-phase applications. The most fundamental of all these are single-phase half bridge and full bridge (H-bridge) VSC and CSC as shown in Fig. 2.2. The single-phase half-bridge is a one-leg converter consisting of two switching elements. This topology can be used to obtain a two-level output of the VSC. The single-phase H-bridge is a two-leg converter with each leg consisting of two switching elements. The H-bridge VSC is more popular for single-phase applications because with same DC input voltage the output of the full bridge is twice that of the half bridge. This topology of VSC can also be used to obtain a two-level output. Additionally a zero

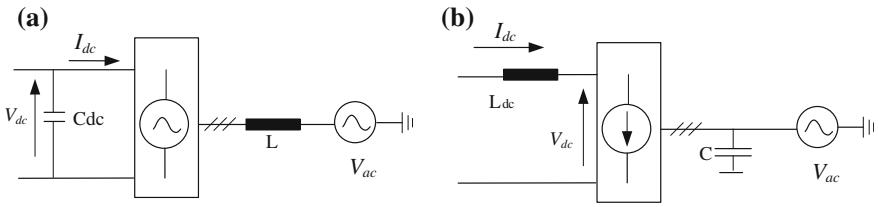

Fig. 2.1 Grid connected converters: **a** VSC **b** CSC

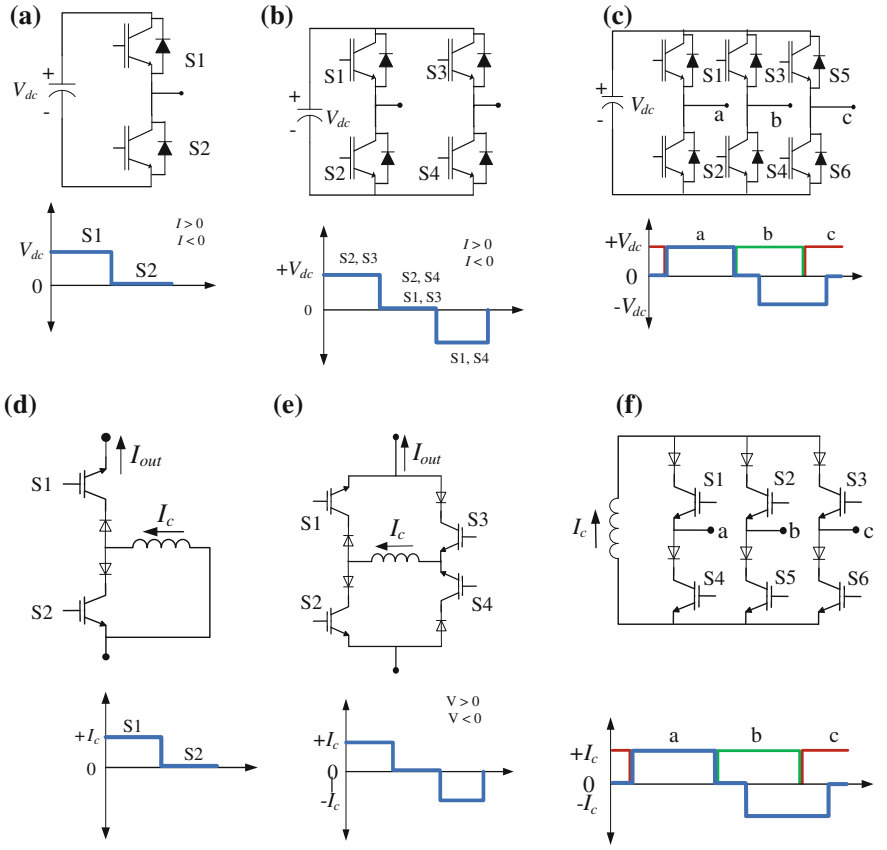

Fig. 2.2 **a** Half bridge VSC, **b** full bridge or H-ridge VSC, **c** three-phase two-level VSC, **d** half-bridge CSC, **e** full bridge CSC and, **f** three-phase two-level CSC

voltage can be placed with the full bridge to obtain a three-level output. The H-bridge topology with the aid of suitable transformers is used for both low voltage and medium voltage distribution system compensation [12]. Finally a three-phase two-level converter can be synthesized by parallel connection of the half-bridge phase legs across the DC-link. CSC topologies may be generated from the respective VSC topologies by employing the duality principles. The half-bridge CSC is shown in Fig. 2.2c which is exactly the dual of the half-bridge VSC converter. Therefore, dual to the voltage source full- and three-phase bridges, is realized by connecting the inductor cells in parallel as shown in Fig. 2.2e, f.

The STATCOM can be used in different power levels depending on the applications. There are mainly three-main areas for the STATCOM application on the basis of different power levels as shown in Fig. 2.3. To implement the STATCOMs at medium and high power level, high power converter is needed that in most cases exceeds the power handling capability of a simple two level converter without

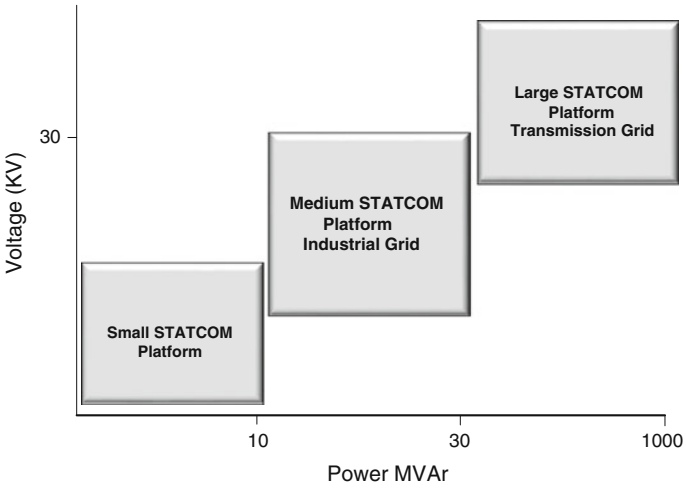

Fig. 2.3 Power level of STATCOMs

device series/parallel connection. Conventionally, for such high power applications and for boosting up the DC bus voltage beyond the voltage rating of an individual switch, the two level converter has to use series connected devices. Similarly, In this case, the series connected low rating devices act as a single switch like one of the switches shown in Fig. 2.1. However, due to the different scattering times of semiconductor devices, the following issues must be well considered in order to avoid voltage-sharing problems among the switches. The electrical and thermal characteristics of the semiconductor devices in the same switch need to be matched. The synchronization of the switching is very difficult and may result in voltage unbalance between the devices. Additional care is needed for the turning-off process of the switch, as well as for its gate currents. As a result of these restrictions, power dissipation during conduction and switching is such that the switching frequency is severely limited. This causes a slow system response and bulky output filter circuits. Large snubber circuit parameters are also required to compensate transient voltage unbalance and to achieve static voltage balancing. It may also lead to more switching losses and relatively longer switching time. Although the blocking voltage of the switch in the two-level converter is increased, a step-up transformer is still needed for coupling to the transmission networks. Moreover, extra efforts are needed to match the harmonic standards at the two-level converter outputs.

Another possible way of achieving such high power requirement is to use magnetic transformer coupled multi-pulse converters [5]. Traditional magnetic coupled multi-pulse converters typically synthesize the staircase voltage wave by varying transformer turns ratio with complicated zigzag connections. For example, a typical 48-pulse converter consists of eight 6-pulse converters connected together through eight zigzag-arrangement transformers using the harmonic cancellation

technique, or connected through Wye/Delta and Delta/Delta connection transformers and using sophisticated control schemes, in order to reduce harmonic distortion and to reach high voltage. The patent of Unified Power Flow Controller (UPFC) [13] shows that the shunt-side and the series- side of the UPFC are based on eight, 2-level, three-phase bridge VSCs. A high power converter arrangement is then achieved by synthesizing the voltage waveform using complicated zigzag transformer connections to ensure that the Total Harmonic Distortion (THD) standards are finally met. In 1995, the first ± 100 MVA STATCOM was installed at the Sullivan substation of Tennessee Valley Authority (TVA) in northeastern Tennessee [14]. This unit is mainly used to regulate 161 kV bus during the daily load cycle to reduce the operation of the tap changer of a 1.2 GVA-161 kV/500 kV transformer. Its 48-pulse power converter consists of eight two-level VSCs with complex-interface magnetic circuits. Because this is a two-level VSC, a series connection of five of gate-turn-off (GTO) thyristors is used as a main switch. The control scheme used in this STATCOM is a 60 Hz staircase. Due to the slow switching speed of the GTOs, the firing angles of the output waveform are fixed; therefore, the amplitude of each output waveform is controlled by exchanging active power of the DC-link capacitor with the power grid. Since it began operating, several weak points of the TVA-STATCOM system have been pointed out [15]. Some of these weak points were due to the use of series connected switching devices as discussed above. Taking feedback from the experiences of this installation, in the AEP UPFC installation, Inez area, eastern Kentucky, USA, the VSCs were designed to make use of three-level configuration instead of a two level used earlier in the TVA STATCOM project [15]. However, this structure still used the multi-pulse arrangement. The limitations with this multi-pulse arrangement with magnetic transformer coupling method are [16]: (i) they are very expensive, (ii) produce about 50 % of the total losses of the system, (iii) occupy up to 40 % of the total system's real estate, (iv) cause difficulties in control due to DC magnetizing and surge overvoltage problems resulting from saturation of the transformers in transient states and (v) are prone to failure. Therefore, the capacitor voltage synthesis method is preferred to magnetic coupling method for achieving higher rating converters. An attractive alternative to the above discussed topologies and most recent development in the field of high power converters is the multilevel converter.

For the STATCOM applications in utility and distribution systems, the conventional two-level converters are most commonly used in low to medium voltage levels. For medium and high-voltage networks, the conventional STATCOM structures are designed on the basis of simple two-level converter and use transformer to meet the desired voltage profile. In some cases, in order to achieve higher power level, converters are connected in parallel to the DC bus. This type of connection requires a transformer with multiple secondary windings, increasing the cost and complexity of the power topology. Further, the transformer adds to the losses in the system and it may saturate once the load draws any DC current. For the STATCOM applications in utility and distribution systems, it is preferable to perform faster switching actions to have fast dynamic response, improved robustness and a continuously spread harmonic spectrum. However, at higher power, the long tail current associated with the

device (IGBT) characteristics prohibits higher switching frequency operation at a high power and the efficiency of the compensator is lower due to significant switching losses [17]. Therefore, the compensator control in high power applications faces difficulties. Further, such higher frequency operation using the two-level converter based compensator is not always possible because of the switching frequency limitation imposed on presently available higher rated devices. Again, the series connection of devices and/or multistep converter configuration is not recommended due to their respective limitations stated above.

For medium to high power applications and to meet the line side imposed current and voltage harmonic distortion standards, the multilevel converter is a logical selection without extending its device ratings. As discussed above, the series connection of the devices faces voltage unbalance problem. In case of a VSC, the best method of stabilizing voltages applied to the devices is by clamping those using DC voltage sources or large capacitors, which transitorily behave as voltage sources. Multilevel VSC topologies are based on this principle and therefore, the voltage applied to the device can be controlled and limited. The multilevel CSC topologies are based on the principle of current clamping using inductors. All the available multilevel CSC topologies have been derived from their corresponding equivalent multilevel VSC topologies using the duality principle [9]. In the following, the discussion presented focuses mostly on the multilevel VSC topologies. However, these can be interpreted similarly for the CSC topologies using the duality principle.

Without semiconductor devices connected in series, the multilevel VSCs show feasible capability of clamping the voltages across individual devices below their limitations. This allows the recent semiconductor devices to be utilized in higher-voltage applications without incurring voltage-sharing problems. In a multilevel converter, the number of possible operating states increases and as a consequence, the flexibility of the converter improves. Another significant advantage of the multilevel configuration is the harmonic reduction in the output waveform with very low switching frequency. Hence the output voltages can be filtered with smaller reactive components. They also provide lower electromagnetic interference and lower acoustic noise. Besides the high-voltage capability, multilevel converters also provide other advantages over the two-level converters. As all the devices are individually controlled, better control over voltage magnitude and harmonic suppression can be achieved. Use of a multilevel converter reduces the required transformer voltage ratio and sometimes even makes possible direct connection of the compensator to the increased voltage supply systems without needing interconnecting transformer. The multilevel converter topologies are attractive for continuous control of system dynamic behavior and to reduce power quality problems such as voltage harmonics, voltage imbalance or sag and have better properties under sudden changes of loads. Besides, a multilevel compensator, in comparison with its two level counterparts, makes more exact formation of the compensating currents possible. Hence, these are suitable for STATCOM applications in both transmission and distribution systems [18–21].

There is a wealth of literature available on the characteristics and controls of the multilevel converters. For the past two decades, multilevel VSC technology has

been a rapidly developing area in power electronics and has been proposed as the best choice in several medium and high voltage applications. It promises power-conversion equipment for applications that operate in the medium-voltage (4.6–13.8 kV) grid without requiring step-up transformers [22]. With the step-up transformer, the multilevel converter may also be operated at higher voltage levels, such as transmission levels. Multilevel VSC technology has recently been utilized in various types of industrial applications, such as AC power supplies, reactive power compensations, adjustable speed drive systems, etc. [3, 4]. Besides, it has also found applications in enabling the use of renewable energy sources. Renewable energy sources such as photovoltaic, wind and fuel cells can be easily interfaced to a multilevel converter system for a high power application [23]. Another application for multilevel converters is to interconnect different power grids [24]. In the following sub-section, the concepts, features, advantages, limitations and classification of multilevel VSCs have been presented.

2.1.1 Multilevel Converters: Basic Concepts and Features

The concept of multilevel converters was first introduced in 1975 [25]. The term multilevel began with the three-level converter. Subsequently, several multilevel converter topologies have been developed [1–4]. The elementary concept of a multilevel VSC to achieve higher power is to use a series of power semiconductor switches with several lower voltage DC sources. The DC voltage sources can be realized by capacitors, batteries, and renewable energy voltage sources. These multiple DC sources are aggregated using the power semiconductor switches in order to achieve high voltage at the output. However, the rated voltage of the power semiconductor switches is kept at only a fraction of the total DC voltage. The AC voltage produced from these DC voltages approaches a sinusoid with increasing the number of levels. The multilevel VSC can work in both rectifier and converter modes as it uses the bi-directional switches.

Fundamentally, as discussed earlier, the output voltage waveform of a multilevel VSC is synthesized from different levels of voltages obtained from DC voltage sources. Figure 2.4 shows an equivalent circuit of a half bridge of a multilevel VSC. A bi-directional, single-pole, multi-throw switch is a key element of the multilevel topology. By controlling the way in which the switch is connected to a portion of the capacitors, a number of output voltage levels can be synthesized. To generate a negative output voltage, the reference of the output can be connected to different segments of the capacitor string. Two or more half bridge of the converter shown in Fig. 2.2 can be utilized to form a multiphase, multilevel converter.

Figure 2.5 illustrates an example of a multilevel converter output voltage waveform. In this figure, an eleven level Pulse Width Modulation (PWM) waveform is shown with a peak-to-peak voltage of 1.0 kV. In this case, the multilevel converter produces a fair approximation to a sinusoidal waveform.

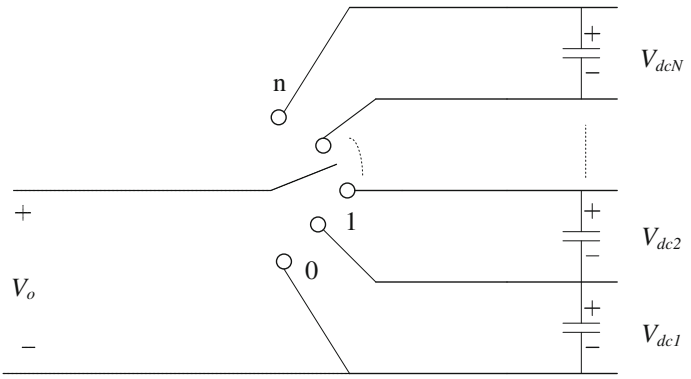

Fig. 2.4 Equivalent circuit of multilevel voltage-source converters

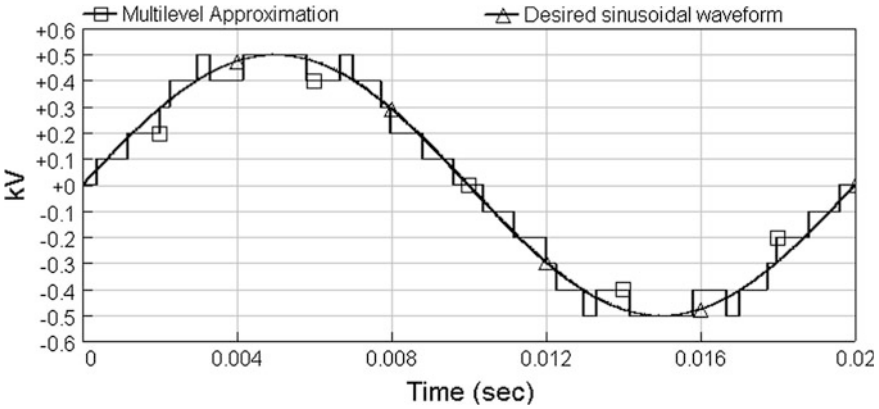

Fig. 2.5 Example multilevel sinusoidal approximation using eleven-levels (V_0)

As one can see in Fig. 2.4, the multilevel converter output stepped waveform contains sharp transitions. This phenomenon results in harmonics, in addition to the fundamental frequency of the sinusoidal waveform. The key issue for a converter modulation is the harmonics elimination. The increased number of levels provides the opportunity to eliminate more harmonic contents. Eliminating some harmonic contents will make it easier to filter the remaining harmonic content. As a result, filters will be smaller and less expensive. There are many schemes available in the literature for reducing the harmonic contents. In Fig. 2.4, the multilevel waveform has been obtained using a multicarrier PWM modulation technique. This scheme simply refers to switching on or off the converter switching devices based on intersection of the modulation signal (mostly, a sinusoidal waveform) with a number of carrier signals (mostly, of triangular shape) in a certain fashion. The number of carrier signals depends on the number of phase output voltage levels of the converter.

A multilevel converter has several advantages over a conventional two-level converter that uses high switching frequency PWM. Some important attractive features of a multilevel converter can be briefly summarized as follows [1–4].

- *Multilevel waveform quality*: The electromagnetic compatibility (EMC) problems can be reduced as the multilevel converters generate the output voltages with lower distortion and reduced *dv/dt* stresses.
- *Common mode* (CM) *voltage*: Multilevel converters produce smaller CM voltage and it can be eliminated using some advanced modulation techniques; therefore, the premature failure of the motor bearings and the EMI issues can be avoided.
- *Input current*: The input current drawn by the multilevel converters is of lower distortion.
- *Voltage transients*: Multilevel waveforms naturally limit the problems of large voltage transients.
- *Switching frequency*: The switching frequency of the power semiconductor switches in a multilevel converter can be much lower than that in a two-level converter for the same harmonic spectrum of the converter outputs. A lower switching frequency implies lower switching loss and higher efficiency.
- *Switch ratings*: Since multilevel converters usually utilize a large number of DC voltages, several switches are required to block smaller voltages. Since switch stresses are reduced, required switch ratings are lowered.
- *System reliability*: If a component fails in a multilevel converter, most of the time it can still be used at a reduced power level. Furthermore, a desired voltage can be produced by more than one way as the multilevel converters tend to have switching redundancies.
- *Application practicality*: Multilevel converters allow for the utilization of smaller, more reliable components.
- *Ride through capability*: Under emergency conditions, like when voltage sags or load swings are experienced at the utility connection, the multilevel converter can also be used to provide ride-through capability if the DC sources are banks of batteries or capacitors.

Unfortunately, multilevel converters do have some disadvantages as listed below [1–4].

- It uses a greater number of power semiconductor switches. Although lower rated switches can be utilized but each switch requires a related gate drive circuit. It may lead to a more expensive and complex system (part of the increased cost may be offset by the fact switches with lower ratings are being used). Using more devices also means the probability of a system failure will increase.
- Another disadvantage of multilevel converters concerns control of the switches. The increased number of switches will result in more complicated control.
- A multilevel converter arrangement requires several DC voltage sources, which are usually provided by capacitors. Balancing the voltages of these capacitors

according to an operating point is a difficult challenge. Capacitors are also prone to failure.

- The number of the achievable voltage levels is limited by voltage-imbalance problems, voltage clamping requirements, circuit layout and packaging constraints, complexity of the controller, and, of course, capital and maintenance costs.

Despite these drawbacks, multilevel converters have emerged as the most preferred candidate for high power applications. Furthermore, as prices of power semiconductors and other associated components continue to decrease, the use of multilevel topologies is expected to extend to medium/low power applications (those of less than 10 kW) as well. Fast power devices (e.g., CMOS transistors), which can operate at very high switching frequencies, can be used for low voltages. Therefore, the values of the reactive components will undergo significant reduction. Furthermore, new power devices are expected to appear in the near future and these may also extend the application of multilevel topologies.

During the last two decades, several state-of-the-art multilevel converter topologies have been introduced by both academia and industries. These topologies can be broadly classified in two groups namely; (i) Monolithic converters and (ii) Modular converters. Both the VSC and CSC configurations are available for these topologies. The monolithic VSC and CSC topologies have been described first in the following section.

2.2 Monolithic Multilevel Converters

Several types of monolithic multilevel converters have been proposed based on different structures of their DC voltage (or current) sources to generate staircase output voltage (or current) levels. The two most actively developed of these topologies are the diode-clamped multilevel converter and flying capacitor multilevel converter. There are other names also used to define these topologies. For example, when referring to the three-level diode-clamped converter, it is called the neutral-point-clamped (NPC) converter. Similarly, the flying capacitor converter is also known as floating capacitor and capacitor clamped converter. In the following sub-sections, these two monolithic multilevel converter topologies have been described. The intention is to give a brief review of these basic topologies with their specific features, advantages, drawbacks, operating principles and their comparison.

2.2.1 Diode-Clamped Multilevel Converter (DCMC)

The first practical (and still widely studied) multilevel topology is the neutral-point-clamped (NPC) PWM topology first introduced by Nabae et al., in 1981 [26]. This is essentially a three-level diode-clamped Converter. The VSC and CSC configurations of DCMC are described in the following sub-sections.

2.2.1.1 DCMC

Figure 2.6 shows the three-phase NPC topology. The NPC consists of two pairs of series switches (e.g., S_1, S_2 and S_{11}, S_{21} in phase-a, Fig. 2.6) in each phase. The DC-link consists of two series capacitors (C_1, C_2 in Fig. 2.6). In each phase, two diodes, called the clamping diodes are used (e.g., D_1, D_2 in phase-a, Fig. 2.6) where the anode of the upper diode is connected to the midpoint (neutral) of the capacitors and its cathode to the midpoint of the upper pair of switches; the cathode of the lower diode is connected to the midpoint of the capacitors and divides the total DC-link voltage into smaller voltages, which is shown in Fig. 2.6. If the point n is taken as the ground reference, the three possible phase voltage outputs are $-V_{dc}/2$, 0, and $V_{dc}/2$. The line-line voltages of two legs with the common DC capacitors are: $V_{dc}, V_{dc}/2, 0, -V_{dc}/2$ and $-V_{dc}$. Table 2.1 lists the switching states for producing three-level phase voltage outputs per phase in the topology of Fig. 2.6. As is evident from this table that the switch pairs (S_1, S_{11}) and (S_2, S_{21}) are complementary. Similar switch states exist in all the three phases to produce corresponding three-level voltage outputs. The key components that distinguish this circuit from a conventional two-level converter are the clamping diodes. These diodes clamp the switch voltage to half the level of the DC-link voltage. For example, when both S_1 and S_2 turn on, the voltage across a and n is $V_{dc}/2$, i.e., $V_{an} = V_{dc}/2$ (Table 2.1). In this case, D_{11} balances out the voltage sharing between S_{11} and S_{21} with S_{11} blocking the voltage across C_1 and S_{21} blocking the voltage across C_2.

The three-level topology discussed above can be extended to higher-level configurations. Several researchers published articles that have reported experimental results for four-, five-, and six-level diode-clamped converters for such uses as static

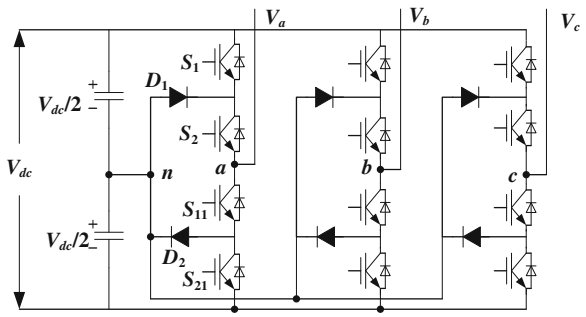

Fig. 2.6 Three-phase three-level structure of a DCMC

Table 2.1 Switching scheme for NPC

S_1	S_2	S_{11}	S_{21}	V_{an}
1	1	0	0	$V_{dc}/2$
0	1	1	0	0
0	0	1	1	$-V_{dc}/2$

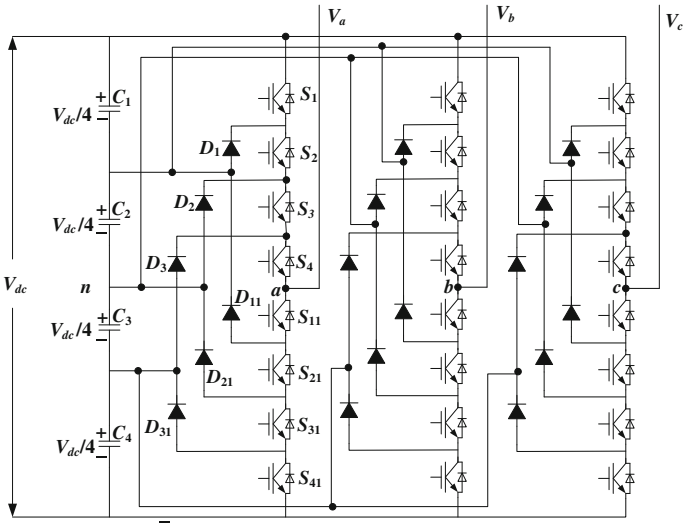

Fig. 2.7 Three-phase five-level structure of a diode-clamped multilevel converter

VAr compensation, variable speed motor drives, and high-voltage system interconnections, etc. [1–4, 27]. A three-phase five-level DCMC is shown in Fig. 2.7. Each of the three phases of the converter shares a common DC bus, which is subdivided by four capacitors into five levels. The voltage across each capacitor is $V_{dc}/4$, and the voltage stress across each switching device is limited to $V_{dc}/4$ through the clamping diodes. Table 2.2 lists the possible output voltage levels for one phase of the five-level converter with the neutral point n taken as a reference. State condition 1 means the switch is on, and 0 means the switch is off. Each phase has four complementary switch pairs such that turning on one of the switches of the pair requires that the other complementary switch be turned off. The complementary switch pairs for phase leg a are (S_1, S_{11}), (S_2, S_{21}), (S_3, S_{31}) and (S_4, S_{41}). Table 2.2 also shows that four adjacent main devices are on and in series for any voltage level output. For the higher voltage levels $(V_{dc}/2,\ -V_{dc}/2)$, the four on devices clamp the phase output to the top or bottom of the DC bus. For the lower voltage levels $(-V_{dc}/4,\ 0, V_{dc}/4)$, the on devices together act as a short connecting two of the clamping diodes back-to-back. The other end of these back-to-back

Table 2.2 Switching scheme for a five-level diode-clamped converter

S_1	S_2	S_3	S_4	S_{11}	S_{21}	S_{31}	S_{41}	V_{an}
1	1	1	1	0	0	0	0	$+V_{dc}/2$
0	1	1	1	1	0	0	0	$+V_{dc}/4$
0	0	1	1	1	1	0	0	0
0	0	0	1	1	1	1	0	$-V_{dc}/4$
0	0	0	0	1	1	1	1	$-V_{dc}/2$

clamping diodes are connected to one of the nodes (2, n, or 3, Fig. 2.7) along the DC bus. The circuit then can be thought of as a type of multiplexer, attaching the output to one of the five available voltage levels.

Figure 2.8 shows a line-line voltage output of a five-level converter, which is a nine-level waveform. This means that an m-level DCMC has an m-level output phase voltage and a $(2m - 1)$-level output line voltage.

In a DCMC, although each active switching device is required to block only a voltage level of $V_{dc}/4$, the clamping diodes require different ratings for reverse voltage blocking. Using phase a of Fig. 2.7 as an example, when all the lower switches S_{11} through S_{41} are turned on, D_3 must block three voltage levels, or $3V_{dc}/4$. Similarly, D_2 must block $V_{dc}/2$ and D_1 must block $V_{dc}/4$. This rule can be similarly defined for an m-level converter. If the converter is designed such that each blocking diode has the same voltage rating as the active switches then D_n and D_{n1} (for $n = 1,\ 2,$ or 3) in Fig. 2.7 will require n diodes in series. Consequently, the number of diodes required for each phase would be $(m - 1) \times (m - 2)$. Similarly, an m-level converter requires $(m - 1)$ capacitors at the DC bus as is also evident from Figs. 2.6 and 2.7. Also, each phase leg consists of $2 \times (m - 1)$ active switches. The net DC voltage (V_{dc}, Figs. 2.6 and 2.7) should be evenly distributed among the DC capacitors for having symmetric and desired m-level waveform.

It should be noted that DCMCs with odd number of levels $(m = 3,\ 5,\ 7,\ \ldots)$ offer a neutral point access. It is also possible to synthesize topologies with even number of levels $(m = 4,\ 6,\ 8,\ \ldots)$. However, in single-phase applications where a neutral point is needed, DCMC with even number of levels cannot be used. Though they have proven to be well suited for drive applications [27].

The DCMC is the most researched topology among the different multilevel converter topologies. One application of the DCMC is an interface between a High Voltage DC (HVDC) transmission line and an AC transmission line [28]. Another application is a variable speed drive for high-power medium-voltage (2.4–13.8 kV)

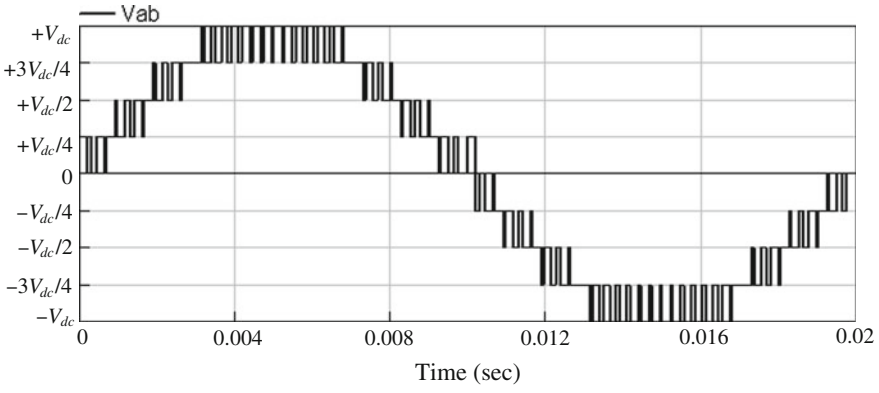

Fig. 2.8 Line voltage waveform of a five-level diode-clamped converter

motors. For drives applications, it is the most widely used structure [27]. STATCOM is another application where the DCMC has found wide acceptance. The world's first UPFC was based on DCMC [14, 15]. Some recent proposals for the STATCOM applications are also based on DCMC [18–22].

The main advantages and disadvantages of multilevel diode-clamped converters are as follows [1–4, 27].

Advantages

- All phases share a common DC bus, which minimizes the capacitance requirements of the converter. Therefore, a back-to-back topology is possible and also practical for uses such as a HVDC and an adjustable speed drive.
- The DC capacitors can be easily precharged as a group unlike the other multilevel converter structures, where precharging and startup are more complex.
- The current ripple in the capacitors is of the order that is greater and or equal to 3rd harmonics (in the flying capacitor converter, the capacitors current ripple may be of the order of fundamental frequency or greater depending on the modulation strategy).
- Although some additional clamping diodes are required, it requires a low number of capacitors. A low number of reactive components is usually preferred from the standpoint of cost.

Disadvantages

- For more than three-level DCMC structure, the voltage stresses across the clamping diodes are non-uniform. For example, in Fig. 2.7, D_1, D_{31} are subjected to the voltage stress of $V_{dc}/4$, D_2, D_{21} are subjected to the voltage stress of $V_{dc}/2$, and D_{11}, D_3 are subjected to the voltage stress of $3V_{dc}/4$. This issue complicates the design and raises reliability and cost concerns.
- For some operating conditions, it has been demonstrated that the charge balance of the DC capacitors cannot be achieved in topologies with a high number of levels (more than three). These balancing problems appear when dealing with high modulation indices and active currents. Therefore, the achievable AC output voltages kept limited. Some solutions for this problem are proposed in the literature.
- When switched in PWM, the reverse recovery of the clamping diodes becomes the major design challenge in high voltage high power applications. Although measures to alleviate this problem can be applied.
- It requires different current ratings for switches due to their conduction duty cycle. This can be verified from Table 2.2 where it can be seen that S_1 conducts only for $V_{an} = V_{dc}/2$, while S_4 conducts over the entire cycle except for $V_{an} = 0$. Such an unequal conduction duty requires different current ratings for switching devices. If the converter design is to suit the worst case then each phase will have $2 \times (m - 2)$ outer devices oversized.

Despite the limitations as mentioned above, the three-level NPC is still the most popular topology that has found widespread practical applications. Its simple structure enables excellent reliability and availability [27]. Based on the highly

competitive Insulated Gate Controlled Thyristor (IGCT) technology a very compact NPC IGCT PEBB, called PowerStack, serving multiple medium-voltage applications has been introduced to the market and the first commercial installations were commissioned in the year 2000 [28]. The NPC IGCT PEBB has been successfully introduced into the market to serve multiple, highly demanding, mature and emerging applications like 15–60 MVA energy storage systems based on regenerative fuel cell technology or NiCd battery technology to enhance grid stability or to reduce power fluctuations, 9–27 MVA medium-voltage applications, and 22 MVA dynamic voltage restorers to safeguard the highly critical processes of a semiconductor plant.

One of the main structural limitations of the 3-level NPC is the asymmetrical loss distribution. To make the loss distribution uniform across the semiconductors, active switches can be used in place of the clamping diodes and the resulting circuit is called three-level Active NPC (ANPC), introduced first in 2001 [29]. Higher level ANPCs can be similarly derived. Based on ANPCs, a wide range of high power MV drives, and STATCOMs are available in the market [27]. The new technologies introduced with the ANPC IGCT have been developed to further improve the power density and the cost competitiveness of the leading IGCT technology which is able to deliver up to 16 MVA output power. The main new technologies introduced to achieve higher output powers are: increased current rating of IGCTs and improved thermal management by means of the ANPC topology [30]. The distribution of junction temperatures among the semiconductors can be balanced applying optimum switch states and commutations.

As discussed above, one of the major problems associated with DCMCs is the unbalancing (or unequalization) of its DC-link capacitors voltage. Marchesoni et al. have theoretically demonstrated that correct voltage balancing of these capacitors cannot be guaranteed in all operating conditions with a large number of levels [32]. Since those conditions include high modulation indices and high power factors, it limits the practical applications of these converters. The unbalancing of DC capacitors voltage results in divergence of capacitor voltages, causing collapse of some and rise of others due to non-uniform power drawn from them. This may result in poor quality voltage outputs, affecting the control performance, causing violation in the safe operating limits leading to converter malfunctioning. Therefore, the DC capacitors voltage balancing is required under all conditions, which determines both the safety and efficiency of DCMCs. Two possible solutions of the voltage imbalance exist: (i) installing of voltage balancing circuits on the converter DC side [20, 21, 32] and (ii) modifying the converter switching pattern according to a control strategy [31, 33]. The latter is preferable in terms of cost, as the former requires additional power hardware, which adds to cost and complexity. For applications involving only reactive power (like STATCOM), the switching pattern modification strategies can be used for voltage balancing. However, reactive power control would be influence if priority were given to voltage balancing. Further, the switching pattern modification strategy cannot be used to control the capacitor voltages, except at low modulation indices [31]. It is also to be noted that for the applications like UPFC, where two such converters are back-to-back connected, the

switching modification strategy necessitates the two converters to operate at a fixed AC voltage ratio for the capacitor voltages equalization. This constraint would seriously limit the flexibility of the UPFC. The voltage balancing circuit based solutions have also been reported for many applications. A schematic of the voltage balancing circuit is shown in Fig. 2.9, where the semiconductor switches (S_{C1}, D_{C1}) − (S_{C4}, D_{C4}) and inductors L_1, L_2 are chopper elements while R_1, R_2 represent the losses. This chopper is shown to be connected to the DC-link of a single-phase DCMC. It works on the principle of transferring the energy from the overcharged capacitor to the undercharged one through an energy storing inductor. In this way, the capacitor voltages at the DC-link are equalized. Although the inclusion of such circuit increases the cost and complexity, it is more reliable and robust against line faults, transients and disturbances. Further, it does not impose any theoretical limits on the operating range of the converter, as is the case with other available methods. Even though utilization of these additional balancing circuits can improve the operation of multilevel converters, the devices of these circuits have to handle high current and voltage ratings, sometimes higher than ratings of the devices of main converter. A voltage balancing circuit employing lower voltage rating devices was proposed in [34]. In [32], four different schemes were presented for controlling of the chopper circuit at DC-bus of DCMC for DC capacitor voltages equalization.

One of the limitations of DCMCs as described above is multiple blocking voltage of the clamping diodes. To overcome this limitation, a modified DCMC configuration was proposed in [35] with the single-phase schematic shown in Fig. 2.10 for the five-level topology. An m-level modified DCMC requires $(m - 1)$ storage capacitors, $2(m - 1)$ switches and $(m - 1) \times (m - 2)$ clamping diodes of same voltage rating, which are the same with the conventional DCMC with

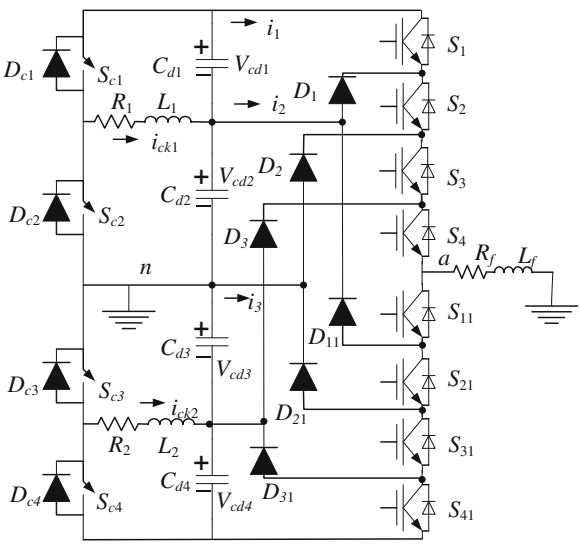

Fig. 2.9 Single-phase five-level DCMC with voltage balancing chopper circuit

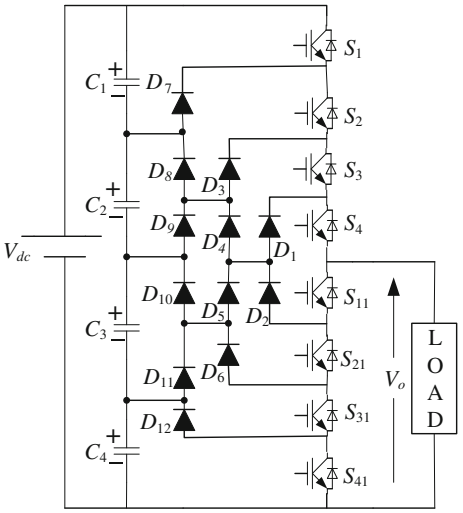

Fig. 2.10 Single-phase five-level schematic of the modified DCMC

clamping diodes in series. The switching scheme for the modified configuration remains same as that for the conventional configuration. However, the main limitation of DCMC, i.e., the unbalancing of its DC-link capacitors voltage is still not resolved for this modified configuration too.

To illustrate the balancing of DC capacitor voltages in DCMC, a three-phase five-level DCMC is simulated with the voltage balancing chopper of the configuration shown in Fig. 2.9 and controlled using the single-pulse control method described in [32]. In Fig. 2.11, e_{vcd1} and e_{vcd2} represent the errors in the corresponding DC capacitor voltages. It is evident from this figure that the capacitor

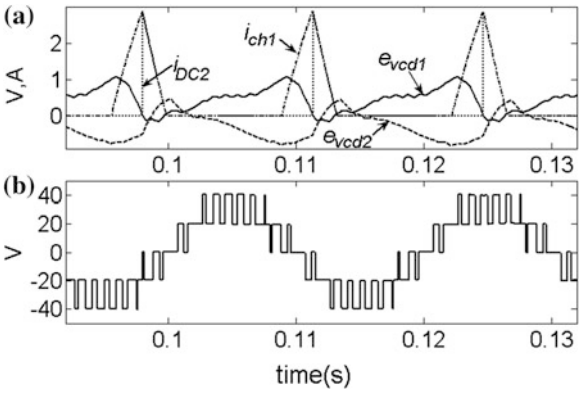

Fig. 2.11 Key results illustrating DC capacitors voltage balancing using voltage balancing chopper circuit in five-level DCMC modulated using PD PWM. **a** Capacitor voltage errors and chopper current, **b** phase-a converter output voltage

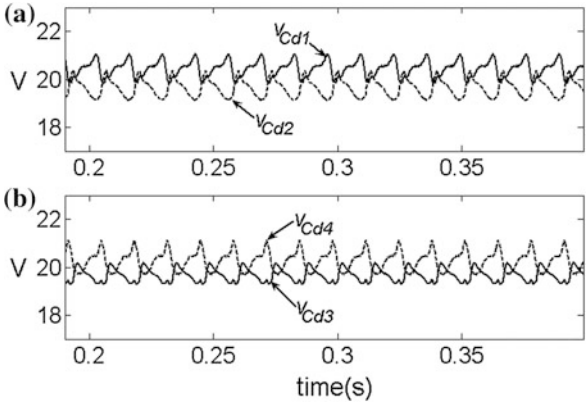

Fig. 2.12 Key results illustrating DC capacitors voltage using voltage balancing chopper circuit in five-level DCMC modulated using PD PWM

voltages are regulated around at their reference value, i.e., 20 V. As the capacitor voltages are balanced, the converter output phase voltage is of good quality five-level waveform as can be seen from Fig. 2.12. The other phase output voltages also have similar waveform.

For STATCOM applications, a CSC has also found to be suitable due to its various advantages [36]. Being a current injection device, the CSC topology injects smaller current harmonics than the voltage harmonics injected by an equivalent VSC based STATCOM. Moreover, a CSC when used to realize a STATCOM requires lower DC energy storage than that of VSC. A VSC and an equivalent CSC are considered to be a pair of dual structures. The multilevel CSC topologies are derived from the dual transform of the corresponding multilevel VSC topologies [9]. In the following sub-section, the dual CSC configuration of DCMC is described.

2.2.1.2 Dual CSC Structure of DCMC

It is known that only planar circuits can be transformed using the duality principle. A planar circuit is a circuit that can be drawn on a plane with no crossing branches. It can easily be verified that the DCMC circuit of Figs. 2.6 and 2.7 are not planar while the modified DCMC topology of Fig. 2.10 is planar. Therefore, the duality transformation can be applied to the circuit of Fig. 2.10 only. As discussed earlier, in duality transformation, the controlled bidirectional conducting switches are transformed into controlled unidirectional switches and capacitors are transformed into inductors. The dual structure of the circuit of Fig. 2.10 is shown in Fig. 2.13, where similar to its VSC counterpart there are four complementary switch pairs: (S_1, S_{11}), (S_2, S_{21}), (S_3, S_{31}) and (S_4, S_{41}) [9]. In Fig. 2.10, the DC capacitors $C_1 - C_4$ corresponds to equal division of DC voltage source V_{dc}. Similarly, in Fig. 2.13, the inductors $L_1 - L_4$ correspond to equal division of DC current source

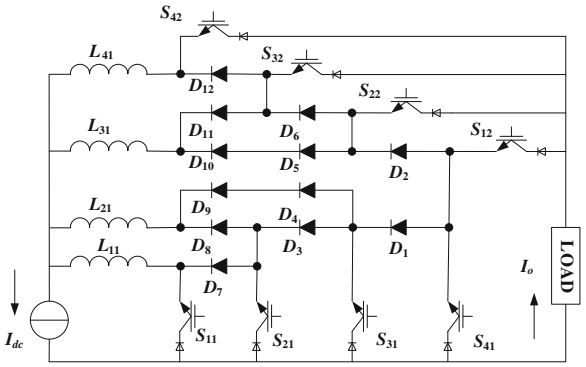

Fig. 2.13 Dual structure of Fig. 2.9

I_d, so that the current carried by each inductor is $(1/4)I_d$. Further, each inductor current passes through only one complementary switch pair. For example, the current through L_1 passes only through the switch pair (S_1, S_{11}) and so on. Based on these considerations, the dual circuit of Fig. 2.10 can be further simplified to the one shown in Fig. 2.14. This topology is called single-rating inductor topology as the DC source current I_d is divided equally among all the inductors. The switching scheme of the circuit of Fig. 2.14 is listed in Table 2.3 for five levels of load current values.

Using different switching states, it is possible to synthesis a multilevel current waveform as a dual of the voltage waveform in VSC NPC. However, similar to the VSC type NPC structure, special consideration needs to be paid on the proper current sharing between the inductors. It is apparent that unbalance current in different inductor branches leads to an excessive current flow through the devices and thus the device failure is occurred. Although the proper current sharing is difficult for the higher level NPC type CSC, similar methods presented for voltage sharing of the VSC type converter is applicable for the CSCs.

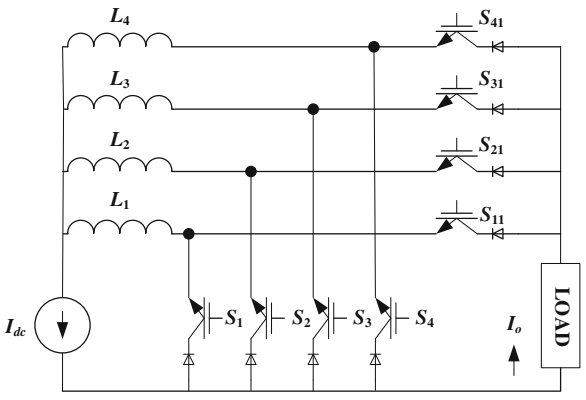

Fig. 2.14 Single phase single-rating inductor five level CSC

Table 2.3 Switching scheme of the single-rating inductor five-level CSC

I_o	Switching scheme							
	S_1	S_2	S_3	S_4	S_{11}	S_{21}	S_{31}	S_{41}
0	1	1	1	1	0	0	0	0
$I_{dc}/4$	0	1	1	1	1	0	0	0
	1	0	1	1	0	1	0	0
	1	1	0	1	0	0	1	0
	1	1	1	0	0	0	0	1
$I_{dc}/2$	0	0	1	1	1	1	0	0
	1	1	0	0	0	0	1	1
	0	1	0	1	1	0	1	0
	0	1	1	0	1	0	0	1
	1	0	1	0	0	1	0	1
	1	0	0	1	0	1	1	0
$3I_{dc}/4$	0	0	0	1	1	1	1	0
	1	0	0	0	0	1	1	1
	0	1	0	0	1	0	1	1
	0	0	1	0	1	1	0	1
I_{dc}	0	0	0	0	1	1	1	1

2.2.2 Flying Capacitor Multilevel (FCM) Converter

Meynard and Foch introduced a flying-capacitor multilevel converter (FCMC) in 1992 [37]. The VSC and CSC configurations of FCMC are described in the following sub-sections.

2.2.2.1 FCM VSC

The structure of FCMC is similar to that of the diode-clamped converter except that instead of using clamping diodes, the converter uses capacitors in their place. In FCMC, the clamping capacitors which 'float' with respect to the DC source are used to achieve multilevel waveform and voltage clamping. These floating capacitors are commonly called as 'flying capacitors' and due this arrangement this topology is named as flying capacitor topology. In the three-level flying capacitor topology shown in Fig. 2.15, the capacitors C_a, C_b and C_c are flying capacitors of the three individual phase legs and C_1, C_2 constitute the DC-link, and the complementary switch pairs are (S_1, S_{11}) and (S_2, S_{21}). It is to be noted that the complementary pair of a switch in the upper half of a phase leg is placed differently in the lower half of the phase leg in flying capacitor topology in contrast to that in the diode-clamped topology, which can be seen by comparing Figs. 2.4 and 2.15. In the three-level converter of Fig. 2.15, all the capacitors shown are regulated at a voltage of $V_{dc}/2$. Depending on the modulation scheme used, the three-level converter is

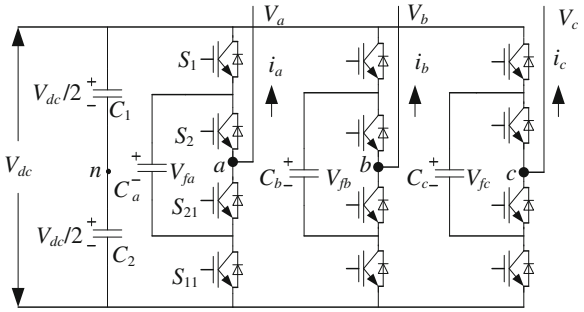

Fig. 2.15 Three-phase 3-level structure of a FCM VSC

switched in such a way to maintain the flying capacitors voltage at $V_{dc}/2$. By doing so, the voltage stress across the semiconductor devices also keeps limited to $V_{dc}/2$. The flying capacitor voltage balancing is achieved by using the redundant switch states available to generate same voltage level at the converter output in this topology. This is further evident from Table 2.4 in which the switching states for producing three-level voltage outputs per phase are listed with respect to the topology of Fig. 2.15. It can be seen that two different switching states can produce '0' voltage level. The corresponding states of flying capacitor with respect to the voltage level output are also listed in Table 2.3. Turning on S_1, S_2 together outputs $+V_{dc}/2$ without changing the state of C_a, which is represented by NC state of the flying capacitor in Table 2.4. Similarly, turning off S_1, S_2 together outputs $-V_{dc}/2$ with NC state of C_a. However, when S_1-ON and S_2-OFF are chosen to output '0' voltage level, charging of C_a is achieved while it's discharging is achieved by choosing S_1-OFF and S_2-ON for 0 voltage level output. It is to be noted that the switch states listed in Table 2.4 are only for positive half cycle of the converter line current waveform (i_a, Fig. 2.15), which is equivalent to the outgoing direction of i_a as shown in Fig. 2.15. For negative half cycle of i_a (incoming i_a), the capacitor states in Table 2.4 for zero voltage level will reverse which can be also analyzed from Fig. 2.15.

It is clear from the configuration of Fig. 2.15 and Table 2.4 that intermediate voltage levels (except the extreme voltage levels $+V_{dc}/2$ and $-V_{dc}/2$) at the converter output are generated by adding or subtracting the flying capacitor voltage with the DC-link voltage. In a generalized way, for any initial state of flying capacitor voltage the three-level FCM VSC output voltage is given by,

Table 2.4 Switching scheme for three-level FCM VSC

S_1	S_2	V_{an}	C_a
ON	ON	$+V_{dc}/2$	*No change* (NC)
ON	OFF	0	*Charging* (+)
OFF	ON	0	*Discharging* (−)
OFF	OFF	$-V_{dc}/2$	*No change* (NC)

$$V_{an} = S_1(V_{dc} - V_{fa}) + S_2 V_{fa} - V_{dc}/2 \tag{2.1}$$

In (2.1), the switching states S_1 and S_2 take the value 1 if the corresponding switch is conducting and 0 otherwise. Based on (2.1), the switch combinations given in Table 2.4 are used to synthesize the output voltage V_{an} of phase-a with respect to n.

In a similar manner as in the diode-clamped topology, higher level flying capacitor topology can be formed by extending the three-level structure of Fig. 2.15. In Fig. 2.16, a three-phase five-level FCM VSC is shown. Assuming that each capacitor has the same voltage rating, the series connection of capacitors in Fig. 2.16 is to indicate the voltage level between the clamping points. Again, three inner loop flying capacitors for phase-a, C_{f1}, C_{f2} and C_{f3} are independent from those for the other two phases. Similar independence exists among all the three phases. All phase legs share the same DC-link capacitors C_1.

Similar to that in a DCMC, the phase voltage of an m-level converter has m levels and the line voltage has $(2m - 1)$ levels. In general, an m-level flying capacitor converter requires $(m - 1)$ pairs of power semiconductor devices and $(m - 1) \times (m - 2)/2$ clamping capacitors per phase leg in addition to $(m - 1)$ main DC bus capacitors provided that all the capacitors are of same size. The number of capacitors can be reduced by sizing the capacitors in a single leg as an equivalent one. In this chapter, from here onwards, a single capacitor, sized equivalently in each clamping leg of the flying capacitor converter has been considered. The size of the voltage increment between two consecutive clamping legs defines the size of voltage steps in the output waveform. The voltage of the innermost clamping leg (e.g. C_{f3} in

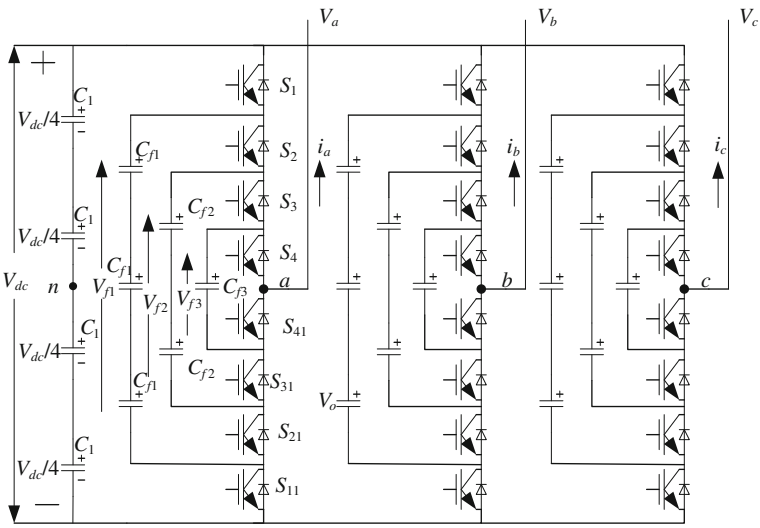

Fig. 2.16 Three-phase five-level structure of a FCM VSC

Fig. 2.16) clamping the innermost two devices is $V_{dc}/(m-1)$. The voltage of the next innermost clamping leg will be $V_{dc}/(m-1)+V_{dc}/(m-1)=2V_{dc}/(m-1)$ and so on. Thus, each next clamping leg will have the voltage increment of $V_{dc}/(m-1)$ from its immediate inner one. The voltage stress across each capacitor is $V_{dc}/(m-1)$. The voltage levels and the arrangements of the flying capacitors in this topology assure that the voltage stress across each main device is same and is equal to $V_{dc}/(m-1)$. Similar to the phase output voltage equation defined by (2.1) for the three-level topology, the five-level converter output voltage is given by

$$V_{an}=S_1(V_{dc}-V_{f1})+S_2(V_{f1}-V_{f2})+S_3(V_{f2}-V_{f3})+S_4V_{f3}-V_{dc}/2 \quad (2.2)$$

Again, as defined earlier, the switching states S_1–S_4 take the value 1 if the corresponding switch is conducting and 0 otherwise in (2.2). Based on (2.2), the switch combinations given in Table 2.5 are used to synthesize the output voltage V_{an} of phase-a of the five-level converter. Table 2.5 also indicates the states of flying capacitors corresponding to the switching combinations chosen. The state NC indicates that the capacitor neither charges nor discharges in this mode. The states + and − denote the charging and discharging of the corresponding capacitors, respectively. The switching states given are for the positive half cycle of the current waveform (indicated as outgoing current i_a in Fig. 2.16). The capacitor states (+ and −) will reverse for the negative half cycle of the current.

It can be seen from Table 2.5 that the structure offers multiple switching combinations for $V_{an}=V_{dc}/4, 0$ and $-V_{dc}/4$. As such redundancies are available, one can choose a preferential switching state that will help in maintaining the capacitor voltages constant. This redundancy is enough to guarantee balanced voltages of the

Table 2.5 Switching scheme for five-level FCM VSC

S_1	S_2	S_3	S_4	C_{f1}	C_{f2}	C_{f3}	V_{an}
ON	ON	ON	ON	NC	NC	NC	$+V_{dc}/2$
ON	ON	ON	OFF	NC	NC	+	$+V_{dc}/4$
ON	ON	OFF	ON	NC	+	–	
ON	OFF	ON	ON	+	–	NC	
OFF	ON	ON	ON	–	NC	NC	
OFF	OFF	ON	ON	NC	–	NC	0
OFF	ON	OFF	ON	–	+	–	
OFF	ON	ON	OFF	–	NC	+	
ON	OFF	OFF	ON	+	NC	–	
ON	OFF	ON	OFF	+	–	+	
ON	ON	OFF	OFF	NC	+	NC	
ON	OF	OFF	OFF	+	NC	NC	$-V_{dc}/4$
OFF	ON	OFF	OFF	–	+	NC	
OFF	OFF	ON	OFF	NC	–	+	
OFF	OFF	OFF	ON	NC	NC	–	
OFF	OFF	OFF	OFF	NC	NC	NC	$-V_{dc}/2$

flying capacitors using proper modulation technique. However, the switching combination chosen affects the current rating of the capacitors. For example, for $V_{an} = V_{dc}/4$, if the first and the last combinations are used (Table 2.5), only one capacitor (C_4 or C_2) is involved. In the other two combinations more than one capacitor are required to be charged or discharged. Therefore, the rms current ratings of the capacitors will necessarily be higher for the single capacitor case than that in the two-capacitor case. This feature of different current rating is present in almost every case (except for the levels of $V_{dc}/2$ and $-V_{dc}/2$). The switching sequence chosen therefore affects the rms current ratings of the capacitors. Thus, optimization of the switching sequence is required, i.e. one which minimizes the capacitor cost and the system losses. As compared to DCMC, the FCMC topology has the advantage that it has redundancies for inner voltage levels, as observed above. Moreover, FCMC has *phase* redundancies, whereas DCMC has only *line-line* redundancies. Unlike DCMC, the FCMC does not require all of the switches that are on (conducting) be in a consecutive series. In DCMC, to avoid the recovery problem associated with the diode, the switching modulation is limited to provide for the voltage unbalance between each leg. Since the FCMC has a wealth of redundant switching states, there are enough combinations between switching states to provide for voltage balancing. Furthermore, compared to DCMC, the FCMC eliminates a mid-capacitor point for each switch pair which results in simple converter structure. The drawback of FCMC is that its control is more complicated and it requires a large number of capacitors. Fortunately, the size of flying capacitors can be reduced by an increased switching frequency [38–41].

After the introduction of FCMC in the 1990s, there have been numerous articles published related to this topology. Both industries as well as academia have shown significant interest in the FCMC topology and its various applications have been explored. At present, around 80 T13 locomotives in the European railways use this topology as input chopper [42]. In the drive applications, as early as 1996, Cegelec (which later became ALSTOM Industry) showed interest in FCMCs and development using the biggest IGBTs available at that time was initiated. Today, a complete range of such drives is proposed to comply with the European standards. For power systems compensation applications as well, the flying capacitor converter has gained significant interests. In [43], a five-level FCMC is selected and designed for a 6.6 kV STATCOM. To decrease size of the flying capacitor by increasing a switching frequency, the Auxiliary Resonant Commutated Pole (ARCP) Converter is used, and its parameters are optimized based on loss-implemented simulation.

In summary, advantages and disadvantages of FCM VSC are as follows [1–4, 37–43].

Advantages

- Large amount of capacitors, in terms of the flying capacitors, may provide extra ride through capabilities during power outages.
- The redundant switching combinations provide added flexibility in controlling and balancing the balancing different voltage levels.

- It eliminates the clamping diode problems present in DCMC topologies and the *dv*/*dt* stress across the devices is naturally limited.
- Unlike DCMC, the redundant switching states in FCMC can control the charge balance in all flying capacitors, even if the phase current is unidirectional. This makes this topology attractive even for the DC/DC converters.
- Each phase leg can be analyzed differently from the others. This is an important difference with DCMC, in which the entire three-phase system must be considered for the balancing issue (without using additional chopper circuits).

Disadvantages

- An excessive number of flying capacitors is required for higher level converter configuration. Such configurations are expensive and more difficult to package with the required bulky capacitors.
- The flying capacitor voltage controller adds complexity to the control of the whole circuit.
- The rms current rating of flying capacitors is higher.
- For low switching frequency operation, large sizes of flying capacitors are required.
- There is a potential for parasitic resonance between decoupling capacitors.
- Precharging and startup are more complex.

As detailed earlier, an FCMC uses flying capacitors to split the input voltage and clamp the voltage stresses across the semiconductor switches. It is the primary requirement of functioning of an FCMC is to have balanced flying capacitor voltages at their corresponding reference values as it dictates both the safe and efficient operation of the converter under all operating conditions. If voltage imbalance occurs, the quality of the output voltages will deteriorate and blocking voltages imposed on certain devices may increase the rated values. Therefore, it is necessary to take into account the balancing of flying capacitor voltages while designing the converter control schemes. Additionally, the evolution of the flying capacitor voltages must be carefully studied since the survival of the converter depends on it. There are many different control strategies available in the literatures taking into account the flying capacitor voltage balancing for FCMCs.

Many studies have shown that under certain conditions, a simple open loop control guarantees natural balancing of the flying capacitor [38–40]. The self-balancing mechanism ensures safe operation under most operating conditions where a high enough switching frequency is chosen and the load is not purely reactive [38, 39]. Nevertheless, in this case, the dynamics involved in the balancing transient depend on the impedance of load at the switching frequency. If the impedance at the switching frequency is high then the natural balancing is very slow and may not be guaranteed. Further, by using such an open-loop control, unbalance may occur in applications with low switching frequencies or if the reference waveform contains harmonics that are close to the switching frequency [38, 39]. Following these observations, a filter circuit of the *R-L-C* type (called, 'balance-booster') tuned at the switching frequency and connected in parallel with

the load may also be used to achieve the natural balancing [39]. It has the advantage of being reliable but the extra filter increases the cost of the overall system, introduces extra power losses especially in high-voltage applications and may be too slow to follow rapid variations of the input voltage [39]. While assuming the natural balancing of the flying capacitors voltages, it is considered that the capacitor voltages are balanced with each switching period provided that the control signals have the same duty cycles, the power devices have the same characteristics and the load currents are symmetrical. However, these conditions cannot be met in real systems due to non-ideal conditions and disturbances, such as unequal capacitance leakage currents, unequal delays in switching, asymmetrical charging/discharging of capacitors and load disturbances. Consequently, the voltages of flying capacitors will vary. Therefore, the need for an external control loop for each flying capacitor voltage may arise for most of its applications due to the dependency of the natural balancing quality on the modulation pattern as well as the load parameters [38–40].

To illustrate the natural balancing property of FCMC, simulation studies using PSCAD/EMTDC are performed on a single-phase five-level FCMC. It is evident from Fig. 2.17a that the flying capacitor voltages attain their target operating values confirming the natural balancing of FCMC. The converter switched output voltage and current are shown in Fig. 2.17b, c, respectively. The five different voltage levels in the phase leg confirms that the flying capacitor voltages have stabilized to their target operating values.

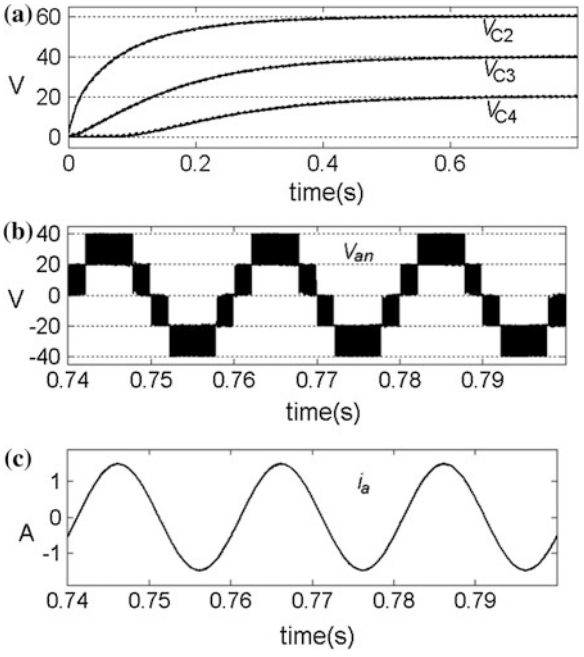

Fig. 2.17 Key results illustrating natural balancing when the single-phase five-level FCMC is modulated using PD PWM. **a** Flying capacitor voltages; **b** FCMC phase-leg switched voltage, and **c** load current in steady state

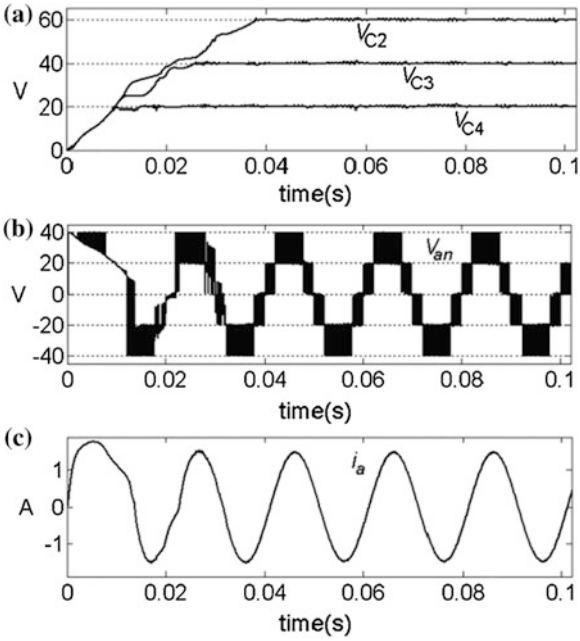

Fig. 2.18 Key results when the single-phase five-level FCMC is controlled using preferential switch state selection scheme. **a** Flying capacitor voltages; **b** FCMC phase-leg switched voltage, and **c** load current in steady state

In Fig. 2.18, the simulation results using the preferential switch state selection scheme proposed in [18] are plotted with the same parameters as considered above. Figure 2.18a shows the start-up transient of the flying capacitor voltages with initially uncharged capacitors. It is evident by comparing the capacitor voltage transients of Figs. 2.17 and 2.18 that the rate of capacitors achieving their respective target voltage values is much faster in the latter case. Once the capacitor voltages reach their respective target values, they are tightly regulated around these values and hence, the load voltage and current achieve their desired waveform shapes as shown in Fig. 2.17.

2.2.2.2 Dual CSC Structure of FCMC

It can be observed from above that FCM VSC has a planar structure. Therefore, its CSC configuration can be derived directly by applying duality transformation. The dual structure of single-phase five-level DCMC configuration is shown in Fig. 2.19. The dual elements in phase-*a* of Fig. 2.16 and in Fig. 2.19 are represented by the same assignations. In phase-a of the five-level FCM VSC configuration of Fig. 2.16, the voltages across the flying capacitors are $V_{f1} = 3V_{dc}/4,\ V_{f2} = V_{dc}/2$ *and* $V_{f3} = V_{dc}/4$. Similarly, in Fig. 2.19, he current through the respective inductors are $3I_{dc}/4,\ I_{dc}/2$ and $I_{dc}/4$, respectively. This implies that all the inductors are of different current ratings. Hence, this configuration of Fig. 2.19 is named as multi-rating inductor converter. In Fig. 2.19, similar to its VSC counterpart there are four

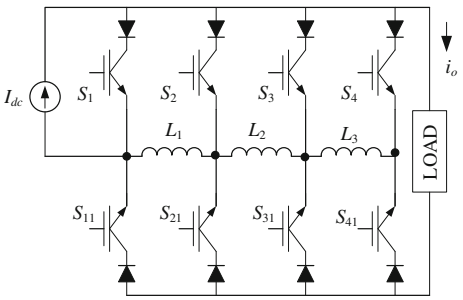

Fig. 2.19 Single phase multi-rating inductor five level CSC

complementary switch pairs: (S_1, S_{11}), (S_2, S_{21}), (S_3, S_{31}) and (S_4, S_{41}) and its switching scheme is listed in Table 2.6 for five levels of load current values. As can be seen, the FCM CSC topology also offers redundant switching combinations. Therefore, in a similar way as in its dual VSC structure, it is possible to synthesize a multilevel current waveform in FCM CSC.

In FCM CSC topology, each semiconductor device blocks the peak line-to-line voltage and conducts Idc/N. However, the inductors carry different current values (e.g., $I_{L1} = 2I_{L2}$). Parallel-connected identical inductors may be used to have a same design rating. With the same switching frequency, and power rating, the FCM CSC requires less energy storage for synthesizing the intermediate levels. This is because the inductors in a FCM CSC are shared by all three phases. However, this topology cannot be easily scaled up for a higher voltage levels.

Table 2.6 Switching scheme of the multi-rating inductor five-level CSC

I_o	Switching scheme							
	S_1	S_2	S_3	S_4	S_{11}	S_{21}	S_{31}	S_{41}
0	1	1	1	1	0	0	0	0
$I_{dc}/4$	0	1	1	1	1	0	0	0
	1	0	1	1	0	1	0	0
	1	1	0	1	0	0	1	0
	1	1	1	0	0	0	0	1
$I_{dc}/2$	0	0	1	1	1	1	0	0
	1	1	0	0	0	0	1	1
	0	1	0	1	1	0	1	0
	0	1	1	0	1	0	0	1
	1	0	1	0	0	1	0	1
	1	0	0	1	0	1	1	0
$3I_{dc}/4$	0	0	0	1	1	1	1	0
	1	0	0	0	0	1	1	1
	0	1	0	0	1	0	1	1
	0	0	1	0	1	1	0	1
I_{dc}	0	0	0	0	1	1	1	1

2.3 Modular Multilevel Converters

Modularity, in general, refers to a technique to develop comparably large systems by combining smaller subsystems. For power converter topologies this means, a cascaded connection of converter cells, so called chain-links, which seems to be an interesting solution to reach high voltage and high quality waveforms [1–4]. However, in order to transfer active power, isolated DC sources are required by means of a transformer and a rectification stage. This fundamental problem has been addressed in [44], opening a new field of possible new solutions. The solution proposed in [37], eliminates the need of separated sources in high power converters by means of an intermediate voltage source or current source, such as a capacitor or inductor, floating with respect to ground potential in the converter circuit. These intermediate sources with passive elements are actively balanced by means of the switching process of the converter. Other circuit configurations including voltage or current sources or their combinations can be tailored in order to make use of the modularity and scalability for high power applications. These solutions require a proper cell or a building block structure. The power electronics building block is an intermediate level towards the modular power converters that incorporate the integration of power devices, passive elements, and other components into functional blocks. Building blocks can be easily added in parallel to increase the current carrying capability or in series in order to handle considerably higher voltages. This section is to provide an overview of the modular multilevel converter topologies from the basic building blocks to the system level modularity, targeting high-power applications and in particular FACTS. As will be discussed further in this section, modular multilevel VSCs and CSCs can be built either straightforward by applying the modular building block cells or by a combination of cells with monolithic multilevel topologies. Therefore, this section summarizes the most recent developments made in this field, covering new promising topologies and operational issues. In addition, emerging trends, challenges, and possible future directions of the multilevel converter technologies are outlined to motivate further work in this field. The following sub-section discusses the first introduced modular topology of multilevel converter introduced in [45].

2.3.1 Chain-Link Multilevel Converters Based on Bipolar Cells

A cascade H-bridge inverter is a series connection of several H-bridges. This topology is the most obvious way of achieving a multilevel waveform. As stated earlier, the H-bridge inverter of Fig. 2.1b can produce voltage waveform with three discrete levels; $+V_{DC}$, 0 and $-V_{DC}$ where V_{DC} is voltage of its DC source. Therefore, a combination of a number of H-bridge inverters should be able to produce more than three level voltage output. Based on this concept the cascade H-bridge inverter

is constructed. A single-phase structure of an m-level cascaded inverter is illustrated in Fig. 2.20. Each Separate DC Source (SDCS) is connected to a single-phase H-bridge inverter. Each inverter level can generate three different voltage outputs, $+V_{DC}$, 0, and $-V_{DC}$ by connecting the DC source to the AC output by different combinations of the four switches, S_1, S_2, S_3, and S_4. To obtain $+V_{DC}$, switches S_1 and S_4 are turned on, whereas $-V_{DC}$ can be obtained by turning on switches S_2 and S_3. By turning on S_1 and S_2 or S_3 and S_4, the output voltage is 0. The AC outputs of each of the different full-bridge inverter levels are connected in series such that the synthesized voltage waveform is the sum of the inverter outputs. The number of output phase voltage levels m in a cascade inverter is defined by $m = 2\,s + 1$, where s is the number of separate DC sources. An example of phase voltage waveform (v_{an}) for an 11-level cascaded H-bridge inverter with 5 SDCSs and 5 full bridges is shown in Fig. 2.21. The phase voltage $v_{an} = v_{a1} + v_{a2} + v_{a3} + v_{a4} + v_{a5}$. Figure 2.21 provides an illustration of this idea of obtaining the total AC voltage produces by the multilevel inverter by adding together five distinct AC voltages of the five H-bridge inverters. Figure 2.21 also illustrates the idea of 'levels' in a cascaded H-bridges multilevel inverter. In this figure, one notices that five distinct DC sources can produce a maximum of 11 distinct levels in the output phase voltage of the multilevel inverter which is in justification of the expression $m = 2s + 1$ given above.

One of the earliest applications for the series connection of single-phase full bridge inverter topology was reported for plasma stabilization [46]. Later this approach was extended to include three-phase systems. Recently, the multilevel cascaded inverters have been proposed for such applications as static VAr generation, an interface with renewable energy sources, and for battery-based applications. Peng has demonstrated a prototype multilevel cascaded static VAr generator connected in parallel with the electrical system that could supply or draw reactive current from an electrical system [47]. The inverter could be controlled to either regulate the power factor of the current drawn from the source or the bus voltage of the connected electrical system. It was also shown that a cascade inverter can be directly connected in series with the electrical system for static VAr compensation. Cascaded inverters are ideal for connecting renewable energy sources with an AC grid, because of the need for separate DC sources, which is the case in applications such as photovoltaics or fuel cells.

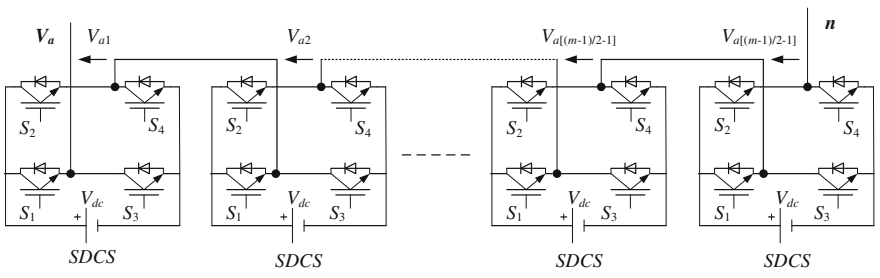

Fig. 2.20 Single phase structure of a multilevel cascaded H-bridge inverter

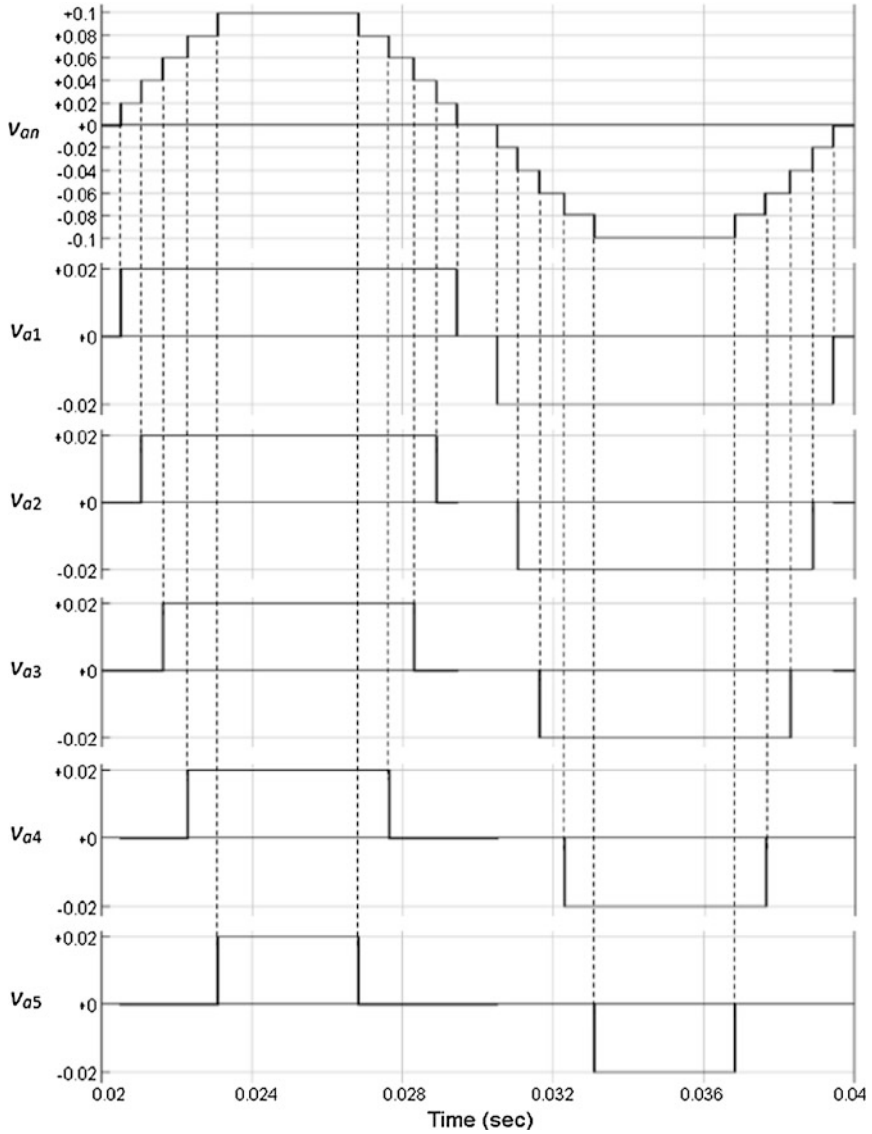

Fig. 2.21 Output phase voltage waveform of an 11-level cascade inverter with 5 separate DC sources

Cascaded inverters have also been proposed for use as the main traction drive in electric vehicles, where several batteries or ultra-capacitors are well suited to serve as SDCSs [48]. The cascaded inverter could also serve as a rectifier/charger for the batteries of an electric vehicle while the vehicle was connected to an AC supply. Additionally, the cascade inverter can act as a rectifier in a vehicle that uses

regenerative braking. Manjrekar has proposed a cascade topology that uses multiple DC levels, which instead of being identical in value are multiples of each other [49]. He also uses a combination of fundamental frequency switching for some of the levels and PWM switching for some other levels to achieve the output voltage waveform. This approach enables a wider diversity of output voltage magnitudes; however, it also results in unequal voltage and current ratings for each of the levels and loses the advantage of being able to use identical, modular units for each level. In the industrial community, Robicon Corporation commercialized their medium-voltage drives utilizing the cascaded multilevel topology in 1999. In 1998, GEC ALSTHOM T&D (now ALSTOM T&D) proposed to use the cascaded topology as a main power converter in their STATCOMs that are associated with the TSR and TCR. To date, several papers have discussed the configurations and control strategies for the reactive power compensation systems that utilize cascaded multilevel converters.

The main advantages and disadvantages of multilevel cascaded H-bridge structures are as follows [1–4, 47–50].

Advantages

- The series of H-bridges structure allows a scalable, modularized layout and packaging due to identical structure of each H-bridge. This will enable the manufacturing process to be done more quickly and cheaply.
- Requires the least number of components considering there are no extra clamping diodes or voltage balancing capacitors to achieve the same number of voltage levels.
- Potential of electric shock is reduced due to separate DC sources.

Disadvantages

- Separate DC sources are required for each of the H-bridges.
- The switching modulation needs to be optimized for high performance applications due to a limited combination of switching patterns.
- For reactive power exchange, the power pulsation at twice the output frequency occurring with the DC-link of each H-bridge inverter necessitates over-sizing of the DC-link capacitors.
- Due to number of DC capacitors voltage to be controlled in its FACTS and custom power applications, it has rather complex DC voltage regulation loop.
- Each H-bridge inverter faces unequal current stress.
- Connecting separate DC sources between two converters in a back-to-back arrangement (e.g., in UPFC) is not possible because a short-circuit will be introduced when two back-to-back converters are not switching synchronously.

In a similar way described for cascaded H-bridge converters, other monolithic multilevel converter configuration defined earlier in Sect. 1.2 may also be used a building block. By expanding the building block configuration from the monolithic converter topologies, various types of chain-link modular converters can be synthesized as shown in Fig. 2.22. In the chain-link structures, for the same switch and capacitor units, the higher the number of cells, the higher the voltage blocking

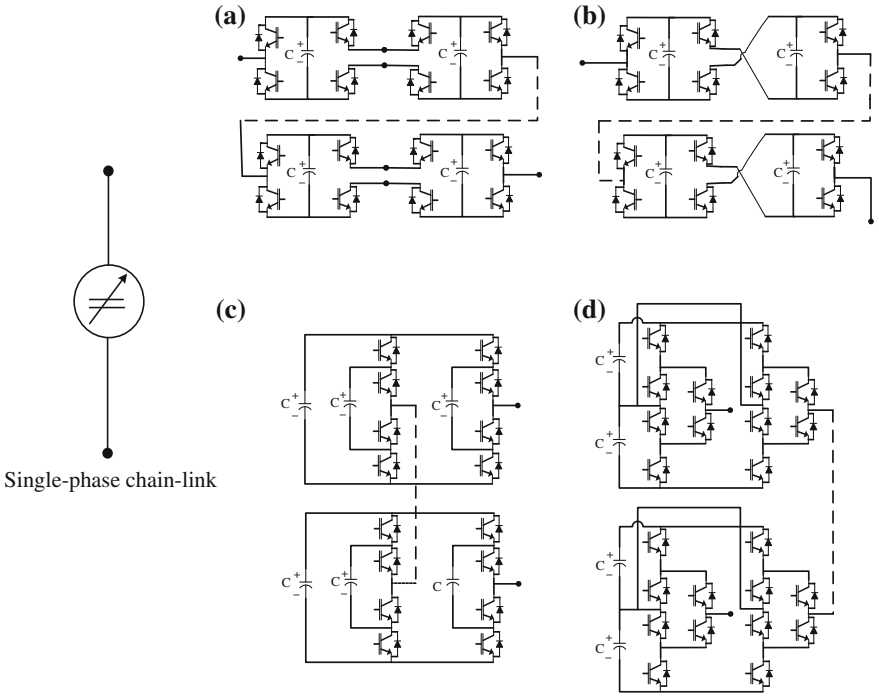

Fig. 2.22 Single-phase chain-link multilevel converter topologies. **a** Series of parallel connected cells. **b** Series of cross connected cells. **c** Stacked commutation cells. **d** Series of NPC commutation cells

capability and the output voltage quality is. The total number of components in the chain-link structure is simply proportional to the number of cells (N). In the chain-link converters, switching frequency of the power devices is reduced by a higher number of cells, while the conduction losses are a function of the number of cells (N) inserted in the conduction path. Therefore, since the chain-link structures bear the same characteristics of their corresponding building blocks, cells with a minimum number of devices are desired to reduce the converter cost and conduction loss in chain-link multilevel converters.

Controlling the floating cell capacitors in the chain-link multilevel converters is one of the main control concerns in such topologies. By changing the switch connection between the intermediate cell capacitors as shown in Fig. 2.22a, the capacitors can be connected in parallel. The parallel connected commutation cells helps the capacitors' voltage ripple reduction. An alternative parallel connection of half-bridge cell capacitors at reduced device current rating is proposed in [51]. The full-bridge cell can be connected in a cross fashion as reported in [52, 53]. The cross connected cell is an alternative symmetrical bipolar cell structure in which by cross connecting more intermediate capacitors in the structure shown in Fig. 2.22b, a higher number of voltage levels can be achieved. This results in reduction of cell

counts and conduction losses while the output quality remains the same as the normal cascaded converters presented in Fig. 2.20. Flying capacitor and neutral point clamped converter can also be utilized as the building block element. By connecting these cells in a nested or series configuration, a single-phase leg structure of the variable VSC can be created as shown in Fig. 2.22c, d. It is worth to mentioning that, the intermediate capacitor voltages should be balanced on the desired DC-voltage value in case of three or more voltage level structure. The chain-link modular multilevel structures in Fig. 2.22, can synthesize a bipolar staircase voltage for high and medium power applications with alternating converter terminal voltages, e.g., STATCOM, matrix converters, etc. For a three-phase system, the output voltage of the three cascaded inverters can be connected in either delta or wye configuration as shown in Fig. 2.23a, b, respectively. Each of these configurations offer various benefits according to the application specifications. The star connection is the most promising as a battery energy storage system (BESS) for positive-sequence active-power control and as a STATCOM for positive-sequence reactive-power control with the lowest converter-cell count. The delta is applicable to a STATCOM for positive- and negative-sequence reactive-power control with $\sqrt{3}$ more current for the same semiconductor as the star connection [54].

The main advantages and disadvantages of the delta connection (Fig. 2.23a) of the chain-link modular multilevel converter topologies for a three-phase systems are as follows:

Advantages

- Modularity of the system is the main advantage of these structures which allows the higher voltage achievement with a minimum mechanical complexity.
- Since each chain-link modular multilevel converter is connected between the lines, a higher current ($\sqrt{3}$ times higher) capability is achieved with the same semiconductor.
- Negative sequence compensation of the delta configuration is achievable by injecting a zero sequence current.

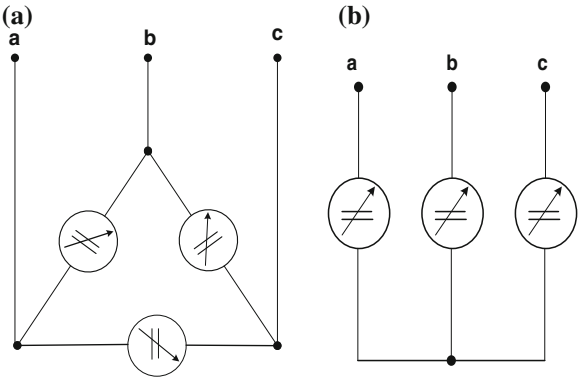

Fig. 2.23 Three-phase chain-link multilevel converter topologies. **a** Delta connection. **b** Star connection

Disadvantages

- Each phase-leg of the delta connection is connected between the line to line network voltages. This increases the required number of series connected cells.
- Current over rating is required for the zero sequence current that exchanges energy between the phases.
- Compensation of unbalance in the network voltages is limited due to restrictions on exchanging energy between the phases during this operational condition.

The main advantages and disadvantages of the start connection (Fig. 2.23b) of the chain-link modular multilevel converter topologies for a three-phase systems are as follows:

Advantages

- Modularity of the system is the main advantage of these structures which allows the higher voltage achievement with a minimum mechanical complexity.
- Since each chain-link modular multilevel converter is connected between the phase network and the neutral, each phase-leg is only subjected to the phase to neutral voltage. This means that theoretically a lower number of series connected cells are required.
- Unbalanced network voltages can be compensated in this structure.

Disadvantages

- For unbalanced loads compensation, a zero sequence voltage must be introduced to exchange energy between the phases. This results in an increased number of series connected cells.
- The required zero sequence voltage increases exponentially when equal amounts of positive and negative sequence compensation are required and this results in a limited compensation capability.

The prominent advantages of modular chain-link multilevel converters in terms of the wider dynamic and greater flexibility, simple mechanical design, maintenance and reliability, low losses make them a suitable choice for different applications such as weak grid support, integration of renewables, industrial steel and mining in order to support heady loads and flicker mitigation. SVC Light® was introduced by ABB in 1997 and improves the efficiency of power transmission systems, increasing the transmission capacity as well as reducing the risk of voltage collapses and blackouts. ABB's latest generation SVC Light is based on a modular, multilevel converter topology to reach even higher transmission efficiency with or without transformer. The new design reduces losses and harmonic emissions and enhances performance, through improved voltage control. Currently, SVC Light® offers a power range of 10–250 MVAr and is available at different voltage and current rating. Siemens offers the SVC PLUS® since 2009 which is the modular multilevel chain-link with the IGBT based full-bridge module. They are also available at different power and voltage ratings. Alstom technology on modular VSC is called MaxSine which is based on power electronic modules.

2.3.2 Modular Multilevel Converters Based on Half-Bridge Cells

In the previous sub-section, the structure of chain-link multilevel converters based on bipolar cells have been presented. Since each chain-link inherits the characteristics of its building block cells, all presented chain-links are capable of synthesizing bipolar voltage waveforms. Despite the non-negative voltage limitation of the unipolar chain-links, which is created by unipolar building blocks, this section is dedicated on STATCOM conversion systems based on half-bridge cells.

2.3.2.1 Modular Multilevel Converter (MMC) with DC Connection

One of the most successful converter topologies for high power applications with respect to today's technology is the MMC proposed in [44]. As shown in Fig. 2.24, this circuit has a similar structure as the conventional two-level converter; however, the series connected devices in each converter phase arm have been replaced by a chain of half-bridge cells shown in Fig. 2.1a. In other words, the energy storage elements at the DC side have been distributed in the converter arms. This structure, positive and negative arms are connected in series from the positive to the negative

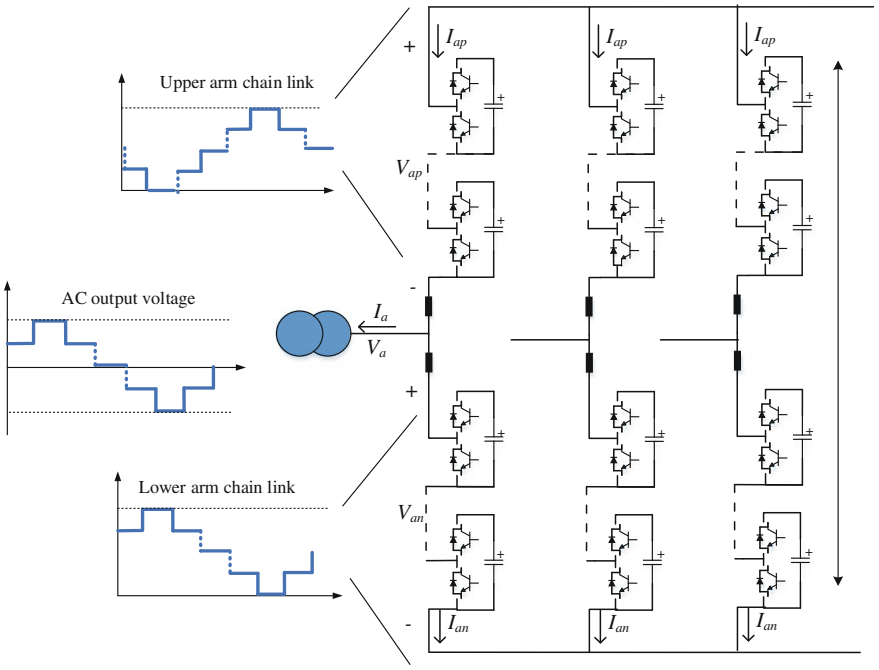

Fig. 2.24 Modular multilevel converter (M2LC)

DC terminals and the AC terminal is connected in the middle of the arms. This topology addresses, low loss, low switching frequency (slightly above the fundamental frequency), voltage scalability due to the simple cascading of identical cells, negligible AC filters due to the synthesized pure sine voltage waveform (for above 20 cells per arm), and mechanical simplicity. Either half- or full-bridge bridge cells can be employed in the converter arms to generate the arm voltage waveforms. In case of the half-bridge cells, each converter arm generates an AC multilevel voltage with a DC offset of the pole-to-ground voltage. This results in a higher converter arm rating (2 times the AC voltage) as they need to provide a DC offset in order to create the output AC voltage. However, when full-bridge cells are used, it is sufficient that each arm generates only the AC voltage with the same amplitude as of the output voltage. Therefore, the number of cells is reduced to half of the one in the half-bridge case while the number of devices in each cell is doubled. A sinusoidal multilevel waveform at the AC terminal is synthesized by devising a proper modulation strategy and creating appropriate insertion indices at each converter arm terminals. One of the other important feature in MMC which can distinguish this topology from the other modular structures, is the lower device current rating due to the AC current sharing between two converter arms and having the circulating current properties. Given the important features of this converter topology, it seems to be an invincible topology for HVDC transmission applications with respect to today's technology. This converter has been developed recently by ABB known as HVDC Light™ [55], by Siemens known as HVDC PLUS™ [56], and known as MaxSine for the Alstom technology. However, various control strategies have been suggested for both MMC and shown the advantages of the high-power MMC-based STATCOM for a full compensation of unbalanced and distorted nonlinear loads [54, 57]. This modular MMC- based STATCOM also introduces a transformerless design. In addition extended version of MMC-based STATCOM was developed in [57] by paralleling a number of MMC to achieve higher efficiency, higher, reliability, lower weight and size, lower switching frequency and lower ratings for the switches. Applying the full-bridge cells instead of the half-bridge cells, the DC and the AC side voltages can be decoupled. Although this requires double the number of switching devices, this is a useful functionality for the renewable sources where the buck or boosting capability of the input voltage is required due to the voltage fluctuation.

Despite all interesting features, this converter suffers from very big a very big capacitor size which is almost ten times greater than the normal monolithic converters. In addition, one of the main challenges in order to control this type of converter is the energy variation balance in each converter arms and different control and capacitor balancing methods have been proposed in literatures [58, 59]. Another critical challenge which corresponds to the high power application requirements is the internal and the external fault tolerance of the converter. Various cell protection schemes and devices have been introduced to deal with internal faults. A device with built-in short circuit failure mode capability or cell bypass switch has been proposed for internal cell faults.

Advantages and disadvantages of the MMC for STATCOM application are as follows:

Advantages

- The system is modular and this allows easy addition of cells for higher phase voltages.
- A DC circulating current can be introduced between the phase legs to facilitate energy exchange under unbalanced conditions for negative sequence compensation. This topology also allows compensation for unbalanced network voltages.
- The line current splits between the two arms of the converter. This means for a constant valve current rating the total output power of the converter is increased.

Disadvantages

- Valve current De-Rating is required due to the DC circulating current added to the required current.
- Each arm of the converter must produce the peak AC output voltage superimposed onto a DC offset. This means the number of cells in the converter is significantly higher than the delta and star chain-link topologies.
- The presence of the DC offset voltage that each arm must create results in a large fundamental frequency component in the arm capacitor voltages. Third harmonic voltage injection does alleviate this issue somewhat, however only by a small fraction (approximately 10 %). The net effect is still an increase in capacitor voltage ripple compared to the delta and star chain-link topologies. This leads to significantly increased amounts of stored energy in the capacitors and hence increased cost for the converter.

To illustrate the MMC operation, a simulation study using MATLAB/Simulink is performed on a three-phase twelve-level MMC. The inverter consists of 12 half-bridge submodules and is connected to the grid and the DC-link voltage is 60 kV. Key MMC waveforms including arm voltage/current and capacitor voltages for 5 MVAr inductive (receiving) and capacitive (sending) reactive power modes have been illustrated in Fig. 2.25a, b, respectively. It is evident from Fig. 2.25 that the submodules capacitor voltages attain their target operating values at 5 kV (60 kV/12). As shown, the capacitor ripple in capacitive modes has a higher maximum ripple while in inductive mode capacitors have a higher minimum ripple. This results in an energy requirement of the converter in the inductive mode as the modulation is limited due to the higher minimum ripple. This can be compensated by having a higher DC voltage in each cell capacitor.

2.3.2.2 Modular Multilevel Converter (MMC) with AC Connection

Since, it is not necessary to have DC connection in STATCOM applications, by series connection of the half bridges as shown in Fig. 2.24, a chain-link multilevel converter based on half-bridge cells can be generated. Since the half-bridge has

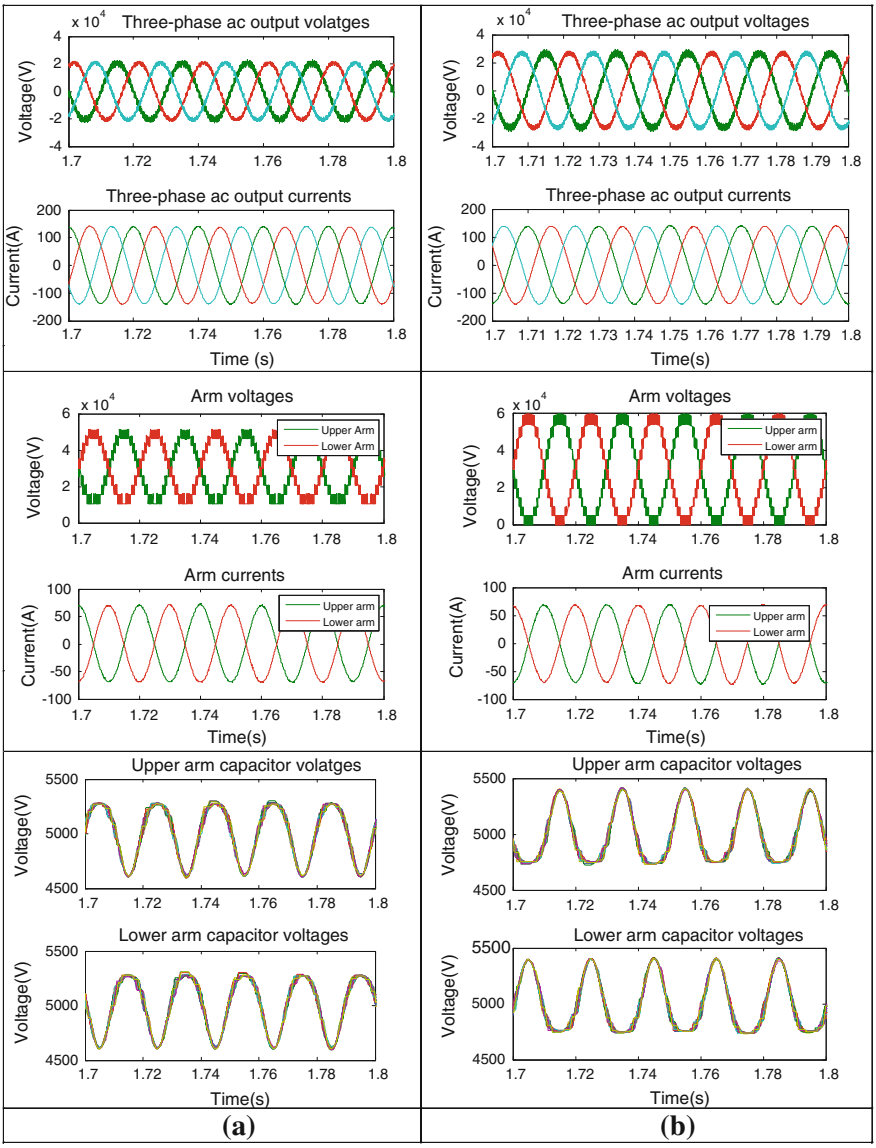

Fig. 2.25 Key MMC waveform with 12 cells in each arm. **a** Inductive mode; **b** capacitive mode

only unipolar output voltage, two sets of series connected half-bridge cells are required for each phase-leg. One set creates positive output voltages while the other creates negative voltages. The corresponding converter schematic is shown in Fig. 2.26. Thus, bipolar multilevel waveform can be generated at the AC output terminal.

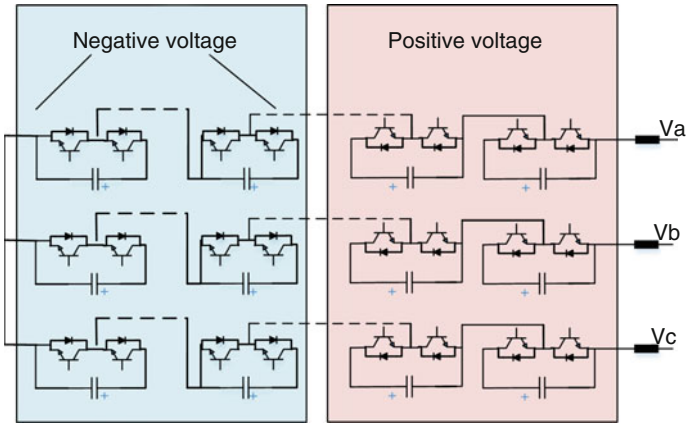

Fig. 2.26 Chain-link multilevel converters with half-bridge cells

Advantage and disadvantages of this topology are as follows:
Advantages

- The system is modular and this allows easy addition of cells for higher phase voltages.
- The system is built based on the half-bridge cells which is very simple and has less mechanics.

Disadvantages

- A zero sequence voltage should be introduced to exchange energy between the phases when compensating unbalanced loads. This results in an increased number of series connected cells.
- Having two set of half-bridge cells results in a high number of cells in the converter, and hence the stored capacitor energy, is not utilized compared to the chain-link delta star topologies.

2.3.3 Modular Current Source Converters (MCSC)

The modular CSCs are the dual configuration of the modular VSCs and provide a good solution for flexibility with scaling in current. The solution is modular and scales well with standard size building blocks, where the devices and passive components (inductors) have the same rating. The challenge with the MCSC current source-based converter is the ability to scale in voltage and obtaining the isolated direct current sources. Although few researches have focused on the analysis and design of CSC based STATCOM systems, with the advents in high

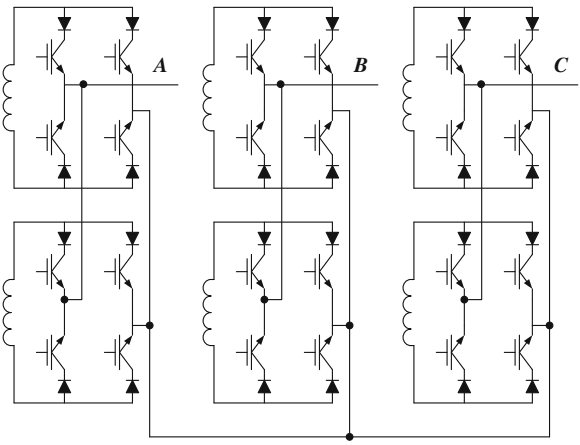

Fig. 2.27 Dual of series connected CHB-parallel connected CHB current sources

voltage, high power semiconductor technology, such as IGCT and high voltage IGBT technologies, CSC based STATCOM systems at different rate of power can be increasingly used in the near future FACTS applications. The most prominent modular multilevel CSC will be discussed in this section.

2.3.3.1 Modular CSCs Using H-Bridge Cells

The cascaded H-bridge (CHB) current source as a dual to a standard voltage-source based CHB is shown in Fig. 2.27. The topology comprises of single-phase current source cells, either half bridge or full bridge cells, which are the dual of the VSC cell (Fig. 2.4). However, a full-bridge functionality is required to achieve a sinusoidal phase current waveform. As shown, despite of the CHB VSC, cells are connected in parallel to synthesize a stepwise current waveform as the current sources cannot be connected in series. Therefore, this topology is more useful for the application with a high current requirement. Basic operation is analogous to a voltage source based CHB, with the cells being connected per-phase. Using a proper Pulse with modulation strategy such as the phase shifted carrier based method, a multilevel current waveform can be generated at the phase output. As the CHB cells are connected in parallel, each cell is rated for the peak phase-to-neutral alternating voltage, hence, the use of this topology in high voltage applications is challenging. It is noted that the current sharing method (similar to voltage balancing method in VSC) needs to be applied on this topology to ensure the same device current rating. This can be done with the selection algorithm method. For instance, at occasion of switching ON, the cell with lower (higher) current is selected to switch on when the voltage across the chain-link is positive (negative) and vice versa.

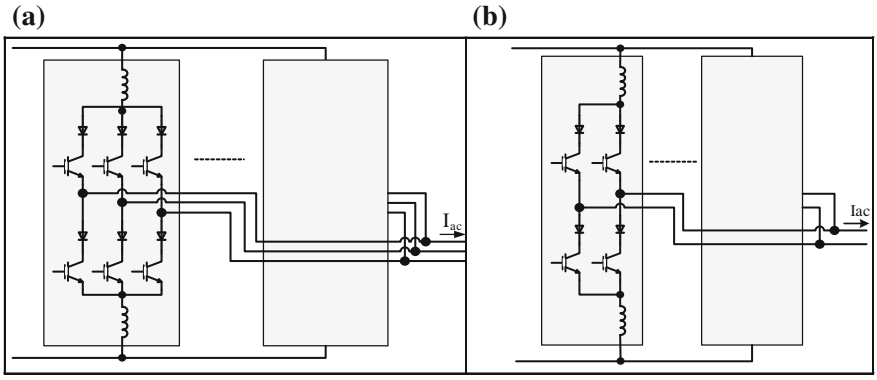

Fig. 2.28 Modular CSCs using cells with a common DC connection, **a** three-phase modular CSC, **b** single-phase modular CSC

2.3.3.2 Modular CSCs Using Cells with Common DC Connection

Because of the nature of current synthesis, a modular multilevel CSC requires current source cells to be connected in parallel. This configuration is the dual of connecting the VSC two or three-phase blocks in series. A three-phase MCSC can be constructed by three single-phase CSCs, or parallel connecting three-phase cells. The conventional modular MCSCs (see Fig. 2.28), that are widely studied in literature [9, 60], consist of parallel- connected full-bridge or three-phase current source cells. The modular CSC topology configuration can also be found by a slight variation to the FCM CSC, described above in Sect. 2.2.2. Figure 2.28a shows a three-phase 5-level example. All inductors conduct the same current level of I_{dc}/N where N is the number of two or three-phases. The DC side of cells is opened, and connected through inductors, which are required to minimize circulating currents between the cells. Same as all modular multilevel structure with the—phase floating energy sources, current balancing strategy is needed to guarantee the device rating. In principle, with a high enough number of cells, each valve can be switched at the fundamental frequency, however the Inductor size is the function of the switching frequency. In order to have a proper design, the optimum switching frequency are chosen to minimize the current ripple. However, using the three-phase CSC block in Fig. 2.28a will result is a lower current ripple compared to the Fig. 2.28b.

2.3.3.3 Current Source M2LC with Half or Full-Bridge Cells

When considering a three-phase current source M2LC, the duality transformations cannot be applied, because a three-phase voltage source M2LC supplying a three-phase load is not a planar structure. One way to construct a three-phase current source M2LC has been discussed in [61], and shown below in Fig. 2.29. This topology copies the higher level circuit structure of the three-phase voltage source

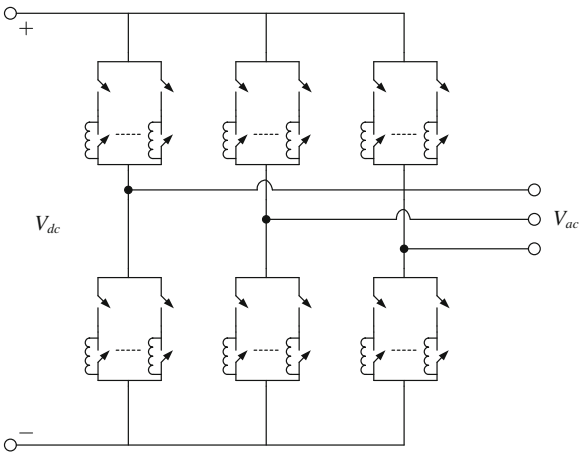

Fig. 2.29 Current source modular multilevel converter–unidirectional cells

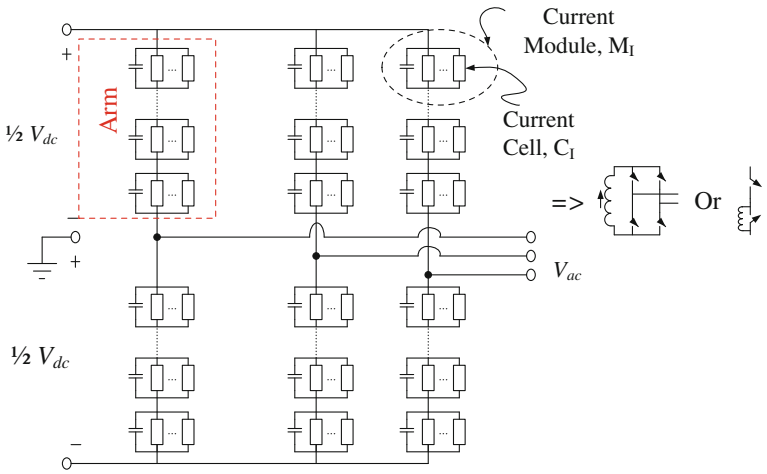

Fig. 2.30 Current source dual of M2LC-configuration to reach a high voltage

M2LC, and thus the operation of this current source M2LC also somewhat copies that of the voltage source M2LC. Each arm in the current source M2LC is a dual circuit of the arm in a voltage source M2LC which has been constructed by parallel connection of either unidirectional (half-bridge), bidirectional (full-bridge), or a mixed. Other types of current source cells may also be used in the current source arm. Each phase consists of two current source arms connecting to the positive and negative poles. When half-bridge cells are used (Fig. 2.29), the current source arm current must be unidirectional, and thus the voltage across each current source arm must be bipolar to ensure zero average arm power.

The current source M2LC can scale in voltage at the arm level. The voltage scaling principle is dual to the current scaling of voltage source M2LC arm. Using

the series-connected current source parallel links as a phase arm, Fig. 2.30 shows a current source MMC topology using half-bridge or full-bridge inductor cells. A capacitor is connected in parallel to each current module to ensure steady-state and dynamic voltage sharing between the series connected current modules. These capacitors are also essential for the series connection of current modules, because all current modules behave as current sources, and their instantaneous currents can never be guaranteed identical in reality. To reach the system voltage level, series-connected current modules are required for each arm. The parallel capacitor voltage should typically have both DC and AC components, which can be actively controlled through the current source parallel links to ensure dynamic voltage sharing. The DC and AC component of the capacitor voltage may be regulated by controlling the DC component and the phase angle of the AC component of the parallel link current, respectively. Having the DC terminals, this converter can be used for either HVDC or FATCS applications. Also, same as the VSC type, using the H-bridge cells can reduce the number of cell in this structure. The main advantages of this topology compared to other modular multilevel CSC are the modularity, scalability to the higher voltage, and the lower voltage rating. Therefore, this topology is more suitable for the high voltage and high current FACTS applications. Due to its scalability, it is possible to remove the transformer for the higher voltage application and thus reduce the extra volume and weight of the system.

2.4 Future Trends in Multilevel Converter Topologies

The evolution of multilevel converters over the last two decades has advanced several commercial applications such as flexible alternating current transmission systems (FACTS). From this technology, as summarized in this chapter, some insight on future trends can be extracted. In addition, despite industrial presence, the technology has not stabilized yet and there are still several challenges for further development of this technology. Some of these trends and challenges are discussed in this section.

The role of the next generation power converter topology becomes significantly important to reduce the total energy consumption by processing the power in electrical transmission systems. The average device switching frequencies are below 300 Hz (for IGBTs and IGCTs) for high power applications. The main reasons for this choice are the device limits, and practical limitations on the cooling system. The switching loss is important in terms of low order harmonics reduction and can be improved by the modulation technique, however, the conduction loss would become dominant, and once the topology is chosen, not much can be done to lower it. Therefore, a trend is to achieve the efficiency of line-commutated thyristor valves converter topologies while gaining valuable insights and overcoming the challenges of the newer topologies.

Reliability and availability at lowered cost is also a key trend in the future development of multilevel converters for high power applications [62].

One important application could be better utilization of the modular building blocks to limit the critical faults in power systems. As discussed earlier in this paper, some multilevel converter topologies have capability to operate under DC fault conditions. The fault detection methods are of vital importance for this ability. As addressed, bipolar cell structures and converter reconfigurations are definitely challenges for further research and development in this field. Another trend to have fault tolerant converters is to move toward the modular current source converters or hybrid VSC/CSC topologies.

Price trends reveals that semiconductors are becoming cheaper while energy is becoming more expensive, and grid codes are becoming more restrictive [63, 64]. Therefore, the use of modular multilevel converters becomes more and more attractive for high power applications, as the long-term operational cost reduction justifies the higher initial costs. The existing and future grid codes and the continued increase of power demand of various applications will be the central focus in modular multilevel converter development. The reduction of the required energy stored in the passive components is highly important. Moreover, the energy consumption in power converters should be minimized [64]. These necessities motivate the trends towards designing building block cells with more functionalities or creating modular converters with paralleled phases.

Currently, the dominating semiconductor technology for high power modular multilevel topologies is the IGBT. This approach has been very successful in modular multilevel topologies due to the low switching frequency, and is expected to exist in the upcoming years in high power application fields. On the other hand, the development of mature wide band gap devices such as silicon carbide (SiC), Gallium Nitride (GaN), and diamond power devices would benefit the establishment of multilevel converters, by drastically reducing the switching losses and minimizing the cooling system requirement [65]. Therefore, it is expected that, in the future, high-voltage SiC devices would affect the building block cells and accordingly modular multilevel topologies for high power applications [66]. This needs to be further evaluated with a proper modeling of the device and considering practical issues in high voltage applications [67].

Modular multilevel converters used for high power applications contain a large number of semiconductors, capacitors and inductors within their structures, which increases the size and weight of theses converter topologies [68]. For some applications such as offshore wind, it is vital to have a compact converter topology.

Although transformers provide galvanic isolation and voltage matching in grid connected high power applications, a transformerless topology is still a desirable feature. The elimination of transformers provides a significant reduction in the cost, volume, and weight, system complexity and losses. An alternative solution to further increase the functionality and efficiency of the grid, is to replace the conventional passive transformers by solid-state transformers. This concept also encounters different challenges, such as very high switching loss when using the silicon devices and special considerations required to both core and winding losses, especially for high power applications [69].

References

1. Rodriguez J, Lai JS, Peng FZ (2002) Multilevel inverters: a survey of topologies, controls, and applications. IEEE Trans Ind Electron 49(4):724–738
2. Rodriguez J, Franquelo LG, Kouro S, Leon JI, Portillo RC, Prats MAM, Perez MA (2009) Multilevel inverters: an enabling technology for high-power applications. Proc IEEE 97 (11):1786–1817
3. Abu-Rub H et al (2010) Medium-voltage multilevel converters—state of the art, challenges, and requirements in industrial applications. IEEE Trans Indust Electron 57(8):2581–2596
4. Kouro S et al (2010) Recent advances and industrial applications of multilevel converters. IEEE Trans Indust Electron 57(8):2553–2580
5. Soto D, Green C (2002) A comparison of high-power converter topologies for the implementation of facts controllers. IEEE Trans Indust Electron 49(5):1072–1080
6. Liang J et al (2013) Current source modular multilevel converter for HVDC and FACTS. In: Proceedings of IEEE 15th European conference on power electronics and applications (EPE)
7. Shen D, Lehn PW (2002) Modelling, analysis and control of a current source inverter-based statcom. IEEE Trans Power Delivery 17(1):248–253
8. Ye Y, Kazerani M, Quintana VH (2005) Current-source converter based statcom: modeling and control. IEEE Trans Power Delivery 20(2):795–800
9. Bai Z, Zhang Z (2008) Conformation of multilevel current source converter topologies using the duality principle. IEEE Trans Power Electron 23(5):2260–2267
10. Rohner S et al (2010) Modulation, losses, and semiconductor requirements of modular multilevel converters. Ind Electron IEEE Trans 57(8):2633–2642
11. Akagi H (2011) Classification, terminology, and application of the modular multilevel cascade converter (MMCC). Power Electron IEEE Trans 26(11):3119–3130
12. Ghosh A, Ledwich G (2002) Power quality enhancement using custom power devices. Kluwer, Norwell
13. Gyugyi L, Schauder C (1994) US Patent, 5,343,139, 30 August 1994
14. Schauder C et al (1997) Operation of ±100 MVAR TVA StatCom. IEEE Trans Power Delivery 12(4), October 1997
15. Schauder C et al (1998) AEP UPFC project: installation, commissioning and operation of the ±160 MVA STATCOM (phase I). IEEE Trans Power Delivery 13(4), October 1998
16. Peng FZ, Lai JS, McKeever JW, VanCoevering J (1996) A multilevel voltage-source inverter with separate DC sources for static var generation. IEEE Trans Ind Applicat 32:1130–1138
17. Kazmierkowski MP, Malesani L (1998) Current control techniques for three-phase voltage-source PWM converters: a survey. IEEE Trans Ind Electron 45(5):691–703
18. Shukla A, Ghosh A, Joshi A (2005) Static shunt and series compensation of an smib system using flying capacitor multilevel inverter. IEEE Trans Power Delivery 20(4):2613–2622
19. Shukla A, Ghosh A, Joshi A (2007) Hysteresis current control operation of flying capacitor multilevel inverter and its application in shunt compensation of distribution systems. IEEE Trans Power Delivery 22(1):396–405
20. Shukla A, Ghosh A, Joshi A (2007) State feedback control of multilevel inverters for dstatcom applications. IEEE Trans Power Delivery 22(4):2409–2418
21. Shukla A, Ghosh A, Joshi A (2008) Control schemes for DC capacitor voltages equalization in diode-clamped multilevel inverter based DSTATCOM. IEEE Trans Power Delivery 23 (2):1139–1149
22. Saeedifard M, Bakhshai AR, Jain P (2003) An active power filter implemented with a 3-level NPC converter in conjunction with the classification technique. Proc IEEE CCECE 1:503–507
23. Ertl H, Kolar JW, Zach FC (2002) A novel multi-cell DC-ac converter for applications in renewable energy systems. IEEE Trans Ind Electron 49(5):1048–1057
24. Flourentzou N, Agelidis V, Demetriades GD (2009) VSC-based HVDC power transmission systems: an overview. IEEE Trans Power Electron 24(3):592–602

25. Baker RH, Bannister LH (1975) Electric power converter. US Patent 3,867,643, February 1975
26. Nabae A, Takahashi I, Akagi H (1981) A new neutral-point clamped PWM inverter. IEEE Trans Ind Applicat IA-17:518–523
27. Rodriguez J, Bernet S, Steimer PK, Lizama IE (2010) A survey on neutral-point-clamped inverters. IEEE Trans Ind Electron 57(7):2219–2230
28. Steimer PK, Apeldoorn O, Ødegård B (2005) Very high power PEBB technology. In: Proceedings of IEEE EPE
29. Brückner T, Bernet S (2001) Loss balancing in three-level voltage source inverters applying active NPC switches. In: Proceedings of IEEE power electronics special conference, Vancouver, pp 1135–1140
30. Brückner T, Bernet S (2001) Loss balancing in three-level voltage source inverters applying active NPC switches. In: Proceedings of IEEE-PESC, Vancouver, pp 1135–1140
31. Marchesoni M, Tenca P (2001) Theoretical and practical limits in multilevel MPC inverters with passive front ends. In: Proceedings of EPE'01, Graz pp 27–29, August 2001
32. Shukla A, Shukla A, Joshi A (2012) Control of dc capacitor voltages in diode-clamped multilevel inverter using bidirectional buck–boost choppers. IET Power Electron 5 (9):1723–1732
33. Ishida T, Matsuse K, Sugita K, Huang L, Sasagawa K (2000) DC voltage control strategy for a five-level converter. IEEE Tran Power Electron 15(3):508–515
34. Shukla A, Shukla A, Joshi A (2010) Flying-capacitor-based chopper circuit for dc capacitor voltage balancing in diode-clamped multilevel inverter. Ind Electron IEEE Trans 57 (7):2249–2261
35. Yuan X, Barbi I (2000) Fundamentals of a new diode clamping multilevel inverter. Power Electron IEEE Trans 15(4):711–718
36. Ye Y, Kazerani M, Quintana VH (2005) Current-source converter based STATCOM: modeling and control. IEEE Tran Power Del 20(2):795–800
37. Meynard TA, Foch H (1992) Multi-level conversion: high voltage choppers and voltage-source inverters. In: IEEE power electronics specialists conference, pp 397–403
38. Yuan X, Stemmler H, Barbi I (2001) Self balancing of clamping-capacitor-voltages in the multilevel capacitor-clamping-inverter under subharmonic PWM modulation. IEEE Trans Power Electron 16(2):256–263
39. Wilkinson RH, Meynard TA, Mouton HDT (2006) Natural balance of multicell converters: the general case. IEEE Trans Power Electron 21(6):1658–1666
40. Shukla A, Ghosh A, Joshi A (2011) Natural balancing of flying capacitor voltages in multicell inverter under PD carrier-based PWM. Power Electron IEEE Trans 26(6):1682–1693
41. Shukla A, Ghosh A, Joshi A (2008) Improved multilevel hysteresis current regulation and capacitor voltage balancing schemes for flying capacitor multilevel inverter. Power Electron IEEE Trans 23(2):518–529
42. Meynard TA, Foch H, Thomas P, Caurault J, Jacob R, Nahrstaedt M (2002) Multicell converter: basic concepts and industry applications. IEEE Trans Ind Electron 49(5):955–964
43. Fuji K, Schwarger U, Doncker RWD (2005) Comparison of hard-switched multi-level inverter topologies for statcom by loss- implemented simulation and cost estimation. In: Proceedings IEEE PESC, pp 340–346
44. Lesnicar A, Marquardt R (2003) An innovative modular multilevel converter topology suitable for a wide power range. In: Proceedings of IEEE power tech conference, Bologna, vol 3, 6p
45. Hochwald W, Kleiner TC (1977) Distribution system for ac electrical energy derived from dc energy sources. US Patent No 4,052,657, 4 October 1977
46. Marchesoni M. Mazzucchelli M, Tenconi S (1988) A non conventional power converter for plasma stabilization. In: IEEE power electronics specialists conference, vol 1, pp 122–129
47. Peng FZ, Lai JS, McKeever JW, VanCoevering J (1996) A multilevel voltage-source inverter with separate DC sources for static var generation. IEEE Trans Ind Appl 32(5):1130–1138

48. Tolbert Leon M, Peng Fang Z, Cunnyngham Tim, Chiasson John N (2002) Charge balance control schemes for multilevel converter in hybrid electric vehicles. IEEE Trans Ind Electron 49(5):1058–1065
49. Manjrekar MD, Lipo TA (1998) A hybrid multilevel inverter topology for drive applications. In: IEEE applied power electronics conference, pp 523–529
50. Malinowski M et al (2010) A survey on cascaded multilevel inverters. Ind Electron IEEE Trans 57(7):2197–2206
51. Ilves K, Taffner F, Norrga S, Antonopoulos A, Harnefors L, Nee HP (2013) A submodule implementation for parallel connection of capacitors in modular multilevel converters. In: Proceedings 15th European conference on power electronics and applications (EPE), Lille
52. Nami A, Wang L, Dijkhuizen F, Shukla A (2013) Five level cross connected cell for cascaded converters. In: Proceedings EPE 2013 ECCE Europe, Lille, 3–5 September 2013
53. Chaudhuri T (2008) Cross connected multilevel voltage source inverter topologies for medium voltage applications. PhD thesis, EPFL
54. Akagi H (2011) Classification, terminology, and application of the modular multilevel cascade converter (MMCC). IEEE Trans Power Electron 26(11):3119–3130
55. Jacobson B, Karlsson P, Asplund G, Harnefors L, Jonsson T (2010) VSC-HVDC transmission with cascaded two-level converters. In: CIGRE, pp B4–B110
56. Friedrich K (2010) Modern HVDC PLUS application of VSC in modular multilevel converter topology. In Proceedings of IEEE international symposium on industrial electronics (ISIE), pp 3807–3810
57. Mohammadi HP, Bina MT (2011) A transformerless medium-voltage STATCOM topology based on extended modular multilevel converters. IEEE Trans Power Electron 26:1534–1545
58. Hagiwara M, Akagi H (2008) PWM control and experiment of modular multilevel converters. In: IEEE power electronics specialists conference, PESC, pp 154–161
59. Angquist L, Antonopoulos A, Siemaszko D, Ilves K, Vasiladiotis M, Nee HP (2011) Open-loop control of modular multilevel converters using estimation of stored energy. IEEE Trans Ind Appl 47:2516–2524
60. Antunes FLM, Braga HAC, Barbi I (1999) Application of a generalized current multilevel cell to current-source inverters. IEEE Trans Ind Electron 46(1):31–38
61. Liang J, Nami A, Dijkhuizen F, Tenca P, Sastry J (2013) Current source modular multilevel converter for HVDC and FACTS. In: Proceedings of EPE 2013 ECCE Europe, Lille, 3–5 September 2013
62. van Wyk JD, Lee FC (2013) On a future for power electronics. IEEE J Emerg Sel Top Power Electron 1(2):59–72
63. Boroyevich D, Cvetkovic I, Burgos R, Dong D (2013) Intergrid: a future electronic energy network?. IEEE J Emerg Sel Top Power Electron 1(3):127–138
64. Popović-Gerber J, Oliver J, Cordero N, Harder T, Cobos JA, Hayes M, O'Mathuna S, Prem E (2012) Power electronics enabling efficient energy usage: energy savings potential and technological challenges. IEEE Trans Power Electron 27(5):2338–2353
65. Peftitsis D, Tolstoy G, Antonopoulos A, Rabkowski J, Lim J, Bakowski M, Ängquist L, Nee H (2012) High-Power modular multilevel converters with SiC JFETs. IEEE Trans Power Electron 27(1):28–36
66. Hudgins JL (2013) Power electronic devices in the futurem. IEEE J Emerg Sel Top Power Electron 1(1):11–17
67. Gong X, Josifović I, Ferreira JA (2013) Modeling and reduction of conducted EMI of inverters with SiC JFETs on insulated metal substrate. IEEE Trans Power Electron 28(7):3138–3146
68. Blaabjerg F, Ma K (2013) Future on power electronics for wind turbine systems. IEEE J Emerg Sel Top Power Electron 1(3):139–152
69. Kassakian JG, Jahns TM (2013) Evolving and emerging applications of power electronics in systems. IEEE J Emerg Sel Top Power Electron 1(2):47–58

Chapter 3
Analysis and Implementation of an 84-Pulse STATCOM

Antonio Valderrabano-Gonzalez, Juan M. Ramirez, Ruben Tapia-Olvera, Julio C. Rosas-Caro, Jose M. Lozano-Garcia and Juan Miguel Gonzalez-Lopez

Abstract This chapter describes the use of STATCOM for the reactive power compensation and the power quality improvement. The assembling of a Voltage Source Converter (VSC) that meets the IEEE Recommended Practices and Requirements for Harmonic Control in Electrical Power Systems (IEEE Std. 519-1992) is emphasized. The low Total Harmonic Distortion (THD) that this VSC generates, qualifies this power conditioner to be considered for its use on stringent applications. The reinjection principle is used, that makes this proposal be considered as an affordable solution to the sinusoidal synthesis due to the reduced number of switches. The reinjection transformer is one of the most important elements in this configuration, and it can have a wide turn ratio variation without

A. Valderrabano-Gonzalez (✉) · J.C. Rosas-Caro
Universidad Panamericana Campus Guadalajara, Calz. Circ. Pte. No.49,
Cd. Granja, 45010 Zapopan, JAL, Mexico
e-mail: avalder@up.edu.mx

J.C. Rosas-Caro
e-mail: crosas@up.edu.mx

J.M. Ramirez
Centro de Investigacion y de Estudios Avanzados del Instituto Politecnico Nacional,
Av. del Bosque 1145, Col. el Bajio, 45019 Zapopan, JAL, Mexico
e-mail: jramirez@gdl.cinvestav.mx

R. Tapia-Olvera
Universidad Politecnica de Tulancingo, Calle Ingenierias No. 100. Col. Huapalcalco,
43629 Tulancingo, HGO, Mexico
e-mail: ruben.tapia@upt.edu.mx

J.M. Lozano-Garcia
Division de Ingenierias Campus Irapuato-Salamanca, Universidad de Guanajuato,
Carr. Salamanca—V. de Santiago, Comunidad de Palo Blanco, 36885 Salamanca,
GTO, Mexico
e-mail: jm.lozano@ugto.mx

J.M. Gonzalez-Lopez
Universidad Tecnologica de Manzanillo, Camino Hacia Las Humedades S/N,
Col. Salahua, 28869 Manzanillo, COL, Mexico
e-mail: jmgonzalez@utmanzanillo.edu.mx

F. Shahnia et al. (eds.), *Static Compensators (STATCOMs) in Power Systems*,
Power Systems, DOI 10.1007/978-981-287-281-4_3

leading out the special application standards. Conventional Proportional-Integral (PI) controllers are applied to hold the output voltage of the STATCOM around nominal conditions. The followed strategy employs the error and its variation to break down the control action into smaller sections that can be selected according to simple rules.

Keywords STATCOM · Multi-pulse · THD · Fuzzy segmented PI · VSC

3.1 Introduction

Deregulation, open access, and cogeneration in electrical power systems are creating transmission congestion scenarios and forced outages. Increasing the number of transmission lines is a non-viable solution to these potential problems, mainly due to costs and environmental issues. To have efficient and reliable power system operation, new control schemes are needed to be developed to handle dynamic disturbances such as transmission lines tripping, loss of generation, short-circuits, load rejection, while the reactive control has to be fast enough to maintain the desired voltage levels and the system stability. Flexible Alternating Current Transmission System (FACTS) devices have been proposed for fast dynamic control of voltage, impedance, and phase angle in high-voltage AC lines. The application of this technology has opened new and better opportunities for an appropriate transmission and distribution control. The series and shunt power systems compensation is used with the purpose of improving the operating conditions. Respect to the voltage, the compensation has the purpose of handling reactive power to maintain bus voltages close to their nominal values, reduce line currents, and reduce system losses. The voltage magnitude in some buses may be controlled through sophisticated and versatile devices such as the STATCOM, which can synthesize the reactive power from small values of storing elements [1], and is a power reactive source [2, 3]. By regulation of the STATCOM output voltage magnitude, the reactive power exchanged between the STATCOM and the transmission system can be controlled [4–8].

Since the STATCOM may cause interference on the system's fundamental sine wave at frequencies that are multiples of the fundamental one, special care should be paid to ensure preventing further harmonic problems. In general, there are three common strategies to construct a VSC while minimizing the harmonic content at the output: (i) the multi-pulse; (ii) the multilevel; (iii) and the Pulse-Width Modulation (PWM) [9, 10].

In the multi-pulse strategies, the period of the signal is broken down into equal sized parts with respect to the pulse number. Switches are triggered once per cycle at the fundamental frequency, and the pulse's amplitude is controlled mainly by the magnetic output stage. Higher number of pulses results in less output THD.

In the multilevel strategy, the DC source has to be broken down into parts of equal amplitude (x), resulting in a signal of $2x - 1$ levels. Switches are also switched once per cycle at the fundamental frequency. The output THD depends on the number of DC sources or divisions available in the DC link.

On the other hand, the PWM strategy uses fast commutations to obtain a low THD. The faster commutations are the lower THD; however, it is limited because of the commutation speed of the switches and requires always an output filter to be coupled to the grid.

This research deals with a combination of multi-pulse and multilevel strategies with emphasis on the use of multi-pulse configurations in order to reach the minimum THD.

Several methods has been investigated for stepping-up the number of pulses in the multi-pulse converter output. The simplest one is by increasing the number of 6-pulse modules through their corresponding transformers (four 6-pulse converters result in 24-pulse, eight 6-pulse converters result in 48-pulse operation, and so forth). The weakness of this method is the large size and high cost due to the number of bridges and transformers. Thus, in order to utilize the VSC in special applications such as airports or hospitals, to attain an 84-pulse signal, an array of fourteen 6-pulse modules with 42 transformers is required, besides a huge control task to have a reduced THD, which makes the entire array an impractical solution. A good strategy to get the 84-pulse waveform from a 12-pulse along with an eight level reinjection converter is presented in [9]. It has 26 extra switches and 7 DC voltage sources (capacitors) compared to the conventional 12-pulse converter. The control task is hard because of the number of gate signals needed, and it is prone to unbalance problems due to the large chain of capacitors. Multilevel Voltage Reinjection (MLVR) H-bridge conversion is another option to generate the 84-pulse signal. It requires 5 additional DC voltage sources and 12 switches compared to the conventional 12-pulse converter, but it can be easily used to have more levels in the reinjection by adding H-bridges in series [11]. An auxiliary multilevel circuit in the DC link side has been proposed for reinjection in [5–7, 10, 12]; it employs fewer components while the THD is bigger than that needed for special applications. This research presents a strategy to generate the 84-pulse VSC, assembled by combining one 12-pulse converter with one seven-level converter used as the reinjection scheme. The extra components, respect to the conventional 12-pulse converter, are: 8 switches, 4 DC voltage sources, 4 diodes for the seven-level converter, and one reinjection transformer. This amount of components and the wide turn ratio allowed by the reinjection transformer constitute an attractive array in terms of cost and reduced output voltage THD.

STATCOM is a FACTS device with a great deal of attributes, such as quick response in the adjustment of the required output levels, fewer space requirements than other shunt FACTS devices, flexibility, and excellent dynamic characteristics under various operating conditions. Its main objective is to generate an almost harmonic-free and controllable three-phase AC output voltage waveform at the Point of Common Coupling (PCC), to regulate reactive current flows by generating and absorbing controllable reactive power through the solid states switching

algorithm [13]. This is one of the most widespread devices studied. However, the state-of-the-art review indicates that a high number of switches, magnetic and reactive elements are needed in order to be able to get a low output THD. This research has been proposed taking into account the current technologies and the advantages of each one on the VSCs assembling, including the advantages of using the multilevel strategies on the synthesis of a staircase signal with a low number of reactive components, but with the low switching speed characteristic of the multi-pulse converters, and also a low number of magnetic devices. The proposed strategy saves the total amount of switching devices, while renders low THD, which is really attractive in special applications.

3.2 84-Pulses STATCOM

STATCOM is a power electronics-based Synchronous Voltage Generator (SVG) which is capable to provide fast and continuous capacitive and inductive reactive power supply. It generates a three-phase voltage, synchronized with the transmission voltage, from a DC energy source, and it is connected to the electric power system by a coupling transformer. The regulation of the STATCOM's output voltage magnitude gives rise to the reactive power exchange between the STATCOM and the transmission system. The STATCOM's basic structure, illustrated on Fig. 3.1, consists of a step-down transformer, a three-phase VSC, and a DC capacitor [2, 5, 6, 8, 14].

3.2.1 Reinjection Configuration

There are three main strategies to implement a VSC: (i) the multi-pulse; (ii) the multilevel; (iii) and the PWM [9, 10].

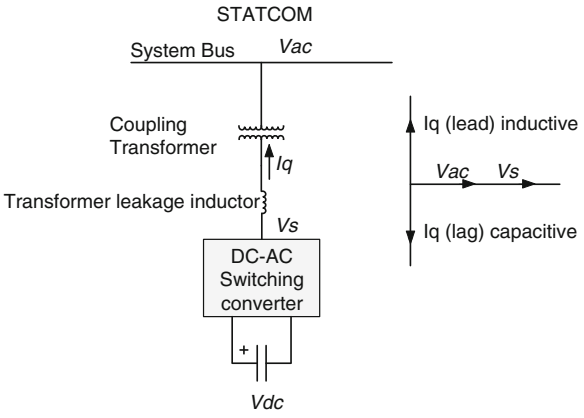

Fig. 3.1 STATCOM basic structure and V–I characteristic

There is a difference on the 12-pulse converter used in this research respect to the standard 12-pulse converter. The DC source is not common to both 6-pulse modules. In this proposition, a positive multi-pulse signal between the main terminals of the first 6-pulse converter and another positive multi-pulse signal with opposite phase between the main terminals of the second 6-pulse converter are connected. In order to have a neutral point, the negative terminal of the first converter is connected to the positive terminal of the second converter.

Each branch in the 6-pulse converters must generate electrical signals with 120° of displacement between them; the upper switch is conducting while the lower one is open and vice versa (180° voltage source operation) [15].

A 30° displacement in the firing sequence of both converters must be considered. Transformer turn ratios are 1:1 and 1:$\sqrt{3}$ on the YY and YΔ transformers, respectively. In order to operate the VSC in special applications such as airports or hospitals, an 84-level voltage signal is generated through a seven-level auxiliary circuit operating as a re-injection scheme. The auxiliary circuit is common to the three phases, reducing the number of extra components. The topology to provide the pulse multiplication is detailed in [9, 10, 12, 16–19], and illustrated in Fig. 3.2.

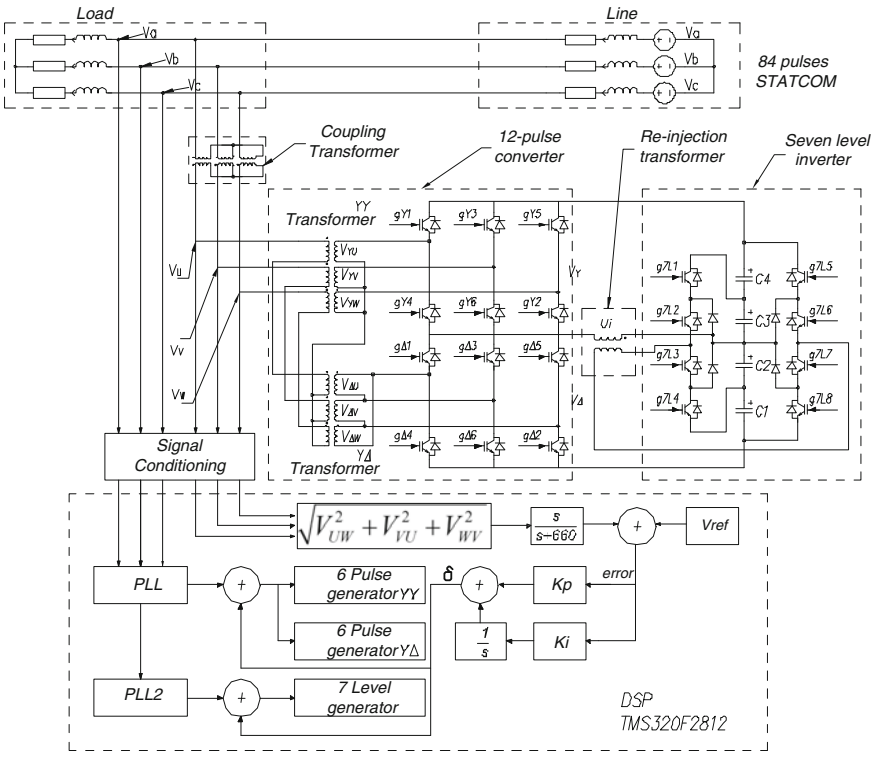

Fig. 3.2 84-pulse STATCOM structure

3.2.2 Total Harmonic Distortion

In order to apply the seven-level inverter output voltage to feed the standard 12-pulse converter, special care should be paid for not applying negative voltage into V_Y or V_Δ; notice the inclusion of the injection transformer between both arrays. Thus, input voltages in the 6-pulse converter may be regulated by adjusting the injection voltage U_i by:

$$V_Y = V_{DC} + U_i \tag{3.1}$$

$$V_\Delta = V_{DC} - U_i \tag{3.2}$$

The injection voltage is determined by the seven-level inverter switching pattern, and the injection transformer turns ratio. When voltages V_Y and V_Δ are used as inputs to the 6-pulse converters, less THD will appear at the output of the VSC. Figure 3.3 exhibits the followed strategy to generate V_{YU} and $V_{\Delta U}$ as the interaction of the seven-level output and the corresponding 6-pulse signals [20]. These signals have been obtained from an electrical simulation developed in PLECS®, within MATLAB/Simulink environment.

Using the 1:1 ratio in the YY transformer, and $1{:}\sqrt{3}$ for the YΔ transformer, adding their corresponding output signals in a series connection, the 84-pulses line-to-neutral signal VU emerges Fig. 3.4a, with the harmonic spectrum in Fig. 3.4b (linear scale) and in Fig. 3.4c (logarithmic scale).

The STATCOM's phase voltage VU is an odd symmetric signal, so that the even terms of the Fourier series become zero. Thus,

$$V_U(t) = \sum_{n=1}^{\infty} V_{U_{2n-1}} \sin((2n-1)\omega t) \tag{3.3}$$

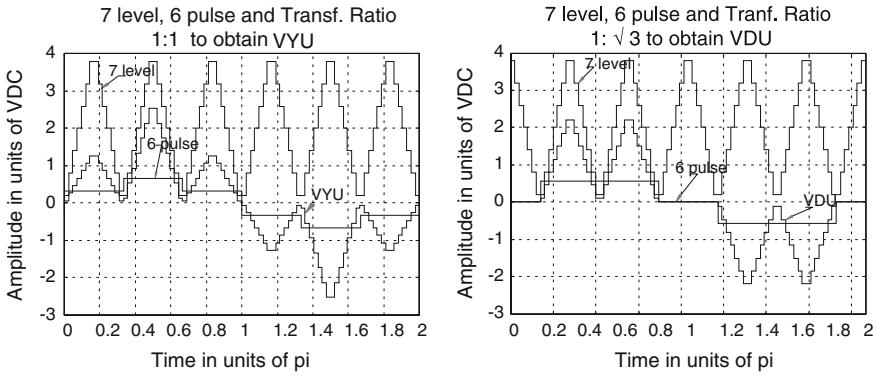

Fig. 3.3 Mixing seven-level, 6-pulse signals, and transformer ratios to attain V_{YU} and $V_{\Delta U}$

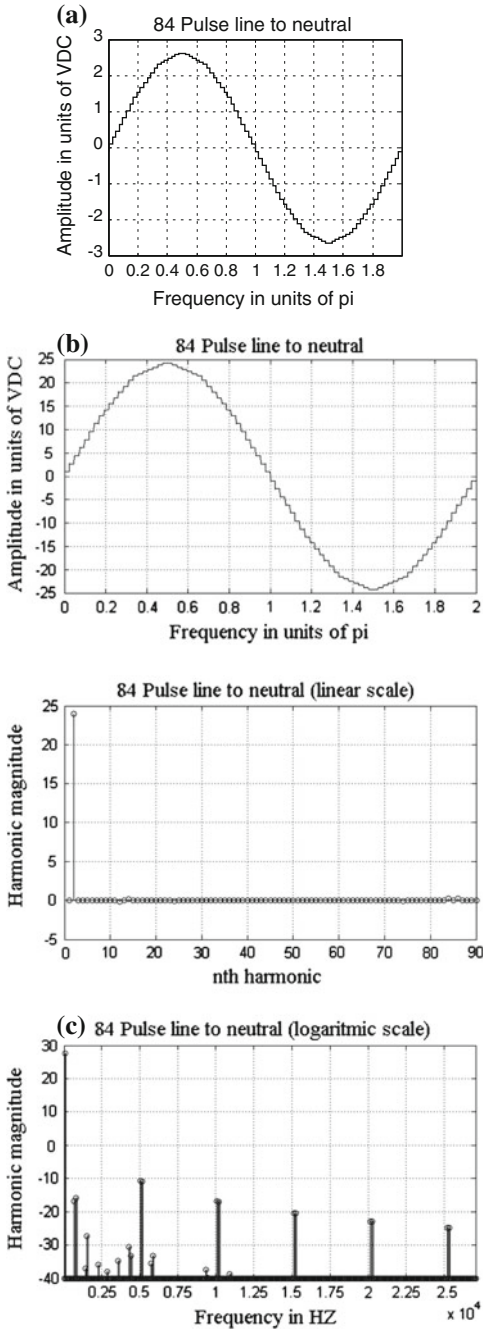

Fig. 3.4 **a** 84-pulses line-to-neutral output voltage, **b** 84-pulses harmonic content (linear scale), 84-pulses harmonic **c** content (logarithmic scale)

$$V_{U_{2n-1}} = \frac{4V}{3\pi(2n-1)}(A_{2n-1} + aB_{2n-1}) \tag{3.4}$$

$$A_{2n-1} = 2 + 2\cos\left(\frac{1}{3}\pi(2n-1)\right) + 2\sqrt{3}\cos\left(\frac{1}{6}\pi(2n-1)\right) \tag{3.5}$$

$$B_{2n-1} = \sum_{i=0}^{20} Coeff_i \cos\left(\frac{i}{42}\pi(2n-1)\right) \tag{3.6}$$

$$Coeff = \left\{ \begin{matrix} -3, & 1, & 1, & 1, & 1, & 1, & 1, \ldots \\ -3\sqrt{3}, & \sqrt{3}-1, & \sqrt{3}-1, & \sqrt{3}-1, & \sqrt{3}-1, & \sqrt{3}-1, & \sqrt{3}-1, \ldots \\ -3, & -\sqrt{3}+2, & -\sqrt{3}+2, & -\sqrt{3}+2, & -\sqrt{3}+2, & -\sqrt{3}+2, & -\sqrt{3}+2 \end{matrix} \right\} \tag{3.7}$$

assuming that a is the turns ratio of the re-injection transformer.

The 84-pulse signal value (VU) depends on a which is determined in order to minimize the THD, defined by [10, 21]

$$THD_{VU} = \sqrt{\frac{\sum_{n=2}^{\infty} V_{Un}^2}{V_{U1}^2}} \tag{3.8}$$

The minimization of THD yields the parameter a. In this research, calculation has been carried out in MATLAB with n = 7,200, and increments of Δa = 0.0001. With these parameters, the minimum THD becomes 2.358 % with a = 0.5609, value used on the previous figures.

The distortion limits according to the IEEE Std. 519 indicate that the allowed THD in voltage is 10 % in dedicated systems, 5 % in general systems, and 3 % for special applications as hospitals and airports [21].

Table 3.1 presents the minimum THD in the output voltage produced with several multi-pulse configurations. The THD produced through this proposition allows its use even in applications with stringent quality requirements; it exhibits less dependence to variations on a, which can have variations until ±12 % to get a maximum THD lower than 3 %. This means that a strict reinjection transformer's turn ratio is not needed to get a THD within a stringent condition. Figure 3.5

Table 3.1 Minimum THD produced through the multi-pulse VSC

Number of pulses	THD (%)
12	15.22
24	7.38
48	3.8
60	3.159
84	2.358

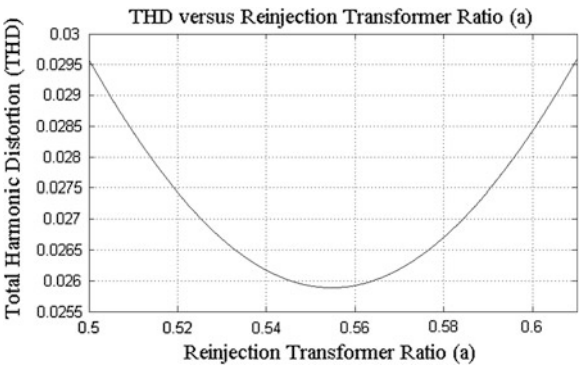

Fig. 3.5 Dependence of the THD respect to the turn ratio of the reinjection transformer

illustrates the dependence of the THD respect to variations in the re-injection transformer turn ratio a. All these values had been obtained using MATLAB.

3.2.3 STATCOM Arrangement

In order to connect the improved VSC to the system for reactive compensation, several points have to be taken into account. This section deals with those details using Fig. 3.2 as the main scheme, including a coupling transformer 13.8:13.8 kV, and considering the following transmission line parameters, at 75° C:

- Conductor code name: Grosbeak Aluminum Conductor Composite Core (ACCC)
- Voltage rating: 13.8 kV peak
- Resistance: 0.0839 Ω/km
- Inductive Reactance: 0.2574 Ω/km
- Line length: 50 km
- Load Resistance: 202.5 Ω
- Load Inductive Reactance: 0.6 H

If we pursue to eliminate the active power exchange between the STATCOM and the system, the DC voltage sources are replaced by capacitors.

Secondly, it must be ensured that the frequency and phase angle at the output of the STATCOM are equal to the system ones; these parameters will be obtained by a synchronizing arrangement which is able to detect instantaneously the phase angle. The seven-level inverter must switch at six times the frequency of the 6-pulse converters to ensure phase and frequency.

The digital signal processor (DSP)-control implementation must take the voltage levels needed for the Analog to Digital Converters (ADC) to detect the signals with appropriate precision, and must refresh the output data before taking new samples to be considered real time. It is also needed to provide isolation from the power stage.

3.2.4 Phase-Locked-Loop

The Phase-Locked Loop (PLL) is the synchronizing circuit responsible for the determination of the system frequency and phase-angle from the fundamental positive sequence voltage of the controlled AC bus [22]. The PLL utilizes the Stationary Reference Frame (SRF) in order to reduce computational costs, and helps to improve the system dynamic performance [23]. Digital PLL is an algorithm which can detect the fundamental component of the phase-voltages to synchronize the output signal to the frequency and phase of the input one. This algorithm does not require a zero crossing detection routine for the input voltage or the generation of internal reference signals for the input current [24]. The proposed PLL strategy employs a—$\tan^{-1}(\alpha/\beta)$ function added to a correction value determined by the signs of α and β, as shown in Fig. 3.6a. This block synchronizes the zero output of the PLL with respect to the startup signal α, when signal β attains its minimum value as shown in Fig. 3.6b.

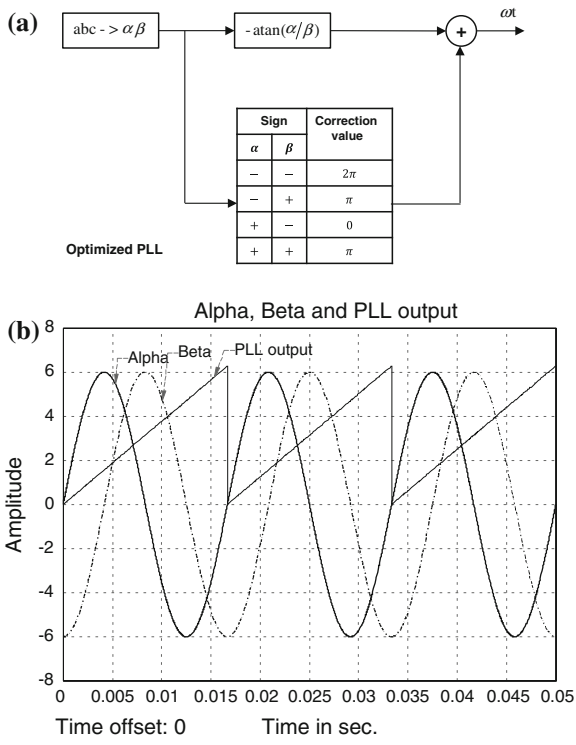

Fig. 3.6 **a** PLL strategy, **b** α, β, and PLL-output

3.2.5 Firing Sequence

The second block is the 6-pulse generator, which is responsible for generating the pulse sequence to fire the three-phase IGBT arrays. It consists of an array of 6-pulse spaced 60° from each other. In this block, the IGBT will operate at full 180° for the *on* period and 180° for the *off* period. Any disturbance in the frequency will be captured by the synchronizing block, preventing errors. The falling border in the synchronizing block output signal is added to a series of six 60° spaced signals that would be sent to the opto-coupler block gate, which will feed each 6-pulse converter. The off sequence turns off in a similar way but waiting 180° to keep the same duration *on* and *off* for each IGBT.

3.2.6 Seven-Level Generator

In order to produce the pulse sequence needed to generate the seven-level inverter, six times the frequency of the 6-pulse generator should be ensured beginning at the same time. This is achieved by monitoring the falling border in the novel PLL output signal, and using it along with the modulus operator with the π/3 argument. This signal will be the period for the seven-level generator, which will modify its state every π/42 rad. Figure 3.7 depicts the asymmetric pulse sequence for such seven-level inverter, along with the voltage for a complete sinusoidal cycle and a π/3 zoom-in, in order to observe the detailed pulse signals.

3.2.7 Angle Control Circuit

The reactive power exchange between the AC system and the compensator is controlled by varying the fundamental component magnitude of the inverter voltage,

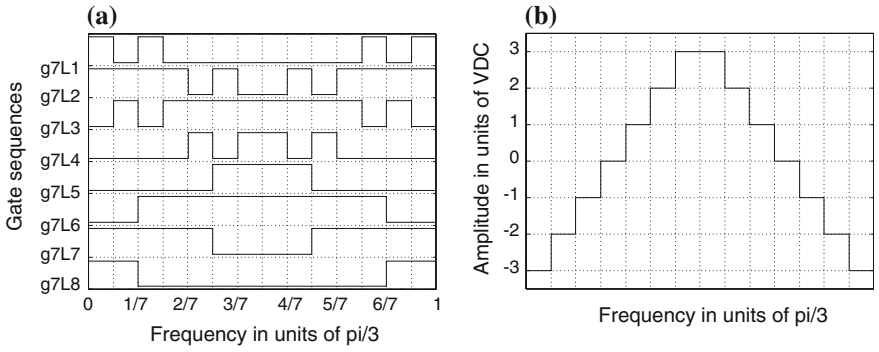

Fig. 3.7 Seven-level gate signals and output. **a** Gate sequence 7 level converter. **b** Output signal 7 level converter

above and below the AC system level. The compensator control is achieved by small variations in the switching angle of the semiconductor devices, so that the first harmonic component of the voltage generated by the inverter is forced to lag or lead the AC system voltage by a few degrees. This causes active power to flow into or out of the inverter, modifying the value of the DC capacitor voltage, and consequently. Subsequently, this will affect the magnitude of the inverter terminal voltage and the resultant reactive power [5]. The angle control block diagram is described in [23] for a PI controller, and depicted in Fig. 3.8.

The inputs are the line-to-line voltages of the controlled AC bus prior to the coupling transformer. The reference voltage VREF is chosen as the RMS value for a pure sinusoidal three-phase signal, which is $\sqrt{1.5}$ times the peak of the line voltage. This value is compared to the filtered RMS voltage at the output of the STATCOM (VRMS) multiplied by the turn ratio of the coupling transformer. The output signal δ corresponds to the displacement angle of the generated multi-pulse voltages, with respect to the controlled AC bus voltage (primary voltage of the converter transformer). The Low Pass Filter (LPF) is tuned to remove the characteristic harmonic content in the multi-pulse configurations; for the 12-pulse and begins with the 11th harmonic. The PI controller has a limiting factor by dividing the error signal by the reference voltage V_{REF} in order to have the δ signal with a maximum value of –1 when the STATCOM output is equal to zero.

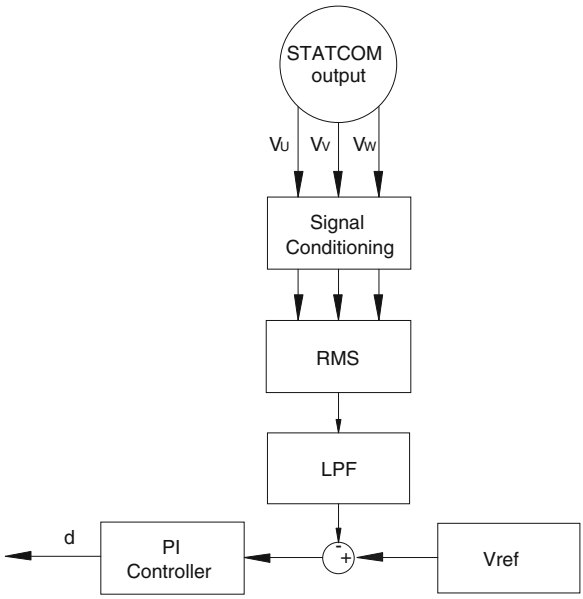

Fig. 3.8 STATCOM power angle control

3.3 Control Strategy

Conventional PI or Proportional-Integral-Derivative (PID) regulators have been applied to control the STATCOM output voltage under nominal and dynamic conditions [25–28]. Such controllers may exhibit poor performance when the error signal jumps with big steps in magnitude. It is desirable to find a controller that can deal with most of the problems detailed in [29]. The strategy followed employs the error and error variation to break down the control action in smaller sections that can be selected according to simple rules [30].

3.3.1 Segmented PI Controller

The complete system presented on Fig. 3.2 was tested under several disturbances using a PI controller tuned for steady state operation. Special attention is paid to measure the error and estimate the error increment when the disturbances are applied. It is verified that a motor startup is a quite demanding situation to test the STATCOM performance, so it was used to define the membership function limits. For simplicity on the controller design, crisp membership functions were used to describe seven linguistic variables similarly to the fuzzy set notation as follows:

- NB → negative big,
- NM → negative medium,
- NS → negative small,
- Z → zero,
- PS → positive small,
- PM → positive medium,
- PB → positive big.

Figure 3.9a displays the error signal, which has a range from −1 to +1, and Fig. 3.9b exhibits the variation of this error. This parameter is estimated using MATLAB ode23t solver with a variable step. The error (E) and its variation (DE) are represented by lowercase as the independent variables; they are continuous values. The uppercase represents the fuzzy set obtained by selecting the indicated membership functions' limits.

Fuzzy control rules are usually obtained empirically. This chapter uses the rules presented in [31] to define the zones of the segmented PI, Table 3.2.

The strategy to tune the segmented PI zones is summarized in the following steps.

1. Tune up a conventional PI at steady state. The proportional and integral gains obtained are: K_P = 0.5411, and K_I = 20.3718. Such values are used on the segmented PI controller as the initial conditions, preserving the same gain values in the seven zones. Thus, originally, the conventional PI and the segmented PI controllers are equivalent.

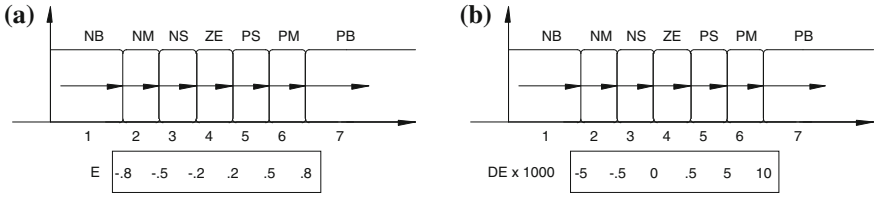

$$E = \begin{cases} \text{NB} & -\infty < e \le -.8 \\ \text{NM} & -.8 < e \le -.5 \\ \text{NS} & -.5 < e \le -.2 \\ \text{ZE} & -.2 < e \le .2 \\ \text{PS} & .2 < e \le .5 \\ \text{PM} & .5 < e \le .8 \\ \text{PB} & .8 < e \le \infty \end{cases} \qquad DE \times 1000 = \begin{cases} \text{NB} & -\infty < de \le -5 \\ \text{NM} & -5 < de \le -.5 \\ \text{NS} & -.5 < de \le 0 \\ \text{ZE} & 0 < de \le .5 \\ \text{PS} & .5 < de \le 5 \\ \text{PM} & 5 < de \le 10 \\ \text{PB} & 10 < de \le \infty \end{cases}$$

Fig. 3.9 Membership functions

Table 3.2 Control rules

E\DE	NB	NM	NS	ZE	PS	PM	PB
NB	1	1	1	2	3	3	4
NM	1	2	2	2	3	4	5
NS	1	2	3	3	4	5	6
ZE	1	2	3	4	5	6	7
PS	2	3	4	5	5	6	7
PM	3	4	5	6	6	6	7
PB	4	5	6	7	7	7	7

2. Taking into account that capacitors are used in the DC link in order to the system operates as STATCOM, and considering them fully discharged, we get a maximum error of −3. It is convenient to adjust the gains' value zone 1 due to it corresponds to the biggest negative error and the biggest negative error variation. To adjust the values of this zone, we must maintain K_P as low as possible to keep the system stable. Then, reduce K_I to the value that allows less oscillation in the segmented PI sections. After this step, zone 1 would have the values for the biggest negative error and error variation, while the remaining zones exhibit the original steady state values.
3. Starting up an induction motor when the capacitors are fully charged is considered one of the most demanding situations and is used for adjusting the remaining zones. To tune the gains of segment 2, use the value of K_P as low as possible to keep the system stable. Then, reduce K_I to the value that allows less oscillation in the zones presented on the right and low corner of Fig. 3.10, which will be discussed later.

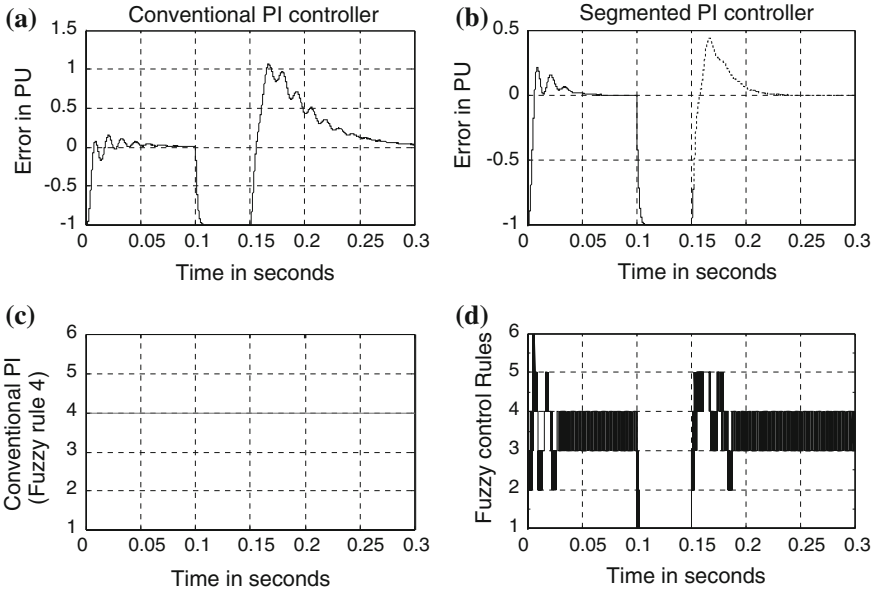

Fig. 3.10 Three-phase fault

Table 3.3 Gain values of the segmented PI

Fuzzy rule	K_P	K_I
1	0.5252	5.0929
2	0.5411	38.9929
3	0.5570	40.7436
4	0.5729	40.7436
5	0.5570	20.3718
6	0.4933	20.3718
7	0.3183	40.7436

4. Repeat step 3 for sections 3, 5, 6, and 7 in sequence. This will bring up to the segmented PI, Table 3.3. After tuning up the seven zones, the output will be between zones 3 and 4 on steady state.

It is important to note that using a different disturbance in the load or the source, the values would vary slightly, but the motor startup after getting to steady state (full capacitors charge) is the most demanding condition. Thus, using these values for tuning the segmented PI the controller will give good results for the most common power problems, such as Sags, Swells, etc.

3.3.2 Study Case

The STATCOM model and the segmented PI controller with the values obtained from the previous section were simulated in MATLAB/Simulink, using PLECS. PLECS is used because it is a fast simulation toolbox for electrical circuits within the Simulink environment specially designed for power electronics systems. It is also a powerful tool for any combined simulation of electrical circuits and controls. The PLL-block feeds the two 6-pulse generators at the fundamental frequency, and it is used to bring forth the seven-level pulses at six times the fundamental frequency to have them synchronized to the system and configured as the 84-pulse STATCOM. The δ signal calculated from the segmented PI controller is utilized to lag or lead the STATCOM voltage respect to the system. While the phase-angle lags the bus voltage ($\delta < 0$), energy is flowing to the DC capacitor, charging it and doing the STATCOM draws capacitive current. Contrarily, inductive current is drawn while ($\delta > 0$) [22].

The main advantages of this controller can be summarized with the system response to an interruption and a motor startup [30].

An interruption occurs when the supply voltage or load current decreases to less than 0.1 pu for a period of time not exceeding one minute. Interruptions can be the result of power system faults, equipment or control failures. An interruption, whether it is instantaneous, momentary, temporary, or sustained, can cause disruption, damage, and it can cause equipment failure, ruination of product, as well as the cost associated with downtime, cleanup, and restart [29, 32]. Figure 3.10 illustrates the controller error behavior after a 3-cycle three-phase fault at the load bus. The error is defined as the difference between the measured voltage and the reference voltage; the greatest error becomes −1 while the fault is on, but, once this one is released; the error is bigger than 1 pu with a conventional PI, as shown in Fig. 3.10a. In contrast, the segmented PI presents an error around 0.4 pu, as shown in Fig. 3.10b. The oscillations in the conventional PI response are smoothed with the use of the segmented controller. Figure 3.10c and d respectively illustrate rule number 4 for the conventional PI controller, and the rules of the segmented PI.

Oscillatory transients and voltage fluctuation commonly arise when a motor is connected. At this point, a sudden change in the steady-state condition of a signal's voltage, current, or both is performed and a series of random changes in magnitude and frequency is presented. A single PI is not as fast as needed to get a smooth startup. Figure 3.11 details the behavior of the error when a motor load is started.

The parameters of the induction motor are as follows:

- 2 250HP (2,300 V),
- Rs = 0.029 Ω,
- Lls = 0.0006 H
- Rr = 0.022 Ω,
- Llr = 0.0006 H,
- Lm = 0.0346 H,
- J = 6.5107 J.

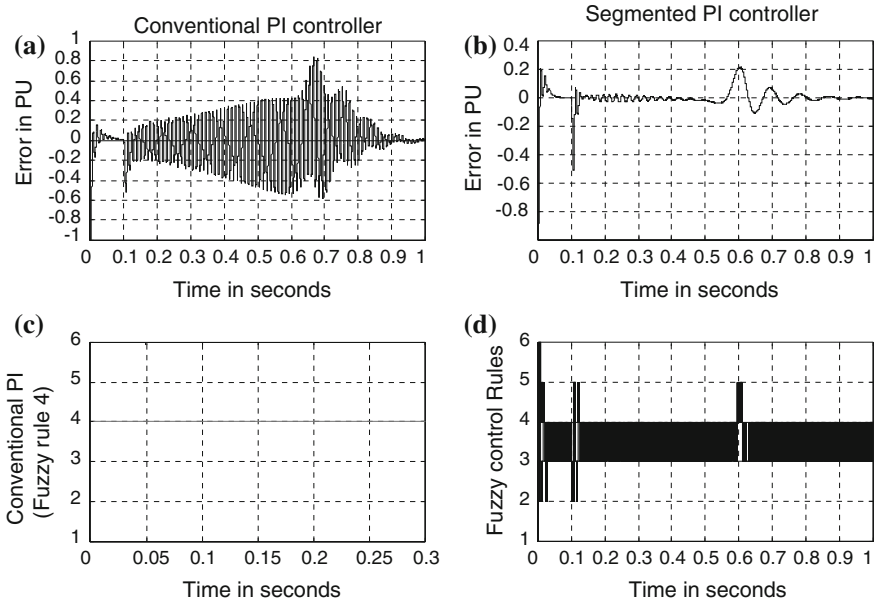

Fig. 3.11 Motor start up

The error signal, for the conventional PI exhibits several big oscillations as shown in Fig. 3.11a, while the segmented one exhibits very fast response to reach the steady state, and minimum oscillation as shown in Fig. 3.11b. Figure 3.13c, d are also included to illustrate the rule number 4 (conventional PI controller), and the rules of the segmented PI, respectively.

With these simulations it is demonstrated that when the system is stressed, the segmented PI controller presents an appropriate response.

3.4 Experimental Results

Previous sections have described the VSC structure as a STATCOM with the controller configuration. This section includes the results gotten on the experimental prototype built to verify the strategy, and are displayed through images coming from an oscilloscope for validation of each part of the device. These experimental results are exhibited as they were collected from the prototype, by increasing the complexity of the whole circuit. Important is to consider the nomenclature used, variables with subscripts a, b, or c, represent the source side, while variables with subscripts U, V, or W, are for the STATCOM output. When it is needed to differentiate both sides on the transmission line, subscripts a, b, or c are used, indicating if the source bus or the load bus is referred [33].

3.4.1 VSC Based on Multi-pulse Strategy

All the images presented in this section are captured with a Tektronix® TDS2024B oscilloscope which has only one reference point for the four acquired signals. Figure 3.12a, reveals the line-to-line voltage V_{UV} and V_{UW} of a 12-pulse VSC output (without connection to the grid), and illustrates that the 12-pulse converter output modified, exhibits exactly the same characteristics of a conventional 12-pulse converter when both input voltages (V_Y and V_Δ) of equal magnitude are used. Figure 3.12b, presents the single-phase seven-level inverter output (U_i) in (3.1) and (3.2) that is the needed signal at the input of the reinjection transformer. This signal has six times the system frequency, which is needed to have a complete cycle for each pulse on the 6-pulse converters output. The zero crossing of this signal must match with each three-phase zero-crossing.

In order to validate the strategy to build V_{YU} and $V_{\Delta U}$, Fig. 3.3 is used as a reference. The seven-level converter output, presented in Fig. 3.12b, is passed through the reinjection transformer connected as a step-down transformer; the transformer output U_i is added to the voltage of capacitors C4 and C3 to build V_Y,

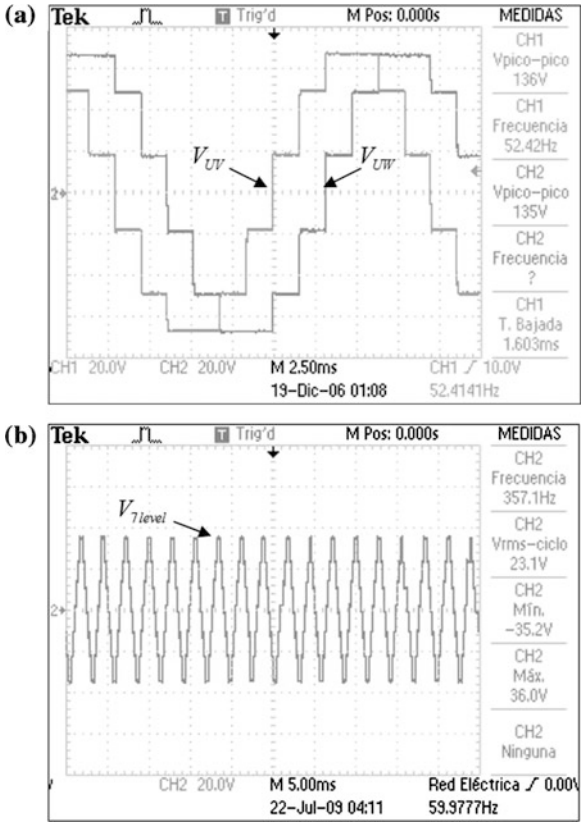

Fig. 3.12 **a** Conventional 12-pulse output voltages, **b** seven-level converter output

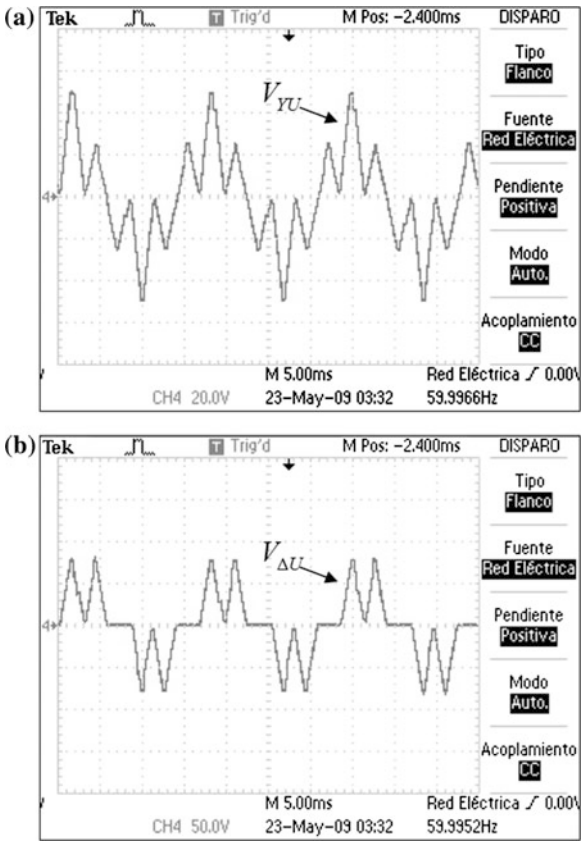

Fig. 3.13 **a** VYU built when the seven-level signal is injected into the 6-pulses converter with (YY-transformer), **b** VΔU built when the seven-level signal is injected into the 6-pulses converter (YΔ-transformer)

and C2 and C1 to build V_{Δ}. Voltage V_{DC}, corresponds to the voltage in capacitors C4 and C3, or C2 and C3. Using voltages V_Y and V_{Δ} as the inputs to the 6-pulse converters, and measuring after transformers YY and YΔ, the VSC outputs are those displayed in Fig. 3.13a, b. These signals have good agreement to the ones illustrated in Fig. 3.3.

Figure 3.14a verifies that by adding the voltages in Fig. 3.13a, b, the resultant waveform has the desired shape. The harmonic content is presented in Fig. 3.14b. It is attained by the Tektronix® TDS2024B oscilloscope. There are significant magnitude harmonics each about 5 kHz, which corresponds to the number $84r \pm 1$ $r = 0, 1, 2, \ldots$ when we use a 60 Hz signal. These harmonics are concurrent to the traditional multi-pulse harmonic content.

3.4.2 STATCOM Synchronized to the Grid

The PLL is the element responsible to determine the system frequency and the fundamental signal phase-angle. In order to verify its usefulness, Fig. 3.15a depicts

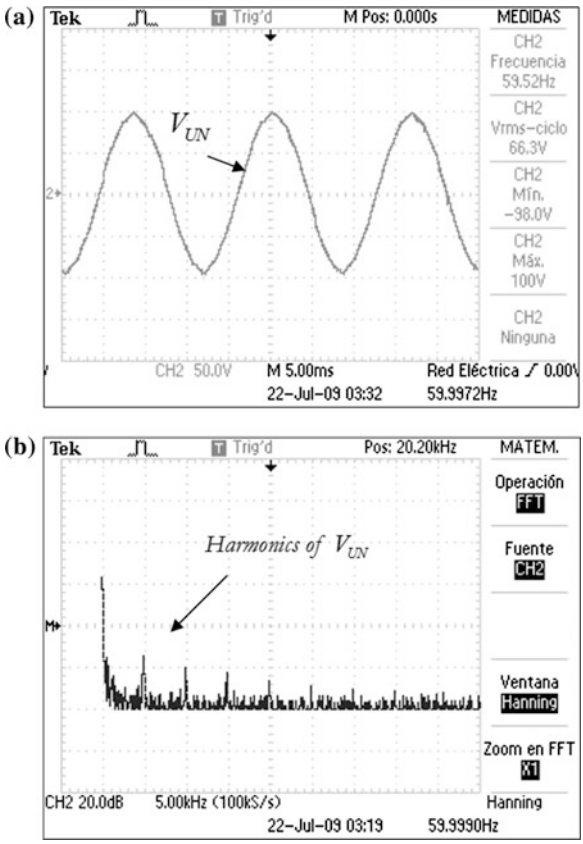

Fig. 3.14 **a** 84-pulses signal obtained through the combination of V_{YU} and $V_{\Delta U}$, **b** 84-pulses output signal harmonic content

the line voltage output of the VSC with respect to the grid line voltage. The waveform, phase, and output frequency, demonstrate the system ability to track the input, and the PLL effectiveness. Figure 3.15b displays the three-phase line-to-line voltages arisen from the VSC. It can be noticed that the angle difference among phases is 120°, as needed in a three-phase signal. The frequency of these signals is equal to that of the grid.

3.4.3 STATCOM Based on Energy Storage and Capacitors on the DC-Link

The use of an energy storage device, such as a bank of batteries, becomes quite important to verify the system behavior in the case of using DC renewable sources or battery storage to provide active power capabilities to the system [34–37]. However, due to the use of the DC source some effects that must be taken into account arise. They are summarized in this section.

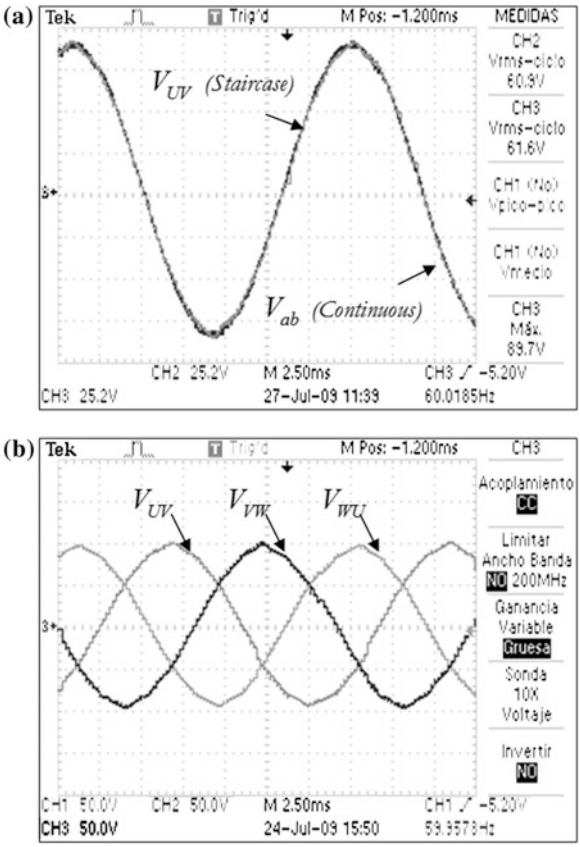

Fig. 3.15 **a** VSC output voltage synchronized in phase, frequency, and amplitude, **b** three phase 84-pulses VSC output

3.4.3.1 Notching

If a conventional 12-pulse STATCOM is used, the resulting voltage signal presents small disturbances in each pulse level change; these disturbances are termed notching [29]. The allowed notching limit according to the IEEE Std. 519 in special applications as hospitals and airports is 10 % [21]. This limit is exceeded by using a 12-pulse converter, especially around the zero crossing, Fig. 3.16a. The notching effect can be considerably reduced if the amount of pulses per cycle is increased. Figure 3.16b illustrates the reduced effect of notching when the 84-pulses STATCOM based on energy storage is employed.

3.4.3.2 Harmonics

The following figures are captured when the STATCOM based on energy storage is synchronized and connected to the grid. They illustrate one phase of the system, assuming that the behavior is similar in the two remaining phases.

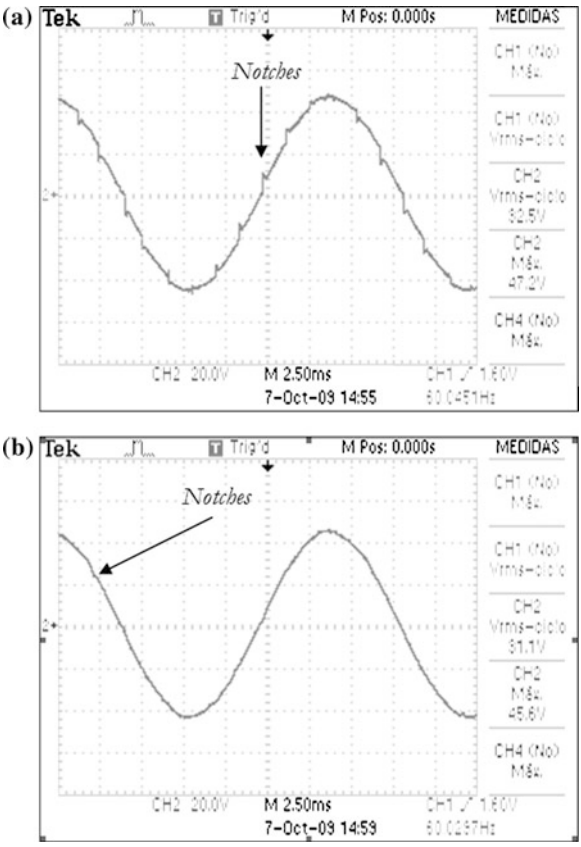

Fig. 3.16 **a** Notching produced by the 12-pulses STATCOM based on energy source, **b** the presence of notching is reduced by the 84-pulses STATCOM with energy source

Harmonic distortion is the pollution of the fundamental sine wave at frequencies that are multiples of the fundamental. Figure 3.17a depicts the phase voltage V_{aDSP} passed through the signal conditioning board, which is fed into the eZdsp TMS320F2812. This voltage is responsible of the synchronization. The VSC output, prior to the coupling transformer is also included and named as $V_U(STATCOM)$. The load voltage is presented as $V_a(Load)$ which has a magnitude of twice of the $V_U(STATCOM)$. These three signals have the same phase and frequency as the power system requires. The Fourier spectrum of $V_a(Load)$, when the STATCOM is not connected to the grid, is illustrated in Fig. 3.17b. The spectrum is calculated in the Tektronix® TPS2024 oscilloscope. Figure 3.17c depicts the spectrum of $V_a(Load)$ when the STATCOM based on energy storage is connected to the grid. In this case, small amplitude harmonics are repeated each 5 kHz.

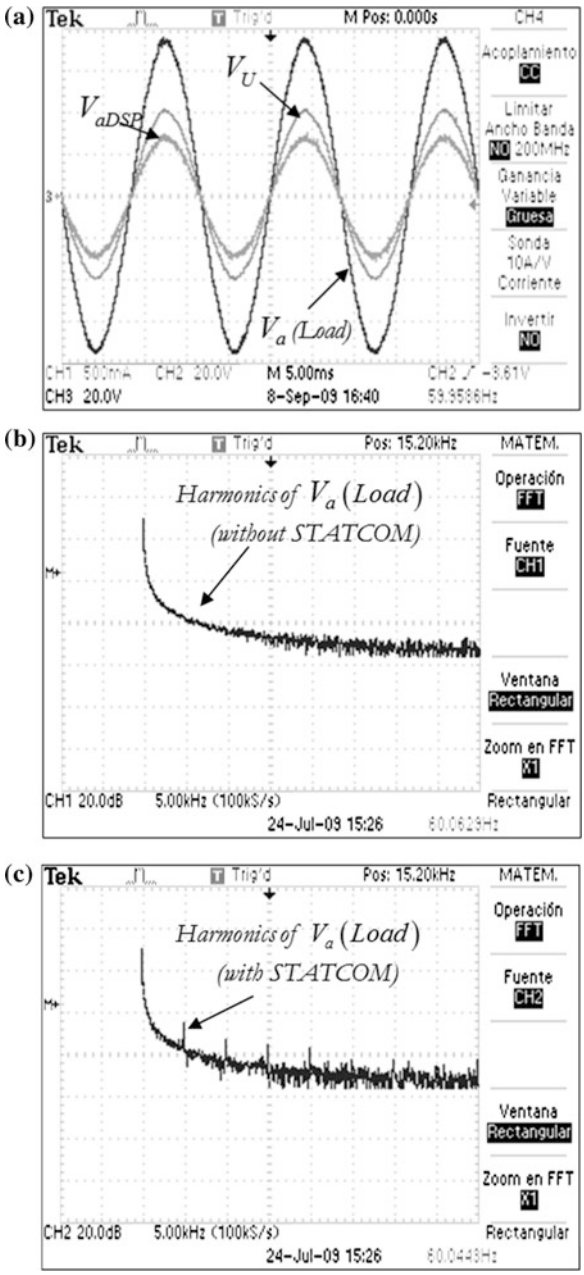

Fig. 3.17 **a** Voltage a fed into the DSP(V_{aDSP}), STATCOM output voltage (V_U), and load voltage of phase-a ($V_a(Load)$), **b** load voltage Fourier spectrum without STATCOM, **c** load voltage Fourier spectrum with the STATCOM based on energy source

3.4.4 STATCOM Reference Voltage Tracking Through a PI Controller

Once the STATCOM is connected to the grid, it is important to include a controller to verify its performance under some common variations. The STATCOM main objective is to maintain the voltage level on the load bus. Thus, the controller reference voltage is the magnitude of the voltage needed on the load, and has to be compared with the measured magnitude. A detailed explanation of the STATCOM operation is found at [8]. Referring to Fig. 3.2, the δ signal used on the pulse generators inside the DSP TMS320F2812 block, represents the phase displacement between the STATCOM and the grid. It is responsible for increasing or decreasing the STATCOM voltage. Through the appropriate δ selection, a conventional proportional-integral controller has been chosen and configured to have a losses' steady state compensation due to the transmission line parameters. This PI controller has been assembled in the DSP TMS320F2812 using the bilinear transformation to validate its behavior. Figure 3.18a shows voltage $V_a(Source)$ and voltage $V_a(Load)$ for the cases of low reference voltage. In this case, $V_a(Load)$ has the frequency and phase-angle corresponding to the $V_a(Source)$, but smaller magnitude. Capacitors were utilized for energy storage. Figure 3.18b depicts the case with nominal reference voltage. In this case, the $V_a(Load)$ has the frequency, the phase-angle, and the amplitude of the $V_a(Load)$, illustrating that the PI controller is able to command the line losses. This is the STATCOM normal operating condition in steady state. Figure 3.18c illustrates the case of high reference voltage. It is noticeable that the load voltage can be adjusted to that of the corresponding reference, although the influence of the 12-pulse converter becomes more evident when V_{ref} is higher than V_{source}. A more robust controller is needed to appropriately respond to commands in load higher voltage. The segmented PI controller proposed on this research demonstrates, via simulation, its ability to track low/high reference voltage.

3.4.5 Load Imbalance

Several researches have been made in order to use the STATCOM for source or load imbalance compensation [27, 38, 39]. Figure 3.19a displays some signals when a resistive load is used; phase-B in the load is in open-circuit to give rise to a load imbalance. The STATCOM is disconnected. Signal $V_a(Source)$ is phase-a voltage. Signal $V_a(Load)$ is the load voltage. It is worth noting the difference in amplitude and phase. The load current is in-phase with the load voltage due to the resistive load. Signal $P_a(Load)$ represents the instantaneous power on the load. Figure 3.19b demonstrates the usefulness of connecting a STATCOM based on

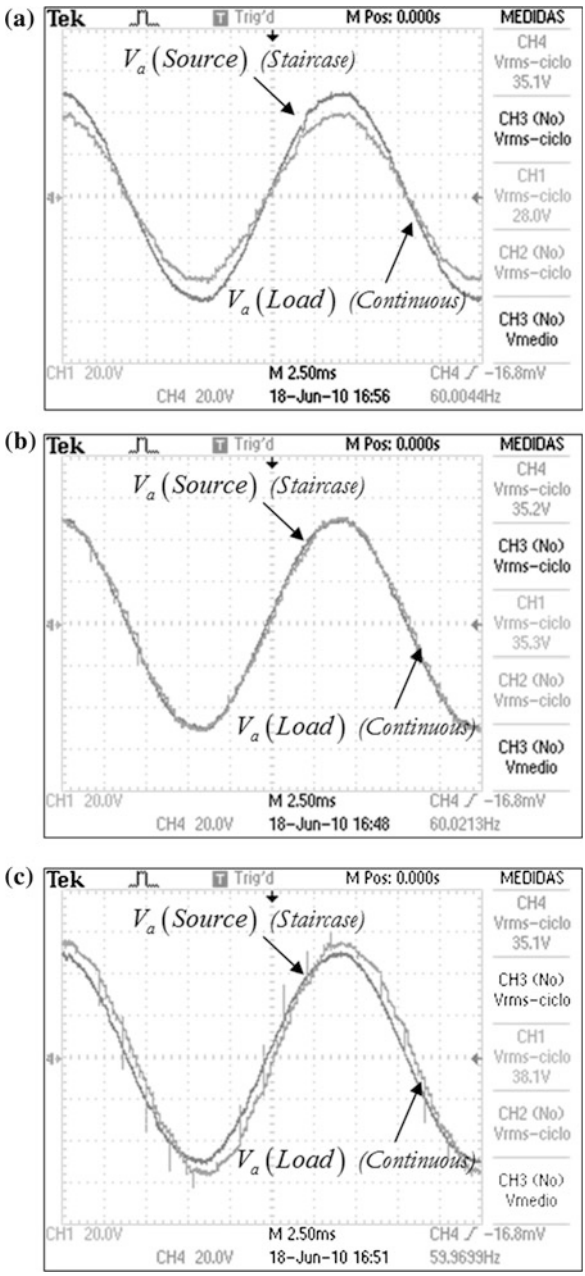

Fig. 3.18 **a** Load voltage when the reference voltage is lower than the source voltage, **b** load voltage when the reference voltage is equal to the source voltage, **c** load voltage when the reference voltage is equal to the source voltage

energy storage to the previous system. Signal $V_a(Source)$ is the phase-a voltage. Signal $V_a(Load)$ is the load voltage. Their overlapping is due to their same magnitude and phase. The load current $I_a(Load)$ becomes in phase with the load

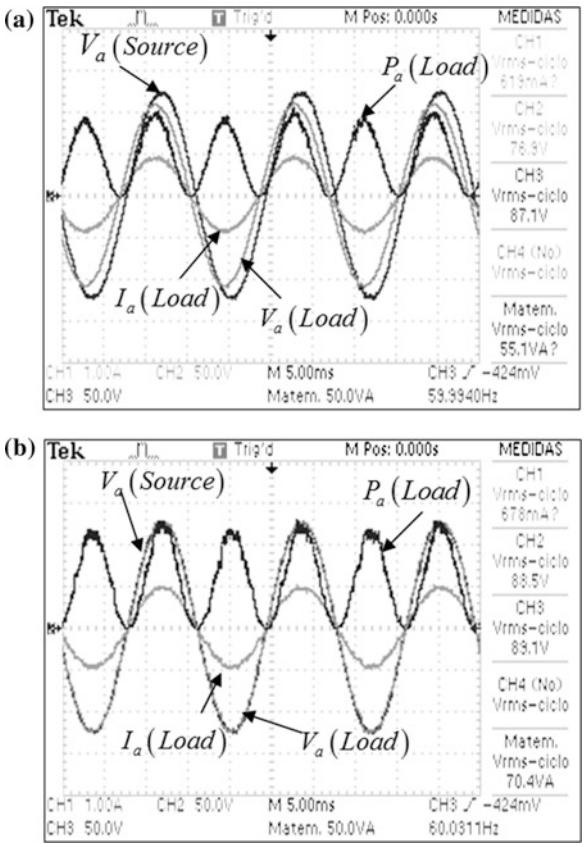

Fig. 3.19 **a** System with resistive load and STATCOM disconnected. **b** system with resistive load and the STATCOM based on energy storage

voltage, as a consequence of the resistive load. The $P_a(Load)$ signal represents the instantaneous power drawn in the load. A bigger power sent to the load is evident. The STATCOM is not designed to deal with unbalanced conditions. Using energy storage, active power can be used to solve unbalancing problems. Such condition needs separate controllers for each STATCOM phase.

References

1. Hingorani NG (2007) FACTS technology—state of the art, current challenges and the future prospects. In: Power engineering society general meeting, IEEE, pp 1–4
2. Song Y-H, Johns A (1999) Flexible ac transmission systems (FACTS). IET, Stevenage
3. Acha E, Fuerte-Esquivel CR, Ambriz-Perez H, Angeles-Camacho C (2004) FACTS: modelling and simulation in power networks. Wiley, New Jersey
4. Wang H (2000) Applications of damping torque analysis to STATCOM control. Int J Electr Power Energy Syst 22:197–204

5. Davalos-Marin R (2003) Detailed analysis of a multi-pulse StatCom. In: Cinvestav–internal report, May 2003. Available at http://www.gdl.cinvestav.mx/jramirez/doctos/doctorado/Predoctoral.pdf
6. El-Moursi M, Sharaf A (2005) Novel controllers for the 48-pulse VSC STATCOM and SSSC for voltage regulation and reactive power compensation. Power Syst IEEE Trans 20:1985–1997
7. Hingorani NG, Gyugyi L (2000) Understanding facts. IEEE press, New Jersey
8. CIGRE, Static Synchronous Compensator (1998) Working group 14.19 in Sept 1998
9. Liu Y, Arrillaga J, Watson N (2004) A new STATCOM configuration using multi-level DC voltage reinjection for high power application. Power Deliv IEEE Trans 19:1828–1834
10. Pan W, Xu Z, Zhang J (2007) Novel configuration of 60-pulse voltage source converter for StatCom application. Int J Emerg Electr Power Syst 8:1–6
11. Arrillaga YH, Liu NR Watson (2007) Flexible power transmission: the HVDC options. Wiley, New Jersey
12. Liu Y, Watson N, Arrillaga J (2003) A new concept for the control of the harmonic content of voltage source converters. In: The 5th international conference on power electronics and drive systems, PEDS 2003, IEEE, pp 793–798
13. Singh B, Saha R, Chandra A, Al-Haddad K (2009) Static synchronous compensators (STATCOM): a review. Power Elect IET 2:297–324
14. Norouzi AH, Sharaf A (2003) A novel control scheme for the STATCOM stability enhancement. In: Transmission and distribution conference and exposition, 2003 IEEE PES, IEEE, pp 24–29
15. Krause PC, Wasynczuk O, Sudhoff SD, Pekarek S (2013) Analysis of electric machinery and drive systems. Wiley, New Jersey
16. Han B, Choo W, Choi J, Park Y, Cho Y (2005) New configuration of 36-pulse voltage source converter using pulse-interleaving circuit. In: Proceedings of the 8th international conference on electrical machines and systems, ICEMS 2005, IEEE, pp 2389–2394
17. Liu YU, Perera LB, Arrillaga J, Watson N (2004) Harmonic reduction in the double bridge parallel converter by multi-level DC-voltage reinjection. In: 2004 international conference on power system technology 2004 PowerCon 2004, IEEE, pp 41–46
18. Voraphonpiput N, Chatratana S (2004) Analysis of quasi 24-pulse STATCOM operation and control using ATP-EMTP. In: Conference analog and digital techniques in electrical engineering
19. Valderrabano-Gonzalez A, Ramirez JM, Beltran-Carbajal F (2013) 84 pulse converter, design and simulations with Matlab
20. Valderrabano A, Ramirez JM (2010) A novel voltage source converter behind the StatCom. Elect Power Compon Syst 38:1161–1174
21. (2014) IEEE recommended practice and requirements for harmonic control in electric power systems, IEEE Std 519-2014 (Revision of IEEE Std 519-1992), pp 1–29
22. Aredes M, Santos G Jr (2000) A robust control for multipulse StatComs. In: Proceedings of IPEC, 2000, pp 2163–2168
23. Cho J-H, Song E-H (2003) Stationary reference frame-based simple active power filter with voltage regulation. In: Proceedings of industrial electronics, ISIE 2003. IEEE international symposium on IEEE 2001, pp 2044–2048
24. Mussa SA, Mohr HB (2004) Three-phase digital PLL for synchronizing on three-phase/switch/level boost rectifier by DSP. In: Power electronics specialists conference, PESC 04. IEEE 35th annual, IEEE, pp 3659–3664
25. Blazic B, Papic I (2006) Improved D-STATCOM control for operation with unbalanced currents and voltages. Power Deliv IEEE Trans 21:225–233
26. Cavaliere CA, Watanabe EH, Aredes M (2002) Multi-pulse STATCOM operation under unbalanced voltages. In: Power engineering society winter meeting, IEEE 2002, pp 567–572
27. Hochgraf C, Lasseter RH (1998) Statcom controls for operation with unbalanced voltages. Power Deliv IEEE Trans 13:538–544

28. Li K, Liu J, Wang Z, Wei B (2007) Strategies and operating point optimization of STATCOM control for voltage unbalance mitigation in three-phase three-wire systems. Power Deliv IEEE Trans 22:413–422
29. Seymour J, Horsley T (2005) The seven types of power problems. White Pap 18:1–24
30. Valderrábano A, Ramirez JM (2010) DStatCom regulation by a fuzzy segmented PI controller. Electr Power Syst Res 80:707–715
31. Pal A, Mudi R (2008) Self-tuning fuzzy PI controller and its application to HVAC systems. Int J Comput Cogn 6:25–30
32. (2009) IEEE recommended practice for monitoring electric power quality, IEEE Std 1159-2009 (Revision of IEEE Std 1159-1995), pp c1–83
33. Valderrábano-González A, Ramírez JM, Beltrán-Carbajal F (2012) Implementation of a 84-pulse voltage-source converter for special applications. IET Power Electron 5:984–990
34. Mahale P, Joshi K, Chandrakar V (2009) Static synchronous compensator (STATCOM) with Energy Storage. In: 2nd international conference on emerging trends in engineering and technology (ICETET), IEEE 2009, pp 560–563
35. Rosas-Caro JC, Ramirez JM, Peng FZ, Valderrabano A (2010) A DC-DC multilevel boost converter. Power Electron IET 3:129–137
36. Yang Z, Shen C, Zhang L, Crow M, Atcitty S (2001) Integration of a STATCOM and battery energy storage. Power Syst IEEE Trans 16:254–260
37. Zhang L, Chen S, Atcitty S, Crow M (2003) A comparison of FACTS integrated with battery energy storage systems. Institute of Electrical and Electronics Engineers, New Jersey
38. Shen D, Liu W, Wang Z (2000) Study on the operation performance of STATCOM under unbalanced and distorted system voltage. In: Power engineering society winter meeting, IEEE 2000, pp 2630–2635
39. Tsai S, Chang Y (2008) Dynamic and unbalance voltage compensation using STATCOM. In: Power and energy society general meeting-conversion and delivery of electrical energy in the 21st century, IEEE 2008, pp 1–8

Chapter 4
Mathematical Modeling and Control Algorithms of STATCOMs

Boštjan Blažič, Leopold Herman, Ambrož Božiček and Igor Papič

Abstract In this chapter, different STATCOM control algorithms will be introduced. The algorithms are derived on the basis of STATCOM mathematical models in the α-β coordinate system and in the synchronously rotating d-q coordinate system. In the first part of the chapter, both mathematical models are derived from the three-phase STATCOM model, and the mathematical process is described in detail. In the second part, four different control algorithms are described: d-q control algorithm for balanced and unbalanced conditions, time-optimal current-control algorithm and Proportional-Resonant (PR) multi-loop controller.

Keywords Control algorithm · Mathematical modeling · STATCOM

4.1 Introduction

Four different control algorithms will be described in the main part of the chapter. The first one is the d-q control algorithm for balanced conditions. The control algorithm is decoupled, enabling independent control of d-axis and q-axis currents. The second one is the d-q control algorithm for unbalanced conditions that enables efficient control of unbalanced compensator currents. With the proposed algorithm, a separate control of positive- and negative-sequence currents is possible. The problem of harmonics generation due to the unbalanced switching function will be

B. Blažič · L. Herman · A. Božiček · I. Papič (✉)
Faculty of Electrical Engineering, University of Ljubljana, Ljubljana, Slovenia
e-mail: igor.papic@fe.uni-lj.si

B. Blažič
e-mail: bostjan.blazic@fe.uni-lj.si

L. Herman
e-mail: leopold.herman@fe.uni-lj.si

A. Božiček
e-mail: ambroz.bozicek@fe.uni-lj.si

F. Shahnia et al. (eds.), *Static Compensators (STATCOMs) in Power Systems*,
Power Systems, DOI 10.1007/978-981-287-281-4_4

also addressed. Modulation of the switching function is proposed as a solution, which enables the use of relatively small capacitor on the DC-side. The controllers' constants for both presented d-q control algorithms are derived from the mathematical models in order to obtain the desired STATCOM response (i.e. first order function). The third control algorithm is a time-optimal current-control (TOCC) algorithm for a space vector modulation-based voltage-source converter. The term "time optimal" refers to optimally controlled reference current tracking in order to gain the shortest durations of current transients. The algorithm uses an internal mathematical model allowing the calculation of the optimal transient current path and in most cases provides a faster transient responses than the hysteresis controller does. The fourth controller is a PR multi-loop controller. The controller is implemented in a synchronous-reference frame (SRF) and allows using half the number of resonators, compared with the solution using proportional-integral controllers in the harmonic-reference frame. The controllers' constants are obtained from the device transfer function. Resonant controllers have taken on significant importance in recent years due to their high selectivity and good performance.

4.2 STATCOM Mathematical Model

The basic building block of the STATCOM is a Voltage Source Converter (VSC) and the device is shunt connected to the network through a coupling inductance. The coupling inductance can be a transformer or a reactor if the device is designed for direct connection to the busbars voltage level. The basic circuit is presented in Fig. 4.1. The STATCOM can be modelled as an AC-voltage source where the magnitude, the phase angle and the frequency of the output voltage are controllable [1, 2].

In all subsequent derivations a per-unit (pu) system is used where i_B and v_B are the base values and ω_B is the angular speed at the system nominal frequency [1]:

$$\begin{aligned}
i'_{pa} &= \frac{i_{pa}}{i_B} \quad & i'_{pb} &= \frac{i_{pb}}{i_B} \quad & i'_{pc} &= \frac{i_{pc}}{i_B} \\
v'_{pa} &= \frac{v_{pa}}{v_B} \quad & v'_{pb} &= \frac{v_{pb}}{v_B} \quad & v'_{pc} &= \frac{v_{pc}}{v_B} \\
v'_{ia} &= \frac{v_{ia}}{v_B} \quad & v'_{ib} &= \frac{v_{ib}}{v_B} \quad & v'_{ic} &= \frac{v_{ic}}{v_B} \\
z_B &= \frac{v_B}{i_B} \quad & L'_p &= \frac{\omega_B L_p}{z_B} \quad & R'_p &= \frac{R_p}{z_B} \\
v'_{dc} &= \frac{v_{dc}}{v_B} \quad & i'_{dc} &= \frac{i_{dc}}{i_B} \quad & C' &= \frac{1}{\omega_B C z_B} \quad & R'_c &= \frac{R_c}{z_B}
\end{aligned} \tag{4.1}$$

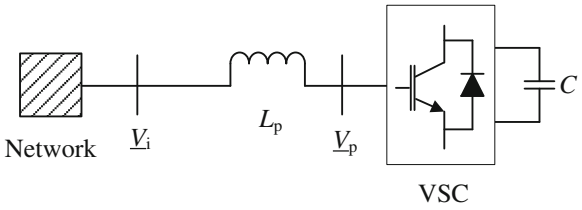

Fig. 4.1 Basic STATCOM circuit and connection to the network

4.2.1 Three-Phase Mathematical Model

The equivalent circuit of a STATCOM is presented in Fig. 4.2. As mentioned, the device is modelled as a voltage source (voltages v'_{pa}, v'_{pb}, v'_{pc}) that is connected to the network through the inductance L'_p/ω_B and the resistance R'_p that represents the losses of the coupling circuit. Please note that the constant L'_p represents the per-unit reactance value, therefore the per-unit inductance is calculated as L'_p/ω_B. The STATCOM current is denoted as i'_p. The DC circuit is modelled as a current source (i'_{dc}) connected to the capacitor C' and the resistance R'_c. The resistance R'_c is used to represent semiconductor and DC-circuit losses.

Based on the three-phase equivalent circuit shown in Fig. 4.2 we can write differential equations for the STATCOM currents. The voltage difference between the network voltages (v'_{ia}, v'_{ib}, v'_{ic}) and the STATCOM voltages (v'_{pa}, v'_{pb}, v'_{pc}) results in the STATCOM current (i'_{pa}, i'_{pb}, i'_{pc}) through the coupling circuit:

$$\frac{d}{dt}\begin{bmatrix} i'_{pa} \\ i'_{pb} \\ i'_{pc} \end{bmatrix} = \frac{-R'_p\omega_B}{L'_p}\begin{bmatrix} i'_{pa} \\ i'_{pb} \\ i'_{pc} \end{bmatrix} + \frac{\omega_B}{L'_p}\begin{bmatrix} \left(v'_{ia} - v'_{pa}\right) \\ \left(v'_{ib} - v'_{pb}\right) \\ \left(v'_{ic} - v'_{pc}\right) \end{bmatrix} \tag{4.2}$$

For an accurate modelling of STATCOM also the DC-side circuit has to be described as the DC-side voltage is not absolutely constant. The DC-side current can be expressed as:

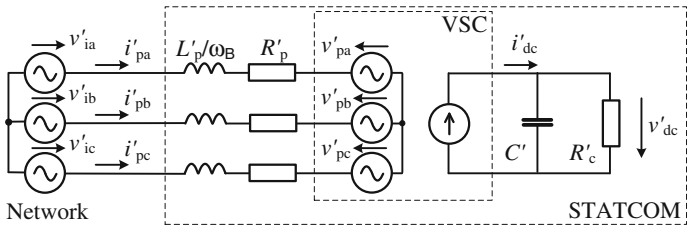

Fig. 4.2 Basic STATCOM equivalent circuit

$$i'_{\mathrm{dc}} = \frac{1}{\omega_{\mathrm{B}} C'} \frac{dv'_{\mathrm{dc}}}{dt} + \frac{v'_{\mathrm{dc}}}{R'_{\mathrm{c}}} \tag{4.3}$$

To describe the connection between the AC and DC side we can consider the VSC instantaneous power. Namely, the instantaneous power on the DC-side of the converter is always equal to the power on the AC-side:

$$v'_{\mathrm{dc}} i'_{\mathrm{dc}} = v'_{\mathrm{pa}} i'_{\mathrm{pa}} + v'_{\mathrm{pb}} i'_{\mathrm{pb}} + v'_{\mathrm{pc}} i'_{\mathrm{pc}} \tag{4.4}$$

The connection between the VSC AC and DC side voltages can be described with the switching function (signals S_{a}, S_{b}, S_{c}), describing the generation of AC voltages from DC voltage:

$$\begin{bmatrix} v'_{\mathrm{pa}} \\ v'_{\mathrm{pb}} \\ v'_{\mathrm{pc}} \end{bmatrix} = k_{\mathrm{p}} \begin{bmatrix} S_{\mathrm{a}} \\ S_{\mathrm{b}} \\ S_{\mathrm{c}} \end{bmatrix} v'_{\mathrm{dc}} \tag{4.5}$$

where the factor k_{p} depends on the converter type. The factor could be also omitted from the derivations, however, it enables to take into account different converter topologies which have different DC-side voltage to AC-side voltage amplitude ratios.

Taking into account (4.4) and (4.5) we get the expression for the DC-side current:

$$i'_{\mathrm{dc}} = k_{\mathrm{p}} S_{\mathrm{a}} i'_{\mathrm{pa}} + k_{\mathrm{p}} S_{\mathrm{b}} i'_{\mathrm{pb}} + k_{\mathrm{p}} S_{\mathrm{c}} i'_{\mathrm{pc}} \tag{4.6}$$

The DC-current (4.6) is included in (4.3) giving a complete description of the DC-side circuit. The complete set of equations describing STATCOM operation, including the DC-side circuit, is [1, 2]:

$$\frac{d}{dt} \begin{bmatrix} i'_{\mathrm{pa}} \\ i'_{\mathrm{pb}} \\ i'_{\mathrm{pc}} \\ i'_{\mathrm{dc}} \end{bmatrix} = \begin{bmatrix} \frac{-R'_{\mathrm{p}} \omega_{\mathrm{B}}}{L'_{\mathrm{p}}} & 0 & 0 & \frac{-k_{\mathrm{p}} \omega_{\mathrm{B}}}{L'_{\mathrm{p}}} S_{\mathrm{a}} \\ 0 & \frac{-R'_{\mathrm{p}} \omega_{\mathrm{B}}}{L'_{\mathrm{p}}} & 0 & \frac{-k_{\mathrm{p}} \omega_{B}}{L'_{\mathrm{p}}} S_{\mathrm{b}} \\ 0 & 0 & \frac{-R'_{\mathrm{p}} \omega_{\mathrm{B}}}{L'_{\mathrm{p}}} & \frac{-k_{\mathrm{p}} \omega_{\mathrm{B}}}{L'_{\mathrm{p}}} S_{\mathrm{c}} \\ k_{\mathrm{p}} \omega_{\mathrm{B}} C' S_{\mathrm{a}} & k_{\mathrm{p}} \omega_{\mathrm{B}} C' S_{\mathrm{b}} & k_{\mathrm{p}} \omega_{\mathrm{B}} C' S_{\mathrm{c}} & -\frac{\omega_{\mathrm{B}} C'}{R'_{\mathrm{c}}} \end{bmatrix} \begin{bmatrix} i'_{\mathrm{pa}} \\ i'_{\mathrm{pb}} \\ i'_{\mathrm{pc}} \\ i'_{\mathrm{dc}} \end{bmatrix} + \frac{\omega_{B}}{L'_{\mathrm{p}}} \begin{bmatrix} v'_{\mathrm{ia}} \\ v'_{\mathrm{ib}} \\ v'_{\mathrm{ic}} \\ 0 \end{bmatrix} \tag{4.7}$$

4.2.2 Mathematical Model in the α-β Coordinate System

For given three-phase system, where x_a, x_b and x_c are individual phases of any electrical parameters, the Clarke transformation $\mathbf{T}_{\boldsymbol{\alpha\beta}}$ is given by (4.8) and (4.9).

$$\mathbf{T}_{\boldsymbol{\alpha\beta}} = \frac{2}{3} \cdot \begin{bmatrix} 1 & -\frac{1}{2} & -\frac{1}{2} \\ 0 & \frac{\sqrt{3}}{2} & -\frac{\sqrt{3}}{2} \\ \frac{1}{2} & \frac{1}{2} & \frac{1}{2} \end{bmatrix} \tag{4.8}$$

$$\begin{bmatrix} x_{\boldsymbol{\alpha}} \\ x_{\boldsymbol{\beta}} \\ x_0 \end{bmatrix} = \mathbf{T}_{\boldsymbol{\alpha\beta}} \cdot \begin{bmatrix} x_a \\ x_b \\ x_c \end{bmatrix} \tag{4.9}$$

Applying (4.9) to the three-phase model (4.2) yields mathematical model in the α-β frame (4.10)

$$\frac{d}{dt}\begin{bmatrix} i'_{\mathrm{p}\alpha} \\ i'_{\mathrm{p}\beta} \end{bmatrix} = \begin{bmatrix} \frac{-R'_{\mathrm{p}}\omega_{\mathrm{B}}}{L'_{\mathrm{p}}} & 0 \\ 0 & \frac{-R'_{\mathrm{p}}\omega_{\mathrm{B}}}{L'_{\mathrm{p}}} \end{bmatrix} \begin{bmatrix} i'_{p\alpha} \\ i'_{p\beta} \end{bmatrix} + \frac{\omega_{\mathrm{B}}}{L'_{\mathrm{p}}} \begin{bmatrix} v'_{\mathrm{i}\alpha} - v'_{\mathrm{p}\alpha} \\ v'_{\mathrm{i}\beta} - v'_{\mathrm{p}\beta} \end{bmatrix} \tag{4.10}$$

Where the zero-sequence component has been omited, due to three phase, three wire STATCOM topology.

In order to include the DC-side circuit into the mathematical model, expressions (4.5) and (4.6) are transformed into α-β frame equations:

$$\begin{aligned} v'_{\mathrm{p}\alpha} &= k_{\mathrm{p}} S_{\alpha} v'_{\mathrm{dc}} \\ v'_{\mathrm{p}\beta} &= k_{\mathrm{p}} S_{\beta} v'_{\mathrm{dc}} \end{aligned} \tag{4.11}$$

$$i'_{\mathrm{dc}} = \frac{3}{2}\left(k_{\mathrm{p}} S_{\alpha} i'_{\mathrm{p}\alpha} + k_{\mathrm{p}} S_{\beta} i'_{\mathrm{p}\beta}\right) \tag{4.12}$$

Where the average switching function in α-β coordinates is given as follows:

$$\begin{bmatrix} S_{\alpha} \\ S_{\beta} \end{bmatrix} = m_{\mathrm{p}} \begin{bmatrix} \cos\delta \\ \sin\delta \end{bmatrix} \tag{4.13}$$

The complete set of equations in α-β coordinates describing STATCOM model is given with (4.14).

$$\frac{d}{dt}\begin{bmatrix} i'_{\mathrm{p}\alpha} \\ i'_{\mathrm{p}\beta} \\ v'_{\mathrm{dc}} \end{bmatrix} = \begin{bmatrix} \frac{-R'_{\mathrm{p}}\omega_{\mathrm{B}}}{L'_{\mathrm{p}}} & 0 & \frac{-k_{\mathrm{p}}\omega_{\mathrm{B}}}{L'_{\mathrm{p}}} S_{\alpha} \\ 0 & \frac{-R'_{\mathrm{p}}\omega_{\mathrm{B}}}{L'_{\mathrm{p}}} & \frac{-k_{\mathrm{p}}\omega_{B}}{L'_{\mathrm{p}}} S_{\beta} \\ \frac{3k_{\mathrm{p}}\omega_{\mathrm{B}}C'}{2} S_{\alpha} & \frac{3k_{\mathrm{p}}\omega_{\mathrm{B}}C'}{2} S_{\beta} & -\frac{\omega_{\mathrm{B}}C'}{R'_{c}} \end{bmatrix} \begin{bmatrix} i'_{\mathrm{p}\alpha} \\ i'_{\mathrm{p}\beta} \\ v'_{\mathrm{dc}} \end{bmatrix} + \begin{bmatrix} \frac{\omega_{\mathrm{B}}}{L'_{\mathrm{p}}} v'_{\mathrm{i}\alpha} \\ \frac{\omega_{\mathrm{B}}}{L'_{\mathrm{p}}} v'_{\mathrm{i}\beta} \\ 0 \end{bmatrix} \tag{4.14}$$

4.2.3 Mathematical Model in the d-q Coordinate System—Balanced Conditions

In the next step, the mathematical model, given in (4.7), is transformed into the d-q synchronous frame by using the classic transformation matrix (4.15) [1]. The zero sequence component is omitted, as a three-wire STATCOM cannot generate zero-sequence currents. The mathematical model is given in (4.16). The detailed transformation into the d-q synchronous frame is given in the Appendix.

$$\mathbf{T_{dq}} = \frac{2}{3}\begin{bmatrix} \cos(\omega t) & \cos\left(\omega t - \frac{2\pi}{3}\right) & \cos\left(\omega t + \frac{2\pi}{3}\right) \\ -\sin(\omega t) & -\sin\left(\omega t - \frac{2\pi}{3}\right) & -\sin\left(\omega t + \frac{2\pi}{3}\right) \end{bmatrix} \tag{4.15}$$

$$\frac{d}{dt}\begin{bmatrix} i'_{pd} \\ i'_{pq} \end{bmatrix} = \begin{bmatrix} \frac{-R'_p\omega_B}{L'_p} & \omega \\ -\omega & \frac{-R'_p\omega_B}{L'_p} \end{bmatrix}\begin{bmatrix} i'_{pd} \\ i'_{pq} \end{bmatrix} + \frac{\omega_B}{L'_p}\begin{bmatrix} v'_{id} - v'_{pd} \\ v'_{iq} - v'_{pq} \end{bmatrix} \tag{4.16}$$

The DC-side current equation was already described with (4.3) and is rewritten here for convenience (4.17).

$$i'_{dc} = \frac{1}{\omega_B C'}\frac{dv'_{dc}}{dt} + \frac{v'_{dc}}{R'_c} \tag{4.17}$$

For the calculation of the DC-side current the power balance equation is used again, this time written in the d-q coordinate system (4.18).

$$v'_{dc}i'_{dc} = \frac{3}{2}\left(v'_{pd}i'_{pd} + v'_{pq}i'_{pq}\right) \tag{4.18}$$

The connection between the AC- and DC-side voltages can be given with the expression (4.19) in the d-q frame. S_d and S_q represent the switching function. The factor k_p is dependent upon the converter type.

$$\begin{bmatrix} v'_{pd} \\ v'_{pq} \end{bmatrix} = k_p\begin{bmatrix} S_d \\ S_q \end{bmatrix}v'_{dc} \tag{4.19}$$

The connection between AC and DC currents, taking into account (4.18) and (4.19), is given in (4.20).

$$i'_{dc} = \frac{3}{2}\left(k_p S_d i'_{pd} + k_p S_q i'_{pq}\right) \tag{4.20}$$

The DC-current (4.20) is included in (4.17) giving the equation for the DC-side circuit.

The complete mathematical model in the d-q coordinate system is given in (4.21). The constant ω is the angular speed of the fundamental frequency voltage component. Because the d-q transformation is frequency dependent, the derived mathematical model is valid only for the fundamental frequency component. For the evaluation of any other harmonic or negative-sequence component, an additional set of equations should be included in (4.21). Figure 4.3 shows the block diagram of the STATCOM model in the rotating d-q frame.

$$\frac{d}{dt}\begin{bmatrix} i'_{pd} \\ i'_{pq} \\ v'_{dc} \end{bmatrix} = \begin{bmatrix} \frac{-R'_p\omega_B}{L'_p} & \omega & \frac{-k_p\omega_B}{L'_p}S_d \\ -\omega & \frac{-R'_p\omega_B}{L'_p} & \frac{-k_p\omega_B}{L'_p}S_q \\ \frac{3k_p\omega_B C'}{2}S_d & \frac{3k_p\omega_B C'}{2}S_q & -\frac{\omega_B C'}{R'_c} \end{bmatrix}\begin{bmatrix} i'_{pd} \\ i'_{pq} \\ v'_{dc} \end{bmatrix} + \begin{bmatrix} \frac{\omega_B}{L'_p}v'_{id} \\ \frac{\omega_B}{L'_p}v'_{iq} \\ 0 \end{bmatrix} \tag{4.21}$$

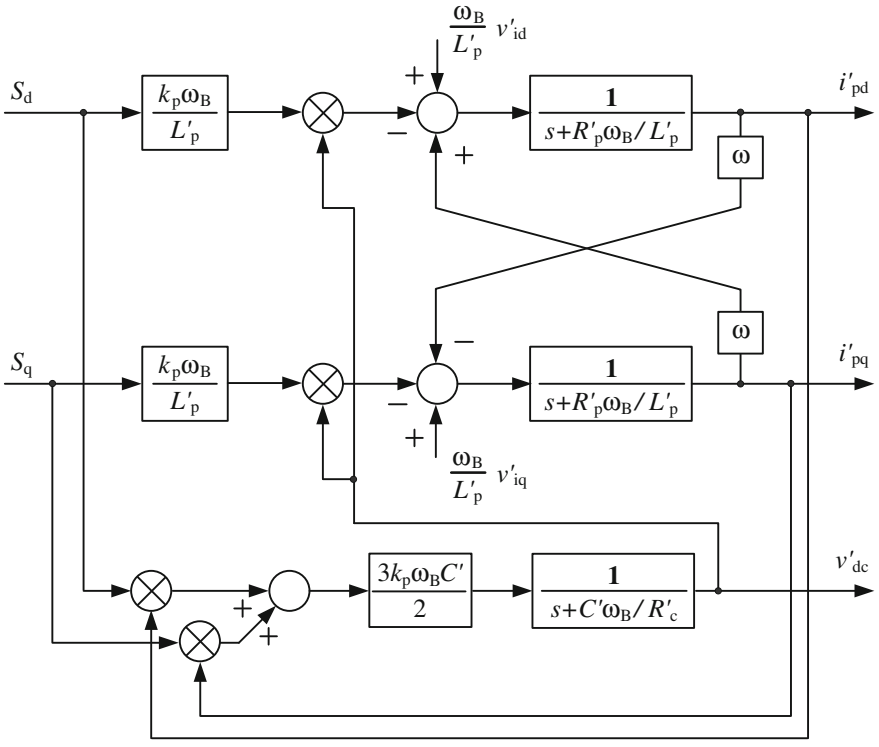

Fig. 4.3 Equivalent block diagram of the STATCOM mathematical model in the rotating d-q frame

4.2.4 Mathematical Model in the d-q Coordinate System - Unbalanced Conditions

As already mentioned, the d-q transformation is frequency dependent, therefore (4.21) is valid only for the positive-sequence fundamental-frequency components. To describe the STATCOM operation under unbalanced conditions another set of equations has to be added to the mathematical model, describing the device operation for the negative-sequence fundamental-frequency components [3]. The developed mathematical model for unbalanced conditions will consist of three parts: the first part describes the device operation with positive-sequence components, the second part describes the operation with negative-sequence components and both parts are linked together with a common DC circuit.

The transformation into the d-q rotating reference frame is a frequency transformation that changes the frequencies of the transformed signals. The positive-sequence components of fundamental frequency are transformed into DC values (under steady-state conditions), while the negative-sequence components of fundamental frequency are transformed into a harmonic component with a frequency equal to the double of the fundamental frequency. The DC component, which represents the positive-sequence part of the signal at fundamental frequency, can be extracted from the transformed signal using a Low-Pass Filter (LPF).

For the calculation of the negative-sequence components a modified transformation matrix is used. In matrix $\mathbf{T_{dq}}$ (4.15) the second and third column are exchanged, thus obtaining the transformed matrix $\mathbf{T_{dqn}}$ (4.22).

$$\mathbf{T_{dqn}} = \frac{2}{3}\begin{bmatrix} \cos(\omega t) & \cos\left(\omega t + \frac{2\pi}{3}\right) & \cos\left(\omega t - \frac{2\pi}{3}\right) \\ -\sin(\omega t) & -\sin\left(\omega t + \frac{2\pi}{3}\right) & -\sin\left(\omega t - \frac{2\pi}{3}\right) \end{bmatrix} \tag{4.22}$$

By using $\mathbf{T_{dqn}}$, the negative-sequence components of fundamental frequency are transformed into DC quantities, whereas positive-sequence components of fundamental frequency are transformed into harmonic components with a frequency equal to the double of the fundamental frequency. The DC component, which represents the negative-sequence part of the signal at fundamental frequency, can be extracted from the transformed signal using a LPF. The whole process is illustrated in Fig. 4.4 [3].

The DC-side current equation was already given in (4.3) and (4.17), and is valid for any DC-side voltage or current. For the derivation of the connection between the DC and AC converter side the procedure is the same as already used in previous chapters. The instantaneous power Eq. (4.3) has to be calculated for unbalanced voltages and currents. The calculated instantaneous power is the sum of a DC and a second harmonic components (4.23).

$$p = p_{\mathrm{DC\_p}} + p_{\mathrm{DC\_n}} + p_{\mathrm{AC\_pn}} + p_{\mathrm{AC\_np}} \tag{4.23}$$

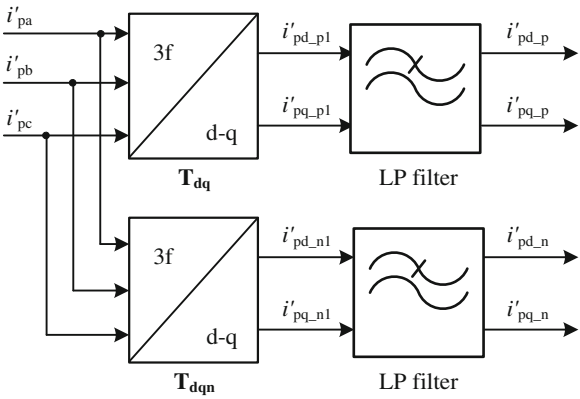

Fig. 4.4 Calculation of positive- and negative-sequence components

The DC components are the result of the product of positive-sequence voltages and currents (p_{DC_p}), and the product of negative-sequence voltages and currents (p_{DC_n}), while the AC components are the result of the product of positive-sequence voltages and negative-sequence currents (p_{AC_pn}) and vice versa (p_{AC_np}). The DC component influences the DC component of the DC-side voltage, while the AC component causes a second harmonic voltage component in the DC-side voltage as a consequence. Clearly, harmonics on the DC side have to be avoided, because they would result in harmonics generation on the converter AC (network) side. Harmonics cancelation can be achieved, for example, with a larger DC-side capacitor or with switching function modulation preventing the generation of harmonics on the AC side (the approach is described in the next section). As the AC components on the DC side have to be avoided, they can also be omitted from the derivation of the mathematical model. With this in mind the power balance equation can be written as in (4.24) where only the DC components of the instantaneous power (4.23) are taken into account.

$$v'_{dc}i'_{dc} = \frac{3}{2}\left(v'_{pd\_p}i'_{pd\_p} + v'_{pq\_p}i'_{pq\_p}\right) + \frac{3}{2}\left(v'_{pd\_n}i'_{pd\_n} + v'_{pq\_n}i'_{pq\_n}\right) \tag{4.24}$$

For the control of unbalanced currents the compensator has to generate unbalanced voltages. This is achieved with the use of an unbalanced switching function that consists of a positive- and a negative-sequence component. The connection between the AC- and DC-side voltages can be given with the expressions (4.25) and (4.26).

$$\begin{bmatrix} v'_{pd\_p} \\ v'_{pq\_p} \end{bmatrix} = k_p \begin{bmatrix} S_{d\_p} \\ S_{q\_p} \end{bmatrix} v'_{dc} \tag{4.25}$$

$$\begin{bmatrix} v'_{\mathrm{pd\_n}} \\ v'_{\mathrm{pq\_n}} \end{bmatrix} = k_{\mathrm{p}} \begin{bmatrix} S_{\mathrm{d\_n}} \\ S_{\mathrm{q\_n}} \end{bmatrix} v'_{\mathrm{dc}} \tag{4.26}$$

The connection between AC and DC currents, taking into account (4.24), (4.25) and (4.26), is given in (4.27).

$$i'_{\mathrm{dc}} = \frac{3}{2} k_{\mathrm{p}} \left(S_{\mathrm{d\_p}} i'_{\mathrm{pd\_p}} + S_{\mathrm{q\_p}} i'_{\mathrm{pq\_p}} \right) + \frac{3}{2} k_{\mathrm{p}} \left(S_{\mathrm{d\_n}} i'_{\mathrm{pd\_n}} + S_{\mathrm{q\_n}} i'_{\mathrm{pq\_n}} \right) \tag{4.27}$$

The DC-current (4.27) is included in (4.17) giving a complete description of the DC-side circuit. A set of equations is added to (4.21) describing the compensator operation with negative-sequence components. The complete mathematical model for unbalanced conditions is given in (4.28) [3].

$$\frac{d}{dt} \begin{bmatrix} i'_{\mathrm{pd\_p}} \\ i'_{\mathrm{pq\_p}} \\ i'_{\mathrm{pd\_n}} \\ i'_{\mathrm{pq\_n}} \\ v'_{\mathrm{dc}} \end{bmatrix} = \begin{bmatrix} \frac{-R'_{\mathrm{p}}\omega_{\mathrm{B}}}{L'_{\mathrm{p}}} & \omega & 0 & 0 & \frac{-k_{\mathrm{p}}\omega_{\mathrm{B}}}{L'_{\mathrm{p}}} S_{\mathrm{d\_p}} \\ -\omega & \frac{-R'_{\mathrm{p}}\omega_{\mathrm{B}}}{L'_{\mathrm{p}}} & 0 & 0 & \frac{-k_{\mathrm{p}}\omega_{\mathrm{B}}}{L'_{\mathrm{p}}} S_{\mathrm{q\_p}} \\ 0 & 0 & \frac{-R'_{\mathrm{p}}\omega_{\mathrm{B}}}{L'_{\mathrm{p}}} & \omega & \frac{-k_{\mathrm{p}}\omega_{\mathrm{B}}}{L'_{\mathrm{p}}} S_{\mathrm{d\_n}} \\ 0 & 0 & -\omega & \frac{-R'_{\mathrm{p}}\omega_{\mathrm{B}}}{L'_{\mathrm{p}}} & \frac{-k_{\mathrm{p}}\omega_{\mathrm{B}}}{L'_{\mathrm{p}}} S_{\mathrm{q\_n}} \\ \frac{3k_{\mathrm{p}}\omega_{\mathrm{B}}C'}{2} S_{\mathrm{d\_p}} & \frac{3k_{\mathrm{p}}\omega_{\mathrm{B}}C'}{2} S_{\mathrm{q\_p}} & \frac{3k_{\mathrm{p}}\omega_{\mathrm{B}}C'}{2} S_{\mathrm{d\_n}} & \frac{3k_{\mathrm{p}}\omega_{\mathrm{B}}C'}{2} S_{\mathrm{q\_n}} & \frac{-C'\omega_{\mathrm{B}}}{R'_{\mathrm{c}}} \end{bmatrix} \begin{bmatrix} i'_{\mathrm{pd\_p}} \\ i'_{\mathrm{pq\_p}} \\ i'_{\mathrm{pd\_n}} \\ i'_{\mathrm{pq\_n}} \\ v'_{\mathrm{dc}} \end{bmatrix} + \begin{bmatrix} \frac{\omega_{\mathrm{B}}}{L'_{\mathrm{p}}} v'_{\mathrm{id\_p}} \\ \frac{\omega_{\mathrm{B}}}{L'_{\mathrm{p}}} v'_{\mathrm{iq\_p}} \\ \frac{\omega_{\mathrm{B}}}{L'_{\mathrm{p}}} v'_{\mathrm{id\_n}} \\ \frac{\omega_{\mathrm{B}}}{L'_{\mathrm{p}}} v'_{\mathrm{iq\_n}} \\ 0 \end{bmatrix} \tag{4.28}$$

The STATCOM mathematical model for unbalanced conditions includes the positive-sequence part, the negative-sequence part and a common DC circuit. The positive- and negative-sequence parts have the same form. That is because the positive-sequence part is computed in the positive-sequence d-q reference frame, while the negative-sequence part is computed in the negative-sequence d-q reference frame. Positive-sequence d-axes and q-axes currents are coupled with the term ω. The same holds for the negative-sequence d- and q-axes currents. The DC-component of the DC-side voltage is affected by both, the positive- and negative-sequence currents. The STATCOM currents and the DC-side voltage are connected with the switching function. Figure 4.5 shows the block diagram of the STATCOM mathematical model for the unbalanced conditions in the rotating d-q frame [3].

4.2.4.1 Harmonics Compensation Due to the Unbalanced Switching Function

As already demonstrated for a VSC, a negative-sequence current component on the AC side causes the presence of a second harmonic component in the DC-side voltage and consequently an additional third harmonic component on the AC side [4, 5]. A conventional approach would aim at ensuring that only a DC component is present in the DC-bus voltage by overrating the DC-side capacitor.

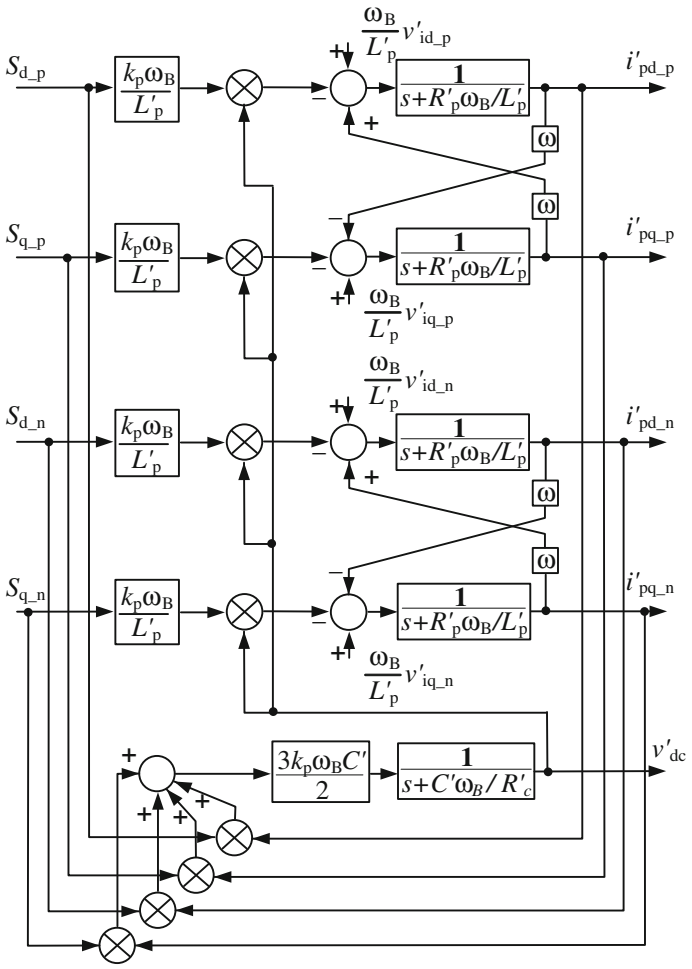

Fig. 4.5 Equivalent block diagram of the STATCOM mathematical model for unbalanced conditions in the rotating d-q frame

Another approach is based on the modulation of the switching function and enables VSC operation with distorted DC-bus voltage [3]. A VSC generates AC voltage from DC voltage. Equation (4.5) is rewritten again for three-phase quantities that are represented with column matrices (4.29).

$$\begin{bmatrix} v'_{pa} \\ v'_{pb} \\ v'_{pc} \end{bmatrix} = k_p \begin{bmatrix} S_a \\ S_b \\ S_c \end{bmatrix} v'_{dc} \Leftrightarrow \mathbf{v'_{pL}} = k_p \mathbf{S_L} v'_{dc} \tag{4.29}$$

A new variable k_m is introduced and represents the modulation factor:

$$k_m = \frac{V_{dcref}}{v'_{dc}} \tag{4.30}$$

where V_{dcref} is the reference DC voltage on the DC side (constant value), whereas v'_{dc} is the instantaneous DC-side voltage.

With the derived modulation factor a new modulated switching function $\mathbf{S_{Lmod}}$ is calculated (4.31) and the Eq. (4.32) for the compensated ac-voltage ($\mathbf{v'_{pLc}}$) is derived.

$$\mathbf{S_{Lmod}} = \mathbf{S_L} k_m \tag{4.31}$$

$$\mathbf{v'_{pLc}} = k_p \mathbf{S_{Lmod}} v'_{dc} \tag{4.32}$$

Introducing (4.30) and (4.31) into (4.32) we get:

$$\mathbf{v'_{pLc}} = k_p \mathbf{S_L} V_{dcref} \tag{4.33}$$

As follows from (4.33) despite the distorted DC-side voltage v'_{dc}, the compensator with the modulated switching function ($\mathbf{S_{Lmod}}$) behaves as if v'_{dc} consisted of the DC component (V_{dcref}) only. Therefore it does not generate additional harmonics at its AC terminals and enables the use of a relatively small capacitor.

4.3 STATCOM Control Algorithms

4.3.1 Frequency Domain: d-q Control Algorithm for Balanced Conditions

The control algorithm is based on the STATCOM mathematical model in the rotating d-q frame (4.21). As it can be seen from the model, we have two controllable parameters (S_d and S_q) and three variables (i'_{pd}, i'_{pq} and v'_{dc}). Therefore, two variables can be controlled independently, while the third one is a dependent variable. The usual choice is to use i'_{pd} to regulate the DC-side voltage v'_{dc}, while i'_{pq} can be used according to STATCOM purpose. The development of the control algorithm on the basis of the mathematical model is described next.

Firstly, we introduce variables w'_{pd} and w'_{pq} which represent the voltage drop on the coupling circuit and variable w'_{dc} which is proportional to the DC-side current [6]:

$$\begin{bmatrix} w'_{pd} \\ w'_{pq} \\ w'_{dc} \end{bmatrix} = \begin{bmatrix} 0 & 0 & \frac{-k_p \omega_B}{L'_p} S_d \\ 0 & 0 & \frac{-k_p \omega_B}{L'_p} S_q \\ \frac{3 k_p \omega_B C'}{2} S_d & \frac{3 k_p \omega_B C'}{2} S_q & 0 \end{bmatrix} \begin{bmatrix} i'_{pd} \\ i'_{pq} \\ v'_{dc} \end{bmatrix} + \begin{bmatrix} \frac{\omega_B}{L'_p} v'_{id} \\ \frac{\omega_B}{L'_p} v'_{iq} \\ 0 \end{bmatrix} \tag{4.34}$$

Taking into account (4.34) the STATCOM mathematical model Eq. (4.21) is transformed to:

$$\frac{d}{dt}\begin{bmatrix} i'_{\mathrm{pd}} \\ i'_{\mathrm{pq}} \\ v'_{\mathrm{dc}} \end{bmatrix} = \begin{bmatrix} \frac{-R'_{\mathrm{p}}\omega_{\mathrm{B}}}{L'_{\mathrm{p}}} & \omega & 0 \\ -\omega & \frac{-R'_{\mathrm{p}}\omega_{\mathrm{B}}}{L'_{\mathrm{p}}} & 0 \\ 0 & 0 & -\frac{\omega_{\mathrm{B}}C'}{R'_{\mathrm{c}}} \end{bmatrix} \begin{bmatrix} i'_{\mathrm{pd}} \\ i'_{\mathrm{pq}} \\ v'_{\mathrm{dc}} \end{bmatrix} + \begin{bmatrix} w'_{pd} \\ w'_{pq} \\ w'_{dc} \end{bmatrix} \tag{4.35}$$

Next, the decoupling between q and d axes is made. The block diagram of the STATCOM control algorithm is shown in Fig. 4.6. The variables w'_{pd}, w'_{pq} and w'_{dc} form the outputs of Proportional-Integral (PI) controller. The input to PI controllers is the difference between the reference and measured values. The output of the current PI controllers would therefore be the voltage drop on the coupling circuit that is required in order that the desired reference current is generated. The output of the DC-side voltage PI controller is proportional to the DC-side current that is required to maintain the DC-side voltage at the reference value.

The d-axis reference current i'^{*}_{pd} is calculated from w'_{dc}.

The switching function that enables the generation of the reference currents is calculated from (4.34).

$$\begin{bmatrix} S_{\mathrm{d}} \\ S_{\mathrm{q}} \end{bmatrix} = \frac{L'}{-k_{\mathrm{p}}\omega_{\mathrm{B}}v'_{\mathrm{dc}}} \left(\begin{bmatrix} w'_{\mathrm{pd}} \\ w'_{\mathrm{pq}} \end{bmatrix} - \begin{bmatrix} \frac{\omega_{\mathrm{B}}}{L'_{\mathrm{p}}}v'_{\mathrm{id}} \\ \frac{\omega_{\mathrm{B}}}{L'_{\mathrm{p}}}v'_{\mathrm{iq}} \end{bmatrix} \right) \tag{4.36}$$

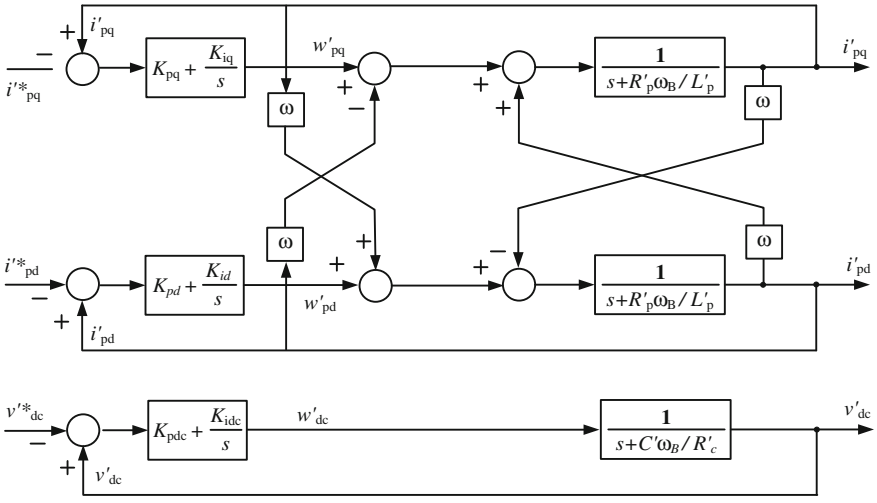

Fig. 4.6 Block diagram of the STATCOM control algorithm in the rotating d-q frame

As can be seen in Fig. 4.6 the cross-coupling terms $\omega \cdot i'_{\mathrm{pd}}$ and $\omega \cdot i'_{\mathrm{pq}}$.
Variables w'_{pd}, w'_{pq} and w'_{dc}.
The transfer functions of the control loops are:

$$\begin{aligned} F_{\mathrm{d}}(s) &= \frac{K_{\mathrm{id}} + sK_{\mathrm{pd}}}{K_{\mathrm{id}} + s\left(R'_{\mathrm{p}}\omega_{\mathrm{B}} \Big/ L'_{\mathrm{p}} + K_{\mathrm{pd}}\right) + s^2} \\ F_{\mathrm{q}}(s) &= \frac{K_{\mathrm{iq}} + sK_{\mathrm{pq}}}{K_{\mathrm{iq}} + s\left(R'_{\mathrm{p}}\omega_{\mathrm{B}} \Big/ L'_{\mathrm{p}} + K_{\mathrm{pq}}\right) + s^2} \\ F_{\mathrm{vdc}}(s) &= \frac{K_{\mathrm{idc}} + sK_{\mathrm{pdc}}}{K_{\mathrm{idc}} + s\left(C'\omega_{\mathrm{B}} \Big/ R'_{\mathrm{c}} + K_{\mathrm{pdc}}\right) + s^2} \end{aligned} \tag{4.37}$$

If we use a simple relation between the integral and proportional constants of PI controllers the transfer function reduces to a first order function (4.38), resulting in fast and stable operation.

$$\begin{aligned} K_{\mathrm{id}} &= \frac{R'_{\mathrm{p}}\omega_{\mathrm{B}}}{L'_{\mathrm{p}}} K_{\mathrm{pd}} \Rightarrow F_{\mathrm{d}}(s) = \frac{K_{\mathrm{pd}}}{K_{\mathrm{pd}} + s} \\ K_{\mathrm{iq}} &= \frac{R'_{\mathrm{p}}\omega_{\mathrm{B}}}{L'_{\mathrm{p}}} K_{\mathrm{pq}} \Rightarrow F_{\mathrm{q}}(s) = \frac{K_{\mathrm{pq}}}{K_{\mathrm{pq}} + s} \\ K_{\mathrm{idc}} &= \frac{C'\omega_{\mathrm{B}}}{R'_{\mathrm{c}}} K_{\mathrm{pdc}} \Rightarrow F_{\mathrm{vdc}}(s) = \frac{K_{\mathrm{pdc}}}{K_{\mathrm{pdc}} + s} \end{aligned} \tag{4.38}$$

4.3.2 Frequency Domain: d-q Control Algorithm for Unbalanced Conditions

On the basis of the presented mathematical model for unbalanced conditions (4.28) a control algorithm is developed next. The purpose of the control algorithm is to enable separate control of positive- and negative-sequence currents and also decoupled control of d- and q-axes current components. The procedure is identical to the one described for the balanced conditions control algorithm.

Firstly, five new variables are introduced ($w'_{\mathrm{pd\_p}}$, $w'_{\mathrm{pq\_p}}$, w'_{dc}, $w'_{\mathrm{pd\_n}}$ and $w'_{\mathrm{pq\_n}}$):

$$\begin{bmatrix} w'_{\mathrm{pd\_p}} \\ w'_{\mathrm{pq\_p}} \\ w'_{\mathrm{pd\_n}} \\ w'_{\mathrm{pq\_n}} \\ w'_{\mathrm{dc}} \end{bmatrix} = \begin{bmatrix} 0 & 0 & 0 & 0 & \frac{-k_{\mathrm{p}}\omega_{\mathrm{B}}}{L'_{\mathrm{p}}} S_{\mathrm{d\_p}} \\ 0 & 0 & 0 & 0 & \frac{-k_{\mathrm{p}}\omega_{\mathrm{B}}}{L'_{\mathrm{p}}} S_{\mathrm{d\_q}} \\ 0 & 0 & 0 & 0 & \frac{-k_{\mathrm{p}}\omega_{\mathrm{B}}}{L'_{\mathrm{p}}} S_{\mathrm{d\_n}} \\ 0 & 0 & 0 & 0 & \frac{-k_{\mathrm{p}}\omega_{\mathrm{B}}}{L'_{\mathrm{p}}} S_{\mathrm{q\_n}} \\ \frac{3k_{\mathrm{p}}\omega_{\mathrm{B}}C'}{2} S_{\mathrm{d\_p}} & \frac{3k_{\mathrm{p}}\omega_{\mathrm{B}}C'}{2} S_{\mathrm{q\_p}} & \frac{3k_{\mathrm{p}}\omega_{\mathrm{B}}C'}{2} S_{\mathrm{d\_n}} & \frac{3k_{\mathrm{p}}\omega_{\mathrm{B}}C'}{2} S_{\mathrm{q\_n}} & 0 \end{bmatrix} \begin{bmatrix} i'_{\mathrm{pd\_p}} \\ i'_{\mathrm{pq\_p}} \\ i'_{\mathrm{pd\_n}} \\ i'_{\mathrm{pq\_n}} \\ v'_{\mathrm{dc}} \end{bmatrix} + \begin{bmatrix} \frac{\omega_{\mathrm{B}}}{L'_{\mathrm{p}}} v'_{\mathrm{id\_p}} \\ \frac{\omega_{\mathrm{B}}}{L'_{\mathrm{p}}} v'_{\mathrm{iq\_p}} \\ \frac{\omega_{\mathrm{B}}}{L'_{\mathrm{p}}} v'_{\mathrm{id\_n}} \\ \frac{\omega_{\mathrm{B}}}{L'_{\mathrm{p}}} v'_{\mathrm{iq\_n}} \\ 0 \end{bmatrix} \tag{4.39}$$

so that the STATCOM mathematical model equation is transformed to

$$\frac{d}{dt}\begin{bmatrix} i'_{\mathrm{pd\_p}} \\ i'_{\mathrm{pq\_p}} \\ i'_{\mathrm{pd\_n}} \\ i'_{\mathrm{pq\_n}} \\ v'_{\mathrm{dc}} \end{bmatrix} = \begin{bmatrix} \frac{-R'_{\mathrm{p}}\omega_{\mathrm{B}}}{L'_{\mathrm{p}}} & \omega & 0 & 0 & 0 \\ -\omega & \frac{-R'_{\mathrm{p}}\omega_{\mathrm{B}}}{L'_{\mathrm{p}}} & 0 & 0 & 0 \\ 0 & 0 & \frac{-R'_{\mathrm{p}}\omega_{\mathrm{B}}}{L'_{\mathrm{p}}} & \omega & 0 \\ 0 & 0 & -\omega & \frac{-R'_{\mathrm{p}}\omega_{\mathrm{B}}}{L'_{\mathrm{p}}} & 0 \\ 0 & 0 & 0 & 0 & \frac{-C'\omega_{\mathrm{B}}}{R'_{\mathrm{c}}} \end{bmatrix} \begin{bmatrix} i'_{\mathrm{pd\_p}} \\ i'_{\mathrm{pq\_p}} \\ i'_{\mathrm{pd\_n}} \\ i'_{\mathrm{pq\_n}} \\ v'_{\mathrm{dc}} \end{bmatrix} + \begin{bmatrix} w'_{\mathrm{pd\_p}} \\ w'_{\mathrm{pq\_p}} \\ w'_{\mathrm{pd\_n}} \\ w'_{\mathrm{pq\_n}} \\ w'_{\mathrm{dc}} \end{bmatrix} \tag{4.40}$$

Newly introduced variables represent the outputs of PI controllers. With the known values of $w'_{\mathrm{pd\_p}}$, $w'_{\mathrm{pq\_p}}$, w'_{dc}, $w'_{\mathrm{pd\_n}}$ and $w'_{\mathrm{pq\_n}}$ all four adjustable parameters ($S_{\mathrm{d\_p}}$, $S_{\mathrm{q\_p}}$, $S_{\mathrm{d\_n}}$ and $S_{\mathrm{q\_n}}$,) can be computed from (4.39). Similarly to the approach shown in Fig. 4.6 decoupling is achieved. The STATCOM mathematical model is reduced to five first-order functions, improving the converter performance. The developed control scheme is shown in Fig. 4.7 showing a general current control loop and the DC-voltage control loop.

The controlled signals (positive- and negative-sequence currents, DC voltage) are first compared to the reference ones (marked with an asterisk). The difference is then applied to a PI controller. The output of each controller is a corresponding variable w'_{pac}. With the solution of (4.39) the values of adjustable parameters ($S_{\mathrm{d\_p}}$, $S_{\mathrm{q\_p}}$, $S_{\mathrm{d\_n}}$ and $S_{\mathrm{q\_n}}$) can be calculated. The two adjustable parameters for the positive sequence ($S_{\mathrm{d\_p}}$, $S_{\mathrm{q\_p}}$) are calculated with the known values of $w'_{\mathrm{pd\_p}}$ and $w'_{\mathrm{pq\_p}}$. The first parameter is used to control positive-sequence active current ($i'_{\mathrm{pd\_p}}$) and the second one is used to control the positive-sequence reactive current ($i'_{\mathrm{pq\_p}}$). Furthermore, with the known values of $w'_{\mathrm{pd\_n}}$ and $w'_{\mathrm{pq\_n}}$ the adjustable parameters for the negative sequence ($S_{\mathrm{d\_n}}$, $S_{\mathrm{q\_n}}$) can be calculated. One is used for negative-sequence active current ($i'_{\mathrm{pd\_n}}$) control and the other is used for negative-sequence reactive current ($i'_{\mathrm{pq\_n}}$) control. From the output of the DC-voltage controller (w'_{dc}) the reference positive-sequence active current ($i'^{*}_{\mathrm{pd\_p}}$) is calculated so that the DC component of the capacitor voltage is maintained at constant value. To sum up, with four adjustable parameters all four currents can be controlled. With the DC

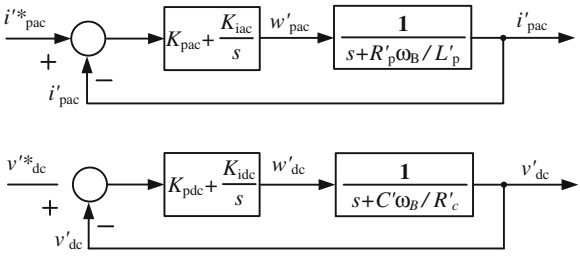

Fig. 4.7 Current control loop and DC-voltage control loop

control loop variable (w'_{dc}), the reference value of the positive-sequence active current is calculated.

With the described control algorithm all four currents (d- and q-axes currents of the positive and negative sequence) are decoupled. However, as all the currents share a common DC bus, a change in the DC component of the DC-side voltage affects all the currents. Therefore the positive-sequence active current control loop has to be fast enough to keep the DC voltage at a constant level.

4.3.2.1 Control Algorithm Simulation

The operation of the proposed STATCOM control algorithm for unbalanced conditions is demonstrated with simulations in the PSCAD. The STATCOM was modelled as a conventional three-phase VSC consisting of six power transistors with a parallel power diode connected in reverse and a capacitor on the DC side, and connected to the network through a transformer. The base values are given in Table 4.1 and the values of STATCOM components are given in Table 4.2.

The STATCOM response was evaluated for a case of a distant single-phase network fault, resulting in a single-phase voltage drop of approximately 0.25 pu at the STATCOM point of common coupling (PCC). Before and during the fault the STATCOM supplies reactive current of 1 pu to the network. The device was controlled with the d-q control algorithm for unbalanced conditions and the proposed switching function modulation. The negative-sequence current reference values ($i'^*_{pd\_n}$, $i'^*_{pq\_n}$) were set to zero.

The STATCOM response with the proposed controls is presented in Fig. 4.8, while Fig. 4.9 shows the same simulation case without the regulation of negative-sequence components and without the switching function modulation. The graphs show the network phase voltages at the PCC (v'_{ia}, v'_{ib}, v'_{ic}), the STATCOM phase currents (i'_{pa}, i'_{pb}, i'_{pc}) and the DC-side voltage (v'_{dc}). All values are given in pu.

Table 4.1 STATCOM base values

Parameter	Value
S_B	2.0 MVA
u_B	0.46 kV
i_B	2.89 kA
z_B	0.16 Ω

Table 4.2 Values of individual STATCOM components

Component	Value	Value (pu)
L_p	0.191 H	0.3 (at v_B)
R_p	6.0 Ω	0.03 (at v_B)
C	39.8 mF	0.5 (at v_B)
R_c	8.0 Ω	50 (at v_B)
v_{dc}^*	1.155 kV	2.5

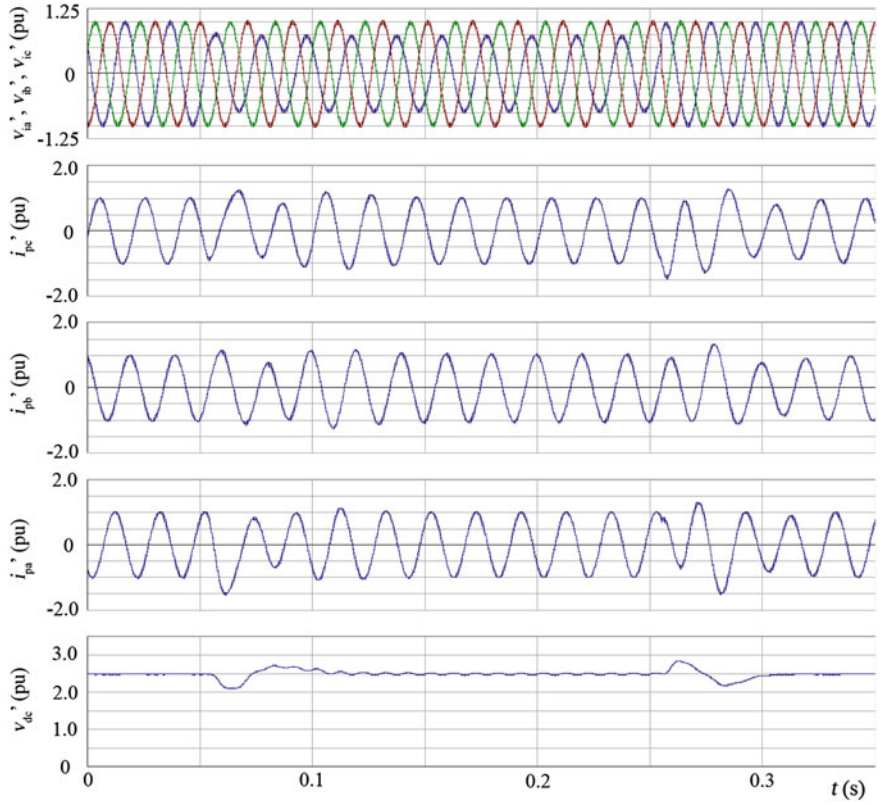

Fig. 4.8 STATCOM response to a distant single-phase fault with the control algorithm for unbalanced conditions and the proposed switching function modulation

As it can be seen from the graphs, the control algorithm for unbalanced conditions successfully controls the negative-sequence currents to zero. The STATCOM still supplies reactive current of 1 pu to the network and does also not generate low-order current harmonics on the AC side (the third harmonic current component is around 1 %). On the other hand, highly unbalanced currents and also overcurrent are evident from Fig. 4.9 where the control of negative-sequence components is not used. The DC-side voltage is significantly more distorted.

4.3.3 Time-Domain: Predictive Control Algorithms (PC)

PC is a general name for a wide range of control approaches that use an explicit model of the controlled device to predict the behavior of a plant [7–18]. Since the electrical machines are relatively well modeled it is possible to use their

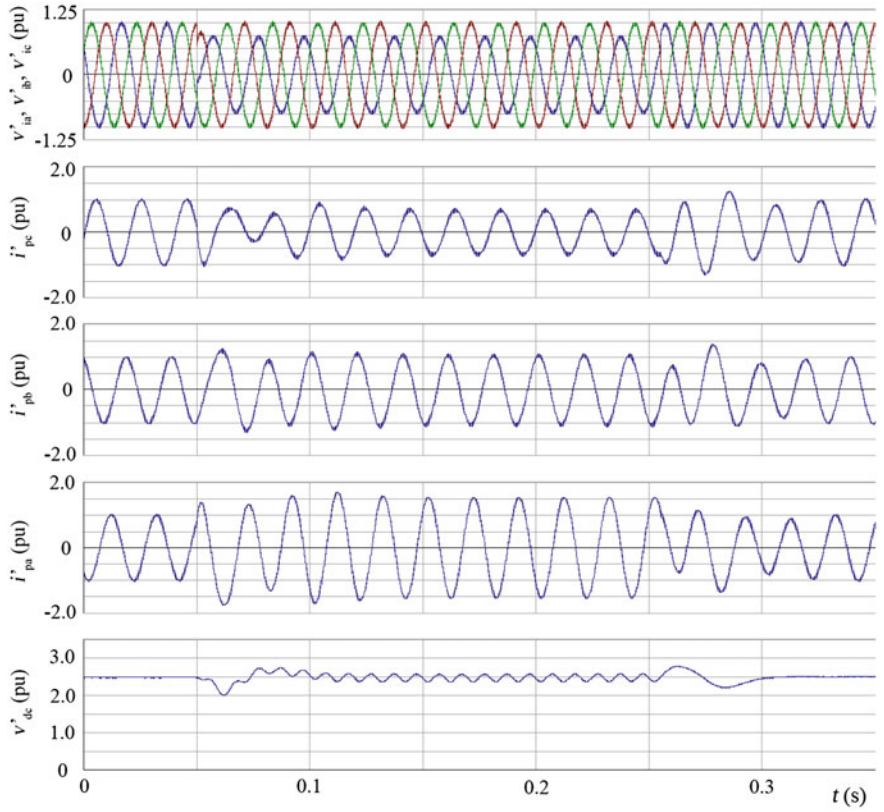

Fig. 4.9 STATCOM response to a distant single-phase fault without the control algorithm for unbalanced conditions and without the proposed switching function modulation

mathematical models to predict the electrical responses and behavior for each combination of input and state variables. The input variables are considered as all the measured quantities that participate in the control algorithm (e.g. grid voltage, STATCOM current). In a simple way, PC defines such VSC output voltage that tracks the reference STATCOM current with minimum error.

The PCs are mainly implemented as a discrete control system based on the Digital Signal Processors (DSP) [8]. Such implementation introduces some dead-time between the data acquisition of input variables and the realization of the output voltage using a Pulse Width Modulation (PWM) from the VSC. Due to one-sample delay is the PC often named as the dead-beat control. Discrete implementation with delays of the output signals influences also the accuracy of the control therefore the signal-predictive approaches needs to be incorporated into control algorithms to gain correct plant response (e.g. control voltage is not generated under the same current or grid voltage conditions as they were used for control voltage calculations). The main goal of the control is to incorporate all the real deviations from the

exact model and control delays into the control algorithm to maximize the control accuracy.

PCs offer excellent control dynamics and accuracy as far as the model is electrically correct represented and all the measured input quantities correctly predicted. Discrete implementation of the PC offers many new options for further development of model-based predictive control algorithms in view of different optimization approaches to meet the desired improvement of the plant behavior.

In the following sections, the basic predictive control approach for the STATCOM will be explained in details. Further on, one of the optimization approaches will be highlighted in view of time-optimization of STATCOM current responses.

4.3.3.1 STATCOM Model—Discretization

As it was already described in previous sections, the STATCOM is often modeled as an ideal voltage source that is shunt connected to the grid through a coupling impedance ($\underline{Z}_\mathrm{p} = R_\mathrm{p} + \mathrm{j}X_\mathrm{p}$). R_p is representing ohmic losses and X_p reactance of the reactor. The one is taking care of minimizing switching ripple in the output current and allows precise control of the output current, defined as a voltage drop over impedance.

A simplified model of the VSC, where the DC-side circuit is neglected, can be for individual phase written as shown in (4.41) or (4.42) and (4.43) for stationary coordinate system (alpha-beta components). The zero-sequence component is in this case omitted and not connected to the STATCOM at middle-voltage. Therefore, zero sequence current is equal to zero.

$$\begin{bmatrix} v'_{\mathrm{ia}} \\ v'_{\mathrm{ib}} \\ v'_{\mathrm{ic}} \end{bmatrix} - \begin{bmatrix} v'_{\mathrm{pa}} \\ v'_{\mathrm{pb}} \\ v'_{\mathrm{pc}} \end{bmatrix} = \begin{bmatrix} R'_\mathrm{p} & 0 & 0 \\ 0 & R'_\mathrm{p} & 0 \\ 0 & 0 & R'_\mathrm{p} \end{bmatrix} \begin{bmatrix} i'_{\mathrm{pa}} \\ i'_{\mathrm{pb}} \\ i'_{\mathrm{pc}} \end{bmatrix} + \begin{bmatrix} \frac{L'_\mathrm{p}}{\omega_\mathrm{B}} & 0 & 0 \\ 0 & \frac{L'_\mathrm{p}}{\omega_\mathrm{B}} & 0 \\ 0 & 0 & \frac{L'_\mathrm{p}}{\omega_\mathrm{B}} \end{bmatrix} \frac{\mathrm{d}}{\mathrm{d}t} \begin{bmatrix} i'_{\mathrm{pa}} \\ i'_{\mathrm{pb}} \\ i'_{\mathrm{pc}} \end{bmatrix} \tag{4.41}$$

$$\begin{bmatrix} v'_{\mathrm{i}\alpha} \\ v'_{\mathrm{i}\beta} \end{bmatrix} - \begin{bmatrix} v'_{\mathrm{p}\alpha} \\ v'_{\mathrm{p}\beta} \end{bmatrix} = \begin{bmatrix} R'_\mathrm{p} & 0 \\ 0 & R'_\mathrm{p} \end{bmatrix} \begin{bmatrix} i'_{\mathrm{p}\alpha} \\ i'_{\mathrm{p}\beta} \end{bmatrix} + \begin{bmatrix} \frac{L'_\mathrm{p}}{\omega_\mathrm{B}} & 0 \\ 0 & \frac{L'}{\omega_\mathrm{B}} \end{bmatrix} \frac{\mathrm{d}}{\mathrm{d}t} \begin{bmatrix} i'_{\mathrm{p}\alpha} \\ i'_{\mathrm{p}\beta} \end{bmatrix} \tag{4.42}$$

or

$$v'_{\mathrm{p}\alpha\beta}(t) = v'_{\mathrm{i}\alpha\beta}(t) - R'_\mathrm{p} i'_{\mathrm{p}\alpha\beta}(t) - \frac{L'_\mathrm{p}}{\omega_\mathrm{B}} \frac{\mathrm{d}i'_{\mathrm{p}\alpha\beta}(t)}{\mathrm{d}t} \tag{4.43}$$

The (4.43) is written in the explicit form to define such VSC output voltage ($v'_{\mathrm{p}\alpha\beta}$) that will cause the STATCOM current ($i'_{\mathrm{p}\alpha\beta}$) to change for a reference current derivative $\mathrm{d}i'_{\mathrm{p}\alpha\beta}/\mathrm{d}t$. Practical realization of the PC within the DSPs demands use of the discrete model of the plant, therefore the model (4.43) needs to be discretized

with precise understanding of discrete actions in digital processors in order to achieve minimal mismatch of discrete system with larger sampling periods.

The first-order differential equation of the plant can be for discrete analysis transformed into discrete form as shown in (4.44). Constant values during whole sample period are considered for the PWM modulated output voltage as well as the grid-side voltage. Voltage drop that is considered on the reactor resistance is considered as constant value defined with average current during one sampling period. Current difference is defined as a difference between the current after and before the PWM update generation. The first value can be replaced with the reference current for that time-instance so the final discrete equation that defines the VSC output voltage which "moves" current vector from $\boldsymbol{i}_{\mathrm{p}}(t_n)$ to $\boldsymbol{i}_{\mathrm{p}}(t_{n+1})^*$ is equal to:

$$\boldsymbol{v}'_{\mathrm{p}\alpha\beta}\left(p_{(n,n+1)}\right) = \boldsymbol{v}'_{\mathrm{i}\alpha\beta}\left(p_{(n,n+1)}\right) - R'_{\mathrm{p}}\boldsymbol{i}'_{\mathrm{p}\alpha\beta}\left(\mathrm{p}_{(n,n+1)}\right) - \frac{L'_{\mathrm{p}}}{\omega_{\mathrm{B}}}\frac{\boldsymbol{i}'^{*}_{\mathrm{p}\alpha\beta}(t_{n+1}) - \boldsymbol{i}'_{\mathrm{p}\alpha\beta}(t_n)}{\mathrm{T_s}} \tag{4.44}$$

where:

- $\mathrm{T_s}$ is the time difference between the two discrete samples and is for this case
- t_n is time-instance of n-th sample
- $p_{(n,\ n+1)}$ is one sample period between sample instance t_n and t_{n+1}.

In practice, the discrete control systems introduce an additional calculation delay of one sample time. Therefore the (4.44) must be written for one sample-time later signals as (4.45). All the variables from (4.45) are at the time of calculation not directly available to be used in equation but need to be appropriately calculated (predicted) from already available measurements from t_n or earlier. The predictions of the unavailable variables need to be incorporated into the control algorithm for the implementation of the (4.45).

$$\begin{aligned}\boldsymbol{v}'_{\mathrm{p}\alpha\beta}\left(p_{(n+1,n+2)}\right) = \boldsymbol{v}'_{\mathrm{i}\alpha\beta\_\mathrm{P}}\left(p_{(n+1,n+2)}\right) - R'_{\mathrm{p}}\boldsymbol{i}'_{\mathrm{p}\alpha\beta\_\mathrm{P}}\left(\mathrm{p}_{(n+1,n+2)}\right) \\ - \frac{L'_{\mathrm{p}}}{\omega_{\mathrm{B}}}\frac{\boldsymbol{i}'^{*}_{\mathrm{p}\alpha\beta\_\mathrm{P}}(t_{n+2}) - \boldsymbol{i}'_{\mathrm{p}\alpha\beta\_\mathrm{P}}(t_{n+1})}{\mathrm{T_s}}\end{aligned} \tag{4.45}$$

The index P stands for predicted variables.

For clearer understanding of signal timings, the Fig. 4.10 is showing the basic timing diagram of control actions and predictions of a single processor control system where delays due to calculation processes are considered. The timings of the actions are as follows:

- Sampling of all electrical quantities (at t_n),
- Data processing, defining new output VSC voltage (within period $p_{(n,n+1)}$)
- Updating of the new calculated duty-cycle to compare register of the PWM (SVM) (at t_{n+1})
- PWM generation of new calculated VSC output voltage (within period $p_{(n+1,n+2)}$).

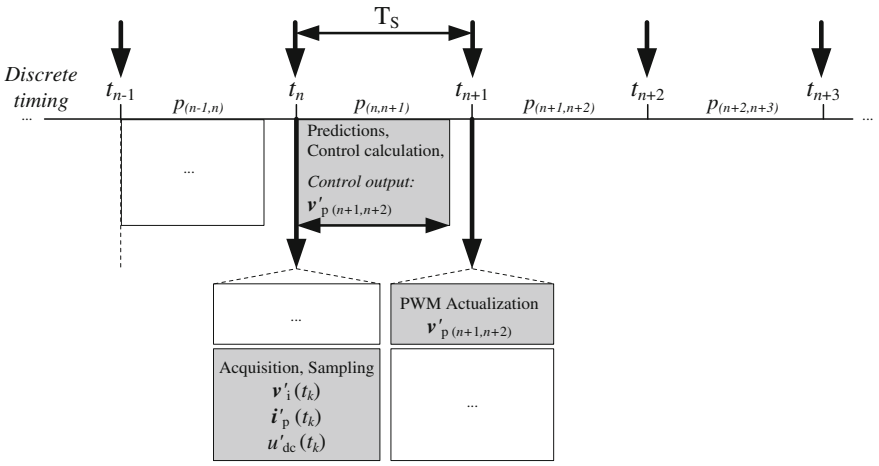

Fig. 4.10 Timing of the DSP actions during one sample period (acquisition of measurements, sampling, processing, PWM update/actualization)

For small values of sampling periods T_s is the accuracy of discrete equation relatively high while higher values could lead to higher mismatch of control output variables and therefore deterioration of the control performance in view of steady state reference tracking accuracy as well as increased harmonic distortion of the output current.

4.3.3.2 Current, Voltage Predictions

All variables from the (4.45) are defined for a time-instance or as an average value over a specified time-period that is not explicitly defined with the sampled value. Variables need to be predicted to suit the correct timing using different approaches. Errors that would eventually occur due to error in prediction could lead to higher steady-state error, higher harmonic distortions and overshoots during transient conditions.

Voltage prediction

Network voltage signal needs to be predicted to an average value for the following (future) sample period (p_{n+1}). Accurate prediction is possible only for strong network under steady state conditions, while the transient conditions could on the weak grids cause relatively high errors in sinusoidal prediction.

For this reason, several prediction methods were introduced with predictive controllers in order to allow minimal mismatch in case of harmonically distorted voltage signals, transients and other non steady state conditions [8–11]. Error of the voltage predictions has the biggest influence to the accuracy of the output current.

Even slight deviation of the predicted voltage could lead to higher currents, which are even higher in systems with small coupling impedance.

The most basic voltage prediction is shown with (4.46) and (4.47), where the voltage value from time-instance t_n is recalculated to a time-instance t_{n+1} and to a middle value in the period $p_{(n+1,n+2)}$. Here, the stiff grid with undistorted and balanced sinusoidal voltage is expected. In a similar way we could predict harmonically distorted voltage, where the prediction would be made for individual harmonic component.

$$\boldsymbol{v}'_{\mathrm{i}\alpha\beta\_\mathrm{P}}(t_{n+1}) = v'_{\mathrm{i}\alpha\beta}(t_n) \cdot e^{j\omega \mathrm{T_s}} \tag{4.46}$$

$$\boldsymbol{v}'_{\mathrm{i}\alpha\beta\_\mathrm{P}}\left(p_{n+1,n+2}\right) = v'_{\mathrm{i}\alpha\beta}(t_n) \cdot e^{j\omega 1.5\mathrm{T_s}} \tag{4.47}$$

Current prediction

Current that appears in the control Eq. (4.45) incorporates the average value of the current during sampling period p_{n+1} and instantaneous value of the current at the following sample instance t_{n+1}.

The prediction can be established by using mathematical model of the plant with the discrete signal timings as follows:

$$\boldsymbol{i}'_{\mathrm{p}\alpha\beta\_\mathrm{P}}(t_{n+1}) = \boldsymbol{i}'_{p\alpha\beta}(t_n) + \frac{\omega_B T_s}{L'_p}\left(\boldsymbol{v}'_{i\alpha\beta\_\mathrm{P}}\left(p_{(n,n+1)}\right) - \boldsymbol{v}'_{\mathrm{p}\alpha\beta\_\mathrm{P}}\left(p_{(n,n+1)}\right)\right) \tag{4.48}$$

where R_p is neglected due to its minimal influence. The actual current $\boldsymbol{i}'_{\alpha\beta}(t_n)$ is the sampled value, network voltage can be predicted as described in the previous section and the VSC output voltage is the control voltage that has been calculated already in the previous sampling period and is applied to the PWM output at period $p_{(n,n+1)}$.

The STATCOM's AC current prediction for the average value over one sampling period can be defined as a average value between currently sampled value (t_n) and predicted value (t_{n+1}), where linear interpolation can be used to define mean value.

Additionally, the reference current needs to be predicted for the time-instance t_{n+2}. According to the mode of operation of the controller for reference definition, different dynamics as well as different harmonic components are expected in the reference signal. However, reference current can be in steady state predicted very accurately by using simple sinusoidal extrapolation for individual harmonic component. Bigger mismatch can be expected during stochastic transients.

$$\boldsymbol{i}'^{*}_{\mathrm{p}\alpha\beta\_\mathrm{P}}(t_{n+2}) = \boldsymbol{i}'^{*}_{\mathrm{p}\alpha\beta}(t_n) e^{\mathrm{j}\omega 2\mathrm{T_S}} \tag{4.49}$$

4.3.3.3 TOCC—Time-Optimal Current Control

The TOCC [18] is an optimization approach that is applied to the predictive control and improves controller dynamics during fast reference current transients. The term "optimal" means the fastest possible response to a change in the operating point of the VSC when operating with the maximal available magnitude of the output voltage vector. The development of the time-optimal current control system is based on the predictive control algorithm where the current predictions for different options can be analyzed in advance and the optimal solution can be chosen and applied to the VSC.

Development of the TOCC is based on the (4.45), which is rewritten to suit further analysis of different durations of predicted transients. The Δt represents the predicted current transient duration between the STATCOM's current and reference current and is used instead of the T_s which represents one sample-time. New form of the control equation is for the sinusoidal reference current is shown in (4.50). The current difference is now defined for the current difference between the predicted STATCOM current (at t_{n+1}) and predicted reference current defined for the last point of the time-optimal current transient. Optimal transient is assumed to be reached under the following conditions:

- Maximal current derivative should be applied during entire transient period (this can be established by applying maximal available output VSC voltage),
- The current path should be optimally selected to reach the reference value in the minimum time.

$$\begin{aligned} \boldsymbol{v}'_{\mathrm{p}\alpha\beta}\left(p_{(n+1,n+1+N)}\right) = {} & \boldsymbol{v}'_{\mathrm{i}\alpha\beta\_\mathrm{P}}\left(p_{(n+1,n+1+N)}\right) - R'_{\mathrm{p}}\boldsymbol{i}'_{\mathrm{p}\alpha\beta\_\mathrm{P}}\left(p_{(n+1,n+1+N)}\right) \\ & - \frac{L'_{\mathrm{p}}}{\omega_{\mathrm{B}}}\frac{\boldsymbol{i}'^{*}_{\mathrm{p}\alpha\beta\_\mathrm{P}}(t_{n+1+N}) - \boldsymbol{i}'^{*}_{\mathrm{p}\alpha\beta\_\mathrm{P}}(t_{n+1})}{N \cdot \mathrm{T}_s} \end{aligned} \tag{4.50}$$

or

$$\begin{aligned} \boldsymbol{v}'_{\mathrm{p}\alpha\beta}\left(p_{(n+1,n+1+N)}\right) = {} & \boldsymbol{v}'_{\mathrm{i}\alpha\beta\_\mathrm{P}}\left(p_{(n+1,n+1+N)}\right) - R'_{\mathrm{p}}\boldsymbol{i}'_{\mathrm{p}\alpha\beta\_\mathrm{P}}\left(p_{(n+1,n+1+N)}\right) \\ & - \frac{L'_{\mathrm{p}}}{\omega_{\mathrm{B}}}\frac{\boldsymbol{i}'^{*}_{\mathrm{p}\alpha\beta\_\mathrm{P}}(t_{n+1}+\Delta t) - \boldsymbol{i}'_{\mathrm{p}\alpha\beta\_\mathrm{P}}(t_{n+1})}{\Delta t} \end{aligned} \tag{4.51}$$

where

- Δt represents predicted duration of the current transient and
- N is an integer which defines count of samples during transient ($N = \Delta t / \mathrm{T}_s$).

The optimization approach includes iterative loop (Fig. 4.11) where the minimal value of the transient duration Δt is defined at individual time-step and for individual set of sampled input signals.

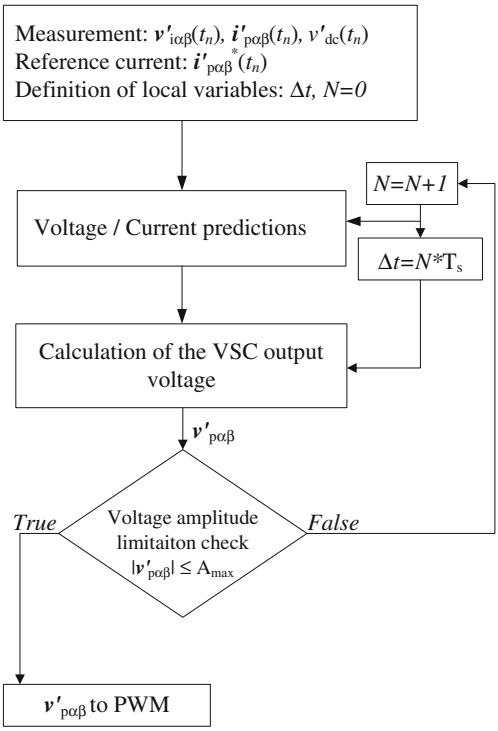

Fig. 4.11 Flow chart of the TOCC iteration loop

In the steady state is the variable Δt is equal to T_s. Under dynamic conditions is Δt increased during each iteration step until the magnitude of the calculated VSC output voltage vector decreases below the maximal available value A'_{max} defined by the DC voltage and maximal modulation factor. The calculated voltage vector $\boldsymbol{v}'_{p\alpha\beta}$ from the last iteration is then generated by the VSC during the following PWM period.

In Fig. 4.11 we can observe the flow diagram of the time-optimal current control algorithm. The entire algorithm is repeated in each discrete calculation step, for every new sample of the measured input data and new reference currents.

Operation of the VSC with the time-optimal current controller is demonstrated in Fig. 4.12a, b. The figures are showing the VSC current transients at the reactive current reference step-change from 0 to 1 pu and from 1 to −1 pu (rotation of the reference current vector for 180°) respectively. The STATCOM losses are for the demonstration purpose neglected ($R_p = 0$) and the VSC output voltage is limited by the maximal available voltage drop across the coupling impedance.

Initial state of the current vector is indicated with the point A and equals to zero. The reference current vector step-changes from point A to B (Fig. 4.12a). The TOCC algorithm predicts that the actual current vector could reach the desired magnitude in the time Δt during which also the reference current vector $i^*_{p\alpha\beta}$ rotates by the angle $\omega\Delta t$. Therefore, the optimal (shortest) track for the current to reach the

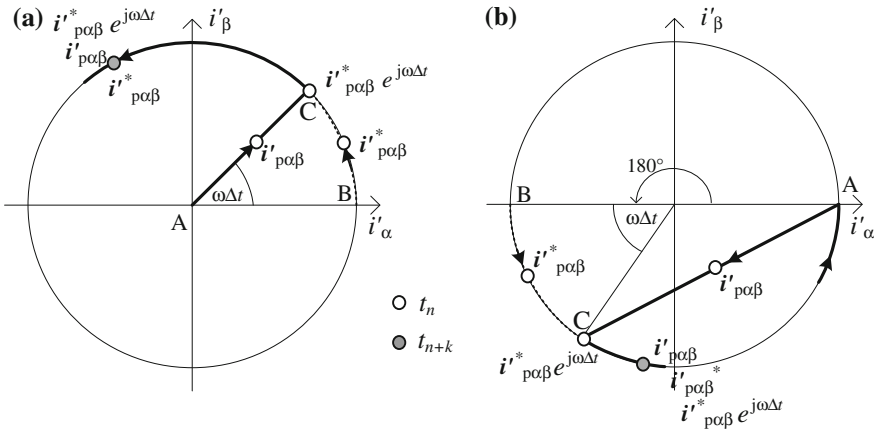

Fig. 4.12 Demonstration of the time-optimal current control system operation: **a** initial current vector equals zero; **b** initial phase displacement between the reference and actual current vector equals 180°

reference value is given by the line between the points A and C. The optimal track is controlled by the TOCC that shifts the instantaneous value of the reference current vector for the $\omega\Delta t$ to the new value $i^{*}_{R\alpha\beta}$. During transient, the Δt is changing linearly while the vector $i^{*}_{R\alpha\beta}$ holds practically the same position. The steady state conditions are established after reaching the point C, then also the reference and the actual current vectors rotate together in the α-β plane.

The current response in Fig. 4.12b shows the same behaviour as the one in Fig. 4.12a. Here is the reference current vector shifted from the point A for 180° to the point B. Again, the TOCC optimizes the current track by shifting the reference current forward to the position that can be reached in minimum time.

The duration of transient period Δt depends on the magnitude of control voltage (the difference between the network and the VSC output voltage), which forces the current through the STATCOM impedance. To improve the operation of the time-optimal controller, the use of a slightly bigger control voltage can provide faster transients and greater stability during disturbances.

Influence of Different VSC Voltage Limitations

One of the important aspects of the control behavior is definition of the operation limits in view of control voltage limitations. The one is in most cases defined with the maximal available VSC output voltage which allows operation under constant switching frequency or with a maximal voltage drop across the coupling impedance or others. However, different voltage limitations show different control behavior and therefore also variable level of TOCC time-optimization advantages.

Simulation Case

With the following simulation case the performance of the two PC (without and with TOCC optimization routine) are compared. It is shown how the optimization

routine (the TOCC) improves the current transients during step-changes of the reference current.

The simulation is performed with a generic VSC that is shunt connected to the grid via 15% coupling impedance. Simulation details are presented in Table 4.3. Reference current of the VSC is changed from zero to the nominal value. The output voltage of the VSC is limited by the maximal value of the voltage drop across the coupling impedance. The voltage limit is with the coupling impedance of 15 % set to the value with 10 % reserve, which is 16.5 % of the nominal network voltage.

The comparison of the control behavior is at reference current step-change for TOCC and basic predictive control shown in Fig. 4.13 and 4.14 in time-graph and stationary coordinate frame respectively.

Table 4.3 Simulation parameters of a generic low voltage STATCOM model

Parameter name	Symbol	Value	Per-unit value
Sampling period	T_S	100 µs	
Sampling frequency	f_S	10 kHz	
PCC phase voltage (RMS)	U_i	1 kV	sqrt(3/2) or 1.225 pu
Nominal current (RMS)	I	1 kA	1.225 pu
DC voltage	u_{dc}	1.9 kV	2.33 pu
Coupling impedance	Z'	5.5 mH	15 %
Reference current (RMS)	I'^*	0–1 kA (ind)	0.707 pu
Output voltage limitations (limitation of voltage drop across coupling impedance)	A_{max}	135 V	0.165 pu

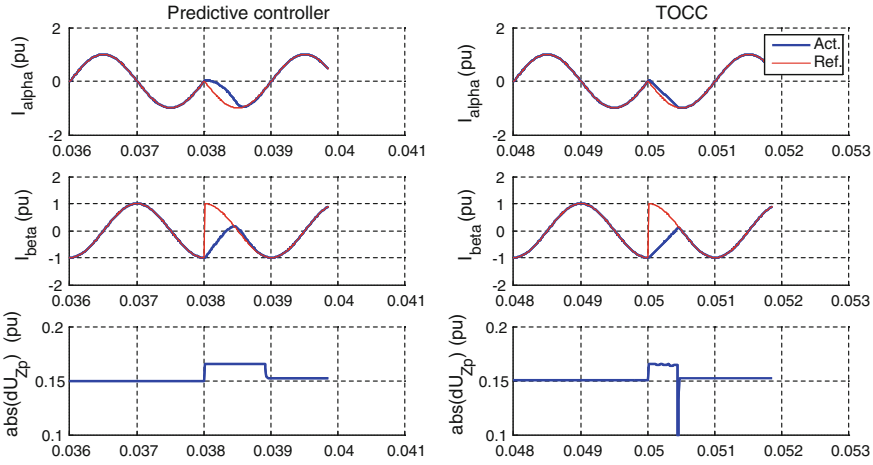

Fig. 4.13 Comparison of the TOCC and basic predictive control (reference reactive current step-change from inductive to capacitive); alpha and beta current components and absolute value of the inductor voltage

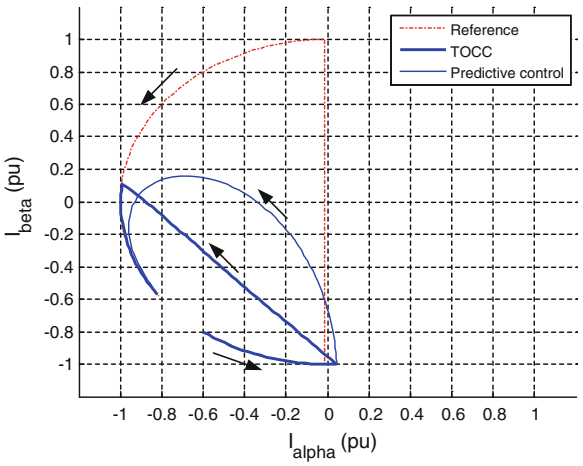

Fig. 4.14 Comparison of the TOCC and basic predictive control (reference reactive current step-change from inductive to capacitive) in stationary coordinate system

From the Fig. 4.13 and 4.14 it can be seen how the current with TOCC controller tracks the reference value in a different way than the controller without optimization. In a particular simulation case is with the TOCC the current transient completed in much shorter time period.

The TOCC is representing only one of many possible optimization approaches that are possible to be realized with the PC. The main drawback of the PC is the modeling of electrical devices which often show nonlinear characteristics, delays and other characters that demand much more complex modeling approach and control realization. Any deviation from the correct model can produce relative high current error in form of harmonic distortion or steady state error.

4.3.4 Resonant Controller

Resonant controllers have taken on significant importance in last years due to their high selectivity and good performance [19–26]. They are equivalent to the PI controllers implemented in the dq-coordinate system for both the positive- and negative-sequences at the same time. Thus, for compensating both sequences only one regulator is needed, which saves computational power. Because transformation into dq-coordinate system is not required for operation of the resonant controller, this makes it simpler and less sensitive to errors in synchronization. It also uses less processing power and for compensating nonsymmetrical quantities less resonators are required compared to PI controllers [19]. Therefore, the PR-controller is nowadays used in many applications and is the subject of intensive studies and fast development. It gives good results when used with active filters, STATCOMs, wind

turbines, photovoltaic inverters, and other devices. Below, multi-loop controller will be developed to be used with STATCOM. Besides main control loop for compensating fundamental frequency component, sever control loops will be added for compensating most problematic harmonics.

4.3.4.1 *PR*-Controller Transfer Function

The relationship between the *dq*-components and the *αβ*-components can be expressed with:

$$i_{\mathrm{d}} = i_{\alpha} \cdot \cos(\omega_{\mathrm{B}} t) + j \cdot i_{\alpha} \cdot \sin(\omega_{\mathrm{B}} t) = i_{\alpha} \cdot e^{j\omega_{\mathrm{B}} \mathrm{t}} \tag{4.52}$$

$$i_{\mathrm{q}} = i_{\beta} \cdot \cos(\omega_{\mathrm{B}} t) - j \cdot i_{\beta} \cdot \sin(\omega_{\mathrm{B}} t) = i_{\beta} \cdot e^{-j\omega_{\mathrm{B}} \mathrm{t}} \tag{4.53}$$

As it can be seen from the above expressions, the influence of the Park transformation can be understood as the frequency shift $\pm\omega_{\mathrm{B}}$ of all the frequencies. The equivalent transfer function of the PR controller $H_{\mathrm{PR}}(s)$ can be derived from a PI controller implemented in positive- and negative-sequence rotating frames, taking into account (4.52) and (4.53).

$$H_{\mathrm{PRi}}(s) = H_{\mathrm{PI}}^{+} + H_{\mathrm{PI}}^{-} \tag{4.54}$$

$$\begin{aligned} H_{\mathrm{PRi}}(s) &= k_{\mathrm{p}} + k_{\mathrm{I}} \frac{s}{s + j\omega_{\mathrm{B}}} + k_{\mathrm{P}} + k_{\mathrm{I}} \frac{s}{s - j\omega_{\mathrm{B}}} = \\ &= 2k_{\mathrm{p}} + 2k_{\mathrm{I}} \frac{s}{s^2 + \omega_{\mathrm{B}}^2} = K_{\mathrm{P}} + \frac{K_{\mathrm{I}}.s}{s^2 + \omega_{\mathrm{B}}^2} \end{aligned} \tag{4.55}$$

The index *i* in (4.54) and (4.55) indicates that this is an ideal PR-controller. At frequency ω_{B}, H_{PRi} has infinite amplification in the case of an open-loop regulator, which for the closed-loop system at this frequency represents an ideal reference tracking, no phase shift and unity gain. Bode diagram of an ideal transfer function is shown in Fig. 4.15. As it can be seen from the figure, an ideal PR controller has an infinite gain at the tuned frequency 250 Hz and almost no phase shift and gain at other frequencies. Disadvantage of such controller in practical application is possible stability problem associated with an infinite gain. Another feature is very narrow bandwidth of ideal PR controllers, which makes them highly sensitive towards slight frequency variation in a typical power system [19].

The expression (4.55) is valid only under the assumption that we are dealing with an ideal integrator, which in practical applications cannot be achieved. Since the integrator in reality has upper and lower limits, we have to take this into account in the

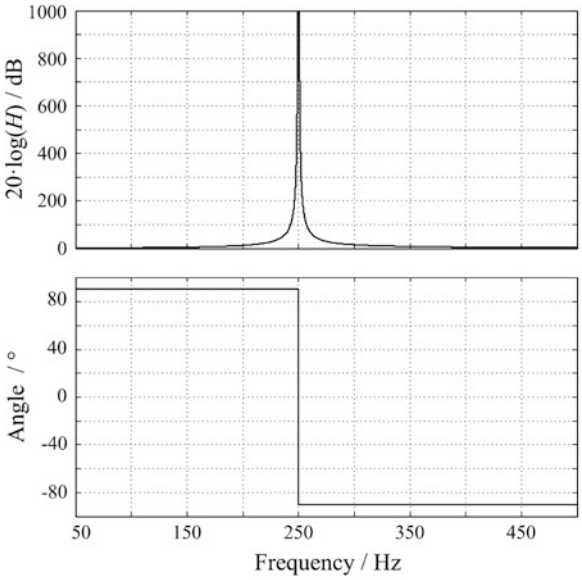

Fig. 4.15 Bode diagram of (4.55). Parameters: $h = \{5\}$, $K_{I5} = 450$ in $K_P = 10$

derivation of PR-controller. For the non-ideal integrators of $H_I = K_I/(1 + (s/\omega_C))$, the PR-controller transfer function takes the form:

$$H_{PR}(s) = K_P + K_I \frac{\omega_{PR} \cdot s}{s^2 + 2\omega_{PR} \cdot s + \omega_B^2} \tag{4.56}$$

where ω_{PR} is the cut-off frequency, representing the limits of the integrator. It is very common that several H_{PR} controllers are added in series to control several harmonics simultaneously. The current controller transfer function takes its final form:

$$H_{PR}(s) = \sum_{h=1,5,7\ldots} K_{Ph} + K_{Ih} \frac{\omega_{PR} \cdot s}{s^2 + 2\omega_{PR} \cdot s + (h \cdot \omega_B)^2} \tag{4.57}$$

Analysis and design of *PR*-regulators

For each application of PR-controllers it is necessary to properly set the proportional and integral constants K_P and K_I. This is usually done by means of Bode diagrams [21]. According to the literature, it is first necessary to set the proportional constant K_P to an appropriate value (as with simple proportional controller), where the stability criterion considering the phase or gain margins must be taken into account. In the second step, several resonators are added in cascade, tuned to the appropriate harmonic frequencies. In doing so, one must take care not to exceed the bandwidth of the filter, as this may cause unstable operation. Such an approach of tuning the controller gives satisfactory results in most practical applications.

4.3.4.2 Control Algorithm

Figure 4.16 shows general control scheme, which includes harmonic detection (Fig. 4.17), the PR-current regulation for fundamental frequency and for harmonics filtering (Eq. 4.55) and the DC-voltage control (Fig. 4.18). The PR-controller is closed with the measured values from the actual system. For fundamental frequency controller these measured values are first compared to the reference values and in the next step transformed into αβ-components. The error is applied to a PR-controller tuned on the fundamental frequency. Next step is to apply Eqs. (4.52) and (4.53) and the output of the controller is the variable $v_{\mathrm{p1,dq}}$, which is added to the voltage reference $v_{\mathrm{p,ref}}$.

Since the objective is also to eliminate the harmonics from the compensator current, this current represents the second controller input. At first, the fundamental-frequency component has to be extracted from the measured current. This is done

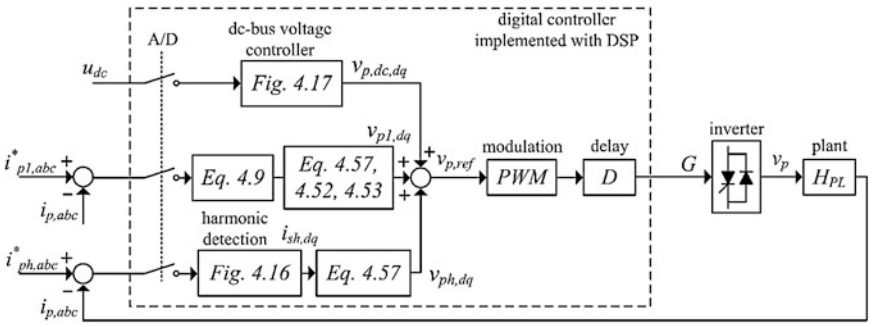

Fig. 4.16 Control block diagram of the HAPF

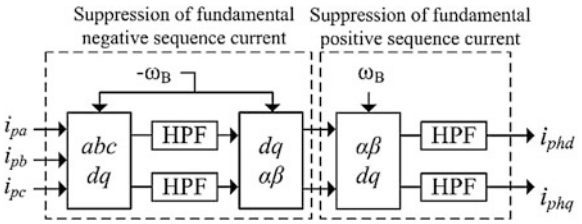

Fig. 4.17 Block diagram of the harmonic current detection

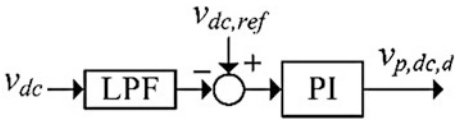

Fig. 4.18 DC-bus voltage control

by using first-order, High-Pass Filters (HPF) in the fundamental frequency, synchronous reference frame. Fundamental angular frequency is obtained using a conventional Phase-Locked Loop (PLL) system [27]. Due to the fact that the supply current may also contain, in the case of unsymmetrical line conditions, some fundamental negative-sequence component, this component is suppressed by the second part of the harmonic detection unit, where the Park transformation is performed with a clockwise synchronous rotation. As a result, the output of the harmonic detection unit is the compensator current harmonics, which in the next step are compared to the reference values. The difference is then applied to a PR controller tuned on the individual resonance frequencies. The output of the controller is the variable $v_{\mathrm{ph,dq}}$, which is added to the voltage reference $v_{\mathrm{p,ref}}$.

4.3.4.3 DC-Bus Voltage Control

Proper control of the DC-bus voltage is essential for the operation of the compensator. The principle of controlling the DC-bus voltage is based on active-power control, i.e., charging the DC capacitor with active power will increase the voltage, while releasing a certain amount of active power, will decrease it. According to the pq-theory, a DC component in the dq-coordinates corresponds to the active power, and thus the DC-bus voltage control is implemented in the SRF.

As can be seen from Fig. 4.18, the difference between the reference value and the measured and filtered actual value is applied to a PI controller, which adjusts the direct axis current (the quadrature axis is set to zero). A LPF eliminates the harmonics from the measured DC-bus voltage. The resultant control signal is added to the voltage reference $v_{\mathrm{p,ref}}$.

Current Control Transfer Function

Figure 4.19 shows the main current-control block diagram of the compensator for harmonic frequencies. The harmonic content of the compensator current is filtered from the measured current. The transfer function for the harmonic-detecting circuit can be expressed as:

$$H_{HPF} = \frac{i_{\mathrm{p},h}}{i_{\mathrm{p}}} = \frac{s - j\omega_{\mathrm{B}}}{s - j\omega_{\mathrm{B}} + \omega_{\mathrm{B}}} \tag{4.58}$$

where ω_{C} is the cut-off angular frequency of the HPFs that extract the DC component in the dq-coordinates, and ω_{B} is the fundamental angular frequency. The detected harmonic current $i_{\mathrm{p},h}$ is compared with the current reference $i_{\mathrm{ph,ref}}$, and the difference e_h represents the input to the PR controller. This results in the production of the reference voltage $v_{\mathrm{p,ref}}$ to be generated by the inverter.

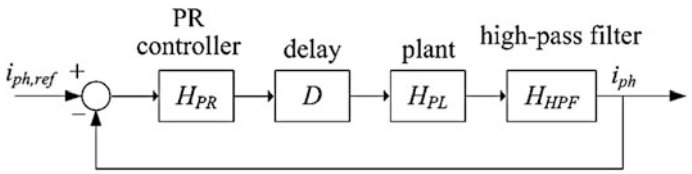

Fig. 4.19 Main current-control block diagram

In the real control circuit (implemented on a DSP), the output signal is inherently delayed with respect to the input signal. The time delay is represented as:

$$D = e^{-sT_s}, \tag{4.59}$$

where T_s is the sampling period. The plant transfer function H_{PL} is defined as (see Fig. 4.1):

$$H_{PL} = \frac{1}{Z_p}. \tag{4.60}$$

Finally, the open-loop transfer function of the controller is given by:

$$H(s) = H_{PR} \cdot H_{HPF} \cdot D \cdot H_{PL}. \tag{4.61}$$

Appendix

The derivation below illustrates the transformation of the STATCOM three-phase mathematical model in the d-q reference frame mathematical model.

The three-phase STATCOM mathematical model is given in (4.62) and is written in a shorter matrix form in (4.63).

$$\frac{d}{dt}\begin{bmatrix} i'_{pa} \\ i'_{pb} \\ i'_{pc} \end{bmatrix} = \frac{-R'_P \omega_B}{L'_P}\begin{bmatrix} i'_{pa} \\ i'_{pb} \\ i'_{pc} \end{bmatrix} + \frac{\omega_B}{L'_p}\begin{bmatrix} \left(v'_{ia} - v'_{pa}\right) \\ \left(v'_{ib} - v'_{pb}\right) \\ \left(v'_{ic} - v'_{pc}\right) \end{bmatrix} \tag{4.62}$$

$$\frac{d}{dt}\left[\mathbf{i'_p}\right] = \frac{-R'_p \omega_B}{L'_p}\left[\mathbf{i'_p}\right] + \frac{\omega_B}{L'_p}\left[\mathbf{v'_{ip}}\right] \tag{4.63}$$

The matrix $\mathbf{T_{dq}}$ (4.64) is used for the transformation in the d-q rotating reference frame and is applied on both sides of (4.62), which results in (4.65).

$$\mathbf{T_{dq}} = \frac{2}{3}\begin{bmatrix} 1/2 & 1/2 & 1/2 \\ \cos(\omega t) & \cos\left(\omega t - \frac{2\pi}{3}\right) & \cos\left(\omega t + \frac{2\pi}{3}\right) \\ -\sin(\omega t) & -\sin\left(\omega t - \frac{2\pi}{3}\right) & -\sin\left(\omega t + \frac{2\pi}{3}\right) \end{bmatrix} \tag{4.64}$$

$$\left[\mathbf{T_{dq}}\right]\frac{d}{dt}\left[\mathbf{i'_p}\right] = \frac{-R'\omega_B}{L'_p}\left[\mathbf{T_{dq}}\right]\left[\mathbf{i'_p}\right] + \frac{\omega_B}{L'_p}\left[\mathbf{T_{dq}}\right]\left[\mathbf{v'_{ip}}\right] \tag{4.65}$$

The transformation of the right-hand side of (4.65) is straightforward and is given in (4.66) and (4.67).

$$\left[\mathbf{T_{dq}}\right]\left[\mathbf{i'_p}\right] = \left[\mathbf{i'_{pdq}}\right] \tag{4.66}$$

$$\left[\mathbf{T_{dq}}\right]\left[\mathbf{v'_{ip}}\right] = \left[\mathbf{v'_{ipdq}}\right] \tag{4.67}$$

The transformation of the left-hand side of (4.65) is a bit more complex. In (4.68) the derivative of the two functions is written. The first term of the left-hand equation side is given with (4.69) and the second term of the left-hand equation side is given with (4.70). The STATCOM mathematical model in the d-q reference frame is given in (4.71)

$$\begin{aligned} \left[\mathbf{i'_p}\right] &= \left[\mathbf{T_{dq}}\right]^{-1}\left[\mathbf{i'_{pdq}}\right] \\ \left[\mathbf{T_{dq}}\right]\frac{d}{dt}\left(\left[\mathbf{T_{dq}}\right]^{-1}\left[\mathbf{i'_{pdq}}\right]\right) &= \left[\mathbf{T_{dq}}\right]\left[\mathbf{T_{dq}}\right]^{-1}\frac{d}{dt}\left[\mathbf{i'_{pdq}}\right] + \left[\mathbf{T_{dq}}\right]\frac{d}{dt}\left[\mathbf{T_{dq}}\right]^{-1}\left[\mathbf{i'_{pdq}}\right] \end{aligned} \tag{4.68}$$

$$\left[\mathbf{T_{dq}}\right]\left[\mathbf{T_{dq}}\right]^{-1}\frac{d}{dt}\left[\mathbf{i'_{pdq}}\right] = \frac{d}{dt}\left[\mathbf{i'_{pdq}}\right] \tag{4.69}$$

$$\begin{aligned} \left[\mathbf{T_{dq}}\right]\frac{d}{dt}\left[\mathbf{T_{dq}}\right]^{-1} &= \begin{bmatrix} 0 & -\omega \\ \omega & 0 \end{bmatrix} \\ \left[\mathbf{T_{dq}}\right]\frac{d}{dt}\left[\mathbf{T_{dq}}\right]^{-1}\left[\mathbf{i'_{pdq}}\right] &= \begin{bmatrix} 0 & -\omega \\ \omega & 0 \end{bmatrix}\begin{bmatrix} i'_{pd} \\ i'_{pq} \end{bmatrix} = \begin{bmatrix} -\omega i'_{pq} \\ -'_{pd} \end{bmatrix} \end{aligned} \tag{4.70}$$

$$\frac{d}{dt}\left[\mathbf{i'_{pdq}}\right] = \frac{-R'_p\omega_B}{L'_p}\left[\mathbf{i'_{pdq}}\right] - \begin{bmatrix} 0 & -\omega \\ \omega & 0 \end{bmatrix}\left[\mathbf{i'_{pdq}}\right] + \frac{\omega_B}{L'_p}\left[\mathbf{v'_{ipdq}}\right] \tag{4.71}$$

References

1. Schauder C, Mehta H (1993) Vector analysis and control of advanced static VAR compensators. In: IEEE proceedings generation, transmission and distribution, pp 299–306
2. Papič I (2000) Mathematical analysis of FACTS devices based on a voltage source converter. Electr Power Syst Res 2:139–148
3. Blažič B, Papič I (2006) Improved D-StatCom control for operation with unbalanced currents and voltages. IEEE Trans Power Deliv 21:225–233
4. Gole AM, Mohaddes M, Elez S (2002) Steady state frequency response of STATCOM. IEEE Trans Power Deliv 16(1):18–23
5. Ekstrom A, Jiang Y (1997) General analysis of harmonic transfer through converters. IEEE Trans Power Electr 12(2):287–293
6. Papič I, Žunko P (2003) UPFC converter-level control system using internally calculated system quantities for decoupling. Electr Power Energ Syst 25(8):667–675
7. Kawabata T, Miyashita T, Yamamoto Y (1990) Dead beat control of three phase PWM inverter. IEEE Trans Power Electron 5(1):21–28
8. Holmes DG, Martin DA (1996) Implementation of a direct digital predictive current controller for single and three phase voltage source inverters. IEEE IAS Annual Meeting, pp 906–913
9. Kukrer O (1996) Discrete-time current control of voltage-fed three-phase PWM inverter. IEEE Trans Power Electr 11(2):260–269
10. Rodríguez J, Pontt J, Silva C, Correa P, Lezana P, Cortés P, Ammann U (2007) Predictive current control of a voltage source inverter. IEEE Trans Ind Electron 54(1):495–503
11. Abu-Rub H, Guzinski J, Krzeminski Z, Toliyat HA (2004) Predictive current control of voltage source inverters. IEEE Trans Ind Electron 51(3):585–593
12. Bode G, Loh PC, Newman MJ, Holmes DG (2005) An improved robust predictive current regulation algorithm. IEEE Trans Ind Appl 41(6):1720–1733
13. Kennel R, Linder A (2000) Predictive control of inverter supplied electrical drives. In: Proceedings of the IEEE 31st annual power electronics specialists conference, pp 761–766
14. Malesani L, Mattavelli P, Buso S (1999) Robust dead-beat current control for PWM rectifier and active filters. IEEE Trans Ind Appl 35(3):613–620
15. Nasiri A (2007) Digital control of three-phase series-parallel uninterruptible power supply systems. IEEE Trans Power Electron 22(4):1116–1127
16. Low KS, Zhuang H (2000) Robust model predictive control and observer for direct drive applications. IEEE Trans Power Electron 15(6):1018–1028
17. Drobnic K, Nemec M, Nedeljkovic D, Ambrozic V (2009) Predictive direct control applied to ac drives and active power filter. IEEE Trans Ind Electron 56(6):1884–1894
18. Božiček A, Blažič B, Papič I (2010) Time–optimal current control with constant switching frequency for STATCOM. Electr Power Syst Res 80(8):925–934
19. Teodorescu R, Blaabjerg F, Liserre M, Loh PC (2006) Proportional-resonant controllers and filters for grid-connected voltage-source converters. IEEE Proc Electron Power Appl 153 (5):750–762
20. Lascu C, Asiminoaei L, Boldea I, Blaabjerg F (2007) High performance current controller for selective harmonic compensation in active power filters. IEEE Trans Power Electron 22 (5):1826–1835
21. Bojoi RI, Griva G, Bostan V, Guerriero M, Farina F, Profumo F (2005) Current control strategy for power conditioners using sinusoidal signal integrators in synchronous reference frame. IEEE Trans Power Electron 20(6):1402–1412
22. Liserre M, Teodorescu R, Blaabjerg F (2006) multiple harmonics control for three-phase grid converter systems with the use of PI-RES current controller in a rotating frame. IEEE Trans Power Electron 21(3):836–841
23. Bojoi R, Limongi L, Roiu D, Tenconi A (2008) Frequency-domain analysis of resonant current controllers for active power conditioners. In: Proceedings of the 34th annual IEEE IECON, pp 3141–3148

24. Yepes AG, Freijedo FD, Doval-Gandoy J, Lopez O, Malvar J, Fernandez-Comesaña P (2010) Effects of discretization methods on the performance of resonant controllers. IEEE Trans Power Electron 25(7):1692–1712
25. Miret J, Castilla M, Matas J, Guerrero J, Vasquez J (2009) Selective harmonic-compensation control for single-phase active power filter with high harmonic rejection. IEEE Trans Ind Electron 56(8):3117–3127
26. Zmood DN, Donald GH, Gerwich HB (2001) Frequency-domain analysis of three-phase linear current regulators. IEEE Trans Ind Appl 37(2):601–610
27. Feola L, Langella R, Testa A (2012) On the behavior of three-phase inverters in the new smart grid context. In: 2nd IEEE energycon conference and exhibition, Florence, 9–12 Sept 2012

Chapter 5
STATCOM Control Strategies

Dionisio Ramirez, Luis Carlos Herrero, Santiago de Pablo and Fernando Martinez

Abstract This chapter reviews the control systems used to enable STATCOMs to carry out their most important task, which is to deliver reactive power to the electrical grid. Later on, other control systems designed for more advanced applications are discussed, such as compensating the nonlinear loads. Later, the design of the control system when STATCOMs are connected to unbalanced electrical networks is presented. Several strategies are presented for controlling the converter, either as a linear current source which is also known as controlled Voltage Source Converter (VSC) based on the use of Proportional-Integral (PI) controllers, or as nonlinear current source, based on the use of hysteresis bands. Other systems, such as the firing algorithm of the switches or system synchronization with the grid, are also discussed.

Keywords STATCOM · DSTATCOM · VSC · Linear current source · Nonlinear current source · Selective harmonic cancellation · Active power filtering · Digital signal cancellation

D. Ramirez (✉)
School of Industrial Engineering, Department of Electrical Engineering,
Technical University of Madrid, Madrid, Spain
e-mail: dionisio.ramirez@upm.es

L.C. Herrero · S. de Pablo · F. Martinez
School of Industrial Engineering, Department of Electronics Technology,
University of Valladolid, Valladolid, Spain
e-mail: lcherrer@tele.uva.es

S. de Pablo
e-mail: sanpab@eii.uva.es

F. Martinez
e-mail: fer_mart@tele.uva.es

F. Shahnia et al. (eds.), *Static Compensators (STATCOMs) in Power Systems*,
Power Systems, DOI 10.1007/978-981-287-281-4_5

5.1 Introduction

STATCOMs are connected to electrical lines in order to improve their performance of the network [1–3] or to help the network parameters to comply with the electrical code in certain countries, principally in those with high penetration of renewable energies [4–6]. These applications are based on injecting reactive power into the grid, so that active and reactive powers exchanged by the STATCOM have to be controlled simultaneously, regulating the former to zero and the latter to the desired value, in an independent way [7–10].

The most widely extended control system for STATCOMs is the linear current source, mainly because of its easier implementation and the fact that it requires a simpler microcontroller. However, if a fast response is necessary, the nonlinear current source control is the best choice although, in return, it needs faster hardware than the former.

In both control systems, the algorithm used in the case of balanced electrical grids relies on the space vector theory and a Phase-Locked Loop (PLL) to carry out the synchronization with the grid; whereas the linear current source uses a Space Vector Modulator (SVM) to control the converter and the nonlinear current source uses hysteresis bands.

Other techniques, such as selective harmonic compensation or active power filtering, can offer special performances, which can be very valuable in some applications; so they have been reviewed later in this chapter.

In the case of an unbalanced grid, the space vector theory is still valid, but now, it is first necessary to break down the electrical voltages into their positive and negative components. One of the most common algorithms used to decompose an unbalanced three-phase voltage system into its sequence networks is Delayed Signal Cancellation (DSC). Once decomposed, each sequence can be controlled independently using PI regulators and, assuming linearity, the resulting space vectors are added before being loaded into a unique SVM.

5.2 Space Vector Model of a VSC Connected to the Grid

In order to establish the equations for the grid connection of a converter, it should be considered that they are usually connected through inductances used as passive filters to reduce the harmonic spectra in the generated voltage and to smooth the peak current between grid and converter. In Fig. 5.1, the inductances have been represented by their resistance and reactance, and these values can include the characteristics of the cables used in the connection.

Therefore, taking into account the circuit shown in Fig. 5.1, the following equation can be written:

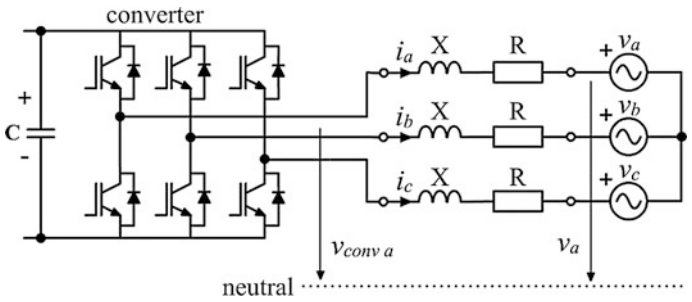

Fig. 5.1 Schematic diagram of the grid connection of a converter

$$\begin{bmatrix} v_{conv\,a} \\ v_{conv\,b} \\ v_{conv\,c} \end{bmatrix} = R \cdot \begin{bmatrix} i_a \\ i_b \\ i_c \end{bmatrix} + \frac{d}{dt} \cdot \begin{bmatrix} \lambda_a \\ \lambda_b \\ \lambda_c \end{bmatrix} + \begin{bmatrix} v_a \\ v_b \\ v_c \end{bmatrix} \tag{5.1}$$

where R and λ represent the resistance and the flux linkage, respectively.

In the case of filter inductances, as no coupling exists between them, (5.1) can be written in a simpler way:

$$\begin{bmatrix} v_{conv\,a} \\ v_{conv\,b} \\ v_{conv\,c} \end{bmatrix} = R \cdot \begin{bmatrix} i_a \\ i_b \\ i_c \end{bmatrix} + L\frac{d}{dt} \cdot \begin{bmatrix} i_a \\ i_b \\ i_c \end{bmatrix} + \begin{bmatrix} v_a \\ v_b \\ v_c \end{bmatrix} \tag{5.2}$$

where L is the self-induction coefficient of the inductances.

Now, considering the definitions for the space vector voltage and current [11]:

$$\vec{U}_{\alpha\beta} = \frac{2}{3} \cdot \left(v_{an} + v_{bn} \cdot e^{j\frac{2\pi}{3}} + v_{cn} \cdot e^{-j\frac{2\pi}{3}} \right) \tag{5.3}$$

$$\vec{I}_{\alpha\beta} = \frac{2}{3} \cdot \left(i_{an} + i_{bn} \cdot e^{j\frac{2\pi}{3}} + i_{cn} \cdot e^{-j\frac{2\pi}{3}} \right) \tag{5.4}$$

and by applying the Clarke transformation:

$$\begin{bmatrix} v_\alpha \\ v_\beta \end{bmatrix} = \frac{2}{3} \begin{bmatrix} 1 & -\frac{1}{2} & -\frac{1}{2} \\ 0 & \frac{\sqrt{3}}{2} & \frac{-\sqrt{3}}{2} \end{bmatrix} \cdot \begin{bmatrix} v_a \\ v_b \\ v_c \end{bmatrix} \tag{5.5}$$

to (5.2), a more compact mathematical expression is achieved:

$$\vec{V}_{\alpha\beta} = \vec{V}_{conv\,\alpha\beta} - R\vec{I}_{\alpha\beta} - L\frac{d\vec{I}_{\alpha\beta}}{dt} \tag{5.6}$$

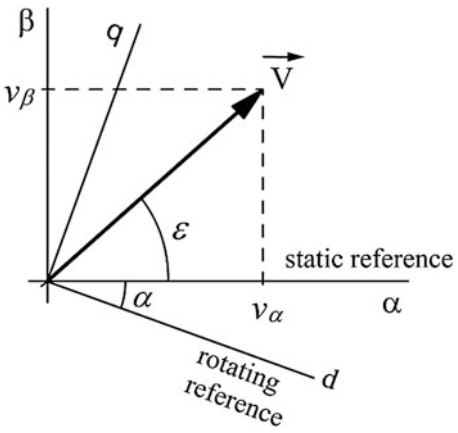

Fig. 5.2 Voltage phasor referred to static and moving reference frames

This equation represents the electrical magnitudes, expressed as space vectors, in a static reference frame.

In a more general way, if the reference system is moving with a velocity, ω_k, then the angle formed by the moving reference frame and the static reference frame, α, is variable. Thus, as is shown in Fig. 5.2, any phasor (for instance, $\vec{V}$) now forms an angle $(\alpha + \beta)$ with respect to the new reference system.

In consequence, to express the space phasors in this new moving reference frame, it is necessary to add the angle alpha, α. By using the Euler formulation to do this, the following is obtained:

$$\vec{V}_{\alpha\beta} \cdot e^{j\alpha} = \vec{V}_{conv\,\alpha\beta} \cdot e^{j\alpha} - R\vec{I}_{\alpha\beta} \cdot e^{j\alpha} - L \cdot \frac{d\vec{I}_{\alpha\beta} \cdot e^{j\alpha}}{dt} \tag{5.7}$$

Now, working on the previous equation:

$$\vec{V}_{\alpha\beta} \cdot e^{j\alpha} = \vec{V}_{conv\,\alpha\beta} \cdot e^{j\alpha} - R\vec{I}_{\alpha\beta} \cdot e^{j\alpha} - e^{j\alpha} L \frac{d\vec{I}_{\alpha\beta}}{dt} - j\frac{d\alpha}{dt} L\vec{I}_{\alpha\beta} \cdot e^{j\alpha} \tag{5.8}$$

and finally

$$\vec{V} = \vec{V}_{conv} - R\vec{I} - L\frac{d\vec{I}}{dt} - j\omega_k L\vec{I} \tag{5.9}$$

This equation is usually broken down into its two orthogonal projections, over the direct and quadrature, d-q, axes:

$$V_d = V_{conv\,d} - RI_d - L\frac{dI_d}{dt} + \omega_k L I_q \tag{5.10}$$

$$V_q = V_{conv\,q} - RI_q - L\frac{dI_q}{dt} - \omega_k LI_d \tag{5.11}$$

In the case of STATCOMs, ω_k is the angular speed of the grid voltage vector and has to be measured by the microcontroller that runs the control algorithm.

Note that all the terms in the first equation correspond to projections on the direct axis except the last one, $\omega_k LI_q$, which is a quadrature term. In the same way, in the second equation, the last term, $\omega_k LI_d$, is different to all the others. Both terms are called decoupling terms and add an extra difficulty to carrying out the control, since any change in one of the axes changes the decoupling term in the other one.

5.3 Power Delivered by the VSC to the Grid

It is well known in Theory of Circuits that the total active power (P) and reactive power (Q) in a three-phase circuit, either balanced or not, can be calculated as the sum of the powers corresponding to each of the symmetric systems into which it can be decomposed.

In a balanced three phase circuit, using the Fresnel notation for phase to neutral voltages and line currents, the apparent Power (S) can be expressed as:

$$\vec{S} = P + jQ = \vec{V}_a \cdot \overrightarrow{I_a^*} + \vec{V}_b \cdot \overrightarrow{I_b^*} + \vec{V}_c \cdot \overrightarrow{I_c^*} \tag{5.12}$$

where the asterisk, *, denotes the complex conjugate of the phasor in polar notation. When (5.12) is expressed as a function of the symmetric components:

$$\vec{S} = 3\vec{V}_{a0} \cdot \overrightarrow{I_{a0}^*} + 3\vec{V}_{a1} \cdot \overrightarrow{I_{a1}^*} + 3\vec{V}_{a2} \cdot \overrightarrow{I_{a2}^*} \tag{5.13}$$

However, as the converter is always connected to the grid with no neutral wire, there is no zero component, and as unbalancing is not considered either, there is no negative component, so that:

$$\vec{S} = 3 \cdot \vec{V}_{a1} \cdot \overrightarrow{I_{a1}^*} \tag{5.14}$$

Now, using space phasors referred to the moving reference frame

$$\vec{V} = \frac{2}{3} \cdot \left(v_{an} + v_{bn} . e^{j\frac{2\pi}{3}} + v_{cn} \cdot e^{-j\frac{2\pi}{3}} \right) \cdot e^{j\alpha} = V_d + jV_q \tag{5.15}$$

$$\vec{I} = \frac{2}{3} \left(i_a + i_b \cdot e^{j\frac{2\pi}{3}} + i_c \cdot e^{-j\frac{2\pi}{3}} \right) \cdot e^{j\alpha} = I_d + j \cdot I_q \tag{5.16}$$

the apparent power can be expressed as

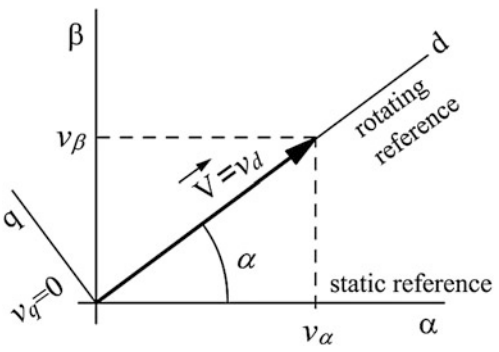

Fig. 5.3 Voltage phasor once aligned with the d axis of the moving reference frame

$$\vec{S} = \frac{3}{2} \cdot \vec{V} \cdot \vec{I}^* = \frac{3}{2} \cdot \left[\left(V_d + jV_q \right) \cdot \left(I_d + jI_q \right)^* \right] \tag{5.17}$$

Splitting this equation into its real and imaginary components, yields

$$\vec{S} = \frac{3}{2} \left(V_d I_d + V_q I_q \right) + j \frac{3}{2} \left(V_q I_d - V_d I_q \right) \tag{5.18}$$

It is convenient to take the direct axis of the reference frame aligned with the direct component of the grid voltage, V_d (Fig. 5.3):

Thus $\vec{V}_d = V_d$ and $V_q = 0$, so the equation of the apparent power is reduced to:

$$\vec{S} = \frac{3}{2} \left(V_d \cdot I_d \right) + j \frac{3}{2} \left(-V_d \cdot I_q \right) \tag{5.19}$$

Therefore, expressed separately, the electric powers are:

$$P = \frac{3}{2} V_d \cdot I_d \tag{5.20}$$

$$Q = -\frac{3}{2} V_d \cdot I_q \tag{5.21}$$

Achieving the synchronization with the grid voltage may require some additional hardware, such as a PLL system, although it can sometimes be enough to use the following mathematical expression:

$$\theta = \tan^{-1} \left(\frac{V_\beta}{V_\alpha} \right) \tag{5.22}$$

to calculate the angle corresponding to the space phasor grid voltage.

5.4 Block Diagram of the Control System

The main objective of the control system of a STATCOM is to control the active and reactive powers delivered to the grid independently. The control block diagram is based on the equations previously obtained for P and Q. Taking into account the fact that the grid voltage, V_d, remains constant, both powers can be regulated by means of the d-q components, I_d and I_q, of the current injected into the electrical network.

By analyzing the terminal equations, it can be checked that the components of the currents depend on the voltage generated by the converter, the resistance and reactance of the filter, and on the decoupling terms, since U_d is usually constant (otherwise, for instance, during a voltage sag, it must be measured):

$$V_{conv\,d} = V_d + \left(RI_d + L \cdot \frac{dI_d}{dt}\right) - \omega_k L I_q \tag{5.23}$$

$$V_{conv\,q} = \left(RI_q + L\frac{dI_q}{dt}\right) + \omega_k L I_d \tag{5.24}$$

or, written in a different way:

$$I_d = f(V_{conv\,d}, R, L;\ decoupling\ term) \tag{5.25}$$

$$I_q = f\left(V_{conv\,q}, R, L; decoupling\ term\right) \tag{5.26}$$

This equation shows that it is possible to control I_d and I_q, indirectly, by means of the d-q components of the inverter voltage, V_d and V_q, with a dynamic that depends on the R and L values of the filtering inductance.

The active power delivered to the grid is usually null, since the STATCOM is not required to generate or absorb this type of power. Nevertheless, since the voltage in the DC bus must be kept constant, it is necessary to compensate for the electric losses, so this is the reference, Fig. 5.4, taken for the PI regulator in the

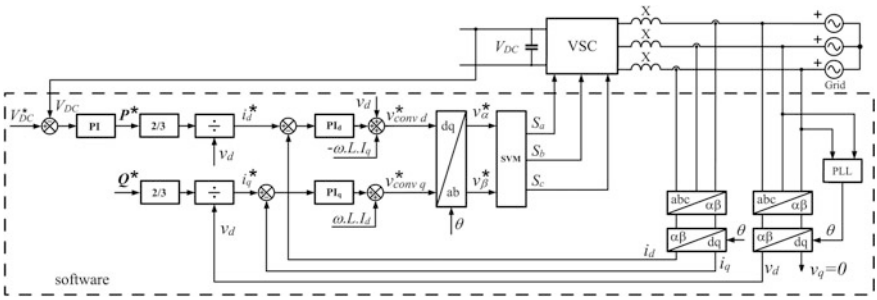

Fig. 5.4 Schematic diagram of the control system

outer loop of the direct axis, d. The PI_d in the inner loop of the same axis, must maintain the measured I_d component close to its reference. Finally, an offset is added, U_d, as well as the decoupling term $(-\omega LI_q)$ in order to make the control in this axis independent from the q axis.

On the other hand, the PI_d regulator used to generate the d reference for the inverter should be initialized $(PI_d(0) = V_d)$ to the grid voltage value to avoid the effect of the transient integral term at the beginning.

There is just one regulator in the q axis, named PI_q, within the equivalent to the inner loop in the other axis. This regulator takes on the task of making the I_q component follow the I_q reference calculated from the reactive power that is to be delivered to the electrical grid. Finally, the decoupling term (ωLI_d) is added.

Taking into account these points, the following equations for generating the d-q voltage references are obtained from the terminal equations:

$$V^*_{conv\,d} = PI_d(0) + PI_d - kI_q \tag{5.27}$$

$$V^*_{conv\,q} = PI_q + kI_d \tag{5.28}$$

where the effect of the term $RI_d + L\frac{dI_d}{dt}$ is substituted by the PI_d term, that of $RI_q + L\frac{dI_q}{dt}$ by the PI_q and ω is considered constant in the absence of grid disturbances.

Next, the voltage references are referred to a static frame, $\alpha\beta$, and are finally turned into three control signals for the converter. In Fig. 5.4, this step has been carried out by means of a Space Vector Modulator, although other techniques can be used, such as Pulse Width Modulation (PWM), non-linear current source, etc.

5.4.1 Determination of the PI Regulator Constants

In order to calculate the proportional and integral constants for the PI regulators, it is necessary to represent the control of the grid connection by means of its transfer function. The method used to calculate the parameters of the inner loop regulators is the cancellation of the largest time constant. Since the time constant in the two axes is the same, the result for the regulators in d and q will also be the same.

The relationship between the electrical current and the voltage generated by the VSC connected to the grid is:

$$\frac{I_d(s)}{V_d(s)} = \frac{I_q(s)}{V_q(s)} = \frac{1}{Ls + R} = \frac{k_{grid}}{\tau_{grid}s + 1} \tag{5.29}$$

where it is clear that the dynamic of the system is determined by the equivalent resistance and inductance between the VSC and the grid, while the static gain and the time constant are:

$$k_g = \frac{1}{R}; \tau_g = \frac{L}{R} \tag{5.30}$$

Next, it is necessary to establish a model for the VSC. This type of converter is normally modeled by a first order system, with a gain equal to one and a delay of τ on both axes:

$$\frac{I_d(s)}{U_d(s)} = \frac{1}{\tau_{conv}s + 1} \tag{5.31}$$

$$\frac{I_q(s)}{U_q(s)} = \frac{1}{\tau_{conv}s + 1} \tag{5.32}$$

In both transfer functions, the delay, τ, represents mainly the elapsed time from the control system changes of the reference value until the VSC changes the state of its semiconductors.

Then, the transfer function for the PI regulator in the inner loop is established in the same way:

$$R(s) = k_{prop} + \frac{k_{intgr}}{s} = k_p \cdot \frac{\frac{k_{prop}}{k_{intgr}}s + 1}{\frac{k_{prop}}{k_{intgr}}s} = k_{reg} \cdot \frac{\tau_{reg}s + 1}{\tau_{reg}s} \tag{5.33}$$

where the new constants are (Fig. 5.5):

$$k_{reg} = k_{prop}; \tau_{reg} = k_{prop}/k_{intgr} \tag{5.34}$$

The time constant for the PI regulator is chosen as equal to the constant time of the electric connection, since this has the greatest of all the time constants in the system. Thus the term $(\tau_{reg}s + 1)$ cancels out $(\tau_{grid}s + 1)$, so that the resulting open loop transfer function is:

$$G(s) = \frac{k_{reg}k_{grid}}{\tau_{reg}\tau_{conv}s^2 + \tau_{reg}s} \tag{5.35}$$

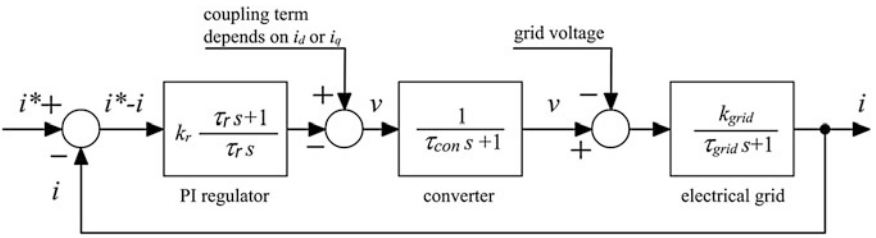

Fig. 5.5 Transfer functions involved in the control loops

and the transfer function for the closed loop is:

$$G^*(s) = \frac{G(s)}{1+G(s)} = \frac{1}{s^2\left[\frac{\tau_{reg}\cdot\tau_{conv}}{k_{reg}\cdot k_{grid}}\right] + s\left[\frac{\tau_{reg}}{k_{reg}\cdot k_{grid}}\right] + 1} \tag{5.36}$$

Taking into account the normalized transfer function equation for second order systems:

$$G^*(s) = \frac{1}{s^2\tau^2 + 2s\tau\xi + 1} \tag{5.37}$$

It is possible to identify coefficients between (5.36) and (5.37):

$$\tau = \sqrt{\frac{\tau_{reg}\cdot\tau_{conv}}{k_{reg}\cdot k_{grid}}} \tag{5.38}$$

Substituting τ in (5.37) and identifying mathematical terms:

$$2\tau\xi = 2\cdot\sqrt{\frac{\tau_{reg}\tau_{conv}}{k_{reg}k_{grid}}}\cdot\xi = \left[\frac{\tau_{reg}}{k_{reg}k_{grid}}\right] \tag{5.39}$$

the following is obtained:

$$\xi = \frac{1}{2}\cdot\sqrt{\frac{\tau_{reg}}{\tau_{conv}k_{reg}k_{grid}}} \tag{5.40}$$

By imposing a damping of $\xi = 1/\sqrt{2}$ so that the overshoot does not exceed 5 %, and $\tau_{reg} = \tau_{grid}$ has been taken, the constant k_r becomes:

$$k_{reg} = \frac{1}{2}\frac{\tau_{grid}}{k_{grid}\tau_{conv}} = k_{prop} \tag{5.41}$$

Finally, taking into account (5.34), and considering again that $\tau_{reg} = \tau_{grid}$, k_{intgr} becomes:

$$k_{intgr} = \frac{k_{prop}}{\tau_{reg}} = \frac{k_{reg}}{\tau_{grid}} \tag{5.42}$$

In the direct axis, the outer regulator keeps the voltage in the DC bus constant, so that its constants have to be designed depending on the efficiency of each particular VSC.

5.4.2 Space Vector Modulation

Using the structure of a three-phase two-level VSC, as shown in Fig. 5.1, the relationship between the controller switching variables (S_a, S_b, S_c) and the phase-to-neutral converter voltages ($v_{conv\,a}$, $v_{conv\,b}$, $v_{conv\,c}$) is given by (5.43), where V_{DC} is the bus voltage and S_k is '1' or '0' when the upper or lower transistor of phase k is on, respectively:

$$\begin{bmatrix} v_{conv\,a} \\ v_{conv\,b} \\ v_{conv\,c} \end{bmatrix} = \frac{1}{3} V_{DC} \begin{bmatrix} 2 & -1 & -1 \\ -1 & 2 & -1 \\ -1 & -1 & 2 \end{bmatrix} \begin{bmatrix} S_a \\ S_b \\ S_c \end{bmatrix} \tag{5.43}$$

Applying the Clarke transformation (5.5) to these voltages, leads to a space vector with the same instantaneous information in a stationary reference frame $\alpha\beta$. There are eight different vectors for the two-level inverter output, named $\vec{V}_0$ to $\vec{V}_7$, as defined in Fig. 5.6, according to the eight possible switching states. To obtain the required output space vector $\vec{v}^*$, which is usually a rotating vector with constant module and pulsation, the conduction times of the inverter switches are modulated according to the angle and magnitude of that reference. The null vectors $\vec{V}_{Z1} = \vec{V}_0$ and $\vec{V}_{Z2} = \vec{V}_7$, and two space vectors adjacent to $\vec{v}^*$, $\vec{V}_X$ and $\vec{V}_Y$, are chosen and modulated during a short switching time, T_S, using the volt-second balance method:

$$\vec{v}^* = \frac{1}{T_S} \int_t^{t+T_S} \vec{v}_{conv\,\alpha\beta} dt = d_{Z1}\vec{V}_{Z1} + d_X\vec{V}_X + d_Y\vec{V}_Y + d_{Z2}\vec{V}_{Z2} \tag{5.44}$$

As the values of d_{Z1} and d_{Z2} have no effect in (5.44) due to the null magnitude of $\vec{V}_0$ and $\vec{V}_1$, solving this equation using rectangular coordinates yields

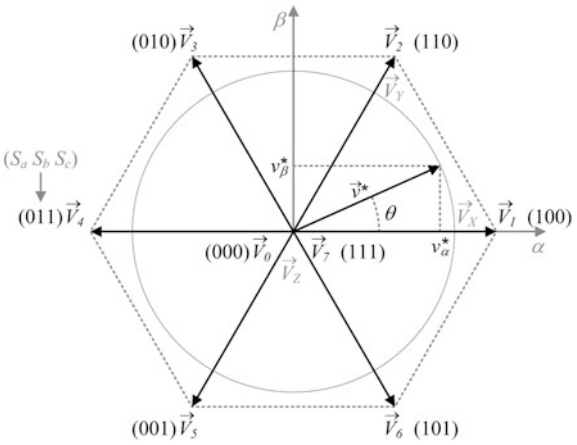

Fig. 5.6 Definitions used for space vector modulation

$$\begin{bmatrix} V_{X\alpha} & V_{Y\alpha} \\ V_{X\beta} & V_{Y\beta} \end{bmatrix} \begin{bmatrix} d_X \\ d_Y \end{bmatrix} = \begin{bmatrix} v_\alpha^* \\ v_\beta^* \end{bmatrix} \tag{5.45}$$

where the matrix arranges the known $\alpha\beta$ components of the adjacent inverter vectors $\vec{V}_X$ and $\vec{V}_Y$. (5.45) can be applied, without loss of generality, to a reference phase θ in the range 0 to $\pi/3$, thus $\vec{V}_1$ and $\vec{V}_2$ will be used jointly with $\vec{V}_0$ and $\vec{V}_7$ to generate $\vec{v}^*$, as shown in Fig. 5.6. Thus, the amount of time for each voltage vector is computed by solving the inverse problem (5.46), leading to the known equations of

$$\begin{bmatrix} d_X \\ d_Y \end{bmatrix} = \begin{bmatrix} d_1 \\ d_2 \end{bmatrix} = \begin{bmatrix} \frac{2}{3}V_{DC} & \frac{1}{3}V_{DC} \\ 0 & \frac{\sqrt{3}}{3}V_{DC} \end{bmatrix}^{-1} \begin{bmatrix} v_\alpha^* \\ v_\beta^* \end{bmatrix} \tag{5.46}$$

$$d_X = d_1 = \frac{\frac{3}{2}v_\alpha^* - \frac{\sqrt{3}}{2}v_\beta^*}{V_{DC}} \tag{5.47}$$

$$d_Y = d_2 = \frac{\sqrt{3}v_\beta^*}{V_{DC}} \tag{5.48))}$$

Finally, the duty cycle of null vectors is computed as

$$d_Z = d_{Z1} + d_{Z2} = 1 - d_X - d_Y \tag{5.49}$$

Applying this method to all six sectors of Fig. 5.6, the duty cycles can be efficiently computed in all situations using different sets of equations, each one valid on one triangle.

Selected vectors are then distributed along the switching period, T_S, in such a way that semiconductor state changes are generated one by one. For the case being dealt with here, the usual switching sequence is as follows: $\vec{V}_0$ will be imposed during $d_Z/4$, then $\vec{V}_1$ will be activated during $d_X/2$, then $\vec{V}_2$ during $d_Y/2$, then $\vec{V}_7$ during $d_Z/2$, and then back to $\vec{V}_2$ during $d_Y/2$, $\vec{V}_1$ during $d_X/2$ and finally $\vec{V}_0$ during $d_Z/4$.

Generic equations valid for all sectors, even in the case of multilevel converters, can be found at [12, 13].

5.4.3 Synchronization with the Grid: PLL Algorithm

A key point in the vector control algorithm for a grid connected VSC is to carry out the synchronization of the control system with the grid with great accuracy.

There are a number of ways to do this, but the most common is to use a phase locked loop whose block diagram is shown in Fig. 5.7 [14].

The algorithm measures the phase to neutral grid voltages and then performs both the Clarke and the Park transformations. The latter is carried out using an

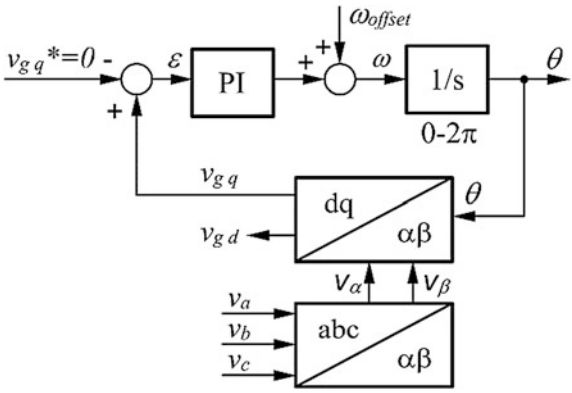

Fig. 5.7 Block diagram of a PLL

incorrect angle at the beginning so that V_q is not zero and, consequently, the error at the PI input is not null either. The PI regulator reacts by changing its output, which represents the angular speed of the grid voltage. Next, this value is integrated into the following integrator, giving a sawtooth (between 0 and 2π) as a result (otherwise the numerical magnitude will overflow sooner or later).

Progressively, the PI regulator speeds up or slows down the dq reference frame until the V_q component becomes null. At this moment, the angular speed, ω, is the actual speed of the space vectors and the angle θ is generated so that the reference frame is aligned with the V_d component of the grid voltage.

Note that an offset, ω_{off}, is added to the PI output to improve the transient behavior of the ω estimation at the very beginning, decreasing the settling time of this variable. Its value should be the expected angular speed for the grid voltage phasor.

In this section, every block in the control system for STATCOMs working as voltage source with current feedback (also named linear current source) have been studied. From this point on, it would be very easy to calculate the equivalent digital control system to be implemented in a microprocessor, by using the z-transformation to finally obtain the difference equations.

5.5 STATCOMs Operating as Nonlinear Current Source

The most important nonlinear controllers used in the STATCOM are current source hysteresis controllers. It is a control method of instantaneous current feedback, where the real current follows the current reference. This is accomplished by setting a hysteresis band over the current reference wave, and when the actual current exceeds the limits stipulated by the hysteresis band, the converter commutates and, so, the current changes its slope to follow the current reference. The hysteresis band controls the values of the switching frequency and the current ripple; when the hysteresis band increases, the switching frequency decreases and the ripple current increases.

Figure 5.8a shows the block diagram of the grid connection control system for the STATCOM application. From the active and reactive power references, the current references in axes d and q, i_d^* and i_q^*, are obtained. Then, using the inverse Clarke and Park transformations, the current references of the three phases, i_a^*, i_b^* and i_c^*, are generated, which are used by means of the hysteresis current regulator. The inverter voltage versus current error has a hysteresis graph (Fig. 5.8b), where the inverter voltage takes the values $+V_{DC}/2$ or $-V_{DC}/2$ depending on the current error values [15].

Figure 5.9 shows the inverter voltage, $v_{conv\,a}$, and phase current, i_a, waveforms obtained using this control method, when the DC neutral (midpoint of the DC voltage) is connected to the grid neutral (Fig. 5.9a), and when they are not connected (Fig. 5.9b). In the first case, when the real current exceeds the upper hysteresis band, the lower semiconductor of the arm is switched on ($v_{conv\,a} = -V_{DC}/2$) and, so, the current decreases. When the current is lower than the lower band, the upper semiconductor is switched on ($v_{conv\,a} = +V_{DC}/2$) and the current increases. When the neutral is not connected (Fig. 5.9b), the converter voltage with respect to the grid neutral has five levels and the phase current does not commutate between both bands as a single line, and also, the current cannot reach or exceed the value of the band. The reason for this is that the current of one phase is influenced by the state of the semiconductor of the other phases. In a real case, the neutral connection does not exist, except perhaps in the distribution STATCOM (DSTATCOM), so the real graphs are in Fig. 5.9b. To make the figures clearer, a STATCOM with the midpoint of DC connected to the grid neutral is usually used (Fig. 5.9a), because it does not remove validity from the control system, although the phase current waveforms can be modified a little; therefore, in the following simulations, the neutral connection will be used.

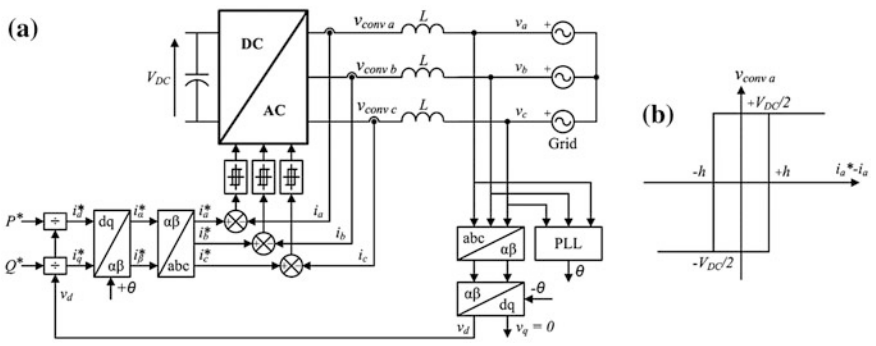

Fig. 5.8 Control system for current source control with hysteresis band: **a** general scheme, **b** inverter voltage versus current error graph, for each phase

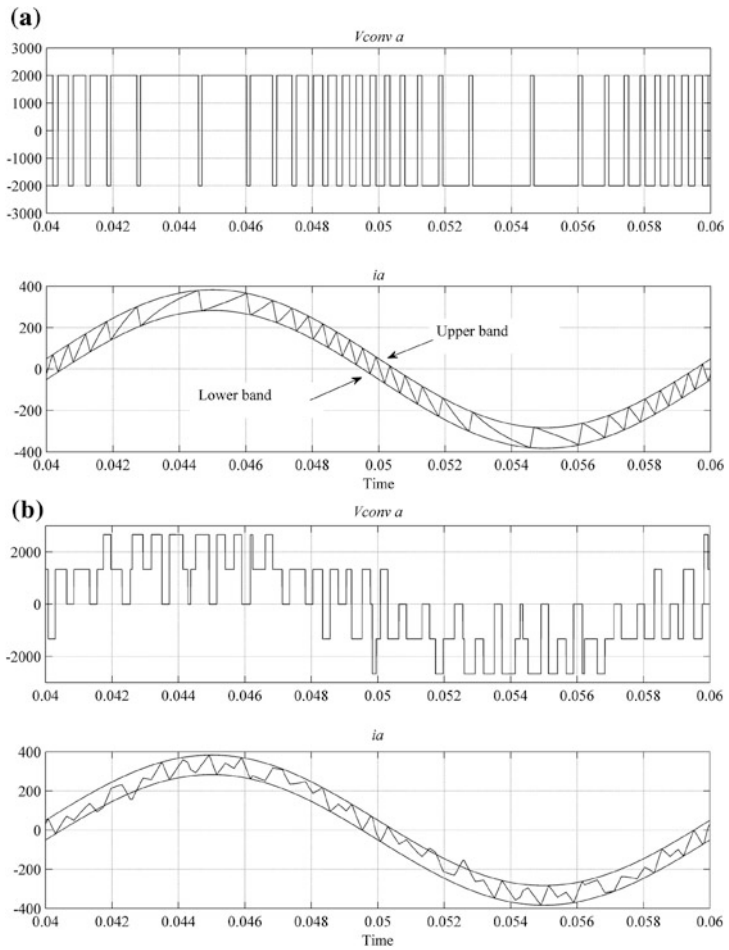

Fig. 5.9 Inverter voltage and phase current waveforms in a two-level converter: **a** with neutral connected, **b** without neutral connected

The algorithm of the hysteresis blocks, for phase-a in Fig. 5.8a, is:

$$
\begin{aligned}
&\textit{if}\left(i_{ak} > i_{ak}^{*} + h\right)\\
&\qquad v_{conv\,ak} = -V_{DC}/2;\\
&\textit{elseif}\left(i_{ak} < i_{ak}^{*} - h\right)\\
&\qquad v_{conv\,ak} = +V_{DC}/2;\\
&\textit{else}\\
&\qquad v_{conv\,ak} = v_{conv\,ak-1};\\
&\textit{end}
\end{aligned}
$$

Neglecting the effect of the electric resistance, the equation that relates the inverter output voltage, $v_{conv\,a}$, the grid voltage, v_a, and the phase current, i_a, for the first phase, is:

$$v_{conv\,a} = L\frac{di_a}{dt} + v_a \tag{5.50}$$

If the current hysteresis band is called h, the time Δt between two commutations is:

$$\Delta t = \frac{2hL}{(v_{conv\,a} - v_a)} \tag{5.51}$$

The time between two consecutive commutations, Δt, is not constant, because the grid voltage is not constant but sinusoidal, and so the switching frequency of the converter is not constant. Logically, the same can be said for phase-b and c. If the hysteresis band is narrow, the current ripple is low, but the switching frequency is large. If the hysteresis band is wide, the opposite takes place.

Variable switching frequency is a drawback because it makes the dimensioning of the grid filter and the compliance with the harmonic injection standards more difficult.

5.5.1 Variable Switching Frequency Controllers with Two-Level and Multilevel Converters

The hysteresis current controller has several advantages and disadvantages with respect to voltage source controllers. The former are:

- Simplicity. From the active and reactive power references, the output current references in axes d and q, i_d^* and i_q^*, are obtained. When using current source control, no more regulators must be adjusted, while when voltage source control is used, two additional PI controllers and the dq decoupling equations must be included.
- Instant control of the output current with high accuracy.
- Intrinsic ability to limit current overloads.
- Extremely good dynamics, limited only by switching speed and the time constant of the load.
- Independence with respect to the variation of the parameters of the load.
- Independence from variations of the voltage drop of semiconductors and dead times of the converter.
- Independence from the DC and AC voltage variations.

And the latter:

- Switching frequency is not constant; it depends on the load and the grid voltage.
- The operation is somewhat random, so it is difficult to establish protections and filters.

The hysteresis band is usually between 1 and 5 % of the nominal current [16]. A very narrow band allows a quick and accurate reference current tracking, but the switching frequency is very high. A very wide band generates a poor tracking of the reference and may produce instabilities.

Converters of two, three or more levels can be used for the STATCOM. Current source hysteresis control can be used in any of them. In the two-level inverter, which is explained above, the error band is h and the graphic of the converter phase to neutral voltage versus current error is shown in Fig. 5.8b. The phase voltage takes the values $+V_{DC}/2$ and $-V_{DC}/2$ and the current oscillates around the reference (Fig. 5.9a).

In the case of a three-level converter, the phase voltage can take the values $+V_{DC}/2$, 0 and $-V_{DC}/2$ (upper graph in Fig. 5.10a), depending on the current error. The current hysteresis graph is shown in Fig. 5.10b. A small dead band δ around the zero error is defined to ensure three-level operation [17]. If the dead band δ is large, the current error will also be great, so it must be the smallest value to ensure the maintenance of the sign of the current error. On the positive half-cycle of the current waveform, the current switches between the reference and the lower band, while in the negative half wave of current, the current switches between the reference and the top band (lower graph in Fig. 5.10a).

The case of the three-level converter can be extended to a larger number of levels. For example, in the case of 7 levels, the current hysteresis graph can be seen in Fig. 5.11b [18]. A small dead band δ is again used to prevent jumps in output voltage. An example of the inverter phase to neutral voltage and phase current waveforms of a 7 level converter can be found in Fig. 5.11a.

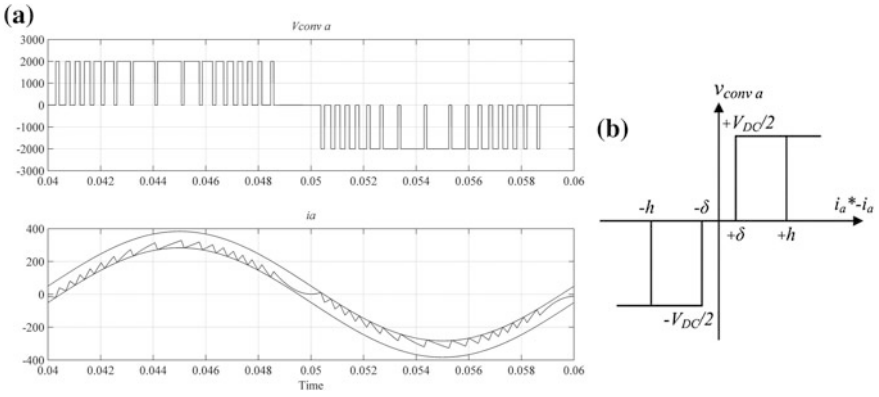

Fig. 5.10 Three-level converter: **a** inverter voltage and phase current waveforms, **b** inverter voltage versus current error graph, for each phase

The inverter voltage (upper graph in Fig. 5.11a) always commutates between two levels, $(+V_{DC}/2; +V_{DC}/3)$, $(+V_{DC}/3; +V_{DC}/6)$, etc., and the current commutates between two hysteresis bands according to the voltage levels, $(I^* + h; I^* + 2h/3 + \delta)$, $(I^* + 2h/3 - \delta; I^* + h/3 + \delta)$, etc. As a result, in the positive half-cycle of the current waveform, the current is very close to the lower band h, while in the negative half wave of current, the current is very close to the upper band h (lower graph in Fig. 5.11a).

The phase current in multilevel converters is slightly lower than the reference value, because in the positive half cycle, the current is closer to the lower band, and the negative half cycle, it is closer to the upper band (Figs. 5.10 and 5.11). The difference between the real current and the reference current is small because the width of the band is small; moreover, this difference is compensated by the action of the PI regulators of active and reactive power.

Below, a second algorithm, using current hysteresis regulation for multilevel converters, is presented [19]. In this case, the explanation is about an example of 5 levels. Phase to neutral converter voltage can take the values $+V_{DC}/2$, $+V_{DC}/4$, 0, $-V_{DC}/4$ and $-V_{DC}/2$. Two bands of error, h and h_1 are defined. Error band h is the main one, and the control will try to maintain the current within this band as long as possible. When the current is within this band, the inverter voltage is zero, since this error is permissible. When the current exceeds this band h, the converter voltage will be $+V_{DC}/4$ or $-V_{DC}/4$ to try to bring the current back within this band. The current can go outside the band, h, due to a very rapid variation of the reference current, or because the voltage of the network takes extreme values. In that case, when the current leaves a supplementary band h_1, the maximum converter voltage is supplied, $+V_{DC}/2$ or $-V_{DC}/2$, to make the current modify its slope and reduce the error. This control logic is shown in Fig. 5.12a, and a waveform simulation is shown in Fig. 5.12b.

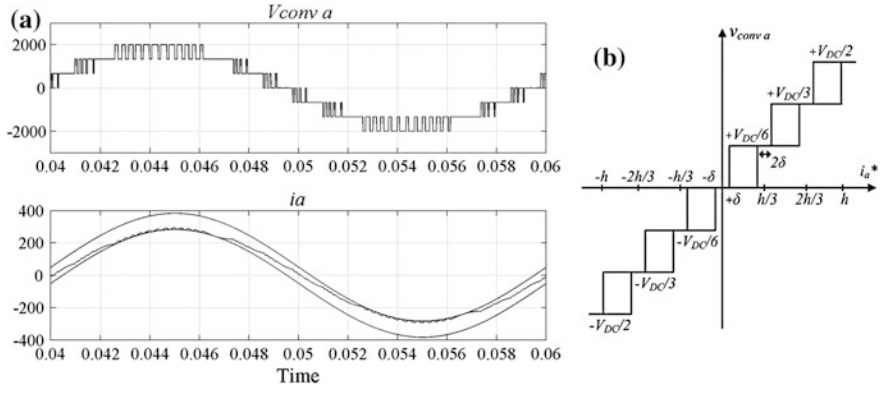

Fig. 5.11 Seven-level converter: **a** inverter output voltage and phase current waveforms, **b** inverter voltage versus current error graph, for each phase

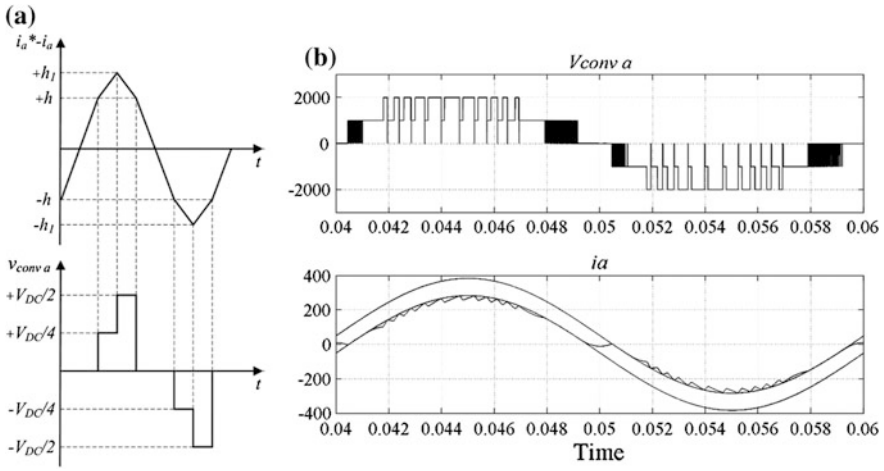

Fig. 5.12 Second algorithm for hysteresis current control in multilevel converters; current phase and converter phase to neutral voltage waveforms: **a** detail, **b** simulation

5.5.2 Constant Switching Frequency Controllers

The hysteresis current controllers, presented in Sect. 5.5.1, have a variable switching frequency, which makes the design of the filters more difficult and can create resonances in the grid.

To get a constant switching frequency, various techniques can be used, such as varying the band of hysteresis depending on the mains voltage, or using a wave carrier. These schemes are more complex, and they eliminate one of the great advantages of hysteresis control, that is the simplicity. They get very fast response speeds, and are suitable for applications that require a high performance.

Nevertheless, variable switching frequency controllers may have too high a switching frequency, causing a high stress in the semiconductors. The switching frequency could be kept constant using a triangular carrier, but the choice of that frequency is not easy, and if it is too high or too low, the effect of not crossing the hysteresis band, or of exceeding it by too much, can be produced [18].

Variable band hysteresis current controllers adjust the width of the band, in order to compensate for variations in the grid voltage, thus making the switching frequency constant [20].

5.6 Advanced Functions of STATCOM Systems

The primary function of STATCOM systems is reactive power compensation, mostly to increase the transmittable power, but also to prevent voltage instability, to provide a dynamic voltage control to increase transient stability and also for

damping power oscillations [21]. However, grid regulation has become more and more demanding in terms of power quality to meet present energy challenges, and harmonic interference problems have also become increasingly serious [22]. Some of the most important effects produced by these harmonic currents are [23, 24]:

- The flow of harmonic currents through the network impedances produces the appearance of harmonic voltages.
- Resonance problems between line impedances and shunt capacitors.
- Increase of motor and transformer losses.
- Telecommunication lines interference.
- Protective equipment, e.g. differential relay protection, which may not work properly.
- Errors in power metering.

There are several devices that compensate for harmonic distortion and/or reactive power [25]:

- Devices based on passive filters: these do not detect changes in the distribution network topology, and therefore, if the load conditions change, their action could disappear and even produce resonance situations.
- Devices based on power electronic converters: these react in response to changes in the distribution system. Compared to passive solutions, like tuned LC filters, filters built using power electronic devices have many advantages, such as their small size and light weight, low power losses, improved tracking of power system frequency changes, faster dynamic response to load changes, and a reduction of resonant problems. Moreover, any increase in nonlinear load capacity, which may exceed the rated power of installed systems, can be addressed using load sharing strategies between several active units [26].

As a consequence, active compensation schemes have recently received more attention. There are two basic modes of harmonic compensation in a STATCOM in terms of bandwidth: on the one hand, the overall harmonic compensation (OHC), also called active power filters (APF), removes all harmonic distortion up to a maximum frequency, limited only by the switching frequency and the system dynamics; on the other hand, the selective harmonic compensation (SHC) generally only removes low order harmonics, usually the 5th, 7th, 11th and 13th. Each of these modes gives a different performance depending on the existing conditions and limitations.

5.6.1 Selective Harmonic Compensation

A deeper analysis of STATCOM control algorithms, see Fig. 5.13, shows that most STATCOM systems with small modifications may contribute to cancelling out, or at least reducing, selected low order current harmonics, in addition to their main task of reactive power compensation. This selectivity can be provided by design,

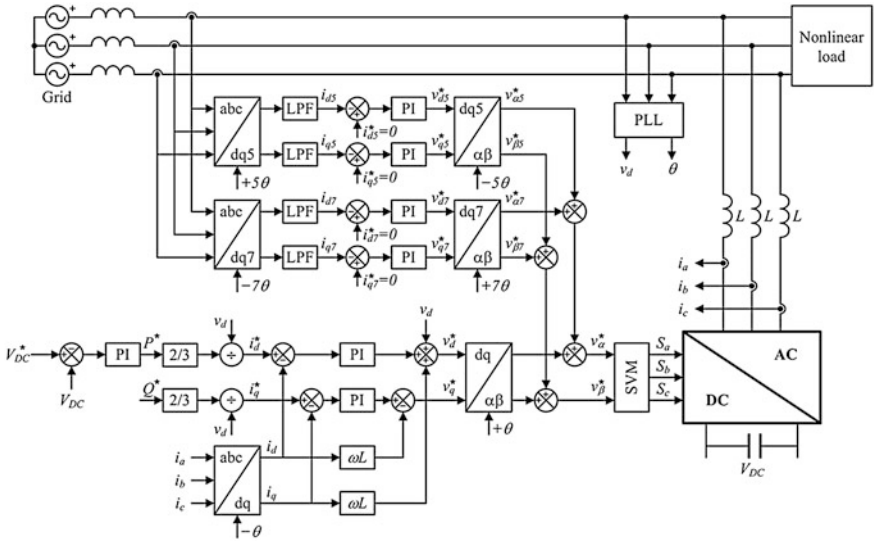

Fig. 5.13 Selective harmonic compensation using STATCOM

through the implemented algorithm, or by the user's choice, dynamically changing the harmonics that are to be compensated.

The complete controller can be carried out as the superposition of many individual harmonic controllers, jointly with the fundamental harmonic controller, whose function is to regulate the DC capacitor voltage and compensate for the reactive power. As stated in 5.4, a voltage reference vector (v_d^*, v_q^*) is generated using external references V_{DC}^* and Q^*. Additional voltage references are then included to mitigate the 5th and 7th harmonics of current, present in the grid because of nonlinear loads. Obviously, any other harmonic component can be cancelled by adding more detectors and compensators.

Harmonic measurement is an important process when designing a selective harmonic compensator. In the time domain, a direct method may use Band-Pass Filters (BPF) to extract each harmonic component directly, phase by phase, with the drawback of a high computational cost, because lots of high order filters are usually required; an alternative method makes use of a generalized Park transformation to convert the selected harmonic component, from a three-phase stationary reference frame to several synchronous reference frames rotating at selected frequencies with an appropriate sequence, and then perform harmonic extraction by means of low-pass filters (LPF) [27, 28].

Frequently, nonlinear loads are front-end three-phase rectifiers used in industrial AC drives, which generate nonsinusoidal currents with Total Harmonic Distortion (THD) factors from 30 to 130 % [29]. The harmonic spectrum of this type of current contains only harmonics of orders $k = 6n \pm 1$, where n is a positive integer. Moreover, in this case, the sequence of the 5th, 11th and 17th harmonics is

negative, while the sequence of the 7th, 13th and 19th harmonics is positive. Therefore, a Park transformation on the fundamental frequency cannot be applied, because the 5th and 7th harmonics shift to the 6th harmonic, the 11th and 13th harmonics shift to the 12th, and so on, thus they cannot be separated in order to compensate them.

The algorithm included in Fig. 5.13 uses two generalized Park transformations at the fifth and seventh harmonics, taking into account their corresponding negative or positive sequence, and then two LPFs extract the amplitude and phase information of those current harmonics through their *dq* components. Then, PI regulators generate the appropriate references that, added to the STATCOM fundamental voltage references, lead the inverter to produce the appropriate current values. As long as those undesired currents are provided by the STATCOM, they are cancelled, or at least mitigated, from the grid. In addition, a limiter (not included in Fig. 5.13) must be added after every PI regulator in order to ensure that the harmonic currents provided by the STATCOM never increase beyond their allowed range. Otherwise, inverter voltage references may become greater than the maximum voltage allowed by the DC capacitor, making the whole system unstable.

The main advantage of SHC over OHC systems is that delay compensation is not required, as long as LPFs introduce no phase shift on DC extracted values and *dq* regulators fix any phase error. On the other hand, OHC designers must take into account, and must compensate for, the delays produced by anti-aliasing filtering and discrete DSP execution, among other things. For example, when running the controller at a 100 μs sampling time on a 50 Hz power system, one single sample delay means from 9° to 45° phase shifts for the 5th to 25th harmonics, respectively. The delay at the 5th harmonic is relatively small, but this delay may cause a noticeable effect because it is one of the dominant harmonics in the spectrum for typical nonlinear loads. Delay compensation is a challenging task; it is usually sensitive to parameter mismatches and relies on the ability to accurately predict the VSC current control performance [30].

Another inherent advantage of SHC systems is that several units can be installed in parallel [26]. They can, in fact, be controlled to cancel individual harmonics from separate units. This possibility is also exploited when using multilevel inverters to implement STATCOMs, using several branches running at low switching frequency to manage the fundamental components (reactive compensation and DC voltage regulation), and other branches running at high switching frequency to cancel out the harmonics [31].

The results of a simulation of the proposed STATCOM working as a SHC are shown in Fig. 5.14. A three-phase rectifier attached to a resistive load has been connected to a 400 V, 50 Hz grid through filtering inductors, sinking 47.3 Arms from the grid. The STATCOM operates at a switching frequency of 10 kHz and regulates its internal DC voltage to 700 V. Before the selective harmonic compensation is activated at 0.02 s, see Fig. 5.14a, the grid current harmonics were 12.59 A (5th), 5.65 A (7th), 4.28 A (11th) and 2.58 A (13th), i.e. 18.8, 8.44, 6.39 and 3.85 %.

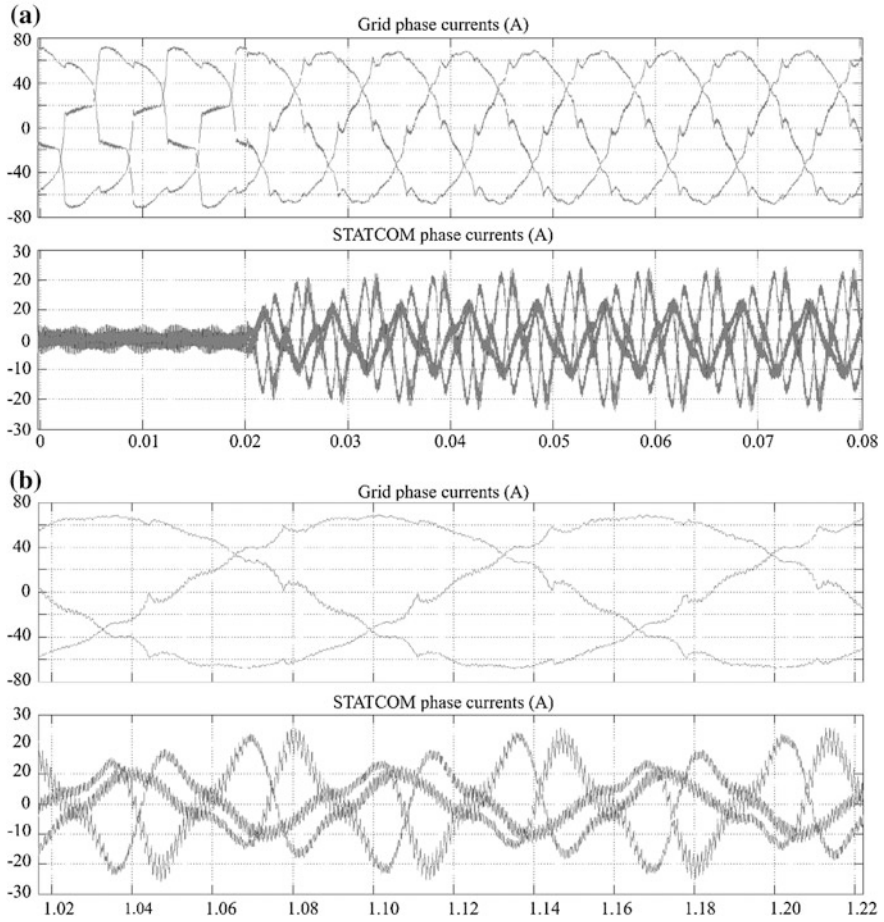

Fig. 5.14 **a** Selective harmonic compensation starts at 0.02 s to mitigate the 5th, 7th, 11th and 13th harmonics generated by a three-phase rectifier, **b** steady state one second later

In steady state, see Fig. 5.14b, those harmonics were reduced to marginal values below 0.05 A (0.07 %). Applying this Selective Harmonic Compensator the THD has been reduced from 22.4 to 4.6 %.

5.6.2 Active Power Filter

The harmonic currents in distribution systems have their main origin in the existence of nonlinear loads such as rectifiers, converters, power supplies, etc. These currents must be compensated to avoid the problems presented in Sect. 5.6. In this section, we analyze the use of STATCOM as a Shunt APF to compensate the

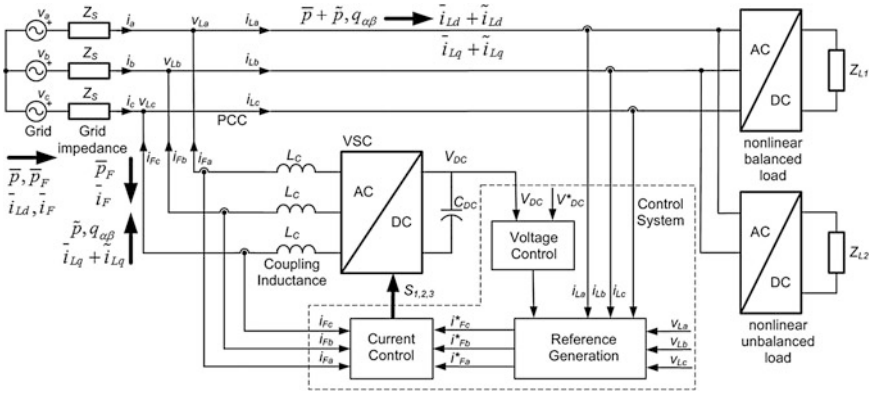

Fig. 5.15 STATCOM as shunt active power filter

harmonic currents caused by nonlinear loads, Fig. 5.15. These devices are also called Overall Harmonic Compensation (OHC).

The Shunt APF is an electronic piece of equipment that uses the energy stored in a capacitor (C_{DC}) to compensate the harmonic distortion caused by the nonlinear load. The basic element of the Shunt APF is the three-phase VSC, which is controlled to inject a current (i_F) at the Point of Common Coupling (PCC), compensating for the harmonic current demanded by the nonlinear load (i_L) of the grid. The purpose of the filter is to compensate for the harmonic currents consumed by the load (i_L) and prevent them from extending through the rest of the electrical system, resulting in the supply current (i_s) being a pure sine. The inverter is connected to the electrical system by coupling inductances (L_C), which filter high frequency current produced by the inverter switching and facilitate the parallel connection of voltage sources (VSC and electrical network) [32]. The Shunt APF characteristics allow the harmonic distortion to be compensated, the reactive power demanded by the load to be injected into the PCC, and also the currents of the supply network to be balanced.

In Fig. 5.15, the basic block diagram of the control system of a Shunt APF is shown. The control system is divided into three sections:

- Determination of the reference current, block "Reference Generation" in Fig. 5.15: the load current (i_L) is measured and harmonics and unbalanced components are extracted to be a part of the reference current (i_F^*). Furthermore, the Shunt APF can compensate reactive power and must regulate the voltage capacitors (V_{DC}). These tasks generate an extra term to be added to the reference current.
- Control of the DC capacitor voltage, block "Voltage Control" in Fig. 5.15: using a PI control, the power to be absorbed from the grid to maintain the constant voltage, V_{DC}, is determined.

- Current control of STATCOM: its function is to make the current, VSC (i_F), follow the reference (i_F^*). For Shunt APF, current regulators based on Hysteresis Control, the Delta Modulation and Dead-Death are the most used [33–35].

The algorithms that generate the reference current can be divided into those developed in the frequency domain and the ones developed in the time domain. Those based in the frequency domain [36] extract the fundamental harmonic component using FFT, DFT, and Kalman Filters, and thus the reference signal is generated. These methods have the disadvantage of requiring a large processing time and they have a slow dynamic response. The methods in the time domain have the advantage of the high speed of response to changes in the system [37–39]. The following section discusses the main methods in the time domain.

In Fig. 5.15, the block "Reference Generation" calculates the reference current for the VSC. Some of the most commonly used methods to generate these references are discussed below.

One of the most common methods is based on the *Instantaneous Power Theory*. In this method, the calculation of the reference current is performed by the intermediate calculation of the instantaneous power of the load. The theory is developed through the application of the Clarke transformation, which allows the transformation of a conventional three-phase system, axes abc, to the static axes system αβ0.

$$\begin{bmatrix} x_\alpha \\ x_\beta \\ x_0 \end{bmatrix} = \sqrt{\frac{2}{3}} \cdot \begin{bmatrix} 1 & -\frac{1}{2} & -\frac{1}{2} \\ 0 & \frac{\sqrt{3}}{2} & -\frac{\sqrt{3}}{2} \\ \frac{1}{\sqrt{2}} & \frac{1}{\sqrt{2}} & \frac{1}{\sqrt{2}} \end{bmatrix} \begin{bmatrix} x_a \\ x_b \\ x_c \end{bmatrix} \tag{5.52}$$

The definitions of instantaneous power, $p(t)$, and instantaneous reactive power, $q(t)$, in a three-phase system (axes abc), are given by:

$$p = v_a i_a + v_b i_b + v_c i_c \tag{5.53}$$

$$q = \frac{-1}{\sqrt{3}}[(v_a - v_b)i_c + (v_c - v_a)i_b + (v_b - v_c)i_a] \tag{5.54}$$

In three-phase systems without harmonic distortion, these powers are constant over time. For systems with harmonic distortion, the powers show an oscillatory term which causes the powers to be no longer constant in time. Both instantaneous powers can be rewritten, in coordinates αβ0, by the Clarke transformation:

- The instantaneous power, $p(t)$, in the reference system αβ0, can be expressed as a sum of two components, p_o and $p_{\alpha\beta}$, where p_o represents the zero-sequence instantaneous power and $p_{\alpha\beta}$ represents the instantaneous active power in axes αβ:

$$p = p_o + p_{\alpha\beta} \tag{5.55}$$

$$p_o = v_o i_o \tag{5.56}$$

$$p_{\alpha\beta} = v_\alpha i_\alpha + v_\beta i_\beta \tag{5.57}$$

$$p = v_o i_o + v_\alpha i_\alpha + v_\beta i_\beta = v_a i_a + v_b i_b + v_c i_c \tag{5.58}$$

- The reactive instantaneous power, $q_{\alpha\beta}$: Akagi [37, 40, 41] defined a vector located on an axis perpendicular to the plane αβ, called instantaneous reactive power. The instantaneous reactive power is a measure of the amount of current or power flowing in each phase without transporting useful energy. It is defined as:

$$q = q_{\alpha\beta} = v_\alpha i_\beta - v_\beta i_\alpha = \frac{-1}{\sqrt{3}}\left[v_a(i_c - i_b) + v_b(i_a - i_c) + v_c(i_b - i_a)\right] \tag{5.59}$$

The set of above equations can be expressed in matrix form as:

$$\begin{bmatrix} p_{\alpha\beta} \\ q_{\alpha\beta} \\ p_o \end{bmatrix} = \begin{bmatrix} v_\alpha & v_\beta & 0 \\ -v_\beta & v_\alpha & 0 \\ 0 & 0 & v_o \end{bmatrix} \begin{bmatrix} i_\alpha \\ i_\beta \\ i_o \end{bmatrix} \tag{5.60}$$

In the case of nonlinear and/or unbalanced loads, the p_o, $p_{\alpha\beta}$ and $q_{\alpha\beta}$ powers have continuous and alternating components. The DC values ($\bar{p}_o$, $\bar{p}_{\alpha\beta}$, and $\bar{q}_{\alpha\beta}$) correspond to the average values of zero-sequence, active and reactive instantaneous power respectively, caused by the positive sequence components of voltages and currents of the load. The alternating components of the powers ($\tilde{p}_o$, $\tilde{p}_{\alpha\beta}$ and $\tilde{q}_{\alpha\beta}$) correspond to the contribution of harmonics and/or the presence of negative sequence components of voltages and current. This can be expressed as:

$$p = p_o + p_{\alpha\beta} = \left(\bar{p}_o + \bar{p}_{\alpha\beta}\right) + \left(\tilde{p}_o + \tilde{p}_{\alpha\beta}\right) = \bar{p} + \tilde{p} \tag{5.61}$$

$$q_{\alpha\beta} = \bar{q}_{\alpha\beta} + \tilde{q}_{\alpha\beta} \tag{5.62}$$

To determine the reference currents, it is assumed that the grid supplies the DC component of the instantaneous power ($\bar{p}$) plus the power required by the VSC ($\bar{p}_F$) and the Shunt APF supplies the remaining power to the load. The instantaneous power that the grid must give is, see Fig. 5.15:

$$p_g = \bar{p} + \bar{p}_F \tag{5.63}$$

Then the powers that VSC must supply to condition the load currents, and compensate the reactive power, correspond to the AC component of the instantaneous power, $\tilde{p}$, and all the reactive power $q_{\alpha\beta}$.

The VSC compensates power losses ($\bar{p}_F$) taking active power from the grid. The power losses presented by the VSC are compensated through using a PI regulator, which, when detects the discharges/charges of the DC capacitor, modifies its output value in order to retrieve the reference voltage of the capacitor (V_{DC}^*).

The currents, in the axes αβ0, depending on the powers and voltages, are:

$$\begin{bmatrix} i_\alpha \\ i_\beta \\ i_o \end{bmatrix} = \begin{bmatrix} v_\alpha & v_\beta & 0 \\ -v_\beta & v_\alpha & 0 \\ 0 & 0 & v_o \end{bmatrix}^{-1} \begin{bmatrix} p_{\alpha\beta} \\ q_{\alpha\beta} \\ p_o \end{bmatrix} = \frac{1}{(v_\alpha^2 + v_\beta^2)} \begin{bmatrix} v_\alpha & -v_\beta & 0 \\ v_\beta & v_\alpha & 0 \\ 0 & 0 & v_\alpha^2 + v_\beta^2 \end{bmatrix} \begin{bmatrix} p_{\alpha\beta} \\ q_{\alpha\beta} \\ p_o \end{bmatrix} \tag{5.64}$$

The currents, in the axes αβ0, are expressed as the sum of two components as

$$i_\alpha = i_{\alpha p} + i_{\alpha q} = \frac{v_\alpha}{v_\alpha^2 + v_\beta^2} p_{\alpha\beta} + \frac{-v_\beta}{v_\alpha^2 + v_\beta^2} q_{\alpha\beta} \tag{5.65}$$

$$i_\beta = i_{\beta p} + i_{\beta q} = \frac{v_\beta}{v_\alpha^2 + v_\beta^2} p_{\alpha\beta} + \frac{v_\alpha}{v_\alpha^2 + v_\beta^2} q_{\alpha\beta} \tag{5.66}$$

$$i_o = \frac{1}{v_o} p_o \tag{5.67}$$

So, the reference currents for compensation, according to the axes αβ0 that the VSC must inject, are:

$$\begin{bmatrix} i_{F\alpha}^* \\ i_{F\beta}^* \end{bmatrix} = \frac{1}{\left(v_{L\alpha}^2 + v_{L\beta}^2\right)} \begin{bmatrix} v_{L\alpha} & -v_{L\beta} \\ v_{L\beta} & v_{L\alpha} \end{bmatrix} \begin{bmatrix} \tilde{p} - \bar{p}_F \\ q_{\alpha\beta} \end{bmatrix} \tag{5.68}$$

$$i_{Fo}^* = \frac{p_o}{v_{L0}} \tag{5.69}$$

The values of the reference currents, in the abc three-phase system, are obtained by the inverse Clarke transformation:

$$\begin{bmatrix} i_{Fa}^* \\ i_{Fb}^* \\ i_{Fc}^* \end{bmatrix} = \sqrt{\frac{2}{3}} \begin{bmatrix} 1 & -\frac{1}{2} & -\frac{1}{2} \\ 0 & \frac{\sqrt{3}}{2} & -\frac{\sqrt{3}}{2} \\ \frac{1}{\sqrt{2}} & \frac{1}{\sqrt{2}} & \frac{1}{\sqrt{2}} \end{bmatrix}^{-1} \begin{bmatrix} i_{F\alpha}^* \\ i_{F\beta}^* \\ i_{Fo}^* \end{bmatrix} = \sqrt{\frac{2}{3}} \begin{bmatrix} 1 & 0 & \frac{1}{\sqrt{2}} \\ -\frac{1}{2} & \frac{\sqrt{3}}{2} & \frac{1}{\sqrt{2}} \\ -\frac{1}{2} & -\frac{\sqrt{3}}{2} & \frac{1}{\sqrt{2}} \end{bmatrix} \begin{bmatrix} i_{F\alpha}^* \\ i_{F\beta}^* \\ i_{Fo}^* \end{bmatrix} \tag{5.70}$$

In a three-phase system without neutral connected, as in Fig. 5.15, there is no homopolar current and, in this case, the compensation is reduced to the equations in axes αβ. So the currents that the Shunt APF must inject are:

$$\begin{bmatrix} i_{Fa}^* \\ i_{Fb}^* \\ i_{Fc}^* \end{bmatrix} = \sqrt{\frac{2}{3}} \begin{bmatrix} 1 & 0 \\ -\frac{1}{2} & \frac{\sqrt{3}}{2} \\ -\frac{1}{2} & -\frac{\sqrt{3}}{2} \end{bmatrix} \begin{bmatrix} i_{F\alpha}^* \\ i_{F\beta}^* \end{bmatrix} \tag{5.71}$$

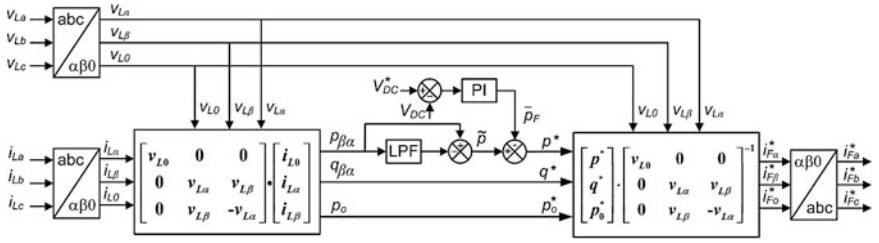

Fig. 5.16 Block diagram of system to generate the reference current based on Instantaneous power theory

When the voltages (v_{La}, v_{Lb}, v_{Lc}) in the grid are distorted, the currents calculated with the above equations do not compensate exactly for the harmonics currents, it being necessary to generate a system of balanced voltages rather than the directly measured ones. This can be done by a PLL tracking system.

Figure 5.16 shows the block diagram to generate the reference current based on Instantaneous Power Theory.

The alternating components can be obtained by filtering the components of the instantaneous active power and instantaneous reactive power. The calculation is done by a LPF whose cutoff frequency must be above the fundamental frequency of the network and below the frequency of the first harmonic filter to be compensated.

To compensate only the current harmonics, the instantaneous power reference are:

$$\begin{bmatrix} p^* \\ q^* \\ p_O^* \end{bmatrix} = \begin{bmatrix} \tilde{p} - \bar{p}_F \\ \tilde{p}_{\alpha\beta} \\ p_o \end{bmatrix} \tag{5.72}$$

If the reactive power compensation is also required, as shown in Fig. 5.16, the reference instantaneous powers are as shown in (5.68).

The results of this compensation method are good when the voltage at the PCC is balanced and it does not present any harmonic distortion. In the literature, there are solutions to eliminate the harmonic voltage distortion measure:

- The filtering of the grid voltage: These filters introduce delays in the voltage measurement, so it requires the application of estimation techniques.
- The use of PLL: One of the most commonly used techniques.

Another problem associated with the algorithm is the computation time required to transform current to power and vice versa.

An improvement of the previous algorithm is based on using the *Synchronous Reference System.* This method is based on the transformation of the three-phase system of currents into a system of moving axes dp0, then, the reference currents

are determined by filtering. The main feature of this method is that it allows the reference currents for compensation to be obtained directly without having to calculate the instantaneous power. The conversion between the conventional three-phase system, in abc axes, to the system of moving axes dq0, is done by the Park transformation.

$$\begin{bmatrix} x_d \\ x_q \\ x_o \end{bmatrix} = \sqrt{\frac{2}{3}} \begin{bmatrix} \cos\theta & \cos(\theta - \frac{2\pi}{3}) & \cos(\theta + \frac{2\pi}{3}) \\ -\text{sen}\theta & -\text{sen}(\theta - \frac{2\pi}{3}) & -\text{sen}(\theta + \frac{2\pi}{3}) \\ \frac{1}{\sqrt{2}} & \frac{1}{\sqrt{2}} & \frac{1}{\sqrt{2}} \end{bmatrix} \begin{bmatrix} x_a \\ x_b \\ x_c \end{bmatrix} \tag{5.73}$$

The Park transformation provides expressions for the real, reactive and zero-sequence instantaneous power:

$$p = v_d i_d + v_q i_q = p_{\alpha\beta} + p_0 \tag{5.74}$$

$$q = v_q i_d - v_d i_q = q_{\alpha\beta} \tag{5.75}$$

$$p_o = v_o i_o \tag{5.76}$$

The Park transform converts the three-phase electrical system (abc axes) to a system of moving dq0 axes, whose position in time is determined by θ. If the moving dq0 axes system is synchronized with the reference voltage signal, the reference current components can be discriminated. The synchronization process is to adjust the axis d of the mobile coordinate system to the load voltage, rotating at the fundamental frequency and with the corresponding direction of rotation to the positive sequence voltages. The three-phase system is considerably simplified, since the current components that rotate at the same speed and with the same sense of rotation as the dq0 axes in motion, will be perceived as constant values. All the other components, including harmonic and fundamental reverse components, appear as alternating values, which facilitates their discrimination by filtering. This can be expressed as:

$$i_d = \bar{i}_d + \tilde{i}_d \tag{5.77}$$

$$i_q = \bar{i}_q + \tilde{i}_q \tag{5.78}$$

$$i_o = \tilde{i}_o \tag{5.79}$$

The DC terms of the current represent the fundamental and balanced component of direct sequence in a three-phase system. The alternating components contain the other phenomena, i.e. harmonics and unbalances of the currents in the abc phase system.

To determine the compensation currents, it is assumed that the grid which provides the DC component along the axis d ($\bar{i}_d$), plus the VSC losses current ($\bar{i}_F$)

and the compensation system, will supply the remaining load currents, as seen in Fig. 5.15. The determination of the VSC losses current ($\bar{i}_F$) is performed by monitoring the voltage V_{DC}, as is done in the method of instantaneous power, with the difference that in this method, the voltage error involves current losses instead of power losses. The reference currents, in the dq0 axes, to be injected by the VSC, are:

$$\begin{bmatrix} i_{Fd}^* \\ i_{Fq}^* \\ i_{F0}^* \end{bmatrix} = \begin{bmatrix} \tilde{i}_{Ld} - \bar{i}_F \\ i_{Lq} \\ i_{Lo} \end{bmatrix} \tag{5.80}$$

From the above equation, using the inverse Park transform, the reference currents, in the abc axes, are obtained:

$$\begin{bmatrix} i_{Fa}^* \\ i_{Fb}^* \\ i_{Fc}^* \end{bmatrix} = \sqrt{\frac{2}{3}} \cdot \begin{bmatrix} \cos\theta & -\text{sen}\theta & \frac{1}{\sqrt{2}} \\ \cos(\theta - \frac{2\pi}{3}) & -\text{sen}(\theta - \frac{2\pi}{3}) & \frac{1}{\sqrt{2}} \\ \cos(\theta + \frac{2\pi}{3}) & -\text{sen}(\theta + \frac{2\pi}{3}) & \frac{1}{\sqrt{2}} \end{bmatrix} \cdot \begin{bmatrix} i_{Fd}^* \\ i_{Fq}^* \\ i_{F0}^* \end{bmatrix} \tag{5.81}$$

Figure 5.17 shows the block diagram to generate the reference currents based on the Synchronous Reference System. It is worth noting that the main characteristic of this method is that the reference currents are calculated by using the Park transform in a synchronous system with the fundamental component of the load voltage.

The synchronization system for tracking the fundamental frequency of the AC voltage may be a PLL-type tracking system.

In Fig. 5.18, the waveforms of STATCOM are shown as Shunt APF. Initially, the applied load is a nonlinear balanced one, the Shunt APF not acting until $t = 0.06$ s. At $t = 0.12$ s, a nonlinear unbalanced load is added.

The Matlab simulation shows that STATCOM can reduce the harmonic distortion of currents caused by nonlinear loads.

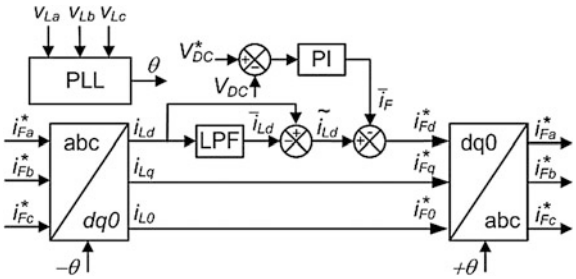

Fig. 5.17 Block diagram to generate the reference current using a synchronous reference system

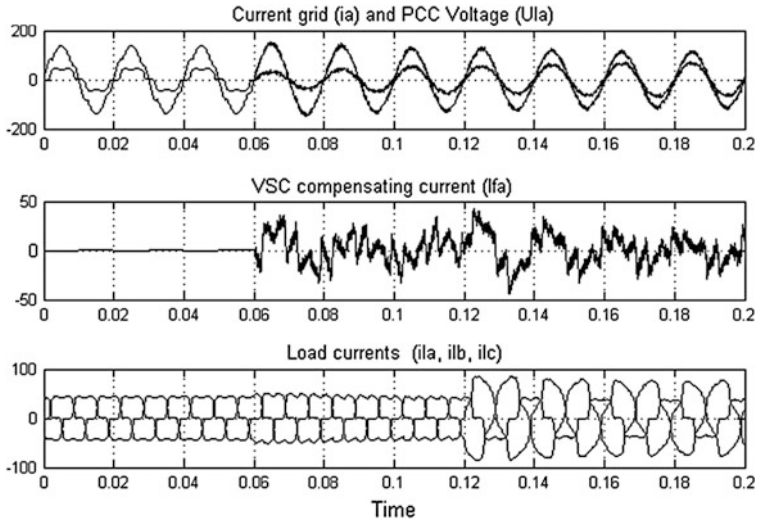

Fig. 5.18 Waveforms of STATCOM as shunt APF

5.7 The Unbalanced Case

5.7.1 Grid Voltage Decomposition into Symmetrical Components

It is well known that an unbalanced system of voltages or electric currents can be broken down into its symmetrical components, named positive component, negative component and zero component.

In the particular case of the STATCOM applications, the electrical grid to which they are connected, are three wire systems because the neutral wire is not connected. Under this condition, the zero component does not exist and the Delayed Signal Cancellation (DSC) algorithm, designed for sampled systems, is applicable to get the other two components using a Digital Signal Processor (DSP) or microcontroller (MCU), Fig. 5.19 [42–44].

The DSC algorithm is based on measuring the three-phase voltages to be decomposed into their symmetrical components (or at least two of them, and getting the third one using the relation $\sum_1^3 v_i$, valid for balanced and unbalanced systems). Next, the measured voltages are referred to a static reference frame, $\alpha\beta$, using the Clarke transformation:

$$\begin{bmatrix} V_\alpha \\ V_\beta \end{bmatrix} = \begin{bmatrix} 1 & 0 & 0 \\ 0 & \frac{\sqrt{3}}{3} & -\frac{\sqrt{3}}{3} \end{bmatrix} \cdot \begin{bmatrix} v_a \\ v_b \\ v_c \end{bmatrix} \tag{5.82}$$

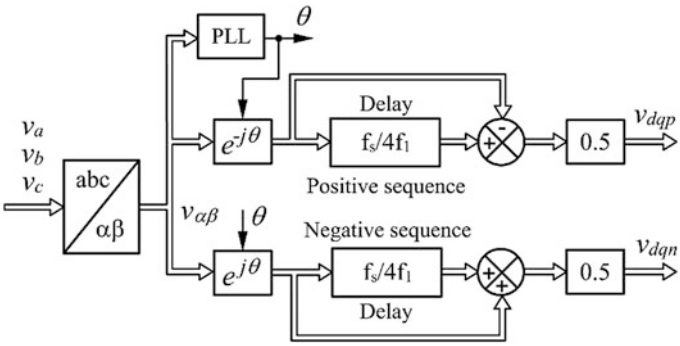

Fig. 5.19 Block diagram of the DSC algorithm

Taking into account that this algorithm is programmed within a sampled system, this operation, and the following, must be carried out on every program cycle once the ADC converters have stored the sampled values in the registers of the DSP.

The next step is to carry out two opposite rotations using the angle of the grid voltage phasor, measured in relation with the resulting static reference frame, θ and $-\theta$, for the positive component:

$$\begin{bmatrix} V_{dp} \\ V_{qp} \end{bmatrix} = \begin{bmatrix} \cos\theta & \sin\theta \\ -\sin\theta & \cos\theta \end{bmatrix} \cdot \begin{bmatrix} V_{\alpha} \\ V_{\beta} \end{bmatrix} \tag{5.83}$$

and for the negative component:

$$\begin{bmatrix} V_{dn} \\ V_{qn} \end{bmatrix} = \begin{bmatrix} \cos\theta & -\sin\theta \\ \sin\theta & \cos\theta \end{bmatrix} \cdot \begin{bmatrix} V_{\alpha} \\ V_{\beta} \end{bmatrix} \tag{5.84}$$

where the PLL algorithm provides the angle used in both transformations.

Then, the obtained dqp and the dqn sample values are successively stored in two independent data buffers for half a period.

Finally, once half a period has been stored in the dqp, dqn samples, and the respective samples stored in the buffers are added to get the final samples for the positive and negative components:

For the positive component:

$$V_{dp}(k) = \frac{1}{2} \cdot \left[v_{dp}(k) + j v_{dp}\left(k - \frac{f_s}{4 \cdot f_g} \right) \right] \tag{5.85}$$

$$V_{qp}(k) = \frac{1}{2} \cdot \left[v_{qp}(k) + j\, v_{qp}\left(k - \frac{f_s}{4 \cdot f_g} \right) \right] \tag{5.86}$$

and for the negative:

$$V_{dn}(k) = \frac{1}{2} \cdot \left[v_{dn}(k) + j\, v_{dn}\left(k - \frac{f_s}{4 \cdot f_g} \right) \right] \tag{5.87}$$

$$V_{qn}(k) = \frac{1}{2} \cdot \left[v_{qn}(k) + j\, v_{qn}\left(k - \frac{f_s}{4 \cdot f_g} \right) \right] \tag{5.88}$$

where f_s is the sampling frequency and f_g is the frequency of the grid voltage. The j term in the previous expressions just means that the samples in the second term are the same as in the first but shifted one-fourth of the period.

Note that the main drawback of this algorithm is related to the elapsed time used to store half a period of the electrical magnitude to be decomposed and the transient period that it introduces. As can be seen in Fig. 5.20, once the grid disturbance takes place, it is necessary to wait for half a period until the DSC algorithm is able to provide the actual values of the symmetrical components.

In some applications, such as unbalanced voltage disturbances in the PCC of renewable energy power plants, STATCOMs are used to collaborate in restoring the positive component and reducing the negative component of the grid voltage by delivering reactive power to the grid and to comply with the grid code.

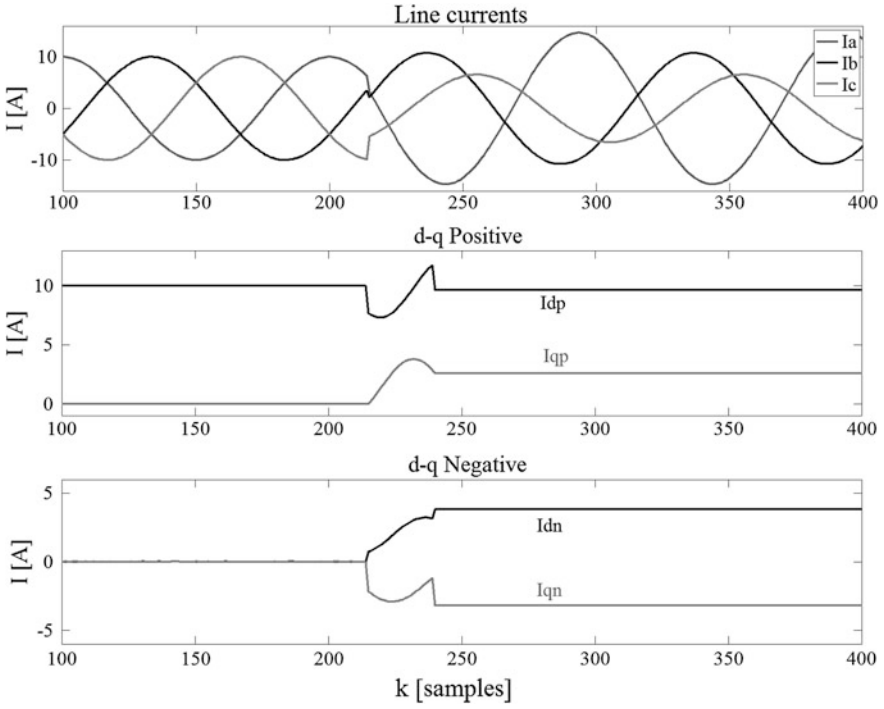

Fig. 5.20 Simulation of the DSC algorithm carried out in Matlab

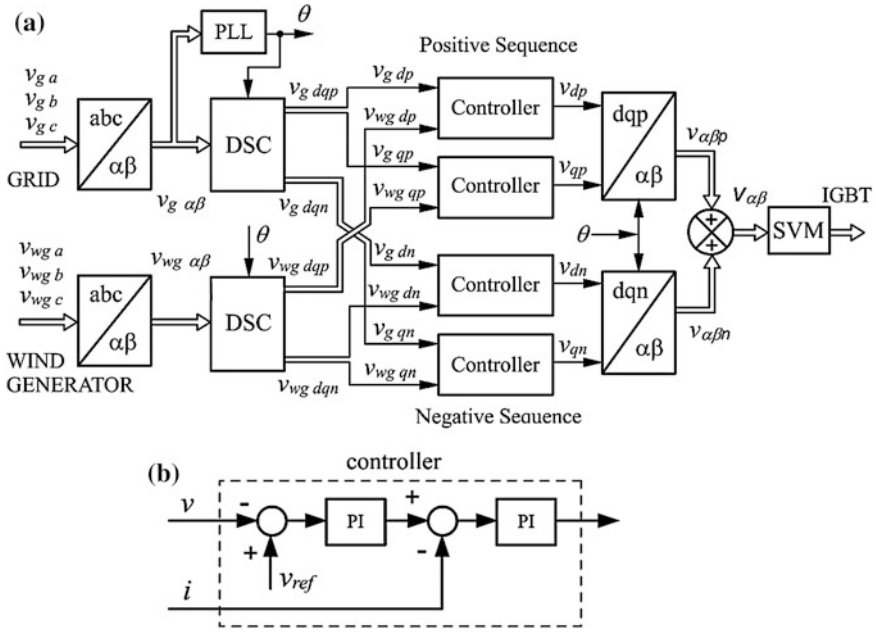

Fig. 5.21 **a** Control block of STATCOMs used to deliver reactive power during electrical disturbances in the grid. **b** Basic control block

The control system monitors the module of the grid voltage phasor and, when a fault is detected, the STATCOM has to start delivering reactive power to the grid in such an amount that the grid code corresponding to the country is complied with.

As is shown in Fig. 5.21a, in such cases, it is necessary to decompose the voltages at the PCC into their component networks, as well as the electric current delivered by the STATCOM, and reproduce the controller block of Fig. 5.21b, once for each axis, d and q, and each component, p and n, with a total of eight PI regulators.

5.7.2 *Calculation of the Power Delivered to the Electrical Grid*

Active and reactive powers delivered to the grid are the variables to be controlled by the control system of the STATCOM. Under unbalanced conditions, these powers can be calculated as the sum of those corresponding to each one of the network sequences into which the system can be decomposed:

$$S = \vec{V}_a \cdot \vec{I}_a + \vec{V}_b \cdot \vec{I}_b + V_c \cdot \vec{I}_c = 3\vec{V}_{a0} \cdot \vec{I}^*_{a0} + 3\vec{V}_{a1} \cdot \vec{I}^*_{a1} + 3\vec{V}_{a2} \cdot \vec{I}^*_{a2} \qquad (5.89)$$

As aforementioned, there is no neutral wire in the connections of STATCOMs to the grid and, therefore, no zero component exists in the corresponding sequence networks. In such cases, active power can be calculated separately (using space vector notation):

$$P = P_p + P_n = \frac{3}{2}(U_{dp}I_{dp} + U_{qp}I_{qp}) + \frac{3}{2}(U_{dn}I_{dn} + U_{qn}I_{qn}) \tag{5.90}$$

and likewise, the reactive power:

$$Q = Q_p + Q_n = \frac{3}{2}(U_{dp}I_{qp} + U_{qp}I_{dp}) + \frac{3}{2}\cdot(U_{dn}I_{qn} + U_{qn}I_{dn}) \tag{5.91}$$

5.8 DC Voltage Determination

By representing the phasor diagram corresponding to the electrical equation of the grid connected inverter:

$$\vec{V}_{conv} = \vec{V}_{grid} + jX\vec{I} \tag{5.92}$$

and then, multiplying it by $3\frac{V_{grid}}{X}$, a proportional diagram is obtained, now in terms of electric power:

$$P^2 + \left(Q + 3\frac{V_{grid}^2}{X}\right)^2 = \left(3\cdot\frac{V_{grid}V_{conv}}{X}\right)^2 \tag{5.93}$$

It is very important to note that one of the projections on the direct axis represents the reactive power delivered to the grid and the other, on the quadrature axis, represents the active power, Fig. 5.22.

In order to work with voltages and the power in the same diagram, it is possible to proportionally graduate the vertical and horizontal axes to the active and reactive powers respectively.

As is known, the maximum voltage generated by the inverter is directly related with the DC voltage value. Therefore, for each DC voltage, the operating points reachable by the inverter describe concentric circumferences. On the other hand, the maximum active power to be delivered to the grid determines the vertical coordinate in the intersection with the vertical axis, graduated as k.*P*, see Fig. 5.23. The point determined in this way on the vertical axis provides the DC voltage necessary to generate a given active power [45].

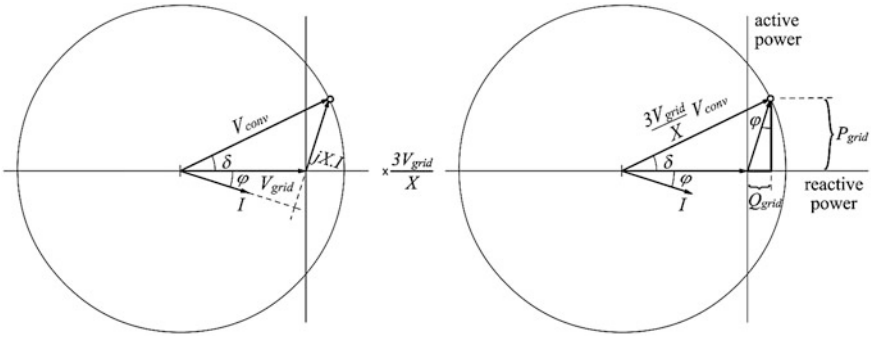

Fig. 5.22 Diagram of voltages and diagram of powers

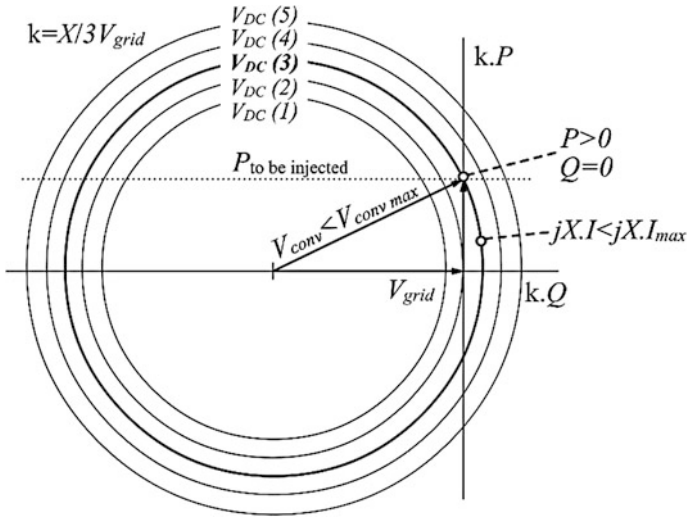

Fig. 5.23 Diagram for several DC voltage values

Nevertheless, at this working point, the reactive power seen from the grid is null (although not from the inverter, since it generates the needed reactive power to the coupling reactance, X).

At this point, it is necessary to take into account the restriction related to the rated voltage for the semiconductors, but also the rated electrical current of the semiconductors.

At the aforementioned working point, there is no projection on the direct axis related to reactive power but, if the V_{DC} voltage increases, keeping the vertical coordinate constant, this projection works out and the inverter would now be able to deliver the same active power as before, but it would also be capable of delivering

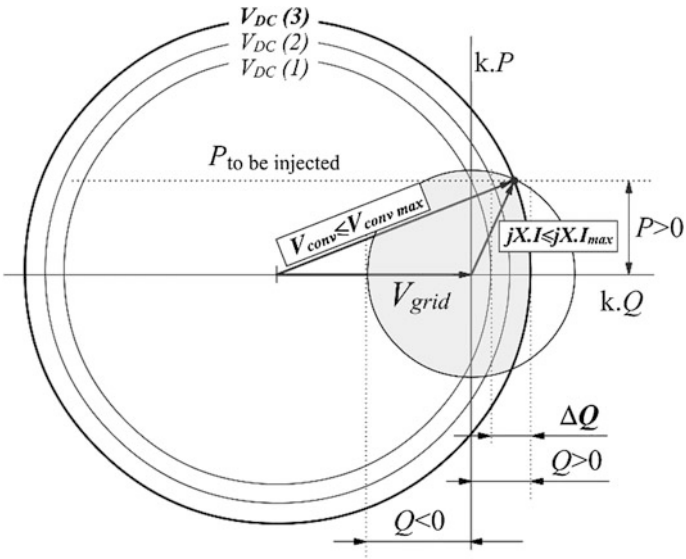

Fig. 5.24 Diagram with P and Q delivered to grid

reactive power, Fig. 5.24. The limit to this power is related with the module of the voltage in the reactance, *X.I*, actually directly related to the rated current.

Therefore, the DC voltage is determined by choosing the active power to be delivered (over the vertical axis) and the reactive power (over the horizontal axis).

The reachable working points are limited by two restrictions: the maximum radius of one of the circumferences is limited by the DC rated voltage of the semiconductors in the inverter, and the radius of the other circumference is limited by the rated current of the semiconductors. The combination of both areas provides the operating area of the inverter.

In the case in which a step-up transformer is used to couple the VSC to the electrical grid, the voltage seen from the inverter, V_{grid}, is lower, so the intersection area between the two circles changes and the operation area increases. In consequence, for the same DC voltage, the maximum active and reactive powers also increase, since the PQ diagram changes with the new $3\frac{V_{grid}}{X}$ factor; whereas the maximum V_{conv} for a given DC voltage, and the related circumference radius, remains constant, Fig. 5.25.

The above reasoning for the determination of the DC bus voltage is still valid considering the new value of V_{grid} seen by the VSC, but now the V_{grid} phasor is shorter and the axis scales change.

On the other hand, if the diagram is now multiplied by $\frac{2}{3V_{grid}}$

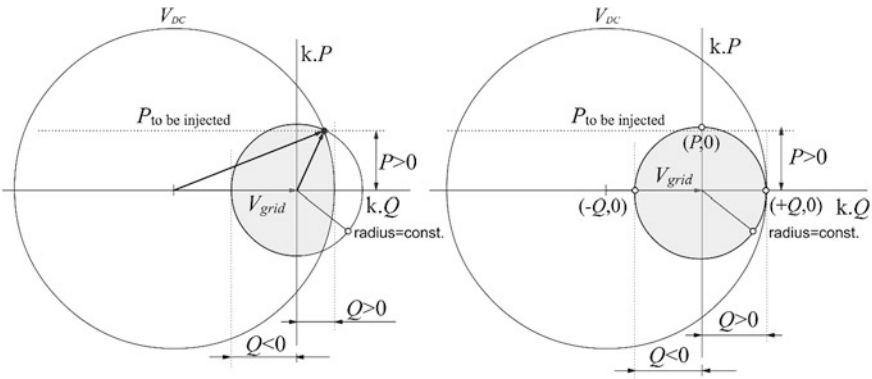

Fig. 5.25 Diagram for the determination of the DC voltage when a step-up transformer is used

$$P^2 + \left(Q + 3\frac{V_{conv}^2}{X}\right) = \left(\frac{3 \cdot V_{grid} V_{conv}}{X}\right)^2 \tag{5.94}$$

then a diagram with the dq currents as coordinates is obtained:

$$I_d^2 + \left(I_q + 2\frac{V_d}{X}\right)^2 = \left(2\frac{V_{conv}}{X}\right)^2 \tag{5.95}$$

This new diagram is very important because it gives the relation for the I_d, I_q currents that are to be delivered to the grid. For instance, the same current in module can be generated with different combinations of active and reactive components and also, for a given rated current, it can be generated giving preference to the reactive power (more usual in STATCOMs) or to the active current.

The study of the electrical diagrams has allowed to choose the necessary DC voltage to generate a certain amount of active and reactive power and establish a mathematical relation between the active and reactive components of the current space vector in order to distribute the rated current value between this two components depending on the application.

References

1. Bongiorno M, Svensson J (2007) Voltage dip mitigation using shunt-connected voltage source converter. IEEE Trans Power Electron 22(5):1867–1874
2. Bollen MHJ (2000) Understanding power quality problems—voltage sags and interruptions. IEEE Press, New York
3. Dixon J, Morán L, Rodríguez J, Domke R (2005) Reactive power compensation technologies: state-of-the-art review. Proc IEEE 93(12):2144–2164

4. National Grid Electricity Transmission plc (2006) The grid code, issue 3, revision 16, Warwick
5. Secretaria General de Energia (2006) Procedimiento de Operacion 12.3. Requisitos de respuesta frente a huecos de tension de las instalaciones eolicas. BOE no. 254—24th Oct 2006 [in Spanish]
6. EirGrid (2007) Grid code, version 2.0
7. Molinas M, Suul JA, Undeland T (2008) Low voltage ride through of wind farms with cage generators: STATCOM versus SVC. IEEE Trans Power Electron 23(3):1104–1117
8. Han C, Huang AQ, Baran ME, Bhattacharya S, Litzenberger W, Anderson L, Johnson AL, Edris A (2008) STATCOM impact study on the integration of a large wind farm into a weak loop power system. IEEE Trans Energy Convers 23(1):226–233
9. Ramirez D, Martinez S, Blazquez F, Carrero C (2012) Use of STATCOM in wind farms with fixed-speed generators for grid code compliance. Renew Energy 37(1):202–212
10. Lahaçani NA, Aouzellag D, Mendil B (2010) Static compensator for maintaining voltage stability of wind farm integration to a distribution network. Renew Energy 35(11):2476–2482
11. Leonhard W (2001) Control of electrical drives. Springer, New York
12. Pablo S, Rey-Boue AB, Herrero LC, Martinez F (2010) Hexagon based algorithm for space vector modulation on multilevel voltage source inverters. In: Proceedings of the international symposium on industrial electronics (ISIE). IEEE, Bari, Italy
13. Celanovic N, Boroyevich D (2001) A fast space-vector modulation algorithm for multilevel three-phase converters. IEEE Trans Ind Appl 37(2):637–641
14. Arruda LN, Silva SM, Filho BJC (2001) PLL structures for utility connected systems. In: Proceedings of the industry applications conference. IEEE, Chicago
15. Kantaria RA, Joshi SK, Siddhapura KR (2011) Novel hysteresis control technique of VSI based STATCOM. In: Proceedings of the India international conference on power electronics (IICPE). IEEE, New Delhi
16. Dinesh L, Sesham H, Manoj V (2012) Simulation of D-Statcom with hysteresis current controller for harmonic reduction. In: Proceedings of the international conference on emerging trends in electrical engineering and energy management (ICETEEEM). IEEE, Chennai
17. Gupta R, Ghosh A, Joshi A (2006) Cascaded multilevel control of DSTATCOM using multiband hysteresis modulation. In: Proceedings of the IEEE Power Engineering Society General Meeting. IEEE, Montreal
18. Gupta R, Ghosh A (2006) Frequency-domain characterization of sliding mode control of an inverter used in DSTATCOM application. IEEE Trans Circ Syst 53(3):662–676
19. Shukla A, Ghosh A, Joshi A (2005) A hysteresis current controlled flying capacitor multilevel inverter based DSTATCOM. In: Proceedings of the IEEE Power Engineering Society General Meeting. IEEE
20. Kazmierkowski MP, Malesani L (1998) Current control techniques for three-phase voltage-source PWM converters: a survey. IEEE Trans Ind Electron 45(5):691–703
21. Hingorani NG, Gyugyi L (2000) Understanding FACTS: concepts and technology of flexible AC transmission systems. Wiley-IEEE Press, New York
22. Peng FZ, Akagi H, Nabae A (1990) A new approach to harmonic compensation in power systems—a combined system of shunt passive and series active filters. IEEE Trans Ind Appl 26(6):983–990
23. Dugan RC, McGranaghan MF, Beaty HW (1996) Electrical power systems quality. McGraw-Hill, New York
24. Ho JM, Liu CC (2001) The effects of harmonics on differential relay for a transformer. In: Proceedings of the international conference and exhibition on electricity distribution. IEEE, Amsterdam
25. Izhar M, Hadzer CM, Syafrudin M, Taib S, Idris S (2004) Performance for passive and active power filter in reducing harmonics in the distribution system. In: Proceedings of the IEEE power and energy conference (PECon). IEEE
26. Zhang S, Dai K, Xie B, Kang Y (2010) Parallel control of shunt active power filters in capacity proportion frequency allocation mode. J Power Electron 10(4):419–427

27. Yuan X, Merk W, Stemmler H, Allmeling J (2002) Stationary-frame generalized integrators for current control of active power filters with zero steady-state error for current harmonics of concern under unbalanced and distorted operating conditions. IEEE Trans Ind Appl 38 (2):523–532
28. Ng CH, Ran L, Putrus GA, Busawon K (2003) A new approach to real time individual harmonic extraction. In: Proceedings of the power electronics and drive systems conference. IEEE
29. Lascu C, Asiminoaei L, Boldea I, Blaabjerg F (2007) High performance current controller for selective harmonic compensation in active power filters. IEEE Trans Power Electron 22 (5):1826–1835
30. Mattavelli P (2001) A closed-loop selective harmonic compensation for active filters. IEEE Trans Ind Appl 37(1):81–89
31. Muñoz JA, Espinoza JR, Baier CR, Moran LA, Guzman JI, Cardenas VM (2014) Decoupled and modular harmonic compensation for multilevel STATCOMs. IEEE Trans Ind Electron 61 (6):2743–2753
32. Dai NY, Wong MC (2011) Design considerations of coupling inductance for active power filters. In: Proceedings of the IEEE conference on industrial electronics and applications (ICIEA). IEEE, Beijing
33. Buso S, Malesani L, Mattavelli P (1998) Comparison of current control techniques for active filter applications. IEEE Trans Ind Electron 45(5):722–729
34. Kazmierkowski MP, Dzieniakowski MA (1994) Review of current regulation techniques for three-phase PWM inverters. In: Proceedings of the IEEE international conference on industrial electronics, control and instrumentation (IECON). IEEE, Bologna
35. Petit JF, Amarıs H, Robles G (2005) Control schemes for shunt active filters to mitigate harmonics injected by inverted-fed motors. Paper presented at the 15th power systems computation conference (PSCC), Liege, Belgium, 22–26 Aug 2005
36. Massoud AM, Finney SJ, Williams BW (2004) Review of harmonic current extraction techniques for an active power filter. In: Proceedings of the IEEE international conference on harmonics and quality of power. IEEE
37. Akagi H, Kanazawa Y, Nabae A (1984) Instantaneous reactive power compensators comprising switching devices without energy storage components. IEEE Trans Ind Appl 20 (3):625–630
38. Sonnenschein M, Weinhold M (1999) Comparison of time-domain and frequency-domain control schemes for shunt active filters. Eur Trans Electr Power 9(1):5–16
39. Valouch V (1999) Active filter control methods based on different power theories. In: Proceedings of the IEEE international symposium on industrial electronics (ISIE). IEEE, Bled
40. Akagi H, Watanabe EH, Aredes M (2007) Instantaneous power theory and applications to power conditioning. Wiley-IEEE Press, New York
41. Akagi H, Nabae A (1993) The p-q theory in three-phase systems under non-sinusoidal conditions. Eur Trans Electr Power 3(1):27–31
42. Bollen MHJ (2003) Algorithms for characterizing measured three-phase unbalanced voltage dips. IEEE Trans Power Deliv 18(3):937–944
43. Svensson J, Bongiorno M, Sannino A (2007) Practical implementation of delayed signal cancellation method. IEEE Trans Power Deliv 22(1):18–26
44. Paap GC (2000) Symmetrical components in the time domain and their application to power network calculations. IEEE Trans Power Syst 15(2):522–528
45. Chinchilla M, Arnalte S, Burgos JC, Rodriguez JL (2005) Power limits of wind energy systems. Renew Energy 31(9):1455–1470

Chapter 6
Robust Nonlinear Control of STATCOMs

Yonghao Gui, Chunghun Kim, Youngseong Han and Chung Choo Chung

Abstract Many nonlinear control techniques for STATCOM systems are available nowadays. In this chapter several nonlinear feedback controller design techniques relatively simpler and more robust are to be introduced: input–output feedback linearization (IOL) method, passivity-based control (PBC) method, port-controlled Hamiltonian (PCH) method with dynamics extension method. The IOL method has been applied to STATCOM and it shows uniform transient performance. However, the oscillatory response owing to the lightly damped internal dynamics could negatively affect the life cycle of the system and power quality. A modified IOL control scheme is introduced to improve the damping of internal dynamics of performance while preserving overall system stability. Although the IOL methods improve the performance of type 2 STATCOM systems, these methods are sensitive to parameter uncertainty. Moreover, when the system is working in the inductive operating range, undesired oscillatory transient response appears in the DC voltage due to its lightly damped internal dynamics with the IOL method. The PBC method considers the dynamics characteristics of type 2 STATCOM systems, in particular its passive characteristics. Employing the PBC method improves the robustness of controller implementation and simplifies implementation compared to the IOL method in such a way that it avoids canceling the system

Y. Gui · C. Kim
Department of Electrical Engineering, Hanyang University, Seoul, Republic of Korea
e-mail: yonghao26@hanyang.ac.kr

C. Kim
e-mail: freidee@hanyang.ac.kr

Y. Han
Power and Industrial Systems, R&D Center, Hyosung Co., Gyeonggi-Do, Republic of Korea
e-mail: yshan@hyosung.com

C.C. Chung (✉)
Division of Electrical and Biomedical Engineering, Hanyang University, Seoul, Republic of Korea
e-mail: cchung@hanyang.ac.kr

F. Shahnia et al. (eds.), *Static Compensators (STATCOMs) in Power Systems*, Power Systems, DOI 10.1007/978-981-287-281-4_6

nonlinearities exactly. However, since the previous methods are designed based on an approximated model of type 2 STATCOM systems, the closed-loop system has a locally stable equilibrium point. Moreover, the stability region is numerically extensively determined. To overcome the aforementioned problem, PCH with the dynamics extension method is developed for a robust and simple structure of nonlinear controller with the non-approximated model of STATCOM systems in order to improve the performance in time domain and enlarge the stability region.

Keywords STATCOM · Nonlinear feedback controller · Input–output feedback linearization · Passivity-based control · Port-controlled Hamiltonian

6.1 Introduction

A STATCOM based on a voltage source converter (VSC) can enhance controllability and increase the power transfer capability of a network by injecting or absorbing reactive power [1]. There are two types of STATCOM systems with respect to the number of control degrees [2]. A STATCOM with two degrees of control for full vector control is a type 1. Type 1 STATCOMs operate under active and reactive power tracking control modes by using a converter with pulse-width modulation technology. Type 2 STATCOMs have only one degree of control, the phase angle, so the system operates under reactive power tracking by using a converter that employs multi-pulse technology. Compared to type 1 STATCOMs, type 2 STATCOMs have simpler structure and are more cost-effective from both manufacturing and operational cost perspectives [3].

In this chapter, several nonlinear feedback controller design techniques for type 2 STATCOMs are explored: input–output feedback linearization (IOL) method, passivity-based control (PBC) method, port-controlled Hamiltonian (PCH) method with dynamics extension method. The IOL method is an efficient method for handling trajectory tracking problems in nonlinear systems. The closed loop of the feedback linearized system has linear input–output behavior resulting in asymptotic tracking performance with a linear controller. In the IOL system, even though the stability and the tracking performance of the output are guaranteed because of an output feedback controller, those of the internal dynamics are not guaranteed [4, 5]. For the STATCOM system, Petitclair et al. designed an IOL controller in [6] and later added a damping term to the input in order to bring the improved stability and transient performance of the internal dynamics [7]. However, it cannot guarantee the system to be internally stable at every operating point with the constant gain of damping term. A modified IOL control scheme was developed to improve the damping of internal dynamics at the cost of output tracking performance while preserving overall system stability in [8]. Although those IOL methods improved the performance of type 2 STATCOM systems, these methods are sensitive to parameter uncertainty. Moreover, when the system is working in the inductive

operating range, undesired oscillatory transient responses appear in the active current and DC voltage since the system has lightly damped internal dynamics while using the IOL method [9]. To compare with the IOL method, the PBC method considers the dynamics characteristics of type 2 STATCOM systems, in particular its passive characteristics. Passivity is a restatement of energy conservation in physical systems, and plays a central role in control techniques [10, 11]. Employing passivity control improves the robustness of controller implementation and simplifies implementation compared to the IOL method, since it avoids canceling the system nonlinearities exactly [12]. A PBC with nonlinear damping (PBCND) to control the reactive current and to improve the performance of the active current and DC voltage for type 2 STATCOMs was developed [13]. This enables fast convergence of errors to zero and reduction of oscillations of the active current and DC voltage. However, since the previous methods were designed based on an approximated model of type 2 STATCOM systems, they only guarantee that the closed-loop system has a locally stable equilibrium point. Moreover, the stability region is numerically extensively determined. The PCH with dynamics extension method was developed for a robust and simple structure of nonlinear controller via the non-approximated model of STATCOM systems in order to improve the performance in time domain and enlarge the stability region [14].

6.2 STATCOM Mathematical Model

In this section, at first, the averaged model of STATCOM is discussed. Figure 6.1a illustrates the equivalent circuit of STATCOM system. The series resistances R_s's describe the converter and transformer conduction losses which are in series with AC lines. The inductances L's denote the leakage of actual power transformer and resistance R_p is switching loss which is shunt with the capacitor. Phase to neutral bus voltage and voltage at the STATCOM AC-side terminals are denoted as $V_{a,b,c}$ and $e_{a,b,c}$ respectively. The circuit equation of AC-side could be as,

$$\begin{bmatrix} \frac{dI'_a}{dt} \\ \frac{dI'_b}{dt} \\ \frac{dI'_c}{dt} \end{bmatrix} = \begin{bmatrix} -\frac{R'_s\omega_b}{L'} & 0 & 0 \\ 0 & -\frac{R'_s\omega_b}{L'} & 0 \\ 0 & 0 & -\frac{R'_s\omega_b}{L'} \end{bmatrix} \begin{bmatrix} I'_a \\ I'_b \\ I'_c \end{bmatrix} + \frac{\omega_b}{L'} \begin{bmatrix} e'_a - V'_a \\ e'_b - V'_b \\ e'_c - V'_c \end{bmatrix}, \tag{6.1}$$

where $I_{(a,b,c)}$ and ω_b are three-phase current and angular velocity at nominal frequency. The parameters and state variables are defined as per-unit value which are denoted as:

$$\begin{aligned} L' &= \frac{\omega_b L}{z_{base}}, \quad C' = \frac{1}{\omega_b C z_{base}}, \quad R'_s = \frac{R_s}{z_{base}}, \quad R'_p = \frac{R_p}{z_{base}}, \\ I'_{(a,b,c)} &= \frac{i_{(a,b,c)}}{I_{base}}, \quad V'_{(a,b,c)} = \frac{V_{(a,b,c)}}{V_{base}}, \quad e'_{(a,b,c)} = \frac{e_{(a,b,c)}}{V_{base}}, \quad z_{base} = \frac{V_{base}}{I_{base}}. \end{aligned} \tag{6.2}$$

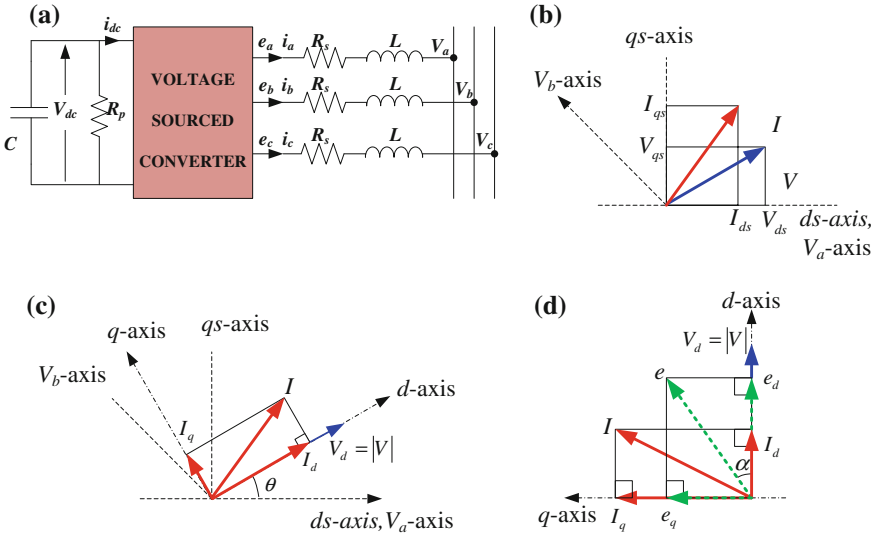

Fig. 6.1 **a** Equivalent circuit of STATCOM. **b** Definition of stationary reference frame. **c** Definition of rotating reference frame. **d** Vectors in synchronous frame

Figure 6.1b illustrates the definition of a stationary orthogonal coordinate frame [9]. Each vector is divided into two quadrature parts which are *ds* and *qs* where *ds*-axis points out the same direction as *a*-axis which is defined by transmission line voltage V_a while *qs*-axis is in quadrature with it. Figure 6.1c describes definition of rotating frame. *d*-axis points out the same direction as *V* and *q*-axis is in quadrature with it. θ is an angle which *d*-axis leads the V_a axis in the direction of rotation and ω is a fundamental frequency of voltage signal which is defined as $\omega = d\theta/dt$. AC-side vectors in rotating frame are illustrated in Fig. 6.1d. The STATCOM is in inductive mode absorbing the reactive power when I_q is positive. On the other hand, negative value of I_q means capacitive mode where the reactive power is supplied from it. The control command, α of the type 2 STATCOM is defined as the phase angle between the STATCOM voltage, *e*, and bus voltage $|V|$. The transformation from phase variables into *d, q* variables could be defined as

$$\begin{bmatrix} I_d \\ I_q \end{bmatrix} = \mathbf{T}_{\mathbf{cor}} \begin{bmatrix} I_a \\ I_b \\ I_c \end{bmatrix}, \tag{6.3}$$

where

$$\mathbf{T}_{\mathbf{cor}} = \frac{2}{3} \begin{bmatrix} \cos \omega t & \cos\left(\omega t - \frac{2\pi}{3}\right) & \cos\left(\omega t + \frac{2\pi}{3}\right) \\ -\sin(\omega t) & -\sin\left(\omega t - \frac{2\pi}{3}\right) & -\sin\left(\omega t + \frac{2\pi}{3}\right) \end{bmatrix}.$$

Here, I_d and I_q denote the active and reactive currents, respectively. Thus, (6.1) can be transformed to the synchronous rotating reference frame as follows:

$$\begin{bmatrix} \frac{dI'_d}{dt} \\ \frac{dI'_q}{dt} \end{bmatrix} = \begin{bmatrix} -\frac{R'_s\omega_b}{L'} & \omega \\ -\omega & -\frac{R'_s\omega_b}{L'} \end{bmatrix} \begin{bmatrix} I'_d \\ I'_q \end{bmatrix} + \frac{\omega_b}{L'} \begin{bmatrix} e'_d - |V'| \\ e'_q \end{bmatrix}. \tag{6.4}$$

The voltage harmonics produced by the inverter are neglected for the simple analysis. Thus, the STATCOM voltages of e'_d and e'_q are described as

$$\begin{aligned} e'_d &= kV'_{dc}\cos\alpha, \\ e'_q &= kV'_{dc}\sin\alpha, \end{aligned} \tag{6.5}$$

where V'_{dc} is the DC voltage. There are two types of STATCOM controllers. Type 1 STATCOM controller uses both the phase angle of voltage term, α, and the factor, k, which relates the DC voltage to the peak voltage on the AC side. On the other hand, type 2 STATCOM controller uses only the phase angle, α. This chapter is focused only on the type 2 STATCOM controller. The instantaneous power at the AC side is equal to the value of DC side of the inverter as

$$V'_{dc}I'_{dc} = \frac{3}{2}\left(e'_dI'_d + e'_qI'_q\right), \tag{6.6}$$

where the DC side equation is

$$\frac{dV'_{dc}}{dt} = -\omega_bC'\left(I'_d + \frac{V'_{dc}}{R'_p}\right). \tag{6.7}$$

The vector of state variables of the STATCOM system is defined as follows:

$$\mathbf{x} = \begin{bmatrix} I'_d & I'_q & V'_{dc} \end{bmatrix}^T \in \mathbb{R}^3.$$

By combining from (6.4) to (6.7), the mathematical model of the STATCOM system in synchronous rotating reference frame could be described as

$$\begin{aligned} \dot{\mathbf{x}} &= f(\mathbf{x}, u), \quad u \in \mathbb{R} \\ y &= h(\mathbf{x}) \end{aligned} \tag{6.8}$$

where

$$f(\mathbf{x},u)=\begin{pmatrix} -\dfrac{R_s'\omega_b}{L'}x_1+\omega x_2+\dfrac{k\omega_b}{L'}x_3\sqrt{1-u^2}-\dfrac{\omega_b}{L'}|V'| \\ -\omega x_1-\dfrac{R_s'\omega_b}{L'}x_2+\dfrac{k\omega_b}{L'}x_3u \\ -\dfrac{3}{2}kC'\omega_b x_1\sqrt{1-u^2}-\dfrac{3}{2}kC'\omega_b x_2u-\dfrac{\omega_b C'}{R_p'}x_3 \end{pmatrix},$$

$$h(\mathbf{x})=x_2,$$

and

$$u=\sin\alpha.$$

Here, $f(\cdot,\cdot)$ is a smooth vector field. For the simple analysis, fluctuation of the AC-side frequency, ω, is not considered. The base frequency, ω_b, is set as the same value of ω in steady state. And it can approximate that $\sqrt{1-u^2}\approx 1$, since α is sufficiently small value. Therefore, the linear state equations from the approximation of the nonlinear model (6.8) at the equilibrium pair $(\mathbf{x_0}, u_0)^T$ can be obtained as

$$\begin{aligned}\Delta\dot{\mathbf{x}}&=\mathbf{A}\Delta x+\mathbf{B}\Delta u,\\ \Delta y&=\mathbf{C}\Delta x,\end{aligned}\tag{6.9}$$

where

$$\mathbf{A}=\left[\frac{\partial f}{\partial \mathbf{x}}\right]_{\begin{pmatrix}\mathbf{x}\\u\end{pmatrix}=\begin{pmatrix}\mathbf{x_o}\\u_o\end{pmatrix}},\quad \mathbf{B}=\left[\frac{\partial f}{\partial u}\right]_{\begin{pmatrix}\mathbf{x}\\u\end{pmatrix}=\begin{pmatrix}\mathbf{x_o}\\u_o\end{pmatrix}},\quad \mathbf{C}=[0\quad 1\quad 0].$$

STATCOM model, which operates in 345 kV, 100 MVA system, is used and the detailed parameters of the system are listed in Table 6.1 [9].

Table 6.1 STATCOM system parameters used in simulation [9]

Parameters	Value	Unit
Network voltage	345	kV_{LL}
Converter rate	100	Mvar
R_s'	0.0071	pu
L'	0.15	pu
R_p'	727.5846	pu
C'	2.78	pu
k	0.6312	

6.3 Feedback Linearization

The IOL is an effective nonlinear control method that transforms a nonlinear system dynamics into a (fully or partly) linear one such that linear control methods (usually a simple proportional controller) can be applied [4, 15]. It is different from the conventional linearization (i.e., Jacobian Linearization), since the IOL is achieved by the output feedback controller that cancels the original plant nonlinearity, rather than by linear approximations of the dynamics at the operating points. The IOL is an effective and powerful output tracking control in nonlinear systems. However, there is an important and open problem to design the controller considering the internal stability and obtaining more improved performance of internal state of IOL system. Since the IOL method only considers the stability and tracking performance of the output from the output feedback controller, and the internal dynamics are not handled properly.

For the type 2 STATCOMs, it has two-dimensional lightly damped internal dynamics including both the active current and DC voltage [6]. Moreover, Petitclair et al. [7] added a damping term to the input in order to decrease the oscillation amplitude of the internal dynamics. However, the stability and/or transient behavior of the internal dynamics was not guaranteed for all operating points due to the fixed gain. Instead of using the fixed gain, Han et al. [8, 9] developed a modified damping controller with a derivative term of the active current multiplied using a nonlinear gain based on the controllability and observability of the system. The control method enhances the stability and performance of the internal dynamics at all operating points. For the closed system with IOL damping controller, a parameter-dependent *Lyapunov* function is used to prove the exponential stability of the error dynamics [16].

In this section, firstly, the definition and theorem related to IOL for single-input single-output (SISO) system are reviewed. Secondly, design of IOL for an application of STATCOM is introduced. The damping controller is designed for the lightly damped internal dynamics. Lastly, the performance of the proposed IOL method is validated by using a topological model in MATLAB/Simulink.

6.3.1 Input–Output Feedback Linearization for Single-Input Single-Output Systems

Let's consider a single-input-single-output (SISO) system such as,

$$\begin{aligned} \dot{\mathbf{x}} &= f(\mathbf{x}) + g(\mathbf{x})u, \\ y &= h(\mathbf{x}), \end{aligned} \tag{6.10}$$

where, $\mathbf{x} \in \mathbf{X} \subset \mathbb{R}^m$ indicates the state vector, $u \in \mathbf{U} \subset \mathbb{R}$ is the input, and $y \in \mathbf{Y} \subset \mathbb{R}$ is the output. In the compact set $\mathbf{X}$, the above three functions, i.e., f: $\mathbf{X} \rightarrow \mathbb{R}^m$,

g: $\mathbf{X} \to \mathbb{R}^m$ and h: $\mathbf{X} \to \mathbb{R}$, are sufficiently smooth. And before beginning with the IOL, all of the states are assumed to be measurable. Then the derivative of output y with respect to time can be obtained as follows:

$$\dot{y} = \frac{\partial h}{\partial \mathbf{x}}[f(\mathbf{x}) + g(\mathbf{x})u] =: L_f h(\mathbf{x}) + L_g h(\mathbf{x})u, \tag{6.11}$$

where, $L_f h(\mathbf{x}) = (\partial h/\partial \mathbf{x}) f(\mathbf{x})$ and $L_g h(\mathbf{x}) = (\partial h/\partial \mathbf{x}) g(\mathbf{x})$. If a dynamic system has a well-defined relative degree γ, $1 \le \gamma \le m$ in a region $\mathbf{X}$ [5]:

$$\begin{cases} L_g L_f^{i-1} h(\mathbf{x}) = 0, & i = 1, 2, \ldots, \gamma - 1, \\ L_g L_f^{\gamma-1} h(\mathbf{x}) = 0. \end{cases}$$

If u does not appear in the $y, \ldots, y^{(\gamma-1)}$ equations and appears in the $y^{(\gamma)}$ with a non-zero coefficient, i.e., $y^{(\gamma)} = L_f^{\gamma} h(\mathbf{x}) + L_g L_f^{\gamma-1} h(\mathbf{x})u$, then the system is input–output linearisable by using the state feedback controller as,

$$u = \frac{v - L_f^{\gamma} h(\mathbf{x})}{L_g L_f^{\gamma-1} h(\mathbf{x})}, \tag{6.12}$$

and it renders the input–output map to $y^{(\gamma)} = v$ which is a chain of γ integrators. Let $e = y_d(t) - y(t)$ be a tracking error, and a new input, v, is chosen as

$$v = y_d^{\gamma} + k_1 e + \cdots + k_{\gamma} e^{(\gamma-1)}, \tag{6.13}$$

where the coefficient, k_i, are chosen such that the polynomial related with the error of the closed-loop system

$$k_1 e + \cdots + k_{\gamma} e^{(\gamma-1)} + e^{\gamma}$$

has all its roots strictly in the left-half plane (LHP). The structure of the closed-loop system with IOL can be referred [4].

Theorem 6.1 [4, 5]: *For the system* (6.10) *with a well-defined relative degree.* γ, *if* γ *is strictly less than m, then it is always possible to find m-*γ *smooth functions,* $\phi_j(\mathbf{x})$, $\forall\ j = 1,\ldots,m - \gamma$, *such that the mapping* T: $\mathbf{X} \to \mathbf{Z_n}$

$$\mathbf{z_n} = \mathbf{T}(\mathbf{x}) = \begin{bmatrix} \phi_1(\mathbf{x}) \\ \vdots \\ \phi_{m-r}(\mathbf{x}) \\ - - - \\ h(\mathbf{x}) \\ \vdots \\ L_f^{\gamma-1} h(\mathbf{x}) \end{bmatrix} =: \begin{bmatrix} \eta_{n,1} \\ \vdots \\ \eta_{n,m-\gamma} \\ - - - \\ \xi_{n,1} \\ \vdots \\ \xi_{n,r} \end{bmatrix} \tag{6.14}$$

has a non-singular Jacobian matrix at $\mathbf{x_o} \in \mathbf{X_0}$*, is a diffeomorphism on* $\mathbf{X}$*. and satisfies the condition:*

$$\frac{\partial \phi_j}{\partial \mathbf{x}} g(\mathbf{x}) = 0, \quad \forall j = 1, \ldots, m - \gamma, \quad \mathbf{x} \in \mathbf{X}. \tag{6.15}$$

In particular, since there is no specific need to keep track individually of each one of the $m - \gamma$ components of the state vector, all of them are represented together as

$$\boldsymbol{\eta}_\mathbf{n} = \begin{pmatrix} z_{n,1} \\ \vdots \\ z_{n,m-\gamma} \end{pmatrix}. \tag{6.16}$$

Sometimes, whenever convenient and not otherwise required, it shall represent also the last γ components together, as

$$\boldsymbol{\xi}_\mathbf{n} = \begin{pmatrix} z_{n,m-\gamma+1} \\ \vdots \\ z_{n,m} \end{pmatrix}. \tag{6.17}$$

By using these notations, the normal form of a SISO nonlinear system having $\gamma < m$ can be divided into two parts: an external part and an internal part, as the following state space model:

$$\begin{aligned} \dot{\eta}_\mathbf{n} &= q(\boldsymbol{\xi}_\mathbf{n}, \eta_\mathbf{n}), \\ \dot{\xi}_\mathbf{n} &= \underbrace{\begin{bmatrix} 0 & 1 & 0 & \cdots & 0 \\ 0 & 0 & 1 & \cdots & 0 \\ \vdots & \vdots & \vdots & \ddots & \vdots \\ 0 & 0 & 0 & \cdots & 1 \\ 0 & 0 & 0 & \cdots & 0 \end{bmatrix}}_{\mathbf{A}_{\xi n}} \boldsymbol{\xi}_\mathbf{n} + \underbrace{\begin{bmatrix} 0 \\ 0 \\ \vdots \\ 0 \\ 1 \end{bmatrix}}_{\mathbf{B}_{\xi n}} v, \\ y &= \xi_{n,1}, \end{aligned} \tag{6.18}$$

where $\boldsymbol{\eta}_\mathbf{n} \in \mathbf{H} \subset \mathbb{R}^{m-\gamma}$, $\boldsymbol{\xi}_\mathbf{n} \in \Xi \subset \mathbb{R}^{\gamma}$, $\mathbf{A}_{\xi n} \in \mathbb{R}^{\gamma \times \gamma}$, and $\mathbf{B}_{\xi n} \in \mathbb{R}^{\gamma \times 1}$. The nominal state is indicated by the subscript n. Due to the IOL, the state variables $\boldsymbol{\eta}_\mathbf{n}$ are rendered unobservable from y and $\dot{\eta}_\mathbf{n} = q(\boldsymbol{\xi}_\mathbf{n}, \boldsymbol{\eta}_\mathbf{n})$ is called internal dynamics [5].

The existence of $\mathbf{T}(\mathbf{x})$ which is a diffeomorphism qualifies as a local coordinate transformation in a neighbourhood of $\mathbf{x_o}$. By using the change of coordinates as described in (6.12), the nominal dynamics could be obtained with the IOL controller of (6.12) as follows:

$$\dot{\mathbf{z}}_{\mathbf{n}} = f_z(\boldsymbol{\xi}_{\mathbf{n}}, \boldsymbol{\eta}_{\mathbf{n}}, v), \tag{6.19}$$

where $\mathbf{z_n} = [\boldsymbol{\eta}_{\mathbf{n}}, \boldsymbol{\xi}_{\mathbf{n}}]^T \in \mathbf{Z_n} \subset \mathbb{R}^m$ denotes a state vector and $v \in \mathbf{N_n} \subset \mathbb{R}$ denotes a new input.

6.3.2 Input–Output Linearization of STATCOM System

For the STATCOM system (6.10), the derivative of output y with respect to time could be described as follows;

$$\dot{y} = -\omega x_1 - \frac{R_s'\omega}{L'}x_2 + \frac{k\omega}{L'}x_3 u. \tag{6.20}$$

A linear relationship between output y and input u from the first derivative of y could be obtained. Therefore, the relative degree of the system is 1. Since $x_3 \neq 0$ in the operating range [9], it is clear that the IOL control law,

$$\alpha = \sin^{-1}\left\{L'\left(v + \omega x_1 + \frac{R_s'\omega_b}{L'}x_2\right)\Big/ k\omega_b x_3\right\}, \tag{6.21}$$

renders the input–output map as $\dot{y} = \dot{x}_2 = v$. The relationship between the new input v and output y is represented as an integrator. Other states such as x_1 and x_3 are unobservable from y. These dynamics are called internal dynamics [4]. Figure 6.2a shows the open loop structures of system. Figure 6.2b shows the closed-loop diagram when tracking the reference, x_{2r}. In this structure, a proportional (P) controller, a constant gain, K, is considered for output feedback controller. By using input–output linearized system, the controller could be designed from the perspectives of linear control theory [5]. By using the IOL control law (6.21), the STATCOM system could be expressed in the form of

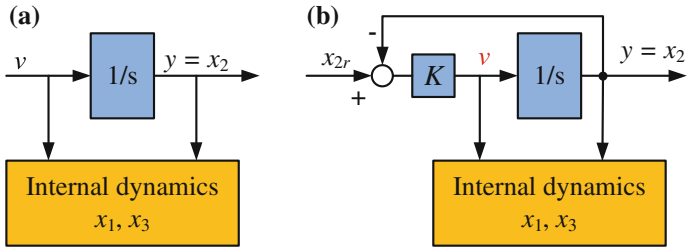

Fig. 6.2 **a** Input–output linearized system, **b** closed-loop control system

$$\begin{aligned}\dot{\mathbf{x}} &= f_F(\mathbf{x}, v),\\ y &= x_2,\end{aligned} \tag{6.22}$$

where

$$f_F(\mathbf{x}, v) = \begin{pmatrix} -\dfrac{R_s'\omega_b}{L'}x_1 + \omega x_2 + \dfrac{k\omega_b}{L'}x_3 - \dfrac{\omega_b}{L'}|V'| \\ -\dfrac{3kC'\omega_b}{2}x_1 - \dfrac{3C'L'x_2}{2x_3}\left(v + \omega x_1 + \dfrac{R_s'\omega_b}{L'}x_2\right) - \dfrac{\omega_b C'}{R_p'}x_3 \end{pmatrix}.$$

It is known that $f_F(\cdot,\cdot)$ is a smooth vector field. At the equilibrium pair ($\mathbf{x_o}$, v_o), the approximated system dynamics could be denoted as,

$$\begin{aligned}\Delta\dot{\mathbf{x}} &= \mathbf{A_F}\Delta\mathbf{x} + \mathbf{B_F}\Delta v,\\ y &= \mathbf{C}\Delta\mathbf{x},\end{aligned} \tag{6.23}$$

where

$$\mathbf{A_F} = \left[\frac{\partial f_F}{\partial \mathbf{x}}\right]_{\begin{pmatrix}\mathbf{x}\\ v_\delta\end{pmatrix}=\begin{pmatrix}\mathbf{x_o}\\ v_o\end{pmatrix}}, \quad \mathbf{B_F} = \left[\frac{\partial f_F}{\partial v}\right]_{\begin{pmatrix}\mathbf{x}\\ v_\delta\end{pmatrix}=\begin{pmatrix}\mathbf{x_o}\\ v_o\end{pmatrix}},$$

which are investigated in [7]. Figure 6.3 describes how the closed-loop poles are affected by the reactive current x_{20} in s-domain within the interval from −1 to 1 pu when K = 300. The magnitude of real pole is same as K. Other poles are independent of K and these poles describe the internal dynamics. The input–output linearised STATCOM system are stable but lightly damped, that is, the poles of internal dynamics are closed to the imaginary axis, In the IOL system, the feedback

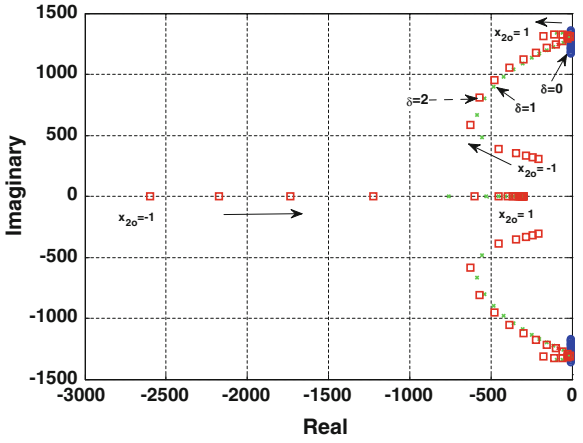

Fig. 6.3 Poles of input–output linearized STATCOM system according to variations of x_{20} in s-domain. (x_{20} = (−1:0.1:1) *blue-circle*:δ = 0; *green*-x: δ = 1; *red-square*: δ = 2)

controller could fail to achieve the transient response and stability of internal states even though the output tracking is properly obtained [4, 5]. These lightly damped dynamics could incur the current ripples on the DC-side capacitor. These ripples have negative effects on the life-cycle of the system as well as the power quality [8].

6.3.3 Input–Output Linearization with Damping Controller

In order to handle the lightly damped dynamics problem, Petitclair et al. designed the input–output linearization with damping (IOLD) controller, which is given by

$$\alpha = \sin^{-1}\left\{ L'\left(v_\delta + \omega x_1 + \frac{R'_s \omega_b}{L'} x_2 + \delta \frac{\mathrm{d}x_1}{\mathrm{d}t} \right) \Big/ k\omega_b x_3 \right\}. \tag{6.24}$$

A damping term which is composed of first derivative of active current multiplied by constant gain, δ, is added to the IOL control law (6.21). Therefore, the STATCOM system including damping term could be described as,

$$\begin{aligned} \dot{\mathbf{x}} &= f_{\delta,1}(\mathbf{x}, v_\delta, \delta), \\ y &= x_2, \end{aligned} \tag{6.25}$$

where

$$f_{\delta,1}(\mathbf{x}, v_\delta, \delta) = \begin{pmatrix} -\frac{R'_s\omega_b}{L'} x_1 + \omega x_2 + \frac{k\omega_b}{L'} x_3 - \frac{\omega_b}{L'} |V'| \\ v_\delta + \delta\left(-\frac{R'_s\omega_b}{L'} x_1 + \omega x_2 + \frac{k\omega_b}{L'} x_3 - \frac{\omega_b}{L'} |V'| \right) \\ -\frac{3kC'\omega_b}{2} x_1 - \frac{3C'L'x_2}{2x_3} \left\{ v_\delta + \omega x_1 + \frac{R'_s\omega_b}{L'} x_2 + \delta\left(-\frac{R'_s\omega_b}{L'} x_1 + \omega x_2 + \frac{k\omega_b}{L'} x_3 - \frac{\omega_b}{L'} |V'| \right) \right\} - \frac{\omega_b C'}{R'_p} x_3 \end{pmatrix},$$

and the linearized system of (6.25) at the equilibrium point ($\mathbf{x_o}$, v_o) is easily obtained as,

$$\begin{aligned} \Delta\dot{\mathbf{x}} &= \mathbf{A_{\delta,1}} \Delta\mathbf{x} + \mathbf{B_{\delta,1}} \Delta v_\delta, \\ \Delta y &= \mathbf{C} \Delta\mathbf{x}, \end{aligned} \tag{6.26}$$

where

$$\mathbf{A_{\delta,1}} = \left[\frac{\partial f_{\delta,1}}{\partial \mathbf{x}} \right] \begin{pmatrix} \mathbf{x} \\ v_o \end{pmatrix} = \begin{pmatrix} \mathbf{x_o} \\ v_o \end{pmatrix}, \quad \mathbf{B}_{\delta,\mathbf{1}} = \left[\frac{\partial f_{\delta,1}}{\partial v_\delta} \right] \begin{pmatrix} \mathbf{x} \\ v_\delta \end{pmatrix} = \begin{pmatrix} \mathbf{x_o} \\ v_\delta \end{pmatrix}.$$

The IOLD controller helps the movement of poles further from the imaginary axis as shown in Fig. 6.3 and the transient response and stability of internal

dynamics could be improved from the IOLD controller [7]. The degree of movement of internal dynamics' poles depends on the controllability of internal dynamics. And for the linearized system (6.23), the controllability for the internal dynamics can be analyzed through a matrix, **CO**, defined as follows:

$$\mathbf{CO} = [\lambda_{\text{int}}\mathbf{I} - \mathbf{A_F} | \mathbf{B_F}], \tag{6.27}$$

where λ_{int} are the poles of internal dynamics at each operating point. Then singular value decomposition is used for the controllability matrix, **CO**. The minimum singular value (MSV) at each operating point of x_2 is plotted in s-domain, as shown in Fig. 6.4. **CO** has the smallest value at at $x_{20} = 2x_{30}/3kC'$ and it could be concluded that this operating point is weakly controllable. Close to this weakly controllable operating point, the approximated linearized STATCOM dynamics, which have the complex conjugate zeroes the same as the complex conjugate poles, are obtained. Thus, there are pole-zero cancellations and these results in unobservable and uncontrollable poles [17]. Therefore, near this weakly operating point, the damping controller has no way to move the closed loop poles of the internal dynamics. For parameters in [7], the value of $2x_{30}/3kC'$ is larger than 1, thus it is out of interesting point and the poles of interesting operating points are in the LHP until the gain, δ, is smaller or equal to zero. In case of Table 6.1, the value of $2x_{30}/3kC'$ is 0.5521. It means that the poles of internal dynamics are hardly handled by damping controller at this operating point. This problem could be resolved by using a large capacitor. Figure 6.5 shows the poles of the closed-loop system (6.26) in s-domain when the operating points of reactive current, x_{20}, is changed from −1 to 1 pu with two times capacitance compared with the case of Table 6.1. The poles are moved further from the imaginary axis with a large value of δ compared to a small one as shown in Fig. 6.5a. However, this approach needs more cost due to the larger capacitance. Figure 6.5b shows the poles of the input–output linearized closed-loop system (6.26)

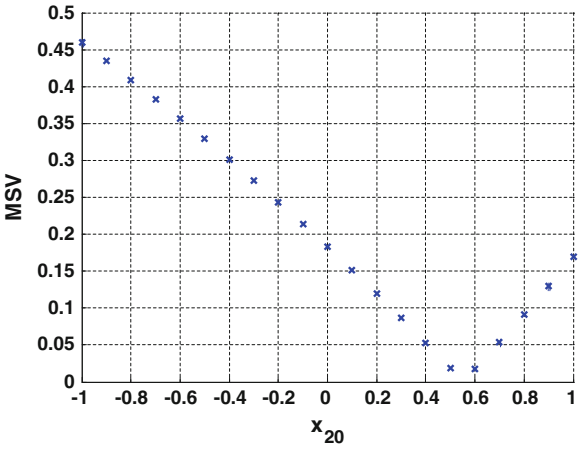

Fig. 6.4 MSVs of the controllability matrix for the internal dynamics

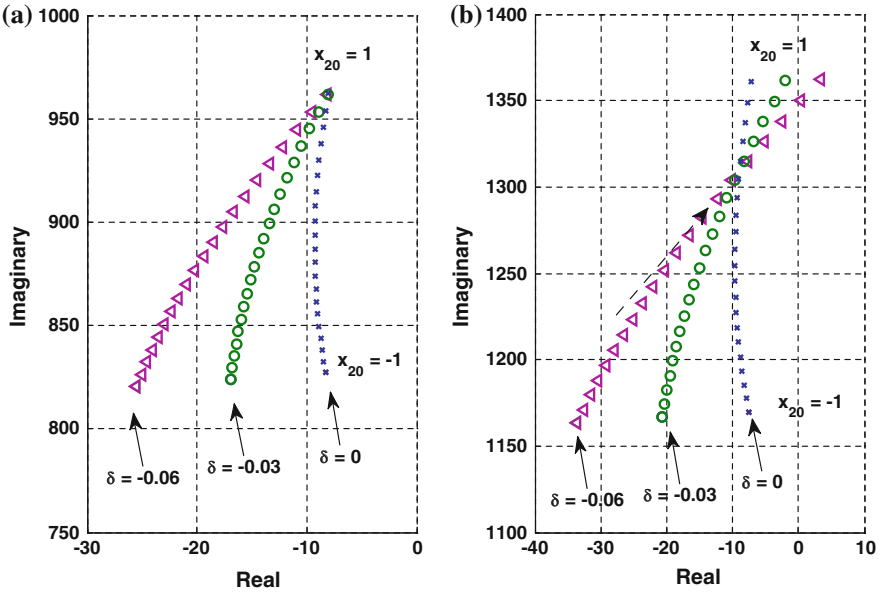

Fig. 6.5 **a** Poles of STATCOM system (6.26) having capacitance of $C' = 1.39$ pu, **b** $C' = 2.78$ pu with damping controller according to the variation of δ and x_{20}

when x_{20} varies from -1 to 1 pu with $C' = 2.78$ pu. The absolute value of real pole has the same value of P controller gain, K when δ is zero. When δ is not zero, the absolute value is not same as the value of K, but stays near within the range of ± 0.5. On the other hand, if δ is a positive real number, then some of poles could be in right half-plane. The performance of the internal states, x_1 and x_3, could be estimated from the complex conjugate poles, since the real part of the complex conjugate poles is 5 times smaller than the magnitude of the real poles. When x_{20} is in the range of $x_{20} > 2x_{30}/3kC'$, the internal dynamics could be more weakly damped or even worse, such as unstable dynamics for small value of δ. On the contrary, if $x_{20} < 2x_{30}/3kC'$, then the poles of internal dynamics move far from the imaginary axis for small δ and therefore more improved transient response could be accomplished. Lastly, when $x_{20} = 2x_{30}/3kC'$, the poles of internal dynamics are hardly moved and this result is coincident with the controllability analysis.

6.3.4 Input–Output Linearization with Modified Damping Controller

It is known that there is little phase margin in inductive mode near the resonant frequency [2]. To handle this problem, Schauder et al. [2, 3] introduced the synthesized feedback controller for improved transient response with the weakly

damped state dynamics in inductive mode. The synthesized feedback controller could be obtained as

$$q(s) = \left(I'_q - I'_{qo(critical)}\right)\left(\frac{s}{1+sT}\right)V'_{dc}, \tag{6.28}$$

where

$$I'_{qo(critical)} = \frac{2}{3kC'}V'_{dc\,o}.$$

This synthesized feedback controller has the effect of relocating the zeroes of the open-loop system so that the root locus of closed-loop system always stays in the LHP, indicating a locally stable operation. In this section, the variable gain of the input–output linearization with a modified damping (IOLMD) controller, which is motivated from Schauder's synthesized feedback controller, is introduced in order to overcome the limitation of the Petitclair's IOLD controller (6.24), such as

$$\alpha = \sin^{-1}\left\{L'\left(v_\delta + \omega x_1 + \frac{R'_s\omega_b}{L'}x_2 + \delta(x_2 - x_{2c})\frac{dx_1}{dt}\right)\Big/ k\omega_b x_3\right\}, \tag{6.29}$$

where

$$x_{2c} = \frac{2}{3kC'}x_3.$$

The term $\delta(x_2 - x_{2c})dx_1/dt$ is added to the IOL control law (6.21). The IOLMD controller has a structure that the variable gain $\delta(x_2 - x_{2c})$ is multiplied by the derivative of x_1 with respect to time. δ is a constant gain and the value of x_{2c} relates with the value of x_3. The STATCOM system dynamics with the IOLMD controller (6.29) could be put in the form of

$$\begin{aligned}\dot{\mathbf{x}} &= f_{\delta,2}(\mathbf{x},\delta) + g_\delta(\mathbf{x})v_\delta,\\ y &= x_2,\end{aligned} \tag{6.30}$$

where

$$f_{\delta,2}(x,\delta) + g_\delta(x)v_\delta = \begin{pmatrix} -\frac{R'_s\omega_b}{L'}x_1 + \omega x_2 + \frac{k\omega_b}{L'}x_3 - \frac{\omega_b}{L'}|V'| \\ v_\delta + \delta\left(x_2 - \frac{2}{3kC'}x_3\right)\left(-\frac{R'_s\omega_b}{L'}x_1 + \omega x_2 + \frac{k\omega_b}{L'}x_3 - \frac{\omega_b}{L'}|V'|\right) \\ -\frac{3kC'\omega_b}{2}x_1 - \frac{3C'L'x_2}{2x_3}\left\{v_\delta + \omega x_1 + \frac{R'_s\omega_b}{L'}x_2\right. \\ \left. +\delta\left(x_2 - \frac{2}{3kC'}x_3\right)\left(-\frac{R'_s\omega_b}{L'}x_1 + \omega x_2 + \frac{k\omega_b}{L'}x_3 - \frac{\omega_b}{L'}|V'|\right)\right\} - \frac{\omega_b C'}{R'_p}x_3 \end{pmatrix}.$$

The approximated linearized system with the IOLMD controller could be expressed as,

$$\begin{aligned} \Delta\dot{\mathbf{x}} &= \mathbf{A}_{\boldsymbol{\delta},2}\Delta\mathbf{x} + \mathbf{B}_{\boldsymbol{\delta},2}\Delta v_{\delta}, \\ \Delta y &= \mathbf{C}\Delta\mathbf{x}, \end{aligned} \tag{6.31}$$

where

$$\mathbf{A}_{\boldsymbol{\delta},2} = \left[\frac{\partial\left(f_{\delta,2} + g_{\delta}v_{\delta}\right)}{\partial\mathbf{x}}\right]_{\begin{pmatrix}\mathbf{x}\\ v_{\delta}\end{pmatrix}=\begin{pmatrix}\mathbf{x_o}\\ v_{\mathrm{o}}\end{pmatrix}}, \quad \mathbf{B}_{\boldsymbol{\delta},2} = g_{\delta}(\mathbf{x})|_{\mathbf{x}=\mathbf{x_o}}.$$

Figure 6.6 describes the poles of the closed-loop system with the IOLD controller (6.24) and the IOLMD controller (6.29) in s-domain. In Fig. 6.6, sky blue (o) marks describe the closed loop poles of system (6.26) with P gain, $K = 300$ and damping controller gain, $\delta = -0.03$ when the variation of x_{20} is within −1 to 1 pu. The violet (*) marks describes the closed loop poles with the IOLMD controller with the same P gain and the modified damping controller gain, $\delta = 2$. The magnitudes of the real poles are no longer the same as K. The polarity of the added term $\delta(x_2 - x_{2c})$ in (6.24) is affected by the value of x_{2c}. By setting the gain δ as a positive real value, the poles of the system (6.26) are in the LHP over the entire operating points. Comparing to the IOLD controller, the IOLMD controller makes the real part of complex poles to be 1.5–129 times larger value of that of the IOLD except at $x_{20} = x_{2co} \coloneqq 2x_{30}/3kC'$. The improved performances of internal dynamics are expected from the IOLMD compared to the IOL (6.22) and the IOLD controller (6.25). At critical point, $x_{20} = x_{2co}$, the poles of the IOLMD case are same as the IOL case. But variable damping gain helps to improve the transient response and this will be described in the next section.

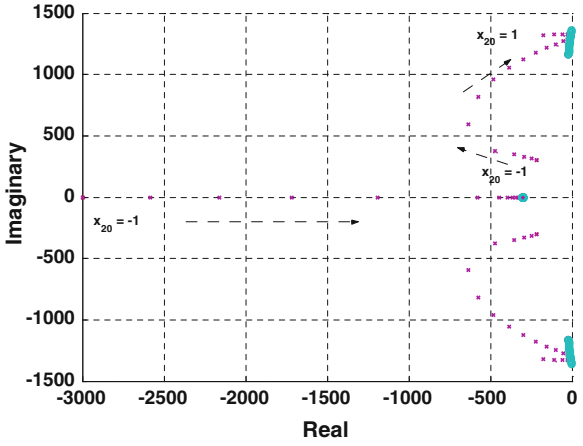

Fig. 6.6 Poles of input–output feedback linearized STATCOM system according to the variations of δ and x_{20} in s-domain (*sky blue* (*circle*) IOLD controller; *violet* (*asterisk*) IOLMD controller)

6.3.5 Controllability and Observability Analysis for STATCOM System

Even an effective contribution in moving the internal dynamics poles to a more stable region could be provided by the IOLMD controller, there is a negative effect on the output performance. Since the output is coupled to the internal states by the damping term and the relationship between the input and output is no longer linear. Therefore, in order to design a most effective damping controller, the movement of the internal dynamics poles and the effect on the output according to the injection of the damping term should be analyzed.

The controllability determines the degree of movement of the internal dynamics poles and this controllability could be analyzed through a matrix which is denoted as,

$$\mathbf{CO} = \left[\lambda_{\text{int},\delta}\mathbf{I_{3\times 3}} - \mathbf{A_\delta}|\mathbf{B_\delta}\right], \tag{6.32}$$

where $\lambda_{\text{int},\delta}$ are complex conjugated poles which have smallest value of real part of damped system (6.31). The *Popov–Belevitch–Hautus* (PBH) rank test shows that the mode of $\lambda_{\text{int},\delta}$ is controllable if and only if rank **CO** = 3 [5].

Remark 6.1 [16] All modes corresponding to the internal dynamics poles of the STATCOM system (6.31) are controllable from the input Δv_δ in the interested operating set.

The singular value decomposition has been used in power system studies [16, 18] in order to quantify the controllability of a mode corresponding to a pole by a given input. The MSV of (6.32) is denoted as,

$$\sigma_{\mathbf{CO},\min} = \min_i\left(\sqrt{\lambda_i\left(\mathbf{COCO}^T\right)}\right) > 0, \quad i = 1, 2, 3 \tag{6.33}$$

and it describes the degree of effectiveness (ability/capability) of the input to control the mode associated with $\lambda_{\text{int},\delta}$. The strength of coupling between the input and the mode is related with the value of $\sigma_{\mathbf{CO}.\min}$ [19]. If $\sigma_{\mathbf{CO}.\min}$. is large, then the mode and the input are strongly coupled, thus the input can easily exert control over the mode. Figure 6.7a shows the values of $\sigma_{\mathbf{CO}.\min}$ at each x_{20}. With the fixed δ, as the value of the MSV is larger, the $\lambda_{\text{int},\delta}$ moves further from the $j\omega$-axis [8]. Clearly, the effectiveness of the input to control the mode will be weak with small the MSV. At the operating point is $x_{20} = 2x_{30}/3kC'$, the zeros of the IOL system have the same values as the internal dynamics poles and the system is weakly controllable. Thus it is hard to move the poles of internal dynamics by using any damping controller at this operating point [9].

Due to inclusion of the damping term, the output becomes coupled to the internal dynamics. Thus, the oscillation of the internal states appears in the output during transient response. This impact of internal state on output could be estimated from

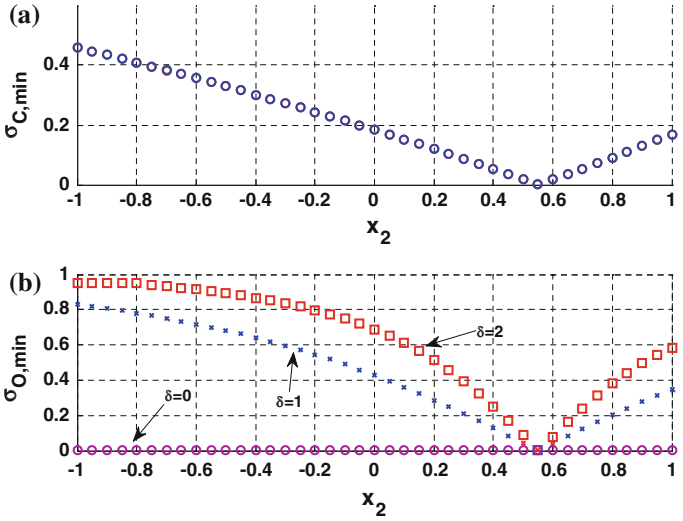

Fig. 6.7 **a** Controllability of internal dynamics **b** observability of internal dynamics. (x_{20} = −1:0.05:1; *violet-circle* = 0; *blue-asterisk* = 1; *red-square* = 2)

the analysis of local observability of the internal dynamics from the output. Here, the matrix, **OV**, is defined as

$$\mathbf{OV} = \left[\lambda_{\text{int},\delta}\mathbf{I_{3\times 3}} - \mathbf{A}_{\boldsymbol{\delta}}^{T} \mid \mathbf{C}_{\boldsymbol{\delta}}^{T}\right]^{T} \tag{6.34}$$

to describe the observability matrix. A pair ($\mathbf{A_\delta}$, $\mathbf{C_\delta}$) could be observable if and only if rank **OV** = 3 for all $\lambda_{\text{int},\delta}$ by using the PBH rank test [19].

Remark 6.2 The IOL controller makes both x_1 and x_3 be unobservable from y [5].

Without the damping term that is $\delta = 0$, the internal dynamics are decoupled from the output (i.e., unobservable from the output), thus, the rank of **OV** is less than 3.

Remark 6.3 [16] The IOL controller with a nonlinear damping term makes both x_1 and x_3 observable from y.

Due to the damping term, $\delta \neq 0$, the rank of **OV** is 3, that means, the mode of $\lambda_{\text{int},\delta}$ is observable from the output. i.e., the observability of the mode corresponding to $\lambda_{\text{int},\delta}$ in the output is recovered because of the IOLMD. The MSV of (6.34) is defined as

$$\sigma_{\mathbf{OV},\min} = \min_i \left(\sqrt{\lambda_i\left(\mathbf{OV}^T\mathbf{OV}\right)}\right) > 0, \quad i = 1, 2, 3. \tag{6.35}$$

The value of $\sigma_{\mathbf{OV},\min}$ is described with δ = 0, 1, 2 at each operating point, x_{20}, as shown in Fig. 6.7b. The value of $\sigma_{\mathbf{OV},\min}$ means the strength of the observability for

the mode associated with $\lambda_{\text{int},\delta}$ in the output [16]. As the value of δ increases from zero, the observability becomes larger and the internal dynamics has the more effect on the output in transient response. However, owing to the stable dynamics of internal dynamics, the value of the time derivative term of the internal dynamics becomes zero at the steady-state. Therefore, the output should approximately track the desired trajectory via the output feedback controller. Notice that, when determining the gain, δ, of the damping control law, the control designer should account a trade-off between the transient response of output and relative stability of the internal dynamics.

6.3.6 Stability Analysis Based on Lyapunov Theorem

By obtaining linearly approximated closed-loop system at each operating point, local stability is analyzed. It is not sufficient for nonlinear system stability [15]. In [16], the stability analysis for the internal dynamics and the boundness of the oscillatory output for STATCOM system has been investigated by using Lyapunov theorem. In this section, the proof of stability and for the internal stability with the IOLMD controller are analyzed, the normal form is derived to decouple the internal states from the control law (6.29). Since the input function of (6.30) is

$$g_\delta(\mathbf{x}) = \begin{bmatrix} 0 & 1 & -\frac{3C'L'x_2}{2x_3} \end{bmatrix}^T, \tag{6.36}$$

and, by defining

$$\eta_1 := x_1,\ \eta_2 := \frac{x_2^2}{2} + \frac{x_3^2}{3L'C'},\quad \xi := x_2 \tag{6.37}$$

to find a function $\phi(\mathbf{x})$ which is independent of v_δ. The mapping could be defined as

$$\mathbf{z} = T(\mathbf{x}) = \begin{bmatrix} \phi(\mathbf{x}) \\ h(\mathbf{x}) \end{bmatrix} \overset{def}{=} \begin{bmatrix} \boldsymbol{\eta} \\ \xi \end{bmatrix}, \tag{6.38}$$

where $T(\mathbf{x})$ is diffeomorphic and qualifies as a local coordinates transformation into the normal form. Thus, it can decouple the internal dynamics from output and analyze the internal dynamics stability.

$$\frac{\partial \phi}{\partial \mathbf{x}} g_\delta(\mathbf{x}) = 0. \tag{6.39}$$

By using the transformation matrix $T(\mathbf{x})$, the system dynamics introduced in (6.30) is converted into a normal form as

$$\begin{aligned}\dot{\boldsymbol{\eta}} &= q(\xi, \boldsymbol{\eta}), \quad \boldsymbol{\eta} \in \mathbb{R}^2, \\ \dot{\xi} &= v_\delta + \delta\varphi(\xi, \boldsymbol{\eta}), \quad \xi \in \mathbb{R}.\end{aligned} \tag{6.40}$$

with the continuously differentiable function

$$q(\xi, \boldsymbol{\eta}) = \begin{pmatrix} \dfrac{-R_s'\omega}{L'}\eta_1 + \omega\xi + \dfrac{k\omega}{L'}q_{\mathbf{x}}(\xi, \eta_2)^{1/2} - \dfrac{\omega}{L'}|V'| \\ -\omega\eta_1\xi - \dfrac{R_s'\omega}{L'}\xi^2 - \dfrac{k\omega}{L'}\eta_1 q_{\mathbf{x}}(\xi, \eta_2)^{1/2} - \dfrac{2\omega}{3L'R_p'}q_{\mathbf{x}}(\xi, \eta_2) \end{pmatrix}, \tag{6.41}$$

and

$$\begin{aligned}\varphi(\xi, \boldsymbol{\eta}) = &\left(\xi - \frac{2}{3kC'}q_{\mathbf{x}}(\xi, \eta_2)^{1/2}\right) \\ &\times \left(-\frac{R_s'\omega}{L'}\eta_1 + \omega\xi + \frac{k\omega}{L'}q_{\mathbf{x}}(\xi, \eta_2)^{1/2} - \frac{\omega}{L'}|V'|\right),\end{aligned} \tag{6.42}$$

where $q_{\mathbf{x}}(\xi,\eta_2) = 3C'L'(\eta_2 - \xi^2/2)$, It can get the continuous function $\mathbf{A_n}(\theta)$ from the linearization of $q(\xi, \boldsymbol{\eta})$ at operating point $(\xi_o, \eta_o)^T$ as follows:

$$\mathbf{A_n}(\theta(t)) = \begin{bmatrix} -\frac{R_s'\omega}{L'} & \frac{3k\omega C'}{2q_{\mathbf{x}}(\xi_o,\eta_{2o})^{1/2}} \\ -\omega\xi_o - \frac{k\omega}{L'}q_{\mathbf{x}}(\xi_o, \eta_{2o})^{1/2} & -\frac{3k\omega C'\eta_{1o}}{2q_{\mathbf{x}}(\xi_o,\eta_{2o})^{1/2}} - \frac{2\omega C'}{R_p'} \end{bmatrix}. \tag{6.43}$$

There are several combinations of $\mathbf{A_i}$ and θ_i to describe $\mathbf{A_n}(\theta)$ as the form described in [20]. For the real fixed matrix $\mathbf{A_0}$, $\mathbf{A_1}$, $\mathbf{A_2}$, and $\mathbf{A_3}$, all of dimension is 2×2, such that

$$\begin{aligned}\mathrm{A_0} &= \begin{bmatrix} -\frac{R_s'\omega}{L'} & 0 \\ 0 & -\frac{2\omega C'}{R_p'} \end{bmatrix}, \quad \mathrm{A_1} = \begin{bmatrix} 0 & \frac{\sqrt{3}k\omega C'}{2\sqrt{C'L'}} \\ 0 & 0 \end{bmatrix}, \\ \mathrm{A_2} &= \begin{bmatrix} 0 & 0 \\ -\omega & 0 \end{bmatrix}, \quad \mathrm{A_3} = \begin{bmatrix} 0 & 0 \\ 0 & -\frac{\sqrt{3}k\omega C'}{2\sqrt{C'L'}} \end{bmatrix},\end{aligned} \tag{6.44}$$

$$\theta_1(t) = \frac{\sqrt{3C'L'}}{q_{\mathbf{x}}(\xi_o, \eta_{2o})^{1/2}}, \quad \theta_2(t) = \xi_o + \frac{k}{L'}q_{\mathbf{x}}(\xi_o, \eta_{2o})^{1/2}, \quad \theta_3(t) = \frac{\sqrt{3C'L'}\eta_{1o}}{q_{\mathbf{x}}(\xi_o, \eta_{2o})^{1/2}}. \tag{6.45}$$

It is obviously that $\mathbf{A_n}(\theta)$ depends affinely on the uncertainties θ_i. The detailed feasibility and existence study of the reference trajectory satisfying Proposition 3.5 were performed in [16].

6.3.7 Performance of the Nonlinear Feedback Controller

Performance of the nonlinear methods introduced in Sect. 6.3 is compared through the simulation using a topological model in SimPowerSystems, MATLAB/Simulink. The parameters and structures are used as the 24-pulses 100MVA STATCOM, which compensates reactive power on a three-bus 345-kV system that has been installed at Migeum S/S, South Korea [9]. The controller block is model by using the Simulink library and the electric blocks are model by using the SimPowerSystems block set, as shown in Fig. 6.8.

Figure 6.9 shows the controller block of the system. The controller block has 3 inputs as V_{abc}, I_{abc}, and V_{dc}, and 1 output as pluses that controls the STATCOM's switches. In Fig. 6.9, block (1) is a measurement system, block (2) is a voltage regulator, block (3) is an $I_{q,ref}$ selector. In the block (3), $I_{q,ref}$ is determined according to the control mode where there are three control objectives: voltage regulation, reactive power and reactive current, and one of them is selected to compute the corresponding $I_{q,ref}$. Block (4) is a Proportional-Integral (PI) controller to generate v_δ in (6.29). Block (5) is the IOLMD controller (6.29) to generate alpha for firing pulses generator. Block (6) is a (PLL) system. Block (7) is a DC balance regulator and block (8) is a firing pulses generator. In this simulation, blocks (4) and (5) are modified to adjust the proposed IOLMD method.

In this simulation, the network voltage, V', may vary within the range 95−105 % according to the power system conditions of the Korea Electric Power Corporation (KEPCO) standard [9]. Sampling time of the controller was set to be 65 microseconds and that of the power electronics was set to be 1 microsecond. Control specifications for I'_q were as follows: settling time, $T_s < 16$ ms, error of steady state. $e_{ss} < 5$ %, and overshoot, %OS < 10 %, and the operating range of reactive current is from −1 to 1 pu [9].

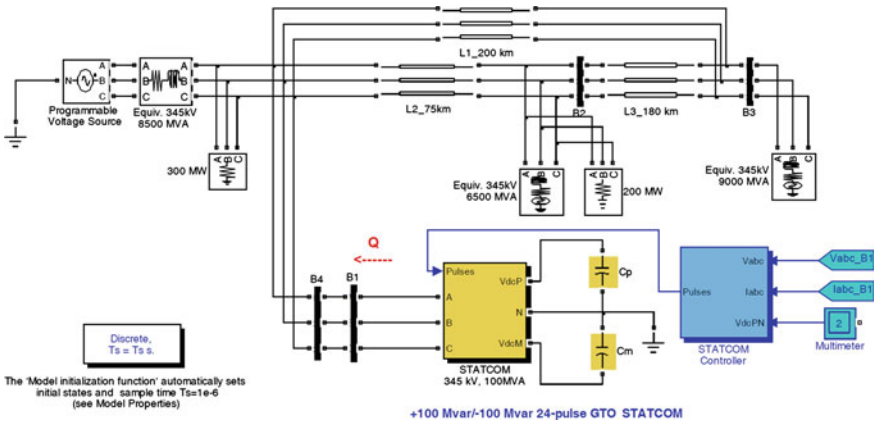

Fig. 6.8 24 pulses 100 MVA STATCOM simulation in SimPowerSystems, MATLAB/Simulink

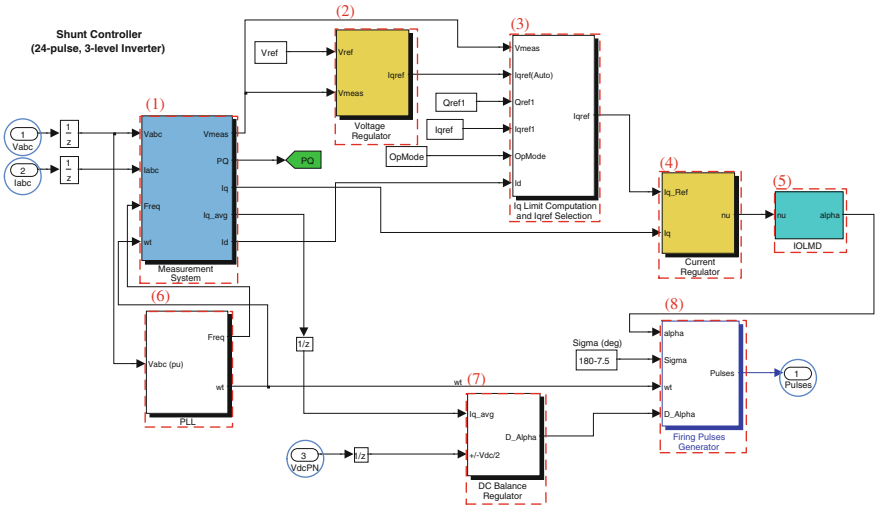

Fig. 6.9 Controller block of STATCOM

Figure 6.10 shows the time responses of the system when the simulation environment is that V' is 1 pu during 0.5 $\sim$ 0.8 s, and it decreases to 0.95 pu at 0.8 s and maintains the value until 1.1 s, then it increases to 1.05 pu and maintains its value until 1.1 s, and then return to the normal value, 1 pu at 1.4 s. The green dashed line indicates the performance of the IOL method, the purple dash-dotted line indicates the performance of the IOLD method, and blue solid line indicates the performance of the IOLMD method. Figure 6.10a and b show the I'_q performance with three IOL controllers introduced in this section when the I'_q reference, I'_{qref}, is changed from −0.8 to 0.8 pu and from 0.8 to −0.8 pu at 0.5 s, respectively. According to [9], the simulation model has additional power electronics components compared to the averaged model. I'_q response has the steady-state error when using only the P controller in the IOL feedback controller. In order to improve the steady-state error without appreciably affecting the transient response, a PI controller is used as a feedback controller. The gain of the PI controller is mainly set for the I'_q racking performance of the system with the IOLMD controller. When using the same PI controller gain, the output response of the systems with the IOL or IOLD controller has transient performances fail to meet the control specifications. These can be improved using a well-tuned PI controller or a derivative compensator. It is observe that time responses have large %OS at 1.1 s, due to the large amount of variation in V' from 0.95 to 1.05 pu. The variation of V' occurred in a very short time interval in order to observe the performance in the worst case. Figure 6.10c and e show the I'_d performance and V'_{dc} performance when I'_{qref} is changed from −0.8 to 0.8 pu, respectively. And Fig. 6.10d and f show the I'_d performance and V'_{dc} performance when I'_{qref} is changed from 0.8 pu to −0.8 pu, respectively. When I'_{qref} is 0.8 pu, the system with the IOLD method has less lightly damped poles than the system with the IOL method, but vice versa at $I'_{qref} = -0.8$ pu as

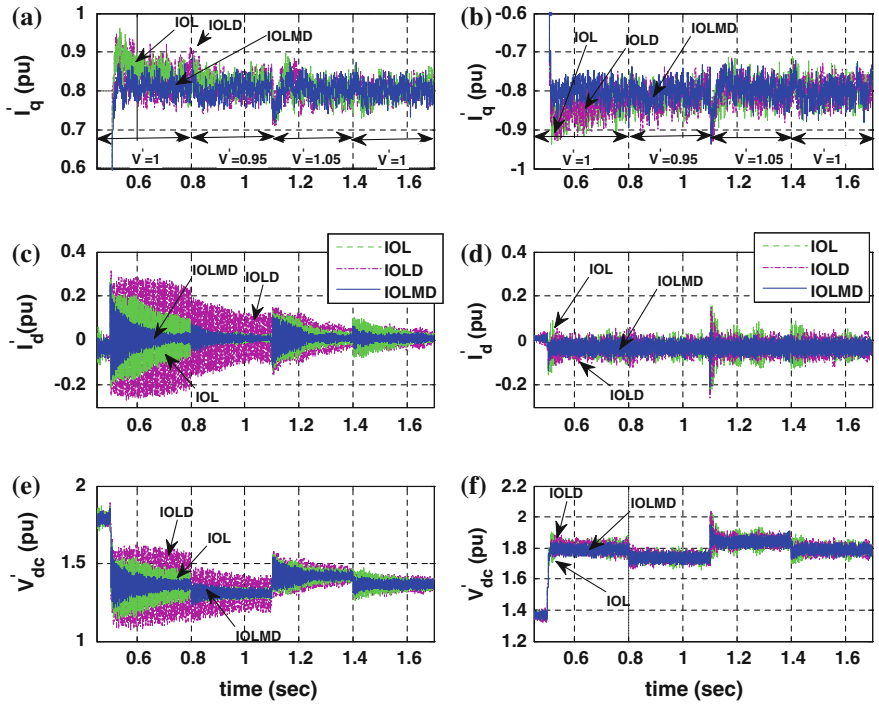

Fig. 6.10 I'_q tracking performances with the three IOL controllers (*Green dashed line* IOL, *Purple dash-dotted line* IOLD, *Blue solid line* IOLMD). **a** Reactive current oscillation comparison at I'_{qr}=0.8 [pu]. **b** Reactive current oscillation comparison at I'_{qr}=-0.8 [pu]. **c** Active current oscillation comparison at I'_{qr}=0.8 [pu]. **d** Reactive current oscillation comparison at I'_{qr}=-0.8 [pu]. **e** DC voltage oscillation comparison at I'_{qr}=0.8 [pu]. **f** DC voltage oscillation comparison at I'_{qr}=-0.8 [pu]

shown in Fig. 6.10. Therefore it cannot be not always guaranteed that the performance of the internal dynamics with the IOLD method gets better than that with the IOL method. Furthermore, if the reference or the network voltage is changed in a short time interval, then remaining oscillations will affect the next control period due to the slow response with either IOL or IOLD method. The IOLMD method shows the best transient performance among them at both operating points since the IOLMD method's poles are always further to the left than the those of the other methods due to the variable gain $\delta(x_2 - x_{2c})$.

6.4 Passivity-Based Control

Although the IOL methods introduced in Sect. 6.3 improves the performance of type 2 STATCOM systems, these methods are sensitive to parameter uncertainty and model mismatch [4, 5, 15]. Moreover, when the system works in the inductive

mode, undesired oscillation appears in the active current and DC voltage, since the system has lightly damped internal dynamics [7]. The undesired oscillations have adverse effects on both the life cycle of the electronic components and the power quality [8]. It can be solved by using a large capacitor, which increases the cost of the system. It is therefore motivated to design a controller considering the dynamics characteristics of type 2 STATCOM systems, in particular its passive characteristics, to resolve the problems without using a large capacitor. Passivity is a restatement of energy conservation in physical systems, and plays a central role in control techniques [10, 11]. Employing passivity control improves the robustness of controller implementation and simplifies implementation compared to the IOL method, since it avoids canceling the system nonlinearities exactly [12]. Tsai et al. designed a PBC consisting of two current inner loops and an outer loop for a type 1 STATCOM system [21]. The two current loops regulated the active and reactive currents, while the outer loop regulated the DC-bus voltage dynamics. However, since type 2 STATCOM systems have a limited degree of control, unlike type 1 systems, the PBC designed in [21, 22] cannot be applied to a type 2 STATCOM system.

In this section, the PBC control method designed in Euler-Lagrange model. Firstly, the general form of Euler-Lagrange (EL) model is introduced, and then the design of the PBC for STATCOM is introduced. A nonlinear damping term is added to PBC in order to achieve improved performance in terms of time response. Moreover, the desired dynamics is calculated by using numerical approximation. Lastly, the performance of the PBCND method is validated by using SimPowerSystems, MATLAB/Simulink.

6.4.1 Euler-Lagrange Formulation

The PBC achieves stabilization of the system; energy dissipative properties and workless force [23]. The EL form can be described as follows:

$$\mathbf{D}\,\dot{\mathbf{x}} = \mathbf{R}\mathbf{x} + \mathbf{J}(u) + \mathbf{b}u + \mathbf{E}, \tag{6.46}$$

where

$$\mathbf{D} = \mathbf{D}^T > 0,\ \mathbf{R} = \mathbf{R}^T < 0, \mathbf{J} + \mathbf{J}^T = 0.$$

Notice that, $\mathbf{D}$ is a diagonal positive definite matrix, $\mathbf{J}$ is skew symmetric matrixes, which represent the conservative forces of the system [23]. The matrix $\mathbf{R}$ is a negative semi-definite symmetric matrix representing the dissipation terms of the circuit model. $\mathbf{b}$ is, generally speaking, a constant vector and it may contain some components which are dependent on the external constant sources. The term $\mathbf{E}$ represents external constant voltage sources.

Based on the EL form, the PBC could be designed with a Lyapunov function candidate. In the next step, a PBC method will be designed for STATCOM based

on the EL form. Firstly, due to the small α, it is approximated that $\cos\alpha \approx 1$ to simplify the controller design [9]. Furthermore, to simplify the analysis, the fluctuation of the frequency ω in the AC system does not considered. The base frequency, ω_b, is set to be equal to that of the steady-state AC system; i.e., $\omega_b \approx \omega$ to [9]. Then, the EL model of STATCOM (6.8) can be expressed as

$$\mathbf{D}\,\dot{\mathbf{x}} = \mathbf{R}\mathbf{x} + \mathbf{J}\mathbf{x} + \mathbf{J}_u(u)\mathbf{x} + \mathbf{E}, \tag{6.47}$$

where

$$\mathbf{D} = \begin{bmatrix} 1 & 0 & 0 \\ 0 & 1 & 0 \\ 0 & 0 & \frac{2}{3C'L'} \end{bmatrix}, \quad \mathbf{R} = \begin{bmatrix} -\frac{R'_s\omega}{L'} & 0 & 0 \\ 0 & -\frac{R'_s\omega}{L'} & 0 \\ 0 & 0 & -\frac{2\omega}{3L'R'_p} \end{bmatrix}, \quad \mathbf{E} = \begin{bmatrix} -\frac{\omega|V'|}{L'} \\ 0 \\ 0 \end{bmatrix},$$

$$\mathbf{J} = \begin{bmatrix} 0 & \omega & \frac{k\omega}{L'} \\ -\omega & 0 & 0 \\ -\frac{k\omega}{L'} & 0 & 0 \end{bmatrix}, \quad \mathbf{J}_u(u) = \begin{bmatrix} 0 & 0 & 0 \\ 0 & 0 & \frac{k\omega}{L'}u \\ 0 & -\frac{k\omega}{L'}u & 0 \end{bmatrix}.$$

The first term, $\mathbf{Rx}$, indicates the dissipative forces in the system; the second terms, $\mathbf{Jx} + \mathbf{J}_u(u)\mathbf{x}$, represent the conservative forces; the last term, $\mathbf{E}$, represents the energy acquisition term [23]. Notice that u is the control input defined as $\sin\alpha$, and $\mathbf{b}$ is zero in this system.

6.4.2 Passivity-Based Controller for STATCOM

The PBC is designed based on error dynamics. The desired dynamics form is

$$\mathbf{D}\dot{\mathbf{x}}^{\mathbf{d}} = \mathbf{R}\mathbf{x}^{\mathbf{d}} + \mathbf{J}\mathbf{x}^{\mathbf{d}} + \mathbf{J}_u(u^d)\mathbf{x}^{\mathbf{d}} + \mathbf{E}, \tag{6.48}$$

and error dynamics are obtained by subtracting (6.48) from (6.46) as follows:

$$\mathbf{D}\,\dot{\mathbf{e}} = \mathbf{R}\mathbf{e} + \mathbf{J}\mathbf{e} + \mathbf{J}_u(u^d)\mathbf{x}^{\mathbf{d}} - \mathbf{J}_u(u)\mathbf{x}, \tag{6.49}$$

where

$$\mathbf{e} = \begin{bmatrix} e_1 \\ e_2 \\ e_3 \end{bmatrix} = \begin{bmatrix} x_1^d - x_1 \\ x_2^d - x_2 \\ x_3^d - x_3 \end{bmatrix}.$$

In order to analyze the stability of the system, a Lyapunov function candidate is considered as follows:

$$V_{ctrl} = \frac{1}{2}\mathbf{e}^T\mathbf{D}\mathbf{e}. \tag{6.50}$$

The derivative of this function (6.50) along the trajectories of the error dynamics (6.49) with respect to time gives

$$\dot{V}_{ctrl} = \frac{1}{2}\dot{\mathbf{e}}^T\mathbf{D}\mathbf{e} + \frac{1}{2}\mathbf{e}^T\mathbf{D}\dot{\mathbf{e}} = \mathbf{e}^T\mathbf{R}\mathbf{e} + \mathbf{e}^T\left[\mathbf{J}_u(u^d)\mathbf{x}^\mathbf{d} - \mathbf{J}_u(u)\mathbf{x}\right]. \tag{6.51}$$

Since $\mathbf{R} = \mathbf{R}^T < 0$ in (6.47), the first-term in (6.51) is negative definite. The second term can be rewritten as

$$\mathbf{e}^T\left[\mathbf{J}_u(u^d)\mathbf{x}^\mathbf{d} - \mathbf{J}_u(u)\mathbf{x}\right] = \frac{k\omega}{L'}(x_2^d x_3 - x_2 x_3^d)(u^d - u). \tag{6.52}$$

In this section, the task is to find a control law to stabilize the system (6.47) at an equilibrium point. A controller is designed as

$$u = \sin\alpha^d + v, \tag{6.53}$$

where

$$v = \left(sat(x_2^d x_3 - x_3^d x_2)\sum_{i=1}^{3}\rho_i e_i^2\right).$$

The saturation function in v is defined as follows:

$$sat(\mathbf{x}) = \begin{cases} v_{low}, & \text{if} \quad \mathbf{x} < v_{low}, \\ v_{up}, & \text{if} \quad \mathbf{x} > v_{up}, \\ \mathbf{x}, & \text{else.} \end{cases} \tag{6.54}$$

When $v_{low} \le v \le v_{up}$, (6.51) is easily rewritten as

$$\dot{V}_{ctrl} = \underbrace{-\frac{R_s'\omega}{L'}e_1^2 - \frac{R_s'\omega}{L'}e_2^2 - \frac{2\omega}{3L'R_p'}e_3^2}_{\mathbf{e}^T\mathbf{R}\mathbf{e}} \underbrace{-\frac{k\omega}{L'}(x_2^d x_3 - x_3^d x_2)^2(\rho_1 e_1^2 + \rho_2 e_2^2 + \rho_3 e_3^2)}_{\text{tunningfactor}}. \tag{6.55}$$

When the errors of states approach zero, the exponential convergence rate is primarily determined by the $\mathbf{e}^T\mathbf{R}\mathbf{e}$ term. However, when the states are far away from steady states, the rate is primarily determined by the magnitudes of the tuning factors as shown in (6.55). The initial value of the error could be defined as

$e_2(t_0) := x_2^d(t_0) - x_2(t_0)$, where $x_2^d(t_0)$ is the initial reference value and $x_2(t_0)$ is the actual initial value of x_2. If

$$\left|x_2^d x_3 - x_3^d x_2\right| > \varepsilon, \qquad \varepsilon > 0,$$

then there exists λ such that

$$|e_2(t)| \leq |e_2(t_0)| e^{-\lambda/2(t-t_0)}, \quad \lambda > 0. \tag{6.56}$$

The weighting factors, $\rho_{1,2,3}$, are the additional convergence rate of the performance, and the selection of $\rho_{1,2,3}$ should be considered via the parameters and the specification of the system.

6.4.3 Additional Nonlinear Damping-Based PBC

From (6.55), when the errors of state approach zero, the term $\left(x_2^d x_3 - x_3^d x_2\right)$ of the tuning factors becomes small. Thus, the tuning factors cannot effectively affect performance in this small error range. The system's convergence rate is determined by $\mathbf{e}^T\mathbf{Re}$ term, which is not large enough to prevent undesirable oscillations in the transient response.

Schauder and Mehta [2] designed a synthesized feedback controller to relocate the open loop transfer function zeroes. The synthesized feedback controller was defined as follows:

$$q = \frac{s}{1+sT}(I'_q - I'_{qo(critical)})V'_{dc}, \tag{6.57}$$

where $I'_{qo(critical)} = 2/3KC'V'_{dc}$. This controller ensures that the closed-loop root-locus is always in the LHP, indicating stable operation. Lee et al. [24] designed a modified non-linear damping controller based on feedback linearization to tame the internal dynamics. They analyzed how this controller affected the poles of the internal dynamics, and showed reduced oscillations in the internal dynamics.

A PBCND is proposed to achieve improved performance in terms of time response. This PBCND is a PBC (6.53) with nonlinear damping, expressed as follows:

$$u = \sin\alpha^d + v + K_g(\mathbf{x})\dot{e}_1, \tag{6.58}$$

where

$$K_g(\mathbf{x}) = g(\mathbf{x})\left(\frac{2}{3kC'}x_3 - x_2\right).$$

Theorem 6.2 [13] *Suppose that the system* (6.8) *uses PBCND* (6.58), *if a gain* $g(\mathbf{x})$ *is designed as*

$$K_g(\mathbf{x}) = a\ \mathrm{sgn}\left(\left(x_2^d x_3 - x_3^d x_2\right)\left(\frac{2}{3kC'}x_3 - x_2\right)(\dot{e}_1)\right), \tag{6.59}$$

where

$$a > 0, \quad \mathrm{sgn}(\mathbf{x}) = \begin{cases} 1, & \text{if } \mathbf{x} > 0, \\ -1, & \text{if } \mathbf{x} < 0, \\ 0, & \text{else}, \end{cases}$$

then the zero equilibrium point of the error dynamics is globally exponentially stable.

The stability of the closed-loop system with PBCND can be easily proven using Lyapunov theorem. Due to the page limit, the detailed proof is omitted in this section [13].

6.4.4 Numerical Approximation of Desired Dynamics

To design the PBCND based on error dynamics (6.49), it is need to determine the desired dynamics. In this section, x_2^d is generated by using 5th-order profile in order to ensure every operating point moves smoothly enough from one to the other. And the other desired states, x_1^d and x_3^d, and input, u^{d}, are calculated approximately for implementation based on the STATCM dynamics.

Firstly, it will be showed that every operating point can be calculated via the output by using the system model (6.8). It is known that if the Jacobian matrix of $f(\mathbf{x}, \alpha)$ at operating points $x_{1\mathrm{o}}$, $x_{3\mathrm{o}}$, α_{o}, as follows:

$$\frac{\partial f(\mathbf{x},\alpha)}{\partial x_2} = \begin{pmatrix} \frac{\partial f_1(\mathbf{x},\alpha)}{\partial x_2} \\ \frac{\partial f_2(\mathbf{x},\alpha)}{\partial x_2} \\ \frac{\partial f_3(\mathbf{x},\alpha)}{\partial x_2} \end{pmatrix} = \begin{pmatrix} -\frac{R'_s\omega_b}{L'} & \frac{k\omega_b}{L'}\cos\alpha_{\mathrm{o}} & -\frac{k\omega_b}{L'}x_{3\mathrm{o}}\sin\alpha_{\mathrm{o}} \\ -\omega & \frac{k\omega_b}{L'}\sin\alpha_{\mathrm{o}} & -\frac{k\omega_b}{L'}x_{3\mathrm{o}}\cos\alpha_{\mathrm{o}} \\ -\frac{3}{2}kC'\omega_b\cos\alpha_{\mathrm{o}} & -\frac{\omega_b C'}{R'_p} & \frac{3}{2}kC'\omega_b(x_{1\mathrm{o}}\sin\alpha_{\mathrm{o}} - x_{2\mathrm{o}}\cos\alpha_{\mathrm{o}}) \end{pmatrix}, \tag{6.60}$$

which is nonsingular in the operating range [9], then, an equilibrium point $\mathbf{x_o} = [\mathrm{x}_{10}\ \mathrm{x}_{20}\ \mathrm{x}_{30}]^T$ and the associated α_{o} can be uniquely obtained via a given operation point of x_2 [25]. In this section, x_2^d is generated by using the 5th-order profile in order to

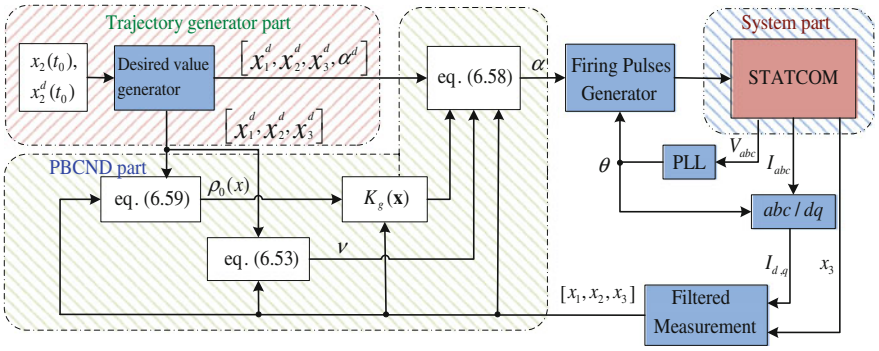

Fig. 6.11 Block diagram of the PBCND method

change the reference smoothly enough, and track it with consideration of control specifications. Finally, a block diagram of the PBCND method is illustrated in Fig. 6.11. It is possible that the system has chattering phenomenon with a signum function in the PBCND method (6.58). However, a dead-band algorithm could be used to overcome this problem, and it will not discuss in detail in this section.

6.4.5 Performance of the PBCND Method

In this part, some simulations are executed to validate the proposed method using the same model introduced in Sect. 6.3 including power electronic devices and driving characteristics in SimPowerSystems, MATLAB/Simulink. Figure 6.12 shows the time responses of the system when V' is varied within the range 95–105 %. The red dashed line indicates the performance of the PBCND method and blue solid line indicates the IOLMD method. It is clear from Fig. 6.12b, d, and f that the time responses of I'_q, I'_d and V'_{dc} using IOLMD and PBCND show similar performance when I'_{qref} is changed from 0.8 to −0.8 pu. In other case, when I'_{qref} is changed from −0.8 to 0.8 pu, the I'_q performance of the IOLMD is better than that of the PBCND. Since the IOL is an effective tracking method. However, the magnitude of oscillations of I'_d in transient responses is smaller when the PBCND is used than that when the IOLMD is used. Large oscillations will negatively affect the lifetime of power electronic components as well as power quality. The PBCND method considers the inherent passivity property of the system, thereby reducing oscillations of both V'_{dc} and I'_d in the transient responses. Moreover, both V'_{dc} and I'_d of the PBCND converged relatively rapidly to steady state, as shown in Fig. 6.12c, e.

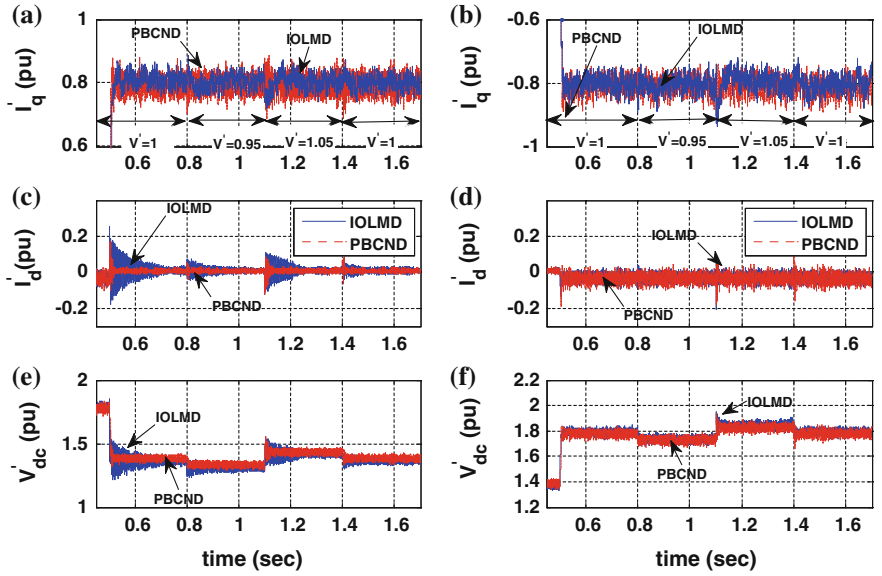

Fig. 6.12 Time responses of the STATCOM when the variation of V' in the range 95–105 %. (*Red dashed line* PBCND, *Blue solid line* IOLMD method). **a** Reactive current oscillation comparison at I'_{qr}=0.8 [pu]. **b** Reactive current oscillation comparison at I'_{qr}=-0.8 [pu]. **c** Active current oscillation comparison at I'_{qr}=0.8 [pu]. **d** Reactive current oscillation comparison at I'_{qr}=-0.8 [pu]. **e** DC voltage oscillation comparison at I'_{qr}=0.8 [pu]. **f** DC voltage oscillation comparison at I'_{qr}=-0.8 [pu]

6.5 Advanced Control Strategy

The IOL and PBC approaches were introduced to apply to type 2 STATCOM systems in Sects. 6.3 and 6.4, respectively. However, all the approaches were designed based on an approximated model of type 2 STATCOM, thus those methods are only guaranteed that the closed-loop system has a locally stable equilibrium point. Moreover, the stability region for the IOLMD method proposed in Sect. 6.3 is numerically extensively determined. Recently, some nonlinear control methods were designed with a non-approximated type 2 STATCOM model.

In this section, our main point is to design a nonlinear controller with a non-approximated model of type 2 STATCOM systems in order to improve the performance in time domain and enlarge the stability region. For these reasons, the dynamic extension algorithm is used to achieve an input-affine system, and generate the tracking control law based on the dynamic extended model. The PCH approach is applied for the extended system. The PCH approach is a method that considers the passivity property.

6.5.1 Dynamic Extension of STATCOM System

It is obvious that the system (6.8) is not an input affine system, since the dynamics includes the multiplication of the state variables by the sinusoidal control. Here, an additional state x_4 and a new input u_a for the system (6.8) could be defined as follows:

$$\begin{aligned} x_4 &:= \sin\alpha, \\ u_a &:= \dot{\alpha}. \end{aligned} \tag{6.61}$$

The system (6.8) is transformed into an input affine system with the extended state, $\mathbf{x_a} = (x_1, x_2, x_3, x_4)^T$, and the new control input, u_a, as follows:

$$\begin{aligned} \dot{\mathbf{x}}_{\boldsymbol{a}} &= f_a(\mathbf{x_a}) + g_a(\mathbf{x_a})u_a, \\ y &= h_a(\mathbf{x_a}), \end{aligned} \tag{6.62}$$

where

$$f_a(\mathbf{x_a}) = \begin{pmatrix} -\frac{R_s'\omega_b}{L'}x_1 + \omega x_2 + \frac{k\omega_b}{L'}x_3\sqrt{1-x_4^2} - \frac{\omega_b}{L'}|V'| \\ -\omega x_1 - \frac{R_s'\omega_b}{L'}x_2 + \frac{k\omega_b}{L'}x_3x_4 \\ -\frac{3}{2}kC'\omega_b x_1\sqrt{1-x_4^2} - \frac{3}{2}kC'\omega_b x_2x_4 - \frac{\omega_b C'}{R_p'}x_3 \\ 0 \end{pmatrix},$$

$$g_a(\mathbf{x_a}) = \begin{pmatrix} 0 \\ 0 \\ 0 \\ \sqrt{1-x_4^2} \end{pmatrix}, \qquad h_a(\mathbf{x_a}) = x_2.$$

For the input affine system (6.62), the system has

$$\frac{\partial h_a}{\partial \mathbf{x_a}} = (\,0 \quad 1 \quad 0 \quad 0\,), \tag{6.63}$$

$$\begin{aligned} L_g h_a(\mathbf{x_a}) &= 0, \\ L_f h_a(\mathbf{x_a}) &= -\omega x_1 - \frac{R_s'\omega_b}{L'}x_2 + \frac{k\omega_b}{L'}x_3x_4, \\ \frac{\partial\left(L_f h_a\right)}{\partial \mathbf{x_a}} &= \left(-\omega - \frac{R_s'\omega_b}{L'}\frac{k\omega_b}{L'}x_4 \frac{k\omega_b}{L'}x_3\right), \\ L_g L_f h_a(\mathbf{x_a}) &= \frac{k\omega_b}{L'}x_3\sqrt{1-x_4^2}. \end{aligned}$$

Thus, the system (6.62) has relative degree $\gamma = 2$ in $\mathbb{R}^4$. In order to find a normal form, it is set as follows

$$\begin{aligned} z_1 &:= \phi_1(\mathbf{x_a}) = h_a(\mathbf{x_a}) = x_2, \\ z_2 &:= \phi_2(\mathbf{x_a}) = L_f h_a(\mathbf{x_a}) = -\omega x_1 - \frac{R_s'\omega_b}{L'}x_2 + \frac{k\omega_b}{L'}x_3 x_4, \end{aligned} \tag{6.64}$$

and the system seeks for two functions ϕ_3 and ϕ_4 such that

$$\begin{aligned} \frac{\partial \phi_3}{\partial \mathbf{x_a}} g_a(\mathbf{x_a}) &= \frac{\partial \phi_3}{\partial x_4}\sqrt{1 - x_4^2} = 0, \\ \frac{\partial \phi_4}{\partial \mathbf{x_a}} g_a(\mathbf{x_a}) &= \frac{\partial \phi_4}{\partial x_4}\sqrt{1 - x_4^2} = 0. \end{aligned} \tag{6.65}$$

For simplification, two new variables are defined as follows:

$$\begin{aligned} z_3 &:= \phi_3 = x_3, \\ z_4 &:= \phi_4 = x_1, \end{aligned} \tag{6.66}$$

satisfy the above conditions (6.65). These four variables, (6.64) and (6.66), define a transformation $\mathbf{z} = [z_1\ z_2\ z_3\ z_4]^T = \Phi(\mathbf{x_a})$ whose Jacobian matrix,

$$\frac{\partial \Phi}{\partial \mathbf{x_a}} = \begin{bmatrix} 0 & 1 & 0 & 0 \\ -\omega & -\frac{R_s'\omega_b}{L'} & \frac{k\omega_b}{L'}x_4 & \frac{k\omega_b}{L'}x_3 \\ 0 & 0 & 1 & 0 \\ 1 & 0 & 0 & 0 \end{bmatrix}, \tag{6.67}$$

is nonsingular in the operating range because of $x_3 \neq 0$. Thus, $\Phi(\mathbf{x_a})$ is a local diffeomorphism [4]. The inverse transformation is given by

$$x_1 = z_4, \quad x_2 = z_1, \quad x_3 = z_3, \quad x_4 = \frac{z_2 + \omega z_4 + \frac{R_s'\omega_b}{L'}z_1}{\frac{k\omega_b}{L'}z_3}. \tag{6.68}$$

In the new coordinates, the system (6.62) is described by

$$\begin{aligned} \dot{z}_1 &= z_2, \\ \dot{z}_2 &= b(\mathbf{z}) + a(\mathbf{z})u_a, \\ \dot{z}_3 &= -\frac{3}{2}kC'\omega_b z_4 q_c(\mathbf{z})^{1/2} - \frac{3}{2}kC'\omega_b z_1(1 - q_c(\mathbf{z}))^{1/2} - \frac{\omega_b C'}{R_p'}z_3, \\ \dot{z}_4 &= -\frac{R_s'\omega_b}{L'}z_4 + \omega z_1 + \frac{k\omega_b}{L'}z_3 q_c(\mathbf{z})^{1/2} - \frac{\omega_b}{L'}|V'|, \end{aligned} \tag{6.69}$$

where

$$b(\mathbf{z}) = -\omega\left(-\frac{R_s'\omega_b}{L'}z_4 + \omega z_1 + \frac{k\omega_b}{L'}z_3 q_c(\mathbf{z})^{1/2} - \frac{\omega_b}{L'}|V'|\right) - \frac{R_s'\omega_b}{L'}z_2$$
$$+\frac{k\omega_b}{L'}(1-q_c(\mathbf{z}))^{1/2}\left(-\frac{3}{2}kC'\omega_b z_3 q_c(\mathbf{z})^{1/2} - \frac{3}{2}kC'\omega_b z_1(1-q_c(\mathbf{z}))^{1/2} - \frac{\omega_b C'}{R_p'}z_3\right),$$
$$a(\mathbf{z}) = \frac{k\omega_b}{L'}z_3 q_c(\mathbf{z})^{1/2}, \quad q_c(\mathbf{z}) = 1 - \left(\frac{z_2 + \omega z_4 + \frac{k\omega_b}{L'}z_1}{\frac{k\omega_b}{L'}z_3}\right)^2.$$

6.5.2 Desired Control Input

If the desired output, z_1^d, is given, then the other desired values of the states can be obtained using the dynamics (6.69) in the new coordinates as follows;

$$\begin{aligned}
z_2^d &= \dot{z}_1^d,\\
\dot{z}_3^d &= -\frac{3}{2}kC'\omega_b z_4^d q_c(\mathbf{z^d})^{1/2} - \frac{3}{2}kC'\omega_b z_1^d(1-q_c(\mathbf{z^d}))^{1/2} - \frac{\omega_b C'}{R_p'}z_3^d,\\
\dot{z}_4^d &= -\frac{R_s'\omega_b}{L'}z_4^d + \omega z_1^d + \frac{k\omega_b}{L'}z_3^d q_c(\mathbf{z^d})^{1/2} - \frac{\omega_b}{L'}|V'|,
\end{aligned} \tag{6.70}$$

where

$$q_c(\mathbf{z^d}) = 1 - \left(\frac{z_2^d + \omega z_4^d + \frac{k\omega_b}{L'}z_1^d}{\frac{k\omega_b}{L'}z_3^d}\right)^2.$$

Thus, from (6.69) and (6.70) the desired new control input can be calculated as

$$u_a^d = \frac{-b(\mathbf{z^d}) + v}{a(\mathbf{z^d})}, \tag{6.71}$$

where

$$v = \ddot{z}_1^d - K_1(z_1 - \dot{z}_1^d) - K_2(z_1 - z_1^d).$$

Here, z_1^d is generated by 5th-order profile, $K_1 > 0$ and $K_2 > 0$. Notice that $\alpha(\mathbf{z^d}) \neq 0$ in the operating range, since $z_3^d = x_3^d \neq 0$ and $q_c(\mathbf{z^d}) = \cos^2\alpha^d \neq 0$.

6.5.3 Port-Controlled Hamiltonian Method

For the original system (6.8), it takes

$$H(\mathbf{x}) = \frac{1}{2}\mathbf{x}^T\mathbf{S}\mathbf{x}, \tag{6.72}$$

where

$$\mathbf{S} = \begin{bmatrix} 1 & 0 & 0 \\ 0 & 1 & 0 \\ 0 & 0 & \frac{2}{3L'C'} \end{bmatrix}.$$

Then the system (6.8) is put in the PCH form described in [14] as follows:

$$\dot{\mathbf{x}} = (\Im(\alpha) - \Re)\frac{\partial H(\mathbf{x})}{\partial \mathbf{x}} + G, \tag{6.73}$$

where

$$\Im(\alpha) = \begin{bmatrix} 0 & \omega & \frac{3}{2}kC'\omega_b\cos\alpha \\ -\omega & 0 & \frac{3}{2}kC'\omega_b\sin\alpha \\ -\frac{3}{2}kC'\omega_b\cos\alpha & -\frac{3}{2}kC'\omega_b\sin\alpha & 0 \end{bmatrix},$$

$$\Re = \begin{bmatrix} \frac{R_s'\omega_b}{L'} & 0 & 0 \\ 0 & \frac{R_s'\omega_b}{L'} & 0 \\ 0 & 0 & \frac{3\omega_b L'C'^2}{2R_p'} \end{bmatrix}, \qquad G = \begin{bmatrix} -\frac{\omega_b}{L'}|V'| \\ 0 \\ 0 \end{bmatrix}.$$

Here, the desired control input is taken based on (6.62) and (6.71) as

$$\alpha^d = \int u_\alpha^d dt, \tag{6.74}$$

that satisfies

$$\dot{\mathbf{x}}^{\mathbf{d}} = (\Im(\alpha^d) - \Re)\frac{\partial H(\mathbf{x}^{\mathbf{d}})}{\partial \mathbf{x}} + G. \tag{6.75}$$

If $\alpha = \alpha^d$ is taken for the system as Theorem 1 in [14], then the error dynamics of the system has an exponentially stable equilibrium point at the origin. The whole procedure of the proposed method is illustrated in Fig. 6.13. The current initial value and final desired value of x_2 are indicated by $x_2(t_0)$ and $x_2(t_f)$, respectively.

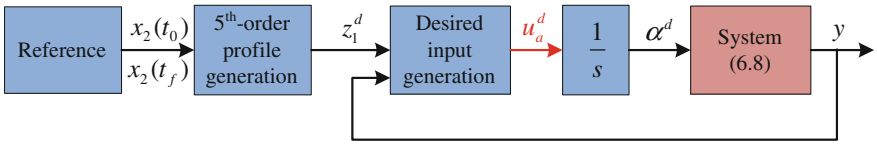

Fig. 6.13 Block diagram of the PCH control system

6.5.4 Performance of PCH Method

To validate this method, the simulation using the topological model was performed in SimPowerSystems, MATLAB/Simulink. The PCH method was compared to the IOLMD developed in Sect. 6.3. Especially, the PCH method improves the transient performance of the system at the weakly controllable operating point as analyzed in Sect. 6.3.3. Figure 6.14 shows the time responses of the system when V' is varied within the range 95−105 %. The red dashed line is the performance of the PCH method and blue solid line is the performance of the IOLMD method. Figure 6.14a, c, and e show the time responses of the STATCOM when I'_{qref} is changed from −0.8 to 0.8 pu, and Fig. 6.14b, d, and f show the time responses of the STATCOM

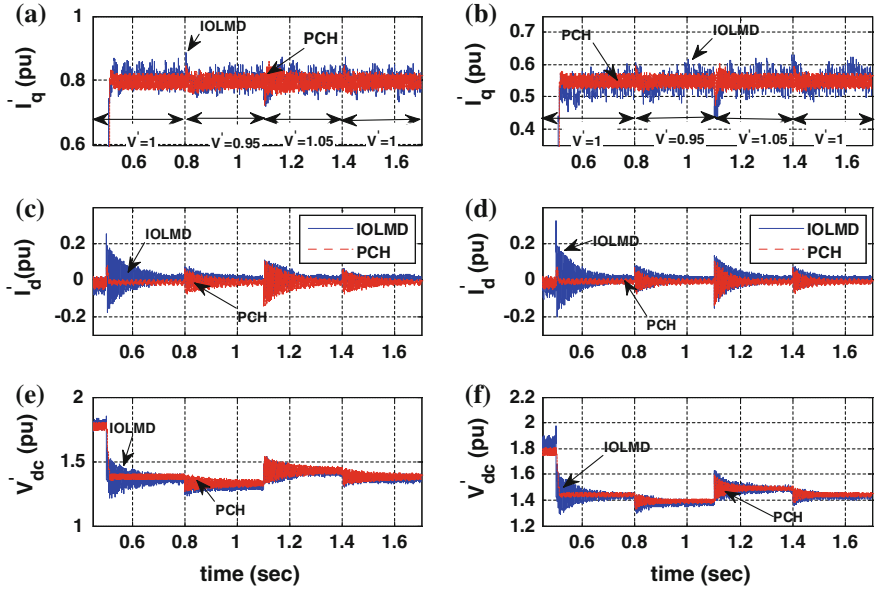

Fig. 6.14 Time responses of the STATCOM when the variation of V' in the range 95–105 %. (*Red dashed line* PCH method, *Blue solid line* IOLMD method). **a** Reactive current oscillation comparison at I'_{qr}=0.8 [pu]. **b** Reactive current oscillation comparison at I'_{qr}=-0.8 [pu]. **c** Active current oscillation comparison at I'_{qr}=0.8 [pu]. **d** Reactive current oscillation comparison at I'_{qr}=-0.8 [pu]. **e** DC voltage oscillation comparison at I'_{qr}=0.8 [pu]. **f** DC voltage oscillation comparison at I'_{qr}=-0.8 [pu]

when I'_{qref} is changed from −0.8 to 0.5521 pu, which is the weakly controllable operating point introduced in Sect. 6.3. It is clear from Fig. 6.14a and b that the time responses of I'_d using IOLMD and PCH show similar performance. Since the desired input of PCH method is generated based on IOL method as shown in (6.71). However, when I'_{qref} is changed from one operating point to another operating point, I'_d and V'_{dc} performance of the PCH method have smaller overshoot and faster convergence to steady state than those of the IOLMD. Since the PCH method considers the inherent passivity property of the system. In addition, the differences between the time performances of IOLMD and PCH to the grid voltage variations are not significant since the objective of the case studies is not to consider the improvement in transient response in the presence of the grid voltage variations but to regulate the reactive current.

References

1. Hingorani N, Gyugyi L, El-Hawary M (2000) Understanding facts: concepts and technology of flexible AC transmission systems. IEEE press, New Jersey
2. Schauder C, Mehta H (1993) Vector analysis and control of advanced static VAR compensators. IET Gen Transm Distrib 140(4):299–306
3. Schauder C (1994) Advanced static VAR compensator control system. US Patent no. US5,329,221
4. Isidori A (1995) Nonlinear control systems, 3rd edn. Springer, Berlin
5. Khalil H (2002) Nonlinear systems, 3rd edn. Prentice Hall, New Jersey
6. Petitclair P, Bacha S, Rognon JP (1996) Averaged modelling and nonlinear control of an advanced static VAR compensator (ASVC). In: Proceedings IEEE power electronics specialists conference, pp 753–758
7. Petitclair P, Bacha S, Ferrieux J-P (1997) Optimized linearization via feedback control law for a STATCOM. In: Proceeding of IEEE industrial applied society annual meeting, pp 880–885
8. Han Y, Lee YO, Chung CC (2009) A modified nonlinear damping of zero-dynamics via feedback control for a STATCOM. In: Proceedings IEEE power technical, pp 1–8
9. Han Y, Lee YO, Chung CC (2011) Modified non-linear damping of internal dynamics via feedback linearisation for static synchronous compensator. IET Gen Transm Distrib 5 (9):930–940
10. Ortega R, Garcia-Canseco E (2004) Interconnection and damping assignment passivity-based control: a survey. Eur J Contr 10(5):432–450
11. Ortega R, Loria A, Nicklasson P, Sira-Ramirez H (1998) Passivity-based control of Euler-Lagrange system: mechanical, electrical and electromechanical applications. Springer, Berlin
12. Lee T-S (2004) Lagrangian modeling and passivity-based control of three- phase AC/DC voltage-source converters. IEEE Trans Ind Electron 51(4):892–902
13. Gui Y, Lee YO, Han Y, Kim W, Chung CC (2012) Passivity-based control with nonlinear damping for STATCOM system. In: Proceedings of IEEE conference decision control, pp 1715–1720
14. Gui Y, Chang DE, Chung CC (2013) Tracking controller design methodology for passive port-controlled Hamiltonians with application to type-2 STATCOM systems. In: Proceedings of IEEE conference decision control, pp 1653–1658
15. Slotine J, Li W (1991) Applied nonlinear control. Prentice-Hall, Englewood Cliffs

16. Lee YO, Han Y, Chung CC (2012) Output tracking control with enhanced damping of internal dynamics and its output boundedness for STATCOM system. IET Contr Theor Appl 6 (10):1445–1455
17. Chen CT (1995) Linear system theory and design. Oxford University Press, Oxford
18. Hamdan AMA (1999) An investigation of the significance of singular value decomposition in power system dynamics. Int J Electr Power Energy Syst 21(6):417–424
19. Kailath T (1980) Linear systems. Prentice-Hall, New Jersey
20. Lee YO, Chung CC (2013) Uniform output regulation via approximated input–output linearisation for lightly damped internal dynamics. Int J Control 86(1):159–171
21. Tsai H-C, Chu C-C, Lee S-H (2005) Passivity-based nonlinear STATCOM controller design for improving transient stability of power systems. In: Proceedings IEEE/PES transmission distribution conference exhibition, pp 1–5
22. Yazdani A (2009) Energy and voltage management methods for multilevel converters for bulk power system power quality improvement. PhD dissertation, Missouri University of Science and Technology
23. Sira-Ramirez H, Silva-Ortigoza R (2006) Control design techniques in power electronics devices. Springer, Berlin
24. Lee YO, Han Y, Chung CC (2010) Output tracking control with enhanced damping of internal dynamics and its output boundedness. In: Proceedings IEEE conference decision control, pp 3964–3971
25. Marsden J, Hoffman M (1993) Elementary classical analysis, 2nd edn. WH Freeman, London

Chapter 7
Versatile Control of STATCOMs Using Multiple Reference Frames

Miguel Ochoa-Giménez, Aurelio García-Cerrada, Javier Roldán-Pérez, Juan L. Zamora-Macho, Pablo García-González and Emilo Bueno

Abstract This chapter first reviews the fundamentals of active and reactive power control using STATCOMs. Then, two current control algorithms, namely selective/resonant controllers and repetitive controllers, are presented that provide a STATCOM with the capability of controlling the harmonics of the current injected into the PCC. Finally, the use of synchronously-rotating reference frames is generalized so that current harmonic control can also be achieved using PI controllers. An efficient application of the last technique is explained in detailed and a number of experimental results are presented. It will be demonstrated that versatile control of STATCOMs is straightforward using this technique even if the grid frequency varies. This technique can be applicable to both, traditional, strong and centralised electric power systems and those to come in the future with large amounts of distributed generation.

Keywords STATCOM · VSC · Harmonic control · Selective control · Repetitive control · Multiple reference frames

M. Ochoa-Giménez · A. García-Cerrada (✉) · J. Roldán-Pérez · J.L. Zamora-Macho · P. García-González
Institute for Research in Technology and Department of Electronics, Control Engineering and Communications, Comillas Pontifical University, Madrid, Spain
e-mail: aurelio@iit.upcomillas.es

M. Ochoa-Giménez
e-mail: miguel.ochoa@iit.upcomillas.es

J. Roldán-Pérez
e-mail: javier.roldan@iit.upcomillas.es

J.L. Zamora-Macho
e-mail: JuanLuis.Zamora@iit.upcomillas.es

P. García-González
e-mail: pablo@dea.icai.upcomillas.es

E. Bueno
Electronics Department, University of Alcalá, Alcalá de Henares, Spain
e-mail: emilio@depeca.uah.es

F. Shahnia et al. (eds.), *Static Compensators (STATCOMs) in Power Systems*, Power Systems, DOI 10.1007/978-981-287-281-4_7

7.1 Introduction

STATCOMs are typical shunt power electronics-based devices (see Fig. 7.1), used in power systems for multiple purposes [1]. Originally, STATCOMs were intended for reactive power control as a superior alternative to thyristor-controlled devices such as Thyristor-Controlled Reactors (TCRs) or Thyristor-Switched Capacitors (TSCs) [2]. Reactive power compensation in TCRs and TSC depends on the point of common coupling (PCC) voltage unlike in STATCOMs which could overcome this limitation thanks to the use of electronic switches capable of controlled ON-OFF and OFF-ON commutation. Also thanks to their controlled commutation, STATCOMs provide a much faster dynamic performance [3]. STATCOMs rapidly evolved from square wave multi-pulse converters [4–6] to pulse width modulation (PWM)-controlled converters [7–9] making it possible a fast and accurate active and reactive power control at the PCC.

Nowadays STATCOMs are used for reactive power compensation mainly, in applications such as improving fault-ride-through of wind generators [10] or compensating voltage drops at the transmission level or voltage fluctuations at the distribution level [11, 12]. When STATCOMs are used in distributions systems they are often called Distribution Static Compensators (DSTATCOMs) [13].

The most classical approach to the control of a STATCOM [9] (reactive power control) only addresses the control of the fundamental components of the current injected in the PCC: the positive-sequence current of the grid frequency. Meanwhile, the same shunt-connected components in Fig. 7.1 (left) namely, a voltage source converter (VSC), a transformer (optional) and a connection filter, are

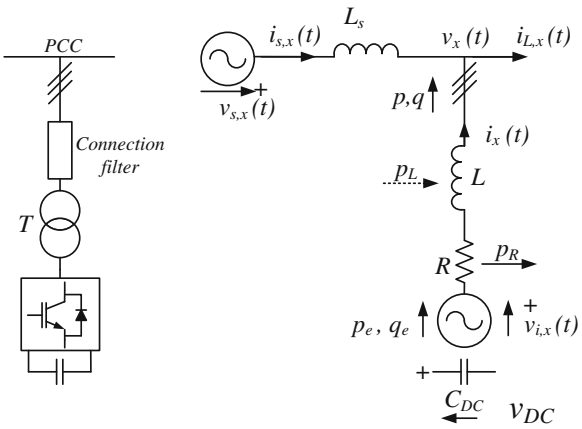

Fig. 7.1 STATCOM schematics (*left*) and simplified model (*right*), nomenclature: p and q are the instantaneous real and reactive power injected by the STATCOM into the PCC, p_R is the power lost in the filter resistance, p_L is the power consumed in the filter plus transformer inductance, p_e and q_e are the real and instantaneous reactive power injected by the electronic converter into the AC system. Subscript x in voltages and currents represents any of the three phases a, b or c

increasingly being used to control the harmonic currents (not only the fundamental component of the grid frequency) injected in the PCC. In this application, the control of the filter current (i, in Fig. 7.1) is carried out using a two-part structure. A main controller tackles the positive sequence of the current component of the grid frequency (active and reactive power control). Meanwhile, an auxiliary controller tackles (a) the negative sequence of the current component of the grid frequency and (b) the current harmonics (frequencies multiple of the grid one). Along these lines, the current injected by the VSC (i) can be forced to compensate the harmonics in the non-linear load current (i_L) so that the grid (v_s) sees an ideal sinusoidal current (i_s). When the parallel compensator is used for this purpose, it is typically called Shunt Active Power Filter (Shunt APF).

Proportional-Integral (PI) controllers using Park's transformation of three-phase electrical variables into the so-called synchronous reference frame (SRF) is often used for power flow control in STATCOMs and other power electronics devices. The speed of the synchronously-rotating frame is made equal to the grid frequency so that all variables of that frequency and positive sequence are DC variables in steady state and simple PI controllers are effective [9, 14, 15]. However, harmonics are still seen as sinusoids in that frame and cannot be tackled so easily. In fact, the internal model principle (IMP) of control systems [16] states, clearly, that to track and/or reject a sinusoidal signal of frequency ω rad/s in a control system, poles at $\pm j\omega$ must be included in the denominator of the controller transfer function.

Current harmonic control was first addressed using resonant terms (selective controllers) as in [17] and [18], with poles, as required, in $\pm mj\omega$ ("m" is the harmonic number). This control method guarantees zero-error in steady-state at the selected frequencies and adaptation to frequency variations could be included. Although frequency variations are not large in traditional power systems, they do exist and are bound to be larger in power systems with a significant contribution of renewable energy sources, above all if some parts of the system must work in island mode. However, one resonant term must be designed and added for each harmonic to be suppressed, increasing the effort in the controller design stage. Furthermore, it is difficult to achieve a precise implementation in discrete time.

A more comprehensive approach was later found with the so-called "repetitive controller" (RC) [19, 20]. The core of a RC is a delay that can be easily implemented in discrete time and it works as a set of selective controllers for all harmonics of interest. However, flexibility is lost when looking at individual harmonics and the controller is very sensitive to frequency variations. The latter problem requires attention, always, and has finally been addressed in power electronics in [21] where a promising solution is presented.

The use of multiple reference frames for active power filters (harmonic control) was proposed in [22]. In this approach, Park's transformation is applied several times to the three-phase magnitudes using, each time, the position of a reference frame which rotates with respect to the fundamental-frequency d-q reference frame with an angular speed related to a harmonic frequency. Consequently, several reference frames rotating synchronously with the harmonic space vectors (harmonic synchronous reference frames or HSRF) are used. In this scenario, PI controllers

can be designed independently for each harmonic once it is referred to the appropriate HSRF. This procedure is very attractive from the design viewpoint but has always been considered as cumbersome and computationally expensive due to the fact that many trigonometric functions have to be calculated in real-time.

Harmonic control has also been tackled using a DFT (discrete fourier transform) or a DCT (discrete cosine transform) as in [23] and [24]. In these cases, the sampling frequency for the harmonic controller must be slower than the one for the main voltage and current controllers and it has to be chosen carefully as a multiple of the fundamental frequency of the signals to be sampled. The second condition is hard to satisfy if the grid frequency varies. In addition. the storage of the DFT coefficients and the management of the data buffers required for each harmonic bring a large computational effort.

In this chapter, current control on STATCOMs with the purpose of controlling instantaneous active (real) and instantaneous reactive power and current harmonics will be addressed. First of all, active and reactive power control using a SRF will be explained. Secondly, the two most popular alternatives for harmonic control will be reviewed, namely, selective and repetitive controllers. Finally, the strategy based on HSRF will be revisited showing that its implementation can be greatly eased whilst maintaining excellent performance. It will be demonstrated that most of the trigonometric functions used in Park's transformations can be avoided in order to reduce the computation effort. Additionally, variations of the grid frequency will be considered to show the excellent frequency-adaptation capability of the algorithm. Results of the HSRF-based controller applied to a laboratory prototype will be presented in the context of the versatile control for a STATCOM where active and reactive power control is addressed together with current harmonic control and voltage support.

7.2 Fundamentals of the Control of a STATCOM

7.2.1 Park's Transformation

A STATCOM was depicted in Fig. 7.1 together with a single-phase simplified model using an L filter for the connection at the PCC. This filter is used to limit the short circuit current to the PCC and to prevent the switching harmonics of the VSC from affecting the grid. Assuming that fast control of the VSC can be achieved using PWM alone or together with a multilevel structure, the VSC output voltage (v_i in Fig. 7.1) can be represented by a fully controllable three-phase voltage source and a three-phase electrical model can be written as follows:

$$L\frac{d}{dt}\begin{bmatrix} i_a(t) \\ i_b(t) \\ i_c(t) \end{bmatrix} = -R\begin{bmatrix} i_a(t) \\ i_b(t) \\ i_c(t) \end{bmatrix} + \begin{bmatrix} v_{i,a}(t) \\ v_{i,b}(t) \\ v_{i,c}(t) \end{bmatrix} - \begin{bmatrix} v_a(t) \\ v_b(t) \\ v_c(t) \end{bmatrix} \tag{7.1}$$

where, $v_a(t)$, $v_b(t)$ and $v_c(t)$, are the components of the three-phase voltage at the PCC, $i_a(t)$, $i_b(t)$ and $i_c(t)$ are the components of the three-phase current injected by the STATCOM in the PCC, $v_{i,a}(t)$, $v_{i,b}(t)$ and $v_{i,c}(t)$ are the components of the three-phase output voltage of the VSC and L and R are the inductance and resistance values of the inductor-based filter. Very often, a transformer is used for the connection of the STATCOM at the PCC, in which case, L should include the transformer leakage inductance and R should include the transformer losses. Subscripts "a, b and c" have been used for each of the three phases.

Three-phase currents and voltages (abc) can be transformed into column vectors ($0dq$) using Park's transformation [25]. For a generic three-phase variable:

$$\mathbf{f}_{0dq}(t) = \mathbf{P}(\theta)\begin{bmatrix} f_a(t) \\ f_b(t) \\ f_c(t) \end{bmatrix}, \quad \mathbf{P}(\theta) = k_1\begin{bmatrix} k_2 & k_2 & k_2 \\ \cos(\theta) & \cos(\theta - \frac{2\pi}{3}) & \cos(\theta + \frac{2\pi}{3}) \\ -\sin(\theta) & -\sin(\theta - \frac{2\pi}{3}) & -\sin(\theta + \frac{2\pi}{3}) \end{bmatrix} \tag{7.2}$$

where k_1 and k_2 are constant values which can be chosen to tune the final result of the transformation. For example, if a power-invariant transformation is to be used k_1 = sqrt(2/3) and k_2 = sqrt(1/3) and the instantaneous real power consumed by a three-phase load, with voltage $\mathbf{v}_{abc}$ and current $\mathbf{i}_{abc}$, is:

$$p(t) = v_a(t)i_a(t) + v_b(t)i_b(t) + v_c(t)i_c(t) = v_0(t)i_0(t) + v_d(t)i_d(t) + v_q(t)i_q(t) \tag{7.3}$$

The first component of $\mathbf{f}_{0dq}(t)$ (0 or homopolar component) in (7.2) can usually be ignored because, in three-wire systems, the homopolar current is zero. Ideally, column vector $\mathbf{f}_{0dq}(t)$ will have constant d-q components in steady state if $d\theta/dt$ in (7.2) is chosen equal to the grid frequency (ω_0). It is then said that the electrical variables are referred to a synchronous d-q reference frame (SRF) and the electrical variables can be represented in a plane by space vectors with d and q perpendicular components. If there are harmonics in the electrical variables, each harmonic can be seen as a rotating space vector (d-q components) in the SRF used so far. Its angular speed will be (see Fig. 7.2):

$$\omega_n = (i \cdot m - 1)\omega_0 = n \cdot \omega_0 \tag{7.4}$$

where m is the harmonic order, ω_0 is the grid frequency in *rad/s* and $i = 1$ if the harmonic is of positive sequence and $i = -1$ if the harmonic is of negative sequence. The positive sequence of $m = 1$ is not considered in (7.4) because would yield a frequency equal zero. The components (d-q) of each harmonic (n) will be DC variables if the resulting rotating space vector is referred to a reference frame rotating with its angular speed, ω_n, (HSRF) which will be here named dq,n reference frame. These components will be sinusoidals of frequency $|n|\cdot\omega_0$ when referred to the SRF. Accordingly, the measured signals have to be rotated many

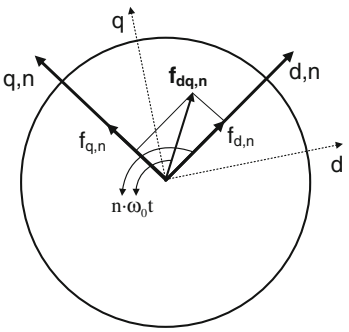

Fig. 7.2 Park's transformation and harmonic space vectors

times, after using Park's transformation, to extract harmonic information as DC variables. It is worth mentioning here that the negative sequence of the grid frequency of any electrical variable ($m = 1$) will be seen in the SRF like a harmonic of frequency $2\omega_0$.

Using a complex-number notation for any electric variable f, rotation is achieved as:

$$\mathbf{f}_{dq,n} = f_{d,n} + jf_{q,n} = e^{-j\theta_n}\left(f_d + jf_q\right) \quad \text{where}: \ \theta_n = \omega_n t \tag{7.5}$$

and:

- f_d and f_q are the components of the space vector $\mathbf{f}$ in the SRF after Park's transformation with $\theta = \omega_0 t$.
- $e^{-j\theta n}$ is a complex number with modulus equal 1 and phase equal $-\theta_n = -\omega_n t$.
- $f_{d,n}$ and $f_{q,n}$ are the components of $\mathbf{f}$ in the dq,n HSRF.

For example the 5th harmonic, which is typically of negative sequence, will be synchronous with a reference frame with $n = -6$ (dq, -6) whilst the 7th harmonic, which is typically of positive sequence, will be synchronous with a reference frame $n = 6$ (dq, 6).

7.2.2 Active and Reactive Power Control in a STATCOM

Applying a power-invariant Park's transformation in (7.1) for a three-wire system in which the homopolar component can be ignored, using $\theta = \omega_0 t$ and recalling that:

$$\mathbf{i}_{0dq} = \mathbf{P}(\theta)\mathbf{i}_{abc}; \ \mathbf{v}_{i,0dq} = \mathbf{P}(\theta)\mathbf{v}_{i,abc}; \ \mathbf{v}_{0dq} = \mathbf{P}(\theta)\mathbf{v}_{abc}, \tag{7.6}$$

one obtains the following state-variable model for the STATCOM in Fig. 7.1:

$$\overbrace{\frac{d}{dt}\begin{bmatrix} i_d \\ i_q \end{bmatrix}}^{d\mathbf{x}/dt} = \overbrace{\begin{bmatrix} -R/L & \omega_0 \\ \omega_0 & -R/L \end{bmatrix}}^{\mathbf{A}} \overbrace{\begin{bmatrix} i_d \\ i_q \end{bmatrix}}^{\mathbf{x}} + \overbrace{\begin{bmatrix} 1/L & 0 \\ 0 & 1/L \end{bmatrix}}^{\mathbf{B}} \overbrace{\begin{bmatrix} \Delta v_d \\ \Delta v_q \end{bmatrix}}^{\mathbf{u}} \tag{7.7}$$

where,

- **x** is the state-variable vector
- **u** is the input vector,
- **A** and **B** are the state matrix and the input matrix respectively,
- ω_0 is the angular speed of the reference frame and
- $\mathbf{u} = \begin{bmatrix} u_d \\ u_q \end{bmatrix}$; $u_d = \Delta v_d = v_{i,d} - v_d \quad and \; u_q = \Delta v_q = v_{i,q} - v_q$

Since the voltage at the PCC is always measured, this transformation can be made using a phase-locked loop (PLL) [26] so that the d-axis of the SRF lays on the space vector of the PCC voltage (**v**) giving, always, $v_q = 0$. Therefore, ω_0 is the angular speed of the space vector **v** and it may vary. In steady state, all variables are ideally DC variables and ω_0 is the system frequency in rad/s. Using the definition of instantaneous reactive power proposed in [27], the real (p) and the instantaneous reactive power (q) injected into the electric system (PCC) by the STATCOM are:

$$p = v_d i_d + v_q i_q = v_d i_d \tag{7.8}$$

$$q = -v_d i_q + v_q i_d = -v_d i_q \tag{7.9}$$

Therefore, the control of the power injected into the electric system reduces to the control of i_d and i_q. The control inputs in (7.7) (Δv_d and Δv_q) can be set arbitrarily since v_d can always be measured, $v_q = 0$ and $v_{i,d}$ and $v_{i,q}$ can be controlled by the VSC.

If the converter losses are neglected, the equation of the energy stored in the DC capacitor of the VSC, in state-space form, is:

$$\frac{d(v_{DC}^2)}{dt} = -\frac{2}{C_{DC}} p_e \quad \text{where } p_e = v_{i,d} i_d + v_{i,q} i_q \tag{7.10}$$

where p_e is the power injected by the converter into the AC system (connection filter and PCC). The state variable and the control input in (7.10) are $(v_{DC})^2$ and p_e, respectively. Clearly, if v_{DC} must remain constant, the steady state value of p_e must be zero.

The schematics of the control for a STATCOM is depicted in Fig. 7.3 as proposed in [4]. The required reactive power (q) injected in the PCC is achieved by the i_q controller (q^r is its reference value). However, keeping the capacitor voltage constant is vital for the VSC. The control of v_{DC} has a cascade configuration. The outer loop (voltage control) generates the reference for the real power (p^r) to be injected by the converter in the PCC (inner loop) so that the capacitor voltage

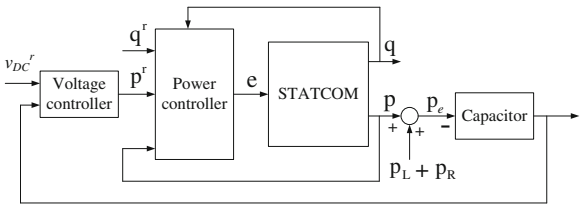

Fig. 7.3 Control for p and q in a STATCOM

remains constant. The capacitor-voltage controller will also take care of the system losses, in steady state, if an integral action is included in it. As shown in [9], the power consumed/lost in the filter (p_L and p_R) can be taken into account to minimise DC-link voltage variations and capacitor size.

7.2.2.1 Decoupled Control of *P* and *Q* in a STATCOM

The control idea shown in Fig. 7.3 requires decoupled control of id and iq. However, d- and q-axis dynamics are clearly coupled in (7.7). Furthermore, since the controller must be implemented in a microprocessor, it is necessary to derive a discrete-time version of the model. Assuming that ω_0 is constant in (7.7) and using a zero-order-hold discretization method, the discrete-time model can be written as [28]:

$$\mathbf{x}[k+1] = \mathbf{\Phi} x[k] + \mathbf{\Gamma} u[k] \tag{7.11}$$

with

$$\mathbf{\Phi} = e^{\mathbf{A}t_s} = \begin{bmatrix} \Phi_1 & \Phi_2 \\ -\Phi_2 & \Phi_1 \end{bmatrix} \tag{7.12}$$

$$\mathbf{\Gamma} = \left(\int_0^{t_s} e^{\mathbf{A}\eta} d\eta \right) \mathbf{B} = \begin{bmatrix} \gamma_1 & \gamma_2 \\ -\gamma_2 & \gamma_1 \end{bmatrix} \tag{7.13}$$

where t_s is the sampling interval. Since ω_0 is not strictly constant in practice, the discrete model is only an approximation. Variations of ω_0 due to power-system oscillations are small and slow and may be neglected in a first approximation, although ω_0 can be estimated using a PLL, as suggested in [29] and [26]. Variations of ω_0 due to system harmonics must be filtered out in the measurement system. Harmonic robust PLLs are also described in [26].

None of the elements of matrices $\mathbf{\Phi}$ and $\mathbf{\Gamma}$ is zero and therefore, the coupling between d- and q-axis dynamics is, again, obvious. Nevertheless, a decoupled discrete-time model can be written from (7.11) using two virtual inputs w_d[k] and w_q[k] (in a column vector $\mathbf{w}$[k]):

$$\mathbf{x}[k+1] = \begin{bmatrix} \Phi_1 & 0 \\ 0 & \Phi_1 \end{bmatrix} \mathbf{x}[k] + \begin{bmatrix} w_d[k] \\ w_q[k] \end{bmatrix} \tag{7.14}$$

$$\begin{bmatrix} w_d[k] \\ w_q[k] \end{bmatrix} = \begin{bmatrix} 0 & \Phi_2 \\ -\Phi_2 & 0 \end{bmatrix} \mathbf{x}[k] + \begin{bmatrix} \gamma_1 & \gamma_2 \\ -\gamma_2 & \gamma_1 \end{bmatrix} \mathbf{u}[k] \tag{7.15}$$

In (7.14), w_d[k] controls the d-axis dynamics while w_q[k] controls de q-axis dynamics. If the required w_d[k] and w_q[k] are known and the filter (L) current and the voltage at the PCC can be measured, the actual VSC outputs $v_{i,d}$ and $v_{i,q}$ can be calculated because matrix $\mathbf{\Gamma}$ in (7.15) can be inverted. However, there are three issues related to the practical implementation of any controller that have to be addressed [30]:

1. The required VSC output calculated with data up to time k will be implemented at time $k + 1$ due to the data-processing time of the controllers. Calling $\mathbf{w}^c$[k] the system inputs calculated by the controller at time k, one can write:

$$\mathbf{w}[k] = \mathbf{w}^c[k-1] \tag{7.16}$$

2. Voltages and currents are measured using anti-aliasing filters. Bessel filters are recommended. They can be designed to look like a one-sample delay in the control-system feedback. Filtered values (superscript f) of measured voltages and currents can be written as:

$$\mathbf{v}^f[k] = \mathbf{v}[k-1] \quad and \quad \mathbf{i}^f[k] = \mathbf{i}[k-1] \tag{7.17}$$

3. Integral action in the controller is provided introducing a new state variable for each axis (ζ_d[k] and ζ_q[k]) which satisfy (giving the d axis as an example):

$$\zeta_d[k+1] = \zeta_d[k] + t_s\left(i_d^r[k] - i_d^f[k]\right) \tag{7.18}$$

where i_d^r [k] is the reference value for the d-axis current and i_d^f [k] is the measured value of the same current.

Summarising, the d-axis model for (7.14) yields:

$$\begin{bmatrix} i_d[k+1] \\ w_d[k+1] \\ i_d^f[k+1] \\ \zeta_d[k+1] \end{bmatrix} = \begin{bmatrix} \Phi_1 & 1 & 0 & 0 \\ 0 & 0 & 0 & 0 \\ 1 & 0 & 0 & 0 \\ 0 & 0 & -t_s & 1 \end{bmatrix} \begin{bmatrix} i_d[k] \\ w_d[k] \\ i_d^f[k] \\ \zeta_d[k] \end{bmatrix} + \begin{bmatrix} 0 \\ 1 \\ 0 \\ 0 \end{bmatrix} w_d^c[k] + \begin{bmatrix} 0 \\ 0 \\ 0 \\ t_s \end{bmatrix} i_d^r[k] \tag{7.19}$$

A state-feedback controller would calculate the input variable for the d axis (w_d^c [k]) as:

$$w_d^c[k] = -\mathbf{K}_d \left[i_d[k],\ w_d[k],\ i_d^f[k],\ \zeta_d[k] \right]^t \tag{7.20}$$

where t means "transposed" of the row vector and $\mathbf{K}_\mathrm{d}$ is a row vector of the appropriate dimension with the controller gains for the d axis (subscript d).

Once the controller determines the values of w_d^c [k] and w_d^c [k], the actual VSC output voltages to be applied at $k + 1$ can be calculated as follows:

$$\begin{bmatrix} u_d[k+1] \\ u_q[k+1] \end{bmatrix} = \mathbf{\Gamma}^{-1} \begin{bmatrix} w_d^c[k] \\ w_q^c[k] \end{bmatrix} - \mathbf{\Gamma}^{-1} \begin{bmatrix} 0 & \Phi_2 \\ -\Phi_2 & 0 \end{bmatrix} \begin{bmatrix} i_d[k+1] \\ i_q[k+1] \end{bmatrix} \tag{7.21}$$

$$\begin{bmatrix} v_{i,d}[k+1] \\ v_{i,q}[k+1] \end{bmatrix} = \begin{bmatrix} u_d[k+1] \\ u_q[k+1] \end{bmatrix} + \begin{bmatrix} v_d[k+1] \\ v_q[k+1] \end{bmatrix} \tag{7.22}$$

Unfortunately, the computation of $v_{i,d}$ and $v_{i,q}$ (VSC outputs) in (7.22) requires the use of the actual filter currents (i_d[k + 1] and i_q[k + 1]) and PCC voltages (v_d[k + 1] and v_q[k + 1]) one step ahead and they are not known. In other words, using the information at time instant k, one has to estimate these values. As demonstrated in [30], the estimation of the currents can be done using (7.14) twice, as a prediction model, because the model state variables are known with one-sample delay (at *k-1*) due to the anti-aliasing filters and the estimation of the voltage can be done assuming that $\mathbf{v}$[k + 1] $\sim$ $\mathbf{v}^f[k\ ] = \mathbf{v}[k\text{-}1]$, because the PCC voltage can be assumed to be fairly constant.

7.2.2.2 DC-Voltage Control

The VSC can behave as an independent voltage source only if the DC-capacitor voltage is maintained constant. Increasing the capacitance value is expensive and it would not be enough to maintain the DC-voltage constant in steady state because losses (particularly inverter losses) can never be calculated accurately. Therefore, a closed-loop control of the DC-voltage is mandatory. As shown in Fig. 7.3, the DC-voltage controller works as an outer loop to calculate the reference value of the active power that the STATCOM has to inject into the grid (p^r) to maintain a constant DC voltage ($p^r < 0$ means, that the STATCOM will take the real power from the PCC).

The discrete-time DC-capacitor model using a forward difference (Euler's method) to approximate the derivative, becomes [28]:

$$v_{DC}^2[k+1] = v_{DC}^2[k] - \frac{2t_s}{C_{DC}} p_e[k] \tag{7.23}$$

A PI controller can be used, using (7.23), to calculate the required instantaneous active power to be injected, p_e^r (drawn $p_e < 0$) by the inverter in order to maintain the DC-link voltage at a constant level. Very often p_e^r can be used directly as p^r in Fig. 7.3, although the filter losses can be taken into account as suggested in [9] to minimise the DC-capacitor voltage excursions during transients. The procedure in [9], uses a simple model to predict the losses in the filter (p_F) as follows:

$$p_F = v_{Fd} i_d + v_{Fq} i_q \tag{7.24}$$

where v_{Fd} and v_{Fq} are the components of the voltage drop in the connection filter. Using (7.7), yields:

$$v_{Fd} = R i_d + L \frac{di_d}{dt} - L\omega_0 i_q \tag{7.25}$$

$$v_{Fq} = R i_q + L \frac{di_q}{dt} + L\omega_0 i_d \tag{7.26}$$

and, therefore,

$$p_F = \overbrace{R i_d^2 + R i_q^2}^{p_R} + \overbrace{\frac{1}{2} L \left[\frac{d\left(i_d^2 + i_q^2\right)}{dt} \right]}^{p_L} \tag{7.27}$$

where, p_R represents the resistive losses in the filter and p_L is the power consumed in the three-phase inductance of the filter to increase the energy stored when there is a transient of reactive power exchanged. Assuming that $i_d \ll i_q$, because the primary objective of the STATCOM is to control the reactive power, p_F simplifies to:

$$p_L = \frac{1}{2} L \frac{di_q^2}{dt} \quad \text{and} \quad p_R = R i_q^2 \tag{7.28}$$

Using the Backward Rectangular Rule approximation of the numerical integration [28], the discrete time model of (7.28) results:

$$p_L[k] = \frac{1}{2} L \frac{i_q^2[k] - i_q^2[k-1]}{t_s} \quad \text{and} \quad p_R[k] = R i_q^2[k] \tag{7.29}$$

As shown in (7.29) transients in the instantaneous reactive power control will be seen as disturbances in the instantaneous active power control loop. A feed forward term can use the reference value of i_q^r to complete the reference value for p^r (or i_q^r)

trying to minimise the effect of the filter losses when the reactive power transient takes place.

In any case, the outer DC-voltage control loop must be made much slower than the inner control loops so that the former does not interfere with the latter. Therefore, the VSC output voltage delay and measurement delay can be neglected altogether when designing the outer control loop.

7.2.2.3 More Complex Connection Filters

Very often, the use of a first order filter consisting of a three-phase inductor (L filter) to connect the STATCOM to the PCC is not sufficient to satisfy the grid requirements. In those cases, a filter consisting of two three-phase inductors plus a three-phase capacitor (LCL filter) has become very popular [31, 32]. This filter adds a lightly damped resonance in the open-loop current control system which has to be tackled actively. A state-feedback approach for the control of the filter output current (the one injected at the PCC) like the one described previously is very appropriate because the closed-loop poles can be placed at well-damped locations. Of course, the state-space model is more complex.

A STATCOM used as a shunt APF with an LCL filter is depicted in Fig. 7.4. Now, currents through inductances L_1 (i_{L1}) and L_2 (i_{L2}) and the voltage across C_f (v_{cf}) must be measured in order to build a state-feedback controller. Current i_{L2} is the variable to be controlled. A state-variable model as in (7.7) can be written:

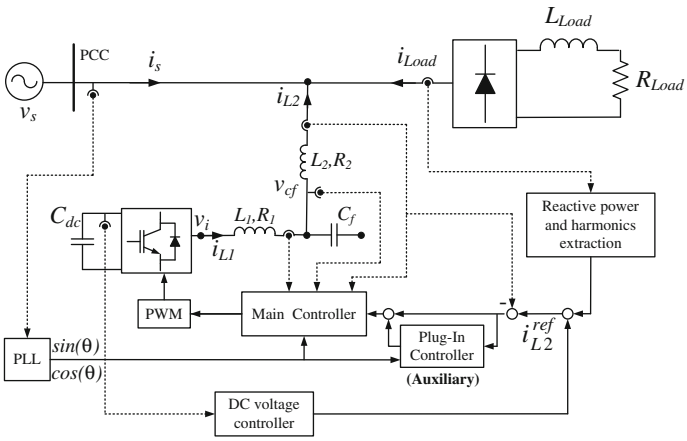

Fig. 7.4 Shunt APF with an LCL filter

$$\mathbf{A} = \begin{bmatrix} \frac{-R_1}{L_1} & \omega_0 & \frac{-1}{L_1} & 0 & 0 & 0 \\ -\omega_0 & \frac{-R_1}{L_1} & 0 & \frac{-1}{L_1} & 0 & 0 \\ \frac{1}{C_f} & 0 & \frac{-1}{R_c C_f} & \omega_0 & \frac{-1}{C_f} & 0 \\ 0 & \frac{1}{C_f} & -\omega_0 & \frac{-1}{R_c C_f} & 0 & \frac{-1}{C_f} \\ 0 & 0 & \frac{1}{L_2} & 0 & \frac{-R_2}{L_2} & \omega_0 \\ 0 & 0 & 0 & \frac{1}{L_2} & -\omega_0 & \frac{-R_2}{L_2} \end{bmatrix}, \quad \mathbf{x} = \begin{bmatrix} i_{L1d} \\ i_{L1q} \\ v_{cfd} \\ v_{cfq} \\ i_{L2d} \\ i_{L2q} \end{bmatrix}, \quad \mathbf{B} = \begin{bmatrix} \frac{1}{L_1} & 0 \\ 0 & \frac{1}{L_1} \\ 0 & 0 \\ 0 & 0 \\ 0 & 0 \\ 0 & 0 \end{bmatrix},$$

$$\mathbf{u} = \begin{bmatrix} v_{id} - v_{sd} \\ v_{iq} - v_{sq} \end{bmatrix} \tag{7.30}$$

where R_c represents the loss resistance in parallel with C_f, and R_1 and R_2 represent the losses in L_1 and L_2, respectively.

As shown in (7.30), a MIMO system is produced by the Park's transformation, including cross-coupling terms between variables of the d and q axis. In this case, it is more practical to use MIMO-design techniques to tackle the state-feedback controller.

7.3 Harmonic Control in a STATCOM

Consider a typical closed-loop control system like the one shown in Fig. 7.5a where $C(s)$ is the controller transfer function, s is the Laplace variable and the plant behaviour is modelled by transfer functions $P_1(s)$ and $P_2(s)$. $R(s)$ and $Y(s)$ are the Laplace Transform of the set-point and the output, respectively, and a disturbance $D(s)$ is also present. Tracking a sinusoidal set-point signal with neither amplitude attenuation nor phase delay using a PI controller in $C(s)$ would require a sufficiently high closed-loop

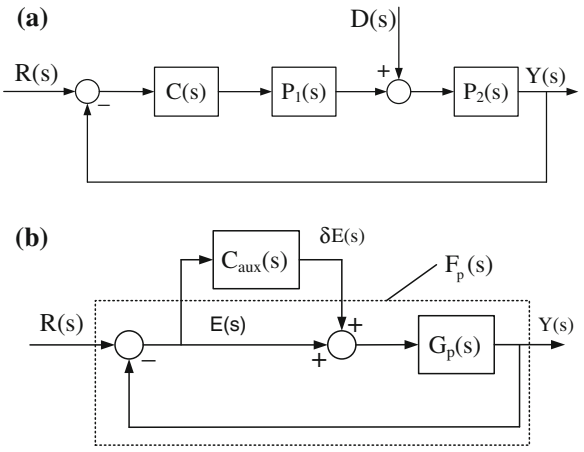

Fig. 7.5 Harmonic feedback control. **a** Feedback-control system. **b** Harmonic controller relative position

bandwidth. This might not always be possible in a STATCOM when controlling the harmonic components of the current injected in the PCC, which are seen as sinusoidal functions in a d-q frame rotating with the grid frequency (SRF) as shown in Sect. 7.2.1. As an alternative, consider the following controller:

$$C(s) = \frac{N(s)}{s^2 + \omega_h^2} \tag{7.31}$$

where $N(s)$ is any polynomial and the controller has two imaginary poles at $\pm j\omega_h$.

The system output is:

$$Y(s) = \overbrace{\frac{\hat{G}(s)}{s^2 + \omega_h^2 + \hat{G}(s)}}^{F(s)} R(s) + \overbrace{\frac{\left(s^2 + \omega_h^2\right)P_2(s)}{s^2 + \omega_h^2 + \hat{G}(s)}}^{F_D(s)} D(s) \tag{7.32}$$

with

$$\hat{G}(s) = N(s)P_1(s)P_2(s) \tag{7.33}$$

Since $F(j\omega_h)_{= 1 \text{ and } FD}(j\omega_h) = 0$, it is clear that the system described here, if closed-loop stable, shows zero set-point tracking error in steady state for sinusoidal set-point signals and disturbances of frequency ω_h. Furthermore, if several frequencies ω_h, $h = 1, 2, 3,\ldots$ are to be followed or rejected, the internal model principle (IMP) [16] demonstrates that a couple of poles $\pm j\omega_h$ must be included in the controller $C(s)$ for each frequency ω_h to be addressed.

The idea explained above suggest that, when controlling harmonic currents with a STATCOM, the PI state-feedback controller described in Sect. 7.2.2 is not enough because, in a SRF, the d- and q-axis reference currents will have a DC value (for active and reactive power control) and harmonics of frequencies as detailed in (7.4) with $h = |n|$. Tracking a single harmonic frequency would require a controller as in (7.31) while tracking a number of harmonics would require several terms as (7.31).

The most typical implementation of harmonic controllers for a STATCOM working as shunt APF was depicted in Fig. 7.4. The main control loop looks after real- and instantaneous reactive power control which are, mainly, a grid-frequency-based problem and can be transformed easily into a DC-variable control system using Park's transformation. The auxiliary (harmonic) controller is placed in a "plug-in" configuration. This facilitates its implementation because it can be easily added to already-working systems. The harmonic extraction of i_{Load} in Fig. 7.4 can be easily done on a SRF, if DC values (related to the positive sequence of the grid-frequency) are filtered out with a High-Pass Filter (HPF). Furthermore, any unbalance in i_{Load}, even at the grid frequency, will also be treated as a harmonic.

The plug-in implementation of a control system can be summarised as in Fig. 7.5b, where $C_{aux}(s)$ is the auxiliary controller, $G_p(s)$ is the original plant

together with the main controller and $R(s)$ and $Y(s)$ are the set-point and output signals in Laplace domain, respectively.

The error in Fig. 7.5b can be written as:

$$E(s) = \frac{1}{1 + [1 + C_{aux}(s)]G_p(s)} R(s) = \frac{1}{[1 + G_p(s)]\left[1 + C_{aux}(s)\left(\frac{G_p(s)}{1+G_p(s)}\right)\right]} R(s) \tag{7.34}$$

and the design of $C_{aux}(s)$ to maintain closed-loop stability can be done after the design of the main control loop which will determine the poles of the main closed-loop control system ($1 + G_p(s) = 0$). A well-designed main control loop is, therefore, of paramount importance before the design of the auxiliary controller is addressed.

7.3.1 Selective Harmonic Control

When several harmonic frequencies have to be tackled in power electronics [33], suggests an auxiliary controller such as:

$$C_{aux}(s) = \sum_{\forall\, h} \left(K \frac{1 + \frac{\alpha_c}{\omega_h} s}{1 + f \frac{\alpha_c}{\omega_h} s} \cdot \frac{\omega_h s}{s^2 + \omega_h^2} \right) \quad with \begin{cases} C_{1h}(s) = K \frac{1+\frac{\alpha_c}{\omega_h} s}{1+f\frac{\alpha_c}{\omega_h} s} \\ C_{2h}(s) = \frac{\omega_h s}{s^2+\omega_h^2} \end{cases} \tag{7.35}$$

where f, K and α_c are design parameters. $C_{2h}(s)$ is tuned for each harmonic and it is a mandatory term if zero error in steady state is required, while $C_{1h}(s)$ can be designed to be a phase-lead ($f < 1$) or a phase-lag ($f > 1$) compensator according to the required phase margin or gain margin at each frequency of interest (ω_h). The parametrisation used in (7.35) is used in [33] to ease the detailed analysis of the closed-loop stability of the control system using Nyquist criterion. Details of how f, K and α_c are designed can be obtained in that reference.

Since each harmonic to be tackled requires a new term in (7.35) and each term can be tuned independently, this approach is usually called "selective" harmonic control. Since $C_{2h}(s)$ in (7.35) is a resonant transfer function, this approach is also called "proportional + resonant" controller.

A typical discrete form for $C_{2h}(s)$ (using Z-Transform) is [34]:

$$C_{2h}(z) = K' \frac{z - 1}{z^2 - 2\cos(\omega_h t_s) z + 1} \tag{7.36}$$

avoiding classical discretization methods (e.g. Tustin) with which closed-loop stability deteriorates as shown in [35]. Meanwhile, the discretization of $C_{1h}(s)$ is less critical.

Obviously, with this approach, the harmonics to be tackled have to be known in advance and zero error in steady state is only achievable if the frequencies of the harmonics are known exactly (a constant and known grid frequency is required). Selective controllers can be applied right from the fundamental harmonic (grid frequency) and the application of Park's transformation is not necessary. However, the use of a reference frame rotating with the grid frequency is normally preferred for the control of real power and instantaneous reactive power.

7.3.2 Repetitive Control

The application of selective controllers as in Sect. 7.3.1 requires to know which harmonics are going to be addressed beforehand. A more comprehensive approach, which is free from previous knowledge of the existing harmonics is, called "repetitive control".

Electrical magnitudes in power systems (voltages and currents) are meant to be periodic in steady state. If ω_0 is the grid frequency, the period of those magnitudes will be:

$$t_p = \frac{2\pi}{\omega_0} \tag{7.37}$$

In the most general case, electrical variables in power systems will, therefore, contain harmonics of frequencies $m\omega_0$ with $m = 0,1,2,\ldots,\infty$. This suggests that, if "all" harmonics have to be tackled by a STATCOM, the controller should have poles such as $s = \pm jm\omega_0$. A transfer function (using Laplace Transform) with poles as required is [36, 37]:

$$C_{rc}(s) = \frac{e^{-t_p s}}{1 - e^{-t_p s}} \tag{7.38}$$

and can be easily implemented digitally, if the sampling period (t_s) is chosen so that:

$$N = t_p/t_s \in \mathbf{N} \tag{7.39}$$

because $e^{-tp \cdot s}$ can be replaced by z^{-N} in (7.38).

Figure 7.6a shows a typical "plug-in" implementation of a repetitive controller (RC) in power electronics, where $C_{rc}(z)$ is the discrete-time RC and $G_x(z)$ and K_x are used to ensure closed-loop stability while $Q(z)$ limits the bandwidth of the closed-loop system. Finally, $G_p(z)$ is the transfer function of the plant plus the controller

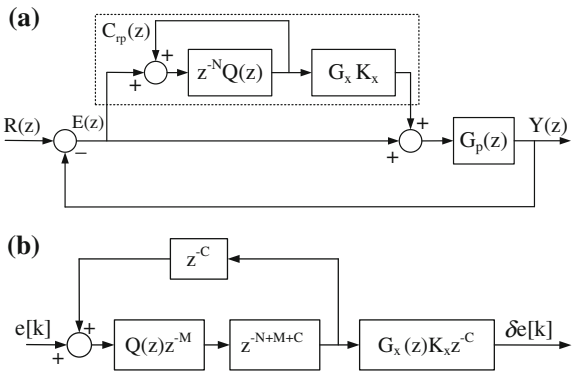

Fig. 7.6 Harmonic feedback control. **a** Plug-in repetitive controller. **b** Implementing a RC

for the grid-frequency component of the electrical variables (the so-called "main controller" in Fig. 7.4).

The complete controller in series with $G_p(s)$ in Fig. 7.6a can be written as:

$$C(z) = 1 + C_{rc}(z) = 1 + \frac{z^{-N}Q(z)}{1 - z^{-N}Q(z)} G_x(z) K_x \tag{7.40}$$

The closed-loop system in Fig. 7.6a will be internally stable if and only if [38]:

1. The transfer function $1 + C(z)G_p(z)$ has no zeros with $|z| \geq 1$.
2. There is no unstable pole-zero cancellation when the product $C(z)G_p(z)$ is formed.

The zeros of $1 + C(z)G_p(z)$ are also the roots of:

$$\left[1 + G_p(z) \right] \cdot \left\{ 1 - z^{-N}Q(z) \cdot \left[1 - K_x G_x(z) F_p(z) \right] \right\} = 0 \tag{7.41}$$

with

$$F_p(z) = \frac{G_p(z)}{1 + G_p(z)} \tag{7.42}$$

and, therefore, if the second condition above is satisfied and $F_p(z)$ is stable, a sufficient condition for stability in Fig. 7.6a is [30]:

$$\max\left\{ |z^{-N}Q(z)| \cdot |1 - K_x G_x(z) F_p(z)| \right\} < 1 \quad with\ z = e^{j\omega t_s}; \quad \forall |\omega| < \frac{\pi}{t_s} \tag{7.43}$$

The importance of a well-designed main controller has to be emphasised here because $F_p(z)$ is clearly the main loop mentioned before.

In the application of a repetitive controller to a STATCOM with shunt APF capabilities reported in [30], a good estimation of $F_p(z)$ is possible and:

1. A zero-delay low-pass FIR filter is used for $Q(z)$ so that the closed-loop bandwidth of the current control system is limited to the 20th harmonic of the grid frequency.
2. $G_x(z)$ is chosen as the inverse of the estimated transfer function for $F_p(z)$.
3. K_x = 0.8 ($K < 2$ guarantees closed-loop stability with the two previous assumptions).

The implementation of some of the transfer functions in a RC is not always possible. For example, in [30], neither $G_x(z)$ nor $Q(z)$ is casual. Fortunately, some of the large number of delays needed in the RC can help and if $z^{-C}G_x(z)$ and $z^{-M}Q(z)$ are proper transfer functions and $N > M + C$ (always the case in practice), the repetitive controller can be easily implemented as shown in Fig. 7.6b.

7.3.3 Grid-Frequency Variations

Selective (resonant) controllers and repetitive controllers rely on the introduction of resonant poles at the frequencies to be tackled by the controller (in set-point signal and in disturbances). If the grid frequency deviates from the expected one, the frequencies of the poles designed for the controller will not coincide with those of the harmonics to be eliminated and zero set-point tracking error cannot be expected.

If the grid frequency varies and can be estimated using a PLL, the selective controllers in (7.35) can be re-tuned recalculating the trigonometric functions required in their discretization in (7.36). Suggestions of how to implement frequency adaptation and to ease the calculation of the trigonometric functions involved can be found in [39]. The tuning can be carried out individually for each harmonic. Nevertheless, the tuning process can be numerically cumbersome if a good number of harmonics have to be addressed. The selective controllers at the low-frequency end may need no modification in a practical application because the errors produced will be small while those controllers at the high-frequency end will surely need to be modified to avoid unacceptable errors.

If a repetitive controller is used with grid-frequency deviations, its tuning can also be done in a reasonably simple way. If the grid period was $t_{p,old}$ and the new grid period t_p has an small variation:

$$t_{p,\,old} = N_{old} t_s, \quad \text{with } N_{old} \in \mathbf{N} \tag{7.44}$$

$$t_p = N t_s + l_e t_s, \quad \text{with } N \in \mathbf{N} \text{ and } l_e \in (0, 1) \tag{7.45}$$

$e^{-tp \cdot s}$ in (7.38) cannot be discretized as z^{-N} any more. In [40], the following discretization of the non-integer delay is proposed:

$$e^{-t_p s} \text{ becomes } z^{-N} L(z) \tag{7.46}$$

where $L(z)$ is a first-order all-pass filter with unity gain which approximates the phase lag of the delay $t_s \cdot l_e$. The most precise solution for $L(z)$ will be one of the so-called Thiran's filters [41] which produce maximally flat group delay. However, [40] shows that a simple approximation of the delay $t_s \cdot l_e$ using a first order Pade's approximation is sufficiently precise in a typical application [42]. With the use of $L(z)$ the stability margins of the repetitive control system are not affected because $|L(e^{j\omega ts})| = 1, \forall\omega$ and the tracking steady-state errors for harmonics of the new grid frequency $\omega_h = 2\ h\pi/t_p$ are greatly reduced if compared to the case in which $L(z)$ is not used.

7.4 Efficient Use of Multiple Reference Frames in STATCOM Control

Figure 7.7a has been drawn recalling that the general form of a versatile controller for a STATCOM consists of (a) a "main controller" to take care of the positive sequence of the fundamental component of the electrical variables (d-q), including active and reactive power-related issues; and (b) a "harmonic controller" placed as a "plug-in controller". Figure 7.7a also includes the plant model **P**(s), which is a matrix of transfer functions, and the relevant signals in the *dq* reference frame such as the set-point $\mathbf{r}_{dq}(t)$, the output variable $\mathbf{y}_{dq}(t)$, the control signals $\mathbf{u}_{dq}(t)$ and $\mathbf{m}_{dq}(t)$, the disturbance $\mathbf{d}_{dq}(t)$ and the error $\mathbf{e}_{dq}(t)$. The physical meaning of all these variables will be explained in the case study used later on in this chapter.

Traditionally the "harmonic controller" consists of [22]:

- Several rotations of the error signal into the chosen harmonic reference frames.
- A Low-Pass Filter (LPF) $1/(1 + T \cdot s)$ in each HSRF to extract the DC components.
- A PI controller $K(1 + I \cdot s)/(I \cdot s)$ to achieve zero steady-state error.

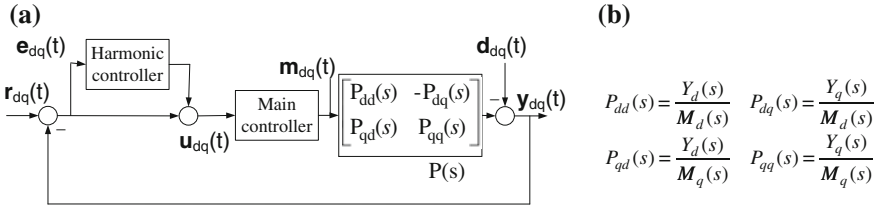

Fig. 7.7 Complete control scheme. Capital letters (i.e. $M_d(s)$) are used not only for the Laplace Transform of the time domain variables (i.e. $m_d(t)$) but also for transfer functions such as $P_{dd}(s)$. All variables are space vectors with d and q components on a reference frame synchronously rotating with the fundamental frequency. **a** Block diagram of the complete control strategy. **b** Plant transfer functions

If the time constant of the LPF (T) is chosen to cancel the zero in the PI controller transfer function, the controller becomes a pure integrator. Only a constant $k_i = K/I$ will have to be designed for each harmonic. This approach simplifies the design and has proved to provide good performance. The relative phase of each harmonic space vector in its reference frame is not required because the controller will eliminate the direct and quadrature components of the harmonic errors.

The use of multiple rotations suggests that many $\cos(n\omega_0 t)$ and $\sin(n\omega_0 t)$ functions must be calculated and this would represent an unaffordable computational burden for most microprocessors. Fortunately, $\cos(n\omega_0 t)$ and $\sin(n\omega_0 t)$ can be easily calculated from $\cos(\omega_0 t)$ and $\sin(\omega_0 t)$, already calculated when performing Park's transformation. In fact, using Moivre's formula [43]:

$$\overbrace{\cos(n\omega_0 t) + j\sin(n\omega_0 t)}^{\cos(\theta_n)+j\sin(\theta_n)} = [\cos(\omega_0 t) + j\sin(\omega_0 t)]^n \tag{7.47}$$

This reduces the computational effort required for multiple-harmonic control as the trigonometric functions are transformed into sums and products. Furthermore, this calculation can be performed in a recursive way:

$$e^{jn\omega_0 t} = [\cos(\omega_0 t) + j\sin(\omega_0 t)]^{(n-1)}[\cos(\omega_0 t) + j\sin(\omega_0 t)] \tag{7.48}$$

where $\cos(\omega_0 t)$ and $\sin(\omega_0 t)$ are obtained for the main controller by means of a PLL.

The outputs of the HSRF controllers have to be rotated back into the fundamental (dq) reference frame where they can all be added together to produce the command signal. Each one of the rotations required uses the angle already calculated but in the opposite direction, and this operation does not require the evaluation of any trigonometric function either, because:

$$[\cos(\omega_0 t) + j\sin(\omega_0 t)]^{-n} = \cos(n\omega_0 t) - j\sin(n\omega_0 t) \tag{7.49}$$

resulting in the complex conjugate of (7.47). So far, referring a space vector to a HSRF has been presented using complex-number notation but it can also be done using matrix notation with the following rotation matrix:

$$\mathbf{R}(n\omega_0 t) = \begin{bmatrix} \cos(n\omega_0 t) & -\sin(n\omega_0 t) \\ \sin(n\omega_0 t) & \cos(n\omega_0 t) \end{bmatrix} \quad \text{with :} \quad \begin{bmatrix} v_d \\ v_q \end{bmatrix} = \mathbf{R}(n\omega_0 t) \begin{bmatrix} v_{d,n} \\ v_{q,n} \end{bmatrix} \tag{7.50}$$

The use of (7.47) provides an efficient procedure to carry out the vector rotations required in controllers using multiple HSRFs without having to solve many trigonometric functions. Therefore, the proposed control strategy using (7.47) will be called efficient multiple-reference-frame (EMRF) controller in the rest of the chapter. Clearly, frequency adaptation is naturally implemented in a EMRF controller if one updates the value of ω_0 accordingly.

7.4.1 Design and Stability Analysis

As the HSRF's are generated without taking into account the phase of the plant at each frequency, a compensation matrix has to be used in each HSRF. Besides, this matrix will decouple the *dq* components at each HSRF and will ensure a good phase margin. The open-loop system to be taken into account for each harmonic controller is depicted in Fig. 7.8a, where the main loop for the fundamental component remains closed. Additional subscript *n* besides *dq* is used in those variables referred to *nth* HSRF while no additional subscripts means that those variables are referred to the fundamental SRF. The rotation matrix **R** in (7.50) satisfies $\mathbf{R}^{-1}(n\omega_o t) = \mathbf{R}(-n\omega_o t)$.

Defining:

- $P'_{dd}(s)$ the transfer function $E_d(s)/U_d(s)$, $P'_{qq}(s)$ the transfer function $E_q(s)/U_q(s)$
- $P'_{dq}(s)$ the transfer function $E_q(s)/U_d(s)$, $P'_{qd}(s)$ the transfer function $E_d(s)/U_q(s)$

where $E_x(s)$ and $U_x(s)$ are the Laplace transforms of e_x and u_x, respectively (x is d or q), and recalling that the use of the Park's transformation produces symmetric plants (i.e. $P'_p(s) = P'_{dd}(s) = P'_{qq}(s)$ and $P'_c(s) = P'_{dq}(s) = P'_{qd}(s)$); the errors produced in the SRF due to the input in the *nth* HSRF rotated to the SRF (with Laplace Transform $\mathbf{E}_{dq}(s)$) can be calculated as:

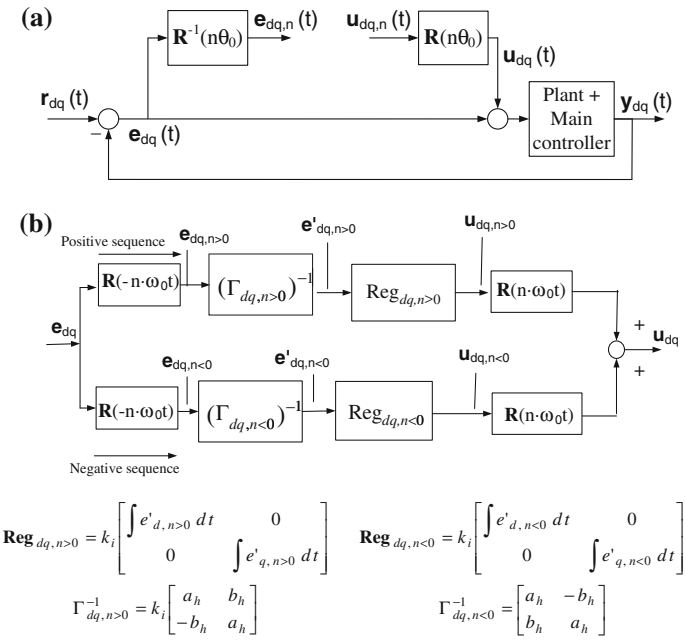

$$\mathbf{Reg}_{dq,n>0} = k_i \begin{bmatrix} \int e'_{d,n>0}\, dt & 0 \\ 0 & \int e'_{q,n>0}\, dt \end{bmatrix} \qquad \mathbf{Reg}_{dq,n<0} = k_i \begin{bmatrix} \int e'_{d,n<0}\, dt & 0 \\ 0 & \int e'_{q,n<0}\, dt \end{bmatrix}$$

$$\Gamma^{-1}_{dq,n>0} = k_i \begin{bmatrix} a_h & b_h \\ -b_h & a_h \end{bmatrix} \qquad \Gamma^{-1}_{dq,n<0} = \begin{bmatrix} a_h & -b_h \\ b_h & a_h \end{bmatrix}$$

Fig. 7.8 Detail of EMRF controller. **a** Open-loop block diagram for harmonic -n- in the SRF. **b** EMRF controller block diagram. Variables with subscript d, q are vectors with *dq* components

$$\mathbf{E}_{dq}(s) = \begin{bmatrix} E_d(s) \\ E_q(s) \end{bmatrix} = \begin{bmatrix} P'_p(s) & -P'_c(s) \\ P'_c(s) & P'_p(s) \end{bmatrix} \cdot \overbrace{\begin{bmatrix} U_d(s) \\ U_q(s) \end{bmatrix}}^{\mathbf{U}_{dq}(s)} \tag{7.51}$$

where $\mathbf{U}_{dq}$(s) is the Laplace transform of the input referred to the fundamental SRF.

The steady-state relationship between $\mathbf{u}_{dq,n}$ and $\mathbf{e}_{dq,n}$ in the time domain, for DC inputs in $\mathbf{u}_{dq,n}$ can be obtained by calculating the inverse Laplace transform and rotating into each HSRF giving:

$$\begin{bmatrix} e_{d,n} \\ e_{q,n} \end{bmatrix} = \underbrace{\begin{bmatrix} \{P'_{p,n}\}_a + \{P'_{c,n}\}_b & -(\{P'_{p,n}\}_b - \{P'_{c,n}\}_a) \\ \{P'_{p,n}\}_b - \{P'_{c,n}\}_a & \{P'_{p,n}\}_a + \{P'_{c,n}\}_b \end{bmatrix}}_{\mathbf{\Gamma}_{dq,n}} \cdot \begin{bmatrix} u_{d,n} \\ u_{q,n} \end{bmatrix} \tag{7.52}$$

with

$$P'_p(s = jn\omega_0) = \{P'_{p,n}\}_a + j\{P'_{p,n}\}_b \tag{7.53}$$

$$P'_c(s = jn\omega_0) = \{P'_{c,n}\}_a + j\{P'_{c,n}\}_b \tag{7.54}$$

The inverse of $\mathbf{\Gamma}_{\mathrm{dq,n}}$ at each harmonic can be used to compensate the open-loop system and to decouple $\mathbf{u}_{dq,n}$ and $\mathbf{e}_{dq,n}$ using a new error signal $\mathbf{e'}_{dq,n}$ written as:

$$\begin{bmatrix} e'_{d,n} \\ e'_{q,n} \end{bmatrix} = \underbrace{(\mathbf{\Gamma}_{dq,n})^{-1} \cdot \mathbf{\Gamma}_{dq,n}}_{\mathbf{I}} \cdot \begin{bmatrix} u_{d,n} \\ u_{q,n} \end{bmatrix} = \mathbf{\Gamma}^{-1}_{dq,n} \begin{bmatrix} e_{d,n} \\ e_{q,n} \end{bmatrix} \tag{7.55}$$

where $\mathbf{I}$ is the identity matrix. Note that decoupling of the closed-loop system consisting of the main controller and the plant is not required. If the closed-loop is not exactly known, identification techniques have to be used at the commissioning stage and/or during operation. The fact that all signals are DC magnitudes would certainly ease the application of these techniques giving the EMRF controller some degree of adaptation to plant changes. The EMRF controller for a positive-sequence harmonic $n > 0$ and its related negative-sequence harmonic $n < 0$ are depicted in Fig. 7.8b, which includes the rotation matrices defined in (7.50), the integral controller and the compensation matrix $\mathbf{\Gamma}_{dq,n}$. The elements a_h and b_h are equal to $\mathbf{\Gamma}^{-1}_{dq,n}(1,1)$ and $\mathbf{\Gamma}^{-1}_{dq,n}(1,2)$ $n > 0$, respectively. Note that $h = |n|$.

The EMRF controller depicted in Fig. 7.8b uses HSRF to transform sinusoidal signals into DC signals avoiding the use of resonant terms in the controller. Nevertheless, the stability analysis cannot be carried out for each HSRF independently. On the contrary, all the synchronous controllers must be transformed into a single *dq* reference frame to carry out the stability analysis. The reference frame rotating

synchronously with the positive-sequence space vector at the fundamental frequency has been used for this purpose.

The EMRF controllers for a given $n > 0$ in Fig. 7.8b and its companion $n < 0$ blended together are equivalent to a resonant controller (h) in the SRF. The transfer function ($C_{d,h}$(s) for d axis and $C_{q,h}$(s) for q axis), equivalent to the pair of EMRF controllers proposed can be obtained by following the procedure in [24] and [44] and taking into account the compensation matrix $\mathbf{\Gamma}_{\mathrm{dq,n}}$. Using the same k_i in all the controllers, one can demonstrate that (subscript x stands for d axis and q axis):

$$C_{x,h}(s) = 2k_i \cdot \frac{(a_h s - b_h h\omega_0)}{s^2 + (h\omega_0)^2} \quad with \quad \begin{cases} a_h = \mathbf{\Gamma}^{-1}_{dq,n}(1,1) \\ b_h = \mathbf{\Gamma}^{-1}_{dq,n}(1,2),\ n > 0 \end{cases} \tag{7.56}$$

According to (7.56), k_i is the only parameter to be designed in the proposed controller and it determines the stability of the system. In fact, k_i can be used, together with the open-loop transfer function, to design the stability margins.

The open-loop block diagram on the fundamental SRF is depicted in Fig. 7.9, where $\mathbf{u}_{dq}$ is the input and $\mathbf{u'}_{dq}$ is the output to carry out the stability analysis. In Fig. 7.9, each of the transfer functions $C_{d,h}$(s) and $C_{q,h}$(s) is a harmonic controller transformed into the fundamental SRF. Adding all the harmonic controllers, the equivalent equation can be written as:

$$C_x(s) = \sum_{h=1}^{N} C_{x,h}(s) = 2k_i \sum_{h=1}^{N} \frac{(a_h s - b_h h\omega_0)}{s^2 + (h\omega_0)^2} \quad with \ \ x = d \ or \ q \tag{7.57}$$

The stability of the proposed algorithm depends only on the parameter k_i, which is the same for all harmonics and can be tuned using the open-loop frequency response of the system. In the next section a case study is used to illustrate the design and stability analysis procedures.

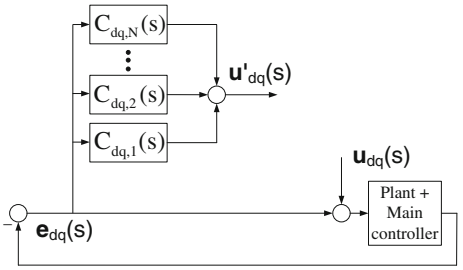

Fig. 7.9 Open-loop block diagram for stability analysis

7.4.2 Description of a Case Study

A STATCOM has been built to illustrate the performance of the proposed controller (EMRF) and the design methodology. The laboratory prototype is like in Fig. 7.4 where the proposed controller (EMRF) has been implemented as the plug-in auxiliary controller. The nominal RMS voltage at PCC was set to 230 V with 50 Hz. These values are also used as base values in this chapter together with a base power equal to 5 kVA. The three phases of the PCC voltage (phase-to-neutral voltages) are used by a PLL in order to synchronize the converter with the grid voltage (see [26] for a detailed description of PLLs for converters in electric power systems). The DC voltage of the VSC was set to 500 V. The VSC has been connected to the grid using a LCL filter with $L_1 = L_2 = 1.5$ mH and $C_f = 20$ μF. The grid inductance is Ls = 700 μH which results in a strong grid. The grid X_s/R_s ratio has been set to 10. A 5 kVA rectifier-type load is connected at the PCC to simulate the demand of harmonic currents. The inverter switching frequency and the control sampling frequency were, both, set to 5 kHz.

All variables described in Fig. 7.7 for the general form of the proposed controller can now be identified in Fig. 7.4: the reference value ($\mathbf{r}_{dq}(t)$) is a current reference ($\mathbf{i}_{L2}^{\text{ref}}$), the output ($\mathbf{y}_{dq}(t)$) is the output current ($\mathbf{i}_{L2}(t)$) and finally the command input ($\mathbf{m}_{dq}(t)$) is the converter output voltage ($\mathbf{v}_i$).

The frequency response of the plant ($P(s)$ in Fig. 7.7), after Park's transformation is applied, is depicted in Fig. 7.10a. A state-feedback control, as in [21], was used as the main controller to eliminate the resonance and to minimise the coupling effect between dq components. This decoupling is required for the independent control of the active and reactive power. The closed-loop poles have been placed in pairs because each variable has components in d and q axis. Damping equal to 1 for the poles has been used to avoid over-current in the transient response. The closed-loop

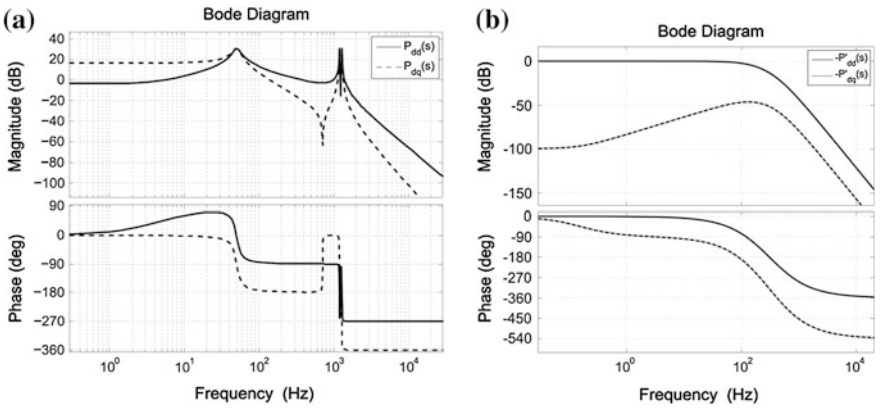

Fig. 7.10 Frequency response of (a) the plant and (b) the closed-loop with the main controller. **a** Bode diagram of $P_{dd}(s)$ and $P_{qq}(s)$. **b** Bode diagram of $-P'_{dd}(s)$ and $-P'_{qq}(s)$

frequency response of the system transfer functions with the main controller in place ($-P'_{dd}(s)$ and $-P'_{dq}(s)$) is depicted in Fig. 7.10b. The resonance is eliminated and the cross coupling is reduced to a negligible level, with a maximum value of −41.8 dB. As a consequence, only $-P'_p(s)$ will have to be used when analysing the design and stability of the EMRF controller.

The situation of the EMRF controller with respect to the main controller is also depicted in Fig. 7.4. In this case, the EMRF controller has to track harmonics at $6k \pm 1$ with $k = 1,2,\ldots,5$. The open-loop transfer function to be considered when designing the EMRF controllers with the contribution of all the harmonics to be tackled is depicted in Fig. 7.9 and can be written as (for the d axis):

$$G_d(s) = -\frac{U'_d(s)}{U_d(s)} = -P'_p(s)\sum_{h=1}^{N}\underbrace{\left(2k_i\frac{(a_h s - b_h h\omega_0)}{s^2 + (h\omega_0)^2}\right)}_{C_{d,h}} \tag{7.58}$$

where k_i has to be designed for stability.

The open-loop frequency response of G_d (s), which includes the equivalent resonant controllers, has been drawn in Fig. 7.11a, for the case study. One can observe several phase margins which are always close to 90° thanks to the use of the plant inverse frequency response to calculate a_h and b_h for all frequencies of interest. Varying k_i will not change much these phase margins because of the sharp magnitude changes shown in the upper plot. The design of k_i will mainly affect the gain margins which have to be evaluated at the ultimate frequencies ω_u^h for each harmonic (h), also shown in the upper plot of Fig. 7.11a. Note that $\omega_u^1 = 0$.

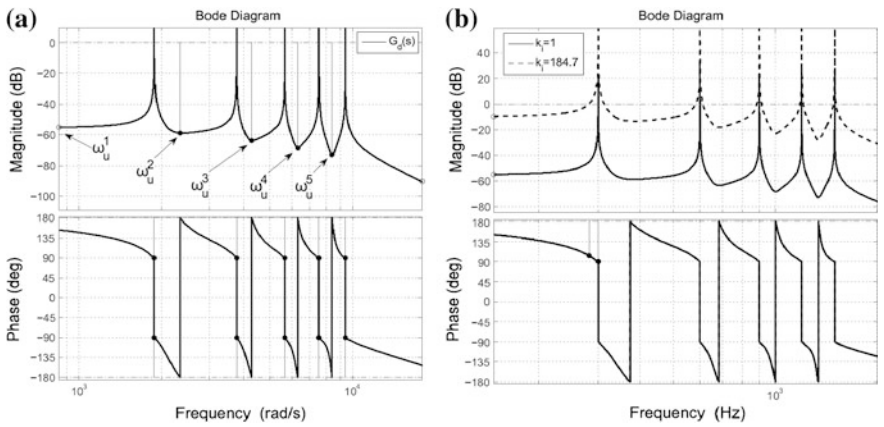

Fig. 7.11 Open-loop frequency response of G_d (s). **a** Bode diagram of G_d (s). **b** Bode diagram of G_d (s) with changes in k_i

Which one of the gain margins is most critical depends on the design of the main controller. The largest possible k_i to be used can be calculated as:

$$k_i^{\max} = \frac{1}{2}\min\left(\left|\frac{1}{G_d(j\omega_u^h)}\right|\right) \tag{7.59}$$

The use of the same value of k_i for all harmonics is a reasonable strategy to ensure closed-loop stability. However, different values of k_i can be used to improve the transient performance for a specific harmonic, if required. If this is the case, the chosen constants k_i^h will have to satisfy:

$$A_m(dB) \leq 20 \cdot log_{10}\left(2\sum_{h=1}^{N}\left[\frac{k_i^h \cdot b_h}{h\omega_0}\right]\right) \tag{7.60}$$

where A_m is the required gain margin in dB at the most critical frequency. Figure 7.11b depicts the frequency response of $G_d(s)$ for two different values of k_i to illustrate the fact that the gain margin is the stability margin most affected by this parameter.

7.4.3 Investigating the Computational Burden of the Proposed Algorithm

The harmonics typically present in a balanced three-phase system are $m = (6k \pm 1)$ with $k = 1, 2,\ldots$ alternating positive (for $k = 1, 3,\ldots$) and negative sequence (for $k = 2, 4,\ldots$). If, for example, harmonics up to the 31st ($k = 5$) are considered, all HSRFs for $n = \pm 6\,k$ have to be calculated. To start with, $\cos(1\omega_0)$ and $\sin(1\omega_0)$ (HSRF with $n = 1$) are required but they are already used for the initial Park's transformation (the only trigonometric functions to be evaluated). The transformation into a HSRF with $n = 2$ can be done by using (7.48) whilst the combination ($n = 1$ and $n = 2$) leads to the HSRF with $n = 3$. This process is repeated with $n = 3$ and $n = 3$ to obtain $n = 6$ and so forth, until the HSRF with $n = 30$ is reached. Only multiplications (M) and sums (S) are used giving:

- HSRFs at $2\omega_0$, $3\omega_0$, $6\omega_0$, $12\omega_0$, $18\omega_0$, $24\omega_0$ and $30\omega_0$ require: $7 \times (4M + 2S)$.
- HSRFs for negative sequences $-2\omega_0$, $-3\omega_0$, $-6\omega_0$, $-12\omega_0$, $-18\omega_0$, $-24\omega_0$ and $-30\omega_0$ using (7.49) require: $7 \times (1M)$.
- The projection of the error signal on the various reference frames ($n = \pm 6, \pm 12, \pm 18, \pm 24, \pm 30$) requires $10 \times (4M + 2S)$.
- The projection of the command signal on the dq ($n = 0$) frame requires $10 \times (4M + 2S)$.
- The compensation of the phase delay at each harmonic requires $10 \times (4M + 2S)$.
- The discrete-time integral controller (Tustin method) and the sum of all command signals on the dq ($n = 0$) frame require $5 \times (2M + 2S) - 1S$.

Table 7.1 Computation effort for different sets of harmonics in the proposed algorithm

Harmonics (m)	*S*	*M*	Mem.	Inst.
5,7	19	41	4	43
5,7,11,13	35	72	8	76
5,7,11,13,17,19	51	103	12	109
5,7,11,13,17,19,23,25	67	134	16	142
5,7,…,17,19,23,25,29,31	83	165	20	175

The process to cover all $m = (6k \pm 1)$ in the proposed controller requires 165 multiplications and 83 sums in this example. These may look like big numbers but most modern microprocessors can combine one sum and one multiplication in a single elementary instruction with a fast cycle-execution time (for example in a TMS320F28335 floating-point digital signal processor, the cycle-execution time is 6.67 ns [45]). Table 7.1 shows the number of sums (S), the number of multiplications (M), the memory used (Mem.) and the number of elementary instructions (Inst.) required in a microprocessor to tackle different harmonic sequences. In each case, the total time required for the algorithm can be calculated multiplying the number of "Inst." by the cycle-execution time of the microprocessor to be used.

Selective and repetitive controllers could produce similar results tackling harmonics in power electronics as shown in the literature [30, 46]. However, there are some clear disadvantages:

- Selective controllers need an extra algorithm to deal with frequency variations, which increases the computational effort [47].
- Repetitive controllers have difficulties to provide adaptation under grid-frequency variations [48].

The estimation of ω_0 in grid-connected VSCs is an unavoidable issue and its common for all types of algorithms and cannot be regarded as an extra cost for the EMRF controller proposed. Obviously, the speed of this adaptation is limited by the speed of the ω_0 estimation algorithm.

In order to make a fair comparison between a resonant controller and the EMRF controller, it is necessary to compare the latter with its equivalent resonant transfer function in (7.58). This equivalent resonant controller can be transformed to discrete time through the Tustin method with pre-warping for the analysis of the calculations required.

Table 7.2 shows the computational effort of implementing the equivalent resonant controller in discrete time (S_1 and M_1 are sums and multiplications for a non-adaptive version of the resonant controller and S_2 and M_2 are for an adaptive version). Note that the EMRF controller requires a few more calculations but it handles harmonics as DC magnitudes and, therefore, it simplifies the implementation of identification techniques, anti-wind-up mechanisms and adaptation algorithms to compensate plant changes. In addition, the implementation of the proposed EMRF algorithm uses less memory.

Table 7.2 Computation effort for the equivalent resonant controller

Harmonics (m)	S_1	M_1	S_2	M_2	Mem.
5,7	10	10	26	36	8
5,7,11,13	20	18	48	62	16
5,7,11,13,17,19	30	26	70	88	24
5,7,11,13,17,19,23,25	40	34	92	114	32
5,7,…,17,19,23,25,29,31	50	42	114	140	40

7.4.4 Experimental Results Using an EMRF Controller for a STATCOM

A STATCOM, as the one depicted in Fig. 7.4, has been built. The full control algorithm was implemented in Matlab/Simulink and, then, it was downloaded into a dSpace 1103 platform which consists of a power PC as the main processing tool, a TMS320F240 DSP for PWM generation and an analog-to-digital conversion system of 16 channels. The analog signals are filtered using 5th-order Bessel filters of 1.7 kHz cut-off frequency before sampling to avoid aliasing. The VSC is a Semikron SKS 22F B6U. All the results presented in these experiments were measured by a Yokogawa DL850 oscilloscope and the data were transferred to a PC for analysis purposes.

In this case, the frequency response of the plant at each harmonic frequency has been identified during the commissioning stage. Only one integral controller had to be designed for all the harmonics to be tackled. A gain margin of 10 dB was specified and the value of the k_i obtained using (7.60) gives 20, which ensures the stability of the closed loop system.

Reactive Power Compensation in Balanced Systems

In this experiment, the STATCOM had to provide the reactive power consumed by an inductive load. The reactive power level can be seen in the q component of the grid and load currents, which are depicted in Fig. 7.12 in grey color. Figure 7.12a shows the transient response when reactive power compensation is enabled at t = 0.4 s. As shown in Fig. 7.12a, the q component of the grid current becomes zero. This implies the full compensation of the reactive power consumed by the load because the q component of the grid voltage is also zero (due to the PLL synchronization). Furthermore, the d component of the grid current remains constant during the transient due to the decoupling feature of the main controller. Figure 7.12b shows the transient response during a load change during reactive power compensation.

Compensation of Load-Current Harmonics in Balanced Systems

In this experiment, the harmonic controller has been set to tackle load-current harmonics from the 5th to the 31st and it was switched on at 1.5 s. Grid and load three-phase currents (abc) are shown in Fig. 7.13 (as measured with an oscilloscope, directly) before and after the controller is switched on. In this case, current

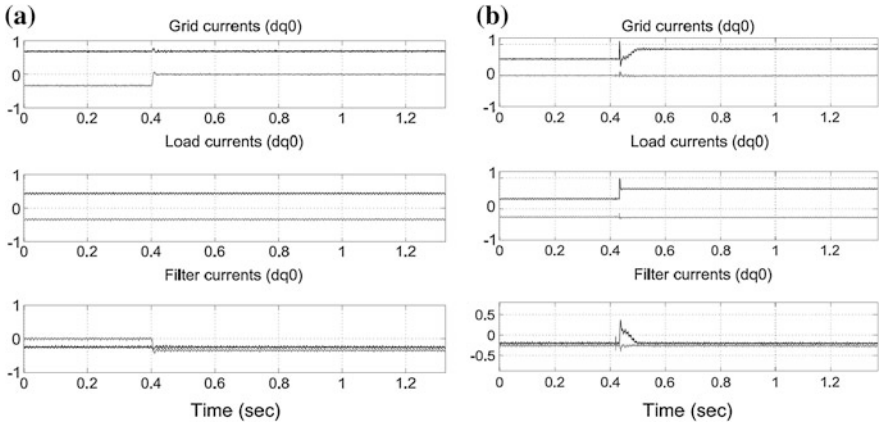

Fig. 7.12 Currents (in pu, base voltage 230 V and base power 5kVA) in *dq* frame during reactive power compensation. Filter current is i_{L2} in Fig. 7.4. **a** Transient response when reactive power compensation is activated. **b** Transient response with a load change during reactive power compensation

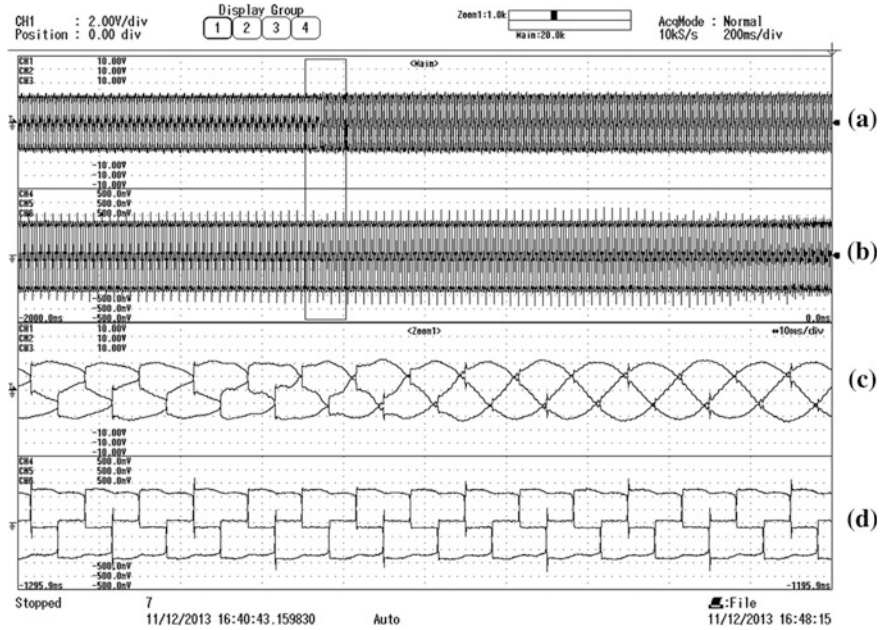

Fig. 7.13 Transient response of the grid and load three-phase currents. **a** Grid current, **b** load current, **c** detail grid current and **d** detail load current. In all channels 1A/div

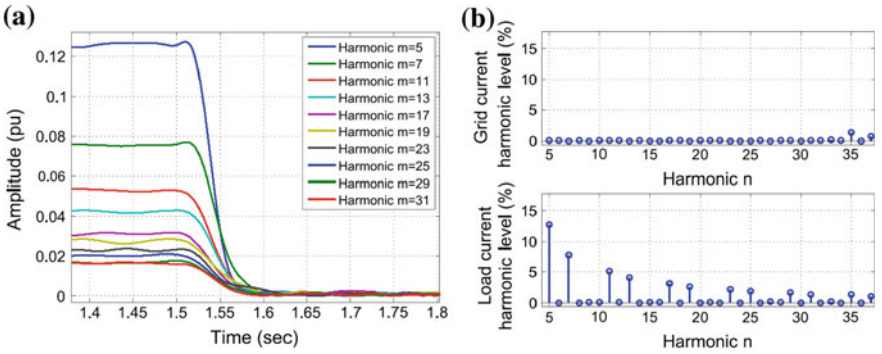

Fig. 7.14 Harmonics in grid currents with EMRF controller. **a** Transient response of current harmonic controller when switching the controller "on". Amplitudes relative to the fundamental. **b** Harmonic level in grid and load currents in steady state. Percentage of the fundamental

harmonics are drawn by a three-phase balanced diode rectifier. The selected harmonics are fully under control after two cycles (40 ms).

Figure 7.14a shows the amplitudes of the harmonics in the grid current calculated using measurements on the fundamental SRF, before and after the controller is turned on. Finally, the amplitude of each harmonic of the load and grid currents in steady-state with the EMRF controller switched on are shown in Fig. 7.14b. The total harmonic distortion (THD) of the load and grid currents are 27.38 and 1.24 %, respectively.

The adaptation capability of the proposed controller when the grid frequency changes is investigated in Fig. 7.15 where the harmonic contents of the grid current is shown when the grid frequency changes instantaneously from 50 to 51 Hz at 1.1 s after starting the experiment. The stepwise frequency change was generated by a fully controlled three-phase laboratory voltage source. The grid frequency is

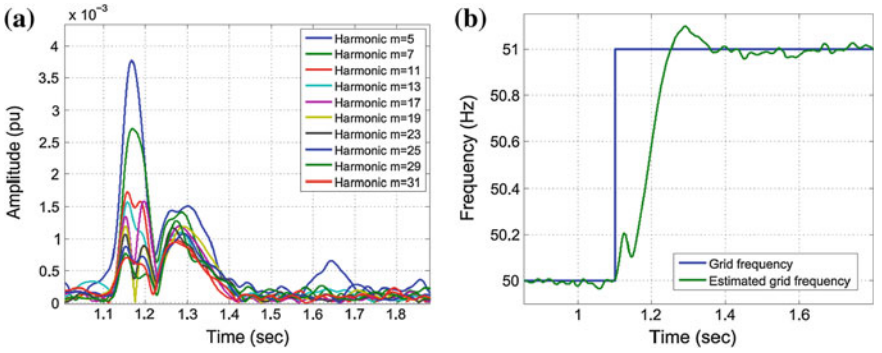

Fig. 7.15 Frequency variation in the experiment with an EMRF controller. **a** Harmonic level in grid current. Amplitudes relative to the fundamental. Grid frequency changes stepwise. **b** Grid frequency step from 50 to 51 Hz

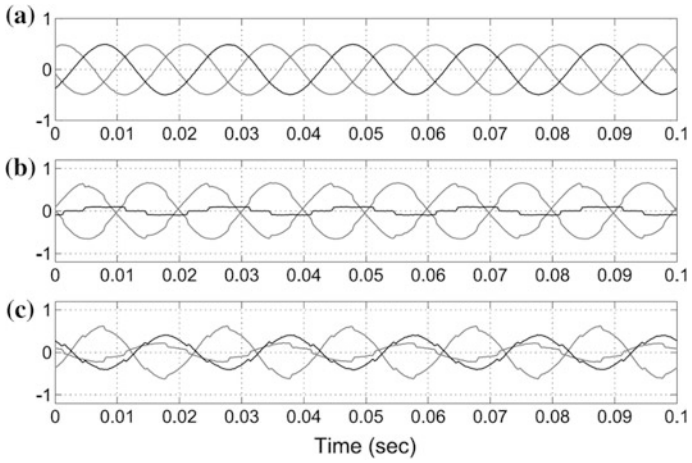

Fig. 7.16 Steady-state response of the grid, load and output-filter currents with an unbalanced load with harmonics: **a** grid three-phase current, **b** load three-phase current and **c** filter output three-phase current i_{L2}. Currents in pu

estimated by a PLL and used to update ω_0 in the EMRF calculations. The load and grid current THD in steady-state when the grid frequency is 51 Hz are 25.24 and 1.1 % respectively.

Compensation of Load-Current Harmonics and Reactive Power with Unbalanced Loads

In this experiment, the EMRF controller, together with the main controller in state-space form have been set to tackle load-current harmonics and reactive power compensation when the load is unbalanced. Three-phase grid, load and filter output currents are shown in Fig. 7.16. In this case, the load consists of a three-phase balanced diode rectifier and a single-phase load placed between phases *a* and *b* (R = 82 Ω, L = 48 mH). As shown in Fig. 7.16, the grid currents are almost sinusoidal and balanced.

Figure 7.17 shows the transient response during the experiment carried out with the unbalanced load but looking at *d* and *q* components of the system currents. To start with, the STATCOM is ON but only the DC-link voltage is controlled. The reactive power reference to be injected in the PCC is set to zero. At t = 0.6 s the current harmonic controller (EMRF) is switched ON. Any unbalance in the load current is seen as a harmonic in the *dq* reference frame following the pattern in Sect. 7.2.1. All harmonics in the grid current disappear while the load current remains the same. At t = 2.3 s the set-point for the reactive power to be injected in the PCC is made equal to the reactive power consumed by the load. After a transient, the STATCOM compensates the load reactive power completely.

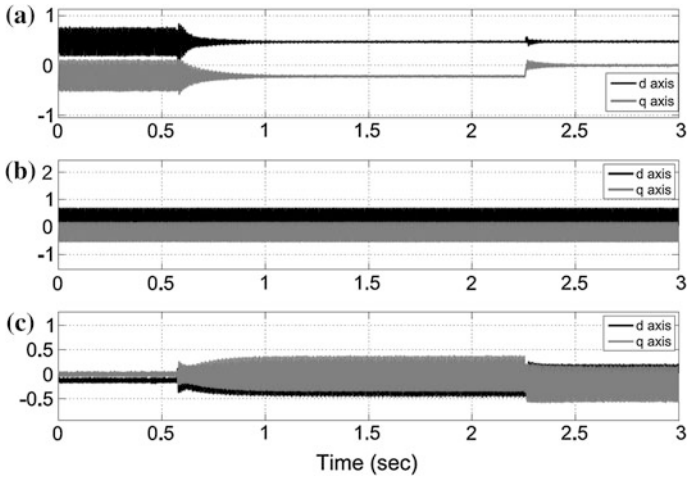

Fig. 7.17 Transient response of the STATCOM in a *dq* reference frame: **a** grid current, **b** load current and **c** filter output current i_{L2}. Currents in pu

7.5 Voltage Support in Unbalanced Power Systems

7.5.1 Problem Description

Nowadays, grid operators may allow the injection of negative-sequence currents during disturbances in order to keep the voltage at the PCC constant and balanced. This can be important for sensitive loads that could disconnect if the AC voltage does not meet restrictive voltage standards. This task can also be accomplished by means of a STATCOM, above all in weak grids whose significant grid impedance may lead to large PCC voltage variations [49].

The general system under investigation for this application is shown in Fig. 7.18, where a balanced non-linear load and a STATCOM are connected to a PCC with unbalanced voltage due to an unbalance in u_s or in the system impedance represented by L_s. The control system to be used is also depicted in Fig. 7.18 but will be explained in Sect. 7.5.2. In this case, the STATCOM is set to tackle two disturbances: harmonic currents of the load and voltage unbalance at the PCC. Notice that, if the unbalance on the PCC voltage were only caused by unbalanced load currents, the problem would be automatically solved by the STATCOM when compensating the harmonics and the unbalance of the load current.

The unbalance of a three-phase supply voltage consists of a loss of symmetry of the phase voltage phasors (magnitude and/or angle). According to the standard

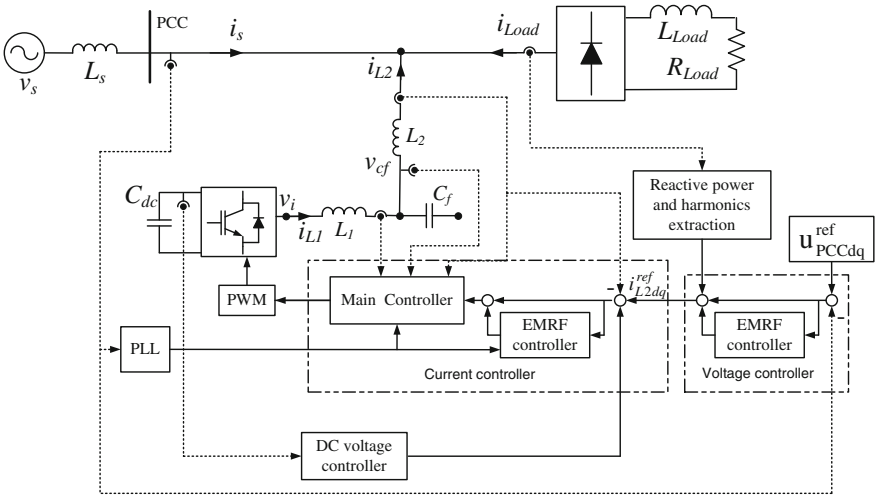

Fig. 7.18 Control scheme of the STATCOM for voltage unbalance and current harmonic compensation

EN50160 [50] voltage unbalance can be quantified using the so-called voltage unbalance factor (VUF) (in %) defined as:

$$VUF = \frac{U^-}{U^+} \cdot 100\,\% \tag{7.61}$$

where U^- is the root mean square (RMS) value of the negative-sequence component and U^+ is the RMS value of the positive-sequence component. The standard EN50160 also establishes that the maximum VUF during normal operation in low voltage (LV) and medium voltage (MV) systems must not exceed 2 %, 95 % of the time.

If the STATCOM in Fig. 7.18 has to reduce voltage unbalance in the PCC, it will have to inject unbalanced currents to produce an unbalanced compensating voltage on the system impedance. Obviously, the negative-sequence current required to reduce the unbalance at the PCC is related to the amount of voltage unbalance at the grid side and the value of the grid impedance. Figure 7.19 shows the amount of the negative-sequence current (in pu) (base current 12.55 A) required for different values of voltage unbalance (in %) and short-circuit ratio (SCR) (see [51] for the definition of SCR when connecting a VSC to the grid). Power losses are neglected for this analysis but the accuracy of the results have been validated looking at various points of Fig. 7.19 with a fully-detailed simulation using Matlab and Simpower Systems. Obviously, the positive-sequence current has to be taken into account in order to calculate the final value of the current injected by the STATCOM. The positive-sequence current depends on the reactive power compensation and the power losses.

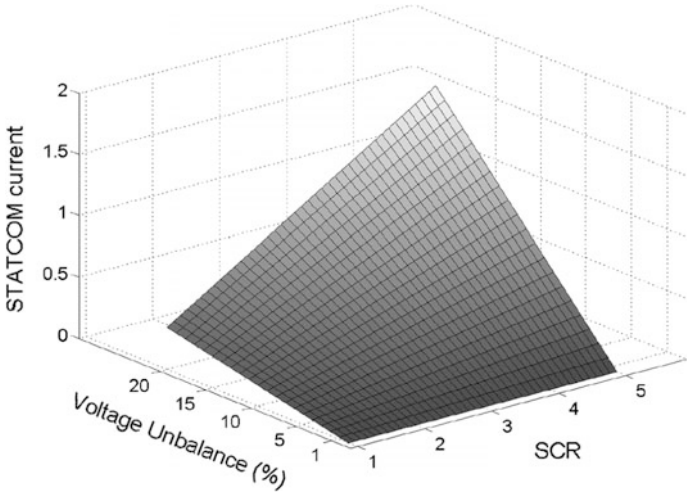

Fig. 7.19 Relationship between SCR, VUF and required STATCOM current (in pu) when balancing the PCC voltage

7.5.2 Voltage Unbalance Compensation Using EMRF Controller

Voltage unbalance is related to the negative-sequence component of the PCC voltage at the fundamental frequency (50 Hz). This component is transformed into a 100-Hz component after Park's transformation is applied into a SRF. From the control point of view, voltage unbalance can be treated as an additional harmonic to track/reject. As a consequence, an EMRF controller can be used to maintain the PCC voltage balanced if the STATCOM's injected current can be calculated. The full-control scheme of the STATCOM, which includes a two-layer control system, is shown in Fig. 7.18. The inner controller contains the main and auxiliary controllers discussed very often in this chapter: the main controller will control active and reactive power injected in the PCC while the auxiliary controller will look after the load-current harmonics and load-current unbalance. The outer layer is used to eliminate the unbalanced voltage from the PCC (100-Hz voltage component on a SRF). The outer-layer controller will complete the harmonic current reference for the inner auxiliary current controller.

The design method of the EMRF controller used in the voltage controller of Fig. 7.18 is similar to the one described in Sect. 7.4.1. With this approach, unbalanced-voltage control and current harmonic control in a STATCOM are treated within the same framework. This is an alternative viewpoint to the one presented in [49] where positive-sequence and negative-sequence controllers are investigated separately.

7.5.3 Experimental Results of Voltage Unbalance Compensation

The laboratory prototype in Sect. 7.4.2 was modified to carry out this experiment. In this case, a grid impedance has been chosen to set SCR = 2.78, which is a weak grid according to [52]. The grid voltage unbalance has been set to 20 % using a laboratory voltage source. This is an extraordinarily large value, but it will help to see the results more clearly. The simulated grid was loaded with a three-phase balanced diode rectifier. Figures 7.20a, b show the PCC voltage before an after switching on the voltage controller, respectively. In Fig. 7.20a the PCC voltage is not only unbalanced but also distorted. Distortion is caused by the non-linear load current and a relatively large short-circuit impedance. The good performance of the proposed voltage controller can be better validated studying positive and negative sequences of the PCC voltage, as shown in Fig. 7.21. The positive sequence $Upcc^{+}_{dq}$

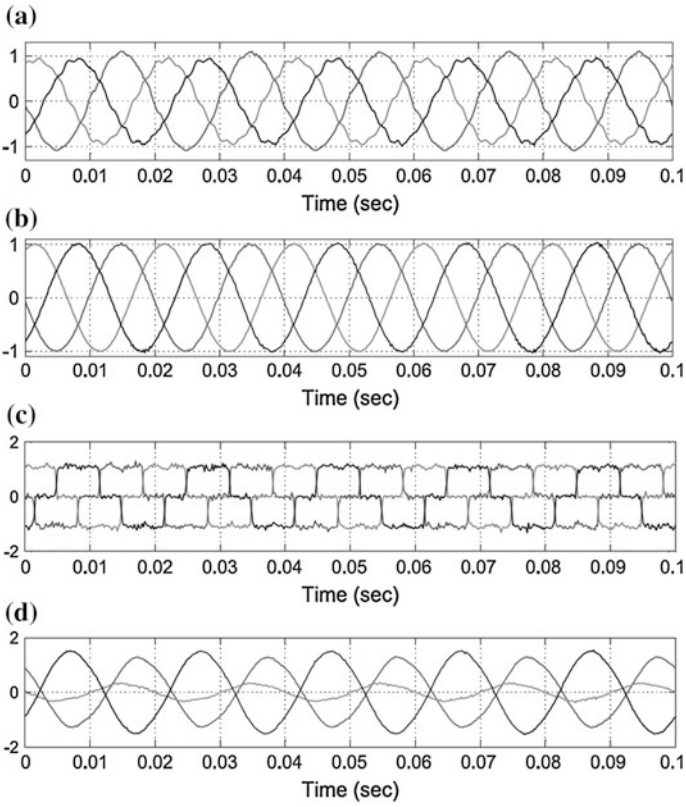

Fig. 7.20 Unbalance compensation: **a** PCC voltage before compensation, **b** PCC voltage after compensation, **c** 3-phase load currents and **d** 3-phase grid currents. Voltages and currents in pu

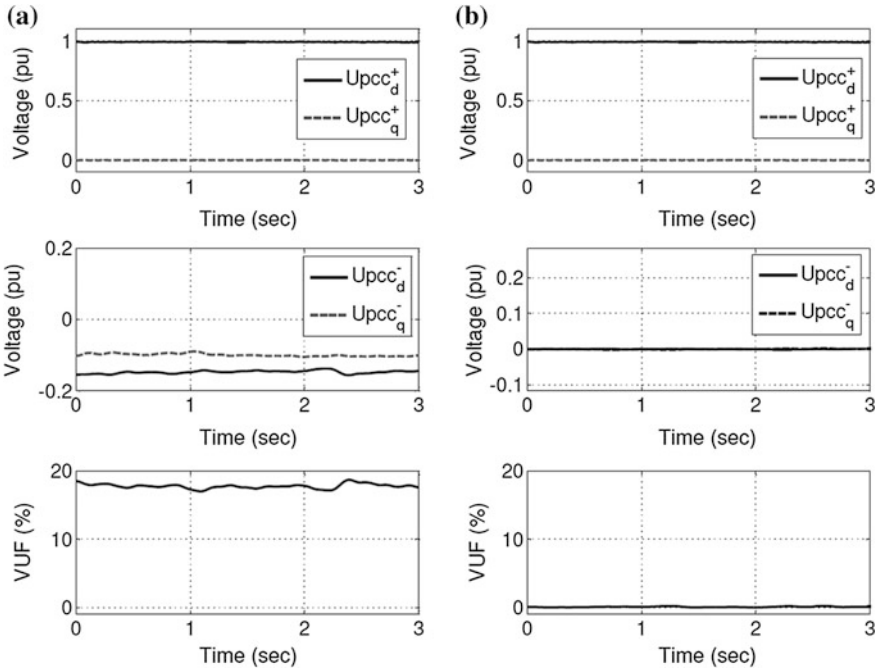

Fig. 7.21 PCC voltage positive and negative sequences and VUF: **a** before compensation, **b** after compensation

remains constant because its reference corresponds to the value it had before enabling the PCC voltage control. The negative sequence $Upcc^{-}_{dq}$ and the VUF become almost zero after the controller is switched ON. The STATCOM not only compensates the PCC voltage unbalance but also the current harmonics consumed by the load. Figures 7.20c, d show the three-phase load currents and the grid currents, respectively when steady state has been reached. The grid currents are unbalanced and almost sinusoidal (current THD < 3 %)

The voltage unbalance is compensated by injecting an unbalanced current into the PCC. Since the PCC voltage is no longer unbalanced, there is an oscillation of active power between the STATCOM and the PCC. This yields an oscillation of the DC-link voltage.

References

1. Singh B, Saha R, Chandra A, Al-Haddad K (2009) Static synchronous compensators (STATCOM): a review. IET Power Electron 2(4):297–324
2. Edris A, Adapa R, Baker M, Bohmann L, Clark K, Habashi K, Gyugyi L, Lemay J, Mehraban A, Meyers A, Reeve J, Sener F, Torgerson D, Eood R (1997) Proposed terms and definitions for flexible AC transmission systems (FACTS). IEEE Trans Power Deliv 12(4):1848–1853

3. Gyugyi L (1994) Dynamic compensation of AC transmission lines by solid-state synchronous voltage sources. IEEE Trans Power Deliv 9(2):904–911
4. Schauder M, Mehta H (1993) Vector analysis and control of advanced static VAR compensator. IEE Proc-C 140(4):299–306
5. Shauder C, Germhardt M, Stacey E, Lemak T, Gyugyi L, Cease TW, Edris A (1997) Operation of_100 MVAr TVA STATCOM. IEEE Trans Power Deliv 12(4):1805–1811
6. Gyugyi L, Hingorani P, Nanmery N, dnd Tai PR (1992) Advanced static VAR compensator using gate turn-off thyristors for utility applications. CIGRE paper, pp 23–302
7. Mwinyiwiwa Z, Wolanski Z., Ooi B-T (1997) Current equalization in SPWM FACTS controllers at lowest switching rates. In: IEEE Power Electronics Specialists Conference (PESC), vol. 1, pp 325–330
8. Mwinyiwiwa Z, Ooi B-T, Wolanski Z (1998) UPFC using multiconverter operated by phase-shifted triangle carrier SPWM strategy. IEEE Trans Ind Appl 34(3):495–500
9. García-González P, García-Cerrada A (2000) Control system for a PWM-based STATCOM. IEEE Trans Power Deliv 15:1252–1257
10. Wessels C, Hoffmann N, Molinas M, Fuchs F (2013) STATCOM control at wind farms with fixed-speed induction generators under asymmetrical grid faults. IEEE Trans Ind Electron 60 (7):2864–2873
11. Sensarma P, Padiyar K, Ramanarayanan V (2001) Analysis and performance evaluation of a distribution STATCOM for compensating voltage fluctuations. IEEE Trans Power Deliv 16 (2):259–264
12. García-Cerrada A, García-González P, Collantes R, Gómez T (2000) Comparison of thyristor-controlled reactors and voltage-source inverters for compensation of flicker caused by arc furnaces. IEEE Trans Power Deliv 15(4):1225–1231
13. Gupta R, Ghosh A, Joshi A (2011) Performance comparison of VSC-based shunt and series compensators used for load voltage control in distribution systems. IEEE Trans Power Deliv 26(1):268–278
14. Roncero-Sánchez P, Feliu-Batlle V, García-Cerrada A (2009) Design and comparison of state-feedback and predictive-integral current controllers for active- and reactive-power control in renewable energy systems. Control Eng Pract 17:255–266
15. Blasko V, Arnedo L, Kshirsagar P, Dwari S (2011) Control and elimination of sinusoidal harmonics in power electronics equipment: A system approach. In: IEEE Energy Conversion Congress and Exposition (ECCE), pp 2827–2837
16. Francis B, Wonham W (1976) The internal model principle of control theory. Automatica 12:456–465
17. Zmood D, Holmes D (2003) Stationary frame current regulation of PWM inverters with zero steady-state error. IEEE Trans Power Electron 18:814–822
18. Newman M, Zmood D, Holmes D (2002) Stationary frame harmonic reference generation for active filter systems. IEEE Trans Ind Appl 38:1591–1599
19. Inoue T, Nakano M (1981) High accuracy control of a proton synchrotron magnet power supply. In: Proceedings of the International Federation of Automatic Control (IFAC), 8th Triennial World Congress, (Kyoto, Japan), pp 216–221
20. Hara S, Yamamoto Y, Omata T, Nakano M (1988) Repetitive control system: a new type of servo system for periodic exogenous signals. IEEE Trans Autom Control AC-33(7):659–668
21. Roldán-Pérez J, García-Cerrada A, Zamora-Macho J, Roncero-Sánchez P, Acha E (2011) Adaptive repetitive controller for a three-phase dynamic voltage restorer. In: International conference on power engineering, energy and electrical drives (POWERENG), pp 1–6
22. Lee S, Sul S (2000) A harmonic reference frame based current controller for active filter. In: proceedings of applied power electronics conference (APEC), pp 1073–1078
23. Lee J, Kang DH, Jeong HG, Lee KB (2011) Active damping for large-scale wind power systems with an LCL-filter using an improved DFT. In: IECON 2011-37th annual conference on IEEE industrial electronics society, pp 1179–1184
24. Mattavelli P (2001) A closed-loop selective harmonic compensation for active filters. IEEE Trans Ind Appl 37:81–89

25. Kraus P (1986) Analysis of electrical machinery. McGraw-Hill Inc., New York
26. Yazdani A, Iravani R (2010) Voltage-sourced converters in power systems: Modeling, control and applications. IEEE and Wiley, Hoboken, New Jersey
27. Akagi H, Kanazawa Y, Nabae A (1984) Instantaneous reactive power compensators comprising switching devices without energy storage. IEEE Trans Ind Appl 20(3):625–630
28. Franklin G, Powell J (1980) Digital Control of Dynamic Systems. Addison-Wesley, Boston
29. Rodriguez P, Teodorescu R, Candela I, Timbus A, Liserre M, Blaabjerg F (2006) New positive-sequence voltage detector for grid synchronization of power converters under fault grid conditions. In: 37th IEEE power electronics specialists conference, 2006; PESC'06, pp 1–7
30. García-Cerrada A, Pinzón-Ardila O, Feliu-Batlle V, Roncero-Sánchez P, García-González P (2007) Application of a repetitive controller for a Three-Phase active power filter. IEEE Trans Power Electron 22:237–246
31. Park M-Y, Chi M-H, Kim H-G, Chun T-W (June 2010) LCL-filter design for grid-connected PCS using total harmonic distortion and ripple attenuation factor. In: Proceedings of the 2010 international power electronics conference, pp 1688–1694
32. Jeong HG, Lee K-B, Choi S, Choi W (2010) Performance improvement of LCL-filter-base grid-connected inverters using PQR power transformation. IEEE Trans Power Electron 25 (5):1320–1330
33. García-Cerrada A, Roncero-Sánchez P, García-González P, Feliu-Batlle V (2004) Detailed analysis of closed-loop control of output-voltage harmonics in voltage-source inverters. IEE Proc-Electr Power Appl 151:734–743
34. Liserre M, Teodorescu R, Blaabjerg F (2006) Multiple harmonics control for three-phase grid converter systems with the use of PI-RES current controller in a rotating frame. IEEE Trans Power Electron 21(3):836–841
35. Yepes A, Freijedo F, Doval-Gandoy J, López O, Malvar J, Fernandez-Comesana P (2010) Effects of discretization methods on the performance of resonant controllers. IEEE Trans Power Electron 25(7):1692–1712
36. Chen S, Lai Y, Tan S, Tse C (2008) Analysis and design of repetitive controller for harmonic elimination in PWM voltage source inverter systems. IET Power Electron 1(4):497
37. Tzou Y, Ou R, Jung S, Chang M (1997) High-performance programmable AC power source with low harmonic distortion using DSP-based repetitive control technique. IEEE Trans Power Electron 12(4):715–725
38. Doyle J, Francis B, Tannenbaum A (1992) Feedback control theory. Macmillan Publishing Company, New York
39. Yepes A, Freijedo F, López O, Doval-Gandoy J (2011) High-performance digital resonant controllers implemented with two integrators. IEEE Trans Power Electron 26(2):563–576
40. Roldán-Pérez J, García-Cerrada A, Zamora-Macho J, Roncero-Sánchez P, Acha E (2014) Troubleshooting a digital repetitive controller for a versatile dynamic voltage restorer. Int J Electr Power Energy Syst 57:105–115
41. Thiran J (1971) Recursive digital filters with maximally flat group delay. IEEE Trans Circuit Theory 18(6):659–664
42. Press W, Teukolsky S, Vetterling W, Flannery B (2007) Numerical recipes: the art of scientific computing, 3rd edn. Cambridge University Press, Cambridge
43. Hazewinkel M (ed) (2001) Encyclopedia of mathematics. Springer, Berlin
44. Zmood D, Holmes D, Bode G (2001) Frequency-domain analysis of three-phase linear current regulators. IEEE Trans Ind Appl 37:601–610
45. Texas Instruments, Texas Instruments TMS320F28335 digital signal controllers data manual, lit. number SPRS439 M ed., August 2012
46. Lascu C, Asiminoaei L, Boldea I, Blaabjerg (2007) High performance current controller for selective harmonic compensation in active power filters. IEEE Trans Power Electron 22 (5):1826–1835

47. Freijedo F, Yepes A, Malvar J, López O, Fernández-Comesaña P, Vidal A, Doval-Gandoy J (2011) Frequency tracking of digital resonant filters for control of power converters connected to public distribution systems. IET Power Electron 4:454–462
48. Chen D, Zhang J, Qian Z (2013) An improved repetitive control scheme for grid-connected inverter with frequency-adaptive capability. Trans Ind Electron 60(2):814–823
49. Rodríguez A, Bueno E, Mayor A, Rodríguez F, García-Cerrada A (2014) Voltage support provided by STATCOM in unbalanced power systems. Energies 7:1003–1026
50. EN50160, Voltage characteristics of electricity supplied by public distribution systems, Technical report, CENELEC (2000)
51. Gavrilovic A (1991) AC/DC system strength as indicated by short circuit ratios. In: IET international conference on AC and DC power transmission, pp 27–32
52. IEEE, IEEE guide for planning DC links terminating at AC locations having low short circuit capacities. IEEE Std 1204-1997, Technical report (1997)

Chapter 8
Control of Multilevel STATCOMs

Javier Muñoz, Pedro Melín and José Espinoza

Abstract Control strategies suitable for multilevel STATCOMs are reviewed in this chapter. First of all, the models are systematically deducted and especial emphasis is given to the dynamic and steady state analysis in order to facilitate the study of the control techniques. Then, these control schemes aimed to achieve the overall compensation objectives are classified in linear and nonlinear approaches. In fact, among the linear alternatives, the Proportional-Resonant (PR) and the Proportional-Integral (PI) controllers are presented as feasible ways to achieve zero steady state error in the stationary and the Synchronous Reference Frame (SRF), respectively. For nonlinear strategies, the input/output linearization control technique is applied. Hysteresis and predictive controllers are also discussed as alternatives to control the STATCOM in the stationary *abc* or α-β frame. The main features of all the aforementioned control techniques will be presented and because the balanced operation of the modules is not natural, dedicated control strategies in charge of balancing the DC side variables, DC voltages for Voltage Source Converters (VSC) and DC currents for Current Source Converters (CSC) based topologies, are shown as an important part of the control of the multilevel STATCOM. Indeed, the inclusion of these dedicated controllers to balance the operation of the different modules is mandatory for multilevel compensators if high performance overall waveforms are required. In order to illustrate the controllers performance operation, key current and voltage waveforms are shown for linear load compensation, using Cascade H-Bridge (CHB), Neutral Point Clamped (NPC) and Multilevel Current Source Converter (MCSC) based STATCOMs.

J. Muñoz (✉)
Department of Industrial Technologies, Universidad de Talca, Talca, Chile
e-mail: jamunoz@utalca.cl

P. Melín
Department of Electrical and Electronic Engineering, Universidad del Bío-Bío, Concepción, Chile
e-mail: pemelin@ubiobio.cl

J. Espinoza
Department of Electrical Engineering, Universidad de Concepción, Concepción, Chile
e-mail: jose.espinoza@udec.cl

F. Shahnia et al. (eds.), *Static Compensators (STATCOMs) in Power Systems*, Power Systems, DOI 10.1007/978-981-287-281-4_8

Keywords Cascade H-bridge · Neutral point clamped · Multilevel current source converter · Multilevel STATCOM

8.1 Introduction

Multilevel topologies have emerged as an alternative to overcome the technological restrictions of the actual semiconductors devices that have limited power ratings. This is the case of multilevel STATCOM topologies that can reach higher compensation levels using standard semiconductor devices, which is particularly useful for medium voltage applications. Among the main features of multilevel topologies we have the use of low commutation frequencies for each device and low dv/dt (or di/dt) waveforms thanks to appropriate modulating techniques that increase the equivalent overall switching frequency.

These multilevel topologies present outstanding advantages as modularity, low harmonic distortion and high power capacity using low rated components. Indeed, just off-the-shelf semiconductor devices are required because the main electrical variables (voltage and current) are shared among all the power valves of the configuration. Nevertheless, these positive features require elaborated control strategies because the number of inputs increases according to the number of levels included in the topology. Fortunately, the actual devices for control purposes (DSPs, FPGAs, etc.) provide feasible alternatives to implement such advanced algorithms.

Moreover, the way to cope with the control task for this kind of systems becomes not trivial due to the nonlinear nature of the modeling equations and the high number of control variables. In fact, it is not easy to define which is the control strategy that achieves the best results, considering both dynamic and steady state behavior, as well as computational burden.

Control objectives for multilevel STATCOMs can be classified as two different tasks: (i) achieve the overall compensation objectives such as power factor control or voltage regulation control; and (ii) ensure equal power distribution among the power modules. This second task must be performed by a dedicated control strategy because the modules in a multilevel configuration do not behave symmetrically as they do not have exactly the same parameters (such as inductance and capacitance sizes), which causes that the power will not be equally shared.

Several approaches have been successfully used for multilevel STATCOMs that are supported with different theoretical considerations. Among the most widespread control strategies used for multilevel power converters, it is possible to highlight the instantaneous power theory based controllers and the SRF based control. The main advantage of the instantaneous power theory approach is that it is possible to generate the current references directly in the stationary frame (*abc* or α-β), and therefore no complex domain transformations are required. On the other hand, when a SRF transformation is performed over the AC variables, their direct and quadrature components are obtained, which are DC quantities, and therefore, the application of classic control theory is straightforward.

Among the linear control strategies suitable for the stationary frame, the PR controller arises as the simplest alternative to implement the controllers transfer function, due to its similarity to the PI controller. Regarding the nonlinear strategies suitable for multilevel STATCOMs in the stationary frame, there have been several proposals in the past years; in fact, two of them will be studied in this chapter: the multilevel hysteresis control and the predictive control, which are suitable to be used in combination with the instantaneous power theory approach.

On the other hand, when the SRF transformation is considered, the easiest linear approach is the PI controller, which has been widely used by researchers and industry. On the side of the nonlinear controllers in the *dq* frame, the input/output exact linearization technique has emerged as a suitable option to be applied in multilevel STATCOMs. It is important to remark that other control strategies are well suited for multilevel converters, such as Fuzzy controllers, Artificial Neural Networks or Linear Matrix Inequalities, just to name a few.

As an important part of control schemes for multilevel STATCOMs, the use of dedicated controllers in charge of the equal power sharing among the circuit elements is vital to achieve the expected high performance multilevel waveforms. If these strategies are not included, unwanted and harmful effects will appear in the resulting AC variables, as will be explained in depth. The key to achieve the equal power distribution among the components is to balance the voltage (or current) of all the DC capacitors (or inductors). To do so, the gating patterns are slightly compensated by means of changing either the modulating signals or the triangular waveform (for carrier based techniques).

8.2 Multilevel STATCOMs Modeling

In order to propose adequate control techniques for multilevel converters, it is vital to know the dynamic and static modeling equations, which allow determining the system behavior. In fact, thanks to a steady state analysis, it is possible to calculate the modulating signals required to reach an arbitrary operating condition, which is especially useful to determine the compensation capabilities of the topologies through an open loop control. This section is devoted to systematically obtain the modeling equations of the three aforementioned representative STATCOM topologies, which will be required to understand the control techniques presented further in this chapter.

8.2.1 Cascade H-Bridge Topology

The CHB STATCOM topology considers the series connection of several H-Bridges modules in order to share the total load voltage among all the modules. This allows a low voltage rating of the semiconductor devices. The main topology for an arbitrary

number of cells n_c per phase is shown in Fig. 8.1. As any other VSC based topology, this configuration needs a passive filter in order to absorb the instantaneous voltage differences between the converter and the grid, and to reduce the harmonic content of the injected AC current. In this case, an inductive first order filter L_c is used.

The dynamic model of the system in Fig. 8.1 can be obtained using Kirchhoff's circuit laws. Just for modeling purposes, let us assume that all the modules have the same capacitance and voltage in their DC side and that the AC voltage is equally shared among all the n_c cells. Applying the voltage law in the AC side for the phase a of the STATCOM, the following equation is obtained,

$$L_c \frac{d}{dt} i_c^a + R_c i_c^a + n_c s_c^a v_{dc}^a = v_s^a, \tag{8.1}$$

where, s_c^a is the commutation function of modules of phase a and the resistor R_c is the parasitic (series) resistance of the inductor L_c.

In order to obtain the dynamic equation of the DC side, the Kirchhoff's current law is applied in the DC node and the resulting expression is,

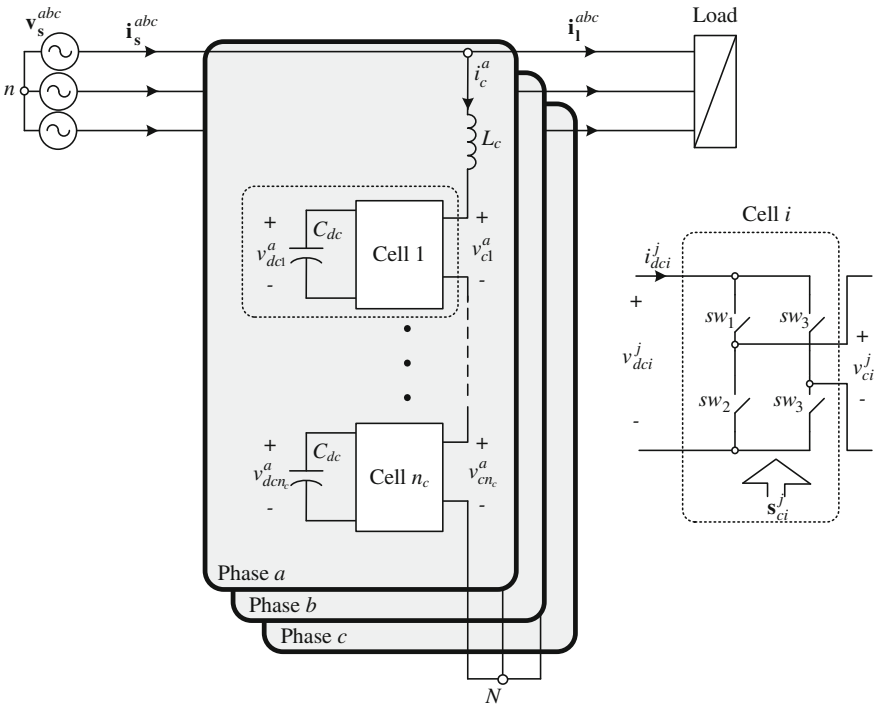

Fig. 8.1 CHB STATCOM

$$s_c^a i_c^a = C_{dc} \frac{d}{dt} v_{dc}^a + \frac{v_{dc}^a}{R_{dc}}, \tag{8.2}$$

where, R_{dc} is a resistor connected in parallel to the capacitor C_{dc} that concentrates the overall losses in the DC side.

Taking into account, (8.1) and (8.2), the total dynamic model for phase a can be obtained as follows,

$$\begin{aligned} \frac{d}{dt} i_c^a &= -\frac{R_c}{L_c} i_c^a - \frac{n_c s_c^a v_{dc}^a}{L_c} + \frac{v_s^a}{L_c}, \\ \frac{d}{dt} v_{dc}^a &= \frac{s_c^a i_c^a}{C_{dc}} - \frac{v_{dc}^a}{R_{dc} C_{dc}}. \end{aligned} \tag{8.3}$$

It is important to remark that this model can be easily extended to the other two phases thanks to the single-phase nature of the H-Bridges. Transients of the source voltage and the load power are also included in the model; however, in order to simplify the analyses, they will be considered as disturbances henceforth.

From (8.3), it is possible to obtain the model of the CHB STATCOM at fundamental frequency, just by replacing the commutation function with its fundamental component, which is usually called the modulating signal. Thus,

$$s_c^a \simeq G_{ac} m_c^a = G_{ac} M_c \sin(\omega_s t + \phi_c) = G_{ac} \left\{ m_c^d \sin(\omega_s t) + m_c^q \cos(\omega_s t) \right\} \tag{8.4}$$

where G_{ac} is the gain of the modulation technique and m_c^a is the modulating signal that is—in steady state—a sinusoidal function with `sine` and `cosine` components, which amplitudes are defined in the dq-axes by m_c^d and m_c^q [1].

Replacing (8.4) into (8.3) and considering the sinusoidal nature of the AC variables, it is possible to express the model in the dq SRF proposed for single-phase systems. Hence, the resulting STATCOM equations are,

$$\begin{aligned} \frac{d}{dt} i_c^d &= -\frac{R_c}{L_c} i_c^d + \omega_s i_c^q - \frac{n_c G_{ac} m_c^d v_{dc}}{L_c} + \frac{v_s^d}{L_c}, \\ \frac{d}{dt} i_c^q &= -\omega_s i_c^d - \frac{R_c}{L_c} i_c^q - \frac{n_c G_{ac} m_c^q v_{dc}}{L_c} + \frac{v_s^q}{L_c}, \\ \frac{d}{dt} v_{dc} &= \frac{G_{ac} \left(m_c^d i_c^d + m_c^q i_c^q \right)}{2 C_{dc}} - \frac{v_{dc}}{R_{dc} C_{dc}}. \end{aligned} \tag{8.5}$$

8.2.1.1 Steady State Analysis

In order to evaluate the stationary behavior of the CHB STATCOM, the state variable equations must be evaluated in steady state, i.e. the derivatives are equal to zero. Then, the resulting equations must be solved and the modulating signals are calculated in order to reach a desired operating condition.

Thus, the steady state equations are,

$$\begin{aligned} 0 &= -\frac{R_c}{L_c} I_c^d + \omega_s I_c^q - \frac{n_c G_{ac} M_c^d V_{dc}}{L_c} + \frac{V_s^d}{L_c}, \\ 0 &= -\omega_s I_c^d - \frac{R_c}{L_c} I_c^q - \frac{n_c G_{ac} M_c^q V_{dc}}{L_c} + \frac{V_s^q}{L_c}, \\ 0 &= \frac{G_{ac}\left(M_c^d I_c^d + M_c^q I_c^q\right)}{2C_{dc}} - \frac{V_{dc}}{R_{dc} C_{dc}}, \end{aligned} \tag{8.6}$$

where the variables in capital letters denote the constant value of each variable in an arbitrary operating point.

In order to force a desired power factor in the source side, or equivalently to impose a phase angle Φ_s between the source current and voltage, the following equation can be considered,

$$\Phi_s = \operatorname{atan}\left(\frac{V_s^q}{V_s^d}\right) - \operatorname{atan}\left(\frac{I_s^q}{I_s^d}\right) = \operatorname{atan}\left(\frac{V_s^q}{V_s^d}\right) - \operatorname{atan}\left(\frac{I_l^q + I_c^q}{I_l^d + I_c^d}\right). \tag{8.7}$$

This previous equation calculates the difference between the source voltage angle and the phase of the source current, which corresponds to the source power factor angle Φ_s. It is important to remark that both d and q components of the source current are composed of the summation of the compensator and load currents.

For sake of simplicity in future calculations, the following definitions are made,

$$K_s = \tan(\Phi_s) = \frac{I_l^q + I_c^q}{I_l^d + I_c^d}, \tag{8.8}$$

$$I_c^q = K_s I_c^d + \left(K_s I_l^d - I_l^q\right) = K_s I_c^d + \lambda_s. \tag{8.9}$$

For a given linear load (I_l^d and I_l^q) and an imposed source power factor, the values of K_s and λ_s will be known. Then, (8.6) and (8.7) can be solved for I_c^d, which gives the following second order polynomial,

$$R_c\left\{1 + K_s^2\right\}\left(I_c^d\right)^2 + \left\{2R_c K_s \lambda_s - V_s^d - K_s V_s^q\right\} I_c^d + \left\{\frac{2V_{dc}^2 n_c}{R_{dc}} - \lambda_s V_s^q + \lambda_s^2 R_c\right\} = 0, \tag{8.10}$$

where the DC voltage V_{dc} must be also imposed in order to solve this equation. This voltage should ensure that the summation of the DC voltages of all the power cells must be higher than the amplitude of the source voltage $|V_s|$, i.e.,

$$n_c V_{dc} > |V_s| = \sqrt{\left(V_s^d\right)^2 + \left(V_s^q\right)^2}. \tag{8.11}$$

This constraint rises because VSCs operate with a DC voltage that must be higher than the peak value of the voltage in the AC side. A suitable value for V_{dc} should consider at least a 10 % security margin. Then (8.11) becomes,

$$V_{dc} = \frac{k_{dc}}{n_c}\sqrt{\left(V_s^d\right)^2+\left(V_s^q\right)^2}, \tag{8.12}$$

where k_{dc} = 1.1 to ensure the 10 % margin.

As (8.10) is a second order polynomial, it has two feasible solutions and just one of them must be selected. The election must consider the lowest absolute value for I_c^d, because this will minimize the current in the compensator and therefore the losses are reduced. It is worth noting from (8.10), that the value of I_c^d depends on neither the value of inductance L_c nor the capacitance C_{dc}, i.e., the current that the compensator requires to inject to achieve a desired power factor is independent of the value of these passive elements.

Once the value of I_c^d is found, I_c^q is easily obtained from (8.9). Then, the value of the modulating signals are calculated as,

$$M_c^d = \frac{V_s^d - R_c I_c^d + \omega_s L_c I_c^q}{n_c G_{ac} V_{dc}}, \tag{8.13}$$

$$M_c^q = \frac{V_s^q - R_c I_c^q - \omega_s L_c I_c^d}{n_c G_{ac} V_{dc}}. \tag{8.14}$$

Example 8.1 Let us consider an inductive load, as described in Table 8.1. Then, the number of cells must be selected, in this example n_c = 3 cells will be included in the topology, which generates a 7-level voltage waveform in each phase. When the number of cells is already defined, the DC voltage of each H-Bridge can be calculated using (8.12). Considering a security margin of 10 % (k_{dc} = 1.1) and taking into consideration that the peak value of the line-to-neutral voltage for the selected case study is 310 V, the DC voltage for each module results in 114 V_{dc} approximately as given by (8.12).

According with the parameters of Table 8.1, direct and quadrature components of the load current are 6 and −6.4 A, respectively. Then, if a unitary power factor is required, (8.8) and (8.9) lead to K_s = 0 and $\lambda_s = -I_l^q$ = 6.4. Using these values, (8.10) turns to

$$R_c\left(I_c^d\right)^2 - V_s^d I_c^d + \left\{\frac{6V_{dc}^2}{R_{dc}} + I_l^q V_s^q + \left(I_l^q\right)^2 R_c\right\} = 0. \tag{8.15}$$

Table 8.1 STATCOM parameters

Parameter	Value
Load nominal line-to-line voltage	380 V_{rms}
Load nominal power	5 kVA
Load power factor	0.8
System nominal frequency	50 Hz
STATCOM AC inductance filter	3 mH
STATCOM DC capacitor	4500 μF

If the SRF transformation is synchronized with the v_s voltage; then, its quadrature component V_s^q can be considered equal to zero. Thus, the only unknown values in (8.15) are the parasitic resistances R_c and R_{dc}. The estimation of the value for these elements is quite complex and it can be done using parameter identification algorithms. For this example, these values are selected as $R_c = 0.09\ \Omega$ and $R_{dc} = 1\ \text{k}\Omega$ just for illustration purposes.

Solving (8.15), with the aforementioned condition, yields to two possible solutions for the direct compensator current: 3.45 kA and 262 mA. Certainly, the second value is the right solution, as the compensator just requires a small amount of active power to maintain the DC voltages in their reference. Then, the *dq* components of the modulating signal for the H-Bridges can be easily obtained using (8.13) and (8.14). Considering the parameters of Table 8.1 and an AC gain of $G_{ac} = 1$ for Phase Shifted Sinusoidal Pulse Width Modulation (PS-PWM), the resulting modulating signals are

$$\begin{aligned} M_c^d &= 0.9267, \\ M_c^q &= -0.0024. \end{aligned} \tag{8.16}$$

An open-loop simulation of the proposed configuration was performed and the results are summarized in Fig. 8.2, where the key waveforms of the multilevel STATCOM are shown. Figure 8.2a illustrates that the overall current is in phase with the load voltage, which is the expected behavior of the STATCOM. The compensator current in Fig. 8.2b is almost 90° shifted with respect to the load voltage, because the compensator mainly delivers reactive current and just a small amount of active power is taken from the three-phase source in order to compensate the converters losses. Figures 8.2c and d, show the total multilevel waveform and the voltage of an individual H-Bridge, respectively. It can be seen the seven levels achieved in the multilevel STATCOM thanks to the adequate phase shift in the individual patterns of each module. In fact, Fig. 8.2f shows the spectra of the aforementioned Pulse Width Modulation (PWM) voltages, where it can be seen that the dominant harmonics are pushed around three times the equivalent commutation frequency of each power cell (equals to 2 times the real switch commutation frequency for unipolar Sinusoidal Pulse Width Modulation (SPWM) [2]), which in this case is 160 times the system frequency (i.e. 8 kHz).

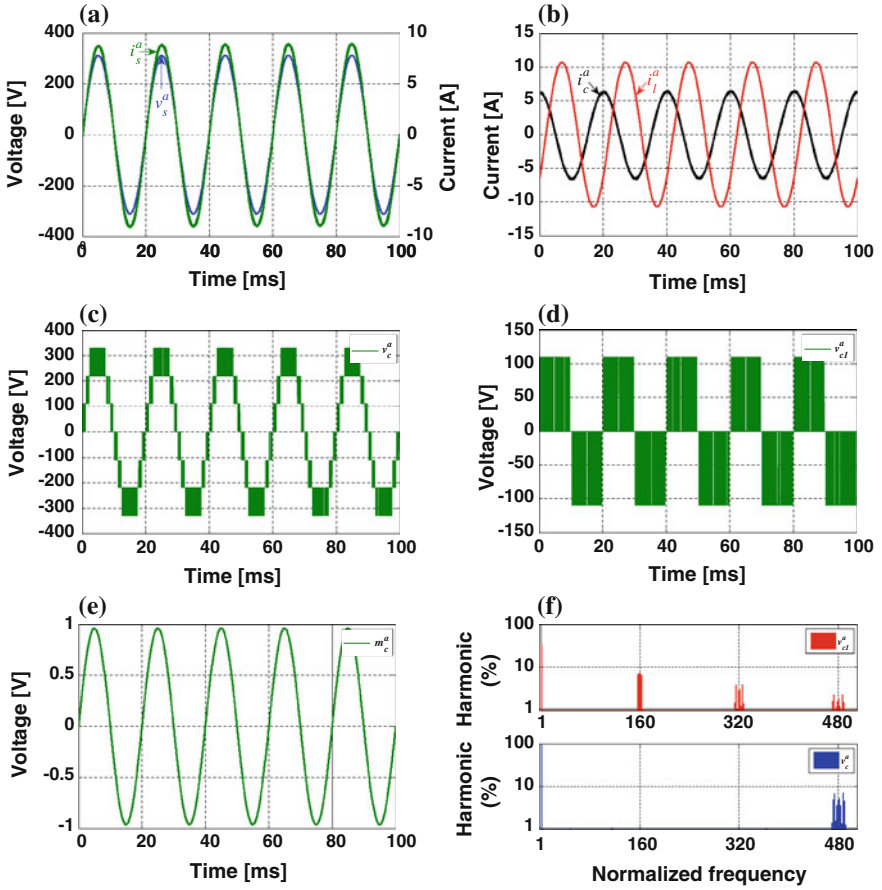

Fig. 8.2 **a** Load voltage and overall current, **b** load current and STATCOM current, **c** multilevel STATCOM voltage, **d** single H-Bridge AC voltage, **e** modulating signal, **f** PWM voltage spectra (single cell and overall multilevel waveform)

8.2.2 Neutral Point Clamped Topology

In an NPC based STATCOM, an NPC converter is connected in parallel to the load through a first-order inductive filter which works as a controlled current source jointly with the NPC. The three-phase NPC topology which generates L voltage levels between each phase and the point N is built using $(L-1)$ capacitors, $6(L-1)$ power valves, $3(L-1)(L-2)$ diodes to share and clamp the total DC voltage in $V_{dc}/(L-1)$ levels [3]. Specifically, for $L = 3$ levels there are two capacitors at the DC side whose voltages add up the voltage of the DC bus bar, 12 power valves and 6 diodes for clamping the capacitor voltages as shown in Fig. 8.3. Each capacitor in

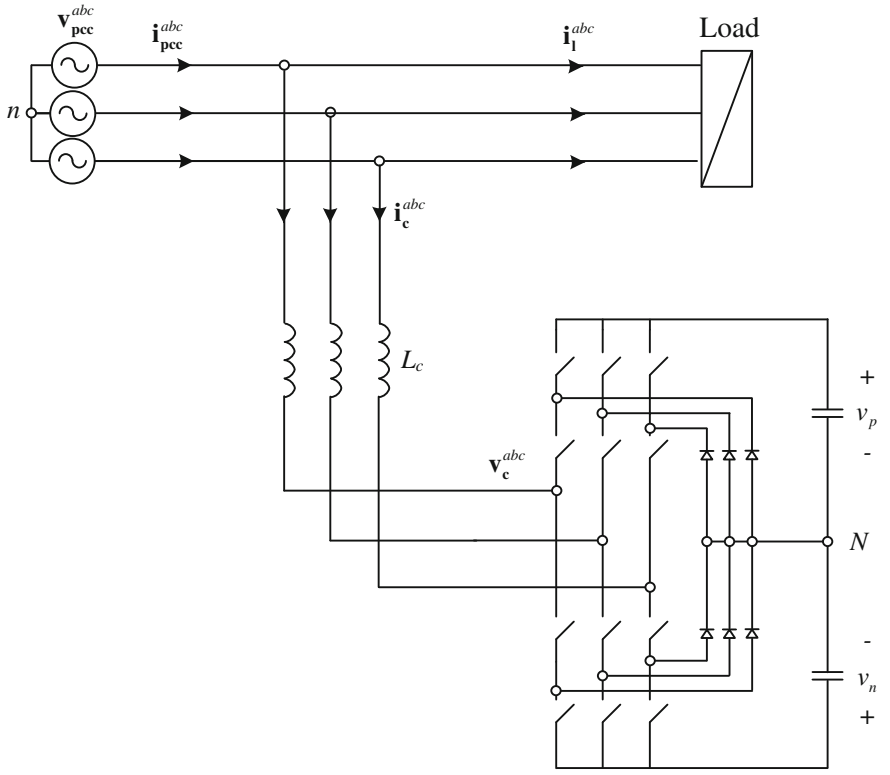

Fig. 8.3 STATCOM based on an NPC Topology

the DC side allows generating two levels—zero or the voltage value of the capacitor voltage—to the line-to-neutral NPC voltage. Reducing the analysis to an NPC with two DC capacitors, the current through each capacitor can be written in terms of the switching function and the NPC input currents, then

$$i_x = \mathbf{s}_{\mathbf{cx}}^{abc^T} \mathbf{i}_{\mathbf{c}}^{abc}, \tag{8.17}$$

where i_x is the current in the positive bar (i_p) or the current in the negative bar (i_n); the capacitors voltage dynamics can be obtained from Kirchhoff current law at the DC side; thus,

$$\frac{d}{dt} v_x = \frac{i_x}{C_{dc}} = \frac{\mathbf{s}_{\mathbf{cx}}^{abc^T} \mathbf{i}_{\mathbf{c}}^{abc}}{C_{dc}}, \tag{8.18}$$

where v_x is either the voltage in the upper capacitor (v_p) or the voltage in the negative capacitor (v_n). The relation of the capacitors voltages can be conveniently defined in terms of the summation and the subtraction of the capacitors voltages; so that,

$$\begin{bmatrix} \Delta v \\ v_{pn} \end{bmatrix} = \begin{bmatrix} v_p + v_n \\ v_p - v_n \end{bmatrix}, \tag{8.19}$$

where v_{pn} is the DC bus voltage and Δv is the difference between the capacitor voltages and it is expected to be zero in order to share evenly the DC voltages. (8.20) allows describing the NPC voltage in terms of the relation of the switching function associated to each capacitor; then,

$$\mathbf{v}_{\mathbf{c}}^{abc} = \frac{1}{2}\mathbf{T}\begin{bmatrix} \underbrace{\left(\mathbf{s}_{\mathbf{cp}}^{abc} + \mathbf{s}_{\mathbf{cn}}^{abc}\right)}_{\mathbf{s}_{\mathbf{cpn}+}^{abc}} & \underbrace{\left(\mathbf{s}_{\mathbf{cp}}^{abc} - \mathbf{s}_{\mathbf{cn}}^{abc}\right)}_{\mathbf{s}_{\mathbf{cpn}-}^{abc}} \end{bmatrix}\begin{bmatrix} \Delta v \\ v_{pn} \end{bmatrix}, \tag{8.20}$$

where the matrix $\mathbf{T}$ is the relation between the phase-to-N-point of the NPC and the phase voltage and it is defined by

$$\mathbf{T} = \frac{1}{3}\begin{bmatrix} 2 & -1 & -1 \\ -1 & 2 & -1 \\ -1 & -1 & 2 \end{bmatrix}. \tag{8.21}$$

On the other hand, on the AC side of the NPC and using Kirchhoff Voltage Law (KVL), one can write

$$\mathbf{v}_{\mathbf{s}}^{abc} = L_c\frac{d}{dt}\mathbf{i}_{\mathbf{c}}^{abc} + R_c\mathbf{i}_{\mathbf{c}}^{abc} + \mathbf{v}_{\mathbf{c}}^{abc} = L_c\frac{d}{dt}\mathbf{i}_{\mathbf{c}}^{abc} + R_c\mathbf{i}_{\mathbf{c}}^{abc} + \frac{1}{2}\mathbf{T}\begin{bmatrix} \mathbf{s}_{\mathbf{cpn}+}^{abc} & \mathbf{s}_{\mathbf{cpn}-}^{abc} \end{bmatrix}\begin{bmatrix} \Delta v \\ v_{pn} \end{bmatrix}, \tag{8.22}$$

from where the STATCOM current $\mathbf{i}_{\mathbf{c}}^{abc}$ can be obtained. Using (8.18) to (8.22), the state model in the *abc* frame can be obtained as,

$$\begin{aligned} \frac{d}{dt}\mathbf{i}_{\mathbf{c}}^{abc} &= \frac{1}{L_c}\mathbf{v}_{\mathbf{s}}^{abc} - \frac{R_c}{L_c}\mathbf{i}_{\mathbf{c}}^{abc} - \frac{1}{2L_c}\mathbf{T}\begin{bmatrix} \mathbf{s}_{\mathbf{cpn}+}^{abc} & \mathbf{s}_{\mathbf{cpn}-}^{abc} \end{bmatrix}\begin{bmatrix} \Delta v \\ v_{pn} \end{bmatrix}, \\ \frac{d}{dt}v_{pn} &= \frac{d}{dt}\left(v_p - v_n\right) = \mathbf{T}\frac{\mathbf{s}_{\mathbf{cpn}-}^{abc}\mathbf{i}_{\mathbf{c}}^{abc}}{C_{dc}}, \\ \frac{d}{dt}\Delta v &= \frac{d}{dt}\left(v_p + v_n\right) = \mathbf{T}\frac{\mathbf{s}_{\mathbf{cpn}+}^{abc}\mathbf{i}_{\mathbf{c}}^{abc}}{C_{dc}}, \end{aligned} \tag{8.23}$$

where it is important to highlight that two dynamics exist in the DC side, which are the dynamic of the difference between the capacitors voltages $\frac{d}{dt}\Delta v$ and the dynamic of the total DC voltage, $\frac{d}{dt}v_{pn}$. For convenience in the analysis, it is recommended to describe the state model in the SRF. Then, using the Park transformation, (8.23) leads to

$$
\begin{aligned}
\frac{d}{dt}i_c^d &= \frac{1}{L_c}\left(v_{\mathbf{s}}^d - R_c i_{\mathbf{c}}^d - \frac{G_{ac}}{2}\begin{bmatrix} m_{cpn+}^d & m_{cpn-}^d \end{bmatrix}\begin{bmatrix} \Delta v \\ v_{pn} \end{bmatrix}\right) + \omega_s i_c^q, \\
\frac{d}{dt}i_c^q &= \frac{1}{L_c}\left(v_{\mathbf{s}}^q - R_c i_{\mathbf{c}}^q - \frac{G_{ac}}{2}\begin{bmatrix} m_{cpn+}^q & m_{cpn-}^q \end{bmatrix}\begin{bmatrix} \Delta v \\ v_{pn} \end{bmatrix}\right) - \omega_s i_c^d, \\
\frac{d}{dt}v_{pn} &= \frac{G_{ac}}{C_{dc}}\left[m_{cpn-}^d i_c^d + m_{cpn-}^q i_c^q\right], \\
\frac{d}{dt}\Delta v &= \frac{G_{ac}}{C_{dc}}\left[m_{cpn+}^d i_c^d + m_{cpn+}^q i_c^q\right],
\end{aligned}
\tag{8.24}
$$

where $\mathbf{m}_{\mathbf{cpn}+}^{dq}$ and $\mathbf{m}_{\mathbf{cpn}-}^{dq}$ are the relation between the modulators $\mathbf{m}_{\mathbf{cp}}^{dq}$ and $\mathbf{m}_{\mathbf{cn}}^{dq}$ described in (8.20). The modulators in the *dq* frame are calculated using a steady state analysis as described in the following section.

8.2.2.1 Steady State Analysis

In order to share the required DC voltage among the power valves of the STATCOM, both DC capacitors must have the same DC voltage level. In steady state, these voltages are kept constant, thus $\Delta v = 0$ and $v_{pn} = V_{dc}$. Hence, the model can be simplified to a classic three-phase VSC. Indeed, solving the DC side expression (last two expressions of (8.24)) the solutions are (i) $\mathbf{i}_{\mathrm{c}}^{dq} = 0$ and (ii) $m_{\mathrm{p}}^d = -m_{\mathrm{n}}^d$ and $m_{\mathrm{p}}^q = -m_{\mathrm{n}}^q$. Solution (i) is trivial and therefore it is discarded; so $m_{\mathrm{cpn}-}^d = 2m_{\mathrm{p}}^d$ and $m_{\mathrm{cpn}-}^q = 2m_{\mathrm{p}}^q$ are the selected values for the modulating signals. Also, considering the power losses in the DC side, (8.24) yields to,

$$
\begin{aligned}
0 &= V_{\mathbf{s}}^d - R_c I_{\mathbf{c}}^d - \frac{G_{ac}}{2} M_{cpn-}^d V_{dc} + L_c \omega_s I_c^q, \\
0 &= V_{\mathbf{s}}^q - R_c I_{\mathbf{c}}^q - \frac{G_{ac}}{2} M_{cpn-}^q V_{dc} - L_c \omega_s I_c^d, \\
0 &= \frac{G_{ac}}{C_{dc}}\left[M_{cpn-}^d I_c^d + M_{cpn-}^q I_c^q\right] - \frac{V_{dc}}{C_{dc} R_{dc}}.
\end{aligned}
\tag{8.25}
$$

As the NPC topology is a boost type of converter, the DC voltage must be higher than the peak value of the line-to-line voltage. Then, the total DC bus voltage can be selected as,

$$
V_{dc} = k_{dc}\sqrt{3}|v_s| = k_{dc}\sqrt{3}\sqrt{\left(V_s^d\right)^2 + \left(V_s^q\right)^2}, \tag{8.26}
$$

where k_{dc} = 1.1 to ensure a 10 % security margin. In order to equally share the converter power, the capacitor voltages must be equal among them. Thus, the voltage in each DC capacitor will depend on the number of levels *L* and they can be calculated as,

$$V_{capacitors} = \frac{V_{dc}}{L-1}. \tag{8.27}$$

From Sect. 8.2.1, the STATCOM quadrature current can be defined in terms of K_s and the load current, then

$$I_c^q = K_s I_c^d + \left(K_s I_l^d - I_l^q\right) = K_s I_c^d + \lambda_s, \tag{8.28}$$

where the direct component of the STATCOM current can be computed in the same way that the CHB case, i.e.,

$$R_c\left\{1+K_s^2\right\}\left(I_c^d\right)^2 + \left\{2R_c K_s \lambda_s - V_s^d - K_s V_s^q\right\} I_c^d + \left\{\frac{V_{dc}^2}{2R_{dc}} - \lambda_s V_s^q + \lambda_s^2 R_c\right\} = 0. \tag{8.29}$$

Computing the direct and quadrature STATCOM currents, the modulators in the *dq* frame can be solved using,

$$\begin{aligned} M_{cpn-}^d &= 2\frac{V_{\mathbf{s}}^d - R_c I_{\mathbf{c}}^d + L_c \omega_s I_c^q}{G_{ac} V_{dc}}, \\ M_{cpn-}^q &= 2\frac{V_{\mathbf{s}}^q - R_c I_{\mathbf{c}}^q - L_c \omega_s I_c^d}{G_{ac} V_{dc}}. \end{aligned} \tag{8.30}$$

Example 8.2 A 3-level NPC converter was considered to compensate the same load presented in the Example 8.1. In this case, the total DC voltage was selected as V_{dc} = 700 V, and therefore, each capacitor must hold just the half of it ($V_{capacitors}$ = 350 V). The same commutating frequency was selected, i.e. f_{sw} = 8 kHz, which corresponds to 160 times the system frequency. Also, the same parasitic resistances R_c = 0.09 Ω and R_{dc} = 1 kΩ were selected. But, for this example, the STATCOM inductance was chosen as L_c = 9 mH.

Solving the steady state equations in order to achieve unitary overall power factor (K_s = 0), the compensator currents give $I_c^d \approx$ 800 mA and $I_c^q = \lambda_s = -I_l^q$ = 6.4 A. Thus, the modulating signals in the *dq* frame result in,

$$\begin{aligned} M_{cpn-}^d &= 2\frac{V_{\mathbf{s}}^d - R_c I_{\mathbf{c}}^d + L_c \omega_s I_c^q}{G_{ac} V_{dc}} = 0.9406, \\ M_{cpn-}^q &= 2\frac{V_{\mathbf{s}}^q - R_c I_{\mathbf{c}}^q - L_c \omega_s I_c^d}{G_{ac} V_{dc}} = -0.0083. \end{aligned} \tag{8.31}$$

The resulting waveforms for these modulating signals are shown in Fig. 8.4, where it is possible to observe that the multilevel STATCOM successfully achieves

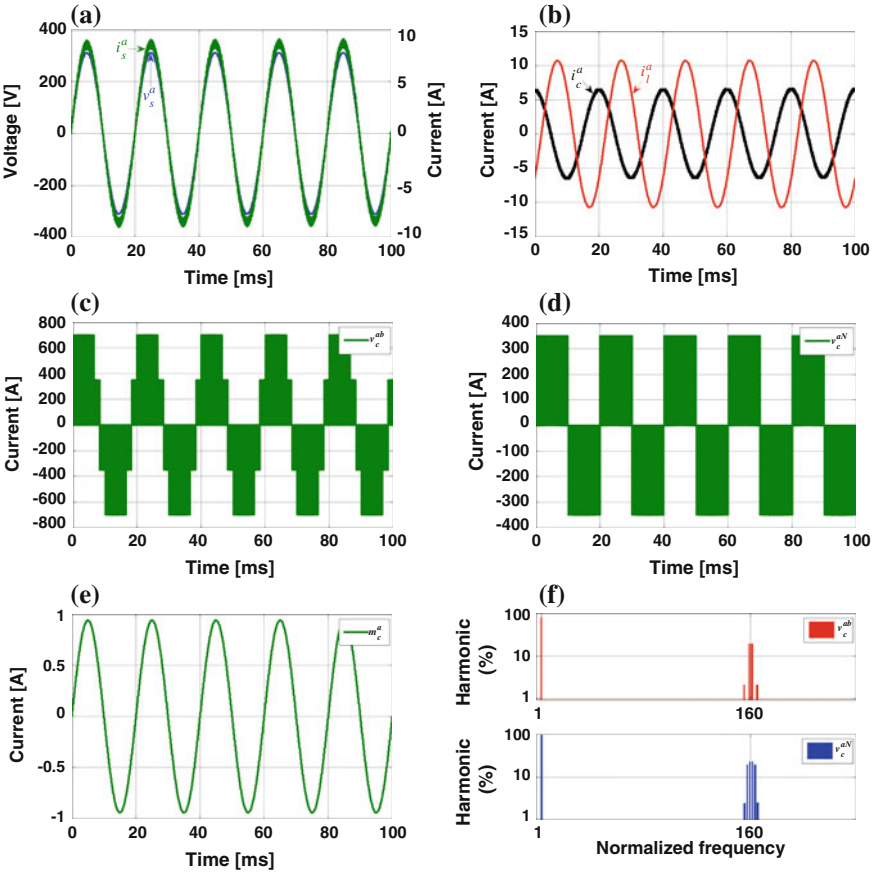

Fig. 8.4 **a** Load voltage and overall current, **b** load current and STATCOM current, **c** multilevel line-to-line STATCOM voltage, **d** multilevel line-to-*N*-point STATCOM voltage, **e** modulating Signal, **f** PWM voltage spectra (line-to-line and line-to-*N*-point)

the compensation condition. In fact, Fig. 8.4a illustrates the steady state behavior of the voltage and current in the AC mains, where the unitary power factor condition can be appreciated. Similar to the CHB topology, the injected current in Fig. 8.4b is almost 90° phase shifted from the load voltage, as it requires active power just to compensate the losses. Figures 8.4c, d, show the phase-to-phase and phase-to-neutral multilevel waveforms, respectively, which are obtained using the modulator shown in Fig. 8.4e. It can be seen the three levels of the NPC STATCOM in the line voltage, which produces a 5-level waveform between two lines of the three-phase system. It is important to remark that the equivalent switching frequency of the resulting multilevel waveforms is equal to the commutation frequency of the semiconductor devices, as Fig. 8.4f shows.

8.2.3 Multilevel Current Source Topology

The use of CSCs in a parallel connection to a common LC filter allows dividing the current in n_c converters [4–7]. Additionally, if a multilevel modulation technique is used, a multilevel current waveform with $L = 2n_c + 1$ levels could be obtained, allowing a smaller LC filter and/or reduce the switching frequency. This increases the current handling capability of the topology compared with classic three-levels CSCs.

For MCSC based STATCOM, three-phase CSCs—each one with its own DC inductor—are arranged in parallel and connected to the electrical grid through a common LC filter. Using a multilevel modulation technique, the LC filter size can be reduced as compared with the use of a conventional modulation technique. On the other hand, sharing the DC current in several converters allows reducing the DC inductors losses with respect to the use of a single converter handling the equivalent DC current level.

Considering Fig. 8.5, each *i*th CSC can be modeled as [8],

$$\mathbf{i}_{\mathbf{r}i}^{abc} = i_{dci}\mathbf{s}_{\mathbf{c}i}^{abc}, \tag{8.32}$$

$$v_{ri} = \left[\mathbf{v}_{\mathbf{c}}^{abc}\right]^T \mathbf{s}_{\mathbf{c}i}^{abc}, \tag{8.33}$$

where $\mathbf{i}_{\mathbf{r}i}^{abc}$ is the pulse-width current at the input of the *i*th CSC, i_{dci} is the DC current in the CSC, v_{ri} is the pulse width voltage at the DC side of the CSC, $\mathbf{v}_{\mathbf{c}}^{abc}$ is the voltage in the AC filter and is common to all the CSCs, and $\mathbf{s}_{\mathbf{c}i}^{abc}$ is the commutation function of the CSC.

The AC side can be modeled using Kirchhoff's laws, where for the current balance at the node for each capacitor it is necessary to consider $\mathbf{i}_{\mathbf{r}i}^{abc}$ as the sum of all the CSCs input currents, each one described in (8.32). Thus,

$$C_c \frac{d}{dt}\mathbf{v}_{\mathbf{c}}^{abc} = \mathbf{i}_{\mathbf{c}}^{abc} - \mathbf{i}_{\mathbf{r}}^{abc} = \mathbf{i}_{\mathbf{c}}^{abc} - \sum_{i=1}^{n_c} \mathbf{i}_{\mathbf{r}i}^{abc} = \mathbf{i}_{\mathbf{c}}^{abc} - \sum_{i=1}^{n_c} i_{dci}\mathbf{s}_{\mathbf{c}i}^{abc}, \tag{8.34}$$

while using voltage law at the filter input, one can write,

$$L_c \frac{d}{dt}\mathbf{i}_{\mathbf{c}}^{abc} = \mathbf{v}_{\mathbf{s}}^{abc} - \mathbf{v}_{\mathbf{c}}^{abc} - R_c\mathbf{i}_{\mathbf{c}}^{abc}, \tag{8.35}$$

where R_c is used to model the losses of the LC filter. On the other hand, the DC side can be modeled using the voltage law; thus,

$$R_{dc}i_{dci} = v_{ri} - L_{dc}\frac{d}{dt}i_{dci}, \tag{8.36}$$

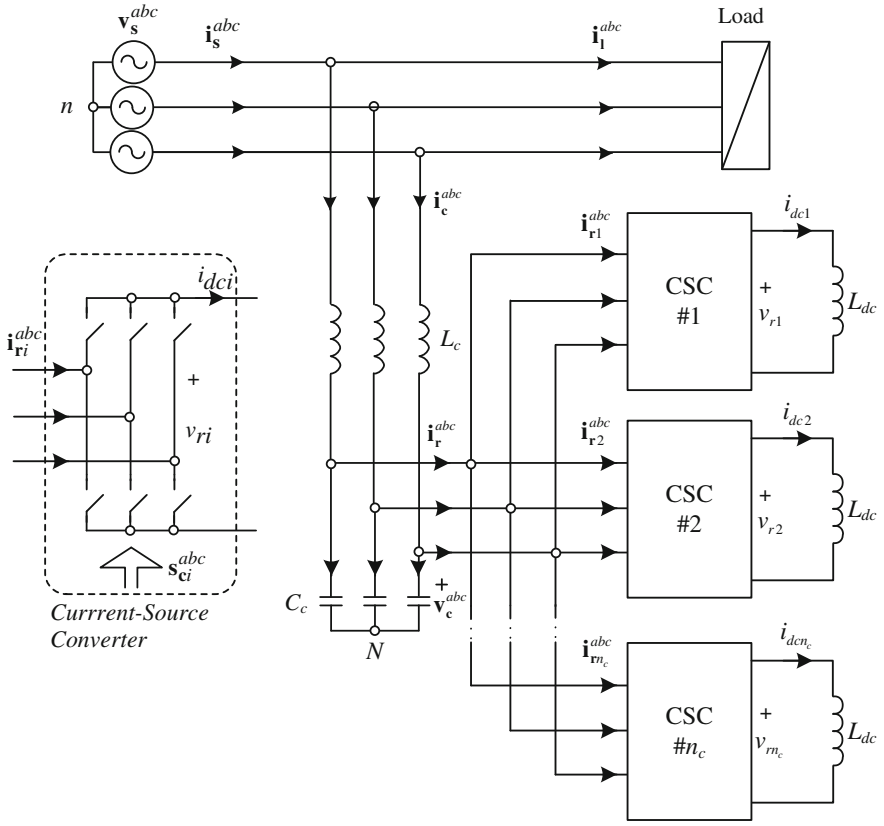

Fig. 8.5 STATCOM based on multilevel current source converters

where R_{dc} is used to model the losses in the CSC. From (8.34) to (8.36), it is possible to obtain the model of the MCSC STATCOM at fundamental frequency. Indeed, $\mathbf{s}_{\mathbf{c}i,}^{abc}$ can be approximated to its fundamental component, thus

$$\mathbf{s}_{\mathbf{c}i}^{abc} \approx G_{ac}\mathbf{m}_{\mathbf{c}i}^{abc}, \tag{8.37}$$

where $\mathbf{m}_{\mathbf{c}i}^{abc}$ is the modulating signal of the ith CSC and G_{ac} is the gain of the modulation technique for the fundamental component. Hence, the model can be written in the dq frame as,

$$\begin{aligned}
\frac{d}{dt}\mathbf{v}_\mathbf{c}^d &= \frac{1}{C_c}\left[\mathbf{i}_\mathbf{c}^d - \sum_{i=1}^{n_c} i_{dci} m_{ci}^d\right] + \omega_s \mathbf{v}_\mathbf{c}^q, \\
\frac{d}{dt}\mathbf{v}_\mathbf{c}^q &= \frac{1}{C_c}\left[\mathbf{i}_\mathbf{c}^q - \sum_{i=1}^{n_c} i_{dci} m_{ci}^q\right] - \omega_s \mathbf{v}_\mathbf{c}^d, \\
\frac{d}{dt}\mathbf{i}_\mathbf{c}^d &= \frac{1}{L_c}\left[\mathbf{v}_\mathbf{s}^d - \mathbf{v}_\mathbf{c}^d - R_c \mathbf{i}_\mathbf{c}^d\right] + \omega_s \mathbf{i}_\mathbf{c}^q, \\
\frac{d}{dt}\mathbf{i}_\mathbf{c}^q &= \frac{1}{L_c}\left[\mathbf{v}_\mathbf{s}^q - \mathbf{v}_\mathbf{c}^q - R_c \mathbf{i}_\mathbf{c}^q\right] - \omega_s \mathbf{i}_\mathbf{c}^q, \\
\frac{d}{dt} i_{dci} &= \frac{1}{L_{dc}}\left[v_{ri} - i_{dci} R_{dc}\right].
\end{aligned} \tag{8.38}$$

8.2.3.1 Steady State Analysis

Considering the average model and the Park transform synchronized with the supply voltage, the steady state equations of the MCSC can be obtained from the operating region of the CSC [9]. Then, the stationary equations can be written in terms of its active and reactive power as,

$$P_c = V_s^d I_c^d = \frac{n_c K_{dc} M_c^d}{\left(1 - \omega_s^2/\omega_{LC}^2\right)^2} V_s^{d^2}, \tag{8.39}$$

$$Q_c = -V_s^d I_c^q = -\left(\frac{n_c K_{dc} M_c^d M_c^q}{\left(1 - \omega_s^2/\omega_{LC}^2\right)^2} + \frac{\omega_s C_c}{\left(1 - \omega_s^2/\omega_{LC}^2\right)}\right) V_s^{d^2}, \tag{8.40}$$

where the R_c has been neglected in order to simplify the expression. For each DC inductor the DC current can be computed using

$$I_{dci} = \frac{K_{dc} M_{ci}^d}{G_{ac}\left(1 - \omega_s^2/\omega_{LC}^2\right)} V_s^d, \tag{8.41}$$

where

$$K_{dc} = \frac{G_{ac}^2}{R_{dc}}, \tag{8.42}$$

$$\omega_{LC} = \frac{1}{\sqrt{L_c C_c}}. \tag{8.43}$$

Unlike the VSCs case, for CSCs the DC current level is expected to be regulated in function of the required power factor compensation for a given load. A way to do so, is to define the modulator index as a function of the required power factor. As shown in Sect. 8.2.1, I_c^q can be written as

$$I_c^q = K_s I_c^d + \left(K_s I_l^d - I_l^q\right) = K_s I_c^d + \lambda_s, \tag{8.44}$$

therefore, a given linear load (I_l^d and I_l^q) and an imposed source power factor, the values of K_s and λ_s will be known. The direct component of the compensator current, I_c^d, is used to keep the DC level in the CSC, so the DC current must first be defined so as to define I_c^d. The DC current can be solved from (8.40), (8.41) and (8.44); thus,

$$I_{dci} = \frac{I_c^q - \omega_s C_c V_c^d}{n_c M_c^q} = \frac{K_s I_c^d + \lambda_s - \omega_s C_c V_c^d}{n_c M_c^q} \tag{8.45}$$

while for, V_c^d

$$V_c^d = V_s^d + \omega_s L_c I_c^q = V_s^d + \omega_s L_c \left(K_s I_c^d + \lambda_s\right), \tag{8.46}$$

thus, the DC current is defined as a function of the desired power factor and the quadrature component of the modulator by

$$I_{dci} = \frac{I_c^q - \omega_s C_c V_c^d}{n_c M_c^q} = \frac{K_s I_c^d + \lambda_s - \omega_s C_c \left(V_s^d + \omega_s L_c \left(K_s I_c^d + \lambda_s\right)\right)}{n_c M_c^q}. \tag{8.47}$$

Because it is expected that I_c^d should be much lower than I_c^q, it can be neglected in (8.47). Then, a simple way to define the DC current level is to choose a desired, M_c^q for a given STATCOM with n_c CSCs. For instance, M_c^q can be chosen as 80 % of its maximum possible value. The direct component of the modulator, M_c^d, must be computed in order to keep the DC current level. Using (8.41), one has

$$M_c^d = \frac{G_{ac} I_{dci} \left(1 - \omega_s^2 / \omega_{LC}^2\right)}{K_{dc} V_s^d}. \tag{8.48}$$

On the other hand, the modulating signal can be computed in terms of an operating point for a given DC current, thus

$$M_c^q = \frac{K_s I_c^d + \lambda_s - \omega_s C_c \left(V_s^d + \omega_s L_c \left(K_s I_c^d + \lambda_s\right)\right)}{n_c I_{dci}}. \tag{8.49}$$

Example 8.3 Because the CSC topology can handle a higher current, a load three times bigger than the used in the VSCs approaches will be used and it is described in Table 8.2. The load currents in *dq* frames are 31.5 and −23.7 A for the direct and quadrature components, respectively. The switching frequency for each CSC is equal to 1,050 Hz, 21 times bigger than the grid frequency. Then, for a unitary power factor requirement ($K_s = 0$ and $\lambda_s = -I_l^q = 23.7$ A) and choosing $M_c^q = 1.2$ the required DC current is given by

Table 8.2 MCSC STATCOM parameters

Parameter	Value
Load nominal line-to-line voltage	380 V_{rms}
Load nominal power	15 kVA
Load power factor	0.8
System nominal frequency	50 Hz
STATCOM AC LC filter	20 mH|40 μF
STATCOM DC inductor	70 mH

$$M_c^q = \frac{I_c^q - \omega_s C_c V_c^d}{n_c M_c^q} \approx \frac{\lambda_s - \omega_s C_c \left(V_s^d + \omega_s L_c \lambda_s\right)}{n_c I_{dci}} = \frac{14.1}{n_c} \text{A}. \tag{8.50}$$

Using three CSCs in parallel ($n_c = 3$), the DC current in each converter is 4.7 A. The direct component of the modulating signal can be calculated using (8.48) and $R_{dc} = 8\ \Omega$, thus

$$M_c^d = \frac{G_{ac} I_{dci} \left(1 - \omega_r^2 / \omega_{LC}^2\right)}{K_{dc} V_s^d} = 0.102. \tag{8.51}$$

Figure 8.6 shows the performance of the MCSC STATCOM. The unitary power factor is achieved (Fig. 8.6a) as the supply current is in phase with the supply voltage. Figure 8.6b shows the load current with the 0.8 inductive power factor and the STATCOM current used to compensate the load reactive power. In order to obtain the required current to compensate the load reactive power, the three CSC are modulated using the modulating signal shown in Fig. 8.6e, previously calculated. Using this modulator in each CSC, the converter current shown in Fig. 8.6d is injected by each CSC to the LC filter. Because CSCs are connected in parallel, the current in the LC filter is the sum of the three CSCs, as shown in Fig. 8.6c. The multilevel current is obtained thanks to the phase shifting among carriers used to generate the gating signals. In this case, the multilevel current has its dominant harmonics near to three times the switching frequency of the CSCs, as shown in Fig. 8.6f.

8.3 Control Requirements for Multilevel STATCOM Topologies

The main control objective for a STATCOM topology can be either voltage regulation or power factor correction at a given point of the distribution system. In the first case, the control reference will be the desired AC mains voltage, which will be regulated with the injection/absorption of reactive power in the shunt branch.

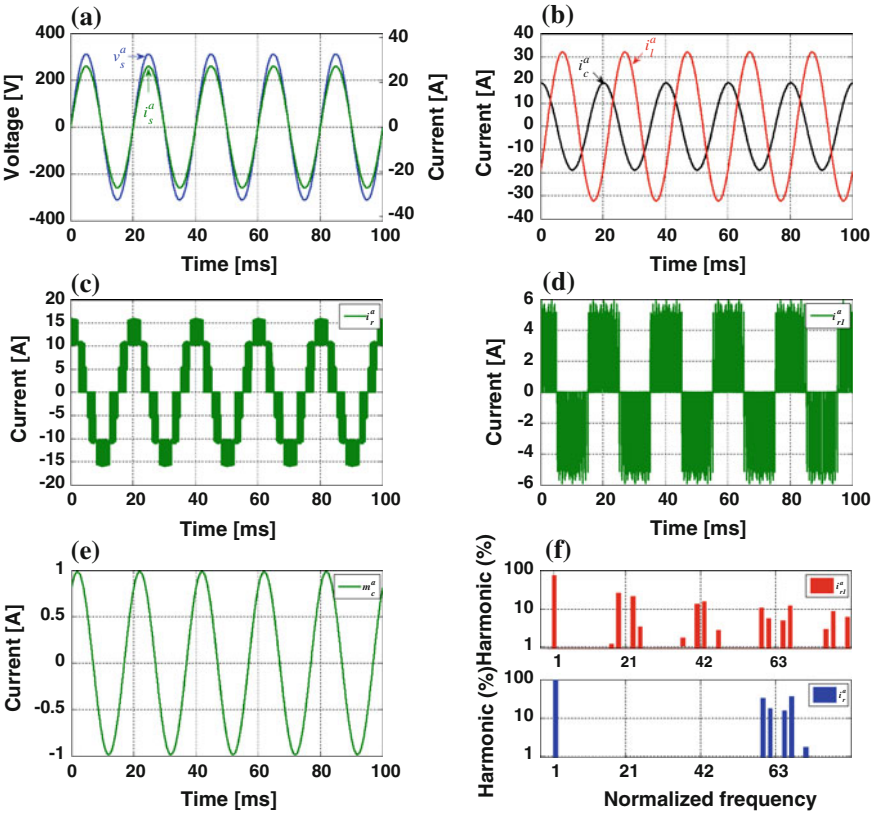

Fig. 8.6 **a** Load voltage and overall current, **b** load current and STATCOM current, **c** multilevel current waveform, **d** current waveform of a single CSC, **e** modulating Signal, **f** PWM current spectra (single CSC and overall multilevel waveform)

For power factor correction, the control reference is the angle between the source current and voltage, which can be manipulated by means of the current drawn by the converter. In both cases, the STATCOM control variables are the active and reactive components of the converter´s current, and therefore, it is usual to find a cascade strategy to control the topology, where the inner loops are for the converter current components and the outer loops are considered for the DC side variables (voltage/current) and the main control goal (AC voltage regulation or power factor correction).

Particularly, for multilevel STATCOMs, besides the aforementioned control schemes, dedicated strategies are included in order to achieve equal power distribution among all the components of the converter. This is required because the compensator parameters differ from their nominal values. These dedicated strategies must modify the gating patterns of the semiconductor devices, which can be done by means of the modulating signals, the triangular carrier (for SPWM) and/or the dead-times (or overlaps) between commutations.

The remaining of this section will depict the main control requirements for three different representative multilevel STATCOM topologies: CHB, NPC and MCSC.

8.3.1 Cascade H-Bridge

The basic requirement from the control point of view is to set the compensator currents in order to achieve the main control goals, which are the reactive power injection and the DC side variables regulation. Moreover, for the specific case of the CHB based STATCOM, due to the inherent parameters deviation among the power modules, the equal distribution of the DC voltages in all the cells must be forced. Otherwise, the harmonic cancellation among the modules will not be achieved as expected, and therefore, the resulting waveforms will contain undesired harmonics.

For instance, Fig. 8.7a shows the AC voltage waveform when the DC voltages of the H-Bridges are unbalanced, and it can observed in the spectra of Fig. 8.7b that the harmonic cancellation is not produced as expected, and therefore, the resulting waveform contains much lower order harmonics than its balanced counterpart (shown in Fig. 8.2). Besides that this DC voltage unbalance produces uncharacteristic harmonics and undesired distortion in the AC currents, it also produces an unequal power distribution among the power modules, which will cause unbalanced power dissipation and semiconductor stress in the H-Bridges. This is also an unwanted effect, and hence the inclusion of a dedicated strategy to balance the DC voltages is indispensable.

8.3.2 Neutral Point Clamped

Similar to the CHB topology, the NPC multilevel STATCOM has two main goals: to inject the required reactive power and to regulate the DC bus voltage. In this

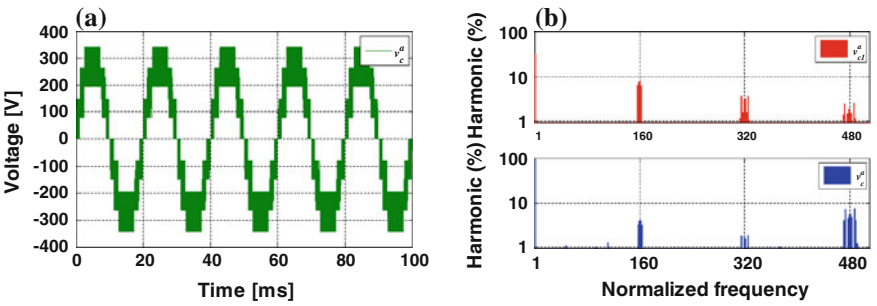

Fig. 8.7 **a** Converter AC voltage with unequal DC voltages, **b** voltage spectra of one cell (*top*) and the total converter (*bottom*) for unequal DC voltages

case, it is also required to include a dedicated strategy to achieve a balanced voltage distribution among the components. The phenomenon that this configuration presents is the unequal voltages in the DC capacitors, just like in the CHB based STATCOM.

As the neutral point *N* ("zero" level) is artificial or linear dependent on the voltages of the capacitors included in the NPC topology (no matter how many levels are considered) [10], when one phase is connected to the neutral point, some capacitors will be charging and others will be discharging [11]. In general, if the whole structure is symmetric, the neutral point currents will be equal to zero. But, under certain conditions, such as asymmetry in the gating patterns or difference in the inductance and/or capacitance values, it is possible that these currents transiently change their mean value, which will cause a voltage unbalance or equivalently, a displacement of the neutral point.

Similar to the CHB STATCOM, the DC link voltage unbalance in the NPC converter will result in distorted AC voltages, particularly, low frequency harmonics will appear. Furthermore, the NPC STATCOM switches are designed just for a fraction of the whole DC side voltage; hence, this assumption will no longer be hold if the DC capacitors voltages are not equally shared [12].

As the currents that flow through the DC capacitors in the NPC topology change according with the commutation states of the converter and usually they are not equal to zero, the DC capacitor voltages of the NPC STATCOM converter fluctuate from their expected values. This is a serious problem for NPC converters because, besides affecting the harmonic performance of the AC currents, it also determines the stable operation of the converter [13]. Therefore, the DC voltage balancing will become an important control goal in the NPC STATCOM. In this context, several schemes have been proposed and based on different approaches [14–16], among them, it is possible to highlight: auxiliary voltage balancing circuit [17], dedicated control schemes [18] and modified modulation techniques [19, 20].

8.3.3 Multilevel Current Source Converter

In the same way as VSC based topologies, MCSC structures must regulate the current level in each DC side, while the required reactive power is injected [21]. It is expected that each CSC supplies equal amount of reactive power, which does not necessarily require the same current level in the DC side of all converters. However, in order to produce a multilevel current waveform in the LC filter and compensate the low-order switching harmonics among the CSCs, an equal DC level is mandatory in each CSC. If the DC current levels are not equal among the CSCs, the harmonic compensation in the LC filter will not be produced as expected, and therefore, uncharacteristic waveforms will be obtained.

Along with the above, the use of an active damping strategy in the control scheme helps to reduce the losses in the LC filter because no extra damping resistor is required [22]. The main function of the active damping strategy is to compensate

the oscillation in the STATCOM currents, therefore—if no active damping is considered—the operating region of the converter will be reduced due to the current oscillations. Hence, a higher DC current level will be required in order to keep the compensation capabilities of the STATCOM, which will produce higher losses.

Finally, in order to reduce the losses in the CSCs and in their DC inductors, a control scheme that includes the capability to change the DC current level is mandatory [23]. This requirement is also included in VSCs topologies, where the DC voltage level must be kept in an imposed value. For CSCs, the DC current must be set according to the reactive power requirements, which makes the use of linear controllers very difficult due to the sensitivity of the operating point with respect to the DC current.

8.4 Linear Control Strategies

8.4.1 p-q *Theory Based Control*

In order to implement the control strategies based on the *p-q* theory, the calculation of the instantaneous active and reactive power in the electrical system is made using the voltages and currents in the α-β frame, obtained from the Clarke transformation. According to [24], the instantaneous complex power can be defined as,

$$s = p + jq = \left(v_\alpha i_\alpha + v_\beta i_\beta\right) + j\left(v_\beta i_\alpha - v_\alpha i_\beta\right), \tag{8.52}$$

where p and q are the instantaneous active and reactive power, respectively. As this expression uses instantaneous voltages and currents, there are no restrictions in s, and therefore it can be used for stationary and dynamic conditions.

Equation (8.52) can be rewritten in a matrix form, as

$$\begin{bmatrix} p \\ q \end{bmatrix} = \begin{bmatrix} v^\alpha & v^\beta \\ v^\beta & -v^\alpha \end{bmatrix} \begin{bmatrix} i^\alpha \\ i^\beta \end{bmatrix}, \tag{8.53}$$

which is the basic equation to compute the instantaneous power used for control purposes.

It is also useful to calculate the currents for given power references, which can be easily obtained inverting the matrix of (8.53) that leads to,

$$\begin{bmatrix} i^\alpha \\ i^\beta \end{bmatrix} = \frac{1}{\left(v^\alpha\right)^2 + \left(v^\beta\right)^2} \begin{bmatrix} v^\alpha & v^\beta \\ v^\beta & -v^\alpha \end{bmatrix} \begin{bmatrix} p \\ q \end{bmatrix}. \tag{8.54}$$

Once these preliminary definitions are made, the overall control scheme based on the *p-q* theory can be presented in Fig. 8.8. There, the system voltages and currents are transformed into the α-β frame in order to calculate the instantaneous active and reactive power using (8.53). These values are used to calculate the

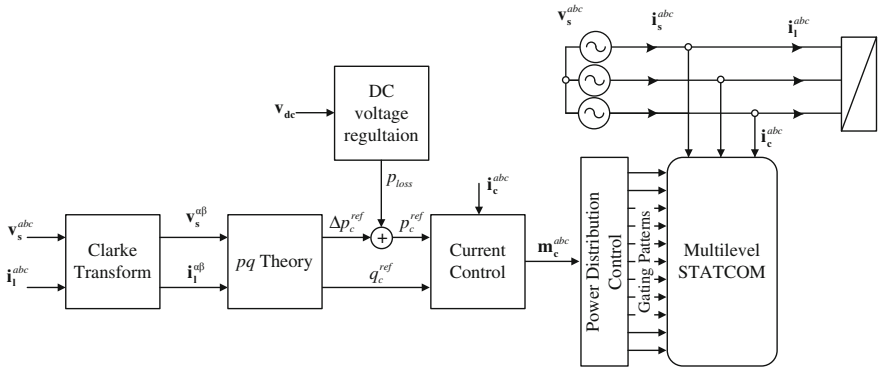

Fig. 8.8 *p-q* Control overall control scheme

required power to be injected by the STATCOM, which ideally delivers all the load reactive power and do not absorb any active power, i.e.

$$\Delta p_c^{ref} = 0, \tag{8.55}$$

$$q_c^{ref} = -q_l = -\left(v_s^{\beta} i_l^{\alpha} - v_s^{\alpha} i_l^{\beta}\right) = v_s^{\alpha} i_l^{\beta} - v_s^{\beta} i_l^{\alpha}. \tag{8.56}$$

These reference values allow having unitary power factor at the grid side, with zero active power delivered to the converter. However, due to inherent losses in the components, this active power cannot be exactly equal to zero and hence, certain amount of power is required to maintain the total DC voltage in its desired value. The DC voltage at this point is considered either as the summation or the average of all the individual DC stages, which is represented as $\mathbf{v_{dc}}$ in Fig. 8.8. The active power associated to the losses and used to charge all the DC stages, can be simply controlled with a PI controller, which output is added to the required active power, as shown in Fig. 8.8.

With the power references already generated, a current control block takes care to generate the modulating signals of the multilevel STATCOM that goes to the power distribution control block in Fig. 8.8, which is in charge to ensure the equal distribution of power among all the components in the multilevel STATCOM. This block will be depicted later in this chapter in a dedicated section.

The current control block can be designed using several techniques, from linear controllers to advanced non-linear schemes. Figure 8.9 shows that this control block can work either in the *abc* frame or the α-β frame. The latter case involves two Clarke transformations as compared with the *abc* approach that only requires one. As it can be seen from Fig. 8.9, the current references are calculated using (8.54) and then a controller block uses the error to track them. As the purpose of this section is to cope with linear control strategies, only this kind of controllers will be depicted.

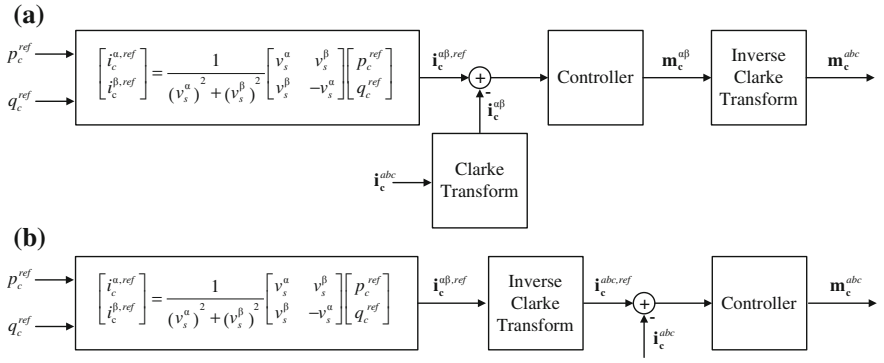

Fig. 8.9 **a** Current control in the α-β frame, **b** current control in the *abc* frame

It is usual to find that the controller block in Fig. 8.9 is considered just a P or PI controller, however these approaches have poor performance because they do not ensure zero steady state error for sinusoidal signals. As both *abc* and α-β are rotating frames [25], PI controllers should be adapted to ensure good stationary performance. In this context, the equivalent of a PI controller for sinusoidal signals is the PR controller, which Transfer Function, suitable to be used in the current controller of the STATCOM, is

$$C(s) = k_p + \frac{k_s s + k_0}{s^2 + \omega_s^2}, \tag{8.57}$$

where ω_s is the system frequency and, k_p, k_s and k_0 are the controllers gains, which can be selected using classical linear control tools such as Bode or Nyquist Diagram. It is important to remark that two transfer functions like these are required if the controller is implemented in the α-β frame and three of them will be used when the controller is in the *abc* stationary frame.

The advantage of using PR controllers is that no extra domain transformations are required to achieve zero steady state error, because it only needs a frequency estimator in order to work properly. Furthermore, the phase angle of the currents and/or voltages is not used to implement the control scheme and therefore a PLL block is not necessary, which simplifies the whole strategy.

8.4.2 dq *Frame Based Control*

Figure 8.10 shows the overall schematic for a *dq* based control strategy. As it can be seen, a PLL block feeds the Park transformation with the synchronism angle θ_s, in order to obtain the *dq* SRF [26]. Once the direct and quadrature components of the load current are obtained, they are used to calculate the reference for the *q* component

of the compensator current, in combination with the power factor reference which is given by the variable K_s^{ref} that can be defined as,

$$K_s^{ref} = \text{atan}\left(\Phi_s^{ref}\right) = \text{atan}\left(\text{acos}\left(pf_s^{ref}\right)\right), \tag{8.58}$$

where pf_s^{ref} is the reference power factor and Φ_s^{ref} is the reference current phase angle. Usually, a unitary reference power factor is required and then K_s^{ref} will be equal to zero, which leads to,

$$i_c^{q,ref} = -i_l^q. \tag{8.59}$$

This case corresponds when all the reactive power is provided by the compensator and therefore all the load quadrature current goes through the STATCOM.

The reference of the compensator direct current is generated by the DC voltage control block, which usually considers a PI controller because it can achieve satisfactory results. As the Park transformation is synchronized with the source voltage, the direct current is associated with the active power, and therefore it can be used to compensate the STATCOM losses, which allows regulating the DC voltage. Similar to the *p-q* control scheme, at this point $\mathbf{v_{dc}}$ corresponds to the sum or average of all the voltages involved in the multilevel converter. The power balance among the components is ensured with the power distribution control block that will be explained later.

The current control block in Fig. 8.10 generates the direct and quadrature components of the signals used in the modulation stage. This control block can be implemented in several ways, but only linear control will be considered in this section. In fact, PI controllers are quite suitable in this scheme, because *dq* components of the converter currents are DC quantities and therefore simple PI controllers can achieve zero steady state error with an acceptable dynamic performance. Hence, Fig. 8.11 shows typical linear current controllers in the SRF that allow to control direct and quadrature currents independently and to obtain satisfactory

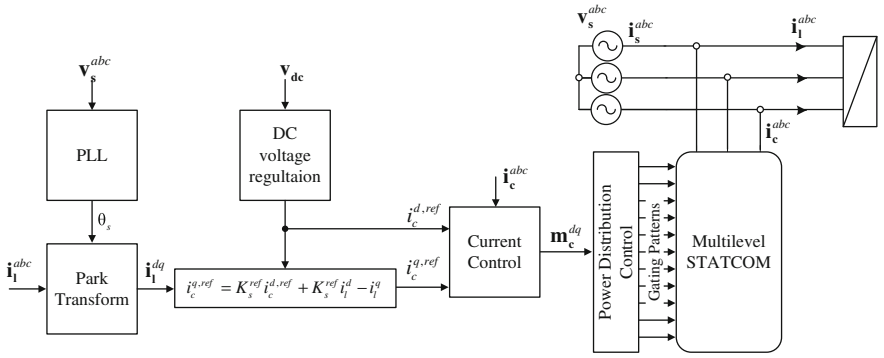

Fig. 8.10 *dq* Control overall schematic

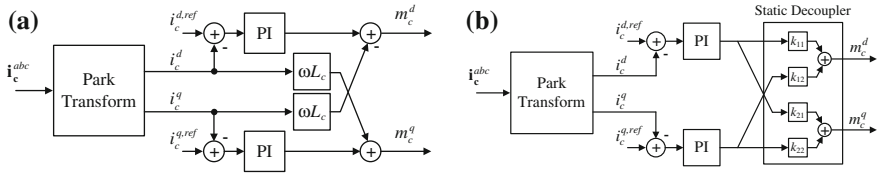

Fig. 8.11 **a** Decoupling control based on the model, **b** decoupling control based on the static decoupler

dynamic response. In Fig. 8.11a the coupled terms of the dynamic model are canceled out in the control strategy, which allows to propose single-variable PI controllers for each loop. On the other hand, in Fig. 8.11b the decoupling stage includes a static de-coupler that is calculated as the inverse of the transfer matrix evaluated in $s = 0$, as classical multivariable control theory proposes [27]. In both cases, a feed forward loop can be added to the controllers output in order to compensate source voltage disturbances.

As both schemes shown in Fig. 8.11 use linear PI controllers, the suitable transfer function that ensures zero steady state error is,

$$C(s) = k_p + \frac{k_i}{s}, \tag{8.60}$$

where k_p and k_i are the proportional and integrative gains, respectively. These gains can be selected using classical linear control tools such as root locus, Bode and/or Nyquist Diagram. Furthermore, empirical tests can be done in order to tune these controllers according with practical criteria that have been established in the technical literature [28].

The advantage of using PI controllers is that they are very well-known and easy to program in any digital platform, such as Digital Signal Processors or Microcontrollers. On the other hand, as a drawback of this approach compared with the PR controller used in the *p-q* theory based strategy is that the Park transformation is required, which involves the use of a PLL algorithm that is not necessary in the power theory based control.

8.4.3 Power Distribution Strategies

In order to achieve a balanced distribution of power among the components in a multilevel STATCOM, it is mandatory to include dedicated strategies to control the DC voltages (or currents). As stated earlier, this must be done because the components are not exactly the same and they do not always perfectly match their nominal values.

There are several approaches to implement the power distribution control, some of them modify the modulating signals according with the amount of levels in the configuration, which can be done either in the *dq*, α-β or the *abc* frames. Other strategies maintain a constant modulating signal, but they modify the modulation technique; for instance, for those modulation strategies based on carriers, triangular waves features are changed in order to achieve the power distribution.

Another option to perform the DC voltage (or current) balance is using variable dead-times for VSC based topologies or equivalently overlap times in CSC topologies. This approach is based on the charging and discharging of the DC energy storage elements; in fact, for given commutation conditions, the DC storage element (capacitor or inductor) will charge or discharge depending on the sign of the AC side variable (current in the case of VSC and voltage for CSCs). Therefore, changing the dead-times (overlap), favorable conditions can be extended, i.e., when the DC variable is higher than its reference, the discharging condition must be extended until the value reaches its set-point. On the other hand, if the DC quantity is lower than its reference, the charging condition must be prolonged in order to lessen the error. Further details of this kind of approaches can be found in [29, 30].

This section will be focused on the power distribution techniques that are applicable to the linear control strategies presented above; however, these schemes are applicable to nonlinear control approaches as well. Only the most representative techniques will be discussed in this part, but it is important to point out that there are many alternatives to achieve equal power distribution in multilevel STATCOMs. Hence, two different balancing control techniques will be presented, one is suitable to be applied in the *dq* SRF and the second one is better for the *abc* stationary frame.

8.4.3.1 Power Distribution Strategy for the *dq* Frame

Figure 8.12a shows a typical power distribution control that uses the *dq* components of the modulating signals generated, for example, with the control strategy presented in Sect. 8.4.2. These *dq* components allow dynamically computing the value of the amplitude and the phase angle of the modulating signal, which is usually the variable used to achieve the power balancing. One of the advantages of this approach is its scalability to any generalized multilevel STATCOM topology with an arbitrary n_c number of DC elements (capacitors or inductors).

The DC variable, in this case the DC voltage, is compared with its reference and then passed through a PI controller, which ensures zero steady state error thanks to its integral part. The controller output is used to change the phase angle of each modulating signal in order to modify the gating patterns of the multilevel STATCOM. For instance, this strategy is suitable for a CHB multilevel STATCOM because the DC voltage control can be repeated as many times as number of cells are include in each phase.

A restriction of this approach is its suitability when direct and quadrature components of the modulating signals are available, because they are required to calculate and modify the phase angle. As it can be seen from Fig. 8.12a, the

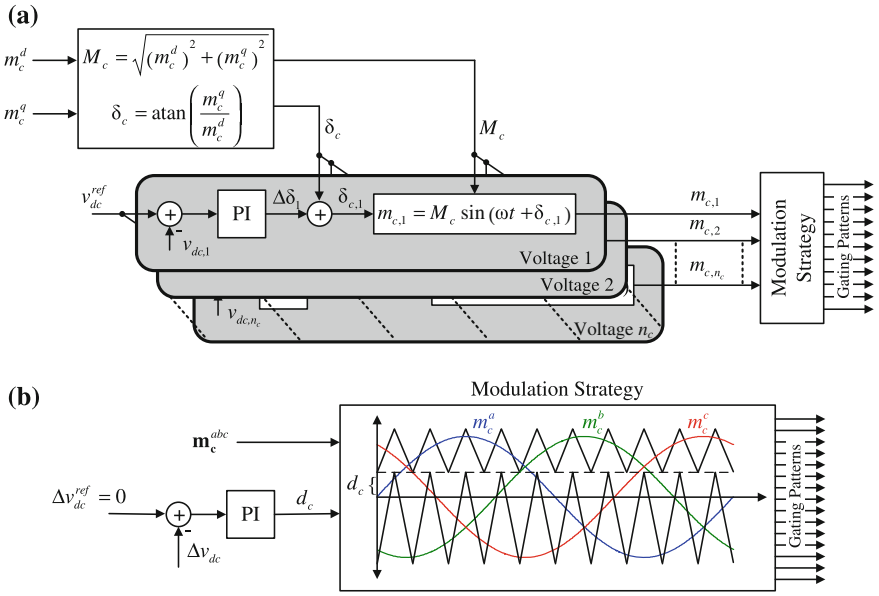

Fig. 8.12 **a** Power distribution strategy for the *dq* frame, **b** power distribution strategy for the *abc* frame

amplitude of the modulating signal is not used because slight variations in the gating patterns are enough to achieve the desired voltage balance. Therefore, only the phase angle of the modulating signal is sufficient to successfully control the DC voltages of the multilevel STATCOM, as many technical articles demonstrate [31, 32].

8.4.3.2 Power Distribution Strategy for the *abc* Frame

When the modulating signal is available in the *abc* frame, as obtained in the *p-q* theory based control shown in Sect. 8.4.1, the phase angle can be hardly modified, then other options can be explored. Thus, instead of changing the modulating signal to obtain the gating patterns of the multilevel STATCOM, it is possible to change the features of the carrier signal, which is usually a triangular waveform for typical modulation techniques.

As an example, when level shifted (LS) SPWM [2] is employed for the multilevel STATCOM, the middle point of the triangular waves has a direct influence in the voltage sharing, as many technical articles state [11, 12]. This strategy is summarized in Fig. 8.12b, where a PI controller modifies the middle point of the Level Shifted Sinusoidal Pulse Width Modulation (LS-SPWM) in order to balance the DC voltages. This kind of approach is suitable for NPC multilevel STATCOMs and further implementation details can be found in [10]. Summarizing the behavior

of this scheme, the difference of the voltages in two DC capacitors Δv_{dc} (e.g. for a 3-level NPC) is compared with its reference equals to zero in order to ensure equal voltage in both components. Then, the PI controller eliminates the steady state error using the middle point of the modulation technique. As it was demonstrated in the technical literature, this approach can achieve satisfactory results for NPC multilevel STATCOMs.

An important disadvantage of this approach is that it is hardly extendible for higher number of levels, because in that case more triangular waves are required and then more intermediate points should be included. Thus, the pairing among inputs and outputs in order to determine which input controls which output in not straightforward. However, some efforts have been made in order to achieve satisfactory results for increased number of levels [33, 34]. Nevertheless, an extension for an arbitrary number of cells, as the one presented in Fig. 8.12a, is very difficult to obtain.

Example 8.4 For illustration purposes, the control strategy proposed in Fig. 8.10 will be implemented for a 7-level CHB STATCOM topology, i.e., $n_c = 3$ cells are included. The parameters of the proposed system are the same presented in the Example 8.1.

The total DC voltage control block is built up with a PI controller and the current control is implemented with the approach shown in Fig. 8.11b. The static decoupler is designed with a linearized model of the system using the small signal approximation [35] and calculating the inverse transfer matrix, as classical multivariable control literature states [27]. The PI current controllers are equal for both d and q axes, and they can be designed using the closed loop pole placement approach, considering each loop as a single-input single-output variable system. Resulting waveforms are shown in Fig. 8.13, where the performance of the multilevel STATCOM under several dynamic tests is shown. In fact, at $t = 50$ ms, a step-up reference change is imposed by the control strategy from a 0.96 (inductive) to unitary power factor. Then, at $t = 300$ ms, a load impact is produced, where the load reactive power doubles its original value. Finally, at $t = 600$ ms, the power factor reference goes back to 0.96, maintaining the same increased load condition.

From all the presented waveforms, it is possible to state that the control strategy allows regulating the variables in their desired reference values, with a transient response imposed by the controllers transfer functions. Figure 8.13a shows the STATCOM current for all the aforementioned conditions, and it is possible to observe that the compensator adjust the injected current in order to dynamically follow the control objectives. This can be also noticed in Fig. 8.13b, where direct and quadrature components of the STATCOM current are shown. As expected, the direct current is approximately zero because the active power required by the STATCOM is only needed to compensate the losses.

On the other hand, the quadrature current follows the dynamic conditions in order to maintain the power factor in its desired value. In fact, Fig. 8.13c shows how the instantaneous power factor tracks its reference with zero steady state error.

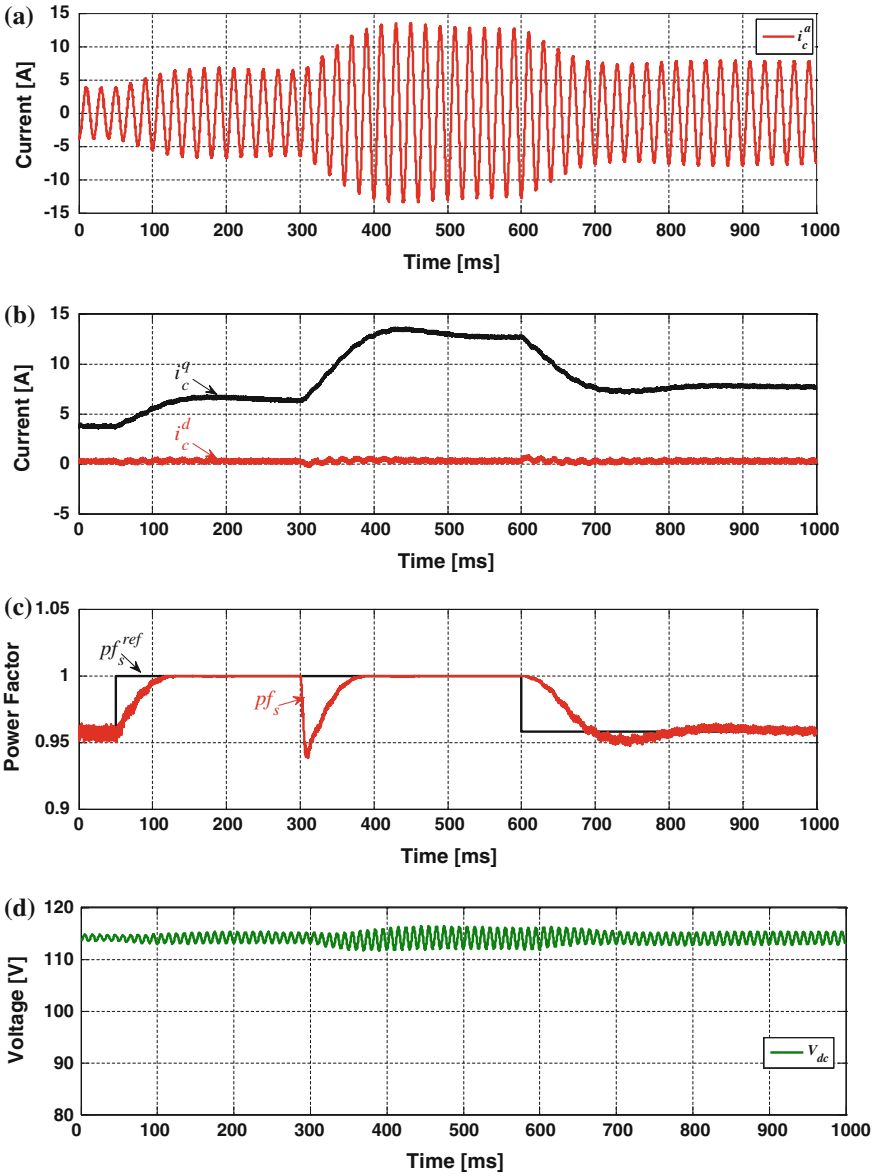

Fig. 8.13 **a** STATCOM current, **b** *d* and *q* components of the STATCOM current, **c** overall power factor and its reference **d** average DC voltage

Finally, the average voltage of the 3 H-bridges is shown in Fig. 8.13d, where the typical second harmonic oscillation can be observed, which value increases and decreases according with the fluctuation of the converter current. In this example, the DC voltages are balanced; however this is only valid for a simulated system,

because in a real set-up these voltages will be unbalanced due to the difference in the parameters of the CHB STATCOM, as it will be shown in the next example.

Example 8.5 In order to illustrate the behavior of the power distribution control in a real multilevel STATCOM system, the scheme of Fig. 8.12a was implemented for a low power laboratory prototype. The implemented topology was a 5-level CHB STATCOM and the performance of the balancing control is shown in Fig. 8.14.

This figure shows that the DC voltages of different H-Bridges from different phases are naturally unbalanced due to the differences in the components values, which cause significant deviations in the expected DC voltages. In this particular case, the differences in the DC voltages went up to ±20 % of the nominal value. Once the DC voltage distribution control was turned on, the voltages reached their references in approximately 1 s, which is enough to ensure a satisfactory dynamic performance. It is important to highlight that that the power distribution control changes the gating patterns of the multilevel STATCOM in order to equalize the DC voltages, this causes a slight modification in the injected current, which is rapidly compensated by the current control. The dynamic response of these controllers is imposed by the PI parameters of Fig. 8.12a and they can be selected using classical linear control tools or using empiric criteria, such as ITAE [28]. As a practical rule, it is highly recommendable to tune these loops at least 10 times slower than the current controllers in order to avoid undesired interactions between the control strategies.

Example 8.6 A 3-Level NPC STATCOM was simulated for the same parameters presented in the Example 8.2. The STATCOM was controlled using the *p-q* theory with the control scheme of Fig. 8.8; the current controller was implemented as Fig. 8.9b depicts and the power distribution control was done modifying the modulation technique as presented in Fig. 8.12b. Key waveforms shown in Fig. 8.15 illustrate the behavior of the proposed topology, where several dynamic tests were performed.

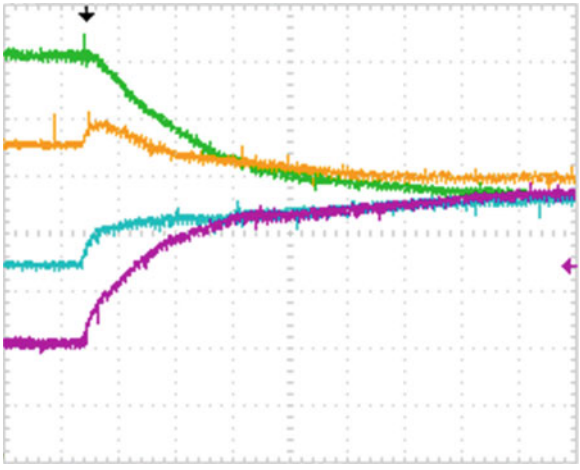

Fig. 8.14 Voltage distribution control in a real STATCOM prototype, 10 V/div and 250 ms/div

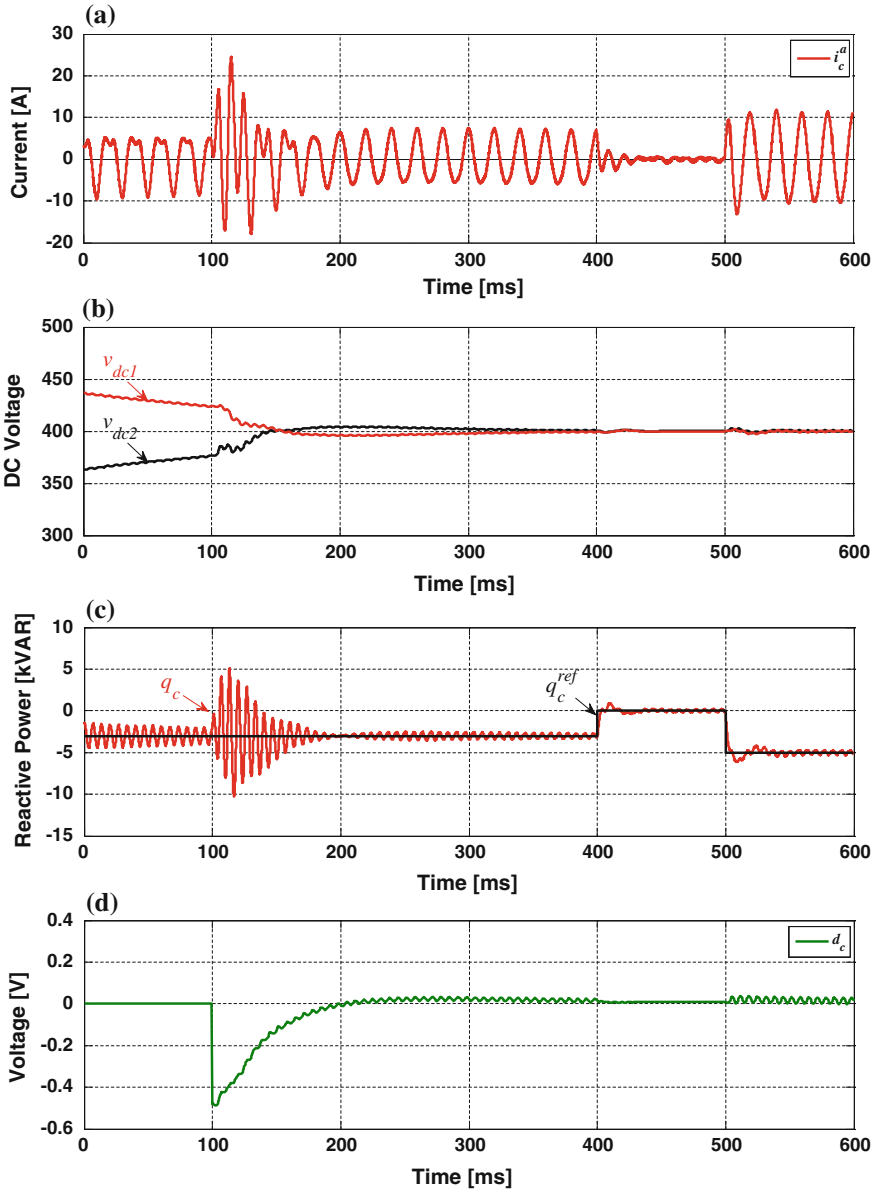

Fig. 8.15 **a** STATCOM current, **b** STATCOM DC voltages, **c** injected reactive power and its reference **d** midpoint of the modulation technique

At the beginning, an artificial voltage imbalance was introduced in order to highlight the harmful effects of this phenomenon. In fact, during the first 100 ms, the waveforms are very distorted, particularly the injected current that has low frequency harmonics and even a DC component, as Fig. 8.15a shows. This distortion also

generates an unwanted oscillation in the instantaneous reactive power, as it can be seen from Fig. 8.15c. At t = 100 ms, the voltage balancing control is activated and the DC voltages reach their equilibrium point after a few hundred milliseconds. During this period, the injected current recovers it expected sinusoidal shape, even though at the beginning of the transient the waveform is quite distorted. Also, the reactive power decreases its steady state oscillation when the DC voltage difference is near to zero. Figure 8.15d shows the behavior of the control variable d_c that corresponds to the midpoint of the modulating technique, as Fig. 8.12b illustrates. When the power distribution control is activated, d_c changes abruptly due to the proportional term of the PI controller, but it rapidly reaches the new steady state condition that ensures the DC voltages balance.

At t = 400 ms, the reactive power reference changes to zero, i.e., the STATCOM will not inject any reactive current, and therefore the load and the overall power factor will be equal. This can be corroborated in the injected STATCOM current, Fig. 8.15a, which is practically equal to zero during this interval. Just a small amount of current is required to maintain the DC voltages in their reference values. In the final stage of the test, the reactive power reference goes up to 5 kVAR and the NPC STATCOM tracks it in less than 3 cycles. The injected current maintained its sinusoidal behavior because the DC voltages remained equal even during the transient condition. As a final remark, it has been demonstrated the importance of the voltage balancing control, as unequal DC sources generate undesired harmonics that distort the overall waveforms.

8.5 Non-Linear Control Strategies

8.5.1 Input/Output Linearizing Control

The Input/Output linearization technique uses the non-linear model of the STATCOM to define a non-linear control law which allows using linear controllers without the requirement to maintain the STATCOM operation in a region near to the operating point where the controller is designed [36]. The above is especially appropriate for CSC topologies, where the DC current level can be defined as a function of the compensation requirement in order to reduce the DC inductor losses [23]. The main drawback of this control approach is the number of electrical variables that must be sensed to implement the strategy. This number is related to the state variables and disturbances, which are used to compute the non-linear law related to the dynamic model of the system.

In order to control the MCSC STATCOM using the *dq* frame approach, the non-linear control scheme is similar to the linear case in terms of the reference for the quadrature component of the STATCOM current. The control scheme is shown in Fig. 8.16a where the quadrature component of the STATCOM current defines the

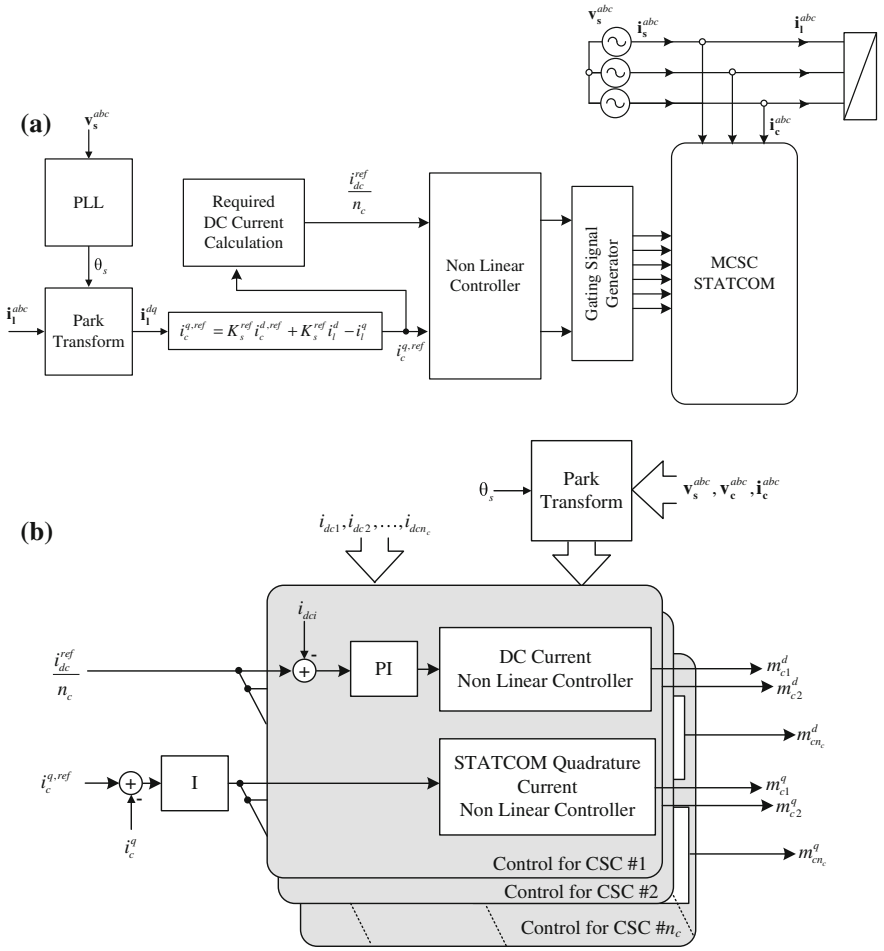

Fig. 8.16 **a** Input/output linearization using *dq* frame, **b** non-linear controller for MCSC STATCOM

DC current level [37]. As it is required that each CSC provides an equal part of the compensated reactive power and considering the parallel connection of the CSCs to the LC filter, the reference current is divided by n_c. The Non-Linear Controller block computes the modulation signal for each CSC which is used by the Gating Signal Generator to produce the gating pattern for each semiconductor.

Two ways can be used to define the non-linear controller. First, the DC current controller can be defined in order to set the direct component of the STATCOM current [38]. This component can be used to control the STATCOM active power and regulate the DC current level in the CSCs, while the reference for the quadrature component of the STATCOM current is defined by the desired power factor. Although each CSCs can provide a part of the required quadrature component,

unfortunately the direct component is common to the CSCs and a power distribution strategy is required (see Sect. 8.4.3).

A second and easier way to control the MCSC topology is to control the STATCOM quadrature current with the quadrature component of the modulating signal and its direct component will control the DC current, as it is shown in Fig. 8.16b [21]. In this way, the DC current reference is calculated in Fig. 8.16a and the controller defines the direct component of the modulating signal; the STATCOM quadrature component is controlled defining a common signal for all the non-linear controllers, which will modify the value of the quadrature component of the modulating signal. From the *dq* state model presented in Sect. 8.2.3, the non-linear laws for the modulator components are,

$$m_{ci}^{d} = \frac{1}{G_{ac} v_c^d}\left(u_{dci} - G_{ac} m_c^q v_c^q\right),$$
$$m_{ci}^{q} = \frac{C_c L_c}{G_{ac} i_{dci}}\left(k_2 u_c^q - k_2 i_c^q - k_1 \tfrac{d}{dt} i_c^q - G_{ac} \sum_{\substack{j=1 \\ j\neq i}}^{n_c} i_{dcj} m_{cj}^q - \tfrac{2\omega_s}{L_c} v_c^d + \left(\tfrac{1}{L_c C_c} + \omega_s^2\right) i_c^d + \tfrac{\omega_s}{L_c} v_s^d - \tfrac{1}{L_c} \tfrac{d}{dt} v_s^q\right), \tag{8.61}$$

where u_{dci} and u_c^q are auxiliary variables conveniently defined. For the STATCOM quadrature component, it is possible to write,

$$\begin{aligned} \frac{i_c^{q,ref}}{u_c} &= \frac{1}{T_{i,i_c} s}, \\ \frac{i_c^q}{i_c^{q,ref}} &= \frac{\frac{k_2}{T_{i,i_c}}}{s^3 + k_1 s^2 + k_2 s + \frac{k_2}{T_{i,i_c}}}. \end{aligned} \tag{8.62}$$

Thus, the dynamic of the STATCOM quadrature component can be set defining T_{i,i_c}, k_1 and k_2 which can be computed using the ITAE criterion. For the DC current controller, one can write

$$\begin{aligned} \frac{i_{dci}}{u_{dci}} &= \frac{1}{L_{dc} s + R_{dc}}, \\ \frac{i_{dc,ref}}{i_{dc}} &= \frac{k_{p,i_{dc}} s + k_{i,i_{dc}}}{L_{dc} s^2 + \left(R_{dc} + k_{p,i_{dc}}\right) s + k_{i,i_{dc}}}. \end{aligned} \tag{8.63}$$

Thus, the dynamic of the DC current can be defined using $k_{p,i_{dc}}$ and $k_{i,i_{dc}}$. Both control loops could use a proportional controller but due that the non-linear controller is based on the STATCOM model, variations in the STATCOM parameters end up not ensuring zero error in steady-state; thus, integral and/or PI controllers are well suited to ensure the tracking of the references. As the control scheme is defined for each CSC, the topology and its control can be adapted to any number of CSCs.

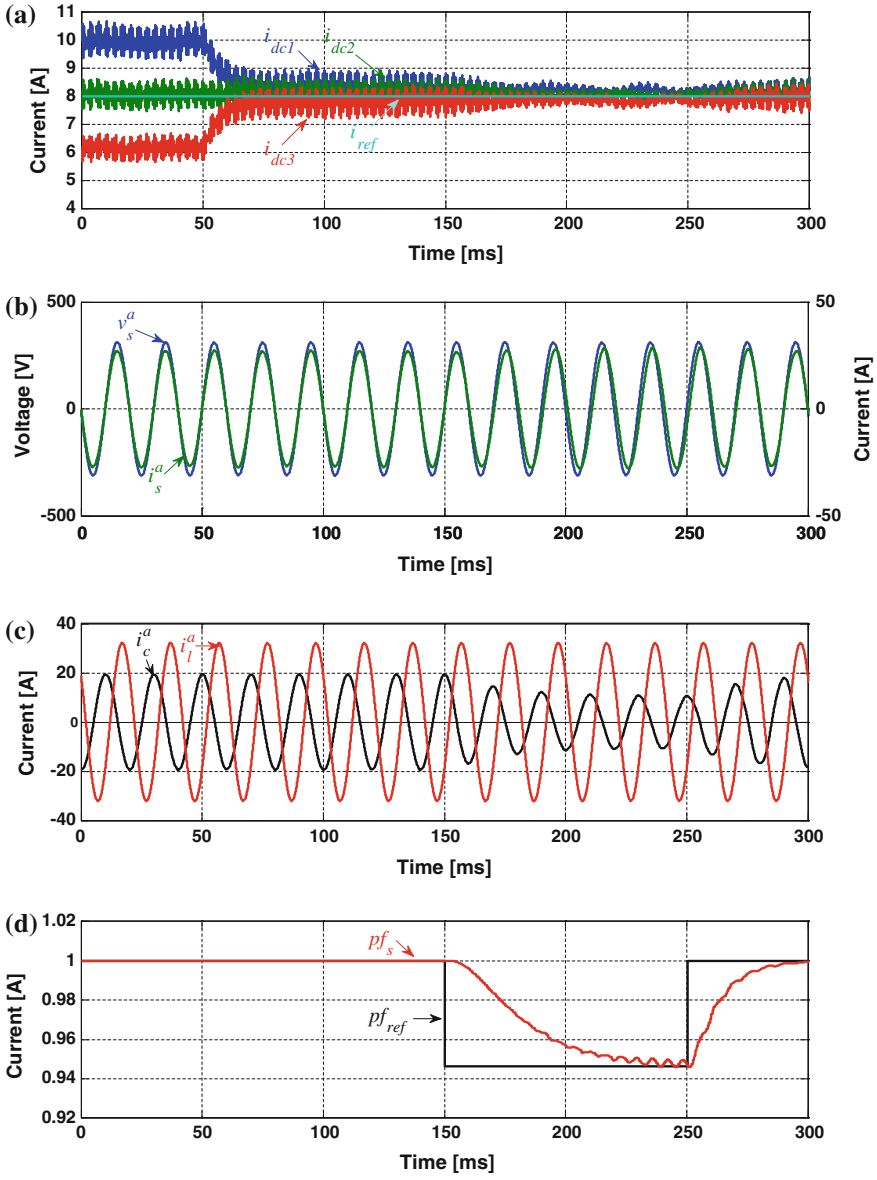

Fig. 8.17 **a** CSCs DC Current and their reference, **b** voltage supply and current supply, **c** STATCOM current and Load current, **d** power factor and its reference

Example 8.7 The MCSC STATCOM was simulated for the parameters of Table 8.2. Three modules in parallel were considered and the results are summarized in Fig. 8.17. At the beginning of the simulation, the DC currents are not evenly distributed due that the current distribution control is deactivated. Then, at

t = 50 ms, this control block is turned on and therefore the DC currents converge rapidly to their desired value. Once the DC currents are evenly distributed among the cells, two power factor reference changes are considered at t = 150 and 250 ms, as Fig. 8.17d clearly shows. The control strategy can successfully reach the power factor references in the expected time, while the DC currents remain equally distributed among the power modules.

It is possible to observe in the STATCOM current, Fig. 8.17c, that its amplitude slightly varies when the current balancing control is activated, because only a redistribution of the modulating signals is produced, which does not majorly affect the overall compensator current.

8.5.2 Hysteresis Control

The hysteresis control of power converters has been widely used due to its simplicity of implementation and good dynamic performance [39]. However, it has an important drawback related to the harmonic content of the resulting waveforms, which is the unknown equivalent switching frequency and also the commutation harmonics are spread all over the spectra.

The implementation of a hysteresis control is quite simple for a 2-level converter. A tolerance band must be defined and whenever the current error goes outside the band, the converter must commute from one state to the other, as Fig. 8.18a depicts. Then, the control law is very easy to program in a digital platform as,

$$\begin{aligned} &\text{if } e_i(t) \geq h, \quad &&\text{then } u(t) = -V_{dc} \\ &\text{else if } e_i(t) \leq -h, \quad &&\text{then } u(t) = +V_{dc}, \end{aligned} \tag{8.64}$$

where, $e_i(t)$ is the current error, h is the hysteresis band and $u(t)$ is the converter output.

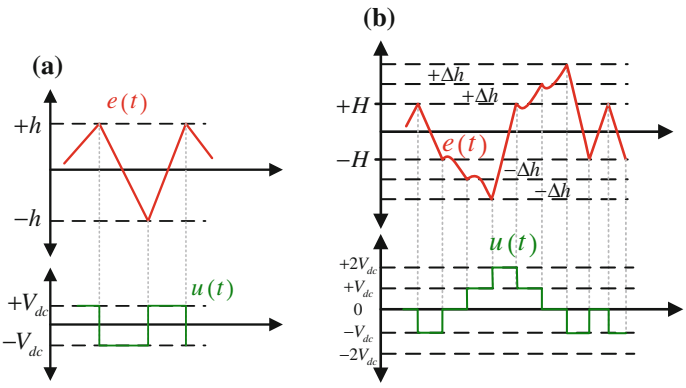

Fig. 8.18 **a** Two level hysteresis controller, **b** multilevel hysteresis controller

The extension of the hysteresis control for multilevel converters is not straightforward and several approaches have been reported in the literature [40, 41]. There are different ways to implement a Multilevel Hysteresis Modulation, among them it is possible to find approaches were multiple bands are considered, that can be symmetric or asymmetric and also time based schemes have been proposed [42].

Figure 8.18b shows an alternative to implement a multi-band hysteresis strategy, suitable for multilevel converters. There, symmetrical bands 2are used to generate the gating patterns, such that the inner bands are used to switch between adjacent levels, while the outer bands produce commutations of additional levels. In the aforementioned figure, H corresponds to the inner band, and outer bands are formed by small Δh steps. Thus, if the error goes further the most outside band, the higher level in the multilevel waveform must be selected in order to correct the error and bring it inside the hysteresis bands.

Example 8.8 A 3-level NPC was simulated using a hysteresis modulation in the current control loop. The system parameters are the same presented in Example 8.6 and the current references are also generated using the *p-q* theory depicted in Fig. 8.8. The main results are summarized in Fig. 8.19, where five different operating conditions were tested. In the first 40 ms, the overall power factor is equal to 0.96 lagging; then, a unitary power factor step reference change is made. At $t = 80$ ms, a load impact is produced and the compensated reactive power increases in a 100 %. After, a reference change is forced in order to over compensate the load reactive power and a 0.96 leading power factor is obtained. Finally, at $t = 160$ ms, the reference changes again to go back to the initial 0.96 inductive power factor.

Waveforms of Fig. 8.19, illustrates the good performance of this strategy in terms of its transient response to reference changes and load impacts. It can be seen that the STATCOM current follows its reference almost instantaneously, which is also reflected in the reactive power graph of Fig. 8.19c. The main drawback of this approach is the uncharacteristic harmonics produced in the multilevel waveform of Fig. 8.19d, which may lead to undesired resonances.

8.5.3 Predictive Control

This control strategy consists in evaluating all the possible commutation states of a given topology and selecting the optimal switches combination that minimizes the error between the desired and the future operating condition. To achieve this, it is essential to count with an accurate model of the system in order to predict the future behavior of the variables. Control objectives of a particular topology will define a cost function that is minimized as an optimization problem in every sampling period. Latest technical literature addresses very important issues about this approach, such as cost function selection, equivalent switching frequency, computational burden, effect of model parameter errors, just to name a few [43].

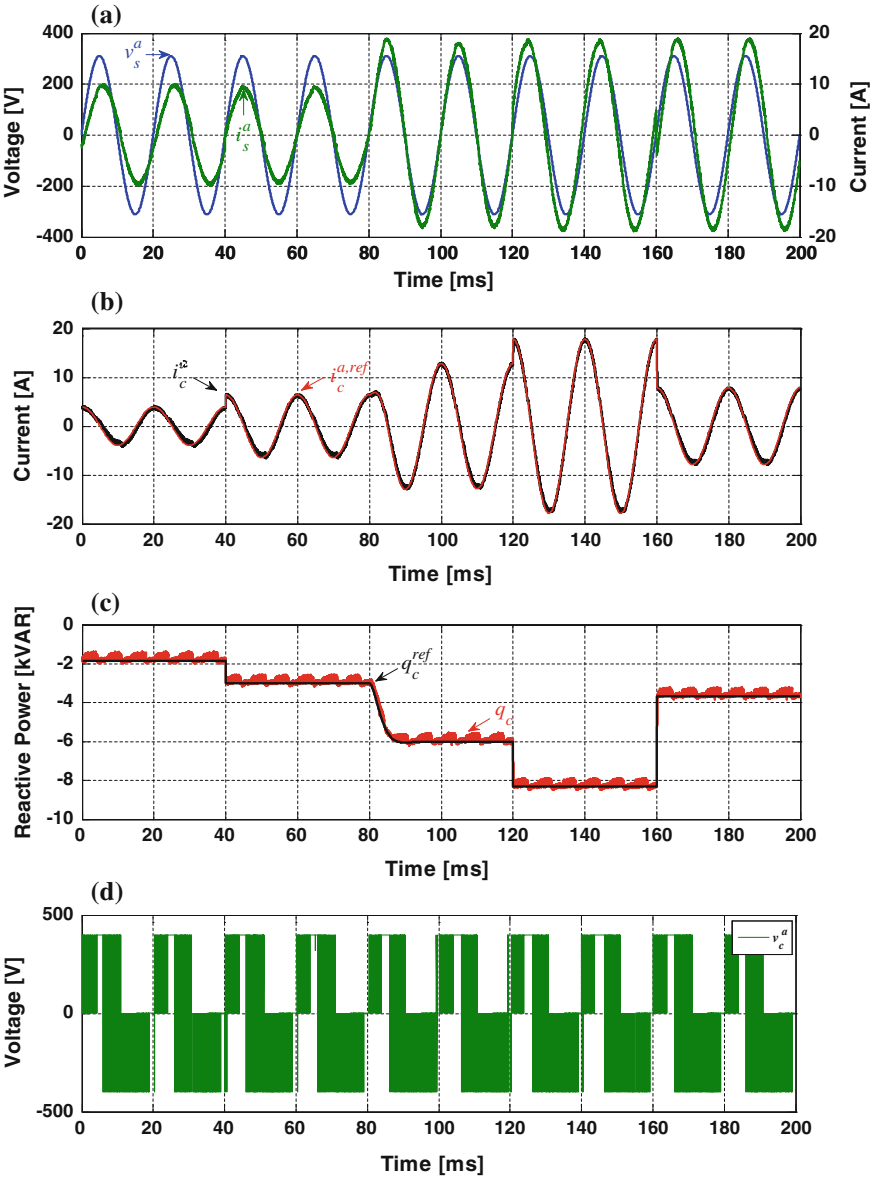

Fig. 8.19 **a** Load voltage and overall current, **b** STATCOM current and its reference, **c** injected reactive power and its reference, **d** multilevel STATCOM voltage

The predictive control technique can be also applied to multilevel STATCOMs, extending the approach to higher amount of switching conditions. The main disadvantage is that the computational burden of considering more commutation states considerably increases due that the number of possible combinations grow

exponentially with the number of switches. For instance, a single H-Bridge has 4 valid states (one for $+V_{dc}$, one for $-V_{dc}$ and two zero states), but if two cells are connected in series, the valid states will be $4^2 = 16$ and for 3 cells $4^3 = 64$ are the valid combinations. In the case of a 3-level NPC the valid states are 27 [43]. As it can be seen, when the number of switches increases, the predictive control requires a high amount of computations; fortunately, modern processors can handle an elevated number of instructions in a small period of time. In fact, devices like FPGAs, can implement all the comparisons simultaneously [44]. Also, it is possible to propose alternatives to reduce the number of evaluations, considering that the adjacent valid states are the most suitable solution when the steady state condition is reached. Also, extra redundancy is produced in multilevel converters, because different commutation states produce the same output level; then, this feature can be used to improve the control strategy. Some research have been proposed in this direction and important results have been published in [45, 46].

According with the model predictive control theory applied to power converters, differential equations that model the system must be firstly discretized in order to evaluate the viable switching conditions. For multilevel STATCOMs, the differential equation that models the AC side is:

$$\mathbf{v}_{\mathbf{s}}^{abc} = L_c \frac{d}{dt}\mathbf{i}_{\mathbf{c}}^{abc} + R_c \mathbf{i}_{\mathbf{c}}^{abc} + \mathbf{v}_{\mathbf{c}}^{abc}. \tag{8.65}$$

Then, considering a first-order Euler approximation, the discrete version of this equation can be expressed as,

$$\mathbf{i}_{\mathbf{c}}^{abc}(k+1) = \left(1 - T_s \frac{R_c}{L_c}\right)\mathbf{i}_{\mathbf{c}}^{abc}(k) + \frac{T_s}{L_c}\left\{\mathbf{v}_{\mathbf{s}}^{abc}(k) - \mathbf{v}_{\mathbf{c}}^{abc}(k)\right\}, \tag{8.66}$$

where T_s is the sampling time of the algorithm. Variables evaluated in the k instant corresponds to the sensed variables and the model is used to predict the future behavior of the system in the next sampling time, $k + 1$.

Once the discrete model is already obtained, a cost function must be proposed. This functional must be evaluated for all the possible switches combinations and the option that minimizes the cost function should be selected and applied in the next sampling time. A typical cost function that minimizes the current error is,

$$g = \left|\mathbf{i}_{\mathbf{c}}^{abc,ref}(k+1) - \mathbf{i}_{\mathbf{c}}^{abc}(k+1)\right|, \tag{8.67}$$

that consists in the absolute value of the difference between the current reference and the predicted value of the STATCOM current, both in the next sampling time. The current reference is usually generated with an external controller that ensures the appropriate reactive power injection and the overall DC voltage (or current) regulation, which in most cases are just PI controllers. As it can be seen, the cost function can be directly proposed in the *abc* frame and then no transformation is required to implement this approach, which simplifies the understanding of the

strategy. However, it is also usual to find in the technical literature the implementation of the model predictive control in the α-β frame [47].

The power distribution control can be implemented separately with any of the aforementioned techniques; however it can be also included in the model predictive control strategy. To do so, the model of the DC side must be well known, based on the elemental equation of the capacitor or inductor (depending of the nature of the topology). For instance, let's consider a VSC multilevel topology, then the capacitor equation will define the DC side dynamics as,

$$i_{dc} = C_{dc}\frac{dv_{dc}}{dt}. \tag{8.68}$$

Using the first order Euler approximation of the derivative, this equation becomes,

$$v_{dc}(k+1) = v_{dc}(k) + \frac{T_s}{C_{dc}} i_{dc}(k), \tag{8.69}$$

where $i_{dc}(k)$ can be sensed, calculated or estimated depending on the specific application and/or topology. After this, the cost function must be redefined in order to include this new control objective, also considering that in a multilevel STATCOM there are several DC storage elements. Thus, the new cost function is,

$$g = \left|\mathbf{i}_{\mathbf{c}}^{abc,ref}(k+1) - \mathbf{i}_{\mathbf{c}}^{abc}(k+1)\right| + \lambda \sum_{i=1}^{n} \left|v_{dc}^{ref}(k+1) - v_{dc,i}(k+1)\right|, \tag{8.70}$$

where $v_{dc,i}$ are all the DC storage elements included in the multilevel STATCOM and λ is a weighting factor that gives priority to the control objectives.

Figure 8.20 shows a flow diagram that describes the predictive control algorithm. In this diagram, $\mathbf{v_{dc}}(k)$ and $\mathbf{i_{dc}}(k)$ correspond to all the DC voltages and currents of the multilevel STATCOM.

Example 8.9 The presented predictive controller was implemented for a 5-level CHB STATCOM and the key waveforms are shown in Fig. 8.21, where in the first 60 ms only a current control is considered, i.e., the cost function was defined by (8.67). At $t = 60$ ms, the voltage balancing control is activated and therefore the cost function changed to (8.70). As it can be seen from the figures, the strategy successfully compensate the reactive power, because the source voltage and current are practically in phase even during the transient condition. Figure 8.21c shows the behavior of the DC capacitors voltage when the voltage balancing control is activated. It can be noticed that this strategy can very quickly reach the new steady state condition, maintaining an accurate current reference tracking. Once the voltage distribution control is activated, the multilevel STATCOM voltage, shown in Fig. 8.21d, becomes symmetrical because the DC voltages are equally distributed in all the cells. It can be also seen in this figure that the DC voltages lack of a

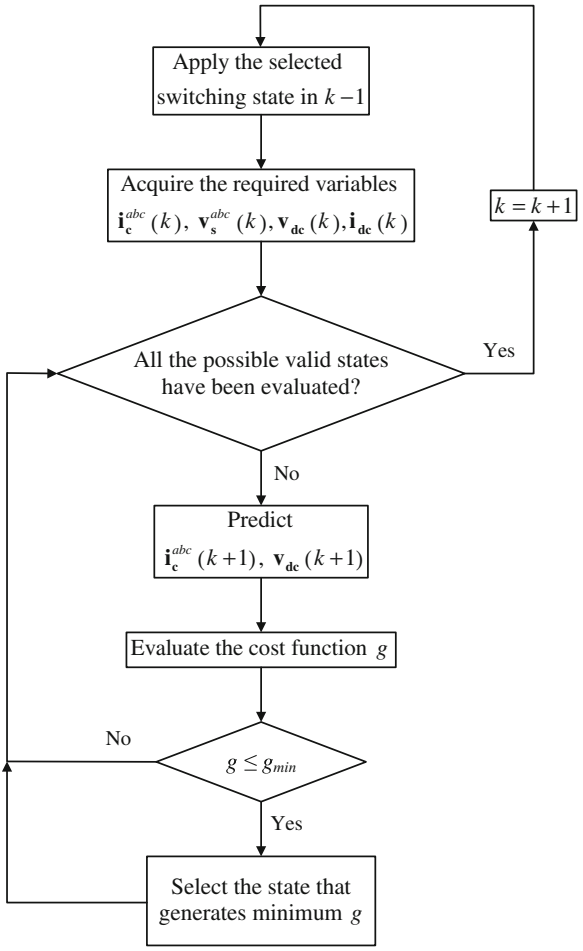

Fig. 8.20 Flow diagram of the predictive control algorithm

significant second harmonic component, which is characteristic of carrier based modulation techniques. It is important to highlight that this strategy can achieve very precise current tracking even when the DC voltages are unbalanced.

The presented waveforms illustrate the fast dynamic performance and the accurate reference tracking of the model predictive control; nevertheless, this technique has also some drawbacks, e.g., it is very sensitive to the parameters deviation and the harmonics do not follow any established pattern. In the first case, when parameters uncertainties are present, this strategy does not ensure zero steady state error; however if the references come from a PI controller this problem can be easily solved. In the second case, regarding the commutation harmonics, the main

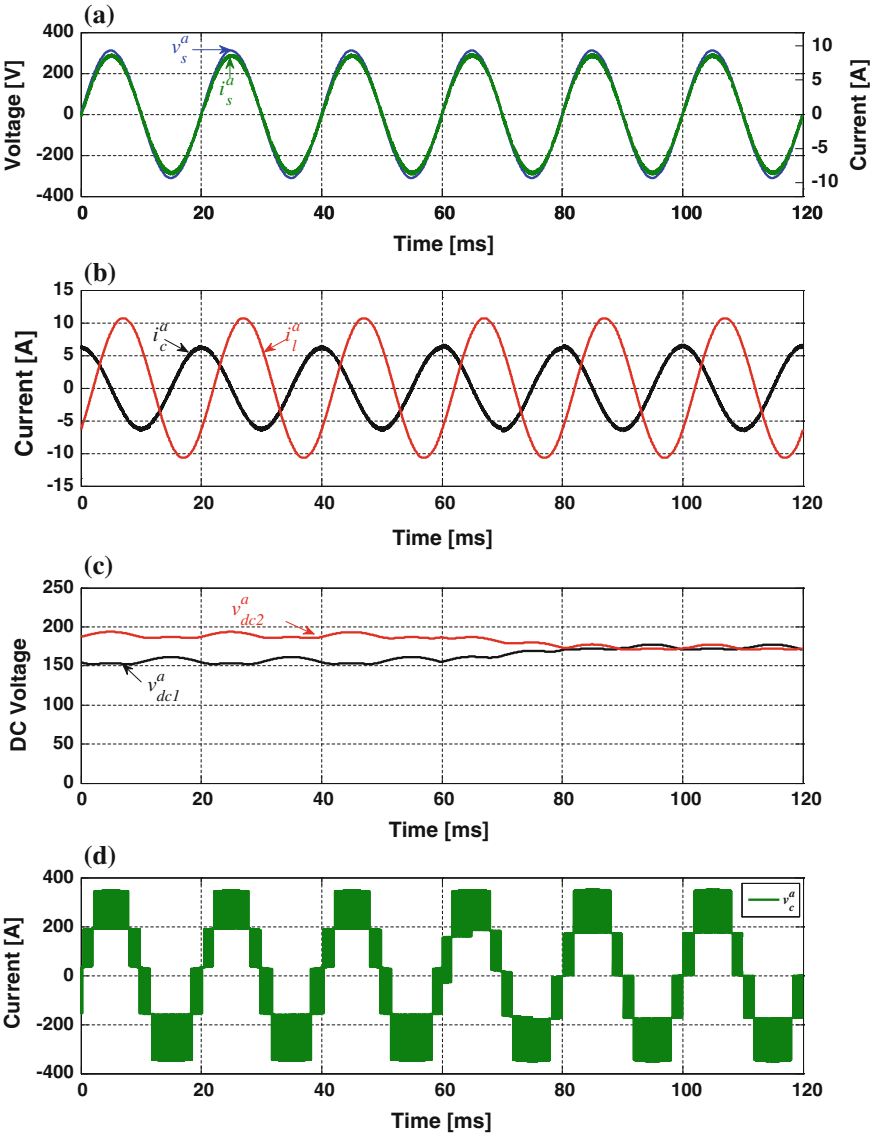

Fig. 8.21 **a** Load voltage and overall current, **b** load current and STATCOM current, **c** DC voltages, **d** multilevel STATCOM voltage

disadvantage is that they can cause unexpected resonances in the electric system, similar to the hysteresis control technique. This issue is not easily solvable and some efforts have been made in order to concentrate the spectra of the resulting waveforms [48, 49].

References

1. Reyes JR, Espinoza JR, Sepulveda CA (2005) Operating region of single-phase UPQCs. In: IEEE 36th power electronics specialists conference, PESC'05, pp 1726–1731, 16 June 2005
2. Wu B (2006) High power converters and AC drives. Wiley-IEEE Press
3. Barrena JA, Aurtenechea S, Canales JM, Rodriguez MA, Marroyo L (2005) Design, analysis and comparison of multilevel topologies for DSTATCOM applications. In: 2005 European conference on power electronics and applications
4. Phillips KP (1972) Current-source converter for AC motor drives. IEEE Trans Ind Appl IA–8 (6):679–683
5. Espinoza JR, Moran LA, Guzman JI (2005) Multi-level three-phase current source inverter based AC drive for high performance applications. In: IEEE 36th power electronics specialists conference, 2005, PESC'05, pp 2553–2559, 16 June 2005
6. Xu D, Zargari NR, Wu B, Wiseman J, Yuwen B, Rizzo S (2005) A medium voltage AC drive with parallel current source inverters for high power applications. In: IEEE 36th power electronics specialists conference, 2005, PESC'05, pp 2277–2283, 16 June 2005
7. Aguirre MP, Calvino L, Valla MI (2013) Multilevel current-source inverter with FPGA control. IEEE Trans Ind Electron 60(1):3–10
8. Melin PE, Espinoza JR, Zargari NR, Sanchez MA, Guzman JI (2006) Modeling issues in three-phase current source rectifiers that use damping resistors. In: 2006 IEEE international symposium on industrial electronics, vol 2, pp 1247–1252, 9–13 July 2006
9. Espinoza JR, Joos G, Perez M, Moran T (2000) Operating region in active-front-end voltage/ current source rectifiers. In: Proceedings of the 2000 IEEE international symposium on industrial electronics, 2000, ISIE 2000, vol 2, pp 459–464
10. Espinoza JE, Espinoza JR, Moran LA (2005) A systematic controller-design approach for neutral-point-clamped three-level inverters. IEEE Trans Ind Electron 52(6):1589–1599
11. Mazuela M, Baraia I, Alvarez S, Atutxa I, Madariaga D (2013) Comprehensive analysis of voltage balancing techniques for 5L-NPC converters. In: 2013 15th European conference on power electronics and applications (EPE), pp 1–10, 2–6 Sept 2013
12. Rubilar IA, Espinoza JR, Munoz JA, Moran LA (2007) DC link voltage unbalance control in three-phase UPQCs based on NPC topologies. In: 42nd IAS annual meeting on industry applications conference. Conference record of the 2007 IEEE, pp 597–602, 23–27 Sept 2007
13. Yue W, Ning L, Su L, Wulong C, Wanjun L, Zhao'an W (2014) Research on DC capacitor voltage self-balancing space vector modulation strategy of five-level NPC converter. In: 2014 twenty-ninth annual IEEE applied power electronics conference and exposition (APEC), pp 2694–2699, 16–20 Mar 2014
14. Sanz I, Bueno EJ, Rodriguez FJ, Moranchel M, Mayor A (2013) Modulation and balancing methods for a NPC converter connected to the grid in a medium voltage application: a STATCOM system. In: 39th annual conference of the IEEE industrial electronics society, IECON 2013, pp 1043–1048, 10–13 Nov 2013
15. Saeedifard M, Nikkhajoei H, Iravani R (2007) A space vector modulated STATCOM based on a three-level neutral point clamped converter. IEEE Trans Power Deliv 22(2):1029–1039
16. Chivite-Zabalza J, Izurza-Moreno P, Madariaga D, Calvo G, Rodríguez MA (2013) Voltage balancing control in 3-level neutral-point clamped inverters using triangular carrier PWM modulation for FACTS applications. IEEE Trans Power Electron 28(10):4473–4484
17. Hasegawa K, Akagi H (2011) A new DC-voltage-balancing circuit including a single coupled inductor for a five-level diode clamped PWM inverter. IEEE Trans Ind Appl 47(2):841–852
18. Umbria F, Gordillo F, Salas F, Vázquez S (2010) Voltages balance control in three phase three-level NPC rectifiers. In: 2010 IEEE international symposium on industrial electronics (ISIE), pp 3018–3023, 4–7 July 2010

19. Hotait HA, Massoud AM, Finney SJ et al (2010) Capacitor voltage balancing using redundant states of space vector modulation for five-level diode clamped inverters. IEEE Trans Power Electron 3(2):292–313
20. Weishaupt CA, Morán LA, Espinoza JR, Dixon JW, Joos G (2010) A reactive power compensator topology based on multilevel single-phase NPC converters. In: 2010 IEEE international conference on industrial technology (ICIT), pp 1339–1344, 14–17 Mar 2010
21. Melin PE, Espinoza JR, Munoz JA, Baier CR, Espinosa EE (2010) Concepts of decoupled control for a shunt active filter based on multilevel current source converters. In: 2010 IEEE international symposium on industrial electronics (ISIE), pp 742–747, 4–7 July 2010
22. Li YW (2009) Control and resonance damping of voltage-source and current-source converters with LC filters. IEEE Trans Ind Electron 56(5):1511–1521
23. Ye Y, Kazerani M, Quintana VH (2005) Current-source converter based STATCOM: modeling and control. IEEE Trans Power Delivery 20(2):795–800
24. Akagi H, Watanabe EH, Aredes M (2007) Instantaneous power theory and applications to power conditioning. Wiley-IEEE Press
25. Ortiz A, Aredes M, Rolim LGB, Bueno E, Rodriguez P (2008) A new current control for the STATCOM based on secondary order generalized integrators. In: Power electronics specialists conference, 2008, PESC 2008, IEEE, pp 1378–1383, 15–19 June 2008
26. Gonzalez-Espin F, Figueres E, Garcera G (2012) An adaptive synchronous-reference-frame phase-locked loop for power quality improvement in a polluted utility grid. IEEE Trans Ind Electron 59(6):2718–2731
27. Skogestad S, Postlethwaite I (2005) Multivariable feedback control analysis and design. Wiley, New York
28. Levine W (2010) The control handbook. CRC Press
29. Sprenger M, Alvarez R, Bernet S (2012) Direct dead-time control-a novel dc-link neutral-point balancing method for the three-level neutral-point-clamped voltage source inverter. In: Energy conversion congress and exposition (ECCE), 2012 IEEE, pp 1157–1163, 15–20 Sept 2012
30. De Alvarenga MB, Pomilio JA (2011) Modulation strategy for minimizing commutations and capacitor voltage balancing in symmetrical cascaded multilevel converters. In: 2011 IEEE international symposium on industrial electronics (ISIE), pp 1875–1880, 27–30 June 2011
31. Fu X, Wang J, Ji Y (2006) A novel STATCOM based on cascaded three-phases voltage source inverter. In: IECON 2006—32nd annual conference on IEEE industrial electronics, pp 2174–2179, 6–10 Nov 2006
32. Li Y, Wu B (2008) A novel DC voltage detection technique in the CHB inverter-based STATCOM. IEEE Trans Power Delivery 23(3):1613–1619
33. Mane JJ, Muley SP, Aware MV (2012) Performance of 5-level NPC inverter with multi-multicarrier multi-modulation technique. In: 2012 IEEE international conference on power electronics, drives and energy systems (PEDES), pp 1–5, 16–19 Dec 2012
34. Yang H, Luo H, Sun P, Li C, Li W, He X (2014) Comprehensive analysis on carrier-based PWM modulations for advanced composited clamping five-level converter. In: Applied power electronics conference and exposition (APEC), pp 2338–2343
35. Ogata K (2004) System dynamics. Pearson Prentice Hall, New Jersey
36. Sekoguchi M, Konishi H, Goto M, Yokoyama A, Lu Q (2002) Nonlinear optimal control applied to STATCOM for power system stabilization. In: Transmission and distribution conference and exhibition 2002: Asia Pacific, vol 1. IEEE/PES, pp 342–347, 6–10 Oct 2002
37. Bilgin HF, Ermis M (2010) Design and implementation of a current-source converter for use in industry applications of D-STATCOM. IEEE Trans Power Electron 25(8):1943–1957
38. Melin PE, Espinoza JR, Baier CR, Guzman JI, Espinosa EE (2011) Unified power quality conditioner based on current source converters for harmonic mitigation using a decoupled control strategy. In: IECON 2011—37th annual conference on IEEE industrial electronics society, pp 4152–4157, 7–10 Nov 2011
39. Rebeiro RS, Uddin MN (2012) Performance analysis of an FLC-based online adaptation of both hysteresis and PI controllers for IPMSM drive. IEEE Trans Ind Appl 48(1):12–19

40. Zare F, Ledwich G (2002) A hysteresis current control for single-phase multilevel voltage source inverters: PLD implementation. IEEE Trans Power Electron 17(5):731–738
41. Gupta R, Ghosh A, Joshi A (2006) Cascaded multilevel control of DSTATCOM using multiband hysteresis modulation. In: IEEE power engineering society general meeting
42. Shukla A, Ghosh A, Joshi A (2011) Hysteresis modulation of multilevel inverters. IEEE Trans Power Electron 26(5):1396–1409
43. Rodriguez J, Cortes P (2012) Predictive control of power converters and electrical drives. Wiley-IEEE Press
44. Thielemans S, Vyncke TJ, Jacxsens M, Melkebeek JA (2011) FPGA implementation of online finite-set model based predictive control for power electronics. 2011 Workshop on predictive control of electrical drives and power electronics (PRECEDE), pp 63–69, 14–15 Oct 2011
45. Wilson A, Cortes P, Kouro S, Rodriguez J, Abu-Rub H (2010) Model predictive control for cascaded H-bridge multilevel inverters with even power distribution. In: 2010 IEEE international conference on industrial technology (ICIT), pp 1271–1276, 14–17 Mar 2010
46. Han J, ZhaoM, Peng D, Tang T (2013) Improved model predictive current control of cascaded H-bridge multilevel converter. In: 2013 IEEE international symposium on industrial electronics (ISIE), pp 1–5, 28–31 May 2013
47. Kouro S, Cortes P, Vargas R, Ammann U, Rodriguez J (2009) Model predictive control—a simple and powerful method to control power converters. IEEE Trans Ind Electron 56 (6):1826–1838
48. Tarisciotti L, Zanchetta P, Watson A, Bifaretti S, Clare JC (2014) Modulated model predictive control for a seven-level cascaded H-bridge back-to-back converter. IEEE Trans Ind Electron 61(10):5375–5383
49. Ramirez RO, Espinoza JR, Villarroel F, Maurelia E, Reyes ME (2014) A novel hybrid finite control set model predictive control scheme with reduced switching. IEEE Trans Ind Electron 61(11):5912–5920

Chapter 9
Adaptive Observer for Capacitor Voltages in Multilevel STATCOMs

J. de León Morales, M.F. Escalante and M.T. Mata-Jiménez

Abstract Control of multilevel STATCOMs is complex mainly due to the internal converter control, where several capacitors are used as a fundamental component of multilevel converters. The capacitor voltage must be regulated to ensure the multilevel output voltage waveform, and to equally distribute the high input voltage among the power semiconductors. Regulation of the capacitor voltages needs the knowledge of the capacitor voltages. In this chapter, a nonlinear adaptive observer for DC capacitor voltages estimation is proposed for a class of multilevel converters. The observation scheme estimates simultaneously the state of the system and the system parameters, adding robustness and improving the state estimation when system parameters are uncertain. The observation scheme is developed using an instantaneous model of the system. The original system model is an n-dimensional system which is not observable. The original model is split into a suitable set of n-interconnected subsystems. This new representation allows overcoming the unobservable condition of the original system, which enables the design of an observation scheme for the capacitor voltages and system parameters. Hence, the observer for the whole system is approached by designing a separate exponential observer for each individual subsystem. As a result, the whole system state is reconstructed from the individual exponential observer designed for each subsystem. Thus, the interconnected system, which is constituted by the interconnected exponential observers, is an observer for the original system.

Keywords Multilevel converters · Nonlinear estimation · STATCOM

J. de León Morales · M.F. Escalante (✉) · M.T. Mata-Jiménez
Facultad de Ingeniería Mecánica y Eléctrica, Universidad Autónoma de Nuevo León,
Av. Universidad s/n; Ciudad Universitaria, 66451 San Nicolás de Los Garza
N.L., Mexico
e-mail: mescalante@ieee.org

J. de León Morales
e-mail: drjleon@gmail.com

M.T. Mata-Jiménez
e-mail: mtulio@ieee.org

F. Shahnia et al. (eds.), *Static Compensators (STATCOMs) in Power Systems*,
Power Systems, DOI 10.1007/978-981-287-281-4_9

9.1 Introduction

The power electronics-based converters are nowadays an essential technology to control and conditioning electrical power. Advancements in areas as power semiconductors, control electronics or control theory, have enabled new applications and new power converter topologies have been created. Thus, in medium or high voltage applications the classical 2-level inverter topology can be replaced by a new breed of power converters called multilevel converters [1–5]. Thereby multilevel converters are very attractive for STATCOMs used in electrical network compensation [6–10].

One common characteristic of multilevel power converters is the use of several capacitors in their power structure. Proper and safe operation of multilevel power converters requires the regulation of the voltage across the capacitors. Capacitor voltage regulation can be obtained by a feedback control loop using voltage sensors. In one hand, using voltage sensors to measure the capacitor voltages is a relative straightforward approach. In the other hand, as the number levels increases it will be necessary to increase the number of voltage sensors and its associated conditioning electronics, resulting in an increased hardware complexity, which impact negatively the system reliability. As an alternative to the physical voltage sensors are the software based sensors. The last ones are known as observers. Observers are computational algorithms that take advantage of the mathematical model of the system to reconstruct the system states from the inputs and some measured outputs [11–14]. Using observers to measure the capacitor voltages will reduce the number of physical sensors reducing the system costs and increasing the system reliability. The use of observers to estimate system states or system parameters have recently been proposed in several applications related to electromechanical and electrical power conversion systems [15–19]. Moreover, observer are becoming standard in applications such as high performance motor drives, as its use have proved to enhance drive performance and reliability [20, 21]. Even though the aforementioned applications of observers are all related or linked to the use of power converters, their main objective is not the observation of the converter states by itself but the observation of variables related to global system performance. As the complexity of power converters has evolved, new requirements in terms of the converter itself have emerged. In the case of multilevel converters, it is required to control and to monitor some of the converter internal states, and specifically the voltages across the capacitors which are used in the multilevel power structure. Recently, some proposals regarding those problems have being presented [22, 23].

9.2 System Description and Modeling

In this section, two known multilevel power converters are modeled. The cascaded H-bridge and the Flying capacitor multilevel converters are modeled as n interconnected subsystems, which allows to design an exponential observer for each subsystem.

9.2.1 Modeling of Cascaded H-Bridge Multilevel Converters

Cascaded H-bridge multilevel inverters are based on serial connection of single phase inverters bridges. A single phase-leg is shown in Fig. 9.1. As shown, each inverter bridge is supplied by a separate and isolated DC power supply. When the inverter is used to compensate reactive power and harmonics in electrical networks, a charged capacitor provides the needed voltage in the DC side of each H-bridge.

The output voltage of a cascaded H-bridge inverter-leg is obtained by adding the single H-bridge output voltages as follows:

$$v_o(t) = \sum_{j=1}^{n} v_{oj}(t) \tag{9.1}$$

where n is the number of cascaded H-bridges. If the DC side of each H-bridge has a value of V_{dc} volts, then the output voltage of each individual H-bridge can take 3 different values: $-V_{dc}, 0$ or $+V_{dc}$, as a function of the switching states. Taking into account that each H-bridge inverter-leg is composed of a series connected pair of switches, (T_{1j}, T_{2j}) and (T_{3j}, T_{4j}), which are commanded in a complementary way, then, it is possible to define a switching function, S_j, to describe the output voltage of each jth H-bridge. This switching function is defined by the switching state and can take 3 different values: -1, 0 or 1. In Table 9.1, the switching function, S_j, is defined as a function of the switching states.

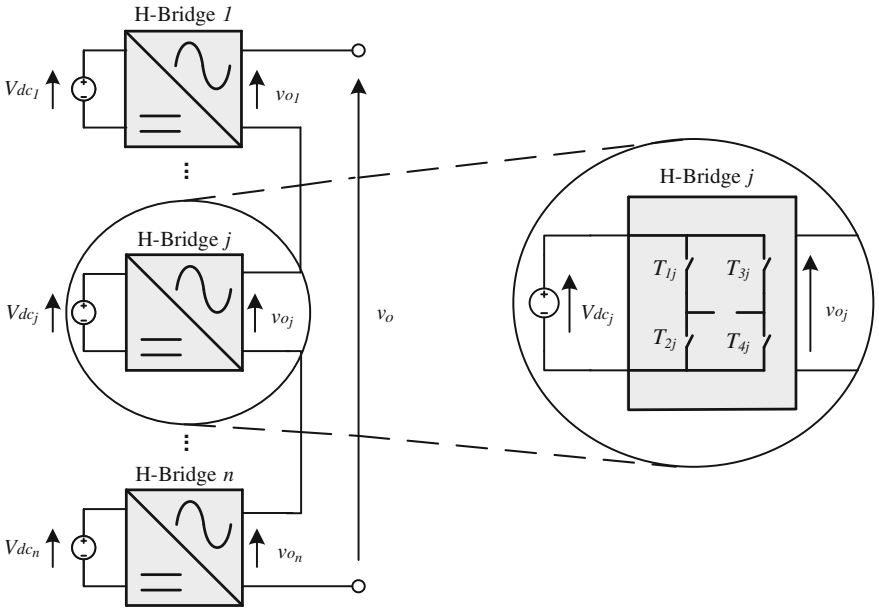

Fig. 9.1 One leg of a three-phase cascaded H-bridge multilevel structure

Table 9.1 Switching function

T_{1j}	T_{3j}	S_j
OFF	OFF	0
OFF	ON	–1
ON	OFF	1
ON	ON	0

Introducing the switching function in (9.1), then:

$$v_o(t) = \sum_{j=1}^{n} V_{dc} S_j \tag{9.2}$$

If a capacitor is used at the DC side of each H-bridge, as shown in Fig. 9.2, then the capacitor voltage for the *j*th bridge, v_{c_j}, is be described by:

$$\frac{d}{dt} v_{c_j} = \frac{1}{C_j} i(t) S_j \tag{9.3}$$

where C_j is the capacitance associated to the *j*th H-bridge.

Using the capacitor voltages, the inverter phase voltage $v_o(t)$ can be expressed as:

$$v_o(t) = \sum_{j=1}^{n} v_{c_j}(t) S_j \tag{9.4}$$

Now, if the multilevel inverter is connected to the electrical power system, the equivalent circuit is shown in Fig. 9.3, where the phase current $i(t)$ is given by:

$$\frac{d}{dt} i(t) = -\frac{1}{l_c} [v_o(t) - v_{net}(t)] - \frac{r_c}{l_c} i(t) \tag{9.5}$$

where $v_{net}(t)$ is the network phase voltage, l_c and r_c are respectively the equivalent inductance and the resistance of the linker transformer or reactor.

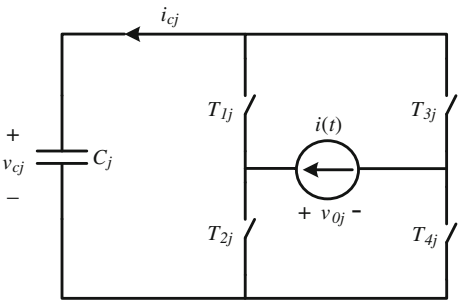

Fig. 9.2 Single-phase H-bridge

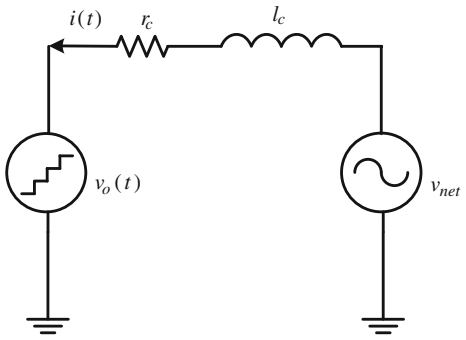

Fig. 9.3 Equivalent circuit of the multilevel converter connected to an electrical power system

Now, using (9.3), (9.4) and (9.5), the dynamical model describing the whole system is given by:

$$\sum_{NH}: \begin{cases} \frac{d}{dt} i(t) & = & -\frac{1}{l_c} \sum_{j=1}^{n} v_{cj}(t) S_j + \frac{1}{l_c} v_{net} - \frac{r_c}{l_c} i(t) \\ \frac{d}{dt} v_{c_1}(t) & = & \frac{1}{C_1} i(t) S_1 \\ \frac{d}{dt} v_{c_2}(t) & = & \frac{1}{C_2} i(t) S_2 \\ \vdots & \vdots & \vdots \\ \frac{d}{dt} v_{c_n}(t) & = & \frac{1}{C_n} i(t) S_n \\ y & = & i(t) \end{cases} \tag{9.6}$$

It is important to remark that the capacitance value C_j for the jth capacitor and the equivalent impedance (l_c, r_c) could be uncertain or unknown. The resulting system is an $(n + 1)$-dimensional nonlinear system where the output is given by $y(t) = i(t)$, and S_j, for $j = 1, \ldots, n$; are the inputs of the system. Assuming that the current $i(t)$ is the only measurable variable of the system (9.6), from the observability rank condition, it is clear that the system is not observable because the observation space is not of full rank.

9.2.2 Modeling of Flying Capacitor Multilevel Converter

Flying capacitor multilevel converters are based on an imbricated structure of commutation cells, as shown in Fig. 9.4. Each commutation cell is composed of a DC source, assured by charged capacitor, and a pair of switches (i.e. T_x, T'_x) which are commanded in a complementary way.

The output voltage of an N-cell converter can be described as a linear combination of DC voltages, given by

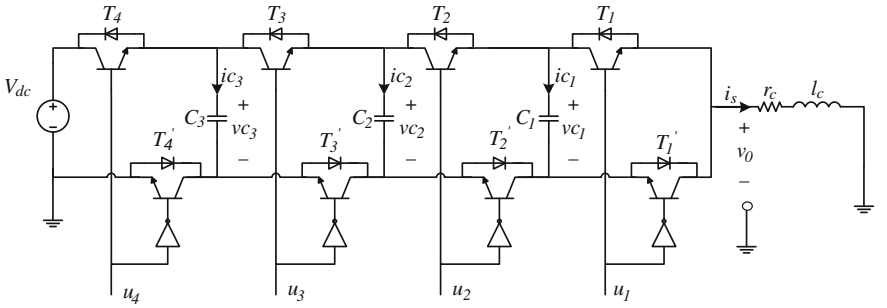

Fig. 9.4 Five-level flying capacitor converter

$$v_o(t) = -\sum_{j=1}^{N} v_{dcj}(t) S_j \tag{9.7}$$

where v_{dc_j} represents the jth DC power supply voltage, and S_j is the switching function linking the jth DC power supply to the output voltage. S_j is defined by the control signals, u_j, applied to the converter switches as

$$S_j = u_{j+1} - u_j \tag{9.8}$$

where u_j is the control signal applied to the jth switch, T_j. Considering that each internal DC power supply is defined by the voltage across a flying capacitor, then the DC voltage dynamics for the jth cell is given by

$$\frac{d}{dt} v_{cj} = \frac{1}{C_j} i(t) S_j \tag{9.9}$$

where C_j is the capacitance. The voltage of the Nth cell is given by $v_{c_N} = E$.

Furthermore, the output current, $i(t)$, is given by

$$\frac{d}{dt} i(t) = -\frac{1}{l_c} v_o(t) - \frac{r_c}{l_c} i(t) \tag{9.10}$$

Then, the whole dynamics system is described by

$$\sum\nolimits_{NF} : \begin{cases} \frac{d}{dt} i(t) & = & -\frac{1}{l_c} \sum_{j=1}^{N-1} v_{cj}(t) S_j + \frac{E}{l_c} S_N - \frac{r_c}{l_c} i(t) \\ \frac{d}{dt} v_{c_1}(t) & = & \frac{1}{C_1} i(t) S_1 \\ \frac{d}{dt} v_{c_2}(t) & = & \frac{1}{C_2} i(t) S_2 \\ \vdots & \vdots & \vdots \\ \frac{d}{dt} v_{c_{N-1}}(t) & = & \frac{1}{C_{N-1}} i(t) S_{N-1} \\ y & = & i(t) \end{cases} \tag{9.11}$$

The resulting system is an n-dimensional nonlinear system, where the output is defined by $y = i(t)$ and S_j, for $j = 1, \ldots, N-1$, are the $N-1$ inputs of the system. It is important to remark that the capacitance value C_j for the jth capacitor and the equivalent impedance (l_c, r_c) could be uncertain or unknown.

Again as in the cascaded H-bridge converter model (9.6), note that $i(t)$ is the only measurable variable of the system (9.11) and, from the observability rank conditions, it is clear that the system (9.11) is not observable, i.e. the space of differentiable elements of the observation space is not of full rank.

9.3 Observer Design

In this section an alternative representation of models (9.6) and (9.11) will be considered, i.e. the original model will be split into a suitable set of n subsystems for which it will be possible to design an observer to estimate the capacitor voltages.

In order to unify the representation of both converter models we define (without loss of generality) $V = v_{net}$ for the H-bridge and $V = -S_{n+1}E$ for the flying capacitors. Note that in both cases V is known.

Equations (9.6) and (9.11) can be split into n subsystems of the form:

$$
\sum\nolimits_1 : \begin{cases} \frac{d}{dt} i(t) = -\frac{r_c}{l_c} i(t) - \frac{1}{l_c} S_1 v_{c_1} + \frac{V}{l_c} \underbrace{- \frac{1}{l_c} (S_2 v_{c_2} + \cdots + S_n v_{c_n})}_{\Gamma_1} \\ \frac{d}{dt} v_{c1} = \frac{1}{C_1} S_1 i(t) \\ y = i(t) \end{cases}
$$

$$
\sum\nolimits_2 : \begin{cases} \frac{d}{dt} i(t) = -\frac{r_c}{l_c} i(t) - \frac{1}{l_c} S_2 v_{c_2} + \frac{V}{l_c} \underbrace{- \frac{1}{l_c} (S_1 v_{c1} + \cdots + S_n v_{c_n})}_{\Gamma_2} \\ \frac{d}{dt} v_{c2} = \frac{1}{C_2} S_2 i(t) \\ y = i(t) \end{cases}
$$

$$
\vdots \quad \vdots \quad \vdots
$$

$$
\sum\nolimits_n : \begin{cases} \frac{d}{dt} i(t) = -\frac{r_c}{l_c} i(t) - \frac{1}{l_c} S_n v_{c_n} + \frac{V}{l_c} \underbrace{- \frac{1}{l_c} (S_1 v_{c_1} + \cdots + S_{n-1} v_{c_{n-1}})}_{\Gamma_n} \\ \frac{d}{dt} v_{c_n} = \frac{1}{C_n} S_n i(t) \\ y = i(t) \end{cases}
$$

Each subsystem can be written in a state affine form as:

$$\sum_j : \begin{cases} \dot{\chi}_j = A(S_j, i)\chi_j + \Phi(S_j, i)\tau + \Psi(S_j, i) + \Gamma_j(\bar{S}_j, \bar{\chi}_j) \\ y = \mathcal{C}\chi_j \end{cases} \tag{9.12}$$

for $j = 1, \ldots, n$, where τ stands for an uncertain parameter; χ_j represents the state of the jth subsystem, S_j are the instantaneous inputs applied to the system and $y = i(t)$ is the measurable output. The matrices $A(S_j, i)$, $\Psi(S_j, i)$ and $\Phi(S_j, i)$ are known and defined by the system parameters and measured input and outputs. The output matrix is

$$\mathcal{C} = (0 \quad 1)$$

and the interconnection

$$\Gamma_j(\bar{S}_j, \bar{\chi}_j) = B\varphi(\bar{S}_j, \bar{\chi}_j)$$

with

$$B = \begin{pmatrix} 1 \\ 0 \end{pmatrix}$$

and

$$\varphi(\bar{S}_j, \bar{\chi}_j) = -\frac{1}{l_c} \sum_{\substack{m=1 \\ m \neq j}}^{n} v_{c_m} S_m$$

where $\bar{S}_j = (S_1, \ldots, S_{j-1}, S_{j+1}, \ldots, S_{n-1})$ and $\bar{\chi}_j = (v_{c_1}, \ldots, v_{c_{j-1}}, v_{c_{j+1}}, \ldots, v_{c_n})$.

The function $\varphi(\bar{S}_j, \bar{\chi}_j)$ is the interconnection term which depends on the inputs and state of each subsystem. Notice that the output is the current $i(t)$ and is the same for each subsystem as shown in Fig. 9.5.

The new set of subsystems will be used to design an observer $\mathcal{O}$ for the n capacitor voltages. It is clear that the observability of the system depends on the applied input. Then, the convergence of this observer can be proved assuming that the inputs S_j are regularly persistent, i.e. it is a class of admissible inputs that allows to observe the system (for more details see [11, 12]).

Now, a further result based on regular persistence is introduced [24, 25].

Lemma *Assume that the input S_j is regularly persistent for system (9.12) and consider the following Lyapunov differential equation:*

$$\dot{P}_j = -\theta_j P_j - A^T(S_j, i)P_j - P_j A(S_j, i) + \mathcal{C}^T\mathcal{C}$$

with $P_j(0) > 0$. Then, $\exists \theta_{j_0} > 0$ such that for any symmetric positive definite matrix $P_j(0)$, $\exists \theta_j \geq \theta_{j_0}$, $\exists \alpha_j, \beta_j > 0, t_0 > 0 : \forall t > t_0$,

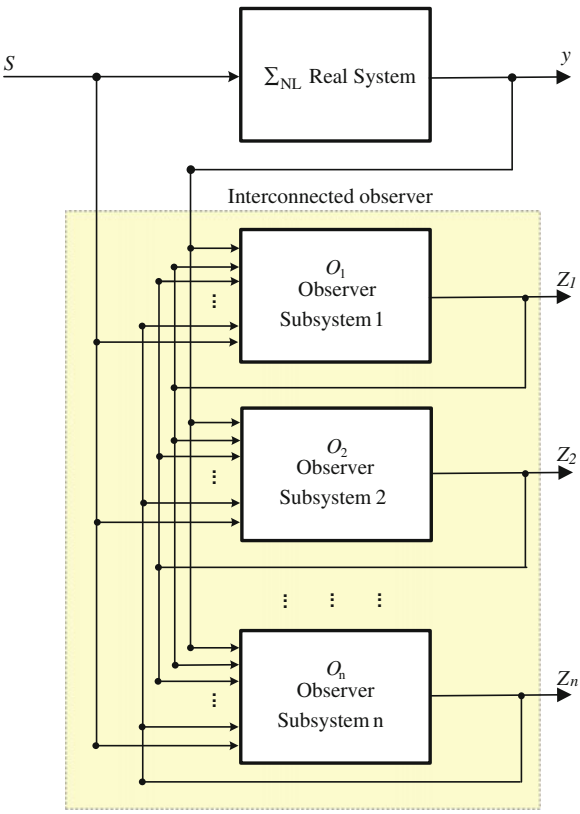

Fig. 9.5 Interconnected observer block diagram

$$\alpha_j I < P_j(t) < \beta_j I,$$

where I is the identity matrix.

This guarantees the matrix P_j is non-singular, and the observer works properly.

Remark The proposed observer $\mathcal{O}$ works for inputs satisfying the regularly persistent condition, which is equivalent to each subsystem Σ_j being observable, and hence, observer $\mathcal{O}_j$ works at the same time while the other subsystems become observable when their corresponding input satisfies the regularly persistent condition.

Now, we will give the sufficient conditions which ensure the convergence of the interconnected observer $\mathcal{O}$. For that, we introduce the following assumptions:

Assumption Assume that the input S_j is a regularly persistent input for subsystem Σ_j and admits an exponential observer $\mathcal{O}_j$ for $j = 1, \ldots, n$. In this case, an observer of the proposed form can be designed and the estimation error will be bounded.

Assumption The term $\Gamma_j(\bar{S}_j, \bar{\chi}_j)$ does not destroy the observability property of subsystem Σ_j under the action of the regularly persistent input S_j. Moreover, $\Gamma_j(\bar{S}_j, \bar{\chi}_j)$ is Lipschitz with respect to $\bar{\chi}_j$ and uniformly with respect to S_j for $j = 1, \ldots, n$.

This technique will be used to design three different observer schemes: an interconnected observer, an adaptive interconnected observer and an extended adaptive interconnected observer. We consider all the assumptions hold for the proposed systems.

9.3.1 Interconnected Observer for the Cascaded H-Bridge Multilevel Converter

In this case we assume that the system parameters are known. The objective of the observer is to reconstruct the capacitor voltages v_{c_j} and the output current $i(t)$. The state is defined as: $\chi_j = (i, v_{c_j})^T$ with:

$$A(S_j, i) = \begin{pmatrix} -\frac{r_c}{l_c} & -\frac{1}{l_c}S_j \\ \frac{1}{C_j}S_j & 0 \end{pmatrix} \quad \Phi(S_j, i) = 0 \quad \Psi(S_j, i) = \begin{pmatrix} \frac{v_{net}}{l_c} \\ 0 \end{pmatrix}$$

Each subsystem can be written in a particular form as:

$$\sum_j : \begin{cases} \dot{\chi}_j = A(S_j, i)\chi_j + \Psi(S_j, i) + \Gamma_j(\bar{S}_j, \bar{\chi}_j) \\ y = \mathcal{C}\chi_j \quad j = 1, \ldots, n \end{cases} \tag{9.13}$$

Note that the term $\Phi(S_j, i)$ is inexistent because we assume that the all parameters are known.

Then, the following system

$$\mathcal{O}_j : \begin{cases} \dot{Z}_j = A(S_j, i)Z_j + \Psi(S_j, i) + \Gamma_j(\bar{S}_j, \bar{Z}_j) + P_j^{-1}\mathcal{C}^T(y - \mathcal{C}Z_j) \\ \dot{P}_j = -\theta_j P_j - A^T(S_j, i)P_j - P_j A(S_j, i) + \mathcal{C}^T\mathcal{C} \end{cases} \tag{9.14}$$

is an observer for the system (9.13) for $j = 1, \ldots, n$ where $P_j^{-1}\mathcal{C}^T$ is the gain of the observer which depends on the solution of the Riccati Equation (9.14) for each subsystem and, $\bar{Z}_j = (\hat{v}_{c_1}, \ldots, \hat{v}_{c_{j-1}}, \hat{v}_{c_{j+1}}, \ldots, \hat{v}_{c_n})$. Furthermore, if the inputs S_j are regularly persistent, the estimation error $\varepsilon_j = Z_j - \chi_j$ converges to zero as t tends to infinite [26]. The parameter $\theta_j > 0$ is called the forgetting factor and it determines the convergence rate of the observer.

Now, consider that the system can be represented as a set of the interconnected subsystems as follows:

$$\sum : \begin{cases} \dot{\chi}_1 &= A(S_j,i)\chi_1 + \Psi(S_1,i) + \Gamma_1(\bar{S}_1,\bar{\chi}_1) \\ \dot{\chi}_2 &= A(S_j,i)\chi_2 + \Psi(S_2,i) + \Gamma_2(\bar{S}_2,\bar{\chi}_2) \\ \vdots & \vdots \quad \vdots \\ \dot{\chi}_n &= A(S_j,i)\chi_n + \Psi(S_n,i) + \Gamma_n(\bar{S}_n,\bar{\chi}_n) \end{cases}$$

Notice that the output is the current $i(t)$ and it is the same for each subsystem.

The main idea of this technique is to construct an observer for the whole system Σ, from the separate observer design of each subsystem Σ_j.

In general, if each $\mathcal{O}_j$ is an exponential observer for Σ_j for $j = 1, \ldots, n$, then the following interconnected system $\mathcal{O}$

$$\mathcal{O}: \begin{cases} \dot{Z}_1 &= A(S_1,i)Z_1 + \Psi(S_1,i) + \Gamma_1(\bar{S}_1,\bar{Z}_1) + P_1^{-1}\mathcal{C}^T(y - \mathcal{C}Z_1) \\ \dot{Z}_2 &= A(S_2,i)Z_2 + \Psi(S_2,i) + \Gamma_2(\bar{S}_2,\bar{Z}_2) + P_2^{-1}\mathcal{C}^T(y - \mathcal{C}Z_2) \\ \vdots & \vdots \quad \vdots \\ \dot{Z}_n &= A(S_n,i)Z_n + \Psi(S_n,i) + \Gamma_n(\bar{S}_n,\bar{Z}_n) + P_n^{-1}\mathcal{C}^T(y - \mathcal{C}Z_n) \\ \dot{P}_1 &= -\theta_1 P_1 - A^T(S_1,i)P_1 - P_1 A(S_1,i) + \mathcal{C}^T\mathcal{C} \\ \dot{P}_2 &= -\theta_2 P_2 - A^T(S_2,i)P_2 - P_2 A(S_2,i) + \mathcal{C}^T\mathcal{C} \\ \vdots & \vdots \quad \vdots \\ \dot{P}_n &= -\theta_n P_n - A^T(S_n,i)P_n - P_n A(S_n,i) + \mathcal{C}^T\mathcal{C} \end{cases}$$

is an observer for the interconnected system Σ.

9.3.2 Adaptive Interconnected Observer for a Flying Capacitor Multilevel Converter

In this subsection an observer is designed for estimating the capacitor voltages v_{c_j} for $j = 1, \ldots, n$ and the resistance value r_c for the flying capacitor multilevel converter (shown in Fig. 9.4). The resistance value is considered uncertain and all the other parameters are supposed constant and known. In order to estimate the resistance, we will define τ as r_c/l_c which is uncertain because it is not known, $\chi_j = (i, v_{c_j})^T$ represents the state of the jth subsystem; with

$$A(S_j,i) = \begin{pmatrix} 0 & -\frac{1}{l_c}S_j \\ \frac{1}{C_j}S_j & 0 \end{pmatrix} \quad \Phi(S_j,i) = \begin{pmatrix} -i \\ 0 \end{pmatrix} \quad \Psi(S_j,i) = \begin{pmatrix} -\frac{E}{l_c}S_j \\ 0 \end{pmatrix}$$

Recalling that each subsystem can be written in a particular state affine form as:

$$\Sigma_j: \begin{cases} \dot{\chi}_j = A(S_j, i)\chi_j + \Psi(S_j, i) + \Phi(S_j, i)\tau + \Gamma_j(\bar{S}_j, \bar{\chi}_j) \\ y = \mathcal{C}\chi_j \quad j = 1, \ldots, n \end{cases} \tag{9.15}$$

Then, the following system

$$\mathcal{O}_j: \begin{cases} \dot{Z}_j = A(S_j, i)Z_j + \Psi(S_j, i) + \Phi(S_j, i)\hat{\tau}_j + \Gamma_j(\bar{S}_j, \bar{Z}_j) \\ \qquad + \{\Lambda_j R_j^{-1}\Lambda_j^T\mathcal{C}^T + P_j^{-1}\mathcal{C}^T\}(y - \mathcal{C}Z_j) \\ \dot{P}_j = -\theta_j P_j - A^T(S_j, i)P_j - P_j A(S_j, i) + \mathcal{C}^T\mathcal{C} \\ \dot{\hat{\tau}}_j = R_j^{-1}\Lambda_j^T\mathcal{C}^T(y - \mathcal{C}Z_j) \\ \dot{\Lambda}_j = \{A^T(S_j, i) - P_j^{-1}\mathcal{C}^T\mathcal{C}\}\Lambda_j + \Phi(S_j, i) \\ \dot{R}_j = -\rho_j R_j + \Lambda_j^T\mathcal{C}^T\mathcal{C}\Lambda_j \end{cases} \tag{9.16}$$

is an adaptive observer for the system (9.15) for $j = 1, \ldots, n$ where $\Lambda_j R_j^{-1}\Lambda_j^T\mathcal{C}^T + P_j^{-1}\mathcal{C}^T$ is the gain of the observer which depends on the solution of the Riccati Equation (9.16) and the adaptation dynamics for each subsystem, $Z_j = (\hat{i}, \hat{v}_{c_j})$, and, $\bar{Z}_j = (\hat{v}_{c_1}, \ldots, \hat{v}_{c_{j-1}}, \hat{v}_{c_{j+1}}, \ldots, \hat{v}_{c_n})$. Furthermore, if the inputs S_j are regularly persistent the observer gain is well defined and the estimation error $\varepsilon_j = Z_j - \chi_j$ converges to zero as t tends to infinite [27]. The parameter $\theta_j > 0$ is called the forgetting factor determining the convergence rate of the observer, and $\rho_j > 0$ is the adaptation gain.

Now, consider that the system can be represented as a set of the interconnected subsystems as follows:

$$\Sigma: \begin{cases} \dot{\chi}_1 &= A(S_1, i)\chi_1 + \Psi(S_1, i) + \Phi(S_1, i)\tau + \Gamma_1(\bar{S}_1, \bar{\chi}_1) \\ \dot{\chi}_2 &= A(S_2, i)\chi_2 + \Psi(S_2, i) + \Phi(S_2, i)\tau + \Gamma_2(\bar{S}_2, \bar{\chi}_2) \\ \vdots &\quad \vdots \quad \vdots \\ \dot{\chi}_n &= A(S_n, i)\chi_n + \Psi(S_n, i) + \Phi(S_n, i)\tau + \Gamma_n(\bar{S}_n, \bar{\chi}_n) \end{cases} \tag{9.17}$$

Again, the main idea is to construct an observer for the whole system Σ, given by (9.17), from the individual observer design of each subsystem Σ_j, given that $\mathcal{O}_j$ is an exponential observer for Σ_j, for $j = 1, \ldots, n$. Then, the interconnected system $\mathcal{O}$, which is constituted by the n adaptive interconnected exponential observers $\mathcal{O}_j$, is an adaptive observer for the interconnected system Σ (see Fig. 9.5).

In general, if each $\mathcal{O}_j$ is an exponential observer for Σ_j for $j = 1, \ldots, n$, then the following interconnected system $\mathcal{O}$

$$
\mathcal{O}:\begin{cases}
\dot{Z}_1 &= A(S_1,i)Z_1+\Psi(S_1,i)+\Phi(S_1,i)\hat{\tau}_1+\Gamma_1(\bar{S}_1,\bar{Z}_1)\\
&\quad +\{\Lambda_1 R_1^{-1}\Lambda_1^T\mathcal{C}^T+P_1^{-1}\mathcal{C}^T\}(y-\mathcal{C}Z_1)\\
\vdots &\vdots \quad \vdots\\
\dot{Z}_n &= A(S_n,i)Z_n+\Psi(S_n,i)+\Phi(S_n,i)\hat{\tau}_n+\Gamma_n(\bar{S}_n,\bar{Z}_n)\\
&\quad +\{\Lambda_n R_n^{-1}\Lambda_n^T\mathcal{C}^T+P_n^{-1}\mathcal{C}^T\}(y-\mathcal{C}Z_n)\\
\dot{P}_1 &= -\theta_1 P_1-A^T(S_1,i)P_1-P_1A(S_1,i)+\mathcal{C}^T\mathcal{C}\\
\vdots &\vdots \quad \vdots\\
\dot{P}_n &= -\theta_n P_n-A^T(S_n,i)P_n-P_nA(S_n,i)+\mathcal{C}^T\mathcal{C}\\
\dot{\hat{\tau}}_1 &= R_1^{-1}\Lambda_1^T\mathcal{C}^T(y-\mathcal{C}Z_1)\\
\vdots &\vdots \quad \vdots\\
\dot{\hat{\tau}}_n &= R_n^{-1}\Lambda_n^T\mathcal{C}^T(y-\mathcal{C}Z_n)\\
\dot{\Lambda}_1 &= \{A^T(S_1,i)-P_1^{-1}\mathcal{C}^T\mathcal{C}\}\Lambda_1+\Phi(S_1,i)\\
\vdots &\vdots \quad \vdots\\
\dot{\Lambda}_n &= \{A^T(S_n,i)-P_n^{-1}\mathcal{C}^T\mathcal{C}\}\Lambda_n+\Phi(S_n,i)\\
\dot{R}_1 &= -\rho_1 R_1+\Lambda_1^T\mathcal{C}^T\mathcal{C}\Lambda_1\\
\vdots &\vdots \quad \vdots\\
\dot{R}_n &= -\rho_n R_n+\Lambda_n^T\mathcal{C}^T\mathcal{C}\Lambda_n
\end{cases}
$$

is an adaptive observer for the interconnected system Σ (see Fig. 9.5). The proof can be found in [28].

9.3.3 Extended Adaptive Interconnected Observer for a Cascaded H-Bridge Multilevel Converter

In this subsection an alternative representation of model (9.6) will be considered, i.e. the original model will be split into a suitable set of n subsystems for which it is possible to design an observer for estimating also the capacitance values C_j for $j=1,\ldots,n$. In order to estimate the capacitance values the state vector can be extended by the vector of constant parameters $dC_j/dt=0$, introducing the capacitance dynamics, and preserving the state affine form:

$$
\sum\nolimits_E:\begin{cases}
\frac{d}{dt}i(t) &= -\frac{1}{l_c}\sum_{j=1}^{n}v_{cj}(t)S_j+\frac{1}{l_c}v_{net}-\frac{r_c}{l_c}i(t)\\
\frac{d}{dt}v_{c_1}(t) &= \frac{1}{C_1}i(t)S_1\\
\frac{d}{dt}C_1^{-1} &= 0\\
\vdots &\vdots \quad \vdots\\
\frac{d}{dt}v_{c_n}(t) &= \frac{1}{C_n}i(t)S_n\\
\frac{d}{dt}C_n^{-1} &= 0\\
y &= i(t)
\end{cases}
\tag{9.18}
$$

Then, the system (9.18) can be split in n subsystems of the form:

$$\sum_j : \begin{cases} \dfrac{d}{dt} i(t) = -\dfrac{r_c}{l_c} i(t) - \dfrac{1}{l_c} S_j v_{cj} + \dfrac{v_{net}}{l_c} \\ \qquad\qquad \underbrace{-\dfrac{1}{l_c}(S_1 v_{c1} + \cdots + S_{j-1} v_{j-1} + S_{j+1} v_{j+1} + \cdots + S_n v_{c_n})}_{\Gamma_j} \\ \dfrac{d}{dt} v_{c_j} = \dfrac{1}{C_j} S_j i(t) \\ \dfrac{d}{dt} C_j^{-1} = 0 \\ \qquad y = i(t) \end{cases}$$

for $j = 1, \ldots, n$. Note that each subsystem can be written in a state affine form as:

$$\sum_j : \begin{cases} \dot{\chi}_j = A(S_j, i)\chi_j + \Psi(S_j, i) + \Phi(S_j, i)\tau + \Gamma_j(\bar{S}_j, \bar{\chi}_j) \\ y = \mathcal{C}\chi_j \quad j = 1, \ldots, n \end{cases} \tag{9.19}$$

where τ stands for r_c/l_c which is uncertain; $\chi_j = (i, v_{c_j}, \mathrm{C}_j^{-1})^T$ represents the extended state of the jth subsystem; with

$$A(S_j, i) = \begin{pmatrix} 0 & -S_j/l_c & 0 \\ 0 & 0 & S_j i \\ 0 & 0 & 0 \end{pmatrix} \quad \Phi(S_j, i) = \begin{pmatrix} -i \\ 0 \\ 0 \end{pmatrix} \quad \Psi(S_j, i) = \begin{pmatrix} \frac{v_{net}}{l_c} \\ 0 \\ 0 \end{pmatrix}$$

The new set of subsystems will be used to design an observer for the n capacitor voltages and capacitance values, obtaining simultaneously the r_c value.

Then, the following system [identical to the adaptive observer (9.16)]

$$\mathcal{O}_j : \begin{cases} \dot{Z}_j = A(S_j, i)Z_j + \Psi(S_j, i) + \Phi(S_j, i)\hat{\tau}_j + \Gamma_j(\bar{S}_j, \bar{Z}_j) \\ \qquad + \{\Lambda_j R_j^{-1} \Lambda_j^T \mathcal{C}^T + P_j^{-1} \mathcal{C}^T\}(y - \mathcal{C}Z_j) \\ \dot{P}_j = -\theta_j P_j - A^T(S_j, i)P_j - P_j A(S_j, i) + \mathcal{C}^T\mathcal{C} \\ \dot{\hat{\tau}}_j = R_j^{-1} \Lambda_j^T \mathcal{C}^T (y - \mathcal{C}Z_j) \\ \dot{\Lambda}_j = \{A^T(S_j, i) - P_j^{-1}\mathcal{C}^T\mathcal{C}\}\Lambda_j + \Phi(S_j, i) \\ \dot{R}_j = -\rho_j R_j + \Lambda_j^T \mathcal{C}^T \mathcal{C} \Lambda_j \end{cases} \tag{9.20}$$

is an adaptive observer for the system (9.19) for $j = 1, \ldots, n$ where $\Lambda_j R_j^{-1} \Lambda_j^T \mathcal{C}^T + P_j^{-1}\mathcal{C}^T$ is the gain of the observer which depends on the solution of the Riccati Equation (9.20) and the adaptation dynamics for each subsystem, $Z_j = (\hat{i}, \hat{v}_{c_j}, \hat{\mathrm{C}}_j^{-1})$, and, $\bar{Z}_j = (\hat{v}_{c_1}, \ldots, \hat{v}_{c_{j-1}}, \hat{v}_{c_{j+1}}, \ldots, \hat{v}_{c_n}, \hat{\mathrm{C}}_1^{-1}, \ldots, \hat{\mathrm{C}}_{j-1}^{-1}, \hat{\mathrm{C}}_{j+1}^{-1}, \ldots, \hat{\mathrm{C}}_n^{-1})$. Furthermore, if the inputs S_j are regularly persistent and the gain is well defined, the estimation

error $\varepsilon_j = Z_j - \chi_j$ converges to zero as t tends to infinite [29]. The parameter $\theta_j > 0$ is called the forgetting factor determining the convergence rate of the observer, and $\rho_j > 0$ is the adaptation gain.

Now consider that the system can be represented as a set of the interconnected subsystems as follows:

$$\sum : \begin{cases} \dot{\chi}_1 & = & A(S_1, i)\chi_1 + \Psi(S_1, i) + \Phi(S_1, i)\tau + \Gamma_1(\bar{S}_1, \bar{\chi}_1) \\ \dot{\chi}_2 & = & A(S_2, i)\chi_2 + \Psi(S_2, i) + \Phi(S_2, i)\tau + \Gamma_2(\bar{S}_2, \bar{\chi}_2) \\ \vdots & \vdots & \vdots \\ \dot{\chi}_n & = & A(S_n, i)\chi_n + \Psi(S_n, i) + \Phi(S_n, i)\tau + \Gamma_n(\bar{S}_n, \bar{\chi}_n) \end{cases}$$

In general, if each $\mathcal{O}_j$ is an exponential observer for Σ_j for $j = 1, \ldots, n$. Then the interconnected system $\mathcal{O}$ which is constituted by interconnected exponential observers $\mathcal{O}_j$ is an adaptive observer for the interconnected system Σ (see Fig. 9.5).

9.4 Simulation and Experimental Results

In this section the presented observer schema are validated through simulation and experimental data which is incorporated into the simulation.

9.4.1 Validation of the Interconnected Observer Using Simulation Experiments

The interconnected observer presented in Sect. 9.3.1 is validated in a system in which the cascaded H-bridge multilevel converter is used to compensate for reactive power and harmonic currents in a power system [27].

The general block diagram is shown in Fig. 9.6. Each multilevel inverter leg has 4 H-bridges per phase (**Block 1**). A capacitor C_{nom} = 50 mF (nominal value) per bridge was used. The capacitors were pre-charged at 50 V. The compensator is coupled to a 100 V utility network through a 0.5 mH inductor and 0.1 Ω resistor (**Block 2**). Simulated load is a combination of linear and nonlinear elements (**Block 3**), with four linear and two nonlinear three-phase symmetrical loads. Load parameters are as follows: Linear loads 1 and 2: R = 10 Ω, L = 5 mH. Linear loads 3 and 4: R = 1 Ω, L = 25 mH. Nonlinear load consists of two three-phase diode rectifiers with the following parameters: Nonlinear load 1: AC input impedance: R = 0.1 Ω, L = 5 mH, DC side: L = 1 mH, C = 2 mF and R_{load1} = 30 Ω. Nonlinear load 2: AC input impedance: R = 0.1 Ω, L = 0.1 mH, DC side: L = 50 mH, C = 20 μF and R_{load2} = 5 Ω. The modulation switching frequency is 5 kHz. Simulations were carried out using PSIM from Powersim and MATLAB/SIMULINK from Mathworks, working in co-simulation mode.

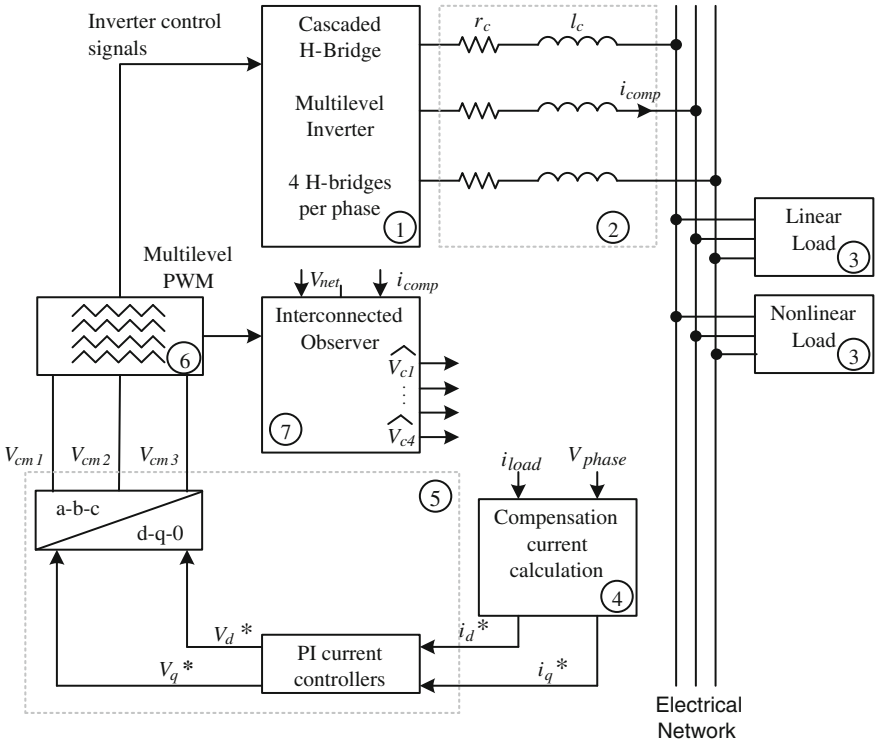

Fig. 9.6 Block diagram of a cascaded H-bridge multilevel-inverter-based compensator and interconnected observer

Compensation currents are calculated in **Block 4** using the instantaneous power concepts [30]. Basically it calculates compensation currents in such a way that reactive power and oscillating power will be supplied by the multilevel compensator. Then compensation currents are controlled using Proportional-Integral (PI) controllers, the PI gains are $k_P = 0.05$, $k_I = 1$ (**Block 5**) in a synchronous reference frame. The proportional-integral current controllers generate the voltage references to command the multilevel inverter. The control signals for the multilevel inverter H-bridges are generated by a Carrier based multilevel Pulse Width Modulation (CPWM) controller shown in **Block 6**. The modulation voltages, v_{cm1}, v_{cm2} and v_{cm3}, calculated by the PI current controllers are fed into the CPWM in order to generate the H-bridge control signals.

Also, in **Block 6**, the switching function, S_j, is generated as defined in Table 9.1. S_j is used in the interconnected observer, **Block 7**, to estimate the H-bridges capacitor voltages according to (9.14) where the observer gain $\theta_j = 10{,}000$ for $j = 1, \ldots, 3$.

During simulation, the loads are connected at different times to study the observer behavior. Nonlinear load 1 is connected at $t = 0.01$ s, then at $t = 0.15$ s

nonlinear load 2 and linear load 1 are connected and finally at $t = 3.5$ s linear loads 2, 3 and 4 are connected.

Figure 9.7 shows the real and estimated capacitor voltages for one phase and their corresponding estimation errors. As shown, the interconnected observer follows the real capacitor voltages accurately. From 1.5 to 1.75 s, direct axis current was commanded to absorb active power from the electrical network and thus, forcing the capacitor voltages to increase. Then, at 3.5 s an increase in reactive current is causing a decrease in the capacitor voltages. In any condition, the observer is able to follow the real capacitor voltages accurately. Once the observer transient is over, the estimated voltages are always close to their real values.

Finally, as the model parameters are always a concern, a simulation with uncertain capacitance values was conducted. The capacitance values at each H-bridge are changed from their nominal values, C_{nom} = 50 mF, as follows: $C_1 = 1.2\ C_{nom}$, $C_2 = 0.8\ C_{nom}$, $C_3 = 1.1\ C_{nom}$, $C_4 = 0.8\ C_{nom}$. Figure 9.8 shows the real and estimated capacitor voltages and their corresponding estimation errors when non-nominal capacitance values are used. As shown, the observer keeps tracking of the real capacitor voltages, but its convergence time is increased. Also, notice that when a capacitor voltage is changing rapidly, when real power is being absorbed from the network (from 1.5 to 1.75 s), the estimation error is increased, but it converges to the real value when the transient at the capacitor voltages is over. That behavior justifies the use of an adaptive observer scheme [27].

9.4.2 *Validation of the Extended Adaptive Interconnected Observer for a Flying Capacitor Converter Using Experimental Data*

The proposed observation scheme introduced in (9.3.3) is validated using experimental data from a 5-level flying capacitor converter. The block diagram of the experimental setup is shown in Fig. 9.9, and the laboratory prototype photo is shown in Fig. 9.10.

The converter prototype has 4 commutation cells, and it is commanded by a dSPACE 1104 system and an Actel ProAsic FPGA board. The capacitors assuring the floating DC sources are 390 µF each. An *R-L* charge is connected at the output. During the test, resistive part, r_c, is changed from 12.6 to 21.6 Ω, while the inductance, l_c, has a constant nominal value of 2.3 mH. The converter modulation scheme is based on a 1 kHz phase-shifted carrier PWM strategy [31], which is implemented in the dSPACE system. Then, the control signals are sent to the FPGA board, where a dead time of 2 µs is introduced to the control signals. The observer scheme needs the input voltage, output current and control signals, which are recorded by a data acquisition system (Agilent U2541A), and then used to evaluate the performance of the proposed estimation scheme. The observer gains were chosen as: $\theta_j = 1$, and $\rho_j = 5$ for $j = 1, \ldots, 3$. Experiment is as follows. The converter

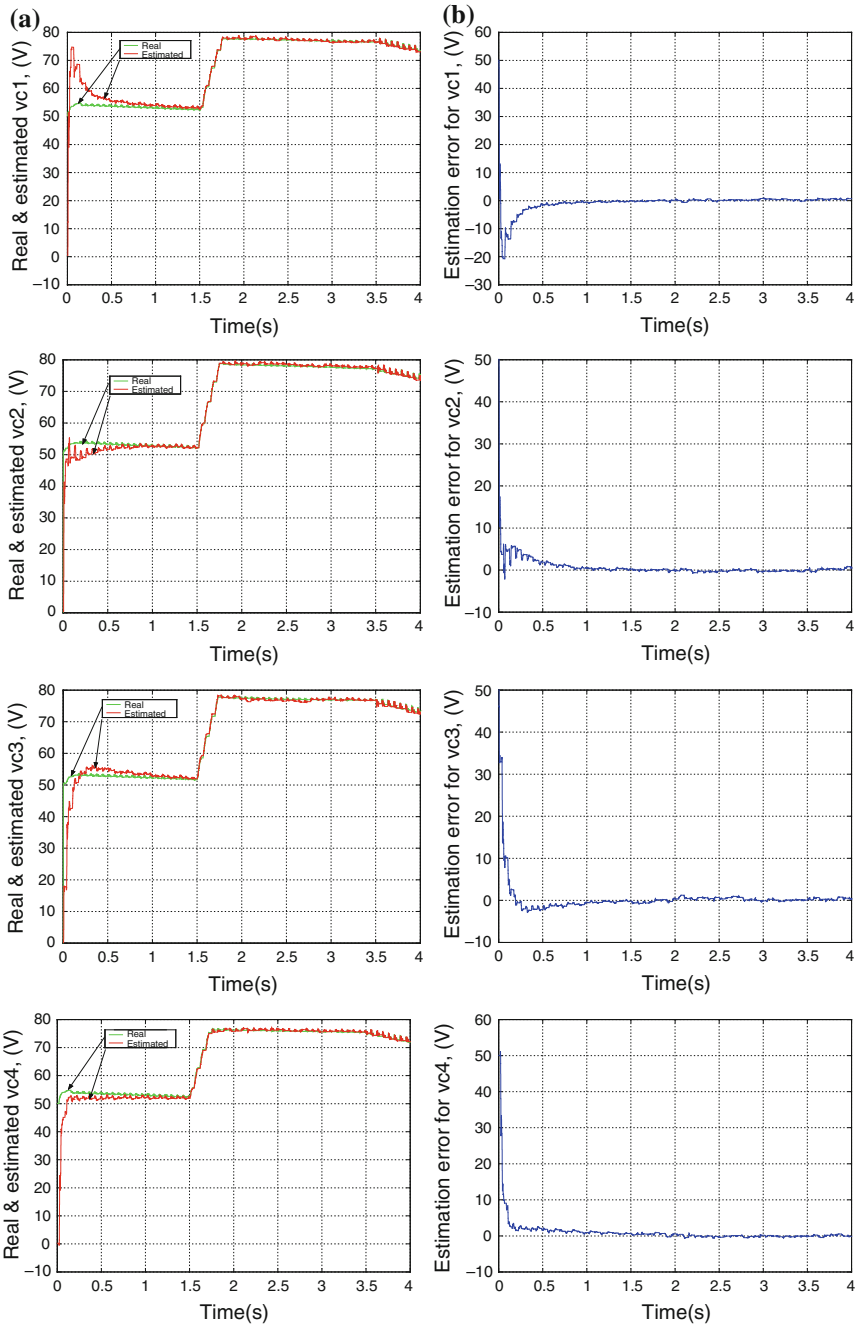

Fig. 9.7 Capacitor voltages and their estimations. **a** Real and estimated capacitor voltages. **b** Estimation errors (considering nominal capacitance values $C_1 = C_2 = C_3 = C_4 = 50$ mF)

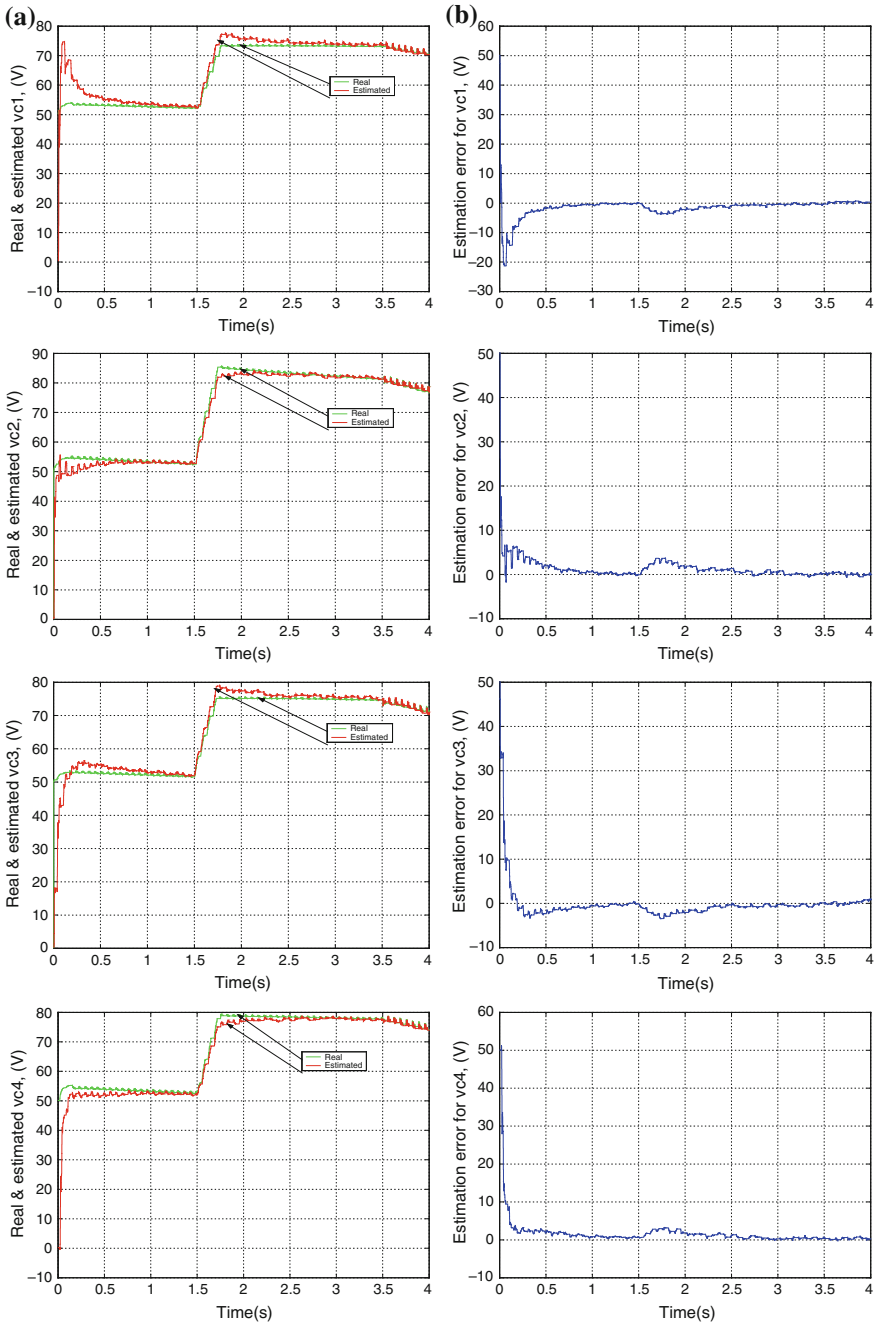

Fig. 9.8 Capacitor voltages and their estimation errors under non-nominal capacitances. **a** Real and estimated capacitor voltages. **b** Estimation errors (considering non-nominal capacitances values: $C_1 = 1.2\ C_{nom}$, $C_2 = 0.8\ C_{nom}$, $C_3 = 1.1\ C_{nom}$, $C_4 = 0.8\ C_{nom}$, $C_{nom} = 50$ mF)

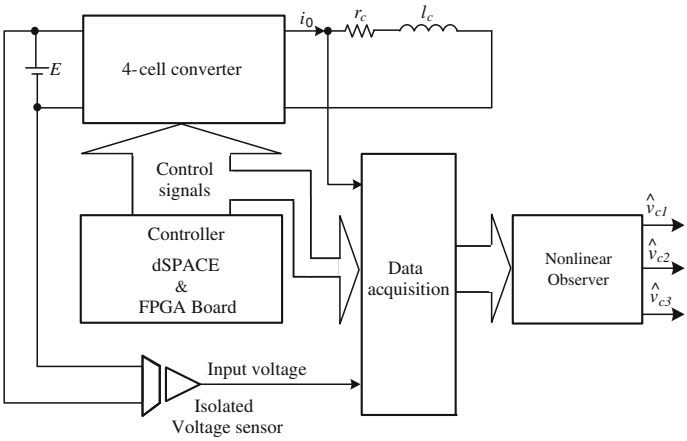

Fig. 9.9 Experimental setup block diagram

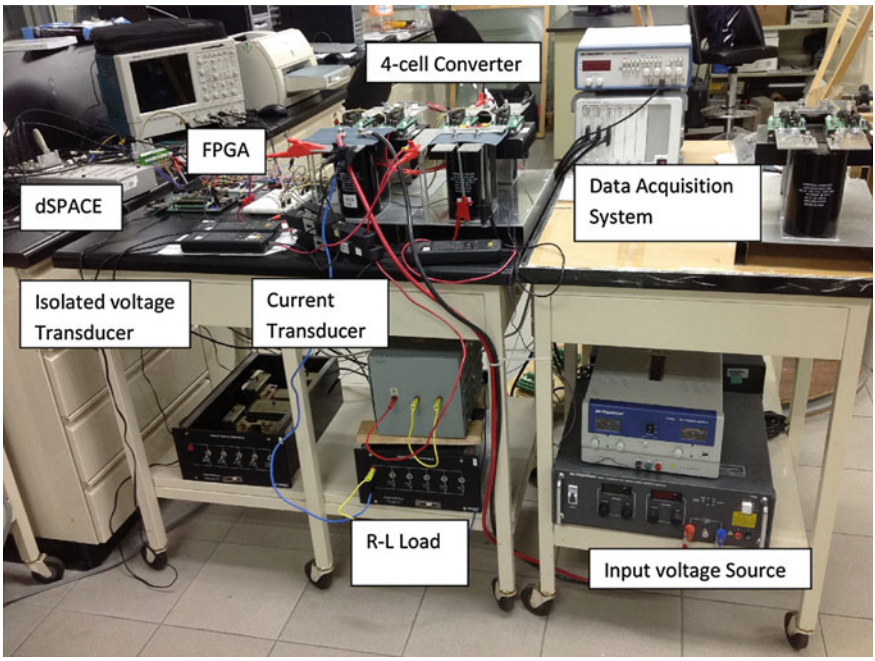

Fig. 9.10 Experimental laboratory prototype

is commanded through the dSPACE board.The modulation algorithm is executed each 50 μs, while the observer input data is collected each 4μs.

The test was run for 8 s. The input voltage source, E, is set to a constant value of 58 V. During the test, input voltage, control signals and output current are sampled

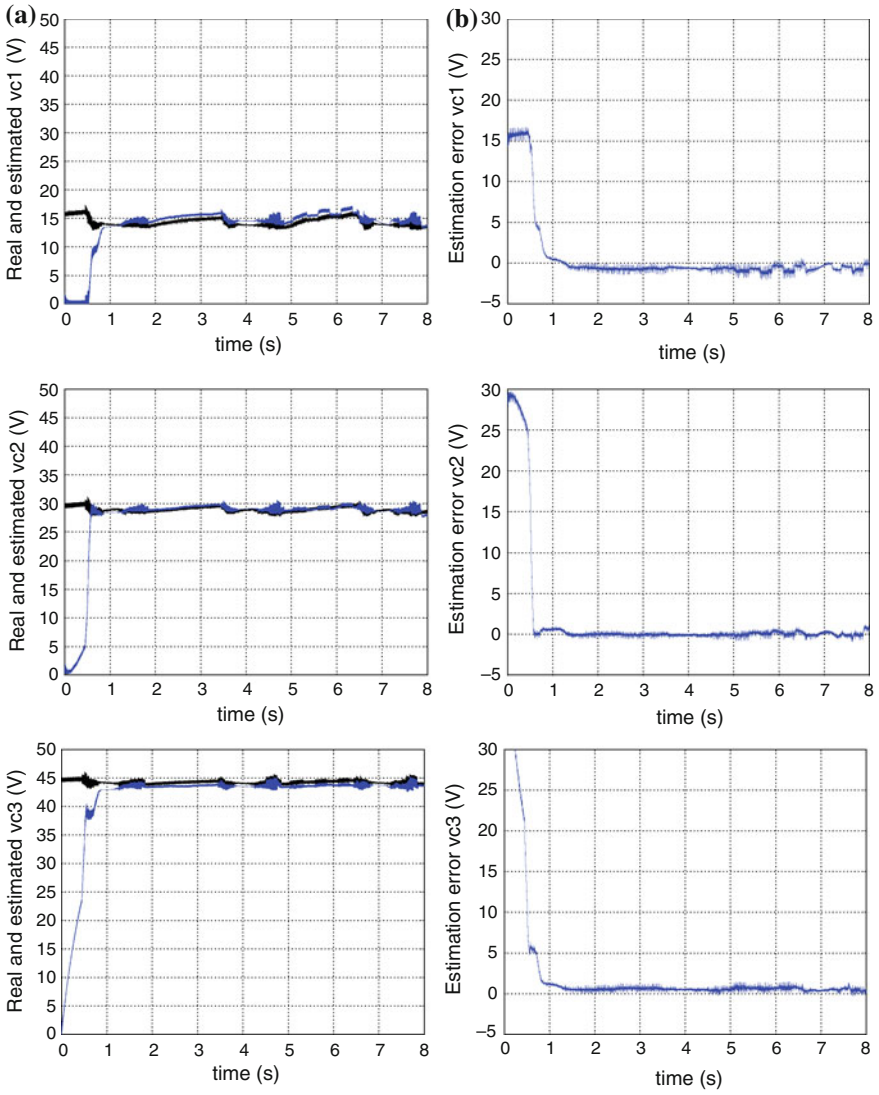

Fig. 9.11 Adaptive observer estimation results. **a** Real (*black traces*) and estimated (*blue traces*) capacitor voltages. **b** Estimation errors

each 4 μs and recorded by a data acquisition system. Then, collected data is fed to the estimation algorithm to get the capacitor voltage estimates.

Following, we present the results obtained with the observation scheme. Initial estimated voltages are set to zero and initial value for r_c is set to 4 Ω. Figure 9.11a shows estimated and measured voltages, and Fig. 9.11b shows estimation errors, which demonstrates that estimated values are close to real values, with estimation

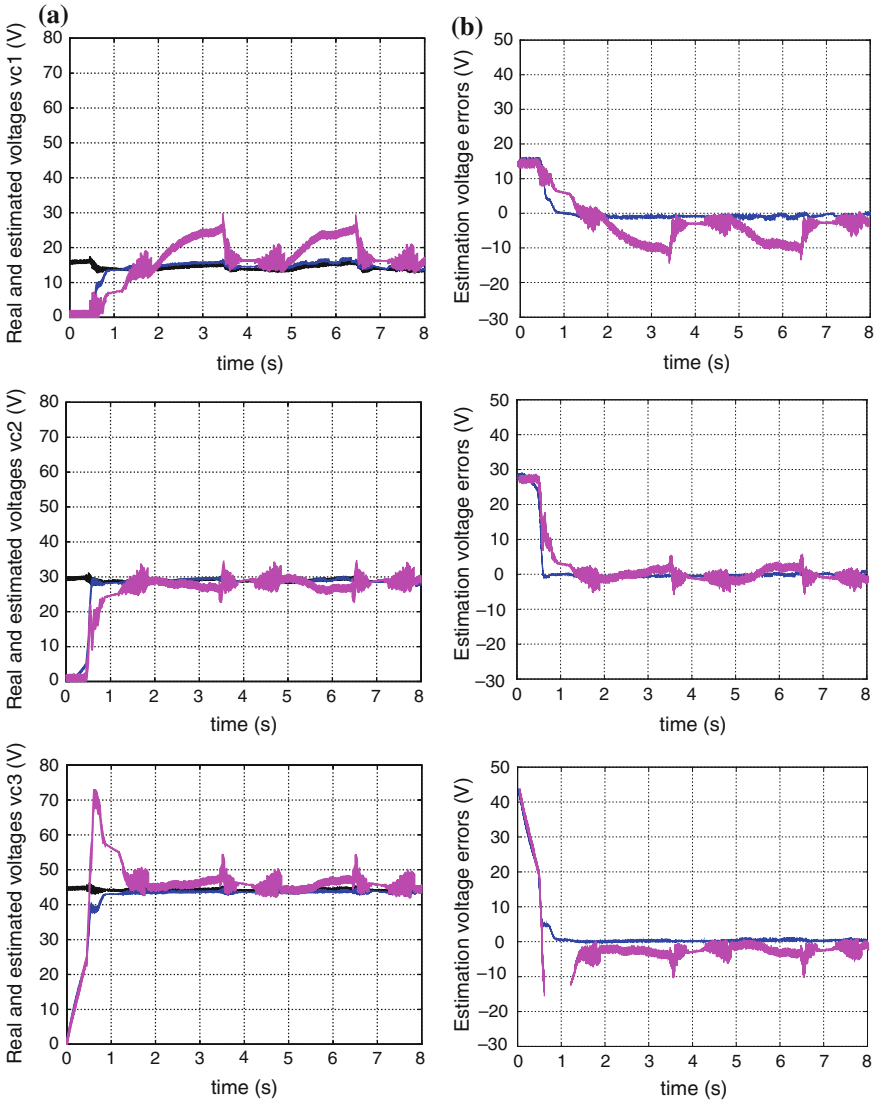

Fig. 9.12 Estimation results for adaptive and non-adaptive schemes. **a** Capacitor voltages: real (*black traces*), adaptive estimation (*blue traces*) and non-adaptive estimation (*magenta traces*). **b** Adaptive estimation errors (*blue traces*) and non-adaptive estimation errors (*magenta traces*)

error being less than 1.5 V once the transient period is over. Note that the transient error is high because initial estimated values start from zero, while the real values are, in this case, at their nominal values. If the initial estimated values are close to the real values then the transient errors and convergence time will be reduced.

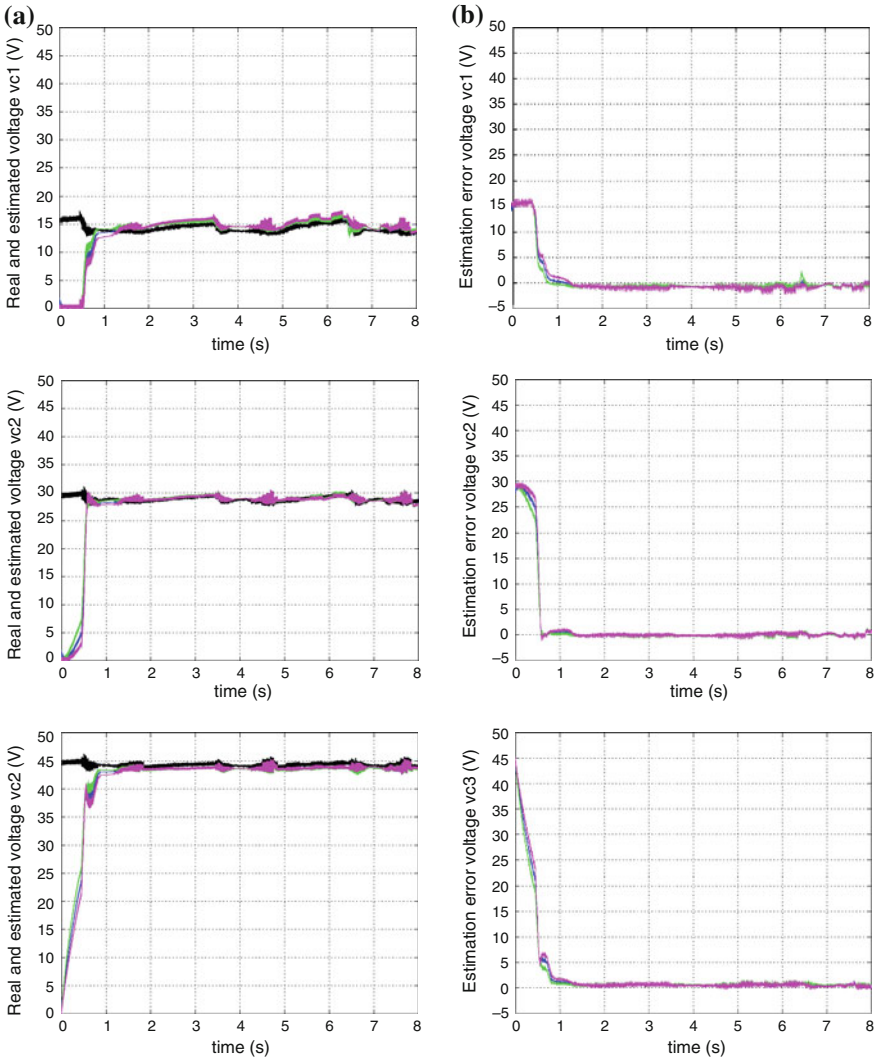

Fig. 9.13 Observer responses under uncertain inductance value. **a** Estimated capacitor voltages: Real (*black traces*), nominal inductance (*blue traces*), 120 % nominal inductance (*magenta traces*), 80 % nominal inductance (*green traces*). **b** Estimation errors nominal inductance (*blue traces*), 120 % nominal inductance (*magenta traces*), 80 % nominal inductance (*green traces*)

The adaptation properties improve the state estimation with respect to the traditional observer scheme, where adaptation correction is zero ($\Lambda_j = 0$). Experiments were carried out to compare both schemes, where the resistive part r_c is changed from 12.6 to 21.6 Ω. For both observer schemes the nominal value of τ is used. Figure 9.12a shows measured voltages and estimated voltages for both adaptive and non-adaptive schemes, and Fig. 9.12b shows estimation errors, which

demonstrates that estimated values are better when using the adaptive scheme. The non-adaptive scheme presents errors 300 % larger than the adaptive observer.

Finally, we run a test to evaluate the observer performance when inductance value is uncertain. Figure 9.13a shows measured voltages and estimated voltages for nominal inductance value l_c, and with uncertainties of ±20 %, and Fig. 9.13b shows the estimation error, which shows that estimated voltages are close to the real voltages in spite of the introduced uncertainties.

References

1. Lai JS, Peng FZ (1996) Multilevel converters—a new breed of power converters. IEEE Trans Ind Appl 32(3):509–517
2. Malinowski M, Gopakumar K, Rodríguez J, Pérez MA (2010) A survey on cascaded multilevel inverters. IEEE Trans Industr Electron 57(7):2197–2206
3. Rodríguez J, Bernet S, Steimer PK, Lizama IE (2010) A survey on neutral-point-clamped inverters. IEEE Trans Industr Electron 57(7):2219–2230
4. Rodríguez J, Lai JS, Peng FZ (2002) Multilevel inverters: a survey of topologies, controls, and applications. IEEE Trans Ind Appl 49(4):724–738
5. Meynard TA, Foch H (1992) Multi-level choppers for high voltage applications. EPE J 2 (1):45–50
6. Hochgraf C, Lasseter R, Divan D, Lipo TA (1994) Comparison of multilevel inverters for static VAR compensation. In: Conference record IEEE—IAS annual meeting, Denver, pp 921–928
7. Peng FZ, Lai JS (1995) A multilevel voltage-source inverter with separate DC sources for static VAR generation. In: Conference record IEEE—IAS annual meeting, Lake Buena Vista, pp 2541–2548
8. Peng FZ, McKeever JW, Adams DJ (1998) A power line conditioner using cascade multilevel inverters for distribution systems. IEEE Trans Ind Appl 34(6):1293–1298
9. Peng FZ, Lai JS (1996) Dynamic performance and control of a static VAR compensator using cascade multilevel inverters. In: Conference record IEEE—IAS annual meeting, San Diego, CA, pp 1009–1015
10. Shukla A, Ghosh A, Joshi A (2010) Flying-capacitor-based chopper circuit for dc capacitor voltage balancing in diode-clamped multilevel inverter. IEEE Trans Industr Electron 57:2249–2261
11. Nijmeijer H, Fossen TI (1999) New directions in nonlinear observer design. Number 244 in lecture notes in control and information sciences. Springer, Heidelberg
12. Besancon G (2000) Remarks on nonlinear adaptive observer design. Syst Control Lett 41 (4):271–280
13. Besancon G, de Leon-Morales J, Huerta-Guevara O (2003) On adaptive observers for state affine systems and application to synchronous machines. In: 42nd Conference on decision and control, USA, pp 1009–1015
14. Djemai M, Manamanni N, Barbot JP (2005) Sliding mode observer for triangular input hybrid system. In: IFAC world congress
15. Lin Yu-Wei, John Cheng J-W (2010) A high-gain observer for a class of cascade-feedback-connected nonlinear systems with application to injection molding. IEEE/ASME Trans Mechatron 15(5):714–727
16. Kenné G, Simo RS, Lamnabhi-Lagarrigue F, Arzandé A, Vannier J-C (2010) An online simplified rotor resistance estimator for induction motors. IEEE Trans Control Syst Technol 18 (5):1188–1194

17. Leon AE, Solsona JA (2010) Design of reduced-order nonlinear observers for energy conversion applications. IET, Control Theor Appl 4(5):724–734
18. Veluvolu KC, Soh YC (2009) High-gain observers with sliding mode for state and unknown input estimations. IEEE Trans Industr Electron 56(9):3386–3393
19. Gensior A, Weber J, Rudolph J, Güldner H (2008) Algebraic parameter identification and asymptotic estimation of the load of a boost converter. IEEE Trans Industr Electron 55(9): 3352–3359
20. Lascu C, Boldea I, Blaabjerg F (2009) A class of speed-sensorless sliding-mode observers for high-performance induction motor drives. IEEE Trans Industr Electron 56(9):3394–3403
21. Khalil HK, Strangas EG, Jurkovic S (2009) Speed observer and reduced nonlinear model for sensorless control of induction motors. IEEE Trans Control Syst Technol 17(2):327–339
22. Lienhardt AM, Gateau G, Meynard TA (2005) Stacked multicell converter (smc): estimation of flying capacitor voltages. In: 2005 European conference on power electronics and applications, Dresden, pp 1–10
23. Almaleki MW, Jon PC (2010) Sliding mode observation of capacitor voltage in multilevel power converters. In: 5th IET international conference on power electronics, machines and drives (PEMD 2010), Brighton, pp 1–6
24. Isidori A (1995) Nonlinear control systems, 3rd edn. Springer, Heidelberg
25. Khalil H (1996) Nonlinear systems, 2nd edn. Prentice Hall, New Jersey
26. de León Morales J, Escalante MF, Mata-Jiménez MT (2007) Observer for DC voltages in a cascaded H-bridge multilevel STATCOM. IET Electr Power Appl 1(6):879–889
27. de León Morales J, Mata-Jiménez MT, Escalante MF (2013) An interconnected adaptive observer for flying capacitor multilevel converters. Electr Power Syst Res 100:7–14
28. Escalante MF, Arellano JJ (2006) Harmonics and reactive power compensation using a cascaded h-bridge multilevel inverter. In: 2006 IEEE international symposium on industrial electronics, Montreal, pp 1966–1971
29. de León Morales J, Mata-Jiménez MT, Escalante MF (2011) Adaptive scheme for DC voltages estimation in a cascaded H-bridge multilevel converter. Electr Power Syst Res 81:1943–1951
30. Ghosh A, Ledwich G (2002) Power quality enhancement using custom power devices. Kluwer's power electronics and power systems series. Kluwer Academic Publishers, Dordrecht
31. Holmes DG, Lippo TA (2003) Pulse width modulation for power converters. IEEE series. Wiley Interscience, Hoboken

Chapter 10
Modeling and Control of STATCOMs

Amit Kumar Jain and Aman Behal

Abstract This chapter addresses modeling and control of the STATCOM and associated power system. Component and system level models of the STATCOM appropriate to objectives are covered. Distinction is made between control objectives on the basis of time scale. For some objectives quasi steady state modeling, where electrical network can be modeled with phasors, is sufficient, while for others, the dynamics of electrical network elements have to be considered on an instantaneous basis. The main control requirements and benefits of STATCOMs in transmission and distribution applications for which quasi steady state analysis suffices are presented in brief. Sub-cycle modeling and control is emphasized since quasi steady state applications will be covered in greater detail in other chapters. Dynamic models of the STATCOM and the local distribution system suited for sub-cycle control are derived. The models include transformation to a particular rotating frame that allows clear definition of voltage and current magnitudes, and active and reactive power on an instantaneous basis. Based on the models, linear and nonlinear control techniques for the control objective of voltage regulation at a load point are covered in detail. Simulation results are included for representative system parameters.

Keywords STATCOM · Modeling · Control · Voltage regulation · Sub-cycle control

A.K. Jain (✉)
Intel Corporation, Hillsboro, OR, USA
e-mail: amit_k_jain@ieee.org

A. Behal
University of Central Florida, Orlando, FL, USA
e-mail: abehal@ucf.edu

F. Shahnia et al. (eds.), *Static Compensators (STATCOMs) in Power Systems*,
Power Systems, DOI 10.1007/978-981-287-281-4_10

10.1 Introduction

STATCOMs find applications in utility transmission and distribution systems, and at customer sites. The applications differ in objectives that translate to different control requirements. For a transmission system, STATCOMs act like a Flexible AC Transmission System (FACTS) device [1]. By injecting controlled reactive power, STATCOMs can increase power transfer capability without infrastructure upgrade, increase stability margins and dampen oscillations. At a distribution system level, a STATCOM can effect local voltage regulation without decreasing voltage stability (unlike tap-changers) [2], correct for imbalanced currents [3, 4], and control active and reactive power transfer in micro-grid environments [5]. At the customer level, STATCOMs can be utilized to suppress current harmonics due to nonlinear loads (active filters) [6], voltage regulation in the presence of distribution system load fluctuations [7], maintaining power factor within the utility allowed limits, and balancing load currents.

Towards meeting the objectives modeling and control strategies with complexity commensurate with application are required. The model has to address the STATCOM implementation and the particular system it is integrated with. For transmission and several distribution level objectives quasi steady state (phasor) modeling of the system along with a matched model for the STATCOM implementation and associated controls is sufficient. At a customer site, fast regulation of voltage is required to avoid costly outages due to voltage sags and swells, or continuous disturbance mitigation due to nearby loads with a random nature [8]. Similarly, suppression of the load current harmonics to meet utility standards on the source currents requires current regulation at as high as the 50th harmonic (3 kHz). In hybrid scenarios, control structure needs to achieve multiple outcomes like harmonic suppression, grid connection of distributed and renewable generation, and power transfer control.

This chapter addresses modeling and control of STATCOMs and associated system for slow and fast (sub-cycle) objectives. Component and system level models of the STATCOM device appropriate to objectives are covered: voltage source inverter and inductive filter with Pulse Width Modulation (PWM) control for fast transients, or magnitude and angle control for quasi state type applications. The main control requirements and benefits of STATCOMs in transmission and distribution applications for which quasi steady state analysis suffices are presented in brief. Sub-cycle modeling and control is emphasized since quasi steady state applications are covered in greater detail in other chapters of the book. Dynamic models of the STATCOM and the local distribution system suited for sub-cycle control are derived. The models include transformations to a rotating frame that allows determination of voltage and current magnitudes and active and reactive power on an instantaneous basis. Extension of the modeling strategy using circuit simulators is presented for addressing systems larger than the one analyzed in detail. Based on the models, linear and nonlinear control techniques for the objective of voltage regulation at load point are covered in detail. Simulation results comparing performance are included for representative system parameters.

10.2 STATCOM Implementations and Models

Circuit implementations of STATCOMs depend on expected functionality as well as the semiconductor devices available for the desired voltage and current magnitudes. An overview of common implementations, dynamic models and control schemes is presented in this section.

10.2.1 Angle and Magnitude Controlled Converters

For high voltage and current levels (transmission applications) requiring slow control over a few cycles or longer time scales, 3 phase inverters with a series inductive filter are utilized (Fig. 10.1a). Although a two level inverter implementation is show in Fig. 10.1a for simplicity, higher voltage system may utilize multilevel inverters [9]. Inverters switches may be realized with thyristors or forced commutated devices like GTOs (gate turn-off thyristors), IGBTs (Insulated Gate Bipolar Transistor) or IGCTs (Integrated Gate Commutated Thyristors) as shown in Fig. 10.1b.

In the configuration of Fig. 10.1a the voltage at one end of the inductor is determined by the grid connection. At the other end of the inductor, the inverter circuit generates a switched voltage waveform—square wave, six-pulse, higher

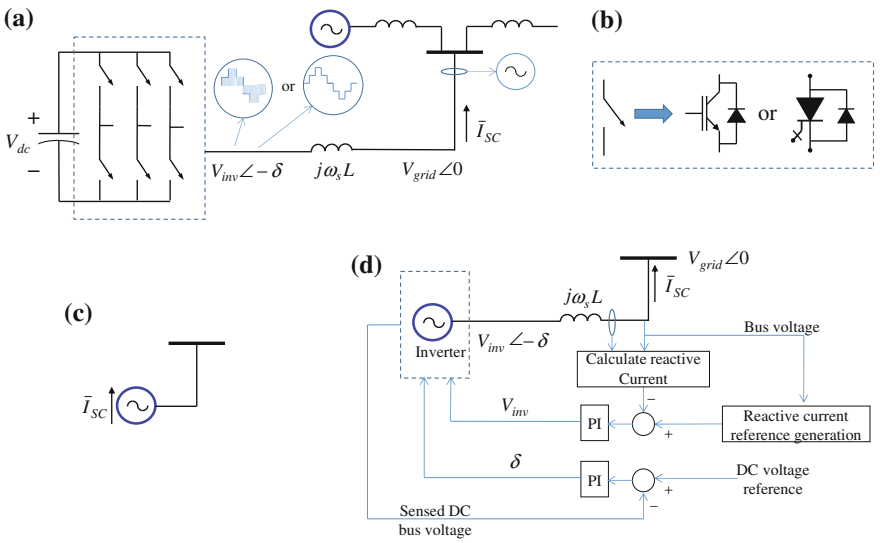

Fig. 10.1 **a** STATCOM realization with angle and magnitude controlled three phase inverter; **b** inverter switch realizations; **c** model for steady state applications; **d** model for dynamic stability studies

number of pulses or PWM, at the grid frequency. The inductor acts as a filter to ensure only sinusoidal current is injected by the STATCOM and also plays a role in the active and reactive power transfer. The angle and magnitude of the fundamental component of the inverter output can be adjusted to control the inductor current, which is also the current output of the STATCOM. Using the equation for power flow between two AC buses separated by an inductor, controlling the phase angle δ controls the active power flow while controlling the magnitude V_{inv} controls the reactive current.

$$\begin{aligned}\bar{I}_{inv} &= -\frac{V_{inv}}{\omega_s L}\sin\delta - j\frac{V_{inv}\cos\delta - V_{grid}}{\omega_s L} \\ &\approx \underbrace{-\frac{V_{inv}}{\omega_s L}\delta}_{\substack{\text{real current} \\ \text{sourced by inverter}}} + j\underbrace{\frac{V_{grid} - V_{inv}}{\omega_s L}}_{\substack{\text{reactive current} \\ \text{sourced by inverter}}} \quad \text{for small } \delta \end{aligned} \tag{10.1}$$

where voltage and currents are as indicated in Fig. 10.1a and ω_s is the power system angular frequency. The above relation is based on phasor analysis where the electrical system is being treated in sinusoidal steady state and the voltage and current dynamics at a shorter time scale (less than a few line frequency cycles, $\sim$50 ms) are ignored. So the time scale of any change in δ and V_{inv} is of the order of a few cycles. This kind of control is therefore suited to slower objectives like power transfer control, reactive power injection for power system stability enhancement and steady state voltage adjustment.

Note that the inverter itself acts like a voltage bus in the AC power system while the filter inductor acts like a line connecting two buses. The angle (δ) and magnitude (V_{inv}) control of the STATCOM interacts with the rest of the system to produce the reactive current supplied by the STATCOM so its dynamics cannot be separated from the dynamic behaviour of the overall system. For steady state analysis (power transfer control or voltage adjustment), this STATCOM realization can be modeled as a reactive current source at the point of connection as shown in Fig. 10.1c. For studying slow moving dynamics as in dynamic stability, this realization of STATCOM has to be modeled as a $V - \delta$ bus with a series inductor along with the associated δ and V_{inv} control loop dynamics as shown in Fig. 10.1d. The inverter can be assumed to be an ideal balanced three phase voltage source with controllable magnitude V_{inv} and angle δ. Magnitude and angle are controlled by the reactive current and DC bus voltage loops, respectively. The reactive current reference generation depends on the STATCOM application: it could be generated to regulate the local bus voltage, introduce damping by varying reactive current in response to disturbance (e.g., rate of change of grid voltage angle) measured at the connection point. The DC bus voltage will typically be fixed. Proportional-Integral (PI) controllers are shown for simple explanation. The exact implementation can be more complex depending on application requirements.

10.2.2 Current Controlled Converters

At lower power levels (up to a few MVA), three phase inverters with PWM control can be used to realize STATCOMs. These inverters employ IGBTs that can switch at a few kHz and are able to control output current with response times in the order of milli-seconds. A three phase three wire implementation is shown in Fig. 10.2a. Such an implementation can be approximated by a three phase current controlled source shown in Fig. 10.2b independent of the interaction with the power system in which it is integrated.

The problem of current control for three phase inverters has been extensively researched for motor drive and grid integration applications. Several linear and nonlinear techniques are reported in literature. Some of these techniques are generic in nature and can be used for STATCOM control. Some others are tailored to the application (e.g., direct torque control for AC machines) and variations inspired by these have been applied to STATCOM current control. We first discuss the basic principles of current control for STATCOM application [10]. Resonant control, which is particularly useful for selective harmonic elimination in an active filter application, and unbalance mitigation are then described briefly. Detailed description of one nonlinear control strategy is deferred till Sect. 10.5.5. Finally, we give an overview of unbalance current mitigation with STATCOM. STATCOM control is typically implemented digitally via combinations of digital signal processors and field programmable gate arrays. Time discretization and sample and hold delays have a significant impact on performance of the controller. Discussion of these impacts and of techniques tailored for discrete implementation are omitted here.

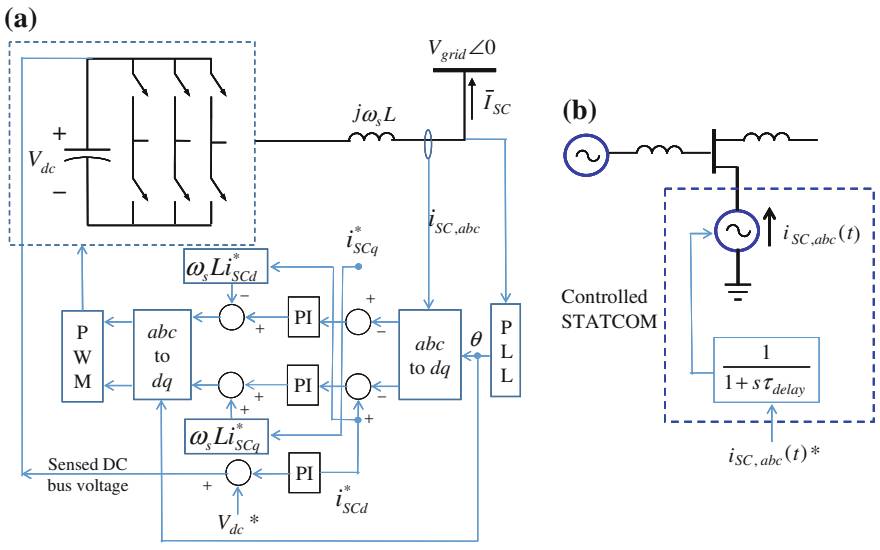

Fig. 10.2 **a** Current controlled converter with a three phase inverter; **b** model for system integration

10.2.2.1 Active and Reactive Current Control

Similar to vector control of three phase AC machines, control of the STATCOM current can be carried out in the rotating reference frame (dq) locked to the grid voltage [10]. The basic scheme is shown in Fig. 10.2a. The grid voltage angle θ is obtained via a Phase-Locked Loop (PLL). The sensed system variables are transformed from the static abc frame to the rotating dq frame using θ with the d-axis of the rotating frame aligned with the grid voltage vector. Thus i_{SCd}, the d-axis component of i_{SC}, is the active current sourced by the STATCOM while i_{SCq}, the q-axis component of i_{SC}, is the reactive current sourced by the STATCOM. These can now be controlled independently. The reactive component of the current tracks the desired reactive current injection to meet the STATCOM application objectives while the active part of the current maintains the DC bus voltage V_{dc} to a fixed value. A simple PI compensator with feed forward terms to decouple the dynamics of i_{SCd} and i_{SCq} is shown in Fig. 10.2a. Several different control strategies rely on the same basic idea of decomposing the active and reactive components with the rotational transform and using the system dynamics in the rotated reference frame. The system integration model for the current controlled STATCOM is indicated in Fig. 10.2b. Neglecting the power loss in the STATCOM, the sinusoidal current source is purely reactive and follows the current reference with a ~ 1 ms lag.

10.2.2.2 Resonant Controller

The resonant controller [11–14] is an idea derived from frequency domain analysis of the dq-axis controller described above viewed from the static reference frame. Essentially, the integral action of the controller implemented in the rotating reference frame appears as an infinite attenuation of the current errors at the positive sequence fundamental frequency. Conceptually, this type of control is ideal for an active filter application where selective harmonic mitigation is required. A generic implementation is indicated in Fig. 10.3. Consider a load like a three-phase thyristor

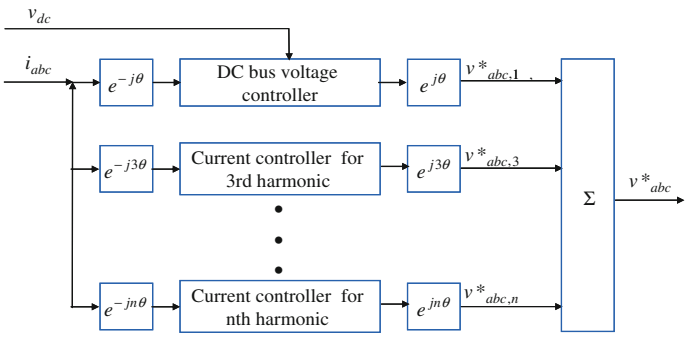

Fig. 10.3 Resonant current controller for active filters

based DC drive that produces negative sequence fifth and positive sequence seventh harmonics. The STATCOM can be made to absorb these harmonics by implementing two parallel control loops, one in a reference frame rotating at $-5\omega_s$ and another in a reference frame rotating at $+7\omega_s$. An additional loop in a reference frame rotating at ω_s is required to maintain the DC bus voltage via the in phase component of the fundamental frequency current. Instead of having separate rotating frames, controllers for the different harmonics can be nested inside a single frame. Such an implementation can result in lower computational overhead. The resonant controller scheme has become very popular and variations of it are now used in commercially available active filters.

10.2.2.3 Unbalance Mitigation

The three wire converter can control positive and negative sequence currents utilizing the theory of instantaneous symmetrical components [3] and aid in current balancing. The positive sequence active and reactive current components are obtained in a reference frame rotating with positive frequency. If negative sequence currents are present they show up as disturbance at double the line frequency in this rotating reference frame. To isolate the positive sequence component, the transformed currents need to be filtered with a low pass or notch filter. The same applies when trying to isolate the negative sequence component in a reference frame rotating with negative frequency. Due to this filtering requirement independent control of the sequence components has an inherent dynamic limitation.

10.3 STATCOM Control Requirements

We can classify STATCOM applications into transmission and distribution levels based on functionality and implementation. Furthermore from a time scale point of view, the following classification can be made:

- *Steady state operation* when both electrical and mechanical systems are in steady state
- *Quasi steady state* when electrical network can be treated in sinusoidal steady state (phasor domain) and slow dynamics of the mechanical components, variable renewable generation, energy storage, and controls acting in the 100 ms to seconds time frame come into play
- *Sub-cycle transients* when electrical dynamics of the STATCOM circuit and the closely coupled network are important while the slower moving variables can be assumed to be constant

The transmission system is concerned with steady state and quasi steady state operation while the distribution system may be concerned with all three. Within the distribution system installations at customer sites will typically be concerned with

instantaneous performance. This section covers STATCOM control requirements based on applications at different levels in the power system. Sub-cycle control is covered in significant detail in the next two sections.

10.3.1 Transmission Level Applications

At the transmission system level, STATCOM is one among the family of Flexible AC Transmission (FACTS) devices [1]. It can be used to increase power transfer capability, enhance stability margins, and add damping for power system oscillations.

10.3.1.1 Power Transfer Capability Enhancement

Figure 10.4 indicates how power transfer capability of a transmission line can be increased by injecting reactive power at its midpoint. The reactive power injection at the mid-point regulates the midpoint voltage to 1 p.u., equal to the magnitude at either end. In this scenario, the power transfer changes according to the following equation increasing the maximum power transfer capability by a factor of two.

$$P = \frac{\sin\delta}{X_L} \xrightarrow{\text{to}} \frac{2\sin(\delta/2)}{X_L} \tag{10.2}$$

This increase in power transfer capability is a steady state benefit depending on the rating of the STATCOM which determines the level of compensation possible. STATCOM control dynamics do not play any role in this.

10.3.1.2 Transient (Angle) Stability Enhancement

The power versus angle curve is used to study the transient (or angle) stability of the transmission line [15]. Figure 10.5 shows the power angle characteristic without compensation and with ideal midpoint compensation of Fig. 10.4. With ideal

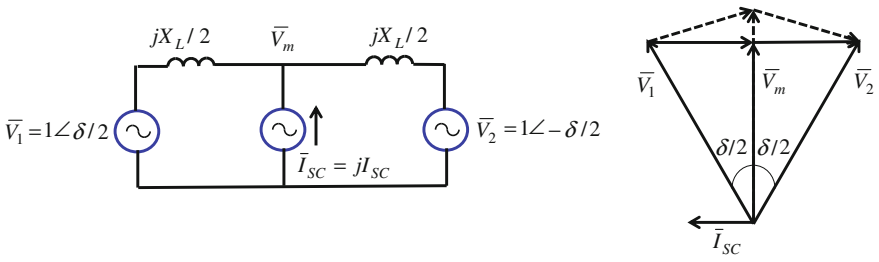

Fig. 10.4 Midpoint compensation of a transmission line with a STATCOM

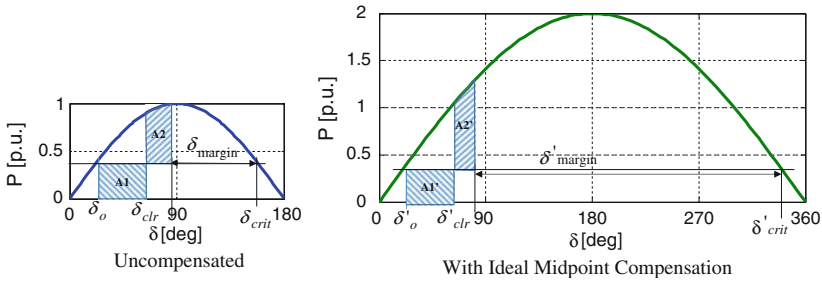

Fig. 10.5 Power angle curve of the original system and with midpoint compensation

midpoint compensation, due to the increase in the maximum power transfer capability, the decelerating area available under the curve from δ'_{clr} to δ'_{crit} is much greater than the area from δ_{clr} to δ_{crit} in the uncompensated case. Thus, the STATCOM increases transient stability margin. This phenomenon unfolds in seconds time frame over which the mechanical power input cannot change, the generation angle (at V_1) advances depending on system inertia, and we are able to assume that the electrical system is in quasi steady state at each time point. To guarantee the power angle curve of Fig. 10.5, it is assumed that STATCOM can regulate the midpoint voltage to 1 p.u. Therefore, transient stability enhancement requires control of STATCOM acting over a few cycles to inject required reactive current. This can be addressed using phasor domain relations between the reactive current and the voltage magnitude.

10.3.1.3 Small Signal (Dynamic) Stability Enhancement

Small signal stability of an interconnected power system refers to the stability of mechanical dynamics of the generators and power oscillations in the network. The objective here is to ensure stability in the event of system changes (load or generation changes or loss of connections) and to provide adequate damping to minimize power oscillations. The electrical network contributes algebraic constraints connecting the electro-mechanical dynamics of the individual generators. Once again, we rely on phasor relations for the electrical network and the time scales of interest are of the order of 100 ms. System stability can be studied via eigen value analysis of the linearized system. Typically, participation factors for different inputs in the unstable or critical modes of the system are used to determine which inputs should be controlled to influence stability and damping of the modes [16]. Reactive power injection at different points can be used to modify eigen values of the system. Further, STATCOMs can serve as a mitigation device by incorporating appropriate feedback, e.g., when regulating the midpoint voltage in the system of Fig. 10.4, a damping term $k_\delta d\tilde{\delta}/dt$ can be added to the reference midpoint voltage; this helps in damping oscillations that result after fault is cleared. The basic idea here is the same

as introducing damping via field excitation control at a generator location without the constraint of location and with potentially larger impact. From STATCOM control point of view, we are relying on quasi steady state phasor relations and augmenting the voltage regulation objective with stability enhancement using sensed local state variables (e.g., $\tilde{\delta}$ or $d\tilde{\delta}/dt$).

10.3.1.4 Voltage Stability

Voltage stability refers to decline in load voltage magnitude due to insufficient reactive power availability and/or high impedance between generation and load [17]. The phenomenon typically unfolds over seconds to minutes due to action of voltage regulation devices like on-load tap changers that attempt to increase power transfer by lowering effective impedance. Constant power loads like power electronic converter controlled loads contribute to the instability due to their negative incremental resistance characteristics (increasing current draw with decreasing voltage). The P-V curve is one method to study the voltage stability. Figure 10.6 shows the P-V curves for an example system. Each of the curves corresponds to a reactive power draw at the load. For inductive load Q is negative while for capacitive loads Q is positive. For a given Q, if the load active power demand increases the load voltage follows the upper part of the curve. The critical load point on the P-V curve, also called the nose of the curve, represents the maximum power point for the system. If the load active power demand exceeds the critical load power voltage instability occurs and the load voltage starts declining along the bottom part of the curve. In steady state higher load reactive power (capacitive) increases the maximum power transfer capability, i.e., the critical load point moves to the right and for a given load power the stability margin increases. This can be accomplished by a STATCOM. However, the more interesting case is when reactive power injection from STATCOM is controlled in response to the voltage. As the load power increases, the load voltage will start dropping (along the top portion of the curve for a fixed Q), and in response to the voltage drop the STATCOM would increase Q injection resulting in an increase in the load voltage as the system transitions to a curve with higher Q injection. The Q injection is in response to deviation of the load voltage from its reference value. The control is implemented so that there is a droop in the voltage reference as the reactive power injection increases. This operation with a V-Q droop leads to the voltage trajectory shown in Fig. 10.6 as the load power demand increases.

The reactive power injection has to be controlled in response to the proximity of the system state to the critical load point. Since voltage instability plays out over seconds to minutes automatic control of STATCOM is required. STATCOM and system models with phasor representation are sufficient for analysis and controller design in this application [2].

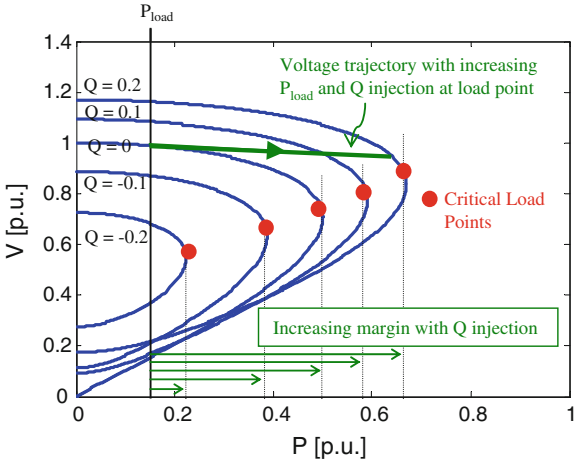

Fig. 10.6 P-V curve showing voltage stability enhancement with STATCOM

10.3.2 Distribution Level Applications

STATCOMs used at the distribution level are also called DSTATCOMs (Distribution STATCOM). STATCOMs in the distribution system (Fig. 10.7) can be used by the utility, at customer sites, or in microgrids where jurisdictions are not clearly defined. At the distribution level, STATCOMs are realized with three phase IGBT based inverters with active and reactive current control as shown in Fig. 10.2. Further, the STATCOM functionality may be integrated in inverters used to connect energy storage and distributed generation sources like photo-voltaics (PV), micro turbines, and fuel cells to the grid.

10.3.2.1 Similarities and Differences Compared with Transmission

Similar to transmission level, STATCOMs in distribution systems can be used for voltage regulation, power transfer capability, and enhancing stability. However, unlike transmission systems where $P - \delta$ and $Q - V$ pairs are strongly coupled with weak cross-coupling, distribution systems exhibit higher cross-coupling so that changes in Q injection can also effect change in active power flow. This functionality could be used in a microgrid environment. In addition STATCOMs can be used to compensate unbalanced currents as indicated in Sect. 10.2.2. Finally, several control objectives could be combined in a single STATCOM, e.g., energy storage, imbalance mitigation, reactive power dispatch by the utility.

Although the potential applications of reactive power injection via STATCOMs in distribution systems abound, regulations are conservative due to insufficient understanding of system level effects. Distributed generation connection to the grid has to comply with the IEEE1547 standard that prohibits reactive power injection unless it is dispatched by the utility. If distributed generation is owned or at least

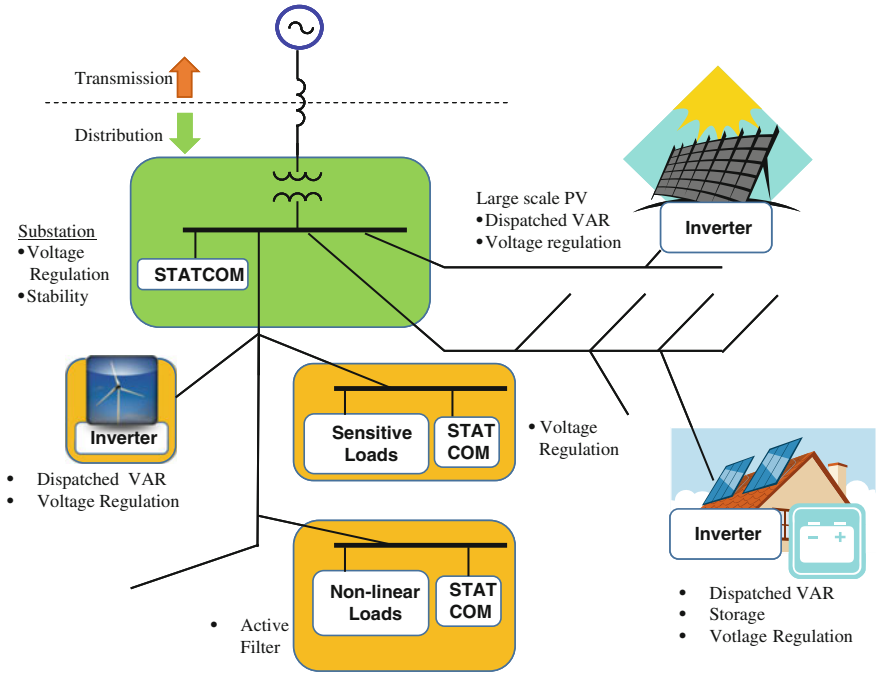

Fig. 10.7 STATCOMs in distribution systems

controlled by the utility, reactive power capability in inverters can be dispatched by the utility to meet reactive power requirements and adjust the voltage profile in the distribution system. Proliferation of roof-top PV results in high voltages at the Point of Common Coupling (PCC) during times of low local loading and high solar availability. According to IEEE1547, the generation source has to disconnect when a PCC voltage rises above a threshold, thereby disconnecting PV generation when it is most available. This problem could be solved if the reactive capability of the interconnection inverter were utilized to suppress the PCC voltage. However, it is not clear if doing this on a larger scale without centralized control will lead to circulating reactive power between inverters and also potentially affect the voltage profile in the distribution system. These aspects are actively being looked at to maximize energy capture without adverse system level impacts.

10.3.2.2 Customer Site Location of STATCOMs

At large customer sites like industrial facilities, STATCOMs are typically used to absorb harmonics and reactive currents in order to meet IEEE519 [18] or EN61000-3-2 [19] for the source currents. Current harmonics and waveforms random in nature are generated by nonlinear and time-varying loads such as diode rectifiers, thyristor controlled DC drives, welding equipment, and electrical arc furnaces.

This application is commonly called active filtering. Control of the inverter for these applications typically involves absorbing the entire load generated current harmonics and random deviations in the current from the fundamental frequency component of the load current. The control can be implemented either in the stationary frame by direct control of the phase currents or using the rotating frame approach indicated in Sect. 10.2.2. Resonant controllers described briefly in Sect. 10.2.2 are now gaining more acceptance due to their ability to mitigate harmonics and negative sequence currents selectively.

Depending on the system impedance at the PCC, nonlinear currents can cause significant voltage distortions that could affect functionality of sensitive loads connected at the PCC or other locations on the same feeder. Short term voltage transients also appear at the PCC due to sudden load changes, faults and subsequent clearance, variable output of generation sources like PV and wind turbines in proximity of the load location. Sensitive loads include process industries like semiconductor fabrication and other electronic equipment like computers. Now the semiconductor fabrication equipment has to be robust enough to comply with the SEMI F47 standard developed by Semiconductor Equipment and Materials Institute [20]. Similarly, computer power supplies have to comply with the CBEMA curve developed by the Information Technology Industry Council [20]. This shifts some of the burden to the equipment manufacturer. The worst case input power quality acceptable by the equipment then has to be guaranteed by the utility, or by a combination of high fidelity utility service and voltage disturbance mitigation solutions at the customer site. In addition to industrial requirements, voltage variations produce flicker in the light output of incandescent lamps. The human eye [21] is very sensitive to light flicker with the sensitivity peaking at a frequency of 8.8 Hz. Common causes of flicker are variable load current drawn by electric arc furnaces and variable power output of renewable generation.

STATCOMs can be used to regulate load voltage in the presence of these disturbances by controlled reactive power injection. While the other distribution system applications indicated above require only quasi steady state modeling for the STATCOM and network elements, voltage regulation at load sites requires fast control in the sub-cycle time scale. The modeling and control for sub-cycle response is presented in detail in the next two sections.

10.4 Distribution System Modeling for Instantaneous Control

Sub-cycle control is required for load voltage regulation in the presence of nonlinear and time varying loads such as electric arc furnaces, fluctuating output power of distributed generation systems, and transients on parallel connected loads (e.g., line start of induction motors) [21, 22]. Due to their high control bandwidth, STATCOMs based on three phase PWM Voltage Source Converter (VSC) are suited for sub-cycle control.

Sub-cycle control requires dynamic models of the distribution system and the STATCOM including electrical system dynamics instead of quasi steady state models with phasor representations. In this section, we address the required distribution system model assuming the STATCOM can be modeled as a controllable balanced three phase current source. Utilizing the *dq* axis theory for balanced three phase systems allows definition of instantaneous reactive current and instantaneous magnitude of phase voltages. However, the choice of angle used for the transformation is extremely important. We need the transformation to allow separation of the active and reactive components and voltage and current magnitudes on an instantaneous basis. If we assume the transformation frequency is constant and equal to the steady state power system frequency the model is only valid on a quasi steady state basis over a few cycles. For example, if the transformation angle is obtained by a PLL, fast transients in the PCC voltage are filtered out by the PLL and the rotation frequency of the transformation is nearly constant. Due to this the transformed system does not capture dynamic properties on a faster time scale: the active and reactive powers and the voltage/current magnitudes are not defined correctly on an instantaneous basis and therefore system and the model cannot be used for sub-cycle control. The transformation presented in this section has a frequency that is not equal to the system steady state frequency, but is derived similar to the approach in field oriented control of AC machines. The transformed dynamic model does not neglect any fast transients and also allows definition of instantaneous active and reactive power and voltage and current magnitude. Typically, empirically tuned PI controllers are used for voltage regulation with reactive current as the control input. However, transforming the electrical dynamics of the distribution system using the proposed transformation gives us a distribution system model that is valid on an instantaneous basis. This model can be used to determine the system dynamic limits with respect to sub-cycle control, and design appropriate linear or non-linear control structures as opposed to use of empirically tuned PI controllers. For scalability, it is explained how circuit simulators with analog behavioral modeling capability can be used to extract linearized dynamics of the transformed system without the need for writing all state equations explicitly. Although the presentation is more tailored to voltage regulation, the model derived can be applied to other sub-cycle system control objectives like instantaneous power control if the STATCOM has the required energy storage capability.

10.4.1 Model Derivation

The simplest system consists of a load supplied on a distribution system, with a STATCOM connected in parallel at the load location. Its single phase model (Fig. 10.8a) consists of: the source modeled as an infinite bus with inductive source impedance, the load as a resistance, the STATCOM as a controllable current source, and a coupling capacitor. The coupling capacitor is included for two reasons: a real STATCOM will have an L-C filter at its output or have fixed compensation capacitors

connected in parallel; the line current and the STATCOM output current become independent making it possible to decouple the STATCOM circuit level control objectives from the system level control. It is assumed that the source, load, and STATCOM are balanced three phase systems. The system dynamics are given by:

$$\begin{aligned} L_s\dot{i}_{s,abc} &= -R_s i_{s,abc} - v_{L,abc} + v_{s,abc} \\ C_c\dot{v}_{L,abc} &= -g_L v_{L,abc} + i_{s,abc} + i_{SC,abc} \end{aligned} \tag{10.3}$$

Here, $i_{s,abc}, i_{SC,abc}, v_{s,abc}$, and, $v_{L,abc}$ are vectors consisting of the individual phase quantities denoted in Fig. 10.8a, $g_L = 1/R_L$ is the load conductance, L_s is the source inductance, R_s is the source resistance, and C_c is the coupling capacitor. For simplicity of presentation, a purely resistive load is considered here. However, this assumption is not restrictive and reactive impedances can be effectively handled as discussed in [23]. Under the assumption that zero sequence components are not present, (10.3) can be transformed to an equivalent two phase $x-y$ system by applying the following three to two phase transformation:

$$v_{s,xy} = v_{sa}\mathrm{e}^{j0} + v_{sb}\mathrm{e}^{j2\pi/3} + v_{sc}\mathrm{e}^{j4\pi/3} \tag{10.4}$$

where the complex number $v_{s,xy} = v_{sx} + jv_{sy}$. This is followed by a rotational transformation:

$$v_{s,dq} = v_{sd} + jv_{sq} = \mathrm{e}^{-j\theta}v_{s,xy} \tag{10.5}$$

Applying the two transformations, Eq. (10.3) can be written as:

$$\begin{aligned} L_s\dot{i}_{s,dq} &= -(R_s + j\omega L_s)i_{s,dq} - v_{L,dq} + v_{s,dq} \\ C_c\dot{v}_{L,dq} &= -(g_L + j\omega C_c)v_{L,dq} + i_{s,dq} + i_{SC,dq} \end{aligned} \tag{10.6}$$

where $\omega = d\theta/dt$ is yet to be chosen and can be a function of time. Corresponding equivalent circuits for the real (d-axis) and imaginary (q-axis) components are shown in Fig. 10.8c.

Now the dq reference frame choice is made similar to that for field oriented control of three phase AC machines. Thus, the angle $\theta = \tan^{-1}(v_{Ly}/v_{Lx})$ so that

$$v_{Lq} \equiv 0 \Rightarrow \dot{v}_{Lq} = 0 \tag{10.7}$$

Defining $\alpha = \theta - \omega_s t$, where ω_s is the frequency of the infinite bus phase voltages, we get $v_{s,dq} = V_s \cdot \mathrm{e}^{-j\alpha}$, where V_s is the constant magnitude of the infinite bus voltage. The relative orientation of the vectors $v_{L,dq}$, $v_{s,dq}$, and the reference frame are shown in Fig. 10.8b. Ignoring losses, a STATCOM only supplies reactive power so that $i_{SCd} \equiv 0$. The system equations can now be rewritten as:

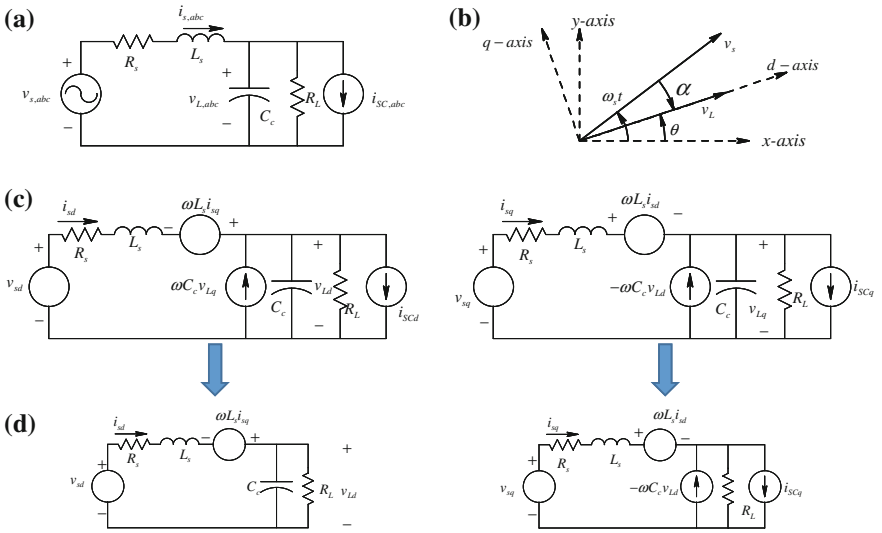

Fig. 10.8 **a** One phase of the system model; **b** choice of reference frame; **c** d-axis and q-axis equivalent circuits; **d** simplified equivalent circuits

$$C_c \dot{v}_{Ld} = -g_L v_{Ld} + i_{sd} \tag{10.8}$$

$$L_s \dot{i}_{sd} = -v_{Ld} - R_s i_{sd} + \omega L_s i_{sq} + V_s \cos\alpha \tag{10.9}$$

$$L_s \dot{i}_{sq} = -R_s i_{sq} - \omega L_s i_{sd} - V_s \sin\alpha \tag{10.10}$$

$$\dot{\alpha} = \omega - \omega_s \tag{10.11}$$

$$\omega = \frac{i_{sq} + i_{SCq}}{C_c v_{Ld}} \tag{10.12}$$

where (10.12) is derived using (10.7). It should be noted that ω varies with time and is different from ω_s. Simplified equivalent circuits with this choice of reference frame are shown in Fig. 10.8d.

10.4.2 Application to Sub-cycle Control

Since $v_{Lq} \equiv 0, v_{Ld}$ represents the instantaneous magnitude of the phase voltages $v_{L,abc}$, while i_{SCq} denotes the instantaneous reactive current supplied by the STATCOM and is the control input to the system. In the absence of negative sequence components, all the state variables in (10.8)–(10.11) are constants in steady state. Thus, the balanced three phase system is effectively transformed to an

equivalent *DC* system and the control problem is simplified to control of *DC* quantities as opposed to the sinusoidally varying quantities. Equation (10.12) defines ω, and therefore θ, using quantities in the *dq* frame so that the *dq* transformation is a diffeomorphism [24] (i.e., the *abc* to *dq* transform and its inverse are continuously differentiable). Thus, (10.8)–(10.12) define the system completely and can be used to design linear or non-linear controllers.

10.4.3 Scalability to Large Systems

The transformed system can be represented in the form of equivalent circuits using circuit simulators with analog behavioral modeling capabilities. The *d*- and *q*-axis equivalent circuits shown in Figs. 10.8b, c can be easily derived from the single phase circuit in Fig. 10.8a. Inductors and capacitors are augmented by appropriate controlled voltage and current sources connected in series and parallel, respectively. Three phase sinusoidal *AC* sources with constant amplitude are replaced by controlled *DC* sources (e.g. $v_{sd} = V_s \cos\alpha$, $v_{sq} = -V_s \sin\alpha$). Finally, two additional equations corresponding to (10.11)–(10.12) are needed to define α and ω. Thus, a more complicated system can be modeled without the need for writing all the state equations explicitly.

Since all the states are constant in steady state, operating point calculation is possible by equating the state derivatives to zero. This can be done by a *DC* bias point calculation in a circuit simulator. The system can be linearized about calculated operating points to obtain either state space data or bode plots of the linearized system. In this chapter, MATLAB/SIMULINK along with the Power System Blockset was used for modeling the equivalent circuits. Figure 10.9 shows the system block diagram for the circuit of Fig. 10.8a indicating the circuit elements and auxiliary equations to be implemented.

10.5 Sub-cycle Voltage Regulation

Based on the model derived in the last section the voltage regulation problem is non-minimum phase for certain operating conditions. Therefore there is an inherent limitation on the achievable dynamic response. Linear and nonlinear control techniques for the voltage regulation problem are discussed and compared via simulations. Next, control of the STATCOM to behave as an instantaneous reactive current source while maintaining its *DC* bus voltage is addressed by a Lyapunov based adaptive controller. Simulation results of the controlled STATCOM integrated with the distribution system model are then presented.

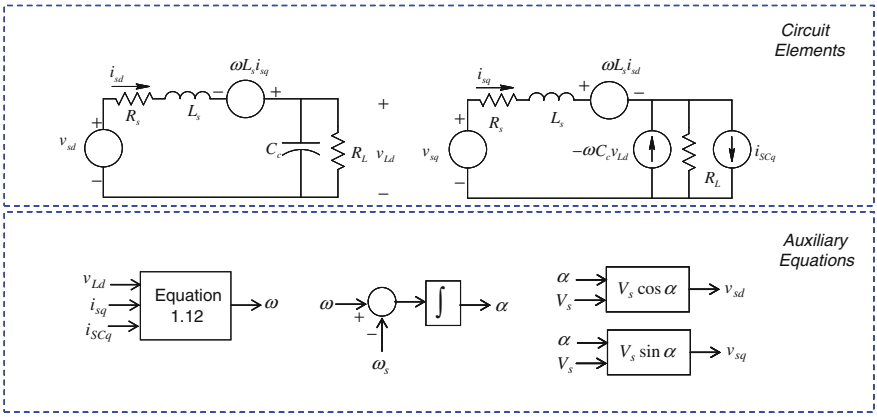

Fig. 10.9 Block diagram of the system model in the rotating frame

10.5.1 Non-minimum Phase Nature of the Voltage Regulation Problem

The distribution system modeled by the dynamics of (10.8)–(10.12) has non-minimum phase when v_{Ld} is chosen as the output of the system with $i'_{SCq} = -i_{SCq}$ as the control input, i.e., the immediate effect of a step increase in i'_{SCq} is a reduction or 'undershoot' in the output after which the output starts increasing and reaches its steady state value. Linearization of the system model reveals that the small signal transfer function $\frac{\tilde{v}_{Ld}(s)}{\tilde{i}'_{SCq}(s)}$ has one right half plane (RHP) zero for certain operating conditions. Bode plots of the transfer function for various operating conditions, each corresponding to a different value of I'_{SCq}, are shown in Fig. 10.10a. The system parameters used are taken from [25] but the load is assumed to be purely resistive:

$$\begin{array}{ll} V_s(\text{L} - \text{L rms}) = 415 \text{ V} & L_s = 9 \text{ mH} \\ C_c = 1 \ \mu\text{F} & R_L = 32 \ \Omega \\ R_s = 0.3 \ \Omega & \omega_s = 120\pi \text{ rad} \times \text{s}^{-1} \end{array}$$

An inspection of the equivalent circuits shown in Fig. 10.8d reveals the peculiar behavior of this system. Assume that at $t = 0$, i'_{SCq} is increased as a step. Since the line inductance prevents an instantaneous change in i_{sq}, the current $\omega C_c v_{Ld}$ reduces instantaneously. Since the coupling capacitor C_c precludes an instantaneous change in v_{Ld}, the immediate effect is a reduction in ω. If the operating condition of the system prior to the step change was such that $i_{sq}(0) > 0$, then i_{sd} starts reducing due to a reduction in value of the controlled voltage source $\omega L_s i_{sq}$. From the first order dynamics of (10.8), a decrease in v_{Ld} is imminent. Once i_{sq} starts increasing due to a reduction of the controlled voltage source $\omega L_s i_{sd}$, then i_{sd} and consequently v_{Ld}, start to increase. If the initial system condition is such that $i_{sq}(0) < 0$, then a

reduction in ω does not cause i_{sd} to decrease. Thus, the system exhibits non-minimum phase behavior only for $i_{sq}(0) > 0$. Figure 10.10b, c shows the simulated step response for the uncontrolled open loop system for cases where $i_{sq}(0) < 0$ and $i_{sq}(0) > 0$ respectively. We refer the interested reader to Appendix 1-A for a nonlinear systems approach to proving the non-minimum phase nature of the system via a study of its zero dynamics.

10.5.2 Linear Control Design

Bode plots of the linearized system shown in Fig. 10.10a were used along with the single input single output design tool in MATLAB to design a simple linear controller with feedback of the load bus voltage alone. The worst case bode plot, corresponding to the minimum value of RHP zero (1,400 rad/s), was used. A purely integral compensator with parameters indicated below sufficed.

K_I	100
Gain Crossover Frequency	55 Hz
Gain Margin (min.)	9 dB
Phase Margin (min.)	78°

More complex linear designs tailored to specific objectives are also possible, e.g., disturbance mitigation in certain frequency range, or aggressive pole placement for faster regulation. Block diagram of the control structure is shown in Fig. 10.11.

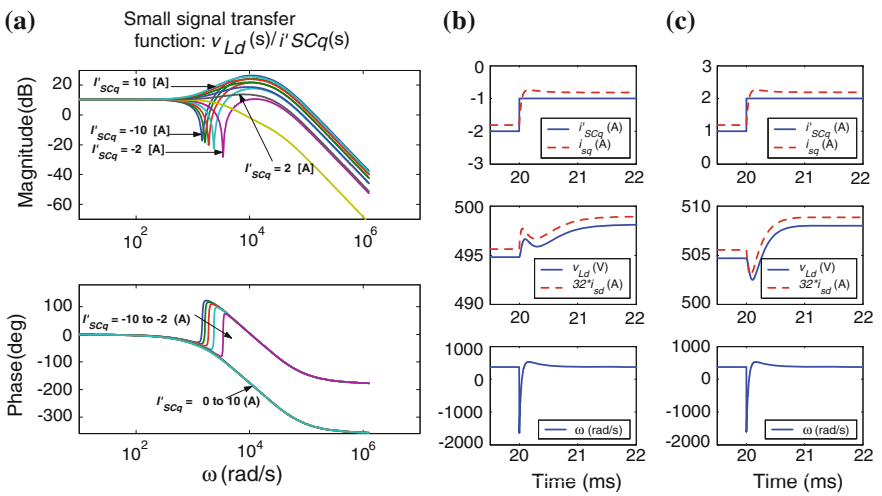

Fig. 10.10 **a** Bode plots of system at different levels of I'_{SCq}; response of open loop system to a step increase in i'_{SCq} for **b** i_{sq} (0) < 0, **c** i_{sq} (0) > 0

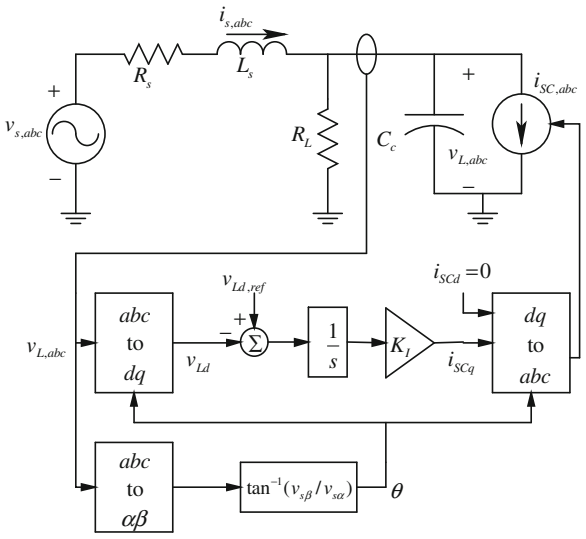

Fig. 10.11 Block diagram of linear control for voltage regulation

10.5.3 Non-linear Control Design

The nonlinear control design for the system dynamics obtained in Sect. 10.4.1 is challenging because of the non-minimum phase nature of the system when v_{Ld} is considered to be the system output. This problem can be circumvented by avoiding direct regulation of v_{Ld}. Instead, direct feedback of another state variable can be employed with respect to which the system dynamics are minimum-phase; the state variable α presents one such choice. Specifically, in [23], an indirect control strategy was devised that relied on feedback regulation of α to its reference value which is statically related to the reference phase voltage magnitude through system parameters. However, since the system parameters are unknown, this can lead to undesirable steady-state errors between v_{Ld} and its reference. To circumvent this issue, a real-time load conductance estimation scheme is devised which adjusts the value of the load conductance estimate based on the phase voltage regulation error. This in turn shifts the reference value for α until the phase voltage error is integrated out to zero. Via a Lyapunov stability analysis, the use of an innovative nonlinear controller and estimator has been shown to achieve asymptotic regulation of the output and exact identification of the load conductance [23]. As opposed to a linearized analysis which is valid only for establishing small signal stability, the Lyapunov stability analysis of [23] is valid in the large.

However, the theoretically guaranteed stability result of [23] relies upon measurement of the system state α which is the angle between the source and load voltage vectors. Since the source voltage is a modeling construct (essentially the Thevenin equivalent voltage of the remainder of the network) it is usually not available for measurement; thus, it is difficult to implement the aforementioned control strategy for a practical system. Therefore, the control structure above was

used as a motivation to design a control strategy dependent only upon measurable system states; specifically, the angle between the direct and quadrature line currents was utilized as the feedback variable. The implementable version of the controller was designed as follows [23]

$$i_{SCq} = -i_{sq} + C_c v_{Ld}\left(\omega_s + \frac{\partial \alpha^*(\hat{g}_L)}{\partial \hat{g}_L}\dot{\hat{g}}_L + k_\rho(\rho - \rho^*(\hat{g}_L)) + \frac{v_{Ld}\sin\rho}{L_s i_{sm}}\right) \quad (10.13)$$

where $i_{sm} = \sqrt{\left(i_{sd}^2 + i_{sq}^2\right)}$, $\rho = \tan^{-1}\left(i_{sq}/i_{sd}\right)$, $\rho^* = \tan^{-1}\left(i_{sq}^*/i_{sd}^*\right)$, and k_ρ is a control gain. Variables with the superscript '*' represent the quasi steady-state solution obtained by setting the left hand side of (10.8)–(10.12) to zero while replacing g_L with its dynamic estimate $\hat{g}_L$ in (10.8). The load conductance estimate was obtained as follows [23]

$$\dot{\hat{g}}_L = -k_g v_{Ld}^*(v_{Ld} - v_{Ld}^*) \quad (10.14)$$

where k_g is a positive control gain. Note that if a load current sensor is available, g_L can be determined directly without the need for an estimator. Local asymptotic stability of this strategy was verified by computing eigen values of the closed loop system linearized about various operating points obtained by using a range of values for the load conductance. This implementable strategy was seen via simulation to outperform both a linear controller and the aforementioned Lyapunov analysis based controller in both transient response and flicker mitigation capability while being robust to system parameter changes as well as changes in the system structure. For more details on the mathematics of the controller design, the interested reader is referred to [23].

Remark While there are many advantages to using nonlinear control, a potential disadvantage is that it is difficult to implement a nonlinear controller in anything other than a digital setting which can lead to conversion and computational delays and consequent loss of bandwidth.

10.5.4 Controller Comparison via Simulation

The controllers designed above were verified via SIMULINK based simulations. The nonlinear controller using feedback of the measurable state ρ, and the output feedback linear controller are compared with respect to regulation of voltage with change in load (g_L) and the ability to mitigate voltage flicker due to a parallel connected load with time varying resistance. For study of flicker mitigation, it is assumed that a time varying load is supplied by the same distribution system and connected as shown in Fig. 10.12. The time varying load has a resistance which is modeled as $R_{EAC} = R_{EAC0} + R_{EAC\_\mathrm{var}}\sin(2\pi f_{fl} t)$, where $f_{fl} = 8.8$ Hz represents the

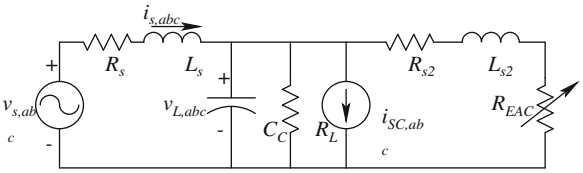

Fig. 10.12 Parallel connection of a time varying load

frequency at which human eye is most sensitive to the resulting light flicker [21]. System parameters additional to those already stated are listed below:

$$R_{EAC0} = R_L \quad R_{EAC\_\text{var}} = R_{EAC0}/3 \quad f_{fl} = 8.8 \text{ Hz}$$
$$L_{s2} = 18 \text{ mH} \quad R_{s2} = 0.3\ \Omega$$

For the nonlinear controller the best overall dynamic response was obtained with control gains $k_\rho = 1e5$, and $k_g = 1.8/V_s$.

Figure 10.13 shows the response of the controllers to step changes in load conductance from 100 % (nominal) to 150 %. Using the linear controller, the load bus voltage error reaches 0.01 p.u. in 5 ms but there are substantial overshoots in v_{Ld} and i_{SCq}. With the nonlinear controller, the voltage settling time is 5 ms and overshoots in v_{Ld}, i_{sd}, i_{sq}, and i_{SCq} are significantly lower than those obtained with the linear controller.

Figure 10.14 compares the ability of the controllers to mitigate voltage flicker. The percentage variation of voltage magnitude from its reference value is given by $\Delta v_{Ld}(\%) = 100 \times \left(v_{Ld} - v_{Ld}^*\right)/v_{Ld}^*$. The percentage mitigation obtained using the two controllers is listed in Table 10.1. The nonlinear controller leads to better mitigation of voltage flicker as compared with the linear controller. The 8.8 Hz parallel load appears at beat frequencies in the *dq*-axis frame. Since the open loop gain crossover frequency for the linear controller is 55 Hz, the STATCOM cannot completely compensate for the disturbance. The controller bandwidth cannot be increased any further due to the non-minimum phase nature of the system. In comparison, the simulation results show that the nonlinear controller is less conservative and gives better performance. Finally, simulations with the system parameters (V_s, ω_s, R_s, L_s, and C_c) allowed to vary around their nominal values confirm that the nonlinear controller is robust to system parameters changes.

10.5.5 STATCOM Control Design

The primary control objective of the STATCOM circuit is to track reactive current i_{SCq} to its reference value. In addition, the STATCOM needs to maintain its DC bus voltage to desired value by drawing active power to compensate for losses. Tracking the active and reactive currents by a PWM inverter can be done by a variety of

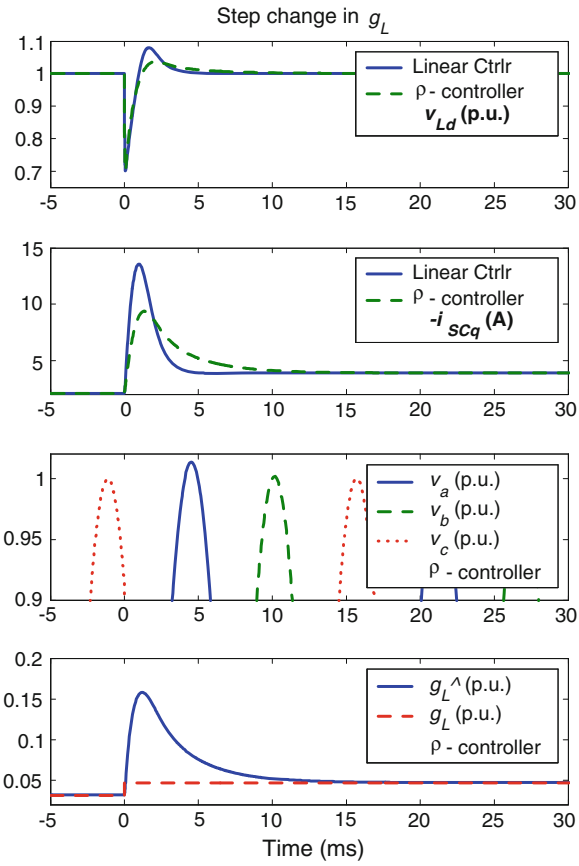

Fig. 10.13 Response to a load increase

methods reported in literature. Here, we illustrate a nonlinear control technique that integrates well with the system level control for voltage regulation [26, 27].

The STATCOM considered here is a three phase inverter with a *DC* bus capacitor and inductive filter on the line side (Fig. 10.15). It is assumed that the internal dynamics of the STATCOM are slower when compared to the switching frequency of the inverter, so that the STATCOM dynamics can be written as:

$$C_{dc}\dot{v}_{dc} = -pv_{dc} - u_{abc}^{T} i_{SC,abc} \tag{10.15}$$

$$L_{sc}\dot{i}_{SC,abc} = u_{abc}v_{dc} - v_{Ld,abc} - R_{sc}i_{SC,abc} \tag{10.16}$$

$$u_{abc} = d_{abc} - (d_a + d_b + d_c)/3 \tag{10.17}$$

Here, v_{dc} is the inverter *DC* bus voltage, i_{SC} is the inverter output current, v_{Ld} denotes the load voltage, d denotes the duty ratios for the inverter, while the subscript 'abc' implies vectors consisting of individual phase quantities. Parameters

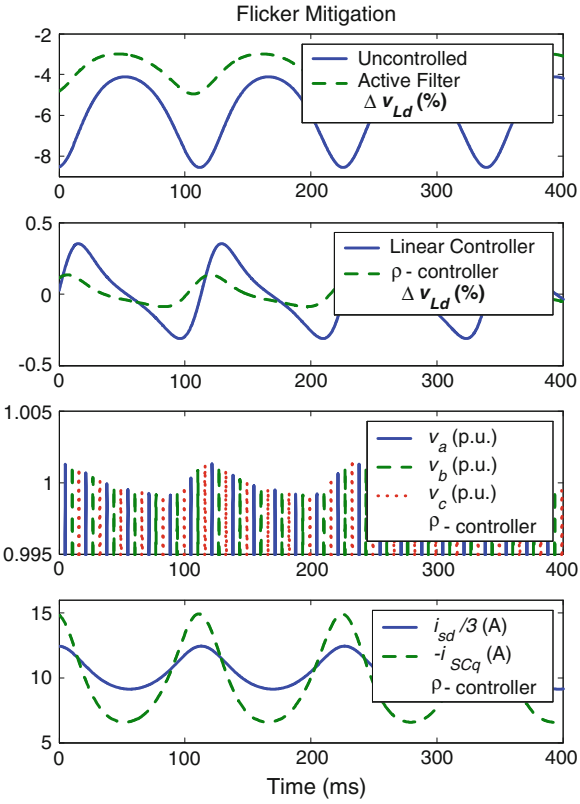

Fig. 10.14 Voltage flicker mitigation

Table 10.1 Flicker mitigation with different control schemes

	Phase voltage magnitude variation (%)	Attenuation (%)
Uncontrolled	4.43	–
Linear controller	0.66	85
Nonlinear controller	0.22	95

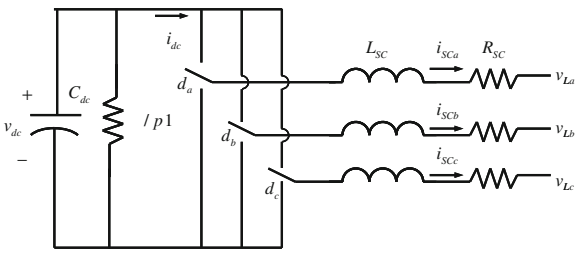

Fig. 10.15 STATCOM schematic showing parasitics

in these equations are as follows. C_{dc}: DC bus capacitance, p: capacitor leakage conductance, L_{sc}: inverter filter inductance, and R_{sc}: combined inverter and inductor parasitic resistance. It should be noted that R_{sc} and p together model all the parasitic losses in the STATCOM. After applying the three phase to two phase transformation followed by the rotational transformation of (10.5), the STATCOM dynamics can be rewritten as:

$$C_{dc}\dot{v}_{dc} = -pv_{dc} - u_d i_{SCd} - u_q i_{SCq} \tag{10.18}$$

$$L_{sc}\dot{i}_{SCd} = -v_{Ld} - R_{sc}i_{SCd} + \omega L_{sc}i_{SCq} + u_d v_{dc} \tag{10.19}$$

$$L_{sc}\dot{i}_{SCq} = -R_{sc}i_{SCq} - \omega L_{sc}i_{SCd} + u_q v_{dc} \tag{10.20}$$

where ω has been previously defined in (10.12), v_{dc}, i_{SCd}, and i_{SCq} represent the state variables of the STATCOM, while u_d and u_q are the control inputs.

The reactive current regulation error e_q is defined as

$$e_q = i_{SCq} - i^*_{SCq} \tag{10.21}$$

From (10.20), it can be seen that u_q can be utilized to achieve the primary control objective. Using (10.21) and (10.20) the control input u_q is designed as:

$$u_q = \frac{1}{v_{dc}}\left(R_{sc}i_{SCq} + \omega L_{sc}i_{SCd} - k_q e_q\right) \tag{10.22}$$

where k_q is a positive control gain.

The secondary control objective is to bound v_{dc} around its reference. This objective cannot be achieved directly by u_d through (10.18) as there might be a possibility of i_{SCd} going to zero during a transient. By evaluating transfer functions of the system linearized about various operating points, it was observed that the dynamics of (10.18)–(10.19) are non-minimum phase when u_d and v_{dc} are chosen as input and output signals, respectively. A stability analysis of the zero dynamics is presented in [28]. Therefore, v_{dc} is controlled indirectly by controlling i_{SCd}. Advantage is taken of the fact that the system states attain constant values in quasi steady state conditions, hence i^*_{SCd} can be calculated by setting (10.18)–(10.21) to zero. Using (10.19), the control input u_d is then designed as:

$$u_d = \frac{1}{v_{dc}}v_{Ld} + R_{sc}i_{SCd} - \omega L_{sc}i_{SCq} + L_{sc}\frac{\partial i^*_{SCd}}{\partial \hat{p}}\dot{\hat{p}} - k_d e_d \tag{10.23}$$

where k_d is a positive control gain, $\hat{p}$ denotes a dynamic estimate for the parasitic conductance which is yet to be designed, and the tracking error $e_d = i_{SCd} - i^*_{SCd}$. To derive $\hat{p}$, we first define an auxiliary signal, $\hat{v}_{dc}$ to mimic the DC bus voltage:

$$\begin{aligned} C_{dc}\dot{\hat{v}}_{dc} &= -\hat{p}v_{dc} - u_d i_{SCd} - u_q i_{SCq} + k_v \tilde{v}_{dc} \\ \hat{v}_{dc}(0) &= v_{dc}(0) \end{aligned} \tag{10.24}$$

where k_v is a positive estimation gain, $\tilde{v}_{dc} = v_{dc} - \hat{v}_{dc}$, and the conductance estimation error $\tilde{p} = p - \hat{p}$. Based on (10.24) and the stability analysis carried out in [29], the dynamic estimate for the parasitic conductance is designed as:

$$\dot{\hat{p}} = -\dot{\tilde{p}} = -k_p v_{dc} \tilde{v}_{dc} \tag{10.25}$$

with k_p a positive constant adaptation gain. Parasitics represented by p and R_{sc} are expected to vary slowly in steady state; hence, along with an estimator for p, an estimator for R_{sc} is also designed as:

$$\dot{\hat{R}}_{sc} = -k_r i_{SCm} \tilde{i}_{SCm} \tag{10.26}$$

where k_r is a positive constant adaptation gain, $i_{SCm} = \sqrt{i_{SCd}^2 + i_{SCq}^2}$, $i_{SCm}^* = \sqrt{i_{SCd}^{*2} + i_{SCq}^{*2}}$, and $\tilde{i}_{SCm}(t) = i_{SCm}^* - i_{SCm}(t)$. For a detailed proof of stability of the above control scheme, see [29].

10.5.6 Integrated System Performance

The STATCOM model and its control can now be integrated with the power distribution system and load voltage controller. The nonlinear bus voltage controller described in Sect. 10.5.3 provide a reactive current reference signal, i_{SCq}^*, to the STATCOM controller. The other reference input to the STATCOM control is the desired constant *DC* bus voltage, V_{dc}^*. Figure 10.16 shows a block diagram indicating the STATCOM and system level control schemes. Simulation results for this integrated system are presented for step change in load (g_L). In addition to the system parameters listed earlier, the following parameters from [7] were used for simulating the integrated system:

$$\begin{aligned} &C_{dc} = 1.75 \text{ mF} && L_{sc} = 9.67 \text{ mH} \\ &p = 1.6667e{-}5\ \Omega^{-1} && V_{dc}^* = 400 \text{ V} \\ &R_{sc} = 3.36\ \Omega \end{aligned}$$

The controller and estimator gains were chosen as:

$$\begin{aligned} &k_d = L_{sc}/\tau_d \quad k_q = L_{sc}/\tau_q \quad \tau_d = 1e{-}3 \quad \tau_q = 0.1e{-}3 \\ &k_v = 0.175 \quad k_p = 166.67 \quad k_r = 2e3 \end{aligned}$$

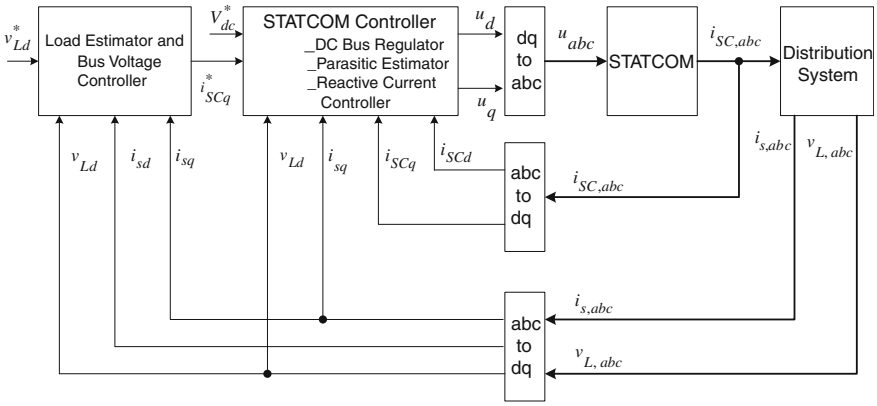

Fig. 10.16 Block diagram of integrated closed loop controller

where τ_d and τ_q are the time constants associated with e_d and e_q, respectively. During each transient, the *DC* bus voltage v_{dc} deviates from its reference value V_{dc}^*. The control inputs u_q and u_d as designed in (10.22) and (10.23) ensure that both i_{SCd} and i_{SCq} reach their reference values. From (10.18)–(10.21) $C_{dc}\dot{e}_v = -pe_v$, where, $e_v = v_{dc} - V_{dc}^*$. This implies that v_{dc} converges to V_{dc}^* with a purely system dependent time constant $\tau_p = C_{dc}/p$, which is of the order of 100 s for the system parameters listed above. The slow convergence of e_v can also be explained by recalling that (a) v_{dc} is controlled indirectly, and (b) the static relationship of i_{SCd}^* and V_{dc}^* leads to a $\partial i_{SCd}^*/\partial V_{dc}^*$ value that is of the order of p ($\approx 2e{-}5$ for our system). Indeed, this poor response is manifested in the simulation results. In order to avoid this slow transient, the design of (10.22) and (10.23) is modified to use the reference value V_{dc}^* instead of v_{dc} giving a satisfactory response for v_{dc}. Details of the stability analysis with this modification are provided in [28].

Figure 10.17 shows the system response to a step increase in load from 100 to 150 %. As seen, i_{SCq} follows its reference value i_{SCq}^* very closely, justifying the assumption of the STATCOM being a controlled reactive current source. Using the controlled STATCOM, the bus voltage controller regulates v_{Ld} to its reference value v_{Ld}^*. The real current drawn by the STATCOM, i_{SCd}, follows its reference value with a small lag, as expected from its higher time constant of $\tau_d = 1$ ms. The DC bus voltage v_{dc} is regulated to its reference value of 400 V. The values of R_{sc} and p used in the system model were maintained constant. However, simulation results omitted here show the convergence of the estimates to the actual values after each transient proving the effectiveness of the estimation schemes.

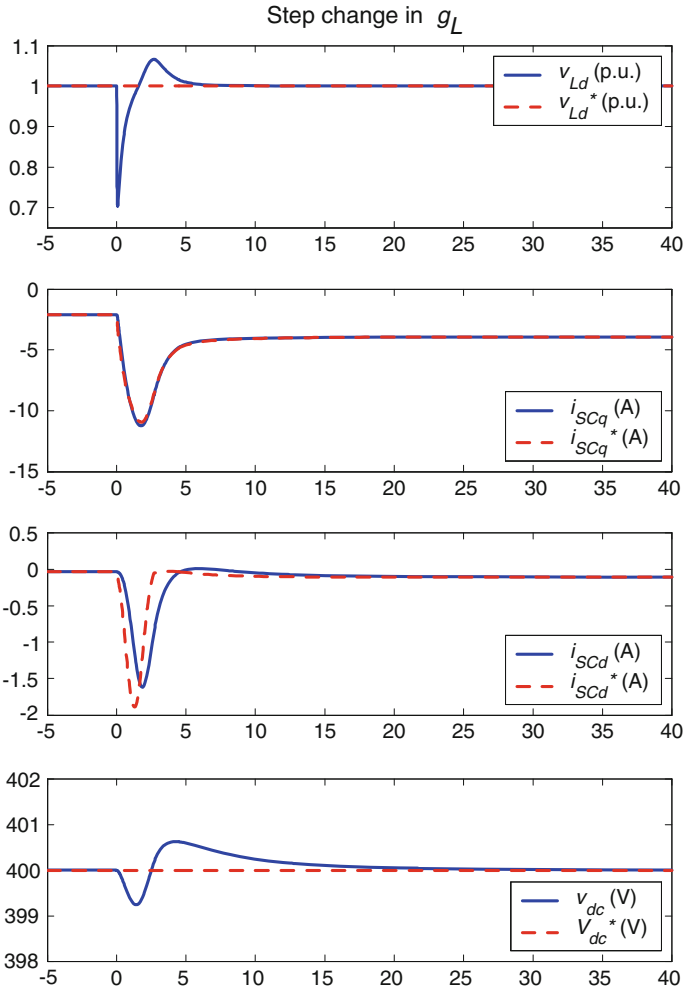

Fig. 10.17 Integrated system performance: system variables for load step change from 100 to 150 %

10.6 Conclusion

The chapter provided an overview of modeling and control requirements for STATCOM applications at different levels in the electric power system. The emphasis was on sub-cycle modeling and control with applications at customer locations in the distribution system. In particular load voltage regulation with reactive current was discussed in detailed. The modeling approach can be applied for other sub-cycle control objectives with active power being another potential control input if energy storage is integrated with the STATCOM. As evident in the

voltage regulation problem an appropriately matched system model plays a key role in determining dynamic limits and control strategies. While transmission level applications may be considered to be mature, new applications for STATCOMs in distribution systems are still being explored. Understanding of quasi steady state behaviour is generally the basis of new applications proposed. Interesting possibilities can arise if sub-cycle models are also considered and the domain of influence at shorter time scales is clearly determined.

Appendix: Stability of the Zero Dynamics

According to [24], a system is non-minimum phase if the *zero dynamics* of the system are not asymptotically stable. Assuming $i_{sq} \neq 0$, the system zero dynamics can be obtained as follows. First, the output v_{Ld} is set to a constant value of v_{Ld}^* in (10.8) which gives $i_{sd}^* = g_L v_{Ld}^*$. Use of v_{Ld}^* and i_{sd}^* in (10.9) obtains i_{SCq} in terms of i_{sq} and α. Finally, substituting for i_{SCq} in (10.10) and (10.11) and using (10.12) for ω obtains the zero dynamics as follows:

$$L_s \dot{i}_{sq} = -R_s i_{sq} - V_s \sin\alpha - g_L v_{Ld}^* \left(v_{Ld}^* (1 + g_L R_s) - V_s \cos\alpha\right) \frac{1}{i_{sq}} \tag{10.27}$$

$$\dot{\alpha} = -\omega_s + \left(v_{Ld}^* (1 + g_L R_s) - V_s \cos\alpha\right) \frac{1}{L_s i_{sq}} \tag{10.28}$$

Choosing v_{Ld}^* as a parameter, equilibrium points for (10.27) and (10.28) can be computed. This allows for local stability analysis of the system via linearization of (10.27) and (10.28) about these equilibrium points. We begin by defining $\chi = \frac{V_s}{\sqrt{(1+R_s g_L)^2 + (\omega_s L_s g_L)^2}}$. For the case when $v_{Ld}^* > \chi$ corresponding to $i_{sq}(0) > 0$, a pair of eigen values is obtained one of which is positive. Since the linearized system corresponding to (10.27) and (10.28) is unstable for $v_{Ld}^* > \chi$, the nonlinear system given by (10.27) and (10.28) is also unstable [24], i.e., the system (10.8)–(10.12) has unstable zero dynamics. For $v_{Ld}^* < \chi$ corresponding to $i_{sq}(0) < 0$, a pair of complex conjugate eigen values with negative real parts is obtained. Since the linearized system corresponding to (10.27) and (10.28) is stable for $v_{Ld}^* < \chi$, the nonlinear system given by (10.27) and (10.28) is *locally* asymptotically stable. For the special case when $v_{Ld}^* = \chi$, the zero dynamics are given by

$$L_s \dot{i}_{sq} = -R_s i_{sq} \tag{10.29}$$

which are clearly asymptotically stable to the equilibrium point. Thus, it can be concluded that the system described by (10.8)–(10.12) is non-minimum phase for $i_{sq}(0) > 0$.

References

1. Hingorani NG, Gyugyi L (1999) Understanding facts: concepts and technology of flexible AC transmission systems. Wiley, New York
2. Diaz de Leon JA, Taylor CW (2002) Understanding and solving short-term voltage stability problems. In: Proceedings of the 2002 IEEE power engineering society summer meeting, vol 2, pp 745–752
3. Hochgraf C, Lasseter RH (1998) STATCOM controls for operation with unbalanced voltages. IEEE Trans Power Deliv 13:538–544
4. Li K, Liu J, Wang Z, Wei B (2007) Strategies and operating point optimization of STATCOM control for voltage unbalance mitigation in three-phase three-wire systems. IEEE Trans Power Deliv 22(1):413–422
5. Majumder R, Ghosh A, Ledwich G, Zare F (2010) Power management and power flow control with back-to-back converters in a utility connected microgrid. IEEE Trans Power Syst 25 (2):821–834
6. Bhattacharya S, Frank TM, Divan DM, Banerjee B (1998) Active filter system implementation. IEEE Ind Appl Mag 4(5):47–63
7. Padiyar KR, Kulkarni AM (1997) Design of reactive current and voltage controller of static condenser. Electr Power Energy Syst 19(6):397–410
8. Preville GD (2001) Flicker mitigation: application to a STATCOM. In: Proceedings of 2001 European conference on power electronics and applications CD-ROM
9. Corzine K (2002) Multilevel converters. In: Skvarenina TL (ed) The power electronics handbook, CRC Press, New York
10. Schauder C, Mehta H (1993) Vector analysis and control of advanced static VAR compensators. IEE Proc C Gener Transm Distrib 140:299–306
11. Zmood DN, Holmes DG, Bode GH (2001) Frequency-domain analysis of three-phase linear current regulators. IEEE Trans Ind Appl 37(2):601–610
12. Zmood DN, Holmes DG (1999) Stationary frame current regulation of PWM inverters with zero steady state error. In: Proceedings of IEEE PESC'99, vol 2, pp 1185–1190
13. Mattavelli P (2001) A closed-loop selective harmonic compensation for active filters. IEEE Trans Ind Appl 37(1):81–89
14. Bojrup M, Karlsson P, Alakula M, Gertmar L (1999) A multiple rotating integrator controller for active filters. In: Proceedings of EPE'99 conference on CD-ROM
15. Kundur P (1994) Power system stability and control. McGraw-Hill Inc., New York
16. Rogers G (1999) Power system oscillations. Springer, Berlin
17. Taylor CW (1993) Power System Voltage Stability. McGraw-Hill Inc., New York
18. IEEE Standard 519-1992 (1992) IEEE recommended practices and requirements for harmonic control in electrical power systems
19. International Electrotechnical Commission (IEC) Standard 1000-3 (1995) Electromagnetic compatibility part 3: limits
20. Kyei J, Ayyanar R, Heydt G, Thallam R, Blevins J (2002) The design of power acceptability curves. IEEE Trans Power Deliv 17(3):828–833
21. Gutierrez M, Venkataramanan G, Sundaram A (2000) Solid state flicker controller using a pulse width modulated AC-AC converter. In: Proceedings of 35th IEEE industry applications society annual meeting, vol 5, pp 3158–3165
22. Moreno CV, Duarte HA, Garcia JU (2002) Propagation of flicker in electric power networks due to wind energy conversions systems. IEEE Trans Energy Convers 17:267–272
23. Jain AK, Behal A, Zhang X, Dawson DM, Mohan N (2004) Nonlinear controllers for fast voltage regulation using STATCOMs. IEEE Trans Control Syst Technol 12(6):827–842
24. Khalil HK (2002) Nonlinear systems, 3rd edn. Prentice Hall, Upper Saddle River, pp 139–142, 512–517
25. Sensharma PS, Padiyar KR, Ramanarayanan V (2001) Analysis and performance of distribution STATCOM for compensating Voltage fluctuation. IEEE Trans Power Deliv 16:259–264

26. Jain AK, Joshi K, Behal A, Mohan N (2006) Voltage regulation with STATCOMs: modeling, control and results. IEEE Trans on Power Deliv 21(2):726–735
27. Jain AK, Joshi K, Behal A, Mohan N (2005) Modeling and nonlinear control of STATCOMs for fast voltage regulation. In: Proceedings of American control conference, Portland, Oregon, June 2005
28. Jain AK, Joshi K, Behal A, Mohan N (2004) Modeling and nonlinear control of STATCOMs for fast voltage regulation. In: Proceedings of IEEE conference on decision and control, Bahamas, Dec 2004
29. Joshi K, Jain AK, Behal A, Mohan N (2004) A comparative study of control strategies for fast voltage regulation with STATCOMs. In: Proceedings of IEEE industrial electronics society (IECON) CD-ROM, Busan, Nov 2004, pp 1–6

Chapter 11
Study of STATCOM in *abc* Framework

Juan M. Ramirez, Juan Miguel Gonzalez-Lopez, Julio C. Rosas-Caro, Ruben Tapia-Olvera, Jose M. Lozano and Antonio Valderrabano-Gonzalez

Abstract In this chapter, the STATCOM characteristics are analyzed when it is utilized for improving the voltage stability. This chapter aims to analyze the STATCOM in the *abc* coordinates, and its impact over the power system under steady state and transient conditions is studied. Mathematical description of the main components is included to represent the dynamic behavior. These elements are formulated by differential equations in order to demonstrate how the STATCOM influences overall power system performance and voltage stability margins. The proposed methodology is validated on a Synchronous Machine Infinite Bus (SMIB) and on the New England test power system, which comprises 39-buses, 46-transmission lines, and 10-generators.

J.M. Ramirez (✉)
Centro de Investigacion y de Estudios Avanzados del Instituto Politecnico Nacional, Av. del Bosque 1145, Col. el Bajio, 45019 Zapopan, JAL, Mexico
e-mail: jramirez@gdl.cinvestav.mx

J.M. Gonzalez-Lopez
Universidad Tecnologica de Manzanillo, Camino hacia las humedades s/n, Col. Salagua, 28869 Manzanillo, COL, Mexico
e-mail: jmgonzalez@utmanzanillo.edu.mx

J.C. Rosas-Caro · A. Valderrabano-Gonzalez
Universidad Panamericana, Campus Guadalajara, Czda Circ Poniente No. 49, Col. Cd Granja, 45010 Zapopan, JAL, Mexico
e-mail: crosas@up.edu.mx

A. Valderrabano-Gonzalez
e-mail: avalder@up.edu.mx

R. Tapia-Olvera
Universidad Politecnica de Tulancingo, Calle Ingenierias No. 100. Col. Huapalcalco, 43629 Tulancingo, HGO, Mexico
e-mail: ruben.tapia@upt.edu.mx

J.M. Lozano
Division de Ingenierias, Universidad de Guanajuato, Campus Irapuato-Salamanca, Carr. Salamanca—V. de Santiago, Comunidad de Palo Blanco, 36885 Salamanca GTO, Mexico
e-mail: jm.lozano@ugto.mx

F. Shahnia et al. (eds.), *Static Compensators (STATCOMs) in Power Systems*, Power Systems, DOI 10.1007/978-981-287-281-4_11

Keywords Power system voltage stability · PV-curves · STATCOM · Voltage stability margin

11.1 Introduction

Figure 11.1a shows a basic representation of a radial power system to define its different electric parameters; a bus feeds a load through a transmission line.

The active and reactive power transfer between power source and load depends on the voltage magnitude in both bus and phase angles; Fig. 11.1a shows the power triangle corresponding to the load bus. P, Q and S represent active, reactive and apparent power, respectively. From the power triangle, the power factor may be expressed by

$$P.F. = \frac{P}{S} = \frac{P}{\sqrt{P^2 + Q^2}} = \cos\phi \tag{11.1}$$

Figure 11.1a is used to relate the active power, reactive power and the voltage in the load bus; the generator or system voltage is assumed constant and it is taken as the reference bus. The line impedance is represented by its series inductive reactance jX, assuming a lossless system, neglecting the line capacitance; all variables are expressed in per unit, pu This small system uses the Thévenin equivalent to the power system seen from the load bus.

The bus voltage is given by the expression:

$$\widetilde{V} = \widetilde{E} - jX\,\widetilde{I} \tag{11.2}$$

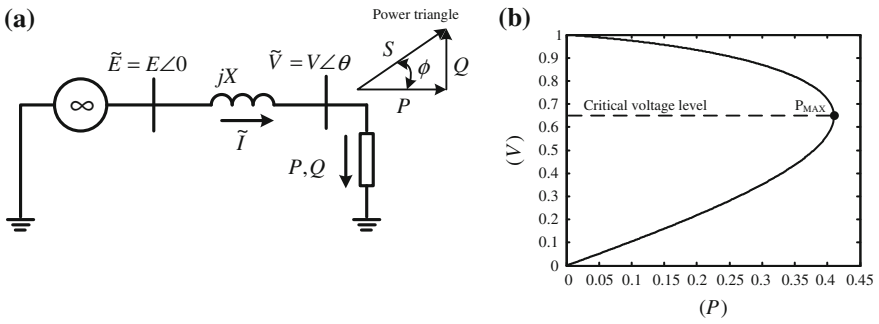

Fig. 11.1 **a** Basic radial power system. **b** PV curve considering $\tan\phi = 0.6$

The active and reactive power delivered to the grid can flow in both directions either absorbed or generated. This equation contains both of them, and may be expressed by:

$$S = P + jQ = \tilde{V}\,\tilde{I}^* = \tilde{V}\,\frac{\tilde{E}^* - \tilde{V}^*}{-jX} = \frac{j}{X}\left(EV\cos\theta + jEV\,\mathrm{sen}\theta - V^2\right) \tag{11.3}$$

The complex power may be separated into the active and reactive component as

$$P = -\frac{EV}{X}\,\mathrm{sen}\theta; \qquad Q = -\frac{V^2}{X} + \frac{EV}{X}\cos\theta \tag{11.4}$$

Equation (11.4) relate the P and Q values to the magnitude V and phase θ of voltage, the angle is normally small providing a close relationship between the load-bus voltage and the reactive power, and a close relationship between the phase angle and the active power [1, 2]. This decoupled behavior holds during normal operation, and not during extreme load operations [3].

It is possible to handle the phase angle θ by an algebraic procedure and write

$$(V^2)^2 + (2QX - E^2)\,V^2 + X^2(P^2 + Q^2) = 0 \tag{11.5}$$

From this second order equation, the necessary condition to have a solution becomes

$$-P^2 - \frac{E^2}{X}Q + \left(\frac{E^2}{2X}\right)^2 \geq 0 \tag{11.6}$$

Assuming this constraint, there are two possible solutions for (11.5),

$$V = \sqrt{\frac{E^2}{2} - QX \pm \sqrt{\frac{E^4}{4} - X^2P^2 - XE^2Q}} \tag{11.7}$$

According to the power triangle, Fig. 11.1a, the reactive power can be also expressed by

$$Q = P\tan\phi \tag{11.8}$$

Once the phase angle has been eliminated from the formulation, the only unknown parameter is the voltage magnitude V; it can be solved since E and X are constants. According to (11.8), Q depends on P, and considering a constant power factor, V depends only on P.

11.1.1 PV-Curves

The relationship between the active power P and the voltage magnitude V is quite important in voltage stability analysis, and their interaction is depicted in the *PV*-curves. For the analyzed case, such curves can be obtained once both solutions (11.5) are known.

A PV-curve for the radial system is depicted in Fig. 11.1b, when $\tan \phi = 0.6$. As above mentioned, for a given power factor, (11.5) has two possible solutions:

1. The one achieved considering a positive sign, results in an operative condition where V is relatively high and the current I is relatively small, which is the segment of the curve shown in Fig. 11.1b above the dotted line; this is the desired operating range.
2. The second solution corresponds to the negative sign, producing an operation bellow the dotted line in Fig. 11.1b, with a low voltage V and a high current I; this is an undesired operation where the systems becomes unstable.

In Fig. 11.1b, the point of $V = 1$ pu (left upper corner) corresponds to the lower load condition. Increasing the load, the voltage decreases gradually approaching to the maximum power transfer point $P_{\max}$. This operating point has different definitions in the voltage stability analysis, for instance, *critical voltage point* or *voltage collapse point*. When the system is operating near this point, a small load increment may produce a high voltage reduction, and after the critical voltage, any increment on the current leads to an unstable operation.

To explain the way power $P_{\max}$ can be calculated, let's assume the load power behaves as impedance. The problem can be formulated by the maximum power transfer theorem, which indicates the maximum power transfer is reached when the load impedance is equal in magnitude to the Thévenin systems impedance [4].

PV-curves are useful to conceptually analyze the voltage stability problem in radial systems. Figure 11.2a shows other PV-curves for the same system shown in Fig. 11.1a but for different power factors. The curves are normalized to the short-circuit power of the system (E^2/X); each curve corresponds to a different power factor.

The power factor has an important effect in the voltage-power characteristic. Another important aspect is when the power factor is leading ($\tan \Phi < 0$), that means the load is capacitive or there is a parallel compensation. In this case, the maximum power point $P_{\max}$ increases with respect to the lagging power factor and the voltage magnitude. This is because for negative values of $\tan(\Phi)$, an increment in the load active power produces an increment in the reactive power produced by the load (or parallel compensator). This situation is difficult to identify because the maximum power-transfer point can be reached when the voltage has a normal magnitude, hiding the real system's condition.

So far, only the load active power versus voltage magnitude has being described, with a constant power factor. In this case, according to (11.8), each value of P corresponds to a value of Q. The reactive power load is analyzed through Fig. 11.2b,

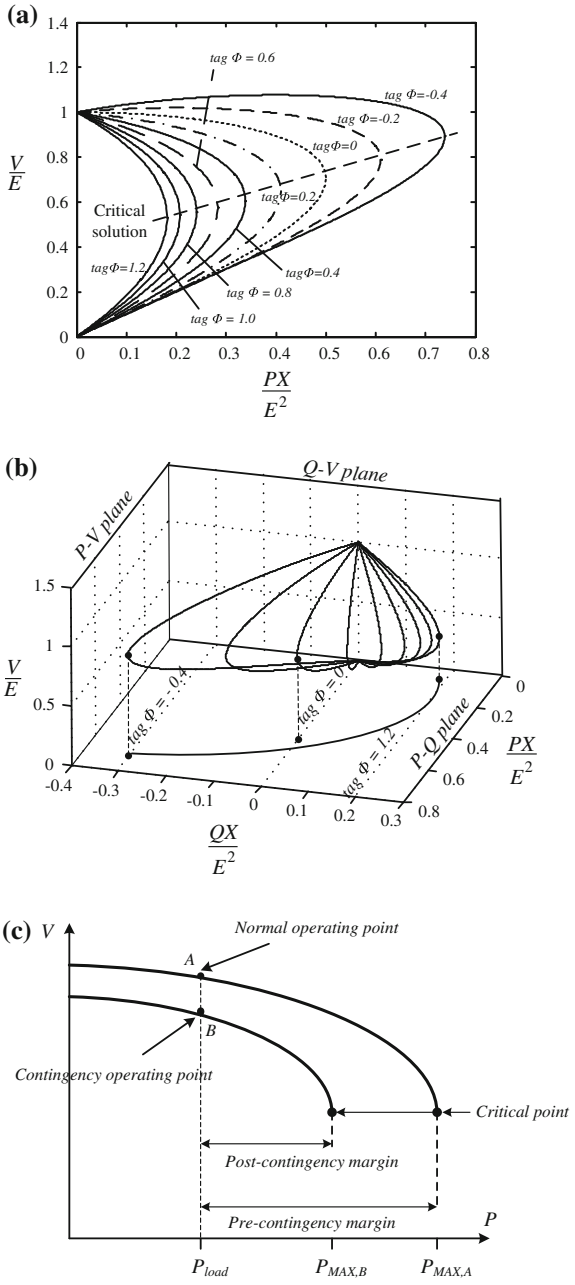

Fig. 11.2 **a** PV-curves for different power factors. **b** Voltage versus active and reactive power. **c** Voltage stability margin of a power system

where all PV-curves displayed in Fig. 11.2a are plotted in a 3D graphic in order to identify the behavior of the reactive power Q, along with the behavior of active power P and voltage magnitude V.

Figure 11.2b includes 3 planes called *PV*, *QV* and *PQ*, respectively; the operative conditions are marked, considering the power factor and the critical voltage point:

1. Leading power factor, tan $\Phi = -0.4$. Under this condition, the load does not require reactive power from the system but it is producing it, this is denoted by the negative sign in *Q*, Fig. 11.2b.
2. Unity power factor, tan $\Phi = 0$. In this case the load is purely resistive. There are not reactive power consumption; the reactive power has a zero value.
3. Lagging power factor, tan $\Phi = 1.2$. Under this condition the load consumes both active and reactive power; this is the most common operating condition.

The projection of the operating points over the planes describes a specific curve, either *PV*, *QV* or *PQ*, for example the PV-plane shown in Fig. 11.2a.

The PV-curves method is also utilized in big power networks, but in that case the variable *P* represents the active power consumed by a full area in MW, and *V* becomes the voltage magnitude in pu Sometimes *P* can represent the active power of a transmission line. In this case, the *PV*-curve is calculated from a load flow calculation. For each specific condition a simulation is executed providing the voltage magnitudes. Several simulations are performed with different load conditions until a curve is built.

11.1.2 Voltage Stability Margin

The voltage magnitude is widely used as security criterion. Voltage levels are observed in simulations before and after an event occur. However, observing only the voltage levels may lead to an erroneous estimation. For this reason, besides of using such security criterion, it is necessary to define margins or distances that allow to predict in a precise way the real system condition, and to prevent the extent of possible changes in the system's operation, under common situations or disturbances [5, 6].

The concept of voltage stability margin has being introduced to reduce the risk of wrong estimations in the system condition. This concept may be defined as an estimation of the power system's proximity of experimenting problems due to bus voltage levels. In the last decade, important efforts have being performed to specify those margins in parameters of the power system that make practical sense to the grid operators.

In general, the voltage stability margin can be defined as the difference between a Key System Parameter (KSP) in the current operating point and the critical voltage stability point [7]. For instance, this KSP can be chosen as the active power, load reactive power, or the total flow capability of the system. There are several options to choose the KSP. However in practice there are two well established categories for this purpose:

1. Choosing the KSP based on the *PV*-curve, for example the total load in an specific area of the system, or the total power flow through a transmission line.
2. Choosing the KSP based on the *VQ*-curve, for example the reactive compensating power provided to a bus or group of buses.

The voltage stability margin is widely accepted to evaluate the voltage stability of a system; it has several advantages such as [8]:

- The concept of this index is not based on a particular model of the system, it can be used in either dynamic or static models independently of how detailed the model is.
- It is precise index which allows taking decisions regardless on the non-linearity of the system and the different device limits as the load is increasing.
- A sensitivity analysis can be applied to determine the effects over the parameters and control systems of the network [9].
- The margin considers the load increment model.

Another additional advantage of this margin is that voltage stability criteria can be defined, to determine how much margin is enough to ensure the system stability.

In general, this criterion may be defined as follows: "A power system can operate in such a way that for the current operating point, and with all possible contingencies, the voltage stability margin is larger than a certain percentage of the selected Key System Parameter" [7].

Figure 11.2c shows the calculation the voltage stability margin for different operating conditions, considering the KSP as the load modeled as constant power. The margin called *pre-contingency*, corresponds to a case where the power system is operated under normal conditions, which means the elements within the system are operating in a satisfactory way. The *post-contingency* margin is related to an undesired operation of the system, which means a perturbation has taken place in the system, for example a generator or a transmission line has tripped or other event that modifies the system operating conditions. Clearly, there is a wider margin in the pre-contingency case, and then there is confidence for operating the system under different circumstances.

Calculating the stability margin only for the pre-contingency case does not offer enough information from the security point of view, since this only describes the leading characteristics of the system for a particular case [10]. However, the analysis has to be complemented with the study of other cases, particularly the contingency cases, since for different reasons contingencies are inherent to the system operation.

From a strict point of view, it would be necessary to calculate the voltage stability margin for all possible contingencies that can take place inside the power system, taking into account either simple contingencies as well as complex events. But this takes a lot of time, and then the most important cases are typically analyzed.

For real-time or on-line analysis, the system state is known or approximately known through a variety of measurements and state estimation, and then the voltage

stability margin is calculated considering a small list of contingencies. The selection of contingencies depends on the safety procedures used for each utility. The statistical data becomes a very useful.

In an off-line environment, where the time is not a constraint and long simulations can be carried out, it is necessary determining the voltage stability margin for a bigger number of contingencies, and also to consider some specific operative conditions, because frequently due maintenance trip of equipment the system rarely operates with all elements connected. For analysis purposes, each element out of service is combined with each contingency to get a set of double contingency simulations. With the result of those studies, sometimes databases are created for being utilized as a back-up for the system operators, with the objective to apply corrective actions for each contingency.

Some criteria established for different utilities are:

(a) Incremental/decremental criteria of voltage: specify that the voltage magnitude should stay within certain nominal range during all contingencies.
(b) Reactive reserve criteria: establish that the reserve of reactive power in a certain group of sources (generators, compensator devices, etc.) should be greater than a margin of their output power in all contingencies.

The combination of the aforementioned limits defines the operating limits; in other words, set the safety range that the system can be operated according to the voltage.

11.2 STATCOM at Steady State

The fundamental structure of the STATCOM is constituted by a Voltage Source Converter (VSC) and a coupling transformer which is utilized as link between the STATCOM and the power system, as illustrated in Fig. 11.3a.

The STATCOM may be considered the power-electronics version of a synchronous capacitor, it generates and injects reactive power into the system, but it can also absorb reactive power and it may change the amount of generated power in

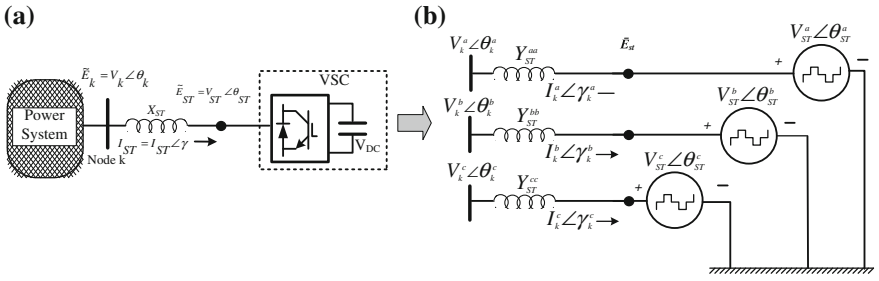

Fig. 11.3 **a** STATCOM basic structure. **b** Three-phase STATCOM equivalent circuit

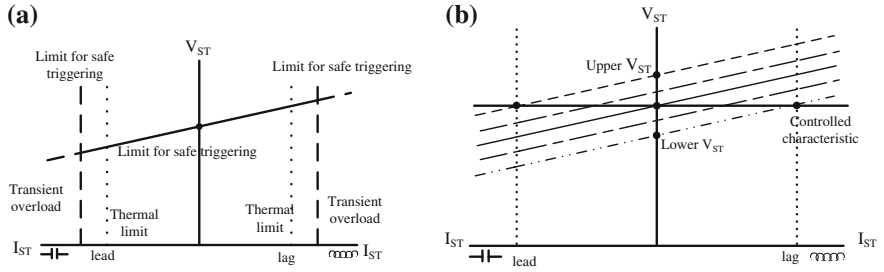

Fig. 11.4 **a** V-I STATCOM's profile. **b** V-I characteristic controlled by the STATCOM

a fast and continuous way; since it is not based on mechanisms, the principle of operation are very similar to a synchronous capacitor.

Figures 11.4a, b indicate that when the voltage generated by the STATCOM is lower than the voltage in the bus where this device is connected, the STATCOM behaves such an inductive load, absorbing reactive power from the grid. On the other hand, when the generated voltage is larger than the grid voltage, it behaves as a capacitive load, injecting reactive power into the system [11]. The STATCOM's losses are active power drawn from the grid; the amount of losses uses to be a small percentage of the device's rated power.

It would not be proper to connect the VSC terminals directly to the power system, which generally exhibits a larger short-circuit capacity. The STATCOM is coupled to the system through a set of inductors or a transformer to provide an inductive link to the grid; depending on the VSC, a set of harmonic filters can be included or a capacitors bank. In such cases also reactors may be used (separated from the coupling transformers), in order to limit the harmonic current from the converter to the capacitor bank.

The natural operation profile of voltage vs current in the STATCOM terminals is illustrated in Fig. 11.4a, this behavior depends fully on the voltage at the STATCOM terminals, and on the transformer or coupling reactance. The transformer reactance has typical values of 10–20 % of the STATCOM's capacity. In other words, the voltage drop is 10–20 % of the bus voltage when the STATCOM is operating at nominal current.

The current magnitude flowing through the Gate Turn-off Thyristors (GTO) or Insulated Gate Bipolar Transistors (IGBT) is independent of the phase this current has with respect to the bus voltage; those semiconductor devices also sustain any over-current only for a short time.

The maximum voltage that a STATCOM can hold at its terminals is usually 1.1 pu. However, the STATCOM can hold dynamic over-voltages and transients over the level provided by the over-voltage protective devices. During this transient condition, diodes in the VSC would allow the current to pass to the DC-link capacitor charging it to a higher value.

In practical applications, the STATCOM is expected to operate with a slope of about 2 and 5 %, Fig. 11.4a, which is smaller than the coupling transformer

reactance, since the transformer reactance is constant, the voltage produced by the VSC in the STATCOM has to behave as shown in Fig. 11.4b.

When voltage V_{ST} increases until $V_{ST}(+)$ to attain a capacitive current, or reducing V_{ST} until $V_{ST}(-)$ to obtain a lagging condition (inductive current). This process can be rapidly achieved through properly handling the semiconductor devices, regulating the VSC's voltage magnitude if necessary [11].

The slope and the reactance, along with the output voltage in the VSC can be set to I_{ST} to control the scheme of the STATCOM, a set of characteristic slopes of voltage-current in the device for several voltage ranges. The STATCOM performance for voltage regulation is quite similar to the static VAr compensator (SVC), but in a more robust way, because the STATCOM operation is not related to low voltage conditions. Under reduced voltage levels the STATCOM can keep working in a leading or lagging way, in contrast to that, the current limits established for a conventional SVC are proportional to the voltage.

A STATCOM is a better option to provide reactive power to a power system, with low voltage problems, while the SVC can generally make more than the STATCOM to limit the dynamic over-voltages [11].

11.3 Embedding a STATCOM into the Power Flow Formulation

At steady state, the STATCOM can be represented in the same way as the synchronous capacitor, which most of the times is modeled as a synchronous generator in which the active power generated is zero. In the power flow problems, a more flexible model can be attained considering the STATCOM as a three-phase variable voltage source, in which the magnitude and phase angle can be regulated to get a constant voltage at the bus where the STATCOM is connected [12]. An expression for the voltage source of a three-phase STATCOM becomes

$$\mathbf{E}_{ST}^{\rho} = V_{ST}^{\rho}(\cos\theta_{ST}^{\rho} + j\ \text{sen}\theta_{ST}^{\rho}) \tag{11.9}$$

where ρ indicates phase a, b, and c quantities; and "$_{ST}$" indicates STATCOM parameters. Figure 11.3b shows the three-phase STATCOM scheme, which can be interpreted as the three-phase Thevenin equivalent from the kth bus of the system.

Some steady state characteristics assumed for the STATCOM model are the following:

- The output voltage $\mathbf{E}_{ST}^{\rho}$ of the converter has only the fundamental frequency component, and then the STATCOM performance does not contribute with harmonic perturbations.
- The magnitude of the voltage V_{ST}^{ρ} is restricted by a maximum and minimum limit, which depends on the STATCOM capability. However, the phase angle θ_{ST}^{ρ} is not restricted to any value and can take values from 0 to 2π radians.

- Inside the power flow algorithms, the *k*th bus, where the STATCOM is connected, it is usually represented by a *PV* controlled voltage, which can change to a *PQ* load bus when the voltage magnitude exceeds the established limits.
- The effects of mutual inductances in the linking transformer between the STATCOM and the power system are neglected.

The circuit in Fig. 11.3b is used to derive the mathematical model of STATCOM, which will be used in the power flow formulation; based on that, the current in the circuit may be written as (11.10)

$$[\mathbf{I}_k^{\rho}] = [\,\mathbf{Y}_{ST}^{\rho\rho} \quad -\mathbf{Y}_{ST}^{\rho\rho}] \begin{bmatrix} \mathbf{E}_k^{\rho} \\ \mathbf{E}_{ST}^{\rho} \end{bmatrix} \tag{11.10}$$

where:

$$\mathbf{I}_k^{\rho} = [I_k^a \angle \gamma_k^a \quad I_k^b \angle \gamma_k^b \quad I_k^c \angle \gamma_k^c]^t \tag{11.11}$$

$$\mathbf{E}_k^{\rho} = [V_k^a \angle \theta_k^a \quad V_k^b \angle \theta_k^b \quad V_k^c \angle \theta_k^c]^t \tag{11.12}$$

$$\mathbf{E}_{ST}^{\rho} = [V_{ST}^a \angle \theta_{ST}^a \quad V_{ST}^b \angle \theta_{ST}^b \quad V_{ST}^c \angle \theta_{ST}^c]^t \tag{11.13}$$

$$\mathbf{Y}_{ST}^{\rho\rho} = \begin{bmatrix} Y_{ST}^{aa} & 0 & 0 \\ 0 & Y_{ST}^{bb} & 0 \\ 0 & 0 & Y_{ST}^{cc} \end{bmatrix} \tag{11.14}$$

Based on (11.10) and (11.14), the next expression can be written for the active and reactive power injected into the *k*th bus:

$$P_k^{\rho} = (V_k^{\rho})^2 G_{ST}^{\rho\rho} + V_k^{\rho} V_{ST}^{\rho} \left[G_{ST}^{\rho\rho} \cos\left(\theta_k^{\rho} - \theta_{ST}^{\rho}\right) + B_{ST}^{\rho\rho} \text{sen}\left(\theta_k^{\rho} - \theta_{ST}^{\rho}\right) \right] \tag{11.15}$$

$$Q_k^{\rho} = -(V_k^{\rho})^2 B_{ST}^{\rho\rho} + V_k^{\rho} V_{ST}^{\rho} \left[G_{ST}^{\rho\rho} \text{sen}\left(\theta_k^{\rho} - \theta_{ST}^{\rho}\right) - B_{ST}^{\rho\rho} \cos\left(\theta_k^{\rho} - \theta_{ST}^{\rho}\right) \right] \tag{11.16}$$

The voltage source expressions become

$$P_{ST}^{\rho} = (V_{ST}^{\rho})^2 G_{ST}^{\rho\rho} + V_{ST}^{\rho} V_k^{\rho} \left[G_{ST}^{\rho\rho} \cos\left(\theta_{ST}^{\rho} - \theta_k^{\rho}\right) + B_{ST}^{\rho\rho} \text{sen}\left(\theta_{ST}^{\rho} - \theta_k^{\rho}\right) \right] \tag{11.17}$$

$$Q_{ST}^{\rho} = -(V_{ST}^{\rho})^2 B_{ST}^{\rho\rho} + V_{ST}^{\rho} V_k^{\rho} \left[G_{ST}^{\rho\rho} \text{sen}\left(\theta_{ST}^{\rho} - \theta_k^{\rho}\right) - B_{ST}^{\rho\rho} \cos\left(\theta_{ST}^{\rho} - \theta_k^{\rho}\right) \right] \tag{11.18}$$

Notice that for considering the STATCOM's variables in the load flow problem, two variables per phase are unknown, V_{ST}^{ρ} and θ_{ST}^{ρ}, and then six additional equations are required in the formulation.

The first equation is related to the active power restriction in the STATCOM, which may be absorbed, injected or being zero, which is included in (11.17). It is worth noting that the STATCOM cannot inject active power to the grid, unless it has a power generator or a long term energy storage element, usually a small

amount of active power is drained into the STATCOM for compensating the losses in switching devices, capacitors, etc.

The second equation can be formulated considering the prevalent conditions in the power system bus where the STATCOM is connected. For instance, in Fig. 11.3b the STATCOM is connected to the kth bus for keeping constant the voltage magnitude V_k^ρ. Thus, V_k^ρ becomes a known parameter, in the power flow formulation it can be modeled as the voltage magnitude in the STATCOM terminals V_{ST}^ρ.

Linearizing (11.15) and (11.17) around the operating point becomes

$$\begin{bmatrix} \Delta P_k^\rho \\ \Delta Q_k^\rho \\ \Delta P_{ST}^\rho \end{bmatrix} = \begin{bmatrix} \frac{\partial P_k^\rho}{\partial \theta_k^\rho} & \frac{\partial P_k^\rho}{\partial V_{ST}^\rho} V_{ST}^\rho & \frac{\partial P_k^\rho}{\partial \theta_{ST}^\rho} \\ \frac{\partial Q_k^\rho}{\partial \theta_k^\rho} & \frac{\partial Q_k^\rho}{\partial V_{ST}^\rho} V_{ST}^\rho & \frac{\partial Q_k^\rho}{\partial \theta_{ST}^\rho} \\ \frac{\partial P_{ST}^\rho}{\partial \theta_k^\rho} & \frac{\partial P_{ST}^\rho}{\partial V_{ST}^\rho} V_{ST}^\rho & \frac{\partial P_{ST}^\rho}{\partial \theta_{ST}^\rho} \end{bmatrix} \begin{bmatrix} \Delta \theta_k^\rho \\ \frac{\Delta V_{ST}^\rho}{V_{ST}^\rho} \\ \Delta \theta_{ST}^\rho \end{bmatrix} \tag{11.19}$$

Then, the STATCOM is now integrated into the steady state model of the power system. From (11.19), the STATCOM account for a row and a column in the Jacobian matrix. The new elements of this matrix has the following expressions,

$$\frac{\partial P_k^\rho}{\partial \theta_k^\rho} = -Q_k^\rho - \left(V_k^\rho\right)^2 G_{ST}^\rho \tag{11.20}$$

$$\frac{\partial P_k^\rho}{\partial V_{ST}^\rho} V_{ST}^\rho = V_k^\rho V_{ST}^\rho \left[G_{ST}^\rho \cos\left(\theta_k^\rho - \theta_{ST}^\rho\right) + B_{ST}^\rho \text{sen}\left(\theta_k^\rho - \theta_{ST}^\rho\right)\right] \tag{11.21}$$

$$\frac{\partial P_k^\rho}{\partial \theta_{ST}^\rho} = V_{ST}^\rho V_k^\rho \left[G_{ST}^\rho \cos\left(\theta_{ST}^\rho - \theta_k^\rho\right) + B_{ST}^\rho \text{sen}\left(\theta_{ST}^\rho - \theta_k^\rho\right)\right] \tag{11.22}$$

$$\frac{\partial Q_k^\rho}{\partial \theta_k^\rho} = P_k^\rho - \left(V_k^\rho\right)^2 G_{ST}^\rho \tag{11.23}$$

$$\frac{\partial Q_k^\rho}{\partial V_{ST}^\rho} V_{ST}^\rho = V_k^\rho V_{ST}^\rho \left[G_{ST}^\rho \text{sen}\left(\theta_k^\rho - \theta_{ST}^\rho\right) - B_{ST}^\rho \cos\left(\theta_k^\rho - \theta_{ST}^\rho\right)\right] \tag{11.24}$$

$$\frac{\partial Q_k^\rho}{\partial \theta_{ST}^\rho} = -V_k^\rho V_{ST}^\rho \left[G_{ST}^\rho \cos\left(\theta_k^\rho - \theta_{ST}^\rho\right) + B_{ST}^\rho \text{sen}\left(\theta_k^\rho - \theta_{ST}^\rho\right)\right] \tag{11.25}$$

$$\frac{\partial P_{ST}^\rho}{\partial \theta_k^\rho} = \frac{\partial Q_k^\rho}{\partial V_{ST}^\rho} \partial V_{ST}^\rho \tag{11.26}$$

$$\frac{\partial P_{ST}^\rho}{\partial V_{ST}^\rho} V_{ST}^\rho = P_{ST}^\rho + \left(V_{ST}^\rho\right)^2 G_{ST}^\rho \tag{11.27}$$

$$\frac{\partial P_{ST}^\rho}{\partial \theta_{ST}^\rho} = -Q_{ST}^\rho - \left(V_{ST}^\rho\right)^2 B_{ST}^\rho \tag{11.28}$$

The STATCOM's reference voltage is set at the end of each iteration to ensure the voltage limits are not exceeded. If a limit is exceeded the magnitude voltage of the STATCOM terminal is set to the exceeded limit value, under this circumstances, in (11.19) V_{ST}^{ρ} is changed by V_k^{ρ}, which indicates that the voltage is no longer controlled in that bus. The linearized equation of the system is presented in (11.29)

$$\begin{bmatrix} \Delta P_k^{\rho} \\ \Delta Q_k^{\rho} \\ \Delta P_{ST}^{\rho} \end{bmatrix} = \begin{bmatrix} \frac{\partial P_k^{\rho}}{\partial \theta_k^{\rho}} & \frac{\partial P_k^{\rho}}{\partial V_k^{\rho}} V_k^{\rho} & \frac{\partial P_k^{\rho}}{\partial \theta_{ST}^{\rho}} \\ \frac{\partial Q_k^{\rho}}{\partial \theta_k^{\rho}} & \frac{\partial Q_k^{\rho}}{\partial V_k^{\rho}} V_k^{\rho} & \frac{\partial Q_k^{\rho}}{\partial \theta_{ST}^{\rho}} \\ \frac{\partial P_{ST}^{\rho}}{\partial \theta_k^{\rho}} & \frac{\partial P_{ST}^{\rho}}{\partial V_k^{\rho}} V_k^{\rho} & \frac{\partial P_{ST}^{\rho}}{\partial \theta_{ST}^{\rho}} \end{bmatrix} \begin{bmatrix} \Delta \theta_k^{\rho} \\ \frac{\Delta V_k^{\rho}}{V_k^{\rho}} \\ \Delta \theta_{ST}^{\rho} \end{bmatrix} \tag{11.29}$$

11.4 Case Study

Figure 11.5 depicts a schematic diagram of the New England system [13], which is being utilized as test system in this chapter.

New England scheme is referred to in the open research since represents an equivalent of 345 kV power system that interconnects New England area in the United States with the Canadian electrical system, which is composed by 10 equivalents generators, 39 buses and 46 transmission links (including transmission lines and transformers). This system has been widely studied from the voltage stability viewpoint [14, 15], the main reason for this is that presents an appropriate test system for different analysis. The shaded area is explained later in this chapter.

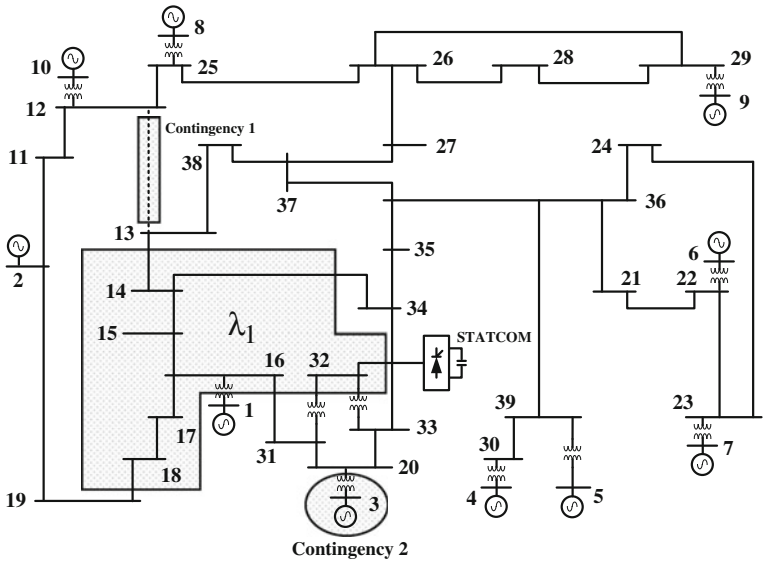

Fig. 11.5 One-line scheme of the test power system

The process to evaluate the voltage stability performance of the New England test system and the effects with the inclusion of the STATCOM mainly involves two steps:

1. Analysis of a reference case.
2. Analysis of three-phase unbalanced cases.

11.4.1 Analysis of the Reference Case

In order to establish a Base Case of Operation (BCOP) to study voltage stability, the analysis' aim of the BCOP is to determine the parameters that are used as a Ref. [16], and then quantify the variations of the reached results for other study cases. Then, it is important to take the following assumptions into account.

Each examined case is defined only on the basis of the interconnection scheme that prevails among the elements of the system. For the BCOP used in this chapter, the system operates with all its elements connected; this means that while the topology is not modified respect to the output of any element, such as a transmission line or a generator. The corresponding operating point is named BCOP. Contingencies are not assumed for the BCOP. Three-phase balanced parameters are another particular feature of the BCOP. Therefore, for such condition it is feasible to use a single-phase power flow analysis program. The main purpose of this assumption is to calculate some parameters as a reference for the unbalanced three-phase cases, without the need to take too much computational time.

A single-phase power flow program follows some recommendations [7], such as:

1. Capacities of Generators are represented by its reactive power limits.
2. Loads are established as constant power.
3. Taps of the transformers are kept in its nominal position.
4. Active power dispatch is fixed.
5. Single slack bus is utilized.

Regarding to the STATCOM characteristics, there are some premises included into the power flow algorithm:

- The bus where the STATCOM is connected is considered as conventional PV bus.
- The STATCOM's operating limits are function of voltage magnitudes kept in their terminals, and are: 1.1 pu as upper limit and 0.9 pu as lower limit. When the STATCOM violates any of these two limits, the voltage magnitude at its terminals is fixed at the violated limit value and the bus where it is connected, change from PV to PQ bus [17].
- The connection process between the STATCOM with the system is considered as instantaneous, this does not cause disturbances on other elements in the system,

and harmonic components that occur due to internal processes are neglected; just the fundamental frequency components are taken into account.

- The active power consumed by the STATCOM is zero, this is controlled by means of the phase angles corresponding to the terminals $\theta_{st} = \theta_k$. This is assumed in all simulations.

Proper management of single-phase power flow algorithm and taking advantage of factors that could be obtained, the next step in the analysis focuses to identify and define the weakest area in terms of voltage. In order to achieve this goal, nodal analysis can be executed [18]. If the most critical areas are properly identified along with their respective elements, then, the most severe operating conditions are identified, which may correspond to different topologies for these particular zones.

The methodology used to delimit the most vulnerable area in the New England test system is described in the following. Starting from an initial state of load, which for convenience is defined as "*current operating point*", an algorithm is implemented to overload the system until the "*critical point of voltage*" is reached. In other words, the algorithm reaches the condition when the system collapses. By modal analysis, the critical modes are a clear index to identify the loadability limit [8, 15, 17].

The procedure executed to bring the power system to an overload is that for building a PV-curve. This consists of increasing active and reactive power according to a specified weighting factor called "*K*". During the implemented simulation process, the load is gradually increased, according to the *K* factor. In each of these steps, power flow analysis is implemented and the attained solution is stored. For each operating point, the Jacobian matrix is calculated J_R [8, 18, 19], and its eigenvalue analysis is carried out. This is done with the aim of verifying the voltage stability condition. If the minimum eigenvalue calculated 'λ_{min}' is bigger than zero, the system is stable in terms of voltage, then power flow analysis is done again increasing the load. This procedure is repeated until the point of voltage collapse arises, which is achieved when 'λ_{min}' is equal to or less than zero.

Simultaneously with the power load increment, the active power generation is also augmented through the same "*K*" factor considered for the loads. Although this guess may not be regarded as realistic, numerical instability problems are avoided in the Newton–Rapshon algorithm [14]. As generators' active power increase, reactive power limits are changing as well; since it is considered that operate under a constant power factor.

Notice that some non-linearities are presented within the process. For instance, those related to the excitation system. Pragmatically, acceptable results have been shown using this technique, with a good approximation to the point of voltage collapse [8, 15, 17].

Once the critical point of voltage has been detected and with the power flow information, all necessary conditions for the voltage stability margin can be calculated; it is a function of the KSP. This margin is defined as the difference between the value of KSP at the current operating point and the critical point of collapse [7]. In the following analysis, the KSP is chosen as the total load active power of the system.

Thus, once the eigenvalues associated to the Jacobian matrix J_R, (λ_1, λ_2,…, λ_n), have been calculated, the purpose is to identify the critical modes [8, 18, 19]. In most cases, critical modes are selected based on the eigenvalues' magnitudes; while smaller the magnitude, lesser stable. It is noteworthy that the minimum eigenvalue calculated does not necessarily become the most critical mode, this is mainly due to some devices' non-linearities cannot be fully captured within the formulation. Although it is impractical and unnecessary to calculate all eigenvalues of the J_R matrix, it is recommended to verify 2–5 eigenvalues in detail [20], since if the smallest eigenvalues "r" are obtained along with their respective eigenvectors, then critical modes are obtained successfully. Regarding to this topic, significant progress has been presented in the applied mathematics, as well as in power systems in order to develop simulation algorithms that allow carrying out partial eigenvalues analysis [20–22].

Since New England test system used in the analysis is small compared to an actual power system with thousands of buses; modal analysis is made with conventional calculation routines, where only the critical mode is examined. For identifying critical modes, elements such as bus, transmission lines, and generator, with greater participation are classified. This is done calculating the factor defined as follows [16, 17]:

(a) Participation factor of a bus: $P_{ki} = \xi_{ki} n_{ik}$

(b) Participation factor of a branch: $PF^{(i)}_{branch\,km} = \dfrac{\Delta Q^{(i)}_{losses\,km}}{\max\left[\Delta Q^{(i)}_{system\,losses}\right]}$

(c) Participation factor of a generator: $PF^{(i)}_{GK} = \dfrac{\Delta Q^{(i)}_{GK}}{\max\left[\Delta Q^{(i)}_{G,\,system}\right]}$

where; 'ξ_{ki}' and 'η_{ik}' are the right and left eigenvectors, respectively.

Through the calculation of these factors, the location of weakest elements within the structure of the system is determined. Some study cases are selected as follows:

- Contingencies to study (output of a transmission line or generator)
- Selection of a bus where the STATCOM is connected.

Once the factors have been established, the most vulnerable area under voltage stability can be delimited and on which implementation of corrective actions must be focused.

Thus, for this analysis, the followed steps become:

1. Specify particular operating conditions.
2. Load increment until the critical point of collapse is detected.
3. Calculation of voltage stability margin.
4. Execute modal analysis.
5. Calculate participation factors.
6. Selection of contingencies, buses to compensate and the most vulnerable area.

These listed steps are applied only for the BCOP; thus modal analysis is mainly utilized to delimit the area of interest for voltage stability study. Then, for the cases

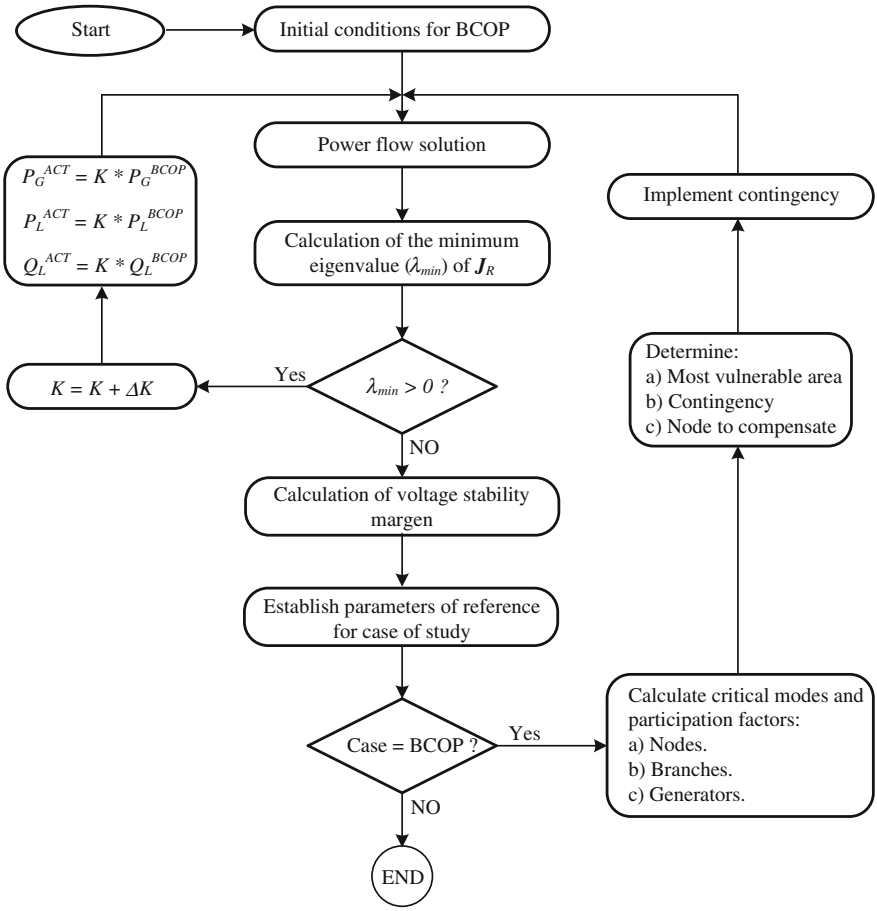

Fig. 11.6 Flowchart to establish reference parameters

where contingencies are deployed, steps 1–3 are applied. Figure 11.6 displays a flowchart of the above-mentioned procedure.

The superscript BCOP indicates original parameters of the current operating point. On the other hand, the superscript ACT, denotes updated values.

11.4.2 Analysis of Three-Phase Unbalanced Cases

Unbalanced operating conditions for steady state three-phase cases are discussed below. In general, the assumptions for single-phase power flow algorithm are also applied to the three-phase power flow study. The specific characteristics that need to be mentioned for this case are as following:

- In order to take into account STATCOM's limits into the three-phase formulation when it operates under unbalanced conditions, once any of its three-phases has violated voltage magnitude limits, automatically the three-phases are placed at the value of the violated limit. The STATCOM's controls do not consider independence between phases, in other words, it only has one degree of freedom. Same concept applies for the generators' reactive power limits.
- Loads are modeled as constant power and they are considered as star neutral connection to ground.

Figure 11.7 describes the essence of the implemented methodology to evaluate voltage stability limits over a three-phase reference frame. For example, factor K is applied in equal magnitude for all three-phases of each load. Therefore, before executing the routine, an unbalance of load is processed, Fig. 11.7.

Regarding to the eigenvalues calculation, 'n_l' describes the number of existing load buses. For the single-phase case, the Jacobian matrix J_R has dimension of ($n_l \times n_l$) with 'n_l' eigenvalues. Hence, on the three-phase case, J_R has dimension ($n_l \times 3 \times n_l \times 3$), with the corresponding '$n_l \times 3$' eigenvalues, where these values may be real or complex conjugates. For this application, just eigenvalues with real part are taken into account, discarding the complex conjugates.

According to the defined criteria to assess the system stability,

- If $\lambda_i > 0$, the system is stable in terms of voltage.
- If $\lambda_i < 0$, the system experiences a condition of voltage instability.
- If $\lambda_i = 0$, this is a voltage collapse condition.

The value and sequence that is attained for each eigenvalue (real or complex conjugates) cannot be determined with precision because it depends on the specific operating condition. In addition, based on the study of different cases, the number of eigenvalues with real part decreases while load is augmented considerably, which leads to an increment of the complex conjugate eigenvalues.

Acceptable results are obtained taking into account only eigenvalues with real part considering a three-phase analysis as shown bellow. This can be concluded based on comparison done with the single-phase analysis, where there is not the case of having complex conjugate eigenvalues, unless the system has a condition of voltage instability fully identified.

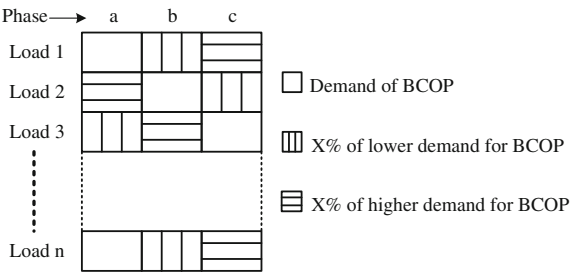

Fig. 11.7 Strategy to implement unbalanced conditions

The calculation of the participation factor is no longer performed for the three-phase analysis; however, a detailed analysis of system's parameters is done to implement the selected contingencies, considering compensation with the STATCOM as well without it. Outlines of the implemented steps are summarized in Fig. 11.8.

11.4.3 Results

In this section, simulating results are presented for the above-mentioned methodology applied to the New England power system, on which the performance of the model used for the three-phase STATCOM is evaluated and its impact on voltage stability. Initially, single-phase case is discussed to use it as a reference, then, an evaluation is reviewed for three-phase unbalanced cases. The synchronous machine 4th order model is used, equipped with an excitation system and a governor; its parameters are taken from [14]. Loads are modeled as constant power. Newton Raphson and Runge Kutta are used to solve the algebraic and differential equations, respectively.

11.4.3.1 Single-Phase Analysis

Some features assumed for the BCOP of New England system have already been defined. Some established conditions are taken into account for its analysis:

- The contingencies are not implemented; therefore, the system normally operates with all its elements.
- Balanced three-phase system.
- Original conditions of total load correspond to 6,126.5 MW and 1,593.4 MVAr. These load are taken as a reference to define the *current operating point* [2].
- Slack generator corresponds to the one installed on bus one illustrated in Fig. 11.5
- Unlike other researchers that have used New England as a test system for voltage stability study, here transformers of generators are not removed from the analysis, since they are a fundamental factor to balance total losses that prevail in the system. As above-mentioned, these transformers as well as those in the transmission network are considered with their taps at the nominal positions.

11.4.3.2 Voltage Stability Margin Calculation

In accordance to the flowchart depicted in Fig. 11.8, the analysis begins with the routine of overload until critical point of voltage collapse is detected for the BCOP. Within the algorithm, the factor K is specified with an increment of K = 0.01;

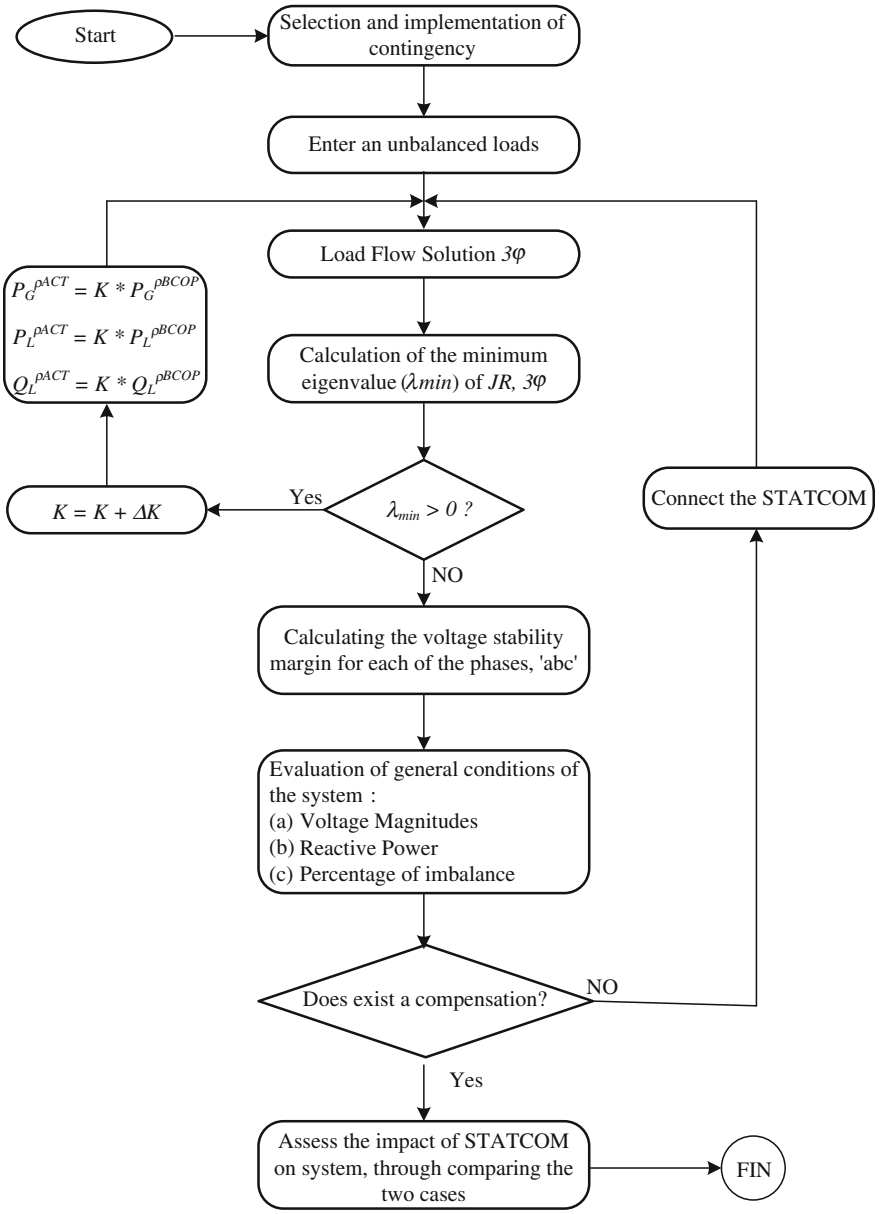

Fig. 11.8 Flowchart of the implemented steps for three-phase analysis

then, this factor remains constant throughout the routine. Therefore, each load is increased by 1 % on their original value. This procedure allows the calculation of the PV-curve for the BCOP. It is worth noting that this factor is the same for all cases simulated.

PV-curves generally depict the active power of total load in MW versus voltage magnitude on any bus of the system in per unit. Therefore, for this purpose it is necessary to choose a bus test.

Table 11.1 summarizes the solution for the BCOP through single-phase power flow algorithm. From this information, voltage magnitudes are analyzed for all load buses. Column four and five correspond to the active and reactive generated power, respectively. Column six and seven represent the active and reactive load power, while last column corresponds to the type of node (1–slack; 2–PV, 3–PQ). Notice that bus 32 has the smallest magnitude with value of 0.9397 pu Thus, this bus is chosen as test bus to plot PV-curves. This process is arbitrary and it is not an established rule; a similar result is obtained to choose another bus in the system without losing the generality of the PV-curve. On the other hand, the calculation of a complete PV-curve is usually not required in conventional studies for planning and operation [16]. According to this recommendation, only the top of the PV-curve is depicted, corresponding to all cases where the system is stable. Figure 11.9 illustrates the PV-curve getting for the BCOP.

Power flow results correspond to an operation condition with all elements of the system in operation, where:

- $|V|$, P_G, Q_G, P_D, Q_D, in (pu).
- θ in degrees.

Type1 = Slack; Type 2 = PV; Type 3 = Q.

The load condition for reaching the collapse, corresponds to 9,725.7 MW and 2,530.3 MVAr. These load values are taken as a reference to define the critical voltage point to the BCOP.

From Fig. 11.9 the voltage stability margin may be estimated; this value corresponds to 3,601.2 MW, which is equivalent to a load increment of 58.8 % over the BCOP.

The advantages of the PV-curve calculation for the BCOP's analysis are clear. There are two operating points that are of particular concern.

1. *Current operating point.*
2. *Critical voltage point.*

Subsequently more cases are defined, each one have their respective operating points to be analyzed (current and critical ones).

11.4.3.3 Modal Analysis

From the prevailing conditions for the BCOP's critical voltage point, modal analysis is performed. The following features are ascertained: if New England power system is considered without generators buses, the system comprises a total of 29 buses to be analyzed.

Tables 11.6, 11.7, 11.8 and 11.9 summarize information related to different parameters of modal analysis for BCOP. Note that provided data, have been

Table 11.1 Steady state solution

Bus	|V|	Θ	P_G	Q_G	P_D	Q_D	Tipo
1	1.0000	0	5.5167	2.0657	0.0920	0.0460	1
2	1.0300	−10.6993	10.000	2.1354	11.040	2.5000	2
3	0.9830	2.5108	6.5000	1.4449	0.0	0.0	2
4	1.0120	3.4129	5.0800	1.5308	0.0	0.0	2
5	0.9970	4.4336	6.3200	0.8011	0.0	0.0	2
6	1.0490	5.4360	6.5000	2.7532	0.0	0.0	2
7	1.0640	8.2210	5.6000	2.2921	0.0	0.0	2
8	1.0280	2.0914	5.4000	0.2430	0.0	0.0	2
9	1.0270	7.7804	8.3000	0.5811	0.0	0.0	2
10	1.0480	−3.7611	2.5000	1.8007	0.0	0.0	2
11	1.0355	−9.0557	0.0	0.0	0.0	0.0	3
12	1.0178	−6.1924	0.0	0.0	0.0	0.0	3
13	0.9879	−9.1862	0.0	0.0	3.2200	0.0240	3
14	0.9545	−10.1203	0.0	0.0	5.0000	1.8400	3
15	0.9572	−8.8885	0.0	0.0	0.0	0.0	3
16	0.9591	−8.1285	0.0	0.0	0.0	0.0	3
17	0.9507	−10.5488	0.0	0.0	2.3380	0.8400	3
18	0.9512	−11.1032	0.0	0.0	5.2200	1.7600	3
19	1.0097	−10.9152	0.0	0.0	0.0	0.0	3
20	0.9627	−5.3847	0.0	0.0	0.0	0.0	3
21	0.9859	−4.0964	0.0	0.0	2.7400	1.1500	3
22	1.0153	0.4294	0.0	0.0	0.0	0.0	3
23	1.0128	0.1566	0.0	0.0	2.7450	0.8466	3
24	0.9748	−6.5530	0.0	0.0	3.0860	0.9220	3
25	1.0266	−4.7182	0.0	0.0	2.2400	0.4720	3
26	1.0135	−5.9545	0.0	0.0	1.3900	0.1700	3
27	0.9932	−8.0732	0.0	0.0	2.8100	0.7550	3
28	1.0172	−2.2195	0.0	0.0	2.0600	0.2760	3
29	1.0195	0.7022	0.0	0.0	2.8350	0.2690	3
30	0.9843	−1.7746	0.0	0.0	6.2800	1.0300	3
31	0.9601	−6.3223	0.0	0.0	0.0	0.0	3
32	0.9397	−6.3025	0.0	0.0	0.0750	0.8800	3
33	0.9602	−6.1649	0.0	0.0	0.0	0.0	3
34	0.9586	−7.9833	0.0	0.0	0.0	0.0	3
35	0.9590	−8.2865	0.0	0.0	3.2000	1.5300	3
36	0.9751	−6.6434	0.0	0.0	3.2940	0.3230	3
37	0.9830	−7.8488	0.0	0.0	0.0	0.0	3
38	0.9834	−8.8315	0.0	0.0	1.5800	0.3000	3
39	0.9852	−0.7757	0.0	0.0	0.0	0.0	3

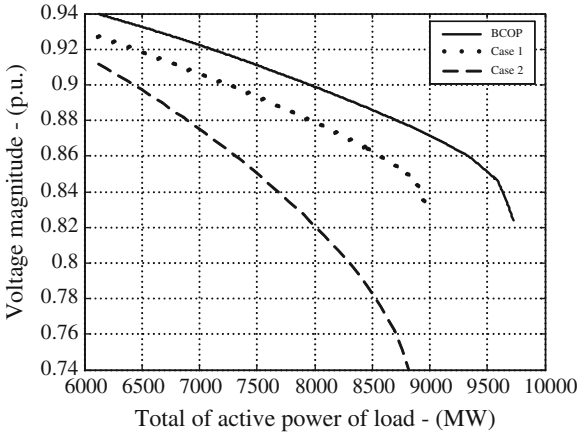

Fig. 11.9 PV-curves at bus 32

Table 11.2 BCOP's critical modes

Mode	Magnitude
1	5.9840
2	13.5383
3	26.1270
4	26.9969
5	39.2448

calculated on the basis of specific conditions for the BCOP's critical point, which corresponds to 9,725.7 MW and 2,530.3 MVAr. Table 11.2 illustrates the 5 modes less stable.

All these modes are positive, indicating that the system is stable in terms of voltage. However, if an extra iteration is made with their respective factor, some negative and complex conjugate eigenvalues will appear, denoting an instability voltage condition.

After that, the bus that are strongly related to the less stable modes are determined. This is done by calculating the participation factor 'FP_n', just for the two less stable modes. Table 11.3 depicts results of the participation factor of bus 'FP_n'.

The main result got from the analysis of participation factor of the bus, draws two areas exposed to problems of voltage stability. The area associated to mode 1 is considered more vulnerable. Buses associated with this area are remarked in Table 11.3, and the buses that are closer to generator 1, Fig. 11.5. In other words, those buses are the most significant modes that influence on the behavior of this phenomenon. Another advantage of this study is that allows determining the bus where the STATCOM should be connected. Since its magnitude is a measure of effectiveness that can be obtained by applying corrective measures. In this case, bus number 32 is selected for the STATCOM allocation.

Regarding to the contribution of transmission lines and generators on the problem, the participation factor of branches 'FP_{branch}' corresponding to mode 1

Table 11.3 Participation factors of buses for BCOP

Mode1		Mode 2	
Bus	FP_n	Bus	FP_n
32	0.1069	27	0.1046
17	0.0664	32	0.1031
34	0.0662	26	0.0727
14	0.0658	37	0.0713
18	0.0642	24	0.0635
15	0.0596	38	0.0539
33	0.0587	36	0.0529
31	0.0554	21	0.0522
16	0.0543	28	0.0475

Table 11.4 Participation factors of branches for mode 1 of BCOP

Transmission line		FP_{branch}
Sending bus	Receiving bus	
36	39	1
12	13	0.8545
18	19	0.8102
19	2	0.5506
21	22	0.4367
13	14	0.4043

Table 11.5 Participation factors of generators for mode 1 of BCOP

Bus	FP_{gen}
3	1
2	0.5777
6	0.5498
10	0.4365
5	0.4297
9	0.3539
8	0.3207
7	0.3199

are evaluated. Results are shown in Table 11.4, while the participation factors of generators 'FP_{gen}' are summarized in Table 11.5.

The participation factors of branches and generators help to determine contingencies that are implemented in simulations. This is a very important point in a voltage stability study, since contingencies are inherently related to the power system operation. In this context two contingencies are selected,

1. Transmission lines tripping.
2. Generators tripping.

In the case of a transmission line tripping, the used criterion is according to the line that exhibits greater participation for the mode under study. Regarding to data of Table 11.4, line 36–39 should be chosen using the mentioned criterion; however, generators 4 and 5 are excluded if this contingency is implemented; since this line links these generators, Fig. 11.5. Hence, this option is discarded. The following option corresponds to the transmission line linking buses 12–13. Although both transmission lines are identified, only one is implemented on the three-phase simulations. On the other hand, the chosen contingency for a generator's tripping becomes the number 3, since is the closest one to the study area. These two contingencies represent severe conditions for the mode under analysis.

In summary, applying modal analysis to the test system, the final result is represented graphically in Fig. 11.5, where it marks the weaker area through the shaded zone associated with the less stable mode. Additionally, two specific contingencies are stated, and the STATCOM's allocation for cases where compensation is required.

According to the algorithm established in Fig. 11.6, particular characteristics are defined for the analyzed cases:

- Case 1: BCOP.
- Case 2: A transmission line contingency.
- Case 3: A generator contingency.

For the three study cases, the current operating point, utilized to calculate PV-curves, the load level is 6,426.5 MW and 1,593.4 MVAr. Therefore, the difference among cases lies on the topology and not on the load level. In addition to the established objectives, the single-phase procedure determines the following parameters:

(a) Voltage stability margin.
(b) Level of voltage magnitude.
(c) Powers in the system.

Some BCOP parameters have already been calculated in the previous section and for the sake of brevity the details for cases 2 and 3 are omitted. Overall, the methodology used in these cases for calculating the PV-curves is done by running the routine when the system is overloaded. Figure 11.9 displays the PV-curves for the three cases. The bus under study is 32.

In Table 11.6, the results of the voltage stability margin for each case are summarized.

Table 11.6 Range of voltage stability (MW)

Case	Current operating point	Critical voltage point	Margin
1	6,126.5	9,725.7	3,601.2
2	6,126.5	8,960.1	2,835.6
3	6,126.5	8,819.3	2,696.8

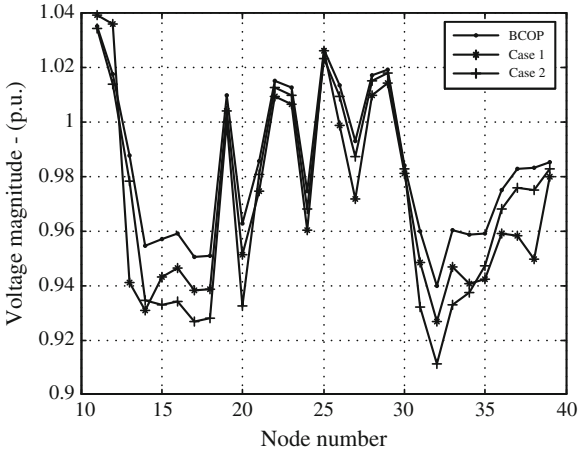

Fig. 11.10 Voltage magnitude at the load buses

Based on Table 11.6, for case 2 the voltage stability margin decreases by about 21 % compared to the BCOP, equivalent to a reduction of 765.6 MW. For case 3, the margin is reduced by 25 %, 906.4 MW lower than the BCOP. Regarding to the voltage magnitude, Fig. 11.10 exhibits the changes experienced by load bus when the system is subjected to operating conditions involving different study cases.

The "current operating point" is taken as a reference of the load conditions for calculating the parameters shown in Fig. 11.10. Generating voltages at buses (1–10) are not shown, since for these load conditions are constant. In Fig. 11.11a, the behaviour of powers is presented, while Fig. 11.11b presents the system losses.

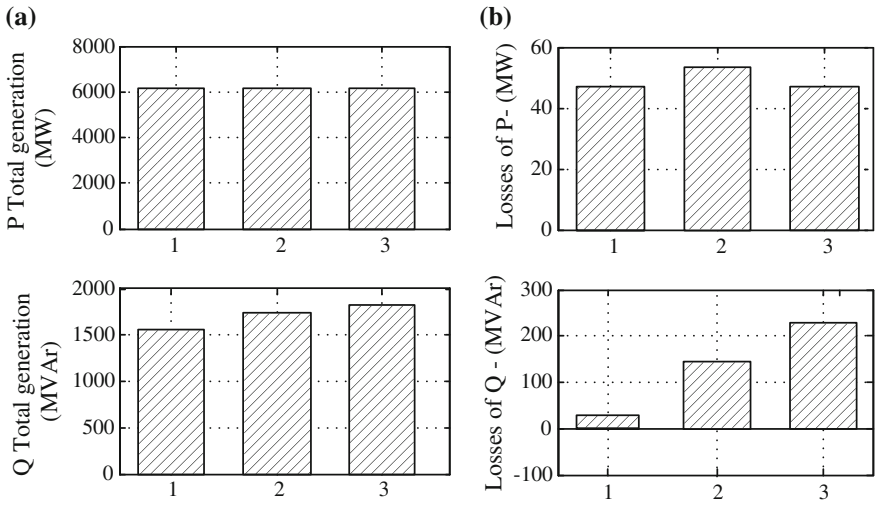

Fig. 11.11 **a** Total generation powers. **b** Total system losses

Furthermore, considering the load condition of the current operating point as a reference, it is possible to conclude that: The changes in the system topology result in minimal variations on the active power behaviour compared with those for the reactive power. It is for this reason that for the three-phase cases discussed in the next section, the analysis is focused only on reactive power changes.

Finally, single-phase simulations are also implemented considering the STATCOM within the system structure; these results are not shown graphically but are cited as references in the three-phase cases.

11.4.3.4 Unbalanced Three-Phase Cases

In this section, the three-phase STATCOM performance is evaluated; this is done through simulations involving severe operating conditions such as unbalanced overloads. One of the main objectives of this evaluation is to examine its operation effects on three-phase voltage stability margin and the voltage level prevailing at each bus, in addition to its overall impact on the system behaviour. According to the results obtained previously for the participation factors, one STATCOM is connected at bus 32. To identify each three-phase unbalanced study, the contingencies are subdivided as follows in the next four cases:

- Case 2a: Implementation of line contingency without compensation.
- Case 2b: Implementation of line contingency with compensation.
- Case 3a: Implementation of generator contingency without compensation.
- Case 3b: Implementation of generator contingency with compensation.

The compensated cases are referred to the STATCOM.
According to Fig. 11.7, the percentages of load unbalance become:

(a) Percentage of BCOP lower than the load: 1.7 %.
(b) Percentage of BCOP higher than the load: 3.2 %.

The New England test system has 19 load buses, which are illustrated in Table 11.1. Applying an unbalance factor to all loads through the specified sequence, Fig. 11.7, the total power demand is calculated, Table 11.7.

For the three-phase unbalanced cases, the power values shown in Table 11.7 are taken as the starting point of analysis. This is equivalent to the current operating point defined by the BCOP. Then cases 2a and 2b are compared. Following the flowchart shown in Fig. 11.8 for the four cases, the three-phase voltage stability margins are illustrated in Fig. 11.12.

Table 11.7 Total power of the unbalanced loads

Total active power (MW)			Total reactive power (MVAr)		
Phase *a*	Phase *b*	Phase *c*	Phase *a*	Phase *b*	Phase *c*
6,159.12	6,177.57	6,128.59	1,606.87	1,600.33	1,598.78

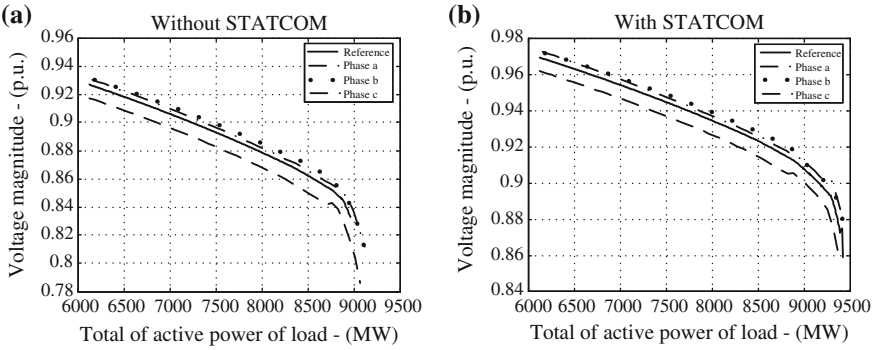

Fig. 11.12 Three-phase voltage stability margins at bus 32. **a** Case 2a; **b** Case 2b

Table 11.8 Voltage stability margins (MW)

Case	Single-phase	Three-phase		
		Phase *a*	Phase *b*	Phase *c*
2a	2,835.6	2,956.4	2,965.2	2,941.7
2b	3,295.1	3,266.4	3,276.1	3,248.2

According to these PV-curves, notice the difference between the attained results for calculating the voltage stability margin considering a single-phase respect to three-phase unbalanced condition. In both cases, the references correspond to that for the single-phase operating condition. Table 11.8 shows the results for different margins, according to the case and the considered phase.

Analysing Table 11.8, notice that depending on the operating conditions and the reference frame in question, different effects arise. For example, for Case 2a, the single-phase reference corresponds to 2,835.6 MW, and instead the three-phase results reveal that the margin is around 2,950 MW per phase; there is a difference of 100 MW between both cases. Furthermore, for Case 2b, the calculated three-phase condition, the margin is lower than that of the single-phase case in an average of 40 MW per phase. This means that in order to get results closer to the actual system, it is necessary to take into account these unbalances.

Note in Fig. 11.12, phases *a* and *b*, that there is a significant unbalance between the voltage magnitudes, regardless the STATCOM operation [16]. It is assumed that the STATCOM is able to keep the voltage magnitude at bus 32 in 1 pu; this is a significant constraint for the demanding conditions of the original test system. The remaining STATCOM's parameters used in these simulations are shown in Table 11.9.

Table 11.9 STATCOM data

Bus	R_{stat}	X_{stat}	V_{esp}	V_{max}	V_{min}
32	0.0	0.1	1.0	1.1	0.9

where:

R_{stat} is the coupling transformer's resistance (pu).
X_{stat} is the coupling transformer's reactance (pu).
V_{esp} desired voltage magnitude at bus 32 (pu).
$V_{\max}$ STATCOM terminal voltage upper limit (pu).
$V_{\min}$ STATCOM terminal voltage lower limit (pu).

Separating each of the stages shown in Fig. 11.12a, b, corresponding to bus 32, the results in Fig. 11.13 are obtained.

Figures 11.13a–c clearly indicate the STATCOM's effects at the compensated bus. Figures show that although operating limits are violated, the STATCOM increases the voltage stability margin by an average of 10 % per phase, which for the analysed cases, corresponds to 300 MW. Furthermore, the voltage magnitude is improved about 5 %, equivalent to 0.05 pu, and this factor is maintained throughout the overload process, which verifies that the STATCOM operation is unaffected by the low-voltage at the bus where it is connected.

STATCOM impacts on the general system's conditions. An overview of voltage levels at the load buses per-phase is illustrated in Fig. 11.14. The operating conditions taken into account for calculating these signals are presented in Table 11.7.

The voltage magnitudes in Fig. 11.14 imply that the effects of STATCOM are higher at the bus where it is connected; such effects are less on the neighbor buses.

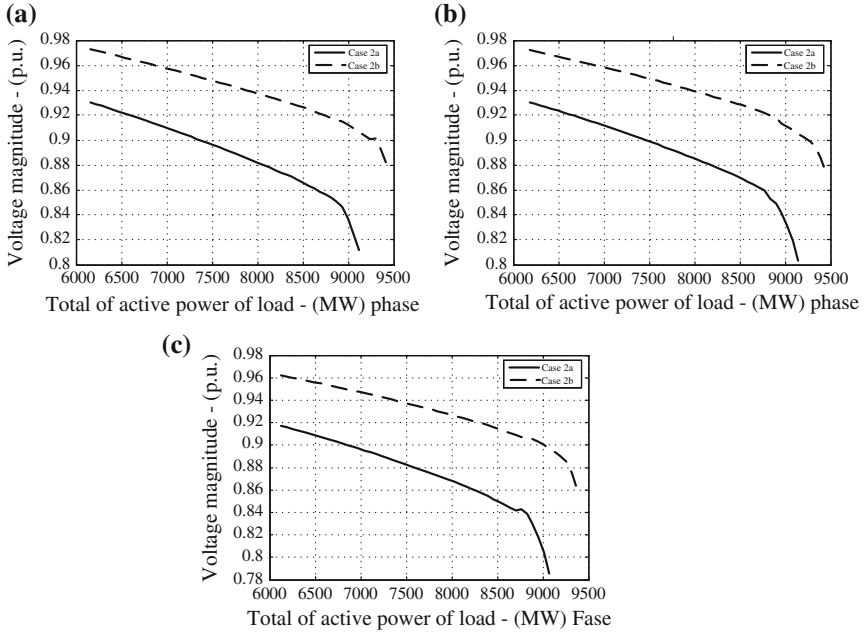

Fig. 11.13 Margins per phase at bus 32. Total of active power of load—(MW) phase (**a**). Total of active power of load—(MW) phase (**b**). Total of active power of load—(MW) Fase (**c**)

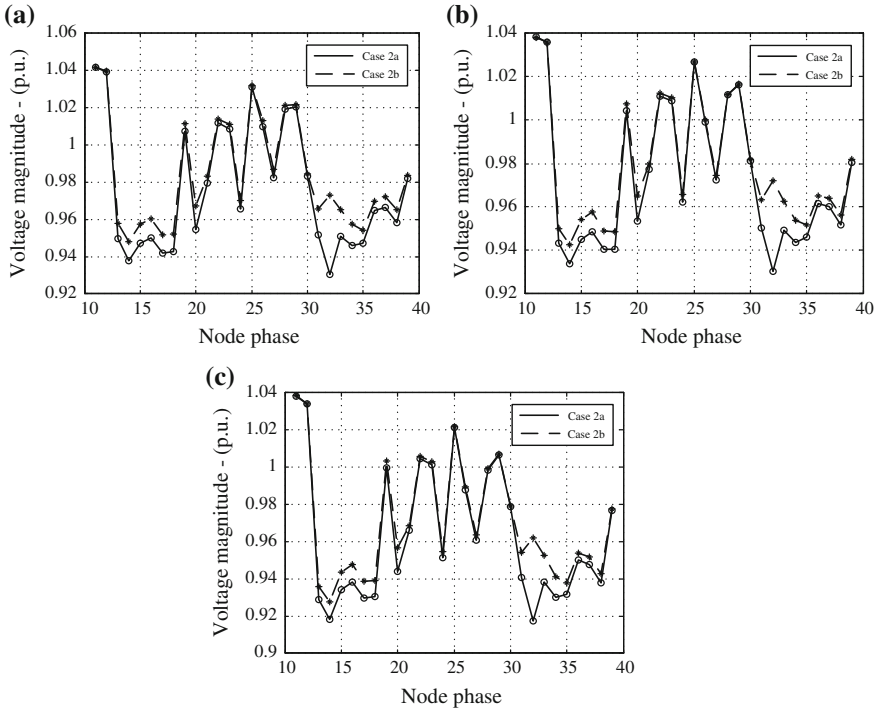

Fig. 11.14 Per phase voltage magnitude at load buses. Node phase (**a**). Node phase (**b**). Node phase (**c**)

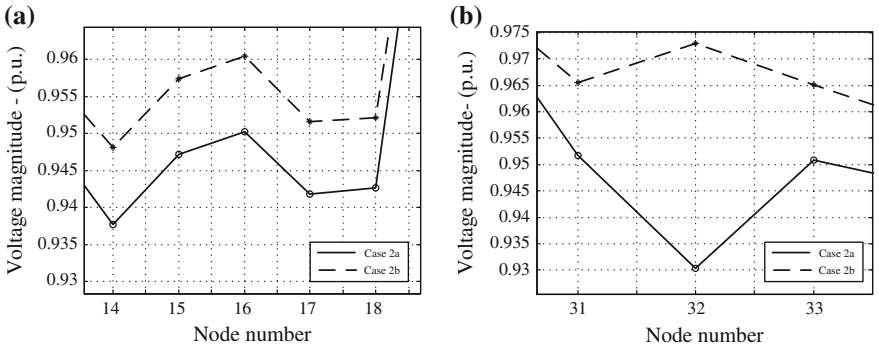

Fig. 11.15 Voltage magnitude at the buses of the weakest area, phase *a*

This can be noticed by referring to the bus involved in the shaded area in Fig. 11.5, identified as the most vulnerable area of the test system. Buses with a lower voltage level are 14–16 and 31–33, Fig. 11.14. A zoom of Fig. 11.14 is depicted in Fig. 11.15.

Table 11.10 Reactive power supplied by the generators (MVAr)

Case	Generator 1			Generator 3		
	Phase *a*	Phase *b*	Phase *c*	Phase *a*	Phase *b*	Phase *c*
2a	276.63	236.66	286.655	197.42	201.64	213.09
2b	237.52	195.46	250.76	136.77	141.55	150.89

Table 11.11 Reactive power supplied by the STATCOM, (MVAr)

Phase *a*	Phase *b*	Phase *c*
139.98	142.81	149.31

Notice from Figs. 11.14 and 11.15 that the results of the modal analysis are verified, because according to these principles, the specific location for the STATCOM, based on the most unstable mode should help to improve the operating conditions in those buses significantly associated with the critical mode. Similar behaviour can be observed for phases *b* and *c*.

A constant power load is assumed to analyse the reactive power behaviour in the system. The studied generators are those at buses 1 and 3. Table 11.10 presents the values of the generated reactive power for Cases 2a and 2b.

Fron Table 11.10 it follows that the STATCOM helps to reduce the reactive power output of generators. For example, the decrement in the generator 1 is about 15 %, and with respect to the generator 3, the reduction is approximately 30 %. With this, the possibilities that generators can achieve their operational limits, especially those for the excitation system are considerably reduced. These two generators are the most favoured by the inclusion of the STATCOM. In general, all generators diminish its reactive power output. The reactive power provided by STATCOM in case 2b is shown in Table 11.11. Likewise, the power losses in the transformers connected to bus 32 are summarized in Table 11.12.

In both transformers, the losses are significantly reduced, about 90 % for the transformer between buses 31–32, and about 80 % for the other, buses 32–33.

Table 11.13 illustrates total losses for cases 2a and 2b. In Tables 11.13 and 11.14 the following concepts stand for:

Margin: Stability voltage margin, (MW).
Magnitude: Voltage magnitude at bus 32, (pu).
Losses: Total reactive power losses, (MVAr).
V-STATCOM: Terminal voltage magnitude of the STATCOM, (pu).
Q-STATCOM: Active power generated by the STATCOM, (MVAr).

Table 11.12 Transformers' reactive power losses (MVAr)

Case	Transformers between buses 31–32			Transformers between buses 32–33		
	Phase *a*	Phase *b*	Phase *c*	Phase *a*	Phase *b*	Phase *c*
2a	1.0608	0.9455	1.2190	0.9312	0.8619	1.0028
2b	0.1371	0.1879	0.1704	0.1738	0.2031	0.2108

Table 11.13 Parameters corresponding to the line's contingency

Parameters	Without STATCOM			With STATCOM		
	Phase *a*	Phase *b*	Phase *c*	Phase *a*	Phase *b*	Phase *c*
Margin	2,956.4	2,965.2	2,941.7	3,266.4	3,276.1	3,248.2
Magnitude	0.9304	0.9325	0.9406	0.9729	0.9721	0.9621
Losses	111.98	138.29	216.68	78.38	113.98	185.83
V-STATCOM	–	–	–	1.1	1.1	1.1
Q-STATCOM	–	–	–	139.99	142.81	149.31

Table 11.14 Parameters corresponding to generator's contingency

Parameters	Without STATCOM			With STATCOM		
	Phase *a*	Phase *b*	Phase *c*	Phase *a*	Phase *b*	Phase *c*
Margin	2,956.4	2,965.2	2,941.7	3,266.4	3,276.1	3,248.2
Magnitude	0.9304	0.9325	0.9406	0.9729	0.9721	0.9621
Losses	111.98	138.29	216.68	78.38	113.98	185.83
V-STATCOM	–	–	–	1.1	1.1	1.1
Q-STATCOM	–	–	–	139.99	142.81	149.31

Notice that there is a notorious unbalance between phases, especially between *a* and *c*, which is about 100 MW. The total losses for Case 2a corresponds to 467.95 MVAr, while for Case 2b becomes 378.21 MVAr. Thus, the STATCOM contributes to improve the general system conditions. A similar analysis is performed for Cases 3a and 3b are summarized in Table 11.14.

References

1. Taylor CW (1996) Power system voltage stability. McGraw-Hill, New York
2. Padiyar KR (1995) Power system dynamics: stability and control. Wiley, New York
3. Van Cutsem T, Vournas C (1998) Voltage stability of electric power system. Kluwer, Norwell
4. Chua LO, Desoer CA, Kuh ES (1987) Linear and nonlinear circuits. McGraw Hill, New York
5. Gao B (1996) Towards the development of a systematic approach for voltage stability assessment of large-scale power systems. IEEE Trans Power Syst 11(3):1314–1324
6. Van Cutsem T et al (1999) Determination of secure operating limits with respect to voltage collapse. IEEE Trans Power Syst 14(1):327–333
7. IEEE/PES Power System Stability Subcommittee Special Publication (2002) Voltage stability assessment: concepts, practice and tools. IEEE/PES Final Document. ISBN 0780378695
8. IEEE/PES Power Systems Stability Subcommittee Special Publications (2001) Voltage stability assessment, procedures and guides, final draft. http://www.power.uwaterloo.ca. Accessed Dec 2013
9. Greene S et al (1999) Contingency ranking for voltage collapse via sensitivities from a single nose curve. IEEE Trans Power Syst 14(1):232–238

10. Repo S (2001) On-line voltage stability assessment of power system-an approach of black-box modelling. Ph.D. dissertation, Tampere University of Technology, Tampere
11. Song YH, Johns AT (1999) Flexible ac transmission system (FACTS). The Institution of Electrical Engineers, UK
12. Acha E, Fuerte-Esquivel CR, Ambriz-Pérez H, Ángeles Camacho C (2006) FACTS: modelling and simulation in power network. Wiley, England
13. Zhang XP, Xue CF, Godfrey KR (2004) Modelling of the static synchronous series compensator (SSSC) in three-phase power flow. IEE Proc Gener Transm Distrib 151 (4):486–494
14. Ajjarapu V, Christy C (1992) The continuation power flow: a tool for steady state voltage stability analysis. IEEE Trans Power Syst 7(1):416–423
15. Mansour Y, Kundur P (1991) Voltage collapse: industry practices: control and dynamic systems. Academic Press, Waltham
16. Gao B, Morison GR, Kundur P (1996) Towards the development of a systematic approach for voltage stability assessment of large-scale power systems. IEEE Trans Power Syst 11 (3):1314–1324
17. Ramirez Juan M, Murillo-Perez José L (2006) Steady state voltage stability with STATCOM. IEEE Trans Power Syst 21(3):1453–1454
18. Mansour Y (1993) Suggested techniques for voltage stability analysis. 93TH0620-5PWR, IEEE/PES
19. Ramírez Juan M, Murillo Jose L (2006) Three-phase voltage stability studies embedding a STATCOM. In: proceedings of the IEEE power engineering society general meeting, Montréal
20. Stewart William J, Jennings Allan (1981) A simultaneous iteration algorithm for real matrices. ACM Trans Math Softw 7(2):184–198
21. Wang L, Semlyen A (1992) Application of sparse eigenvalue techniques to the small signal stability analysis of large power system. IEEE Trans Power Syst 5(2):635–642
22. Martin N (1986) Efficient eigenvalue and frequency response methods applied to power system small-signal stability studies. IEEE Trans Power Syst 1(2):217–225

Chapter 12
Modeling of STATCOM in Load Flow Formulation

Salah Kamel and Francisco Jurado

Abstract This chapter presents an easy modeling of STATCOM into a recent Newton–Raphson (NR) load flow method. This load flow formulation is based on power and current injection mismatches. In this new load flow, the current mismatch equations are used to represent the PQ buses while the power mismatches are used for PV buses. This load flow formulation decreases the required number of equations, the computation time and improves the convergence performance especially in case of PV buses. The developed STATCOM model is considered as an application for the representation of PV buses in the new NR power and current injection mismatches load flow formulation. In this model, the connected buses with STATCOM are converted to PV buses with zero active power generation and the voltage magnitudes are fixed at the pre-request values. The controlled buses are incorporated in load flow algorithm as power injection mismatch equations. The parameters of STATCOM can be calculated during the iterative process using simple equations based on its configuration.

Keywords Power flow control · Hybrid mismatches load flow formulation · STATCOM

S. Kamel (✉) · F. Jurado (✉)
Department of Electrical Engineering, University of Jaén, EPS, Linares, Jaén, Spain
e-mail: skamel@ujaen.es

F. Jurado
e-mail: fjurado@ujaen.es

S. Kamel
Department of Electrical Engineering, Aswan Faculty of Engineering, Aswan University, Aswan, Egypt

F. Shahnia et al. (eds.), *Static Compensators (STATCOMs) in Power Systems*,
Power Systems, DOI 10.1007/978-981-287-281-4_12

12.1 Introduction

With the rapid development of power electronics, the flexible A.C transmission system (FACTS) devices have been proposed and implemented in electrical power systems. The semiconductor devices such as diodes, transistors, thyristors and Gate Turn-off Thyristors (GTO) have been applied to develop various types of FACTS. These devices are used to increase the controllability and enhance the power transfer capability of existing transmission network.

The FACTS technology opens up new opportunities to control power and enhance the usable capacity of electrical power network. These opportunities arise through the ability of FACTS devices to control many parameters of transmission systems such as, the series impedance, the shunt impedance, the current, the voltage magnitude, the phase angle, and the damping of oscillations at various frequencies below the rated frequency [1–6]. The FACTS devices can be classified according to the mode of their connection to the transmission system as; series compensator, shunt compensator, combined series-series compensator and combined series-shunt compensator. STATCOM is considered a shunt controller. This controller has capability of controlling the power flow through the line by injecting appropriate reactive power to electrical power system.

The incorporating of STATCOM in load flow algorithm needs some modifications such as [7]:

- New terms owing to the contributions from the STATCOM devices need to be included in the existing power flow equations of the concerned buses.
- STATCOM impedance should be added into the admittance matrix.
- New sub-blocks of Jacobian related to the STATCOM device should be included.
- The power contributed by STATCOM at the connected bus should be included into power mismatches vector.

Acha et al. [8], has presented a comprehensive STATCOM model based on a straightforward extension of the power flow equations. Where, the STATCOM control parameters are taken as independent variables and their values are calculated during the iterative process. Hence, a good convergence characteristic can be obtained. The comprehensive technique is considered a unified approach links the alternating current network and STATCOM state variables in a single system of simultaneous equations. As a result of that, the Jacobian matrix is increased according to the number of STATCOMs.

Bhowmick et al. [9], tried to reduce the complexities of the load flow program codes with STATCOM controller. This target has been done by developing an indirect approach for modeling of STATCOM in NR load flow algorithm. In this approach, the power system network with the STATCOM is represented with amended equivalent network without this device. Then, the standard load flow program can be used to find the load flow solution and the required voltage parameters of STATCOM. The main advantage of the indirect approach is the

reducing of load flow complexity when contains STATCOM device. The main disadvantage of this approach is the increasing in the size of Jacobian matrix in order to accommodate the additional state variables of STATCOM. As a result of that, the Jacobian elements related to STATCOM have to be modified.

Nor et al. [10], has applied the matrix partitioning approach to model STATCOM in NR load flow algorithm. This approach tried to avoid the modification of original Jacobain matrix and achieve the reusability. This approach based on partitioning of the Jacobian matrix into original matrix and new sub-matrices related to STATCOM. This approach is based on the comprehensive STATCOM model; hence, the advantages of the comprehensive approach have been collected in this technique. Moreover, the adding and changing in load flow codes can be done with some modification in the original codes. The main disadvantage of this technique is that new codes related to the STATCOM have to be written, as a result of that, the complexity of load flow program with STATCOM is still kept.

Regarding to the power flow techniques, The Newton-Raphson method is considered an excellent load flow method used in industry applications. The main disadvantage of NR method is considered the necessity for updating the Jacobian matrix during the iteration process. New technique has been presented to solve this drawback. This technique is based on current injections formulation [11–13].

The main advantage of this new method is the calculation of Jacobian matrix. Where, the off-diagonal and few diagonal elements of Jacobian matrix are constant and equal to the nodal admittance matrix.

The current injection mismatch equations are very suitable especially for large scale system that contains on only PQ buses and few PV buses like the distribution systems. However, in the case of PV buses, this new formulation has slow convergence character. Consequently, another technique has been developed to improve the convergence character of the method (NR-RCIM). This technique has been based on additional equations to represent the voltage mismatches for all PV buses [14]. The total required number of equations has been increased according to the number of PV buses. Hence, the Newton-Raphson based on current injection approach is not reliable for solving transmission systems and found wide usage in distribution systems [13].

This chapter presents an easy modeling of STATCOM in Newton-Raphson load flow based on power and current injection mismatches. In this new load flow, the current mismatch equations are used to represent the PQ buses while the power mismatches are used for PV buses. The STATCOM is represented as PV bus with desired voltage magnitude and zero generated power in terms of power mismatches. The developed model decreases the complexity of load flow programming codes with STATCOM device. However, the model is considered simple and more suitable for implementation of shunt FACTS devices into load flow algorithm.

12.2 Operation Principles and Equivalent Circuit of STATCOM

12.2.1 STATCOM

STATCOM has a characteristic similar to the synchronous condenser, but as an electronic device it has no inertia and is superior to the synchronous condenser in several ways, such as better dynamics, a lower investment cost and lower operating and maintenance costs. The STATCOM could generate a controllable ac voltage source behind a transformer leakage reactance when a dc source is applied [15–18]. The schematic diagram of STATCOM is shown in Fig. 12.1.

STATCOM can provide smooth, continuous voltage regulation, prevent voltage collapse and improve transmission stability [19–23]. A recent installation of STATCOM in Turkish transmission system is shown in Fig. 12.2 [24].

The advantage of a STATCOM is that the reactive power provision is independent from the actual voltage on the connection point. This can be seen in the diagram for the maximum currents being independent of the voltage in comparison to the SVC as shown in Fig. 12.3. This means, that even during most severe contingencies, the STATCOM keeps its full capability.

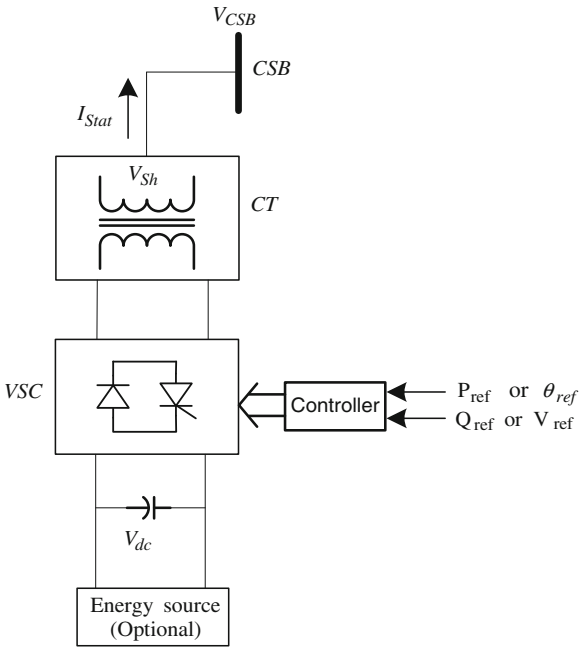

Fig. 12.1 Schematic diagram of STATCOM

Fig. 12.2 STATCOM prototype in Turkish transmission system

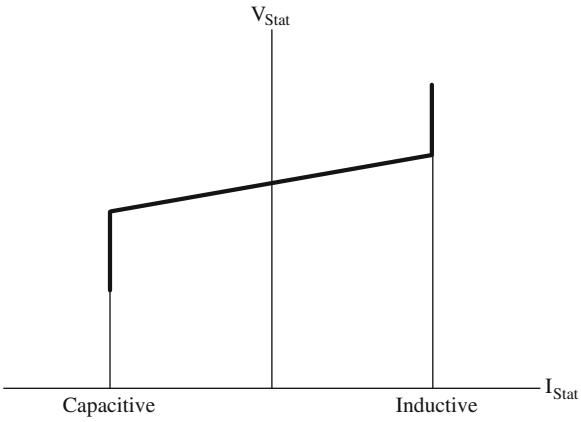

Fig. 12.3 V-I characteristics of STATCOM

12.2.2 The Shunt Compensation Concept on STATCOM

The basic principle of reactive power generation using a voltage source converter can be explained based on conventional rotating synchronous machine as shown in Fig. 12.4a [15, 25, 26]. For purely reactive power flow, the three-phase induced

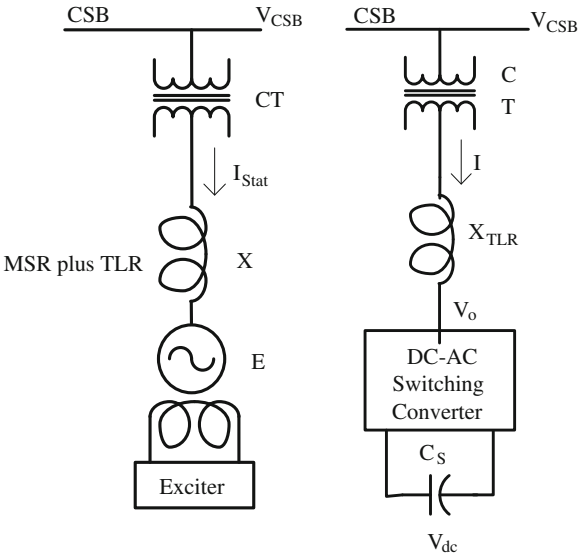

Fig. 12.4 Reactive-power generations: **a** Using rotating synchronous compensator, **b** using rotating VSSC

EMFs, e_a, e_b and e_c of the synchronous rotating machine are in-phase with the system voltage, v_a, v_b, v_c.

The reactive current I_{Stat} drawn by the STATCOM is calculated by the magnitude of the connected system voltage bus V_{CSB}, that of the internal E, and the total equivalent circuit reactance X as:

$$I_{Stat} = \frac{V_{CSB} - E}{X} \tag{12.1}$$

The corresponding reactive power Q_{Stat} exchanged can be done as follows:

$$Q_{Stat} = \frac{1 - \frac{E}{V_{CSB}}}{X} V_{CSB}^2 \tag{12.2}$$

With controlling the excitation of the machine, and hence the amplitude E of its internal voltage relative to the amplitude V_{Stat} of the system voltage, the reactive power flow can be controlled. The increasing of E above V (i.e., over-excited) results in a leading current, where the machine is behaving as a capacitor by the ac system. The decreasing E below V (i.e. operating under-excited) produces a lagging current, where in this case the machine is behaving as an inductor by the ac system. In all these operating conditions, a small amount of active power flows from the ac system to the machine to supply its mechanical and electrical losses. Also, if the excitation of the machine is controlled with the corresponding reactive output maintain or varies a specific parameter of the system like bus voltage, the rotating VAr generator functions as a rotating synchronous compensator.

Figure 12.4b shows the basic Voltage Source Converter (VSC) scheme of STATCOM. The charged capacitor C_s provides dc input voltage source. The AC-DC converter produces a set of controllable three-phase output voltages with the same frequency of the power system. Each output voltage is in phase with and coupled to the corresponding ac system voltage via a relatively small tie reactance in general, from 0.1 to 0.15 pu, which in practice is provided by the per phase leakage inductance of the CT. By varying the amplitude of the output voltages, V_o, the reactive power exchange between the converter and the ac system can be controlled in a manner similar to that of the rotating synchronous machine.

If the amplitude of output voltage is increased above the ac system voltage, the current will flow through the tie reactance from the converter to the ac system, which made the converter generates capacitive power for the ac system. On the other hand, if the amplitude of the output voltage is decreased below the ac system, the reactive current will flow from the ac system to the converter, which made the converter absorbs inductive power. If the amplitude of the output voltage is made equal to the ac system voltage, the reactive power exchange is zero.

12.2.3 STATCOM Equivalent Circuit

Unlike the SVC, the STATCOM is represented as a voltage source for the full range of operation, enabling a more robust voltage support mechanism. The equivalent circuit of STATCOM as shown in Fig. 12.5 is used to derive the mathematical model of the controller for inclusion in power flow algorithms [27].

12.2.3.1 Power Equations

The power flow equations of STATCOM are derived below from first principles and assuming the following ideal voltage source representation:

$$V_{stat} = |V_{stat}|(\cos\theta_{Stat} + j\sin\theta_{Stat}) \tag{12.3}$$

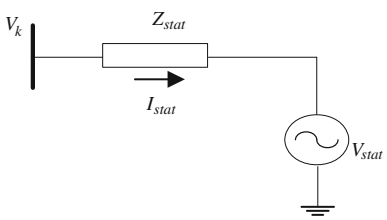

Fig. 12.5 Equivalent circuit of STATCOM controller

The following active and reactive power equations are obtained for the converter and bus k, respectively:

$$P_{stat} = V_{stat}^2 G_{stat} + V_{stat} V_k [G_{stat} \cos(\theta_{stat} - \theta_k) + B_{stat} \sin(\theta_{stat} - \theta_k)] \quad (12.4)$$

$$Q_{stat} = -V_{stat}^2 B_{stat} + V_{stat} V_k [G_{stat} \sin(\theta_{stat} - \theta_k) - B_{stat} \cos(\theta_{stat} - \theta_k)] \quad (12.5)$$

$$P_k = V_k^2 G_{stat} + V_{stat} V_k [G_{stat} \cos(\theta_k - \theta_{stat}) + B_{stat} \sin(\theta_k - \theta_{stat})] \quad (12.6)$$

$$Q_k = -V_k^2 B_{stat} + V_{stat} V_k [G_{stat} \sin(\theta_k - \theta_{stat}) - B_{stat} \cos(\theta_k - \theta_{stat})] \quad (12.7)$$

12.3 NR Load Flow Formulations

A new development on Newton-Raphson load flow based on current injections formulation was presented in [11, 12]. This technique was emerged to solve the problem of updating the Jacobian elements in conventional Newton-Raphson load flow (NR-PM). In this method, The Jacobian matrix can be obtained faster than the conventional power flow Jacobian. Where, the off-diagonal elements plus a few diagonal ones are constant and equal to the terms of the nodal admittance matrix, except for the PV buses whose elements are required to additional effort. Also this method does not require at all the use of transcendental functions during the iterative process. In this method, the PV and PQ buses are represented by two equations comprising the real and imaginary components of the current injection mismatches expressed in terms of the voltage rectangular coordinates. There are two versions for this method has been developed:

12.3.1 NR Current Injection Load Flow Formulation (Version-1)

In the first version of this formulation, a new dependent variable (ΔQ) is introduced for each PV bus together with an additional equation imposing the constraint of zero deviations in the bus voltage. The algorithm of the first version of Newton-Raphson load flow based on current injection mismatches is given by (12.8), Bus k is taken as PV-type and connected with many PQ buses [11, 12].

$$
\begin{bmatrix}
\Delta I_{m1}\\ \Delta I_{r1}\\ \Delta I_{m2}\\ \Delta I_{r2}\\ \vdots\\ \Delta I_{mk}\\ \Delta I_{rk}\\ \vdots\\ \vdots\\ \Delta I_{mN}\\ \Delta I_{rN}
\end{bmatrix}
=
\begin{bmatrix}
B_{11}^{*} & G_{11}^{*} & B_{12} & G_{12} & \cdots & \left(G_{1k}-\frac{B_{1k}V_{mk}}{V_{rk}}\right) & 0 & \cdots & \cdots & B_{1N} & G_{1N}\\
G_{11}^{**} & B_{11}^{**} & G_{12} & -B_{12} & \cdots & \left(-B_{1k}-\frac{G_{1k}\Delta V_{mk}}{V_{rk}}\right) & 0 & \cdots & \cdots & G_{1N} & -B_{1N}\\
B_{21} & G_{21} & B_{22}^{*} & G_{22}^{*} & \cdots & \left(G_{2k}-\frac{B_{2k}V_{mk}}{V_{rk}}\right) & 0 & \cdots & \cdots & B_{2N} & G_{2N}\\
G_{21} & -B_{21} & G_{22}^{**} & B_{22}^{**} & \cdots & \left(-B_{2k}-\frac{G_{2k}\Delta V_{mk}}{V_{rk}}\right) & 0 & \cdots & \cdots & G_{2N} & -B_{2N}\\
\vdots & \vdots & \vdots & \vdots & \vdots & \vdots & \vdots & \iddots & \iddots & \vdots & \vdots\\
B_{k1} & G_{k1} & B_{k2} & G_{k2} & \cdots & \left(G_{kk}^{*}-\frac{B_{kk}^{*}V_{mk}}{V_{rk}}\right) & \frac{V_{rk}}{V_{k}^{2}} & \cdots & \cdots & B_{kN} & G_{kN}\\
G_{k1} & -B_{k1} & G_{k2} & -B_{k2} & \cdots & \left(B_{kk}^{**}-\frac{G_{kk}^{**}\Delta V_{mk}}{V_{rk}}\right) & -\frac{V_{mk}}{V_{k}^{2}} & \cdots & \cdots & G_{kN} & -B_{kN}\\
\vdots & \vdots & \vdots & \vdots & \vdots & \vdots & \vdots & \iddots & \iddots & \vdots & \vdots\\
\vdots & \vdots & \vdots & \vdots & \vdots & \vdots & \vdots & \iddots & \iddots & \vdots & \vdots\\
B_{n1} & G_{n1} & B_{n2} & G_{n2} & \cdots & \left(G_{nk}-\frac{B_{nk}V_{mk}}{V_{rk}}\right) & 0 & \cdots & \cdots & B_{NN}^{*} & G_{NN}^{*}\\
G_{n1} & -B_{n1} & G_{n2} & -B_{n2} & \cdots & \left(-B_{nk}-\frac{G_{nk}\Delta V_{mk}}{V_{rk}}\right) & 0 & \cdots & \cdots & G_{NN}^{**} & B_{NN}^{**}
\end{bmatrix}
\begin{bmatrix}
\Delta V_{r1}\\ \Delta V_{m1}\\ \Delta V_{r2}\\ \Delta V_{m2}\\ \vdots\\ \Delta V_{mk}\\ \Delta Q_{k}\\ \vdots\\ \vdots\\ \Delta V_{rN}\\ \Delta V_{mN}
\end{bmatrix}
\tag{12.8}
$$

In (12.8), the mismatches vector is represented as real and imaginary injected currents as described in (12.9) and (12.10). While the real and imaginary components of the nodal voltage are taken as corrections vector. Hence, the Jacobian matrix can be obtained faster than the conventional NR power flow Jacobian matrix by differentiation the mismatches vector with regard to the corrections vector. It can be observed that the off-diagonal elements are constant and equal to the elements of nodal admittance matrix. Equations (12.11) to (12.14) are presented the diagonal elements of Jacobian matrix related to PQ buses. It can be observed that the first part of these equations equals to the elements of admittance matrix and only the second part in need of update during the iterative process.

$$
I_{rk} = I_{rk}^{sp} - \left(\frac{P_k^{sp}V_{rk} + Q_k^{sp}V_{mk}}{(V_{rk})^2+(V_{mk})^2}\right) + \sum_{i=1}^{N}\left(G_{ki}V_{ri} - B_{ki}V_{mi}\right) \tag{12.9}
$$

$$
I_{mk} = I_{mk}^{sp} - \left(\frac{P_k^{sp}V_{mk} - Q_k^{sp}V_{rk}}{(V_{rk})^2+(V_{mk})^2}\right) + \sum_{i=1}^{N}\left(G_{ki}V_{mi} - B_{ki}V_{ri}\right) \tag{12.10}
$$

$$B^{*}_{kk} = B_{kk} - \left(\frac{Q^{sp}_{k}\left((V_{rk})^2 - (V_{mk})^2 \right) - 2P^{sp}_{k} V_{rk} V_{mk}}{V^{4}_{k}} \right) \tag{12.11}$$

$$B^{**}_{kk} = -B_{kk} - \left(\frac{Q^{sp}_{k}\left((V_{rk})^2 - (V_{mk})^2 \right) - 2P^{sp}_{k} V_{rk} V_{mk}}{V^{4}_{k}} \right) \tag{12.12}$$

$$G^{*}_{kk} = G_{kk} - \left(\frac{P^{sp}_{k}\left((V_{rk})^2 - (V_{mk})^2 \right) + 2V_{rk} V_{mk} Q^{sp}_{k}}{V^{4}_{k}} \right) \tag{12.13}$$

$$G^{**}_{kk} = G_{kk} + \left(\frac{P^{sp}_{k}\left((V_{rk})^2 - (V_{mk})^2 \right) + 2V_{rk} V_{mk} Q^{sp}_{k}}{V^{4}_{k}} \right) \tag{12.14}$$

12.3.2 NR Current Injection Load Flow Formulation (Version-2)

The second version of the current injection load flow has been presented in [14]. This algorithm tried to solve the drawback of the original representation of PV buses in the first version. Where, the original representation was based on the imposition that the voltage mismatches at PV bus equal to zero from the first iteration [11, 12]. But this condition is only true after convergence of the iterative process happen. In this version, an additional equation has been introduced to represent the voltage mismatches for every PV bus.

$$\begin{bmatrix} \Delta I_{m1} \\ \Delta I_{r1} \\ \Delta I_{m2} \\ \Delta I_{r2} \\ \vdots \\ \Delta I_{mk} \\ \Delta I_{rk} \\ \Delta V^{2}_{k} \\ \vdots \\ \Delta I_{mN} \\ \Delta I_{rN} \end{bmatrix} = \begin{bmatrix} B^{*}_{11} & G^{*}_{11} & B_{12} & G_{12} & \cdots & B_{1k} & G_{1k} & 0 & \cdots & B_{1N} & G_{1N} \\ G^{**}_{11} & B^{**}_{11} & G_{12} & -B_{12} & \cdots & G_{1k} & -B_{1k} & 0 & \cdots & G_{1N} & -B_{1N} \\ B_{21} & G_{21} & B^{*}_{22} & G^{*}_{22} & \cdots & B_{2k} & G_{2k} & 0 & \cdots & B_{2N} & G_{2N} \\ G_{21} & -B_{21} & G^{**}_{22} & B^{**}_{22} & \cdots & G_{2k} & -B_{2k} & 0 & \cdots & G_{2N} & -B_{2N} \\ \vdots & \vdots & \vdots & \vdots & \vdots & \vdots & \vdots & 0 & \vdots & \vdots & \vdots \\ B_{k1} & G_{k1} & B_{k2} & G_{k2} & \cdots & B^{*}_{kk} & G^{*}_{kk} & \frac{V_{rk}}{V^{2}_{k}} & \cdots & B_{kN} & G_{kN} \\ G_{k1} & -B_{k1} & G_{k2} & -B_{k2} & \cdots & G^{**}_{kk} & B^{**}_{kk} & \frac{-V_{mk}}{V^{2}_{k}} & \cdots & G_{kN} & -B_{kN} \\ 0 & 0 & 0 & 0 & \cdots & 2V_{rk} & 2V_{mk} & 0 & \cdots & 0 & 0 \\ \vdots & \vdots & \vdots & \vdots & \vdots & \vdots & \vdots & \vdots & \vdots & \vdots & \vdots \\ B_{N1} & G_{N1} & B_{N2} & G_{N2} & \cdots & B_{Nk} & G_{Nk} & 0 & \cdots & B^{*}_{NN} & G^{*}_{NN} \\ G_{N1} & -B_{N1} & G_{N2} & -B_{N2} & & G_{Nk} & -B_{Nk} & 0 & & G^{**}_{NN} & B^{**}_{NN} \end{bmatrix} \begin{bmatrix} \Delta V_{r1} \\ \Delta V_{m1} \\ \Delta V_{r2} \\ \Delta V_{m2} \\ \\ \Delta V_{rk} \\ \Delta V_{mk} \\ \Delta Q_{k} \\ \\ \Delta V_{rN} \\ \Delta V_{mN} \end{bmatrix} \tag{12.15}$$

The algorithm of Revised Newton-Raphson load flow based on current injection mismatches given in (12.15).

Also it can be observed that the off-diagonal elements J in the Jacobian matrix are identical to the corresponding elements in the bus admittance matrix.

Advantages of NR Current Injection Load Flow Method
The main advantage of NR load flow based on current injection mismatches method is that the majority of the Jacobian matrix elements related to PQ buses are constant and equal to the admittance elements. Also the method does not require at all the use of transcendental (sine, cosine) functions during the iterative process.

Drawbacks of NR Current Injection Load Flow Method
The main disadvantage for this method is that an additional equation for every PV bus is required. This method is not reliable for solving transmission systems and found wide usage in distribution systems [28–38]. Where, the transmission systems are characterized with many PV nodes; hence the size of the Jacobian matrix increases as the number of PV nodes increase. Also according to that the average execution time is increased.

12.4 Recent NR Power-Current Injection Load Flow Formulation

The revised representation of PV buses in NR current injection (NR-RCIM) method has been presented in [14]. This algorithm tried to solve the drawback of the original representation of PV buses in (NR-CIM). Where, the original representation was based on the imposition that the voltage mismatches at PV bus equal to zero from the first iteration [11]. But this condition is only true after convergence of the iterative process. In the revised representation of PV bus, the number of required equations has increased and became three for each PV bus, where the reactive power is introduced as a new additional state variable.

$$\begin{bmatrix} \Delta I_{m1} \\ {}^{r1} \\ \Delta I_{m2} \\ \Delta I_{r2} \\ \vdots \\ \Delta P_f \\ \vdots \\ \Delta I_{mN} \\ \Delta I_{rN} \end{bmatrix} = \begin{bmatrix} \frac{\partial I_{m1}}{\partial V_{r1}} & \frac{\partial I_{m1}}{\partial V_{m1}} & \frac{\partial I_{m1}}{\partial V_{r2}} & \frac{\partial I_{m1}}{\partial V_{m2}} & \cdots & \cdots & \frac{\partial I_{m1}}{\partial \delta_f} & \cdots & \cdots & \frac{\partial I_{m1}}{\partial V_{rN}} & \frac{\partial I_{m1}}{\partial V_{mN}} \\ \frac{\partial I_{r1}}{\partial V_{r1}} & \frac{\partial I_{r1}}{\partial V_{m1}} & \frac{\partial I_{r1}}{\partial V_{r2}} & \frac{\partial I_{r1}}{\partial V_{m2}} & \cdots & \cdots & \frac{\partial I_{r1}}{\partial \delta_f} & \cdots & \cdots & \frac{\partial I_{r1}}{\partial V_{rN}} & \frac{\partial I_{r1}}{\partial V_{mN}} \\ \frac{\partial I_{m2}}{\partial V_{r1}} & \frac{\partial I_{m2}}{\partial V_{m1}} & \frac{\partial I_{m2}}{\partial V_{r2}} & \frac{\partial I_{m2}}{\partial V_{m2}} & \cdots & \cdots & \frac{\partial I_{m2}}{\partial \delta_f} & \cdots & \cdots & \frac{\partial I_{m2}}{\partial V_{rN}} & \frac{\partial I_{m2}}{\partial V_{mN}} \\ \frac{\partial I_{r2}}{\partial V_{r1}} & \frac{\partial I_{r2}}{\partial V_{m1}} & \frac{\partial I_{r2}}{\partial V_{r2}} & \frac{\partial I_{r2}}{\partial V_{m2}} & \cdots & \cdots & \frac{\partial I_{r2}}{\partial \delta_f} & \cdots & \cdots & \frac{\partial I_{r2}}{\partial V_{rN}} & \frac{\partial I_{r2}}{\partial V_{mN}} \\ \vdots & \vdots & \vdots & \vdots & \vdots & \vdots & \vdots & \vdots & \vdots & \vdots & \vdots \\ \vdots & \vdots & \vdots & \vdots & \vdots & \vdots & \vdots & \vdots & \vdots & \vdots & \vdots \\ \frac{f}{\partial V_{r1}} & \frac{f}{\partial V_{m1}} & \frac{f}{\partial V_{r2}} & \frac{f}{\partial V_{m2}} & \cdots & \cdots & \frac{\partial P_f}{\partial \delta_f} & \cdots & \cdots & \frac{\partial P_f}{\partial V_{rN}} & \frac{\partial P_f}{\partial V_{mN}} \\ \vdots & \vdots & \vdots & \vdots & \vdots & \vdots & \vdots & \vdots & \vdots & \vdots & \vdots \\ \vdots & \vdots & \vdots & \vdots & \vdots & \vdots & \vdots & \vdots & \vdots & \vdots & \vdots \\ \frac{\partial I_{mN}}{\partial V_{r1}} & \frac{\partial I_{mN}}{\partial V_{m1}} & \frac{\partial I_{mN}}{\partial V_{r2}} & \frac{\partial I_{mN}}{\partial V_{m2}} & \cdots & \cdots & \frac{\partial I_{mN}}{\partial \delta_f} & \cdots & \cdots & \frac{\partial I_{mN}}{\partial V_{rN}} & \frac{\partial I_{mN}}{\partial V_{mN}} \\ \frac{\partial I_{rN}}{\partial V_{r1}} & \frac{\partial I_{rN}}{\partial V_{m1}} & \frac{\partial I_{rN}}{\partial V_{r2}} & \frac{\partial I_{rN}}{\partial V_{m2}} & \cdots & \cdots & \frac{\partial I_{rN}}{\partial \delta_f} & \cdots & \cdots & \frac{\partial I_{rN}}{\partial V_{rN}} & \frac{\partial I_{rN}}{\partial V_{mN}} \end{bmatrix} \begin{bmatrix} {}^{r1} \\ \Delta V_{m1} \\ \Delta V_{r2} \\ \Delta V_{m2} \\ \vdots \\ \Delta \delta_f \\ \vdots \\ {}^{rN} \\ \Delta V_{mN} \end{bmatrix} \tag{12.16}$$

In this chapter, a new formulation has been used to present a good representation of PV buses in current injection load flow method and decrease the number of

required equations from three to only one at every PV bus with robust convergence characteristic for well and ill-conditioned systems [39]. In the developed load flow method, combination between two NR techniques is used. Where, the PQ nodes are represented as revised NR current injection load flow method, which based on real and imaginary parts of injected currents at these nodes. While, PV nodes are represented using the power injection mismatches formulation. The combined power and current injection mismatches load flow formulation can be calculated from (12.16).

12.4.1 Representation of PQ Buses

The complex current mismatch at bus k is given by:

$$\Delta I_k = \frac{P_k^{sp} - jQ_k^{sp}}{V_k^*} - \sum_{i=1}^{n} Y_{ki} V_i \tag{12.17}$$

where,

$$V_k^2 = V_{mk}^2 + V_{rk}^2 \tag{12.18}$$

In case of where bus k has only a constant power load:

$$P_k^{sp} = P_k^g - P_k^l \tag{12.19}$$

$$Q_k^{sp} = Q_k^g - Q_k^l \tag{12.20}$$

(12.17) can be expanded into real and imaginary components as:

$$\Delta I_{rk} = \frac{P_k^{sp} V_{rk} + Q_k^{sp} V_{mk}}{V_{rk}^2 + V_{mk}^2} - \sum_{i=1}^{n} (G_{ki} V_{ri} - B_{ki} V_{mi}) = I_{rk}^{sp} - I_{rk}^{cal} \tag{12.21}$$

$$\Delta I_{mk} = \frac{P_k^{sp} V_{mk} - Q_k^{sp} V_{rk}}{V_{rk}^2 + V_{mk}^2} - \sum_{i=1}^{n} (G_{ki} V_{mi} - B_{ki} V_{ri}) = I_{mk}^{sp} - I_{mk}^{cal} \tag{12.22}$$

(12.21) and (12.22) can be rewritten as follows:

$$I_{rk}^{cal} = I_{rk}^{sp} - \left(\frac{P_k^{sp} V_{rk} + Q_k^{sp} V_{mk}}{V_{rk}^2 + V_{mk}^2} \right) + \sum_{i=1}^{n} (G_{ki} V_{ri} - B_{ki} V_{mi}) \tag{12.23}$$

$$I_{mk}^{cal} = I_{mk}^{sp} - \left(\frac{P_k^{sp} V_{mk} - Q_k^{sp} V_{rk}}{V_{rk}^2 + V_{mk}^2} \right) + \sum_{i=1}^{n} (G_{ki} V_{mi} - B_{ki} V_{ri}) \tag{12.24}$$

By assuming all buses in the system are PQ types. Then, the Jacobian matrix which corresponds these PQ buses (J_{PQ}) are determined by differential of (12.23) and (12.24) with respect to the real and imaginary parts of buses voltage as presented in (12.25).

$$\begin{bmatrix} \Delta I_{r1} \\ \Delta I_{m1} \\ \vdots \\ \Delta I_{rk} \\ \Delta I_{mk} \\ \vdots \\ \Delta I_{rN} \\ \Delta I_{mN} \end{bmatrix} = [J_{PQ}] \begin{bmatrix} \Delta V_{m1} \\ \Delta V_{r1} \\ \vdots \\ \Delta V_{mk} \\ \Delta V_{rk} \\ \vdots \\ \Delta V_{mN} \\ \Delta V_{rN} \end{bmatrix} \tag{12.25}$$

The derivatives of the Jacobian matrix can be calculated as follows:
Diagonal elements of $\frac{\partial I_{mk}}{\partial V_{rk}}$ $(i = k)$

$$\frac{\partial I_{mk}}{\partial V_{rk}} = \frac{2P_k^{sp} V_{rk} V_{mk}}{V_k^4} + \frac{Q_k^{sp}(V_{rk}^2 - V_{mk}^2)}{V_k^4} + B_{kk} \tag{12.26}$$

(12.18) can be rewritten as:

$$V_k = V_k^2 V_k^{-1} = (V_{mk}^2 + V_{rk}^2) V_k^{-1} \tag{12.27}$$

By using the above equation, (12.26) can be rewritten to be as follows:

$$\frac{\partial I_{mk}}{\partial V_{rk}} = B_{kk}^* = B_{kk} - \left(\frac{Q_k^{sp}(V_{rk}^2 - V_{mk}^2) - 2P_k^{sp} V_{rk} V_{mk}}{V_k^4} \right) \tag{12.28}$$

$$\frac{\partial I_{mk}}{\partial V_{rk}} = B_{kk}^* = B_{kk} - a_k \tag{12.29}$$

where:

$$a_k = \frac{Q_k^{sp}(V_{rk}^2 - V_{mk}^2) - 2P_k^{sp} V_{rk} V_{mk}}{V_k^4} \tag{12.30}$$

Off-diagonal elements of $\frac{\partial I_{mk}}{\partial V_{ri}}$ $(i \neq k)$

$$\frac{\partial I_{mk}}{\partial V_{ri}} = B_{ki} \tag{12.31}$$

Diagonal elements of $\frac{\partial I_{mk}}{\partial V_{mk}}$ *(i = k)*

$$\frac{\partial I_{mk}}{\partial V_{mk}} = G^{*}_{kk} = G_{kk} - \left(\frac{(P^{sp}_{k}(V^{2}_{rk} - V^{2}_{mk}) + 2V_{rk}V_{mk}Q^{sp}_{k})}{V^{4}_{k}}\right)$$

$$\frac{\partial I_{mk}}{\partial V_{mk}} = G^{*}_{kk} = G_{kk} - b_{k} \tag{12.32}$$

where:

$$b_{k} = \frac{(P^{sp}_{k}(V^{2}_{rk} - V^{2}_{mk}) + 2V_{rk}V_{mk}Q^{sp}_{k})}{V^{4}_{k}} \tag{12.33}$$

Off-diagonal elements of $\frac{\partial I_{mk}}{\partial V_{ri}}$ $(i \neq k)$

$$\frac{\partial I_{mk}}{\partial V_{mi}} = G_{ki} \tag{12.34}$$

Diagonal elements of $\frac{\partial I_{rk}}{\partial V_{rk}}$ *(i = k)*

$$\frac{\partial I_{rk}}{\partial V_{rk}} = G^{**}_{kk} = G_{kk} - \left(\frac{P^{sp}_{k}(V^{2}_{mk} - V^{2}_{rk}) - 2Q^{sp}_{k}V_{rk}V_{mk})}{V^{4}_{k}}\right)$$

$$\frac{\partial I_{rk}}{\partial V_{rk}} = G^{**}_{kk} = G_{kk} - c_{k} \tag{12.35}$$

where,

$$c_{k} = -b_{k}\frac{P^{sp}_{k}(V^{2}_{mk} - V^{2}_{rk}) - 2Q^{sp}_{k}V_{rk}V_{mk})}{V^{4}_{k}} \tag{12.36}$$

Off-diagonal elements of $\frac{\partial I_{rk}}{\partial V_{ri}}$ $(i \neq k)$

$$\frac{\partial I_{rk}}{\partial V_{ri}} = G_{ki} \tag{12.37}$$

Diagonal elements of $\frac{\partial I_{rk}}{\partial V_{mk}}$ *(i = k)*

$$\frac{\partial I_{rk}}{\partial V_{mk}} = B^{**}_{kk} = -B_{kk} - \left(\frac{Q^{sp}_{k}(V^{2}_{rk} - V^{2}_{mk}) - 2P^{sp}_{k}V_{rk}V_{mk}}{V^{4}_{k}}\right)$$

$$\frac{\partial I_{rk}}{\partial V_{mk}} = B^{**}_{kk} = -B_{kk} - d_{k} \tag{12.38}$$

where,

$$d_k = a_k = \frac{Q_k^{sp}(V_{rk}^2 - V_{mk}^2) - 2P_k^{sp}V_{rk}V_{mk}}{V_k^4} \tag{12.39}$$

Off-diagonal elements of $\frac{\partial I_{rk}}{\partial V_{mi}}$ $(i \neq k)$

$$\frac{\partial I_{rk}}{\partial V_{mi}} = -B_{ki} \tag{12.40}$$

Finally, the Jacobian matrix (J_{PQ}) can be calculated using (12.41):

$$J_{PQ} = \begin{bmatrix} \begin{bmatrix} B_{11}^* & G_{11}^* \\ G_{11}^{**} & B_{11}^{**} \end{bmatrix} & \cdots & \begin{bmatrix} B_{1k} & G_{1k} \\ G_{1k} & -B_{1k} \end{bmatrix} & \cdots & \begin{bmatrix} B_{1N} & G_{1N} \\ G_{1N} & -B_{1N} \end{bmatrix} \\ \vdots & \ddots & \vdots & \ddots & \vdots \\ \begin{bmatrix} B_{k1} & G_{k1} \\ G_{k1} & -B_{k1} \end{bmatrix} & \cdots & \begin{bmatrix} B_{kk}^* & G_{kk}^* \\ G_{kk}^{**} & B_{kk}^{**} \end{bmatrix} & \cdots & \begin{bmatrix} B_{kN} & G_{kN} \\ G_{kN}^{**} & -B_{kN}^{**} \end{bmatrix} \\ \vdots & \ddots & \vdots & \ddots & \vdots \\ \begin{bmatrix} B_{1N} & G_{1N} \\ G_{1N} & -B_{1N} \end{bmatrix} & \cdots & \begin{bmatrix} B_{Nk} & G_{Nk} \\ G_{nN} & -B_{Nk} \end{bmatrix} & \cdots & \begin{bmatrix} B_{nN}^* & G_{nN}^* \\ G_{nN}^{**} & B_{nN}^{**} \end{bmatrix} \end{bmatrix} \tag{12.41}$$

The diagonal elements of Jacobian matrix related to PQ buses can be calculated using (12.11)–(12.14). From (12.41), it can be observed that the off-diagonal element are constant and equal to the admittance elements, also the first part of each diagonal element is constant and the another needs to update during the iterative process.

12.4.2 Improved Representation of PV Buses

In this new representation, the PV nodes are represented using the power injection mismatches formulation. The angles at these buses are updated during the iteration process similar to the NR-PM load flow method. The combined power and current injection mismatches load flow formulation can be calculated using (12.42).

$$\begin{bmatrix} \Delta\mathbf{I}_{mk} \\ \Delta\mathbf{I}_{rk} \\ \Delta\mathbf{P}_f \end{bmatrix} = \begin{bmatrix} \mathbf{J_{PQ}} & & \frac{\partial\mathbf{I}_{mk}}{\partial\boldsymbol{\delta}} \\ & & \frac{\partial\mathbf{I}_{rk}}{\partial\boldsymbol{\delta}} \\ \frac{\partial\mathbf{P}_f}{\partial\mathbf{V_r}} & \frac{\partial\mathbf{P}_f}{\partial\mathbf{V_m}} & \frac{\partial\mathbf{P}_f}{\partial\boldsymbol{\delta}} \end{bmatrix} \begin{bmatrix} \Delta\mathbf{V}_{rk} \\ \Delta\mathbf{V}_{mk} \\ \Delta\delta_f \end{bmatrix} \tag{12.42}$$

where,

$$P_f = \sum_{i=1}^{n} V_f V_i (G_{fi} \cos \delta_{fi} + B_{fi} \sin \delta_{fi}) \tag{12.43}$$

The J_{PQ} is given in (12.41) and the other elements can be calculated as follows:
Element of $\frac{\partial I_{mk}}{\partial \delta_f}$

$$\frac{\partial I_{mk}}{\partial \delta_f} = V_f (G_{kf} \cos \delta_f - B_{kf} \sin \delta_f) \tag{12.44}$$

Element of $\frac{\partial I_{rk}}{\partial \delta_f}$

$$\frac{\partial I_{rk}}{\partial \delta_f} = -V_f (G_{kf} \sin \delta_f + B_{kf} \cos \delta_f) \tag{12.45}$$

Element of $\frac{\partial P_f}{\partial V_{mk}}$
In this case, the (12.43) can be rewritten as follows:

$$P_f = V_f V_k (G_{fk} \cos \delta_{fk} + B_{fk} \sin \delta_{fk})$$

$$P_f = V_f V_k \left(G_{fk} \cos\left(\delta_f - \delta_k\right) + B_{fk} \sin\left(\delta_f - \delta_k\right)\right)$$

where,

$$\sin(\delta_f - \delta_k) = \sin \delta_f \cos \delta_k - \sin \delta_k \cos \delta_f \tag{12.46}$$

$$\cos(\delta_f - \delta_k) = \cos \delta_f \cos \delta_k + \sin \delta_k \sin \delta_f \tag{12.47}$$

then,

$$P_f = V_f \left[G_{fk}\left(V_{rk} \cos \delta_f + V_{mk} \sin \delta_f\right) + B_{fk}\left(V_{rk} \sin \delta_f - V_{mk} \cos \delta_f\right)\right] \tag{12.48}$$

According to above equation,

$$\frac{\partial P_f}{\partial V_{mk}} = V_f (G_{fk} \sin \delta_f - B_{fk} \cos \delta_f) \tag{12.49}$$

Element of $\frac{\partial P_f}{\partial V_{rk}}$

$$\frac{\partial P_f}{\partial V_{rk}} = V_f (G_{fk} \cos \delta_f + B_{fk} \sin \delta_f) \tag{12.50}$$

Diagonal element of $\frac{\partial P_f}{\partial V_{rk}}$ (12.43) can be rewritten as:

$$P_f = V_f^2 G_{ff} + \sum_{\substack{i=1 \\ i \neq f}}^{n} V_f \begin{bmatrix} G_{fi}\left(V_i \cos\delta_i \cos\delta_f + V_i \sin\delta_i \sin\delta_f\right) \\ +B_{fi}\left(V_i \cos\delta_i \sin\delta_f - V_i \sin\delta_i \cos\delta_f\right) \end{bmatrix} \tag{12.51}$$

Then,

$$\frac{\partial P_f}{\partial \delta_f} = -V_f \sum_{\substack{i=1 \\ i \neq f}}^{n} V_i (G_{fi} \sin\delta_{fi} - B_{fi} \cos\delta_{fi}) \tag{12.52}$$

Off-diagonal element of $\frac{\partial P_f}{\partial \delta_i}$

$$\frac{\partial P_f}{\partial \delta_i} = V_f V_i (G_{fi} \sin\delta_{fi} - B_{fi} \cos\delta_{fi}) \tag{12.53}$$

12.4.3 Current Mismatches for PQ Buses

From (12.21) and (12.22), the real and imaginary current mismatches at bus k can be expressed as:

$$\Delta I_{rk} = \frac{P_k^{sp} V_{rk} + Q_k^{sp} V_{mk}}{V_{rk}^2 + V_{mk}^2} - I_{rk}^{cal} \tag{12.54}$$

where,

$$I_{rk}^{cal} = \sum_{i=1}^{n} (G_{ki} V_{ri} - B_{ki} V_{mi}) \tag{12.55}$$

$$\Delta I_{mk} = \frac{P_k^{sp} V_{mk} - Q_k^{sp} V_{rk}}{V_{rk}^2 + V_{mk}^2} - I_{mk}^{cal} \tag{12.56}$$

where,

$$I_{mk}^{cal} = \sum_{i=1}^{n} (G_{ki} V_{mi} - B_{ki} V_{ri}) \tag{12.57}$$

The specified active and reactive power can be calculated as follows:
From,

$$\Delta P_k = P_k^{sp} - P_k^{cal} \tag{12.58}$$

$$\Delta Q_k = Q_k^{sp} - Q_k^{cal} \tag{12.59}$$

And,

$$P_k^{cal} = V_{rk} I_{rk}^{cal} + V_{mk} I_{mk}^{cal} \tag{12.60}$$

$$Q_k^{cal} = V_{mk} I_{rk}^{cal} - V_{rk} I_{mk}^{cal} \tag{12.61}$$

Then,

$$P_k^{sp} = \Delta P_k + P_k^{cal} = \Delta P_k + V_{rk} I_{rk}^{cal} + V_{mk} I_{mk}^{cal} \tag{12.62}$$

$$Q_k^{sp} = \Delta Q_k + Q_k^{cal} = \Delta Q_k + V_{mk} I_{rk}^{cal} - V_{rk} I_{mk}^{cal} \tag{12.63}$$

By substituting (12.62) and (12.63) into (12.54) and (12.56), the current mismatches can be expressed only in terms of power mismatches and voltages at bus k as presented in (12.64) and (12.65).

$$\Delta I_{rk} = \frac{\Delta P_k V_{rk} + \Delta Q_k V_{mk}}{V_k^2} \tag{12.64}$$

$$\Delta I_{mk} = \frac{\Delta P_k V_{mk} - \Delta Q_k V_{rk}}{V_k^2} \tag{12.65}$$

12.4.4 Power Mismatches for PV Buses

The active power mismatches are used to represent the mismatches of PV buses as follows:

$$\Delta P_f = P_f^{sp} - \sum_{i=1}^{n} |V_f||V_i|\left(G_{fi} \cos \delta_{fi} + B_{fi} \sin \delta_{fi}\right) \tag{12.66}$$

12.4.5 Bus Voltage Corrections

Case (1) *PQ Bus*

The bus voltage is updated after each iterative process as real and imaginary components as follows:

$$V_{rk}^{(h+1)} = V_{rk}^{h} + \Delta V_{rk}^{h} \tag{12.67}$$

$$V_{mk}^{(h+1)} = V_{mk}^{h} + \Delta V_{mk}^{h} \tag{12.68}$$

$$V_k = \sqrt{V_{rk} + V_{mk}} \tag{12.69}$$

$$\delta_k = \tan^{-1}\left(\frac{V_{mk}}{V_{rk}}\right) \tag{12.70}$$

Case (2) *PV Bus*
In this case, the bus angle is used and updated as follows:

$$\delta_f^{(h+1)} = \delta_f^{h} + \Delta\delta_f^{h} \tag{12.71}$$

In the new representation of PV buses in NR current injection load flow method, it can be observed that there is no change in Jacobian elements related to PQ buses. Only the elements related to PV buses are changed, also only one equation for each PV bus is required. The advantages of NR-RCIM in the case of PQ bus are saved. Where, the off-diagonal plus a few diagonal elements are constant and equal to the terms of the admittance matrix [11]. To show the above advantages of the new load flow method, the structure of the Jacobian matrix for the 9-bus system (Fig. 12.6.) is presented in Fig. 12.7, where buses 2 and 3 are PV type, bus 1 is slack type and the others buses are PQ type. As described in the developed algorithm both of slack and second row of PV buses have to be discarded during the iterative process to yield the load flow Jacobian matrix.

12.5 Developed STATCOM Model

A simple implementation for STATCOM steady-state model in NR power and current injection load flow (NR-PCIM) program is presented. Also, the model is considered as an application for the new representation of PV bus in NR current injection load flow formulation [40]. The equivalent circuit of STATCOM is shown in Fig. 12.5.

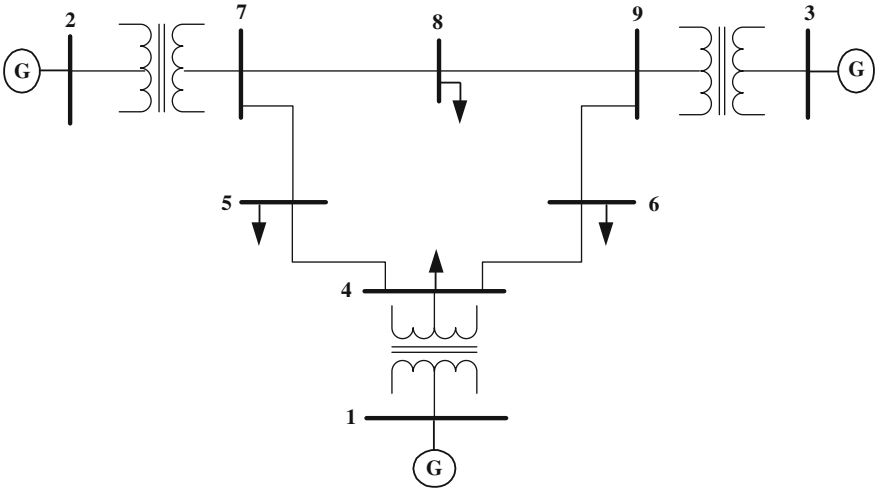

Fig. 12.6 9-bus system with two PV nodes

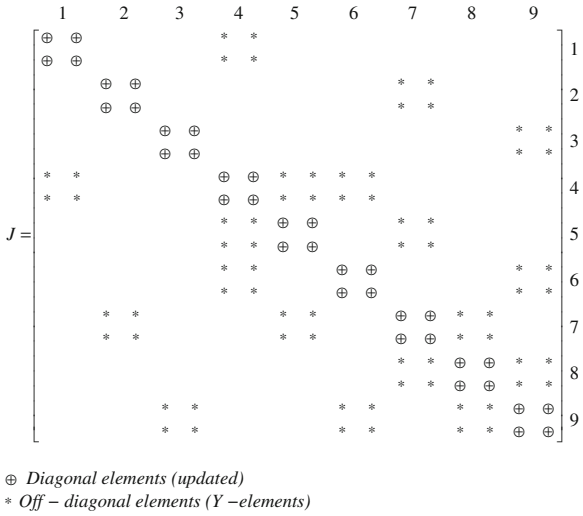

Fig. 12.7 NR-PCIM Jacobian matrix structure of the 9-bus system

$$\begin{bmatrix} \Delta I_{m1} \\ \Delta I_{r1} \\ \Delta I_{m2} \\ \Delta I_{r2} \\ \vdots \\ \Delta P_{PV} \\ \vdots \\ \Delta P_{Stat} \\ \vdots \\ \vdots \\ \vdots \\ {}_{mN} \\ \Delta I_{rN} \end{bmatrix} = \begin{bmatrix} B_{11}^{*} & G_{11}^{*} & B_{12} & G_{12} & \cdots & \frac{\partial I_{m1}}{\partial \delta_{PV}} & \cdots & \frac{\partial I_{m1}}{\partial \delta_{CSB}} & \cdots & & \cdots & B_{1N} & G_{1N} \\ G_{11}^{**} & B_{11}^{**} & G_{12} & -B_{12} & \cdots & \frac{\partial I_{r1}}{\partial \delta_{PV}} & \cdots & \frac{\partial I_{r1}}{\partial \delta_{Stat}} & \cdots & & \cdots & G_{1N} & -B_{1N} \\ B_{21} & G_{21} & B_{22}^{*} & G_{11}^{*} & \cdots & \frac{\partial I_{m2}}{\partial \delta_{PV}} & \cdots & \frac{\partial I_{m2}}{\partial \delta_{Stat}} & \cdots & & \cdots & B_{2N} & G_{2N} \\ G_{21} & -B_{21} & G_{22}^{**} & B_{22}^{**} & \cdots & \frac{\partial I_{r2}}{\partial \delta_{PV}} & \cdots & \frac{\partial I_{r2}}{\partial \delta_{Stat}} & \cdots & & \cdots & G_{2N} & -B_{2N} \\ \vdots & \vdots & \vdots & \vdots & \ddots & \vdots & & \vdots & & \ddots & & \vdots & \vdots \\ \frac{\partial P_{PV}}{\partial V_{r1}} & \frac{\partial P_{PV}}{\partial V_{m1}} & \frac{\partial P_{PV}}{\partial V_{r2}} & \frac{\partial P_{PV}}{\partial V_{m2}} & \cdots & \frac{\partial P_{PV}}{\partial \delta_{PV}} & \cdots & \frac{\partial P_{PV}}{\partial \delta_{Stat}} & \vdots & & \vdots & \frac{\partial P_{PV}}{\partial V_{rN}} & \frac{\partial P_{PV}}{\partial V_{mN}} \\ \vdots & \vdots & \vdots & \vdots & \ddots & \vdots & \vdots & \vdots & & \ddots & \vdots & \vdots & \vdots \\ \frac{\partial P_{Stat}}{\partial V_{r1}} & \frac{\partial P_{Stat}}{\partial V_{m1}} & \frac{\partial P_{Stat}}{\partial V_{r2}} & \frac{\partial P_{Stat}}{\partial V_{m2}} & \cdots & \frac{\partial P_{Stat}}{\partial \delta_{PV}} & \cdots & \frac{\partial P_{Stat}}{\partial \delta_{Stat}} & \cdots & & \cdots & \frac{\partial P_{Stat}}{\partial V_{rN}} & \frac{\partial P_{Stat}}{\partial V_{mN}} \\ \vdots & \vdots & \vdots & \vdots & \vdots & \vdots & \vdots & \vdots & \vdots & & \vdots & \vdots & \vdots \\ \vdots & \vdots & \vdots & \vdots & \vdots & \vdots & \vdots & \vdots & \vdots & & \vdots & \vdots & \vdots \\ \vdots & \vdots & \vdots & \vdots & \vdots & \vdots & \vdots & \vdots & \vdots & & \vdots & \vdots & \vdots \\ B_{N1} & G_{N1} & B_{N2} & G_{N2} & \cdots & \frac{\partial I_{mN}}{\partial \delta_{PV}} & \cdots & \frac{\partial I_{mN}}{\partial \delta_{Stat}} & \cdots & & \cdots & B_{NN}^{*} & G_{NN}^{*} \\ G_{N1} & -B_{N1} & G_{N2} & -B_{N2} & \cdots & \frac{\partial I_{rN}}{\partial \delta_{PV}} & \cdots & \frac{\partial I_{rN}}{\partial \delta_{Stat}} & \cdots & & \cdots & G_{NN}^{**} & B_{NN}^{**} \end{bmatrix} \begin{bmatrix} \Delta V_{r1} \\ \Delta V_{m1} \\ \Delta V_{r2} \\ \Delta V_{m2} \\ \vdots \\ \Delta \delta_{PV} \\ \vdots \\ \Delta \delta_{Stat} \\ \vdots \\ \vdots \\ \vdots \\ \Delta V_{rN} \\ \Delta V_{mN} \end{bmatrix} \tag{12.72}$$

The developed model decreases the complexities of the computer load flow program codes with STATCOM controller. The model is based on the representation of the connected STATCOM bus by generator (PV-type) bus with the desired voltage magnitude and zero active power generation. The mismatches of the PV buses are the power mismatches and the corresponding corrections are the angles. For the other load buses (PQ-type), the mismatches are the real and imaginary components of injected currents similar to Newton-Raphson current injection mismatches load flow (NR-CIM) formulation [8]. The load flow is carried-out with the simple equivalent STATCOM model using (12.72). During the iterative process, the parameters of STATCOM can be calculated using the simple (12.73).

$$V_{stat} = V_k + Z_{stat}(S_{stat}/V_k)^{*} \tag{12.73}$$

where,

$$S_{stat} = P_{stat} + jQ_{stat} \tag{12.74}$$

P_{stat} is equal to zero (there is no active power generation from STATCOM side) and Q_{stat} can be calculated each iterative process using (12.75).

$$Q_{stat} = Q_k = \sum_{i=1}^{n} |V_k||V_i|\left(G_{k,i}\sin\delta_{k,i} - B_{k,i}\cos\delta_{k,i}\right) + Q_k^{l} \tag{12.75}$$

After load flow convergence, the final values of STATCOM parameters can be updated using the same above equations. The developed STATCOM model enhances the reusability of load flow codes without any modification in Jacobian matrix.

12.6 Load Flow Solution Process with Developed STATCOM Model

The following steps are required for a simple implementation of STATCOM model into Newton-Raphson power and current injection load flow (NR-PCIM) method:

Step 1: Modify the bus data of the network by converting the connected STATCOM bus to PV bus with the desired voltage magnitude:
Step 2: Calculate the current mismatches for PQ buses and power mismatches for PV buses.
Step 3: Using (12.72), the NR power and current injection load flow method can be solved without any changes in the Jacobian matrix.
Step 4: Update the parameter of STATCOM during the iterative process using (12.73) and calculate the final values after the convergence.

12.7 Numerical Examples

Various slandered IEEE bus test systems such as: 14-bus, 30-bus, 57-bus and 118- are used for validating the developed power mismatch STATCOM model in Newton-Raphson power and current injection load flow (NR-PCIM) program.

12.7.1 IEEE 14 Bus Test System

The objective of this test is to validate the result obtained from the developed power mismatch STATCOM model in NR-PCIM and comprehensive STATCOM model in NR-PM load flow method [8]. The IEEE 14-bus system with a STATCOM controller is shown in Fig. 12.8. The STATCOM is connected at bus number 11 to control the voltage magnitude to be 1.01 pu The convergence tolerance for power mismatch is set to 10–4. The final values of STATCOM parameters are computed after the convergence and presented in Table 12.1. The obtained results from the two methods are similar.

The buses voltage and line flows of test system without and with STATCOM are presented in Table 12.1 and Table 12.2. From Table 12.1, it is clear that the voltages at slack bus and generator buses are same without and with STATCOM with significant change in load buses voltage. From Table 12.2, it can be seen that there is significant change in the line flows.

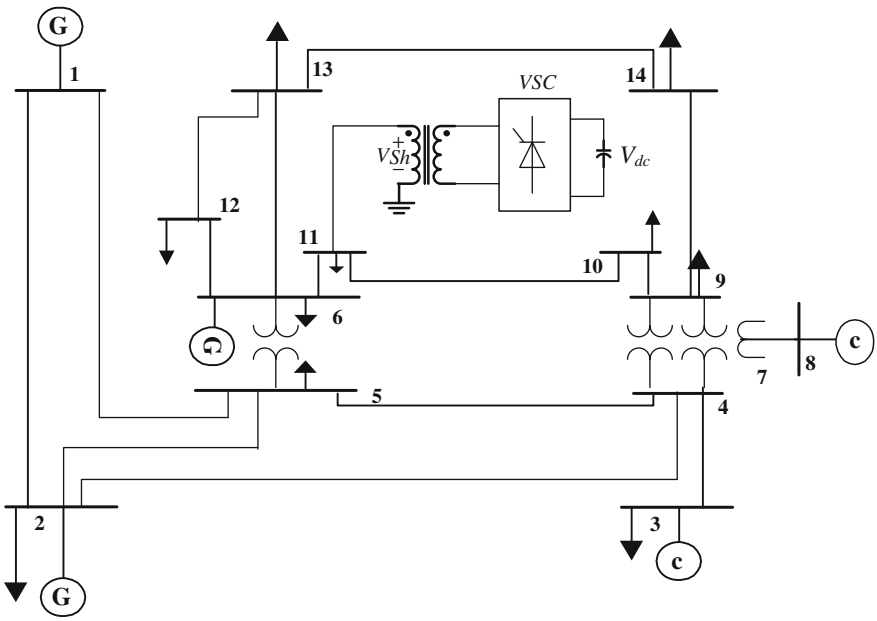

Fig. 12.8 IEEE 14-bus test system with STATCOM

Table 12.1 Buses voltage with and without STATCOM model

Bus number	Voltage magnitude (pu)		Angle of voltage (deg.)	
	W/O STATCOM	With STATCOM	W/O STATCOM	With STATCOM
1	1.0600	1.0600	0.0000	0.0000
2	1.0450	1.0450	−4.9511	−4.9699
3	1.0100	1.0100	−12.6141	−12.6510
4	1.0295	1.0270	−10.4188	−10.4123
5	1.0349	1.0332	−8.9546	−8.9807
6	1.0700	1.0700	−14.6700	−14.9146
7	1.0559	1.0481	−13.5516	−13.5239
8	1.0900	1.0900	−13.5516	−13.5239
9	1.0497	1.0342	−15.1674	−15.1488
10	1.0458	1.0214	−15.3638	−15.1431
11	1.0543	1.0100	−15.1436	−14.3606
12	1.0547	1.0535	−15.5140	−15.7526
13	1.0495	1.0472	−15.5734	−15.7799
14	1.0315	1.0216	−16.3510	−16.4485
STATCOM parameters	–	0.9776	–	−14.3607

Table 12.2 Line flow with and without STATCOM model

Bus number	Active power flow (MW)		Reactive power flow (MVAr)	
	W/O STATCOM	With STATCOM	W/O STATCOM	With STATCOM
1–2	155.95	156.52	−20.19	−20.32
1–5	76.42	76.71	−3.34	−2.57
2–3	72.53	72.69	3.63	3.61
2–4	56.01	56.07	−8.35	−6.93
2–5	41.47	41.78	−7.87	−6.94
3–4	−23.95	−23.80	−2.33	−0.91
4–5	−62.31	−61.30	7.40	5.23
4–7	28.41	27.94	−12.21	−9.59
4–9	16.09	15.77	−3.07	−0.68
5–6	43.76	45.35	−12.24	−12.75
6–11	7.11	8.28	5.07	28.35
6–12	7.80	7.95	2.70	3.13
6–13	17.65	17.92	7.99	9.71
7–8	0.00	0.00	−20.45	−24.94
7–9	28.41	27.94	6.35	13.62
9–10	5.48	5.07	2.73	13.78
9–14	9.52	9.15	2.65	0.60
10–11	−3.53	−4.00	−3.10	7.81
12–13	1.63	1.77	0.95	1.36
13-14	5.55	5.94	2.71	4.79

12.7.2 Performance Characteristics

The convergence characteristic for load flow method with the STATCOM model is tested using IEEE 14-bus test system. In this test the voltage at bus (11) is controlled to be 1.01 pu The active and reactive power mismatches against the number of iterations are drawn as shown in Fig. 12.9. Figure 12.9. From this figure, it can be observed that the developed model has good convergence characteristics than comprehensive STATCOM model in conventional NR-PM load flow.

12.7.3 Robustness of the Developed STATCOM Model in Many IEEE Test Systems

The IEEE 30 bus, the IEEE 57 bus and the IEEE 118 bus systems are tested with power mismatch STATCOM model at different case studies. Table 12.3 shows the ability of STATCOM model to solve different test systems, when one and more

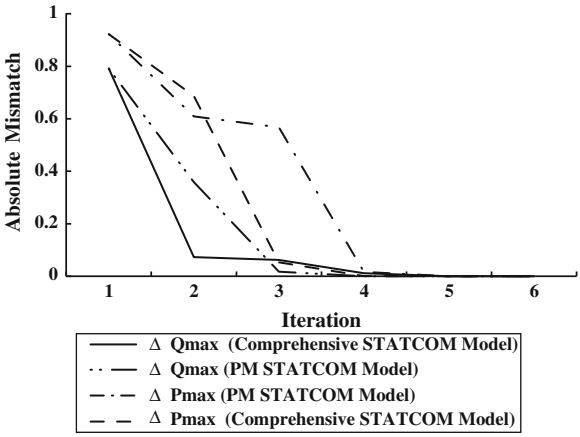

Fig. 12.9 Absolute power mismatches graphs for IEEE 14 bus system with STATCOM model

Table 12.3 Different cases for various IEEE test systems with STATCOM model

Case	Connected bus	IEEE 30		IEEE 57		IEEE118	
		$\lvert V_{stat} \rvert$ (pu)	δ_{stat} (deg.)	$\lvert V_{stat} \rvert$ (pu)	δ_{stat} (deg.)	$\lvert V_{stat} \rvert$ (pu)	δ_{stat} (deg.)
A	7	1.0195	−12.9452	1.0812	−8.0970	1.1699	62.7356
B	7	1.0199	−12.9522	1.0789	−7.9439	1.1699	62.6784
	14	1.0199	−16.0358	1.1028	−9.8241	1.0617	59.9252
C	7	1.0203	−12.9569	1.0789	−7.9497	1.1699	62.6249
	14	1.0072	−16.1656	1.1028	−9.8296	1.0617	59.8790
	16	1.0034	−15.7917	1.0041	−8.7404	1.0597	59.4116
D	7	1.0201	−12.9566	1.0781	−7.9360	1.1699	62.5752
	14	1.0065	−16.1179	1.0991	−9.8371	1.0617	59.8258
	16	1.0025	−15.7648	1.0041	−8.7405	1.0597	59.3608
	20	1.0133	−17.0829	1.0219	−15.0650	1.0674	53.9331
E	7	1.0201	−12.9566	1.0710	−7.8844	1.1699	62.5698
	14	1.0065	−16.1192	1.0691	−9.8240	1.0617	59.8204
	16	1.0025	−15.7657	1.0041	−8.7125	1.0597	59.3554
	20	1.0133	−17.0845	1.0157	−15.6908	1.0617	53.9262
	22	1.0098	−16.5331	1.0737	−15.0503	1.0213	52.3937

STATCOM(s) are implemented in the network to control the voltage at different places with constant value equals to 1.01 pu The load flow solution of IEEE 118-bus test system in the last test case is presented in Table 12.6. Based on Table 12.6, the ability of the developed model to work in large scale system has been validated. The required voltage magnitude at buses 7, 14, 16, 20, and 22 has been achieved after at the specified tolerance (0.00001).

Table 12.4 Execution time (seconds) of NR-PCIM with STATCOM

IEEE 14	IEEE 118
> 0.001	0.047

Tolerance = 0.0001 p.u

Table 12.5 Comparative convergence characteristics of NR-PCIM with STATCOM

Test system	Mismatch tolerance		
	0.01	0.001	0.0001
IEEE 14-bus	2	3	3
IEEE 118-bus	4	6	6

12.7.4 Execution Time and Numbers of Iterations

This test has been carried out using the personal computer (Pentium IV, 2 GHz processor and 2 GB RAM). In this test, the average execution time for NR-PCIM load with the developed power mismatch STATCOM model flow is tested. The STATCOM is connected to bus (11) to maintain the voltage magnitude at 1.01 p.u for both of IEEE 14-bus system and IEEE 118-bus system. The results are presented in Table 12.4. It can be observed that in case of IEEE 14-bus system, the time is very small and cannot be measured. In case of IEEE 118-bus system, the computation time is similar to the NR-PCIM load flow solution without STATCOM as presented in [2]. The number of iterations for NR-PCIM load flow method with STATCOM is presented in Table 12.5. Also it equals to number of iterations for NR-PCIM load flow method in uncontrolled case as presented in [2].

Appendix

See Table 12.6.

Table 12.6 Load flow solution of 118-bus system without and with STATCOM (Tolerance = 0.00001)

Bus no	Without STATCOM		With STATCOM	
	| V | (p.u)	Angle (deg.)	| V | (p.u)	Angle (deg.)
1	0.9713	62.3220	0.9713	62.1164
2	0.9550	63.9829	0.955	63.7778
3	0.9661	62.7630	0.9666	62.55
4	0.9980	63.0746	0.998	62.8692
5	0.9985	62.8321	1.0005	62.6013
6	0.9900	63.9709	0.99	63.7163
7	0.9894	63.0810	1.01	62.5694
8	1.0150	62.2493	1.015	62.0446

(continued)

Table 12.6 (continued)

Bus no	Without STATCOM		With STATCOM	
	| V | (p.u)	Angle (deg.)	| V | (p.u)	Angle (deg.)
9	1.0516	62.9063	1.0516	62.7016
10	1.0500	63.7536	1.05	63.5489
11	0.9847	61.5662	0.985	61.359
12	0.9900	61.9892	0.99	61.7834
13	0.9677	59.7092	0.968	59.5186
14	0.9831	60.4728	1.01	59.8201
15	0.9700	57.9257	0.97	57.7879
16	0.9809	59.9424	1.01	59.3551
17	0.9874	57.9938	0.989	57.8339
18	0.9730	58.6127	0.973	58.4687
19	0.9620	57.5914	0.962	57.441
20	0.9584	54.6368	1.01	53.9259
21	0.9610	53.4346	1.006	52.8844
22	0.9732	52.8387	1.01	52.3935
23	0.9999	52.7979	1.0048	52.6727
24	0.9920	47.9224	0.992	47.903
25	1.0500	56.8805	1.05	56.7669
26	1.0150	57.4306	1.015	57.3052
27	0.9680	59.4888	0.968	59.379
28	0.9614	58.8358	0.9614	58.7235
29	0.9628	59.0389	0.9628	58.924
30	0.9842	56.1419	0.9851	55.9856
31	0.9670	59.5811	0.967	59.4652
32	0.9630	58.9775	0.963	58.8704
33	0.9624	51.7173	0.9633	51.596
34	0.9840	46.7980	0.984	46.7333
35	0.9794	46.7924	0.9797	46.7202
36	0.9800	47.0233	0.98	46.9558
37	0.9841	46.5927	0.9859	46.4979
38	0.9525	45.6793	0.9538	45.5775
39	0.9681	44.7478	0.9687	44.6779
40	0.9700	44.5753	0.97	44.5175
41	0.9666	42.8660	0.9666	42.8083
42	0.9850	41.0079	0.985	40.9501
43	0.9623	38.4108	0.9555	38.5144
44	0.9767	28.6785	0.9591	28.8722
45	0.9866	26.1384	0.974	26.2406
46	1.0050	25.9568	1.005	25.8786
47	1.0067	22.1717	1.0067	22.1152

(continued)

Table 12.6 (continued)

Bus no	Without STATCOM		With STATCOM	
	| V | (p.u)	Angle (deg.)	| V | (p.u)	Angle (deg.)
48	1.0210	25.8985	1.0148	25.9531
49	1.0250	26.5040	1.025	26.4461
50	1.0016	26.9028	1.0016	26.8468
51	0.9692	27.3772	0.9692	27.3238
52	0.9599	27.2403	0.9599	27.1875
53	0.9473	28.5161	0.9473	28.4651
54	0.9550	31.0971	0.955	31.0474
55	0.9520	31.6356	0.952	31.5865
56	0.9540	31.2197	0.954	31.1703
57	0.9706	28.9539	0.9706	28.9016
58	0.9599	28.7045	0.9599	28.6527
59	0.9850	29.3477	0.985	29.3054
60	0.9932	27.7342	0.9932	27.6943
61	0.9950	28.0285	0.995	27.989
62	0.9980	28.4345	0.998	28.3941
63	0.9752	27.7294	0.9752	27.6902
64	0.9875	26.8596	0.9875	26.8219
65	1.0050	24.2978	1.005	24.2643
66	1.0500	26.4777	1.05	26.4336
67	1.0202	26.5551	1.0202	26.5127
68	0.9969	17.9593	0.997	17.9369
69	1.0350	0.0000	1.035	0
70	0.9840	17.9521	0.984	17.9428
71	0.9838	20.6220	0.9838	20.6119
72	0.9800	34.1631	0.98	34.1488
73	0.9910	20.7075	0.991	20.6974
74	0.9580	15.9344	0.958	15.9229
75	0.9648	13.2718	0.9649	13.2595
76	0.9430	17.3183	0.943	17.2994
77	1.0060	16.2047	1.006	16.1763
78	1.0035	15.9780	1.0018	15.9764
79	1.0092	16.4255	1.0042	16.4655
80	1.0400	19.0840	1.04	19.0691
81	0.9939	18.3619	0.9939	18.3421
82	0.9777	22.3464	0.9688	22.5033
83	0.9738	24.8854	0.965	25.0818
84	0.9751	29.5503	0.9723	29.6689
85	0.9850	32.1136	0.985	32.1763
86	0.9896	33.4811	0.9896	33.5438

(continued)

Table 12.6 (continued)

Bus no	Without STATCOM		With STATCOM	
	| V | (p.u)	Angle (deg.)	| V | (p.u)	Angle (deg.)
87	1.0150	38.0801	1.015	38.1428
88	0.9881	34.4891	0.9881	34.5437
89	1.0050	38.0258	1.005	38.0748
90	0.9850	41.9407	0.985	41.9884
91	0.9800	41.1237	0.98	41.1697
92	0.9900	37.1563	0.99	37.1998
93	0.9792	33.3650	0.9783	33.419
94	0.9795	30.5156	0.9778	30.5742
95	0.9667	27.2660	0.964	27.3313
96	0.9777	24.2442	0.9736	24.3161
97	1.0027	21.3006	1.0006	21.322
98	1.0140	23.7539	1.014	23.7538
99	1.0100	31.3465	1.01	31.36
100	1.0170	35.0289	1.017	35.0545
101	0.9925	35.0589	0.9925	35.092
102	0.9900	36.3519	0.99	36.3919
103	1.0100	39.6010	1.01	39.6266
104	0.9710	42.1625	0.971	42.1881
105	0.9650	43.0899	0.965	43.1155
106	0.9607	41.3471	0.9607	41.3727
107	0.9520	45.4796	0.952	45.5052
108	0.9654	45.3730	0.9654	45.3986
109	0.9660	46.3420	0.966	46.3676
110	0.9730	49.2297	0.973	49.2553
111	0.9800	50.9234	0.98	50.949
112	0.9750	52.1759	0.975	52.2015
113	0.9930	59.0680	0.993	58.9385
114	0.9601	58.6297	0.9601	58.5214
115	0.9600	58.6191	0.96	58.5106
116	1.0050	18.1163	1.005	18.094
117	0.9738	60.4484	0.9738	60.2426
118	0.9476	14.6813	0.9476	14.6659

References

1. Gotham DJ, Heydt GT (1998) Power flow control and power flow studies for systems with FACTS devices. IEEE Trans Power Syst 13:60–66
2. Kamel S, Abdel-Akher M, Jurado F, Ruiz-Rodríguez FJ (2013) Modeling and analysis of voltage and power control devices in current injections load flow method. Electric Power Compon Syst 41:324–344
3. Radman G, Raje SR (2007) Power flow model/calculation for power systems with multiple FACTS controllers. Electric Power Syst Res 77:1521–1531
4. Canizares CA, Pozzi M, Corsi S, Uzunovic E (2003) STATCOM modeling for voltage and angle stability studies. Int J Electric Power Energy Syst 6:421–422
5. Yankui Z, Yan Z, Bei W, Jian Z (2006) Power injection model of STATCOM with control and operating limit for power flow and voltage stability analysis. Electric Power Syst Res 76:1003–1010
6. Kamel S, Abdel-Akher M, Song MK (2012) Analysis and modeling of a unified power flow controller in Newton-Raphson load flow. Adv Sci Lett 8:884–889
7. Bhowmick S, Das B, Kumar N (2011) An advanced static synchronous compensator model to reuse Newton and decoupled power flow codes. Electric Power Compon Syst 39:1647–1666
8. Acha E, Ambriz-Pérez H, Fuerte-Esquivel CR, Angeles-Camacho C (2004) FACTS: modelling and simulation in power networks, Wiley-Blackwell, New York
9. Bhowmick S, Das B, Kumar N (2011) An advanced static synchronous compensator model to reuse Newton and decoupled power flow codes. Electric Power Compon Syst 39 (15):1647–1666
10. Nor KM., Mokhlis H, Gani TA (2004) Reusability techniques in load-flow analysis computer program. IEEE Trans Power Syst 19 (4):1754–1762
11. da Cost VM, Martins N, Pereira JLR (1999) Developments in the Newton-Raphson power flow formulation based on current injections. IEEE Trans Power Syst 14:1320–1326
12. da Cost VM, Martins N, Pereira JLR (2001) An augmented Newton-Raphson power flow formulation based on current injections. Electr Power Energy Syst 23:305–312
13. Garcia PAN, Pereira JLR, Carneiro S, da Cost VM, Martins N (2000) Three-phase power flow calculations using the current injection method. IEEE Trans Power Syst 15:508–514
14. Garcia PAN, Pereira JLR, Carneiro S, Vinagre MP, Gomes FV (2004) Improvements in the representation of PV buses on three-phase distribution power flow. IEEE Trans Power Deliv 19:894–896
15. Hingorani NG, Gyugyi L (2000) Understanding FACTS—concepts and technology of flexible AC transmission systems. IEEE Press, NewYork
16. Yang Z, Crow ML, Shen C, Zhang L (2000) The steady-state characteristics of A STATCOM with energy storage. IEEE Power Eng Soc Summer Meet 2:669–674
17. Hanson DJ, Woodhouse ML, Horwill C, Monkhouse DR, Osborne MM (2002) STATCOM: a new era of reactive compensation. Power Eng J 151–160
18. Wang HF, Li H, Chen H (2002) Application of cell immune response modelling to power system voltage control by STATCOM. IEE Proc—Gener, Trans Distrib 149(1):102–107
19. Haque MH (2004) Use of energy function to evaluate the additional damping provided by a STATCOM. Electric Power Syst Res 72(2):195–202
20. Abido MA (2005) Analysis and assessment of STATCOM-based damping stabilizers for power system stability enhancement. Electric Power Syst Res 73(2):177–185
21. Padiyar KR, Parkash VS (2003) Tuning and performance evaluation of damping controller for a STATCOM. Int J Electric Power Energy Syst 25(2):155–166
22. Cong L, Wang Y (2002) Coordinated control of generator excitation and STATCOM for rotor angle stability and voltage regulation enhancement of power systems. IEE Proc—Gener, Trans Distrib 149(6):659–666
23. Rahim AHMA, Al-Baiyat SA, Al-Maghrabi HM (2002) Robust damping controller design for a static compensator. IEE Proc—Gener, Trans Distrib 149(4):491–496

24. STATCOM Prototype in the Turkish Transmission System, (Online). Available http://www.guckalitesi.gen.tr/en/projects/alt08.php
25. Gyugyi L (1994) Dynamic compensation of ac transmission lines by solid-state synchronous voltage source. IEEE Trans Power Deliv 9(2):904–911
26. Sen KK (1999) STATCOM—STATic synchronous COMpensator: theory, modeling, and applications. IEEE proceeding of: power engineering society winter meeting
27. Zhang X.-P, Rehtanz C, Pal BC (2006) Flexible AC transmission systems: modelling and control Monograph. Springer Power Systems Series
28. Ferreira CA, da Costa VM (2005) A second order power flow based on current injection equations. Int J Electric Power Energy Syst 27(4):254–263
29. Garcia PAN, Pereira JLR, Carneiro S, da Cost VM, Martins N (2000) Three-phase power flow calculations using the current injection method. IEEE Trans Power Syst 15(2):508–514
30. Penido DRR, de Araujo LR, Carneiro S, Pereira JLR, Garcia PAN (2008) Three-phase power flow based on four-conductor current injection method for unbalanced distribution networks. IEEE Trans Power Syst 23(2):494–503
31. de Araujo LR, Penido DRR, Junior SC, Pereira JLR, Garcia PAN (2010) Comparisons between the three-phase current injection method and the forward/backward sweep method. Int J Electric Power Energy Syst 32(7):825–833
32. Penido DRR, de Araujo LR, Carneiro Jr S, Pereira JLR, Garcia PAN (2007) Power factor correction on distribution networks including distributed generation. IEEE Power Engineering Society General Meeting
33. Penido DRR, de Araujo LR, Junior SC, Pereira JLR (2013) A new tool for multiphase electrical systems analysis based on current injection method. Int J Electric Power Energy Syst 44(1):410–420
34. Garcia PAN, Pereira JLR, Carneiro S Jr (2001) Voltage control devices models for distribution power flow analysis. IEEE Trans Power Syst 16(4):586–594
35. Penido DRR, de Araujo LR, Carneiro Jr S, Pereira JLR (2006) Unbalanced three-phase distribution system load-flow studies including induction machines. IEEE Power Engineering Society General Meeting
36. da Costa VM, de Oliveira ML, Guedes MR (2007) Developments in the analysis of unbalanced three-phase power flow solutions. Int J Electric Power Energy Syst 29(2):175–182
37. de Araujo LR, Penido DRR, Júnior SC, and Pereira JLR (2010) Power-flow analysis of the IEEE 8500-node test feeder using the current injection method. IEEE PES transmission and distribution conference and exposition
38. Penido DRR, de Araujo LR, Pereira JLR, Garcia PAN, and Carneiro S (2004) Four wire Newton-Rapshon power flow based on the current injection method. IEEE PES power systems conference and exposition
39. Kamel S, Abdel-Akher M, Jurado F (2013) Improved NR current injection load flow using power mismatch representation of PV bus. Int J Electr Power Energy Syst 53:64–68
40. Kamel S, Jurado F, Vera D (2013) A simple implementation of power mismatch STATCOM model into current injection Newton-Raphson power-flow method. Electri Eng (Archiv für Electrotechnik). doi:10.1007/s00202-013-0288-4

Chapter 13
Optimal Placement and Sizing of STATCOM in Power Systems Using Heuristic Optimization Techniques

Reza Sirjani

Abstract The benefits of reactive power compensation depend greatly on the placement and size of the compensators. STATCOM is a shunt compensator and one of the important members of the Flexible AC Transmission Systems (FACTS) family that are increasingly being used in long transmission lines in modern power systems. The FACTS devices placement problem is commonly solved using heuristic optimization techniques which are diverse and have been the subject of ongoing enhancements. This chapter, in the first stage, presents a survey of the literature from the last decade that has focused on the various heuristic optimization techniques applied to determine optimal placement and sizing of the STATCOM. In the second stage, the application of the global harmony search (GHS) algorithm as a new meta-heuristic optimization method for determining the optimal location and size of STATCOM in a transmission network is presented. The algorithm is easy to be implemented and capable of finding multiple optimal solutions to the constrained multi-objective problem, providing more flexibility in making decisions about the location of STATCOM. Power system loss reduction, bus voltage profile improvement, voltage stability enhancement and device size are employed as measures of power system performance in the optimization algorithm. The proposed multi-objective GHS algorithm is validated on 57 and 118-bus transmission networks.

Keywords STATCOM · Power loss · Modal analysis · Optimization techniques · Harmony search algorithm

R. Sirjani (✉)
Faculty of Engineering, Cyprus International University, Nicosia, Mersin 10, Northern Cyprus, Turkey
e-mail: rsirjani@ciu.edu.tr

F. Shahnia et al. (eds.), *Static Compensators (STATCOMs) in Power Systems*, Power Systems, DOI 10.1007/978-981-287-281-4_13

13.1 Introduction

Reactive power compensation is used to influence the natural electrical characteristics of a transmission line to increase the steady-state transmittable power and to control the voltage profile along the line. A number of reactive compensation devices such as shunt capacitor, static VAr compensator (SVC) and STATCOM have long been applied by electric power utilities for this purpose. STATCOMs have a variety of applications in the operation and control of power systems, such as scheduling power flow, decreasing unsymmetrical components, damping power oscillations and enhancing transient stability [1–4]. STATCOM is a shunt-connected reactive compensation device that is capable of generating and absorbing reactive power. Its output can be varied to maintain and control specific parameters of an electric power system [5]. The improvement in static voltage stability and the reduced losses that result from using a STATCOM have been demonstrated in Shaygan et al. [6]. The results show that the installation of a STATCOM in critical buses is an effective solution for reducing active and reactive losses, and this type of FACTS device can improve static voltage stability for both the base system and the stressed system. The system dynamics influencing voltage stability are usually slow. Therefore, many aspects of the power system can be analysed effectively by using static methods that examine the viability of an equilibrium point representing a specific condition of the system. The static analysis techniques allow the examination of a wide range of system conditions and, if appropriately used, can provide much insight into the nature of the problem and the identification of the key contributing factors. One of the suitable methods for static voltage stability analysis is modal analysis. In this method, the system voltage stability characteristics can be identified by computing the eigenvalues and eigenvectors of a reduced Jacobian matrix [7].

Because of economical considerations, the installation of a FACTS controller in every bus is impossible and unnecessary. Identifying the best locations for STATCOMs entails calculating steady-state conditions for the network. However, because the load flow equations are nonlinear, the problem becomes very complex, and an extensive investigation has to be undertaken to solve the problem.

Several studies on the use of these controllers for voltage and angle stability applications have been conducted and reported in the literature. A variety of methods are used to optimize the allocation of these devices in power systems. These methods may be classified into the following categories [6]:

- Loss sensitivity analysis
- Voltage stability analysis using modal analysis and Continuation Power Flow (CPF)
- Cost analysis using Optimal Power Flow (OPF)
- Heuristic optimization techniques

From the categories, the heuristic optimization techniques have been widely applied in solving the optimal STATCOM placement problem. In this chapter, a comprehensive analysis of the heuristic optimization techniques for optimal placement and sizing of STATCOMs that have been proposed recently by various researchers is presented. This analysis includes important heuristic optimization techniques such as Evolution Strategies (ES), Genetic Algorithms (GA), Particle Swarm Optimization (PSO), and Harmony Search (HS) algorithms used in solving power system optimization problems. In addition, applications of hybrid techniques in optimal STATCOM placement problems are discussed.

In the next stage, a new optimization technique, the GHS algorithm is used to find the optimal placement and sizing of STATCOM in power systems. The harmony search algorithm is a meta-heuristic optimization method that is inspired by musicians adjusting the pitches of their instruments to find better harmony [8]. It has several advantages over other methods, such as not requiring initial value settings for the decision variables and handling both discrete and continuous variables. In this research, the suitable buses are first identified using modal analysis. Next, the global harmony search algorithm is employed to determine the amount of shunt compensation required for loss minimization and voltage improvement with respect to the size of the STATCOM. The results obtained using the proposed algorithm in 57 and 118-bus test systems are compared with other optimization methods for validation.

13.2 STATCOM Placement and Sizing Using Optimization Techniques

Recently, heuristic optimization techniques have become a popular choice for solving complex and intricate problems which are otherwise difficult to solve by traditional methods [9]. In the past few decades, several global optimization algorithms have been developed that are based on the nature inspired analogy. These are mostly population based heuristics, also called general purpose algorithms because of their applicability to a wide range of problems [9]. Some popular global optimization algorithms include ESs [10], GAs [11, 12], Simulated Annealing (SA) [13], Artificial Immune Systems (AIS) [14], Ant Colony Optimization (ACO) [15], PSO [16], HS algorithms [8], Bee Colony Optimization (BCO) [17], and others.

This section presents the basic knowledge of evolutionary computation and other heuristic optimization techniques as well as how they are combined with knowledge elements in computational intelligence systems. Applications to the optimal placement and sizing of STATCOMs in power networks are emphasized, and recent research is presented and discussed.

13.2.1 Evolution Strategies (ES)

The ES optimization technique was introduced in the early 1960s and developed further in the 1970s by Rechenberg and Schwefel at the University of Berlin in Germany. It was originally created to solve technical optimization problems, and its first application was in the area of hydrodynamics [18]. Nowadays, the ES is recognized as a very strong optimization method capable of solving large scale, multimodal, highly constrained, nonlinear problems. The main search procedure in the ES is the mutation operator that generates random samples around search points (solution candidates) selected from a population of different search points. The original strategy, denoted by 1 + 1, generates one offspring from a single parent by applying mutation. If the child performs better than its ancestor, it will be the parent of the next generation [19].

An ES was developed to obtain the best points of operation of FACTS devices [20]. The objective function was defined to adjust the control variables of the SVC, STATCOM, and UPFC in order to improve the power system operation by reducing losses that electric network suffers under a certain load condition, taking into account the voltage drop constraints and operation limits of the devices. The ES developed in this paper was applied to various power systems with satisfactory results and low computational effort.

13.2.2 Genetic Algorithm (GA)

GA is one of the most popular types of evolutionary algorithms. To be more precise, it constitutes a computing model for simulating natural and genetic selection that is related to the biological evolution described in Darwin's Theory [11, 12]. In this computing model, a population of abstract representations called as chromosomes or the genome of candidate solutions called as individuals, to an optimization problem could result in better solutions. They are traditionally represented in binary form as strings comprised of 0s and 1s with fixed length. But other kinds of encoding are also possible which include real values and order chromosomes. The program then assigns proper number of bits and coding [9].

Being a member of the evolutionary computation family, the first step in GA is population initialization, which is usually done stochastically. GA usually uses three simple operators called as selection, recombination or crossover and mutation [9]. Selection is the step of a GA in which a certain number of individuals are chosen from the current population for later breeding (recombination or crossover); the rate of choosing is normally proportional to the individual's fitness value. There are several general selection techniques, namely, tournament selection and fitness proportionality selection which is also known as roulette-wheel selection.

Other techniques only choose those individuals with a fitness value greater than a given arbitrary constant. Taken together, crossover and mutation are called reproduction which is analogous to biological crossover and mutation [9]. The advantages and disadvantages of GA are described as follows [9, 11]:

The advantages of GA:

- It can solve every optimization problem which can be described with the chromosome encoding.
- It solves problems with multiple solutions.
- Since GA execution technique is not dependent on the error surface, it can be used for solving multi-dimensional, non-differential, non-continuous, and even non-parametrical problems.
- GA is a technique which is easy to be understood and it practically does not demand the knowledge of mathematics.
- GA is easily transferred to existing simulations and models.

The disadvantages of GA:

- Certain optimization problems cannot be solved by GA probably due to poorly known fitness functions which generate bad chromosome blocks.
- There is no absolute assurance that a GA will find a global optimum.
- GA cannot assure constant optimization response times. In addition, the difference between the shortest and the longest optimization response times is much larger than with conventional gradient methods. This disadvantage limits the use of GA in real time applications.
- GA application in real time control is limited because of random solutions and convergence. This means that while the entire population is improving, there is no assurance that an individual within this population will converge to its specified value. Therefore, it is unreasonable to use GA for on-line control in real systems without testing it first on a simulation model.

A GA based optimization procedure has been implemented to find the best placement, type, and size of selected FACTS devices for reducing total financial losses in the network caused by voltage sags [21]. Three types of FACTS devices were considered, namely, SVC, STATCOM, and Dynamic Voltage Restorer (DVR).

Another GA based allocation of FACTS devices considered the cost function of FACTS devices and power system losses [22]. Simulation of the test system for different scenarios showed that the placement of multi-type FACTS devices leads to an improvement in the voltage stability margin of power system and reduction of losses.

An optimization method termed “the Queen Bee assisted GA” has been explored to obtain optimal placement of FACTS devices for voltage profile enhancement [23]. The proposed algorithm is a modification of the standard GA incorporating the evolution of a queen bee in a hive. This algorithm converges much faster than the standard GA with smaller number of parameters and reduced computational burden. A performance criterion using a voltage stability index was defined to

quantify voltage stability at any given bus. The effectiveness of the approach was confirmed through simulation results.

Tavakoli et al. [24] examined the average model of STATCOM in the time domain and then adapted its power flow analysis. A combinatorial optimization was arranged which focused on voltage stability, reactive power, and losses of transmission lines as three main objectives for the power system. GA was employed to seek the optimal solution for sizing and placing STATCOMs across the IEEE 14-bus network, while a correcting power ratio was defined for adapting the optimized values with those obtained by the average model.

An approach based on sensitivity analysis and GA was applied to optimally locate STATCOM in a distribution network [25]. A step-by-step sensitivity analysis approach is utilized to find optimal placement of compensators. In this process, a compound voltage-loss sensitivity index is used to meet various optimization requirements. In the next step, reactive power injection of the STATCOM is defined by the GA. The objective function takes into account voltage stability, reduction of active losses and reduction of reactive power in a power network.

13.2.3 Particle Swarm Optimization (PSO)

PSO algorithm belongs to the category of evolutionary computation for solving global optimization problems. The the PSO algorithm was first introduced for solving optimization problem in 1995 by Eberhart and Kennedy [16]. PSO is a well known and popular search strategy that has gained widespread appeal amongst researchers and has been shown to offer good performance in a variety of application domains, with potential for hybridization and specialization. It is a simple and robust strategy based on the social and cooperative behaviour shown by various species like flocks of bird, schools of fish, and so on. PSO and its variants have been effectively applied to a wide range of real life optimization problems [9].

From the literature, it is noted that PSO has advantages and disadvantages which are described as follows [9, 16]:

The advantages of PSO:

- PSO is based on intelligence which can be applied for both scientific research and engineering use.
- PSO have no overlapping and mutation calculation and the search can be carried out based on the speed of a particle. In the development of several generations, only the most optimist particle can transmit information onto the other particles, and the speed of the researching is very fast.
- The calculation in PSO is very simple compared with other optimization techniques and its optimization ability is stronger.
- PSO adopts real number code, and it is decided directly by a solution. The number of the dimension is equal to the constant of a solution.

The disadvantages of PSO:

- PSO easily suffers from partial optimism, which reduces the accuracy and speed of finding the velocity and position vectors.
- PSO has difficulty in finding optimal design parameters and its accuracy depends on the initial conditions and the parameter values selected.

Del Valle et al. [26] demonstrated the application of PSO for optimal sizing and location of STATCOM in a power system, considering voltage deviation constraints at each bus. Results from the illustrative example showed that the PSO is able to find the solution with the best size and location with a high degree of convergence and with statistical significance when the minimum, maximum, average and standard deviation values of the voltage deviation metric are evaluated.

Hernandez et al. [27] demonstrated the feasibility of applying the PSO technique in solving optimal allocation of a STATCOM in a 45-bus section of the Brazilian power system. The technique was able to find the best location for the STATCOM in order to optimize the system voltage profile with a low degree of uncertainty. Another approach for optimal placement of STATCOMs in power systems was proposed using simultaneous application of PSO and CPF in order to improve the voltage profile, minimize the power system's total losses, and maximize the system load-ability with respect to the size of the STATCOM [5].

The PSO technique has also been applied to determine the optimal location and controller parameters of STATCOM [28]. Here, a systematic procedure to determine the optimal location of the STATCOM for transient stability improvement following a severe disturbance was presented. The application of PSO for sizing and locating a STATCOM in a power system while considering voltage deviation constraints was demonstrated in [29]. Results from the illustrative example showed that the PSO techniques is able to find the best size and location with statistical significance and a high degree of convergence when evaluating the minimum, maximum, average, and standard deviation values of the voltage deviation metric.

To find the optimal location and sizing of a STATCOM in a power system for voltage profile improvement, different variations of the PSO techniques have been applied [30]. From among the various PSO techniques, namely, the classical PSO, PSO time varying inertia weight, PSO random inertia weight and PSO time varying acceleration coefficients (PSO-TVAC), the PSO-TVAC model was found to be superior in terms of computational speed and accuracy of solution [30]. The effect of population size and initial and final values of acceleration coefficients was also investigated in this paper.

13.2.4 Harmony Search (HS) Algorithm

The HS algorithm is an optimization technique that is inspired by musicians improvising their instrument pitches to find better harmony [8]. In the same way as musical instruments can be played with discrete musical notes based on player

experience or based on random processes in improvisation, optimal design variables can be obtained with certain discrete values based on computational intelligence and random processes [31]. Music players improve their experience based on aesthetic standards while design variables in computer memory can be improved based on an objective function. Among the advantages of the HS algorithm are that it can consider both discontinuous and continuous functions because it does not require differential gradients, it does not require initial value setting for the variables, it is free from divergence, and it may escape local optima [31]. The HS algorithm has the following merits [8, 31]:

- HS does not require differential gradients, thus it can consider discontinuous functions as well as continuous functions.
- HS can handle discrete variables as well as continuous variables.
- HS does not require initial value setting for the variables.
- HS is free from divergence.
- HS may escape local optima.
- HS may overcome the drawback of GA building block theory which works well only if the relationship among variables in a chromosome is carefully considered. If neighbour variables in a chromosome have weaker relationship than remote variables, the building block theory may not work well because of crossover operation. However, HS explicitly considers the relationship using ensemble operation.
- HS has a novel stochastic derivative applied to discrete variables, which uses musician's experiences as a searching direction.

In [32], the improved harmony search algorithm (IHS) is used to determine the optimal location and size of STATCOMs in a transmission network. The problem is decomposed into two sub-problems. The first sub-problem is the optimal placement of STATCOM devices using the modal analysis method. The second sub-problem is the optimization of the load flow by setting STATCOM parameters using the improved harmony search algorithm. A multi-criterion objective function is defined to enhance the voltage stability, improve the voltage profile and minimise power loss while considering the total STATCOM size. The results from a 57-bus test system show that the IHS algorithm produces a lower power loss, better voltage profile and greater voltage stability than the traditional harmony search algorithm and particle swarm optimization techniques in solving the STATCOM placement and sizing problem.

13.2.5 Hybrid Artificial Intelligence Techniques

To create a hybrid intelligent system, two or more artificial intelligence techniques are applied. During the last decade, hybrid systems have been applied in engineering applications. A combination of Modified Simulated Annealing (MSA) and

PSO techniques has been proposed to minimize total losses in a power system with FACTS devices [33]. The problem was decomposed into two sub-problems in which the first sub-problem considered optimal placement of FACTS devices using a line loss sensitivity index and the second sub-problem considered load flow with FACTS parameters using the MSA/PSO techniques.

13.2.6 Comparison of Various Heuristic Optimization Techniques

The number of publications and the heuristic optimization techniques applied to solve the optimal STATCOM placement problem in the specified period are shown in Fig. 13.1. The PSO, GA, and hybrid methods have been the most popular optimization techniques for solving the optimal STATCOM placement problem in the last decade.

From the figure, PSO is the most popular technique applied because of its advantages, which include simple implementation, small computational load, and fast convergence. PSO is efficient for solving many problems for which it is difficult to find accurate mathematical models. However, the PSO algorithm is prone to relapsing into local minima and premature convergence when solving complex optimization problems. The GA, which is considered one of the first global optimization techniques for solving the optimal FACTS placement problem, has some drawbacks such as divergence and local optima problems. Many recent publications use hybrid techniques or multi-stage methodologies to find the optimal locations and sizes of STATCOMs. In most of these hybrid techniques, approaches are proposed to find the critical buses, while other optimization techniques such as PSO and GA are used to find the optimal sizes of the STATCOM.

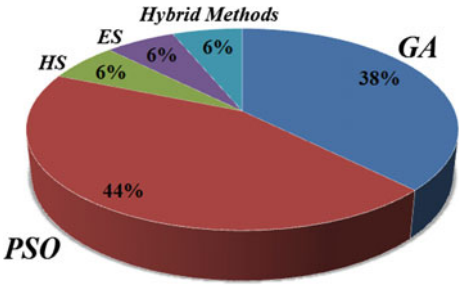

Fig. 13.1 Number of papers published on different optimization techniques for optimal STATCOM placement

13.3 Optimal Placement and Sizing of STATCOM Using GHS Algorithm

13.3.1 STATCOM Modelling

Typically, a STATCOM consists of a coupling transformer, an inverter, and a DC capacitor. For an ideal steady-state analysis, the active power exchange between the AC system and the STATCOM is assumed negligible and only reactive power is exchanged between them [6, 34]. The schematic representation of STATCOM and its equivalent circuit are shown in Fig. 13.2a, b, respectively.

In Fig. 13.2a, the shunt-connected transformer is assumed to be ideal. STATCOM is implemented so that the active power flow between the AC source and the Voltage Source Converter (VSC) is controlled by a phase angle, and the reactive power flow is determined mainly by the magnitude of the voltage source (V_k) and the VSC output fundamental voltage (V_{vR}). VSC generates reactive power when $V_{vR} > V_k$ and consumes reactive power when $V_{vR} < V_k$. During normal operation, a small amount of active power flows into the VSC to compensate for the power losses inside the VSC, and δ is kept slightly larger than zero for lagging power factor [34]. The STATCOM equivalent circuit shown in Fig. 13.2b is used to derive the mathematical model of the controller for inclusion in the power flow algorithm. The power flow equations for bus i of the power system with no FACTS controllers are given by,

$$P_i = \sum_{m=1}^{n} \left(V_i^2 G_{ii} - V_i V_m [G_{im} \cos(\theta_i - \theta_m) + B_{im} \sin(\theta_i - \theta_m)] \right) \tag{13.1}$$

$$Q_i = \sum_{m=1}^{n} \left(-V_i^2 B_{ii} + V_i V_m [G_{im} \cos(\theta_i - \theta_m) - B_{im} \cos(\theta_i - \theta_m)] \right) \tag{13.2}$$

With the addition of a STATCOM connected at bus k, the system power flow equations remain the same as the equations of a system without a STATCOM for all buses given by (13.1) and (13.2) except for bus k. The power flow equations for

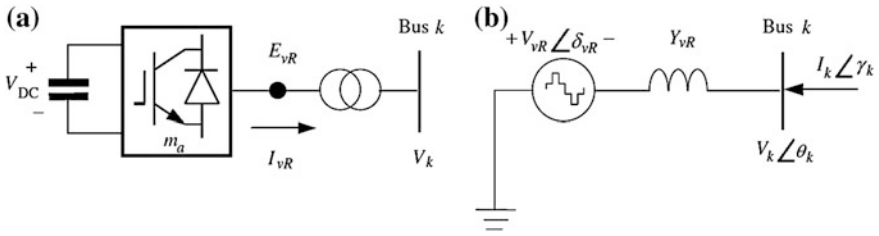

Fig. 13.2 STATCOM representation **a** VSC connected to the AC network via a transformer, **b** Shunt solid-state voltage source [34]

the STATCOM in a two-bus system shown in Fig. 13.2b are derived by first considering the voltage source and the complex power which are given by,

$$E_{vR} = V_{vR}(\cos\delta_{vR} + j\sin\delta_{vR}) \tag{13.3}$$

$$S_{vR} = V_{vR}I_{vR}^{*} = V_{vR}Y_{vR}^{*}(V_{vR}^{*} - V_{k}^{*}) \tag{13.4}$$

By substituting (13.3) into (13.4), the active and reactive power equations at the converter terminal and bus k are obtained as follows [6]:

$$P_{vR} = V_{vR}^{2}G_{vR} - V_{k}V_{vR}[G_{vR}\cos(\delta_{vR} - \theta_{k}) + B_{vR}\sin(\delta_{vR} - \theta_{k})] \tag{13.5}$$

$$Q_{vR} = -V_{vR}^{2}B_{vR} + V_{k}V_{vR}[B_{vR}\cos(\delta_{vR} - \theta_{k}) - G_{vR}\sin(\delta_{vR} - \theta_{k})] \tag{13.6}$$

$$P_{k} = V_{k}^{2}G_{vR} - V_{k}V_{vR}[G_{vR}\cos(\theta_{k} - \delta_{vR}) + B_{vR}\sin(\theta_{k} - \delta_{vR})] \tag{13.7}$$

$$Q_{k} = -V_{k}^{2}B_{vR} + V_{k}V_{vR}[B_{vR}\cos(\theta_{k} - \delta_{vR}) - G_{vR}\sin(\theta_{k} - \delta_{vR})] \tag{13.8}$$

These equations for two-bus power system are obtained. Thus, for an n-bus power system, the active and reactive power equations at bus k (i.e. the bus where the STATCOM is connected) are given as follows:

$$\begin{aligned} P_{K} = {} & V_{vR}^{2}G_{vR} - V_{K}V_{vR}[G_{vR}\cos(\delta_{vR} - \theta_{K}) + B_{vR}\sin(\delta_{vR} - \theta_{K})] \\ & + \sum_{m=1}^{n}\left(V_{K}^{2}G_{KK} - V_{K}V_{m}[G_{Km}\cos(\theta_{K} - \theta_{m}) + B_{im}\sin(\theta_{K} - \theta_{m})]\right) \end{aligned} \tag{13.9}$$

$$\begin{aligned} Q_{K} = {} & -V_{K}^{2}B_{vR} + V_{K}V_{vR}[B_{vR}\cos(\theta_{K} - \delta_{vR}) - G_{vR}\sin(\theta_{K} - \delta_{vR})] \\ & + \sum_{m=1}^{n}\left(-V_{K}^{2}B_{KK} + V_{K}V_{m}[G_{Km}\cos(\theta_{K} - \theta_{m}) - B_{Km}\sin(\theta_{K} - \theta_{m})]\right) \end{aligned} \tag{13.10}$$

Using these power equations, the linearized STATCOM model is derived as shown in (13.11), where the voltage magnitude V_{vR} and phase angle δ_{vR} are considered as state variables:

$$\begin{bmatrix} \Delta P_{K} \\ \Delta Q_{K} \\ \Delta P_{vR} \\ \Delta Q_{vR} \end{bmatrix} = \begin{bmatrix} \frac{\partial P_{K}}{\partial \theta_{K}} & \frac{\partial P_{K}}{\partial V_{K}}V_{K} & \frac{\partial P_{K}}{\partial \delta_{vR}} & \frac{\partial P_{K}}{\partial V_{vR}}V_{vR} \\ \frac{\partial Q_{K}}{\partial \theta_{K}} & \frac{\partial Q_{K}}{\partial V_{K}}V_{K} & \frac{\partial Q_{K}}{\partial \delta_{vR}} & \frac{\partial Q_{K}}{\partial V_{vR}}V_{vR} \\ \frac{\partial P_{vR}}{\partial \theta_{K}} & \frac{\partial P_{vR}}{\partial V_{K}}V_{K} & \frac{\partial P_{vR}}{\partial \delta_{vR}} & \frac{\partial P_{vR}}{\partial V_{vR}}V_{vR} \\ \frac{\partial Q_{vR}}{\partial \theta_{K}} & \frac{\partial Q_{vR}}{\partial V_{K}}V_{K} & \frac{\partial Q_{vR}}{\partial \delta_{vR}} & \frac{\partial Q_{vR}}{\partial V_{vR}}V_{vR} \end{bmatrix} \times \begin{bmatrix} \Delta\theta_{K} \\ \frac{\Delta V_{K}}{V_{K}} \\ \Delta\delta_{vR} \\ \frac{\Delta V_{vR}}{V_{vR}} \end{bmatrix} \tag{13.11}$$

.

13.3.2 Modal Analysis for Determining STATCOM Placement

Modal or eigenvalue analysis of the Jacobian (J) matrix of system load flow equation, near the point of voltage collapse, has been widely used to identify buses vulnerable to voltage collapse and locations for injecting reactive power into the system [6]. The participation of each load in the critical mode determines the importance of the load in voltage collapse. The degree of participation is determined from an inspection of the entries of the left eigenvector of the critical mode. Right eigenvector components indicate the degree to which given variables are involved in a given mode. The use of both left and right eigenvector information leads to the notion of participation factors that indicate which generators should be motivated to inject more active or reactive power into the system [35]. Here, modal analysis is used for determining optimal placement of VAr compensators which are normally installed in power transmission systems for voltage stability improvement.

In the modal analysis method, the Jacobian matrix of the operating point of a power system is calculated [36]. For this purpose, the power flow equation linearized around the operating point is considered and given as follows:

$$\begin{bmatrix} \Delta P \\ \Delta Q \end{bmatrix} = \begin{bmatrix} J_{P\theta} & J_{PV} \\ J_{Q\theta} & J_{QV} \end{bmatrix} \begin{bmatrix} \Delta\theta \\ \Delta V \end{bmatrix} \tag{13.12}$$

where ΔP is the incremental change in the bus active power, ΔQ is the incremental change in the bus reactive power, $\Delta\theta$ is the incremental change in the bus voltage angle, and ΔV is the incremental change in the bus voltage magnitude. $J_{p\theta}$, J_{PV}, $J_{Q\theta}$, and J_{QV} are the Jacobian matrix elements representing the sensitivity of the power flow to bus voltage changes.

System voltage stability is affected by both P and Q, however, at each operating point, P can be kept constant and voltage stability can be evaluated by considering the incremental relationship between Q and V. If the active power P is kept constant in (13.1), then $\Delta P = 0$ and (13.12) becomes,

$$\Delta Q = J_R \Delta V \tag{13.13}$$

where J_R is the reduced Jacobian matrix system given by

$$J_R = [J_{QV} - J_{Q\theta} J_{P\theta}^{-1} J_{PV}] \tag{13.14}$$

The power network modes can be defined by the eigenvalues and eigenvectors of J_R which can be written as

$$J_R = \xi \, \Lambda \, \eta \tag{13.15}$$

where ξ is the right eigenvector matrix of J_{R}, η is the left eigenvector matrix of J_{R}, and Λ is the diagonal eigenvalue matrix of J_{R}.

The inverse of J_R is then given by,

$$J_R^{-1} = \xi\, \Lambda^{-1}\, \eta \tag{13.16}$$

Substituting (13.16) into (13.13) yields

$$\Delta V = (\xi\, \Lambda^{-1}\, \eta)\, \Delta Q \tag{13.17}$$

or

$$\Delta V = \sum_i \frac{(\xi_i \eta)_i}{\lambda_i} \Delta Q \tag{13.18}$$

where λ_i is the ith eigenvalue, ξ_i is the ith column right eigenvector of J_{R}, and η_i is the ith row left eigenvector of J_{R}. λ_i, ξ_i, and η_i define the ith mode of the system. The ith modal reactive power variation is given by,

$$\Delta Q_{mi} = \kappa_i \xi_i \tag{13.19}$$

where k_{i} is a normalization factor such that

$$\kappa_i^2 \sum_J \xi_{ij}^2 = 1 \tag{13.20}$$

and ξ_{ij} is the jth element of ξ_i.

The ith modal voltage variation can therefore be written as

$$\Delta V_{mi} = {}^{1}/_{\lambda_i} \Delta Q_{mi} \tag{13.21}$$

From (13.21), the stability of mode i with respect to reactive power changes is defined by the modal eigenvalue, λ_i. Large values of λ_i suggest small changes in the modal voltage for reactive power changes. As the system is stressed, the value of λ_i becomes smaller, and the modal voltage becomes weaker. If the magnitude of λ_i is equal to zero, the corresponding modal voltage collapses because it undergoes an infinite change for a finite reactive power change. A system is therefore defined as voltage stable if all the eigenvalues of J_{R} are positive. The bifurcation or voltage stability limit is reached when at least one eigenvalue reaches zero, i.e., when one or more modal voltages collapse. If any of the eigenvalues are negative, the system is unstable. The magnitude of the eigenvalues provides a relative measure of the proximity of the system to voltage instability [36, 37].

The left and right eigenvectors corresponding to the critical modes in the system can provide information concerning the mechanism of voltage instability by

identifying the elements involved in these modes. The bus participation factor that measures the participation of the kth bus in the ith mode can be defined as

$$P_{ki} = \xi_{ki}\, \eta_{ik} \tag{13.22}$$

Bus participation factors corresponding to critical modes can predict areas or nodes in the power system susceptible to voltage instability. Buses with large participation factors in the critical mode are the most critical system buses. Thus, by using the modal analysis method, the critical buses can be determined and these buses are considered as suitable location for VAr compensators installation.

13.3.3 Problem Formulation for Optimal Sizing of STATCOM

A multi-objective function consisting of shunt VAr compensator cost is considered in searching for an optimal solution. This multi-objective function which not only maximizes voltage stability margin but also minimizes voltage deviation, active-power loss and cost which are described as follows:

Active power loss: The total active-power loss in a power system is given by [38]:

$$P_{loss} = \sum_{l=1}^{n} R_l I_l^2 = \sum_{l=1}^{n} \sum_{j=1, i\neq j}^{n} [V_i^2 + V_j^2 - 2V_i V_j \cos(\theta_i - \theta_j)] Y_{ij} \cos \varphi_{ij} \tag{13.23}$$

where n is the number of lines, R_l is the resistance of line l, I_l is the current through line l, V_i and θ_i are the voltage magnitude and angle at node i, respectively, and Y_{ij} and φ_{ij} are the magnitude and angle of the line admittance, respectively.

Voltage deviation: The voltage improvement index of a power system is defined as the deviation from unity voltage magnitude at a bus. Thus, for a given system, the voltage improvement index is given by [38]:

$$L_v = \sqrt{\sum_{i=1}^{n} \left(\frac{V_{iref} - V_i}{V_{iref}} \right)^2} \tag{13.24}$$

where n is the number of buses, V_{iref} is the reference voltage at bus i, and V_i is the actual voltage at bus i.

Voltage stability margin: From the voltage stability viewpoint, critical modes with the lowest eigenvalues are considered very important. The minimum eigenvalue should be increased to maximize the voltage stability margin [37].

Total injected reactive power: The total injected reactive power of VAr compensator is given by [5]:

$$Q_{ST} = \sum_{j=1}^{ns} Q_j \tag{13.25}$$

where ns is the number of VAr compensators, and Q_j is the injected reactive power of the VAr compensators.

Investment cost: Shunt VAr compensators are expensive devices and therefore the investment cost for installing such controllers must be considered to justify the economic viability of the devices. The total cost also depends on the size of fixed and controlled portion of the shunt controllers. The FACTS equipment cost represent only half of the total FACTS project cost. Other costs like civil works, installation, commissioning, insurance, engineering and project management constitute the other half of the FACTS project cost.

The objective of using shunt VAr compensator is to control system variables such as the active and reactive line power flows and bus voltages, and therefore the following constraints are considered:

Power flow balance equations: The balance of active and reactive powers must be satisfied at each bus. Power balance with respect to a bus can be formulated as [38] :

$$P_{Gi} - P_{Li} = V_i \sum_{j=1}^{n} [V_j [G'_{ij} \cos(\delta_i - \delta_j) + B'_{ij} \sin(\delta_i - \delta_j)] \tag{13.26}$$

$$Q_{Gi} - Q_{Li} = V_i \sum_{j=1}^{n} [V_j [G'_{ij} \sin(\delta_i - \delta_j) - B'_{ij} \sin(\delta_i - \delta_j)] \tag{13.27}$$

where P_{Gi} and Q_{Gi} are the generated active and reactive powers and P_{Li} and Q_{Li} are the load active and reactive powers at node i. The conductance G'_{ik} and the susceptance B'_{ik} represent the real and imaginary components of element Y'_{ij} of the $[Y'_{nn}]$ matrix, which are obtained by modifying the initial nodal admittance matrix.

Power flow limit: The apparent power that is transmitted through a branch l must not exceed its limiting value, $S_{l\,\max}$, which represents the thermal limit of a line or transformer in steady-state operation:

$$S_l \leq S_{l\max} \tag{13.28}$$

Bus voltage limits: For several reasons, such as stability and power quality, the bus voltages must be maintained within limits around its nominal value which is given by

$$V_{i\min} \leq V_{inom} \leq V_{i\max} \tag{13.29}$$

In practice, the accepted deviation can reach up to 10 % of the nominal voltage value.

The fitness function for solving the optimal sizing of VAr compensator problem is calculated using the objective functions described in Sect. 13.3.3. The constraints of this problem do not explicitly contain the variables. Therefore, the effect of the constraints must be included in the fitness function value. The constraints are separately checked, and the violations are handled using a penalty function approach. Incorporating all of the constraints in the same mathematical function is impossible because the three objectives are different. Thus, an overall fitness function, in which each objective function is normalized with respect to the base system without a VAr compensator, is considered. This fitness function is given by,

$$\begin{aligned}\mathrm{Min}\{f(x)\} = \mathrm{Min}\Bigg\{ & \omega_1 \frac{P_{loss}}{\sum \Delta Loss_{base}} + \omega_2 \frac{L_v}{\sum \Delta V_{base}} + \omega_3 \frac{\lambda_{Crtical(base)}}{\lambda_{Critical}} + \omega_4 \frac{Cost_{shunt}}{Cost_{Max}} \\ & -\chi_1 . \sum_{i=1}^{nr} bal_i - \chi_2 . \sum_{k=1}^{n} thermal_k - \chi_3 . \sum_{k=1}^{n} voltage_k \Bigg\}\end{aligned} \tag{13.30}$$

Subject to:

$$\begin{aligned}\omega_1 + \omega_2 + \omega_3 + \omega_4 = 1 \\ 0 < \omega_1, \omega_2, \omega_3, \omega_4 < 1\end{aligned} \tag{13.31}$$

where P_{loss}, L_{v}, $\lambda_{\mathrm{Critical}}$, and $Cost_{\mathrm{shunt}}$ are the total active power loss, voltage deviation index, smallest eigenvalue, and total VAr compensator cost, respectively. ω_1, ω_2, ω_3, and ω_4 are the coefficients of the corresponding objective functions, $\sum \Delta Loss_{base}$ is the total active power loss in the network of the base system, $\sum V_{base}$ is the total voltage deviation of the base system, $\lambda_{\mathrm{Critical(base)}}$ is the smallest eigenvalue of the base case, and $Cost_{\mathrm{Max}}$ is the maximum cost.

In Eq. (13.30), the power loss as well as voltage deviation should be minimized and the base case values are written in denominator whereas, for voltage stability enhancement the eigenvalue should be maximized and the critical eigenvalue at base case is written in numerator.

The bal_i element in (13.30) is a factor equal to 0 if the power balance constraint at bus i is not violated; otherwise, bal_i is equal to 1. The sum of these violations represents the total number of buses in the network that do not follow constraints (13.26) and (13.27). This sum is multiplied by a penalty factor that increases the fitness function to an unacceptable value, which results in an infeasible solution that must be discarded. The second and third sums in the fitness function represent the total number of violations of constraints (13.28) and (13.29), respectively, and are also multiplied by penalty factors. The last three sums in this fitness function are the measures of infeasibility for each candidate solution. The penalty factors used in this study are χ_1, χ_2, and χ_3, and each is set to a value equals to 100.

STATCOM is an expensive device and therefore optimum placement and sizing of only one STATCOM in a transmission system is considered. For calculating the

cost of STATCOM there is no specific equation like the SVC [5]. Hence, the fourth objective function component in Eq. (13.30) has been defined to having the minimum possible STATCOM sizes regarding to the control of STATCOM, instead of considering the total STATCOM cost [5]. Since only one STATCOM has been considered, it is reasonable that:

$$\underbrace{\frac{Cost_{ST}}{Cost_{MAX}} \cong \frac{Q_{ST}}{Q_{ST\max}}}_{For\ One\ STATCOM} \tag{13.32}$$

where Q_{ST} is the STATCOM size and $Q_{ST\max}$ is the maximum possible STATCOM size.

Thus, the fitness function in Eq. (13.30) has been redefined by considering STATCOM size. The new fitness function is given by

$$\begin{aligned}\text{Min}\{f_{STATCOM}(x)\} = \text{Min}\Bigg\{ & \omega_1 \frac{P_{loss}}{\sum \Delta Loss_{base}} + \omega_2 \frac{L_v}{\sum \Delta V_{base}} + \omega_3 \frac{\lambda_{Crtical(base)}}{\lambda_{Critical}} + \omega_4 \frac{Q_{ST}}{Q_{ST\max}} \\ & - \chi_1 . \sum_{i=1}^{nr} bal_i - \chi_2 . \sum_{k=1}^{n} thermal_k - \chi_3 . \sum_{k=1}^{n} voltage_k \Bigg\}\end{aligned} \tag{13.33}$$

In the optimum STATCOM placement and sizing method, modal analysis method is first used to determine the critical system buses which are buses with large participation factors. These buses are considered as possible locations for STATCOM installation.

Next, the optimal placement and sizing of only one STATCOM among the candidate buses is found by using the the GHS algorithm in which the optimal STATCOM set $\{0, 0 \ldots Q_i^{ST}, \ldots, 0, 0\}$ leads to maximum power loss reduction, minimum voltage deviation and maximum eigenvalue in critical mode while considering the STATCOM size.

13.3.4 Global Harmony Search Algorithm

The harmony search (HS) algorithm is a meta-heuristic optimization algorithm inspired by the playing of music. It uses rules and randomness to imitate natural phenomena. Inspired by the cooperation within an orchestra, the HS algorithm achieves an optimal solution by finding the best "harmony" among the system components involved in a process. Just as discrete musical notes can be played based on a player's experience or on random processes in improvisation, optimal design variables in a system can be obtained with certain discrete values based on computational intelligence and random processes [12]. Musicians improve their

experience based on aesthetic standards, whereas design variables can be improved based on an objective function.

The HS algorithm looks for the vector or the path of X that reduces the computational cost or shortens the path. The computational procedure of the HS algorithm is as follows [39]:

Step 1: *Initialisation of the Optimization Problem*

Consider an optimization problem that is described as

$$Minimize\, F(x)\, subject\, to\, x_i \in X_i,\ i = 1, 2, 3, \ldots N.$$

where *F(x)* is the objective function, *x* is the set of design variables (x_i), X_i is the set of the range of possible values for each design variable ($Lx_i < X_i < Ux_i$) and *N* is the number of design variables. The following HS algorithm parameters are also specified: the harmony memory size (HMS), or number of solution vectors in the harmony memory; the harmony memory considering rate (HMCR); the pitch adjusting rate (PAR); the number of decision variables (*N*); the number of improvisations (NI) and the stopping criterion.

Step 2: *Initialisation of the Harmony Memory*

The harmony memory (HM) matrix shown in Eq. (13.34) is filled with HMS randomly generated solution vectors and sorted by the values of the objective function *f(x)*.

$$HM = \begin{bmatrix} x_1^1 & x_2^1 & \ldots & x_{N-1}^1 & x_N^1 \\ x_1^2 & x_2^2 & \ldots & x_{N-1}^2 & x_N^2 \\ . & . & . & . & . \\ . & . & . & . & . \\ . & . & . & . & . \\ x_1^{HMS-1} & x_1^{HMS-1} & \ldots & x_{N-1}^{HMS-1} & x_N^{HMS-1} \\ x_1^{HMS} & x_1^{HMS} & \ldots & x_{N-1}^{HMS} & x_N^{HMS} \end{bmatrix} \begin{matrix} \Rightarrow & f(x^{(1)}) \\ \Rightarrow & f(x^{(2)}) \\ . & . \\ . & . \\ . & . \\ \Rightarrow & f(x^{(HMS-1)}) \\ \Rightarrow & f(x^{(HMS)}) \end{matrix} \tag{13.34}$$

Step 3: *Improvising a New Harmony from the HM set*

A new harmony vector, $x' = (x_1', x_2', \ldots, x_n')$, is generated based on three rules: random selection, memory consideration and pitch adjustment.

- *Random Selection*: To determine the values x_i' for the new harmony $x' = (x_1', x_2', \ldots x_n')$, the HS algorithm randomly picks a value from the total value range with a probability of (1-HMCR). Random selection is also used for memory initialisation.

- *Memory Consideration*: To determine a value x_i', the HS algorithm randomly picks a value x_i^j from the HM with a probability of HMCR, where $j = \{1, 2, ..., \text{HMS}\}$.

$$x_i' \leftarrow \begin{Bmatrix} x_i' \in \{x_i^1, x_i^2, \ldots, x_i^{HMS}\} & with\ probablity\ HMCR \\ x_i' \in X_i & with\ probablity\ \ (1 - HMCR) \end{Bmatrix} \quad (13.35)$$

- *Pitch Adjustment*: Every component of the new harmony vector $x' = (x_1', x_2', \ldots x_n')$ is examined to determine whether it should be pitch-adjusted. After the value x_i' is randomly picked from the HM in the memory consideration process, it can be further adjusted by adding a certain amount to the value with probability *PAR*. This operation uses the *PAR* parameter, which is the probability of pitch adjustment, given as follows:

$$x_i' \leftarrow \begin{Bmatrix} Yes & with\ probablity\ PAR \\ No & with\ probablity\ (1 - PAR) \end{Bmatrix} \quad (13.36)$$

The value of (1-PAR) sets the probability of doing nothing. If the pitch adjustment decision for x_i' is yes, then x_i' is replaced as follows:

$$x_i' \leftarrow x_i' \pm bw \quad (13.37)$$

where *bw* is the arbitrary distance bandwidth for a continuous design variable. In this step, pitch adjustment or random selection is applied to each variable of the new harmony vector.

Step 4: *Updating the HM*

If the new harmony vector $x' = (x_1', x_2', \ldots x_n')$ is better than the worst harmony in the HM, as determined from the objective function value, the new harmony is inserted into the HM, and the worst harmony is removed from the HM [31].

Step 5: *Checking the stopping criterion*

If the stopping criterion, which is based on the maximum number of improvisations, is satisfied, computation is terminated. Otherwise, steps 3 and 4 are repeated.

Inspired by the swarm intelligence of particle swarm, a novel GHS algorithm is proposed by Zou et al. [40, 41] to solve optimization problems. The GHS algorithm includes two important operations; position updating and genetic mutation with a small probability. The new approach modifies the improvisation step of the HS such that the new harmony can mimic the global best harmony in the HM. The GHS and the HS algorithms are different in three aspects described as follows [40]:

i. The HMCR and PAR are excluded from the GHS algorithm and genetic mutation probability (p_m) is included in the GHS algorithm.

ii. The GHS algorithm modifies the improvisation step of the HS algorithm and this modification is represented by the following pseudo code.

```
for each i ∈ [1,N] do
  x_R = 2 × x_i^best − x_i^worst
  if x_R > x_iU
    x_R = x_iU
  elseif x_R < x_iL
    x_R = x_iL
  end
  x'_i ← x_i^worst + r1_i × (x_R − x_i^worst) %position updating
  if r2_i ≤ p_m then
    x'_i ← x_iL + r3_i × (x_iU − x_iL) %genetic mutation
  end
end
```

Here, "*best*" and "*worst*" are the indexes of the global best harmony and the worst harmony in HM, respectively. r_{1i}, r_{2i} and r_{3i} are all the uniformly generated random numbers in [0, 1]. r_{1i} is used for position updating, r_{2i} determines whether the GHS should carry out genetic mutation, and r_{3i} is used for genetic mutation. Figure 13.3 illustrates the principle of position updating [40].

$step_i = |x_i^{best} - x_i^{worst}|$ is defined as adaptive step of the ith decision variable. The region between P and R is defined as trust region for the ith decision variable. The trust region is actually a region near the global best harmony. In the early stage of optimization, all solution vectors are sporadic in solution space, so most trust regions are wide, which is beneficial to the global search of the GHS; while in the late stage of optimization, all non-best solution vectors are inclined to move to the global best solution vector, so most solution vectors are close to each other. Here, most trust regions are narrow, which is beneficial to the local search of the GHS algorithm. A reasonable design for adaptive step can guarantee that the proposed algorithm has strong global search ability in the early stage of optimization, and has strong local search ability in the late stage of optimization. Dynamically adjusted $step_i$ keeps a balance between the global search and the local search [40, 41]. As for genetic mutation operation with a small probability, it is carried out for the worst harmony of HM after updating position, so as to enhance the capacity of escaping from the local optimum for the proposed algorithm.

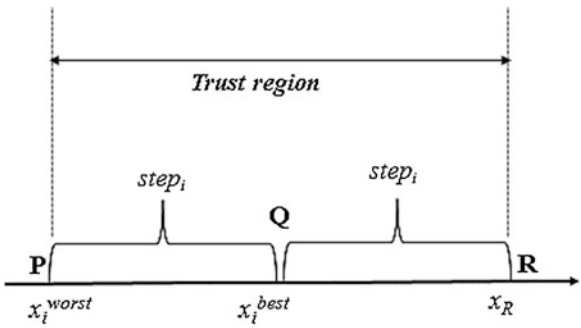

Fig. 13.3 The schematic diagram of position updating [40]

iii. The GHS algorithm replaces the worst harmony x^{worst} in HM with the new harmony x' even if x' is worse than x^{worst}.

For clarity, the GHS algorithm is described in terms of a flow chart as shown in Fig. 13.4.

In modified improvisation steps, adaptive step and trust region are defined for the GHS, and according to these two factors, a novel position updating equation is designed to make the worst harmony of harmony memory move to the global best harmony in each iteration. Using position updating equation can accelerate the convergence rate of the GHS, however, it also accelerates the premature convergence of the GHS and make it get into the local optimum. To overcome these disadvantages, genetic mutation with a small probability is introduced in the GHS algorithm [40, 41].

13.3.5 Application of GHS Algorithm for Optimal Placement and Sizing of STATCOM

The procedures for implementing the GHS algorithm in the optimal placement and sizing of STATCOM are described follows:

i. Input the system parameters such as bus, branch, and generator data.
ii. Form the Jacobian matrix and calculate the eigenvalues for the base case.
iii. Calculate the eigenvectors and determine bus participation factors for the smallest eigenvalue.
iv. Determine buses with large participation factors and consider these buses as possible locations for STATCOM installation.
v. Randomly add one STATCOM for reactive power compensation at the bus among suitable buses. Each STATCOM set is considered a harmony vector. The HM arrays are randomly initialized using (13.34). The number of columns in the HM is equal to the number of buses in the test system. The optimal parameters of the test system, $x\mathrm{L_i}$ and $x\mathrm{U_i}$, are assumed to have minimum and maximum values of STATCOM in MVar, respectively. The HMS value is assumed to be 10.
vi. Improvise a new harmony through position updating and genetic mutation. In this step, the genetic mutation probability is assumed as $p_{\mathrm{m}} = 0.2$.
vii. Run the power flow program to calculate power loss, voltage deviation, and the eigenvalues.
viii. Calculate the objective function using (13.30).
ix. Replace the worst harmony in HM with the new harmony.
x. Evaluate whether the stopping criterion (maximum generation ≥5,000) is satisfied. If not, return to step (vi) and repeat the procedure.
xi. Determine the optimal VAr compensator set (i.e., the best harmony) that provides maximum power loss reduction, minimum voltage deviation, maximum voltage satiability enhancement and minimum STATCOM size.

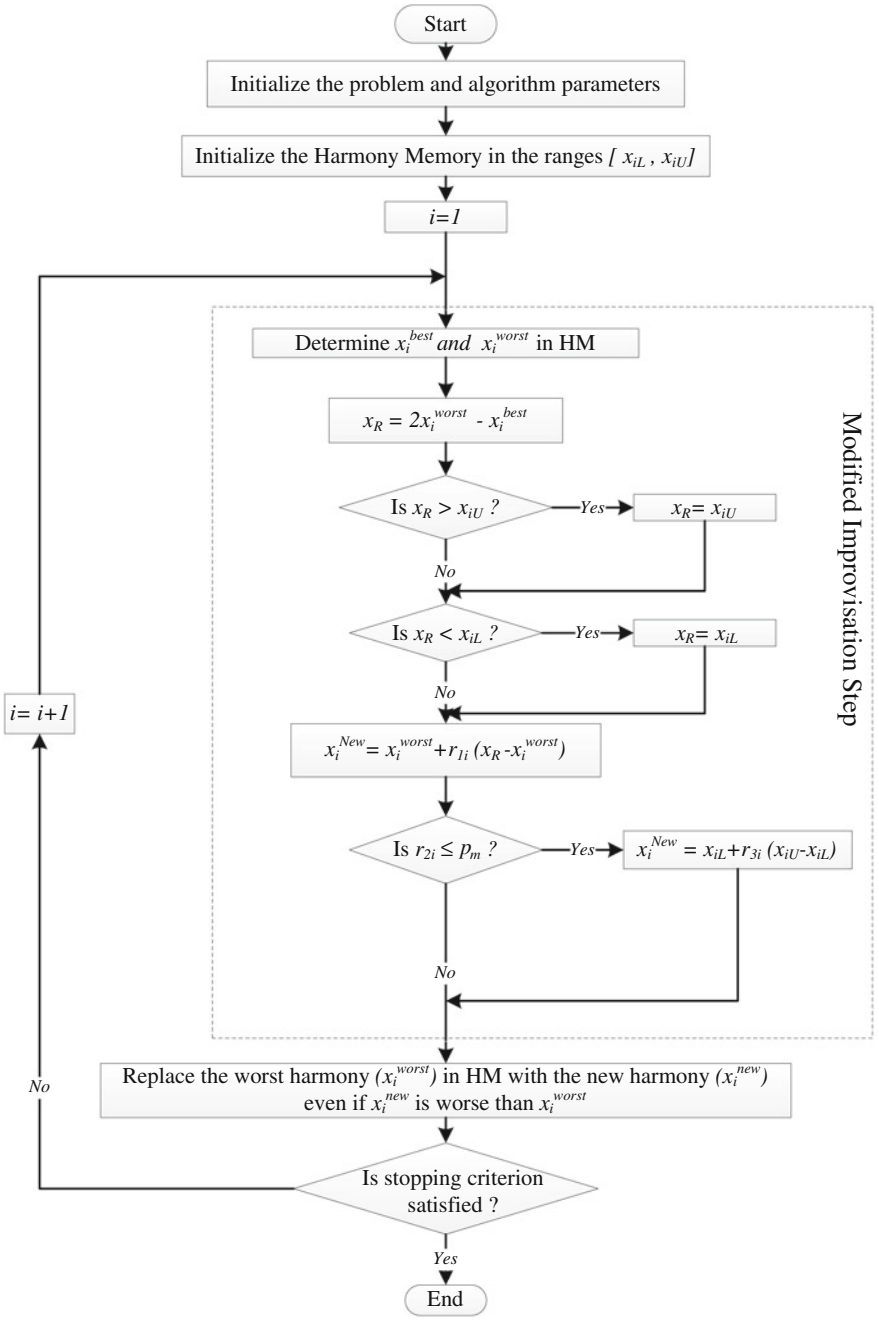

Fig. 13.4 The procedures of the GHS algorithm

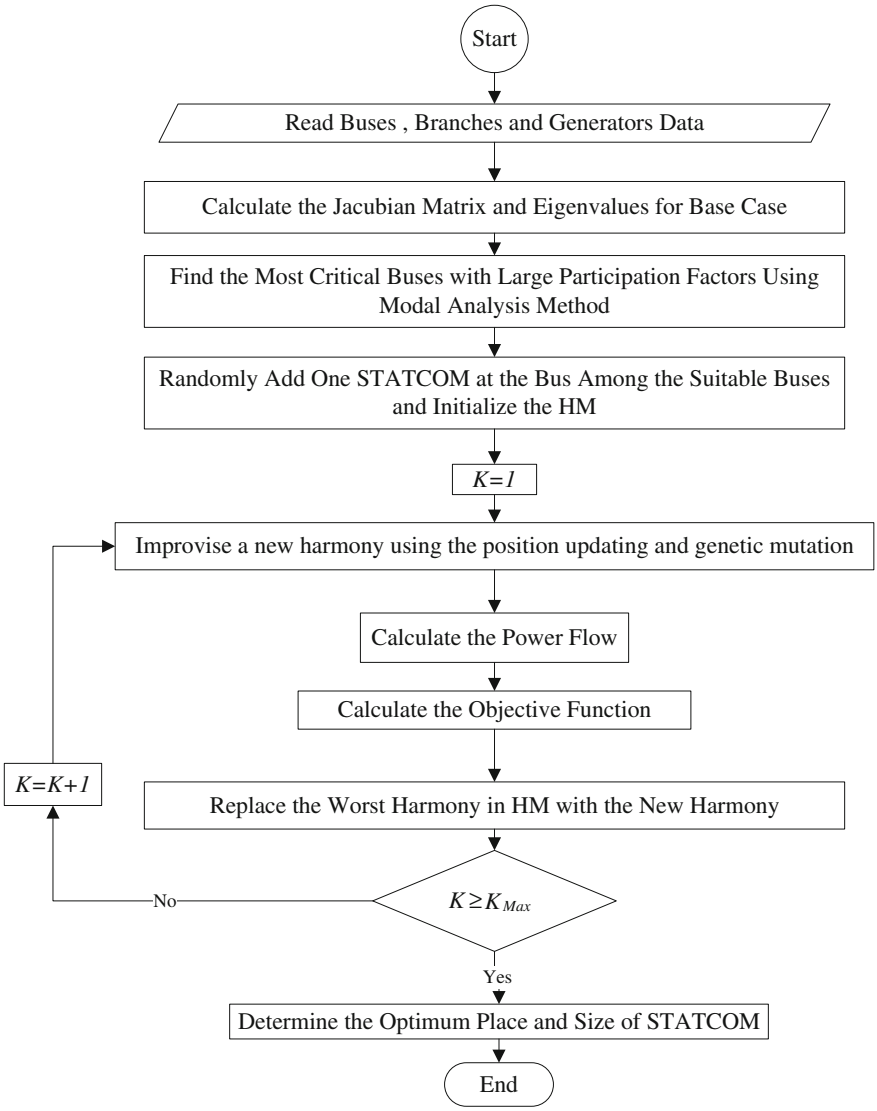

Fig. 13.5 Procedures used in solving the optimal STATCOM placement and sizing problem

Figure 13.5 shows a schematic diagram of the procedures used in solving the optimal STATCOM placement and sizing problem using modal analysis and the GHS algorithm.

13.3.6 Case Studies and Results

In determining the optimal location and size of STATCOM in a transmission network, modal analysis is first applied to determine suitable placement of STATCOM and then GHS algorithm is applied to determining optimal placement and size of STATCOM. For the optimization problem formulation, a multi-criterion objective function has been considered to enhance voltage stability, improve voltage profile and minimize power loss and total cost. The results obtained using the proposed GHS techniques in the IEEE 57-bus and 118-bus test systems are compared with other optimization techniques for validation purpose. The 57 bus system shown in Fig. 13.6 consists of seven generators with bus 1 as the slack bus, 50 load buses and 80 lines. The system data can be found in Appendix 1. At base case condition, the system load is 12.508 p.u. and the system power loss is 28.41 MW [42].

The 118-bus system consists of 54 generators (in which one is the slack node), 91 load buses and 186 lines. The system power loss is 132.86 MW and the system data can be found in Appendix 2 [42].

The eigenvalues of the reduced Jacobian matrix are first generated to obtain the relative proximity of the system to voltage instability. The bus participation factors are then generated for the critical mode to identify the critical buses in the system.

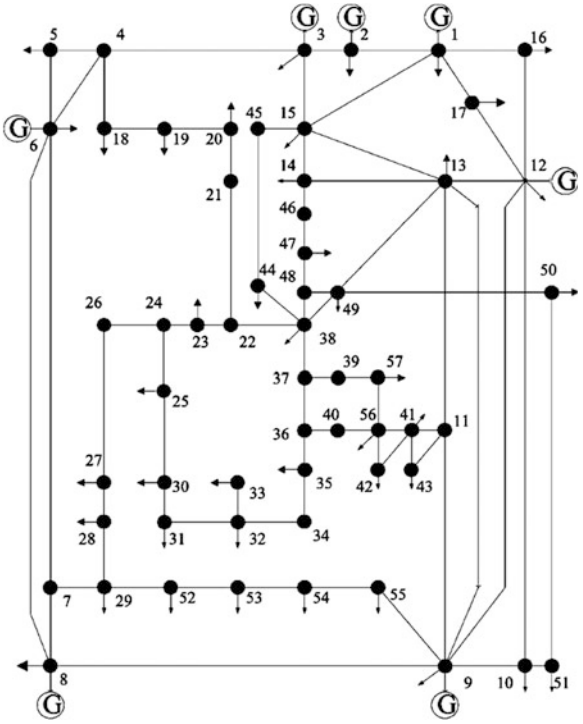

Fig. 13.6 Network configuration of the IEEE 57-bus test system

The smallest eigenvalue for this system at base case is found to be 0.2344. The bus participation factor values for the smallest eigenvalue of the reduced Jacobian matrix are calculated for all load buses and sorted as shown in Table 13.1.

Considering the results of modal analysis shown in Table 13.1, the ten buses with high participation factor values are considered suitable for STATCOM installation. The identified ten buses are buses 24, 25, 30, 31, 32, 33, 34, 35, 36 and 40. Table 13.2 shows the place and size of STATCOM using the five optimization techniques. The results obtained from the IHS and GHS algorithms are compared with results obtained using the GA, PSO and conventional HS algorithm. Table 13.2 also shows the total power loss, voltage deviation and the smallest eigenvalue after the installation of the STATCOM. This study is performed with the restriction that the injected Q does not exceed 50 MVar.

Table 13.2 shows that STATCOM placement using the GHS algorithm not only produces greater voltage stability enhancement and greater reductions in power loss and voltage deviation than GA, PSO and conventional HS algorithm, but it also gives the lowest fitness function value compared to other optimization techniques. It is also observed that the result of STATCOM placement using the IHS algorithm in terms of power loss reduction, voltage deviation minimization and voltage stability enhancement is comparable to the GHS algorithm. However, the STATCOM size found by the GHS algorithm is lower than that found by the IHS algorithm.

The smallest eigenvalue of the IEEE 118-bus test system at the base case which is without STATCOM installation is calculated as 3.9425. The bus participation

Table 13.1 The participation factor values of all load buses in the IEEE 57-bus test system

Bus no.	Participation factor	Bus no.	Participation factor	Bus no.	Participation factor
31	0.1833	21	0.0067	52	0.0005
33	0.1744	22	0.0067	14	0.0004
32	0.1704	38	0.0057	53	0.0004
30	0.133	20	0.0043	11	0.0002
25	0.1004	44	0.0041	13	0.0002
34	0.0306	27	0.0038	15	0.0002
35	0.0229	41	0.0038	18	0.0002
40	0.0177	48	0.0037	51	0.0002
36	0.0176	47	0.0031	7	0.0001
24	0.0165	19	0.0024	10	0.0001
39	0.0142	49	0.0024	54	0.0001
37	0.014	28	0.0015	4	0
26	0.0138	46	0.0015	5	0
57	0.0114	50	0.0014	16	0
56	0.0092	45	0.0013	17	0
23	0.0072	43	0.0008	55	0
42	0.0070	29	0.0006		

Table 13.2 A comparison of different optimization techniques for optimal placement and sizing of STATCOM in the IEEE 57-bus test system

Objective function	Base case	GA	PSO	HS	IHS	GHS
Optimum location (Bus no.)	–	33	32	31	31	31
Size of STATCOM (MVar)	–	17.44	15.35	12.87	12.41	12.37
Total power losses (MW)	28.41	28.19	28.02	27.88	27.76	27.74
Total voltage deviation	0.265	0.209	0.215	0.181	0.178	0.177
Smallest eigenvalue	0.234	0.302	0.261	0.291	0.314	0.322
Fitness function value	1.000	0.802	0.839	0.765	0.743	0.736

factor values for the smallest eigenvalue of the reduced Jacobian matrix are calculated for all load buses. Among all load buses the bus participation factor values of six buses are sorted and shown in Table 13.3. The bus participation factor values of other load buses are found to be 0. It means that only six buses have participation to the critical mode. From the table, the buses with participation factors correspond to the critical system buses which are at buses 20, 21, 22, 23, 37 and 38. These buses are considered as suitable locations for STATCOM installation.

The proposed IHS and GHS algorithms were implemented to determine the optimal location and size of only one STATCOM in the IEEE 118-bus test system. The coefficient values for the objective functions are assumed to be the same as those in the IEEE 57-bus test system. This study is performed with the restriction that the injected Q does not exceed 120 MVar. As shown in Table 13.3, the most critical buses in the system are buses 20, 21, 22, 23, 37 and 38 and these buses are considered as candidate location for STATCOM installation.

Table 13.4 shows a comparison of the optimal STATCOM placement results of the IHS and GHS algorithms with the other optimization techniques in terms of total power loss, voltage deviation, smallest eigenvalue and size of STATCOM. The results in the table show that the GHS algorithm gives the lowest fitness function value and the greatest reduction in terms of power loss and voltage deviation as compared to GA, PSO, conventional HS and IHS algorithms.

The convergence characteristics of the different optimization techniques for the optimal placement and sizing of STATCOM in the IEEE 118-bus test system are shown in Fig. 13.7. From the figure, the GHS algorithm converges faster compared with the other optimization techniques.

Table 13.3 The participation factor values of critical buses in the 118 bus test system

Bus no.	Participation factor
21	0.4268
22	0.3390
20	0.2274
23	0.0068
37	0.0039
38	0.0014

Table 13.4 A comparison of different optimization techniques in optimal placement and sizing of STATCOM in the IEEE 118-bus test system

Objective function	Base case	GA	PSO	HS	IHS	GHS
Optimum location (Bus no.)	–	20	22	21	21	21
Size of STATCOM (MVar)	–	69.11	71.39	64.11	64.17	64.23
Total power losses (MW)	132.86	132.57	132.56	131.52	131.43	131.23
Total voltage deviation	0.294	0.291	0.290	0.289	0.287	0.285
Smallest eigenvalue	3.9425	5.108	5.166	5.282	5.284	5.292
Fitness function value	1.000	0.875	0.865	0.857	0.853	0.845

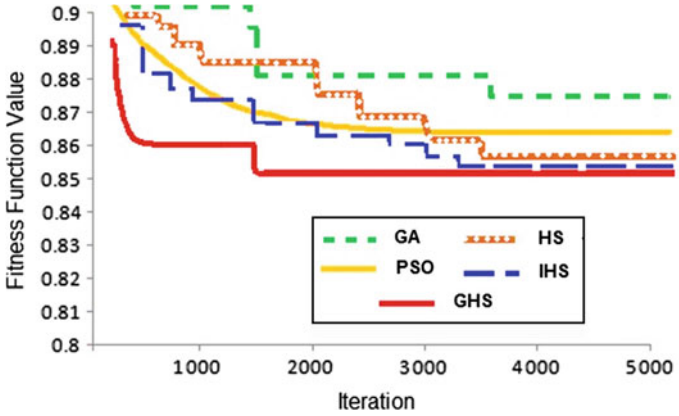

Fig. 13.7 Convergence characteristics of different optimization techniques in the IEEE 118-bus test system

Table 13.5 Accuracy of different optimization techniques for the optimal STATCOM placement and sizing in the IEEE 118-bus test system

Fitness function value	GA	PSO	HS	IHS	GHS
Minimum	0.8583	0.8605	0.8567	0.8529	0.8451
Maximum	0.9163	0.8661	0.8581	0.8532	0.8451
Mean	0.8753	0.8651	0.8572	0.8531	0.8451
Standard deviation	5.80e−04	5.61e−05	1.42e−05	3.78e−06	3.47e−08

The minimum, maximum, mean and standard deviation of the fitness function values from 50 executions of the GA, PSO, HS, IHS and GHS algorithm are shown in Table 13.5. From the table, it is noted that the GHS algorithm gives the lowest fitness function values and lowest standard deviation values compared to other optimization techniques. This proves that the proposed GHS algorithm for solving the optimal placement and sizing of STATCOM in the IEEE 118-bus test system is more accurate than GA, PSO, conventional HS and IHS algorithms.

Appendix 1

Tables 13.6–13.8

Table 13.6 Bus data of IEEE 57-bus test system

Bus	Type	P_d (MW)	Q_d(MVar)	Bus	Type	P_d (MW)	Q_d(MVar)
1	S	55	17	30	L	3.6	1.8
2	G	3	88	31	L	5.8	2.9
3	G	41	21	32	L	1.6	0.8
4	L	0	0	33	L	3.8	1.9
5	L	13	4	34	L	0	0
6	G	75	2	35	L	6	3
7	L	0	0	36	L	0	0
8	G	150	22	37	L	0	0
9	G	121	26	38	L	14	7
10	L	5	2	39	L	0	0
11	L	0	0	40	L	0	0
12	G	377	24	41	L	6.3	3
13	L	18	2.3	42	L	7.1	4.4
14	L	10.5	5.3	43	L	2	1
15	L	22	5	44	L	12	1.8
16	L	43	3	45	L	0	0
17	L	42	8	46	L	0	0
18	L	27.2	9.8	47	L	29.7	11.6
19	L	3.3	0.6	48	L	0	0
20	L	2.3	1	49	L	18	8.5
21	L	0	0	50	L	21	10.5
22	L	0	0	51	L	18	5.3
23	L	6.3	2.1	52	L	4.9	2.2
24	L	0	0	53	L	20	10
25	L	6.3	3.2	54	L	4.1	1.4
26	L	0	0	55	L	6.8	3.4
27	L	9.3	0.5	56	L	7.6	2.2
28	L	4.6	2.3	57	L	6.7	2
29	L	17	2.6				

Table 13.7 Generator data of IEEE 57-bus test system

Bus	P_g(MW)	Q_g(MVar)	Q_{max}(MVar)	Q_{min}(MVar)	V_g (pu)
1	128.9	−16.1	200	−140	1.04
2	0	−0.8	50	−17	1.01
3	40	−1	60	−10	0.985
6	0	0.8	25	−8	0.98
8	450	62.1	200	−140	1.005
9	0	2.2	9	−3	0.98
12	310	128.5	155	−150	1.015

Table 13.8 Branch data of IEEE 57-bus test system

Bus (From)	Bus (To)	R (Ω)	X (Ω)	B (Ω)	Bus (From)	Bus (To)	R (Ω)	X (Ω)	B (Ω)
1	2	0.0083	0.028	0.129	7	29	0	0.0648	0
2	3	0.0298	0.085	0.0818	25	30	0.135	0.202	0
3	4	0.0112	0.0366	0.038	30	31	0.326	0.497	0
4	5	0.0625	0.132	0.0258	31	32	0.507	0.755	0
4	6	0.043	0.148	0.0348	32	33	0.0392	0.036	0
6	7	0.02	0.102	0.0276	34	32	0	0.953	0
6	8	0.0339	0.173	0.047	34	35	0.052	0.078	0.0032
8	9	0.0099	0.0505	0.0548	35	36	0.043	0.0537	0.0016
9	10	0.0369	0.1679	0.044	36	37	0.029	0.0366	0
9	11	0.0258	0.0848	0.0218	37	38	0.0651	0.1009	0.002
9	12	0.0648	0.295	0.0772	37	39	0.0239	0.0379	0
9	13	0.0481	0.158	0.0406	36	40	0.03	0.0466	0
13	14	0.0132	0.0434	0.011	22	38	0.0192	0.0295	0
13	15	0.0269	0.0869	0.023	11	41	0	0.749	0
1	15	0.0178	0.091	0.0988	41	42	0.207	0.352	0
1	16	0.0454	0.206	0.0546	41	43	0	0.412	0
1	17	0.0238	0.108	0.0286	38	44	0.0289	0.0585	0.002
3	15	0.0162	0.053	0.0544	15	45	0	0.1042	0
4	18	0	0.555	0	14	46	0	0.0735	0
4	18	0	0.43	0	46	47	0.023	0.068	0.0032
5	6	0.0302	0.0641	0.0124	47	48	0.0182	0.0233	0
7	8	0.0139	0.0712	0.0194	48	49	0.0834	0.129	0.0048
10	12	0.0277	0.1262	0.0328	49	50	0.0801	0.128	0
11	13	0.0223	0.0732	0.0188	50	51	0.1386	0.22	0
12	13	0.0178	0.058	0.0604	10	51	0	0.0712	0
12	16	0.018	0.0813	0.0216	13	49	0	0.191	0
12	17	0.0397	0.179	0.0476	29	52	0.1442	0.187	0
14	15	0.0171	0.0547	0.0148	52	53	0.0762	0.0984	0
18	19	0.461	0.685	0	53	54	0.1878	0.232	0
19	20	0.283	0.434	0	54	55	0.1732	0.2265	0
21	20	0	0.7767	0	11	43	0	0.153	0
21	22	0.0736	0.117	0	44	45	0.0624	0.1242	0.004
22	23	0.0099	0.0152	0	40	56	0	1.195	0
23	24	0.166	0.256	0.0084	56	41	0.553	0.549	0
24	25	0	1.182	0	56	42	0.2125	0.354	0
24	25	0	1.23	0	39	57	0	1.355	0
24	26	0	0.0473	0	57	56	0.174	0.26	0
26	27	0.165	0.254	0	38	49	0.115	0.177	0.003
27	28	0.0618	0.0954	0	38	48	0.0312	0.0482	0
28	29	0.0418	0.0587	0	9	55	0	0.1205	0

Appendix 2

Tables 13.9–13.11, Fig. 13.8

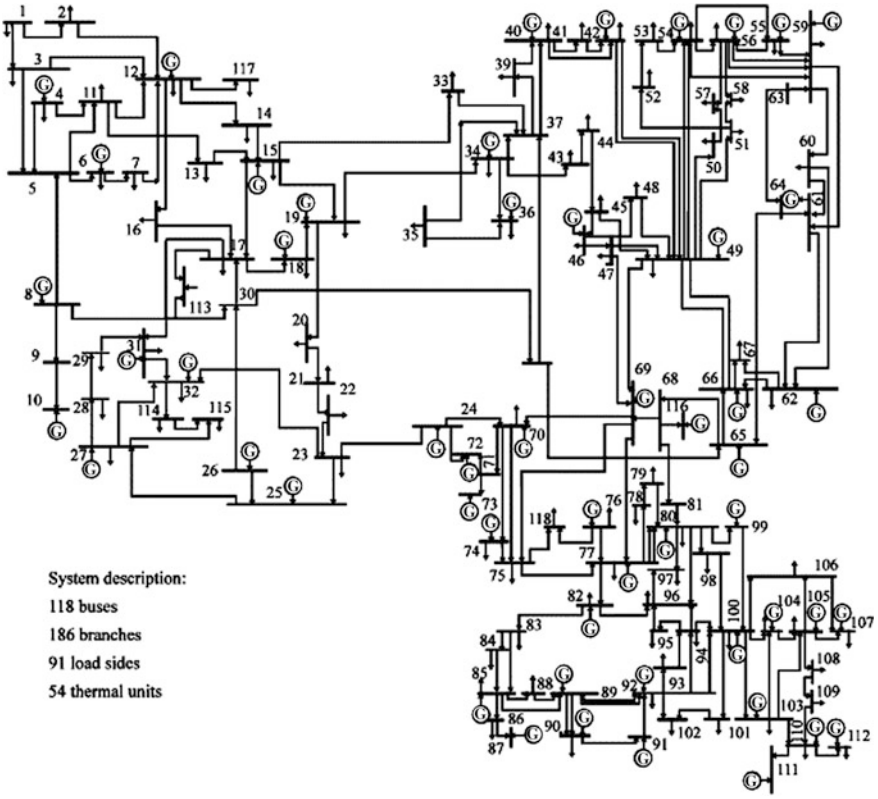

Fig. 13.8 Network diagram for the IEEE 118-bus test system

Table 13.9 Bus data of IEEE 118-bus test system

Bus	Type	P_d (MW)	Q_d (MVar)	Bus	Type	P_d (MW)	Q_d (MVar)	Bus	Type	P_d (MW)	Q_d (MVar)
1	G	51	27	41	L	37	10	81	L	0	0
2	L	20	9	42	G	96	23	82	L	54	27
3	L	39	10	43	L	18	7	83	L	20	10
4	G	39	12	44	L	16	8	84	L	11	7
5	L	0	0	45	L	53	22	85	G	24	15
6	G	52	22	46	G	28	10	86	L	21	10
7	L	19	2	47	L	34	0	87	G	0	0
8	G	28	0	48	L	20	11	88	L	48	10
9	L	0	0	49	G	87	30	89	G	0	0
10	G	0	0	50	L	17	4	90	G	163	42
11	L	70	23	51	L	17	8	91	G	10	0
12	G	47	10	52	L	18	5	92	G	65	10
13	L	34	16	53	L	23	11	93	L	12	7
14	L	14	1	54	G	113	32	94	L	30	16
15	G	90	30	55	G	63	22	95	L	42	31
16	L	25	10	56	G	84	18	96	L	38	15
17	L	11	3	57	L	12	3	97	L	15	9
18	G	60	34	58	L	12	3	98	L	34	8
19	G	45	25	59	G	277	113	99	G	42	0
20	L	18	3	60	L	78	3	100	G	37	18
21	L	14	8	61	G	0	0	101	L	22	15
22	L	10	5	62	G	77	14	102	L	5	3
23	L	7	3	63	L	0	0	103	G	23	16

(continued)

Table 13.9 (continued)

Bus	Type	P_d (MW)	Q_d (MVar)	Bus	Type	P_d (MW)	Q_d (MVar)	Bus	Type	P_d (MW)	Q_d (MVar)
24	G	13	0	64	L	0	0	104	G	38	25
25	G	0	0	65	G	0	0	105	G	31	26
26	G	0	0	66	G	39	18	106	L	43	16
27	G	71	13	67	L	28	7	107	G	50	12
28	L	17	7	68	L	0	0	108	L	2	1
29	L	24	4	69	S	0	0	109	L	8	3
30	L	0	0	70	G	66	20	110	G	39	30
31	G	43	27	71	L	0	0	111	G	0	0
32	G	59	23	72	G	12	0	112	G	68	13
33	L	23	9	73	G	6	0	113	G	6	0
34	G	59	26	74	G	68	27	114	L	8	3
35	L	33	9	75	L	47	11	115	L	22	7
36	G	31	17	76	G	68	36	116	G	184	0
37	L	0	0	77	G	61	28	117	L	20	8
38	L	0	0	78	L	71	26	118	L	33	15
39	L	27	11	79	L	39	32				
40	G	66	23	80	G	130	26				

Table 13.10 Generator data of IEEE 118-bus test system

Bus	P_g (MW)	Q_g (MVar)	Q_{max} (MVar)	Q_{min} (MVar)	V_g (pu)	Bus	P_g (MW)	Q_g (MVar)	Q_{max} (MVar)	Q_{min} (MVar)	V_g (pu)
1	0	0	15	−5	0.955	65	391	0	200	−67	1.005
4	0	0	300	−300	0.998	66	392	0	200	−67	1.05
6	0	0	50	−13	0.99	69	516.4	0	300	−300	1.035
8	0	0	300	−300	1.015	70	0	0	32	−10	0.984
10	450	0	200	−147	1.05	72	0	0	100	−100	0.98
12	85	0	120	−35	0.99	73	0	0	100	−100	0.991
15	0	0	30	−10	0.97	74	0	0	9	−6	0.958
18	0	0	50	−16	0.973	76	0	0	23	−8	0.943
19	0	0	24	−8	0.962	77	0	0	70	−20	1.006
24	0	0	300	−300	0.992	80	477	0	280	−165	1.04
25	220	0	140	−47	1.05	85	0	0	23	−8	0.985
26	314	0	1,000	−1,000	1.015	87	4	0	1,000	−100	1.015
27	0	0	300	−300	0.968	89	607	0	300	−210	1.005
31	7	0	300	−300	0.967	90	0	0	300	−300	0.985
32	0	0	42	−14	0.963	91	0	0	100	−100	0.98
34	0	0	24	−8	0.984	92	0	0	9	−3	0.99
36	0	0	24	−8	0.98	99	0	0	100	−100	1.01
40	0	0	300	−300	0.97	100	252	0	155	−50	1.017
42	0	0	300	−300	0.985	103	40	0	40	−15	1.01
46	19	0	100	−100	1.005	104	0	0	23	−8	0.971
49	204	0	210	−85	1.025	105	0	0	23	−8	0.965

(continued)

Table 13.10 (continued)

Bus	P_g (MW)	Q_g (MVar)	Q_{max} (MVar)	Q_{min} (MVar)	V_g (pu)	Bus	P_g (MW)	Q_g (MVar)	Q_{max} (MVar)	Q_{min} (MVar)	V_g (pu)
54	48	0	300	−300	0.955	107	0	0	200	−200	0.952
55	0	0	23	−8	0.952	110	0	0	23	−8	0.973
56	0	0	15	−8	0.954	111	36	0	1,000	−100	0.98
59	155	0	180	−60	0.985	112	0	0	1000	−100	0.975
61	160	0	300	−100	0.995	113	0	0	200	−100	0.993
62	0	0	20	−20	0.998	116	0	0	1,000	−1,000	1.005

Table 13.11 Branch data of IEEE 118-bus test system

Bus (From)	Bus (To)	R (Ω)	X (Ω)	B (Ω)	Bus (From)	Bus (To)	R (Ω)	X (Ω)	B (Ω)
1	3	0.0129	0.0424	0.01082	64	61	0	0.0268	0
4	5	0.00176	0.00798	0.0021	38	65	0.00901	0.0986	1.046
3	5	0.0241	0.108	0.0284	64	65	0.00269	0.0302	0.38
5	6	0.0119	0.054	0.01426	49	66	0.018	0.0919	0.0248
6	7	0.00459	0.0208	0.0055	49	66	0.018	0.0919	0.0248
8	9	0.00244	0.0305	1.162	62	66	0.0482	0.218	0.0578
8	5	0	0.0267	0	62	67	0.0258	0.117	0.031
9	10	0.00258	0.0322	1.23	65	66	0	0.037	0
4	11	0.0209	0.0688	0.01748	66	67	0.0224	0.1015	0.02682
5	11	0.0203	0.0682	0.01738	65	68	0.00138	0.016	0.638
11	12	0.00595	0.0196	0.00502	47	69	0.0844	0.2778	0.07092
2	12	0.0187	0.0616	0.01572	49	69	0.0985	0.324	0.0828
3	12	0.0484	0.16	0.0406	68	69	0	0.037	0
7	12	0.00862	0.034	0.00874	69	70	0.03	0.127	0.122
11	13	0.02225	0.0731	0.01876	24	70	0.00221	0.4115	0.10198
12	14	0.0215	0.0707	0.01816	70	71	0.00882	0.0355	0.00878
13	15	0.0744	0.2444	0.06268	24	72	0.0488	0.196	0.0488
14	15	0.0595	0.195	0.0502	71	72	0.0446	0.18	0.04444
12	16	0.0212	0.0834	0.0214	71	73	0.00866	0.0454	0.01178
15	17	0.0132	0.0437	0.0444	70	74	0.0401	0.1323	0.03368
16	17	0.0454	0.1801	0.0466	70	75	0.0428	0.141	0.036
17	18	0.0123	0.0505	0.01298	69	75	0.0405	0.122	0.124
18	19	0.01119	0.0493	0.01142	74	75	0.0123	0.0406	0.01034

(continued)

Table 13.11 (continued)

Bus (From)	Bus (To)	R (Ω)	X (Ω)	B (Ω)	Bus (From)	Bus (To)	R (Ω)	X (Ω)	B (Ω)
19	20	0.0252	0.117	0.0298	76	77	0.0444	0.148	0.0368
15	19	0.012	0.0394	0.0101	69	77	0.0309	0.101	0.1038
20	21	0.0183	0.0849	0.0216	75	77	0.0601	0.1999	0.04978
21	22	0.0209	0.097	0.0246	77	78	0.00376	0.0124	0.01264
22	23	0.0342	0.159	0.0404	78	79	0.00546	0.0244	0.00648
23	24	0.0135	0.0492	0.0498	77	80	0.017	0.0485	0.0472
23	25	0.0156	0.08	0.0864	77	80	0.0294	0.105	0.0228
26	25	0	0.0382	0	79	80	0.0156	0.0704	0.0187
25	27	0.0318	0.163	0.1764	68	81	0.00175	0.0202	0.808
27	28	0.01913	0.0855	0.0216	81	80	0	0.037	0
28	29	0.0237	0.0943	0.0238	77	82	0.0298	0.0853	0.08174
30	17	0	0.0388	0	82	83	0.0112	0.03665	0.03796
8	30	0.00431	0.0504	0.514	83	84	0.0625	0.132	0.0258
26	30	0.00799	0.086	0.908	83	85	0.043	0.148	0.0348
17	31	0.0474	0.1563	0.0399	84	85	0.0302	0.0641	0.01234
29	31	0.0108	0.0331	0.0083	85	86	0.035	0.123	0.0276
23	32	0.0317	0.1153	0.1173	86	87	0.02828	0.2074	0.0445
31	32	0.0298	0.0985	0.0251	85	88	0.02	0.102	0.0276
27	32	0.0229	0.0755	0.01926	85	89	0.0239	0.173	0.047
15	33	0.038	0.1244	0.03194	88	89	0.0139	0.0712	0.01934
19	34	0.0752	0.247	0.0632	89	90	0.0518	0.188	0.0528
35	36	0.00224	0.0102	0.00268	89	90	0.0238	0.0997	0.106
35	37	0.011	0.0497	0.01318	90	91	0.0254	0.0836	0.0214

(continued)

Table 13.11 (continued)

Bus (From)	Bus (To)	R (Ω)	X (Ω)	B (Ω)	Bus (From)	Bus (To)	R (Ω)	X (Ω)	B (Ω)
33	37	0.0415	0.142	0.0366	89	92	0.0099	0.0505	0.0548
34	36	0.00871	0.0268	0.00568	89	92	0.0393	0.1581	0.0414
34	37	0.00256	0.0094	0.00984	91	92	0.0387	0.1272	0.03268
38	37	0	0.0375	0	92	93	0.0258	0.0848	0.0218
37	39	0.0321	0.106	0.027	92	94	0.0481	0.158	0.0406
37	40	0.0593	0.168	0.042	93	94	0.0223	0.0732	0.01876
30	38	0.00464	0.054	0.422	94	95	0.0132	0.0434	0.0111
39	40	0.0184	0.0605	0.01552	80	96	0.0356	0.182	0.0494
40	41	0.0145	0.0487	0.01222	82	96	0.0162	0.053	0.0544
40	42	0.0555	0.183	0.0466	94	96	0.0269	0.0869	0.023
41	42	0.041	0.135	0.0344	80	97	0.0183	0.0934	0.0254
43	44	0.0608	0.2454	0.06068	80	98	0.0238	0.108	0.0286
34	43	0.0413	0.1681	0.04226	80	99	0.0454	0.206	0.0546
44	45	0.0224	0.0901	0.0224	92	100	0.0648	0.295	0.0472
45	46	0.04	0.1356	0.0332	94	100	0.0178	0.058	0.0604
46	47	0.038	0.127	0.0316	95	96	0.0171	0.0547	0.01474
46	48	0.0601	0.189	0.0472	96	97	0.0173	0.0885	0.024
47	49	0.0191	0.0625	0.01604	98	100	0.0397	0.179	0.0476
42	49	0.0715	0.323	0.086	99	100	0.018	0.0813	0.0216
42	49	0.0715	0.323	0.086	100	101	0.0277	0.1262	0.0328
45	49	0.0684	0.186	0.0444	92	102	0.0123	0.0559	0.01464
48	49	0.0179	0.0505	0.01258	101	102	0.0246	0.112	0.0294
49	50	0.0267	0.0752	0.01874	100	103	0.016	0.0525	0.0536

(continued)

Table 13.11 (continued)

Bus (From)	Bus (To)	R (Ω)	X (Ω)	B (Ω)	Bus (From)	Bus (To)	R (Ω)	X (Ω)	B (Ω)
49	51	0.0486	0.137	0.0342	100	104	0.0451	0.204	0.0541
51	52	0.0203	0.0588	0.01396	103	104	0.0466	0.1584	0.0407
52	53	0.0405	0.1635	0.04058	103	105	0.0535	0.1625	0.0408
53	54	0.0263	0.122	0.031	100	106	0.0605	0.229	0.062
49	54	0.073	0.289	0.0738	104	105	0.00994	0.0378	0.00986
49	54	0.0869	0.291	0.073	105	106	0.014	0.0547	0.01434
54	55	0.0169	0.0707	0.0202	105	107	0.053	0.183	0.0472
54	56	0.00275	0.00955	0.00732	105	108	0.0261	0.0703	0.01844
55	56	0.00488	0.0151	0.00374	106	107	0.053	0.183	0.0472
56	57	0.0343	0.0966	0.0242	108	109	0.0105	0.0288	0.0076
50	57	0.0474	0.134	0.0332	103	110	0.03906	0.1813	0.0461
56	58	0.0343	0.0966	0.0242	109	110	0.0278	0.0762	0.0202
51	58	0.0255	0.0719	0.01788	110	111	0.022	0.0755	0.02
54	59	0.0503	0.2293	0.0598	110	112	0.0247	0.064	0.062
56	59	0.0825	0.251	0.0569	17	113	0.00913	0.0301	0.00768
56	59	0.0803	0.239	0.0536	32	113	0.0615	0.203	0.0518
55	59	0.04739	0.2158	0.05646	32	114	0.0135	0.0612	0.01628
59	60	0.0317	0.145	0.0376	27	115	0.0164	0.0741	0.01972
59	61	0.0328	0.15	0.0388	114	115	0.0023	0.0104	0.00276
60	61	0.00264	0.0135	0.01456	68	116	0.00034	0.00405	0.164
60	62	0.0123	0.0561	0.01468	12	117	0.0329	0.14	0.0358
61	62	0.00824	0.0376	0.0098	75	118	0.0145	0.0481	0.01198
63	59	0	0.0386	0	76	118	0.0164	0.0544	0.01356
63	64	0.00172	0.02	0.216					

References

1. Saranjeet K (2009) Evolutionary algorithm assisted optimal placement of FACTS controllers in power system. Master Thesis Thapar University, India, p11
2. Gyugyi ML, Shauder CD, SenKK (1997) Static synchronous series compensator a solid state approach to the series compensation of transmission line. IEEE Trans Power Deliv 12 (3):406–417
3. Hassan MO, Cheng SJ, Zakaria ZA (2009) Steady-state modelling of static synchronous compensator and thyristor controlled series compensator for power flow analysis. Inf Technol J 8(3):347–353
4. Radam GG, Raje RS (2007) Power flow model/calculation for power systems with multiple FACTS controllers. Electric Power Syst Res 77(12):1521–1531
5. Azadani EN, Hosseinian SH, Janati M, Hasanpor P (2008) Optimal Placement of Multiple STATCOM. In: 12th International Middle-East power system conference, pp 523–528
6. Shaygan M, Seifossadat SGH, Razaz M (2011) Study the effects of STATCOM on the static voltage stability improvement and reduction of active and reactive losses. Int Rev Electr Eng 6 (4):1862–1869
7. Natesan R, Radman G (2004) Effects of STATCOM, SSSC and UPFC on voltage stability. In: Proceedings of the 36th Southeastern symposium on system theory, pp 546–550
8. Geem ZW, Kim JH, Loganathan G (2001) A new heuristic optimization algorithm: harmony search. Simulation 76(2):136–701
9. Khajehzadeh M, Taha MR, El-Shafie A, Eslami M (2011) A survey on meta-heuristic global optimization algorithms. Res J Appl Sci, Eng Technol 3(6):569–578
10. Rechenberg I (1965) Cybernetic solution path of an experimental problem. Royal Aircraft Establishment, brary Translation, p 1122
11. Holland J (1975) An introduction with application to biology, control and artificial intelligence adaptation in natural and artificial system. MIT Press
12. Holland JH (1975) Adaptation in natural and artificial systems. The University of Michigan Press, AnnArbor
13. Kirkpatrick S, Gelatt CD, Vecchi MP (1983) Optimization by simulated annealing. Science 220(4598):671–680
14. Farmer JD, Packard NH, Perelson AS (1986) The immune system, adaptation, and machine learning. Physica D 22(1–3):187–204
15. Dorigo M, Maniezzo V (1992) Optimization, learning and natural algorithms. Ph.D. thesis Politecnico di Milano, Italy
16. Kennedy J, Eberhart R (1995) Particle swarm optimization. IEEE international conference on neural networks Perth, Australia, pp 1942–1948
17. Nakrani S, Tovey C (2004) On honey bees and dynamic server allocation in internet hosting centers. Adapt Behav 12(3–4):223
18. Mendes JC, Saavedra OR, Pessanha JO (2002) Power system restoration restoration with priority loads using an evolutionary strategy. In: Proceedings of 34th North American power symposium, Arizona, pp 254–260
19. Santiago M, Maldonado R (2006) Optimal placement of FACTS controllers in power systems via evolutionary strategies. In: Proceedings of IEEE international conference on transmission and distribution evolutionary computation, pp 1–6
20. Dominguez-Navarro JA, Bernal-Agustin JL, Diaz A, Requena D, Vargas EP (2007) Optimal parameters of FACTS devices in electric power systems applying evolutionary strategies. Electri Power Energy Syst 29:83–90
21. Zhang Y, Milanovic JV (2007) Voltage sag cost reduction with optimally placed FACTS devices. In: 9th international conference on Electrical power, quality and utilisation, pp 1–6
22. Baghaee HR, Jannati M, Vahidi B, Hosseinian SH, Rastegar H (2008) Improvement of voltage stability and reduce power system losses by optimal GA-based allocation of multi-type

FACTS devices. In: 11th international conference on optimization of Electrical and Electronic equipment, pp 209–214
23. Sundareswaran K, Bharathram P, Siddharth M, Vaishnavi G, Shrivastava NA, Sarma H (2009) Voltage profile enhancement through optimal placement of FACTS devices using queen-bee-assisted GA. In: Third international conference on power systems, pp 1–5
24. Bina TM, Siahbidi JR, Kanzi K (2005) Application of averaging technique to the power system optimum placement and sizing of static compensators. In: The 7th international power engineering conference, pp 1–6
25. Samimi A, Golkar MA (2011) A novel method for optimal placement of STATCOM in distribution networks using sensitivity analysis by DIgSILENT software. Asia-Pacific power and energy Engineering conference, pp 1–5
26. Del-Valle Y, Hernandez JC, Venayagamoorthy GK, Harley RG (2006) Optimal STATCOM sizing and placement using particle swarm optimization. In: Proceedings of the IEEE transmission and distribution conference and exposition Latin America, pp 1–6
27. Hernandez JC, Del-Valle Y, Venayagamoorthy GK, Harley RG (2006) Optimal allocation of a STATCOM in a 45 bus section of the Brazilian power system using particle swarm optimization. In: Proceedings of the IEEE swarm intelligence symposium, pp 69–75
28. Panda S, Padhy NP (2008) Optimal location and controller design of STATCOM for power system stability improvement using PSO. J Franklin Inst 345:166–181
29. Del-Valle Y, Venayagamoorthy GK, Harley RG (2009) Comparison of enhanced-PSO and classical optimization methods: a case study for STATCOM placement. In: Proceedings of the IEEE 15th international conference on intelligent system applications to power systems, pp 1–7
30. Varshney S, Srivastava L, Pandit M (2011) Comparison of PSO models for optimal placement and sizing of STATCOM. In: 2nd international conference on sustainable energy and intelligent system, pp 346–351
31. Lee K, Geem Z (2005) A new meta-heuristic algorithm for continuous engineering optimization: harmony search theory and practice. Comput Methods Appl Mech Eng 194 (2005):3902–3933
32. Sirjani R, Mohamed A, Shareef H (2012) Optimal placement and sizing of static synchronous compensators in power systems using improved harmony search algorithm. Int Rev Electr Eng 7(2):4183
33. Majumdar S, Chakraborty AK, Chattopadhyay PK (2009) Active power loss minimization with FACTS devices using SA/PSO techniques. In: 3rd international conference on power systems, pp 1–5
34. Acha E, Fuerte-Esquivel CR, Ambriz-Perez H, Angeles-Camacho C (2004) FACTS modelling and simulation in power network. Wiley, New York
35. Zhang XP, Rehtanz C, Pal B (2006) Flexible AC transmission systems modelling and control. Springer, Berlin
36. Kundur P (1994) Power system stability and control. McGraw-Hill Inc
37. Sharma C, Ganness MG (2007) Determination of power system voltage stability using modal analysis. IEEE Int Conf Power Eng, Energy Electri Drives, POWERENG 2007:381–387
38. Pisica I, Bulac C, Toma L, Eremia M (2009) Optimal SVC placement in electric power systems using a genetic algorithms based method. In: IEEE Bucharest power tech conference, pp 1–6
39. Kazemi A, Parizad A, Baghaee H (2009) On the use of harmony search algorithm in optimal placement of FACTS devices to improve power system security. In: Proceedings of the IEEE EUROCON, pp 570–576
40. Zou D, Gao L, Li S, Wu J, Wang X (2010) A novel global harmony search algorithm for task assignment problem. J Syst Softw 83(10):1678–1688
41. Zou D, Gao L, Wu J, Li S, Li Y (2010) A novel global harmony search algorithm for reliability problems. Comput Ind Eng 58(2):307–316
42. Power Systems Test Case Archive, Uni. of Washington, http://www.ee.washington.edu/research/pstca/

Chapter 14
Optimal Placement of STATCOMs Against Short-Term Voltage Instability

Yan Xu, Zhao Yang Dong and Kit Po Wong

Abstract Short-term voltage stability is an increasing concern in today's power systems given growing penetration of induction motors. The instability can lead to catastrophic consequences such as cascading failures and/or wide-spread blackouts. STATCOMs are able to provide rapid and dynamic reactive power (VAr) support into the system and therefore improve system's short-term voltage performance following a large disturbance. Importantly, the sizing and locating of the STATCOM integration determine how much the short-term voltage performance can be improved. This chapter presents a novel systematic method for optimal placement of STATCOMs against short-term voltage instability. The problem is formulated as a multi-objective optimization model minimizing two conflicting objectives: (1) total investment cost and (2) expected unacceptable short-term voltage performance subject to a set of probable contingencies. Indices for quantifying short-term voltage stability and the related risk level are proposed for problem modeling. Candidate buses for STATCOM installations are analytically selected based on trajectory sensitivity technique. Load dynamics are fully considered using a composite load model comprising induction motor and other typical components. For the proposed model, rather than a single solution, a set of trade-off solutions called Pareto optimal solutions can be obtained, and the decision-maker may select one from them depending on practical needs. A relatively new and superior multi-objective evolutionary algorithm called multi-objective evolutionary algorithm

Y. Xu (✉)
Center for Intelligent Electricity Networks, The University of Newcastle, Newcastle, Australia
e-mail: daniel.xu@newcastle.edu.au

Z.Y. Dong
School of Electrical and Information Engineering, The University of Sydney, Sydney, Australia
e-mail: joe.dong@sydney.edu.au

K. Po Wong
School of Electrical, Electronic and Computer Engineering, The University of Western Australia, Perth, Australia
e-mail: kitpo.wong@uwa.edu.au

F. Shahnia et al. (eds.), *Static Compensators (STATCOMs) in Power Systems*, Power Systems, DOI 10.1007/978-981-287-281-4_14

based on decomposition (MOEA/D) is introduced and employed to find the Pareto optimal solutions to the model. The proposed method is verified on the New England 10-machine 39-bus system using industry-grade simulation tool and system models. Simulation results have validated the effectiveness of the proposed method. The method can be practically applied to provide decision-support for STATCOM installations.

Keywords Dynamic VAr support · Multi-objective optimization · Reactive power planning · Pareto optimality · Short-term voltage stability · STATCOM

14.1 Introduction

Voltage instability is a major threat in power system operation. This phenomenon can manifest in the form of progressive voltage drop or rapid voltage collapse after the power system being subjected to a disturbance. The loss of voltage stability can lead to catastrophic consequences such as cascading failures and/or wide-spread blackouts. Over past decades, many major blackouts around the world have been found directly associated with this phenomenon [1–3].

The driven force for voltage instability is usually the loads. In general, the instability stems from the attempt of load dynamics to restore the power consumption beyond the capability of the combined transmission and generation system [1]. According to an IEEE and CIGRE joint taskforce [2], the voltage stability can be divided into short-term and long-term phenomenon in terms of time frame (a more detailed classification and definition is given in the Appendix). In power system planning stage, VAr compensation is an effective means to improve the voltage stability. Conventional voltage stability assessment and associated VAr planning practices are mostly based on power flow methods. While these static methods are effective for steady-state long-term voltage stability, they usually overlook the short-term voltage instability phenomenon, where dynamic load components such as induction motors tend to restore their consumed power in a very short time-frame (typically, several seconds) [3]. Following a large disturbance, the induction motors decelerate dramatically by the voltage dip or may stall if the electrical torque fails to overcome the mechanical load. This in turn draws very high reactive current which affects strongly the voltage magnitudes and impedes the voltage recovery. Without adequate VAr support, unacceptable transient voltage performance (such as prolonged voltage depression, slow voltage recovery, etc.) may be experienced, and/or fast voltage collapse may occur. With increasing penetration of induction motor loads (e.g., air-conditioners), today's power systems tend to be more vulnerable to short-term voltage instability [3].

In terms of VAr planning, traditional static capacitor banks alone are inadequate to mitigate the short-term voltage instability due to the lack of fast response and that their VAr output decreases in a quadratic order with the voltage drop. As a superior

alternative, STATCOMs are able to provide rapid and dynamic VAr support against the voltage depression following a large disturbance, thus can more effectively counteract the short-term voltage instability [3]. Moreover, proper allocation of dynamic VAr support can effectively improve the low-voltage-ride-through (LVRT) capability of wind farms [4]. This chapter studies the optimal placement (i.e., sizing and locating) of STATCOMs into the power system for improving the short-term voltage stability.

Although a number of methods have been reported for optimal placement of STATCOMs, most of them focused on improving the steady-state voltage stability level [5–9] or mitigating static voltage sags [10], yet very few consider short-term voltage instability phenomenon. These works are reviewed as follows.

In [11], an optimal power flow (OPF) model was used to optimize the VAr placement considering steady-state voltage stability first. Then, time-domain simulation is performed to adjust the optimized VAr placement to verify the short-term voltage stability requirements. The VAr sources are sequentially allocated for one contingency at a time.

To allocate static and dynamic VAr sources against both steady-state and dynamic voltage instability problems, a mixed-integer programming (MIP) algorithm was developed in [12]. Based on linear sensitivities of performance measure with respect to the VAr injection, the MIP model can be solved efficiently and many contingencies can be considered simultaneously. However, due to the use of approximate linear sensitivities, it can only provide near-optimal solutions.

Reference [13] presented a heuristic approach for placing the STATCOM against the short-term voltage instability based on trajectory sensitivity technique. The best placement locations are selected from the buses with highest trajectory sensitivity index values. The STATCOM size is determined based on the existing fixed capacitors at a bus. Although effective, the method is heuristic and cannot guarantee the optimality of the cost-effectiveness of the project.

In [14], a mixed-integer dynamic optimization (MIDO) model was proposed. Using discretizing scheme, the MIDO model is converted to a mixed-integer nonlinear programming (MINLP) model and solved by standard solvers. However, the load is represented as the static ZIP (constant impedance, constant current, and constant power) model which is unable to reflect the dynamic nature of various load components (in particular induction motors), thus the optimization results tend to be inaccurate.

More recently, this MIDO model was improved in [15] using the control vector parameterization (CVP), trajectory sensitivity, singular value decomposition and linear programming techniques, and the load dynamics is taken into account. Moreover, it is noted that the works [13–15] only considered a single contingency during allocating the dynamic VAr resources.

This chapter presents a novel systematical method for optimal placement of STATCOMs against short-term voltage instability. Compared with existing works, the contributions and salient features of this chapter are as follows:

- For the optimal cost-effectiveness of the STATCOM integration project, the problem is formulated as a multi-objective optimization problem (MOP), minimizing two conflicting objectives: (1) the total investment cost (including purchasing cost and installation cost) of the STATCOM device, and (2) the expected unacceptable short-term voltage performance subject to a set of probable contingencies.
- System dynamic performance is realistically analyzed using full time-domain simulations and a composite load model comprising induction motors and other typical components is used to reflect the load dynamics.
- An index called transient voltage severity index (TVSI) is proposed for quantifying the short-term voltage stability degree, considering both unacceptable voltage deviation magnitude and corresponding duration time.
- Multiple contingencies are considered, and to reflect the probabilistic nature of the contingencies, the second objective is quantified by a risk index.
- A relatively new and superior multi-objective evolutionary algorithm called MOEA/D is introduced and employed to find Pareto optimal solutions of the MOP model. The MOEA/D can be potentially employed for solving other MOP problems in power engineering.

14.2 Problem Descriptions

14.2.1 Basics of STATCOM

STATCOM is a Voltage Source Converters (VSC)-based power electronics device able to generate rapid and continuously variable VAr output for voltage regulation. The VAr output of a STATCOM is the product of its current injection and the voltage magnitude of the connected bus. In response to a sudden voltage dip, the VAr output of the STATCOM decreases linearly with the bus voltage drop, which is superior over its competitor—SVC, whose VAr output decreases squarely with the bus voltage drop.

The Voltage-Current characteristic of STATCOM and SVC are compared in Fig. 14.1, where it can be seen that STATCOM can provide constant reactive current injection down to low voltage. For example, at 70 % voltage level, the SVC output becomes 70 % reactive current or 49 % reactive power, while for STATCOM, its reactive current output remains 100 % and its VAr output is 70 %. This difference is critical in supporting re-acceleration of motor loads—a major driving force for short-term voltage instability.

Besides, STATCOM has shorter response time and smaller size than SVC. All these advantages make it a better option for dynamic VAr support [3, 13, 16, 17].

During a dynamic event in the power system, e.g., a short-circuit fault, STATCOMs are able to provide rapid and dynamic VAr injection within the system to support the bus voltages. Figure 14.2 illustrates the impact of STATCOM to bus

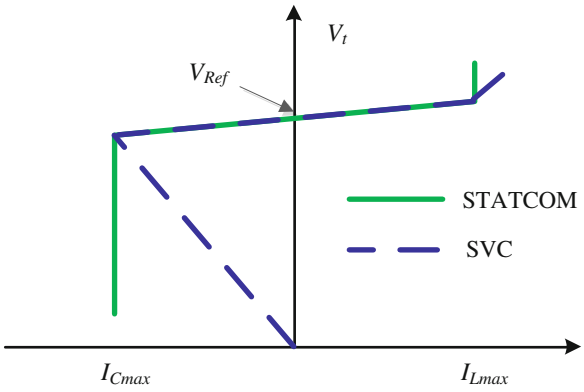

Fig. 14.1 Voltage-current characteristic of the STATCOM and SVC [3]

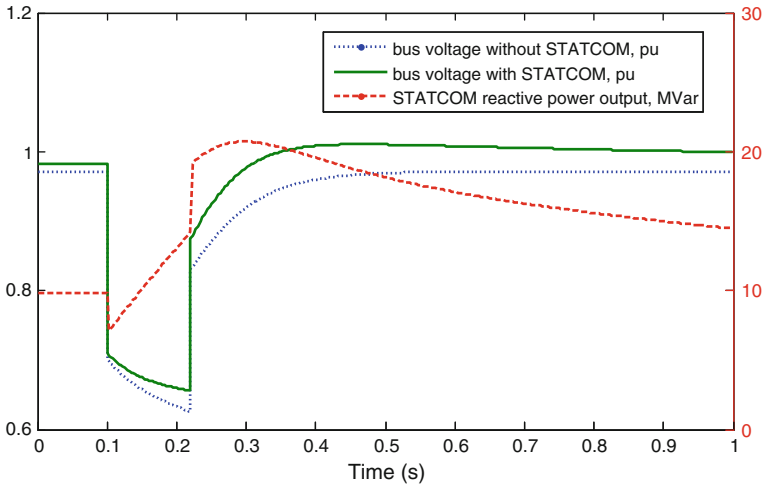

Fig. 14.2 An illustration of the STATCOM reactive power output during a fault

voltage at pre- and post-disturbance states. The trajectories are obtained from time-domain simulation of a short-circuit disturbance to an induction motor load-based distribution feeder with a 10 MVA STATCOM [29]. According to Fig. 14.2, before the disturbance occurs (0–0.1 s), the STATCOM is exporting 10 MVAr reactive powers (see red broken line). The bus voltage (see green unbroken line) is maintained at the normal level. When the short-circuit fault incepts (0.1 s), the bus voltage drops down to 0.7 pu and the STATCOM's output decrease a little accordingly. During the fault-duration period (0.1–0.22 s), the STATCOM reacts rapidly to export increasing reactive power to boost the bus voltage. After the fault cleared (0.22 s), the bus voltage jumps up and the STATCOM exports more reactive

power due to the augmented voltage magnitude. Subsequently, with variable STATCOM reactive power support to the nominal value, the bus voltage recovers gradually back to the normal level. The voltage profile without the STATCOM is also shown in Fig. 14.2 (see blue broken line), where it can be seen that the voltage level is generally depressed during the whole post-disturbance states.

The dynamic model of the STATCOM used here is the "SVMO3" model, which is developed by the Western Electricity Coordinating Council (WECC) [17]. This model is a generic VSC-based STATCOM model and has been implemented in by several main-stream software vendors including Siemens PTI PSS®E and GE PLSF for STATCOM modeling [17, 18]. The model has also been validated with several recorded digital fault recorder traces from actual static VAr system installations through WECC task force efforts [17]. This STATCOM model will also be used in the later numerical tests of this chapter. The block diagram and the model parameters are given in Appendix 1 and 2.

14.2.2 Load Modeling

The key driving force of voltage instability is the tendency of dynamic loads to restore their consumed power within a very short time frame [2]. Hence, appropriate modeling of the load dynamics is necessary in dynamic VAr planning studies.

In this chapter, the composite load model "CLOD" [18] is employed (note that other load models can also be considered when necessary). As illustrated in Fig. 14.3, this load model is an aggregation of induction motors, lighting, and other types of equipment that are fed from many typical substations [18].

This composite load model is defined by an 8-dimensional vector$[\rho_L, \rho_S, \rho_D, \rho_T, \rho_C, K_P, R_e, X]$, each element indicates respectively the percentage value of large motors (LM), small motors (SM), discharge lighting, transformer exciting current, and constant power load, as well as the exponent of voltage-dependent real power load, and branch resistance and reactance (pu on load MW base). The model

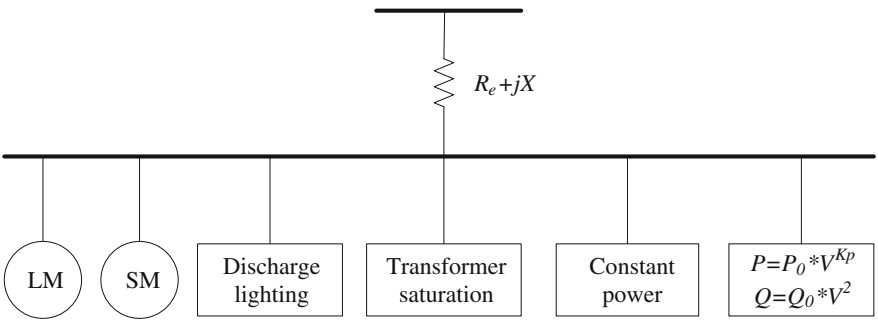

Fig. 14.3 Structure of the composite load model "CLOD"

is suitable in situations where loads are to be represented in dynamic level, but where detailed dynamics data is not available, it has been implemented by PSS®E as a standard composite load model [18]. More details about this model can be found in [18].

14.2.3 Transient Voltage Severity Index

Short-term voltage stability assessment mainly focuses on unacceptable transient voltage deviation, delayed voltage recovery, and/or fast voltage collapse following a disturbance. Some industrial criteria such as NERC/WECC criteria, TVA criteria, ITIC curve, etc. [19] related to short-term voltage stability defines the unacceptable voltage dip magnitude and the duration time, but they can only provide a binary answer to the voltage stability, namely, stable or unstable.

To quantitatively measure the short-term voltage stability degree, several indices have been proposed in the literature. Reference [14] proposed a contingency severity index which is the sum of two indices respectively accounting for the voltage magnitude violation and the duration time, however, it only considers the maximum voltage deviation magnitude. Reference [20] proposed an index called transient voltage dip acceptability to consider both the voltage dip magnitude and its duration time, but a nonlinear curve-fitting process is needed during its calculation.

This chapter proposes an alternative yet more straightforward index called transient voltage severity index (*TVSI*) to quantify the transient voltage performance of the system buses following the clearance of the disturbance:

$$TVSI = \frac{\sum_{i=1}^{N} \sum_{t=T_c}^{T} TVDI_{i,t}}{N \times (T - T_c)} \tag{14.1}$$

where N is the total number of buses in the system, T is the considered transient time frame, T_c is the fault clearing time, *TVDI* is the transient voltage deviation index, calculated by:

$$TVDI_{i,t} = \begin{cases} \frac{|V_{i,t} - V_{i,0}|}{V_{i,0}}, & \text{if } \frac{|V_{i,t} - V_{i,0}|}{V_{i,0}} \geq \mu \\ 0, & \text{otherwise} \end{cases} \quad \forall t \in [T_c, T] \tag{14.2}$$

where $V_{i,t}$ denotes the voltage magnitude of bus i at time t, which is obtained from time-domain simulation, and μ is the threshold to define unacceptable voltage deviation level, which can be set according to the industrial criteria [19], e.g., 20 %.

The concept of the *TVSI* is illustrated in Fig. 14.4. It only accounts for the buses with unacceptable voltage violation during the transient period, and it measures not only the voltage violation magnitude but also the corresponding duration time in the

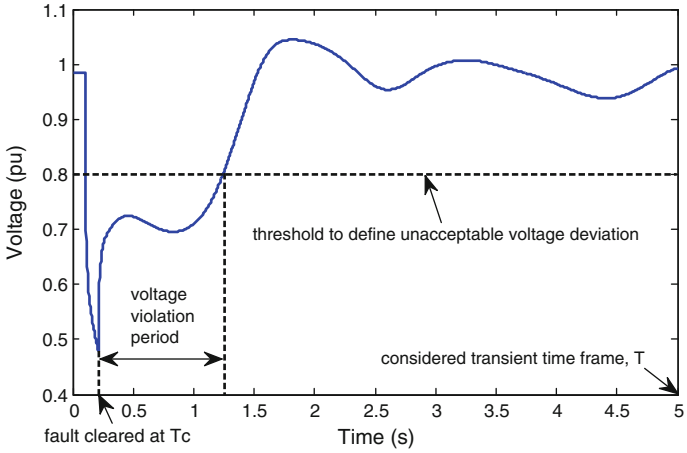

Fig. 14.4 Illustration of the concept of *TVSI*

system level. It can provide a quantitative comparison of the system transient voltage performance following a disturbance. A smaller *TVSI* value means the transient voltage performance is better.

14.2.4 Risk-Based Criterion

Previous research such as [11, 13–15] only consider a single contingency in placing the STATCOM, and the contingency evaluation is based on a deterministic criterion, i.e., all the contingences are equally treated and each should satisfy the stability requirement. In practice, the STATCOM placement should cover multiple contingencies taking into account both their probability and severity. In this chapter, a risk index (*RI*) is proposed to quantify the expected unacceptable transient voltage performance under a set of probable contingencies:

$$RI = \sum_{k=1}^{M} TVSI_k \times p_k \tag{14.3}$$

where p_k is the probability of the contingency k, which can be obtained from historical fault statistics, and M is the total number of the contingencies to be considered.

14.2.5 Candidate Bus Selection

The optimal placement of STATCOM is essentially a MINLP problem. To reduce the whole problem size, it is usually needed to select only potential buses as the

candidate locations for STATCOM installation. Previous works [13–15] show that the trajectory sensitivity technique is an effective means to identify potential buses.

Trajectory sensitivity is referred to as the time-varying sensitivity of (small) changes in a parameter with respect to the system dynamic behavior [21]. It can either be calculated analytically [21] or numerically approximated through two successive time-domain simulation runs as follows:

$$\frac{\partial \phi(x_0, t)}{\partial x} = \frac{\phi(x_0 + \Delta x_0, t) - \phi(x_0, t)}{\Delta x_0} \tag{14.4}$$

where $\partial \phi(x_0, t)/\partial x$ denotes the trajectory sensitivity along with time t given the initial system condition x_0,ϕ denotes the dynamic trajectory of the system, Δx_0 is the small perturbation.

Based on the concept of trajectory sensitivity, this chapter proposes a sensitivity index (SI) to assess the sensitivity of the change in *RI* with respect to the dynamic VAr injection at a bus:

$$SI_i = \frac{RI(B_i) - RI(B_i + \Delta B)}{\Delta B} \tag{14.5}$$

where B_i is the capacitive capacity of the STATCOM installed at bus i, and ΔB is the small perturbation, e.g., 10 MVAr. Note that the SI is a positive value since the *RI* can generally be reduced after the STATCOM integration.

The proposed SI measures the overall effectiveness of a bus for deploying the STATCOM to improve the system short-term voltage stability for a set of probable contingencies. Hence, the buses with larger SI values should be selected as the candidate locations in the optimization model.

14.3 Mathematical Model

In this chapter, the STATCOM placement problem is formulated as a multi-objective mixed-integer programming model with the following objectives and constraints.

14.3.1 Objectives

The objective function comprises two individual objectives:

$$\min_x \mathbf{f} = [f_1(x, u), f_2(x, u)] \tag{14.6}$$

where x and u stand for decision variables and state variables, respectively. The decision variables include the STATCOM size and the placement location.

The first objective f_1 is the risk level of unacceptable transient voltage performance under a set of probable contingencies, calculated by (14.3). Note that (14.3) cannot be explicitly calculated, rather, it requires time-domain simulation to obtain the post-disturbance voltage trajectories.

The second objective f_2 is the total investment costs of the STATCOM deployment project, calculated by:

$$f_2 = \sum_{i=1}^{H} I_i \times C_{\text{install}} + \sum_{i=1}^{H} I_i \times B_i \times C_{\text{purchase}} \tag{14.7}$$

where I_i is the binary decision variable 1 or 0, indicating whether or not to install the STATCOM at bus i, B_i is the integer decision variable denoting the capacity limit of the STATCOM at bus i, C_{install} and C_{purchase} denote respectively the installation cost and the purchasing cost of the STATCOM, H is the total number of candidate buses.

14.3.2 Steady-State Constraints

The steady-state constraints consist of power flow balance and steady-state operational limits for pre-contingency state:

$$\begin{cases} P_G - P_L - P(V,\theta) = 0 \\ Q_G - Q_L - Q(V,\theta) = 0 \end{cases} \tag{14.8}$$

$$\begin{cases} S(V,\theta) \le S^{\max} \\ V^{\min} \le V \le V^{\max} \\ P_G^{\min} \le P_G \le P_G^{\max} \\ Q_G^{\min} \le Q_G \le Q_G^{\max} \end{cases} \tag{14.9}$$

where (14.8) represent the active and reactive power balance for each bus, P_G and Q_G denote the active and reactive power generation, P_L and Q_L denote the active and reactive power load, P and Q denote the power flow equations, θ is the voltage angle; (14.9) represents the operational limits on line flow, steady-state voltage magnitude, and generator output capacity.

14.3.2.1 Dynamic Constraints

It is usually the case that short-term voltage instability or collapse occurs along with the loss of synchronism of generators. It is however usually difficult to distinguish the major driving force, voltage or generator angle, for the short-term instability phenomenon [2]. Consequently, it is necessary to add the rotor angle stability constraint in the optimization model to prevent the voltage instability caused by the rotor angle instability.

Conventionally, the rotor angle stability is checked by examining the rotor angle deviation against a certain threshold [22]. In this chapter, the following constraint is included to ensure the rotor angle stability for each contingency:

$$\left[\max\left(\Delta\delta_{ij}^{T}\right)\right]_{k} \leq \sigma \tag{14.10}$$

where $\left[\max\left(\Delta\delta_{ij}^{T}\right)\right]_{k}$ denotes, for contingency k, the maximum rotor angle deviation between any two generators during the transient period T, σ is the threshold and can be set to π for the extreme case [22].

It should be indicated that (14.10) is consistent with industry practice since a real-world power system is always operated such that any generator rotor angle will not exceed a threshold. If a generator's rotor angle is larger than such a threshold, the generator will be tripped by out-of-step relay to protect it from being damaged [22]. Other rotor angle stability criteria can also be considered when necessary.

It is important to note that since the transient voltage performance is already reflected by the RI and is one optimization objective, the dynamic voltage magnitudes are not needed to be constrained in the MOP model.

14.4 Solution Method

14.4.1 Pareto Optimality

In contrast to a single-objective optimization problem which has a definite single solution, a MOP model optimizes simultaneously two or more objectives. When these objectives are in conflict with each other, e.g., in (14.6), a lower value of f_1 will result in a higher value of f_2, there is not a single solution that can minimize all the objectives simultaneously. Rather, a set of trade-off solutions can be obtained, and the decision-maker may select one from them depending on practical needs.

Pareto optimality theory [23] is a predominant concept to define the trade-off solutions. Given the feasible decision space $\mathbf{X}$, a solution $x^* \in \mathbf{X}$, is called *Pareto optimal* (or *non-dominated*), if there does not exist another solution, $x \in \mathbf{X}$, such that $\mathbf{f}(x) \leq \mathbf{f}(x^*)$ and $f_i(x) \leq f_i(x^*)$ for at least one function. In other words, none of the objective functions can be improved in value without impairment in some of the other objective values. The vector of objective function values given by a Pareto optimal solution $\mathbf{f}(x^*)$ is called a *Pareto optimal objective vector*. The set of all the Pareto optimal solutions is called *Pareto set* (PS) and the set of all the Pareto optimal objective vectors is the *Pareto front* (PF).

To approximate the PF, one way is to aggregate (e.g., through weight factors) the individual objectives as a composite one such that the MOP can be decomposed into a number of scalar objective optimization sub problems. However, this approach can suffer from several limitations: first, it is usually difficult to select an

appropriate weight factor; second, only one single Pareto optimal solution can be obtained from each simulation run. An alternative yet more efficient way is to apply a multi-objective evolutionary algorithm (MOEA) [24]. Based on the emulation of the mechanism of natural selection, the MOEA treats the MOP as a whole and is able to find multiple optimal solutions in a single simulation run, and systematically approximate the PF without any subjectivity. Besides, the MOEA is not limited to the convexity and/or differentiability of the mathematical model of the problem.

14.4.2 Decomposition-Based MOEA

State-of-the-art MOEAs are Non-dominated Sorting Genetic Algorithm II (NSGA-II) and Multi-objective Genetic Local Search (MOGLS) [23, 24]. This chapter introduces a relatively new yet more superior algorithm called MOEA/D here, and employs it to find the PF of the proposed MOP model. This algorithm can be considered for solving other MOP problems in power engineering.

Proposed in [25], MOEA/D combines the aggregation strategy and MOEA together. It explicitly decomposes the MOP into a set of scalar optimization sub problems, and then solves them by evolving a population of solutions. Compared with NSGA-II and MOGLS, it has been shown that MOEA/D has lower computational complexity, and can find higher-quality solutions for many benchmark problems [25].

For a MOP with m objectives, given a set of evenly spread weight vectors $\boldsymbol{\lambda}^1, \ldots, \boldsymbol{\lambda}^j, \ldots, \boldsymbol{\lambda}^S$, where $\boldsymbol{\lambda}^j = \left(\lambda_1^j, \ldots, \lambda_m^j\right)$, the MOP is decomposed into S scalar optimization subproblems using *Tchebycheff* approach and the objective function of the *j*th subproblem is:

$$\min \left[\vartheta^{te}\left(x \middle| \boldsymbol{\lambda}^j, z^*\right) = \max_{1 \le i \le m} \left\{ \lambda_i^j \middle| f_i(x) - z_i^* \right\} \right] \tag{14.11}$$

where z^* is the reference point.

At each generation, the population is composed of the best solution found so far for each sub problem. The neighborhood relations among these sub problems are defined based on the distance between their aggregation coefficient vectors, and the optimal solutions to two neighboring sub problems should be very similar. Each sub problem is optimized by using the information only from its neighboring sub problems.

The major operations of MOEA/D are introduced below, and more technical details and explanations can be found in [25].

14.4.2.1 Step (A) Initialization

(A.1) Generate S evenly spread weight vectors: $\boldsymbol{\lambda}^1, \ldots, \boldsymbol{\lambda}^S$.
(A.2) Set the external population (EP) = $\varnothing$.
(A.3) Compute the *Euclidean* distance between any two weight vectors and find the R closest weight vectors to each weight vector. For each $i = 1, \ldots, S$, set $E(i) = \{i_1, \ldots, i_R\}$, where $\boldsymbol{\lambda}^{i_1}, \ldots, \boldsymbol{\lambda}^{i_R}$ are the R closest neighboring weight vectors to $\boldsymbol{\lambda}^i$.
(A.4) Generate an initial population $x^1, \ldots, x^S$ randomly. Set the objective function value $FV^i = f(x^i)$.
(A.5) Initialize $z = (z_1, \ldots, z_m)$ by a problem-specific method.

14.4.2.2 Step (B) Updating

For $i = 1, \ldots, S$, perform the following steps:

(B.1) Reproduction: randomly select two indices k, l from $E(i)$ and generate a new solution y from x^k and x^l by a specific operator (e.g., genetic operator).
(B.2) Improvement: apply a specific repair/improvement heuristic on y to producey'.
(B.3) Update z: for each $j = 1, \ldots, m$, if $z_j < f_j(y')$, set $z_j = f_j(y')$.
(B.4) Update neighboring solutions: for each index $j \in E(i)$, if $\vartheta^{te}\left(y' \middle| \boldsymbol{\lambda}^j, z\right) \leq \vartheta^{te}\left(x^j \middle| \boldsymbol{\lambda}^j, z\right)$, set $x^j = y'$ and $FV^j = F(y')$.
(B.5) Update EP: remove from EP all the vectors dominated by $F(y')$, and add $F(y')$ to EP otherwise.

14.4.2.3 Step (C) Termination

If any stopping criterion is met, e.g., the maximum iteration number is reached or no changes are found in EP in a predefined number of successive iterations, stop and export EP. Otherwise, go back to Step (2).

14.4.3 Coding Rule

The decision variables I and B are coded as an individual shown in Fig. 14.5. An individual contains two parts of values, where the left part represents the binary decision on installing the STATCOM at each candidate bus, and the right part represents the corresponding STATCOM size (MVAr). Hence, given H candidate buses, the length of an individual is $2 \times H$.

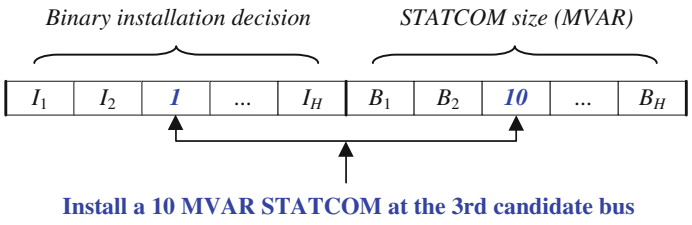

Fig. 14.5 Structure of a coded individual

14.4.4 Computation Process

The overall computation flowchart of the proposed methodology for optimal STATCOM placement against short-term voltage instability is shown in Fig. 14.6.

The whole computation process can be divided into the following 7 stages:

- In the 1st stage, the system model, contingency set together with their probabilities, and computing parameters are input.
- In the 2nd stage, the candidate STATCOM installation buses are selected using the process presented in Sect. 14.2.5. Only the selected candidate buses are included in the subsequent optimization process.
- In the 3rd stage, the optimization procedure starts, with the initial population generated according to Step (A).
- In the 4th stage, for each of the generated individual, the objective function value f_2 is calculated according to (14.7), and then full time-domain simulation is performed to evaluate f_1 according to (14.3).
- In the 5th stage, the individuals are assessed according to their objective function values and constraints (14.8–14.10), an individual is "infeasible" if it cannot meet (14.8–14.10), only "feasible" individuals are saved and the EP is updated according to Step (B).
- Stopping criterion is then checked at the 6th stage, if any of them is met, the whole computation can stop and the current EP is exported; otherwise, offspring generation is produced at the 7th stage according to Step (B). The new individuals are sent back to the 4th stage.
- The whole computation iterates until one stopping criterion is met. It is worth mentioning that due to the parallel nature of the MOEA, the method is open to parallel processing techniques [26, 28] for accelerating the computation speed when necessary.

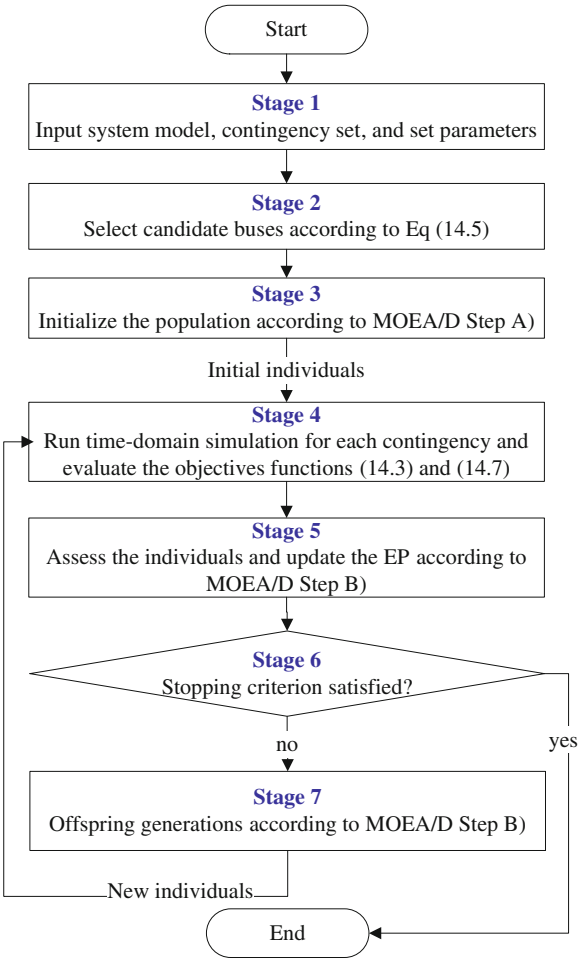

Fig. 14.6 Computation flowchart

14.5 Numerical Results

The proposed methodology is validated on the New England 10-machine 39-bus system, which is a benchmark test system for stability studies [14]. The on-line diagram of this system is shown in Fig. 14.7, and its total load is 6,150.5 MW and 2,555.6 MVAr.

During the test, the time-domain simulation is performed using the PSS®E package [18], the MOEA/D algorithm is implemented in the MATLAB platform, and an I/O is developed to interface MATLAB and PSS®E [26].

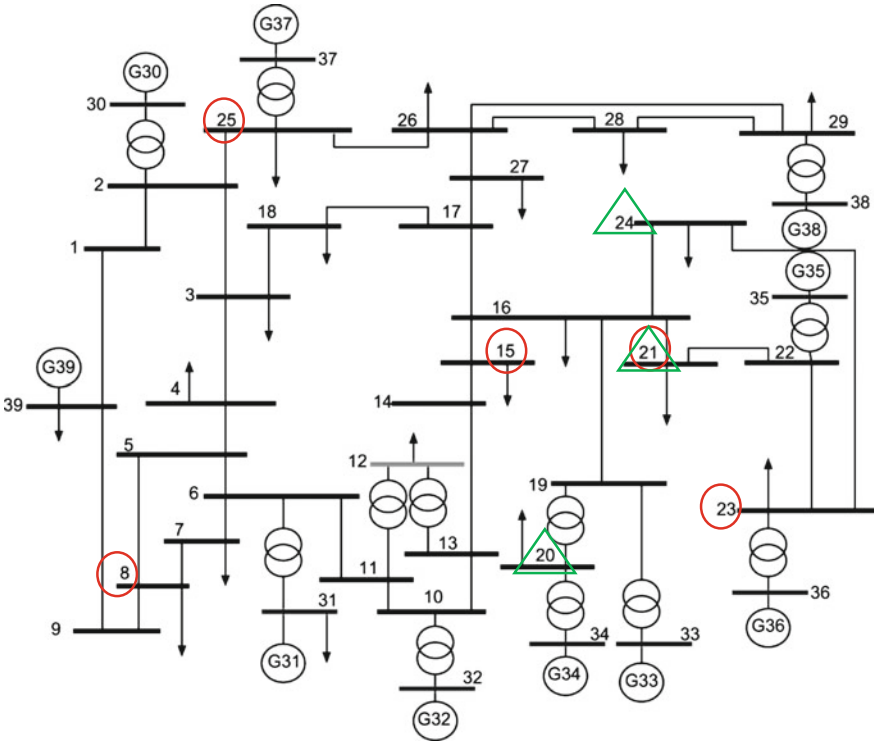

Fig. 14.7 One-line diagram of the New England 10-machine 39-bus system

14.5.1 Parameter Settings

The STATCOM cost coefficients C_{install} and C_{purchase} are assumed to be \$1.5 million and \$0.05 million/MVAr, respectively [14]. It is assumed that the total VAr compensation at one bus is all provided by one STATCOM device. In practice, different sized STATCOM can be used in combination when necessary.

Since this chapter focuses on the planning stage, the STATCOM control parameters are set to typical values based on [17]. These parameters can also be fine-tuned when necessary, but it is usually a reasonable choice to use the typical values during the planning stage. The parameters of the STATCOM are given in Appendix Table 14.6.

A total of 5 contingencies spreading different geographical regions of the network are assumed (see Table 14.1). In practice, the probabilities of the

Table 14.1 Contingency set

Fault bus no.	8	21	15	23	25
Probability (%)	20	20	20	20	20
Fault details	3-phase short-circuit bus fault, cleared after 0.11 s				

contingencies should be obtained from historical statistics. Without any priori knowledge and for a test without loss of generality, the contingency probabilities are assumed to be the same here, being 20 %. Besides, for network planning/reinforcement studies, it is usually a common practice to consider the severest fault scenario, hence, the 3-phase short-circuit bus fault is assumed here (however, other types of contingencies, e.g., single-phase to line short-circuit or phase-to-phase short-circuit can also be considered if necessary). The locations of the 5 contingencies are also marked in Fig. 14.7 (see the red cycles).

The load model parameters are set to values presented in Table 14.2. For practical application, these parameters should be derived from load modeling efforts.

For the time-domain simulation, the total simulation time T is set to 2 s, the simulation step is set to 0.0025 s. For *TVDI* calculation, μ is set to 20 %.

To implement the MOEA/D, the whole problem is decomposed into 51 sub problems and the stopping criteria are (1) when the maximum iteration number 100 is reached or (2) no changes are found in EP after 10 successive iterations.

14.5.2 Short-Term Voltage Stability Assessment

At first, the short-term voltage stability of the test system is assessed and quantified in terms of *TVSI*. To demonstrate the impact of load dynamics, two time-domain simulation runs are performed and compared. For the first, the composite load model is not included, rather, the load is represented as constant power, hence no load dynamics will be involved during the transient period; for the second, the dynamic load model (defined in Table 14.2) is used. The *TVSI* values of each fault for the two load models are compared in Table 14.3.

As the Table 14.3 reports, the load dynamics can substantially affect the system's short-term voltage stability (a larger *TVSI* value corresponds to a lower voltage stability level). Considering the five probable contingencies together, the *RI* values are 0.046 and 3.15 for the system without and with load dynamics, respectively.

To illustrate this, the voltage responses (0–5 s) under the fault at bus 21 and bus 15 with different load models are shown in Figs. 14.8 and 14.9, respectively. It can

Table 14.2 PSS®E "CLOD" load model parameters

Parameter	ρ_L	ρ_S	ρ_D	ρ_T	ρ_C	K_P	R_e	X
Value	20 %	30 %	5 %	5 %	30 %	2	0	0

Table 14.3 Short-term voltage stability assessment before STATCOM installation

Fault bus no.	8	21	15	23	25
TVSI (constant power load model)	0.018	0.061	0.043	0.067	0.041
TVSI (dynamic load model)	0.56	3.70	6.87	2.30	2.30

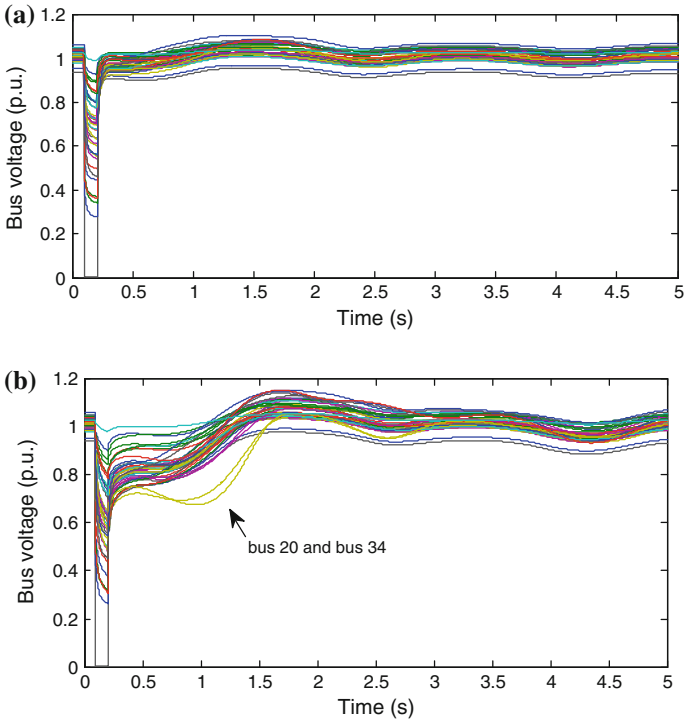

Fig. 14.8 Bus voltage responses under the bus 21 fault. **a** Constant power load model, and **b** Dynamic load model

be seen that, without the load dynamics, the system post-fault bus voltages recover very fast to the normal level and there is no short-term voltage instability issue—see Figs. 14.8a and 14.9a.

By marked contrast, when load dynamics are involved, for the bus 21 fault, a number of buses experience much slower voltage recovery—see Fig. 14.8b, in particular, bus 20 and 34 undergo a prolonged voltage depression during 0.2–1.4 s; for the bus 15 fault, the voltage collapses occurs at 1.6 s—see Fig. 14.9b, together with the loss of rotor angle stability—see Fig. 14.9c (note that the oscillatory voltage response after 1.6 s is as the result of the loss of synchronism). It is manifest that without considering the load dynamics, the STATCOM placement results tend to be optimistic. In the following of the test, the dynamic load model is used.

Compared with the existing methods in the literature [13–15] which only provide a binary classification for the voltage stability, the proposed TVSI can quantitatively evaluate the voltage stability degree.

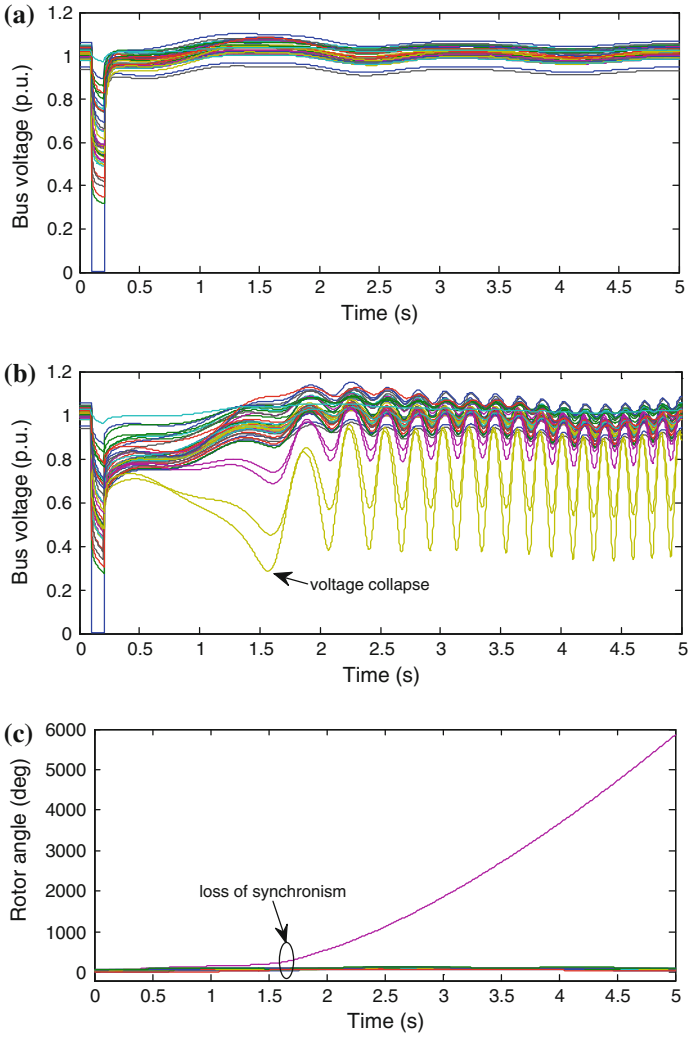

Fig. 14.9 System dynamic response under the bus 15 fault. **a** Bus voltage responses using constant power load model, **b** Bus voltage responses using dynamic load model, and **c** rotor angle response using dynamic load model

14.5.3 Candidate Bus Selection

For this test system, only the load buses are considered as the candidate locations for STATCOM installation. There are a total of 17 load buses in this system. To select the best candidate buses from them, the *SI* value of each load bus is evaluated using the method presented in Sect. 14.2.5. The results are shown in Fig. 14.10.

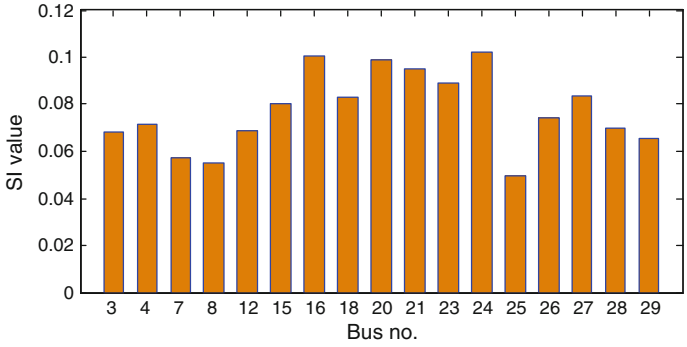

Fig. 14.10 *SI* of each bus with respect to the *RI*

According to Fig. 14.10, the *SI* values vary among different buses, implying that the buses have different effects to improve the short-term voltage stability for a STATCOM connection. In this test, the top 5 buses with highest *SI* values are selected as the candidate locations for STATCOM placement. The numbers of selected buses are 16, 20, 21, 23, and 24, respectively.

14.5.4 STATCOM Placement Results

Compared with Refs. [13–15] which can only provide a single and deterministic solution, the proposed MOP approach in this paper is able to provide a range of trade-off solutions for better decision-making support. The MOP (14.6–14.10) is solved using the MOEA/D. A PS containing 9 Pareto optimal solutions are obtained, which presents the cost-benefit characteristics of the STATCOM installation project to the decision-makers. The obtained PS is shown in Fig. 14.11, where the fitted PF to the PS is also plotted.

As Fig. 14.11 shows, generally, a lower *RI* corresponds to a higher investment cost, i.e., more STATCOM installations. Based on the obtained PF, decision can be made to select a final solution according to practical needs and engineering judgments. One appropriate criterion can be given the maximum acceptable risk level, select the solution with lowest investment cost on the Pareto front. In this test, we assume that the maximum acceptable risk level in terms of *RI* is 1.0. A solution is correspondingly selected in Fig. 14.11. It should be indicated that other decision-making criteria for selecting a final solution from the PF can also be considered, such as fuzzy logic, *Nash*-equilibrium, etc. [27].

The details of the selected solution are listed in Table 14.4. The corresponding locations of STATCOM are also marked in Fig. 14.6 (see the green triangles). 3 buses are installed with STATCOM, the total size is 116 MVAr, the investment cost is $10.3 million and the resulting *RI* is 0.85. The *TVSI* under each specific

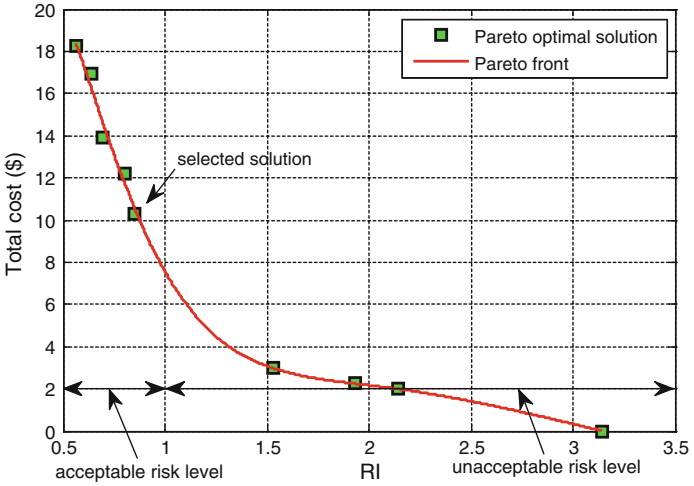

Fig. 14.11 Pareto optimal solutions and the fitted Pareto front

Table 14.4 Selected STATCOM installation scheme

Installation bus no.	16	20	21	23	24	Total
STATCOM size (MVAr)	0	33	42	0	41	116

Table 14.5 Short-Term voltage stability assessment after STATCOM installation

Fault bus no.	8	21	15	23	25
TVSI	0.42	0.85	1.14	0.58	1.28

contingency is given in Table 14.5. Comparing Table 14.5 with Table 14.3, it can be seen that, after the STATCOM installation, the system short-term voltage stability is significantly improved for each fault, and the overall risk level (*RI*) is reduced by 73 %.

To illustrate the improvement of the short-term voltage stability by the STATCOM, the system responses (0–5 s) under the bus 21 fault and the bus 15 fault are shown in Fig. 14.12 for comparison with Figs. 14.8 and 14.9. With the dynamic VAr support by the STATCOM, for the bus 21 fault, the bus voltage can recover much faster after fault clearing, and for the bus 15 fault, the voltage collapse and rotor angle instability is prevented, and the voltage recovers very fast to the normal level.

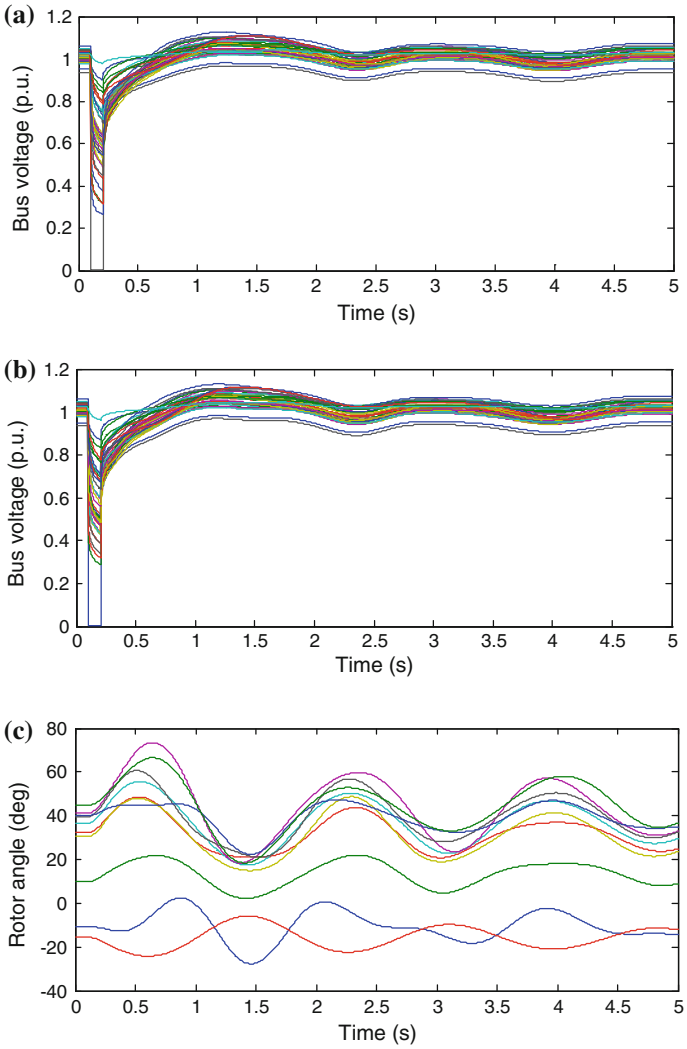

Fig. 14.12 System dynamic response after STATCOM installations. **a** Bus voltage responses under the bus 21 fault, **b** Bus voltage responses under the bus 15 fault, and **c** Rotor angle response under the bus 15 fault

It is worth pointing out that given the same STATCOM cost rates and the same test system as Ref. [14], the total cost for the selected final solution is $10.3 million considering 5 contingencies simultaneously. While in [14], the simulation results report that the total cost is $19.53 million for the single contingency "16–17" and $12.45 million for the single contingency "21–22", which is much more expensive than the obtained results here.

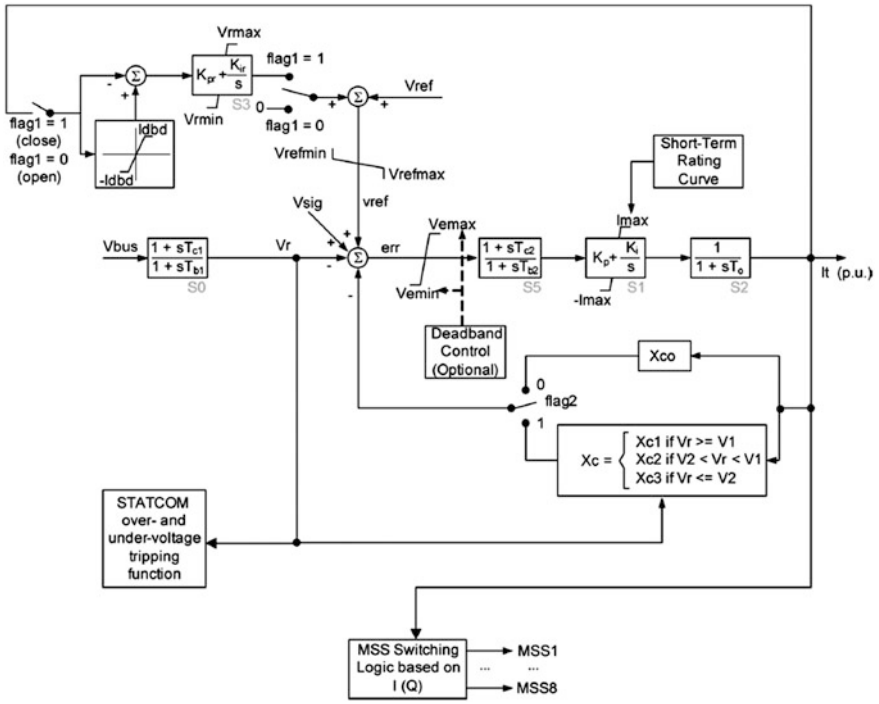

Fig. 14.13 Block diagram of the SVSMO3 STATCOM model [18]

Appendix 1

The block diagram of the "SVSMO3" model for STATCOM is shown in Fig. 14.13 [18].

Appendix 2

Table 14.6 SVSMO3U1 model parameters used in this chapter [17]

Value	Model parameter
0.01	*Xc*0, linear droop
0	*Tc*1, voltage measurement lead time constant (sec)
0.1	*Tb*1, voltage measurement lag time constant (sec)
4	*Kp*, proportional gain
25	*Ki*, integral gain
0.5	*Ve*max, voltage error max. (pu)

(continued)

Table 14.6 (continued)

Value	Model parameter
−0.5	*Ve*min, voltage error min. (pu)
0.005	*T0*, firing sequence control delay (sec)
10	*I*max1, max. continuous current rating (pu on STBASE)
0	*dbd*, deadband range for voltage control (pu)
10	*Kdbd*, ratio of outer to inner deadband
0.1	*Tdbd*, deadband time (sec)
0	*Kpr*, proportional gain for slow-reset control
0.001	*Kir*, integral gain for slow-reset control
0.01	*Idbd*, deadband range for slow-reset control (pu on STBASE)
0.1	*Vr*max, max. limit on slow-reset control output (pu)
−0.1	*Vr*min, min. limit on slow-reset control output (pu)
1.4	*Ishrt*, max. short-term current rating multiplier of max. continuous curr
0.5	*UV*1, voltage at which STATCOM limit starts to be reduced linearly (pu)
0.2	*UV*2, voltage below which STATCOM is blocked (pu)
1.08	*OV*1, voltage above which STATCOM limit linearly drops (pu)
1.2	*OV*2, voltage above which STATCOM blocks (pu)
1.3	*Vtrip*, voltage above which STATCOM trips after time delay Tdelay2 (pu)
1	*Tdelay*1, short-term rating time (sec)
0.08	*Tdelay*2, trip time for V > Vtrip (sec)
1	*Vsched*, VOLTAGE REFERENCE (pu)
1.05	*Vref*max, max. limit on voltage reference (pu)
0.95	*Vref*min, min. limit on voltage reference (pu)
0	*Tc*2, lead time constant (sec)
0	*Tb*2, lag time constant (sec)
0	*I2t*, I2t limit
0	*Reset*, reset rate for I2 t limit
0	*hyst*, width of hysteresis loop for I2 t limit
0.01	*Xc*1, non-linear droop slope 1
1	*Xc*2, non-linear droop slope 2
0.01	*Xc*3, non-linear droop slope 3
1.025	*V*1, non-linear droop upper voltage (pu)
0.975	*V*2, non-linear droop lower voltage (pu)
0.1	*Tmssbrk*, time for MSS breaker to operate—typically ignor e(sec)
300	*Tout*, time MSC should be out before switching back in (sec)
0.5	*TdelLC*, time delay for switching in a MSS (sec)
0.3	*Iupr*, upper threshold for switching MSSs (pu on STBASE)
−0.3	*Ilwr*, lower threshold for switching MSSs (pu on STBASE)
10	*STBASE* (>0), STATCOM BASE MVA

Appendix 3

The IEEE/CIGRE Joint Task Force on Stability Terms and Definitions (2004) suggested a classification criterion for voltage stability, as shown in Fig. 14.14 [2].

- *Large-disturbance voltage stability* refers to the system's ability to maintain steady voltages following large disturbances such as system faults, loss of generation, or circuit contingencies. This ability is determined by the system and load characteristics, and the interactions of both continuous and discrete controls and protections. Determination of large-disturbance voltage stability requires the examination of the nonlinear response of the power system over a period of time sufficient to capture the performance and interactions of such devices as motors, underload transformer tap changers (ULTCs), and generator field-current limiters. The study period of interest may extend from a few seconds to tens of minutes.
- *Small-disturbance voltage stability* refers to the system's ability to maintain steady voltages when subjected to small perturbations such as incremental changes in system load. This form of stability is influenced by the characteristics of loads, continuous controls, and discrete controls at a given instant of time. This concept is useful in determining, at any instant, how the system voltages will respond to small system changes. With appropriate assumptions, system equations can be linearized for analysis thereby allowing computation of valuable sensitivity information useful in identifying factors influencing stability. This linearization, however, cannot account for nonlinear effects such as tap changer controls (dead-bands, discrete tap steps, and time delays).
- *Short-term voltage stability* involves dynamics of fast acting load components such as induction motors, electronically controlled loads, and HVDC converters. The study period of interest is in the order of several seconds, and analysis requires solution of appropriate system differential equations; this is similar to

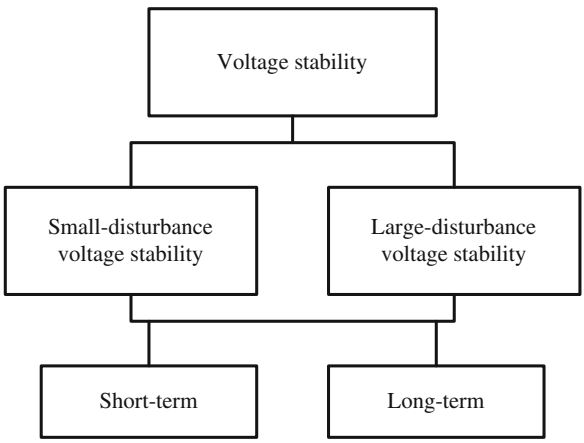

Fig. 14.14 Classification of voltage stability

analysis of rotor angle stability. Dynamic modeling of loads is often essential. In contrast to angle stability, short circuits near loads are important.

- *Long-term voltage stability* involves slower acting equipment such as tap-changing transformers, thermostatically controlled loads, and generator current limiters. The study period of interest may extend to several or many minutes, and long-term simulations are required for analysis of system dynamic performance. Stability is usually determined by the resulting outage of equipment, rather than the severity of the initial disturbance. Instability is due to the loss of long-term equilibrium (e.g., when loads try to restore their power beyond the capability of the transmission network and connected generation), post-disturbance steady-state operating point being small-disturbance unstable, or a lack of attraction toward the stable post-disturbance equilibrium (e.g., when a remedial action is applied too late). The disturbance could also be a sustained load buildup (e.g., morning load increase). In many cases, static analysis can be used to estimate stability margins, identify factors influencing stability, and screen a wide range of system conditions and a large number of scenarios. Where timing of control actions is important, this should be complemented by quasi-steady-state time-domain simulations.

References

1. Cutsem TV, Vournas C (1998) Voltage stability of electric power systems. Kluwer, Norwell
2. Kundur P, Paserba J, Ajjarapu V, Andersson G, Bose A, Canizares C, Hatziargyriou N, Hill DJ, Stankovic A, Taylor C, Cutsem TV, Vittal V (2004) Definition and classification of power system stability. IEEE Trans Power Syst 19(2):1387–1401
3. Diaz de Leon JA, Taylor CW (2002) Understanding and solving short term voltage stability problems. In: IEEE power engineering society summer meeting, July 2002
4. Molinas M, Suul JA, Undeland T (2008) Low voltage ride through of wind farms with cage generators: STATCOM versus SVC. IEEE Trans Power Electron 23(4):1104–1117
5. Gerbex S, Cherkaoui R, Germond AJ (2001) Optimal location of multi-type FACTS devices in a power system by means of genetic algorithms. IEEE Trans Power Syst 16(3):537–544
6. Yorino N, El-Araby EE, Sasaki H, Harada S (2003) A new formulation for FACTS allocation for security enhancement against voltage collapse. IEEE Trans Power Syst 18(1):3–10
7. Sode-Yome A, Mithulananthan N, Lee KY (2006) A maximizing loading margin method for static voltage stability in power system. IEEE Trans Power Syst 21(2):799–808
8. Chang Y-C (2012) Multi-objective optimal SVC installation for power system loading margin improvement. IEEE Trans Power Syst 27(2):984–992
9. Ghahremani E, Kamwa I (2013) Optimal placement of multiple-type FACTS devices to maximize power system loadability using a generic graphical user interface. IEEE Trans Power Syst 28(2):764–778
10. Milanovic JV, Zhang Y (2010) Modelling of FACTS devices for voltage sag mitigation studies in large power systems. IEEE Trans Power Deliv 25(4):3044–3052
11. Pourbeik P, Koessler RJ, Quaintance W, Wong W (2006) Performing comprehensive voltage stability studies for the determination of optimal location, size and type of reactive compensation. In: IEEE power engineering society general meeting, Jul 2006

12. Krishnan V, Liu H, McCalley JD (2009) Coordinated reactive power planning against power system voltage instability. In: IEEE PES power systems conference and exposition (PSCE'09), Mar 2009
13. Sapkota B, Vittal V (2010) Dynamic var planning in a large power system using trajectory sensitivities. IEEE Trans Power Syst 25(1):461–469
14. Tiwari A, Ajjarapu V (2011) Optimal allocation of dynamic VAR support using mixed integer dynamic optimization. IEEE Trans Power Syst 26(1):305–314
15. Paramasivam M, Salloum A, Ajjarapu V, Vittal V, Bhatt NB, Liu S (2013) Dynamic optimization based reactive power planning to mitigate slow voltage recovery and short term voltage instability. IEEE Trans Power Syst 28(4):3865–3873
16. Noroozian M, Petersson AN, Thorvaldson B, Nilsson BA, Taylor CW (2003) Benefits of SVC and STATCOM for electric utility application. In: IEEE transmission and distribution conference and exposition, Sep 2003
17. Pourbeik P, Sullivan DJ, Bostrom A, Sanchez-Gasca J, Kazachkov Y, Kowalski J, Salazar A, Meyer A, Lau R, Davies D, Allen E (2012) Generic model structures for simulating static Var systems in power system studies—a WECC task force effort. IEEE Trans Power Syst 27 (3):1618–1627
18. Siemens Power Technologies International (2011) PSS®E 33.0 program application guide, vol II
19. Shoup DJ, Paserba JJ, Taylor CW (2004) A survey of current practices for transient voltage dip/sag criteria related to power system stability. In: IEEE power systems conference and exposition
20. Xue Y, Xu T, Liu B, Li Y (2000) Quantitative assessment of transient voltage security. IEEE Trans Power Syst 15(3):1077–1083
21. Hiskens IA, Pai MA (2000) Trajectory sensitivity analysis of hybrid systems. IEEE Trans Circuits Syst 47(2):204–220
22. Gan D, Thomas RJ, Zimmerman RD (2000) Stability-constrained optimal power flow. IEEE Trans Power Syst 15(2):535–540
23. Miettinen K (1999) Nonlinear multiobjective optimization. Kluwer, Norwell
24. Coello Coello CA (2006) Evolutionary multi-objective optimization: a historical view of the field. IEEE Comput Intell Mag 1(1):28–36
25. Zhang Q, Li H (2007) MOEA/D: a multiobjective evolutionary algorithm based on decomposition. IEEE Trans Evol 11(6):712–731
26. Meng K, Dong ZY, Wong KP, Xu Y, Luo F (2010) Speed-up the computing efficiency of PSSE-based power system transient stability simulations. IET Gen Trans Dist 4(5):652–661
27. Zhou B, Chan KW, Yu T, Chung CY (2013) Equilibrium-inspired multiple group search optimization with synergistic learning for multiobjective electric power dispatch. IEEE Trans Power Syst 28(4):3534–3545
28. Xu Y, Dong ZY, Luo F, Zhang R, Wong KP (2014) Parallel-differential evolution approach for optimal event-driven load shedding against voltage collapse in power systems. IET Gen Trans Dist 8(4):651–660
29. Technical Report, "Singleton Ring STATCOM Study", prepared by Centre for Intelligent Electricity Networks of University of Newcastle for Ausgrid Co., Australia, 2013

Chapter 15
STATCOM Application for Enhancement of Available Power Transfer Capability in Transmission Networks

Trapti Jain, Sri Niwas Singh and Suresh Chandra Srivastava

Abstract The introduction of open access in transmission network has given rise to increased power transactions, thereby pushing them closer to their operating limits. Thus, the power transfer capability of the transmission network should be increased so that all the desired transactions can be accommodated. However, the addition of new transmission lines is restricted due to the environmental, right-of-way and economic issues, making it essential to utilize the existing transmission corridors efficiently. Available Transfer Capability (ATC) of a transmission system, which refers to the unutilized transfer capability over and above already committed usage, should be adequate to ensure fair electricity trading. This chapter presents an application of STATCOM to enhance the dynamic ATC for bilateral as well as multilateral transactions in an open market environment. The performance of STATCOM is dependent on its location in the system. Hence, to enhance the dynamic ATC effectively, STATCOM has been placed optimally in the network by carrying out a sensitivity analysis of structure preserving energy margin with respect to its control parameter. The hybrid approach, utilizing the benefits of the direct methods as well as time domain simulation methods, has been used to determine the dynamic ATC with detailed model of generators, exciters and loads. The potential energy contributed by the STATCOM has also been included in the structure preserving energy function to include their influence on transient stability.

T. Jain (✉)
School of Engineering, Discipline of Electrical Engineering,
Indian Institute of Technology Indore, Indore, India
e-mail: traptij@iiti.ac.in

S.N. Singh · S.C. Srivastava
Department of Electrical Engineering, Indian Institute of Technology Kanpur,
Kanpur, India
e-mail: snsingh@iitk.ac.in

S.C. Srivastava
e-mail: scs@iitk.ac.in

F. Shahnia et al. (eds.), *Static Compensators (STATCOMs) in Power Systems*,
Power Systems, DOI 10.1007/978-981-287-281-4_15

Keywords Available transfer capability · Direct method · Hybrid method · Sensitivity analysis · STATCOM · Structure preserving energy function · Time domain simulation

15.1 Introduction

The ability of a power system to meet the load demand without unduly stressing its apparatus or allowing network variables to stray from prescribed range is referred as power system security [1]. Maintaining security of a power system has become more challenging in the deregulated environment due to the involvement of several market entities and satisfaction of many types of contractual obligations. The System Operator (SO) is responsible to maintain the security and reliability of power system while ensuring the contractual power flow.

In a restructured electricity market, the market participants utilize a common transmission network for wheeling power from the point of generation to the point of consumption. All the participants, in an open market environment, may try to maximize their profit and procure the energy from the cheaper sources, which may, sometimes, lead to congestion of certain transmission corridors, thereby undermining the system security. Therefore, it is important to assess the power transfer capabilities along different corridors of the transmission systems to ensure that system security is maintained while serving a wide range of transactions.

ATC is a term defined to reflect additional secure power transfer in an electricity market environment. Accurate evaluation of ATC is essential to maximize the utilization of the existing transmission system. Further, adequate ATC is required to be maintained for reliable and secure operation of the system as well as to ensure fair electricity trading. This can be achieved through the use of Flexible AC Transmission System (FACTS) devices, which have the capability to control line power flows and bus voltages [2]. STATCOM, one of the versatile FACTS devices, facilitate steady state power flow control as well as stability control, thereby enhancing power transfer capability of the transmission network. The extent to which a STATCOM can enhance ATC depends on its location in the system. Hence, in order to enhance the ATC effectively, it should be placed optimally in the system.

Different methodologies have been reported in the literature [3–6] to determine the optimal locations of FACTS controllers in order to enhance the ATC. These methodologies can be grouped into sensitivity-based methods, Optimal Power Flow (OPF) based methods, mixed integer linear programming based approaches and heuristic approaches. However, these methods considered only static criteria for the placement of FACTS controllers and therefore, lead to effective improvement in the static ATC only. Dynamic considerations in placement of FACTS devices are important for obtaining significant enhancement in dynamic ATC but, only a few placement method based on dynamic criteria appeared in the literature. In [7], analytical expressions based on structure preserving energy margin sensitivity were

derived to determine the effective location of shunt and series FACTS devices to improve transient stability. The advantage of this method is that it does not require introducing compensation in the post fault system to determine the energy margin sensitivity indices. However, it fails in a case, when the mode of instability is changed on introducing compensation in the system. In order to overcome this drawback, numerical computation of structure preserving energy margin sensitivity was proposed in [8].

This chapter presents an application of STATCOM to enhance the dynamic ATC for bilateral as well as multilateral transactions in an open market environment, which is a part of the work published by the authors in [8]. The optimal placement of STATCOM has been obtained by computing the sensitivity of the structure preserving energy margin with respect to its control parameter. The hybrid approach [9], combining the structure preserving energy function and time domain simulation methods, has been used to determine the dynamic ATC with detailed model of generators, exciters and loads.

15.2 Available Transfer Capability

According to the framework established by North American Electric Reliability Council (NERC) in 1996 [10], ATC is a measure of the power transfer capability remaining in the physical transmission network for further commercial activity over and above already committed usage. The term capability refers to the ability of the line(s) to reliably transfer power from one bus/area to another. It is different from the transfer capacity, which usually refers to the thermal rating of a particular transmission element or component. The ATC gives the upper limit of additional power that can be transferred over the network for a specified time period under given system conditions, when power is injected and extracted at the specified seller and buyer buses, respectively. The calculation of ATC is subject to uncertainties in the system parameters, such as generation dispatch patterns, load fluctuations and equipment availabilities. These uncertainties may cause significant variations on the ATC. Due to this, North American Electric Reliability Council (NERC) has defined ATC [10], shown in Fig. 15.1, as,

$$\mathrm{ATC} = \mathrm{TTC} - \mathrm{TRM} - \{\mathrm{ETC} + \mathrm{CBM}\} \tag{15.1}$$

where, TTC is Total Transfer Capability, TRM is Transmission Reliability Margin, ETC is Existing Transmission Commitments and CBM is Capacity Benefit Margin. Total Transfer Capability is the maximum amount of electric power that can be transferred over the interconnected transmission network in a reliable manner under a reasonable range of uncertainties and contingencies. Existing Transfer Commitments refers to the power transfer capability that must be reserved for already committed transactions. The uncertainties in the transmission system and generation are accounted by Transmission Reliability Margin and Capacity Benefit Margin,

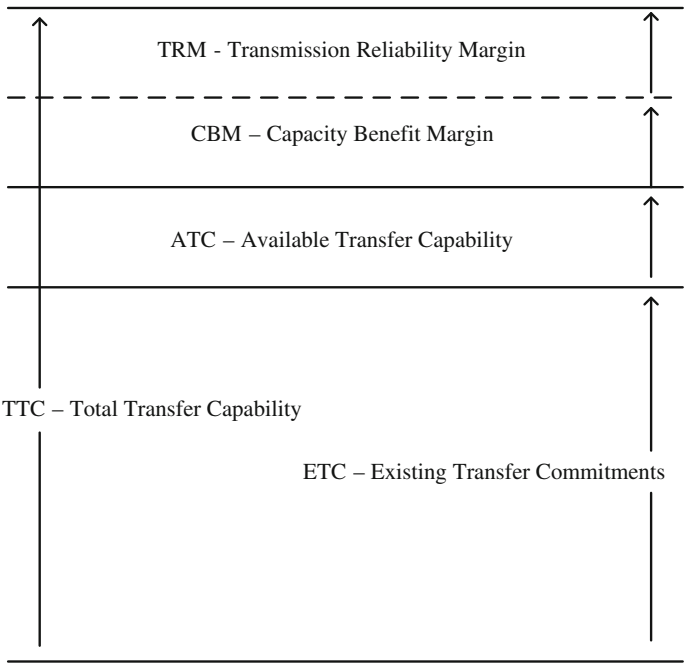

Fig. 15.1 Basic definition of ATC (Reproduced from NERC 1996)

respectively. Transmission Reliability Margin is defined as the amount of transmission transfer capability necessary to ensure that the interconnected network is secure under a reasonable range of uncertainties in the transmission system conditions. Capacity Benefit Margin is the amount of transmission transfer capability reserved by the load serving entities to ensure access to generation from interconnected systems to meet generation reliability requirements.

The Existing Transfer Commitment (ETC) is known precisely in the real time applications. For any other time interval in future, this has to be approximated through some forecasting techniques. The ETC determines the base case operating point for the specified time interval. It includes the generation schedule, load dispatch, system configuration, state of all the circuit breakers and contingencies, if any. Assuming that the TRM and CBM can be decided by the utilities according to their specific system conditions and reliability requirements, the ATC can be defined as,

$$\mathrm{ATC} = \mathrm{TTC} - \mathrm{ETC}. \tag{15.2}$$

The above equation shows that all the constraints applicable to the TTC calculation are also applicable to the ATC calculation and vice versa. The constraints required to determine ATC include static constraints as well as dynamic constraints. ATC, determined using the static constraints only, is termed as static ATC and that,

determined using both static and dynamic constraints, is termed as dynamic ATC. Static constraints comprise line flow limits, bus voltage limits, generator active and reactive power limit and steady state stability limit while dynamic constraints comprise small signal stability limit and large signal stability limit. If the stability limits are underestimated, the system tends to be operated conservatively, with an associated economic penalty. However, if the limits are overestimated, the system may be operated in a vulnerable state. Hence, it is essential to consider transient stability constraints for accurate assessment of the ATC.

In an open power market, the electricity trading is carried out through a competitive bidding process administered by power exchange/market operator, apart from the direct transactions through bilateral or multilateral negotiations. Every intended transaction is communicated to the system operator. The transactions are evaluated by the system operator on the basis of the ATC of the system. Power transactions between a specific seller bus/area can be committed only when sufficient ATC is available for that interface. Thus, such transfer capability can be used for reserving transmission services, scheduling firm and non-firm transactions and for arranging emergency transfers between seller bus/area and buyer bus/area of an interconnected power system network. Since the transmission system is shared by all the market entities, the information about the ATC is required to be continuously updated in real time and made available to the market participants through the web based systems, such as Open Access Same time Information Systems (OASIS) in the US markets. Thus, the ATC, among areas of an interconnected power system network and also for critical transmission paths between areas, is required to be continuously computed, updated and posted following any change in the system conditions.

15.3 Modeling of Power System Components

The dynamic behavior of various power system components is described by mathematical model of the system. Accurate system model is important to accurately analyze system stability. Different models of synchronous generator, exciter and loads have been developed in the literature. However, one has to select these models according to the type of stability problem to be addressed. The models of various power system components, used in this chapter, to determine the dynamic ATC are described in the following subsections.

15.3.1 Generator Model

The synchronous generators are represented by two-axis flux decay dynamic model [11]. The model is shown in Fig. 15.2. The model assumes negligibly small direct and quadrature axes sub-transient time constants T'_{doi} and T'_{qoi}. The fast dynamics associated with the damper windings are, thus, ignored.

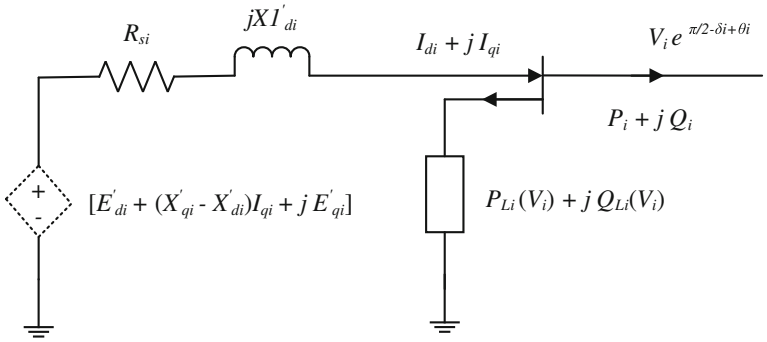

Fig. 15.2 Two-axis flux decay dynamic model of a synchronous machine

The dynamics of an *i*th generator, represented by a two-axis flux decay model, are described by the following differential algebraic equations with respect to the Center of Inertia (COI) reference frame.

$$\dot{\theta}_i = \omega_i \tag{15.3}$$

$$M_i\,\dot{\omega}_i = P_{mi} - P_{ei} - (M_i/M_T)P_{COI} \tag{15.4}$$

$$T'_{doi}\,\dot{E}'_{qi} = E_{fdi} - E'_{qi} - (X_{di} - X'_{di})I_{di} \tag{15.5}$$

$$T'_{qoi}\,\dot{E}'_{di} = -E'_{di} + (X_{qi} - X'_{qi})I_{qi} \tag{15.6}$$

where

$$P_{ei} = E'_{qi}I_{qi} + E'_{di}I_{di} + (X'_{qi} - X'_{di})I_{di}I_{qi} \tag{15.7}$$

$$P_{COI} = \sum_{i=1}^{m}(P_{mi} - P_{ei}) \tag{15.8}$$

$$M_T = \sum_{i=1}^{m} M_i \tag{15.9}$$

$$V_{qi} = E'_{qi} - X'_{di}I_{di} \tag{15.10}$$

$$V_{di} = E'_{di} + X'_{qi}I_{qi} \tag{15.11}$$

$$V_i = (V_{di} + jV_{qi})e^{j\theta_i} \tag{15.12}$$

The COI variables are defined as

$$\theta_i = \delta_i - \delta_0, \quad M_T \delta_0 = \sum_{i=1}^{m} M_i \delta_i, \tag{15.13}$$

This gives

$$\sum_{i=1}^{m} M_i \theta_i = 0 \text{ and } \sum_{i=1}^{m} M_i \omega_i = 0 \tag{15.14}$$

where

δ_i = rotor angle of generator i
δ_0 = angle of Center of Inertia (COI)
θ_i = rotor angle of generator i with respect to COI
ω_i = rotor speed of generator i with respect to COI
M_i = inertia constant of generator i
P_{Mi} = mechanical power input to generator i
P_{ei} = active power output of generator i
T'_{doi}, T'_{qoi} = transient direct axis and quadrature axis time constants of generator i
X_{di}, X_{qi} = steady state direct and quadrature axis reactance of generator i
X'_{di}, X'_{qi} = direct and quadrature axis transient reactance of generator i
E'_{di}, E'_{qi} = voltages induced behind the quadrature and direct axis transient reactance of generator i
E_{fdi} = voltage induced due to rotor field excitation of generator i
I_{di}, I_{qi} = direct and quadrature axis armature currents of generator i
V_i = terminal voltage of generator i
V_{di}, V_{qi} = direct and quadrature axis components of the terminal voltage of generator i.

15.3.2 Excitation System

Each generator is assumed to be provided with IEEE Type DC-1 excitation system [12]. Its transfer function block diagram is shown in Fig. 15.3. It represents a field controlled DC commutator exciter with continuously acting voltage regulator. The block with the transfer function $((1 + sT_C)/(1 + sT_B))$ represents the Transient Gain Reduction (TGR) with $T_B > T_C$ and has the function similar to that of the Excitation System Stabilizer (ESS). Normally either TGR (in forward path) or ESS (in the feedback path) is used. By choosing $T_B = T_C$, the transient gain reduction is neglected.

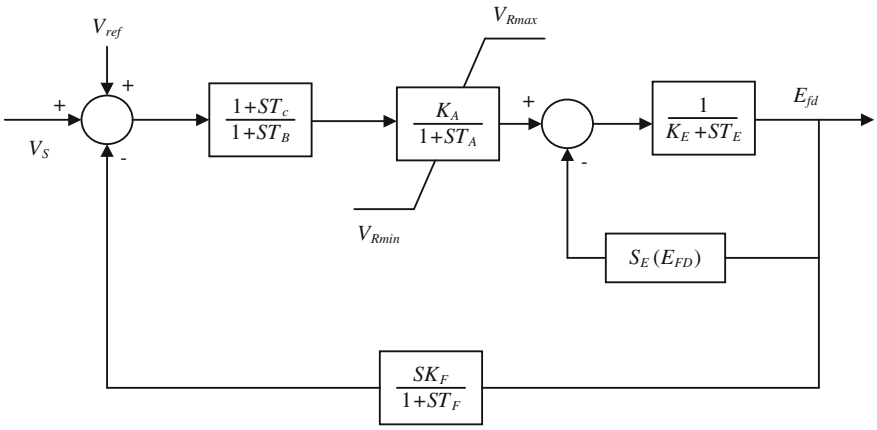

Fig. 15.3 IEEE type DC-1 exciter

The dynamical equations, representing the exciter model, are given as,

$$T_{Ei}\dot{E}_{fdi} = -\left(K_{Ei} + S_{Ei}\left(E_{fdi}\right)\right)E_{fdi} + V_{Ri} \tag{15.15}$$

$$T_{Fi}\dot{R}_{fi} = -R_{fi} + \frac{K_{Fi}}{T_{Fi}}E_{fdi} \tag{15.16}$$

$$T_{Ai}\dot{V}_{Ri} = -V_{Ri} + K_{Ai}R_{fi} - \frac{K_{Ai}K_{Fi}}{T_{Fi}}E_{fdi} + K_{Ai}\left(V_{refi} - V_i\right) \tag{15.17}$$

where

K_{Ei}, T_{Ei} = exciter gain and time constant
$S_{Ei}\left(E_{fdi}\right)$ = field saturation function
V_{Ri} = regulator amplifier output voltage
K_{Ai}, T_{Ai} = regulator amplifier gain and time constant
R_{fi} = exciter rate feedback
K_{Fi}, T_{Fi} = rate feedback gain and time constant
V_{refi} = reference setting voltage
V_i = terminal voltage of generator i.

15.3.3 Network Equations

Load flow equations decide the operating point in terms of bus voltages and phase angles for a specified generation schedule and load dispatch. The steady state load flow equation at a bus-i can be written as

$$-P_i - jQ_i + \sum_{k=1}^{n} V_i V_k Y_{ik} e^{j(\phi_i - \phi_k - \alpha_{ik})} = 0 \tag{15.18}$$

where

P_i, Q_i = active and reactive power injections at bus-i
ϕ_i = phase angle of voltage at bus-i
$Y_{ik}\angle\alpha_{ik}$ = ikth element of the bus admittance matrix

The power injections at the load buses can be given as,

$$P_i + jQ_i = -P_{Li}(V_i) - jQ_{Li}(V_i) \tag{15.19}$$

where

P_{Li}, Q_{Li} = active and reactive power load at bus-i.

The power balance equation at the generator terminals is given as,

$$P_i + jQ_i = V_i(I_{di} - jI_{qi}) e^{j\left(\frac{\pi}{2} + \phi_i - \delta_i\right)} - P_{Li}(V_i) - Q_{Li}(V_i) \tag{15.20}$$

Using (15.18) to (15.20), the load flow equation at the generator buses become,

$$V_i\left(I_{di} - jI_{qi}\right) e^{j\left(\frac{\pi}{2} + \phi_i - \delta_i\right)} - P_{Li}(V_i) - jQ_{Li}(V_i) - \sum_{k=1}^{n} V_i V_k Y_{ik} e^{j(\phi_i - \phi_k - \alpha_{ik})} = 0 \tag{15.21}$$

For the load bus-i, the power flow equation is given by

$$-P_{Li}(V_i) - jQ_{Li}(V_i) - \sum_{k=1}^{n} V_i V_k Y_{ik} e^{j(\phi_i - \phi_k - \alpha_{ik})} = 0. \tag{15.22}$$

15.3.4 Load Model

The active power loads are represented as composite ZIP ('Z' represents constant impedance, 'I' represents constant current and 'P' represents constant power components) load model. However, the reactive power loads are represented as constant impedance type. Composite model of the active power loads, in terms of the load bus voltage 'V' is expressed as following,

$$P = P_0 \left[a_0 + a_1 \left(\frac{V}{V_0} \right) + a_2 \left(\frac{V}{V_0} \right)^2 \right] \tag{15.23}$$

where, a_0, a_1, a_2 are the per unit load coefficients, such that $a_0 + a_1 + a_2 = 1$. P_0 is the active power load at nominal voltage V_0. For constant impedance type load, a_0, a_1 are zero and $a_2 = 1$.

However, it is established in [13] that the composite load model is not realistic at low voltages and leads to computational problems. Hence, it is used when the corresponding terminal voltage is above a threshold value. At low voltage, the nonlinear composite load model at a bus is converted into an equivalent constant impedance type. The load model is converted back to the composite load model, when the voltage reaches above the given threshold value. In this work, the voltage threshold is considered as 0.8 pu [14].

15.3.5 STATCOM

STATCOM consists of a DC capacitor connected to a DC-AC converter, which is connected to the AC network bus through a coupling transformer [2], as shown in Fig. 15.4. The DC-AC converter is operated as a voltage source. The STATCOM produces reactive power, without reactive energy storage device, by circulating

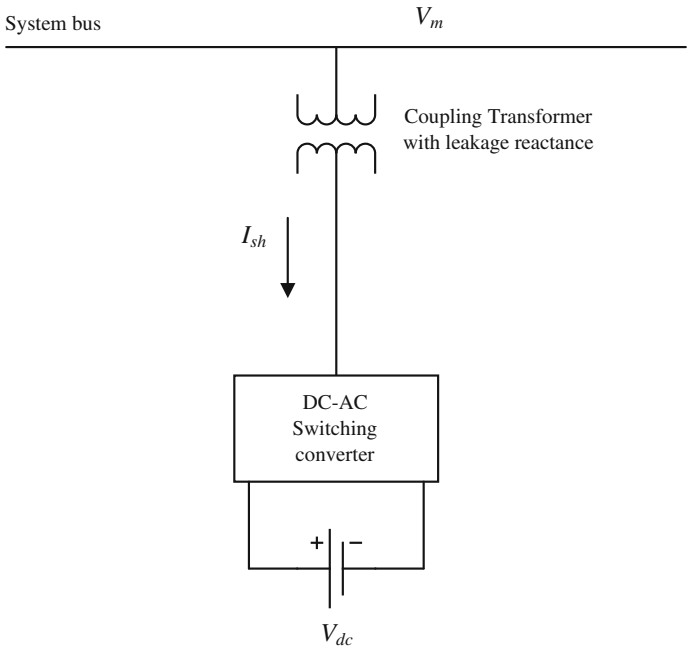

Fig. 15.4 Basic model of a STATCOM

alternating current among the phases of the AC system. From the point of reactive power generation, their operation is similar to that of an ideal synchronous machine, whose reactive power output is varied by excitation control. The expression for the shunt current flowing and the reactive power injection by the STATCOM are given as

$$I_{sh} = \frac{(V_{sh} - V_m)\angle\phi_m}{jX_l} \tag{15.24}$$

$$Q_{sh} = I_{sh}V_m \tag{15.25}$$

where

V_{sh} = magnitude of the voltage of the Voltage Source Converter (VSC)
V_m = magnitude of the bus voltage
ϕ_m = phase angle of the bus voltage
X_l = leakage reactance of the coupling transformer.

Since STATCOM injects controllable reactive current into the system, it can be represented by a shunt reactive current source. The reactive power exchange of the STATCOM with the AC system is controlled by regulating the output voltage amplitude of the VSC.

A typical V–I characteristic of the STATCOM is given in Fig. 15.5. $I_{C\max}$, $I_{L\max}$ are the maximum capacitive and inductive currents that can be injected by the STATCOM. The reactive shunt current injected by STATCOM is varied according to the voltage droop characteristics. The slope of the droop characteristics depends on the voltage regulation required. From Fig. 15.5, it can be observed that the STATCOM can be operated over its full output current range even at very low,

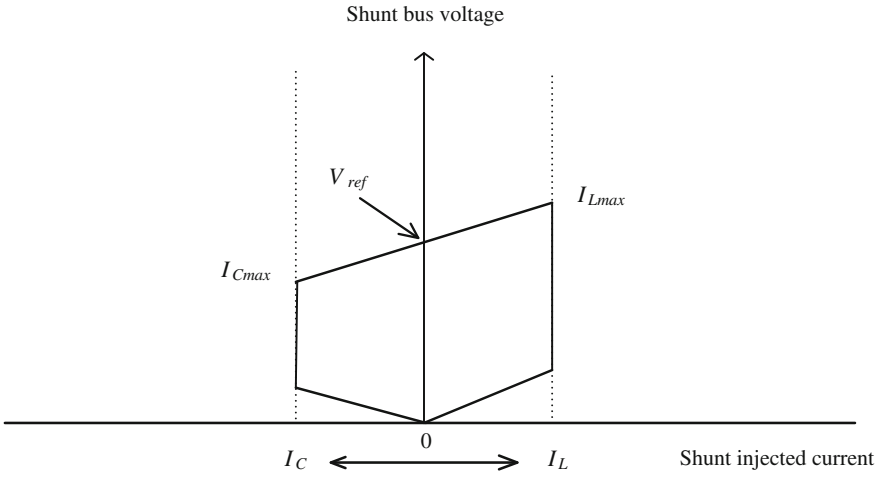

Fig. 15.5 A typical V–I characteristics of STATCOM

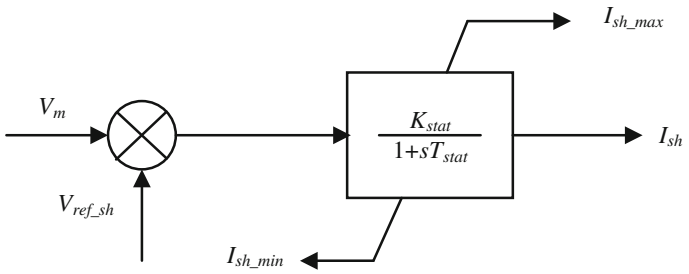

Fig. 15.6 A dynamic model of STATCOM [15]

typically about 0.2 pu (theoretically zero), system voltage levels. In other words, the maximum capacitive or inductive output current of the STATCOM can be maintained independent of the AC system voltage and the maximum VAr generation or absorption changes linearly with the AC system voltage. Thus, the STATCOM is capable of providing voltage support under large system disturbances during which the voltage excursions would be well outside the linear operating range of the compensator.

In steady state, the STATCOM is operated to keep the bus voltage at a desired level. This allows treatment of the device as an equivalent generator (PV-type bus) with the active power injection equal to zero and the load flow algorithm is used to find the required reactive power.

A simplified first order dynamic model of the STATCOM is shown in Fig. 15.6. The differential equation, describing the dynamics of the STATCOM [15], can be written as:

$$T_{stat}\,\dot{I}_{sh} = -I_{sh} + K_{stat}(V_{ref\_sh} - V_m) \tag{15.26}$$

where

V_m, I_{sh} = terminal voltage and shunt reactive current, respectively
K_{stat}, T_{stat} = regulator gain and time constant of STATCOM, respectively
V_{ref_sh} = reference voltage

The STATCOM regulator has a non-windup limiter, thus the current I_{sh} is locked if one of its limits is reached and the first derivative is set to zero.

15.4 Optimal Placement of STATCOM

STATCOMs can enhance the power transfer capability and stability of the network by regulating the bus voltages. However, their performance is dependent on their location in the system. Further, they cannot be deployed extensively due to their considerable cost. Hence, it is important to ascertain their optimal location in the

network to enhance the ATC effectively. Since the power transfer capability of long distance transmission lines is mainly restricted by transient stability limits, optimal placement of STATCOMs should be based on dynamic criteria to demonstrate its effectiveness in increasing dynamic ATC.

Direct methods of stability analysis using network preserving power system models are more attractive than traditional network-reduction techniques for assessment of the stability limits. This is due to the fact that power system components, especially the load behaviors, can be represented more realistically in network preserving model. Apart from this, use of the sparse matrix technique reduces the CPU time in solving nonlinear algebraic equations enabling it to determine the stability limits faster than the traditional methods. It determines stability limits of the system by computing a stability index, called the energy margin. A positive energy margin indicates that the system is stable, while its magnitude indicates the margin from the instability. If the energy margin is negative, the system is unstable. Placement of STATCOM in the system would change the energy margin of the system. Thus, sensitivity analysis of the energy margin is used to get an idea of the optimal locations of STATCOM for improving stability of the system.

The structure preserving energy function for the detailed power system model including STATCOM is presented in the next sub-section followed by computation of energy margin and energy margin sensitivity to determine the optimal placement of STATCOM.

15.4.1 Structure Preserving Energy Function

The structure preserving energy function incorporating the effect of exciter, damper winding, voltage dependent active and reactive power loads [16] and STATCOM has been used in this work. The total system energy can be represented as the sum of kinetic energy W_1 and potential energy W_2 of the system. The system possesses kinetic energy due to the rotation of generator rotors whereas; the potential energy of the system is the summation of the energy contributed by each individual component of the system. If rotating motor loads are present in the system, the energy stored in their rotors will also be added to the kinetic energy of the system. For an n-bus system having m-machines, the kinetic energy, which is a function of rotor speed, can be expressed as

$$W_1(\omega) = \frac{1}{2}\sum_{i=1}^{m} M_i \omega_i^2 \tag{15.27}$$

The potential energy of all the rotors can be represented as (subscript '0', in all the expressions given below is used to indicate the quantities at the initial equilibrium point)

$$W_{21}(\theta) = -\sum_{i=1}^{m} P_{mi}(\theta_i - \theta_{i0}) \tag{15.28}$$

Potential energy contributed by the voltage dependent active power loads can be given by W_{22}

$$W_{22}(t) = \sum_{i=1}^{n} \int_{t_0}^{t} P_{Li}(V_i) \frac{d\phi_i}{dt} dt \tag{15.29}$$

If active power load P_{Li} is variable, W_{22} becomes a path dependent term and has to be integrated numerically. Using trapezoidal rule of integration,

$$W_{22}(t+h) = W_{22}(t) + \frac{1}{2}[P_{Li}(t) + P_{Li}(t+h)][\phi_i(t+h) - \phi_i(t)] \tag{15.30}$$

The potential energy W_{23} considers the energy added by voltage dependent reactive power loads

$$W_{23}(V) = \sum_{i=1}^{n} \int_{V_{i0}}^{V_i} \frac{Q_{Li}(V_i)}{V_i} dV_i \tag{15.31}$$

The energy component W_{23} is path independent as the integral can be obtained as a function of the bus voltage V_i. For constant impedance loads, $Q_{Li} = b_2 V_i^2$,

$$\int_{V_{i0}}^{V_i} \frac{Q_{Li}}{V_i} dV_i = \frac{b_2}{2}(V_i^2 - V_{i0}^2) \tag{15.32}$$

Change in the energy stored in the machine reactances and transmission lines are represented by W_{24} and W_{25}, respectively.

$$\begin{aligned} W_{24}(\theta, E'_q, V, \phi) = \sum_{i=1}^{m} \{ & E'^2_{qi} + V_i^2 - 2E'_{qi} V_i \cos(\theta_i - \phi_i) \\ & - [E'^2_{qi0} + V_{i0}^2 - 2E'_{qi0} V_{i0} \cos(\theta_{i0} - \phi_{i0})]\} (1/2X'_{di}) \end{aligned} \tag{15.33}$$

$$W_{25}(V, \phi) = -\frac{1}{2} \sum_{i=1}^{n} \sum_{j=1}^{n} B_{ij} \left(V_i V_j \cos \phi_{ij} - V_{i0} V_{j0} \cos \phi_{ij0} \right) \tag{15.34}$$

If the damper windings are also present, the change in the energy stored in damper winding is given by W_{26} and W_{27}.

$$W_{26}(\theta, E'_d, V, \phi) = \sum_{i=1}^{m} \{E'^2_{dt} + V_i^2 - 2E'_{dt}V_i \cos(\theta_i - \phi_i) - [E'^2_{di0} + V_{i0}^2 - 2E'_{di0}V_{i0}\cos(\theta_{i0} - \phi_{i0})]\}(1/2X'_{qi}) \tag{15.35}$$

$$W_{27}(V) = -\sum_{i=1}^{m} \frac{(V_i^2 - V_{i0}^2)}{2X'_{qi}} \tag{15.36}$$

The exciter dynamics is taken into account by W_{28} as given below

$$W_{28}(t) = -\sum_{i=1}^{m} \int_{t_0}^{t} \left[\frac{E_{fdi}}{X_{di} - X'_{di}}\right] \frac{dE'_{qi}}{dt} dt \tag{15.37}$$

In the absence of AVR, E_{fd} is constant and W_{28} becomes path independent function of $E_q^{'}$, expressed as

$$W_{28}(t) = -\sum_{i=1}^{m} E_{fdi} \frac{(E'_{qi} - E'_{qi0})}{(X_{di} - X'_{di})} \tag{15.38}$$

If AVR is considered, then E_{fd} is variable and W_{28} has to be computed by numerical integration. Using trapezoidal rule,

$$W_{28}(t+h) = W_{28}(t) - \frac{1}{2}\sum_{i=1}^{m} \frac{[E_{fdi}(t+h) + E_{fdi}(t)][E'_{qi}(t+h) - E'_{qi}(t)]}{(X_{di} - X'_{di})} \tag{15.39}$$

The effects of flux decay along d-axis and q-axis are taken into account by W_{29}, W_{210} and W_{211}, W_{212}, respectively.

$$W_{29}(E'_q) = \sum_{i=1}^{m} \left[\frac{(E'^2_{qi} - E'^2_{qi0})}{2(X_{di} - X'_{di})}\right] \tag{15.40}$$

$$W_{210}(t) = \sum_{i=1}^{m} \int_{t_0}^{t} \left[\frac{T'_{doi}}{X_{di} - X'_{di}}\right] \left(\frac{dE'_{qi}}{dt}\right)^2 dt \tag{15.41}$$

$$W_{211}(E'_d) = \sum_{i=1}^{m} \left[\frac{(E'^2_{di} - E'^2_{di0}}{2(X_{qi} - X'_{qi})}\right] \tag{15.42}$$

$$W_{212}(t) = \sum_{i=1}^{m} \int_{t_0}^{t} \left[\frac{T'_{qoi}}{(X_{qi} - X'_{qi})}\right] \left(\frac{dE'_{di}}{dt}\right)^2 dt \tag{15.43}$$

The effect of STATCOM in the energy function is considered by $W_{STATCOM}$, proposed by Padiyar et al. [17] for SVC. Since the SVC and the STATCOM, both, inject shunt reactive current to control bus voltage, the structure preserving energy function proposed in [17] can be used for the STATCOM. The only difference is that the SVC injects shunt reactive current by varying the shunt susceptance, whereas the STATCOM itself is modeled by a variable shunt current source. $W_{STATCOM}$ is expressed below

$$W_{STATCOM} = \int_{V_{i0}}^{V_i} I_{stat} dV_i \tag{15.44}$$

The structure preserving energy function for the complete system can be obtained as given below.

$$W(\theta, \omega, E'_q, E'_d, V, E_{fd}, t) = W_1 + W_2 = W_1 + \left(\sum_{i=1}^{12} W_{2i} + W_{STATCOM} \right). \tag{15.45}$$

15.4.2 Computation of Energy Margin

Energy margin is the difference between the critical energy and the total energy of the system at the fault clearing time. There are two general approaches to compute the critical energy W_{cr}, the controlling Unstable Equilibrium Points (UEP) approach and the Potential Energy Boundary Surface (PEBS) approach. In the former approach, W_{cr} is taken as the potential energy of the post fault system at the controlling UEP. In the latter approach, the critical energy is approximated as the peak attained by the potential energy during faulted trajectory. Determination of the controlling UEP is complex with a structure-preserving model and, hence, the PEBS method is used in the present work. During a transient, the power flow equations are solved twice, once for the faulted system to evaluate the generated power and again for the post fault system to evaluate the transient energy. The presence of nonlinear voltage dependent loads introduces nonlinear algebraic equations, which are solved using iterative methods.

The steps involved in the computation of the energy margin are given below.

Step-1: Base case load flow is performed to obtain the pre-fault operating point.

Step-2: The bus admittance matrix **Y** is formed for the faulted and the post-fault network.

Step-3: Execution of forward numerical integration is initiated for the equations corresponding to the faulted system. At the end of each integration interval, power flow of the faulted system is performed with injected

currents at the generator buses as inputs. Load bus voltages and angles, obtained from this load flow solution, are used to evaluate P_{ei}.

Step-4: At the end of each integration interval, using the same inputs as in the step 3, power flow of the post-fault system is performed to obtain the bus voltages and angles to be used for calculation of the energy function.

Step-5: The integration process is continued for the faulted system equations. The values of W and W_2 are monitored for each interval of the integration. The critical energy W_{cr} is obtained as the maximum value of W_2 occurring when the faulted trajectory crosses the PEBS.

Step-6: The difference in W_{cr} and W, at the fault clearing time, gives the value of the energy margin.

15.4.3 Energy Margin Sensitivity

Sensitivity analysis of energy margin determines the influence of placing STATCOM on the energy margin of the system. The placement of STATCOM at a bus is modeled by injecting a shunt reactive current at that bus. The energy margin sensitivity with respect to the shunt reactive current, I_{sh}, is given by

$$\eta_{STAT} = \frac{EM_C - EM}{I_{sh}} \tag{15.46}$$

where, η_{STAT} is the energy margin sensitivity of STATCOM with respect to I_{sh}, EM is the energy margin without compensation and EM_C is the energy margin with compensation. To compute the energy margin with compensation, a fixed amount of the shunt reactive current I_{sh} has been introduced at the bus, where the STATCOM is assumed to be placed. This has been repeated for all the buses. The bus having the highest sensitivity is considered as the most optimal location to place the STATCOM.

15.5 Evaluation of Dynamic ATC

ATC is computed as the additional power transfer capability available under the worst case, out of various critical contingencies and the system intact condition. Thus, the first and the foremost step in the assessment of ATC is contingency screening to identify the critical contingencies. Accuracy of ATC determination depends on the proper selection of the severe contingencies in the contingency list. Inaccurate selection of contingencies may give higher value of the ATC. Conventionally, contingency screening is performed by computing performance indices and ranking the contingencies based on the value of performance indices. Higher ranked

contingencies are considered in the contingency list. However, in an open power market, different transactions are likely to take place and the severity order of a contingency may not be the same for each transaction. The transfer capability is limited by a contingency whose severity is largely affected by introduction of the transaction. Hence, it is necessary to quantify the severity of contingencies considering the influence of the transaction. This has been taken care of by computing an index, based on the deviation in the value of the performance indices computed at the base case loading and with additional transaction, to perform contingency screening.

The dynamic ATC is computed using a hybrid method, which was proposed by the authors in [9] and for the benefit of the readers, it is recounted here. This method combines the merits of both the direct method as well as the time domain simulation method. Hybrid method based dynamic ATC computation is divided into three stages, as shown in Fig. 15.7. The brief description of each stage is given below.

Stage A: In this stage, first of all, the critical contingencies are identified by carrying out static contingency screening. A static contingency screening index SPI_k, for a kth contingency, is defined as,

$$SPI_k = \frac{PI_{Tk} - PI_{Bk}}{PI_{Bk}} \tag{15.47}$$

where PI_{Bk} and PI_{Tk} are the performance index values at the base case loading and for an additional transaction T, respectively. The index SPI_k becomes large, if the performance index increases considerably by the introduction of the transaction. The contingencies, with the larger SPI_k are considered in the list of severe contingencies.

After performing static contingency screening, static ATC is computed at the base case as well as for all the critical contingencies, considering bus voltage limit,

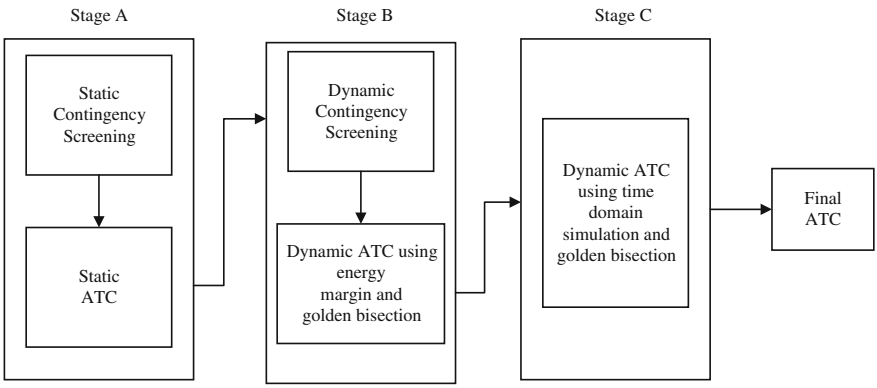

Fig. 15.7 Hybrid method for dynamic ATC calculation

line flow limit and generator active and reactive power limits. To determine static ATC, an optimization problem formulated in [18] is used. This is given below.

Maximize λ

subject to,

$$P_{Gi} - P_{Di} - \sum_{j=1}^{n} V_i V_j (G_{ij} \cos \delta_{ij} + B_{ij} \sin \delta_{ij}) = 0 \tag{15.48}$$

$$Q_{Gi} - Q_{Di} - \sum_{j=1}^{n} V_i V_j (G_{ij} \sin \delta_{ij} - B_{ij} \cos \delta_{ij}) = 0 \tag{15.49}$$

$$P_{Gp} - P_{Lq} = 0 \tag{15.50}$$

$$V_{i\min} \leq V_i \leq V_{i\max}, \quad \forall i \in n \tag{15.51}$$

$$P_{Gi\min} \leq P_{Gi} \leq P_{Gi\max}, \quad \forall i \in N_g \tag{15.52}$$

$$Q_{Gi\min} \leq Q_{Gi} \leq Q_{Gi\max}, \quad \forall i \in N_g \tag{15.53}$$

$$P_{ij} \leq P_{ij\max}, \quad \forall ij \in N_l \tag{15.54}$$

where, P_{Gi} and Q_{Gi} are the active and reactive power generation at bus-i, δ_{ij} is the voltage angle difference between bus-i and bus-j, $V_{i\min}$ and $V_{i\max}$ are the lower and upper limits of voltage magnitude at bus-i, P_{ij} is the power flow in line connected between bus-i and bus-j, $P_{ij\max}$ is the upper limit of power flow in a line connected between bus-i and bus-j, N_g is the number of generators and N_l is the number of lines.

Here, $\lambda = 0$ corresponds to the base case transfer and $\lambda = \lambda_{\max}$ corresponds to the maximum power transfer. ATC in each case (normal or contingency case) is calculated as follows:

$$ATC_i = P_{Di}(\lambda_{\max}) - P_{Di}^0, \quad \forall i \in t_k \tag{15.55}$$

where t_k is the number of transactions.

The worst-case ATC is selected as an initial point for dynamic ATC determination in the next stage.

Stage B: In this stage, a dynamic contingency screening index S_k, as proposed in [19], is used to perform dynamic contingency screening. The contingency screening index S_k, for a kth contingency, is defined as,

$$S_k = \frac{E_{Bk} - E_{Tk}}{E_{Tk}} \tag{15.56}$$

where E_{Bk} and E_{Tk} are the energy margin at the base case loading and for additional transaction T, respectively. The index S_k becomes large, if the energy margin

decreases considerably by the introduction of the transaction. The contingencies, with the larger values of S_k, have been included in the list of severe contingencies.

At a base case loading, energy margin is computed for all the contingencies. Contingencies, with sufficiently high energy margin, are discarded and the severity index S_k for the rest of the contingencies is computed. The contingency, with the highest value of S_k, is the severest one. For a large power system, computing energy margin for all the contingencies at the base case loading is not practical. While carrying out the contingency analysis, it has been observed that the severity index S_k needs to be computed only for those line outages, which are in the neighborhood of the generators participating in the transaction.

This stage utilizes energy margin approach to determine dynamic ATC. The transaction is increased by the value obtained in stage A and energy margin is computed for the severest contingency. If the energy margin is greater than the tolerance value ε, signifying that the system is stable, then go to stage C. The value of ε has been taken as 0.01 pu in this work. If it is less than ε, then decrease the transaction by an amount such that the energy margin becomes just greater than ε. Now, the energy margin is required to be minimized during the interval $[T_1, T_2]$, where, T_1 is the transaction value at which the energy margin is positive and T_2 is the transaction value at which the energy margin is negative. To obtain the transaction amount with tolerable and positive energy margin, the golden bisection based interpolation method has been used. It can be obtained as,

$$\begin{aligned} T_0^{(1)} &= 0.618T_1 + 0.382T_2 \\ T_0^{(2)} &= 0.618T_2 + 0.382T_1 \end{aligned} \tag{15.57}$$

The transaction amount is made equal to $T_0^{(1)}$ and the energy margin is computed. If the energy margin is negative, then set $T_2 = T_0^{(1)}$ and check for the convergence ($|T_1 - T_2| \leq \varepsilon_1$); otherwise set $T_1 = T_0^{(1)}$ and compute the energy margin at $T_0^{(2)}$. If the energy margin is positive, set $T_1 = T_0^{(2)}$, otherwise, set $T_2 = T_0^{(2)}$. Repeat this interpolation method till convergence is achieved. The transaction amount, with tolerable and positive energy margin, is the dynamic ATC, which is used as the initial condition in the next stage.

Stage C: In this stage, accurate value of the dynamic ATC is obtained using time domain simulation method. Time domain simulation is performed at the dynamic ATC value estimated in stage B. If the post-fault system is unstable, decrease the transaction by an amount such that it becomes stable. Let the corresponding transaction be T_3. If the post-fault system is stable, then increase the transaction by an amount such that it becomes unstable. Let the corresponding transaction be T_4. The golden bisection based interpolation method has been used to obtain the transaction amount at which the post-fault system is marginally stable. At this transaction, $|T_3 - T_4| \leq \varepsilon_1$, where threshold ε_1 is taken as 0.01 pu This transaction amount is the dynamic ATC value.

The flowchart of the hybrid approach is shown in Fig. 15.8.

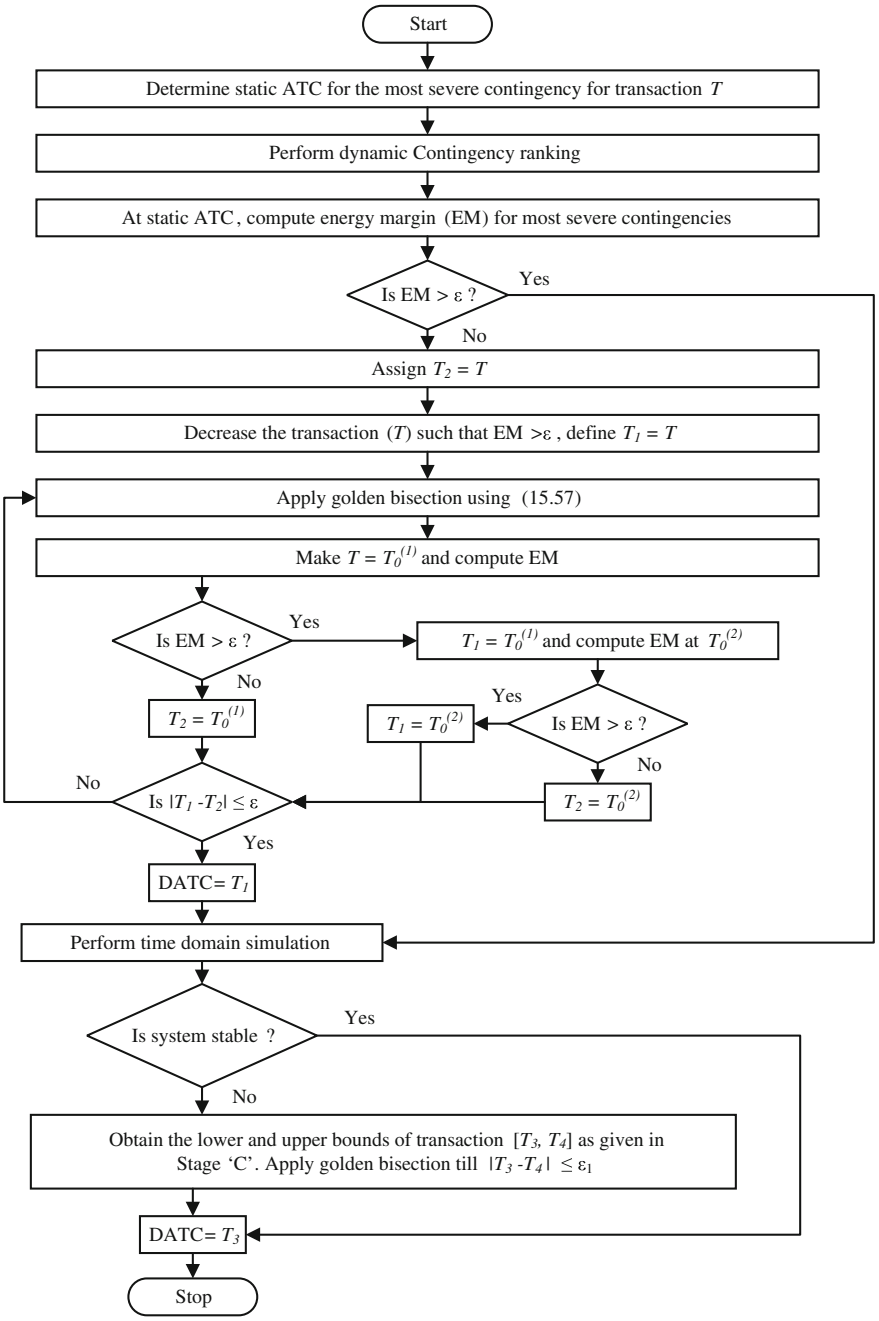

Fig. 15.8 Flowchart of the hybrid method

15.6 Case Studies

The impact of STATCOM on the dynamic ATC enhancement has been studied on a practical 60-machine, 246-bus system, representing 400 and 220 kV buses of the Northern Regional Power Grid (NRPG) network of India. NRPG network is the largest among all five regional grids in India, comprising of nine states. The details of this system can be found from [20]. Dynamic ATC is determined considering different types of transactions, involving both bilateral and multilateral contracts. Generator outages, shunt reactor outages and few single line outages, which caused islanding of the system, are not considered in this work. Outage of one of the circuits in the double circuit parallel transmission lines is viewed as single line outage. Reactive power loads are assumed to be constant impedance type, whereas active power loads are represented as composite type load containing 60 % constant power, 20 % constant current and 20 % constant impedance components. A three-phase fault has been applied at one of the buses in the system and is assumed to be cleared in 5 cycles for determination of the dynamic ATC.

To determine the dynamic ATC values for this system, following seven types of transactions have been simulated. These include four cases of bilateral transactions (T1–T4) and three cases of multilateral transactions (T5–T7).

(i) Transaction—T1: A seller at bus-40 alone supplies the increase in the load of the buyer at bus-200.
(ii) Transaction—T2: A seller at bus-40 alone supplies the increase in the load of the buyer at bus-205.
(iii) Transaction—T3: A seller at bus-32 alone supplies the increase in the load of the buyer at bus 205.
(iv) Transaction—T4: A seller at bus-32 alone supplies the increase in the load of the buyer at bus 202.
(v) Transaction—T5: Sellers at buses 40 and 32 equally share the increase in the load of the buyer at bus 200.
(vi) Transaction—T6: Sellers at buses 40 and 32 supply the increased load at buses 200 and 205 in the ratio of 0.6 and 0.4, respectively.
(vii) Transaction—T7: Sellers at buses 7, 32, 38 and 40 supply the increased load at buses 200 and 190 in the ratio of 0.2, 0.2, 0.2 and 0.4, respectively.

In all the above multilateral transactions, loads at buyer buses are assumed to be changed in the same ratio except for the transaction T7, in which loads at buyer buses 200 and 190 have been changed in the ratio of 0.4 and 0.6, respectively. Table 15.1 shows the dynamic contingency ranking for all the transactions. Fault has been considered at bus 40 and bus 32, which are the generator buses. The severity index is relatively high for transactions T1, T2, T5, T6 and T7 whereas, it is low and negative for transactions T3 and T4.

Table 15.1 Dynamic contingency ranking for different transactions

Transaction	Faulted bus	Line tripped	S_k
T1	40	40–211	1.0011
	40	40–239	0.9967
	40	40–241	0.9234
T2	40	40–211	1.0112
	40	40–239	1.0074
	40	40–241	0.9548
T3	32	32–59	−0.0531
	32	32–221	−0.0663
	32	32–218	−0.0595
T4	32	32–59	−0.0570
	32	32–221	−0.0654
	32	32–218	−0.0608
T5	40	40–211	0.4895
	40	40–239	0.4877
	40	40–241	0.4136
T6	40	40–211	0.6024
	40	40–239	0.5996
	40	40–241	0.5270
T7	40	40–211	0.7382
	40	40–239	0.7377
	40	40–241	0.6588

In order to find the critical faults in the system, a detailed analysis has been carried out by applying faults at various buses and finding their Critical Clearing Time (CCT). The faults, which had least critical clearing time, are considered as the most critical faults. The fault at bus 40, which is the generator bus, cleared by tripping of line (40–211) or cleared by tripping of line (40–239) or cleared by tripping of line (40–241), all having CCT equal to 0.11 s, are identified as the most critical faults. Thus, only these three faults were considered while computing the energy margin sensitivity for the placement of the STATCOM in this system. This sensitivity is shown in Table 15.2. Only 400 kV buses and lines have been considered for the placement of the STATCOM in this system. It can be observed that the bus 216 has the highest sensitivity for placement of the STATCOM in all the three fault cases considered. Hence, the STATCOM has been placed at bus 216.

In order to show the effectiveness of the STATCOM in improving the ATC values, these values are first computed without placing STATCOM in the system. Table 15.3 shows the results of the dynamic ATC for all the transactions and critical fault locations without STATCOM, whereas, dynamic ATC values with the STATCOM at bus 216 are shown in Table 15.4. The results for enhancement in the

Table 15.2 Energy margin sensitivity for STATCOM

Bus	Sensitivity η_{STAT} for fault at bus 40, cleared by tripping the line (40–211)	Sensitivity η_{STAT} for fault at bus 40, cleared by tripping the line (40–241)	Sensitivity η_{STAT} for fault at bus 29, cleared by tripping the line (40–239)	Average η_{STAT}
216	0.050	0.038	0.042	0.043
217	0.040	0.022	0.034	0.032

Table 15.3 Dynamic ATC for different transactions and fault locations without STATCOM

Transaction	Static ATC (MW)	Fault at bus	Line tripped	Dynamic ATC (MW)
T1	158	40	40–211	54
		40	40–239	54
		40	40–241	83
T2	129	40	40–211	51
		40	40–239	51
		40	40–241	77
T3	129	32	32–59	129
		32	32–221	129
		32	32–218	129
T4	94	32	32–59	94
		32	32–221	94
		32	32–218	94
T5	158	40	40–211	123
		40	40–239	123
		40	40–241	158
T6	255	40	40–211	92
		40	40–239	92
		40	40–241	140
T7	296	40	40–211	150
		40	40–239	150
		40	40–241	230

static as well as dynamic ATC values obtained by placing the STATCOM are given in Table 15.5 for all the transactions. It can be seen that though there is slight improvement in the static ATC values, the impact of the STATCOM is more pronounced in enhancing the dynamic ATC. This is because the objective considered for the placement of the STATCOM is to improve the transient stability.

Table 15.4 Dynamic ATC for different transactions and fault locations with STATCOM

Transaction	Static ATC (MW)	Fault at bus	Line tripped	Dynamic ATC (MW)
T1	158	40	40–211	84
		40	40–239	84
		40	40–241	113
T2	130	40	40–211	79
		40	40–239	79
		40	40–241	105
T3	130	32	32–59	130
		32	32–221	130
		32	32–218	130
T4	96	32	32–59	96
		32	32–221	96
		32	32–218	96
T5	158	40	40–211	158
		40	40–239	158
		40	40–241	158
T6	256	40	40–211	146
		40	40–239	146
		40	40–241	193
T7	296	40	40–211	237
		40	40–239	238
		40	40–241	296

Table 15.5 Worst case ATC with STATCOM

Transaction	Static ATC (MW)		Dynamic ATC (MW)		Improvement in dynamic ATC (MW)
	Without STATCOM	With STATCOM	Without STATCOM	With STATCOM	
T1	158	158	54	84	30
T2	129	130	51	79	28
T3	129	130	129	130	01
T4	94	95	94	95	01
T5	158	158	123	158	35
T6	255	256	92	146	54
T7	296	296	150	237	87

References

1. Singh SN (1995) Voltage security and loss minimization studies in electric power systems. Indian Institute of Technology Kanpur, Kanpur
2. Hingorani NG, Gyugyi L (2001) Understanding FACTS, concepts and technology of flexible ac transmission systems. IEEE Press, New York
3. Verma KS, Singh SN, Gupta HO (2001) FACTS devices location for enhancement of total transfer capability. In: Proceedings of IEEE PES winter meeting, Ohio, 2001
4. Xiao Y, Song YH, Liu CC, Sun YZ (2003) Available transfer capability enhancement using FACTS devices. IEEE Trans Power Syst 18(1):305–312
5. Lima FGM, Munoz J, Kockar I, Galiana FD (2002) Optimal location of phase shifters in a competitive market by mixed integer linear programming. In: Proceedings of 14th power systems computation conference, Spain
6. Ongsakul W, Jirapong P (2005) Optimal allocation of FACTS devices to enhance total transfer capability using evolutionary programming. In: Proceedings of IEEE international symposium on circuits and systems
7. Shubhanga KN, Kulkarni AM (2002) Application of structure preserving energy margin sensitivity to determine the effectiveness of shunt and series FACTS devices. IEEE Trans Power Syst 17(3):730–738
8. Jain T, Singh SN, Srivastava SC (2009) Dynamic ATC enhancement through optimal placement of FACTS controllers. Electr Power Syst Res 79(11):1473–1482
9. Jain T, Singh SN, Srivastava SC (2008) Dynamic available transfer capability computation using a hybrid approach. IET Proc Gener Transm Distrib 2(6):775–788
10. North American Electric Reliability Council (NERC) (1996) Report. Available transfer capability definitions and determination
11. Sauer PW, Pai MA (1990) Power system steady state stability and the load flow Jacobian. IEEE Trans Power Syst 5(4):1374–1382
12. Padiyar KR (1996) Power system dynamics stability and control. Wiley, Singapore
13. Kundur P (1994) Power system stability and control. Mc Graw-Hill Inc., New York
14. Arrillaga J, Arnold CP (1983) Computer modeling of electrical power system. Wiley, London
15. Nassif AB, Castro MS et al (2005) H_2 norm-oriented STATCOM tuning for damping power system oscillations. Electr Power Compon Syst 33(5):1363–1383
16. Padiyar KR, Ghosh KK (1989) Direct stability evaluation of power systems with detailed generator models using structure preserving energy functions. Int J Electr Power Energy Syst 11(1):47–56
17. Padiyar KR, Immanuel V (1994) Modeling of SVC for stability evaluation using structure preserving energy function. Int J Electr Power Energy Syst 16(5):339–348
18. Jain T, Singh SN, Srivastava SC (2007) A neural network based method for fast ATC estimation in electricity markets. Paper presented in IEEE PES general meeting held at Tampa, Florida, USA, 24–28 Jun 2007
19. Yamada Y, Nagata M, Tanaka K (2002) An energy function based contingency screening method for ATC assessment with transient stability constraints. In: Proceedings of transmission and distribution conference and exhibition 2002. Asia Pacific, Yokohama, Japan, 6–10 Oct 2002
20. Department of Electrical Engineering, Indian Institute of Technology Kanpur. http://www.iitk.ac.in/ee/facilities/Research_labs/Power_System/NRPG-DATA.pdf. Accessed 21 Jul 2014

Chapter 16
STATCOM Application for Decentralized Secondary Voltage Control of Transmission Networks

Hasan Mehrjerdi, Serge Lefebvre and Maarouf Saad

Abstract Recent wide-area blackouts throughout the world highlight the need of smart power networks that could eliminate catastrophic outages by having the ability to react fast and efficient to risky operating conditions. Decentralized voltage control using STATCOM based on partitioning algorithm is discussed in this chapter. The partitioning algorithm technique divides power system into partitions to eventually prevent the propagation of disturbances if interaction between partitions is minimized. The optimized number of partitions is found based on the bus voltage sensitivity to disturbances being applied to loads in each partition. Then, a number of representative buses are labelled as pilot (control) buses displaying the critical point for installation of STATCOM for voltage control in each partition. The control uses decentralized controllers to eliminate voltage violations resulting from load variations and disturbances in each partition of the power system. The decentralized controllers are implemented by fuzzy control which is trained via offline simulations. Required reactive power is injected into the partitions by STATCOMs to correct voltage violations.

Keywords Fuzzy model and control · Graph theory · Power network · Pilot buses · Secondary voltage control

H. Mehrjerdi (✉) · S. Lefebvre
Power Systems and Mathematics Department, Research Institute of Hydro-Quebec, Varennes, Canada
e-mail: hasan.mehrjerdi.1@ens.etsmtl.ca

S. Lefebvre
e-mail: Lefebvre.Serge@ireq.ca

M. Saad
Electrical Engineering Department, Quebec University (ETS), Montreal, Canada
e-mail: maarouf.saad@etsmtl.ca

F. Shahnia et al. (eds.), *Static Compensators (STATCOMs) in Power Systems*, Power Systems, DOI 10.1007/978-981-287-281-4_16

16.1 Introduction

Today's power systems operate close to their limits, resulting a greater vulnerability to disturbances. Recent examples such as the blackout in North America in 2003, Italy in 2003, Greece in 2004 and in European countries on November 4, 2006 are representative of this vulnerability. To withstand outages/blackouts, the power industry is investing to protect its network against different disturbances, but large interconnected power systems require innovative solutions to make these practical. In transmission systems with long lines with loads remote from production, it is generally difficult to maintain constant voltage when the demand varies under highly loaded conditions. Without control, the voltage will exceed its operating range. This is harmful to quality and security.

Thus, investing efficient and secure voltage regulation for power systems by controls suitable to real-time and large networks is necessary. The goal is to maintain voltages within the ranges permitted, at all buses, following a change in the operating conditions using STATCOM. Voltage control means to regulate voltage profile by adjusting automatically reactive power control devices. The primary objective of secondary voltage control using STATCOM is to achieve better closed loop voltage regulation in power systems. Partitioning techniques, STATCOM location, partitioning model estimation and decentralized secondary voltage control using STATCOM is explained in this chapter.

Power network partitioning (PNP) that intentionally divides a power network into partitions is an appropriate method to stop the propagation of disturbances and avoid power system failure. PNP is a technique that enhances the reliability and robustness of the power system by eliminating the cascading events that inevitably lead to a total system shut down. The goal of PNP is to increase the performance and robustness of a large power network with the aim of reducing large scale power outages. Different methods have been developed for partitioning recognition and model reduction. The electrical distance method, time domain, and frequency domain approaches have been used in [1, 2]. As presented in [3], a coherency identification technique incorporating bus voltages and rotor angles improves the accuracy of the dynamic equivalent. For large systems, the above mentioned methods are fairly complex and as a result require considerable computational effort.

Model based approaches, related to the slow-coherency or eigenstructure decomposition studied in [4], are one of the important algorithms in network partitioning. These approaches focus on generator coherency and tend to ignore some important nonlinear modeling details such as nonlinear controls. Other important methods are based on measurement-based approaches, which process the wide-area response signals to find clusters of coherent buses [5]. Measurement-based coherency recognition fits within the framework of online security control.

A decomposition algorithm for coherency recognition by analyzing and quantifying the strength of connection among generating units using factors has been proposed in [4] that take into account interconnection constraints among dynamic components of the system. The results demonstrated that the coherency recognition

obtained with this procedure is independent of fault location and the size of the disturbance, since it is based on structural characteristics of coupling factors.

Voltage control problems has been studied in [6] using a model incorporating predictive/optimal control and proposing a centralized control scheme that is solved using a distributed fashion through a Lagrangian decomposition algorithm.

A network graph technique is presented in [7] to find internal and boundary buses of a local network. The local network graph is defined by finding the internal and boundary buses. The buses with voltage violations must be identified to build the local network graph. These buses may or may not be within one local network. The bus with the largest voltage violation is designated the target bus, and the respective local network is constructed. The bus voltage violations are corrected one at a time, until all violations are eliminated.

An area partitioning algorithm that minimizes both active and reactive power imbalances between generation and load within partitions has been proposed in [8]. The proposed algorithm uses a multi-objective graph partitioning technique that can be applied to very large power grids. The proposed algorithm improves the voltage profile of an island after system reconfiguration compared with algorithms that only consider active power balance.

An integrated algorithm is studied in [9] to identify a cutset for a large power system for the application of a slow coherency based controlled islanding scheme. The large scale power system is represented as a graph and a simplification algorithm is used to reduce the complexity of the system. Generators belonging to the same slowly coherent group are collapsed into a dummy node, and a graph partition library is used to split the graph into a given number of parts.

A slow coherency based islanding strategy for large disturbances is studied in [10]. The slow coherency grouping is based on a linearized electromechanical model of the system which is applicable to highly nonlinear power systems. To verify the applicability and validity of the procedure, the algorithm is tested on a 179-bus, 29-generator test system.

A clustering approach based on the fuzzy C-medoid algorithm is proposed in [11] for separating large power systems into coherent electric areas centered on a representative medoid-bus. The method is demonstrated on two test systems. They develop a formulation of the coherency matrix that is recursive in time to enable online grid partitioning.

A slow coherency based network partitioning technique which groups generators and load buses simultaneously into several coherent areas is proposed in [12]. The technique uses the slow eigenbasis matrix which is extended to include load buses. A simple method of calculating the closeness of each row eigenvector to the reference row eigenvectors is used for grouping the load buses with the respective reference machine.

The scheme proposed here separates the power system into smaller partitions using graph theory with the goal to avoid cascading events. The algorithm is tested on the IEEE 39-bus and IEEE 118-bus networks. These networks are divided into partitions that are designed to have minimum interaction and therefore any disturbances in a particular partition will not strongly propagate to the other partitions.

The partitions can be reconfigured and updated in accordance with variations in grid structure. Disturbances are defined as increasing of active and reactive power to the loads.

Selection of the pilot buses (STATCOM location) is the most crucial point for an appropriate controller design to obtain efficient voltage regulation. Methods have been already proposed for the choice of pilot buses [13, 14]. The location of STATCOM in the chapter is based on the largest variation and sensitivity of the voltage on the buses among all the buses in the same partition.

Fuzzy controller is individually designed for each partition which injects required reactive power by STATCOMs into the partition in case of disturbances and regional voltage variations. To act properly, the controller in each partition needs a regional model. In order to obtain this model, an offline fuzzy learning algorithm is applied in each partition and a nonlinear system model is estimated based on load disturbance inputs and bus voltage outputs.

Several methods to design secondary voltage controllers have been proposed [15–20]. The applications of coordinated voltage control have been tested and successfully used in France and Italy. Recently, much research work has been focused on the optimization of coordinating secondary voltage control [21–29].

An optimal coordinated voltage controller is presented in [24] based on a model predictive control (MPC) scheme. MPC has been used in secondary voltage control to coordinate different control actions in order to maintain desired voltage profiles in emergencies at different locations. A single-stage Euler state predictor upon on the system model is employed to predict voltage performance under selected control actions.

An algorithm for optimizing the voltage control systems based on jumping genes paradigm in the format of hierarchical genetic algorithm has been studied in [28]. The advantage of this algorithm is that it finds solutions that can be used for stabilizing the voltage drop or even voltage collapse in a power system.

A method is proposed in [29] that divides a power system into smaller islands with consideration of fast restoration. Self-healing approach for large disturbances is considered to deal with tragic events when vulnerability analysis shows that the power system is approaching an emergency state. A load shedding scheme based on the rate of frequency decline is applied by shedding less load compared to the conventional load shedding.

An algorithm is presented in [12] to identify a cutset for the application of a slow coherency based controlled islanding for large power system. They use controlled islanding for a corrective measure of last resort to prevent cascading outages caused by large disturbances. Generators belonging to the same slowly coherent group are integrated into a node, and a graph partition is used to divide the graph into a given number of partitions.

Replacing conventional open-loop or centralized voltage control systems with intelligent decentralized control has many advantages such as: robustness, practical feasibility, ease of hardware implementation and low cost. Intelligent control such as fuzzy control has great advantages to solve nonlinear problems and to analyze the uncertain information associated with the model of system or process being

controlled. In [30] a two layer fuzzy logic with hierarchical levels is described for control of regional as task-oriented control level and set-point control level. The high level control updates high-side voltage set points at power plants, and switches capacitor/reactor banks at the transmission network. The low level control is an automatic voltage regulator (AVR) at the power plants.

Here, fuzzy rules are used to obtain a nonlinear model of system partitions, and then fuzzy control is used to hold the buses voltage as close as possible to their regional reference values, especially useful when the power demand is heavy.

This is applied to IEEE 118-bus network with three partitions and STATCOMs installed on pilot buses in order to eliminate voltage violations in system.

16.2 Partitioning Based on Graph Theory

The graph partitioning problem is involving many different branches of engineering. Graph representation is employed to simplify the structure of power systems by utilizing the following notations: nodes representing buses in the power systems, branches representing transmission lines and transformers, weights of a branch equal to the active/reactive power flow in MW/MVAr through the line or a transformer representing the branch.

The goal of electrical network graph partitioning is to divide the vertices of a graph with weighted edges into several subsets while minimizing the interconnections among those sub-graphs. Graph theory can be applied to the large electrical networks by dividing them into subsystems to gain the facility of control and overcome the problems of black-out and load shedding. Spectral partitioning methods are known to produce good partitions for a wide class of problems, and they are used quite extensively.

This chapter firstly describes a spectral graph-based partitioning method to perform a k-way partitioning based on the k-dimensional spectral embedding of a graph [31]. In spectral partitioning techniques, the eigenvectors and eigenvalues (spectrum) of a graph are computed and a cost function is shown to be minimized by a function of the spectrum. The proposed scheme separates the power system into smaller partitions to avoid cascading events. The algorithm is tested on IEEE 39-bus and IEEE 118-bus networks. In this graph representation, only connections and the power flows through these connections are considered for evaluation.

16.2.1 Spectral K-Way Partitioning

The graph-partitioning problem involves a graph, $G = (\mathcal{V}, \varepsilon)$ with vertices, $\mathcal{V} = \{\upsilon_1, \upsilon_2, \ldots, \upsilon_n\}$ and weighted edges where the weight of edge $e = (v_i, v_j)$ represents the cost of putting υ_i and υ_j in separate partitions.

The notion of weighted graphs where each edge carries a cost, is fundamental to many applications of graph theory. We may associate to G a weight matrix W which satisfies the following properties: (1) $\omega_{ij} = \omega_{ji}$. (2) $\omega_{ii} = 0$. (3) $\omega_{ij} \geq 0$ and (4) $\omega_{ij} = 0$ if i is not adjacent to j in G.

The problem is to find a partition for the set of vertices $\mathcal{P} = \{p_1, p_2, \ldots, p_k\}$ for a given k, which optimizes some cost criterion based on the weights of the edges. Spectral-based partitioning extracts global information about the structure of a graph from eigenvalues/eigenvectors for graph matrices. The adjacency matrix of G is the $n \times n$ matrix $A(G) = \left[a_{ij}\right]$ where a_{ij} is the weight of the edge between v_i and v_j. The degree matrix of G is the $n \times n$ matrix $D(G) = \left[d_{ij}\right]$ is defined by

$$d_{ij} = \begin{cases} \sum_{k=1}^{n} a_{ik} & \text{if } i = j \\ 0 & \text{if } i \neq j \end{cases} \tag{16.1}$$

The Laplacian of G is the $n \times n$ symmetric matrix $L(G) = D(G) - A(G)$. Since the rows (and columns) sum to 0, the Laplacian is singular; it has rank at most $n - 1$ and 0 as an eigenvalue. In fact, the multiplicity of the 0 eigenvalue is the number of connected components of G. Matrix $L(G)$ is positive semidefinite and has only real eigenvalues.

The smallest eigenvalue is zero and all other eigenvalues are positive. The multiplicity of zeros as eigenvalue represents the number of connected sub-graphs. The power flow problem is solved by using the Newton-Raphson method algorithm.

This section presents a spectral k-way partitioning formulation. All k partitions are found simultaneously using all the global information available in the eigenvectors. $\lambda_1, \lambda_2, \ldots, \lambda_k$ are the k smallest eigenvalues of matrix L and $X = \{x_1, x_2, \ldots, x_k\}$ eigenvectors associated with eigenvalues from which the first eigenvectors partition vector will be built. The partition matrix $\widehat{P}$

$$\widehat{P} = Z(X)XX^T Z(X) \tag{16.2}$$

Where $Z(X)$ is a diagonal matrix with

$$z_{ij} = \frac{1}{\sqrt{\sum_{h=1}^{k} x_{ih}^{2}}} \tag{16.3}$$

$\widehat{P}_{ij}$ is the cosine of the angle between the two row vectors i and j of X and presents the closeness of vertices to each other. First vertex will be chosen by random and can be considered as center of the first partition (for example vertex c_1). To find the second vertex as center of the second partition, $\widehat{P}_{ic_1}$ *for* $i = 1, \ldots, n$ is calculated

and the minimum of $\widehat{P}_{ic_1}$ presents the second center of the second partition. When searching other partitions to find the k partition, the following equation is used:

$$Min\ Y = \left(1 - \widehat{P}_{ic_1}\right) + \left(1 - \widehat{P}_{ic_2}\right) + \ldots + (1 - \widehat{P}_{ic_k}) \tag{16.4}$$

16.2.2 Case Study I (Graph Partitioning for IEEE 39-Bus)

In this section, we discuss the results of the partitioning for IEEE 39-bus. In this network, there are 10 generators, 21 loads, 39 buses, and 46 branches (edges). The power flow has been obtained using the Matpower software [32]. Figure 16.1a shows the weighted graph model of the IEEE 39-bus. The weights are 'apparent power' between branches.

Figure 16.1b shows the result of partitioning when all weights are considered (apparent power on branches). Comparing this partitioning with the case when all of weights are considered as one shows that adding weights on the edges change slightly the partitions. For example, buses 17 and 18 move to partition three in this weighted partitioning.

Figure 16.2 shows the connection matrix including nodes (bus numbers) and weighted edges. Figure 16.3 shows the eigenvalues calculated by the Laplacian matrix, as can be seen in this figure the minimum eigenvalue is zero and all eigenvalues are positives which represents one of the main properties of the Laplacian matrix.

Figure 16.4 shows the closeness of buses 18 and 19 with other buses $((\widehat{P}_{i18}, \widehat{P}_{i19}\ for\ i = 1, \ldots, 39))$. These two buses are chosen at random to give an example of the closeness between these buses and other buses. When this closeness parameter reduces close to the value of one, it indicates that the buses are very close together and probably enclosed in the same partition. As this closeness parameter reduces toward zero or becomes even negative, it indicates that the buses are far and probably will be enclosed in a different partitions.

To check the robustness and performance of the partitioning algorithm based on the graph theory, some disturbances are added to the loads. The disturbances have been initiated from 5 % and increasing to 20 %. The results are satisfactory and show the partitions stay approximately the same with a little change on the boundaries. Figure 16.5 shows the result of the partitioning when all weights are considered and 20 % disturbance is added on the all loads. As this figure shows, compared to Fig. 16.1, buses two and eighteen, and thirty are moving to partition one.

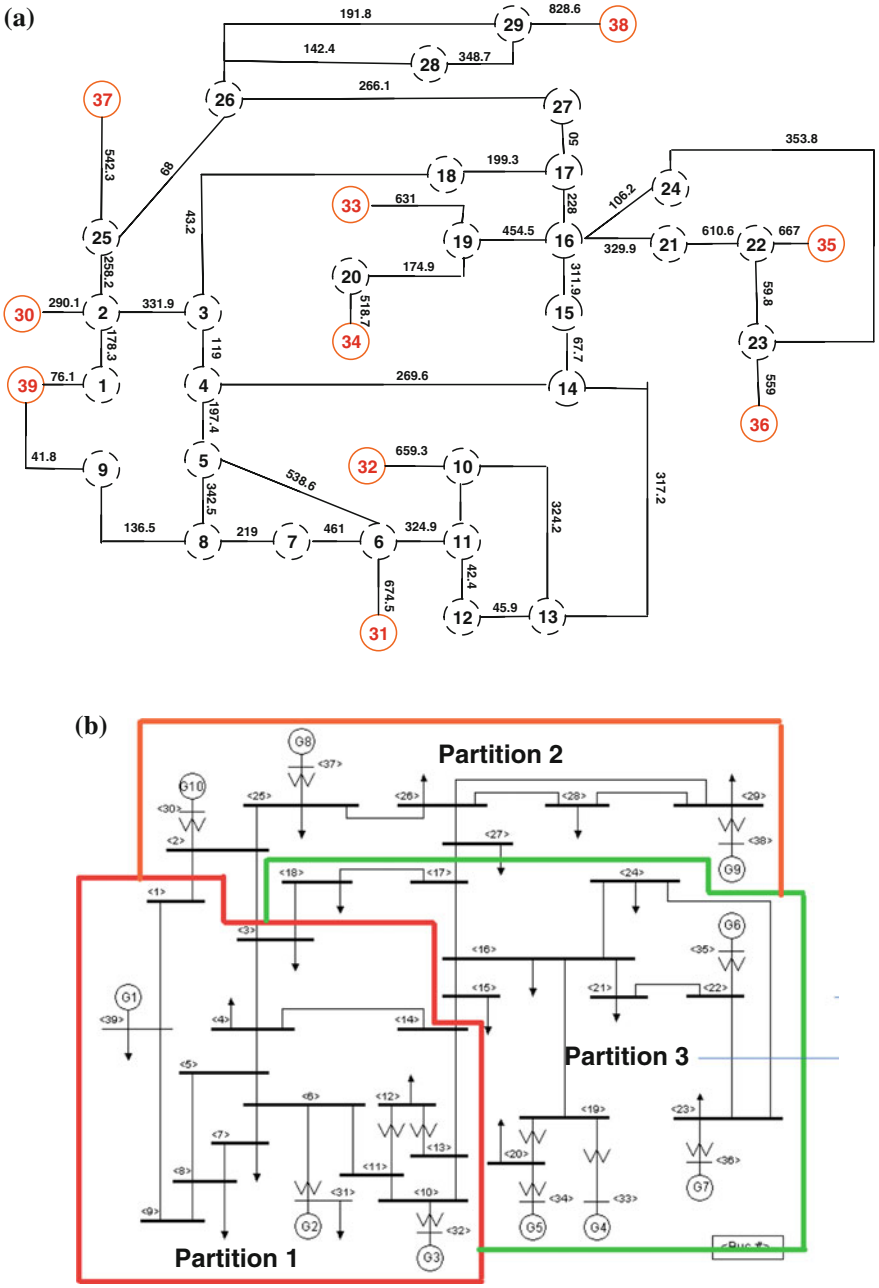

Fig. 16.1 Partitioning (IEEE 39-bus)

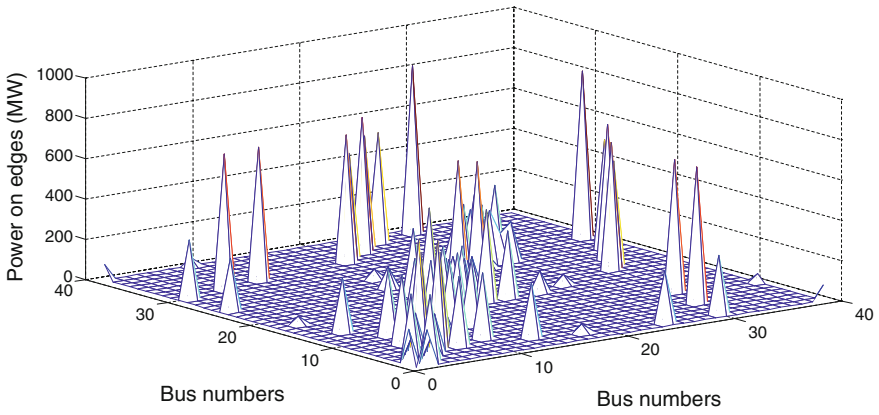

Fig. 16.2 Connection Matrix (IEEE 39-bus)

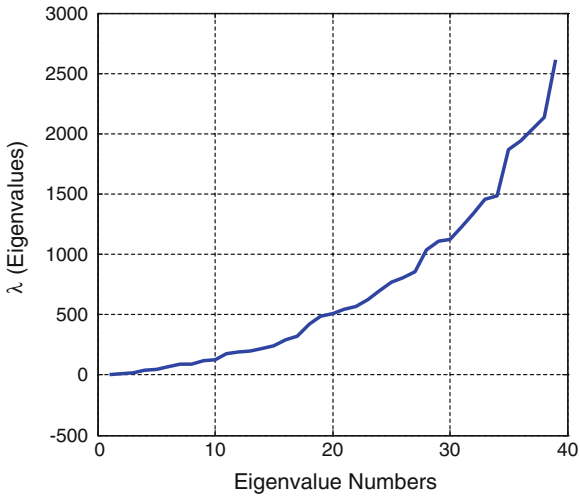

Fig. 16.3 Eigenvalues of Laplacian matrix (IEEE 39-bus)

16.2.3 Case Study II (Graph Partitioning for IEEE 118-Bus)

In this section, we discuss the results of the partitioning for IEEE 118-bus based on the graph theory. In this network, there are 54 generators, 99 loads, 118 buses, and 186 branches (edges).

Figure 16.6 shows the result of partitioning when all weights are considered (apparent power between buses). The bus centers are 3, 73 and 87.

Figure 16.7 shows the eigenvalues calculated by the Laplacian matrix, as can be seen in this figure the minimum eigenvalue is zero and all eigenvalues are positives.

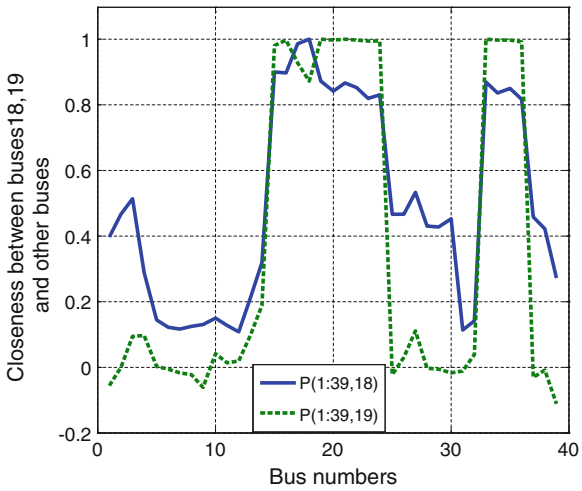

Fig. 16.4 Closeness between buses 18 and 19 with other buses (IEEE 39-bus)

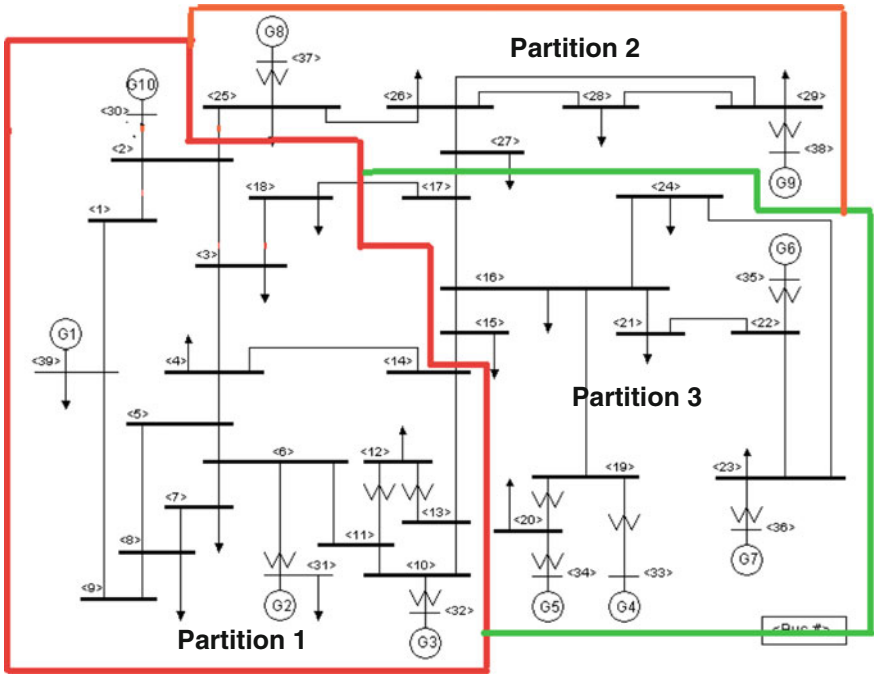

Fig. 16.5 Weighted partitioning (IEEE 39-bus) with 20 % disturbances on the loads

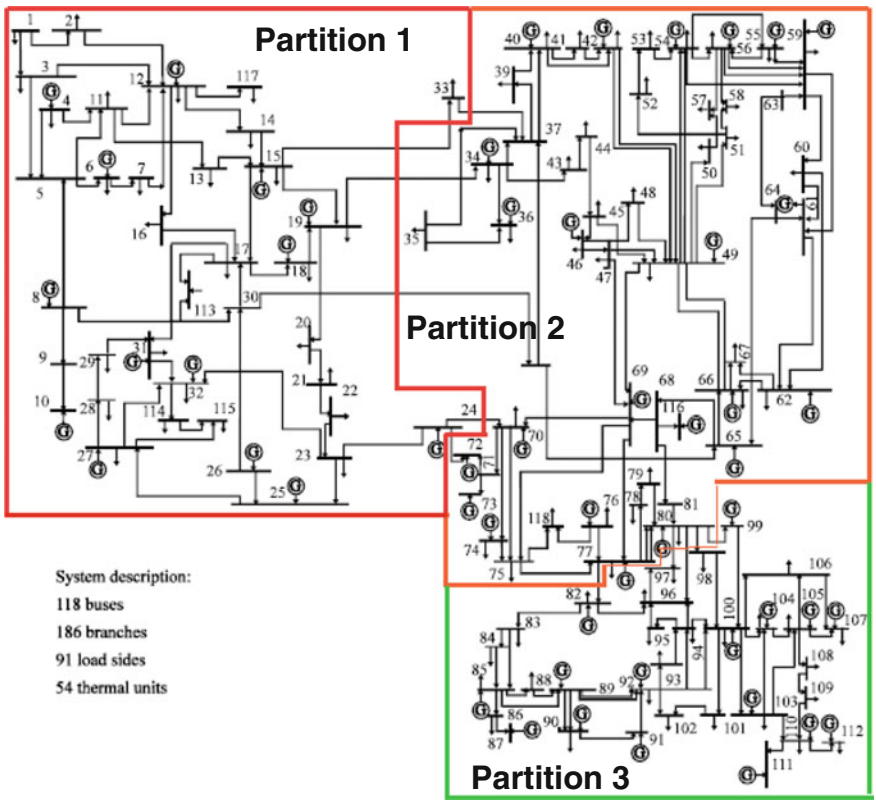

Fig. 16.6 Weighted partitioning (IEEE 118-bus)

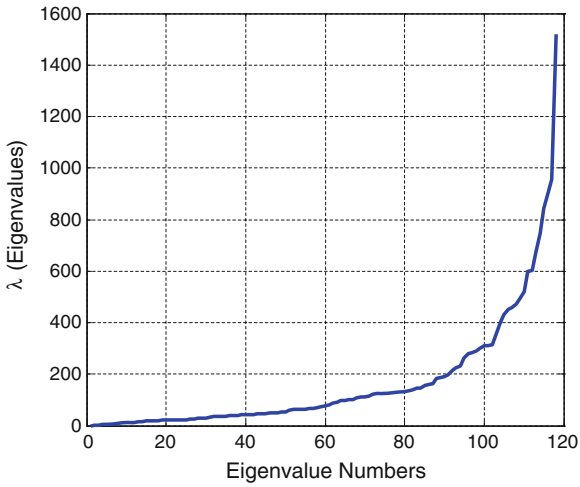

Fig. 16.7 Eigenvalues of Laplacian matrix (IEEE 118-bus)

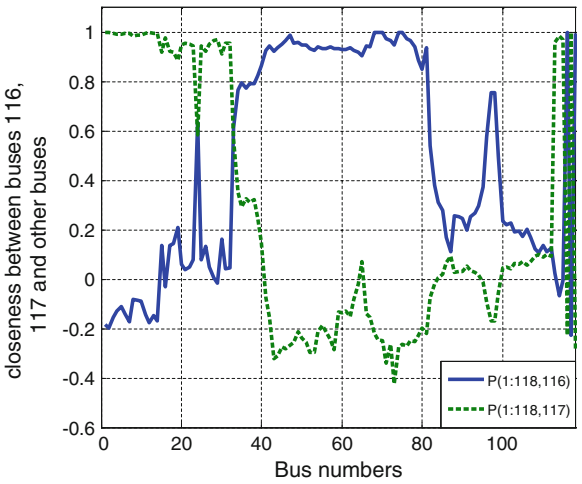

Fig. 16.8 Closeness between buses 18 and 19 and other buses (IEEE 39-bus)

Figure 16.8 shows the closeness of buses 116 and 117 and other buses. These two buses are chosen at random to show the closeness between these buses and the other buses in the experiment. When this closeness parameter reduces close to the value of one, it indicates that the buses are very close together and probably enclosed in the same partition.

16.3 Location of STATCOM

In this section, the disturbances are applied separately to loads in each partition of Fig. 16.6 to measure the interaction between partitions and to check the buses voltage variations. This is instrumental to identify those buses with the highest sensitivity (pilot buses). In the following tables v_{var} and Q_{var} are calculated by the following equations:

$$v_{var}(\%) = \frac{\left|v_{ad(avg)} - v_{bd(avg)}\right|}{v_{bd(avg)}} \times 100 \tag{16.5}$$

$$Q_{var}(\%) = \frac{\left|Q_{ad(avg)} - Q_{bd(avg)}\right|}{Q_{bd(avg)}} \times 100 \tag{16.6}$$

where $v_{ad(avg)}$ and $Q_{ad(avg)}$ are respectively the average voltage of buses and the reactive power of generators in each partition after disturbances applied to the loads while $v_{bd(avg)}$ and $Q_{bd(avg)}$ are the pre-disturbances values.

In the first step, load disturbances are in partition 1. This partition has 21 buses and 16 generators and the percentage of generators to all buses is 43.2 %.

Table 16.1 Percentage of voltage variations (disturbance in partition 1)

IEEE 118-bus network	v_{var} (%)	v_{var} (%)	v_{var} (%)
	5 % *Dis*	10 % *Dis*	20 % *Dis*
Partition 1	0.0312	0.0640	0.1348
Partition 2	0.0073	0.0203	0.0486
Partition 3	0.0001	0.0002	0.0004

Table 16.1 presents the percentage of buses voltage variations in each partition.

As can be seen in this table, load disturbances in partition 1 affect the voltages in this partition more than that in other partitions. This indicates that partition 1 is adequately isolated from the two other partitions.

Figure 16.9a shows the buses voltage differences ($\Delta v = v_{ad} - v_{bd}$) in presence of disturbances in partition 1. As illustrated, buses voltage in partition 1 decrease more than voltages of the other partitions. This confirms partition 1 is separated from other partitions.

Table 16.2 presents the percentage of the reactive power variations in each partition for this event. It turns out that generators in partition 1 produce more reactive power to regulate the voltage. Therefore in partition 1 the generators are able to compensate against a drop in voltage. This explains why this partition adequately isolated from the disturbances in other partitions.

The results show buses 20, 21 and 22 are the most sensitive buses in this partition and can be considered as STATCOMs location buses. Because these buses are close, bus 21 is considered as a main pilot bus in this partition.

Next, load disturbances are applied in partition 2. This partition has 27 buses, 23 generators, and the percentage of generators to all buses is 46 %. Table 16.3 presents the percentage of bus voltage variations in each partition and shows that load disturbances in partition 2 affects the voltages in this partition more than that in other partitions. Thus partition 2 is adequately isolated from the two other partitions.

Figure 16.9b shows Δv in presence of disturbances in partition 2. The buses voltage in this partition decreases more than the ones in the other partitions. This confirms that partition 2 is adequately separated from other partitions. Table 16.4 presents the percentage of reactive power variations in each partition for this event.

As can be seen from this table, the generators in partition 2 produce more reactive power to regulate the voltage. Therefore in partition 2 the generators are able to compensate against a drop in voltage. This explains again why this partition adequately isolated from the disturbances in other partitions. The results show bus 44 is the most sensitive bus in this partition and can be considered as the main pilot bus.

Finally, the disturbances are applied to the loads in partition 3. This partition has 16 buses, 15 generators and the percentage of generators to all buses is 48.4 %. Table 16.5 presents the percentage of the buses voltage variations in each partition. As can be seen in this table, load disturbances in partition 3 affect the voltages in this partition more than that in other partitions. This indicates that partition 3 is adequately isolated from the two other partitions.

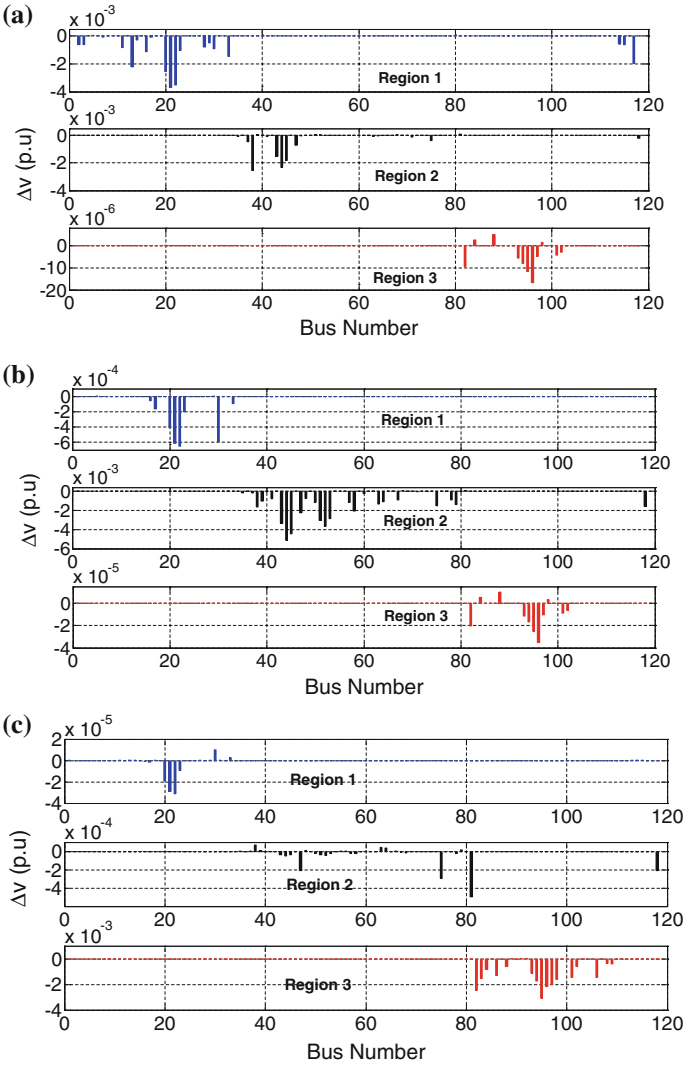

Fig. 16.9 Buses voltage difference in presence of disturbance (IEEE 118-bus network)

Table 16.2 Percentage of reactive power variations (disturbance in region 1)

IEEE 118-bus network	Q_{var} (%)	Q_{var} (%)	Q_{var} (%)
	5 % *Dis*	10 % *Dis*	20 % *Dis*
Partition 1	3.24	8.1	18.2
Partition 2	2.19	4.57	10.03
Partition 3	0.27	0.28	0.29

Table 16.3 Percentage of voltage variations (disturbance in partition 2)

IEEE 118-bus network	v_{var} (%)	v_{var} (%)	v_{var} (%)
	5 % *Dis*	10 % *Dis*	20 % *Dis*
Partition 1	0.0038	0.0077	0.0162
Partition 2	0.0424	0.0861	0.1776
Partition 3	0.004	0.0003	0.0008

Table 16.4 Percentage of reactive power variations (disturbance in partition 2)

IEEE 118-bus network	Q_{var} (%)	Q_{var} (%)	Q_{var} (%)
	5 % *Dis*	10 % *Dis*	20 % *Dis*
Partition 1	0.6	1.19	3.1
Partition 2	8.4	19.2	43
Partition 3	0.27	0.29	0.30

Table 16.5 Percentage of voltage variations (disturbance in partition 3)

IEEE 118-bus network	v_{var} (%)	v_{var} (%)	v_{var} (%)
	5 % *Dis*	10 % *Dis*	20 % *Dis*
Partition 1	0.0001	0.0002	0.0005
Partition 2	0.0012	0.0027	0.0066
Partition 3	0.0348	0.0742	0.1674

Table 16.6 Percentage of reactive power variations (disturbance in partition 3)

IEEE 118-bus network	Q_{var} (%)	Q_{var} (%)	Q_{var} (%)
	5 % *Dis*	10 % *Dis*	20 % *Dis*
Partition 1	0.007	0.011	0.028
Partition 2	0.66	1.61	4.51
Partition 3	3.2	7.68	18.05

Figure 16.9c shows Δv for disturbances in partition 3. The buses voltage in this partition decreases more than the ones in other partitions. This confirms that partition 3 is adequately separated from other partitions.

Table 16.6 presents the percentage of reactive power variations in each partition for this event. It turns out that generators in partition 3 produce more reactive power to regulate the voltage. Therefore in partitions 3 the generators are also able to compensate against a drop in voltage and adequately isolated this partition from the disturbances in other partitions.

The results show bus 95 is the most sensitive bus in this partition and can be considered as main pilot bus.

Table 16.7 shows the STATCOMs location for the three partitions of the IEEE 118-bus network.

Table 16.7 STATCOM locations (IEEE118-bus network)

IEEE 118-bus network	STATCOM location
Partition 1	21,13,117,33,3
Partition 2	44,52,47,75,118
Partition 3	95,82,98,106

16.4 Controller Design Using STATCOM

16.4.1 Partitioning Model Estimation

In this section, the generation of training data is explained based on variations of active/reactive power in load buses as inputs and buses voltage measurement as outputs. The key idea is to construct a mapping between load disturbances and buses voltage in order to plan and carry out voltage regulation. The first step is the generation of the training data set.

Different sets of inputs and outputs are applied to obtain the nonlinear model of each partition. For the first set of input/output data, disturbances have been added to all of the loads in the partition. Then for the other set of input/output data, disturbances have been added randomly to different loads in the partition to constitute sufficiently rich and meaningful data. After the training data set has been prepared, fuzzy rule antecedent membership functions have been identified by using the subtractive clustering algorithm. The consequent parameters of the rules are optimized by least square estimation (LSE). The subtractive clustering parameters that have been used for extracting the rules are: radii = 0.4, squash factor = 0.4, accept ratio = 0.3 and reject ratio = 0.15. With these parameters, a model with four fuzzy rules is identified. Figure 16.10 shows the fuzzy system structure with desired inputs and outputs. The nonlinear model of each partition is obtained using fuzzy model estimation.

Figure 16.11 shows the system and estimated model obtained by the fuzzy algorithm for each of the three partitions separately.

As shown, after applying load disturbances in the partitions, the error between the system and the estimated model increase. Table 16.8 presents the errors for each partition separately. The error is calculated with the following equation.

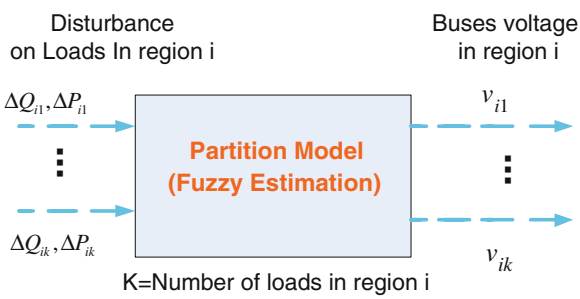

Fig. 16.10 Fuzzy partition model estimation

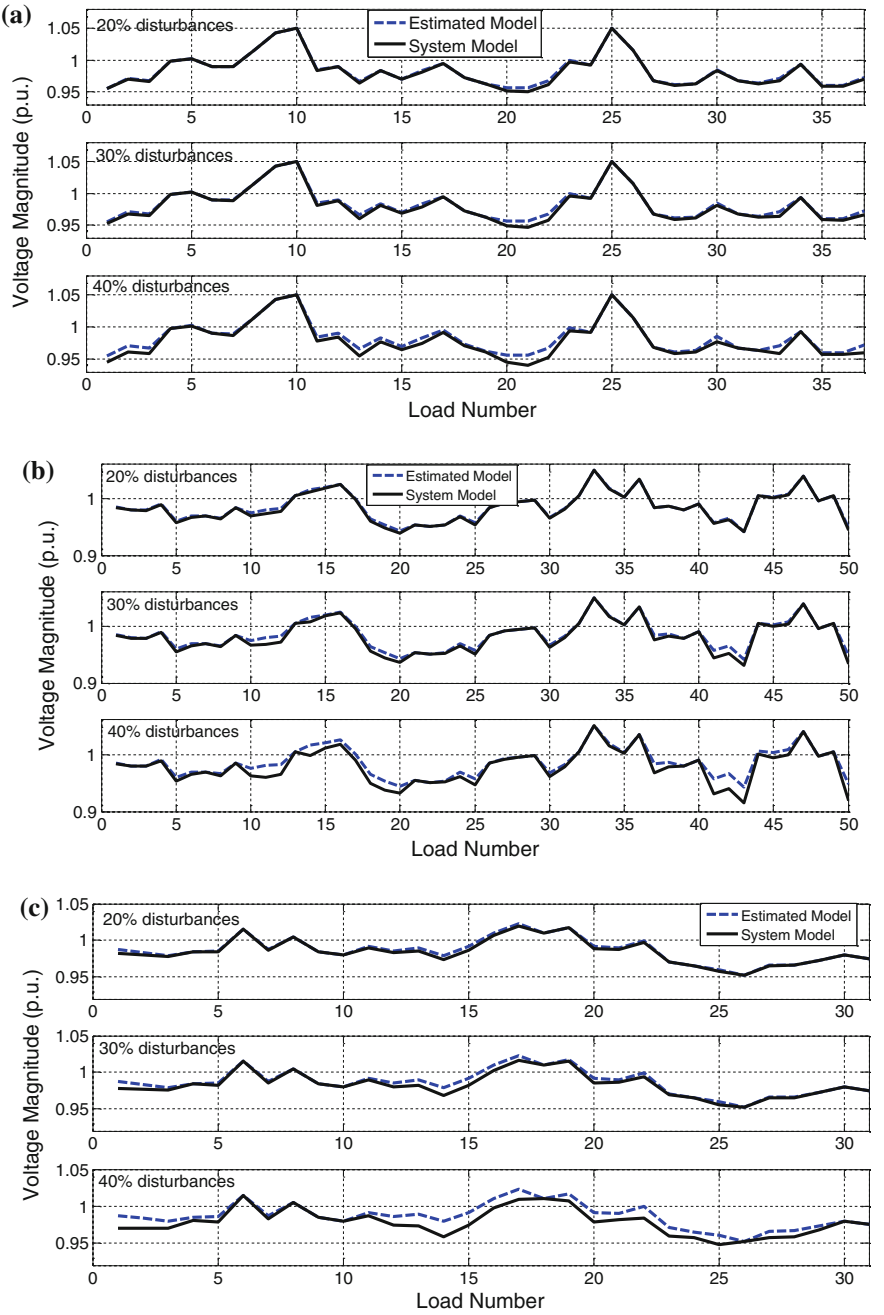

Fig. 16.11 System model and fuzzy model estimation

Table 16.8 Error between system and estimated model

IEEE 118-bus network	20 % Disturbance	30 % Disturbance	30 % Disturbance
Error Partition 1	0.0010	0.0022	0.0045
Error Partition 2	0.0014	0.0034	0.0069
Error Partition 3	0.0016	0.0031	0.0080

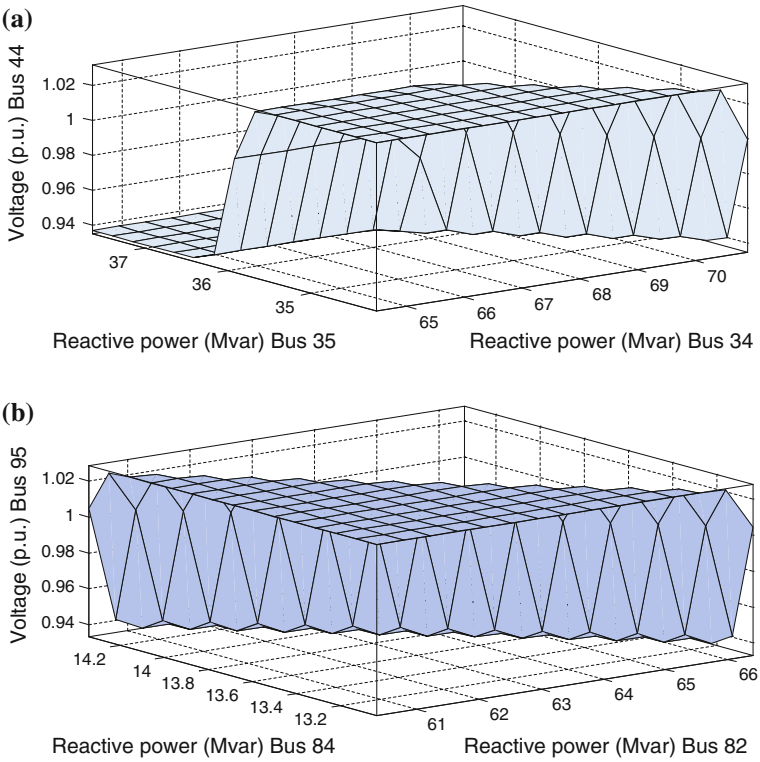

Fig. 16.12 Pilot bus voltage obtained by the fuzzy model and reactive power variations as inputs

$$Error = \frac{\sum_{i=1}^{k} V_{system}(i) - V_{estimation}(i)}{k} \tag{16.7}$$

where k is number of load buses in the partition.

Figure 16.12 shows the voltage of two representative pilot buses in partitions 2 and 3 respectively. Inputs are chosen at random (they are variations of the loads reactive power).

16.4.2 Decentralized Voltage Control Design by STATCOMs

Controls in each partition are required to improve buses voltage when a disturbance occurs. This section addresses the design of controller at pilot buses through a fuzzy approach using STATCOMs.

First the location of STATCOM is identified and represents the most sensitive point for secondary voltage control. The location of STATCOM is based on the largest bus voltage variation and sensitivity among all the buses in the same partition as explained in section III. In practice, the pilot bus voltage are updated and coordinated considering the operating conditions. Then decentralized controllers are designed separately for each partition. This step requires a model of each region affected by interaction.

Figure 16.13 presents the design of decentralized control in each partition. The controller inputs are buses voltage variations in each partition and its outputs are reactive power injected by STATCOMs. If a partition is affected by disturbances and the buses voltage approach their operating limits (especially on the pilot buses), the controller will check the ability of the generators in that partition to provide the required reactive power and will supply it. If generators operate close to their limits, then the controller will adjoin control elements (inductors, capacitors and etc.) to the system to provide the needed reactive power to the partition to prevent voltage violations.

The control-law equations for voltage regulation are:

$$\begin{bmatrix} Q\_con_{i1} \\ \vdots \\ Q\_con_{in} \end{bmatrix} = \begin{bmatrix} f_1(Q_{i1}, v_{i1}) \\ \vdots \\ f_n(Q_{ip}, v_{ik}) \end{bmatrix} \tag{16.8}$$

The functions f_1 and f_n are the control laws of a Sugeno-type fuzzy controller. Sugeno controllers take in fuzzy inputs and outputs. In this equation $v_{i1} \ldots v_{ik}$ are buses voltage in partition, $Q\_con_{i1} \ldots Q\_con_{in}$ are reactive power injected into the partition i by controllers, and $Q\_{i1} \ldots Q\_{ip}$ are the reactive power generated by generators in partition i. Table 16.9 presents an example of the fuzzy training outputs for control of partition 1. A similar training has been performed for partitions 2 and 3 respectively. As can be seen in this table, the disturbances ranging from 10–50 % are applied to the loads in this partition and the reactive power is modified to prevent voltage violations.

Next, load disturbance is applied in partition 2. This partition has 27 buses, 23 generators, and the percentage of generators to all buses is 46 %. Table 16.10 shows the reactive power produced by controllers in partition 2 to compensate the disturbance. Disturbance is increasing from 0–40 %.

Finally, the disturbance is applied to the loads in partition 3. This region has 16 buses, 15 generators and the percentage of generators to all buses is 48.4 %. Table 16.11 shows the reactive power produced by controllers in partition 3 to compensate the disturbance. Disturbance is increasing from 0 to 50 %.

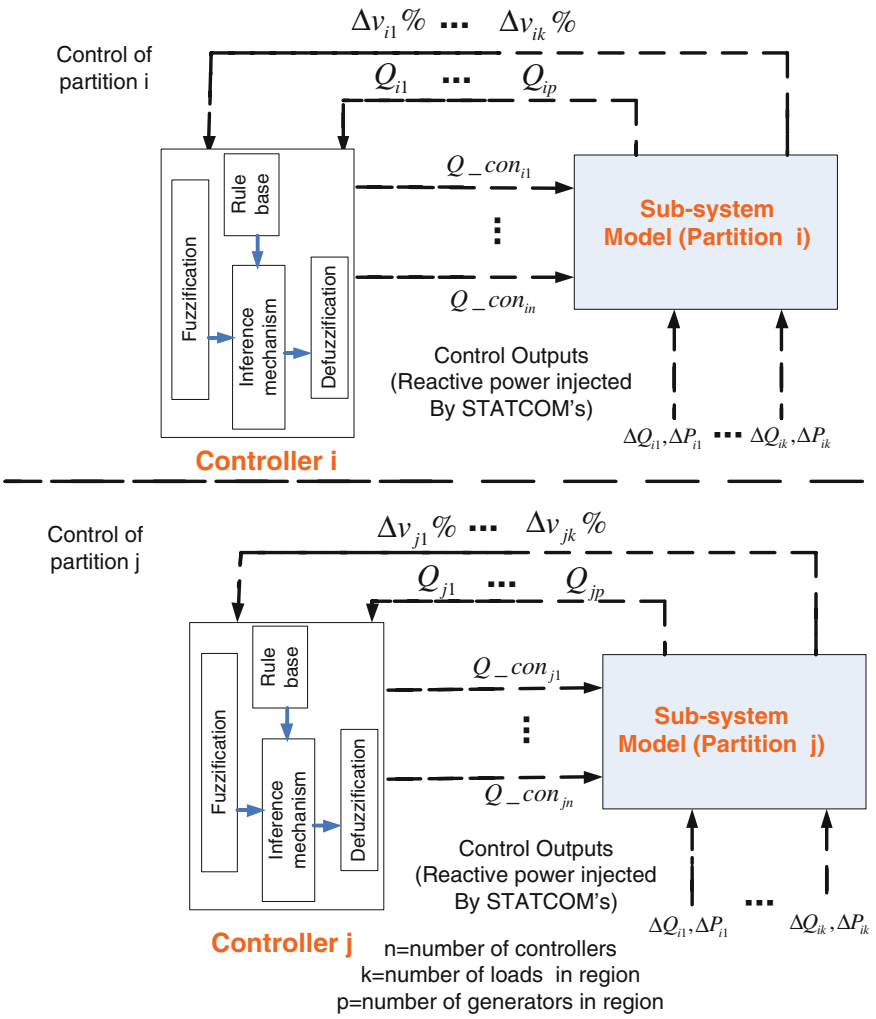

Fig. 16.13 Fuzzy control block diagram

Table 16.9 Fuzzy training outputs for control of partition 1 (reactive power injected by STATCOMs)

	Disturbances on Partition 1						
	10 %	20 %	25 %	30 %	35 %	40 %	50 %
STATCOM location (Partition 1)	Reactive power injected by STATCOMs (MVAr)						
21	0	0	2	4	6	10	12
13	0	0	0	0	2	6	10
117	0	0	0	0	2	4	5
33	0	0	0	0	0	3	8
3	0	0	0	0	0	0	8

Table 16.10 Fuzzy training outputs for control of partition 2 (Reactive power injected by STATCOMs)

	Disturbances on Partition 2						
	10 %	20 %	25 %	30 %	35 %	40 %	50 %
STATCOM location (partition 2)	Reactive power injected by STATCOMs (MVAr)						
44	0	0	2	4	8	15	20
52	0	0	0	2	4	8	12
118	0	0	0	2	10	18	25
75	0	0	0	0	4	10	22
47	0	0	0	0	0	8	18

Table 16.11 Fuzzy training outputs for control of partition 2 (Reactive power injected by STATCOMs)

	Disturbances on Partition 2						
	10 %	20 %	25 %	30 %	35 %	40 %	50 %
STATCOM location (partition 3)	Reactive power injected by STATCOMs (MVAr)						
95	0	0	0	15	18	25	50
82	0	0	0	0	15	18	30
98	0	0	0	0	0	15	30
106	0	0	0	0	0	0	18

16.4.3 Decentralized Voltage Control Design

The simulation is to demonstrate the performance characteristics inferred from the theoretical development. A case study on the IEEE 118-bus network confirms the robustness and performance of the algorithm. In this section, we discuss the results of different tests on the IEEE 118-bus network. These tests are as follows:

1. Increase loads in each partition individually, verify the voltage of the main pilot bus; when this voltage violates a limit then inject required power into the partition,
2. Increase loads in each partition individually, verify the voltage of the pilot buses; when this voltage violates a limit then inject required power into the partition,

In the first test, 30 % disturbances are applied to the loads in the partition 1. Allowable variations on buses voltage are set to $\mp 1\%$. If buses voltage variations exceed 1 %, the controller will modify reactive power to keep voltages in the desired ranges. Figure 16.14(a) shows buses voltage in partition 1 without and with controller.

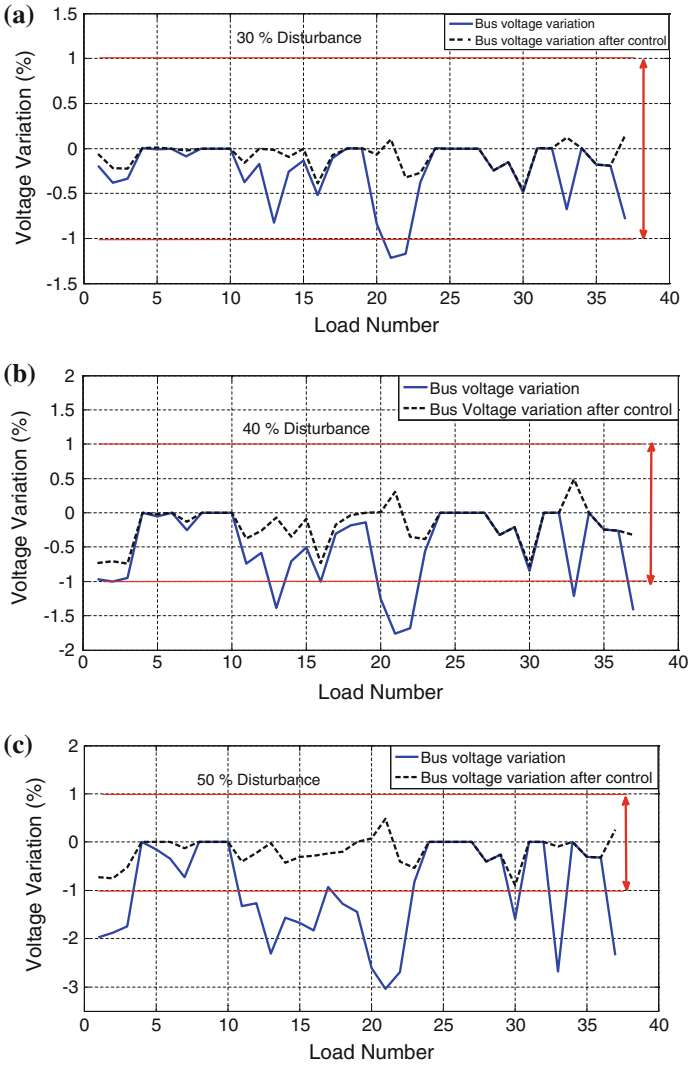

Fig. 16.14 Buses voltage before and after injection of reactive power to partition 1

As illustrated, the 30 % disturbances cause voltage of pilot bus 21 to drop more than 1 %. In this situation, reactive power is supplied at this pilot bus, bus voltage increases and stays within the desired voltage range. Next, disturbances are increased to 40 % and 50 % respectively and Fig. 16.14b, c show the buses voltage. As can be seen in these figures, the controller for pilot bus 21 is not sufficient to regulate the voltages and therefore, other controllers installed in pilot buses add reactive power to the partition to compensate voltages drop. These controllers are installed in pilot buses 21, 13, 117, 33 and 3 respectively.

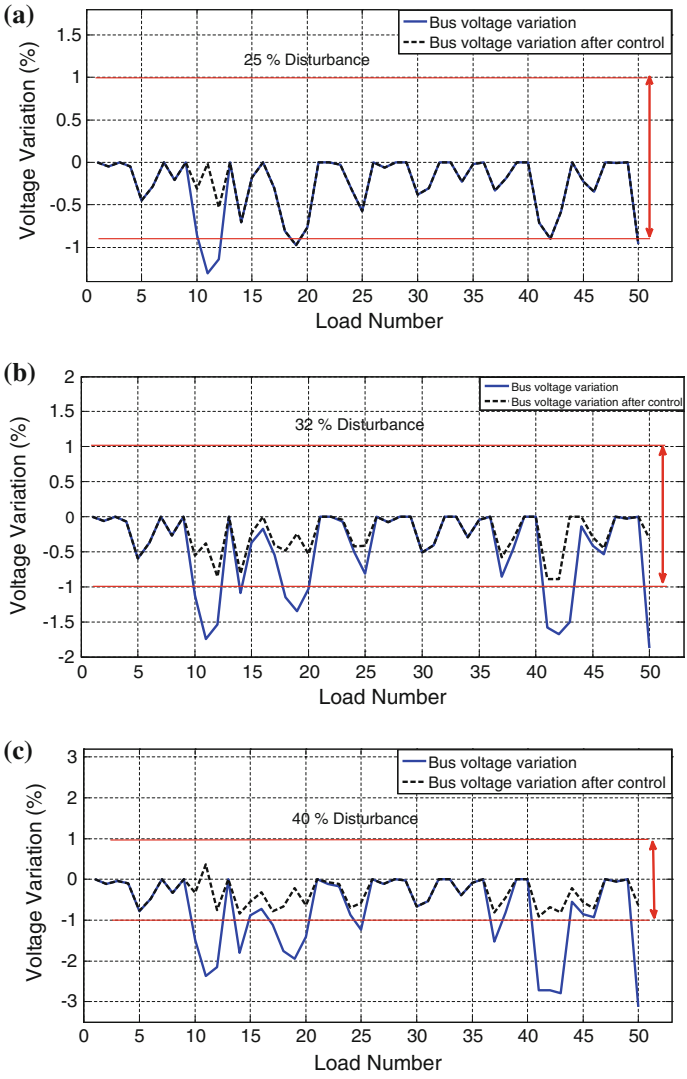

Fig. 16.15 Buses voltage before and after injection of reactive power to partition 2

In the second test, the loads in the partition 2 are increased to 25 %. Figure 16.15a shows buses voltage in partition 2 without and with the controller.

The scenario cause voltage of pilot bus 44 drops under 1 % of variation. In this situation, reactive power is added on this pilot bus and its bus voltage increases and stays within the allowable range. Next, disturbances are 32 % and 40 % respectively in Fig. 16.15b, c. Here, the controller for pilot bus 44 is not enough to regulate the voltages and therefore, other controllers installed on pilot buses supply reactive

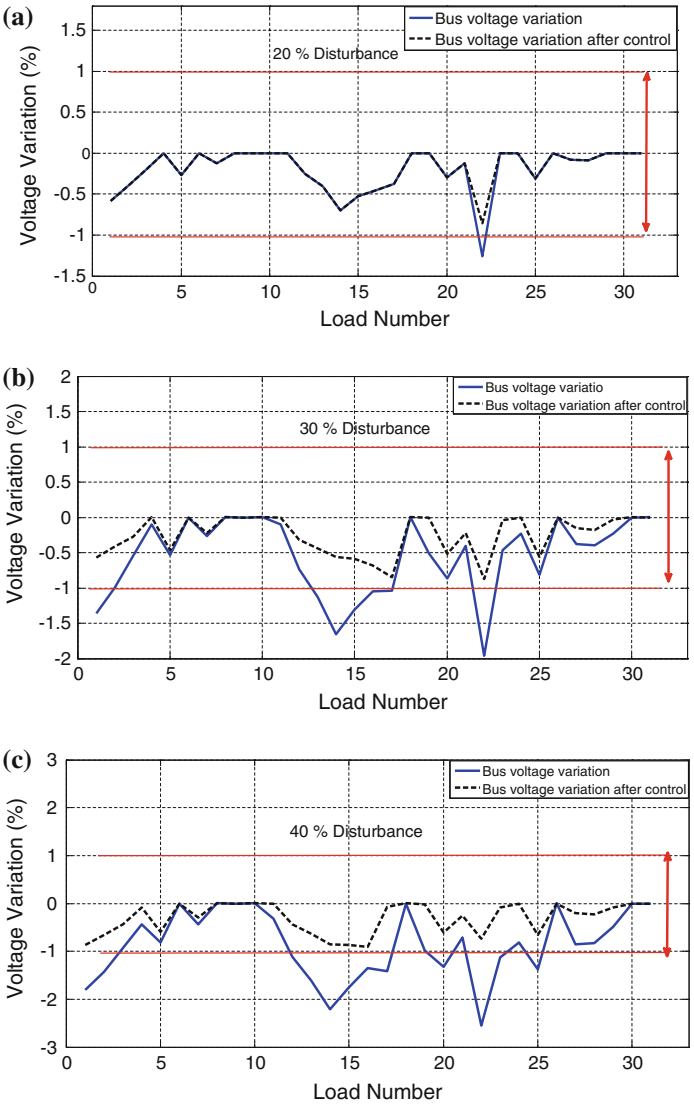

Fig. 16.16 Buses voltage before and after injection of reactive power to partition 3

power to the partition. These controllers are installed at pilot buses 44, 52, 47, 75, and 118 respectively.

In the third test, the loads in the partition 3 are increased by 20 %. Figure 16.16a shows the buses voltage in partition 3 without and with the controller.

The scenario causes voltage of pilot bus 95 falls under its accepted range. In this situation, reactive power is added in this pilot bus, bus voltage increases and there is no violation.

Next, disturbances are increased to 30 % and 40 % respectively and Fig. 16.16b, c show the buses voltage. Here, the reactive power injected by the controller in pilot bus 95 is not enough to regulate the voltages and therefore other controllers come in. These controllers are installed at pilot buses 95, 82, 98, and 106 respectively.

References

1. Chow JH (1982) Time-scale modelling of dynamic network with applications to power systems, vol 46. Springer Verlag, New York
2. Jonsson M, Begovic M, Daalder J (2004) A new method suitable for real-time generator coherency determination. IEEE Trans Power Syst 19(3):1473–1482
3. Joo S-K, Liu C-C, Jones LE, Choe J-W (2004) Coherency and aggregations techniques incorporating rotor and voltage dynamics. IEEE Trans Power Syst 19(2):1068–1075
4. De Tuglie E, Iannone SM, Torelli F (2008) A coherency recognition based on structural decomposition procedure. IEEE Trans Power Syst 23:555–563
5. Kamwa I, Pradhan AK, Joos G (2007) Automatic segmentation of large power systems into fuzzy coherent areas for dynamic vulnerability assessment. IEEE Trans Power Syst 22 (4):1974–1985
6. Beccuti AG, Demiray TH, Andersson G, Morari M (2010) A lagrangian decomposition algorithm for optimal emergency voltage control. IEEE Trans Power Syst 25(4):1769–1779
7. Wagner WR, Keyhani A, Hao S, Wong TC (1990) A rule-based approach to decentralized voltage control. IEEE Trans Power Syst 5(2):643–651
8. Li J, Liu CC, Schneider KP (2010) Controlled partitioning of a power network considering real and reactive power balance. IEEE Trans Smart Grid 1(3):261–269
9. Xu G, Vittal V (2010) Slow coherency based cutset determination algorithm for large power systems. IEEE Trans Power Syst 25(2):877–884
10. You H, Vittal V, Wang X (2004) Slow coherency-based islanding. IEEE Trans Power Syst 19 (1):483–491
11. Kamwa I, Pradhan AK, Joos G, Samantaray SR (2009) Fuzzy partitioning of a real power system for dynamic vulnerability assessment. IEEE Trans Power Syst 24(3):1356–1365
12. Yusof SB, Rogers GJ, Alden RTH (1993) Slow coherency based network partitioning including load buses. IEEE Trans Power Syst 8(3):1068–1075
13. Conejo A, Aguilar M (1996) A nonlinear approach to the selection of pilot buses for secondary voltage control. In: IEEE proceedings—power systems control and management
14. Lerm AAP (2006) Using the bifurcation theory to select pilot busbars in a secondary voltage regulation scheme. In: IEEE/PES power systems conference and exposition, pp 2096–2100
15. Paul JP, Leost JY, Tesseron JM (1987) Survey of the secondary voltage control in France: present realization and investigation. IEEE Trans Power Syst 2:505–511
16. Lagonotte P, Sabonnadiere JC, Leost JY, Paul JP (1989) Structure analysis of the electrical system: application to secondary voltage control in France. IEEE Trans Power Syst 4:479–486
17. Stancovie' A, Ili'c M, Maratukulam D (1991) Recent results in secondary voltage control of power systems. IEEE Trans Power Syst 6:94–101
18. Marinescu B, Bourles H (1999) Robust predictive control for the flexible coordinated secondary voltage control of large-scale power systems. IEEE Trans Power Syst 14:1262–1268
19. Mehrjerdi H, Lefebvre S, Saad M, Asber D (2013) A decentralized control of partitioned power networks for voltage regulation and prevention against disturbance propagation. IEEE Trans Power Syst 28(2):1461–1469
20. Mehrjerdi H, Ghahremani E, Lefebvre S, Saad M, Asber D (2013) An authenticated voltage control of partitioned power networks with optimal allocation of STATCOM using heuristic algorithm. IET Gener Transm Distrib 7(9):1037–1045

21. Corsi S, Pozzi M, Sabelli C, Serrani A (2004) The coordinated automatic voltage control of the Italian transmission grid—Part I: reasons of the choice and overview of the consolidated hierarchical system. IEEE Trans Power Syst 19(4):1723–1732
22. Corsi S, Pozzi M, Sforna M, Dell'Olio G (2004) The coordinated automatic voltage control of the Italian transmission grid—Part II: control apparatuses and field performance of the consolidated hierarchical system. IEEE Trans Power Syst 19(4):1733–1741
23. Larsson M, Hill DJ, Olsson G (2002) Emergency voltage control using search and predictive control. Electr Power Energy Syst 24(2):121–130
24. Wen JY, Wu QH, Turner DR, Cheng SJ, Fitch J (2004) Optimal coordinated voltage control for power system voltage stability. IEEE Trans Power Syst 19(2):1115–1122
25. Wang HF, Li H, Chen H (2003) Coordinated secondary voltage control to eliminate voltage violations in power system contingencies. IEEE Trans Power Syst 18(2):588–595
26. Wu Q, Popovic DH, Hill DJ, Parker CJ (2001) Voltage security enhancement via coordinated control. IEEE Trans Power Syst 16(1):127–135
27. Mehrjerdi H, Lefebvre S, Saad M, Asber D (2013) Coordinated control strategy considering effect of neighborhood compensation for voltage improvement in transmission systems. IEEE Trans Power Syst 28(4):4507–4515
28. Ma HM, Ng KT, Man KF (2008) Multiobjective coordinated power voltage control using jumping genes paradigm. IEEE Trans Power Syst 55(11):4075–4084
29. You H, Vittal V, Yang Z (2003) Self-healing in power systems: an approach using islanding and rate of frequency decline-based load shedding. IEEE Trans Power Syst 18(1):174–181
30. Marques AB, Taranto GN, Falcao DM (2005) A knowledge-based system for supervision and control of regional voltage profile and security. IEEE Trans Power Syst 20(4):400–407
31. Chan PK, Schlag DF, Zien JY (1994) Spectral K-way ratio-cut partitioning and clustering. IEEE Trans Comput Aided Des Integr Circuits Syst 11(9):1088–1096
32. Zimmerman RD, Murillo-Sánchez CE, Thomas RJ (2011) MATPOWER: steady-state operations, planning, and analysis tools for power systems research and education. IEEE Trans Power Syst 26(1):1088–1096

Chapter 17
Analysis and Damping of Subsynchronous Oscillations Using STATCOM

Nagesh Prabhu

Abstract Series compensation of long transmission lines is an economic solution to the problem of enhancing power transfer and improving system stability. However, series compensated transmission lines connected to the turbo generator can result in Subsynchronous Resonance (SSR) leading to undamped Subsynchronous Oscillations (SSO). The advent of Flexible AC Transmission System (FACTS) controllers using high power semiconductors has made it possible to apply these controllers in conjunction with fixed series compensation, not only to improve system performance, but also to overcome the problem of SSR. FACTS controllers based on Voltage Source Converter (VSC) are emerging controllers that have several advantages over the conventional ones using thyristors. STATCOM is a shunt FACTS controller suitable for voltage regulation and damping of oscillations. This chapter describes the analysis and simulation of a series compensated system with STATCOM connected at the electrical center of the transmission line. The SSR characteristic of the combined system is discussed. A new technique of SSR damping is presented in which a STATCOM injects subsynchronous current.

Keywords Subsynchronous resonance (SSR) · FACTS · Voltage source converter (VSC) · STATCOM · Damping torque · Eigenvalue · Transient simulation

17.1 Introduction

The continuous increase for the demand of electrical energy and constraints on additional right of way for transmission lines has caused the power systems to operate under more stressed conditions. Hence the electrical utilities are forced to expand the generation and transmissions facilities. In view of difficulties involved

N. Prabhu (✉)
Department of Electrical and Electronics Engineering, NMAM Institute of Technology, Nitte, Udupi District 574 110, India
e-mail: prabhunagesh@nitte.edu.in; prabhunagesh@rediffmail.com

F. Shahnia et al. (eds.), *Static Compensators (STATCOMs) in Power Systems*, Power Systems, DOI 10.1007/978-981-287-281-4_17

in the addition of new transmission lines, it is challenging for power system engineers to efficiently utilize the existing transmission facilities in a secure manner.

The long transmission lines are used for utilization of remotely located resources. The reasons for limitation of transmission capability of long transmission lines extend from thermal considerations to transient and dynamic stability of the networks. The power flow pattern in the transmission system is unfavourable if some of the transmission lines may be very close to their thermal limits while other lines have large thermal margins. The increase in power flow over a given transmission network can be achieved by compensating the AC network by (a) Series compensation to partly compensate for the transmission line reactance by series capacitors. (b) Shunt compensation to maintain voltage dynamically at appropriate buses in the network by reactive power compensators.

Series capacitive compensation is an economical and direct approach for increasing the transmission capability of long distance transmission lines. The series capacitor decreases electrical length of compensated transmission line. They also help in voltage regulation and reactive power control among parallel transmission paths. However, introduction of Series capacitors in a transmission system can give rise to SSR by interacting with the turbo-generators [1, 2]. The SSR phenomenon was discovered when it resulted in the destruction of two generator shafts at the Mohave power station (in USA) on December 9, 1970 and again on October 26, 1971.

It has been defined by the IEEE SSR working group [3] that, SSR is an electrical power system condition where the electric network exchanges energy with the turbine-generator at one or more of the natural frequencies of the combined system below the synchronous frequency of the system. During the incidents of generator shaft damage at Mohave [4], it was found that the frequency of one of the torsional modes was close to the complementary frequency of subsynchronous currents present in the electrical system. This resulted in large torque in the shaft section between the generator and exciter which subsequently damaged the shaft.

SSR is a major concern for the stability of turbine-generators connected to transmission systems which employ series capacitors. A disturbance in the power system can cause excitation of turbine-generator natural torsional modes. When the generator is connected to a series capacitor compensated transmission system, these oscillations can be amplified and sustained due to interaction between the electrical and the multi-mass mechanical system. The oscillations of the shaft at natural modes may build up to dangerously high value resulting in shaft failure.

17.2 SSR Phenomenon

The physical basis for the detrimental effects of SSR phenomenon can be explained by taking up a basic series compensated system as shown in Fig. 17.1.

The oscillations of the generator rotor at subsynchronous frequency 'f_m' result in voltages induced in the armature having components of (a) subsynchronous frequency ($f_o - f_m$) and (b) supersynchronous frequency ($f_o + f_m$) where 'f_o' is the

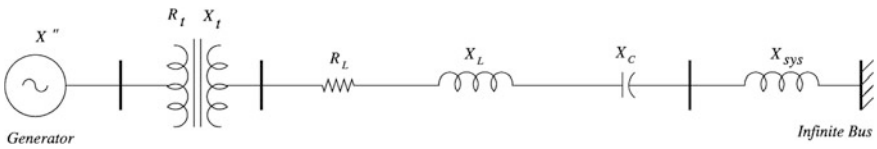

Fig. 17.1 A series compensated system

operating system frequency. These voltages set up currents in the armature (and network) whose magnitudes and phase angles depend on the network impedances. Both current components (sub and supersynchronus) set up electromagnetic torques of the same frequency 'f_m'. In general, supersynchronous frequency currents result in positive damping torque while the subsynchronous frequency currents result in negative damping torque [1]. The net torque can result in negative damping if magnitudes of the subsynchronous frequency currents are high and in phase with the voltages (of subsynchronous frequency). This situation can arise when the electrical network connected to the generator armature is in resonance around the frequency of ($f_o - f_m$). A series compensated transmission line has a resonance frequency of 'f_{er}' given by

$$f_{er} = f_0 \sqrt{\frac{X_c}{x'' + X_t + X_L + X_{sys}}} \tag{17.1}$$

where x'' is the subtransient reactance of the generator, X_t is the leakage reactance of the transformer, X_L and X_C are the transmission line inductive and capacitive reactance respectively. Since $X_C < X_L$, $f_{er} < f_o$. Thus for a particular level of series compensation, it is possible that $f_{er} \approx f_o - f_m$.

There are two aspects of the SSR problem [1]. These are (i) Self excitation (also called as steady state SSR) and (ii) Transient torques (also called as transient SSR).

Self excitation

Subsynchronous frequency currents entering the generator terminals produce subsynchronous frequency terminal voltage components. These voltage components may sustain the currents to produce the effect that is termed as self excitation. There are two types of self excitation, one involving only rotor electrical dynamics and the other involving both rotor electrical and mechanical dynamics. The first one is termed as induction generator effect while the second one is called as torsional interaction.

Induction generator effect

Induction generator effect results from the fact that subsynchronous frequency (f_{er}) currents in the armature set up a rotating magnetic field which induce currents in the rotor of frequency $f_{er} < f_o$. As the rotating mmf produced by the subsynchronous frequency armature currents is moving slower than the speed of the rotor, the resistance of the rotor (at the subsynchronous frequency viewed from the armature

terminals) is negative as the slip of the machine viewed as an induction generator is negative. When the magnitude of this negative resistance exceeds the sum of the armature and network resistances at a resonant frequency, there will be self excitation. However, this problem can be tackled by suitable design of amortisseuer windings of the generator rotor.

Torsional Interaction

Generator rotor oscillations at a torsional mode frequency fm, induce armature voltage components at frequencies (f_{em}) given by $f_{em} = f_o - f_m$. When the subsynchronous component of f_{em} is close to f_{er} [electrical resonant frequency defined in (17.1)], the subsynchronous torques produced by subsynchronous voltage component can be sustained. This interaction between electrical and mechanical systems is termed as torsional interaction (TI). The torsional interaction can also be viewed as the insertion of negative resistance in the generator armature viewed from the terminals. This effect is much more significant compared to the induction generator effect.

The self excitation aspect of SSR can be considered as a stability problem under small disturbances and can be analyzed using linear models. Transient torques and system disturbances resulting from switching in the network can excite oscillatory torques on the generator rotor. The transient electrical torque, in general has many components including unidirectional, exponentially decaying and oscillatory torques from subsynchronous to multiples (typically second harmonic) of network frequency. Due to SSR phenomenon, the subsynchronous frequency components of torque can have large amplitudes immediately following the disturbance, although they may decay eventually. Each occurrence of these high amplitude transient torques can result in expenditure of the shaft life due to fatigue damage. Since the system is nonlinear, the effect of transient torque can be studied by numerical integration of system differential equations by incorporating all nonlinearities. The EMTP permits nonlinear modelling of complex system components and is well suited for analyzing transient torque SSR problems [2].

17.3 Modelling of Electomechanical System

The steady-state SSR relates to the stability of the operating point whereas the transient SSR problem refers to the possibility of high values of oscillatory shaft torques caused by a major disturbance, even though such torsional oscillations may eventually be damped out.

The mathematical models that are considered for the SSR analysis are invariably non-linear and in general, the solution is obtained by transient simulation. However, for operating point stability (small signal stability), it is adequate to linearize the system equations around the operating point to simplify the analysis [1]. Major differences in the modelling for SSR analysis compared to conventional stability analysis are (a) Inclusion of network transients and (b) The detailed modelling of the

mechanical system made up of turbine, generator, exciter rotors and shafts as multimass-spring-damper system. The transient SSR problem requires the use of transient simulation (as the nonlinearities cannot be neglected while considering large disturbances). The following methods have been used for the analysis of steady-state SSR based on linearized models: (1) Damping torque analysis (Frequency domain method) (2) Eigenvalue analysis. The various methods of analysis are illustrated based on case studies on IEEE first benchmark model (FBM) [5] where a single machine is connected to infinite bus through a series compensated line. The overall system model is derived from the component models of the synchronous generator, excitation system, Power System Stabilizer (PSS), mechanical system and the AC network.

The power system comprises of turbine-generator and electrical network. The mechanical system is represented by multi-mass spring damper system. For SSR studies, it is necessary to model generator in detail. Generator model 2.2 [1, 6] is usually considered where the stator and rotors are represented by six differential equations. It is required to model the excitation system and PSS also. The electrical network consists of transmission lines, transformers, series capacitors and shunt reactance if any. For the steady state SSR analysis, the entire system is described by a set of first order differential equations, which are linearized about an operating point to perform damping torque and eigenvalue analysis. The modelling of various subsystems of the electromechanical system are described in the sections to follow.

17.3.1 Synchronous Generator

The study of torsional interactions demands a detailed model of the synchronous generator. The synchronous machine model 2.2 considered is shown in Fig. 17.2.

The stator 3 phase windings are replaced by fictitious d, q and o coils from Park's transformation. Out of these, the o coil (in which zero sequence current i_o flows) has no coupling with the rotor coils and may be neglected if $i_o = 0$. The fictitious d and q coils rotate at the same speed of rotor. The four rotor windings include field winding f, d-axis damper winding h and q-axis damper windings g and k.

The equations governing the 2.2 generator model are given as [1, 6],

The d-axis equivalent circuit equations:

$$\frac{d\Psi_h}{dt} = \frac{1}{T_d''}[-\Psi_h + \Psi_d] \tag{17.2}$$

$$\frac{d\Psi_f}{dt} = \frac{1}{T_d'}\left[-\Psi_f + \Psi_d + \frac{x_d'}{x_d - x_d'}E_{fd}\right] \tag{17.3}$$

$$\Psi_d = x_d'' i_d + \frac{x_d' - x_d''}{x_d'}\Psi_h + \frac{x_d - x_d'}{x_d}\frac{x_d''}{x_d'}\Psi_f \tag{17.4}$$

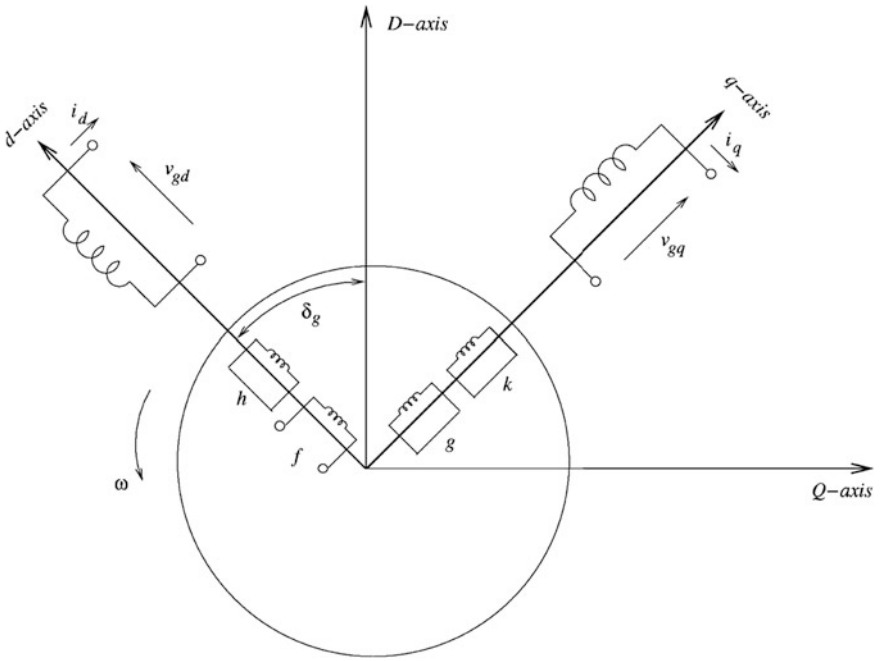

Fig. 17.2 Synchronous machine with rotating armature windings

The q-axis equivalent circuit equations:

$$\frac{d\Psi_g}{dt} = \frac{1}{T_q'}\left[-\Psi_g + \Psi_q\right] \tag{17.5}$$

$$\frac{d\Psi_k}{dt} = \frac{1}{T_q''}\left[-\Psi_k + \Psi_q\right] \tag{17.6}$$

$$\Psi_q = x_q'' i_q + \frac{x_q' - x_q''}{x_q'}\Psi_k + \frac{x_q - x_q'}{x_q}\frac{x_q''}{x_q'}\Psi_g \tag{17.7}$$

The stator equations can be expressed as,

$$\frac{d\Psi_d}{dt} = -\omega\Psi_q - \omega_B R_a i_d - \omega_B v_{gd} \tag{17.8}$$

$$\frac{d\Psi_q}{dt} = \omega\Psi_d - \omega_B R_a i_q - \omega_B v_{gq} \tag{17.9}$$

where, ω is the generator rotor speed. The armature current components i_d and i_q are not independent, but can be expressed in terms of the flux linkages from equations.

To have a common axis of reference with the network, the voltages v_{gd} and v_{gq} are transformed to Kron's (D-Q) reference frame using the following transformation.

$$\begin{bmatrix} v_{gd} \\ v_{gq} \end{bmatrix} = \begin{bmatrix} \cos\delta_g & -\sin\delta_g \\ \sin\delta_g & \cos\delta_g \end{bmatrix} \begin{bmatrix} v_{gD} \\ v_{gQ} \end{bmatrix} \tag{17.10}$$

17.3.2 Modeling of Excitation Control System

A simplified block diagram of the single time constant static exciter [1] is shown in Fig. 17.3. Here V_g is the terminal voltage of the generator and the signal V_{PS} is the output of PSS. The equations for the excitation system are given below.

$$\frac{dV_R}{dt} = \frac{1}{T_A}\left[-V_R + K_A(V_{ref} - V_g + V_{ps})\right] \tag{17.11}$$

$$\begin{aligned} E_{fd} &= V_R \quad if\ E_{fd\,\min} < V_R < E_{fd\,\max} \\ &= E_{fd\,\min} \quad if\ V_R < E_{fd\,\min} \\ &= E_{fd\,\max} \quad if\ V_R > E_{fd\,\max} \end{aligned} \tag{17.12}$$

$$V_g = \sqrt{v_{gD}^2 + v_{gQ}^2} \tag{17.13}$$

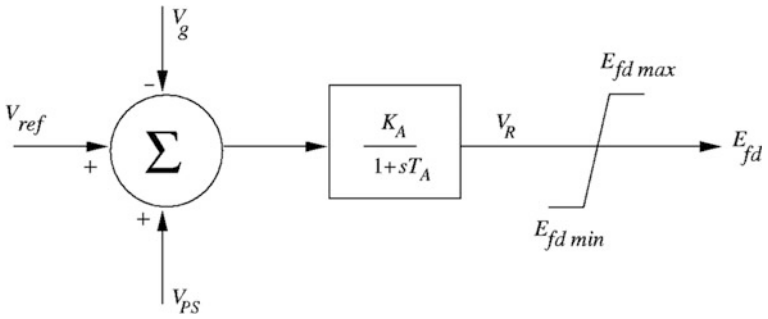

Fig. 17.3 Excitation system

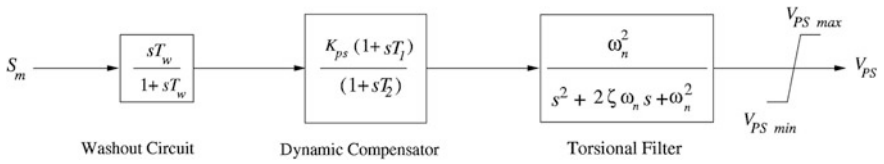

Fig. 17.4 Block diagram of power system stabilizer

17.3.3 Power System Stabilizer (PSS)

Modern power systems are affected by the problem of spontaneous low frequency oscillations particularly when operating under stressed system conditions associated with increased loading on transmission lines. A cost effective and satisfactory solution to the problem of undamped low frequency oscillations is to provide Power PSS which are supplementary controllers in excitation systems [1]. PSS is represented by the block diagram as shown in Fig. 17.4.

PSS consists of a washout circuit, dynamic compensator, a torsional filter. The input signal to the PSS is generator slip S_m. Where $S_m = \frac{\omega-\omega_B}{\omega_B}$ and $S_{m0} = \frac{\omega_0-\omega_B}{\omega_B}$, ω is the speed of the generator rotor (in rad/s).

The transfer function of PSS is taken as,

$$PSS(s) = \frac{sT_\omega}{1+sT_\omega} K_{PS} \frac{1+sT_1}{1+sT_2} \frac{\omega_n^2}{s^2+2\varsigma\omega_n s+\omega_n^2} \tag{17.14}$$

17.3.4 Electrical Network

For power system dynamic performance studies involving frequencies below fundamental (synchronous frequency) a single π equivalent of the transmission is adequate. When the line charging is not considered, the transmission line is modelled by a lumped resistance (R_L) and reactance (X_L). The transformers are modelled by resistance (R_t) and leakage reactance (X_t) between two busses. A single machine infinite bus system is shown in Fig. 17.1.

Defining $X_e = X_t + X_L + X_{sys}$, $R_e = R_t + R_L$ and X_C representing the compensating series capacitor, the equations governing the transmission line are given as,

$$\frac{dV_{cD}}{dt} = -\omega_0 V_{cQ} + \omega_B X_c i_D \tag{17.15}$$

$$\frac{dV_{cQ}}{dt} = \omega_0 V_{cD} + \omega_B X_c i_Q \tag{17.16}$$

where,

$$\begin{bmatrix} i_D \\ i_Q \end{bmatrix} = \begin{bmatrix} \cos\delta_g & \sin\delta_g \\ -\sin\delta_g & \cos\delta_g \end{bmatrix} \begin{bmatrix} i_d \\ i_q \end{bmatrix}$$

$$\begin{bmatrix} v_{gd} \\ v_{gq} \end{bmatrix} = \begin{bmatrix} R_e & -\sin\delta_g \\ -\frac{\omega}{\omega_B} X_e & R_e \end{bmatrix} \begin{bmatrix} i_d \\ i_q \end{bmatrix} + \frac{X_e}{\omega_B} \begin{bmatrix} \frac{di_d}{dt} \\ \frac{di_d}{dt} \end{bmatrix} + \begin{bmatrix} \cos\delta_g & -\sin\delta_g \\ \sin\delta_g & \cos\delta_g \end{bmatrix} \left\{ \begin{bmatrix} V_{cD} \\ V_{cQ} \end{bmatrix} + \begin{bmatrix} 0 \\ 1 \end{bmatrix} E_b \right\} \tag{17.17}$$

In (17.17), armature currents i_d and i_q are to be substituted from (17.4) and (17.7). The derivatives of armature currents, $\frac{di_d}{dt}$, $\frac{di_q}{dt}$ are expressed in terms of state variables representing flux linkages ($\psi_h, \psi_f, \psi_g, \psi_k, \psi_d$ *and* ψ_q from (17.2)–(17.9) respectively) to obtain the final expression for v_{gd} and v_{gq}.

17.3.5 Turbine Generator Mechanical System

The mechanical system consisting of rotors of generator, exciter and turbine shafts can be viewed as a mass-spring-damper system (see Fig. 17.5).

The equations for the *i*th mass (connected by elastic shaft sections to mass $(i-1)$ and mass $(i+1)$ is given by

$$M_i \frac{d^2\delta_i}{dt^2} + D_i' \frac{d\delta_i}{dt} + D_{i,i-1}' \left(\frac{d\delta_i}{dt} - \frac{d\delta_{i-1}}{dt} \right) + D_{i,i+1}' \left(\frac{d\delta_i}{dt} - \frac{d\delta_{i+1}}{dt} \right) + K_{i,i-1}(\delta_i - \delta_{i-1}) + K_{i,i+1}(\delta_i - \delta_{i+1}) = T_{mi} - T_{ei} \tag{17.18}$$

Combining all the equations, for a '*N*' mass system,

$$[M]p^2\delta + \left[D'\right]p\delta + [K]\delta = [T_m] - [T_e] \tag{17.19}$$

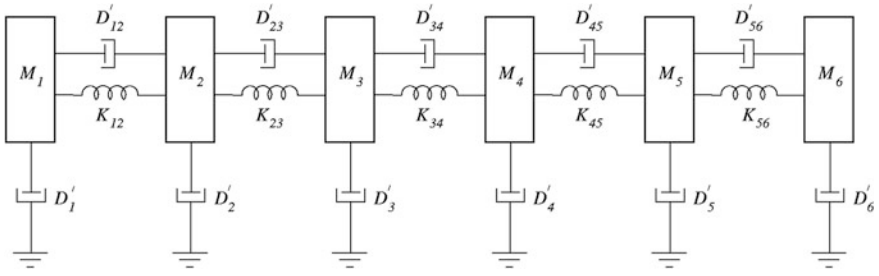

Fig. 17.5 Mass-spring-damper system with six masses

where [M] is a diagonal matrix, [D′] and [K] are tridiagonal symmetric matrices. [T_m] and [T_e] are the N Vectors of mechanical and electrical torques. [T_e] has only one non zero element corresponding to the generator rotor. Also, the mechanical torque directly acting on the generator rotor (T_{mg}) is zero. The inertia M_i is given by

$$M_i = \frac{2H_i}{\omega_B} D_i^{'} = \frac{D_i}{\omega_B} \tag{17.20}$$

where H_i is the inertia constant defined as, $\frac{1}{2}\frac{J_i \omega B^2}{S_B}$ J_i is the moment of inertia, S_B is the base MVA and D_i is the per unit damping coefficient, ω_B is the base speed in rad/s.

Alternate representation using electrical analogy

The mechanical system equations can also be written from analogy to an electrical (RLC) network [1]. Defining the per unit slip of a mass (M_i) as

$$S_i = \frac{\omega_{i-}\omega_B}{\omega_B} \tag{17.21}$$

where ω_i is the speed of rotor i. We can express

$$\frac{d\omega_i}{dt} = \omega_B (S_i - S_{i0}) \tag{17.22}$$

$$\begin{aligned} 2H_i \frac{dS_i}{dt} + D_i(S_i - S_{i0}) + D_{i,i-1}(S_i - S_{i-1}) + D_{i,i+1}(S_i - S_{i+1}) \\ + T_{i,i-1} + T_{i,i+1} = T_{mi} - T_{ei} \end{aligned} \tag{17.23}$$

$$\frac{dT_{i,i-1}}{dt} = K_{i,i-1}(S_i - S_{i-1})\omega_B \tag{17.24}$$

$$\frac{dT_{i,i+1}}{dt} = K_{i,i+1}(S_i - S_{i+1})\omega_B \tag{17.25}$$

where $T_{i,i-1}$ is the torque in the shaft section connecting mass i and $i-1$. It is not difficult to see that inertia (2H) is analogous to capacitance, slip analogous to voltage and torque analogous to current. The spring constant in pu ($K\omega B$) is analogous to the reciprocal of inductance. The pu damping coefficient (D) is analogous to conductance. For the six mass system shown in Fig. 17.6, the electrical analogy is shown in Fig. 17.6. There is no loss of generality in assuming S_{i0} (slip at the operating point) as zero.

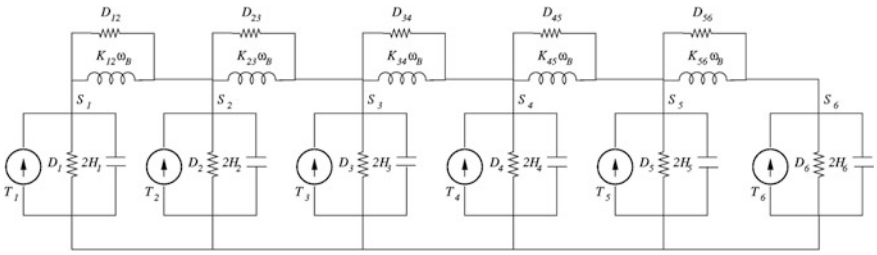

Fig. 17.6 An electrical analogue for the mass-spring-damper system of Fig. 17.5

The state variable for the network shown in Fig. 17.6 are only 11 given by

$$X_m = [S_1 S_2 S_3 S_4 S_5 S_6 T_{12} T_{23} T_{34} T_{45} T_{56}]^T \tag{17.26}$$

The additional state variable (required when writing equations for the electrical system) is δ_g (rotor angle corresponding to the generator. The equation for δ_g is given by

$$\frac{d\delta_g}{dt} = \omega_B (S_m - S_{m0}) \tag{17.27}$$

where $S_m = \frac{\omega - \omega_B}{\omega_B}$ and $S_{m0} = \frac{\omega_0 - \omega_B}{\omega_B}$, ω is the speed of the generator rotor (in rad/s). Substituting in Eq. (2.33) we get

$$\frac{d\delta_g}{dt} = (\omega - \omega_0) \tag{17.28}$$

Normally, the operating speed ω_0 is considered to be same as the nominal or rated speed which is taken as base speed ω_B and $S_{m0} = 0$.

17.4 Analytical Tools for SSR Study

The steady state SSR can be studied by damping torque analysis and eigenvalue analysis for which the system is linearized about an operating point. The transient SSR (transient torques) requires the system to be modelled in detail which takes care about all the non-linearity. The transient simulation can be done by EMTP or using MATLAB-SIMULINK [7]. The various methods of SSR analysis are described in the sections to follow.

17.4.1 Damping Torque Analysis

Frequency domain methods (based on the linearized system model) are used to screen the system conditions that give rise to potential SSR problems and identify those system conditions that do not influence the SSR phenomenon. Frequency domain studies are widely used for planning because of their computational advantage. The significance of this approach is that it allows planners to decide upon a suitable countermeasure for the mitigation of detrimental effects of SSR and to establish acceptable series compensation levels for a specified stage of system development. The damping torque analysis is a frequency domain method, which gives quick check to determine the torsional mode stability. The system is assumed to be stable if the net damping torque at any of the torsional mode frequency is positive [8]. However, damping torque method does not give an idea about the stability of the entire system.

In the method of damping torque analysis, the torsional interaction phenomenon between the electrical and mechanical system, is explained with the aid of complex torque coefficients. At any given oscillation frequency of the generator rotor, the developed electrical torque can be divided into two components, one in phase with the machine rotor angle δ_g and the other in phase with the machine rotor speed ω The former is termed as synchronizing torque and the latter as damping torque. An inadequate level of either of these two torque components may lead to the instability of the rotor oscillation modes. Synchronizing torque is a measure of the internally generated force to restore the machine rotor angle following an arbitrary small displacement of this angle. Instability is also indicated by the negative value of damping torque at a frequency of oscillation. For performing an analysis of the damping and synchronizing torques, the overall electromechanical system can be visualized as shown in Fig. 17.7 where ΔT_e, ΔS_m and $\Delta\delta_g$ are the incremental magnitudes of electrical torque, generator rotor speed and rotor angle respectively.

The output of electrical system comprising of generator and AC network, is the change in the electrical torque ΔT_e being input to the mechanical system.

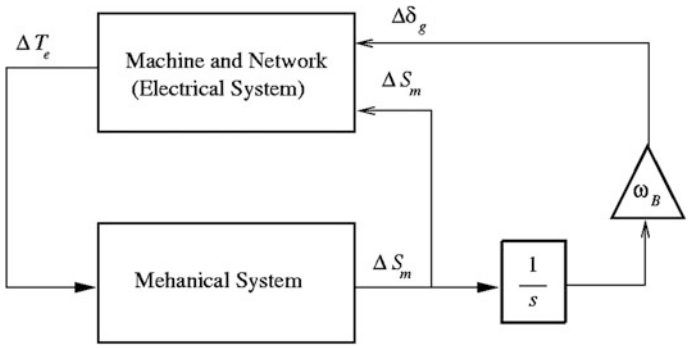

Fig. 17.7 Block diagram showing interaction between electrical and mechanical systems

The output of the mechanical system is the change in generator slip which is the input to the electrical system. The effect of the electrical system on the rotor torsional dynamics can be expressed in terms of the open-loop transfer function from generator slip S_m to electrical torque T_e which is defined in the frequency domain as,

$$\frac{\Delta T_e(j\omega)}{\Delta S_m(j\omega)} = T_{de}(\omega) - j\frac{T_{se}(\omega)}{\omega}\omega_B \tag{17.29}$$

where,

T_{de} Damping torque due to electrical system
T_{se} Synchronizing torque due to electrical system
ω Frequency in rad/s

The mechanical system dynamics can be given as below [8].

$$K_m + \frac{j\omega}{\omega_B}D_i = 0 \tag{17.30}$$

where, $K_m = \left(\frac{-2H_{mi}}{\omega_B}(\omega)^2 + K_i\right)$ and H_{mi}, K_i and D_i are the modal inertia constant, modal spring constant and modal damping for the ith torsional mode of frequency ω_i respectively. For the electrical system, the electrical spring constant K_e and damping constant D_e can be calculated as,

$$\frac{\Delta T_e(j\omega)}{\Delta \delta_g(j\omega)} = (K_e + \frac{j\omega}{\omega_B}D_e) \tag{17.31}$$

When both mechanical and electrical systems are interconnected, the entire system dynamics are governed by the equation as below [8].

$$(K_m + K_e + \frac{j\omega}{\omega_B}D_i + \frac{j\omega}{\omega_B}D_e) = 0 \tag{17.32}$$

when there is no damping $(D_i + D_e = 0)$, the frequencies of shaft oscillations must satisfy only the following criterion.

$$K_m + K_e = 0 \; when \; \omega = \omega_i \tag{17.33}$$

Since K_e is relatively small, the condition of (17.33) is satisfied at a point close to ω_i which is the modal frequencies. In the case of a resultant damping $(D_i + D_e \neq 0)$, the oscillation frequency will deviate only insignificantly from the undamped case. If the resultant damping is positive, then the oscillations will decay. Therefore an interaction between the electrical and mechanical systems occurs only

if the resultant damping for the frequencies satisfying (17.33) is negative [8] and the criterion is given by

$$K_m + K_e \cong 0 \quad and \quad D_i + D_e < 0 \tag{17.34}$$

Without the contribution from the electrical system, a torsional system has associated with it positive damping due to steam flows, friction, and windage losses which can be lumped together and termed mechanical damping T_{dm}. A torsional mode will become unstable when the electrical damping contribution T_{de} is negative and exceeds in magnitude T_{dm} (the inherent mechanical damping associated with the turbine-generator), leading to net damping torque (T_D) becoming negative. The instability of the ith torsional mode at frequency ω_i can be determined from the criterion.

$$T_D(\omega_i) = T_{dm}(\omega_i) + T_{de}(\omega_i) < 0 \tag{17.35}$$

The above criterion is equivalent to the net decrement factor (σ_i) satisfying

$$\sigma_i = \sigma_{mi} + \sigma_{ei} > 0 \tag{17.36}$$

where σ_i is defined as decrement factor and equivalent to the negative of the real part of eigenvalue (estimated in s^{-1}) which is a indicative of how fast the oscillations decay and can be expressed as,

$$\sigma_i = -\frac{T_D(\omega_i)}{4H_{mi}} \tag{17.37}$$

When mechanical damping is zero, (17.37) becomes,

$$\sigma_i = -\frac{T_{de}(\omega_i)}{4H_{mi}} \tag{17.38}$$

The impedance functions of the network as viewed from the generator internal bus are of significance and can be expressed with respect to Kron's (D-Q) synchronously rotating frame of reference. The electrical torque (ΔT_e) as a function of the change in per unit rotor speed (ΔS_m) can be derived from the knowledge of the impedance functions. At the generator internal bus, the following equation applies

$$\begin{bmatrix} \Delta_{iD} \\ \Delta_{iQ} \end{bmatrix} = \begin{bmatrix} Y_{DD}(s) & Y_{DQ}(s) \\ Y_{QD}(s) & Y_{QQ}(s) \end{bmatrix} \begin{bmatrix} \Delta_{eD} \\ \Delta_{eQ} \end{bmatrix} \tag{17.39}$$

The expression for determining contribution of damping torque coefficient (T_{de}) and synchronizing torque by the external transmission network can be written as [1],

$$T_{de}(\omega) = \mathrm{Re}\left[Y_{QD}(j\omega)\frac{\omega_0}{j\omega} + Y_{QQ}(j\omega)\right](E')^2 \tag{17.40}$$

$$T_{se}(\omega) = \mathrm{Im}\left\{\left[Y_{QD}(j\omega)\frac{\omega_0}{j\omega} + Y_{QQ}(j\omega)\right](E')^2 + i_{d0}\frac{\omega_B}{j\omega}E'\right\} \tag{17.41}$$

The damping torque coefficient T_{de} evaluated for a particular torsional mode frequency ω_m can be obtained by substituting $\omega = \omega_m$ in (17.40).

17.4.2 Eigenvalue Analysis

Eigenvalue technique is based on the mathematical model of the system using a set of differential equations which are linearized about an operating point. This technique was used by Found and Khu [9] and Bowler et al. [10] to study the torsional interactions and to determine the various conditions which lead to instability. The eigenvalues are computed by formulating the linearized state and output equations of the entire system. The eigenvalues are given by the solution of the matrix equation

$$det[\lambda I - A] = 0 \tag{17.42}$$

The eigenvalues are of the form $\lambda_{,i} = \sigma_i \pm j\omega_i$, where the real part σ_i is the decrement factor and imaginary part ω_i gives the oscillation frequency. If any $\sigma_i \geq 0$, then the system is unstable. The system is stable with $\sigma_i < 0$ for all i.

Since eigenvalues are dependent on the operating point, this analysis is useful for studying the steady state SSR and used to examine the effect of different series compensation levels and system configurations on the damping of torsional modes. In addition, eigenvalue analysis can be used to design controllers for damping torsional modes.

17.4.3 Transient Simulation

Transient simulation programs are used to analyze a broad range of problems. These programs use a step-by-step numerical integration method to solve the set of differential equations representing the overall system under study. The differential equations can be both linear and nonlinear. This technique allows detailed modelling of generators, system controllers, switching devices and various types of faults. This is advantageous to use when it is necessary to accurately model nonlinear devices. Since simulation allows detailed modelling of system taking into account the nonlinearities which cannot be neglected in the presence of a large disturbance, it is helpful in studying the transient torque problem.

The transient simulation can also be done by using the MATLAB-SIMULINK [7]. Here, the differential equations describing the system can be represented either in state-space form or in the transfer function form or by representing each differential equation as a combination of the basic blocks of SIMULINK such as summer, gain block and integrator. Nonlinearities can also be modelled and the system response to various inputs can be studied.

17.5 A Case Study

The system considered is adapted from IEEE First Benchmark Model (FBM) [5]. The generator, mechanical system and the transmission line parameters for the system under study is given in Appendix.

The system is represented schematically in Fig. 17.8 and consists of a generator, turbine and series compensated long transmission line.

Mechanical system consists of 6 masses including high pressure (HP), intermediate pressure (IP), low pressure-A (LPA), low pressure-B (LPB), generator (GEN), and exciter (EXC).The modelling aspects of the electromechanical system comprising the generator modelled with 2.2 model, mechanical system, the excitation system, PSS with torsional filter and the transmission line are given in Sect. 17.3.

The analysis is carried out on the IEEE FBM based on the following initial operating condition and assumptions.

1. The generator delivers 0.9 pu power to the transmission system with terminal voltage magnitude of 1.0 pu.
2. The input mechanical power to the turbine is assumed constant (dynamics of the turbine governor is neglected).
3. The turbine-generator mechanical damping is neglected for damping torque analysis.
4. Infinite bus voltage is taken as 1.0 pu.

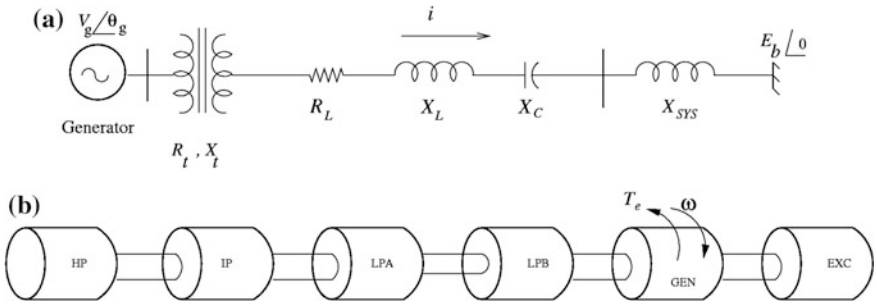

Fig. 17.8 IEEE first benchmark model. **a** Electrical system. **b** Mechanical system

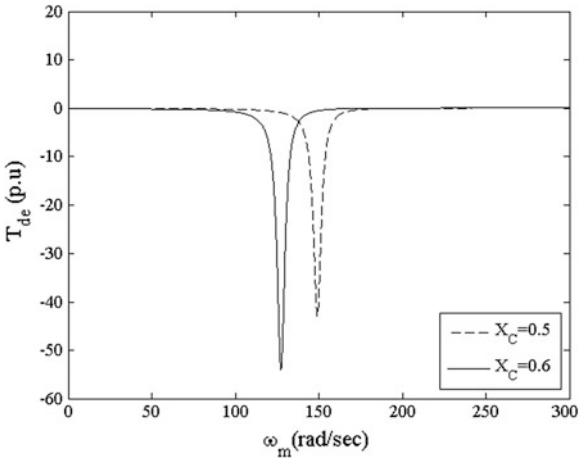

Fig. 17.9 Variation of damping torque with frequency for IEEE FBM

17.5.1 Results of Damping Torque Analysis

The damping torque analysis is carried out with X_C = 0.50 and X_C = 0.60. The variation of damping torque for these compensation levels are shown in Fig. 17.9 where the resonant frequencies shown are the complements ($f_0 - f_{er}$) of the electrical resonant frequency (f_{er}). If the complement of electrical resonant frequency ($f_0 - f_{er}$) matches with any of the mechanical system natural frequency (f_m), adverse torsional interaction is expected due to electromechanical resonance condition.

It is to be noted that, when X_C = 0.60 (here f_{er} = 250 rad/s), the peak negative damping occurs at about 127 rad/s ($f_0 - f_{er}$ = 377−250 rad/s) which matches with mode-2 of the FBM and adverse torsional interactions are expected. However, with X_C = 0.50 (here f_{er} = 228 rad/s), peak negative damping occurs at 149 rad/s ($f_0 - f_{er}$ = 377−228 rad/s) and since this network mode is not coinciding with any of the torsional modes, the system is expected to be stable. It is observed that, with the increased level of series compensation, the peak negative damping increases and causes significant increase in the electrical resonance frequency (f_{er}) and decrease in the frequency ($f_0 - f_{er}$) at which resonance occurs. It is to be noted that, the frequencies of torsional modes are practically unaffected by the electrical system.

17.5.2 Eigenvalue Analysis

In this analysis, the turbine-generator mechanical damping is considered and generator is modelled with 2.2 model (as indicated in Sect. 17.3.1). The entire electromechanical system is linearized about an operating point. The variation of real

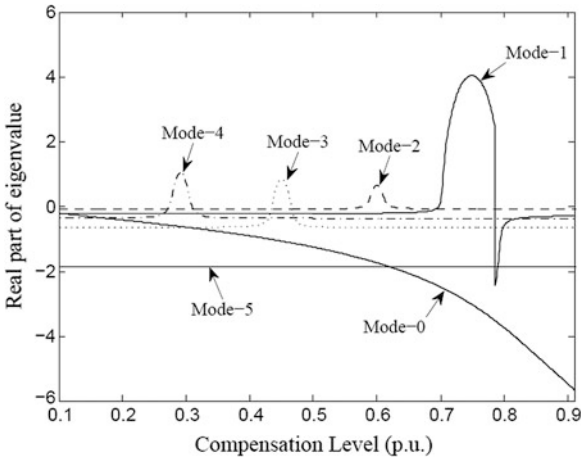

Fig. 17.10 Variation of real part of eigenvalue with compensation level for IEEE FBM

part of eigenvalues with series compensation is shown in Fig. 17.10 and it should be noted that, mode-2 becomes unstable at $X_C = 0.6$. When $X_C = 0.5$, real part of eigenvalues of all the torsional modes are found to be negative and the system is stable. The eigenvalues of the system matrix [A] when $X_C = 0.5$ and $X_C = 0.6$ are given in Table 17.1. It should be noted that, when $X_C = 0.60$, the subsynchronous network mode ($\omega_0 - \omega_{er}$) (is the complement of the network series resonance frequency) coincides with the torsional frequency of mode-2 and adverse torsional interactions are expected. Thus the results obtained by eigenvalue analysis are in agreement with that obtained by the damping torque method.

The following observations can be made with reference to Table 17.1.

1. The frequency and damping of the swing mode (mode-0) increases with the level of series compensation.
2. As the complement of network resonance frequency reduces, with higher compensation levels, it can be said that the lower torsional modes are most affected as the series compensation is increased. The damping of mode-1 is reduced and mode-2 is destabilized with increase of compensation from $X_C = 0.50{-}0.60$.
3. The damping of higher torsional modes 3 and 4 is marginally increased with increase of compensation.
4. Mode-5 is not affected with change in series compensation as its modal inertia is very high.
5. It is observed that, the damping of subsynchronous network mode with $X_C = 0.60$ increases with respect to the case when $X_C = 0.50$. However, this fact may not be always true as the eigenvalue of subsynchronous network mode with $X_C = 0.45$ and with $X_C = 0.65$ is found to be $-3.2364 \pm j160.57$ and $-0.92295 \pm j116.53$ respectively. In general, the damping of subsynchronous mode can decrease with the higher level of series compensation. The damping of supersynchronous network mode is marginally increased with higher level of series compensation.

Table 17.1 Eigenvalues of the entire system for IEEE FBM

Mode	With $X_C = 0.50$	With $X_C = 0.60$
0	–1.2528 ± *j* 8.1336	–1.7367 ± *j* 8.9280
1	–0.2278 ± *j* 99.1500	–0.2143 ± *j* 99.4580
2	–0.0718 ± *j*127.0000	0.6658 ± *j*127.0000
3	–0.6213 ± *j* 160.2000	–0.6459 ± *j* 160.4200
4	–0.3637 ± *j* 202.7900	–0.3646 ± *j* 202.8200
5	–1.8504 ± *j* 298.1700	–1.8504 ± *j* 298.1700
Network mode subsynchronous ($\omega_0 - \omega_{er}$)	–1.6108 ± *j* 149.1200	–1.9029 ± *j* 126.9500
Network mode supersynchronous ($\omega_0 + \omega_{er}$)	–2.9688 ± *j* 605.0300	–2.9806 ± *j* 626.7900
Exciter mode	–21.0700 ± *j* 25.8080	–21.7900 ± *j* 25.0460
Voltage measurement	–499.1700	–498.9900
PSS	–100.1900	–100.1900
PSS	–0.1003	–0.1004
Torsional filter	–6.5589 ± *j* 18.9270	–5.8579 ± *j* 18.5790
Generator	–39.9000	–39.9110
Generator	–20.2110	–20.2260
Generator	–2.8804	–2.8700

17.5.3 Transient Simulation

The transient simulation of the combined electromechanical system has been carried out using MATLAB-SIMULINK [7]. The simulation results for 10 % decrease in the input mechanical torque applied at 0.5 s and removed at 1 s with $X_C = 0.50$ and with $X_C = 0.60$ are shown in Fig. 17.11a, and b respectively.

It is clear from the Figs. 17.11 that, the system is stable with $X_C = 0.50$ and unstable with $X_C = 0.60$. The FFT analysis of the LPA-LPB section torque is performed between 3 and 7 s with the time spread of 1 s with $X_C = 0{:}60$. The results of FFT analysis is shown in Fig. 17.12. Referring to Fig. 17.12, it is observed that, in the time span of 3–4 s, the mode-1 component is higher compared to mode-2 component. As the time progresses, mode-2 component increase while all other torsional mode components decay. The decrement factor σ of mode-2 calculated from FFT analysis is found to be 0.6561 and is comparable to the real part of eigenvalue (0.6658) corresponding to mode-2 given in Table 17.1 and in agreement with eigenvalue results.

17.6 Modelling of STATCOM

STATCOM [11–13] is a second generation FACTS controller used for reactive power compensation. It is based on VSCs and uses power semiconductor devices such as GTOs or IGBTs. A 6-pulse 2-level STATCOM is shown in Fig. 17.13.

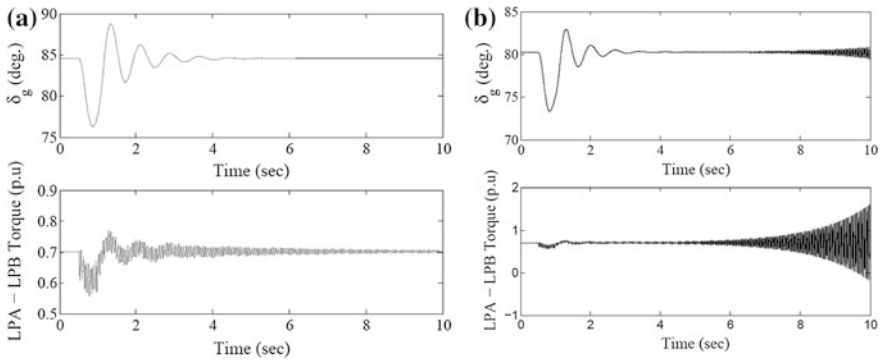

Fig. 17.11 Variation of rotor angle and LPA-LPB section torque for pulse change in input mechanical torque **a** $X_C = 0.50$, **b** $X_C = 0.60$

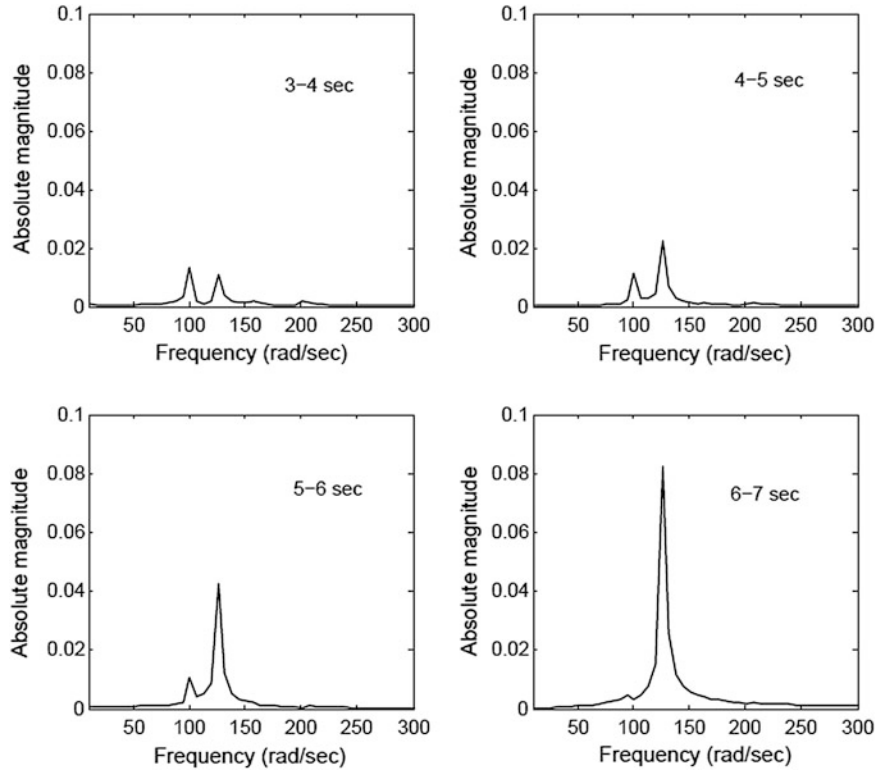

Fig. 17.12 FFT analysis of LPA-LPB section torque ($X_C = 0.60$)

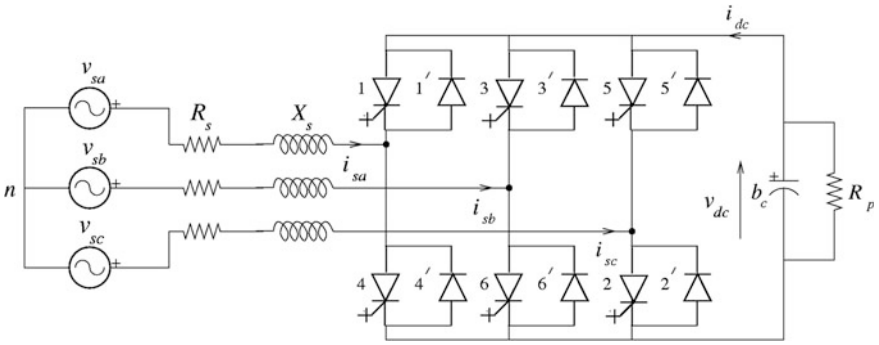

Fig. 17.13 6-pulse 2-level STATCOM

The 6-pulse STATCOM has substantial harmonics in the output voltage. The harmonics can be reduced by various PWM switching strategies. Alternatively, the 12-pulse operation of 2-level STATCOM eliminates 5th and 7th harmonics. When STATCOM is realized by 12-pulse 3-level converter, it is possible to obtain an operating condition where the 12-pulse three level converter works nearly like a 24 pulse converter and the harmonic components are reduced substantially.

The steady state representation of STATCOM is shown in Fig. 17.14. The primary control in the STATCOM is reactive current control. Since the reactive current in a STATCOM depends on the system parameters also, a closed loop control is essential. The reactive current reference of the STATCOM can be kept constant or regulated to control the bus voltage magnitude constant in which case a voltage controller sets the reactive current reference and forms an outer loop.

The work reported in this section is mainly focussed on the analysis and simulation of a series compensated system with STATCOM connected at the electrical center of the transmission line. The objective is to investigate the SSR characteristic of the combined system and suggest a possible SSR countermeasure by providing a subsynchronous damping controller (SSDC) which uses local signals.

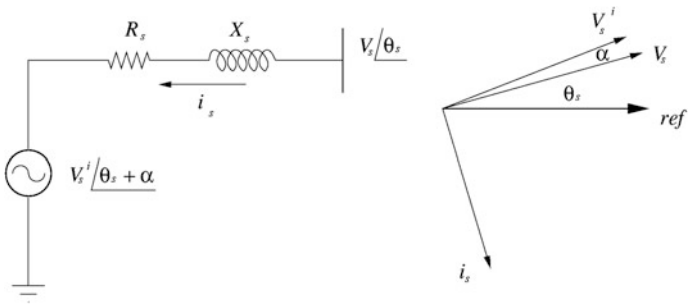

Fig. 17.14 Phasor diagram and steady state representation

17.6.1 Modelling of a 2-Level Converter Based STATCOM

A 6-pulse 2-level STATCOM [14, 15] is shown in Fig. 17.13. R_s and X_s are the resistance and leakage reactance of the converter transformer respectively. The following assumptions are made.

1. The devices are assumed to be ideal switches (lossless).
2. The bottom device of the converter leg turns on immediately after the top device is turned on and vice versa. In practice a small delay is provided to prevent both switches of a leg being on at the same time.

The differential equations for the STATCOM are

$$\frac{di_{sa}}{dt} = -\frac{\omega_B}{X_s}(R_s i_{sa} + v^i_{sa} - v_{sa)} \tag{17.43}$$

$$\frac{di_{sb}}{dt} = -\frac{\omega_B}{X_s}(R_s i_{sb} + v^i_{sb} - v_{sb)} \tag{17.44}$$

$$\frac{di_{sc}}{dt} = -\frac{\omega_B}{X_s}(R_s i_{sc} + v^i_{sc} - v_{sc)} \tag{17.45}$$

$$\frac{dv_{dc}}{dt} = -\frac{\omega_B}{b_c}\left(\frac{v_{dc}}{R_p} + i_{dc}\right) \tag{17.46}$$

where v^i_{sa}, v^i_{sb} and v^i_{sc} are the converter output phase voltages with respect to neutral and obtained as

$$\begin{bmatrix} v^i_{sa} \\ v^i_{sb} \\ v^i_{sc} \end{bmatrix} = \begin{bmatrix} S_{a2} \\ S_{b2} \\ S_{c2} \end{bmatrix} v_{dc} \tag{17.47}$$

S_{a2}, S_{b2} and S_{c2} are the switching functions [14, 16] for a 2-level 6-pulse VSC as shown in Fig. 17.15 and ω_B is the base frequency. v_{sa}, v_{sb} and v_{sc} are the STATCOM bus phase voltages with respect to neutral.

Since the switches are assumed to be ideal,

$$v_{dc} i_{dc} + v^i_{sa} i_{sa} + v^i_{sb} i_{sb} + v^i_{sc} i_{sc} = 0 \tag{17.48}$$

From (17.47) and (17.48), the following equation is obtained.

$$i_{dc} = -[i_{sa} S_{a2} + i_{sb} S_{b2} + i_{sc} S_{c2}] \tag{17.49}$$

The switching functions for 6-pulse converter have odd harmonics excluding triplen harmonics. Harmonics of the order $12\,k - 7$ and $12\,k - 5$, $k = 1, 2, 3\ldots$ can be

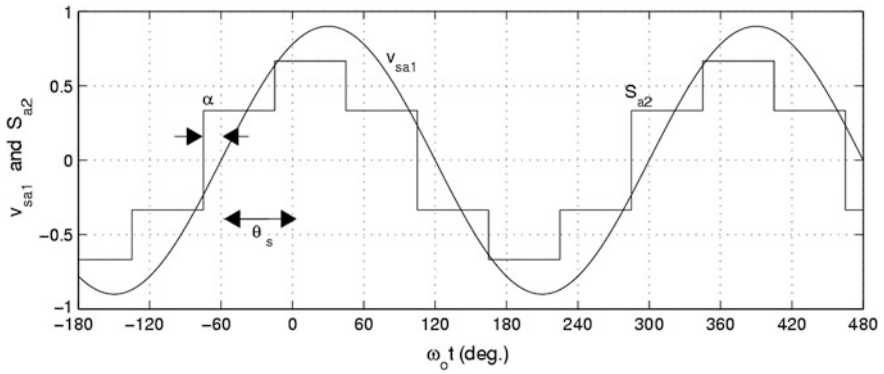

Fig. 17.15 Switching function Sa2, for a 2-level 6-pulse VSC

eliminated by using a 12-pulse converter which combines the output of two 6-pulse converters using transformers [11, 14, 16].

17.6.2 Equations in D-Q Reference Frame

Neglecting harmonics, the STATCOM bus phase voltages and converter output voltages in D-Q frame (v^i_{sD}, and v^i_{sQ}) are obtained by Kron's transformation [6] given below.

$$\begin{bmatrix} v^i_{sa} \\ v^i_{sb} \\ v^i_{sc} \end{bmatrix} = \sqrt{\frac{2}{3}} \begin{bmatrix} \cos(\omega_0 t) & \sin(\omega_0 t) & \frac{1}{\sqrt{2}} \\ \cos\left(\omega_0 t - \frac{2\pi}{3}\right) & \sin\left(\omega_0 t - \frac{2\pi}{3}\right) & \frac{1}{\sqrt{2}} \\ \cos\left(\omega_0 t + \frac{2\pi}{3}\right) & \sin\left(\omega_0 t + \frac{2\pi}{3}\right) & \frac{1}{\sqrt{2}} \end{bmatrix} \begin{bmatrix} v^i_{sD} \\ v^i_{sQ} \\ v^i_{sO} \end{bmatrix} \tag{17.50}$$

The zero sequence component v^i_{sO} is neglected as it is zero for balanced operation. The currents $i_{sa}i_{sb}i_{sc}$ and the voltages $v_{sa}v_{sb}v_{sc}$ are transformed to $i_{sD}i_{sQ}$ and $v_{SD}v_{SQ}$ in a similar manner.

The following equations in the D-Q variables can be given for describing STATCOM.

$$\frac{di_{sD}}{dt} = -\frac{R_s\omega_B}{X_s} i_{sD} - \omega_0 i_{sQ} + \frac{\omega_B}{X_s}\left[v_{sD} - v^i_{sD}\right] \tag{17.51}$$

$$\frac{di_{sQ}}{dt} = \omega_0 i_{sD} - \frac{R_s\omega_B}{X_s} i_{sQ} + \frac{\omega_B}{X_s}\left[v_{sQ} - v^i_{sQ}\right] \tag{17.52}$$

$$\frac{dv_{dc}}{dt} = -\frac{\omega_B}{b_c} i_{dc} - \frac{\omega_B}{b_c R_p} v_{dc} \tag{17.53}$$

where

$$v_{sD}^{i} = kv_{dc}\sin(\alpha + \theta_s)$$

$v_{sQ}^{i} = kv_{dc}\cos(\alpha + \theta_s), k = \frac{2\sqrt{6}}{\pi}$ for a 12-pulse converter, $\theta_s = \tan^{-1}\left(\frac{v_{sD}}{v_{sQ}}\right)$ angle of STATCOM bus voltage, $v_s = \sqrt{v_{sD}^2 + v_{sQ}^2}$ magnitude of STATCOM bus voltage.

In terms of D-Q components, the (17.48) can be expressed as,

$$v_{dc}i_{dc} + v_{sD}^{i}i_{sD} + v_{sQ}^{i}i_{sQ} = 0 \tag{17.54}$$

Substituting for v_{sD}^{i}, and v_{sQ}^{i} we get,

$$i_{dc} = -[k\sin(\alpha + \theta_s)i_{sD} + k\cos(\alpha + \theta_s)i_{sQ}] \tag{17.55}$$

The final state equations in the D-Q variables for a 2-level VSC based STATCOM are given by the following equations.

$$\frac{di_{sD}}{dt} = -\frac{R_s\omega_B}{X_s}i_{sD} - \omega_0 i_{sQ} - \frac{\omega_B k\sin(\alpha + \theta_s)}{X_s}v_{dc} + \frac{\omega_B}{X_s}v_{sD} \tag{17.56}$$

$$\frac{di_{sQ}}{dt} = \omega_0 i_{sD} - \frac{R_s\omega_B}{X_s}i_{sQ} - \frac{\omega_B k\cos(\alpha + \theta_s)}{X_s}v_{dc} + \frac{\omega_B}{X_s}v_{sQ} \tag{17.57}$$

$$\frac{dv_{dc}}{dt} = \frac{\omega_B k\sin(\alpha + \theta_s)}{b_c}i_{sD} + \frac{\omega_B k\cos(\alpha + \theta_s)}{b_c}i_{sQ} - \frac{\omega_B}{b_c R_p}v_{dc} \tag{17.58}$$

17.7 Controller Structures for STATCOM

The primary control loop for a STATCOM is the reactive current loop. Closed loop control is necessary as the reactive current depends not only on the control parameters (k and α) but also on the system voltage magnitude V_s and angle θ_s. Schauder and Mehta [17] define type-2 control structure for a 2-level (fundamental frequency Modulation with 180° conduction) STATCOM.

17.7.1 Type-2 Controller

With a 2-level VSC, Type-1 control requires PWM. In type-2 control, the PWM techniques are avoided in the interest of reducing switching losses and 180° conduction is practiced. The reactive current control can be achieved by controlling the magnitude of the converter output voltage $v_{sD}^{i} = kv_{dc}$. Since k is constant in Type-2

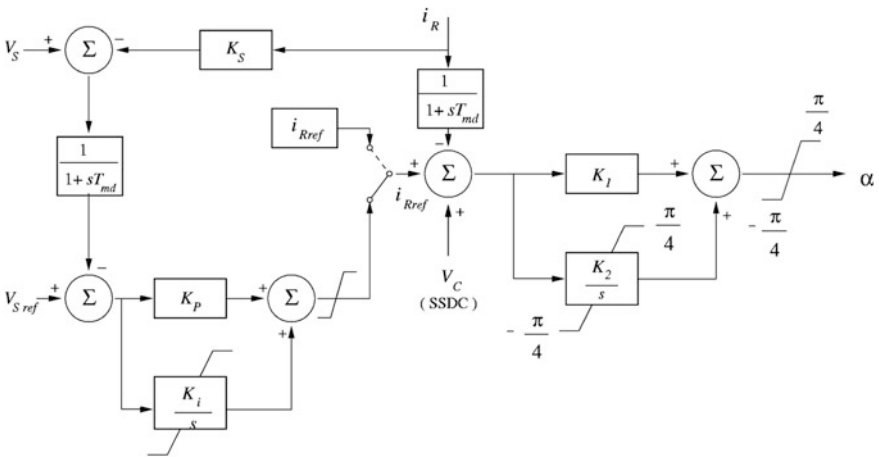

Fig. 17.16 Type-2 controller for 2-level VSC based STATCOM

control, the converter output voltage is varied by varying phase angle α over a narrow range [17]. The capacitor voltage is not regulated but depends upon the phase difference α between the converter output voltage and the bus voltage (very small, about 1°). This causes the variation of capacitor voltage over a small range with change in operating point. The capacitor voltage varies over a narrow range with α and reactive current is hence controlled.

From control view point, it is convenient to compute active (i_P) and reactive (i_R) currents drawn from the STATCOM as,

$$i_P = \frac{v_{sD}i_{sD} + v_{sQ}i_{sQ}}{V_s} = i_{sD}\sin\theta_s + i_{sQ}\cos\theta_s \tag{17.59}$$

$$i_R = \frac{v_{sD}i_{sQ} - v_{sQ}i_{sD}}{V_s} = -i_{sD}\cos\theta_s + i_{sQ}\sin\theta_s \tag{17.60}$$

The controller block diagram of Type-2 controller is shown in Fig. 17.16. The reactive current i_R is positive when STATCOM is operating in the inductive region and negative when STATCOM is operating in the capacitive region. The active current i_P is positive when STATCOM draws active power from the system.

17.8 Case Study with STATCOM

The system considered is a modified IEEE FBM [5]. The complete electromechanical system is represented schematically in Fig. 17.17, which consists of a generator, turbine, and series compensated long transmission line and STATCOM

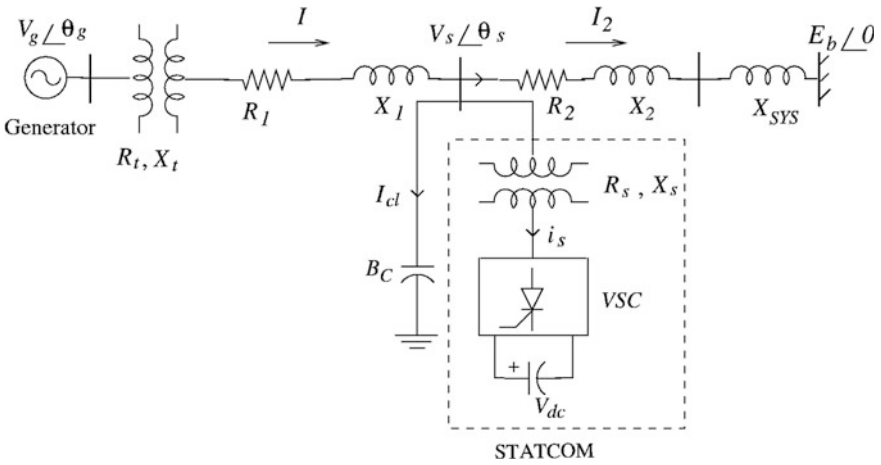

Fig. 17.17 Modified IEEE first benchmark model with STATCOM

connected at the electrical center of the transmission line. The data of the system are given in Appendix.

The Analysis is carried out based on the following initial operating condition and assumptions.

1. The generator delivers 0.9 pu power to the transmission system.
2. The dynamics of the turbine-governor systems are neglected and the input mechanical power to the turbine is assumed constant.
3. The compensation level provided by the series capacitor is set at 0.6 pu.
4. The dynamic voltage support at the midpoint of the transmission line is provided by STATCOM. In order to effectively utilize the full rating of STATCOM in both inductive as well as capacitive range, a fixed shunt capacitor is also used at the STATCOM bus. The rating of STATCOM is selected as ± 150 MVAr. At the operating point considered, the STATCOM supplies 99 MVAr and the remaining reactive power is supplied by fixed capacitor to maintain bus voltage 1.015 pu. Under dynamic conditions STATCOM supplies/absorbs the reactive power to maintain the bus voltage at the specified value. The type-2 controller (refer Fig. 17.16) is adopted for the control of reactive power output of STATCOM.

17.8.1 Damping Torque Analysis

The damping torque analysis is performed with detailed D-Q model of STATCOM [18]. The admittance function $[Y] = \begin{bmatrix} Y_{DD}(s) & Y_{DQ}(s) \\ Y_{QD}(s) & Y_{QQ}(s) \end{bmatrix}$ seen at the generator internal bus in D-Q axes is computed with the presence of STATCOM and damping

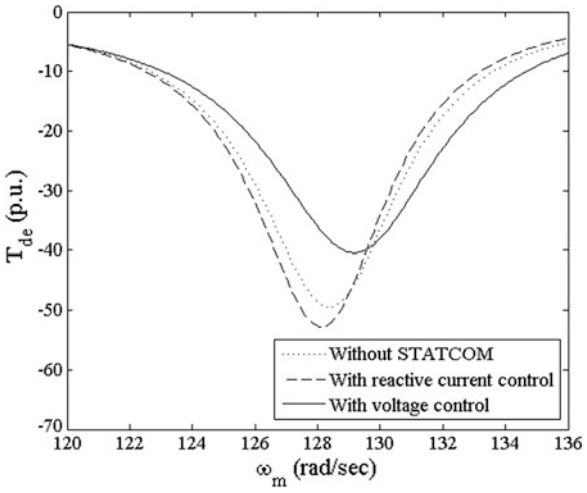

Fig. 17.18 Variation of damping torque with detailed D-Q model of a 2-level VSC based STATCOM

torque is evaluated as given by (17.40). The damping torque with detailed D-Q model of STATCOM is shown in Fig. 17.18.

The system is unstable since the peak negative damping occurs near about 127 rad/s which matches with the mode-2 of IEEE FBM. The voltage control reduces the peak negative damping and marginally increases the resonance frequency. It is interesting to note that, the reactive current control marginally increases the undamping compared to the case without STATCOM. This is not surprising as the contribution of positive supersynchronous damping torque due to shunt capacitor has reduced with the lesser value of shunt capacitor used. It is also observed that, the voltage control reduces the damping of the torsional modes particularly in the range of frequencies greater than 130 rad/s as compared to reactive current control.

17.8.2 Eigenvalue Analysis

The overall system with STATCOM is linearized about an operating point and the eigenvalues of the system matrix [A] are given in Table 17.2.

Table 17.2 shows that, mode 2 is unstable at the operating point considered. The frequency of the swing mode (mode-0) marginally increases with the inclusion of STATCOM. The negative damping of critical torsional mode-2 has marginally increased compared to the case without STATCOM. The voltage control reduces the undamping of critical torsional mode-2 and improves the damping of swing mode. This latter fact is not in agreement with the results of damping torque analysis shown in Fig. 17.18 and indicates the generator model affects the damping

Table 17.2 Torsional mode eigenvalues of the system with a 2-level VSC based STATCOM

Mode	Without STATCOM	With STATCOM	
		Reactive current control	Voltage control
0	–2.0489 ± *j* 9.3762	–2.0619 ± *j* 9.3784	–2.4301 ± *j* 9.5310
1	–0.2293 ± *j* 99.4370	–0.2290 ± *j* 99.4410	–0.2074 ± *j* 99.4100
2	0.5523 ± *j*127.2900	0.6300 ± *j*127.2500	0.3310 ± *j*127.3000
3	–0.6450 ± *j* 160.4400	–0.6470 ± *j* 160.4400	–0.6440 ± *j* 160.4400
4	–0.3643 ± *j* 202.8400	–0.3654 ± *j* 202.8400	–0.3648 ± *j* 202.8400
5	–1.8504 ± *j* 298.1700	–1.8504 ± *j* 298.1700	–1.8504 ± *j* 298.1700
Network mode subsynchronous ($\omega_0 - \omega_{er}$)	–1.7926 ± *j* 127.6900	–1.6920 ± *j* 127.5100	–1.6920 ± *j* 128.4100
Network mode supersynchronous ($\omega_0 + \omega_{er}$)	–2.9801 ± *j* 625.7700	–3.0868 ± *j* 625.4400	–3.0734 ± *j* 625.4500

of swing mode. Mode-5 is not affected with the inclusion of STATCOM as its modal inertia is very high. The damping of subsynchronous network mode increases with voltage control.

17.8.3 Transient Simulation

The eigenvalue analysis uses equations in D-Q variables where the switching functions are approximated by their fundamental frequency components (neglecting harmonics in the output voltages of the converters). To validate the results obtained from damping torque and eigenvalue analysis, transient simulation of the overall nonlinear system is carried out using the detailed 3 phase model of STATCOM where the switching of the converter is modelled by switching functions (The harmonics generated by VSC are considered).The transient simulation of the overall system including STATCOM (with voltage control) has been carried out using 3 phase model using MATLAB-SIMULINK [7]. The simulation results for 10 % decrease in the input mechanical torque applied at 0.5 s and removed at 1 s with 3 phase model of STATCOM are shown in Fig. 17.19. It is clear from the Fig. 17.19 that, the system is unstable as the oscillations in rotor angle and LPA-LPB section torque grow with time.

The FFT analysis of the LPA-LPB section torque (variation are obtained with 3 phase model of STATCOM) is performed between 6 and 10 s with the time spread of 1 s. The results of FFT analysis is shown in Fig. 17.20. It is observed that as the time progresses, mode-2 component increases while all other torsional mode components (particularly mode-1) decay. The decrement factor σ of mode-2 calculated from FFT analysis is found to be 0.3326 and is comparable to the real part of eigenvalue (0.3310) corresponding to mode-2 given in Table 17.2 and in agreement with eigenvalue results. Hence the D-Q model is quite accurate in predicting the system performance.

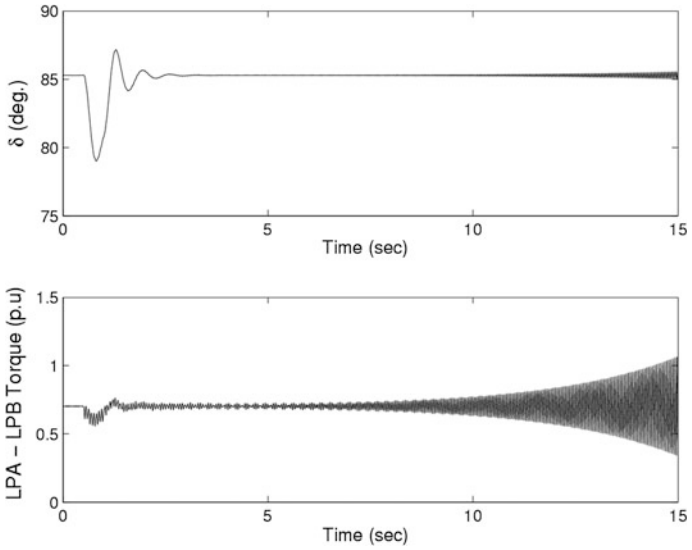

Fig. 17.19 Variation of rotor angle and LPA-LPB section torque for pulse change in input mechanical torque [3 phase model of a 2-level VSC based STATCOM (with voltage control)]

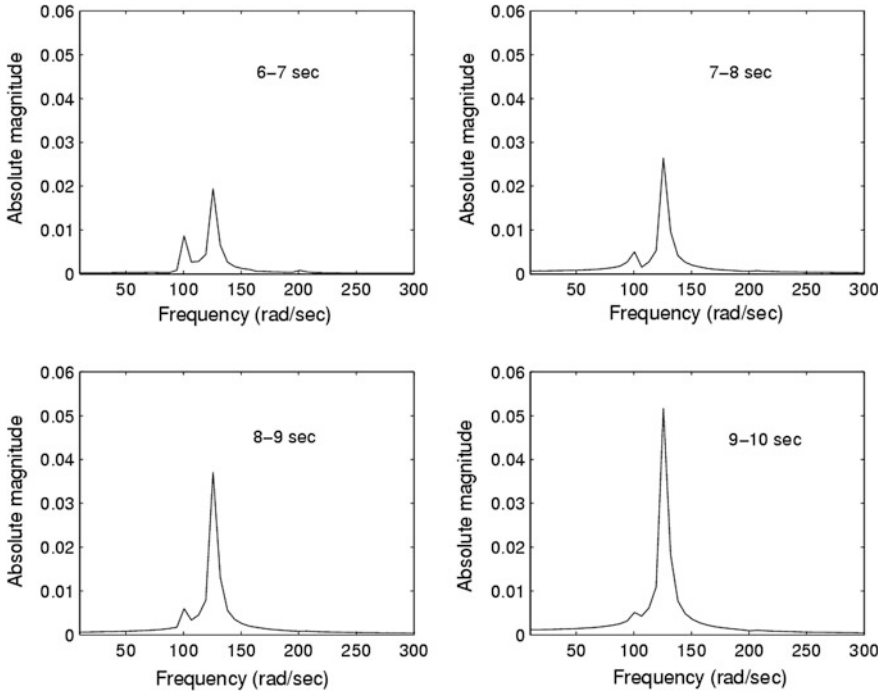

Fig. 17.20 FFT analysis of LPA-LPB section torque [3 phase model of a 2-level VSC based STATCOM (with voltage control)]

17.9 Design of SubSynchronous Damping Controller (SSDC)

Improvement of the damping of SSR modes can be achieved by SSDC. The Thevenin voltage signal (V_{th} = Vs + X_{th}·is) derived from the STATCOM bus voltage (Vs) and the reactive current (is) is used for damping of power swings in references [19, 20]. Here the SSDC [represented by a transfer function $T_2(s)$] which takes the Thevenin voltage signal as input is used to modulate the reactive current reference $i_{R\ ref}$ to improve the damping of the unstable torsional mode. The block diagram of SSDC [18] is shown in Fig. 17.21.

The objective of SSDC is to enhance the damping torque at the critical range of torsional frequencies such that the net damping torque is positive. The critical range of frequencies is decided by the negative damping introduced by the electrical system in the absence of SSDC.

It is observed from the damping torque analysis with STATCOM voltage control (as shown in Fig. 17.18) that, the negative damping is more significant in the range of frequency of 110–135 rad/s. In order that, the SSDC contributes to the positive damping the $T_{de(des)}$ is taken to be positive. The $T_{de(des)}$ is set to ensure that, the damping controller increases the damping without affecting the synchronizing torque contribution. Here the desired damping torque $T_{de(des)}$ is taken as 1 (pu) as larger $T_{de(des)}$ causes network mode eigenvalue unstable.

It is simpler to design the SSDC transfer function by parameter optimization with the objective of minimizing the deviations between the desired damping torque ($T_{de(des)}$) and the actual damping torque (T_{de}).

The structure of the transfer function $T_2(s)$ is taken as,

$$T_2(s) = \frac{as + b}{s^2 + cs + d} \tag{17.61}$$

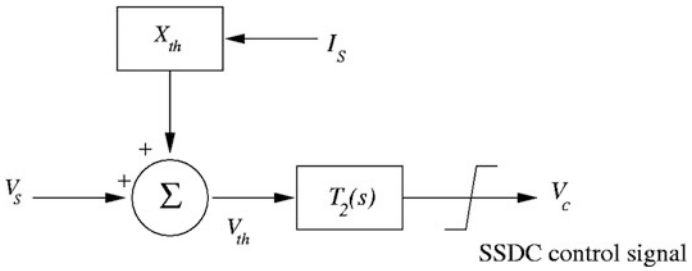

Fig. 17.21 Block diagram of subsynchronous damping controller (SSDC) for STATCOM

The objective function for optimizing of the parameters 'r' (a, b, c and d) of the transfer function $T_2(s)$ is taken as,

$$\begin{aligned} \text{Minimize} \quad & f(r) = \sum_{\omega_{\min}}^{\omega_{\max}} \left(T_{de(des)} - T_{de}\right)^2 \\ \text{subjected to,} \quad & \begin{cases} c > 0 \\ c^2 - 4d < 0 \end{cases} \end{aligned} \tag{17.62}$$

$\omega_{\min} \leq \omega \leq \omega_{\max}$, $\omega_{\min}$ and $\omega_{\max}$ are taken to be 110 rad/s and 135 rad/s (the critical frequency range).

The constraints ensure that the poles of the transfer function $T_2(s)$ are complex and have negative real parts. The optimization routine 'fmincon' of MATLAB is used for the solution.

The designed value of $T_2(s)$ (SSDC) is obtained as [18],

$$T_2(s) = \frac{-13,631s + 41,611}{s^2 + 8.9135s + 23,492}$$

The X_{th} is Thevenin reactance (a tunable parameter) and selected so as to maximize the damping torque of the overall system computed with the designed transfer function $T_2(s)$.

17.10 Analysis with SSDC

The analysis with SSDC is carried out based on damping torque analysis, eigenvalue analysis and transient simulation. While damping torque and eigenvalue analysis considers D-Q model of STATCOM, the transient simulation considers both the detailed D-Q and 3 phase nonlinear models of STATCOM.

17.10.1 Damping Torque Analysis with SSDC

The damping torque with detailed D-Q model of 2-level VSC based STATCOMs are shown in Fig. 17.22. It is seen that, the peak negative damping is significantly reduced with SSDC and occurs at a lower frequency of about 52 rad/s. Since this frequency does not match with any of the torsional modes the system is expected to be stable. It should be noted that, the damping torque is positive with SSDC in the

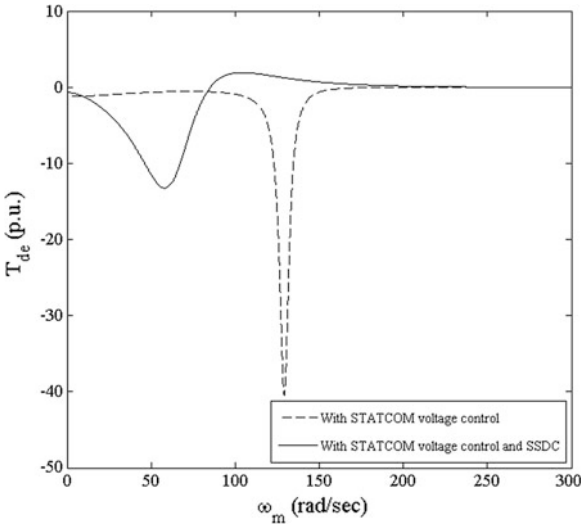

Fig. 17.22 Variation of damping torque with detailed D-Q model of a 2-level VSC based STATCOM and SSDC

range of torsional mode frequencies and causes the damping of SSR It is expected that, the designed SSDC contributes positive damping in the range of critical torsional mode frequencies and ensures stable system.

17.10.2 Eigenvalue Analysis

The eigenvalues of the overall system for a 2-level VSC based STATCOM on voltage control and SSDC are shown in Table 17.3.

Table 17.3 Torsional mode eigenvalues of the system with a 2-level VSC based STATCOM and SSDC

Mode	Eigenvalues
0	–2.4421 ± *j* 9.5275
1	–0.2399 ± *j* 99.3810
2	–0.0613 ± *j*127.2700
3	–0.6643 ± *j* 160.4700
4	–0.3655 ± *j* 202.8400
5	–1.8504 ± *j* 298.1700
Network mode subsynchronous ($\omega_0 - \omega_{er}$)	–0.1829 ± *j* 132.8800
Network mode supersynchronous ($\omega_0 + \omega_{er}$)	–3.1030 ± *j* 625.4400

Comparing the eigenvalue results without SSDC (refer Table 17.2 and with SSDC (Table 17.3), the following observations can be made.

1. The damping of critical mode-2 has significantly improved with SSDC.
2. The damping of all torsional modes is increased with SSDC.
3. Mode-5 is not affected as its modal inertia is very high.
4. The damping of subsynchronous network mode is reduced with SSDC.

17.10.3 Transient Simulation

The transient simulation of the overall system including STATCOM with SSDC has been carried out with 3 phase model of STATCOM using MATLAB-SIMULINK [7]. The simulation results for 10 % decrease in the input mechanical torque applied at 0.5 s and removed at 1 s with a 2-level VSC based STATCOM along with SSDC is shown in Fig. 17.23.

The FFT analysis of line current magnitude with SSDC is shown in Fig. 17.24 and it is very clear that, the system is stable with SSDC. The FFT analysis of line current when SSDC is used (refer Fig. 17.24) shows that, it contains a predominant 21 Hz component corresponding to torsional mode-2 which decays with time. The damping torque analysis, eigenvalue analysis and transient simulations show that, the SSDC is effective in stabilizing the critical torsional modes.

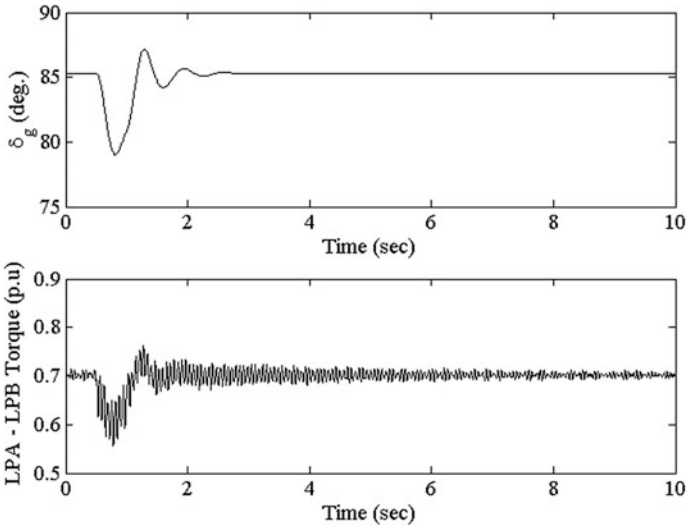

Fig. 17.23 Variation of rotor angle and LPA-LPB section torque for pulse change in input mechanical torque (with 3 phase model of a 2-level VSC based STATCOM with SSDC)

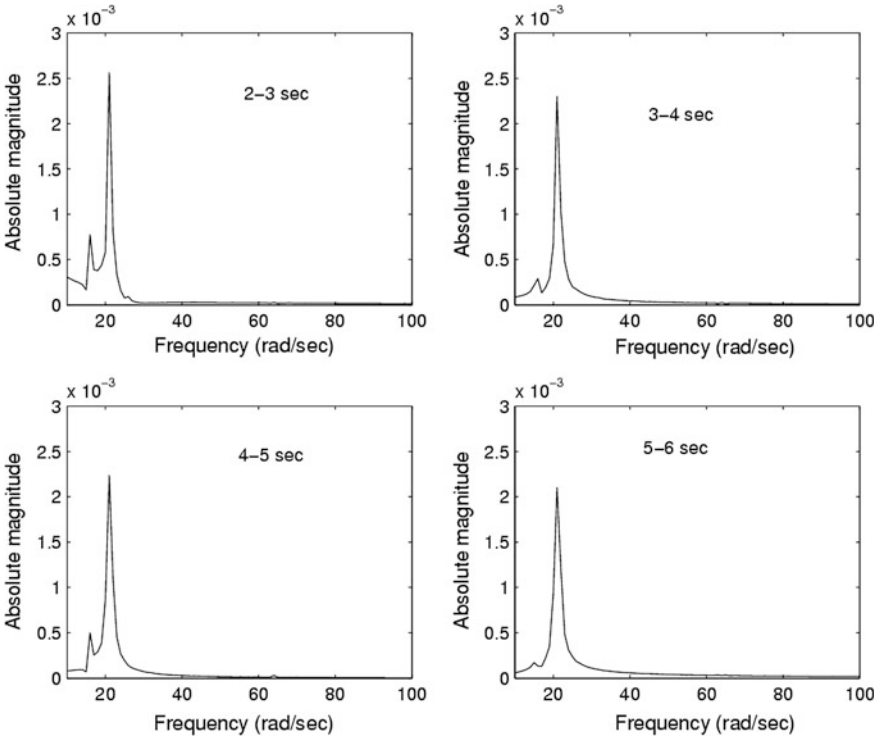

Fig. 17.24 FFT analysis of line current magnitude (with D-Q model of VSC based STATCOM with SSDC)

Appendix

System Data

The technical data for the case studies are summarized below.

IEEE FBM

The system data is the modified IEEE First benchmark model. Data are given on 892.4 MVA, 500 kV base. The base frequency is taken as 60 Hz.

Generator Data

$$x_d = 1.79, \quad x_d^{'} = 0.169, \quad x_d^{''} = 0.135, \quad x_q = 1.71, \quad x_q^{'} = 0.228, \quad x_q^{''} = 0.20, \quad R_a = 0$$

$$T_{do}^{'} = 4.3,\ T_{do}^{''} = 0.032,\ T_{qo}^{'} = 0.85,\ T_{qo}^{''} = 0.05,\ T_d^{'} = 0.4,$$
$$T_d^{''} = 0.0259,\ T_q^{'} = 0.1073,\ T_q^{''} = 0.0463$$

Multimass mechanical system

The self damping of 0.20 is considered for HP, IP, LPA and LPB turbines. The mutual damping between HP-IP, IP-LPA, LPA-LPB and LPB-GEN are taken as 0.30 whereas for GEN-EXC it is taken as 0.005 (Table 17.A.1).

The fractions of total mechanical torque T_m for HP, IP, LPA and LPB turbines are takes as 0.30, 0.26, 0.22 and 0.22 respectively.

Transformer and transmission line data

$$R_t = 0.00,\ X_t = 0.14,\ R_L = 0.02,\ X_L = 1.0,\ X_{SYS} = 0.06$$

Excitation System

$$K_A = 200,\ T_A = 0.025,\ E_{fd\max} = 6,\ E_{fd\min} = -6$$

Power System Stabilizer

$$T_w = 10, K_{PS} = 6, T_1 = 0.10, T_2 = 0.01, \xi = 0.5, \omega_n = 22\text{rad/s}$$

$$V_{PS\max} = 0.10, V_{PS\min} = -0.10$$

Table 17.A.1 Multimass mechanical system data

Mass	Inertia constant H (s)	Shaft sections	Spring constant K in pu torque/rad
HP turbine	0.092897	HP-IP	19.303
IP turbine	0.155589	IP-LPA	34.929
LPA turbine	0.858670	LPA-LPB	52.038
LPB turbine	0.884215	LPB-GEN	70.858
Generator	0.868495	GEN-EXC	2.8220
Exciter	0.0342165		

Data for Analysis with STATCOM

Transformer and transmission line data

$$R_t = 0.00,\ X_t = 0.14,\ R_1 = 0.016,\ X_1 = 0.8,\ X_C = 0.6$$

$$B_C = 0.25213,\ R_2 = 0.004,\ X_2 = 0.2,\ X_{SYS} = 0.06$$

STATCOM Data

$$R_s = 0.0381, X_s = 0.5711, b_C = 0.2984, R_P = 299.66$$

Voltage controller

$$K_s = 0.15, K_p = 0.0, K_i = -100, i_{Rmax} = 0.1681, i_{Rmin} = -0.1681$$

Type II Controller

$$K_1 = 0.175, K_2 = 3.5, SSDC : X_{th} = 0.16, \textit{Limits on SSDC output} = \pm 0.00285$$

References

1. Padiyar KR (1999) Analysis of subsynchronous resonance in power systems. Kluwer Academic Publishers, Boston
2. Anderson PM, Agarwal BL, Van Ness JE (1989) Subsynchronous resonance in power systems. IEEE Press, New York
3. IEEE SSR Task Force (1980) Proposed terms and definitions for subsynchronous resonance in series capacitor compensated transmission lines. IEEE Trans Power Apparatus Syst PAS-92:506-511
4. Hall MC, Hodges DA (1976) Experience with 500 kV subsynchronous resonance and resulting turbine generator shaft damage at mohave generating station. IEEE PES winter meeting, Publication CH1066-0-PWR, pp 22–30
5. IEEE SSR working group (1977) First benchmark model for computer simulation of subsynchronous resonance. IEEE Trans Power Apparatus Syst PAS-96(5):1565–1572
6. Padiyar KR (2002) Power system dynamics—stability and control, 2nd edn. B. S. Publications, Hyderabad
7. The Math Works Inc (1999) Using MATLAB-SIMULINK
8. Canay IM (1982) A novel approach to the torsional interaction and electrical damping of the synchronous machine, part-I: theory, part-II: application to an arbitrary network. IEEE Trans Power Apparatus Syst PAS-101(10):3630–3647
9. Found AA, Khu KT (1978) Damping of torsional oscillations in power systems with series compensated systems. IEEE Trans Power Apparatus Syst PAS-97: 744–753

10. Bowler CEJ, Ewart DN, Concordia C (1973) Self excited torsional frequency oscillations with series capacitors. IEEE Trans Power Apparatus Syst PAS-92:1688–1695
11. Hingorani NG, Gyugyi L (2000) Understanding FACTS—concepts and technology of flexible AC transmission systems. IEEE Press, New York
12. Gyugyi L (1994) Dynamic compensation of AC transmission lines by solid state synchronous voltage sources. IEEE Trans Power Deliv 9(2):904–911
13. Schauder C, Gernhardt M, Stacey E, Cease TW, Edris A, Lemak T, Gyugyi L (1995) Development of § 100 Mvar Static Condenser for Voltage Control of Transmission Systems. IEEE Trans Power Deliv 10(3):1486–1496
14. Prabhu N (2004) Analysis of subsynchronous resonance with voltage source converter based FACTS and HVDC controllers. PhD thesis, Indian Institute of Science, Bangalore
15. Padiyar KR, Kulkarni AM (1997) Design of reactive current and voltage controller of static condenser. Int J Electr Power Energy Syst 19(6):397–410
16. Padiyar KR (2007) FACTS controllers in power transmission and distribution. New Age International (P) Limited, New Delhi
17. Schauder C, Mehta H (1993) Vector analysis and control of advanced static var compensator. IEE Proc-C 140(4):299–306
18. Padiyar KR, Prabhu N (2006) Design and performance evaluation of sub synchronous damping controller with STATCOM. IEEE Trans Power Deliv 21(3):1398–1405
19. Kulkarni AM, Padiyar KR (1998) Damping of power swings using shunt FACTS controllers. Fourth workshop on EHV technology, Bangalore
20. Padiyar KR, Swayam Prakash V (2003) Tuning and performance evaluation of damping controller for a STATCOM. Int J Electr Power Energy Syst 25:155–166

Chapter 18
STATCOM Application for Mitigation of Subsynchronous Resonance in Wind Farms Connected to Series-Compensated Transmission Lines

Akshaya Kumar Moharana and Rajiv K. Varma

Abstract Large-scale integration of wind farms in transmission networks has led to several challenges; one of which is the need for increased transmission capacity to transport bulk amounts of wind power. Series compensation is an established means of enhancing the power transfer capability of existing transmission lines and is being increasingly considered for integrating large wind power plants. However, series-compensated transmission lines may cause subsynchronous resonance (SSR) in turbine-generators, which can lead to electrical instability at subsynchronous frequencies and potential turbine-generator shaft failures. This chapter presents a thorough mathematical analysis of SSR in a double-cage induction generator (IG) based wind farm connected to a series-compensated transmission line and its mitigation. The prediction of SSR is done for a wide range of wind farm sizes and series compensation levels through eigenvalue studies and equivalent circuit analysis. Two types of STATCOM controllers are proposed and tested with an aggregated wind farm model. In the proposed controller-I the DC voltage remains uncontrolled and only the angular difference between the STATCOM terminal and the Point of Common Coupling (PCC) bus voltage is controlled. In controller-II, the DC link capacitor voltage is controlled by the phase angle difference between the STATCOM terminal and PCC bus voltage. Both the modulation index and angle are controlled in this controller. Studies are conducted for three different induction generators used in commercial wind farms. Fault studies are also conducted at different locations.

Keywords Wind turbine · Induction generator · Series compensation · Subsynchronous resonance · Induction generator effect · Torsional interaction · Torque amplification · Eigenvalue analysis · Equivalent circuit analysis · STATCOM

A.K. Moharana (✉)
Power System Studies, Powertech Labs Inc., Surrey, BC, Canada
e-mail: akshaya.moharana@powertechlabs.com

R.K. Varma
Department of Electrical and Computer Engineering, University of Western Ontario, London, ON, Canada
e-mail: rkvarma@uwo.ca

F. Shahnia et al. (eds.), *Static Compensators (STATCOMs) in Power Systems*, Power Systems, DOI 10.1007/978-981-287-281-4_18

18.1 Introduction

In the last thirty years the wind energy industry has seen a rapid growth in comparison to other renewable energy industries. Enhanced technology and design improvements have played a significant role in increasing their penetration levels. The size of the wind turbines has increased, the cost has been reduced, and controllability of the wind power plants has been improved, in recent years. The advancements in power electronics have placed wind energy as a serious and competitive alternative to other renewable sources [1–4]. Particularly North Europe, Germany, Spain, USA, Canada, China, and India have shown a strong achievement in expanding the wind energy systems.

With the recent developments in power electronics, most wind farms in Europe and North America use Doubly Fed Induction Generators (DFIG) and the most recent trend is to use full converter based wind turbine generators [5–7]. However, there are large number of wind farms across USA, India, and Australia, etc., which utilize fixed speed Induction Generator based wind turbines. Currently many of these larger scale wind farms are either in operation or under construction. Brahmanvel wind farm in India has a total rating of 549.1 MW. The largest IG based wind farm in USA is the Twin Groves wind farm in Illinois with an installed capacity of 396 MW. A few of the other large scale IG based wind farms are Maple Ridge wind farm (321.75 MW) in New York, Fowler Ridge wind farm (300.30 MW) in Indiana, Pioneer Prairie wind farm (301.95 MW) in Iowa, and Stateline wind farm (300.96 MW) on the border of Washington and Oregon, USA [1].

18.1.1 SSR in Wind Farms

Large-scale integration of wind farms in the transmission and distribution networks has led to several challenges [8, 9]. One of these challenges is the need for substantial upgrade of transmission infrastructures including the construction of new transmission lines to accommodate the increased power flow from the wind plants [10–12]. It is well known that series compensation is an effective means of enhancing the power transfer capability of existing transmission lines. Hence, it is being increasingly considered for integrating large wind generation plants [12, 13]. However, series capacitors have been known to cause SSR as described above. Furthermore, the presence of series capacitors in the line may also potentially cause SSR in induction generator based wind turbine generators [10, 14].

References [15, 16] presented a detailed analytical and experimental result of SSR of a squirrel-cage induction motor and a deep bar induction motor, respectively, fed by a series-compensated feeder.

In 2003, the impact of a large-scale integration of wind farms into a utility grid was studied [10], which focused on major interconnection issues. In this paper, both conventional IG based wind farms and DFIG based wind farms were considered.

Wind farm interaction with series-compensated transmission line was discussed for the first time in this paper.

In December 2005, Xcel energy released a report on the study of a series capacitor in the Wilmarth-Lakefield transmission system [17]. This report specifically discussed the impact of the series capacitor on the interconnected network and wind turbine generators connected at various points in the network. Series compensation of 65 % was considered for the analysis according to this report. A 107 MVA wind farm based on 100 DFIGs was proposed at the Lakefield system. Induction generator effect and torsional interaction were studied thoroughly using the frequency scanning method. Induction generator effect was found to be dependent on the rotor circuit parameter and operating slip of the DFIG. This study suggested that when a large number of wind turbines are aggregated, the SSR issue might become more prominent. Different sizes of wind farms and their impact on the SSR were a major contribution of the work. However, no small-signal analysis or electromagnetic transient studies were performed.

Five papers published between 2006 and 2008 discussed SSR issues in wind farms and its mitigation using Flexible AC Transmission (FACTS) Controllers [18–22]. In [18] the authors studied the potential of SSR through a frequency domain model of the induction generator based wind farm. It was found that torsional modes can be excited by an electrical fault in the network but any unstable torsional interaction was not found. In [23] a double-cage induction generator based 500 MW wind farm was connected to a series-compensated transmission line. Several electromagnetic transient simulation results shown in this paper indicated the potential of induction generator effect in the wind farm following a fault in the network. However, it only happened with a high level of series compensation. A FACTS device-static VAr compensator (SVC) was proposed to mitigate the SSR oscillation in the wind farm [20]. The authors proposed a damping controller in which speed deviation was considered as the input signal. However, no eigenvalue analysis was presented to illustrate the improved stability in a closed loop system. Since wind farms are spread over a large geographical area, the specific generator speed which can be used for the damping of SSR oscillation was not discussed. Another paper [21] showed the mitigation of SSR using Thyristor Controlled Series Capacitor (TCSC). A damping controller was also proposed in this paper to mitigate the SSR oscillation in the wind farm. A further paper [22] presented a comparative study of mitigation of SSR oscillation using two FACTS devices: (a) SVC and (b) TCSC. Several electromagnetic transient simulations carried out in PSCAD/EMTDC were shown in this paper for SSR in wind farms of size between 100 and 500 MW. TCSC with and auxiliary damping controller was found to be superior over the SVC with a similar damping controller for mitigation of the SSR oscillation in the wind farm following a symmetrical fault in the network.

Two papers were published on the mitigation of SSR in wind farms using static synchronous compensators (STATCOM) and static synchronous series compensators (SSSC) [24, 25]. In these papers a 100 MW squirrel-cage induction generator based wind farm was connected to a series-compensated transmission line. A shaft monitoring system was proposed to monitor the shaft oscillation following the

disturbance in the network. Several low-pass and band-pass filters were proposed to achieve the objective of monitoring the torsional oscillations. Auxiliary damping controllers were proposed to mitigate the oscillation in the wind turbines. A generator speed feedback signal was used for the damping of the torsional interactions. Another damping signal was also derived from the active power generated by the wind farm in a fixed time interval. However, in a large wind farm, selection of an appropriate speed signal for the damping would be a challenging task for the control engineer. In these two papers, no induction generator effect was found; rather a torsional interaction was reported following a fault in the network.

Modelling of DFIG based wind farm connected to a series-compensated transmission line was presented in [23]. Smallsignal analysis and time domain simulations were carried out in this paper. Impact of a series capacitor and control parameters on the SSR oscillation were reported. Further studies of SSR with DFIG based wind farms were reported in [26–29]. A detailed modelling of the DFIG based wind farm connected to a series-compensated transmission line was reported in these papers. Small-signal analysis followed by a time-domain simulation was performed to examine the SSR conditions. DFIG converter controller design and its interactions with series capacitor were studied. Through participation factor analysis, authors established a criterion to detect and mitigate the SSR by choosing suitable controller parameters.

There are two events related to SSR that have already occurred in the wind farms connected to a series-compensated transmission line. In October 2009 a single line to ground fault occurred on a 345 kV series-compensated line connected to two large wind farms of capacity ≈485 MW in Texas. After the fault, once the faulted line was cleared, the wind farm continued to operate radially with a single 345 kV line with 50 % series compensation. Then, the SSR interaction between the wind turbine generator control and series capacitor initiated and grew sufficiently large to damage the wind turbines as voltage exceeded 2 pu before the series capacitor was bypassed. From preliminary analysis it was found that the control interaction of the DFIG based wind turbine controller and series capacitor caused the un-damped voltage oscillations [30].

Another incident was witnessed in the Buffalo Ridge area of Minnesota. Many wind farms are planned and connected to the 345 kV series-compensated transmission line in southwestern Minnesota. In one case, the series compensation level was chosen to be 60 % in a 54 mile line. One end of the line was connected to a 150 MW wind farm. During the commissioning process of the series capacitor, one line was taken out before the series capacitor was bypassed. During this operation the wind farm output was 15 MW and only one of the six synchronous generators (46 MW) was connected to line. The switching operation resulted in the radial operation of the wind farm with the series-compensated transmission line. The system tripped due to the flashover in the generator bus duct resulting in the bypass of the series capacitor. Generator current recorded during the event was analyzed and the presence of DC component along with a low frequency component (9–13 Hz) was confirmed. This was later confirmed as the SSR that was caused due

to the interaction of the DFIG controller and the series-compensated transmission line [17, 31].

A report on the impact of wind farms in SSR in a power system was released in 2011 [32]. This report was prepared based on the incident witnessed in the Zorillo Gulf wind farm in Texas. Through frequency scanning method only, an analysis of the SSR was performed. The major focus was given to the converter and its control on the basis of practical experience. The impact of rotor current controller bandwidth and DC link voltage controller bandwidth was tested by performing a time domain simulation in PSCAD/EMTDC. The study was later extended to see the impact of the grid side converter's reactive power controller bandwidth and PLL bandwidth. From these simulations it was found that rotor side converter current controller and PLL exhibit a greater impact on the SSR oscillation. The impact of the DC link controller bandwidth was found to be the least. At the same time, the magnitude of power flow was also found to impact the SSR oscillations.

To protect wind farms from SSR oscillations, a relay has recently been developed by ERL phase power technologies [31]. This relay is useful to detect the oscillation of frequency band between 5–25 Hz. This development was the result of collaborative research between the Xcel energy and ERL phase power technology. A real issue of SSR oscillation in a DFIG based wind farm connected to a series-compensated transmission line was the motivation of this development.

18.1.2 Subsynchronous Resonance

SSR is an electrical power system condition where the electric network exchanges energy with a turbine generator at one or more of the natural frequencies of the combined system below the synchronous frequency of the system [33–36]. Series compensation in the line results in excitation of subsynchronous currents at an electrical frequency f_{er} given by

$$f_{er} = f_0 \sqrt{\frac{X_c}{X_N}} \tag{18.1}$$

where, X_c is the reactance of the series capacitor, X_N is the reactance of the line including that of the generator and transformer, and f_0 is the nominal frequency of the power system. Typically X_c can be up-to 60–70 % of X_N. Hence, $f_{er} < f_0$. The subsynchronous currents result in rotor torques and currents at the complementary frequency as f_r.

$$f_r = f_0 - f_{er} \tag{18.2}$$

These rotor currents result in subsynchronous armature voltage components that may enhance subsynchronous armature currents to produce SSR. There are two

aspects of the SSR: (i) Self-excitation involving both an induction generator effect and torsional interaction, and (ii) Transient torque (also called transient SSR). More details on the SSR can be found in [33–36].

18.1.3 Subsynchronous Resonance Study Techniques

There are several techniques available for the study of SSR in power systems. The most common techniques are:

- Frequency scanning
- Eigenvalue analysis
- Electromagnetic transient simulation

18.1.3.1 Frequency Scanning

The frequency scanning technique is a fundamental technique for preliminary analysis of SSR. It involves the determination of the driving point impedance over the frequency range of interest as viewed from the neutral bus of the generator under study. In this technique, the equivalent resistance and reactance are computed by looking into the network from a point behind the stator winding of a particular generator, as a function of the frequency. Should there be a frequency at which the reactance is zero and resistance is negative, self-sustaining oscillations at that frequency would be expected due to the induction generator effect. Frequency scanning can sometimes provide information regarding the possible problems with torsional interaction and transient torques. This method is fast and easy to use [33–41].

18.1.3.2 Eigenvalue Analysis

Eigenvalue analysis is extensively utilized for the study of torsional interaction and induction generator effect. This is an exact method studied through the detailed model of the power system. The basic procedure of the eigenvalue analysis encompasses:

- Development of a positive sequence model of the power system
- Modeling of generator electrical circuits
- Modeling of turbine-generator spring mass system
- Calculation of eigenvalues of the interconnected systems
- Real component of eigenvalues corresponding to the subsynchronous modes of the turbine-generator spring mass system indicates the severity of torsional interaction

- Real component of eigenvalues corresponding only to electrical system resonant frequencies reveals the severity of the induction generator effect problem

The real part of the eigenvalue is a direct measure of the positive or negative damping for each mode [37, 38, 42, 43].

18.1.3.3 Transient Torque Analysis

In order to determine the potential for SSR torque amplification, electromagnetic transient analysis is performed to find the peak transient shaft torque that is to be expected when a fault or equipment switching takes place in a series-compensated line [33, 34, 37, 38].

In this chapter, SSR analysis is carried out through a comprehensive eigenvalue analysis that is then reasonably validated through the electromagnetic transient simulation using PSCAD/EMTDC software.

18.2 System Modelling

The study system considered for the SSR study in wind farm is shown in Fig. 18.1. In this system, a double-cage induction generator based wind farm is connected to a series-compensated transmission line. This system is a modified IEEE First SSR Benchmark System [35]. The synchronous generator is replaced with an equivalent induction generator. The wind farm size is varied between 100 and 500 MW, whereas the series compensation level is varied from 10 to 90 %.

The wind farm is split into two sub-systems. One sub-system represents the mechanical drive train, whereas the other sub-system accounts for the electrical circuit of the generator. The wind turbine generator system model is reasonably validated in one case by considering a symmetrical fault in the electrical network and also a step change in mechanical torque input. Small-signal analysis is carried out utilizing the user written programs in MATLAB, while all electromagnetic transient simulations are carried out with PSCAD/EMTDC software [44–46].

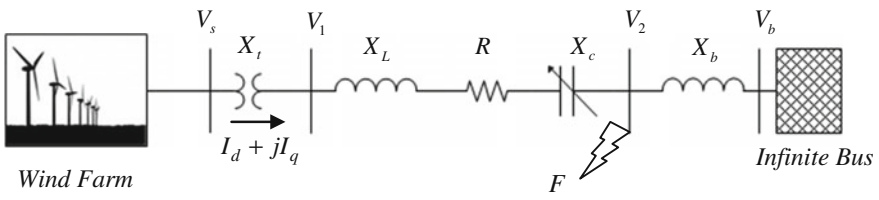

Fig. 18.1 Study system

18.2.1 Wind Farm

18.2.1.1 Drive-Train System

The vibrational modes of a wind turbine can be excited by external influences such as stochastic fluctuations of the rotor torque caused by wind turbulence and output torque of the electrical generator. The vibrational response of a torsional system is determined by three elasto-mechanical parameters such as (i) the moment of inertia of the rotating masses, (ii) the torsional stiffness of the elastic shafts and connecting elements, and (iii) the torsional damper constants. These three parameters are usually determined from the design and material properties of the drive train components involved [47].

The drive train of a wind turbine generator system typically consists of a blade pitching mechanism with a spinner, a hub with three/two blades, a rotor shaft, and a gear box with a breaker and electrical generator. Considering it as a three-mass drive train system, the proportion of the inertial moments of these sub-systems contributing to the overall inertial moment of the drive train of wind turbines with widely differing sizes and technical concepts can be distributed as follows [48]. The hub with blades comprises 85–92 % of the total polar moment of inertia, whereas the generator rotor constitutes 5–10 %, and the rest of the drive train system contributes 1–2 %. Unlike the moment of inertia, the generator represents the largest torsional stiffness, which is approximately 100 times the rotor shaft stiffness and approximately 50 times the stiffness of the hub with blades [48]. In general, for modal analysis of a multi-mass drive train system the rotor is treated as a combination of discrete masses connected together by springs represented by their damping and stiffness coefficient.

The two-mass drive train system is widely used for studying the power system stability including the wind turbine generators [43, 47–52]. A typical two-mass drive train system is shown in Fig. 18.2.

The equivalent shaft stiffness can be obtained from the parallel equivalent shaft stiffness given below. The equivalent inertia constant can be expressed as the summation of the inertia constants of the blade and the hub.

$$\frac{1}{K_{tg}} = \frac{1}{K_{bh}} + \frac{1}{K_{hg}} \tag{18.3}$$

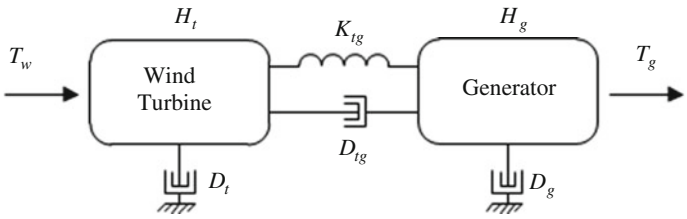

Fig. 18.2 Two-mass drive train system

$$H_t = H_b + H_h \tag{18.4}$$

The differential equations of a two-mass system are written as:

$$\frac{d}{dt}(\delta_t) = \omega_t \tag{18.5}$$

$$\frac{d}{dt}(\delta_g) = \omega_g \tag{18.6}$$

$$2H_t \frac{d}{dt}(\omega_t) = T_w - K_{tg}(\delta_t - \delta_g) - D_{tg}(\omega_t - \omega_g) - D_t\omega_t \tag{18.7}$$

$$2H_g \frac{d}{dt}(\omega_g) = K_{tg}(\delta_t - \delta_g) + D_{tg}(\omega_t - \omega_g) - D_g\omega_g - T_g \tag{18.8}$$

Equations (18.5)–(18.8) can be reduced to a third order system as written below. The self-damping is neglected here.

$$\frac{d}{dt}(\delta_{tg}) = \frac{d}{dt}(\delta_t) - \frac{d}{dt}(\delta_g) = \omega_t - \omega_g \tag{18.9}$$

$$2H_t \frac{d}{dt}(\omega_t) = T_w - K_{tg}\delta_{tg} - D_{tg}(\omega_t - \omega_g) \tag{18.10}$$

$$2H_g \frac{d}{dt}(\omega_g) = K_{tg}\delta_{tg} + D_{tg}(\omega_t - \omega_g) - T_g \tag{18.11}$$

where,

δ_{tg} Torsional angle between wind turbine and generator (rad)
ω_t Angular speed of wind turbine (rad/s)
ω_g Angular speed of generator (rad/s)
H_t Inertia constant of wind turbine (s)
H_g Inertia constant of generator (s)
D_t Damping coefficient of wind turbine (pu)
D_g Damping coefficient of generator (pu)
D_{tg} Damping coefficient between wind turbine and generator (pu)
K_{tg} Shaft stiffness between wind turbine and generator (pu)
T_w Mechanical torque input to wind turbine (pu)
T_g Electromagnetic torque output of generator (pu)

In practice, the large difference between the speed of the wind turbine and the generator makes the gear box an essential part of the system. The gearbox separates the two shaft systems. The impact of the generator rotor shaft can be neglected being of very small size. In the presence of the gearbox, all of the parameters must

be transformed to either high-speed shaft side or low-speed shaft side. In this work since the electrical network is present in the high-speed shaft side, all of the turbine parameters are referred to the generator rotor side. The low-speed shaft stiffness and inertia constants when referred to the high-speed side can be expressed as:

$$H_t^G = \frac{H_t}{N^2} \tag{18.12}$$

$$K_{tg}^G = \frac{K_{tg}}{N^2} \tag{18.13}$$

where, $N = \frac{\omega_g}{\omega_t}$ is the gearbox ratio.

The equations of motion of a two-mass torsional system are now presented in the state space form.

$$\dot{x}_{WT} = [A_{WT}]x_{WT} + [B_{WT}]u_{WT} \tag{18.14}$$

$$y_{WT} = [C_{WT}]x_{WT} \tag{18.15}$$

where, $x_{WT}^t = [\,\Delta\omega_t \quad \Delta\delta_{tg} \quad \Delta\omega_g\,]$ and $u_{WT} = \Delta T_w$.

18.2.1.2 Aggregation of Drive Train System

Since a large number of wind turbines are connected to a common bus, it is assumed that the disturbance originating in the bus affects the performance of all of the individual machines identically, and the individual rotor oscillations lie in phase with each other. All of the wind turbines are therefore considered to be connected in parallel, mechanically [11, 49, 53]. Considering number of turbines the equivalent model variables of a wind farm are expressed as:

$$H_t = \sum_{k=1}^{N} H_{tk} \tag{18.16}$$

$$H_g = \sum_{k=1}^{N} H_{gk} \tag{18.17}$$

$$K_{tg} = \sum_{k=1}^{N} K_{tgk} \tag{18.18}$$

$$D_{tg} = \sum_{k=1}^{N} D_{tgk} \tag{18.19}$$

18.2.1.3 Induction Generator

A wind turbine generator system converts the mechanical energy from the wind into electrical energy. Based on the rotational speed, the wind turbine generators are classified into two categories: (i) fixed speed generator, and (ii) variable speed generator [11–13].

A fixed-speed wind turbine generator consists of a conventional squirrel-cage induction generator that is directly connected to the grid. The slip of the induction generator varies with the power generated. However, the variations remain within 1–2 % of the rated generator speed. In this type of generator, since the rotor speed cannot be controlled, variation in the wind speed causes fluctuation in the input torque that is directly translated into variable power output. The fluctuation in the mechanical torque input also puts stress on the drive train system of a wind turbine. Since there is large speed difference between the wind turbine hub and the generator, a gearbox is used to connect the low-speed shaft of the wind turbine with the high-speed wind turbine generator.

Most of the time the induction generators are modelled as a simple squirrel-cage induction machine as in previous section. However, most of the induction generators above 5 kW have a double squirrel-cage rotor. In comparison to single-cage machines, these generators are widely used in the wind farms where slip varies over a wide range. In the double-cage rotor there are two electrical circuits. One circuit is placed at the outer surface of the rotor, very close to the stator winding. The other circuit is located in the deeper part of the cage. When the current flows in the outer conductor, it is tightly coupled with the stator, thus exhibiting a smaller leakage reactance but higher resistance due to a smaller cross section of the copper bar. Similarly when the current flows in the deeper bar, being very lightly coupled, it exhibits a larger leakage reactance but smaller resistance due to a large cross section of the copper bar. The rotor circuit acts as if two separate circuits are connected in parallel to each other.

During rated power output of a wind farm, the rotor reactance of the induction generator remains low due to the smaller slip (0–1 %). This results in a uniform current flow in the rotor bars. Further, due to the large cross section of inner rotor bars the efficiency remains high because of less power loss in the rotor. During any transient events in the network, when the speed deviates from the rated value, the slip increases significantly. During those high slip conditions the reactance of the inner rotor circuit increases and forces the current to flow in the circuit on the surface of the rotor that offers low reactance. Due to a smaller cross section of these outer circuit conductors, a high resistance is experienced which offers a higher torque in comparison to a single-cage induction generator operating with same slip [54–57].

In literature, two types of double-cage induction generator models are available Figs. 18.3a, b represent two models that are equivalent. References [56, 57] have shown the conversion of parameters from the name plate data of a double-cage machine to an electromagnetic transient model. Since manufacturers' data are not

readily available to the researchers, the constant parameter model of the double-cage is adopted for various studies related to the grid integration of fixed-speed wind farms. A new method has been proposed to derive different parameters of a double-cage induction generator from the manufacturer provided data: nominal mechanical power, nominal power factor, maximum torque, starting torque, and current [58]. In [56, 57] a detailed study of the equivalence between different double-cage induction machine models with six, seven and eight parameters have been presented. For a fair comparison between the small-signal model and non-linear model available in PSCAD/EMTDC software, the model shown in Fig. 18.3b is adopted in this chapter.

The mathematical model of a double-cage induction generator is developed in a manner that closely resembles the derivation of the per unit *d-q* model of a single-cage induction generator. Several assumptions are considered which are as follows:

- The core and mechanical losses are neglected.
- The machine is symmetric.
- Both rotor windings are magnetically coupled and the effects of space harmonics are neglected.
- Each of the two cages is short circuited by independent end rings.
- No inter-bars current can flow as rotor bars are insulated from the iron.
- Saturation effect and other nonlinearities are neglected.

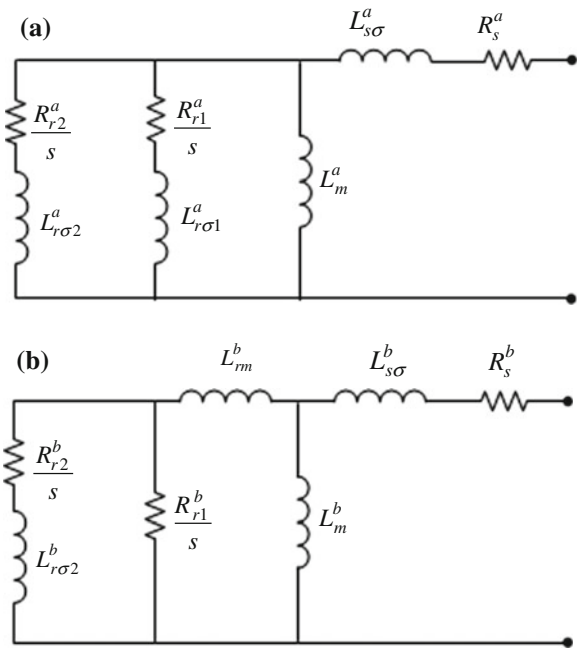

Fig. 18.3 Equivalent circuit of double-cage induction generator. **a** Model-I. **b** Model-II

The basic differential equations of the double-cage induction generators are written in *d-q* reference frame as [57, 58]:

$$\frac{1}{\omega_s}\frac{d}{dt}\lambda_{ds} = -R_s I_{ds} + \lambda_{qs} - V_{ds} \tag{18.20}$$

$$\frac{1}{\omega_s}\frac{d}{dt}\lambda_{qs} = -R_s I_{qs} - \lambda_{ds} - V_{qs} \tag{18.21}$$

$$\frac{1}{\omega_s}\frac{d}{dt}\lambda_{dr1} = -R_{r1} I_{dr1} + s\lambda_{qr1} \tag{18.22}$$

$$\frac{1}{\omega_s}\frac{d}{dt}\lambda_{qr1} = -R_{r1} I_{qr1} - s\lambda_{dr1} \tag{18.23}$$

$$\frac{1}{\omega_s}\frac{d}{dt}\lambda_{dr2} = -R_{r2} I_{dr2} + s\lambda_{qr2} \tag{18.24}$$

$$\frac{1}{\omega_s}\frac{d}{dt}\lambda_{qr2} = -R_{r2} I_{qr2} - s\lambda_{dr2} \tag{18.25}$$

The flux linkage equations are:

$$\lambda_{ds} = X_s I_{ds} + X_m I_{dr1} + X_m I_{dr2} \tag{18.26}$$

$$\lambda_{qs} = X_s I_{qs} + X_m I_{qr1} + X_m I_{qr2} \tag{18.27}$$

$$\lambda_{dr1} = X_m I_{ds} + X_{r1} I_{dr1} + X_{12} I_{dr2} \tag{18.28}$$

$$\lambda_{qr1} = X_m I_{qs} + X_{r1} I_{qr1} + X_{12} I_{qr2} \tag{18.29}$$

$$\lambda_{dr2} = X_m I_{ds} + X_{12} I_{dr1} + X_{r2} I_{dr2} \tag{18.30}$$

$$\lambda_{qr2} = X_m I_{qs} + X_{12} I_{qr1} + X_{r2} I_{qr2} \tag{18.31}$$

where,

$$X_{12} = X_m + X_{rm} \tag{18.32}$$

$$X_s = X_{s\sigma} + X_m \tag{18.33}$$

$$X_{r1} = X_{r1\sigma} + X_{12} \tag{18.34}$$

$$X_{r2} = X_{r2\sigma} + X_{12} \tag{18.35}$$

The electromagnetic torque can be expressed as,

$$T_g = X_m\big((I_{qr1} + I_{qr2})I_{ds} - (I_{dr1} + I_{dr2})I_{qs}\big) \tag{18.36}$$

where,

R_s	Stator resistance per phase (pu)
$X_{s\sigma}$	Stator leakage reactance per phase (pu)
R_{r1}	First-cage rotor resistance per phase (pu)
$X_{r1\sigma}$	First-cage rotor leakage reactance per phase (pu)
R_{r2}	Second-cage rotor resistance per phase (pu)
$X_{r2\sigma}$	Second-cage rotor leakage reactance per phase (pu)
X_m	Mutual reactance between the stator and rotor windings (pu)
V_{ds}, V_{qs}	*d-q* axis voltage at generator terminal (pu)
I_{ds}, I_{qs}	*d-q* axis stator current (pu)
I_{dr1}, I_{qr1}	*d-q* axis first-cage rotor current (pu)
I_{dr2}, I_{qr2}	*d-q* axis second-cage rotor current (pu)

Differential equations presented in (18.20)–(18.25) are linearized to develop the state space model of the induction generator. The system now can be written in the form of

$$\dot{x}_G = [A_G]x_G + [B_G]u_G \tag{18.37}$$

where,

$$x_G^t = [\,\Delta I_{ds} \quad \Delta I_{qs} \quad \Delta I_{dr1} \quad \Delta I_{qr1} \quad \Delta I_{dr2} \quad \Delta I_{qr2}\,] \tag{18.38}$$

$$u_G^t = [\,\Delta\omega_g \quad \Delta V_{ds} \quad \Delta V_{qs}\,] \tag{18.39}$$

This model is implemented as a voltage source behind the transient reactance, which is similar to the derivation of the single-cage induction generator [43, 59]. The detailed derivations can be found in [46]. The model can be expressed as follows,

$$\frac{1}{\omega_s}X_0\frac{d}{dt}I_{ds} + \frac{1}{\omega_s}\frac{d}{dt}E_{q1} = -R_sI_{ds} + X_0I_{qs} - E_{d1} - V_{ds} \tag{18.40}$$

$$\frac{1}{\omega_s}X_0\frac{d}{dt}I_{qs} - \frac{1}{\omega_s}\frac{d}{dt}E_{d1} = -R_sI_{qs} - X_0I_{ds} - E_{q1} - V_{qs} \tag{18.41}$$

$$\frac{d}{dt}E_{d1} = -\frac{\omega_sR_{r1}}{X_r}\left(X_{r2}E_{d1} - (X_mX_{r2\sigma})E_{d2} + \frac{(X_mX_{r2\sigma})^2}{X_r}I_{qs}\right) + s\omega_sE_{q1} \tag{18.42}$$

$$\frac{d}{dt}E_{q1} = -\frac{\omega_s R_{r1}}{X_r}\left(X_{r2}E_{q1} - (X_m X_{r2\sigma})E_{q2} - \frac{(X_m X_{r2\sigma})^2}{X_r}I_{ds}\right) - s\omega_s E_{d1} \quad (18.43)$$

$$\frac{d}{dt}E_{d2} = -\frac{\omega_s R_{r2}}{X_r}\left(-\frac{X_{12}^2}{X_m X_{r2\sigma}}E_{d1} + X_{12}E_{d2}\right) + s\omega_s E_{q2} \quad (18.44)$$

$$\frac{d}{dt}E_{q2} = -\frac{\omega_s R_{r2}}{X_r}\left(-\frac{X_{12}^2}{X_m X_{r2\sigma}}E_{q1} + X_{12}E_{q2}\right) - s\omega_s E_{d2} \quad (18.45)$$

The electromagnetic torque can now be expressed in terms of rotor-induced voltages, as

$$T_g = -\left(E_{d1}I_{ds} + E_{q1}I_{qs}\right) \quad (18.46)$$

In order to perform eigenvalue analysis, the differential equations. (18.40)–(18.45) are linearized and arranged in a linear state space form.

$$\dot{x}_G = [A_G]x_G + [B_G]u_G \quad (18.47)$$

where,

$$x_G^t = [\,\Delta I_{ds} \quad \Delta I_{qs} \quad \Delta E_{d1} \quad \Delta E_{q1} \quad \Delta E_{d2} \quad \Delta E_{q2}\,] \quad (18.48)$$

$$u_G^t = [\,\Delta\omega_g \quad \Delta V_{ds} \quad \Delta V_{qs}\,] \quad (18.49)$$

18.2.1.4 Aggregation of Induction Generators

Aggregation of wind turbines is an important issue during the planning of grid integration of large-scale wind farms and stability studies. One of the important considerations for the aggregation is to understand the potential for mutual interaction between the various wind turbines in a wind farm. Reactive power compensation and stability study of wind farms are typically done considering the aggregated model of wind turbine generators [60–64]. Aggregation of wind turbine generators is somewhat different from the aggregation of simple induction machines for motor application [53]. The oscillation in the power output of the induction generator is dominated by the dynamics of the mechanical drive train due to the fact that the inertia constant of the wind turbine is much higher than that of induction generator.

In general, representing large number of induction generators by a single equivalent induction generator may not be accurate under certain circumstances which are as follows:

1. If different wind turbines are subjected to different wind speeds due to being located over a wide geographical region, or subjected to different types of disturbances.
2. If different sizes of same type of induction generator based wind turbines (having different drive trains, blades structure, etc.) are aggregated together by one equivalent IG based wind turbine.

In this chapter, the aggregation of the wind turbines has been performed for the investigation of SSR. The rating of an aggregated wind farm can be expressed as the summation of the rating of each machine:

$$S_{eq} = \sum_{k=1}^{N} S_k \tag{18.50}$$

where, S_k is the kVA rating of single machine and S_{eq} is the rating of the equivalent machine. This is known as the kVA weighted averaging, one of the most commonly used methods of aggregating induction machines for power system stability studies. In a wind farm, if all the induction machines are not identical then aggregated parameters are calculated as the weighted average of the respective parameter of individual machines [60, 61]. The generalized method for the calculation of the aggregated parameters $\left(x_{agg}\right)$ of the generator is as follows:

$$x_{agg} = \sum_{k=1}^{N} \alpha_k x_k \tag{18.51}$$

where, x_k is the parameter of k-th generator and α_k is a factor, which is calculated as

$$\alpha_k = \frac{S_k}{\sum_{k=1}^{N} S_k} \tag{18.52}$$

The aggregation of shunt capacitors $\left(C_g\right)$ at the terminal of an induction generator can be done as,

$$C_g = \sum_{k=1}^{N} C_{gk} \tag{18.53}$$

where, C_{gk} is the shunt capacitance at the k-th generator terminal.

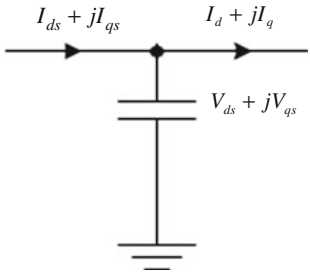

Fig. 18.4 Shunt capacitor at the terminal of the wind turbine generator

18.2.1.5 Shunt Capacitor at Generator Terminal

The reactive power demand of the induction generator that is catered by a local capacitor bank depends on its terminal voltage and the power output. For a constant voltage at the terminal, the reactive power demand of the wind turbine generator increases with increase in the power output. However, the reactive power demand is not linearly dependent on the active power output of the wind turbine. For wind power application, shunt capacitor banks are split into multiple stages. Each stage of the capacitor bank is connected based on the active power output. A simple shunt capacitor is shown in Fig. 18.4. For the analysis, the voltage across the capacitor can be written in the synchronously rotating *d-q* reference frame as given below [37].

$$C_g \frac{d}{dt} V_{ds} = I_{ds} - I_d + \omega_s C_g V_{qs} \tag{18.54}$$

$$C_g \frac{d}{dt} V_{qs} = I_{qs} - I_q - \omega_s C_g V_{ds} \tag{18.55}$$

where,

C_g	Shunt capacitor at the terminal of induction generator (pu)
I_{ds}, I_{qs}	*d-q* axis current of induction generator (pu)
I_d, I_q	*d-q* axis current of series-compensated transmission line (pu)
V_{ds}, V_{qs}	*d-q* axis voltage at the wind turbine generator terminal (pu)

18.2.2 AC Network

The series-compensated line is depicted in Fig. 18.5. The dynamic equations expressed in the synchronously rotating *d-q* reference frame [33, 37] are:

$$L \frac{d}{dt} I_d = V_{ds} - RI_d + \omega_s L I_q - V_{cd} - V_{bd} \tag{18.56}$$

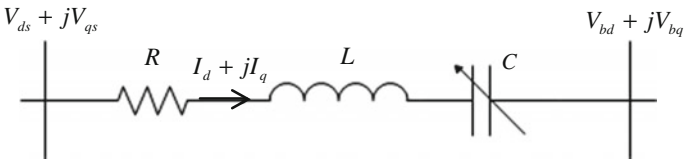

Fig. 18.5 Series-compensated transmission line

$$L\frac{d}{dt}I_q = V_{qs} - RI_q - \omega_s LI_d - V_{cq} - V_{bq} \tag{18.57}$$

$$C\frac{d}{dt}V_{cd} = I_d + \omega_s CV_{cq} \tag{18.58}$$

$$C\frac{d}{dt}V_{cq} = I_q - \omega_s CV_{cd} \tag{18.59}$$

where,

R	Transmission line resistance (pu)
L	Transmission line inductance including transformer and infinite grid inductance (pu)
C	Series capacitance (pu)
V_{ds}, V_{qs}	*d-q* axis voltage at the wind turbine generator terminal (pu)
I_d, I_q	*d-q* axis current of series-compensated transmission line (pu)
V_{cd}, V_{cq}	*d-q* axis voltage across series capacitor (pu)
V_{bd}, V_{bq}	*d-q* axis voltage at the infinite bus (pu)

Linearizing the differential equations, the state space model of the network including the shunt capacitor is now written as:

$$\dot{x}_N = [A_N]x_N + [B_N]u_N \tag{18.60}$$

where

$$x_N^t = [\,\Delta V_{ds} \quad \Delta V_{qs} \quad \Delta I_d \quad \Delta I_q \quad \Delta V_{cd} \quad \Delta V_{cq}\,] \tag{18.61}$$

$$u_N^t = [\,\Delta I_{ds} \quad \Delta I_{qs} \quad \Delta V_{bd} \quad \Delta V_{bq}\,] \tag{18.62}$$

18.2.3 Complete System Model

In order to develop a complete state space model of the study system, all the subsystems defined in (18.14), (18.47) and (18.60) are interconnected to each other with suitable feedback. The complete system can now be expressed as:

$$\dot{x}_{WT} = [A_{TT}]x_{WT} + [A_{TG}]x_G + [B_T]u_{WT} \tag{18.63}$$

$$\dot{x}_G = [A_{GT}]x_{WT} + [A_G]x_G + [A_{GN}]x_N \tag{18.64}$$

$$\dot{x}_N = [A_{NG}]x_G + [A_{NN}]x_N + [B_N]u_N \tag{18.65}$$

Combining (18.63)–(18.65), the state space model of the study system is written as:

$$\dot{x}_{sys} = \left[A_{sys}\right]x_{sys} + [B_1]u_1 + [B_2]u_2 \tag{18.66}$$

$$y_{sys} = \left[C_{sys}\right]x_{sys} \tag{18.67}$$

where,

$$x_{sys}^t = [\, x_{WT}^t \quad x_G^t \quad x_N^t \,] \tag{18.68}$$

$$y_{sys}^t = [\, \Delta P_{WF} \quad \Delta Q_{WF} \,] \tag{18.69}$$

$$u_1 = [\Delta T_W] \tag{18.70}$$

$$u_2 = \begin{bmatrix} \Delta V_{bd} \\ \Delta V_{bq} \end{bmatrix} \tag{18.71}$$

The state matrix and input matrix are defined as follows:

$$\left[A_{sys}\right] = \begin{bmatrix} A_{TT} & A_{TG} & 0_{3\times6} \\ A_{GT} & A_{GG} & A_{GN} \\ 0_{6\times3} & A_{NG} & A_{NN} \end{bmatrix} \tag{18.72}$$

$$[B_1] = \begin{bmatrix} B_T \\ 0_{6\times1} \\ 0_{6\times1} \end{bmatrix}, \quad [B_2] = \begin{bmatrix} 0_{3\times2} \\ 0_{6\times2} \\ B_N \end{bmatrix} \tag{18.73}$$

The state matrix $\left[A_{sys}\right]$ in (18.72) is used for the eigenvalue analysis discussed in the next section where, $\left[A_{sys}\right]$ is a 15 × 15 sized matrix, $[B_1]$ is a 15 × 1 matrix and $[B_2]$ is a 15 × 2 matrix.

18.3 SSR Analysis

18.3.1 Small-Signal Stability Analysis

18.3.1.1 Eigenvalue Analysis

The complete system state space model presented in (18.66) is utilized for the calculation of system eigenvalues. Eigenvalues are calculated by considering various initial conditions. The wind farm size is varied between 100 and 500 MW and the series compensation level is varied between 10 and 90 %. The eigenvalues are also calculated for a 500 MW wind farm producing variable output. This is performed from the viewpoint of evaluating the impact of series compensation during the wind speed variation.

(a) **Variation in Wind Farm Size**

The state space model mentioned in (18.66) results in seven complex conjugate eigenvalues and one real eigenvalue. The eigenvalues for different operating conditions are depicted in Table 18.1. The oscillatory modes obtained are: (i) network mode 1 and network mode 2, (ii) super synchronous mode, (iii) electrical mode, (iv) rotor mode, (v) electromechanical mode, and (vi) torsional mode. The only non-oscillatory mode is represented by the real eigenvalue. However, for the SSR analysis electrical mode, electro-mechanical mode and torsional modes are of main interest. The impact of series compensation on these three modes is studied through a comprehensive eigenvalue analysis depicted in Table 18.1.

The electrical mode that is characterized by the series capacitor is largely affected by the level of series compensation. The impact of wind farm size is also found to be substantial. Table 18.1 illustrates that for all wind farm sizes, an increase in the series compensation level causes the electrical mode to become less stable and then become unstable beyond a specific compensation level, known as the critical compensation level. An unstable electrical mode always indicates the potential for induction generator effect SSR in the network. On the other hand, oscillatory frequency (f_{er}) associated with the electrical mode also gets reduced with increasing level of series compensation.

Now, keeping the level of series compensation constant, when size of the wind farm is increased from 100 to 500 MW, the electrical mode shows a unique behaviour. Initially it become less stable and then becomes more stable for larger wind farms. For example, in the case of a 100 MW wind farm with 50 % series compensation, the electrical mode eigenvalues are calculated as -0.415 ± 237.08i, which become 0.165 ± 202.08i and 0.1569 ± 182.46i for 200 and 300 MW wind farms, respectively. However, when the wind farm size increases to 400 and 500 MW, the electrical mode becomes stable again. The electrical mode damped frequency also decreases with respect to the increasing size of the wind farm. Similar behaviour is also observed for all series compensation levels depicted in Table 18.1. This shows that instability due to SSR can occur at a realistic level of series compensation.

Table 18.1 System eigenvalues for different sizes of wind farm

Modes	100 MW	200 MW	300 MW	400 MW	500 MW
No compensation					
Network mode-1	−7.740 ± 2599.2i	−8.947 ± 2132.8i	−9.657 ± 1935.4i	−10.11 ± 1802.4i	−10.41 ± 1677.2i
Network mode-2	−8.788 ± 1845.2i	−11.07 ± 1378.8i	−12.64 ± 1181.5i	−13.86 ± 1048.5i	−14.94 ± 923.23i
Sup. Sync. mode	−9.800 ± 376.59i	−10.01 ± 376.67i	−10.15 ± 376.73i	−10.24 ± 376.77i	−10.31 ± 376.79i
Electrical mode	X	X	X	X	X
Rotor mode	−62.03 ± 2.8866i	−60.51 ± 3.1177i	−59.54 ± 3.3131i	−58.84 ± 3.5633i	−58.26 ± 3.9728i
Elect-mech. mode	-5.658 ± 34.578i	−4.506 ± 31.003i	−3.841 ± 28.141i	−3.461 ± 25.601i	−3.334 ± 23.071i
Torsional mode	−0.552 ± 3.5799i	−0.625 ± 3.5629i	−0.742 ± 3.588i	−0.890 ± 3.7309i	−0.925 ± 4.0691i
Non-osc. mode	−7.684	−5.464	−3.669	−2.002	−0.433
40 % Series compensation					
Network mode-1	−7.703 ± 2613.1i	−8.863 ± 2163.5i	−9.5929 ± 1977.5i	−10.074 ± 1872.9i	−10.42 ± 1797.9i
Network mode-2	−8.728 ± 1859.1i	−10.89 ± 1409.5i	−12.433 ± 1223.5i	−13.539 ± 1118.9i	−14.42 ± 1044i
Sup. Sync. mode	−6.818 ± 501.74i	−6.789 ± 533.07i	−6.6586 ± 550.61i	−6.5325 ± 561.61i	−6.420 ± 569.5i
Electrical mode	−1.118 ± 251.73i	−0.762 ± 220.39i	−0.86505 ± 202.84i	−1.092 ± 191.85i	−1.352 ± 183.98i
Rotor mode	−62.80 ± 3.0335i	−61.55 ± 3.3139i	−60.632 ± 3.4701i	−59.951 ± 3.5803i	−59.40 ± 3.6859i
Elect-mech. mode	−6.334 ± 36.361i	−5.388 ± 33.973i	−4.6926 ± 31.874i	−4.1921 ± 30.064i	−3.813 ± 28.385i
Torsional mode	−0.530 ± 3.5918i	−0.557 ± 3.5761i	−0.59757 ± 3.5653i	−0.6502 ± 3.5647i	−0.720 ± 3.5837i
Non-osc. mode	−8.755	−7.210	−5.8976	−4.7785	−3.7286
50 % Series compensation					
Network mode-1	−7.694 ± 2616.1i	−8.848 ± 2168.3i	−9.575 ± 1984.9i	−10.05 ± 1884i	−10.41 ± 1814.3i
Network mode-2	−8.713 ± 1862.2i	−10.86 ± 1414.3i	−12.38 ± 1231i	−13.47 ± 1130.1i	−14.34 ± 1060.4i
Sup. Sync. mode	−6.986 ± 516.37i	−6.939 ± 551.31i	−6.790 ± 570.89i	−6.649 ± 583.18i	−6.525 ± 592.01i
Electrical mode	−0.415 ± 237.08i	+0.165 ± 202.08i	+0.156 ± 182.46i	−0.041 ± 170.14i	−0.306 ± 161.31i
Rotor mode	−63.02 ± 3.0866i	−61.85 ± 3.4067i	−60.96 ± 3.5792i	−60.30 ± 3.6858i	−59.75 ± 3.7703i

(continued)

Table 18.1 (continued)

Modes	100 MW	200 MW	300 MW	400 MW	500 MW
Elect-mech. mode	−6.537 ± 36.849i	−5.683 ± 34.809i	−5.020 ± 32.981i	−4.520 ± 31.384i	−4.120 ± 29.897i
Torsional mode	−0.525 ± 3.5951i	−0.545 ± 3.5814i	−0.572 ± 3.5703i	−0.607 ± .5641i	−0.653 ± 3.5659i
Non-osc. mode	−9.048	−7.6941	−6.525	−5.528	−4.607
55 % Series compensation					
Network mode-1	−7.690 ± 2617.6i	−8.840 ± 2170.5i	−9.566 ± 1988.2i	−10.05 ± 1888.8i	−10.41 ± 1821.2i
Network mode−2	−8.706 ± 1863.7i	−10.85 ± 1416.5i	−12.36 ± 1234.3i	−13.44 ± 1134.9i	−14.30 ± 1067.3i
Sup. Sync. mode	−7.061 ± 523.11i	−7.006 ± 559.71i	−6.849 ± 580.23i	−6.702 ± 593.12i	−6.572 ± 602.39i
Electrical mode	−0.061 ± 230.32i	+0.652 ± 193.64i	+0.709 ± 173.05i	+0.539 ± 160.11i	+0.281 ± 150.82i
Rotor mode	−63.13 ± 3.1162i	−62.01 ± 3.4618i	−61.15 ± 3.6484i	−60.48 ± 3.7587i	−59.94 ± 3.8386i
Elect-mech. mode	−6.644 ± 37.1i	−5.847 ± 35.25i	−5.211 ± 33.572i	−4.719 ± 32.095i	−4.314 ± 30.714i
Torsional mode	−0.523 ± 3.5967i	−0.539 ± 3.5842i	−0.561 ± 3.5735i	−0.589 ± 3.5662i	−0.625 ± 3.5638i
Non-osc. mode	−9.199	−7.947	−6.856	−5.922	−5.063
60 % Series compensation					
Network mode-1	−7.685 ± 2619.1i	−8.832 ± 2172.6i	−9.557 ± 1991.3i	−10.04 ± 1893.2i	−10.40 ± 1827.4i
Network mode-2	−8.698 ± 1865.1i	−10.83 ± 1418.6i	−12.34 ± 1237.3i	−13.42 ± 1139.2i	−14.27 ± 1073.4i
Sup. Sync. mode	−7.130 ± 529.54i	−7.068 ± 567.73i	−6.903 ± 589.14i	−6.750 ± 602.61i	−6.616 ± 612.28i
Electrical mode	+0.296 ± 223.87i	+1.158 ± 185.58i	+1.297 ± 164.06i	+1.166 ± 150.52i	+0.926 ± 140.79i
Rotor mode	−63.24 ± 3.148i	−62.181 ± 3.5235i	−61.33 ± 3.7288i	−60.68 ± 3.8471i	−60.14 ± 3.9266i
Elect-mech. mode	−6.755 ± 37.356i	−6.023 ± 35.706i	−5.424 ± 34.193i	−4.948 ± 32.849i	−4.545 ± 31.584i
Torsional mode	−0.521 ± 3.5984i	−0.534 ± 3.5872i	−0.551 ± 3.5771i	−0.573 ± 3.5694i	−0.600 ± 3.5646i
Non-osc. mode	−9.352	−8.209	−7.201	−6.333	−5.535

A double-cage induction generator has one electromechanical mode that is represented by the eigenvalues having an oscillatory frequency in the range of 3–8 Hz. The electromechanical mode becomes more stable with increasing level of series compensation. At a constant level of series compensation, if size of the wind farm increases, the electromechanical mode becomes less stable. However, no instability in the electromechanical mode is seemingly caused by the series capacitor, as depicted in Table 18.1.

The torsional mode becomes relatively more stable with increasing size of the wind farm. However, increase in the percent of series compensation affects the torsional mode marginally, without causing any concern of the torsional interaction. Hence, no potential for torsional interaction is expected.

Figure 18.6 shows the variation in the electrical mode eigenvalues for different sizes of wind farm and series compensation levels. As the series compensation increases the real part of the electrical mode eigenvalue decreases. The oscillatory frequency of this mode also decreases consistently. The crossover series compensation level, known as the critical compensation, is different for different sizes of wind farms. Figure 18.7 shows the damping ratio of the electrical mode. It illustrates

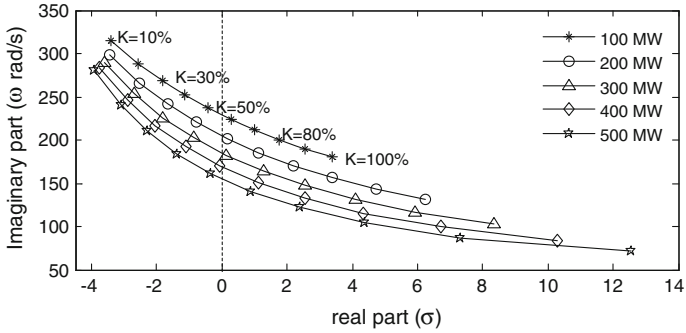

Fig. 18.6 Electrical mode eigenvalues

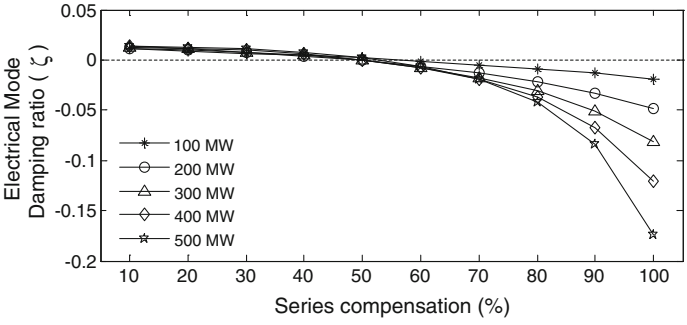

Fig. 18.7 Electrical mode damping ratio

Table 18.2 Critical series compensation level (%) for different size of wind farm

Wind farm size	100 MW	200 MW	300 MW	400 MW	500 MW
Critical series-compensation level (%)	56.00	48.25	48.60	50.50	52.60

that the effective damping ratio decreases gradually with the increasing series compensation level and becomes negative beyond the critical level of series compensation. Further increase in the series compensation yields a faster rise in the negative damping. Table 18.2 shows the critical compensation levels for different sizes of wind farms.

Figure 18.8 shows the damping ratio of the electromechanical mode for different sizes of wind farms. It is observed that the smaller wind farms exhibit larger damping to the electromechanical mode in comparison to the larger wind farms. The damping ratio increases marginally with increasing series compensation until 85 %, beyond which the larger wind farms show a faster rise in the damping ratio. The torsional mode-damping ratio is shown in Fig. 18.9. The large wind farm offers larger damping ratio during low series compensation. The damping ratio decreases steadily with the increase in the level of series compensation.

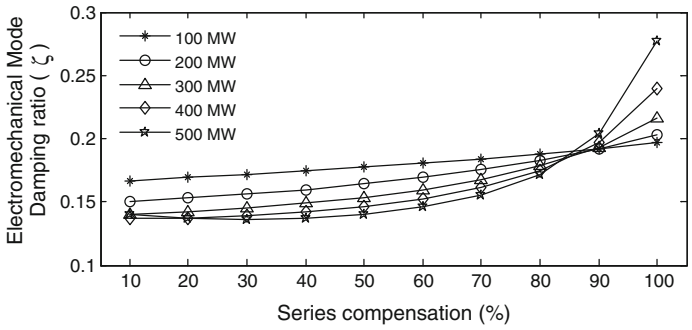

Fig. 18.8 Electromechanical damping ratio

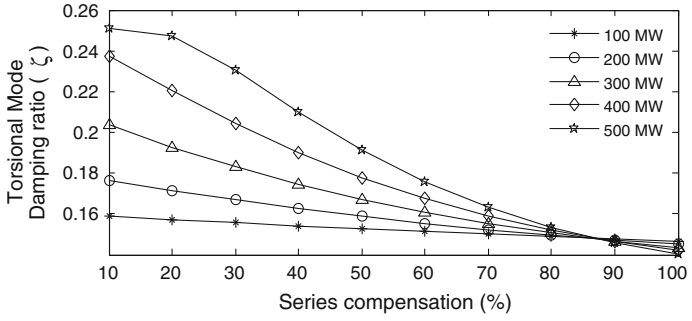

Fig. 18.9 Torsional mode damping ratio

(b) **Variation in Wind Farm Output**

In the previous section, the wind farm size has been varied by aggregating an appropriate number of wind turbines. In this section, the wind farm size is kept constant at 500 MW and the output of the wind farm is varied by varying the mechanical torque input to the aggregated wind turbine. The eigenvalues calculated for different outputs and series compensation levels are depicted in Table 18.3.

It is observed that the electrical mode becomes less stable consistently with increasing series compensation level and finally becomes unstable beyond the critical compensation level. Simultaneously, the damped frequency of the electrical mode is found to decrease with increased level of series compensation. Now when the compensation level is kept constant and wind farm outputs are varied, the electrical mode eigenvalues change very little with the increase in power output. When the output power varies, the slip of the induction generator only varies narrowly which does not cause significant change in the rotor resistance. Since the numbers of wind turbines are kept constant, the effective equivalent impedance of the wind farm remains almost constant. Thus, variation in the output of a large wind farm is less sensitive to the issue of SSR. The critical compensation levels for different wind farm outputs are depicted in Table 18.4.

Figures 18.10, 18.11 and 18.12 show the damping ratio of electrical mode, electromechanical mode and torsional mode, respectively, for different wind farm power output conditions. The electrical mode damping ratio remains almost constant for all of the outputs of a large wind farm, as shown in Fig. 18.10. It only decreases with increased percent series compensation level. The electromechanical mode damping ratios are shown in Fig. 18.11. It is observed that during a low level of series compensation the damping ratios for different outputs are different. However, as the compensation level increases the damping ratios increase and become similar. Figure 18.12 shows the variation in the torsional mode-damping ratio. With a low level of series compensation and large power output, the damping ratio remains high, but it decreases linearly with increase in the series compensation level. However, for low power output conditions the variation is negligible. After comparing Tables 18.1 and 18.3, it is observed that the various subsynchronous modes primarily depend on the size of the wind farm rather than this power output.

18.3.1.2 Participation Factor Analysis

From the eigenvalue analysis, stability of the subsynchronous modes is studied. The normalized participation factor analysis is performed to investigate the influence of various system states on the subsynchronous modes. A 100 MW wind farm connected to a 50 % series-compensated line is considered to perform the study. Figure 18.13 shows the participation factors associated with the electrical, electromechanical, torsional, and rotor mode. The participation factor associated with the electrical mode is shown in Fig. 18.13a, which is mainly contributed by the *d-q* axis

Table 18.3 System eigenvalues with different power outputs

Modes	100 MW	200 MW	300 MW	400 MW	500 MW
40 % Series compensation					
Network mode-1	−10.86 ± 2408.8i	−10.8 ± 2299.8i	−10.70 ± 2147.4i	−10.58 ± 1974.8i	−10.42 ± 1797.9i
Network mode-2	−13.56 ± 1654.9i	−13.66 ± 1545.8i	−13.84 ± 1393.4i	−14.08 ± 1220.9i	−14.42 ± 1044i
Sup. Sync. mode	−6.409 ± 570i	−6.41 ± 569.94i	−6.411 ± 569.85i	−6.415 ± 569.71i	−6.420 ± 569.5i
Electrical mode	−1.357 ± 183.43i	−1.363 ± 183.48i	−1.364 ± 183.59i	−1.360 ± 183.75i	−1.352 ± 183.98i
Rotor mode	−59.65 ± 0.8033i	−59.62 ± 1.4707i	−59.57 ± 2.1425i	−59.50 ± 2.8659i	−59.40 ± 3.6859i
Elect-mech. mode	−3.142 ± 29.967i	−3.210 ± 29.829i	−3.331 ± 29.531i	−3.521 ± 29.06i	−3.813 ± 28.385i
Torsional mode	−0.407 ± 3.4973i	−0.43 ± 3.4988i	−0.476 ± 3.5033i	−0.562 ± 3.5199i	−0.720 ± 3.5837i
Non-osc. mode	−6.056	−5.834	−5.43	−4.775	−3.728
50 % Series compensation					
Network mode-1	−10.84 ± 2410.1i	−10.78 ± 2301.8i	−10.69 ± 2151.7i	−10.56 ± 1983.9i	−10.41 ± 1814.3i
Network mode-2	−13.53 ± 1656.1i	−13.64 ± 1547.8i	−13.80 ± 1397.8i	−14.03 ± 1229.9i	−14.34 ± 1060.4i
Sup. Sync. mode	−6.508 ± 592.67i	−6.510 ± 592.6i	−6.513 ± 592.47i	−6.518 ± 592.28i	−6.525 ± 592.01i
Electrical mode	−0.315 ± 160.58i	−0.322 ± 160.65i	−0.323 ± 160.79i	−0.318 ± 161.01i	−0.306 ± 161.31i
Rotor mode	−59.98 ± 0.95387i	−59.95 ± 1.619i	−59.90 ± 2.2843i	−59.84 ± 2.9897i	−59.75 ± 3.7703i
Elect-mech. mode	−3.518 ± 31.191i	−3.580 ± 31.086i	−3.691 ± 30.844i	−3.864 ± 30.454i	−4.120 ± 29.897i
Torsional mode	−0.409 ± 3.5161i	−0.428 ± 3.5175i	−0.466 ± 3.521i	−0.534 ± 3.5315i	−0.653 ± 3.5659i
Non-osc. mode	−6.593	−6.393	−6.036	−5.472	−4.607
55 % Series compensation					
Network mode-1	−10.84 ± 2410.7i	−10.78 ± 2302.7i	−10.68 ± 2153.7i	−10.56 ± 1987.8i	−10.41 ± 1821.2i
Network mode-2	−13.52 ± 1656.8i	−13.63 ± 1548.8i	−13.79 ± 1399.7i	−14.01 ± 1233.9i	−14.30 ± 1067.3i
Sup. Sync. mode	−6.552 ± 603.14i	−6.554 ± 603.05i	−6.558 ± 602.91i	−6.564 ± 602.69i	−6.572 ± 602.39i
Electrical mode	0.272 ± 150i	0.264 ± 150.08i	0.2629 ± 150.24i	0.268 ± 150.48i	0.281 ± 150.82i
Rotor mode	−60.16 ± 1.0498i	−60.13 ± 1.7131i	−60.08 ± 2.3755i	−60.02 ± 3.0736i	−59.94 ± 3.8386i

(continued)

Table 18.3 (continued)

Modes	100 MW	200 MW	300 MW	400 MW	500 MW
Elect-mech. mode	−3.745 ± 31.882i	−3.804 ± 31.793i	−3.911 ± 31.576i	−4.075 ± 31.221i	−4.314 ± 30.714i
Torsional mode	−0.410 ± 3.5256i	−0.427 ± 3.527i	−0.461 ± 3.53i	−0.521 ± 3.5384i	−0.625 ± 3.5638i
Non-osc. mode	−6.897	−6.708	−6.372	−5.850	−5.063
60 % Series compensation					
Network mode-1	−10.83 ± 2411.3i	−10.77 ± 2303.7i	−10.67 ± 2155.5i	−10.55 ± 1991.3i	−10.40 ± 1827.4i
Network mode-2	−13.51 ± 1657.4i	−13.61 ± 1549.7i	−13.77 ± 1401.6i	−13.99 ± 1237.4i	−14.27 ± 1073.4i
Sup. Sync. mode	−6.593 ± 613.13i	−6.595 ± 613.03i	−6.600 ± 612.87i	−6.607 ± 612.62i	−6.616 ± 612.28i
Electrical mode	0.9178 ± 139.87i	0.9081 ± 139.97i	0.9059 ± 140.15i	0.9116 ± 140.41i	0.9260 ± 140.79i
Rotor mode	−60.35 ± 1.1627i	−60.32 ± 1.8238i	−60.28 ± 2.4835i	−60.22 ± 3.175i	−60.14 ± 3.9266i
Elect-mech. mode	−4.008 ± 32.638i	−4.064 ± 32.565i	−4.165 ± 32.37i	−4.320 ± 32.048i	−4.545 ± 31.584i
Torsional mode	−0.412 ± 3.5351i	−0.426 ± 3.5365i	−0.4571 ± 3.5392i	−0.510 ± 3.5458i	−0.600 ± 3.5646i
Non-osc. mode	−7.229	−7.051	−6.736	−6.252	−5.535

Table 18.4 Critical series compensation level (%) for different outputs of a 500 MW wind farm

Wind farm output	100 MW	200 MW	300 MW	400 MW	500 MW
Critical series-compensation level (%)	52.75	52.80	52.85	52.80	52.60

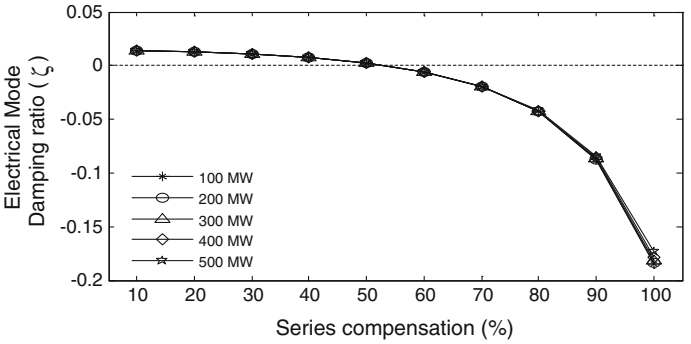

Fig. 18.10 Electrical mode damping ratio

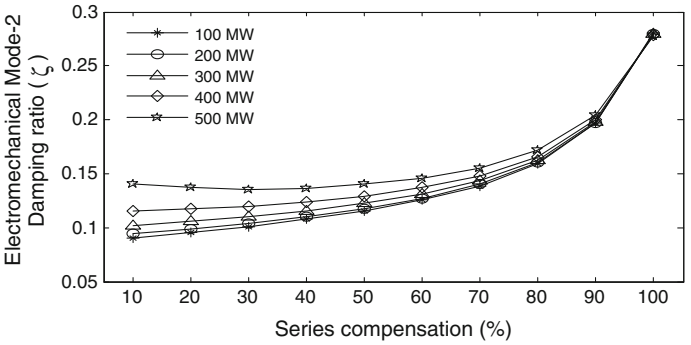

Fig. 18.11 Electromechanical mode damping ratio

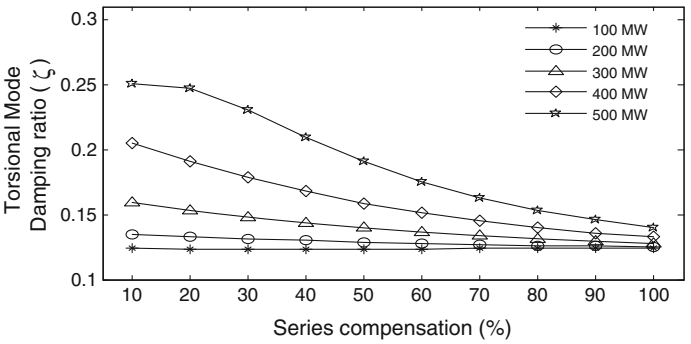

Fig. 18.12 Torsional mode damping ratio

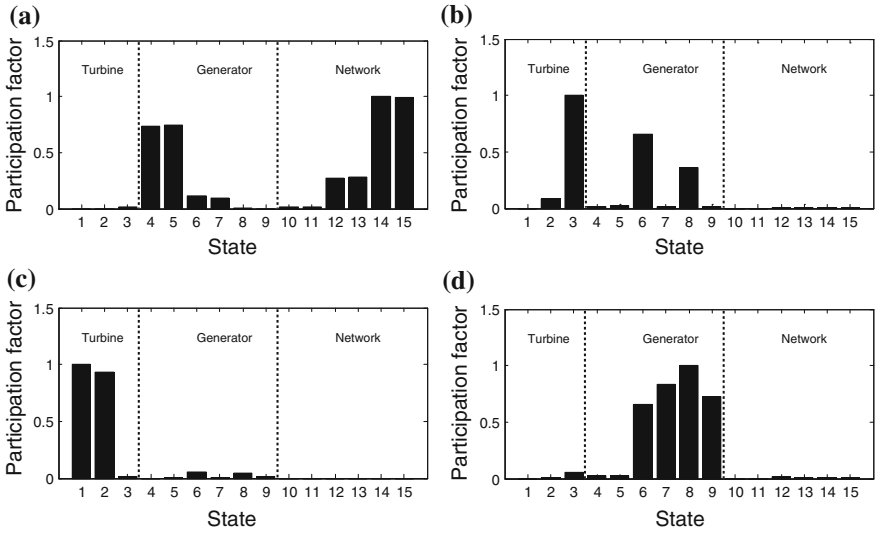

Fig. 18.13 Participation factors of various modes. **a** Electrical mode. **b** Electromechanical mode. **c** Torsional mode. **d** Rotor mode

voltage across the series capacitor, *d-q* axis stator current of the induction generator and line current. Although very small, rotor circuit influence is also observed here. Figure 18.13b illustrates the participation factor associated with the electromechanical mode. This shows the contribution from the generator speed, and *d* axis induced voltage of two rotor cages. Similarly the torsional mode participation factor is depicted in Fig. 18.13c, which is mostly contributed by the dynamics of the drive train system and no interaction from the electrical network is found in this case. The participation factor associated with the rotor mode is shown in Fig. 18.13d. This mode is largely contributed by the rotor circuit parameters.

18.3.2 Electromagnetic Transient Analysis

18.3.2.1 Steady State SSR

This section presents the investigation of steady state SSR in two scenarios: (i) variation in the wind farm size and (ii) variation in the output of a 500 MW wind farm.

(a) **Variation in Wind Farm Size**

Figure 18.14 shows the steady state performance of a 100 MW wind farm connected to 50 and 60 % series-compensated lines, respectively. The motivation behind the chosen series compensation is that one is below and another is above the

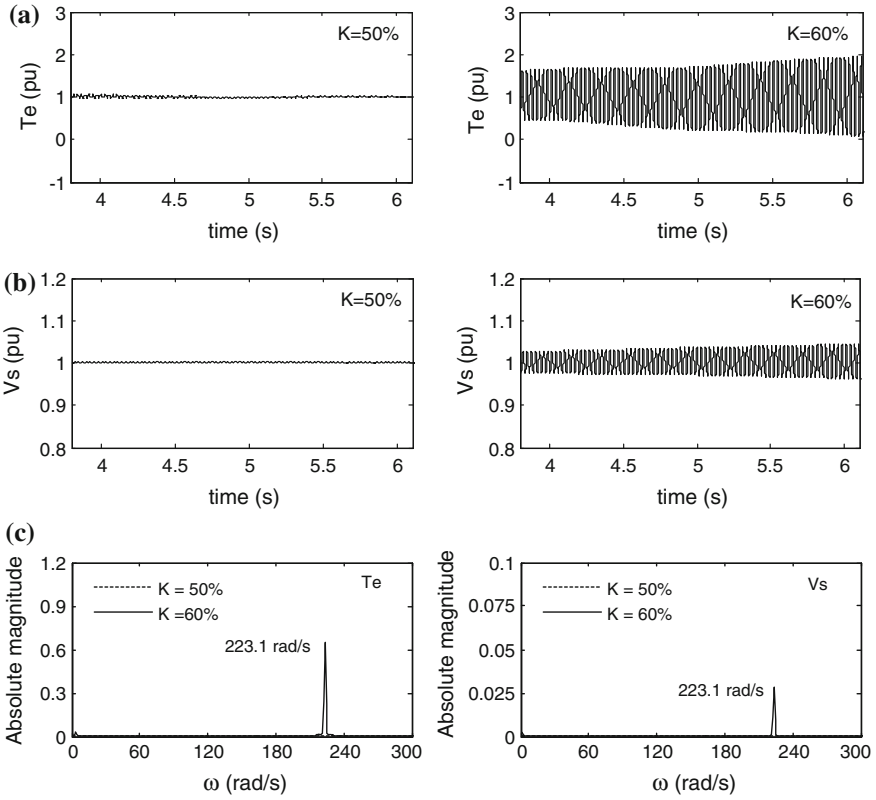

Fig. 18.14 Steady state SSR in a 100 MW wind farm. **a** Electromagnetic torque. **b** PCC voltage. **c** FFT of electromagnetic torque

critical compensation level as shown in Table 18.2. As predicted from eigenvalues in Table 18.1, the 100 MW wind farm connected to a 50 % series-compensated line exhibits a stable electrical mode and no self-excited oscillations are found in the electromagnetic torque as shown in Fig. 18.14a. However, with 60 % series compensation the electromagnetic torque experiences self-excitation that grows with time. PCC voltage shown in Fig. 18.14b also exhibits similar behaviour. Beyond the critical compensation level of 56 % shown in Table 18.2, self-excitation occurs in the system. The FFT analysis of the electromagnetic torque and the PCC voltage is shown in Fig. 18.14c. The estimated frequencies of both the oscillations are found to be 223.1 rad/s which matches very closely with the calculated value of 223.87 rad/s (damped frequency of the electrical mode at 60 % series compensation) shown in Table 18.1. Similar study is conducted for a 300 MW wind farm. In this case the compensation levels are 40 and 50 % because of the lower critical compensation level (48.25 %) shown in Table 18.2. No oscillation is witnessed with 40 % series compensation but the electromagnetic torque and PCC voltage start

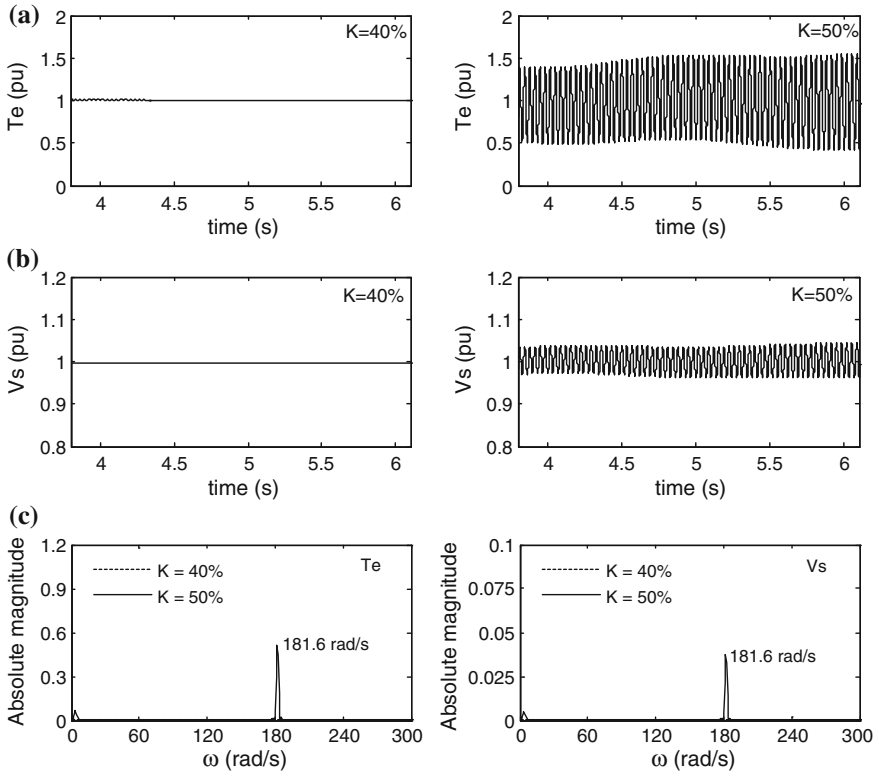

Fig. 18.15 Steady state SSR in a 300 MW wind farm. **a** Electromagnetic torque. **b** PCC voltage. **c** FFT of electromagnetic torque

oscillating when the series compensation level is increased to 50 %, as shown in Fig. 18.15a, b, respectively. This is predicted from the eigenvalue analysis. The FFT of the torque and voltage is shown in Fig. 18.15c. The estimated frequency (181.6 rad/s) matches closely with the electrical mode damped frequency (182.46 rad/s) of the 300 MW wind farm with 50 % series compensation. Similar results are obtained for 500 MW wind farm.

(b) Variation in Wind Farm Output

The study of steady state SSR is now done with a large 500 MW wind farm producing 100 and 300 MW output. Table 4.4 shows the critical compensation levels for different output conditions. Thus, 50 and 55 % series compensation are chosen to simulate one stable and unstable operating condition. Figure 18.16a shows the electromagnetic torque of 100 MW output at steady state for the two compensation levels. Similarly the PCC voltage is shown in Fig. 18.16b. To estimate the oscillatory frequency FFT analysis of the electromagnetic torque and the PCC voltage are carried out and shown in Fig. 18.16c. The estimated frequencies

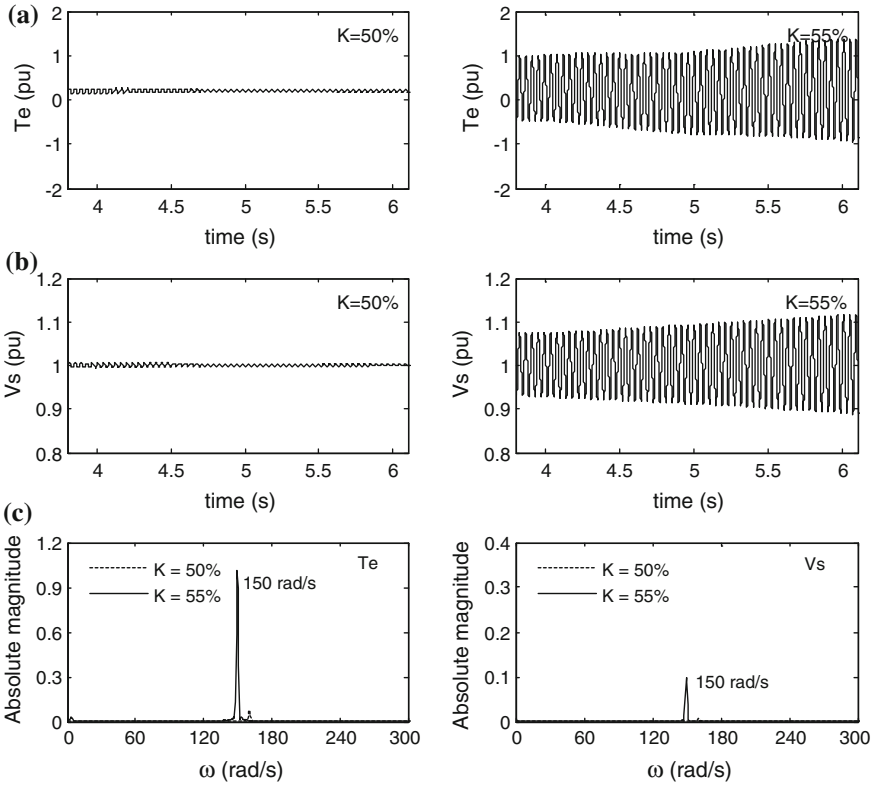

Fig. 18.16 Steady state SSR in a 500 MW wind farm producing 100 MW output. **a** Electromagnetic torque. **b** PCC voltage. **c** FFT of electromagnetic torque

shown in Fig. 18.16c correspond to 55 % series compensation, which match with the calculated values shown in Table 18.3. A similar study is conducted with 300 MW output. The self-excitation in electromagnetic torque and PCC voltage are observed, and shown in Fig. 18.17a, b, respectively. The FFT of the two quantities are shown in Fig. 18.17c. The estimated frequencies match with the calculated damped frequencies shown in Table 18.3.

18.3.2.2 Transient SSR

(a) Variation in Wind Farm Size

Transient SSR in wind farms may result from large disturbances such as fault, or line outages etc. To study the potential of SSR during transients in the system, a three-phase fault is simulated at *F* (Bus-2) as shown in Fig. 18.1 The fault is simulated at t = 4 s and cleared after six cycles (100 ms). When the fault occurs, a

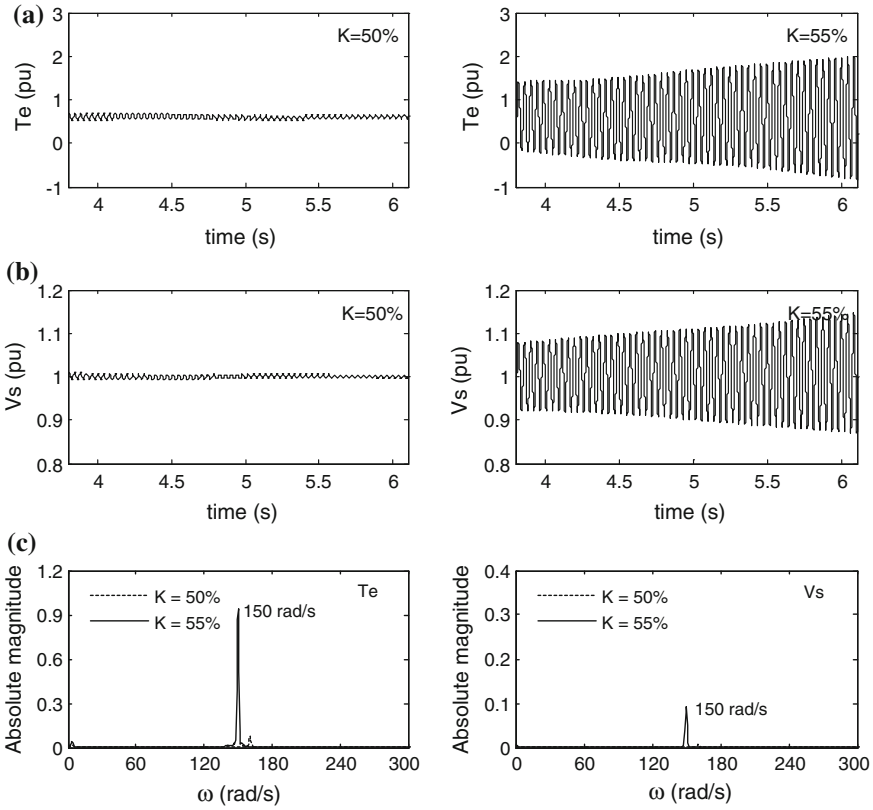

Fig. 18.17 Steady state SSR in a 500 MW wind farm producing 300 MW output. **a** Electromagnetic torque. **b** PCC voltage. **c** FFT of electromagnetic torque

large disturbance is experienced in the electromagnetic torque, shaft torque, speed of the generator, terminal voltage and voltage across series capacitor. Each of the mentioned variables contains multiple frequency components. Thus FFT analysis is carried out to determine the various frequency components.

A 100 MW wind farm with 50 and 60 % series compensation is considered and simulation results are shown in Fig. 18.18. The electromagnetic torque following the disturbance is shown in Fig. 18.18a. Since 50 % series compensation is a stable operating condition the oscillation in electromagnetic torque decays. However, with 60 % series compensation the oscillation in electromagnetic torque grows gradually and becomes unstable. Corresponding shaft torque is shown in Fig. 18.18b. With 60 % series compensation, the shaft torque destabilizes due to the influence of the electrical mode instability. The FFT of electromagnetic torque and shaft torque is shown in Fig. 18.18c. The frequencies 237.1 and 223.8 rad/s corresponding to the 50 and 60 % series compensation, respectively, match with the calculated frequencies of 237.08 and 223.87 rad/s, respectively, shown in Table 18.1. Similarly,

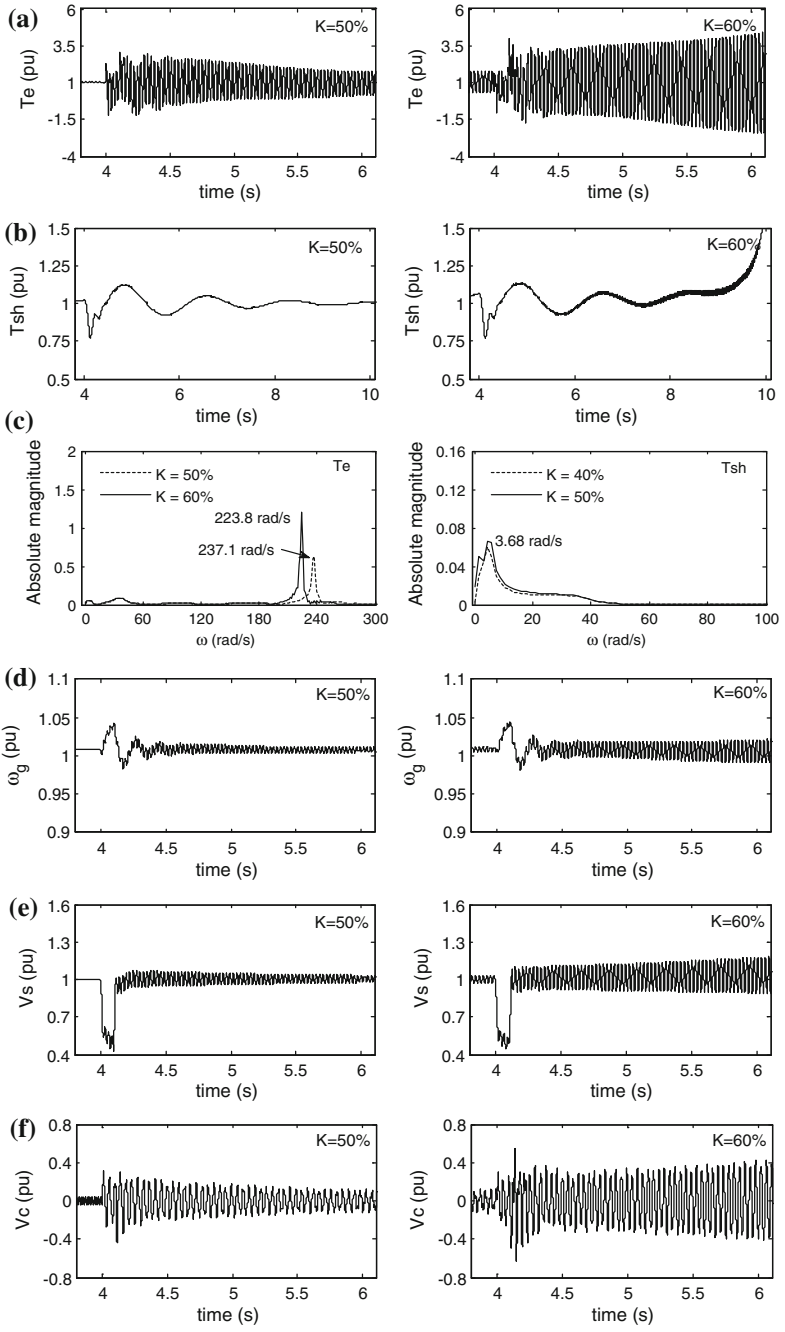

Fig. 18.18 Transient SSR in a 100 MW wind farm. **a** Electromagnetic torque. **b** Shaft torque. **c** FFT of electromagnetic and shaft torque. **d** Generator speed. **e** PCC voltage. **f** Series capacitor voltage

the FFT of shaft torque shows the torsional mode frequency of 3.68 rad/s which corresponds to the calculated damped frequency of ≈ 3.57 rad/s. This correlation validates the small-signal analysis carried out in this chapter. The generator speed, PCC voltage, and voltage across series capacitor are shown in Fig. 18.18d–f, respectively. The oscillations in the generator speed and PCC voltage contain multiple frequency components that are similar to the detected components found in electromagnetic torque and shaft torque. The series capacitor voltage contains a frequency component that is the 60 Hz compliment of the electrical mode oscillatory frequency.

Similar study is carried out with a 300 MW wind farm connected to 40 and 50 % series-compensated transmission line. The response of the wind farm following the three-phase fault at the remote end is depicted in Fig. 18.19. The electromagnetic torque oscillation shown in Fig. 18.19a is similar to the 100 MW wind farm illustrated in Fig. 18.19a. Shaft torque oscillation is shown in Fig. 18.19b. In this case since the instability does not occur within the time frame (10 s) of simulation, the shaft torque seems to be stabilized. However, the electrical mode instability destabilizes the shaft torque after 10 s, not shown here. The FFT of the electromagnetic torque (see Fig. 18.19c) shows two frequencies: 203.1 and 182.6 rad/s, corresponding to 40 and 50 % series compensation, respectively. FFT of the shaft torque depicted in Fig. 18.19c shows a torsional mode frequency of 3.68 rad/s. All of the measured frequencies match very well with the corresponding calculated damped frequencies shown in the Table 18.1. The generator speed, PCC voltage, and series capacitor voltage also exhibit similar responses to the fault which are displayed in Fig. 18.19d–f.

(b) **Variation in Wind Farm Output**

Due to the variation in the wind speed, variable output power from the wind farm flows through the series-compensated line. To evaluate the impact of series compensation on the wind farm during the above scenario, several simulations are carried out with a 500 MW wind farm producing variable power outputs. The series compensation levels considered are 50 and 55 %. Figure 18.20 shows the performance of the wind farm producing 100 MW (0.2 pu) output. With 55 % series compensation the electrical mode is found to be unstable as shown in Table 18.3. This is now reasonably validated through the time domain simulation shown in Fig. 18.20a. The shaft torque for the corresponding series compensation level is shown in Fig. 18.20b. Due to the electrical mode instability, shaft torque is also amplified and attains a very high magnitude which can potentially damage the wind turbine shafts. The FFT of electromagnetic torque and shaft torque are shown in Fig. 18.20c. The estimated frequencies match very closely with the calculated values shown in Table 18.3. Generator speed and PCC voltage are shown in Fig. 18.20d, e, respectively. With 50 % series compensation, the oscillations in the speed and voltage are stabilized. However, the oscillation grows with 55 % series compensation. The estimated frequencies are identical to the measured frequencies obtained from the FFT of electromagnetic torque.

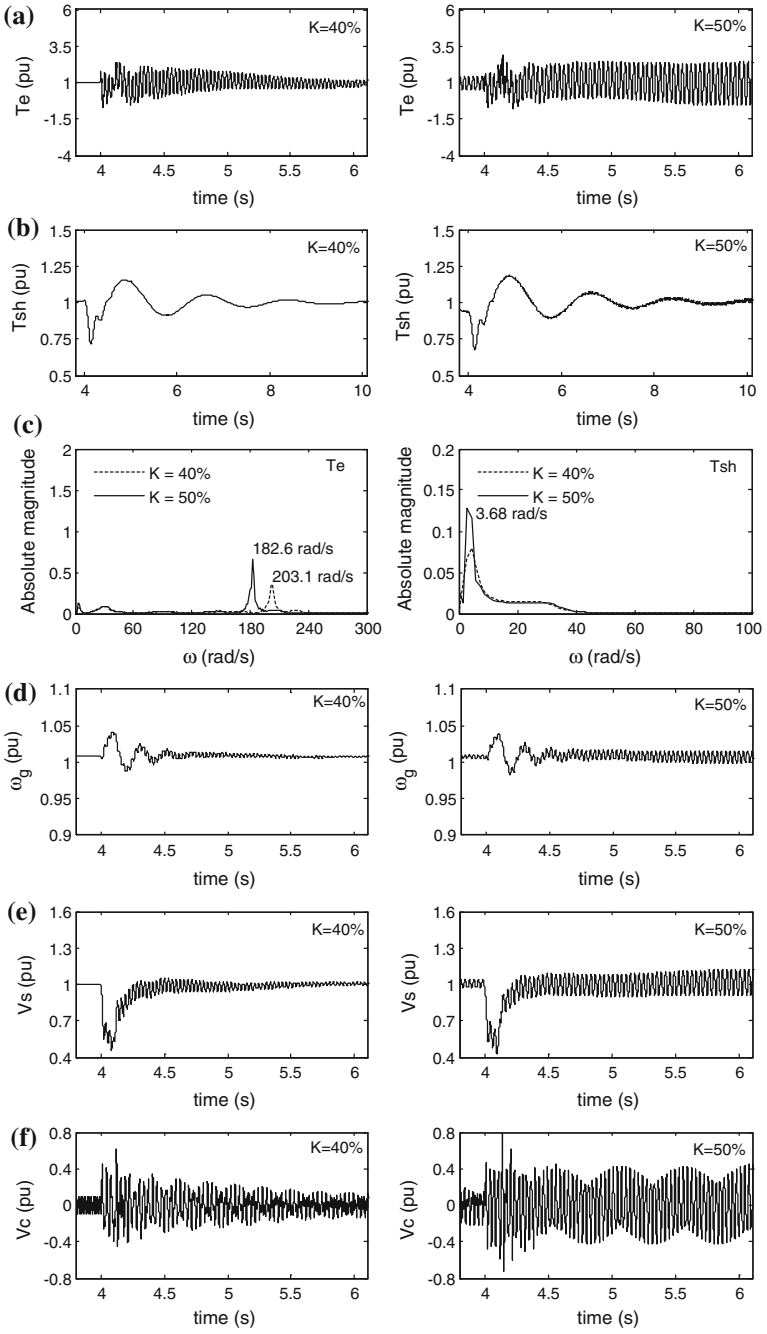

Fig. 18.19 Transient SSR in a 300 MW wind farm. **a** Electromagnetic torque. **b** Shaft torque. **c** FFT of electromagnetic and shaft torque. **d** Generator speed. **e** PCC voltage. **f** Series capacitor voltage

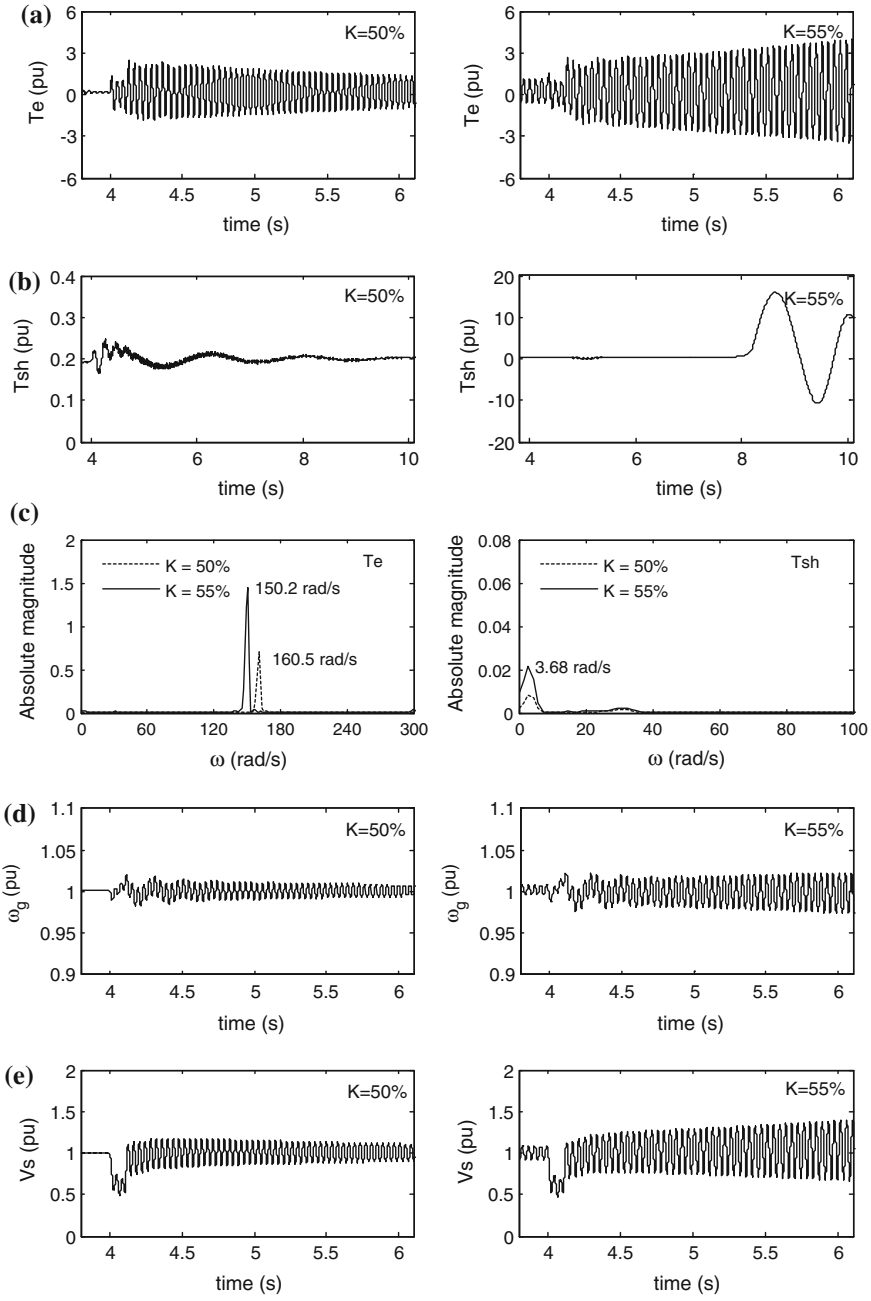

Fig. 18.20 Transient SSR in a 500 MW wind farm producing 100 MW output. **a** Electromagnetic torque. **b** Shaft torque. **c** FFT of electromagnetic torque and shaft torque. **d** Generator speed. **e** PCC voltage

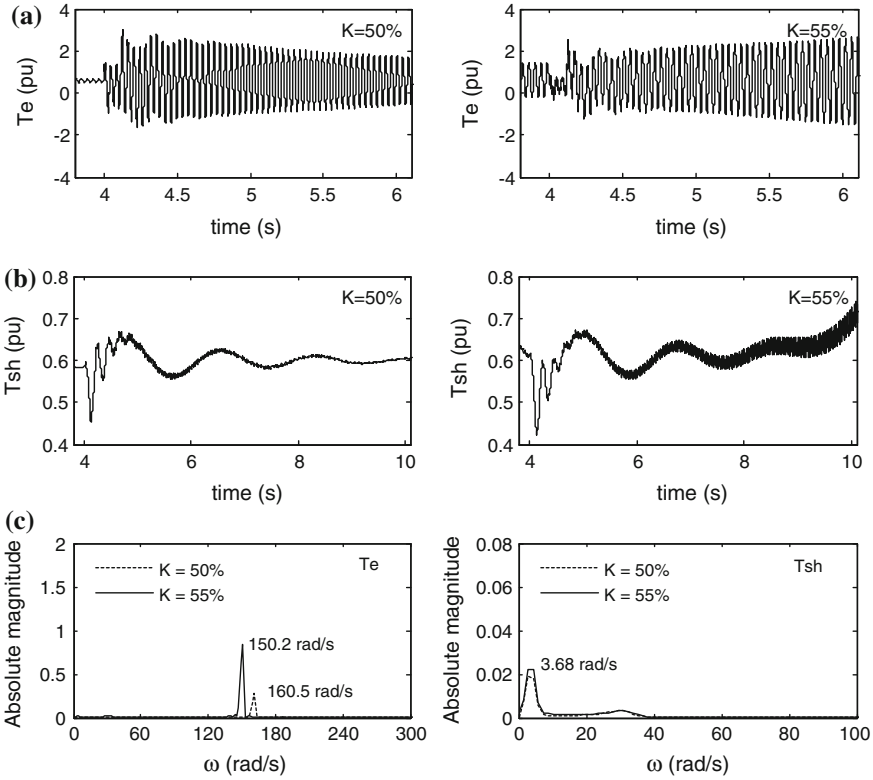

Fig. 18.21 Transient SSR in a 500 MW wind farm producing 300 MW output. **a** Electromagnetic torque. **b** Shaft torque. **c** FFT of electromagnetic torque and shaft torque

Figure 18.21 illustrates the performance of the wind farm with 300 MW output. The electromagnetic torque and shaft torque are shown in Fig. 18.21a, b, respectively. The oscillations are almost similar to the oscillations observed with 100 MW output shown in Fig. 18.20. The estimated frequencies from the FFT are depicted in Fig. 18.21c, which match with the calculated damped frequencies. From the study with other outputs and sizes of wind farm, it is confirmed that beyond the critical compensation, symmetrical fault in the network may cause significant rise in the electromagnetic torque and shaft torque. Repetitive high shaft torque may lead to cyclic fatigue of the shaft.

18.4 SSR Mitigation Using STATCOM

In recent global power scenarios, wind power generator technology has occupied a significant space and it is growing continuously. The wind energy penetration has increased substantially in some countries. To comply with the grid code, the wind

farms are expected to remain connected during the low voltage and/or fault in the grid. Significant reactive power support is therefore required for the wind farms to meet the grid code. STATCOM leads amongst the different devices used for dynamic reactive power compensation, due to its advantages stated earlier. Stability of the power system also depends upon the stability of the large wind farms, which can be improved by putting a STATCOM of suitable rating at the PCC. With increased threat of SSR in an induction generator based wind farm, a STATCOM is proposed at the PCC as shown in Fig. 18.22. The size of the STATCOM is set around 60 MVA/100 MW wind farm size.

STATCOM was developed as an advanced VAr compensator. STATCOM consists of a Voltage Source Converter (VSC) instead of controllable reactors and switched capacitors used in static VAr compensator (SVC). The first STATCOM in the world was commissioned in Japan in 1991. The STATCOM have several advantages over the SVC. Few of them are [37]:

- Faster response
- Less space requirement
- Relocatable
- Can be interfaced with battery, fuel cell, SMES or PV modules
- Superior performance during the transient
- Does not contribute to the short circuit current
- No issue related to loss of synchronism

A STATCOM is comparable to the synchronous condenser, which can supply variable reactive power and regulate the bus voltage. The STATCOM is realized as a voltage source with variable magnitude. If the STATCOM voltage magnitude is set to a higher value than the grid voltage (in pu), it injects reactive power into the grid. This mode of operation very often is referred to as the "over-excited" mode. Similarly, when the STATCOM per unit voltage magnitude is lower than the grid voltage, it absorbs reactive power and is known as "under-excited" mode. In the over excited mode operation the STATCOM acts like a variable capacitor and

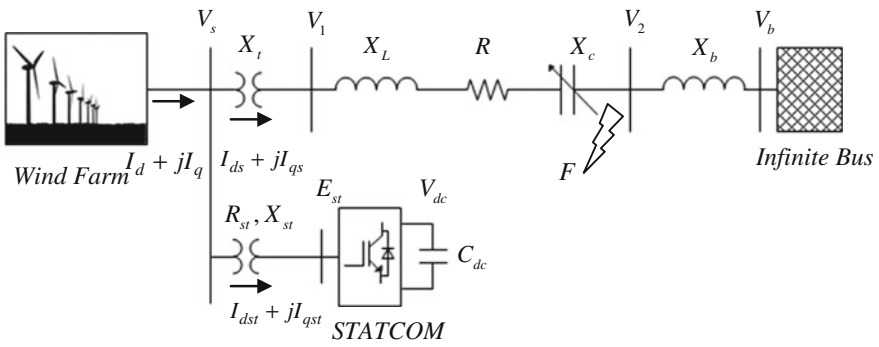

Fig. 18.22 STATCOM proposed at the PCC of wind farm

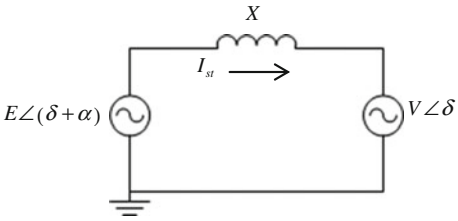

Fig. 18.23 Equivalent circuit of a synchronous condenser

during the under excited mode it behaves like a variable inductor. An equivalent circuit of the system with a VAr compensator is shown in Fig. 18.23. The reactive current is derived as

$$I_{st} = \frac{E - V}{X} \tag{18.74}$$

18.4.1 Power Circuit Modeling

The single line diagram of the STATCOM is shown in Fig. 18.24. The STATCOM bus AC voltage is directly proportional to the DC side voltage. A capacitor is connected at the DC side of the converter, whose voltage is to be kept constant [37, 65, 66]. The modeling and analysis of the STATCOM is carried out with the following:

- The system voltages are balanced and sinusoidal
- The switches are ideal
- Transformer impedances are equal in all three phases

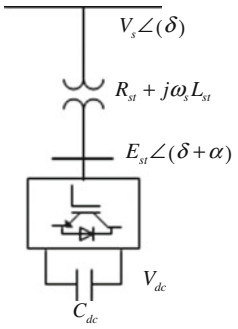

Fig. 18.24 Equivalent circuit of STATCOM

Considering a six-pulse converter the STATCOM can be described by the differential equations:

$$L_{st}\frac{dI_{sta}}{dt} = V_{sa} - R_{st}I_{sta} - E_{sta} \tag{18.75}$$

$$L_{st}\frac{dI_{stb}}{dt} = V_{sb} - R_{st}I_{stb} - E_{stb} \tag{18.76}$$

$$L_{st}\frac{dI_{stc}}{dt} = V_{sc} - R_{st}I_{stc} - E_{stc} \tag{18.77}$$

$$C_{dc}\frac{dV_{dc}}{dt} = I_{dc} - \frac{V_{dc}}{R_{dc}} \tag{18.78}$$

where,

R_{st}	Resistance in series with the STATCOM represents the sum of transformer winding resistance losses and the inverter conduction losses (pu)
L_{st}	Leakage resistance of the transformer (pu)
C_{dc}	DC side capacitor (pu)
R_{dc}	Resistance in shunt with the capacitor C_{dc} represents the switching loss of the inverter and the power loss in the capacitor (pu)
$I_{sta}, I_{stb}, I_{stc}$	Three phase currents of the STATCOM (pu)
V_{sa}, V_{sb}, V_{sc}	Three phase voltages at the PCC (pu)
$E_{sta}, E_{stb}, E_{stc}$	Three phase voltages at the STATCOM terminal (pu)
V_{dc}	DC side voltage (pu)
I_{dc}	DC side current (pu)

Applying Kron's transformation [37] to transform Eqs. (18.75)–(18.77) to a synchronously rotating reference frame the dynamic equations are written as:

$$L_{st}\frac{d}{dt}I_{dst} = V_{ds} - R_{st}I_{dst} + \omega_s L_{st}I_{qst} - E_{dst} \tag{18.79}$$

$$L_{st}\frac{d}{dt}I_{qst} = V_{qs} - R_{st}I_{qst} - \omega_s L_{st}I_{dst} - E_{qst} \tag{18.80}$$

where,

V_{ds}, V_{qs}	d-q axis PCC voltage (pu)
I_{dst}, I_{qst}	d-q axis STATCOM current (pu)
E_{dse}, E_{qst}	d-q axis STATCOM terminal voltage (pu)

Assuming the switches are ideal, they are lossless and from the conservation of energy principle, in terms of *d-q* form,

$$V_{dc}I_{dc} = E_{dst}I_{dst} + E_{qst}I_{qst} \tag{18.81}$$

E_{dst} and E_{qst} are now expressed as the function of modulation index (m), DC voltage (V_{dc}), angle of the PCC voltage (θ) and the angular difference between the PCC voltage and the STATCOM terminal voltage (α).

$$E_{dst} = mV_{dc}\sin(\theta + \alpha) \tag{18.82}$$

$$E_{qst} = mV_{dc}\cos(\theta + \alpha) \tag{18.83}$$

$$m = \frac{\sqrt{6}}{\pi} \tag{18.84}$$

Substituting (18.82) and (18.83) in (18.81)

$$P_{dc} = mV_{dc}\sin(\theta + \alpha)I_{dst} + mV_{dc}\cos(\theta + \alpha)I_{qst} \tag{18.85}$$

Comparing (18.81) and (18.85)

$$I_{dc} = mI_{dst}\sin(\theta + \alpha) + mI_{qst}\cos(\theta + \alpha) \tag{18.86}$$

It is to be noted that

$$\tan(\theta) = \frac{V_{ds}}{V_{qs}}, \quad V_s = \sqrt{V_{ds}^2 + V_{qs}^2} \tag{18.87}$$

$$V_{ds} = V_s\sin(\theta), \quad V_{qs} = V_s\cos(\theta) \tag{18.88}$$

The active current I_{st}^P, and reactive current I_{st}^R, of the STATCOM can be written as:

$$I_{st}^P = \frac{V_{ds}I_{dst} + V_{qs}I_{qst}}{V_s} \tag{18.89}$$

$$I_{st}^R = \frac{-V_{ds}I_{qst} + V_{qs}I_{dst}}{V_s} \tag{18.90}$$

Using (18.88) in (18.89) and (18.90)

$$I_{st}^P = I_{dst}\sin(\theta) + I_{qst}\cos(\theta) \tag{18.91}$$

$$I_{st}^R = I_{dst}\cos(\theta) - I_{qst}\sin(\theta) \tag{18.92}$$

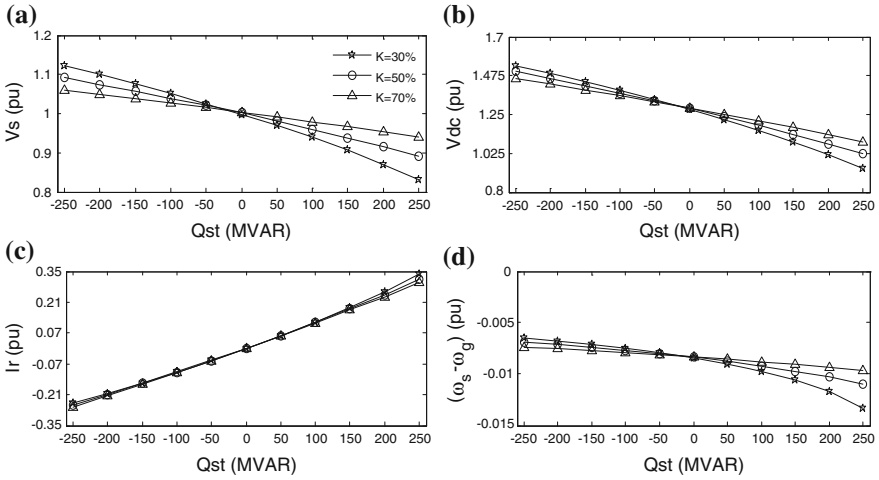

Fig. 18.25 Steady state performance of STATCOM. **a** PCC voltage. **b** DC Voltage. **c** Reactive current. **d** Generator slip

18.4.2 Steady State Performance of the STATCOM

The steady state performance of the proposed STATCOM when connected to the study system is presented in Fig. 18.25. Variation in the PCC voltage for different reactive power rating of the STATCOM is shown in Fig. 18.25a. This is carried out for three different series compensation levels (K): 30, 50 and 70 %. It is seen that, with the low series compensation level the STATCOM controls the voltage more effectively and the slope decreases with the increase in the series compensation level. Similar analysis is carried out for the DC voltage that is shown in Fig. 18.25b. Variation in DC voltage is very much similar to that of PCC voltage. Figure 18.25c shows the reactive power injection from the STATCOM for different series compensation level. Variation in the slip of the induction generator is shown in Fig. 18.25d. It is seen that in inductive mode of the STATCOM, the slip decreases faster with lower series compensation. As the series compensation level increases the variation in the slip is small.

18.4.3 Modeling of STATCOM Controller

Two types of STATCOM controllers are proposed for the mitigation of SSR in wind farms. The detailed model of each controller is discussed here.

18.4.3.1 Controller-I

The proposed controller-I (C–I) is similar to the Type-2 controller originally proposed in [66]. In this controller DC voltage remains uncontrolled and only the angular difference between the STATCOM terminal and the PCC bus voltage is controlled. This controller is mostly used in transmission network for dynamic reactive power support. However, the uncontrolled DC voltage may cause over voltage in the AC side bus. Figure 18.26 shows the block diagram of the controller-I.

The state space model of the controller is developed for small-signal analysis. The linearized dynamic equations of controller-I are:

$$T_{LP}\frac{d}{dt}(\Delta x_1) = \Delta V_s - K_s \Delta I_R - \Delta x_1 \tag{18.93}$$

$$GT_1\frac{d}{dt}(\Delta x_1) + T_2\frac{d}{dt}(\Delta x_2) = G\left(V_S^{Ref} - \Delta x_1\right) - \Delta x_2 \tag{18.94}$$

$$T_I\frac{d}{dt}(\Delta x_3) = \Delta x_2 \tag{18.95}$$

Arranging (18.93)–(18.95) in the state space form,

$$\dot{x}_{Ct} = [A_{Ct}]x_{Ct} + [B_{Ct}]u_{Ct} \tag{18.96}$$

$$y_{Ct} = [C_{Ct}]x_{Ct} \tag{18.97}$$

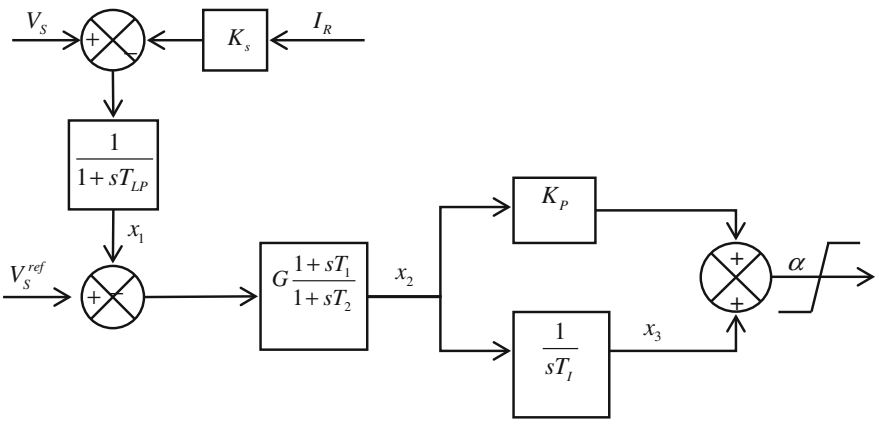

Fig. 18.26 Block diagram of controller-I

where,

$$x_{Ct}^{t} = [\Delta x_1 \quad \Delta x_2 \quad \Delta x_3], \quad y_{Ct} = [\Delta\alpha] \tag{18.98}$$

$$u_{Ct}^{t} = [\Delta V_s \quad \Delta I_R] \tag{18.99}$$

$$[C_{Ct}] = [K] = [0 \quad K_P \quad 1] \tag{18.100}$$

18.4.3.2 Controller-II

In controller-II (C-II), the DC link capacitor voltage is controlled by the phase angle difference between the STATCOM terminal and PCC bus voltage. The reactive current is controlled by regulating V_s to V_s^{ref}. In this controller, modulation index (m) and angle (α) are controlled. The proposed controller-II is shown in Fig. 18.27, where both the inputs are decoupled from each other. The modulation index is

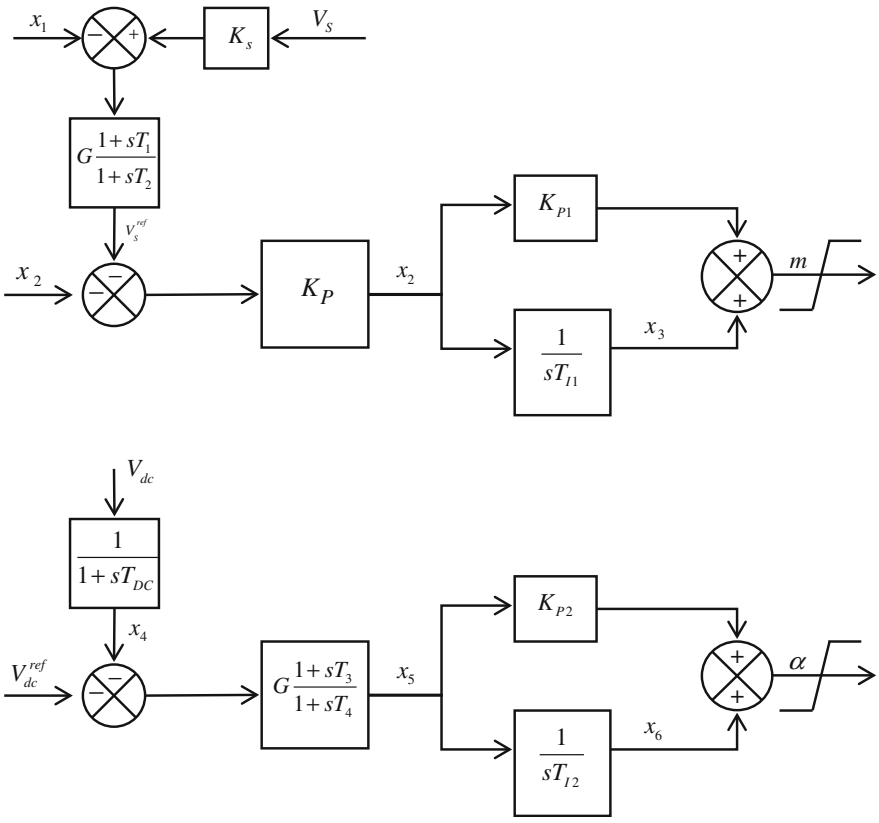

Fig. 18.27 Block diagram of controller-II

derived from the voltage error, where a voltage droop characteristic is introduced for control of the voltage at the PCC. Regulating the magnitude of the converter bus voltage now regulates the reactive power injection, or absorption by the STATCOM. The phase angle difference (α) is derived from the DC voltage error. For the damping of subsynchronous oscillations, an additional lead lag compensator is used in each control path. Since no torsional interaction is witnessed in the wind farm due to series compensation, no damping controller is required here. For the small-signal analysis, the proposed controller is now modeled as a linear time invariant system that is described through a set of differential equations. The dynamic equations of the controller-II are written as:

$$T_{LP}\frac{d}{dt}(\Delta x_1) = \Delta V_S - K_S \Delta I_R - \Delta x_1 \tag{18.101}$$

$$G_1 T_1 \frac{d}{dt}(\Delta x_1) + T_2 \frac{d}{dt}(\Delta x_2) = G_1\left(V_S^{Ref} - \Delta x_1\right) - \Delta x_2 \tag{18.102}$$

$$T_{I1}\frac{d}{dt}(\Delta x_3) = \Delta x_2 \tag{18.103}$$

$$T_{DC}\frac{d}{dt}(\Delta x_4) = \Delta V_{DC} - \Delta x_4 \tag{18.104}$$

$$G_2 T_3 \frac{d}{dt}(\Delta x_4) + T_4 \frac{d}{dt}(\Delta x_5) = G_2\left(V_{DC}^{Ref} - \Delta x_4\right) - \Delta x_5 \tag{18.105}$$

$$T_{I2}\frac{d}{dt}(\Delta x_6) = \Delta x_5 \tag{18.106}$$

Equations (18.101)–(18.106) are written in the linear state space form as

$$\dot{x}_{Ct} = [A_{Ct}]x_{Ct} + [B_{Ct}]u_{Ct} \tag{18.107}$$

$$y_{Ct} = [C_{Ct}]x_{Ct} \tag{18.108}$$

where,

$$x_{Ct}^t = [\,\Delta x_1 \quad \Delta x_2 \quad \Delta x_3 \quad \Delta x_4 \quad \Delta x_5 \quad \Delta x_6\,] \tag{18.109}$$

$$y_{Ct}^t = [\,\Delta m \quad \Delta\alpha\,] \tag{18.110}$$

$$[C_{Ct}] = [K] = \begin{bmatrix} 0 & K_{P1} & 1 & 0 & 0 & 0 \\ 0 & 0 & 0 & 0 & K_{P1} & 1 \end{bmatrix} \tag{18.111}$$

18.4.4 Complete System Model

18.4.4.1 Complete System Model with Controller-I

Keeping the drive train and induction generator model intact only the network models are redefined. These equations are linearized while constructing the small-signal model. The differential equations are:

$$C_g \frac{d}{dt} V_{ds} = I_{ds} - (I_d + I_{dst}) + \omega_s C_g V_{qs} \tag{18.112}$$

$$C_g \frac{d}{dt} V_{qs} = I_{qs} - (I_q + I_{qst}) - \omega_s C_g V_{ds} \tag{18.113}$$

$$L \frac{d}{dt} I_d = V_{ds} - R I_d + \omega_s L I_q - V_{cd} - V_{bd} \tag{18.114}$$

$$L \frac{d}{dt} I_q = V_{qs} - R I_q - \omega_s L I_d - V_{cq} - V_{bq} \tag{18.115}$$

$$C \frac{d}{dt} V_{cd} = I_d + \omega_s C V_{cq} \tag{18.116}$$

$$C \frac{d}{dt} V_{cq} = I_q - \omega_s C V_{cd} \tag{18.117}$$

where,

V_{ds}, V_{qs}	d-q axis voltage at the PCC (pu)
I_{ds}, I_{qs}	d-q axis stator current of induction generator (pu)
I_d, I_q	d-q axis series-compensated line current (pu)
V_{cd}, V_{cq}	d-q axis voltage across series capacitor (pu)
V_{bd}, V_{bq}	d-q axis voltage at the infinite bus (pu)

The state space model of the drive train, induction generator and network are expressed as:

$$\dot{x}_{WT} = [A_{TT}]x_{WT} + [A_{TG}]x_G + [B_T]u_{WT} \tag{18.118}$$

$$\dot{x}_G = [A_{GT}]x_{WT} + [A_{GG}]x_G + [A_{GN}]x_N \tag{18.119}$$

$$\dot{x}_N = [A_{NG}]x_G + [A_{NN}]x_N + [A_{NSt}]x_{St} + [B_N]u_N \tag{18.120}$$

Arranging the dynamic equations of the power circuit of the STATCOM presented in (18.78)–(18.80), the STATCOM model is defined in the state space form as:

$$\dot{x}_{St} = [A_{StN}]x_N + [A_{StSt}]x_{St} + [B_{St}]u_{St} \tag{18.121}$$

where,

$$u_{st} = [\Delta\alpha] \tag{18.122}$$

Combining (18.118)–(18.121) the open loop equation of the complete system is written as:

$$\dot{x}_{sys} = [A_{sys}]x_{sys} + [B_1]u_1 + [B_2]u_2 + [B_3]u_3 \tag{18.123}$$

where,

$$x^t_{sys} = [\,x^t_{WT} \quad x^t_G \quad x^t_N \quad x^t_{St}\,] \tag{18.124}$$

$$x^t_{WT} = [\,\Delta\omega_t \quad \Delta\delta_{tg} \quad \Delta\omega_g\,] \tag{18.125}$$

$$x^t_G = [\,\Delta I_{ds} \quad \Delta I_{qs} \quad \Delta E_{d1} \quad \Delta E_{q1} \quad \Delta E_{d2} \quad \Delta E_{q2}\,] \tag{18.126}$$

$$x^t_N = [\,\Delta V_{ds} \quad \Delta V_{ds} \quad \Delta I_d \quad \Delta I_q \quad \Delta V_{cd} \quad \Delta V_{cq}\,] \tag{18.127}$$

$$x^t_{St} = [\,\Delta I_{dst} \quad \Delta I_{qst} \quad \Delta V_{dc}\,] \tag{18.128}$$

$$u_1 = [\Delta T_W], \quad u_2 = \begin{bmatrix} \Delta V_{bd} \\ \Delta V_{bq} \end{bmatrix}, \quad u_3 = u_{St} \tag{18.129}$$

The state space model of controller-I defined in (18.96) is rewritten as:

$$\dot{x}_{Ct} = [A_{Ct}]x_{Ct} + [B_{Ct}][M]x_{sys} \tag{18.130}$$

where,

$$[M]x_{sys} = u_{Ct} \tag{18.131}$$

Further

$$u_3 = [K]\Delta x_{Ct} \tag{18.132}$$

The combined equation of the system including controller-I is now expressed as:

$$\begin{bmatrix} \dot{x}_{sys} \\ \dot{x}_{Ct} \end{bmatrix} = \begin{bmatrix} A_{sys} & B_3K \\ B_{Ct}M & A_{Ct} \end{bmatrix} \begin{bmatrix} x_{sys} \\ x_{Ct} \end{bmatrix} + B_1u_1 + B_2u_2 \tag{18.133}$$

The total number of states of the closed loop system is 21. The detailed eigenvalue analysis of the closed loop system defined in (18.133) is presented in Sect. 18.5.

18.4.4.2 Complete System Model with Controller-II

The augmentation of the controller-II is carried out in a similar way as described for controller-I. The closed loop state space model of the system is developed as mentioned in (18.133). With controller-II the total number of states becomes 24.

18.5 Small-signal Stability Analysis

The eigenvalue analysis of the study system is carried out for a wide range of operating conditions. The wind farm size is varied from 100 to 500 MW, while the series compensation is varied between 10 and 90 %. In this study the size of STATCOM is chosen about 60 MVA/100 MW. The choice of STATCOM size is based on the previous study conducted in [26–16] and STATCOMs used in integration of wind farm. Table 18.5 shows all the eigenvalues of the systems (300 MW wind farm with 50 % series compensation) including controller-I and controller-II. Out of six complex conjugate eigenvalues and one real eigenvalue only three oscillatory modes that are useful for the analysis of SSR are shown explicitly. In the absence of STATCOM (Table 18.1) as the compensation level increases, the electrical mode becomes less stable and then becomes unstable for all sizes of wind farm considered. Now when the STATCOM with proposed controller-I is employed at the PCC, the system eigenvalues are calculated and shown in Table 18.6. Being the most sensitive mode, the electrical mode is studied thoroughly. It is found that with the controller-I the electrical mode becomes unstable for all wind farm sizes. For example, the electrical mode eigenvalues for 300 MW wind farm with 50 % series

Table 18.5 Complete system eigenvalues

Mode	Without STATCOM	With STATCOM	
		Controller-I	Controller-II
Sup. Sync. mode	−6.790 ± 570.89i	−6.752 ± 539.98i	−5.470 ± 605.57i
Electrical mode	+0.156 ± 182.46i	−2.188 ± 176.68i	−2.233 ± 175.88i
Elect-mech. mode	−5.020 ± 32.981i	−4.743 ± 33.079i	−5.127 ± 33.076i
Torsional mode	−0.572 ± 3.5703i	−0.502 ± 3.5372i	−0.522 ± 3.5515i
Other modes	−9.575 ± 1984.9i	−5.808 ± 2537.7i	−2.213 ± 2507.4i
	−12.38 ± 1231i	−9.801 ± 1466.4i	−8.526 ± 1456i
	−60.96 ± 3.5792i	−3.558 ± 660.37i	−5.491 ± 605.81i
	−6.525	−167.3 ± 59.511i	−11.25 ± 478.25i
		−61.49 ± 3.3024i	−5.159 ± 128.56i
		−8.919 ± 5.5316i	−62.04 ± 2.596i
		−2.071	−245.0, −178.39
			−8.649, −2.7203
			−0.0062, −0.031231

Table 18.6 System eigenvalues with STATCOM controller-I

Modes	100 MW	200 MW	300 MW	400 MW	500 MW
40 % Series compensation					
Electrical mode	−2.462 ± 238.74i	−2.391 ± 212.56i	−2.372 ± 198.02i	−2.410 ± 188.41i	−2.483 ± 181.42i
Elect-mech. mode	−6.201 ± 36.437i	−5.123 ± 34.018i	−4.355 ± 31.965i	−3.777 ± 30.133i	−3.327 ± 28.423i
Torsional mode	−0.506 ± 3.5829i	−0.503 ± 3.5534i	−0.503 ± 3.5229i	−0.506 ± 3.4899i	−0.512 ± 3.4523i
50 % Series compensation					
Electrical mode	−2.732 ± 221.71i	−2.402 ± 192.82i	−2.188 ± 176.68i	−2.091 ± 166i	−2.074 ± 158.2i
Elect-mech. mode	−6.429 ± 36.927i	−5.463 ± 34.868i	−4.743 ± 33.079i	−4.182 ± 31.465i	−3.729 ± 29.953i
Torsional mode	−0.506 ± 3.5872i	−0.503 ± 3.5625i	−0.502 ± 3.5372i	−0.503 ± 3.5104i	−0.505 ± 3.4807i
55 % Series compensation					
Electrical mode	−2.959 ± 213.81i	−2.482 ± 184.15i	−2.132 ± 166.78i	−1.947 ± 155.59i	−1.867 ± 147.42i
Elect-mech. mode	−6.547 ± 37.183i	−5.665 ± 35.36i	−4.960 ± 33.681i	−4.412 ± 32.189i	−3.962 ± 30.785i
Torsional mode	−0.507 ± 3.5894i	−0.503 ± 3.5676i	−0.502 ± 3.5443i	−0.502 ± 3.5204i	−0.503 ± 3.4942i
60 % Series compensation					
Electrical mode	−3.249 ± 206.24i	−2.585 ± 174.87i	−2.098 ± 157.28i	−1.805 ± 145.6i	−1.650 ± 137.07i
Elect-mech. mode	−6.669 ± 37.447i	−5.842 ± 35.794i	−5.194 ± 34.32i	−4.667 ± 32.963i	−4.224 ± 31.677i
Torsional mode	−0.507 ± 3.5916i	−0.504 ± 3.5716i	−0.502 ± 3.5514i	−0.501 ± 3.5303i	−0.502 ± 3.5075i

compensation are 0.156 ± 182.46i without STATCOM. With STATCOM these eigenvalues become 2.188 ± 176.68i.

Table 18.7 shows the system eigenvalues with STATCOM controller-II that shows a further enhancement in the electrical mode stability in comparison to the controller-I. The proposed controller-II also improves the stability of electromechanical modes of the wind turbine generator. For instance, without STATCOM the electromechanical mode eigenvalues for a 100 MW wind farm with 50 % series compensation are −6.537 ± 36.849i. With controller-I and controller-II these eigenvalues change to −6.4289 ± 36.927i and −6.892 ± 36.733i, respectively. The torsional mode is not much affected by the two STATCOM controllers. The stable eigenvalues of the torsional mode indicate there is no potential of torsional instability.

The improvement of the electrical mode stability with STATCOM is illustrated in Fig. 18.28, which shows the variation in the electrical mode eigenvalues with series compensation level and wind farm size. As observed in Fig. 18.28a, the electrical mode eigenvalues become less stable with increase in the series compensation and cross the imaginary axis at the critical compensation level. Figure 18.28b shows the improvement in the electrical mode stability with the proposed STATCOM controller-I. Only at a very high unrealistic series compensation level the electrical mode of 500 MW wind farm tends to be unstable. The trend of the variation in the electrical mode eigenvalues with controller-II is quite similar to the controller-I, though not reported here.

18.6 Electromagnetic Transient Analysis

This section presents the time domain simulations of the study system carried out with PSCAD/EMTDC software. The detailed model of the wind farm, series-compensated line, and STATCOM with two proposed controllers are implemented with PSCAD/EMTDC. The time-domain simulations are done in steady state and transient condition. The small-signal analysis results are correlated with the time domain simulation results.

18.6.1 Steady State SSR

Steady state SSR refers to the self-excitation due to induction generator effect. This is indicated by an unstable electrical mode. The imaginary part of the electrical mode eigenvalue predicts the oscillatory frequency of the self-excitation in the wind farm. From the eigenvalue analysis it is observed that only the electrical mode becomes unstable beyond a critical compensation level for different sizes of wind farms. Therefore, beyond this compensation level, occurrence of self-excitation is expected. Figure 18.29a shows the self-excitation of the electromagnetic torque and

Table 18.7 System eigenvalues with STATCOM controller-II

Modes	100 MW	200 MW	300 MW	400 MW	500 MW
40 % Series compensation					
Electrical mode	−3.566 ± 227.06i	−2.804 ± 207.5i	−2.511 ± 195.29i	−2.418 ± 187.05i	−2.417 ± 180.81i
Elect-mech. mode	−6.632 ± 36.256i	−5.529 ± 34i	−4.698 ± 31.997i	−4.085 ± 30.255i	−3.603 ± 28.631i
Torsional mode	−0.508 ± 3.5852i	−0.516 ± 3.5623i	−0.529 ± 3.5383i	−0.549 ± 3.5139i	−0.579 ± 3.4879i
50 % Series compensation					
Electrical mode	−3.600 ± 209.54i	−2.628 ± 188.83i	−2.233 ± 175.88i	−2.079 ± 167.08i	−2.033 ± 160.35i
Elect-mech. mode	−6.892 ± 36.733i	−5.909 ± 34.818i	−5.127 ± 33.076i	−4.525 ± 31.538i	−4.034 ± 30.096i
Torsional mode	−0.508 ± 3.5893i	−0.513 ± 3.5708i	−0.522 ± 3.5515i	−0.536 ± 3.5323i	−0.556 ± 3.5122i
55 % Series compensation					
Electrical mode	−3.652 ± 201.87i	−2.635 ± 180.94i	−2.257 ± 167.95i	−2.142 ± 159.2i	−2.141 ± 152.51i
Elect-mech. mode	−7.031 ± 36.983i	−6.122 ± 35.256i	−5.377 ± 33.663i	−4.788 ± 32.242i	−4.297 ± 30.901i
Torsional mode	−0.508 ± 3.5913i	−0.512 ± 3.575i	−0.519 ± 3.558i	−0.530 ± 3.5412i	−0.546 ± 3.5237i
60 % Series compensation					
Electrical mode	−3.736 ± 194.93i	−2.733 ± 174.08i	−2.446 ± 161.38i	−2.437 ± 152.97i	−2.544 ± 146.65i
Elect-mech. mode	−7.179 ± 37.242i	−6.355 ± 35.718i	−5.658 ± 34.289i	−5.090 ± 33i	−4.604 ± 31.772i
Torsional mode	−0.507 ± 3.5934i	−0.511 ± 3.5791i	−0.517 ± 3.5644i	−0.525 ± 3.5499i	−0.537 ± 3.5349i

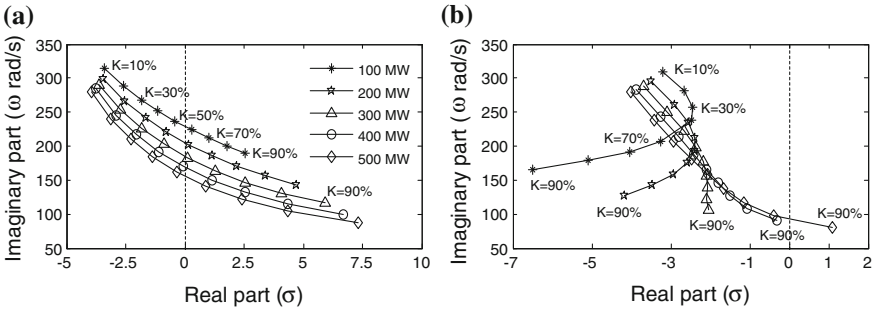

Fig. 18.28 Electrical mode eigenvalues. **a** Without STATCOM. **b** With STATCOM (C-I)

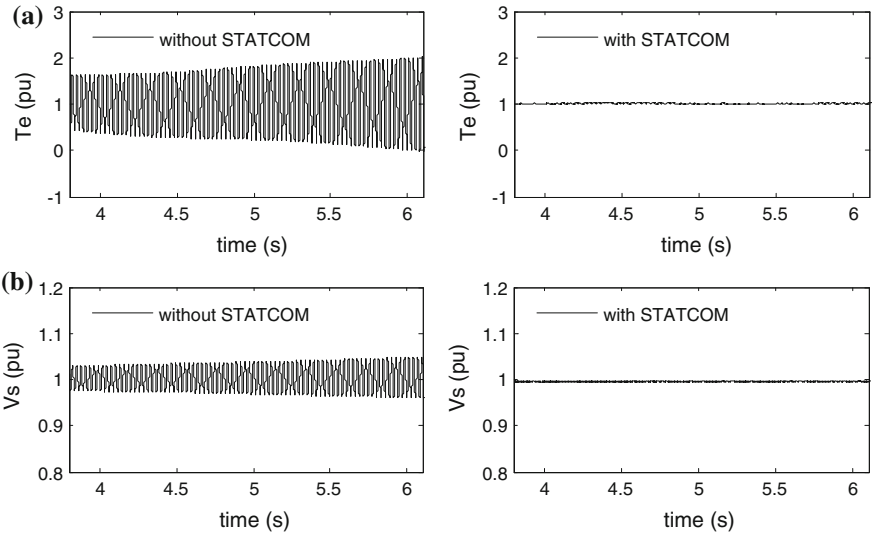

Fig. 18.29 Steady state performance of a 100 MW wind farm. a Electromagnetic torque. **b** PCC voltage

its mitigation with a 60 MVA STATCOM for a 100 MW wind farm connected to 60 % series-compensated line. The size of the STATCOM is determined from the PSCAD/EMTDC studies to be adequate to stabilize the electrical mode. The PCC voltage is shown in Fig. 18.29b. In steady state since both the proposed controllers behave identically, performance with only controller-I is shown. Figures. 18.30 and 18.31 show the self-excitation of the PCC voltage and its mitigation through the STATCOM for a 300 and 500 MW wind farm, respectively, connected to 50 and 55 % series compensation, respectively. For a 300 MW wind farm the critical compensation level is 48.60 %, thus 50 % series compensation presents a marginally unstable operating condition which can be seen from a slowly growing

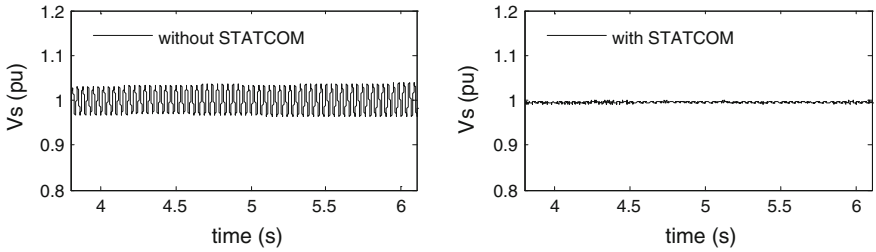

Fig. 18.30 Steady state PCC voltage of a 300 MW wind farm

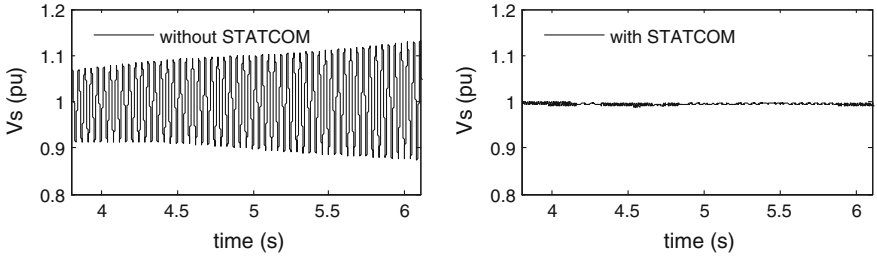

Fig. 18.31 Steady state PCC voltage of a 500 MW wind farm

oscillation in the PCC voltage depicted in Fig. 18.30. However, in the case of a 500 MW wind farm with 55 % series compensation, the electrical mode is unstable; therefore the oscillations in the PCC voltage grow faster. Similar responses are seen with the electromagnetic torque, though not shown here. The STATCOM controllers effectively stabilize the electrical mode oscillations.

18.6.2 Transient SSR

This section presents the performance of STATCOM during systems faults for various cases that includes variation in the size of wind farm, variation in the output of a wind farm, and variation in the series compensation level.

18.6.2.1 Variation in Wind Farm Size

Wind farm sizes from 100 to 500 MW are considered for the transient SSR analysis. Performances of both the controllers are reported together. For each wind farm the series compensation level is chosen marginally above its critical series compensation level. Figure 18.32 shows the performance of the 100 MW wind farm with

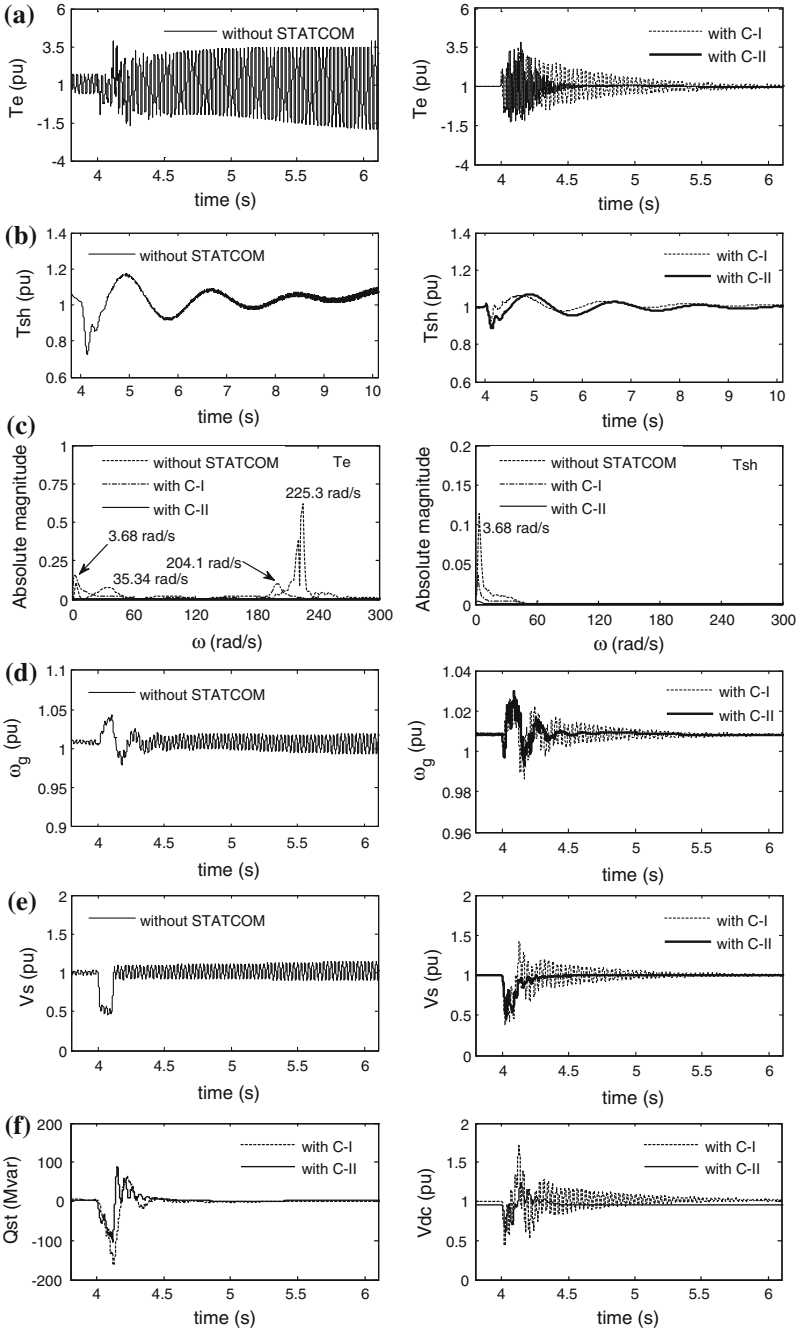

Fig. 18.32 Transient SSR and its mitigation in a 100 MW wind farm. **a** Electromagnetic torque. **b** Shaft torq. **c** FFT of electromagnetic and shaft torque. **d** Generator speed. **e** PCC voltage **f** STATCOM reactive power and DC link voltage

60 % series compensation and the effectiveness of the proposed controllers in damping the SSR oscillations. The electromagnetic torque without STATCOM and with STATCOM is shown in Fig. 18.32a. In the absence of the STATCOM, fault in the network causes induction generator effect SSR. The electromagnetic torque grows and attains a large value. With the proposed controller C-I though the oscillation is damped out successfully, it takes approximately 2 s. Meanwhile, the controller C-II offers improved performance and the SSR oscillation is damped out successfully within 0.6 s.

The shaft torque for the corresponding operating condition is shown in Fig. 18.32b. The peak shaft torque reaches up to 1.2 pu after the fault is cleared. However, influence of the unstable electromagnetic torque continues and later destabilizes the shaft torque. The proposed controllers now avoid the destabilisation. The peak overshoot is reduced and oscillation in the shaft torque is stabilized rapidly. The performance of both controllers is quite similar in this case. FFT analysis of the electromagnetic torque and shaft torque is shown in Fig. 18.32c. The FFT of electromagnetic torque shows the estimated frequency of 225.3 rad/s without STATCOM, which matches with the electrical mode frequency shown in Table 18.1. The estimated frequency of 204.1 rad/s matches with the calculated damped frequency (206.24 rad/s) of the electrical mode with controller I shown in Table 18.6. With the STATCOM controller–II no electrical mode oscillation is detected in the electromagnetic torque. The electromechanical mode frequency detected at 35.34 rad/s matches very closely with the calculated values of 37.55, 37.44 and 37.24 rad/s which are the electromechanical mode eigenvalues of the wind turbine generators without STATCOM, with STATCOM controller-I and STATCOM controller-II, respectively. The torsional mode frequency in all cases is found to be approximately 3.6 rad/s, which matches closely with the FFT estimated value of 3.68 rad/s. Figure 18.32d, e depict the generator speed and PCC voltage, respectively. The generator is stabilized faster with controller C-II than with controller C-I. With C-II, the over voltage following the fault clearance is also reduced significantly. The reactive power output of the STATCOM and the DC voltage are shown in Fig. 18.32f. The negative reactive power output of the STATCOM indicates the capacitive mode of operation. The DC voltage is stabilized faster with C-II and the overshoot also gets reduced. During transients the STATCOM injects large (two times of rating) reactive power for few cycles only which can be seen from Fig. 18.32f.

Transient simulation results of a 300 MW wind farm with 50 % series compensation are shown in Fig. 18.33. The electromagnetic torque, shaft torque, generator speed, and PCC voltage with and without the STATCOM are shown in Fig. 18.33a–d, respectively. Figure 18.33e shows the reactive power output and DC voltage of the STATCOM. It is observed that controller C-II reduces the post fault oscillations in electromagnetic torque, generator speed, and PCC voltage more effectively than the controller C–I. DC voltage is also now controlled effectively. The estimated frequencies of electromagnetic torque and shaft torque match very closely with the calculated values shown in Tables 18.1, 18.6 and 18.7. With controller C-II, reactive power output of the STATCOM is also reduced which is an added benefit. This indicates the reduced requirement of the MVA capacity of the STATCOM.

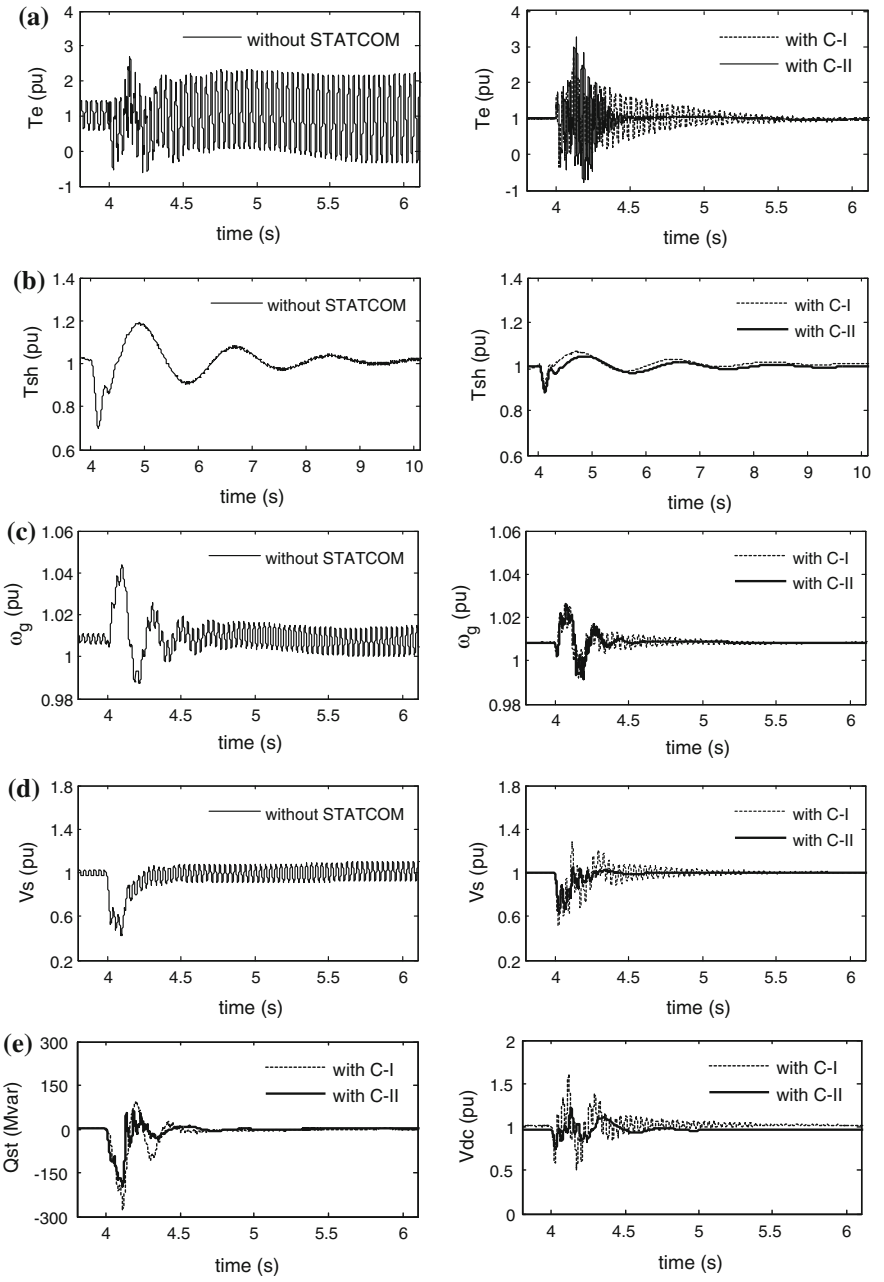

Fig. 18.33 Transient SSR and its mitigation in a 300 MW wind farm. **a** Electromagnetic torque. **b** Shaft torque. **c** Generator speed. **d** PCC voltage. **e** STATCOM reactive power and DC link voltage

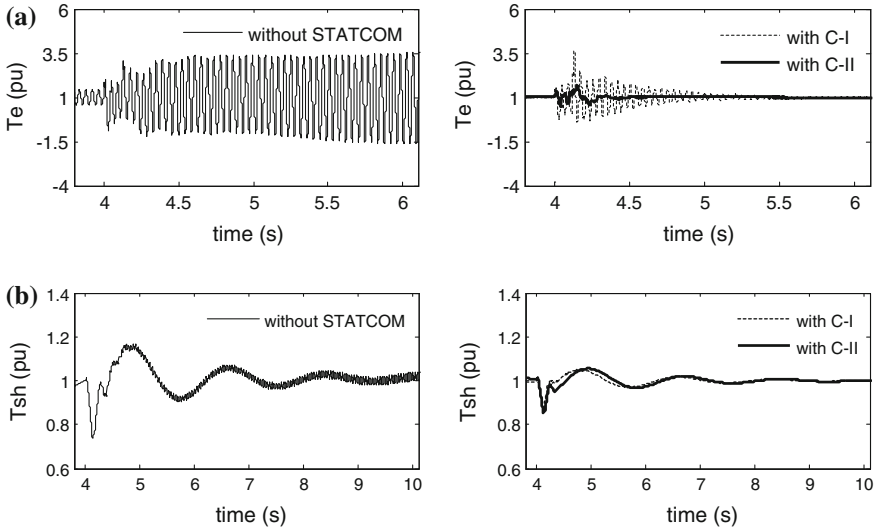

Fig. 18.34 Transient SSR and its mitigation in a 500 MW wind farm. **a** Electromagnetic torque. **b** Shaft torq

Now the performance of the 500 MW wind farm with 55 % series compensation is shown in Fig. 18.34. The growing oscillation of the electromagnetic torque is successfully stabilized by the proposed controllers. Also in this case, performance of C-II is found to be superior over of that of C-I. The STATCOM substantially reduces the peak over shoot in the shaft torque following the fault.

18.6.2.2 Variation in Wind Farm Output

In the previous section different sizes of wind farms were considered. This section deals with different outputs of a large wind farm. A 500 MW wind farm is considered and keeping the series compensation level constant at 55 %, the study is conducted with 100 and 300 MW output of a wind farm. A symmetrical six-cycles fault is created at the remote end (location-*F*) of the series-compensated line and the simulation results are shown in Fig. 18.35. The 100 MW (0.2 pu at 500 MW base) output with 55 % series compensation represents an unstable electrical mode scenario that can be seen from the growing oscillation in the electromagnetic torque and the PCC voltage of the wind farm. The unstable electrical mode is damped out by the proposed controllers C–I and C-II. The electromagnetic torque with and without the STATCOM are shown in Fig. 18.35a. The PCC voltage is shown in Fig. 18.35b, which is also stabilized following the fault clearance. Reactive power and DC voltage of the STATCOM shown in Fig. 18.35c show a significant improvement in the performance with controller C-II over the performance with controller C–I. Particularly controller C-II reduces the peak over shoot in the DC

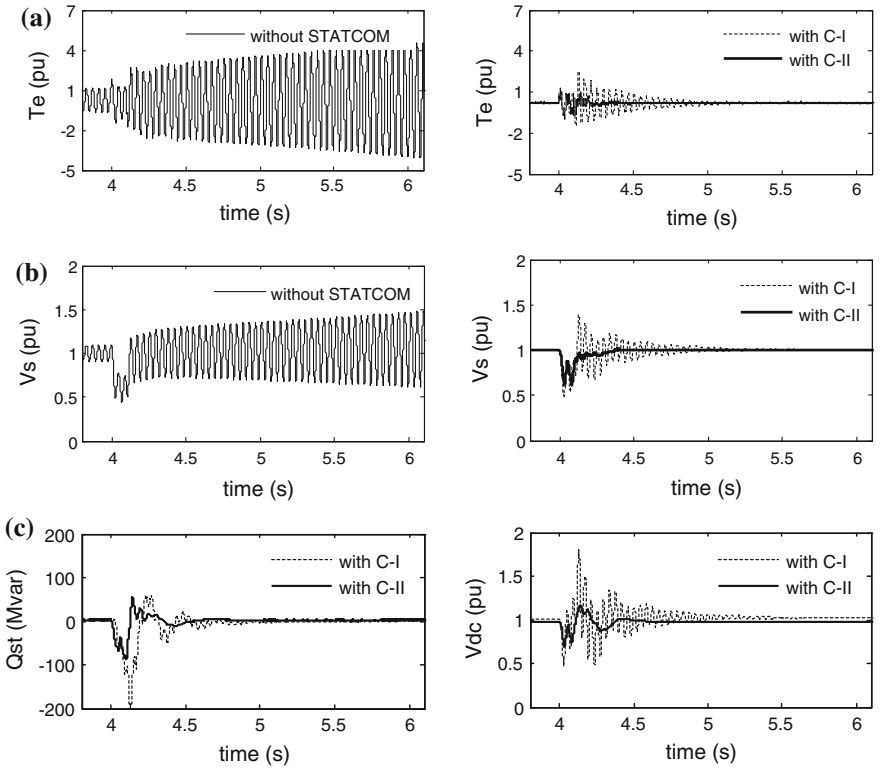

Fig. 18.35 Transient performance of a 500 MW wind farm producing 100 MW. **a** Electromagnetic torque. **b** PCC voltage. **c** STATCOM reactive power and DC link voltage

voltage that reflects as a reduced overshoot in the AC voltage at the PCC. The reactive power output of the STATCOM is also reduced with C-II without compromising the aim of stabilizing the unstable electrical mode oscillation.

Figure 18.36 shows the performance of the wind farm at a 300 MW output condition, which is quite similar to the 100 MW output case. The electromagnetic torque and the PCC voltage, both are stabilized successfully with the proposed STATCOM controllers and the potential of SSR is mitigated.

The case studies presented above validate the proposed controllers for the mitigation of SSR in a double-cage induction generator based wind farm. With the control of the modulation index, the DC voltage is controlled smoothly, which then minimizes the voltage overshoot at the PCC. Dynamic response of the STATCOM is also improved noticeably with controller C-II. From the transient simulations no torsional interaction is found which corroborates the small-signal analysis. Accurate correlation of the FFT estimated frequencies and calculated damped frequencies validate the small-signal model of the study system and the proposed controllers of the STATCOM.

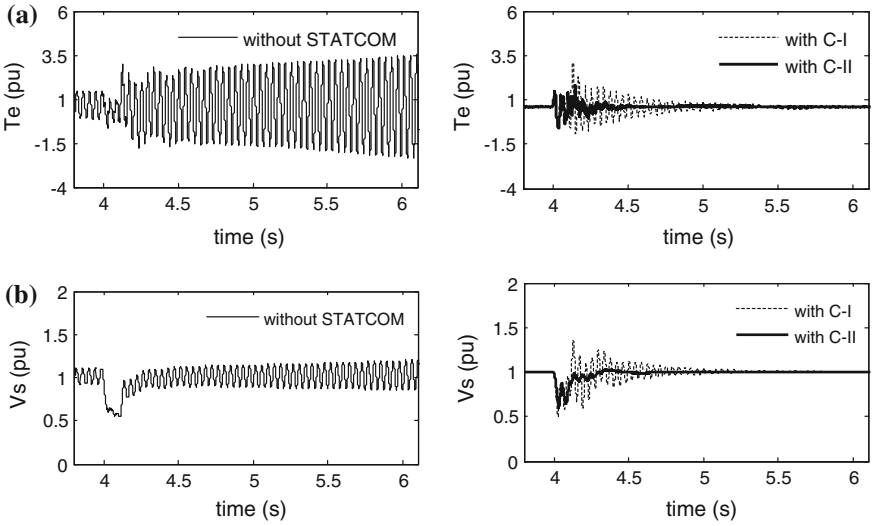

Fig. 18.36 Transient performance of a 500 MW wind farm producing 300 MW. **a** Electromagnetic torque. **b** PCC voltage

18.7 Discussion

A detailed analysis of the potential of SSR and its mitigation using STATCOM in a double-cage induction generator based wind farm connected to a series-compensated transmission line is reported in this chapter. System eigenvalues are computed for a wide range of wind farm sizes and a broad range of series compensation levels. The FFT analysis is used to further correlate the frequencies of the critical modes obtained from small-signal studies. The following conclusions are made with respect to the potential of SSR:

(a) Induction generator effect (i.e. the electrical mode becoming unstable) may be experienced even at realistic levels of series compensation, with large wind farms in the range of 100–500 MW.
(b) The critical levels of series compensation for SSR to occur are 56 % for 100 MW, 48.25 % for 200 MW, 48.6 % for 300 MW, 50.5 % for 400 MW and 52.6 % for 500 MW wind farms, respectively.
(c) In the case of a 500 MW wind farm, the critical levels of series compensation for SSR to occur are 52.75 % for 100 MW, 52.80 % for 200 MW, 52.85 % for 300 MW, 52.80 % for 400 MW and 52.6 % for 500 MW power output, respectively.
(d) Torsional interaction does not seem to occur for the range of wind farm sizes and series compensation levels considered.

(e) Large MW rated wind farms producing small MW power outputs do not exhibit high shaft torques in response to terminal faults, as observed with the small power rated wind farms.
(f) A STATCOM with voltage control installed at the PCC can successfully alleviate the potential of SSR both in steady state and during faults.

From the studies conducted with the study system, it appears that SSR may occur even for realistic levels of series compensation levels (typically 50 %) for a 100 MW or lesser size wind farm. Since small size wind farms can be subjected to high shaft torques in response to terminal faults, detailed analysis must be performed to understand such impacts before connecting these induction generator based wind farms to a series-compensated transmission line. Suitable preventive measures may also be undertaken to avoid any potential damage to the torsional system of the wind turbines.

Appendix

Table 18.8 Wind turbine torsional system data [11, 51]

Parameter	Per unit value
H_t	4 s
K_{tg}	0.3 pu/el. rad
H_g	0.5 s

Table 18.9 Double-cage induction generator data [57, 67]

Parameters	IG-1	IG-2	IG-3
P (MW)	2.3	2.3	1.3
V (Volt)	690	690	690
f (Hz)	60	60	60
$R_S(pu)$	0.00506	0.00506	0.0074
$X_{s\sigma}(pu)$	0.13176	0.12552	0.1485
$R_{r1}(pu)$	0.01199	0.011658	0.0129
$R_{r1}(pu)$	0.01923	0.018624	0.0124
$X_{r\sigma1}(pu)$	0	0	0
$X_{r\sigma2}(pu)$	0.21172	0.28565	0.1345
$X_{rm}(pu)$	0.072175	0.078995	0.0499
$X_m(pu)$	3.8892	4.0058	4.369

Table 18.10 STATCOM data [67]

STATCOM size	~60 MVA/100 MW wind farm
Base MVA	300
Base voltage	25 kV

Table 18.11 STATCOM parameters

R_{st}	0.0006 pu
X_{st}	0.1 pu
C_{dc}	5000 μF

Table 18.12 STATCOM controller parameters [67]

Controller-I (C–I)		Controller-II (C-II)	
T_{LP}	0.0024	T_{LP}, T_{DC}	0.004, 0.004
G	0.05	G_1, G_2	1, 0.1
T_1	0.015	T_1, T_2	0.007, 0.05
T_2	0.005	T_3, T_4	0.002, 0.05
K_P	0.1	K_{P1}, T_{I1}	0.54, 0.016
T_I	0.5	K_{P2}, T_{I2}.	50, 5

References

1. American Wind Energy Association (Online). http://www.awea.org/
2. Canada Wind Energy Association (Online). http://www.canwea.ca/
3. European Wind Energy Association (Online). http://www.ewea.org/
4. Electric Reliability Council of Texas (Online). http://www.ercot.com/
5. Ackerman T (2005) Wind power in power systems. Wiley, New York
6. Akhmatov V (2007) Induction generators for wind power. Multi Science, UK
7. Boldea I (2006) Variable speed generators. CRC Press, New York
8. Fox B, Flynn D, Bryans L, Jenkins N, Milborrow D, O'Malley M, Watson R, Anaya-Lara O (2007) Wind power integration: connection and system operation aspects. IET power and energy series, United Kingdom
9. Jenkins N, Allan R, Crossley P, Krschen D, Strbac G (2008) Embedded generation. IET power and energy series, United Kingdom
10. Pourbeik P, Koessler RJ, Dickmander DL, Wong W (2003) Integration of large wind farms into utility grids (Part 2—performance issues). In: Proceedings 2003 IEEE PES GM, pp 1520–1525
11. Henderson M, Bertagnolli D, Ramey D (2009) Planning HVDC and FACTS in New England. In: Proceedings 2009 IEEE/PES PSCE, pp 1–3
12. Ercot CREZ Transmission optimization study (Online). Available www.ercot.com http://transmission.bpa.gov/business/generation_interconnection/documents/STD-N-000001-00-01_071509.pdf

13. Southern Alberta Transmission Reinforcement Needs Identification Document (Online). Available http://www.aeso.ca
14. Wagner CF (1941) Self-excitation of induction motors with series capacitors. Trans Am Inst Electr Eng 60(12):1241–1247
15. Limebeer DJN, Harley RG (1981) Subsynchronous resonance of single-cage induction motors. IEE Proc B Electr Power Appl 128(1):33–42
16. Limebeer DJN, Harley RG (1981) Subsynchronous resonance of deep-bar induction motors. IEE Proc B Electr Power Appl 128(1):43–51
17. Bowler CE, Khan E (2005) Wilmarth-Lakefield 345 kV transmission series capacitor study: phase 2 SSR evaluation report Rev.1.0. Xcel Energy Inc. internal report
18. Tabesh A, Iravani R (2006) Small-signal dynamic model and analysis of a fixed-speed wind farm—a frequency response approach. IEEE Trans Power Deliv 21(2):778–787
19. Varma RK, Auddy S (2006) Mitigation of subsynchronous oscillations in a series compensated wind farm with static var compensator. In: Proceedings 2006 IEEE power engineering society general meeting, pp 1–7
20. Varma RK, Auddy S (2006) Mitigation of subsynchronous resonance by SVC using PMU-acquired remote generator speed. In: Proceedings 2006 IEEE power India conference, pp 1–8
21. Varma RK, Semsedini Y, Auddy S (2007) Mitigation of subsynchronous oscillations in a series compensated wind farm with thyristor controlled series capacitor (TCSC). In: Proceedings 2007 power systems conference: advanced metering, protection, control, communication, and distributed resources, pp 331–337
22. Varma RK, Auddy S, Semsedini Y (2008) Mitigation of subsynchronous resonance in a series-compensated wind farm using FACTS controllers. IEEE Trans Power Deliv 23(3):1645–1654
23. Ostadi A, Yazdani A, Varma RK (2009) Modeling and stability analysis of a DFIG-based wind-power generator interfaced with a series-compensated line. IEEE Trans Power Deliv 24 (3):1504–1514
24. El-Moursi MS, Bak-Jensen B, Abdel-Rahman MH (2010) Novel STATCOM controller for mitigating SSR and damping power system oscillations in a series compensated wind park. IEEE Trans Power Electron 25(2):429–441
25. El-Moursi MS (2012) Mitigating subsynchronous resonance and damping power system oscillation in a series compensated wind park using a novel static synchronous series compensator control algorithm. Wind Eng 15(3):363–377
26. Fan L, Kavasseri R, Miao ZL, Zhu C (2010) Modeling of DFIG-based wind farms for SSR analysis. IEEE Trans Power Deliv 25(4):2073–2082
27. Fan L, Zhu C, Miao Z, Hu M (2011) Modal analysis of a DFIG-based wind farm interfaced with a series compensated network. IEEE Trans Energy Convers 26(4):1010–1020
28. Irwin GD, Jindal AK, Isaacs AL (2011) Subsynchronous control interactions between type 3 wind turbines and series compensated AC transmission systems. In: Proceedings 2011 IEEE PES GM, pp 1–6
29. Fan L, Miao Z (2012) Mitigating SSR using DFIG-based wind generation. IEEE Trans Sustain Energy 3(3):349–358
30. Subsynchronous interaction between Series-Compensated Transmission Lines and Generation (Online). Available http://www.nerc.com/files/LL_45_SubsynchronousInteraction.pdf
31. Narendra K, Fedirchuk D, Midence R, Zhang N, Mulawarman A, Mysore P, Sood V (2011) New microprocessor based relay to monitor and protect power systems against sub-harmonics. In: Proceedings 2011 IEEE electrical power and energy conference, pp 438–443
32. Bongiorno M, Peterson A, Agneholm E (2011) The impact of wind farms on subsynchronous resonance in power systems. Elforsk Report 11:29
33. Anderson PM, Farmer RG (1996) Series compensation of power systems. PBLSH Publication, California
34. Anderson PM, Agrawal BL, Van Ness JE (1990) Subsynchronous resonance in power systems. IEEE Publication, New York
35. IEEE committee report (1977) First benchmark model for computer simulation of subsynchronous resonance. IEEE Trans Power Apparatus Syst 96(5):1565–1572

36. IEEE Committee Report (1985) Terms, definitions and symbols for subsynchronous oscillations. IEEE Trans Power Apparatus Syst PAS-104(6):1326–1334
37. Padiyar KR (1999) Analysis of subsynchronous resonance in power system. Kluwer Academic Publisher, USA
38. IEEE Committee Report (1992) Reader's guide to subsynchronous resonance. IEEE Trans Power Syst 7(1):150–157
39. Johansson N, Angquist L, Nee HP (2011) A comparison of different frequency scanning methods for study of subsynchronous resonance. IEEE Trans Power Syst 26(1):356–363
40. Agrawal BL, Farmer RG (1979) Use of frequency scanning techniques for subsynchronous resonance analysis. IEEE Trans Power Apparatus Syst PAS-98(2):341–349
41. El-Marsafawy M (1983) Use of frequency-scan techniques for subsynchronous-resonance analysis of a practical series-capacitor compensated AC network. In: IEE proceedings C generation, transmission and distribution vol 130, no 1, pp 28–40
42. Crow ML (2010) Computational methods for electric power systems. CRC Press, New York
43. Anaya-Lara O, Jenkins N, Ekanayake J, Cartwright P, Guges M (2009) Wind energy generation: modeling and control. Wiley, USA
44. MATLAB (2011) The language for technical computing. The Mathworks Inc
45. Application guide PSCAD/EMTDC (Online). Available https://pscad.com/sites/default/files/documents/Application_Guide_2008.pdf
46. Moharana AK (2012) Subsynchronous resonance in wind farms. PhD dissertation, University of Western Ontario, Canada
47. Hau E (2006) Wind turbines: fundamentals, technologies, application, economics, 2nd edn. Springer, Germany
48. Lubosny Z (2003) Wind turbine operation in electric power systems. Springer, Germany
49. Muyeen SM, Ali MH, Takahashi R, Murata T, Tamura J, Tomaki Y, Sakahara A, Sasano E (2007) Comparative study on transient stability analysis of wind turbine generator system using different drive train models. IET Renew Power Gener 1(2):131–141
50. Petru T, Thiringer T (2002) Modeling of wind turbines for power system studies. IEEE Trans Power Syst 17(4):1132–1139
51. Mei F, Pal B (2007) Modal analysis of grid-connected doubly fed induction generators. IEEE Trans Energy Convers 22(3):728–736
52. Pal B, Mei F (2008) Modelling adequacy of the doubly fed induction generator for small-signal stability studies in power systems. IET Renew Power Gener 2(3):181–190
53. Perdana A (2008) Dynamic model of wind turbines. PhD dissertation, Chalmers University of Technology, Sweden
54. Levi E, Rauski D (1993) Modeling of deep-bar and double cage self-excited induction generators for wind-electricity generation studies. Electr Power Syst Res 27(1):73–81
55. Levi E (1997) General method of magnetizing flux saturation modeling in d-q axis models of double-cage induction machines. IEE Proc—Electr Power Appl 144(2):101–109
56. Pedra J, Candela I, Sainz L (2009) Modelling of squirrel-cage induction motors for electromagnetic transient programs. IET Electr Power Appl 3(2):111–122
57. Pedra J, Corcoles F, Monjo L, Bogarra S, Rolan A (2012) On Fixed-speed WT generator modeling for rotor speed stability studies. IEEE Trans Power Syst 27(1):397–406
58. Pedra J, Corcoles F (2004) Estimation of induction motor double-cage model parameters from manufacturer data. IEEE Trans Energy Convers 19(2):310–317
59. Kundur P (1994) Power system stability and control. McGraw-Hill, New York
60. Germond AJ, Podmore R (1978) Dynamic aggregation of generating unit models. IEEE Trans Power Apparatus Syst PAS-97(4):1060–1069
61. Chan SM, Cresap RL, Curtice DH (1984) Wind turbine cluster model. IEEE Trans Power Apparatus Syst PAS-103(7):1692–1698
62. Nozari FK, David Price M, William W (1987) Aggregation of induction motors for transient stability load modeling. IEEE Trans Power Syst 2(4):1096–1103
63. Taleb M, Akbaba M, Abdullah EA (1994) Aggregation of induction machines for power system dynamic studies. IEEE Trans Power Syst 9(4):2042–2048

64. Louie KW (2006) Aggregating induction motors in a power system based on their standard specifications. In: Proceedings 2006 international conference *on* power system technology, pp 1–8
65. Patil KV, Senthil J, Jiang J, Mathur RM (1998) Application of STATCOM for damping torsional oscillations in series compensated AC systems. IEEE Trans Energy Convers 13 (3):237–243
66. Schauder C, Mehta H (1993) Vector analysis and control of advanced static VAr compensators. In: IEE proceedings C generation, transmission and distribution vol 140, no. 4, pp 299–306, Jul 1993
67. Moharana A, Varma RK, Seethapathy R (2014) SSR alleviation by STATCOM in induction-generator-based wind farm connected to series compensated line. IEEE Trans Sustain Energy 5(3):947–957

Chapter 19
STATCOM on the Mexican Power Systems: Two Case Studies

Miguel A. Olguín-Becerril, Esther Barrios-Martínez and César Ángeles-Camacho

Abstract Mexico, as other countries, has set targets for using renewable energy generation; however, because of its variability, it may affect the electricity system operation and lead to electrical breakdown. STATCOM is a power electronic device used to mitigate those risks. To analyze the STATCOM behavior for integrating wind generation into the Mexican Electrical System, without compromising its integrity, two cases were studied. In the first case a region of the Northeast of Mexico is analyzed, where there are two power plants with a total of 990, and 1,600 MW more will be added soon for wind generation. Under these circumstances, an electrical failure close to generator stations is risky for the system stability. For this reason, the behavior of the network was analyzed by incorporating a STATCOM to maintain the voltage values close to nominal, after introducing a three-phase fault at a bus bar near generation. In the second case, the Southeast region of Mexico is considered, where there are three parallel transmission lines of 243 km each. Capacitive reactance is presented because of the lines length, and it raises the voltage in bus bars during low demand. To avoid such overvoltage, currently one of the lines is disconnected. A STATCOM is proposed for absorbing reactive power to maintain the nominal voltage without disconnecting the transmission line during low demand.

Keywords FACTS · STATCOM · Voltage stability · Coupling transformer

M.A. Olguín-Becerril (✉) · C. Ángeles-Camacho
Instituto de Ingeniería, Universidad Nacional Autónoma de México,
Mexico City, Mexico
e-mail: miguelangelmx@hotmail.com

C. Ángeles-Camacho
e-mail: cangelesc@iingen.unam.mx

E. Barrios-Martínez
Facultad de Ingeniería, Universidad Nacional Autónoma de México,
Mexico City, Mexico
e-mail: ebarriosm@fi-b.unam.mx

F. Shahnia et al. (eds.), *Static Compensators (STATCOMs) in Power Systems*,
Power Systems, DOI 10.1007/978-981-287-281-4_19

19.1 Introduction

The Mexican Electrical System (MES) is formed by a main electrical power systems that electrically interconnect most of the country, except the Baja California peninsula which has two networks operating independently: the north and the Baja California Sur electric power systems. There have been projects to interconnect them, via submarine cables either by DC or AC, but such connections have not yet been carried out.

The cost and difficulties involved in the construction of transmission lines because of rights of way and environmental impact can limit the transmission capacity. On the other hand, when the power transfer increases, power systems come to have a more complex operation, and the system may become less secure or even electrical power outages may occur. This may be more severe when large power flows are presented with inadequate controls, dynamic oscillations between different parts of the system and bottlenecks in the flow of electrical power [1]. The effect of these situations can be decreased with the use of Flexible AC Transmission Systems (FACTS).

In some MES areas, electric power transfer complications and voltages different from nominal are presented. Those situations could be solved using traditional compensations or a most flexible compensation, as those provided by FACTS devices. The Static VAr Compensators (SVCs) have been used since the 80s to solve some of these problems in the MES. Currently there are 27 SVCs interconnected in 400, 230 and 115 kV electrical substations. Those devices have been used to improve voltage magnitude levels in the point of connection and proved an invaluable tool in that function. More flexible devices that offer other features besides the voltage support such as the STATCOM, however, have not been exploited by the MES. The STATCOM has the advantage over SVC that delivers the same amount of current despite low voltages caused by electrical failures [2].

19.2 Mexican Electrical System Features

For planning and operation reasons the MES divides Mexico into nine regions for generation and transmission. These regions are the following: Northwest, North, Northeast, West, Central, East, Southeast, Peninsular and Baja California and Baja California Sur. Thus, regional electric systems share resources capacity and efficient economic and reliable operation as a whole. The two regions of the peninsula of Baja California (Baja California and Baja California Sur) remain electrically isolated because their interconnection with the rest of the network is technically and economically not justified.

The electricity market in Mexico is through nine interconnections between the USA and one interconnection with Belize. These connections are used primarily to import and export electricity in emergencies.

19.2.1 Electric Generation

The natural resources of each geographic area are used to generate electricity; for example, taking into account the hydrography of the Southeast, there are several hydroelectric power plants. Similarly, considering the amount of wind in the Isthmus of Tehuantepec, wind power plants have been installed there; additionally, there are combined cycle power plants in several areas of the country. A variety of generation sources exists, and it is used to make the most economic generation dispatch, considering the Laguna Verde nuclear power plant as based generation.

In Mexico, approximately 72 % of electricity is generated using fossil fuels (fuel oil, natural gas and coal), with fuel oil and natural gas being predominant. The fuel oil is used mainly in Generator Stations which are located near ports or refineries. The use of natural gas is increasingly important in new combined cycle power plants. Additionally, because of ecological constraints, the use of natural gas has increased in conventional thermoelectric plants supplying power to large cities of Mexico. The main thermoelectric power plants and their capacity are indicated in Table 19.1.

In the Northeast region, there exists the largest thermoelectric generation block. On the other hand, diesel is used in power plants which operate during demand peak hours, to supply isolated areas.

Approximately 21 % of the electricity produced in Mexico comes from hydroelectric resources because of Mexican hydrography. The largest hydroelectric plant in Mexico is Chicoasén in Chiapas in Southeast region; it is the fourth most productive hydroelectric plant in the world. In the Grijalva River, the largest hydroelectric development in the country is located; comprised of Angostura, Chicoasén, Malpaso and Peñitas plants, it represents 45.6 % of the total hydroelectric operation capacity.

Another important development is in the Balsas River, located in the west. It consists of Caracol, Infiernillo and La Villita with a total of 17.8 % of the hydroelectric capacity.

In the Santiago River, in the state of Nayarit in the West region, there are Aguamilpa and El Cajon hydroelectric power plants with a total capacity equivalent to 16.2 %. The main hydroelectric plants and their capacity are indicated in Table 19.2.

Table 19.1 Main thermoelectric plants in Mexico

Thermoelectric plant	Effective installed capacity (MW)
Tuxpan	2,100
Tula	1,500
Manzanillo I	1,200
Valle de México	1,000
Salamanca	866
Altamira	800

Table 19.2 Main hydroelectric plants in Mexico

Hydroelectric plant	Effective installed capacity (MW)
Chicoasén	2,400
Malpaso	1,080
Infiernillo	1,040
Aguamilpa	960
Angostura	900
El Cajón	750

The only nuclear power plant in Mexico is Laguna Verde, located in the east, which consists of two units, 682.4 MW each. Its operating cost is the lowest of all power plants in the MES, and its participation represents 4.93 % of the total energy produced, with a capacity factor of 90.37 %.

The potential wind power generation in the state of Oaxaca in the East region is 33,200 MW. Other states with wind potential are Zacatecas, Hidalgo in the Central region, Tamaulipas in the Northeast and Baja California. It is estimated that public investment in wind power for the period 2006–2015 will be US$791 million.

19.2.2 The Mexican Network

In the MES electricity consumption centers are often located far from the generation centers, so there are several long transmission lines (over 150 km) in service. Operating those lines efficiently to prevent energy losses, power transfer problems and an inadequate voltage regulation in maximum and minimum demands is necessary. Thus, in every area of MES various complex operating conditions exist which must be properly analyzed and resolved.

The transmission network has been developed taking into account the size and geographic dispersion of the electrical demand, as well as the power plants location. In some areas of the country, the centers of electrical generation and consumption are far apart, so that interconnection was made gradually, when projects were technically and economically justified. The MES consists of networks at different voltage levels.

- The main network consists of transmission lines and electrical substations to ultra-high voltage (400 and 230 kV), which carry large amounts of energy between regions. This network is powered by power plants and supplies to subtransmission system to facilities at 400 and 230 kV. There are currently about 45,000 km of these lines,
- Sub transmission networks in high voltage (between 161 and 69 kV) have regional coverage and supply power to medium voltage distribution lines and loads connected to these voltages. At present there are approximately 46,000 km from those lines,

- The transmission medium voltage networks (60 and 2.4 kV) distribute energy within relatively small geographic areas and deliver to those in low voltage and connected facilities in this voltage range with a total length of about 364,000 km, which includes 14,500 km of underground lines,
- Distribution networks in low voltage (220 or 240 V) power loads of low-consumption users are also included. There are about 233,000 km of lines in these voltages [3].

The MES has around 760,000 km of transmission and distribution lines in total. It corresponds to 6.0 % of 400 and 230 kV lines, 6.1 % from 161 to 60 kV and the remaining 87.9 % medium and low voltage from 60 to 220 V.

The transmission capacity between system regions depends on the instantaneous conditions of the electrical demand and the generation capacity available. In general terms, the maximum power that can be transmitted by a line depends on the more restrictive of the following limits:

- Heating in conductors,
- Voltage drop in line,
- System stability due to disconnection caused by generators and/or transmission lines failure.

In MES, the voltage drops in line and system stability because of disconnection factors are the limits which most often restrict the maximum transmission power.

19.2.3 Operating Conditions of the MES

The main function of the National Energy Control Center is to plan, lead and to supervise the MES to achieve the objectives, i.e. safety, continuity, quality and economy in the electrical service. Its functions are also related to the operation of the electrical installations and equipment, which are administered in conjunction with other resources such as energy. In addition, the center coordinates and supervises electrical interconnections operation with national and foreign companies with external power producers.

The MES operation aims to make the power supply efficient by meeting the following objectives:

i. SAFETY: Skill of the MES to endure disturbances occurrence. The system is considered in safe operation when it is able to withstand the occurrence of the more severe simple contingency without the action of additional control schemes,
ii. CONTINUITY: The uninterrupted electricity service supply to users, according to rules and regulations,
iii. QUALITY: Refers to the voltage condition, frequency and waveform of the electrical service supplied to users, in compliance with the provisions of the Law Regulation,

iv. ECONOMY: Involves the lowest overall cost of production per kWh, resulting from the energy resources optimal use. The following are all considered: the most efficient Generator Stations and the provision of more adequate power, depending on environmental constraints, cost and energy consumption, transmission network losses, network restrictions and existing contracts.

For medium-term operation planning, the following are considered: energy requirements and demand, maintenance program and availability of generators, prices forecast and availability of energy, rain forecast, transmission and environmental constraints as well as the energy supply from external producers. The operation planning in the short-term considers those relating to the transmission network, starting and stopping of thermoelectric power plants and their availability to the curves of thermal regime, the offer prices of energy producers, hydraulic coupling cascade reservoirs and water travel times from one reservoir to another. The outcome is the schedule plan of an operation per unit plan, minimizing the production total cost for energy consumption.

The electric dispatch is made taking into account the estimated demand, the producer geographic area and network constraints, hydraulic availability, availability of all Generator Stations, interruptible loads and short-term total energy costs or prices offered by all producers [4].

19.3 Benefits of FACTS Devices

For an appropriate power compensation, in most of the electricity networks in the world, conventional controllers such as series capacitor banks and shunt reactors have been used. Employing modern controls which use power electronics with greater speed and operational reliability, however, is more convenient; these are called FACTS controllers. These devices have already been implemented in several electricity transmission companies in various countries in recent years, with notably reliable behavior because of their long-existing usage.

FACTS allow operation near the point of economic operation, as well as help to increase the power transfer capability of the network and to perform a specific control between interconnected subsystems.

FACTS devices can be used to solve problems caused by network transmission limitations [5, 6]. The benefits of using fast operation electronic controllers according to the Electric Power Research Institute include the following [7, 8]:

- Improved response time to stability problems. The control device can react quickly to the generator's electromechanical oscillation speed as a result of a disturbance in the network. The margin of stability results in an increase in the use of the transmission network at the required times, such as after a contingency,

- Transmission of a larger amount of electrical power safely through of transmission lines, close to their thermal limits levels. This results in increased power transfer capacity of existing lines and savings in new transmission lines building,
- Saving by reducing the generation reserve margins. FACTS devices enable connectivity between different electrical systems or subsystems, so the ability to control the power transfer between areas is increased; furthermore, output operating margins by equipment failure is prevented.
- Power system oscillations damping which could damage equipment or lead to system collapse.

19.3.1 FACTS Applications in Mexico

Because of the growth in demand in the transmission network in Mexico, finding new ways to optimize the transmission capacity is necessary, as well as maintaining levels of safety and electrical stability. To achieve this, the devices based on power electronics have proved to be a good choice.

The FACTS that have been used in Mexico are as follows:

The Static VAR Compensator (SVC): Its function is to deliver or absorb volts-amperes reactive to the transmission system, according to the needs of the network.

It is used for voltage dynamic control and improved stability because it can provide the required reactive power for compensating the reactive power deviations caused by the load variation. In Mexico SVCs have been installed since the early 80s, and there are currently 27 SVCs installed in the country in 400, 230 and 115 kV. The total capacity provided by SVC technology to the MES is about 2,961 inductive MVAr and 5,520 capacitive MVAr.

Some of these most relevant compensators are installed in the following electrical substations:

- Baja California Sur region: El Palmar,
- Northwest region: Cananea and Santa Ana,
- North region: Camargo and Durango,
- Northeast region: Güemez,
- West region: Acatlán and La Pila,
- Central region: Texcoco, Topilejo and Cerro Gordo,
- East region: Temazcal and Cerro de Oro,
- Peninsular region: Escárcega [9].

Table 19.3 shows the distribution of SVCs capacity by region. The SVC components are thyristor switched capacitor (TSC), thyristor controlled reactor (TCR) and 5th and 7th harmonic filters.

SVCs must be able to vary the voltage system at least ±5 %. Its working range is between 10 and 20 % of the short-circuit power at the system connection point.

Table 19.3 SVCs capacity installed in Mexico in 400, 230 and 115 kV

Region	Voltage (kV)	Inductive (MVAr)	Capacitive (MVAr)
Baja California	230	0	+200
South Baja California	230	–50	+150
Northwest	230	–156	+180
North	230	–190	+650
Northeast-400	400	–100	+300
Northeast-230	230	–90	+300
West-400	400	–340	+450
West-230	230	–70	+200
Central-400	400	–570	+1,200
Central-230	230	–125	+450
East	400	–900	+900
Peninsular-400	400	–300	+300
Peninsular-115	115	–70	+240
Total		–2,961	+5,220

These FACTS elements can be installed near to major load centers such as big cities or industrial areas and in critical substations where compensating voltage is required.

Back-to-back High Voltage Direct Current: Although it is not installed in Mexico, the MES benefits from HVDC light®. This was installed in 1999 in the Eagle Pass substation in the American Electric Power-Central Power Light's (AEP-CPL) power system. Eagle Pass has a 138 kV transmission line that ties into the MES Piedras Negras substation; it is mainly used in emergency conditions to transfer load from one network to the other.

This type of electric power transmission system isolates two electrical AC networks (in this case, the USA network and the MES) via a DC link. By connecting USA and Mexico systems through a HVDC, conditions for development in the border region are provided and also allow for the sharing of power and energy in the future.

The HVDC technology will reduce the risk of erratic power flows and instability that typically bring negative behaviors in CA interconnections.

The main components of a HVDC system are converters, transmission lines, smoothing reactors, electrodes and transformers.

19.4 STATCOM Projects

STATCOM has played an important role in the suitable functioning of electric power systems. In particular, some projects have set the guideline in the application of STATCOM; Table 19.4 shows the most important projects and their representative characteristics.

Table 19.4 The most important STATCOMs and their representative characteristics

STATCOM installed	Feature most important	Inverters	Rating (MVAr)	Application	Year	Country
Kita Osaka [10]	First	Thyristors	±20	Voltage and dynamic stability	1980	Japan
Rejsby Hede [11]	With wind farm	IGBT	±8	Dynamic stability	1997	Denmark
Eagle Pass/Piedras Negras [12]	Interconnecting grids	GTO	±36	Asynchronous tie	1999	USA/Mexico
Marcy [13]	Largest	IGBT	±200	Increase the transmission capacity	2001	USA

Problems in power transmission have been the same through time. Presently, however, these have been compounded by large size and/or new characteristics of the power electric systems. Particularly, the STATCOM has demonstrated proper functioning in order to mitigate these large problems. Table 19.5 shows a technical benefits record of STATCOM.

The STATCOM projects have become more sophisticated and have complemented one or more of the services shown in Table 19.5. Thus, STATCOM is expected to continue to be a promising countermeasure to solve these problems.

Table 19.5 Service performed by STATCOM

STATCOM service	Performance		
	Excellent	Good	Limited
Reactive power compensation	✓		
Active power compensation			✓
Voltage regulation	✓		
Voltage stability improvement	✓		
Steady-state improvement		✓	
Transient stability improvement		✓	
Dynamic stability improvement		✓	
Power flow control			✓
Power oscillation damping		✓	
Low frequency oscillation damping		✓	
Rotor angle stability			✓
Power quality improvements		✓	
Transmission line capacity enhancement		✓	
Asynchronous tie	✓		

19.4.1 STATCOM Model Description

The interest in the STATCOM models has presented constant growth, because of the worthy results obtained in simulations that are followed by successful applications.

The STATCOM is a shunt FACTS controller that allows the support of voltage in the power system, which results in reactive power compensation; it is composed of one Voltage Source Converter (VSC) and its associated shunt-connected transformer. Thus, STATCOM has been considered as one source of voltage for steady-state and dynamic analysis of an electrical system [14, 15]. As a typical configuration, the VSC is a three-phase, two-level, six-pulse converter consisting of six power semiconductor switching devices with an anti-parallel connected diode, as described in Fig. 19.1a.

A larger number of series or/and parallel semiconductors becomes in others power converter. A schematic representation of the STATCOM is illustrated in Fig. 19.1b. Fig. 19.1c demonstrates the three-phase STATCOM, where the phases are electrically decoupled.

The equivalent circuit corresponds to the Thevenin equivalent as seen from node k with a sinusoidal voltage V_k; the fundamental component of the STATCOM voltage is a voltage source variable $E_{vR} = V_{vR}\angle\delta_{vR}$ with the superscript ρ denoting phases a, b and c. The voltage magnitude, V_{vR}, is given by maximum and minimum limits, which are a function of the DC source. Hence, the reactive power flow is determined mainly by the magnitude of the nodal voltage and the voltage source. For $V_{vR} > V_k$, the STATCOM generates reactive power and consumes reactive power when $V_{vR} < V_{k.}$, STATCOM models have been derived from the above operation principle.

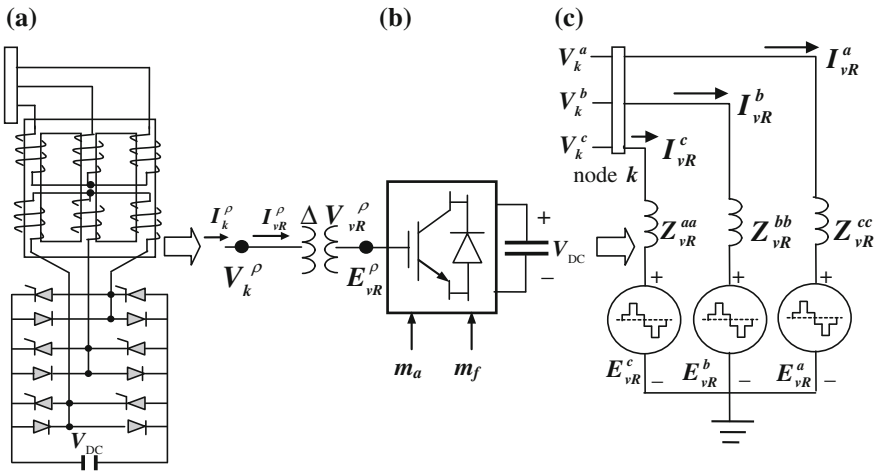

Fig. 19.1 STATCOM: **a** basic VSC diagram connected to the AC network via a shunt-connected transformer, **b** STATCOM schematic representation and **c** three-phase equivalent circuit [15]

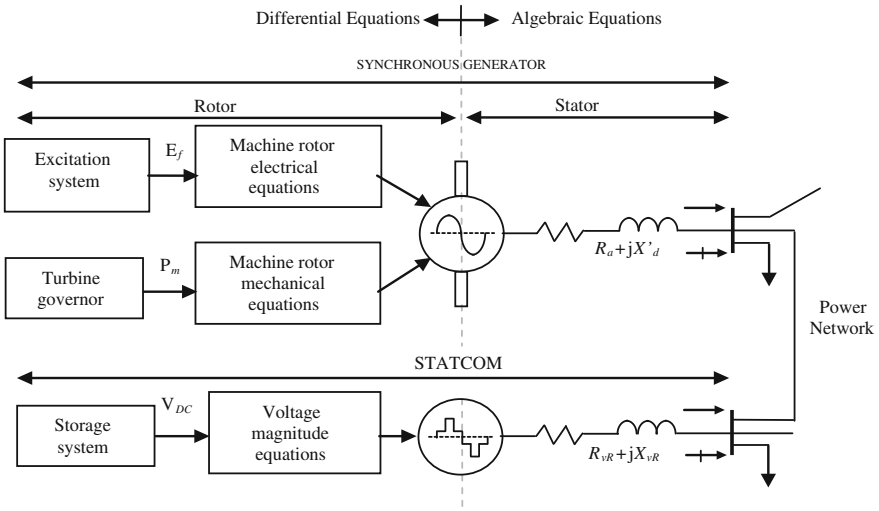

Fig. 19.2 The synchronous generator and STATCOM models connected to transmission network

These can be modelled and included with other models of power system conventional elements in any simulation tool, as shown in Fig. 19.2.

The applicability of the models STACOM has is always based on how easy it is to incorporate into a simulation program with conventional elements of the power system. Furthermore, STATCOM modelling depends on the type of analysis being performed.

The STATCOM model developed by the German company Siemens in the Power System Simulator for Engineering (PSS®E) program was considered for this work [16].

The PSS®E program was first used in 1976 and is used to simulate, analyze and optimize the behavior of a power system. Among the analysis that can be performed include:

- Power flows,
- Reduction Network,
- Dynamic Simulation.

This program has two simulation options: (1) the steady-state simulation option, where studying the network under conditions of opening/closing of transmission lines as well as connection/disconnection of loads and generation is possible, and (2) the dynamic simulation option, where any type of disturbance is considered such as line failure, generators tripping, etc.

Additionally, with the PSS®E program modelling some FACTS devices in both steady-state and dynamic simulation is possible. The STATCOM is included in PSS®E as a shunt element which is connected between the send bus bar and

Table 19.6 STATCOM variables for steady-state

Variable	Description
Control mode	Normal is specified, because the link to serial part is out of service
P setpoint	Desired active power flow which reaches the terminal bus bar. Input in MW
Q setpoint	Desired reactive power flow which reaches the terminal bus bar. Input in MVAr
V send setpoint	Voltage setting at the bus bar terminal. Input in pu
Shunt max	Maximum reactive power in parallel. Input in MVAr
Bridge max	Maximum active power transfer bridge. Input in MW
V term max	Maximum voltage at the terminal bus bar. Input in pu
V term min	Minimum voltage at the terminal bus bar. Input in pu
V series max	Maximum voltage series. Input in pu
I series max	Maximum series current. Input in MVA
Dummy series X	Series elements reactance used for the model solution. Input in pu
V series reference	Series voltage reference
Owner number	Owners number

ground. It has models for steady-state and dynamic simulation options. Data required by steady-state models are indicated in Table 19.6.

The control diagram and the dynamic model parameters used are shown in Fig. 19.3.

The model inputs are basically the reference voltage and terminal voltage. The output is current reactive
where

V_{ref} is the reference voltage on the node where the STATCOM is connected (usually 1 pu).

$|V|$ is the voltage in the node to regulate.

VAR (*L*) are other input signals such as stabilizers.

$|VT|$ is the STATCOM internal voltage.

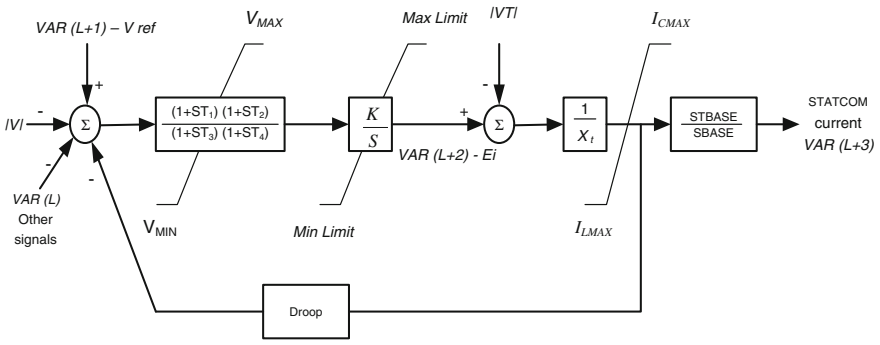

Fig. 19.3 STATCOM control diagram used by program PSS®E dynamic model

If the internal voltage amplitude of the STATCOM increases more than network voltage, then a current flows from the converter to the electrical system, and the converter generates capacitive reactive power to the system.

Conversely, if the STATCOM voltage amplitude is less than the network voltage, then the current flows from the power system to the converter, and it absorbs the inductive reactive power of the system. If STATCOM voltage amplitude is equal to the system voltage amplitude, the reactive power exchange becomes zero, in which case the STATCOM is said to be in a floating state.

The control block diagram refers to the following:

Abatement Function Block
This relates to a lead-lag compensator which will provide the appropriate characteristics of lead or lag of phase to compensate between the voltage input reference and the voltage at node to regulate.

Gain Control Block
This type of block is the transfer function of the integral controller. The K parameter is used as gain control. The recommended value is 25 dV/dE_i, where V is the system voltage, and E_i is the STATCOM internal voltage (behind the coupling transformer). Using higher gain could result in faster responses; therefore, it will be necessary to reduce the time.

Drop Block
It refers to the variation slope of the STATCOM output current based on the system voltage, i.e. the voltage drop. The drop value established is the per unit variation of nominal system voltage which causes STATCOM to produce the maximum output current.

For example, if the operating voltage is 1.0 pu, and the drop is set to 0.05 pu, the STATCOM output current will be zero when the system voltage is 1.0 pu The capacitive current will be 100 % when the voltage is 0.95 pu, and the inductive current will be 100 % when the voltage is 1.05 pu; for intermediate values, current varies linearly.

Coupling Transformer Block
Is the coupling transformer reactance in pu, the typical value is 0.1, on the basis of nominal MVA.

Change Base Block
A change of MVA base is performed.

19.5 STATCOM Application in the MES

The cost of the transmission lines construction, its electrical losses and the difficulties encountered in new lines construction because of rights of way and environmental impact can limit the transmission capacity in a power network.

Additionally, when the power transfer increases, then power systems come to have a more complex operation [17]. The effect of these situations can be decreased by using STATCOM.

Because of the short circuit faults occurrence in a power system, the electrical stability is endangered, and it could result in electrical equipment being out of service because failure with the corresponding economical cost. Therefore, performing an analysis to determine the possible installation of a device with a fast response to power failures such as the STATCOM is convenient. The analysis should consider the following [18]:

- Power flow study to know the active and reactive power behavior in the interest area,
- Electrical stability study to know stability loss risk during any contingency or equipment failure,
- Network weak nodes or with voltage support problems,
- Long transmission lines, where the capacitive reactance increases the voltage at the sending/receiving nodes,
- Cost/benefit study for using a STATCOM against SVC.

19.5.1 STATCOM Application in Northeast Region

The objective of this case study is to keep the node voltage close to nominal values, after a fault appears.

The implementation of STATCOM was considered in the Northeast region at 400 kV, because there is a significant amount of electrical generation. The power stations Rio Bravo 3 and Rio Bravo 4, which are turbo-gas power plants, have three generating units each, with 530 MW altogether. In addition to the existing generation, in the near future wind generation will be in service in the state of Tamaulipas, with a total of 1,666.5 MW, since industrial development has been introduced to this area of the country, and it is still waiting for further increase in demand for electricity for domestic and industrial consumption [19].

There is an important potential wind generation in this area. This generation is delivered to the power substation Anahuac Tamaulipas (ATP). The STATCOM behavior is analyzed at this point. The interest area is shown in Fig. 19.4 which includes the power station and substation Rio Bravo 3 (RBT), the power station and substation Rio Bravo 4 (RBC), the Frontera substation (FRO), the Aeropuerto substation (AER), the Villa de García substation (VDG), the Anahuac Tamaulipas Potencia substation (ATP) and the Huinalá substation (HUI).

Additionally, the transmission lines linking the nodes were considered. Furthermore, Fig. 19.4 indicates where the fault is simulated and where a STATCOM is connected with a capacity of ±500 MVAr.

A three-phase failure in bus bar ATP (400 kV) was simulated, with a duration of 0.23 s, to analyze the network performance with and without STATCOM.

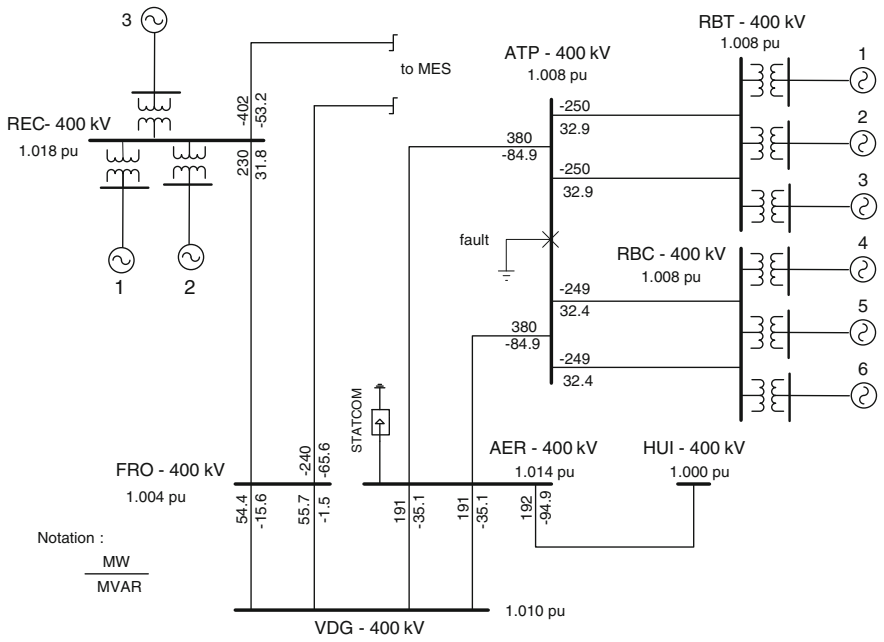

Fig. 19.4 400 kV network of the Northeast region, indicating power flows of active and reactive power

Figure 19.5a, b shows the voltage magnitude in pu obtained in AER (which is adjacent to the substation ATP). By applying the failure at the second two, the short circuit presence involves a voltage drop in the fail. It tends to zero, and it drops to near 0.2 pu; a drastic current increase then occurs in the network. The voltage magnitude drops sharply from 2.0 to 2.23 s, in the contingency. As shown in Fig. 19.5a. Once the fault is released, the system attempts to restore its initial conditions, but in this case the failure was so great that the system is disturbed, presenting oscillations and alterations.

It was not recovered despite voltage controls of adjacent power stations, as seen with the ripple appearing in the voltage magnitude once the fault disappears.

As a consequence of the three-phase fault, the machines in nearby nodes are also affected in their performance and behavior. After the contingency, the machines clearly try to deliver the required reactive power for the network recovery, but they fail because the signal voltage becomes unstable after the fault disappears.

In order to evaluate the STATCOM impact in voltage control, a simulation is now performed, by applying the same fault. The STATCOM is connected to the AER. The voltage magnitude obtained as shown in Fig. 19.5b. The STATCOM model used for this analysis was the Power System Simulator for Engineering (PSS®E) model [16].

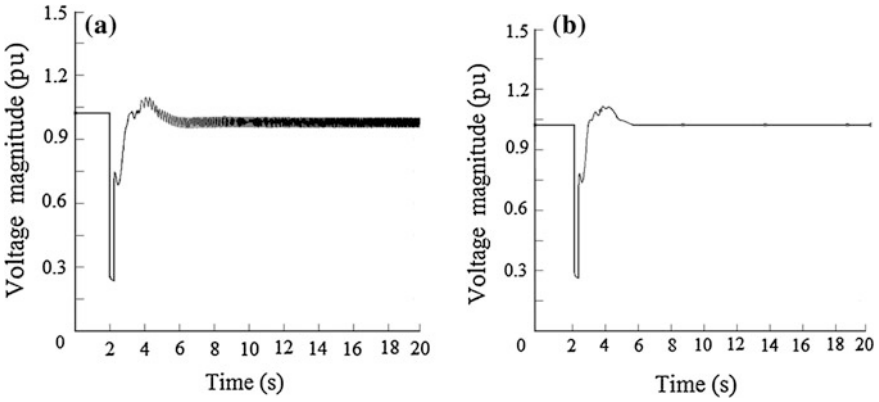

Fig. 19.5 Voltage magnitude response at AER under a three-phase fault in ATP without STATCOM (**a**), and with STATCOM (**b**)

During the fault, as observed in the same case without STATCOM, AER voltage drops to near 0.2 pu because failure occurs. When STATCOM is applied, AER benefits, because when failure occurs, STATCOM injects reactive power into the network in order to raise the voltage magnitude in these nodes. STATCOM has a greater responsiveness because it raises the voltage magnitude in less operating time with respect to a SVC.

Once the fault occurred, and the rate increases considerably because of STATCOM; the rotor of the machine is able to stabilize its speed and return to normal operation in less time compared to the case of a SVC. After the fault is cleared, the voltage is stabilized rapidly which indicates that the STATCOM connected at AER exerts control to keep the voltage magnitude at its nominal value, delivering reactive power according to the needs of the network, despite the long-time failure.

STATCOM has a high response speed and is able to normalize the system in a short period of time. During the fault, the rotor speed in nearby generators considerably increases. Because of STATCOM, the machines are able to stabilize the speed and return to normal operation in less time compared to the case of a SVC.

Once the fault has been released, the system is able to regain stability after a certain time due to the action of STATCOM during and after the contingency. At the time when the disturbance occurs STATCOM almost immediately stops the injection of reactive power and it switches to a state where it absorbs MVAr, while machines recover stability, STATCOM absorbs reactive power and then starts again injecting reactive power to recover its initial value, allowing the generators voltage to return to normal operation. Note that the STATCOM returns to its normal operation in less time than SVC. Besides maintaining the voltage, the loss of electrical stability is also prevented.

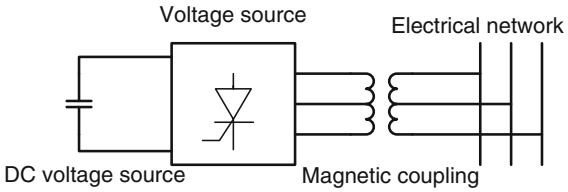

Fig. 19.6 STATCOM components, indicating the magnetic coupling

19.5.1.1 Consideration of Various Values of the Coupling Transformer

One of the main components of the STATCOM is the coupling transformer or magnetic coupling; this can be constructed with different reactance values. In Fig. 19.6 the magnetic coupling of the STATCOM and the capacitor as a DC source are shown.

Connecting the VSC terminals directly to the network is not suitable, because it has a larger short circuit than the VSC. For this reason, a coupling transformer is used between the STATCOM terminals and the network. When STATCOM is connected to the system through a transformer, it has an adequate reactance in order to permit a satisfactory STATCOM operation.

The STATCOM operational characteristic voltage-current is completely dependent on VSC voltage and coupling transformer reactance. The typical transformer reactance has values between 10 and 20 % of the drop voltage. It corresponds to 10 or 20 % of the network nominal voltage in the range of the STATCOM nominal current.

The coupling transformer could be a delta-star three-phase transformer bank and should be considered the core losses and the nonlinear characteristics, because transformers with the ability to saturate affect the performance of power electronic controllers.

In some STATCOM applications where network disturbances appear because of harmonics, applying a harmonic filter or a capacitor bank is necessary. In order to limit the flow of harmonic currents, employing reactors, in addition to the coupling transformer, may be required as well or they could be eliminated by using harmonic controller instead of increasing the filter [20].

Considering the three-phase failure in the bus bar ATP substations indicated above, the reactive power behavior in the transmission lines ATP to AER is analyzed, as well as the current and voltage in AER by adjusting the transformer coupling of the STATCOM with three different reactance values: 0.1, 0.5 and 1.0 Ω. The reactive power and the current injected by the STATCOM for the three cases are shown in Figs. 19.7, 19.8 and 19.9, whereas the voltage magnitude is shown in Fig. 19.10.

The behavior variation of both the reactive power in transmission lines AER-ATP and the voltage magnitude in bus bar AER were small in the three cases, because the power stations nearby (RBT and RBC) provide the reactive power

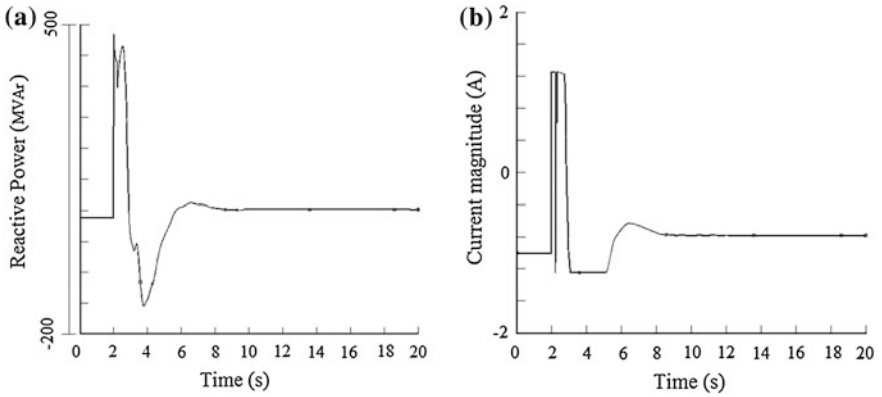

Fig. 19.7 **a** Reactive power flowing in lines AER-ATP. **b** Current injected by the STATCOM, when $X = 0.1\ \Omega$

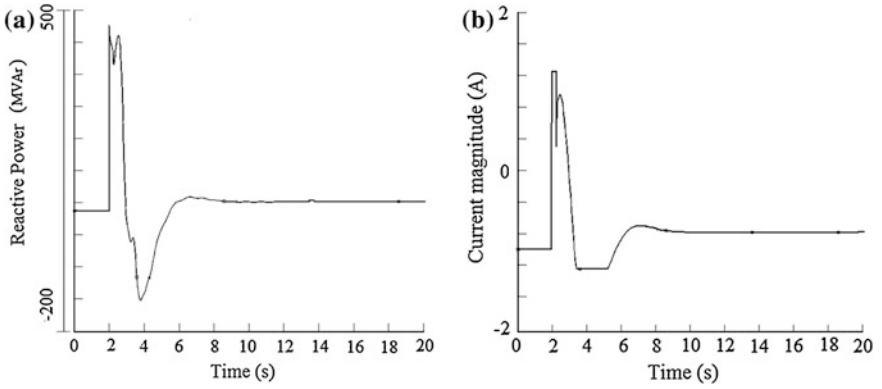

Fig. 19.8 **a** Reactive power flowing in lines AER-ATP. **b** Current injected by STATCOM, when $X = 0.5\ \Omega$

required; therefore the voltage magnitude is maintained. The variation of the inductance in the transformer coupling was then not determinant.

The magnitude of the reactive power is shown in Table 19.7, for each transmission line ATP-AER to its maximum value: when the failure has been applied and was required to exchange reactive power. Initial reactive power was 62 MVAr in each case.

By increasing the reactance of the coupling transformer, the reactive power contribution decrease, i.e. for the higher transformer reactance, the STATCOM delivers less reactive power, which is important when evaluating economic projects for installing a STATCOM.

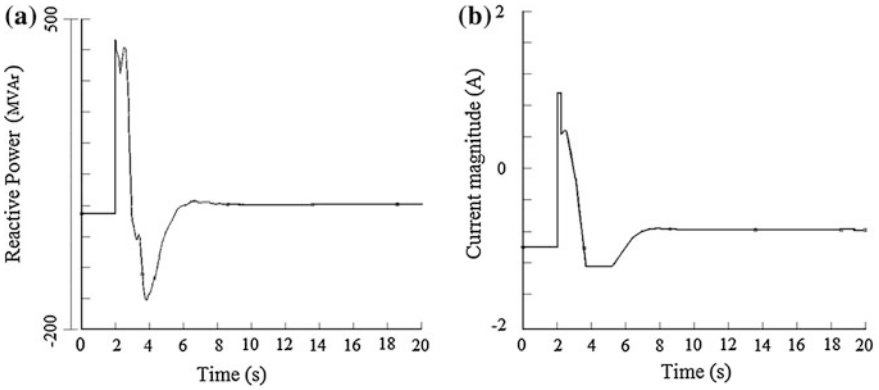

Fig. 19.9 **a** Reactive power flowing in lines AER-AT. **b** Current injected from the STATCOM, when $X = 1.0\ \Omega$

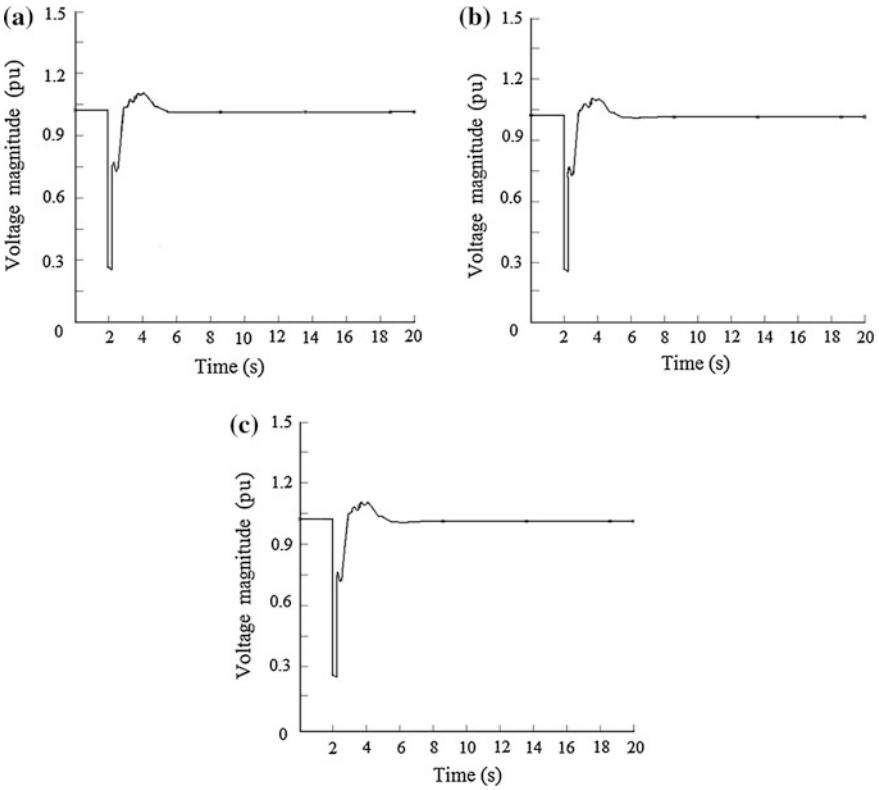

Fig. 19.10 Voltage magnitude in bus bar AER with **a** $X = 0.1\ \Omega$, **b** $X = 0.5\ \Omega$ and **c** $X = 1.0\ \Omega$

Table 19.7 Behavior of reactive power in lines AER-ATP

Reactance X (Ω)	Reactive power lines AER to ATP (MVAr)
0.1	486
0.5	470
1.0	456

19.5.2 STATCOM Application in the Southeast Region

The objective of this case study is to provide the exchange of enough reactive power when high voltage in bus bars appears, caused by power network operating conditions.

The largest block of hydroelectric energy is in the southeast of the country, and the largest thermoelectric power block is located in the Northeast. Moreover, the main energy demand centers are located in the center (Mexico City), the northeast (Monterrey) and the west (Guadalajara), as indicated in Fig. 19.11.

Some generation centers are far from consumption centers, making long transmission lines necessary. The power station Manuel Moreno Torres (MMT) is located in the southeast of the country, and it has three parallel 400 kV transmission lines connecting to substation Juile (JUI).

The lengths of these lines are shown in Table 19.8. When low generation exists in MMT, low active power is sent to JUI and because of the long lines capacitive reactance, a nominal voltage increase occurs, which could result in damage to electrical equipment because of overvoltage.

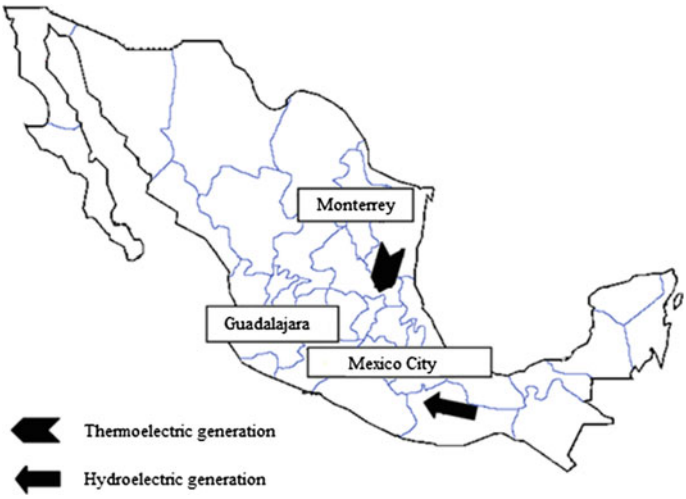

Fig. 19.11 Energy consumption centers and generation blocks in Mexico

Table 19.8 Lengths of transmission lines MMT-JUI

Transmission line	Name	Length (km)
MMT-JUI	A3040	243
MMT-JUI	A3140	243
MMT-JUI	A3T90	241.9

For this reason, maneuvers are performed to open one of the transmission lines (commonly line A3T90) for voltage control at JUI. This practice is not recommended, because the design of the circuit breakers do not consider opening and closing constantly, and there is a risk of mechanical damage to the device with the consequent possible electrical failure in the network. Additionally, there is a risk of human error which may consequently bring a disturbance to the power network. To eliminate the above practice, the installation of a STATCOM is proposed with a capacity of ±500 MVAr.

19.5.2.1 Considerations of STATCOM Simulations

The purpose of proposing a STATCOM in electrical substation JUI is to maintain the voltage at 400 kV, even during periods of low generation, which could also contribute to the reactive compensation requirements in this area of the Mexican Electrical System. To model the MES transmission lines, transformers and generators, the PSS®E program in the steady-state option was applied [16].

Figure 19.12 shows actual measured values of active power in each MMT-JUI line during the third week of January 2006, in minimum demand in Mexico. Because of a minimum load demand, power generation in station MMT decreases

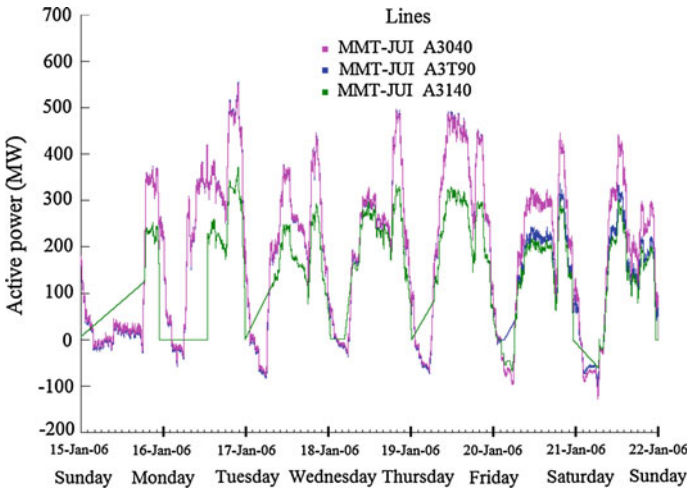

Fig. 19.12 Active power in the three transmission lines of MMT-JUI January 15–22, 2006

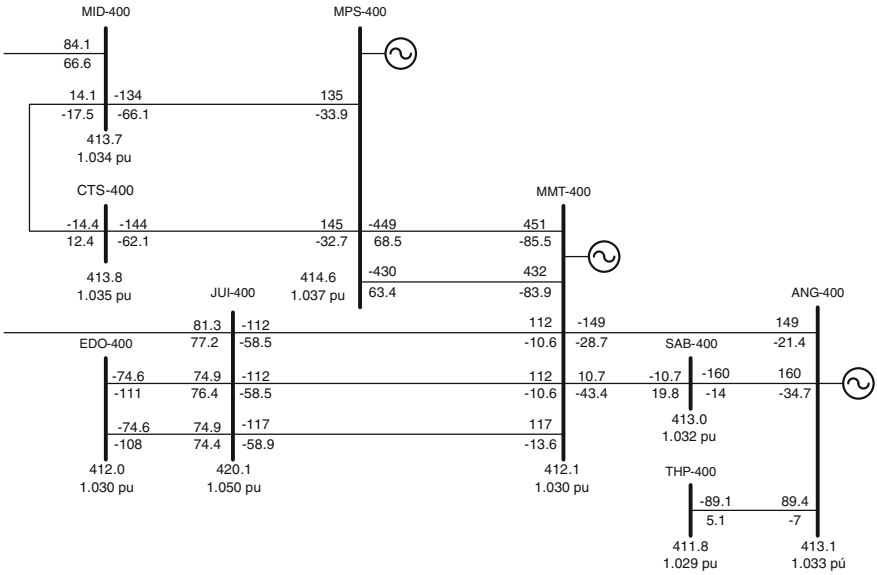

Fig. 19.13 Active and reactive power flow behavior minimum demand

its contribution from 22:00 to 10:00 h. Thus in JUI, the voltage magnitude becomes greater than 4 % from the nominal voltage because of the capacitive effect on the lines. To mitigate this capacitive effect, one line is disconnected when there are about 100 MW of power flow in each line of MMT to JUI (normally line A3T90).

In Fig. 19.13 the network section in analysis is shown, and details of both active and reactive power are shown at the transmission lines of interest (JUI-MMT) with minimum demand.

The electrical substations investigated are Manuel Moreno Torres (MMT), Minatitlán II (MID), Coatzacoalcos (CTS), Juile (JUI), Cerro de Oro (EDO), El Sabino (SAB), Angostura (ANG), Tapachula (THP) and Brillantes (BRZ), as well as transmission lines connecting them and power stations. At minimum demand, JUI voltage magnitude is 420 kV, i.e. 5 % above the nominal, creating overvoltage.

From Fig. 19.13, the bus bars have overvoltages at steady-state in the southeast region of MES; furthermore, the voltage profile is 3–5 % above the nominal voltage.

This is a critical situation, if we consider that these are the normal operating conditions of this part of the power network during minimum load demand.

To prevent overvoltage or the continued disconnection of one transmission line, the use of a STATCOM is proposed [21]. To validate it, a power flow analysis was carried out in steady-state, and results are shown in Fig. 19.14. Analyses of Fig. 19.14 show that significant changes occur in nodal voltage magnitudes when the STATCOM is present in the network. For example, the voltage magnitude in the STATCOM bus bar (JUI-400) is maintained at 404.8 kV, and the voltage

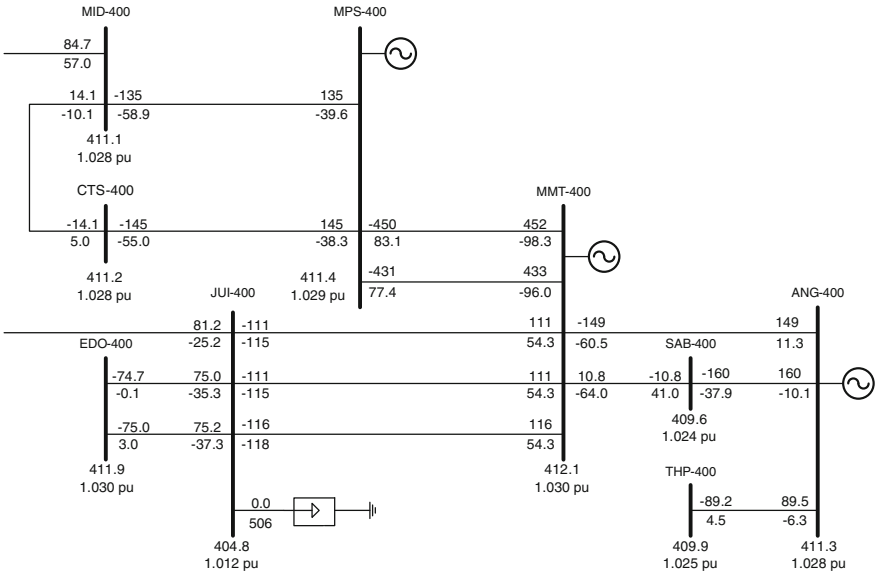

Fig. 19.14 Active and reactive power flow behavior minimum demand with STATCOM

magnitude in the network area is near to nominal because of the STATCOM performance.

As can be observed, by using the STATCOM, the transmission lines opening is not required because the voltage magnitude profile has moved away from the steady-state limits. The results indicate that the STATCOM exerts voltage control in the power system by absorbing reactive power. A comparison between Figs. 19.13 and 19.14 revealed that without STATCOM, JUI absorbed a total of 175.9 MVAr and gave a total of 228 MVAr, whereas with STATCOM, JUI now absorbs a total of 445.8 MVAr to maintain the voltage value close to 1 pu.

Figure 19.15 shows the voltage magnitude profile in the bus bar of the interest region in both cases with and without STATCOM connected. Analyses of Fig. 19.15 show that with the connection of STATCOM in JUI, the voltage magnitude profile in adjacent nodes is significantly near to nominal.

One STATCOM application is for voltage support because considering the typical voltage-current characteristic this device can provide both capacitive and inductive compensation, as well as control its output current at full capacity, regardless of system voltage. In other words, STATCOM provides full capacitive reactive power to any system voltage. STATCOM has an additional transitional capacity in both capacitive and inductive regions.

The maximum overcurrent transient in capacitive region is determined by the ignition-off inverters maximum current capacity. In the inductive region, investors are naturally commutated and therefore the transient current capacity is limited by the maximum allowable junction temperature in electronic switches [22].

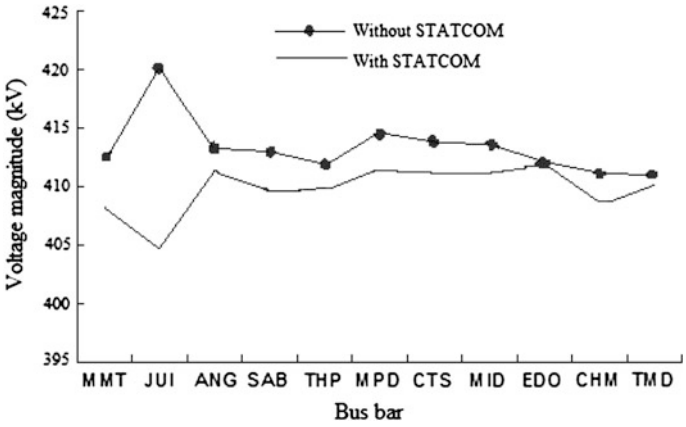

Fig. 19.15 Voltage magnitude at nodes in interest zone

References

1. Acha E, Fuerte-Esquivel CR, Ambriz-Pérez H, Angeles-Camacho C (2005) FACTS modelling and simulation in power networks. Wiley, West Sussex
2. Hingorani NG, Gyugyi L (2000) Understanding FACTS: concepts and technology of flexible AC transmission systems. IEEE Inc., New York
3. Comisión Federal de Electricidad (2006) Programa de obras e inversiones del Sector Eléctrico 2007–2016. Gerencia de Programación de Sistemas Eléctricos, Mexico City
4. Comisión Federal de Electricidad (2005) Reglas de despacho y operación del Sistema Eléctrico Nacional. Diario Oficial, Mexico City
5. Li-Jun C, Erlich I (2005) Simultaneous coordinated tuning of PSS and FACTS damping controllers in large power systems. IEEE Trans Power Syst 20:294–300
6. Breuer W, Povh D, Retzmann, Teltsch E, Lei X (2004) Role of HVDC and FACTS in future power systems. Paper presented at conference of electric power supply industry, Shanghai, October 2004
7. Angeles-Camacho C (2005) Phase domain modelling and simulation of large-scale power systems with VSC-based FACTS equipment. PhD thesis, University of Glasgow, Glasgow
8. Hernández J, Messina A (2001) Utilización de Dispositivos de Control en la Red de Transmisión para Amortiguar Oscilaciones de Potencia. Paper presented at the 2nd Biennial Congress, CIGRE-Mexico, Irapuato, 13–15 June 2001
9. Comisión Federal de Electricidad (2013) CFE y la electricidad en México. http://www.cfe.gob.mx/ConoceCFE/1_AcercadeCFE/CFE_y_la_electricidad_en_Mexico/Paginas/CFEylaelectricidadMexico.aspx. Accessed 20 Aug 2013
10. Matsuno K, Iyoda I, Oue Y (2002) An experience of FACTS development 1980s and 1990s. Paper presented at transmission and distribution conference and exhibition: asia pacific, IEEE/PES, Yokohama, 6–10 Oct 2002
11. Sobtink KH, Renz KW, Tyll H (1998) Operational experience and field tests of the SVG at Rejsby Hede. Paper presented at power system technology, POWERCON '98, International Conference Beijing, 18–21 Aug 1998
12. Kidd D, Mehraban B, Ekehav B, Ulleryd J (2003) Eagle pass back-to-back VSC installation and operation. Paper presented at power engineering society general meeting, IEEE, Toronto, 13–17 July 2003

13. Fardanesh B, Schuff A (2007) Dynamic studies on the NYS transmission system with the Marcy CSC in the UPFC and IPFC configurations. Paper presented at transmission and distribution conference and exposition, IEEE PES, Dallas, 7–12 Sept 2003
14. Angeles-Camacho C, Acha E, Barrios-Martinez E (2007) Three-phase STATCOM models for large-scale Newton-Raphson power flow studies. Paper presented at power tech, Lausanne, 1–5 July 2007
15. Barrios-Martinez E, Angeles-Camacho C, Acha E (2009) Dynamic phase-domain modeling and simulation of STATCOM in large-scale power systems. Paper presented at Power Tech, Bucharest, 28 June–2 July 2009
16. Siemens Power Transmission and Distribution (2007) PSS®E 31.0 program application guide volumes 1 and 2. New York
17. Coronado I, Zúñiga P, Ramírez J (2001) FACTS: soluciones modernas para la industria eléctrica. Avance y Perspectiva 20:235–244
18. Torres A, Torres M, Ríos M (2001) FACTS technologies to improve the colombian national transmission system. Paper presented at IEEE transmission and distribution conference and exposition, Atlanta, 28 Oct–2 Nov 2001
19. Comisión Reguladora de Energía (2014) Temporadas abiertas de reserva de capacidad de transmisión y transformación. http://www.cre.gob.mx/documento/2317.pdf. Accessed 2 Feb 2014
20. Ben-Sheng Ch, Yuan-Yih H (2008) A minimal harmonic controller for a STATCOM. IEEE Trans Ind Electron 55:655–664
21. CIGRÉ (2000) FACTS technology for open access. Final draft report, JWG 14/37/38/39-24. Paris
22. Dávalos RJ, Ramírez JM (2001) Características funcionales del STATCOM. Paper presented at Segundo Congreso Bienal CIGRÉ-Mexico, Irapuato, 13–15 June 2001

Chapter 20
Stability Analysis of STATCOM in Distribution Networks

Juan Segundo-Ramírez, Aurelio Medina Ríos and Gerard Ledwich

Abstract This chapter presents the stability analysis based on bifurcation theory of the distribution static compensator (DSTATCOM) operating both in current control mode as in voltage control mode. The bifurcation analysis allows delimiting the operating zones of nonlinear power systems and hence the computation of these boundaries is of interest for practical design and planning purposes. Suitable mathematical representations of the DSTATCOM are proposed to carry out the bifurcation analyses efficiently. The stability regions in the Thevenin equivalent plane are computed for different power factors at the Point of Common Coupling (PCC). In addition, the stability regions in the control gain space are computed, and the DC capacitor and AC capacitor impact on the stability are analyzed in detail. It is shown through bifurcation analysis that the loss of stability in the DSTATCOM is in general due to the emergence of oscillatory dynamics. The observations are verified through detailed simulation studies.

Keywords Bifurcation · DSTATCOM · Floquet multiplier · Stability regions

J. Segundo-Ramírez (✉)
Facultad de Ingeniería, Departamento de Ingeniería Mecánica y Eléctrica,
Universidad Autónoma de San Luis Potosí, San Luis Potosí, México
e-mail: juan.segundo@uaslp.mx

A.M. Ríos
Facultad de Ingeniería Eléctrica, División de Estudios de Posgrado,
Universidad Michoacana de San Nicolás de Hidalgo, Morelia, México
e-mail: amedinr@gmail.com

G. Ledwich
School of Electrical Engineering and Computer Science,
Queensland University of Technology, Brisbane, Australia
e-mail: a.ghosh@qut.edu.au

F. Shahnia et al. (eds.), *Static Compensators (STATCOMs) in Power Systems*,
Power Systems, DOI 10.1007/978-981-287-281-4_20

20.1 Introduction

The transient and steady state response of a power system can be computed by conventional numerical integration methods; this method is known as a Brute Force approach [1]. Therefore the stability of any electric system may be computed through time domain simulations. On the other hand, with bifurcation theory it is possible to predict the system behavior around the operating points without resorting to the numerical integration solution. The results obtained with this analysis can be represented in a bifurcation diagram providing qualitative information about the behavior of the periodic steady state solutions as the parameters vary. In bifurcation points, infinitesimal changes in system parameters can cause significant qualitative changes in periodic solutions. Knowing the set of bifurcation values in the parameter space, it is possible to design an electrical circuit within stable operating conditions, but an important problem is the computation of these bifurcation sets. Upon obtaining the global feature of the bifurcation set, various non-linear phenomena, such as the coexistence of many stable states [2], the jump behavior of periodic responses [3], the phenomenon of hysteresis and the appearance of chaotic states [4], etc., can be observed. In general terms, the construction of a bifurcation diagram consists of the following steps [1, 5]: (1) find a first periodic steady-state solution, (2) based on the first solution, find other equilibrium solutions using a continuation method [1, 5], and (3) determine the stability of each solution.

The bifurcation theory has been used in stability analysis [6] for the demonstration of chaotic motions in the two-degree freedom swing equations. Subsequent applications of this theory have been directed to diverse studies such as voltage collapse [7], subsynchronous resonance [8], voltage source converters [9, 10], ferroresonance oscillations [4], and design of nonlinear controllers [11]. Furthermore, this theory has been applied to assess the dynamical behavior of nonlinear components such as induction motors [3], load models [12, 13], tap changing transformers [14], Flexible AC Transmission Systems (FACTS) [15, 16], and custom power devices [17, 18]. In addition, bifurcation theory has been used to analyze the stability of power converter and nonlinear switched circuits. In [19, 20] a wide collection of results related to nonlinear phenomena in power electronics is presented.

Conventional stability analyses in power systems are basically based on brute force approach and eigenanalysis. In these analyses, the system is modeled using root mean square (rms) quantities and the network dynamics are neglected. In this chapter, the power system is represented through instantaneous quantities, the network transients are taken into account and the electric sources voltage are assumed to be sinusoidal.

20.2 DSTATCOM

The basic purpose of the DSTATCOM is to compensate the load in such a way that at the PCC the source current and the PCC voltage are balanced and sinusoidal. The DSTATCOM can compensate the load, correct the power factor and reduce the

harmonic content in the network. This device can even regulate the voltage at the connection bus. There are important differences between the DSTATCOM and the STATCOM. The STATCOM injects almost sinusoidal a balanced three-phase current, whereas the DSTATCOM must be able to inject an unbalanced and harmonically distorted current in order to balance and eliminate the harmonic distortion in the source current. Therefore, the compensation algorithm and the control are significantly different between DSTATCOM and STATCOM. Additionally, there are two operating modes of the DSTATCOM associated to the control scheme and compensation algorithm. These operating modes are named voltage control mode and current control mode.

In order to cancel-out unbalance or harmonics in the line current, the voltage source converter that constitutes the DSTATCOM must be able to inject currents in one phase independently of the other two phases. From this point of view the structure of a DSTATCOM is very important. The DSTATCOM structure adopted in our analysis is shown in Fig. 20.1. This structure contains three H-bridge Voltage Source Converters (VSC) connected to a common DC storage capacitor. Each VSC is connected to the network through a transformer. The purpose of the transformers is to provide isolation between the inverter legs and prevents the DC capacitor from being shorted through switches of the different inverters. The converter allows three

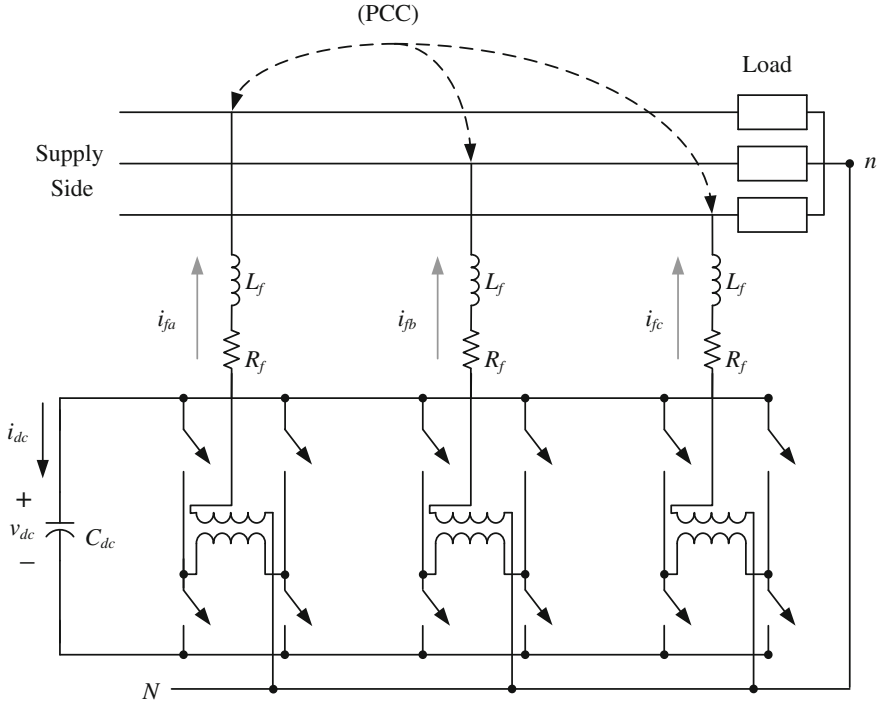

Fig. 20.1 Structure of the DSTATCOM

independent current injections. It is to be noticed that due to the presence of transformers, this topology is not suitable for canceling any DC component in the load current [21]. The inductance L_f represents the leakage inductance of each transformer and additional external inductance, if any. The switching losses of an inverter and the copper loss of the connecting transformer are represented by a resistance R_f. For more details about this structure please see [21]. This converter topology with a hysteresis modulation technique is used in this chapter for the DSTATCOM operating in voltage and current control mode; however, other topologies or modulation techniques can be used.

Now, let us consider the following nonlinear system periodically excited with a T-periodic function (20.1), which can describe the dynamic behavior of the equivalent circuit of the compensated system shown in Fig. 20.2.

$$\dot{\mathbf{x}}(t) = \mathbf{f}(t, \mathbf{x}; \mathbf{M}) \tag{20.1}$$

where $\mathbf{x}$ and $\mathbf{f}$ are n-dimensional vectors and $\mathbf{M}$ is a m-dimensional parameter vector. In particular, for the electric system shown in Fig. 20.1, the dynamic system is

$$\frac{d}{dt}\begin{bmatrix} i_s \\ v_t \\ i_l \\ i_f \\ r \end{bmatrix} = \begin{bmatrix} -\frac{R_s}{L_s} i_s - \frac{1}{L_s} v_t + \frac{v_s}{L_s} \\ \frac{1}{C_{fil}} i_s - \frac{1}{C_{fil}} i_l + \frac{1}{C_{fil}} i_f \\ -\frac{R_l}{L_l} i_l + \frac{1}{L_l} v_t - K_3 \frac{i_l}{L_l r^{m+2}} \\ -\frac{R_f}{L_f} i_f - \frac{1}{L_f} v_t + \frac{V_{dc}}{L_f} u \\ \frac{K_3}{K_2} \frac{i_1^2}{r^{m+3}} - \frac{K_1}{K_2} r^{n-1} \end{bmatrix} \tag{20.2}$$

Please notice that in (20.2) each variable is a three-phase variable. The nonlinear load is an Electric Arc Furnace (EAF); however, a different load can be connected to the PCC. The dynamic behavior of the v–i characteristic of the EAF is described by the differential equation introduced in [22]. This differential equation is based on the principle of energy balance.

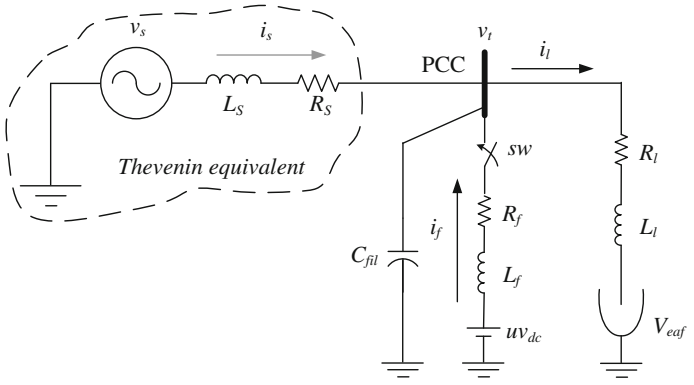

Fig. 20.2 Compensation of a weak system with an EAF

It is possible to represent the different stages of the arcing process by simply modifying the parameters of m and n in the EAF. The complete set of combinations of these parameters for different stages of the electric arc can be found in [22].

20.2.1 Simplified Representation of the DSTATCOM

In the detailed model, the switching devices, the modulation process and the DC capacitor dynamic are explicitly represented. The switching elements are modeled as ideal switches. This model sometimes requires very short time steps to well represent the commutation process; thus, the simulation time can be considerably long. If we are not interested in the switching phenomena, we can use a source having the average value computed upon a switching period. With the simplified model, one can simulate the system using a larger time step and consequently a smaller simulation time. Of course, these simplifications have to be accurate enough to preserve the information of interest. Here, two ways for obtaining simplified representations of the DSTATCOM are developed. The first one is to assume the converter as a set of ideal current or voltage sources. The second one is to assume a zero hysteresis band for the modulation technique, which is called smooth hysteresis band approach.

20.2.1.1 Ideal Sources

For this approach, the converter can be replaced by three ideal current or voltage sources, depending on the case. The link between the DC side and the AC side of the converters is well represented using the energy preservation principle. This modeling approach is equal to suppose an instantaneous response of the power electronic converters without commutation harmonics; in other words, this approach assumes that the DSTATCOM converters follow perfectly the control references.

20.2.1.2 Smooth Hysteresis Band Approach

In the ideal sources approach we assume an instantaneous response of the converter to generate the reference currents or voltages. However, this approach does not take into account neither the switching control nor the converter structure. The smooth hysteresis band approach is simpler than the ideal sources approach, since it is possible to obtain the simplified model from the detailed model in a straightforward way. In addition, this approach takes into account the converter structure and the switching control.

This model is based on the assumption that the hysteresis band shown in Fig. 20.3 is decreased until $h = 0$, as a consequence the harmonic distortion introduced by the commutation process no longer exists. The hysteresis curve in the

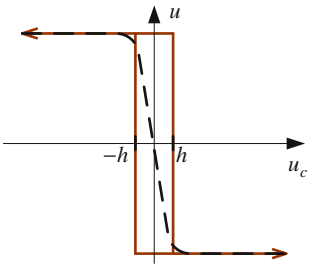

Fig. 20.3 Hysteresis modulation technique and the smooth hysteresis approximation

detailed model can be replaced for a sigmoid function or a hyperbolic tangent. The approximation of the hysteresis curve using the sigmoid function is defined as

$$u = \frac{2}{1 + e^{4u_c/h}} - 1 \tag{20.3}$$

The approximation through the hyperbolic tangent is defined as

$$u = -\tanh(u_c/h) \tag{20.4}$$

here, u_c is a continuous function defined as the controlled current or voltage obtained from measurements minus the reference signal. Figure 20.3 shows the hysteresis function represented with solid lines and the smooth hysteresis curve is drawn with dashed lines.

20.2.2 DSTATCOM Operating in Current Control Mode

In the current control mode, the DSTATCOM compensates for any unbalance or distortion in the load; thus, a balanced current from the system for any unbalance or harmonic distortion in the load is drawn [23]. One of the most important issues for the load compensation is the generation of the reference compensator currents. There are several techniques proposed [24, 25]. However, most of these methods assume that the voltage at the PCC is stiff. Unfortunately this is not a valid assumption for the most practical applications. In this chapter, the computation of the reference currents will be done using instantaneous symmetrical components [26]. For a more realistic case, the source is not assumed to be stiff.

20.2.2.1 Compensation Algorithm and Control

In (20.2), u is the control signal constrained between +1 and −1. Once the reference currents are generated, they are tracked-down in a hysteresis band current control scheme. The control signal is computed through,

$$u = hys\left(i_f - i_f^*\right) \tag{20.5}$$

where i_f^* is the reference compensation current. These are given by [26],

$$\begin{aligned} i_{fa}^* &= i_{la} - \frac{v_{ta} + (v_{tb} - v_{tc})\beta}{\sum_{x=a,b,c} v_{tfx}^2}\left(P_l^{av} + P_{loss}\right) \\ i_{fb}^* &= i_{lb} - \frac{v_{tb} + (v_{tc} - v_{ta})\beta}{\sum_{x=a,b,c} v_{tfx}^2}\left(P_l^{av} + P_{loss}\right) \\ i_{fc}^* &= i_{lc} - \frac{v_{tc} + (v_{ta} - v_{tb})\beta}{\sum_{x=a,b,c} v_{tfx}^2}\left(P_l^{av} + P_{loss}\right) \end{aligned} \tag{20.6}$$

where β is computed based on the desired power factor. In (20.6), P_l^{av} is the average power drawn by the load, P_{loss} is the power loss due to R_f, and v_{tfx} is the fundamental component of v_{tx}, for $x = a, b, c$.

The hysteresis function hys is defined by,

$$hys(w) = \begin{cases} 1 & for \quad w \leq -h \\ -1 & for \quad w > h \end{cases} \tag{20.7}$$

where 2 h is the hysteresis band.

The power loss P_{loss} is computed through the proportional controller [23], i.e.,

$$P_{loss} = K_{pdc}\left(v_{dc}^* - v_{dc}^{av}\right) + K_{idc}\int \left(v_{dc}^* - v_{dc}^{av}\right) dt \tag{20.8}$$

where v_{dc}^* is the reference DC voltage, v_{dc}^{av} is the average voltage across the DC capacitor.

To compute β, we introduce a simple *proportional-integral* control given by,

$$\beta = K_{p\beta}\left(\beta_t^* - \beta_t\right) + K_{i\beta}\int \left(\beta_t^* - \beta_t\right) dt \tag{20.9}$$

where

$$\beta_t^* = \frac{1}{\sqrt{3}}\tan\left(\cos^{-1}(PF^*)\right) \tag{20.10}$$

$$\beta_t = \frac{1}{\sqrt{3}}\tan\left(\cos^{-1}(PF)\right) \tag{20.11}$$

and PF* is the desired reference power factor at the PCC bus and PF is the measured power factor at PCC.

20.2.2.2 Simplified DSTATCOM Model

The ideal switch model has some disadvantages [27]. One way to mitigate the adverse effects on the simulation related to the switching process is to use a small integration time step to carry-out the simulation. However, it takes long simulation time. The source of numerical problems for the integration process arises from the discontinuities and the non-differentiability introduced by the ideal switch model [20, 28], and one way to avoid these problems is to smooth the switching transitions.

In Fig. 20.4 the schematic representation of the simplified DSTATCOM model in current control mode is shown. Figure 20.5 shows the schematic representation of the DC link model. The power balance between the DC and AC side can be given as,

$$\begin{aligned} P_{dc} &= v_{dc} i_{dc} \\ &= i_{fa} v_{ta} + i_{fb} v_{tb} + i_{fc} v_{tc} + R_f\left(i_{fa}^2 + i_{fb}^2 + i_{fc}^2\right) + L_f\left(i_{fa}\frac{di_{fa}}{dt} + i_{fb}\frac{di_{fb}}{dt} + i_{fc}\frac{di_{fc}}{dt}\right) \end{aligned} \tag{20.12}$$

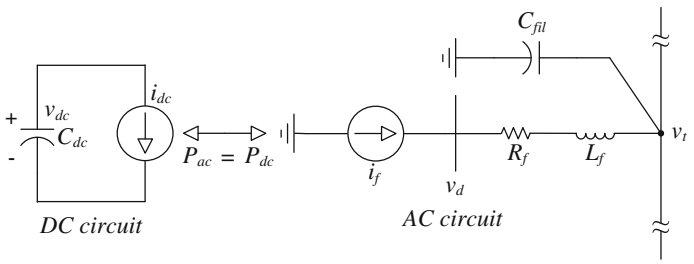

Fig. 20.4 Schematic representation for the simplified model

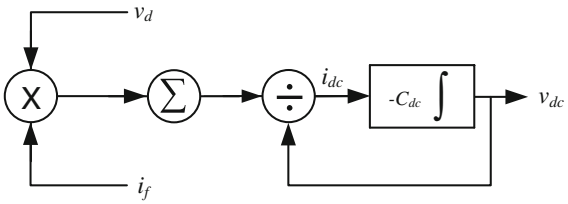

Fig. 20.5 DC link model

where

$$\frac{di_{fa}}{dt} = -\frac{\Delta\left(\frac{dv_{ta}}{dt} + \left(\frac{dv_{tb}}{dt} - \frac{dv_{tc}}{dt}\right)\beta + (v_{tb} - v_{tc})\frac{d\beta}{dt}\right) + \frac{d\Delta}{dt}}{\Delta^2}\left(P_l^{av} + P_{loss}\right) + \frac{di_{la}}{dt} - \frac{v_{ta} + (v_{tb} - v_{tc})\beta}{\Delta}\left(\frac{dP_{dc}}{dt} + \frac{dP_{loss}}{dt}\right) \tag{20.13}$$

$$\frac{di_{fb}}{dt} = -\frac{\Delta\left(\frac{dv_{tb}}{dt} + \left(\frac{dv_{tc}}{dt} - \frac{dv_{ta}}{dt}\right)\beta + (v_{tc} - v_{ta})\frac{d\beta}{dt}\right) + \frac{d\Delta}{dt}}{\Delta^2}\left(P_l^{av} + P_{loss}\right) + \frac{di_{lb}}{dt} - \frac{v_{tb} + (v_{tc} - v_{ta})\beta}{\Delta}\left(\frac{dP_{dc}}{dt} + \frac{dP_{loss}}{dt}\right) \tag{20.14}$$

$$\frac{di_{fc}}{dt} = -\frac{\Delta\left(\frac{dv_{tc}}{dt} + \left(\frac{dv_{ta}}{dt} - \frac{dv_{tb}}{dt}\right)\beta + (v_{ta} - v_{tb})\frac{d\beta}{dt}\right) + \frac{d\Delta}{dt}}{\Delta^2}\left(P_l^{av} + P_{loss}\right) + \frac{di_{lc}}{dt} - \frac{v_{tc} + (v_{ta} - v_{tb})\beta}{\Delta}\left(\frac{dP_{dc}}{dt} + \frac{dP_{loss}}{dt}\right) \tag{20.15}$$

$$\Delta = \sum_{x=a,b,c} v_{tfx}^2 \tag{20.16}$$

20.2.2.3 Comparative Analysis of Models for the DSTATCOM in Current Mode

In this section, the performance of the simplified model presented in the previous section is compared against the detailed model where the voltage source inverter based on the three H-bridge inverter is used. The test system is shown in Fig. 20.2. The system and the DSTATCOM parameters are given in Table 20.1. The hysteresis band for the detailed model is $h = 1$ A.

Initially, for $t < 0$ the switch *sw* is open and the electric circuit is in periodic steady-state. At $t = 0$ s the switch *sw* is closed and the DSTATCOM starts the compensation with the DC capacitor pre-charged at 1,200 V. Selected waveforms are presented in Fig. 20.6. Figure 20.6a shows the compensation current i_{fa}, while

Table 20.1 System parameters of the DSTATCOM in current mode

System	DSTATCOM
Voltage ($\|V_s\|$): 440 V (peak), sinusoidal and may contain harmonics, exhibit sags and swells, and possible unbalance.	Voltage controllers gains of DC capacitor loops: $K_{pdc} = 80$, $K_{idc} = 500$.
Feeder impedance (R_s, L_s): $1 + j7.54\ \Omega$	β control loop gains: $K_{p\beta} = 0.5$, $K_{i\beta} = 300$.
AC capacitor (C_{dc}): 70 μF	DC capacitor(C_{dc}): 1,500 μF
Feeder load impedance (R_l, L_l): $0.5 + j3.77\ \Omega$	Interface circuits (R_f, L_f): $0.05 + j3.77\ \Omega$
EAF constants: $K_1 = 15$, $K_2 = 0.05$, $K_3 = 800$, $m = 0$ and $n = 2$.	Reference value of DC capacitor voltage: 1,200 V

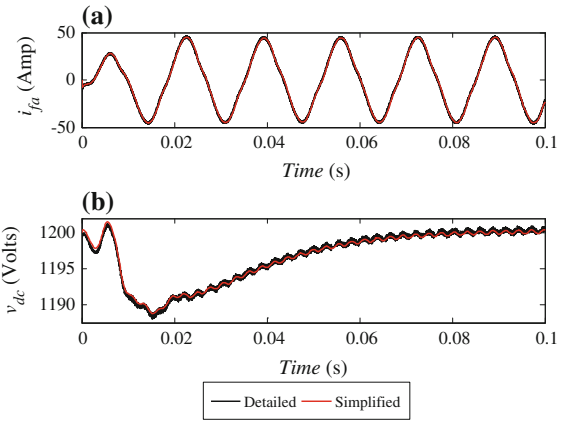

Fig. 20.6 Comparison in the time domain between the detailed and the simplified model for **a** compensation current i_{fa} and **b** DC capacitor voltage v_{dc}

Fig. 20.6b shows the DC voltage v_{dc} with the simplified model and with the detailed model for an integration step size of 65 and 1 μs, respectively. A good agreement between the two models has been achieved, even though the simplified model has a considerably larger integration step size (125 times).

20.2.3 DSTATCOM Operating in Voltage Control Mode

Here, the control strategy proposed in [29] is used. With this algorithm, the DSTATCOM operates as a voltage regulator to maintain constant the voltage of a specified bus (PCC). The magnitude of the bus voltage is pre-specified while its phase angle is generated from a DC capacitor control loop. A deadbeat controller for the inverter is used for voltage tracking. With this algorithm, the DSTATCOM can compensate the terminal voltage, for any distortion or unbalance in the load or in the voltage source.

20.2.3.1 Simplified DSTATCOM Model

In the simplified model, the three H-bridge converters are replaced by three controllable voltage sources. The main advantage of this model is to allow larger integration steps with high precision and reliability. In Fig. 20.7, the schematic representation for the simplified model of DSTATCOM operating in voltage mode is shown. This model is based on the assumption that $v_{tx} = v_{tx}^*$, where v_{tx}^* is the reference terminal voltage. Figure 20.8 shows the schematic representation of the DC link model.

The reference terminal voltage v_{tx}^* is

$$v_{tx}^* = V_m \sin(\omega t - \delta - \phi_x) \tag{20.17}$$

and δ is computed using a proportional-integral controller described by,

$$\delta = K_{p\delta}\left(P_{sh} - P_{sh}^*\right) + K_{i\delta}\int \left(P_{sh} - P_{sh}^*\right) dt \tag{20.18}$$

P_{sh} is the instantaneous power reference in the shunt link and P_{sh}^* is its reference; P_{sh} is given by

$$P_{sh} = v_{ta}i_{fa} + v_{tb}i_{fb} + v_{tc}i_{fc} \tag{20.19}$$

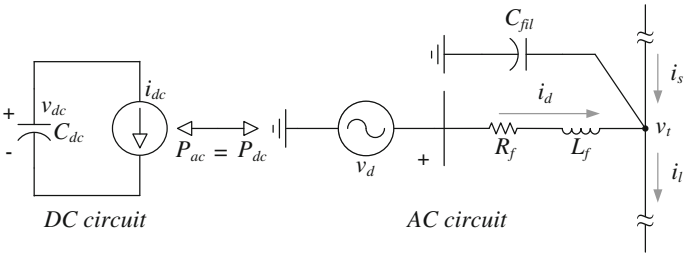

Fig. 20.7 Schematic representation for the simplified model

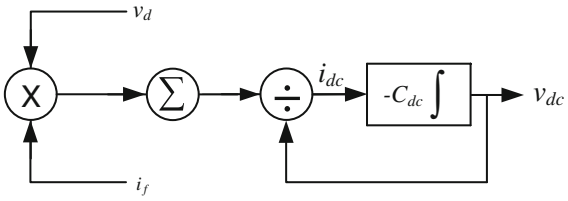

Fig. 20.8 DC link model

P_{sh}^{*} is obtained as,

$$P_{sh}^{*} = K_{pdc}\left(v_{dc}^{average} - v_{dc}^{*}\right) + K_{idc}\int \left(v_{dc}^{average} - v_{dc}^{*}\right)dt \tag{20.20}$$

where v_{dc}^{*} is the reference DC voltage, $v_{dc}^{average}$ is the average voltage across the DC capacitor. The converter terminal voltage is given by,

$$v_{dx} = R_f i_{dx} + L_f \frac{di_{dx}}{dt} + v_{tx} \tag{20.21}$$

The current injected by the compensator is calculated by,

$$i_{dx} = -C_{fil} V_m \sin(\omega t - \delta - \phi_x)\left(\omega - \frac{d\delta}{dt}\right) + i_{lx} - i_{sx} \tag{20.22}$$

The first derivative of i_{dx} is computed as,

$$\frac{di_{dx}}{dt} = \frac{d(i_{lx} - i_{sx})}{dt} - C_{fil} V_m \left(\sin(\omega t - \delta - \varphi_x)\frac{d^2\delta}{dt^2} + \cos(\omega t - \delta - \varphi_x)\left(\omega - \frac{d\delta}{dt}\right)^2\right) \tag{20.23}$$

The dynamic capacitor voltage is given by,

$$C_{dc}\frac{dv_{dc}}{dt} = -\frac{i_{da}v_{da} + i_{db}v_{db} + i_{dc}v_{dc}}{v_{dc}} \tag{20.24}$$

where

$$x =$$
$$\phi_a = 0,\ \phi_b = 2\pi/3,\ \phi_a = -2\pi/3$$

$$\frac{d\delta}{dt} = K_{p\delta}\left(\frac{dP_{sh}}{dt} - K_{pv}\frac{dv_{dc}^{average}}{dt}\right) + K_{i\delta}\left(P_{sh} - P_{sh}^{*}\right) \tag{20.25}$$

$$\frac{d^2\delta}{dt^2} = K_{p\delta}\left(\frac{d^2P_{sh}}{dt^2} - K_{pv}\frac{d^2v_{dc}^{average}}{dt^2}\right) + K_{i\delta}\left(\frac{dP_{sh}}{dt} - K_{pv}\frac{dv_{dc}^{average}}{dt}\right) \tag{20.26}$$

Table 20.2 System parameters of the DSTATCOM in voltage mode

System Parameters	DSTATCOM
Voltage (V_s): 440 V (peak), sinusoidal and may contain harmonics, exhibit sags and swells, and possible unbalance	Voltage controllers gains of DC capacitor loops: K_{pdc} = 154, K_{idc} = 3,500
Feeder impedance (R_s, L_s): 1 + j7.54 Ω	δ control loop gains: $K_{p\delta}$ = 27e−6, $K_{i\delta}$ = 8e−3
AC capacitor (C_{ac}):70 μF	DC capacitor(C_{dc}): 1,500 μF
Feeder load impedance (R_l, L_l): 0.5 + j3.77 Ω	Interface circuits (R_f, L_f): 0.05 + j3.77 Ω
EAF constants: K_1 = 15, K_2 = 0.05, K_3 = 800, m = 0 and n = 2	Reference value of DC capacitor voltage: 1,200 V

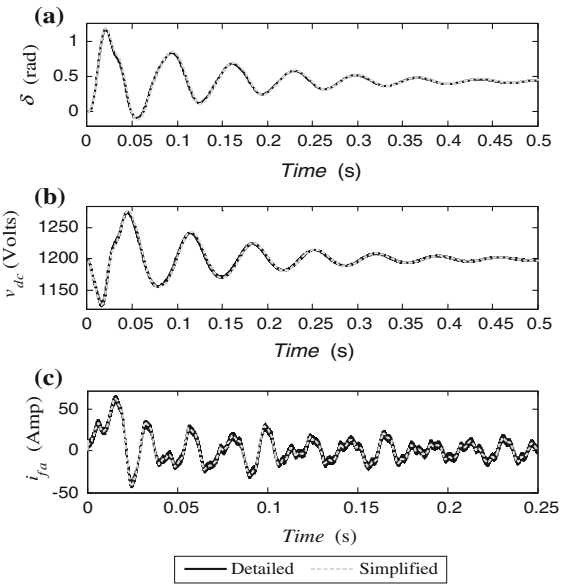

Fig. 20.9 Comparison in the time domain between the detailed and the simplified model for **a** phase angle δ, **b** DC capacitor voltage v_{dc}, and **c** compensation current i_{fa}

20.2.3.2 Comparative Analysis of Models for the DSTATCOM in Voltage Control Mode

In this section, the performance of the simplified DSTATCOM model is compared against the detailed model. The system parameters and the DSTATCOM parameters for the circuit shown in Fig. 20.2 are given in Table 20.2. The hysteresis band for the detailed model is h = 10.

Initially, the electric system is in periodic steady state and the switch sw is open. At t = 0 s, the switch sw is closed, thus, the DSTATCOM starts to regulate the terminal voltage v_t at the PCC bus. Figure 20.9a shows the results comparison for the phase angle δ, Fig. 20.9b shows the comparison for the voltage across the DC

capacitor v_{dc}, and Fig. 20.9c for the compensation current ifa. The results show a very good agreement between the simplified model and the detailed model, with an integration step size of 60 and 1 μs, respectively. An excellent agreement between the two models is achieved, even though the simplified model has a considerably larger integration step (60 times).

20.2.4 Comparison of the Simplified Modeling Approaches

20.2.4.1 DSTATCOM Operating in Current Mode

A comparison between the detailed model and the simplified model based on the ideal source approach is shown in Fig. 20.10. The compensator current i_{fa}, the terminal voltage v_{ta}, and the DC voltage capacitor v_{dc}, are shown in Fig. 20.10a, b, and c respectively.

The same comparison for the simplified model based on the hyperbolic tangent approach is presented in Fig. 20.11. For this numerical experiment, the hysteresis band has been selected as $h = 5$ A. Observe that the DC voltage capacitor computed with the ideal current source models has a small error. This error is because this model assumes that the DSTATCOM generates the compensation currents instantaneously. The model based on the hyperbolic tangent gives much better solutions since it is not based on this assumption.

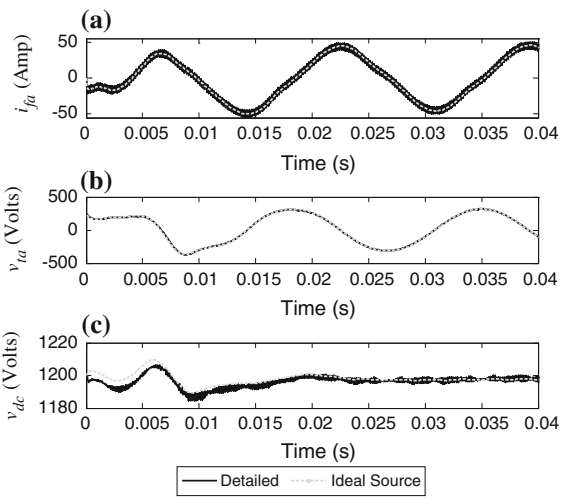

Fig. 20.10 Comparison in the time domain between the detailed and the simplified model based on the ideal source approach for **a** compensation current i_{fa}, **b** terminal voltage v_{ta}, and **c** DC capacitor voltage v_{dc}

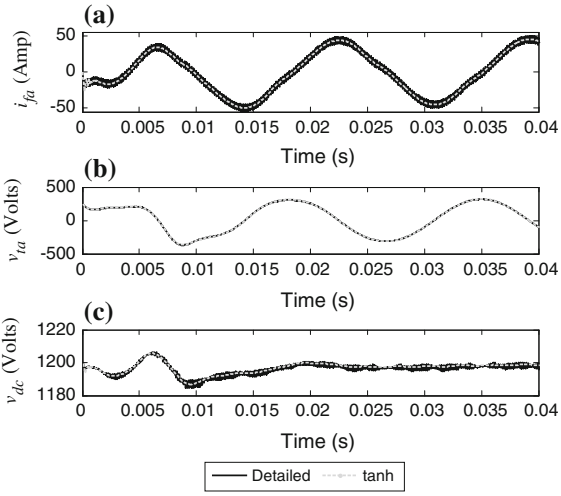

Fig. 20.11 Comparison in the time domain between the detailed and the simplified model based on the smooth hysteresis band approach for **a** compensation current i_{fa}, **b** terminal voltage v_{ta}, and **c** DC capacitor voltage v_{dc}

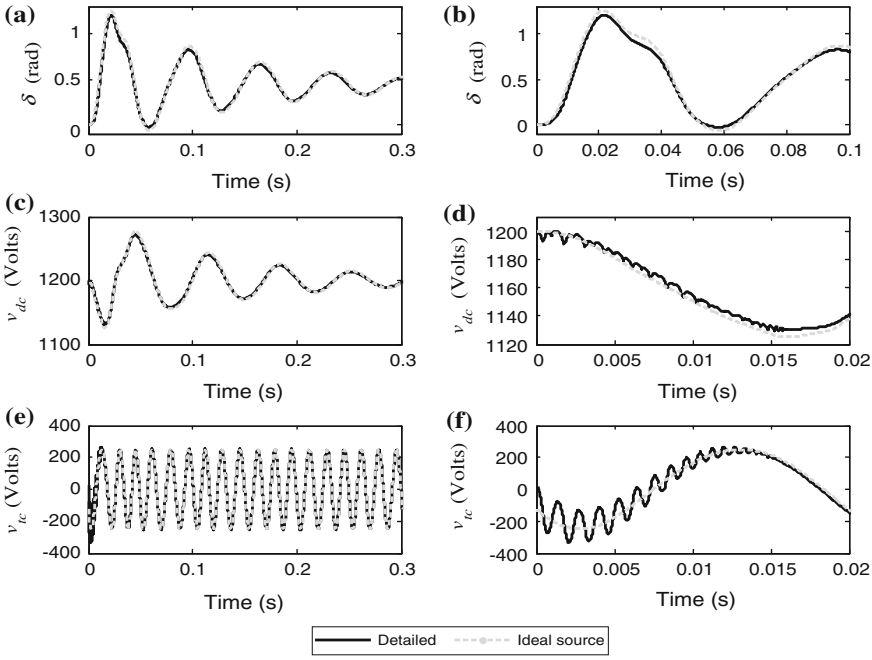

Fig. 20.12 Comparison in the time domain between the detailed and the simplified based on the ideal source approach for **a** phase angle δ, **b** phase angle δ during the first 0.02 s, **c** DC capacitor voltage v_{dc}, **d** DC capacitor voltage v_{dc} during the first 0.02 s, **e** terminal voltage v_{tc}, and **f** terminal voltage v_{tc}

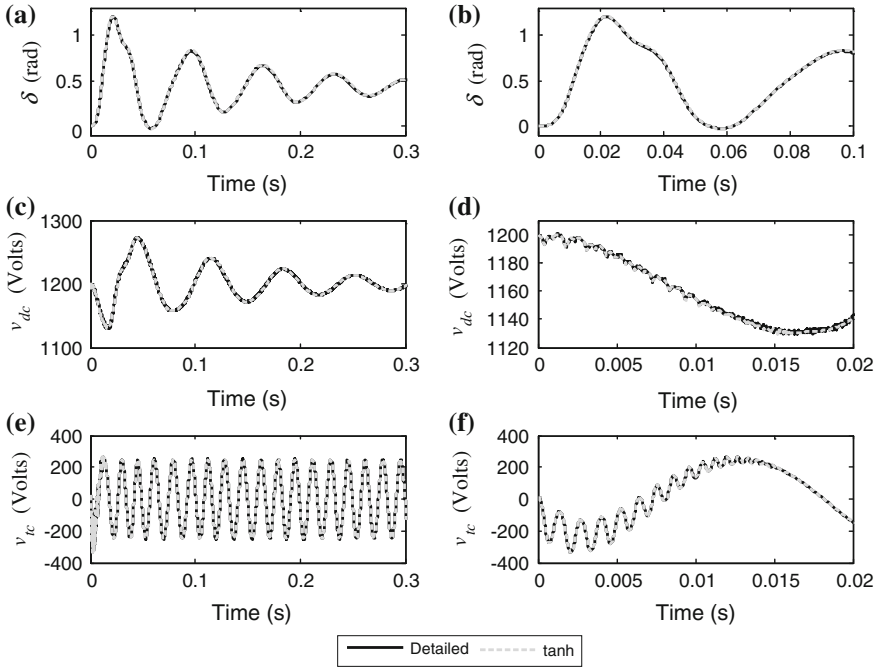

Fig. 20.13 Comparison in the time domain between the detailed and the simplified based on the smooth hysteresis band approach for **a** phase angle δ, **b** phase angle δ during the first 0.02 s, **c** DC capacitor voltage v_{dc}, **d** DC capacitor voltage v_{dc} during the first 0.02 s, **e** terminal voltage v_{tc}, and **f** terminal voltage v_{tc}

20.2.4.2 DSTATCOM Operating in Voltage Mode

The solution comparison for the DSTATCOM operating in voltage mode for the phase angle δ, the DC capacitor voltage v_{dc}, and the terminal voltage v_{ta} are presented in the Fig. 20.12a, c and e respectively. Observe from Fig. 20.12b, d and f that for this particular case, the solution obtained with the simplified model based on ideal voltage sources is not accurate during the first cycles.

The same comparison for the simplified model based on the hyperbolic tangent is presented in Fig. 20.13. Please notice that the initial transients can be accurately reproduced with the simplified model based on this approach.

The presented simplified models allow the fast computation of the periodic steady state solution by time domain simulations and by the application of an iterative method such as the Newton method. This method computes the periodic steady state solution despite its stability and it is commonly used as the corrector in the continuation methods for tracing bifurcation diagrams. Due to the discontinuity of the detailed model, the Newton method presents convergence issues and becomes difficult the construction of stability regions. To tackle these issues, the previously presented simplified models can be used instead. In particular, the fastest

and best suited modeling approach was that based on ideal sources, therefore, this will be used for the bifurcation analysis and the detailed models will be used to corroborate the computed stability regions.

20.3 Stability Analysis of Periodic Steady State Solutions

Continuation schemes are used to determine how the solutions of a system vary with a given parameter. Implementing a predictor–corrector scheme, a continuation algorithm can trace the path of an already established solution as the parameters are varied. XPPAUTO [30] is a software package widely used for this purpose; however, this software has not been used in the presented analyses since it has convergence problems to trace the bifurcation diagrams of periodically forced nonlinear-switched systems. In this chapter, the sequential method [5] is used as the predictor; in this method, the periodic solution determined in the previous step is used as an initial guess for the periodic solution to be determined in the next step. After the third point, an extrapolation method based on the cubic spline is used as a predictor. The Newton method based on the direct exponential expansion (DEE) process [31] is used as the corrector.

The stability of a periodic solution is computed from its Floquet multipliers; they describe the stability near the limit cycle of interest. Floquet theory is based on the observation that a periodic solution can be represented through a fixed point of an associated Poincaré map. Consequently, the stability of a periodic solution can be determined by computing the stability of the corresponding fixed point of the Poincaré map. The Floquet multipliers are the eigenvalues of the Jacobian of this Poincaré map obtained in the DEE method. Stable periodic solutions correspond to Floquet multipliers inside the unit circle; on the other hand, unstable periodic solutions have at least one Floquet multiplier outside the unit circle. Therefore, loss of stability is encountered when a multiplier leaves the unit circle; this can occur in three different ways: A fold bifurcation is encountered when a single real Floquet multiplier crosses the unit circle at +1. The flip bifurcation or period-doubling bifurcation takes place when a single real Floquet multiplier crosses the unit circle at −1. At this bifurcation point, the prevailing solution branch becomes unstable and a new branch is born. Solutions on this new branch have twice the period of the previous limit cycle. The generalized Hopf bifurcation or Neimark bifurcation is found when two complex conjugated Floquet multipliers leave the unit cycle.

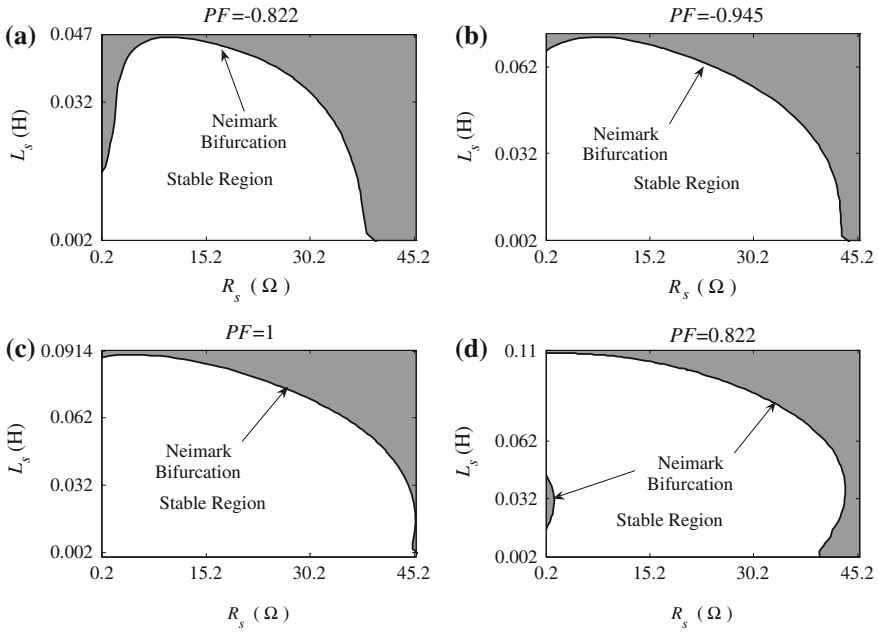

Fig. 20.14 Stability regions for the DSTATCOM operating in current control for different power factors at the terminal bus with $|V_s|$ = 440 V

20.3.1 Stability Analysis of the DSTATCOM in Current Control Mode

20.3.1.1 Stability Regions in the L_s-R_s Plane

The network of Fig. 20.2 has been represented through its Thevenin equivalent. The network upstream from the PCC towards the source side may contain different feeders and loads. Thus, the radial line and the source shown in figure is a Thevenin representation of the upstream network, where v_s, R_s, and L_s represent the Thevenin equivalent looking towards the left into the network. Since the Thevenin equivalent can change at any time depending on the load at left side of the PCC, it is desirable to assess a set of v_s, R_s, and L_s, for which the DTATCOM performance is stable.

For the electric system shown in Fig. 20.2, only the Neimark bifurcation was located in the parametrical-space used in this analysis. In analogy with the Hopf bifurcation, a bifurcation is expected at a critical value, as the limit cycle losses its stability, so that an attracting torus is born; this is the secondary Hopf bifurcation or a Neimark bifurcation. Besides, the bifurcated solution can be either stable and supercritical or unstable and subcritical [5].

Figure 20.14 shows the bifurcation set on the R_s–L_s plane. This Figure shows the stability regions for different power factor corrections with $|V_s|$ = 440 V, where $|V_s|$

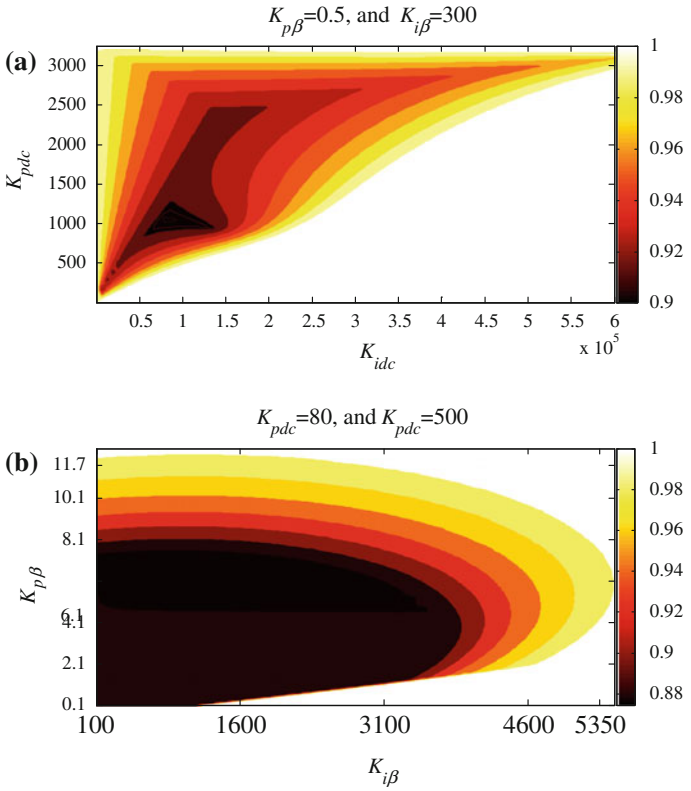

Fig. 20.15 Stability regions for the DSTATCOM operating in current control mode in **a** the K_{idc} – K_{pdc} space, and **b** $K_{i\beta}$ – $K_{p\beta}$ space

is the peak value. The solid line represents the Neimark bifurcation set. Inside the contour line the solutions are T-periodic and the gray zones represent the unstable regions. The stable region in the R_s–L_s plane changes according to the power factor at the PCC. For instance, Fig. 20.14d shows that for a 0.822 lead power factor, an unstable region within the stable region exists. In a practical distribution system, the set (R_s, L_s) is smaller than those stable sets computed through the bifurcation analysis, which means that for all the possible operating points the DSTATCOM operating in current control mode will properly compensate.

20.3.1.2 Stability Regions in the Gains Plane

In this section, the stability region in the K_{idc} – K_{pdc} space, and in the $K_{i\beta}$ – $K_{p\beta}$ space, as well as the contour lines for different Floquet multipliers are computed. Figure 20.15a shows the stability regions in the K_{idc} – K_{pdc} space, and Fig. 20.15b shows the stability regions in the $K_{i\beta}$ – $K_{p\beta}$ space. Also, in these figures, contour

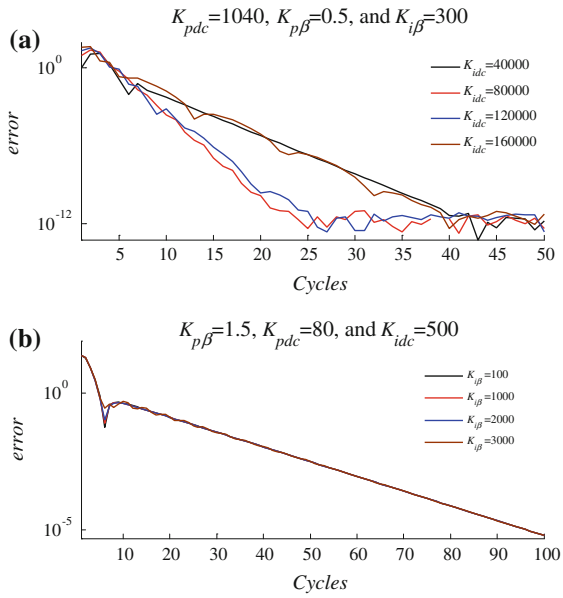

Fig. 20.16 Convergence errors for different gains in the DSTATCOM controllers. **a** For DC capacitor voltage controller. **b** For power factor controller

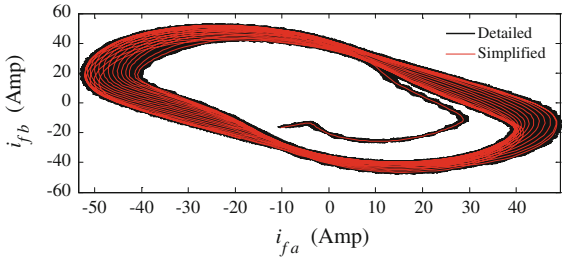

Fig. 20.17 Quasiperiodic solution for $K_{p\beta} = 0.5$, $K_{i\beta} = 300$, $K_{pdc} = 1{,}040$, and $K_{idc} = 2.5 \times 10^5$. i_{fa} versus i_{fb}

lines are presented for different Floquet multipliers to show the different speed of response. For example, from the Fig. 20.15a, it is easy to notice that the pair of gains $K_{idc} = 80{,}000$ and $K_{pdc} = 1{,}040$ give the fastest response. The implementation of this set of gains in a physical controller depends on the precision available in the hardware and software employed.

Figure 20.16a shows time domain simulations of the convergence error for $K_{pdc} = 1{,}040$ and different K_{idc}. It can be observed that this agrees with the bifurcation diagram of Fig. 20.15a. From Fig. 20.15b, it is easy to notice that in the stable region, there is an important area for which the maximum Floquet multiplier

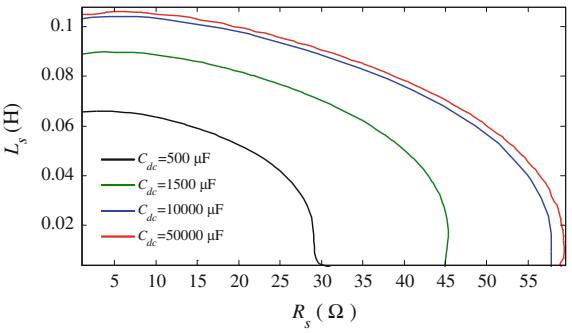

Fig. 20.18 Comparison between the stability regions for different DC capacitors

is constant. This means that for this area, the speed of response should be almost the same. To corroborate this observation, the convergence error for $K_{p\beta} = 1.5$ and different $K_{i\beta}$ is shown in Fig. 20.16b. As expected, the convergence error is almost the same in this area.

Figure 20.17 shows the torus solution for compensation current i_f for $K_{p\beta} = 0.5$, $K_{i\beta} = 300$, $K_{pdc} = 1{,}040$, and $K_{idc} = 2.5 \times 10^5$. This operating point corresponds to a quasiperiodic solution. Please notice that the detailed model and the simplified model are in very good agreement, even in the unstable regions.

20.3.1.3 DC Capacitor Impact on the Stability

The impact of the DC capacitor size in the stability regions in the $R_s - L_s$ plane is qualitatively shown through bifurcation analysis. This analysis shows that the stable region increases asymptotically as the DC capacitor size increases, thus, the size of the DC capacitor can be chosen to suit the load demand. Figure 20.18 shows the stability regions in the $R_s - L_s$ plane for different DC capacitor sizes.

20.3.1.4 AC Capacitor Impact on the Stability

The purpose of the capacitor filter C_{fil} is to provide a path for the switching harmonic current introduced by the DSTATCOM. However, it is shown in [23], that this passive filter has an important impact on the DSTATCOM performance and on its stability. High capacitances in the capacitor filter provide a low impedance path for the harmonic currents. However, there are three problems related to high capacitances. The first one is the cost, the second one is that the speed of response becomes slower, and the third one is that the stable region decreases as the capacitance becomes larger. This is shown in Fig. 20.19, where the stability region in the $R_s - L_s$ plane has been computed for three different capacitor filters.

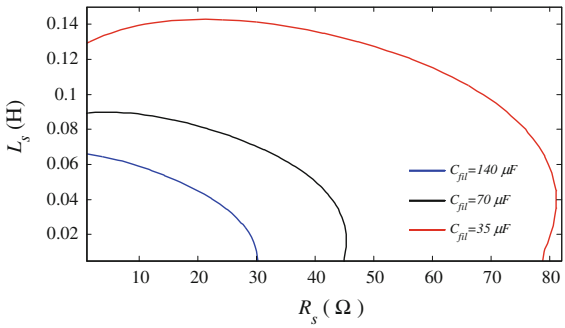

Fig. 20.19 Comparison between the stability regions for different AC capacitors

20.3.2 Bifurcation Analysis for DSTATCOM in Voltage Control Mode

In this section, the bifurcation theory is applied to the same system to assess the stability regions of the electric system including the DSTATCOM operating in voltage control mode. In the section to follow, bifurcation diagrams in the Thevenin space are computed to show the set of L_s, R_s, and v_s (derived from Thevenin reactance) for which the DSTATCOM contains stable solutions. The stability regions on the gains space are calculated through bifurcation theory, and the set of gains for the fastest speed response of the DSTATCOM is obtained from this analysis. Besides, the gains impact on the stability regions in the Thevenin space is analyzed. Finally, the AC and DC capacitors size impact on the stability in the Thevenin space is analyzed.

The simplified DSTATCOM model based on ideal sources is used in this analysis; however, the solutions will be compared against the detailed DSTATCOM model to validate the results. The simplified model is used in this analysis rather than the detailed model basically because the detailed model does not allow the correct implementation of the shooting method during the correcting process in the computation of the bifurcation branches through the continuation methods.

20.3.2.1 Stability Regions in the $R_s - L_s$ Plane

The Fig. 20.20 shows the bifurcation set on the $L_s - R_s$ plane for different Thevenin voltages. The dotted line represents the Neimark bifurcation set. Inside the contour line the solutions are T-periodic, and the dark zone is the unstable region. The stability region for $|V_s| = 350$ V, $|V_s| = 400$ V, and $|V_s| = 440$ V, are shown in Fig. 20.20a–c, respectively. In Fig. 20.20d a comparison is presented between the different stability boundaries; the stability region decreases as the source voltage becomes smaller. Also, Fig. 20.20a–c can be seen as bifurcation diagrams in the Thevenin space.

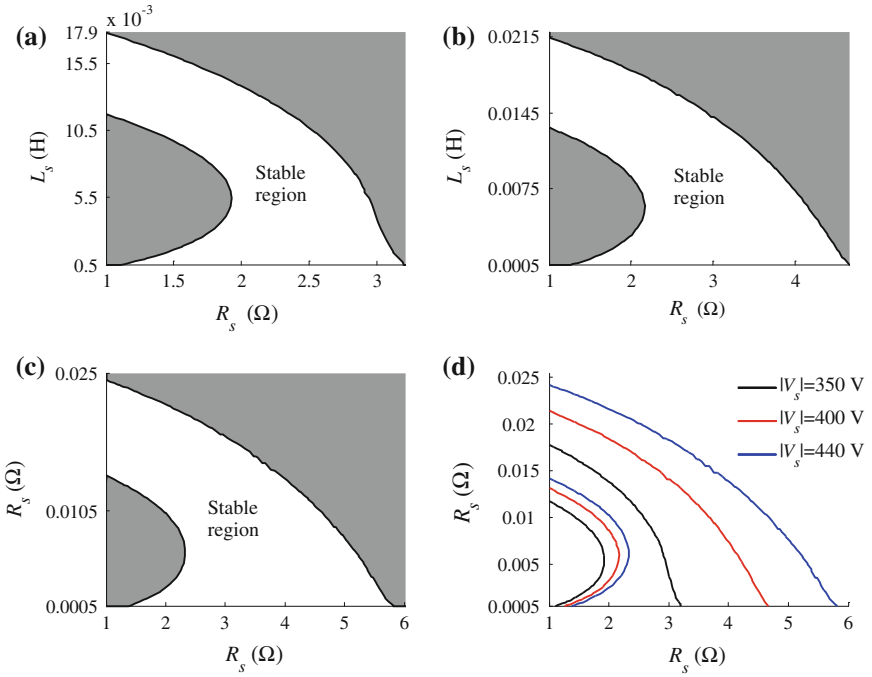

Fig. 20.20 Stability regions for the DSTATCOM operating in voltage control in the $L_s - R_s$ plane for different Thevenin equivalent voltages; **a** $|V_s| = 350$ V, **b** $|V_s| = 400$ V, and **c** $|V_s| = 440$ V and **d** comparison of the stability boundaries

Figure 20.20d shows that the only region for which the DSTATCOM properly operates in the Thevenin space for $|V_s|$ is from 350 to 440 V; between the inner stability boundary of $|V_s| = 440$ V and the outer stability boundary of $|V_s| = 350$ V. In this region, the DSTATCOM can compensate any disturbance from the network.

20.3.2.2 Stability Regions in the Gains Plane

The dynamic behaviour of the DSTATCOM in transient state is strongly related to the gain of the PI controllers; therefore, an important task to do deals with the proper gains assessment. In addition, the set of gains has an important impact on the DSTATCOM steady state performance, since they modify the stability regions. In this section the stability region in the $K_{idc} - K_{pdc}$ space, and in the $K_{i\delta} - K_{p\delta}$ space are computed, as well as the contour lines for different Floquet multipliers, with the purpose of assessing the set of gains for which the fastest speed of response is obtained. Figure 20.21b in the $K_{idc} - K_{pdc}$ space. Also, in these figures, contour lines are presented for different Floquet multipliers to show the different speed of response. Figure 20.22a shows the convergence error for different pairs of gains $K_{i\delta}$

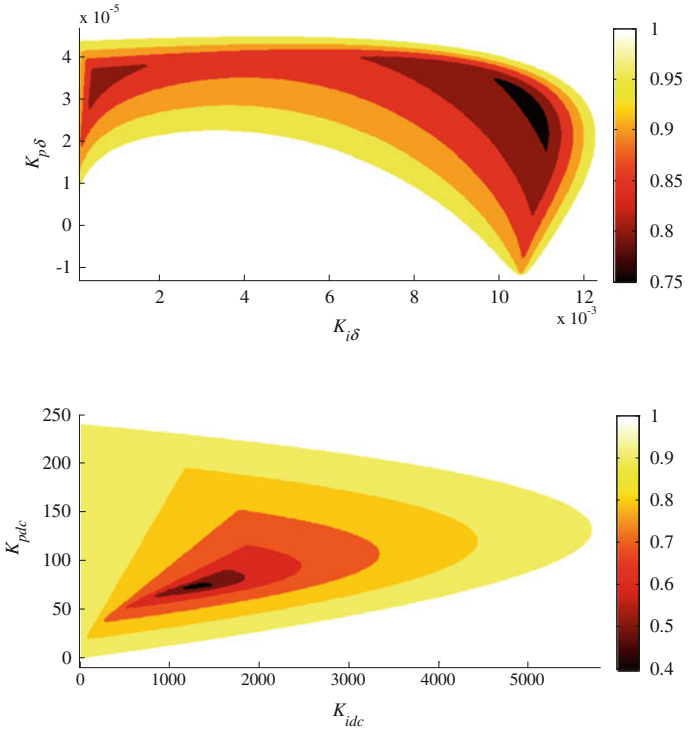

Fig. 20.21 Stability regions for the DSTATCOM operating in voltage control mode. (*Top*) $K_{i\delta}$ $-K_{p\delta}$ space. (*Bottom*) K_{idc} $-K_{pdc}$ space

$-K_{p\delta}$. In Fig. 20.22a, the convergence error for $K_{p\delta} = 30 \times 10^{-6}$, and different $K_{i\delta}$ are shown. From this figure, we can see that the fastest response is around $K_{i\delta} = 10.5 \times 10^{-3}$ and $K_{p\delta} = 30 \times 10^{-6}$. Figure 20.22b shows the convergence error for $K_{pdc} = 74$, and different K_{idc}. From this figure, it is easy to see that the fastest response is around $K_{pdc} = 74$ and $K_{idc} = 1{,}320$. These results are in agreement with the bifurcation analysis illustrated in Fig. 20.21.

As mentioned previously, the gains of the controller have a direct impact on the system stability. However, it is not known how the size of the stable region in the Thevenin space varies as the gains are varied. To investigate the effect of the gains variation in the stability of the system, a bifurcation analysis is carried-out to assess the stable and unstable regions for different sets of gains. In particular, the stability region obtained for $K_{idc} = 1{,}320$, $K_{pdc} = 74$, $K_{i\delta} = 8 \times 10^{-3}$, and $K_{p\delta} = 27 \times 10^{-6}$ with $|V_s| = 440$ V is compared against that shown in Fig. 20.20c. This comparison is shown in Fig. 20.23; it can be noticed that the size of the stable regions significantly change as we change the set of gains. Figure 20.23 has been computed using the parameters given in Table 20.2; only the gains are varied.

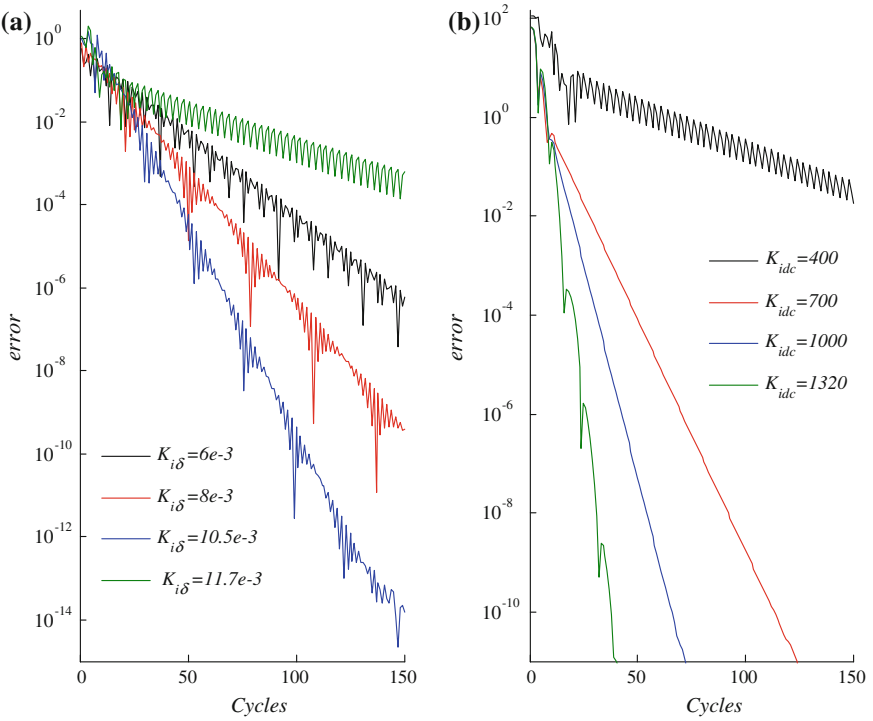

Fig. 20.22 Convergence errors for different gains of the DSTATCOM controllers. **a** For δ controller. **b** For the DC capacitor voltage controller

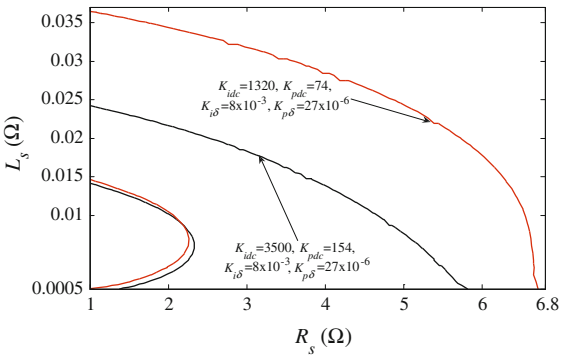

Fig. 20.23 Comparison between the stability regions for two sets of gains

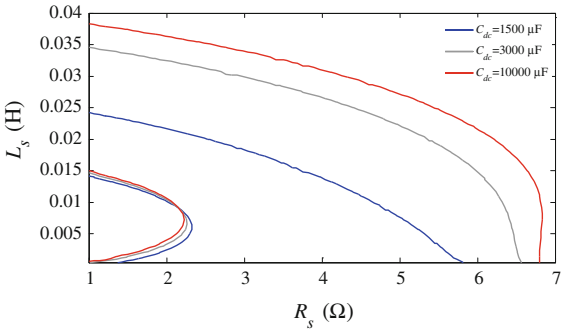

Fig. 20.24 Comparison between the stability regions for different DC capacitors

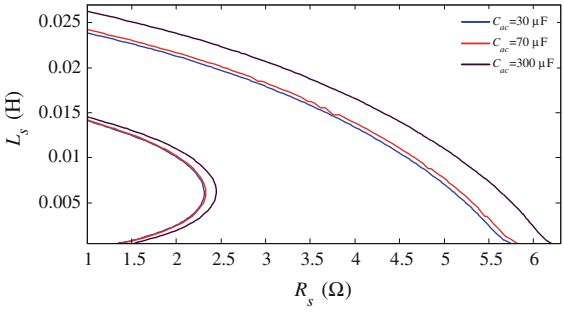

Fig. 20.25 Comparison between the stability regions for different AC capacitors

20.3.2.3 DC Capacitor Impact on the Stability Region

The DC capacitor is a very important element in the design of DSTATCOM, as it stores the energy necessary to compensate the load during disturbances. In steady state, the DSTATCOM has to provide the active power fluctuation and the reactive power demanded by the system, in order to maintain the voltage at the PCC bus. Thus, the DC capacitor size is important for the compensator performance, i.e., larger capacitances the storage more energy, consequently the DSTATCOM could bear larger and more severe disturbances. This observation suggests that the stable region increases as the DC capacitor size becomes larger. To corroborate this, a comparison between the stability regions for different DC capacitor sizes is presented in Fig. 20.24. It can be seen that the stable regions on the $L_s - R_s$ asymptotically increases as the DC capacitor becomes larger. Please notice that even the inner unstable region decreases as the AC capacitor size increases. Figure 20.24 has been computed using the parameters given in Table 20.2. From this analysis, the DC capacitor size can be selected to suit the load demand. Obviously, the selected DC capacitor size also depends on its cost.

20.3.2.4 AC Capacitor Filter Impact on the Stability Region

The main purpose of the AC capacitor filter is to drain the harmonic currents coming from the DSTATCOM converters. A small AC capacitor size presents high impedance to the harmonic currents; in consequence, the harmonic currents are not efficiently drained. For a large AC capacitor size, the harmonic currents are efficiently drained; however, there are some problems with a large AC capacitor filter. For instance, the transients in a capacitor increase as its size increases. To assess the AC capacitor filter impact on the stability, the stable regions in the Thevenin plane have been compared for three different AC capacitors; this comparison can be seen in Fig. 20.25. From this figure, it easy to notice that the AC capacitor has a positive impact on the stability, since the stable region on the L_s–R_s plane increases as the AC capacitor becomes larger. However, it should be noticed that not only the outer boundary increases; the inner boundary becomes larger as well. Basically, the AC capacitor filter size has a positive effect on the stability because the AC capacitor acts as reactive power compensator as well, and this action reduces the reactive power injected by the DSTATCOM to maintain the reference terminal voltage. Figure 20.25 has been computed using the parameters of Table 20.2.

References

1. Parker TS, Chua LO, Parker TS (1989) Practical numerical algorithms for chaotic systems. Springer, Reissue
2. Wan C, Huang M, Tse CK, Wong SC, Ruan X (2013) Nonlinear behavior and instability in a three-phase boost rectifier connected to a nonideal power grid with an interacting load. IEEE Trans Power Electron 28(7):3255–3265
3. Deivasundari P, Uma G, Santhi R (2014) Experimental verification of Hopf bifurcation in pulse-width modulated inverter fed cage induction motor drive system. IET Power Electron 7 (2):340–349
4. Ben Amar F, Dhifaoui R (2011) Study of the periodic ferroresonance in the electrical power networks by bifurcation diagrams. Int J Electr Power Energy Syst 33(1):61–85
5. Nayfeh AH, Balachandran B (1995) Applied nonlinear dynamics: analytical, computational and experimental methods. Wiley, New York
6. Kopell N, Washburn RB (1982) Chaotic motions in the two-degree-of-freedom swing equations. IEEE Trans Circuits Syst 29(11):738–746
7. Grijalva S (2012) Individual branch and path necessary conditions for saddle-node bifurcation voltage collapse. IEEE Trans Power Syst 27(1):12–19
8. Alomari MM, Zhu JG (2011) Bifurcation control of subsynchronous resonance using TCSC. Commun Nonlinear Sci Numer Simul 16(5):2363–2370
9. Wan C, Huang M, Tse CK, Wong S-C, Ruan X (2013) Nonlinear behavior and instability in a three-phase boost rectifier connected to a nonideal power grid with an interacting load. IEEE Trans Power Electron 28(7):3255–3265
10. Segundo-Ramírez J, Medina A, Ghosh A, Ledwich G (2012) Stability boundary analysis of the dynamic voltage restorer in weak systems with dynamic loads. Int J Circuit Theory Appl 40(6):551–569
11. Lee S-H, Park J-K, Lee B-H (2001) A study on the nonlinear controller to prevent unstable Hopf bifurcation. In: Power engineering society summer meeting, vol 2, pp 978–982

12. Canizares CA (1995) On bifurcations, voltage collapse and load modeling. IEEE Trans Power Syst 10(1):512–522
13. Pai MA, Sauer PW, Lesieutre BC, Adapa R (1995) Structural stability in power systems-effect of load models. IEEE Trans Power Syst 10(2):609–615
14. Liu C-C, Vu KT (1989) Analysis of tap-changer dynamics and construction of voltage stability regions. IEEE Trans Circuits Syst 36(4):575–590
15. Kamarposhti MA, Lesani H (2011) Effects of STATCOM, TCSC, SSSC and UPFC on static voltage stability. Electron Eng 93(1):33–42
16. Mithulananthan N, Canizares CA, Reeve J, Rogers GJ (2003) Comparison of PSS, SVC, and STATCOM controllers for damping power system oscillations. IEEE Trans Power Syst 18 (2):786–792
17. Segundo-Ramírez J, Medina A, Ghosh A, Ledwich G (2010) Non-linear oscillations assessment of the distribution static compensator operating in voltage control mode. Electron Power Compon Syst 38(12):1317–1337
18. Segundo-Ramirez J, Medina A, Ghosh A, Ledwich G (2009) Stability analysis based on bifurcation theory of the DSTATCOM operating in current control mode. IEEE Trans Power Deliv 24(3):1670–1678
19. Tse C (2003) Complex behavior of switching power converters. CRC Press, Boca Raton, FL
20. Banerjee S, Verghese GC (2001) Nonlinear phenomena in power electronics: attractors, bifurcations, chaos, and nonlinear control. IEEE Press, New York
21. Ghosh A (2002) Power quality enhancement using custom power devices. Kluwer Academic Publishers, Dordrecht
22. Acha E, Semlyen A, Rajakovic N (1990) A harmonic domain computational package for nonlinear problems and its application to electric arcs. IEEE Trans Power Deliv 5 (3):1390–1397
23. Ghosh A, Ledwich G (2003) Load compensating DSTATCOM in weak AC systems. IEEE Trans Power Deliv 18(4):1302–1309
24. Hingorani NG, Gyugyi L (2000) Understanding FACTS: concepts and technology of flexible AC transmission systems. Wiley, New York
25. Mishra MK, Ghosh A, Joshi A (2003) Load compensation for systems with non-stiff source using state feedback. Electron Power Syst Res 67(1):35–44
26. Ghosh A, Joshi A (2000) A new approach to load balancing and power factor correction in power distribution system. IEEE Trans Power Deliv 15(1):417–422
27. Vlach J, Wojciechowski JM, Opal A (1995) Analysis of nonlinear networks with inconsistent initial conditions. IEEE Trans Circuits Syst Fundam Theory Appl 42(4):195–200
28. Mohan N, Undeland TM, Robbins WP (2002) Power electronics: converters, applications, and design, 3rd edn. Wiley, Hoboken
29. Mishra MK, Ghosh A, Joshi A (2003) Operation of a DSTATCOM in voltage control mode. IEEE Trans Power Deliv 18(1):258–264
30. Ermentrout B (2002) simulating, analyzing, and animating dynamical systems: a guide to XPPAUT for researchers and students. SIAM, Philadelphia
31. Segundo-Ramírez J, Medína A (2010) Computation of the steady-state solution of nonlinear power systems by extrapolation to the limit cycle using a discrete exponential expansion method. Int J Nonlinear Sci Numer Simul 11(8):655–660

Chapter 21
Network Protection Systems Considering the Presence of STATCOMs

Premalata Jena and Ashok Kumar Pradhan

Abstract STATCOM is a shunt type Flexible AC Transmission System (FACTS) device that maintains the voltage at the connection point by injecting/absorbing the reactive power. With the presence of STATCOM, the current magnitude during fault is modulated and the performance of available overcurrent relay is constrained. Distance relay, in such a situation, finds problem due to the compensation effect during the dynamic performance of STATCOM. The dynamic response time of STATCOM may overlap with the operating time of distance relay. The control action associated with the STATCOM also affects the performance of distance relay during line faults. The chapter presents the analytical and simulation studies for demonstrating the performance of Mho and quadrilateral type distance relay protecting a line with STATCOM. The performance of Inverse Definite Minimum Time (IDMT) overcurrent relay is also discussed.

Keywords Static compensator (STATCOM) · Overcurrent relay · Distance relay · Mho relay · Quadrilateral characteristic · Line fault · Line protection

21.1 Introduction

With the ongoing growth of the electric power demand and deregulation in the electrical power industry, numerous changes have been introduced to modern electricity industry. Transmission systems are now being pushed to function closer

P. Jena
Department of Electrical Engineering, Indian Institute of Technology Roorkee, Roorkee, India
e-mail: pjenafee@iitr.ac.in

A.K. Pradhan (✉)
Department of Electrical Engineering, Indian Institute of Technology Kharagpur, Kharagpur, India
e-mail: akpradhan@ee.iitkgp.ernet.in

F. Shahnia et al. (eds.), *Static Compensators (STATCOMs) in Power Systems*, Power Systems, DOI 10.1007/978-981-287-281-4_21

to their stability and thermal limits and the energy needs to be transported from the generation point to the end user along the most desirable path. Upgrading transmission system by constructing new transmission lines is extremely difficult because of economic and environmental constraints. To obtain higher efficiency by better utilization of existing transmission lines without compromising quality and reliability of electrical power supply, has to be derived using alternative means. In this respect, FACTS technology has been implemented to solve this problem [1–2]. Due to the interaction of FACTS devices with the power system, the transients superimposed on the power frequency voltage and current waveforms (particularly during faults) can be significantly different for systems not employing such devices. Further introduction of such a device results in rapid changes in system parameters resulting in change in power angle and seen impedance by line relays. It is thus important to study the impact of the FACTS devices on the traditional protection relaying schemes such as distance relay [3].

STATCOM is one of the most widely used shunt FACTS devices. It uses Voltage Source Converter (VSC) and can inject an almost sinusoidal current with variable magnitude in quadrature with the connecting line voltage. It can be applied at the midpoint of a transmission line or at heavy load area to maintain the voltage which is obtained by supplying or absorbing reactive power of the power system [4]. Because of the presence of STATCOM devices in a fault loop, the voltage and current signals at relay point will be affected in both steady and transient states. This will affect the performance of exiting protection methods such as distance relay scheme.

STATCOM is one of the shunt devices that can provide the desired voltage support and power quality improvement as required [1–5]. It has been analyzed that the presence of STATCOM introduces new system dynamics which affects protection schemes in a power system. The new dynamics include (i) rapid changes in system parameters such as line impedance, power angle and line currents, (ii) transients introduced by the associated control action and (iii) the harmonics introduced into the power system [3].

With the onset of a fault in a power system, the STATCOM being a shunt active device will add current to the fault and as a result associated instantaneous overcurrent and the time delayed overcurrent protection are affected. With the inclusion of STATCOM in a power network overcurrent protection settings and coordination have to be assessed. Distance protection has been widely applied for protecting transmission lines. At the time of fault, the system voltage decreases and the STATCOM tries to restore the voltage to its reference value. As a result of such action the impedance seen by a distance relay is modulated depending on its location and participation. Injected current by STATCOM introduces modulation in seen impedance by distance relay resulting in underreach or overreach phenomenon [6]. The location of STATCOM; midpoint or at the end of a line modulates the current and voltage during fault differently.

The distance protection available for a line needs to be reassessed for different system contingencies and associated control modes of STATCOM. Today many of the distance relaying schemes are communication assisted where relay decision of other end is available. Such a scheme has to be reviewed in the presence of a

STATCOM. Delayed operation of distance relay can affect system stability. Presence of STATCOM will also affect distance relays on the nearby transmission lines including Zone-2 and Zone-3 [7–10]. The operating time and tripping schemes of the distance relay are to be specified in the new scenario. A comprehensive solution strategy for protection in such a scenario should be available.

21.2 The Power System

A 115 kV, 50 Hz three-phase power system, as shown in Fig. 21.1, is considered for simulation using EMTDC/PSCAD software. The power system is modelled with a long transmission line having distributed parameter and a STATCOM is connected at the middle of the line. Two 115 kV, 300 MVA sources with angle difference between them maintained at 30 is connected by a transmission line. Detail system data are provided in Appendix 1. In this chapter both analytical and simulation studies are carried out to investigate the impact of presence of STATCOM on protection relay located at the sending end bus.

21.2.1 The STATCOM

A 24-pulse VSC-type 11 kV, 100 MVA STATCOM connected at the mid-point of the transmission line is shown in Fig. 21.1. First the response of STATCOM is studied by creating fault in the power system. The STATCOM uses 24-pulse VSC

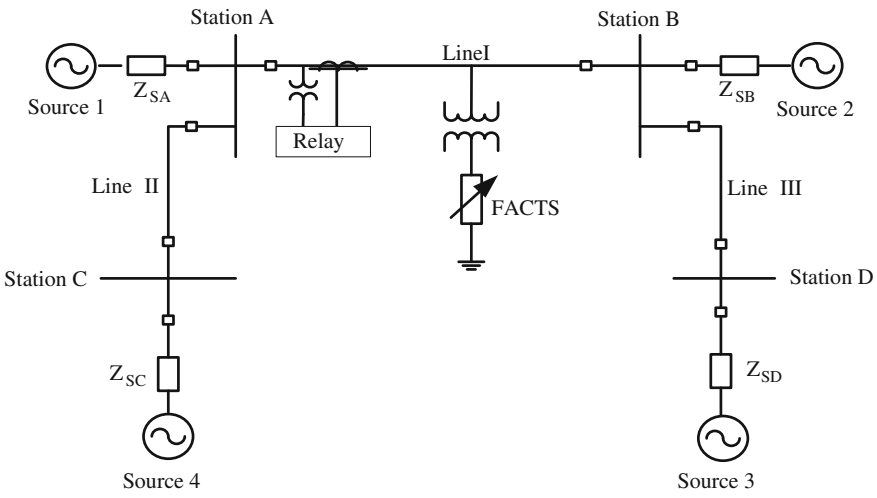

Fig. 21.1 A 115 kV, 50 Hz three-phase power system with STATCOM

which is connected with two 300 μF series DC capacitors. The converter connects to the transmission system through two 11/115 kV, Δ/Y and Y/Y shunt transformers, injects or consumes reactive power to the transmission system to regulate the voltage at the connecting point. The main purpose of use of STATCOM is to control the voltage at different weak points in the power system.

The STATCOM compensates for the reactive power and its value varies with the power transfer between the sending and receiving ends to maintain constant voltage at the midpoint. The SVC consists of a Thyristor Switched Capacitor (TSC) and Thyristor Controlled Reactor (TCR) connected in parallel to the compensation point of the system. With proper coordination of the capacitor switching and reactor control, the reactive output can be varied within the capacitive and inductive ratings of it. Figure 21.2 shows the V-I characteristics of an SVC. The STATCOM is assumed to operate within its reactive power rating to maintain the voltage at its location under all operating conditions. In this study, the STATCOM is modelled as a controlled voltage source that responds instantaneously to changing The SVC converts the DC voltage to AC voltage with desired magnitude, frequency and phase. The STATCOM maintains the voltage at its location within its reactive power limits with all operating conditions. In this study, the STATCOM is modeled as a controlled voltage source that responds instantaneously to changing system conditions. During fault, the STATCOM operates as long as its reactive power limit does not exceed. The power rating of STATCOM is selected such that it can provide sufficient compensation for all conditions of loading and different faults. The control circuit is tuned for different abnormal conditions. To model the STATCOM device used in transmission system, a three-phase balanced firing scheme is adopted. This implies that all the three phases are fired at the same angle but 120° apart. It is observed that this firing scheme affects the relay performance for different types of faults. The topology for 24-pulse STATCOM is provided in Fig. 21.3. The control strategy which is used in the simulation is provided in Fig. 21.4.

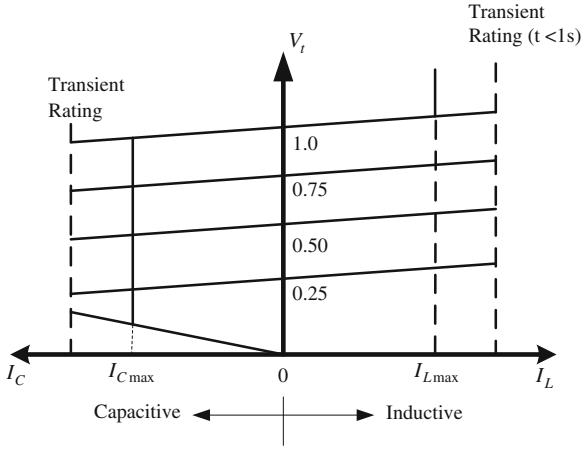

Fig. 21.2 The V-I characteristics of STATCOM

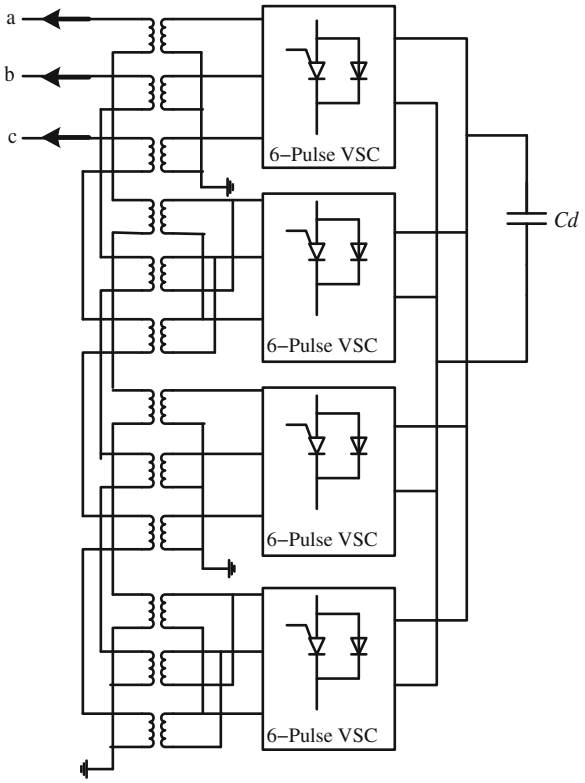

Fig. 21.3 STATCOM topology used in the simulation for the case study

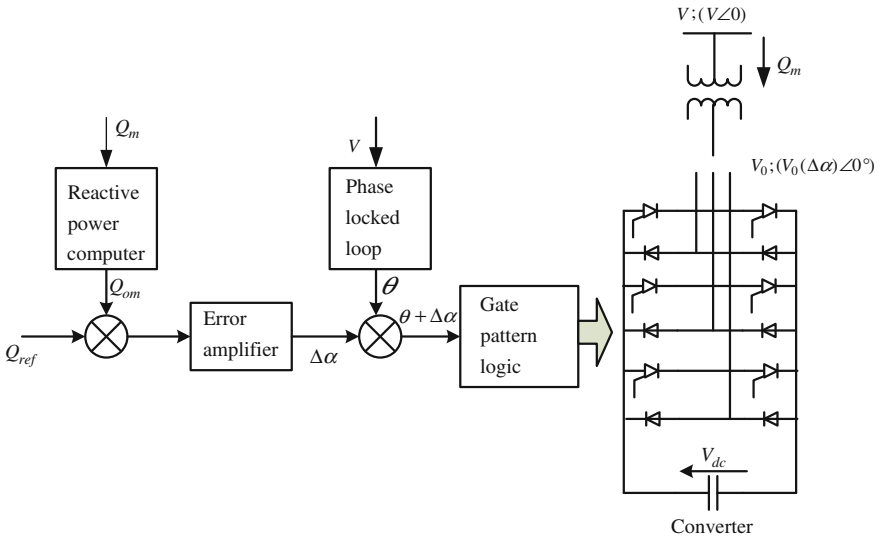

Fig. 21.4 Basic control scheme for the VSC-type VAr generator

21.3 Analytical Study of Impedance Seen by Distance Relay

The impedance seen by the distance relay can be analytically calculated which will provide information on the effect of STATCOM on the relay performance. A three-phase fault is created in line-I beyond the STATCOM and the equivalent circuit is shown in Fig. 21.5. From the figure, the impedance seen by the relay, for a three-phase fault beyond the STATCOM location can be expressed as

$$Z_m = Z_{k1} + \frac{Z'_{lb1} \times X_{sh}}{Z'_{lb1} + X_{sh}} = Z_{k1}\left(1 + \frac{(2m-1) \times X_{sh}}{(2m-1) \times Z_{la1} + X_{sh}}\right) \tag{21.1}$$

where

Z_m Impedance seen by the relay
Z_{k1} Positive sequence impedance of line section up to the device location
Z'_{lb1} Positive sequence impedance of line section following STATCOM up to the fault point
Z_{line} Total line impedance
X_{sh} Positive sequence reactance of the STATCOM
m Fault location in per unit of line length

When there is no shunt compensation or STATCOM is operating on the floating mode, the term X_{sh} in (21.1) tends to infinity and then (21.1) reduces to

$$Z_m = Z_{k1} + Z'_{lb1} = mZ_{line} = Z'_m \tag{21.2}$$

With shunt compensation, the value of X_{sh} depends on the level of compensation. It is found that during faults on the line, voltage reduces at the fault point as well as at the relay location and the reactive power is supplied by the STATCOM to improve the voltage at the desired location. During fault the STATCOM always

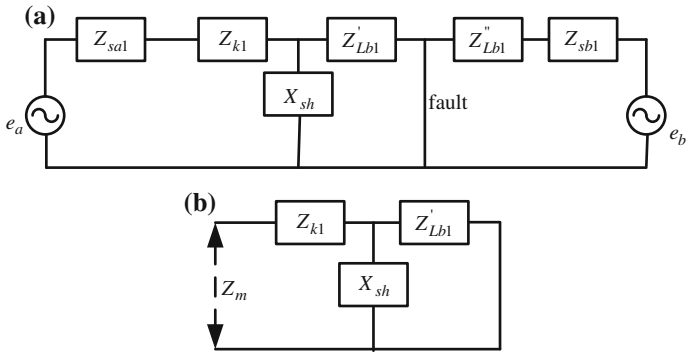

Fig. 21.5 Equivalent circuit for three-phase fault beyond the STATCOM. **a** Equivalent circuit for three phase fault. **b** Reduced equivalent circuit

operates in capacitive mode and the reactance depends on how much reactive power is supplied by the device. The higher the reactive power support, the lower the value of X_{sh}.

From (21.1), it is observed that as the value of X_{sh} reduces compared to Z'_{lb1}, the calculated impedance is affected with variation in Z'_{lb1}. It is also investigated that, the resultant calculated impedance has a nonlinear relationship with the fault location as the shunt reactance is capacitive and the series reactance of the line is inductive. This concept is explained using Fig. 21.4. The calculated impedance at the relay location without STATCOM, given by (21.2), is used for comparison with calculated impedances with the presence of STATCOM. The impedance ratio is given by

$$\frac{Z_m}{Z'_m} = \left(\frac{1}{2m}\right) \times \left(1 + \frac{(2m-1) \times 2 \times K}{(2m-1) + 2 + K}\right) \tag{21.3}$$

where $K = \frac{X_{sh}}{X_{line}}$.

The impedance seen by the distance relay is affected when $m > 0.5$ (fault beyond the STATCOM). For $m \leq 0.5$ (fault before the compensation point), the impedance seen by the relay is not affected by the presence of STATCOM. Z_{line} is taken as inductive as the value of line resistance is very small as compared to its reactance. The value of resistance can be ignored as it will not introduce any appreciable amount of error in the impedance analysis. As a result the K factor is scalar quantity for a lossless line (resistance is neglected). With inductive compensation offered by STATCOM, the value of the K is positive in case of capacitive compensation it is negative. The plot for the ratio of the impedance seen with STATCOM to without STATCOM as provided in (21.1) is shown in Fig. 21.6 with variation in fault location (m) and compensation factor (K). The curves for $m > 1$ represent faults beyond the protected line. The ratio of the fault impedance seen at the relay location in the presence of STATCOM to the fault impedance seen without STATCOM for the same fault location is taken along vertical axis of Fig. 21.6. This ratio provides the information about the degree of underreaching or overreaching of the distance relay. The horizontal axis represents the values of compensation with respect to the

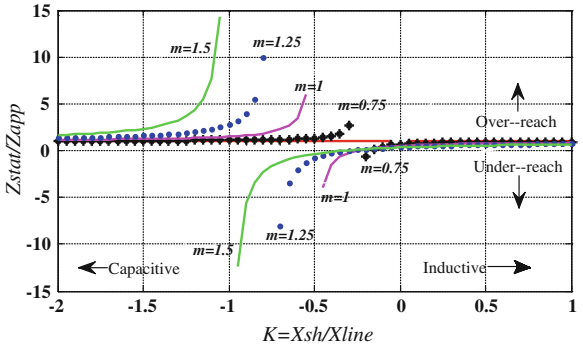

Fig. 21.6 Impedance curves for three-phase faults in the presence of STATCOM

line impedance. The compensation factor K becomes positive/ negative for inductive/capacitive region as evident from Fig. 21.6.

For faults beyond the STATCOM, the reactance offered by the device (due to the compensation) affects the fault impedance seen by the relay. The resonance condition is obtained at the point where the value of reactance offered by STATCOM is equal to the reactance of the line between the STATCOM and fault location. At resonance condition the device should not operate as the ratio of impedance provided in (21.1) tends to infinity. For a far end fault (fault located at the end of the line), the resonance will occur when capacitive reactance is equal to half of the line impedance with the seen impedance tends to infinity. It can be observed that the resonance point splits the curves into overreach and underreach regions. The influence of the shunt compensation decreases as the ratio of X_{sh} to Z_{line} increases. It is also observed from the Fig. 21.6 that with increase in fault location from the STATCOM, there is more chances of region of under/overreaching. It can be observed from the above analysis that the proper choice of X_{sh} will help in avoiding the underreach and overreach problem of distance relay.

21.4 The Simulation Results

The power system as shown in Fig. 21.1 is simulated using PSCAD/EMTDC software. The voltage and current samples are acquired at a sampling rate of 1 kHz. The voltage and current phasors are estimated using one cycle least square technique. The fault is detected using cycle-to-cycle comparison technique. Detail system data are provided in Appendix-1 and the least square technique model is described in Appendix-2. The power system and STATCOM model discussed in the earlier section were built in the PSCAD/EMTDC software.

21.4.1 Performance of IDMT Overcurrent Relay

The IDMT overcurrent relay is located at the sending end bus-A. The relationship between the time of operation (T_{set}), plug setting multiplier (PSM) and Time multiplier setting (TMS) of IDMT overcurrent relay is given by

$$T_{\text{op}} = \frac{0.14 \times TMS}{PSM^{0.02} - 1} \tag{21.4}$$

where PSM = $\frac{I_{relay}}{Plug\ Setting}$ and TMS = $\frac{T_{op}}{Time\ Setting}$

The magnitude of maximum fault current is obtained by creating the three-phase fault very close to the relay bus. The magnitude of the maximum fault current (I_{max}) is 3,500 A for both with and without STATCOM situations. In both the cases the

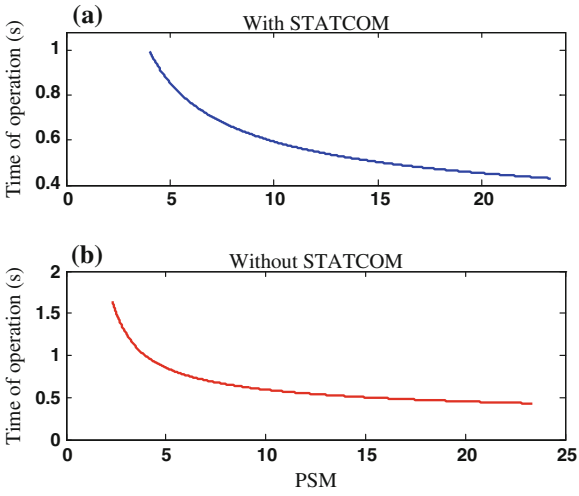

Fig. 21.7 The characteristic of IDMT overcurrent relay for **a** With STATCOM. **b** Without STATCOM

magnitude is equal as the fault position is close to the relay bus and current contributed by source-1 is more in comparison to source-2. The minimum fault current (I_{min}) is obtained by creating line-to-ground fault of AG-type at far end of line-1 (at 90 % of the line length). The magnitude of minimum fault currents are 600 and 350 A without and with STATCOM respectively. The load current flowing through line *I* is 150 A. The corresponding Current Transformer (CT) ratio is taken as 150:5. The overcurrent relay located at station-A, has a plug setting of 5 A. With STATCOM, for I_{max} the PSM = (I_{max} × 0.03/PS) = 3,500 × 0.03/5 = 21. The value of PSM is equal for both with and without STATCOM for maximum fault case. It is observed that with STATCOM the magnitude of minimum fault current is more in comparison to without STATCOM. It is because at the relay location the fault current is sum of current contributed by source-1 and STATCOM (direction of current contributed by STATCOM is same direction to the current supplied by source-1). The IDMT characteristics for with and without STATCOM case are provided in Fig. 21.7. From the characteristics it is clear that as the magnitude of minimum fault current varies with and without STATCOM and the overcurrent relay should be adaptive in nature for the presence/absence of STATCOM. For selectivity test of overcurrent relay (to test the overlapping between the maximum loading current in line and the minimum fault current level), the minimum fault current information is required.

21.4.2 Performance of Mho Relay

The line is tapped at the middle to connect a shunt STATCOM as shown in Fig. 21.1. Mho Distance relays with a positive sequence voltage polarization are connected at each end of the line with their first zone set to cover 90 % of the

protected line section. The network was analyzed and simulated under different normal as well as fault conditions. The apparent impedance seen by the protection relays is also calculated under the action of changing load flow and STATCOM response using both the analytical approach as well as simulation using the PSCAD/EMTDC. A Mho relay is placed at the sending end with a directional operating region in between −90° and 90°. In this case for the zone-1 protection, Z_{set} is 80 % of length of line-1.

21.4.2.1 Performance During Balanced Fault

In the system shown in the Fig. 21.1, three-phase faults are created at different locations (25, 50, 75 and 100 % from the relay bus). The voltage and current phasors for the relay are estimated using one cycle least square technique as provided in Appendix-1. The impedance is calculated using the relation provided in [6]. The apparent impedance trajectories of the system with and without STATCOM are shown in Fig. 21.8. It is observed that in case of three-phase fault, the impedance seen by the relay is accurate as the calculated impedance trajectory is well within the trip region for both the cases. The distance relay does not overreach or underreach for balanced fault case. For without STATCOM situation, the same impedance trajectory is obtained as for the case with the STATCOM (shown in Fig. 21.8).

21.4.2.2 Performance During Unbalanced Fault

To test the performance of Mho relay for unbalanced fault, a line-to-ground fault of BG-type is created for 0 and 100 Ω at 50 km from the relay location. The BG-type fault with 0 ohm fault resistance is created without the presence of STATCOM. For this case the impedance trajectory-1 is within the trip region as shown in Fig. 21.9.

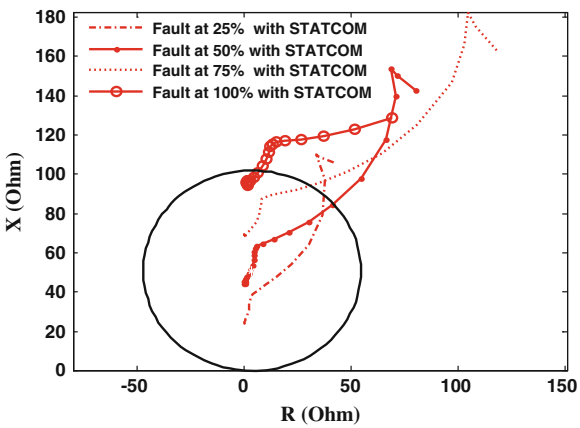

Fig. 21.8 Performance of Mho relay for three-phase fault with STATCOM

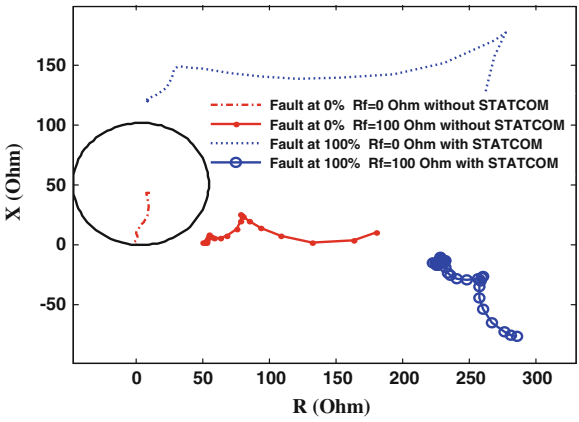

Fig. 21.9 Performance of Mho relay for line-to-ground fault of BG-type fault with and without STATCOM

A BG-type fault with 100 Ω is created without STATCOM and corresponding impedance trajectory-2 does not enter the trip region. In this case the distance relay has underreach problem. For BG-type fault with zero fault resistance, with STATCOM, corresponding impedance trajectory-3 does not enter into the trip region. It can be seen that both resistance and reactance of the apparent impedance of the transmission system with STATCOM are larger than those for the system without STATCOM; distance relay will underreach. For BG-type fault, 100 Ω fault resistance, with STATCOM the impedance trajectory-4 also lies outside the trip region.

21.4.2.3 Performance of Mho relay with fault location

Another line-to-ground fault of AG-type is created at 50 % of the line length with a fault resistance of 0 ohm with and without the presence of STATCOM. The impedance trajectories are shown in Fig. 21.10. It is observed that the impedance trajectory is well within the trip region for both the cases. Next AG-type fault is created at 75 % of the line length with and without the presence of STATCOM. The apparent impedance seen by the relay (blue one) as shown in Fig. 21.11 is greater than the actual fault impedance as a result the relay has underreach problem. The apparent impedance seen by the relay (red one) without STATCOM is within the trip region as shown in Fig. 21.12.

Another line-to-ground fault of AG-type is created at 100 % (far end fault) of the line length with a fault resistance of 0 Ω with and without STATCOM. The impedance trajectories are shown in Fig. 21.12. It is observed that the impedance trajectory is well within the trip region for both the cases. Next AG-type fault is created at 100 % of the line length with STATCOM. The apparent impedance seen by the relay (blue one) as shown in Fig. 21.12 is outside the trip region. For far-end fault case, the apparent impedance seen by the Mho relay with presence of STATCOM is more in comparison to without. During this situation the relay finds

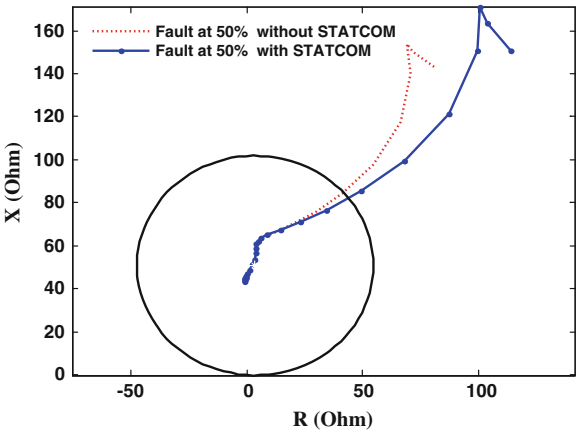

Fig. 21.10 Apparent impedance seen by the distance relay for AG-fault at 100 km from the relay bus with and without STATCOM without fault resistance

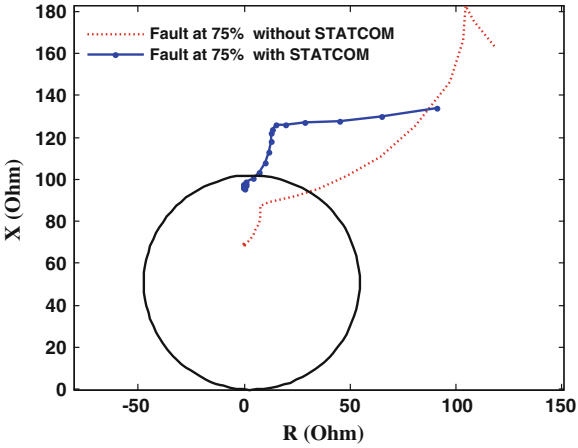

Fig. 21.11 Apparent impedance seen by the distance relay for AG-fault at 150 km from the relay bus with and without STATCOM without fault resistance

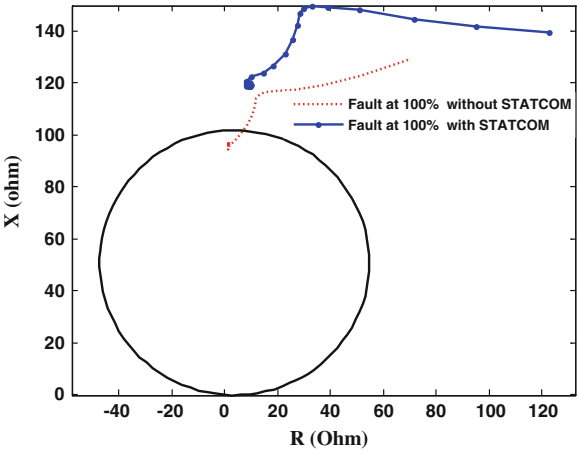

Fig. 21.12 Apparent impedance seen by the distance relay for AG-fault without fault resistance at 200 km from the relay bus with and without STATCOM

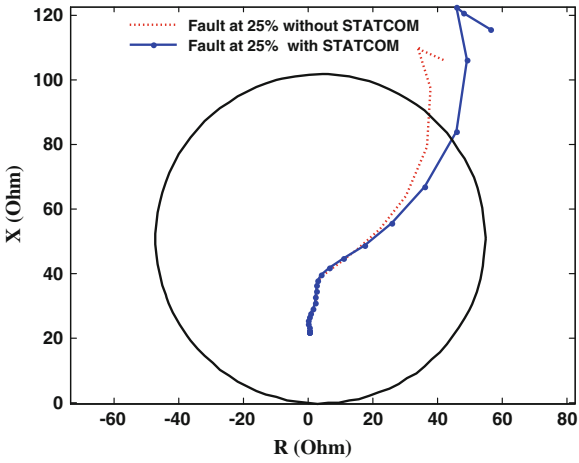

Fig. 21.13 Apparent impedance seen by the distance relay for AG-fault with fault resistance of 0 ohm at 50 km from the relay bus with and without STATCOM

underreach problem. A line-to-ground fault of AG-fault without fault resistance is created at 50 km from the relay bus with and without STATCOM and the corresponding impedance trajectories are within the trip region as shown in Fig. 21.13.

21.4.2.4 Performance During High Resistance Fault

Line-to-ground fault of AG-type is created with fault resistance of 100 ohm at the far end (towards the receiving end) and the apparent impedance trajectories are shown in Fig. 21.14. It can be seen that both the resistance and reactance of the apparent impedance of the transmission system with STATCOM are larger than those for the system without STATCOM (i.e. it will underreach).

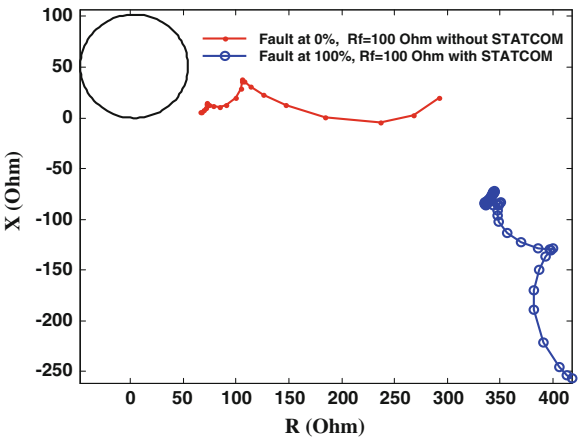

Fig. 21.14 Apparent impedance seen by the distance relay for AG-fault with fault resistance of 100 Ω at 200 km from the relay bus with and without STATCOM

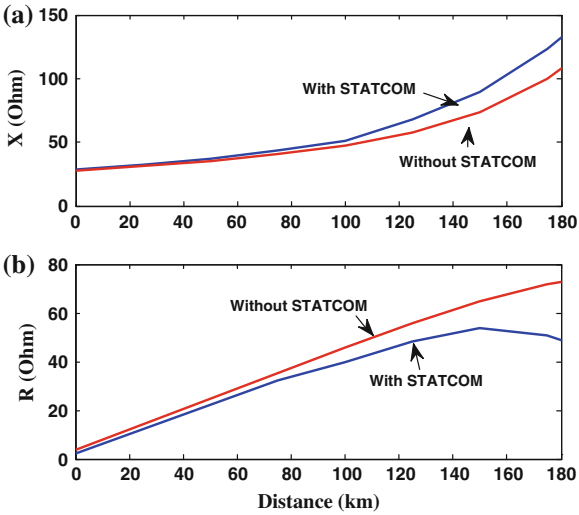

Fig. 21.15 Impedance plots for AG-type fault for different fault locations. **a** Variation of reactance. **b** Variation of resistance

21.4.2.5 Performance with fault location variation

To study the coverage of the mho characteristic, faults at different positions have been studied, and the apparent resistance and reactance for different fault locations are shown in Fig. 21.15a, b. Line-to-ground faults of BG-type are created at different locations from the relay bus and respective resistances and reactances are calculated. It is observed that the magnitude of reactance is more without STATCOM in comparison to with STATCOM. In case of resistance the value is less in comparison to with STATCOM situation. For unbalanced fault, the value of reactance is more in case of without STATCOM than with STATCOM. Due to this for far end faults with STATCOM, the distance relay finds underreach problem.

21.4.3 Performance of Distance Relay with Quadrilateral Characteristic

The distance relay is located at the bus A. The sample values of three-phase voltage and current are stored at sampling frequency of 1 kHz. The least square technique is used to estimate the phasors of the three-phase voltage and current. Line-to-ground fault of AG-type is created at different locations (the location is varied from 0 to 90 % and with variation in fault resistance (fault resistance is varied between 0 and 120 Ω) and corresponding the three-phase voltage and current phasors are estimated. Using the relation as provided in (21.1), the desired quadrilateral characteristics are obtained for both without and with STATCOM are shown in Fig. 21.16. From the figure it is observed that there is deviation in trip region for both the cases.

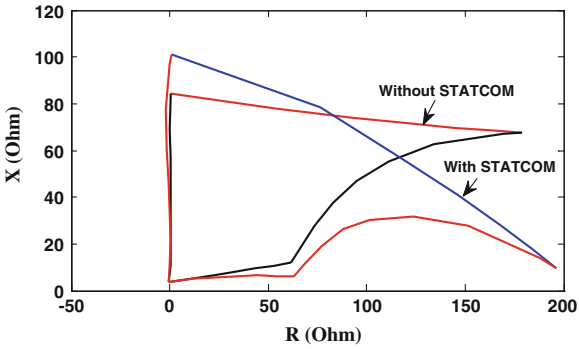

Fig. 21.16 Quadrilateral characteristics of distance relay with and without STATCOM

With STATCOM in a line, the conventional quadrilateral characteristic is to be adaptive to allow the relay to respond during fault in the line.

$$Z_{\text{app}} = \frac{V_{\text{a}}}{I_{\text{a}} + k_0 I_0} \tag{21.5}$$

where

V_a the voltage of phase-a,
I_a the current of phase-a,
K_0 compensation factor,
I_0 zero sequence current.

21.4.3.1 Performance during unbalanced fault

The desired quadrilateral characteristic trip region is drawn using the relation as in (21.5) and it is shown in Fig. 21.17. A line-to-ground fault of AG-type is created at 5 % of the line-1 without and with a fault resistance of 100 ohm without STATCOM and the corresponding impedance trajectories have entered the desired trip region. It is seen that the apparent impedance is within the trip region and the relay takes correct decision during fault. Again AG-fault is created at 75 % of line-1 with fault resistance of 0 and 100 ohm with STATCOM and the impedance trajectories are also within the trip region.

21.4.3.2 Performance with variation in fault location

The performance of the distance relay for variation in fault location has been analyzed. The fault location is varied up to 90 % of the line length. Line-to-ground fault of AG-type is created with a fault resistance of 50 ohm at different fault locations with STATCOM. The corresponding voltage and current samples are stored at a sampling frequency of 1 kHz. The phasors are estimated using one cycle

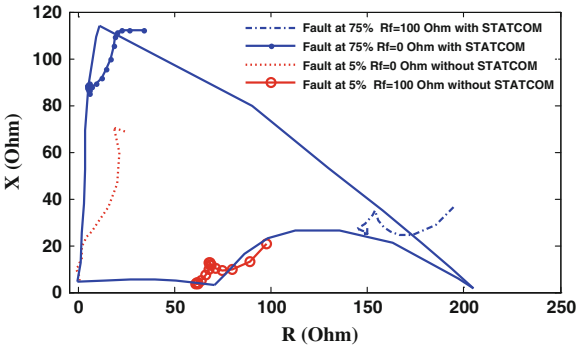

Fig. 21.17 Quadrilateral characteristic of distance relay with and without STATCOM with variation in fault resistance

least square technique. The apparent impedance is calculated using the relation provided in (21.5). The resistance and reactance values for different fault locations are shown in Fig. 21.18. It is observed that the magnitude of reactance increases with increase in fault distance whereas the fault resistance decreases with increase in fault distance from the relay location.

21.4.3.3 Performance with close-in fault and load angle variation

The performance of distance relay is tested for close-in fault case. A line-to-ground fault of BG-type is created at 10 % of the line length. The corresponding seen apparent impedance locus is entered to the desired trip region as shown in Fig. 21.19. The load angle of the system is also varied from 5° to 30° and AG-type fault is created. Using (21.5), the apparent impedance is calculated and the corresponding

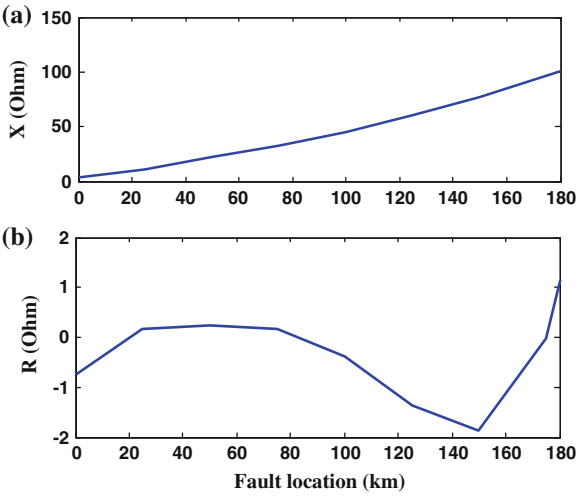

Fig. 21.18 Impedance plots for AG-type fault for different fault locations with STATCOM. **a** Variation of reactance. **b** Variation of resistance

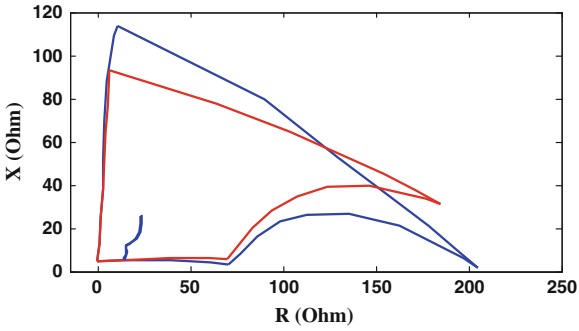

Fig. 21.19 Close-in BG-fault with and without STATCOM with quadrilateral characteristics

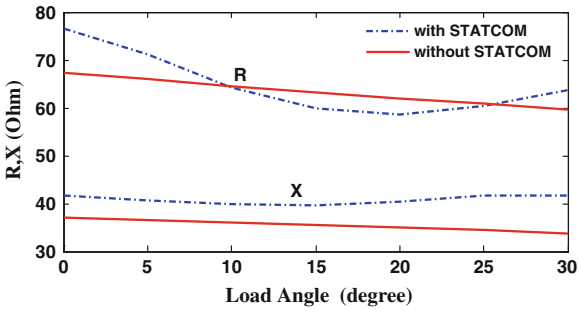

Fig. 21.20 Quadrilateral characteristic of distance relay with and without STATCOM, variation in load angle

resistance and reactance are shown in Fig. 21.20. It is observed that for lower power angle, the seen resistance is more in comparison to with STATCOM case. The value of reactance is more in case of with STATCOM in comparison to the without STATCOM. With higher load angle the distance relay underreaches for with STATCOM in the system.

21.4.3.4 Performance with STATCOM located at the end of line I

Performance of distance relay with Mho characteristic is studied with STATCOM at the end of the line. A line-to-ground fault of AG-type is created at 50 % of the line I. The impedance trajectories seen by the distance relay with and without STATCOM are entered the desired trip region as shown in Fig. 21.21. Again AG-type fault is created at the 50 % line length with fault resistance of 100 Ω and the corresponding impedance trajectory is outside the trip region as shown in Fig. 21.22. During this case the relay underreaches.

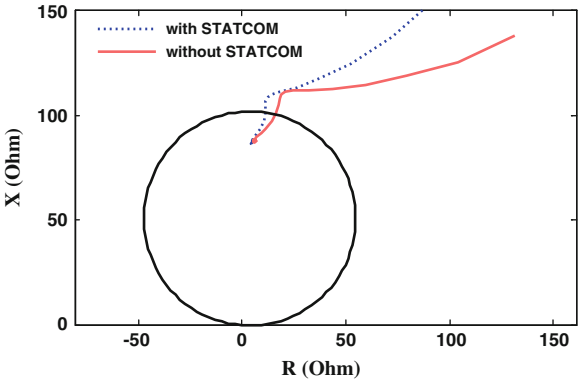

Fig. 21.21 Mho relay characteristic of distance relay without and with STATCOM located at end of line-I (with AG-type fault with fault resistance of 0 Ω at 50 % of line-I)

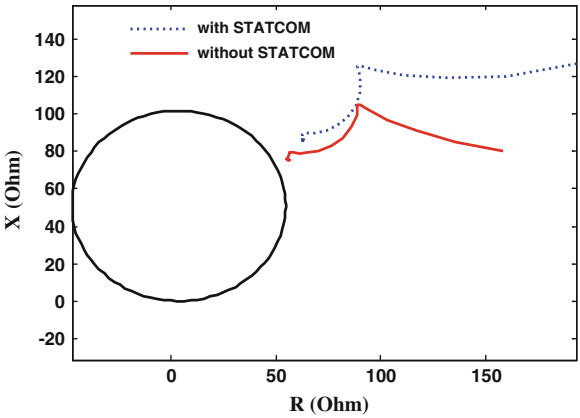

Fig. 21.22 Mho characteristic of distance relay without and with STATCOM located at end of line-I (with AG-type fault of fault resistance of 100 Ω at 50 % of line-I)

21.5 The Adaptive Distance Relaying Scheme

The presence STATCOM changes the apparent resistance and reactance values of distance relay as demonstrated in results. The fault case studies show that both resistance and reactance values varies with STATCOM compared to the case without STATCOM. There are different propositions to mitigate this challenge. New settings of the distance relay have been calculated using active, reactive powers of sending end and reactive power of STATCOM [11]. Apparent resistance and reactance of the distance relay can also be evaluated based on cycle-to-cycle active power and reactive power transfer at relay point [11]. In [4], it is described that the apparent impedance seen by the distance relay used for protecting the line

with STATCOM is dependent on current flowing through STATCOM. With the current through STATCOM known and the value of fault resistance, the apparent impedance can be updated to make the impedance estimation accurate. The zone-2 and zone-3 settings can be updated with certain set rules. The zone 2 maximum setting could be line 1 plus 71 % of line 2 and zone 3 maximum setting could be 124 % of line-2 to protect both the lines [8].

Appendix 1

The least error square algorithm is a powerful tool for estimation of phasors of power system signals. The fault current signal in a series compensated line can be modelled as

$$i_k = I_1 \sin(k\omega_0 T_s + \phi) + I_S \sin[k(\omega_0 - \omega_m)T_s + \phi_s] \; + k_0 e^{\frac{-kT_s}{\tau}} \tag{21.6}$$

where,

I_1 the peak of the fundamental component,
I_S the peak of the subsynchronous frequency component,
ω_0 the fundamental frequency, rad/s
ω_m the subsynchronous frequency, rad/s,
T_s sampling interval, s,
ϕ the phase angle of the fundamental frequency component,
ϕ_s the phase angle of the subsynchronous frequency component,
k_0 the magnitude of the decaying DC component,
τ the time constant of the decaying DC component, s.

The above equation can be written in a linear form as

$$i(k) = a_{11}x_1 + a_{12}x_2 + a_{13}x_3 + a_{14}x_4 + a_{15}x_5 + a_{16}x_6 \tag{21.7}$$

where,

$$a_{11} = \sin(k\omega_0 T_s), a_{12} = \cos(k\omega_0 T_s), a_{13} = \sin(k(\omega_0 - \omega_m)T_s),$$
$$a_{14} = \cos(k(\omega_0 - \omega_m)T_s), a_{15} = 1, a_{16} = -kT_s,$$
$$x_1 = I_1 \cos\phi,\; x_2 = I_1 \sin\phi,\; x_3 = I_S \cos\phi_S,\; x_4 = I_S \sin\phi_S,\; x_5 = k_0,\; x_6 = \frac{k_0}{\tau}$$

The above linear equation can be written as,

$$[A][X] = [B] \tag{21.8}$$

where, $[A] = \begin{bmatrix} \sin(\omega_0 T_s) & \cos(\omega_0 T_s) & \sin((\omega_0-\omega_m)T_s) & \cos((\omega_0-\omega_m)T_s) & 1 & -T_s \\ \sin(\omega_0 2T_s) & \cos(\omega_0 2T_s) & \sin((\omega_0-\omega_m)2T_s) & \cos((\omega_0-\omega_m)2T_s) & 1 & -2T_s \\ \vdots & \vdots & \vdots & \vdots & \vdots & \\ \vdots & \vdots & \vdots & \vdots & \vdots & \\ \sin(\omega_0 NT_s) & \cos(\omega_0 NT_s) & \sin((\omega_0-\omega_m)NT_s) & \cos((\omega_0-\omega_m)NT_s) & 1 & -NT_s \end{bmatrix}$

and $[B] = [i(t_0 + T_s)\ i(t_0 + 2T_s)\ \ldots i(t_0 + NT_s)]'$ and $[B] = [i(t_0 + T_s)\ i(t_0 + 2T_s)\ \ldots\ i(t_0 + NT_s)]'$.

In the above relation, N represents for number of sample points per cycle. The unknown vector becomes, $[X] = [x_1\, x_2\, x_3\, x_4\, x_5\, x_6]'$.

To estimate $[X]$, following equation is used and fundamental component is obtained thereafter.

$$[X] = \left[[A]^T[A]\right]^{-1}[A]^T[B] \tag{21.9}$$

For (A4), ω_m is obtained. The electrical resonance frequency of a series compensated line is described by

$$\omega_e = \omega_0\sqrt{m} \tag{21.10}$$

where ω_0 = the fundamental frequency, rad/s and m = degree of compensation. The perturbation frequency is,

$$\omega_m = \omega_0 - \omega_e \tag{21.11}$$

Appendix 2

System Data

The parameters of each line (Line-I-200 km, Line-II and Line-III-300 km);
Positive sequence impedance = 0.03293 + *j*0.3184 Ω/km,
Positive sequence capacitance = 0.01136 μF/km
Zero sequence impedance = 0.2587 + *j*1.1740 Ω/km,
Zero sequence capacitance = 0.00768 μF/km
The parameters of each source are;
Positive sequence impedance = 0.06979 + *j*1.99878 Ω,
Zero sequence impedance = 0.2094 + *j*5.9963 Ω.

STATCOM Specifications

1. STATCOM Specifications: Thee-phase, two-level 24-pulse GTO-based VSC, 300 MVA rated power, 11 kV rated bus voltage. PWM switching frequency, 500 Hz.
2. Coupling transformer: Two transformers Y-Y (115 kV:11 kV, 50 MVA) and Y-Δ (115 kV:11 kV, 50 MVA).

References

1. Sidhu TS, Varma RK, Gangadharan PK, Albasri FA, Ortiz GR (2005) Performance of distance relays on shunt-FACTS compensated transmission lines. IEEE Trans Power Delivery 20 (3):1837–1845
2. Dash PK, Pradhan AK, Panda G, Liew AC (2000) Adaptive relay setting for flexible ac transmission systems (FACTS). IEEE Trans Power Delivery 15(1):38–43
3. El-Arroudi K, Joos G, McGillis DT (2002) Operation of impedance protection relays with the STATCOM. IEEE Trans Power Delivery 17(2):381–387
4. Khederzadeh M, Ghorbani A (2011) STATCOM modeling impacts on performance evaluation of distance protection of transmission lines. Euro Trans Electr Power 8(20):63–79
5. Sham MV, Chethan KS, Vittal KP (2011) Development of adaptive distance relay for STATCOM connected transmission line. In: Proceedings of IEEE PES innovative smart grid technologies, pp 1–6
6. Jamali S, Kazemi A, Shateri H (2008) Comparing effects of SVC and STATCOM on distance relay tripping characteristic. In Proceedings of IEEE international symposium on industrial electronics, pp 1568–1573
7. Zhang W, Lee S, Choi M (2010) Setting considerations of distance relay for transmission line with STATCOM. J Electr Eng Technol 5(4):522–529
8. Zhang W, Lee S, Choi M, Oda S (2010) Considerations on distance relay setting for transmission line with STATCOM. In: Proceeding of IEEE power and energy society general meeting
9. Hingorani NG, Gyugyi L (1999) Understanding FACTS: concepts & technology of flexible ac transmission systems. Wiley, New York
10. Sidhu TS, Varma RK (2007) Performance comparison of distance protection schemes for shunt-FACTS compensated transmission lines. IEEE Trans Power Delivery 22(4):2116–2125
11. Bapiraju JVVN, Shenoy UJ, Sheshadri KG, Khincha HP, Thukaram D (2004) Implementation of DSP based relaying with particular reference to effect of STATCOM on transmission line protection. In: Proceedings of international conference on power system technology POWERCON, Singapore